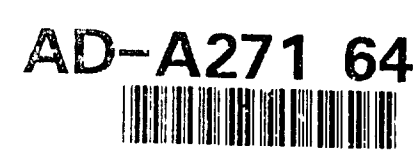
AD-A271 640



2 9

(1)

9th International Conference on High-Power Particle Beams

Beams 92



Washington, DC
May 25–29, 1992

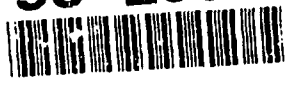
N00014-91-J-1955

S ELECTED OCT 2

This document has been approved for public release and sale; its distribution is unlimited

VOLUME III

93-25563



Microwaves
Free Electron Lasers
Advanced Accelerators
Applications
Plasma Discharges

93 10 21 149

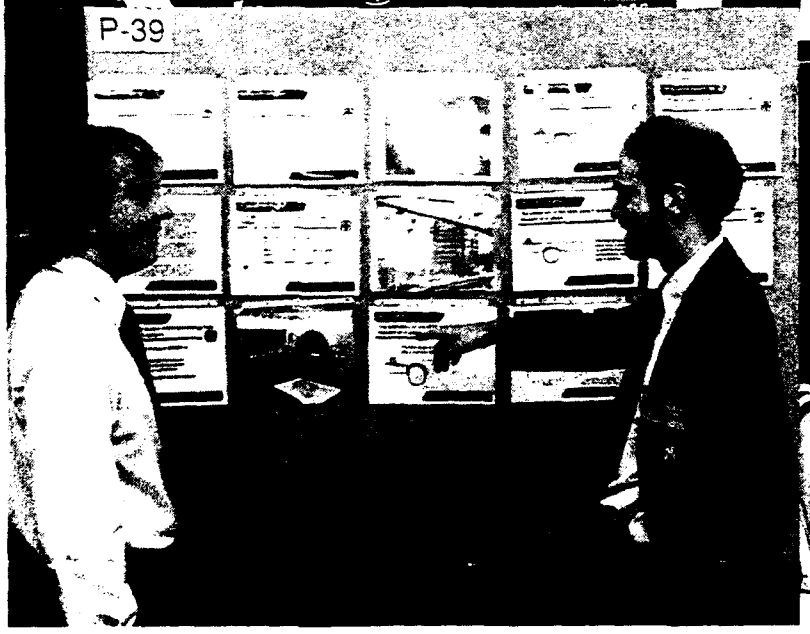
Edited by
David Mosher
and
Gerald Cooperstein










P-39



Beams 92

Proceedings of the
9th International Conference on High-Power Particle Beams

Washington, DC
May 25 - 29, 1992

Edited by

David Mosher and Gerald Cooperstein
Naval Research Laboratory

Volume III

Accesion For
NTIS CRA&I ☑
DTIC TAB ☐
Unannounced ☐
Justification .....
By .....
Distribution/
Availability Codes
Dist | Avail and/or Special
A-1

Beams 92

Proceedings of the
9th International Conference on High-Power Particle Beams

NTIS PB92-206168

Copies of these proceedings can be ordered from the National Technical Information Service (NTIS).

NTIS
PO Box 1425
Springfield, VA 22151
(703) 487-4690

Paper Index - Volume I

Invited Ion Beam Papers

PROGRESS IN LITHIUM BEAM FOCUSING AND BEAM-TARGET INTERACTION EXPERIMENTS AT SANDIA NATIONAL LABORATORIES, T.A. Mehlhorn, L.D. Bacon, J.E. Bailey, D.D. Bloomquist, G.A. Chandler, R.S. Coats, D.L. Cook, M.E. Cuneo, M.S. Derzon, M.P. Desjarlais, R.J. Dukart, A.B. Filuk, T.A. Haill, D.L. Hanson, D.J. Johnson, R.J. Leeper, T.R. Lockner, C.W. Mendel Jr., L.P. Mix, A.R. Moats, J.P. Quintenz, T.D. Pointon, T.J. Renk, G.E. Rochau, S.E. Rosenthal, C.L. Ruiz, D.B. Seidel, S.A. Slutz, R.W. Stinnett, W.A. Stygar, G.C. Tisone, R.E. Olson, J.P VanDevender, D.F. Wenger 31

EXTRACTION GEOMETRY ION DIODE PHYSICS: THEORETICAL MODELING AND EXPERIMENTAL RESULTS, J.B. Greenly, C.K. Struckman, B.R. Kusse, W.A. Noonan 43

FOCUSING PROPERTIES OF A STRONGLY INSULATED APPLIED BR-PROTON DIODE WITH A PREFORMED ANODE PLASMA SOURCE, H. Bluhm, P. Hoppe, M. Althaus, H. Bachmann, W. Bauer, K. Baumung, L. Buth, H.U. Karow, H. Laqua, D. Rusch, E. Stein, O. Stoltz 51

TRANSPORT AND FOCUSING CONSIDERATIONS FOR LIGHT ION ICF SYSTEMS, P.F. Ottinger, D. Mosher, J.M. Neri, D.V. Rose, C.L. Olson 60

HYDRODYNAMIC TARGET EXPERIMENTS WITH PROTON BEAMS AT KALIF: DIAGNOSTICS OF THE ABLATION PRESSURE BY LASER DOPPLER INTERFEROMETRY; GENERATION OF MULTI-MBAR PRESSURES BY ABLATIVE FOIL ACCELERATION AND IMPACT, K. Baumung, H.U. Karow, V. Licht, D. Rusch, J. Singer, O. Stoltz, H. Bachmann, W. Bauer, H. Bluhm, L. Buth, B. Goel, M.F. Goez, H. Guth, P. Hoppe, H. Lotz, C.D. Munz, G.I. Kanel, A.L. Ni, A. Shutov, O.Yu. Vorobjev 68

MULTISTAGE ION ACCELERATOR FOR INERTIAL FUSION ENERGY, K. Imasaki, C. Yamanaka, S. Miyamoto, K. Yasuike, N. Shirai, S. Nakai, T. Aoki, S. Kawata 76

INTENSE ION BEAM RESEARCH AT LOS ALAMOS, D.J. Rej, R.R. Bartsch, H.A. Davis, R.J. Faehl, D.C. Gautier, J.B. Greenly, I. Henins, T.W. Linton, R.E. Muenchausen, W.J. Waganaar 88

Invited Electron Beam, Bremsstrahlung, and Diagnostics Papers

CHARGED PARTICLE BEAM PROPAGATION STUDIES AT THE NAVAL RESEARCH LABORATORY, R.A. Meger, R.F. Hubbard, J.A. Antoniades, R.F. Fernsler, M. Lampe, D.P. Murphy, M.C. Myers, R.E. Pechacek, T.A. Peyser, J. Santos, S.P. Slinker 99

RADLAC II HIGH CURRENT ELECTRON BEAM PROPAGATION EXPERIMENT, C.A. Frost, S.L. Shope, M.G. Mazarakis, J.W. Poukey, J.S. Wagner, B.N. Turman, C.E. Crist, D.R. Welch, K.W. Struve 109

GENERATION, CONTROL, AND TRANSPORT OF A 19-MEV, 700-KA, PULSED ELECTRON BEAM, T.W.L. Sanford, J.A. Halbleib, J.W. Poukey, D.R. Welch, R.C. Mock, P.J. Skogmo, K.A. Mikkelson 119

RECENT RESULTS ON THE GOL-3 DEVICE, A.V. Arzhannikov, A.V. Burdakov, V.V. Chikunov, A.F. Huber, A.V. Karyukin, V.A. Kapitonov, V.S. Koidan, S.V. Lebedev, K.I. Mekler, P.I. Melnikov, A.A. Nikiforov, V.S. Nikolaev, V.V. Postupaev, D.D. Ryutov, E.P. Semenov, S.L. Sinitsky, M.A. Shcheglov, S.G. Voropaev, M.V. Yushkov 127

INNOVATIVE BREMSSTRAHLUNG RESEARCH AT PHYSICS INTERNATIONAL COMPANY, S.L. Wong, J.C. Riordan, J.S. Meachum 136

SPECTROSCOPIC STUDIES OF PULSED-POWER PLASMAS, Y. Maron, R. Arad, G. Dadusc, G. Davara, R.E. Duvall, V. Fisher, M.E. Foord, A. Fruchtman, L. Gregorian, Ya.E. Krasik, C. Litwin, L. Perelmutter, M. Sarfaty, E. Sarid, S. Shkolnikova, R. Shpitalnik, L. Troyansky, A. Weingarten, R.E.H. Clark, A. Fisher, C. Litwin 143

Invited Radiating Z-Pinch Papers

A REVIEW OF Z-PINCH RESEARCH AT PHYSICS INTERNATIONAL, C. Deeney, P.D. LePell, T. Nash, B. Failor, S.L. Wong, R.R. Prasad, M. Krishnan, K.G. Whitney, J.W. Thornhill, F.L. Cochran, M.C. Coulter, J.L. Giuliani, Jr., J.P. Apruzese, F.C. Young, D.D. Hinshelwood, J.D. Sethian 159

RADIATIVE Z-PINCH COUPLING TO AN INDUCTIVE GENERATOR, J.L. Giuliani, Jr., M. Mulbrandon, R. Terry, P.F. Ottinger, R.J. Commisso, C. Deeney, P.D. LePell 167

THE LOS ALAMOS FOIL IMPLOSION PROJECT, J. Brownell, J. Parker, R.R. Bartsch, J. Benage, R. Bowers, J. Cochrane, P. Forman, J. Goforth, A. Greene, H. Kruse, J. Ladish, H. Oona, D. Peterson, R. Reinovsky, N.F. Roderick, J. Trainor, P.J. Turchi 175

Invited Microwave Papers

GYROKLYSTRON RESEARCH FOR APPLICATION TO TEV LINEAR COLLIDERS, W. Lawson, V.L. Granatstein, B. Hogan, U.V. Koc, P.E. Latham, W. Main, H.W. Matthews, G.S. Nusinovich, M. Reiser, C.D. Striffler, S.G. Tantawi 185

NANOSECOND RADAR SYSTEM BASED ON REPETITIVE PULSED RELATIVISTIC BWO, B.V. Bunkin, A.V. Gaponov-Grekhov, A.S. Eltchaninov, F.Ya. Zagulov, S.D. Korovin, G.A. Mesyats, M.L. Osipov, E.A. Otlivantchik, M.I. Petelin, A.M. Prokhorov, V.V. Rostov, A.P. Saraev, I.P. Sisakyan, A.V. Smorgonsky, V.A. Suvorov 195

HIGH POWER MICROWAVE GENERATION AT HIGH REPETITION RATES, N. Aiello, J. Benford, N. Cooksey, B. Harteneck, J. Levine, D. Price, R. Smith, D. Sprehn, M. Willey 203

RELATIVISTIC MULTIWAVE CERENKOV GENERATOR, V.I. Kanavets, A.S. Nifanov, A.I. Slepkov .. 211

HIGH POWER MICROWAVE GENERATION IN VIRCATORS, A.N. Didenko, V.I. Rashchikov 219

THE EXPERIMENTAL AND THEORETICAL DEVELOPMENT OF A ONE GIGAWATT, REPETITIVELY PULSED, ONE MICROSECOND PULSE LENGTH, HIGH CURRENT RELATIVISTIC KLYSTRON AND MODULATOR, M.V. Fazio, B.E. Carlsten, R.J. Faehl, W.B. Haynes, R.F. Hoeberling, T.J.T. Kwan, D.G. Rickel, R.M. Stringfield, F.W. VanHaaften, R.F. Wasierski, A. Erickson, K. Rust .. 227

HIGH PEAK POWER TUBES AND GATE EFFECT KLYSTRONS, N. Gerbelot, J.M. Buzzi, M. Bres, G. Faillon 237

Invited Free Electron Laser Papers

THE ETA II LINEAR INDUCTION ACCELERATOR AND IMP WIGGLER: A HIGH-AVERAGE-POWER MILLIMETER-WAVE FREE-ELECTRON LASER FOR PLASMA HEATING, S.L. Allen, E.T. Scharlemann 247

IREB TRANSPORT IN A FOCUSING WIGGLER AND FEL EXPERIMENTS AT JAERI, S. Kawasaki, T. Kobayashi, K. Sakamoto, Y. Kishimoto, A. Watanabe, S. Musyoki, H. Oda, S. Tokuda, Y. Nakamura, T. Nagashima, M. Shiho 255

SELF-CONSISTENT NONLINEAR SIMULATIONS OF HIGH-POWER FREE-ELECTRON LASERS, H.P. Freund, R.H. Jackson 263

Invited Advanced Accelerator Papers

LINEAR ACCELERATOR WITH RADIAL LINES - LIA-30, A.I. Pavlovskii, V.S. Bossamykin, A.I. Gerasimov, V.A. Tananakin, A.S. Fedotkin, K.A. Morunov, V.F. Basmanov, G.M. Skripka, A.D. Tarasov, A.V. Grishin, V.P. Gritzina, V.Ya. Averchenkov, O.N. Syutin, S.A. Lazarev, V.S. Gorkunov, V.P. Veresov 273

TECHNOLOGY DEMONSTRATION FOR THE DARHT LINEAR INDUCTION ACCELERATORS, M. Burns, P. Allison, J. Downing, D.C. Moir, G. Caporaso, Y.J. Chen 283

SLIA THEORY REVIEW, J.J. Petillo, A.A. Mondelli, C. Kostas, K.T. Tsang, D.P. Chernin 291

STUDY OF RECIRCULATING INDUCTION ACCELERATOR AS DRIVERS FOR HEAVY ION FUSION, H.D. Shay, J.J. Barnard, A.L. Brooks, F. Coffield, F. Deadrick, L.V. Griffith, H.C. Kirbie, V.K. Neil, M.A. Newton, A.C. Paul, L.L. Reginato, W.M. Sharp, J. Wilson, S.S. Yu, D.L. Judd 297

LOW EMITTANCE ACCELERATOR CAVITY DESIGN TO MINIMIZE AMPLIFICATION OF BEAM BREAKUP MODES, M.L. Sloan, J.R. Thompson, C.S. Kueny 305

OPTICAL GUIDING AND ELECTRON ACCELERATION IN THE LASER WAKEFIELD ACCELERATOR, P. Sprangle, E. Esarey, J. Krall, G. Joyce, A. Ting 313

Invited Beam and Pulsed Power Applications Papers

CURRENT STATUS OF PULSE-POWER TECHNOLOGY AND APPLICATIONS AT LBT, NAGAOKA, K. Yatsui, W. Masuda, K. Masugata, W. Jiang, Y. Sekimoto, G. Imada, T. Sonegawa, X.D. Kang 323

INITIAL RESULTS FROM THE RHEPP MODULE, H.C. Harjes, K.J. Penn, K.W. Reed, C.R. McClenahan, G.E. Laderach, R.W. Wavrik, J.L. Adcock, M.E. Butler, G.A. Mann, G.E. Pena, G.J. Weber, D. VanDeValde, L.E. Martinez, D. Muirhead, P.D. Kiekel, D.L. Johnson, E.L. Neau 333

APPLICATIONS OF HIGH POWER MICROWAVES, J. Benford, J. Swegle 341

X-PINCH SOFT X-RAY SOURCE FOR MICROLITHOGRAPHY, S.C. Glidden, D.A. Hammer, D.H. Kalantar, N. Qi 349

MAGNETIC FUSION WITH HIGH ENERGY SELF-COLLIDING ION BEAMS, N. Rostoker, F.J. Wessel, B. Maglich, A. Fisher 357

PRACTICAL APPLICATIONS OF HIGH-POWER ION BEAMS, G.E. Remnev, V.A. Shulov 365

Invited Pulsed Power Papers

MICROSECOND-CONDUCTION-TIME POS EXPERIMENTS, B.V. Weber, J.R. Boller, R.J. Commisso, P.J. Goodrich, J.M. Grossmann, D.D. Hinshelwood, J.C. Kellogg, P.F. Ottinger, G. Cooperstein 375

INDUCTIVE ENERGY STORE (IES) TECHNOLOGY FOR MULTI-TERRAWATT GENERATORS, P.S. Sincerny, S.R. Ashby, F.K. Childers, C. Deeney, D. Kortbawi, J.R. Goyer, J.C. Riordan, I.S. Roth, C. Stallings, L. Schlitt 385

HIGH CURRENT PULSED POWER GENERATOR GIT-16. STATE OF PROJECT. EXPERIMENTAL RESULTS, S.P. Bugaev, A.M. Volkov, A.A. Kim, V.N. Kiselev, B.M. Kovalchuk, N.F. Kovsharov, V.A. Kokshenev, G.A. Mesyats, A.P. Huseev 394

PULSED POWER INDUCTIVE ENERGY STORAGE IN THE MICROSECOND RANGE, W. Rix, A.R. Miller, J. Thompson, E. Waisman, M. Wilkinson, A. Wilson 402

A LONG CONDUCTION TIME COMPACT TORUS PLASMA FLOW SWITCH, R.E. Peterkin,Jr., D.E. Bell, J.H. Degnan, M.R. Douglas, T.W. Hussey, B.W. Mullins, N.F. Roderick, P.J. Turchi 408

Contributed Pulsed Power Papers

ACCELERATORS WITH VACUUM INSULATED MARX GENERATORS, E.N. Abdullin, S.P. Bugaev, A.M. Efremov, V.B. Zorin, B.M. Kovalchuk, S.V. Loginov, G.A. Mesyats, V.S. Tolkachev, P.M. Schanin, A.A. Chistov 419

ELECTRON BEAM GENERATORS AT ANGARA-5 FACILITY, V.V. Bulan, E.V. Grabovsky, A.N. Gribov, O.G. Egorov, V.V. Zajivikhin, E.P. Kojokhin, K.V. Kurbatov, I.N. Kukharenko, V.G. Lujnov, V.E. Pichugin, O.A. Smolenkova **425**

PROGRESS IN TECHNOLOGY OF THE MICROSECOND E-BEAM GENERATORS WITH ENERGY CONTENT IN THE RANGE 100 - 500 KJ, A.V. Arzhannikov,V.T. Astrelin, V.B. Bobylev, V.S. Koidan, V.S. Nikolaev, M.A. Shcheglov, S.L. Sinitsky, A.V. Smirnov, R.P. Zotkin **431**

HIGH-CURRENT ACCELERATOR "SIRIUS" WITH ELECTRON BEAM CURRENT OF 2 KA, ELECTRON ENERGY OF MEV-RANGE AND PULSE DURATION OF 50 MCSEC, V.I. Engelko, N.G. Beruchev, V.V. Ershov, O.L. Komarov, V.G. Kovalev, O.P. Pechersky, A.A. Petukhov, Yu.M. Saveljev, L.V. Smirnov, K.I. Tkachenko **436**

INDUCTIVE PULSED POWER SOURCE FOR PLASMA RADIATOR, B.D. Yankovskiy **443**

SUPER-POWER ACCELERATOR FOR MICROWAVE ELECTRONICS, G.I. Batskikh, L.N. Kazansky, A.A. Oreshin, P.A. Samarsky, V.D. Seleznev, A.V. Sinelshikov, A.I. Khomenko, S.P. Bugaev, B.M. Kovalchuk, V.I. Koshelev, G.A. Mesyats, M.I. Petelin **449**

IGUR-3 - POWERFUL BREMSSTRAHLUNG RADIATION PULSE GENERATOR, V.S. Diyankov, A.I. Kormilitsin, V.P. Kovalev **455**

HEAVEN-LIGHT II INTENSE PULSED ELECTRON BEAM ACCELERATOR, N. Zeng, R. Zhao, D. Yang, X. Jiang, X. Wang **462**

THE EXPERIMENTAL RESEARCH OF A FIELD-ENHANCED MULTICHANNEL OIL SWITCH, R. Zhao, N. Zeng, D. Yang, X. Jiang, X. Wang **468**

THE MAGPIE PROJECT: CURRENT STATUS, I.H. Mitchell, P. Choi, J.P. Chittenden, J.F. Worley, J.M. Bayley, A.E. Dangor, M.G. Haines **474**

OPTIMISATION OF THE POWER COUPLING IN THE MAGPIE 4-WAY JUNCTION USING A 1/6TH SCALE MODEL, I.H. Mitchell, P. Choi, J.P. Chittenden, J.F. Worley **480**

NEW HALF VOLTAGE AND DOUBLE PULSE OPERATION OF THE HERMES III LINEAR INDUCTION ACCELERATOR, K.A. Mikkelson, R.L. Westfall, S.M. Neely, V.J. Harper-Slaboszewicz.. **486**

APPLICATION OF MAGNETICALLY INSULATED TRANSMISSION LINES FOR HIGH CURRENT, HIGH VOLTAGE ELECTRON BEAM ACCELERATORS, S.L. Shope, M.G. Mazarakis, C.A. Frost, J.W. Poukey, B.N. Turman **492**

MODELLING PULSED-POWER TRANSMISSION LINES, C.W. Mendel, Jr., D.B. Seidel, W.A. Johnson, S.E. Rosenthal **499**

PULSED POWER ELECTRON ACCELERATORS WITH THE FORMING SYSTEMS BASED ON STEPPED TRANSMISSION LINES, V.S. Bossamykin, V.S. Gordeev, A.I. Pavlovskii, A.P. Klement'ev, O.N. Syutin, A.V. Budakov, V.F. Basmanov, A.P. Gridasov, V.O. Filippov, G.A. Myskov **505**

NEW SCHEMES FOR HIGH-VOLTAGE PULSED GENERATORS BASED ON STEPPED TRANSMISSION LINES, V.S. Bossamykin, V.S. Gordeev, A.I. Pavlovskii **511**

DEVELOPMENT OF MICROSECOND GENERATORS WITH PLASMA CURRENT INTERRUPTING SWITCH IN I. V. KURCHATOV INSTITUTE OF ATOMIC ENERGY: FREQUENCY OPERATION OF GENERATORS, V.M. Babykin, R.V. Chikir, G.I. Dolgachev, Yu.P. Golovanov, Yu.I. Kovalev, A.G. Ushakov, L.P. Zakatov 517

EXPERIMENTAL RESEARCH OF MICROSECOND PLASMA INTERRUPTING SWITCH (PCIS): CANAL CONCEPT OF PCIS OPERATION, G.I. Dolgachev, L.P. Zakatov, A.G. Ushakov 523

EXPERIMENTAL STUDIES OF A MICROSECOND PLASMA OPENING SWITCH IN THE POSITIVE POLARITY REGIME, V.M. Bystritskii, I.V. Lisitsyn, Ya.E. Krasik 529

NUMERICAL SIMULATIONS OF PLASMA DYNAMICS IN A MICROSECOND PLASMA OPENING SWITCH, V.M. Bystritskii, I.V. Lisitsyn, A.A. Sinebryukhov 535

A PLASMA OPENING SWITCH WITH A RETAINED PLASMA, V.L. Gumennyj, Yu.A. Zhdanov, I.N. Naugol'nyj, A.V. Pashchenko, Yu.V. Tkach 541

ANTHEM SIMULATIONAL STUDIES OF THE PLASMA OPENING SWITCH, R.J. Mason 547

TWO-DIMENSIONAL STUDIES OF CURRENT CONDUCTION IN PLASMA OPENING SWITCHES, D. Parks, E. Waisman, R. Ingermanson, E. Salberta 553

ELECTRON AND ION MAGNETOHYDRODYNAMIC EFFECTS IN PLASMA OPENING SWITCHES, J.M. Grossmann, C.R. DeVore, P.F. Ottinger 559

A SELF-CONSISTENT THEORY OF PLASMA FILLED DIODES AND PLASMA OPEN SWITCHES, L.I. Rudakov 565

OPENING SWITCH MODEL WITH VORTEX STRUCTURES, N.B. Volkov, T.A. Golub, N.A. Gondarenko, A.M. Iskoldsky 575

COMPACT GENERATOR WITH PLASMA FLOW OPENING SWITCH, B.A. Kablambajev, V.A. Poskonin, N.A. Ratakhin 581

THE INFLUENCE OF THE B-THETA FIELD ON MPOS PERFORMANCE, A.A. Kim, D.V. Getman 586

POS USE EFFICIENCY IN MULTIMODULE ACCELERATOR WITH SELF-MAGNETIC INSULATION, V.V. Zajivikhin 592

EXPERIMENTS ON MICROSECOND CONDUCTION TIME PLASMA OPENING SWITCH MECHANICS, W. Rix, M. Coleman, A.R. Miller, D. Parks, K. Robertson, J. Thompson, E. Waisman, A. Wilson 598

DENSITY MEASUREMENTS OF MICROSECOND-CONDUCTION-TIME POS PLASMAS, D.D. Hinshelwood, B.V. Weber, R.J. Commisso, P.J. Goodrich, J.M. Grossmann, J.C. Kellogg 603

MICROSECOND PLASMA OPENING SWITCH EXPERIMENTS ON HAWK WITH AN E-BEAM DIODE LOAD, P.J. Goodrich, R.C. Fisher, D.D. Hinshelwood, J.R. Boller, R.J. Commisso, B.V. Weber 609

PLASMA OPENING SWITCH FOR LONG-PULSE INTENSE ION BEAM, H.A. Davis, R.J. Mason, R.R. Bartsch, J.B. Greenly, D.J. Rej 615

LONG CONDUCTION TIME PLASMA OPENING SWITCH EXPERIMENTS AT SANDIA NATIONAL LABORATORIES, M.E. Savage, W.W. Simpson, G.W. Cooper, M.A. Usher **621**

PLASMA EROSION OPENING SWITCH USING LASER-PRODUCED PLASMA, H. Akiyama, T. Fukuzawa, S. Ihara, S. Katsuki, S. Maeda **627**

SPECTROSCOPIC INVESTIGATIONS OF A PLASMA OPENING SWITCH USING A NOVEL GASEOUS PLASMA SOURCE, M. Sarfaty, Ya.E. Krasik, R. Arad, A. Weingarten, S. Shkolnikova, Y. Maron, A. Fisher **633**

THE AURORA ACCELERATOR'S TRIGGERED OIL SWITCH, D.M. Weidenheimer, N.R. Pereira, D.C. Judy, K.L. Stricklett **640**

HIGH-PRESSURE GAS SWITCH FOR A WIDEBAND SOURCE, P.A. Pincosy, P. Poulsen, W.R. Cravey **646**

PREDICTION OF ELECTROMAGNETIC PULSE GENERATION BY PICOSECOND AVALANCHES IN HIGH-PRESSURE AIR, D.J. Mayhall, J.H. Yee **652**

HYDROGEN SPARK SWITCHES FOR REP-RATED ACCELERATORS, S.L. Moran, M.G. Grothaus, L.W. Hardesty **659**

SIMPLE METHODS OF SQUARE PULSE GENERATION BY INDUCTIVE PULSE FORMING LINES AND A FIELD EFFECT TRANSISTOR AS AN OPENING SWITCH, M.J. Rhee, B.N. Ding **665**

HIGH REPETITION RATE MEGAVOLT MARX GENERATORS, Yu.A. Kotov, S.N. Rukin **670**

150 KEV INTENSE ELECTRON BEAM ACCELERATOR SYSTEM WITH HIGH REPEATED PULSE, Q. Zhang, T. Li, H. Tang, N. Xia, Z. Wang, B. Zheng **676**

QUICK CHARGING BLUMLEIN PFL, K. Masugata, S. Tsuchida, H. Saitou, K. Shibata, M. Shigeta, Y. Sekimoto, K. Yatsui **682**

THE DEVELOPMENT OF A ONE MICROSECOND PULSE LENGTH, REPETITIVELY PULSED, HIGH POWER MODULATOR AND A LONG-PULSE ELECTRON BEAM DIODE FOR THE PRODUCTION OF INTENSE MICROWAVES, R.M. Stringfield, R.J. Faehl, M.V. Fazio, R.F. Hoeberling, T.J.T. Kwan, D.G. Rickel, F.W. VanHaaften, R.F. Wasierski, A. Erickson, K. Rust **688**

Paper Index - Volume II

Contributed Ion Beam Papers

NEW RESULTS FROM EXPERIMENTAL AND NUMERICAL INVESTIGATIONS OF THE SELF-MAGNETICALLY B-THETA-INSULATED ION DIODE, W. Bauer, H. Bachmann, H. Bluhm, L. Buth, P. Hoppe, H.U. Karow, H. Lotz, D. Rusch, Ch. Schultheiss, E. Stein, O. Stoltz, Th. Westermann **735**

GENERATION OF STRONG RADIAL MAGNETIC INSULATION FIELDS IN HIGH POWER ION DIODES IN EXTRACTION GEOMETRIES, P. Hoppe, H. Bluhm, H. Laqua, O. Stoltz **741**

ION BEAM GENERATION WITH INHOMOGENEOUS ANODE AND CATHODE PLASMAS, V. Fedorov, W. Schmidt, Th. Westermann **747**

ION DIODE SIMULATION FOR PULSED POWER GENERATORS WITH STATIONARY CODES, M. Alef, V.T. Astrelin, L. Feher, St. Illy, M. Kuntz, W. Schmidt, R. Schuldt, D. Seldner, E. Stein, Th. Westermann **756**

SIMULATION OF A BR ION DIODE, R.J. Faehl, D.J. Rej **762**

ION BEAM DIVERGENCE FROM UNSTABLE FLUCTUATIONS IN APPLIED-B DIODES, R.N. Sudan, D.W. Longcope **769**

QUICKSILVER SIMULATIONS OF APPLIED-B EXTRACTION DIODES, M.P. Desjarlais, T.D. Pointon **775**

OPERATION OF A HIGH IMPEDANCE APPLIED-B EXTRACTION ION DIODE ON THE SABRE POSITIVE POLARITY LINEAR INDUCTION ACCELERATOR, D.L. Hanson, M.E. Cuneo, P.F. McKay, J.E. Maenchen, R.S. Coats, J.W. Poukey, S.E. Rosenthal, W.E. Fowler, D.F. Wenger, M. Bernard, J.R. Chavez, W.F. Stearns **781**

LIF ION SOURCE PERFORMANCE ON PFBA II, R.W. Stinnett, T.A. Green, D.J. Johnson, T.R. Lockner, T.A. Mehlhorn, J.E. Bailey, A.B. Filuk, L.P. Mix, J. Panitz, P. Schwoebel **788**

SPECTROSCOPIC CHARACTERIZATION OF LEVIS ACTIVE ION SOURCE ON PBFA II, A.B. Filuk, J.E. Bailey, K.W. Bieg, A.L. Carlson, T.J. Renk, G.C. Tisone, Y. Maron **794**

LASER FORMATION OF LITHIUM PLASMA ION SOURCES FOR APPLIED-B ION DIODES ON THE PBFA-II ACCELERATOR, G.C. Tisone, T.J. Renk, D.J. Johnson, R.A. Gerber, R.G. Adams **800**

FORMATION PROCESS OF NEGATIVE IONS IN A MAGNETICALLY INSULATED DIODE, K. Horioka, Q. Yu, K. Kasuya **806**

MAGNETICALLY INSULATED H- DIODES, A. Fisher, V.M. Bystritskii, E. Garate, R. Prohaska, N. Rostoker **812**

ANODE DISCHARGE TO FACILITATE CATHODE PLASMA FORMATION FOR GENERATION OF H-, C-, F-, I-, AND PB- IONS, A.G. Mozgovoy, V.A. Papadichev **818**

H- GENERATION USING AN EXTERNALLY APPLIED PREPULSE, A.G. Mozgovoy, V.A. Papadichev **824**

LASER PLASMA PRODUCTION AND LASER DIAGNOSTICS FOR PULSED ION SOURCES, K. Kasuya, K. Horioka, T. Hushiki, N. Matsuura, T. Miyoshi, K. Nakata, Y. Miyai, Y. Kawakita, E. Ohshita **829**

IMPROVED FLASH-BOARD FOR PLASMA INJECTION DIODE, K. Kasuya, K. Horioka, H. Hayase . **835**

PRODUCTION OF PULSED F- BEAMS, A. Kitamura, K. Takahashi, A. Shinmura, Y. Furuyama, T. Nakajima **841**

CHARACTERISTICS OF HIGH POWER ION DIODE WITH REAL CATHODE, H. Sugimura, E. Chishiro, T. Tachibana, K. Masugata, K. Yatsui **847**

CHARACTERISTICS OF ION BEAM AND ANODE PLASMA IN "POINT PINCH DIODE", K. Masugata, T. Tazima, K. Yatsui **853**

POINT FOCUSING OF INTENSE ION BEAM BY SPHERICAL "PLASMA FOCUS DIODE", W. Jiang, T. Sakagami, K. Masugata, K. Yatsui **859**

CHARACTERISTICS OF THE INTENSE ION BEAMS GENERATED WITH THE POINT PINCH DIODE, M.Sato, T. Tazima **865**

EXPERIMENTAL STUDY OF THE PINCH-BEAM DIODE WITH THIN, UNBACKED FOIL ANODES, S.J. Stephanakis, J.R. Boller, G. Cooperstein, B.V. Weber, F.C. Young **871**

EXPERIMENTS ON GENERATION OF HIGH POWER ION BEAM IN PLASMA-FILLED DIODE, V.M. Bystritskii, A.V. Kharlov, G.A. Mesyats, A.V. Mytnikov, A.A. Sinebryukhov **878**

LIGHT ION DRIVER RESEARCH FOR INERTIAL FUSION, S. Miyamoto, K. Yasuike, S. Nakai, K. Imasaki, C. Yamanaka **884**

FAST MAGNETIC FIELD PENETRATION INTO AN INTENSE NEUTRALIZED ION BEAM, R. Armale, N. Rostoker **890**

DIVERGENCE IN INTENSE ION BEAMS CAUSED BY INCOMPLETE CHARGE NEUTRALIZATION, C.L. Olson, J.W. Poukey **897**

SPECTROSCOPIC STUDIES OF INTENSE ION BEAM PROPAGATION IN THE PBFA-II GAS CELL, J.E. Bailey, A.L. Carlson, D.J. Johnson, E.J. McGuire, T. Nash, C.L. Olson, J.J. MacFarlane, P. Wang **903**

BALLISTIC FOCUS LIGHT ION BEAMS FOR AN INERTIAL CONFINEMENT FUSION REACTOR, R.R. Peterson **909**

ION BEAM TRANSPORT AND FOCUSING EXPERIMENTS, J.C. Olson, B.R. Kusse **915**

FOCUSING OF INTENSE ION BEAMS WITH A PLASMA-FILLED SOLENOIDAL MAGNETIC LENS INCLUDING SELF-FIELDS, B.V. Oliver, R.N. Sudan **921**

ION BEAM MODELING USING ARGUS, J.J. Petillo, A.A. Mondelli, A. Mankofsky, C.L. Chang **927**

ESQ FOCUSING FOR AN INTENSE, HIGH-BRIGHTNESS H- BEAM: EMITTANCE GROWTH AND ITS REMEDY, S.K. Guharay, C.K. Allen, M. Reiser **933**

ORION PROJECT: ACCELERATION OF CLUSTER IONS AND HIGHLY CHARGED BIOMOLECULES FROM 10 MEV TO 1GEV, S. Della-Negra, Y. Le Beyec, A. Brunelle, D. Gardes, B. Waast, E. Parilis, P. Hakansson, B.U.R. Sundquist **939**

ION BEAM TRANSPORT IN A PREIONIZED PLASMA CHANNEL, S.P. Slinker, R.F. Hubbard, M. Lampe, G. Joyce, I. Haber **945**

STEERING ALGORITHMS FOR A HEAVY-ION RECIRCULATING ACCELERATOR, W.M. Sharp, J.J. Barnard, S.S. Yu **951**

GENERATION OF ULTRA HIGH PRESSURE WITH LIGHT ION BEAMS, B. Goel, O.Yu. Vorobjev, A.L. Ni **957**

TARGET EXPERIMENTS WITH LIGHT-ION BEAMS AT KALIF: MEASUREMENTS OF THE DYNAMIC STRENGTH AND SPALLATION THRESHOLD OF METALS AT HIGH STRAIN RATES, H. Bachmann, K. Baumung, G.I. Kanel, H.U. Karow, V. Licht, D. Rusch, J. Singer, O. Stoltz **963**

GENERATION OF EXTREME STATES IN CONDENSED MATTER BY HIGH-POWER ION BEAMS, V.E. Fortov, V.A. Skvortsov, V.V. Kostin, O.Yu. Vorobjev, I.V. Lomonosov, A.L. Ni, I. Hofmann, B. Goel **969**

PULSED-ION-BEAM DRIVEN ABLATION OF MATERIAL NEAR ITS SUBLIMATION ENERGY, A. Kitamura, T. Asahina, Y. Furuyama, T. Nakajima **976**

CHARGE FLUCTUATIONS, ENERGY STRAGGLING, AND MULTIPLE SCATTERING IN INTENSE ION BEAM-TARGET INTERACTIONS, Z. Zinamon, E. Nardi **982**

PARTICLE DRIVEN INERTIAL FUSION THROUGH CLUSTER ION BEAM, C. Deutsch, N.A. Tahir .. **988**

AN ANALYSIS OF CLUSTER-DRIVEN INERTIAL CONFINEMENT FUSION, M. Piera, S. Eliezer, J.M. Martinez-Val **995**

SMALL-SCALE TARGETS FOR HEAVY-ION DRIVEN INERTIAL CONFINEMENT FUSION EXPERIMENTS, J.M. Martinez-Val, G. Velarde, P. Velarde, M. Piera, M. Perlado, E. Minguez, J.J. Honrubia, J.M. Aragones **1001**

Contributed Electron Beam Papers

THEORETICAL EVALUATION OF THE ANGULAR SPREAD OF THE ELECTRON BEAM GENERATED IN A GUIDING MAGNETIC FIELD, D.D. Ryutov **1009**

NEW RESULTS ON MICROSECOND E-BEAM GENERATION FOR PLASMA HEATING EXPERIMENTS, Yu.I. Deulin, V.V. Filippov, A.V. Karyukin, S.V. Lebedev, M.A. Shcheglov, S.G. Voropaev **1015**

BREMSSTRAHLUNG PRODUCTION BY MICROSECOND E-BEAM FROM THIN FOIL IN A MIRROR TRAP, V.V. Filippov, V.S. Koidan, S.V. Lebedev, P.I. Melnikov, M.A. Shcheglov, S.G. Voropaev **1021**

FOILLESS INJECTION OF REB INTO A DENSE PLASMA, I.V. Kandaurov, Eh.P. Kruglyakov, O.I. Meshkov **1027**

FREQUENCY REGIME OF HIGH CURRENT RELATIVISTIC ELECTRON BEAMS INTERACTING WITH VARIOUS GASEOUS MEDIA, N.A. Kondratiev, V.I. Smetanin, Yu.P. Usov, V.E. Kulbeda..... **1033**

SPECTRA OF LANGMUIR TURBULENCE EXCITED BY HIGH-CURRENT REB, I.V. Kandaurov, Eh.P. Kruglyakov, M.V. Losev, O.I. Meshkov, A.L. Sanin, L.N. Vyacheslavov **1037**

ELECTRIC FIELD STRENGTH MEASUREMENTS IN A MEGAVOLT VACUUM DIODE USING LASER INDUCED FLUORESCENCE OF AN ATOMIC BEAM, B.A. Knyazev, V.V. Chikunov, P.I. Melnikov **1043**

TWO-STAGE DENSE PLASMA HEATING BY 100 KJ E-BEAM, A.V. Burdakov, V.V. Chikunov, A.F. Huber, A.V. Karyukin, V.S. Koidan, S.V. Lebedev, K.I. Mekler, P.I. Melnikov, A.A. Nikiforov, V.V. Postupaev, M.A. Shcheglov, S.G. Voropaev **1049**

SOFT X-RAY MEASUREMENTS OF MICROSECOND-E-BEAM-HEATED PLASMA, A.V. Burdakov, V.V. Postupaev, V. Piffl **1055**

ULTRAVIOLET FLASH LAMP ON THE NOBLE GAS DIMERS EXCITED BY AN E-BEAM, V.I. Klimov, G.P. Mkheidze, A.A. Savin **1061**

CONDUCTIVITY OF PLASMA CREATED BY REB IN ARGON, V.I. Klimov, G.P. Mkheidze, A.A. Savin **1067**

MICROWAVE GENERATION AND CHARGED PARTICLE ACCELERATION BY HIGH CURRENT RELATIVISTIC ELECTRON BEAMS, Yu.V. Tkach, I.F. Kharchenko, V.A. Balakirev, V.V. Dolgopolov, Yu.V. Kirichenko, S.M. Latinsky, E.M. Lats'ko, E.A. Lisenko, V.E. Novikov, A.O. Ostrovsky, A.V. Pashchenko, E.A. Prasol, S.S. Romanov **1073**

ELECTRON BEAM DIODES USING FERROELECTRIC CATHODES, J.D. Ivers, L. Schachter, J.A. Nation, G.S. Kerslick **1081**

THE NSWC MICROCHANNEL ELECTRON SOURCE PROGRAM, K.A. Boulais, J.Y. Choe, S.T. Chun, A. Krall, K. Irwin, S.E. Saddow, M.J. Rhee **1087**

LONG PULSE, PLASMA CATHODE E-GUN, D.M. Goebel, R.W. Schumacher, R.M. Watkins..... **1093**

CONTROLLING THE EMISSION CURRENT FROM A PLASMA CATHODE, S.P. Bugaev, V.I. Gushenets, P.M. Schanin **1099**

FORMATION OF INTENSE CONVERGENT PARTICLE BEAMS IN A GAS-DISCHARGE-PLASMA-EMITTER DIODE, N.V. Gavrilov, Yu.E. Kreindel, G.A. Mesyats, O.A. Shubin **1105**

FORMATION AND TRANSPORTATION OF A MICROSECOND HIGH CURRENT ELECTRON BEAM IN A PLASMA-ANODE GUN, M.Yu. Kreindel, E.A. Litvinov, G.E. Ozur, D.I. Proskurovsky **1111**

RIBBON REB RESEARCH ON 0.7 MJ GENERATOR U-2, A.V. Arzhannikov, V.B. Bobylev, V.S. Nikolaev, S.L. Sinitsky, M.V. Yushkov, R.P. Zotkin **1117**

HIGH BRIGHTNESS HOLLOW CATHODE ELECTRON BEAM SOURCE, G. Kirkman, N. Reinhardt, B. Jiang, M.A. Gundersen, T.Y. Hsu, R.L. Liou, R.J. Temkin **1123**

HIGH-CURRENT-DENSITY CATHODE OPERATION AND BEAM TRANSPORT WITH STEADY-STATE AND PULSED CATHODE HEATING METHODS, W.D. Getty, K.D. Pearce, M.E. Hemiter **1129**

HIGH GRADIENT ACCELERATION IN A 17 GHZ PHOTOCATHODE RF GUN, S.C. Chen, B.G. Danly, J. Gonichon, C.L. Lin, R.J. Temkin, S. Trotz, J.S. Wurtele **1135**

BEAM GENERATION WITH THE 4-MV RLA INJECTOR AND ACCELERATION THROUGH THE ET-2 POST-ACCELERATING CAVITY, M.G. Mazarakis, D.L. Smith, J.W. Poukey, P.J. Skogmo, L.F. Bennett, M. George, W.R. Olson, M.J. Harden, B.N. Turman, S.A. Moya, J.L. Henderson, K.W. Struve **1141**

DESIGN AND EVALUATION OF THE XBT DIODE, E.L. Wright, A. Vlieks, K. Fant, C. Pearson, R. Koontz, D. Jensen, G. Miram **1147**

THE PHYSICS OF "VACUUM" BREAKDOWN, F. Schwirzke, M.P. Hallal, Jr., X.K. Maruyama **1153**

SIMULATIONS OF A PLASMA-FILLED PINCHED ELECTRON BEAM DIODE, S.B. Swanekamp, J.M. Grossmann, P.F. Ottinger, S.J. Stephanakis, B.V. Weber, J.C. Kellogg, G. Cooperstein **1159**

ONE-DIMENSIONAL NUMERICAL SIMULATION OF PLASMA FILLED PLANAR DIODE, I.V. Glazyring, V.S. Diyankov, A.A. Kondratyev, A.I. Kormilitsin, A.P. Yalovets **1165**

NONLINEAR DYNAMICS IN A REFLEX DIODE, M.S. Litz, J. Golden **1170**

POST ACCELERATION OF A PSEUDOSPARK-PRODUCED HIGH-BRIGHTNESS ELECTRON BEAM, B.N. Ding, M.J. Rhee **1176**

TIME-RESOLVED BEAM ENERGY MEASUREMENT OF SHORT ELECTRON BEAM BUNCHES WITH A LONGITUDINAL VELOCITY TILT, D.X. Wang, J.G. Wang, M. Reiser **1182**

THE EFFECTS OF BEAM PARAMETERS ON BREMSSTRAHLUNG EXPOSURE ANGULAR DISTRIBUTION, S. Jiangjun, M. Qian **1188**

BREMSSTRAHLUNG RADIATION ON THE SNOP FACILITIES, A.V. Luchinsky, V.K. Petin, N.A. Ratakhin, N.A. Smirnov, V.F. Fedushchak **1194**

THEORY OF THE BREMSSTRAHLUNG CONVERTER FOR RAISING ENERGY EXTRACTION IN THE RANGE 10-100 KEV, V.V. Ryzhov, A.A. Sapozhnikov **1199**

HIGH-INTENSITY FLASH X-RAY PRODUCTION BY REB, V.F. Zinchenko, V.V. Timofeyev, V.D. Shiyan **1205**

HARMONIC EMISSION IN A DIELECTRIC MEDIUM WITH A UNIFORM MAGNETIC FIELD, J. Soln **1211**

BREMSSTRAHLUNG RISETIME SHORTENING BY DIODE GEOMETRY RECONFIGURATION, M. Bushell, R. Fleetwood, D.C. Judy, G. Merkel, M. Smith, D.M. Weidenheimer **1215**

APPLICATION OF A SMALL ANGULAR SPREAD BEAM IN THE REFLECTED REB REGIME ON REBEX MACHINE, V. Piffl, V. Bohacek, M. Clupek, J. Raus, P. Sunka, J. Ullschmied **1221**

AN EXPERIMENTAL STUDY OF STRONG TURBULENCE DRIVEN BY AN INTENSE RELATIVISTIC ELECTRON BEAM, M. Masuzaki, R. Ando, M. Yoshikawa, H. Morita, J. Yasuoka, K. Kamada **1227**

INTENSE ELECTRON BEAM RADIUS-TAILORING EXPERIMENT FOR PROPAGATION STUDIES, D.J. Weidman, J.D. Miller, K.T. Nguyen, M.J. Rhee, R.F. Schneider, R.A. Stark **1233**

THEORY OF WAKEFIELD AND JXB DRIFT EFFECTS OF A RELATIVISTIC ELECTRON BEAM PROPAGATING IN A PLASMA, H.S. Uhm **1239**

RELATIVISTIC ELECTRON BEAM PROPAGATION IN HIGH PRESSURE GASEOUS MEDIA, J.A. Antoniades, M.C. Myers, D.P. Murphy, R.F. Hubbard, T.A. Peyser, R.F. Fernsler, R.E. Pechacek, J. Santos, R.A. Meger **1245**

TRANSPORT OF HIGH CURRENT, RELATIVISTIC ELECTRON BEAMS USING ACTIVE-WIRE B-THETA CELL TECHNIQUES, D.P. Murphy, R.E. Pechacek, M.C. Myers, J.A. Antoniades, T.A. Peyser, R.F. Fernsler, R.F. Hubbard, J. Santos, R.A. Meger **1251**

IFR TRANSPORT EXPERIMENTS ON THE SUPERIBEX ACCELERATOR, M.C. Myers, J.A. Antoniades, T.A. Peyser, D.P. Murphy, R.E. Pechacek, R.F. Hubbard, R.A. Meger **1257**

BEAM PROFILE DIAGNOSTICS ON THE NRL SUPERIBEX EXPERIMENT, T.A. Peyser, M.C. Myers, R.E. Pechacek, D.P. Murphy, J.A. Antoniades, R.A. Meger **1263**

ASYMPTOTIC AND NONLINEAR EVOLUTION OF THE ELECTRON-HOSE INSTABILITY OF A REB PROPAGATING IN THE ION-FOCUSED REGIME, M. Lampe, G. Joyce, S.P. Slinker, D.H. Whittum **1270**

THEORY AND SIMULATION OF THE RESISTIVE HOSE INSTABILITY IN RELATIVISTIC ELECTRON BEAMS, R.F. Fernsler, S.P. Slinker, R.F. Hubbard, M. Lampe **1276**

ELECTRON BEAM PROPAGATION IN THE ION-FOCUSED AND RESISTIVE REGIMES, R.F. Hubbard, M. Lampe, R.F. Fernsler, S.P. Slinker **1282**

CONDITIONS FOR STABLE OPERATION IN A HELICAL QUADRUPOLE FOCUSING ACCELERATOR, C.M. Tang, J. Krall **1288**

A HIGH-ORDER MOMENT SIMULATION MODEL, K.T. Tsang, C. Kostas, D.P. Chernin, J.J. Petillo, A.A. Mondelli **1294**

REFINED DEFINITION OF THE BEAM BRIGHTNESS AS THE ARITHMETIC MEAN OF THE DISTRIBUTION FUNCTION, T.J. Myers, K.A. Boulais, M.J. Rh... ..... **1300**

ELECTRON BEAM TRANSPORT, Yu.V. Rudjak, V.B. Vladyko **1306**

GENERATION AND CHARACTERISTICS OF HIGH POWER LONG PULSE ELECTRON BEAM (PROPAGATION IN VACUUM WITH DIFFERENT PRESSURE), G.I. Alexeev, A.M. Bishaev, A.A. Golubev, V.A. Gudovich, A.H. Kadimov, G.I. Klenov, V.P. Larionov, O.I. Radkevich, O.V. Shterbina **1312**

GENERATION OF MICROWAVE OSCILLATIONS IN AN ELECTRODYNAMIC SYSTEM WITH PLASMA-BEAM INTERACTION, V.I. Perevodchikov, M.A. Zavialov, V.F. Martynov, L.A. Mitin, V.N. Tskhai, A.L. Shapiro **1318**

CYCLOTRON RADIATION OF AN REB INJECTED INTO INCREASING MAGNETIC FIELD, B.A. Alterkop, V.M. Mikhailov, A.A. Rukhadze, V.P. Tarakanov **1322**

LONG PULSE ELECTRON BEAM PROPAGATION, J.R. Smith, I.R. Shokair, K.W. Struve, P.W. Werner, S. Hogeland, P.D. Kiekel, I. Molina, B.N. Turman, R.B. Miller **1328**

Contributed Beam Diagnostics Papers

FAST H-ALPHA LINE BROADENING DURING THE 100 NS REB INJECTION INTO A PLASMA, K. Kolacek, M. Ripa, J. Ullschmied, K. Jungwirth, P. Sunka **1337**

THE BEAM CURRENT DIAGNOSING IN LARGE AREA DIODES, D. Huang, W. Ma, X. Wang, N. Zeng, Y. Shan, Y. Wang, D. Zhang **1343**

THE STRENGTH CALCULATION FOR A FOIL COAXIAL SHUNT, D. Huang **1349**

AN OFFSET MODEL RADIATION CALORIMETER, S. Fu, Y. Chen, K. Hu **1354**

INTRABAND RADIOLUMINESCENCE OF DIELECTRICS: PROPERTIES AND APPLICATIONS TO HIGH POWER BEAM DIAGNOSTICS, D.I. Vaysburd, B.N. Syomin **1360**

COMPUTER ASSISTED DIAGNOSTICS ON A HIGH-POWER MICROWAVE SYSTEM, M.T. Crawford, M. Kristiansen, L.L. Hatfield, S.E. Calico **1367**

SQUEEZED STATES OF HIGH-CURRENT ELECTRON BEAM IN A SYSTEM WITH VIRTUAL CATHODE, A.V. Fedotov, A.M. Ignatov, V.P. Tarakanov **1373**

ELECTRON BEAM DEFLECTION DIAGNOSTIC, M.T. Ngo, J.A. Pasour **1379**

ELECTRON BEAM POTENTIAL MEASUREMENTS ON AN INDUCTIVE-STORE, OPENING-SWITCH ACCELERATOR, J.C. Riordan, J.R. Goyer, D. Kortbawi, J.S. Meachum, R.S. Mendenhall, I.S. Roth **1385**

A NEW TIME-RESOLVED ENERGY-FLUX GAUGE FOR PULSED ION BEAMS, S.H. Richter, D.V. Keller **1391**

THEORETICAL SPECTROSCOPIC ANALYSIS OF INTENSE ION BEAM-PLASMA INTERACTION IN THE PBFA II GAS CELL, P. Wang, J.J. MacFarlane, G.A. Moses, J.E. Bailey **1397**

MULTI-DIMENSIONAL DIAGNOSTICS OF HIGH POWER ION BEAMS BY ARRAYED PINHOLE CAMERA SYSTEM, K. Yasuike, S. Miyamoto, N. Shirai, T. Akiba, S. Nakai, K. Imasaki, C. Yamanaka **1403**

Paper Index - Volume III

Contributed Microwave Papers

OPTIMIZATION OF THE OUTPUT CAVITY FOR A THREE CAVITY X-BAND GYROKLYSTRON AMPLIFIER, W. Main, S.G. Tantawi, P.E. Latham, B. Hogan, W. Lawson, C.D. Striffler, V.L. Granatstein **1449**

THEORETICAL INVESTIGATION OF ANOMALOUSLY HIGH EFFICIENCY IN A THREE CAVITY GYROKLYSTRON AMPLIFIER, P.E. Latham, U.V. Koc, W. Main, S.G. Tantawi **1455**

HIGH EFFICIENCY, LOW MAGNETIC FIELD GYROKLYSTRON AMPLIFIERS, P.E. Latham, G.S. Nusinovich, B. Levush **1461**

MODE-PRIMED OPERATION OF AN 85 GHZ QUASIOPTICAL GYROKLYSTRON, R.P. Fischer, A.W. Fliflet, W.M. Manheimer **1467**

LARGE ORBIT GYROKLYSTRON DEVELOPMENT AT LOS ALAMOS, R.M. Stringfield, R.M. Wheat, D.J. Brown, M.V. Fazio, J. Kinross-Wright, B.E. Carlsten, G. Rodenz, R.J. Faehl, R.F. Hoeberling **1473**

THE NRL 11.4 GHZ MAGNICON AMPLIFIER EXPERIMENT, S.H. Gold, C.A. Sullivan, B. Hafizi, W.M. Manheimer, W.M. Black **1479**

HIGH PERFORMANCE 33.2 GHZ GYROKLYSTRON, J.D. McNally, M.P. Bobys, D.B. McDermott, N.C. Luhmann, Jr. **1485**

HARMONIC GYRO-TWT AMPLIFIER FOR HIGH POWER, Q.S. Wang, D.B. McDermott, N.C. Luhmann, Jr., A.T. Lin, C.S. Kou, K.R. Chu **1491**

STABILITY AND NONLINEAR DYNAMICS OF GYROTRONS AT CYCLOTRON HARMONICS, G.P. Saraph, G.S. Nusinovich, T.M. Antonsen, Jr., B. Levush **1497**

PROSPECTS FOR DEVELOPMENT OF POWERFUL, HIGHLY EFFICIENT, RELATIVISTIC GYRODEVICES, G.S. Nusinovich, V.L. Granatstein **1503**

DEPRESSED COLLECTORS FOR MILLIMETER WAVE GYROTRONS, A. Singh, V.L. Granatstein **1508**

COHERENT FAST WAVE RADIATION FROM SPATIOTEMPORALLY MODULATED GYRATING RELATIVISTIC ELECTRON BEAMS, J.L. Hirshfield, A.K. Ganguly **1514**

CYCLOTRON AUTORESONANCE MASERS: RECENT EXPERIMENTS AND PROJECTS, V.L. Bratman, G.G. Denisov, S.V. Samsonov **1520**

CYCLOTRON AUTORESONANCE MASER (CARM) AMPLIFIER EXPERIMENTS AT 17 GHZ, W.L. Menninger, B.G. Danly, S. Alberti, C. Chen, D.L. Goodman, E. Giguet, J.L. Rullier, J.S. Wurtele, R.J. Temkin **1526**

CYCLOTRON AUTORESONANCE MASER (CARM) OSCILLATOR EXPERIMENT AT 28 GHZ, G. Gulotta, S. Alberti, B.G. Danly, T. Kimura, W.L. Menninger, J.L. Rullier, R.J. Temkin **1532**

THE ELECTRODYNAMICS OF A CO-AXIAL PLASMA SLOW-WAVE STRUCTURE OF A PLASMA CHERENKOV AMPLIFIER DRIVEN BY A HIGH-CURRENT REB IN FINITE MAGNETIC FIELD, I.A. Selivanov, A.G. Shkvarunets, V.P. Tarakanov **1538**

EXPERIMENTAL STUDY AND PIC-SIMULATION FOR THE PCM OPERATION, P.S. Strelkov, A.G. Shkvarunets, V.P. Tarakanov **1545**

INFLUENCE OF CATHODE PLASMA UPON THE RADIATION PULSE DURATION OF VACUUM MICROSECOND RELATIVISTIC MICROWAVE GENERATOR, O.T. Loza, P.S. Strelkov, S.N. Voronkov **1550**

THE "HOSE TYPE" INSTABILITY OF REB AND MICROWAVE GENERATION IN A WAVEGUIDE, A.A. Rukhadze, P.V. Rybak, V.P. Tarakanov **1556**

ON SOME PRACTICAL CONSIDERATION OF THE ELECTRON BEAM BREAKUP TRANSIT TIME OSCILLATOR, T.J.T. Kwan **1562**

EXTERNAL QUASI-OPTICAL FEEDBACK SYSTEM FOR NARROWING RADIATION BAND, V.A. Bogachenkov, V.A. Papadichev, I.V. Sinilshikova, O.A. Smith **1568**

RELATIVISTIC MAGNETRONS: OPTIMIZATION OF PARAMETERS AND MODELLING OF PHASE LOCKING PROCESSES, D.V. Alexandrovich, S.V. Baranov, A.N. Didenko, N.M. Filipenko, G.P. Fomenko, A.S. Maidanovskii, S.S. Novikov, V.V. Pozdeev, A.S. Sulakshin **1574**

THE NONUNIFORM-PHASE-VELOCITY RELATIVISTIC BWO, S.D. Korovin, S.D. Polevin, V.V. Rostov, A.M. Roitman **1580**

THE STATE OF ART OF INVESTIGATIONS OF RELATIVISTIC MULTIWAVE MICROWAVE GENERATORS, A.N. Bastrikov, S.P. Bugaev, I.A. Chernyavsky, M.P. Deichuli, P.A. Khryapov, V.I. Koshelev, V.V. Lopatin, N.S. Sochugov, K.N. Sukhushin, A.N. Zakharov, V.I. Kanavets, V.M. Pikunov, A.I. Slepkov **1586**

CHERENKOV MICROWAVE GENERATOR OF HIGH-CURRENT RELATIVISTIC ELECTRON BEAMS, N.F. Kovalev **1592**

MULTIWAVE RELATIVISTIC ELECTRON DEVICES: PROGRESS AND PROSPECTS, V.A. Cherepenin **1596**

HIGH POWER X-BAND MICROWAVE AMPLIFIERS AND THEIR APPLICATION FOR PARTICLE ACCELERATION, T.J. Davis, J.D. Ivers, G.S. Kerslick, E. Kuang, J.A. Nation, M. Oppenheim, L. Schachter **1601**

RECENT RESULTS FROM THE UNIVERSITY OF MARYLAND OVERMODED BWO AND MWCG PROGRAM, D.K. Abe, T.M. Antonsen, Jr., Y. Carmel, B. Levush, S.M. Miller, A. Bromborsky **1607**

THEORY OF RELATIVISTIC BACKWARD WAVE OSCILLATORS OPERATING NEAR CUTOFF, S.M. Miller, T.M. Antonsen, Jr., B. Levush, A. Bromborsky **1613**

THEORY OF RELATIVISTIC BACKWARD WAVE OSCILLATORS OPERATING NEAR CYCLOTRON RESONANCE, A. Vlasov, G.S. Nusinovich, B. Levush, A. Bromborsky **1619**

DIELECTRIC CHERENKOV MASER AS A POWERFUL AMPLIFIER WITH SUPERWIDE BANDWIDTH, A.S. Shlapakovskii, K.A. Chirko **1625**

EXPERIMENTAL STUDY OF A PLASMA-FILLED BACKWARD WAVE OSCILLATOR, X. Zhai, E. Garate, R. Prohaska, A. Fisher, G. Benford **1631**

PASOTRON HIGH-ENERGY MICROWAVE SOURCE, J.M. Butler, D.M. Goebel, R.W. Schumacher, J. Hyman, J. Santoru, R.M. Watkins, R.J. Harvey, F.A. Dolezal, R.L. Eisenhart, A.J. Schneider..... **1637**

THEORY OF THE INTERACTION OF ELECTRON BEAMS WITH THE WAVES IN PLASMA FILLED WAVEGUIDES, N.I. Karbushev, Yu.A. Kolosov, Ye.I. Ostrenskiy, A.I. Polovkov, A.D. Shatkus, L.A. Mitin, I.L. Volokitenkova, V.A. Balakirev, G.V. Sotnikov..... ..... **1643**

RESEARCH ON A 1.3 GHZ ANNULAR ELECTRON BEAM POWERED MULTI-GIGAWATT MICROWAVE AMPLIFIER, K.J. Hendricks, W.R. Fayne, L.A. Bowers, C.E. Davis, M.D. Haworth, R.C. Platt, R.W. Lemke, M.C. Clark **1649**

APPLICATION OF HIGH-CURRENT ACCELERATORS WITH INDUCTORS, BASED ON DISTRIBUTED PARAMETER LINES FOR GENERATION OF HIGH-POWER MICROWAVE PULSES, A.I. Pavlovskii, V.D. Selemir, V.V. Ivanov, I.V. Konovalov, I.G. Prikhod'ko, V.G. Suvorov, K.V. Shibalko, V.G. Kornilov, V.Y. Vatrunin, V.S. Zhdanov..... **1655**

EFFECT OF INTENSE SPACE CHARGE IN RALATIVISTIC KLYSTRON AMPLIFIERS, B.E. Carlsten, R.J. Faehl, M.V. Fazio, T.J.T. Kwan, D.G. Rickel, R.D. Ryne, R.M. Stringfield..... **1661**

A PROPOSED EXTENDED CAVITY FOR COAXIAL RELATIVISTIC KLYSTRONS, L. Schachter, T.J. Davis, J.A. Nation..... **1667**

RELATIVISTIC HIGH POWER KLYSTRONS, A.N. Sandalov, V.M. Pikunov, V.E. Rodiakin, A.A. Stogov..... **1673**

A NONLINERAR THEORY OF ENERGY AND CURRENT MODULATION IN RELATIVISTIC KLYSTRON AMPLIFIERS, H.S. Uhm **1679**

THE TIME ENERGY COMPRESSION OF PULSE MICROWAVE VIRCATOR RADIATION, P.Yu. Chumerin, G.V. Melnikov, S.A. Novikov, S.V. Razin, Yu.G. Yushkov, A.G. Zcherlitsin, A.N. Didenko **1685**

FREQUENCY CONTROL OF VIRCATOR MICROWAVE RADIATION, A.N. Didenko, M.Yu. Antoshkin, G.P. Fomenko, V.P. Grigoryev, T.V. Koval, G.V. Melnikov, V.I. Tsvetkov, A.G. Zherlitsin..... **1690**

NUMERICAL SIMULATION AND EXPERIMENT STUDY OF VIRCATOR, Z.X. Wang, Y.Q. Chen, Y.S. Chen, R.Y. Fan..... **1696**

EXPERIMENTAL STUDY OF VIRTUAL CATHODE OSCILLATOR IN UNIFORM MAGNETIC FIELD, K.G. Kostov, N.A. Nikolov, I.P. Spasovsky, R. Atanassov..... **1700**

Contributed Free Electron Laser Papers

NONLINEAR SIMULATION OF A HIGH-POWER COLLECTIVE FREE-ELECTRON LASER, H.P. Freund, A.K. Ganguly 1709

ANALYSIS OF THE ELECTRON DYNAMICS IN A RAMAN FREE ELECTRON LASER WITH REVERSED AXIAL GUIDE MAGNETIC FIELD, G. Spindler, G. Renz, M.E. Conde, G. Bekefi 1715

HELICAL SMALL PERIOD WIGGLER FOR THE RAMAN FREE ELECTRON LASER OF SIOFM, M.C. Wang, B. Feng, Z. Wang, Z. Lu, L. Zhang 1721

DEVELOPMENT OF A HIGH POWER MILLIMETER WAVE FREE-ELECTRON LASER AMPLIFIER, S.W. Bidwell, Z.X. Zhang, T.M. Antonsen, Jr., W.W. Destler, V.L. Granatstein, B. Levush, J. Rodgers, H.P. Freund 1728

A KIND OF MICRO-FEL DEVICE WITH SUPER-HIGH GAIN, W. Ding 1734

OPTICAL GUIDING AND SUPERRADIANCE EFFECTS IN FREE ELECTRON LASERS, N.S. Ginzburg 1740

NONLINEAR ANALYSIS OF A GRATING FREE-ELECTRON LASER, B. Hafizi, P. Sprangle, P. Serafim, A. Fisher 1746

EUPHROSYNE, A PULSED ELECTRON GENERATOR FOR FEL APPLICATION, C. Bonnafond, J. Bardy, H. Bottollier-Curtet, A. Devin, J. Gardelle, G. Germain, J. Labrouche, J. Launspach, P. Le Taillandier, J. de Mascureau 1752

FEL PROJECT FOR INDUSTRIAL APPLICATIONS IN JAPAN, K. Imasaki, S. Sato, Y. Miyauchi, T. Keishi, A. Kobayashi, A. Koga, E. Nishimura, K. Saeki, I. Bessho, M. Okano, S. Abe, A. Nagai, T. Tomimasu 1758

A FREE ELECTRON LASER AT P. N. LEBEDEV INSTITUTE, Accelerator Physics Laboratory Staff 1764

FREE ELECTRON LASER -FEL- BASED ON MSU RM-100 RACE-TRACK MICROTRON, V.K. Grishin, B.S. Ishkhanov, A.N. Sandalov, V.I. Shvedunov 1770

HIGH CURRENT CERENKOV FREE ELECTRON LASER-CFEL AT FAR INFRARED WAVELENGTHS, V.K. Grishin, C.M. Cricket, I.F. Lenski 1776

Contributed Advanced Accelerator Papers

MODEL OF CAVITY COUPLING FOR BEAM BREAKUP CONTROL, D.G. Colombant, Y.Y. Lau, D.P. Chernin 1783

EXPERIMENTS ON THE EXCITATION AND COUPLED-CAVITY SUPPRESSION OF BEAM-BREAKUP-INSTABILITY IN LONG-PULSE ELECTRON BEAM TRANSPORT, R.M. Gilgenbach, P.R. Menge, M.T. Walter, C.H. Ching, J. Foster, P.L.G. Ventzek 1789

ELECTRON FLOW IN POSITIVE-POLARITY MULTIGAP INDUCTIVE ACCELERATORS, B.W. Church, R.N. Sudan **1795**

SIMULATIONS OF MULTISTAGE INTENSE ION BEAM ACCELERATION, S.A. Slutz, J.W. Poukey **1801**

PROSPECTS OF CYCLOTRON RESONANCE LASER ACCELERATION, C. Chen **1807**

NUMERICAL SIMULATIONS OF DENSITY CHANNEL GUIDING AND RELATIVISTIC OPTICAL GUIDING OF LASER PULSES IN A PLASMA, J. Krall, G. Joyce, P. Sprangle, E. Esarey **1813**

TWO-BEAM VIRTUAL CATHODE ACCELERATOR, W. Peter **1819**

EXPERIMENTAL STUDIES OF BEAM ACCELERATION WITH A SHORT PULSE X-BAND ELECTRON CYCLOTRON MASER, K. Kamada, T. Kanazawa, M. Sakamoto, N. Matsumura, F. Tamagawa, R. Ando, M. Masuzaki, S. Kawasaki **1825**

COLLECTIVE ACCELERATION OF LIGHT ION BEAMS IN KALI-200, T. Vijayan, P. Roychowdhury, S.K. Iyyengar **1831**

MODELING HIGH-POWER RF ACCELERATOR CAVITIES WITH SPICE, S. Humphries, Jr. **1837**

SUPERFISH POST-PROCESSOR FOR IBM-PC COMPATIBLE COMPUTERS, S. Humphries, Jr. **1843**

SIMULATION STUDIES OF BEAM QUALITY IN HIGH-GRADIENT ACCELERATORS, G. Joyce, J. Krall **1849**

CLIA - A COMPACT LINEAR INDUCTION ACCELERATOR SYSTEM, S.R. Ashby, D. Drury, P.S. Sincerny, L. Thompson, L. Schlitt **1855**

THE LELIA INDUCTION INJECTOR: FIRST RESULTS, J. Bardy, P. Anthouard, P. Eyharts, P. Eyl, M. Thevenot, A. Roques, D. Villate **1861**

HIGH-CURRENT LINEAR ACCELERATOR, A.G. Mozgovoy **1867**

RECENT ADVANCES IN INDUCTION ACCELERATION AND POSTACCELERATION OF HIGH-CURRENT BEAMS AT TOMSK NUCLEAR PHYSICS INSTITUTE, V.V. Vasiljev, I.B. Ivanov, G.G. Kanaev, O.N. Tomskikh, Yu.P. Usov, E.G. Furman **1870**

A 3.4 MEV LINEAR INDUCTION ACCELERATOR, C. Nianan, S. Zhang, Z. Tao **1876**

BEAM MATCHING INTO THE DARHT LINAC, T.P. Hughes, D.C. Moir, R.L. Carlson **1881**

HITMI: EXPERIMENTS WITH AN ELECTRON-BEAM DRIVEN VACUUM LINEAR INDUCTION ACCELERATOR, C. Ekdahl, S. Humphries, Jr., W. Rix, C. Warn **1887**

Contributed Beam Applications Papers

FOCUSING AND PROPAGATION OF PROTON BEAM AS DRIVER OF ICF, K. Niu **1895**

LIBRA-LITE, A BALLASTIC FOCUS LIGHT ION INERTIAL CONFINEMENT FUSION REACTOR, R.R. Peterson, D. Bruggink, R.L. Engelstad, G.L. Kulcinski, E.G. Lovell, J.J. MacFarlane, E.A. Mogahed, G.A. Moses, S. Rutledge, M.E. Sawan, I.N. Sviatoslavsky, G. Sviatoslavsky, L.J. Wittenberg 1901

IONIZATION OF A HIGH ENERGY NEUTRAL BEAM PROPAGATING IN THE IONOSPHERE, S.T. Lai 1907

LARGE AREA ELECTRON BEAM GENERATION AND PROPAGATION FOR KRF LASERS, C.J. Pawley, J.D. Sethian, S.P. Obenschain, S.J. Czuchlewski 1912

DEVELOPMENT OF A 100 JOULE LEVEL XECL LASER PUMPED BY INTENSE RELATIVISTIC ELECTRON BEAM, J.R. Liu, R.F. Sun, A.C. Qiu, X. Yuan, Y.G. Gan, X.H. Wang, Y.M. Zhang, X.Q. Zhao, S.Q. Ren, L. Nie, D.S. Yao, L.G. Wang, M. Zhang, Y.M. Wei, L.H. Wang 1918

REB PUMPED SYSTEMS WITH MULTIPOLE MAGNETIC FIELD WALL SHIELDING, G.P. Mkheidze, A.A. Savin, F.B. Trintchouk 1924

LARGE-APERTURE E-BEAM PUMPED EXCIMER LASERS FOR ICF, E.P. Bolshakov, V.A. Burtsev, M.A. Vasilevsky, V.M. Vodovosov, V.V. Jeremkin, V.E. Kuznetsov, V.A. Ovsyannikov, O.P. Pechersky, V.F. Prokopenko, R.F. Fidelskaya, K.I. Finkelstein, V.I. Chernobrovin, V.I. Chetvertkov, V.Yu. Baranov, A.P. Streltsov 1930

PULSE HEAT TREATMENT OF MATERIAL SURFACE BY HIGH-CURRENT ELECTRON BEAM, V.I. Engelko, A.V. Lazarenko, O.P. Pechersky 1935

DISSIPATION OF STRESS WAVE ENERGY AND STRUCTURAL MODIFICATION OF STEELS IRRADIATED BY A LOW-ENERGY HIGH-CURRENT ELECTRON BEAM, V.I. Itin, Yu.F. Ivanov, S.V. Lykov, G.A. Mesyats, G.E. Ozur, D.I. Proskurovsky, V.P. Rotshtein 1942

ACTION OF A NANOSECOND MEGAVOLT HIGH-CURRENT ELECTRON BEAM ON METALS AND ALLOYS, I.M. Goncharenko, A.M. Efremov, Yu.F. Ivanov, V.I. Itin, B.M. Kovalchuk, S.V. Lykov, A.B. Markov, V.P. Rotshtein, A.A. Tukhfatullin 1948

HIGH ENERGY ELECTRON BEAM MATERIALS PROCESSING, R.A. Stark, R.F. Schneider, E.E. Nolting, M. Skopec, J.C. Danko, C.D. Lundin, T.T. Meek 1954

ENHANCEMENT OF METAL PROPERTIES BY IRRADIATION WITH INTENSE, HIGH-ENERGY ELECTRON BEAMS, K.W. Struve, A.C. Smith, E.L. Neau 1960

HIGH-RATE DEPOSITION OF THIN FILMS BY HIGH-POWER ION BEAM, I.F. Isakov, G.E. Remnev, A.N. Zakutayev 1966

QUICK PREPARATION OF THIN FILMS AND CHARACTERISTICS OF ABLATION PLASMA PRODUCED BY ION-BEAM EVAPORATION, T. Sonegawa, X.D. Kang, H. Hoshino, M. Ohashi, Y. Shimotori, S. Furuuchi, K. Masugata, K. Yatsui 1971

Contributed Plasma Discharge Papers

ELECTROTHERMAL PLASMA SOURCE AS A HIGH HEAT FLUX SIMULATOR FOR PLASMA-FACING COMPONENTS AND LAUNCH TECHNOLOGY STUDIES, M. Bourham, J. Gilligan, O. Hankins, W. Eddy, J. Hurley **1979**

PLASMA DYNAMICS AND HOTSPOTS STUDIES FROM A PLASMA FOCUS DEVICE, C.C. Tzeng, C.K. Yeh, Y.J. Yu, Y.Y. Kuo, M. Wen, W.S. Hou, T.R. Yeh **1984**

DEUTERIUM-FIBER-INITIATED Z-PINCHES: SIMULATION COMPARED TO EXPERIMENT, P. Sheehey, I.R. Lindemuth, R.H. Lovberg, R.A. Riley, Jr. **1990**

RADIATIVE COLLAPSE OF A DENSE PLASMA, H.U. Rahman, N. Rostoker, F.J. Wessel **1996**

GOLD Z-PINCHES ON SATURN, R.B. Spielman **2002**

DIFFERENT STABILIZATION PROCESSES IN Z-PINCH PLASMA EXPERIMENTAL APPROACH, B. Etlicher, A.S. Chuvatin, L. Veron, F.J. Wessel, C. Rouille, S. Attelan, P. Choi **2008**

HIGH POWER IMPODING PLASMA FOR THE X-RAY LASER, R.B. Baksht, I.M. Datsko, V.A. Kokshenev, A.A. Kim, A.V. Luchinsky, V.V. Loskutov, V.I. Oreshkin, A.G. Russkich **2014**

MULTICHANNEL X-RAY SPECTRAL MEASUREMENT OF HOT PLASMA EVOLUTION IN NITROGEN-PUFF Z-PINCH, A. Krejci, J. Raus, V. Piffl, A.V. Golubev, Yu.Ya. Platonov, E. Krousky, O. Renner **2020**

INVESTIGATION OF INTENSE XUV EMISSION OF NITROGEN-PUFF Z-PINCH WITH SMAL ENERGY INPUT, J. Raus, A. Krejci, V. Piffl **2026**

TIME RESOLVED INTERFEROMETRY OF PLASMA RADIATION SOURCE LOADS, E.J. Yadlowsky, R.C. Hazelton, J.J. Moschella, T.B. Settersten **2032**

MAGNETIC PICKUP LOOP ANALYSIS OF AN EXPLODING WIRE Z-PINCH, J.J. Moschella, E.J. Yadlowsky **2038**

PHENOMENOLOGICAL MODELING OF ARGON Z-PINCH IMPLOSIONS, K.G. Whitney, J.W. Thornhill, C. Deeney, P.D. LePell, M.C. Coulter **2044**

RADIATION HYDRODYNAMICS OF AN IMPODING ARGON PUFF GAS PLASMA, J. Davis, F.L. Cochran **2050**

ANOMALOUS RESISIVITY IN A Z-PINCH SYSTEM, P.E. Pulsifer, K.G. Whitney **2056**

A NUMERICAL STUDY OF THE STAGNATING COMPACT TOROID AND ITS APPLICABILITY AS A RADIATION SOURCE, M.R. Douglas, R.E. Peterkin, Jr., T.W. Hussey, D.E. Bell, N.F. Roderick **2062**

HYDRODYNAMICS OF A STAGNATING RING-PUFF PLASMA, R.W. Clark, J. Davis, J. Les **2068**

Contributed Microwave Papers

OPTIMIZATION OF THE OUTPUT CAVITY FOR A THREE CAVITY X-BAND GYROKLYSTRON AMPLIFIER

W. Main, S. Tantawi, P.E. Latham, B. Hogan, W. Lawson,
C.D. Striffler and V.L.Granatstein
Laboratory for Plasma Research and Department of Electrical Engineering
University of Maryland, College Park, Maryland 20742

Abstract

Experimental results of the University of Maryland three-cavity gyroklystron indicate that interactions past the output cavity have enhanced the tube's efficiency. The tube operated at 10 GHz in the TE_{01} mode. At beam parameters of 425 kV, 204 A, and α=0.7, the three-cavity gyroklystron produced 27 MW at 32% efficiency with gain of 36 dB and pulse energy of 39 J [1]. Four different three-cavity circuits were studied experimentally. These circuits differed mainly in the geometry of the output cavity. Each of these circuits was found to have two distinct operating regimes, which were controlled by the magnetic guide field taper across the circuit. By observing the effects of perturbing the guide field after the output cavity; and using an electric field probe in the output cavity it is shown that one regime corresponds to a CARM-like interaction after the output cavity.

I. Introduction

The University of Maryland is developing a three-cavity gyroklystron to show the feasibility of this device as an RF driver for future advanced linear accelerators. For these accelerators to achieve energies in the TeV range, over a thousand phase locked drivers will be required. For this reason, achieving high gain will be important. To achieve this high gain will require gyroklystrons with three or more cavities. Our early work focused on two-cavity gyroklystrons which gave promising results [2,3].

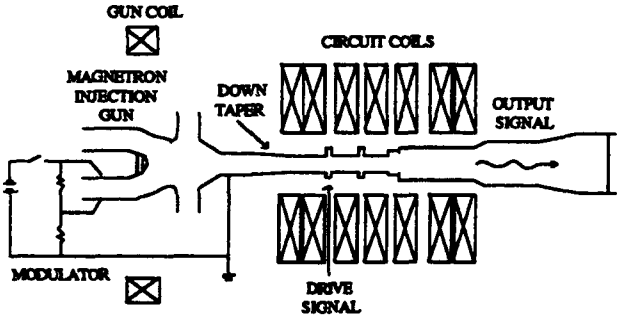


Figure 1. Schematic diagram of gyroklystron system.

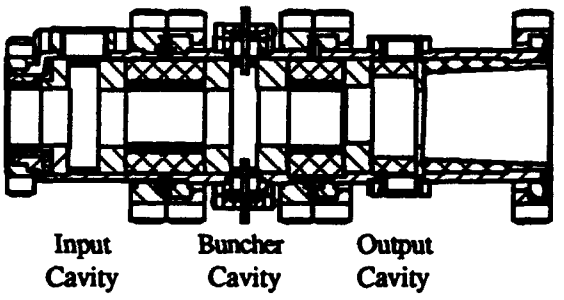


Figure 2. Diagram of Microwave circuit.

A schematic diagram showing the major components of the system appears in Figure 1, and the microwave circuit appears in Figure 2. In the first three-cavity circuit, achieving stable operation was our main concern. Output power rose with increasing α until instabilities prevented further beam compression. This problem was reduced in the second and subsequent circuits by increasing the loading in the down-taper region, the region between the cathode and the input cavity (Figure 1).

All of the tubes had at least two distinct operating regimes. The operating regime was controlled by the magnetic field taper. Figure 3 shows the axial variation of the magnetic guide field for these two regimes. We characterize the tapers by the percent decrease in field going from the input to output cavity,

and the field at the output cavity. The tapers which optimize each of the operating regimes vary slightly from tube to tube, so we give the range of tapers used. The steep taper has a 30-32% decrease and a field of 4.58 kG in the output cavity, and the weak taper has a decrease of 17-22% and a field of 4.53-4.90 kG in the output cavity.

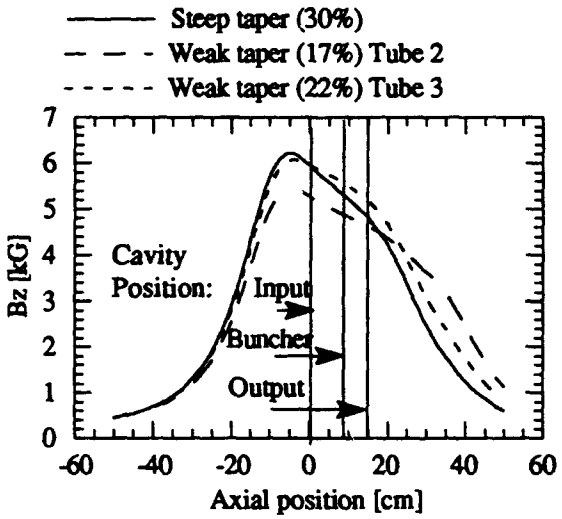


Figure 3. Axial variation of the guide field for the steep and weak tapers used in Tubes 2 and 3.

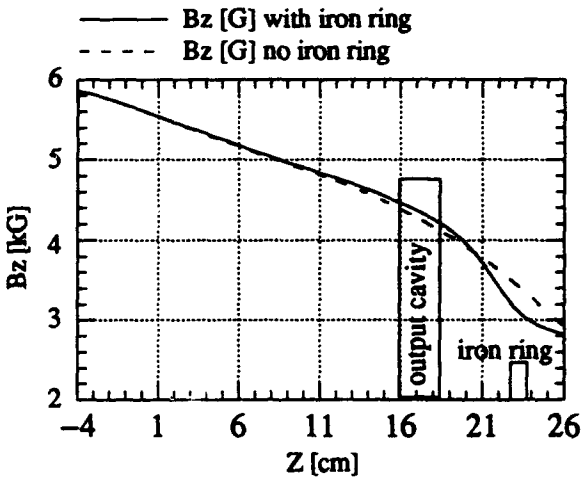


Figure 4. Axial dependence of magnetic guide field, with and without iron ring (Tube 2).

In addition to affecting the best output power, gain and efficiency, the operating regime (steep or weak taper) also affected the achievable α, and the dependence of output power on α. The two regimes were also affected differently by increased load reflection, and the effect was different for different tubes. In Section II we present the experimental arrangement. In Section III we will summarize the results of each of the four tubes, and in Section IV we discuss these results.

II. Experimental Arrangement

The magnetron injection gun (MIG) was designed to give optimum beam quality at 500 kV for 160 A and a velocity ratio $\alpha \equiv v_\perp/v_\parallel = 1.5$. Our modulator produced pulses with 1 μs flat-top and we typically operated at 1 Hz rep-rate. Eight d.c. water-cooled pancake coils produced the axial magnetic guide-field. These coils were powered by four separate power supplies so that we could adjust the magnetic compression of the beam and vary the magnetic field taper across the circuit. This system could operate up to 6.5 kG at the circuit.

The important features of this circuit are the remotely tunable buncher cavity and the lossy dielectrics (Fig. 2). To tune the cavity we insert two metal rods (OD= 5.1 mm) from opposite sides of the cavity. The tip of the rods travels from the outer wall of the cavity to within 5 mm of the drift tube radius. Most of the 120 MHz of tunability occurred when the probes were extended well into the cavity. The lossy dielectrics were placed on the outer wall of the cavities to suppress unwanted modes; and in the drift regions to damp unwanted oscillations and to provide isolation for the cavities.

Input power for the gyroklystron was supplied by a 200 kw pulsed magnetron capable of producing 2 μs pulses. Forward and reverse power were monitored. Coupling varied form 20% to 50% depending on beam parameters.

III. Design and Operation of the Four Three-Cavity Circuits

The primary difference between the four tubes presented is in the geometry of the output cavities. Figure 5 shows the output cavity cross-section of each of the four tubes. The design of the first three-cavity circuit was based on the theoretical design of a four-cavity circuit by Chu et al. [4]. The design was based on a beam of 500 kV, 160 A and $\alpha = 1.5$. To realize the cavity Qs of the theoretical design we loaded the input and buncher cavities on the outer wall with lossy dielectric. Loading the cavities on the outer wall also gave the best suppression of unwanted modes. Due to the finite gyro-radius of the beam, the drift regions were not cutoff to all modes at the operating frequency. To attenuate these unwanted modes, the drift regions were lined with lossy dielectric (black regions in Figure 2).

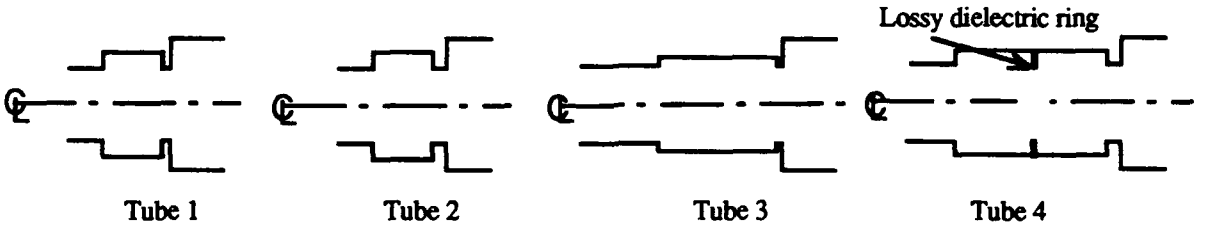


Figure 5. Cross-sectional diagrams of the output cavities of the four tubes presented.

Tube 1 operated well at high input power, producing 23 MW at 27% efficiency and 31 dB gain. Table I summarizes the output cavity design and operating parameters for all four tubes. At low input power, instabilities limited operation to lower α, or lower beam power. This prevented operation at high gain and high power. We also discovered that the tube produced higher power when operated with the calorimeter (2% reflection) as opposed to the anechoic chamber (<0.1% reflection).

Tube	**1**	**2**	**3**	**4**
Length [cm]	2.45	2.45	4.52	5.53
Radius [cm]	2.14	2.14	1.94	2.14
Lip Len. [cm]	0.29	0.49	0.25	0.49
Q	200	350	465	700
Mode	TE_{011}	TE_{011}	TE_{011}	TE_{012}
Performance at max. power:				
Power MW	23	27	22	22
Sat. Gain dB	31	36	44	32
Efficiency %	27	32	25	27

Table I. Summary of output cavity design and operating parameters for Tubes 1-4.

We suspected that the down-taper instabilities observed in Tube 1 were suppressed when higher input power was used because some of the input power leaked from the input cavity into the down taper region (Fig. 1). To allow better operation at low input power we significantly increased the attenuation in the down-taper in Tube 2. We also suspected that the enhanced operation with a more reflective load indicated that a higher Q in the output cavity was necessary. At our optimum beam power (425 kV and 205 A) Tube 1 was only able to operate at α=0.65 which was far below the design goal of α=1.5. At this point we were only operating at 5% of start oscillation current in the output cavity so we also increased the output cavity Q from 200 (Tube 1) to 350 (Tube 2).

These changes were successful. Tube 2 achieved 50 dB saturated gain at 20 MW, and 36 dB at the high power point of 27 MW where the efficiency was 36% [1]. The tube was able to operate stably with input power near one hundred watts. In contrast to Tube 1, the best power was now achieved with the low reflection anechoic chamber as the load. There were also two distinct regimes of operation. The steep taper produced the highest power using the anechoic load, however, the operation was seriously degraded when the system was terminated by the (more reflective) calorimeter. In the weak taper regime the system was not significantly affected by the load, however the best power achieved was 24 MW. In this regime the efficiency was 36%. In contrast, ongoing numerical modeling of this device which considered only cavity modes has shown efficiencies from 23% to 31% [5]. The different numerical efficiencies correspond to different assumptions of how the beam loading affects the cavity Qs.

To resolve this discrepancy we investigated the possibility of a beneficial interaction after the output cavity. Because the output power was extracted axially, there is a region of over 20 cm where the RF could have additional interaction with the beam just past the output cavity. In Tube 2 we investigated this interaction by perturbing the guide field after the output cavity with an iron ring. We found that by decreasing the field after the output cavity by 12%, the power was reduced by 15% even though the field in the output cavity was unchanged (Figure 4).

Concerned that some of the interaction was occurring after the output cavity we decided to increase the length of the output cavity. This would reduce the length of the region where the post output cavity interaction could occur while increasing the length of the desired interaction. The cavity could be lengthened while keeping the same operating frequency, either by reducing the radius or by going to the second axial harmonic (TE_{012}). We proceeded with both of these approaches, the first as Tube 3 and the second as Tube 4. In each of the designs, the longer cavity would allow operation closer to the point of start oscillation. Tube 3 was designed to operate at the start oscillation point to study phase locked oscillator operation. We also included a probe in the radial wall of the output cavity in Tubes 3 and 4 to directly monitor the cavity interaction.

Tube 3 had the additional advantage that the reduced cavity radius caused it to operate at a higher magnetic field and thus higher α. Experimentally, the magnetic field at the optimum operating point was increased; however, due to instabilities, the achievable α was not. The best power and gain occurred at the same operating point and were 22 MW and 44 dB. In contrast to the previous tubes the best operating point occurred at the weak magnetic field taper.

Tube 3 also gave the first measurement of power from inside the output cavity. In this tube the probe coupling was over 100 dB and thus was not calibrated. In the weak taper regime the probe signal was directly proportional to the measurement made in the anechoic chamber. Figure 6 shows that as the field taper was increased, the signal from the output cavity decreased to zero while the power measured at the anechoic chamber increased. Figure 7 shows the field profiles used in this measurement. This suggests that the weak taper corresponds to an interaction in the output cavity and the strong taper corresponds to an interaction somewhere else.

The output cavity in Tube 4 had the same radius as both Tube 1 and 2. The output cavity lip thickness was the same as Tube 2. The cavity length, which was almost twice that of Tube 1 and 2 was intended to operate in the TE_{012} mode. The long length of the cavity caused the TE_{011} and similar lower order modes with one axial variation to have high Q, and hence low start oscillation currents (< 10 A). Most of these modes would start to oscillate at the same magnetic field range as the TE_{012}. To suppress these modes, a thin ring of lossy dielectric was placed on the axial mid-plane of the cavity . Cold tests

showed that this ring did not affect the Q of the TE_{012} mode while substantially reducing the Q of all single axial variation modes. The tube was also equipped with a probe to sample a signal from the output cavity. Testing of this tube was under way at the time of writing this paper. However we report our initial observations.

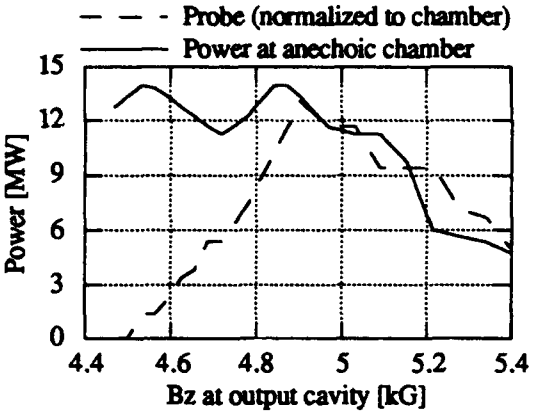


Figure 6. Comparison of anechoic chamber and probe signals vs. output cavity magnetic field.

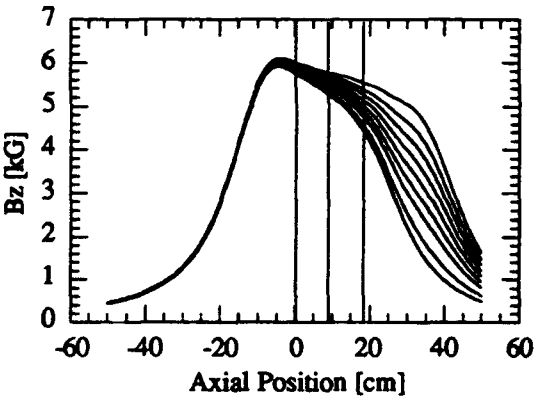


Figure 7. Magnetic field profiles used in comparison of probe and chamber signals.

Tube 4 had two regimes of operation. In one regime the output power was almost solely due to interaction after the output cavity. In this regime, the magnetic field at the output section was 3.5 kG and the maximum output power was 9.7 MW. The output power was enhanced by 25% when we introduced a small amount of reflection after the output window using a 1 cm thick acrylic plate. The output power was measured after the plate, which means that the enhancement in performance was due to increased radiation from the electron beam owing to reflection from the plate. The other regime of operation occurred at a magnetic field of 4.0 kG at the center of the output cavity and a taper of 39%. The output power was due to interaction primarily in the output cavity. This magnetic field was lower than that used in both Tubes 1 and 2, although they all shared the same output cavity radius. In Tube 4 the maximum output power was 22 MW. By comparing the anechoic chamber and output cavity signals it appeared that we could not operate in a regime where both the output cavity and the output taper were contributing to the interaction. Although the region where interactions could occur after the output cavity was greatly reduced in this tube, we still observed interactions there. The performance of the Tube 4 was generally weaker than that of Tube 2.

IV. Discussion

To compare the operation of the four tubes in simple terms, Figure 8 shows plots of efficiency vs. beam current for each tube at the beam voltage of 425 kV. As expected from their similar designs, Tubes 1 and 2 gave similar operation. The increased Q in Tube 2 allowed it to operate better in the lower current regime of 100-200 A. The efficiency of Tube 3 showed a strong dependence on beam current in the range of 150-200 A, as would be expected from a frequency-locked oscillator. Below 100 A, where large alphas could be achieved, the tube free-oscillated at the operating frequency. Tube 4, which had the longest output cavity, had significantly lower efficiency that Tubes 1 and 2. This may have been due to the longer cavity's increased sensitivity to axial velocity spread.

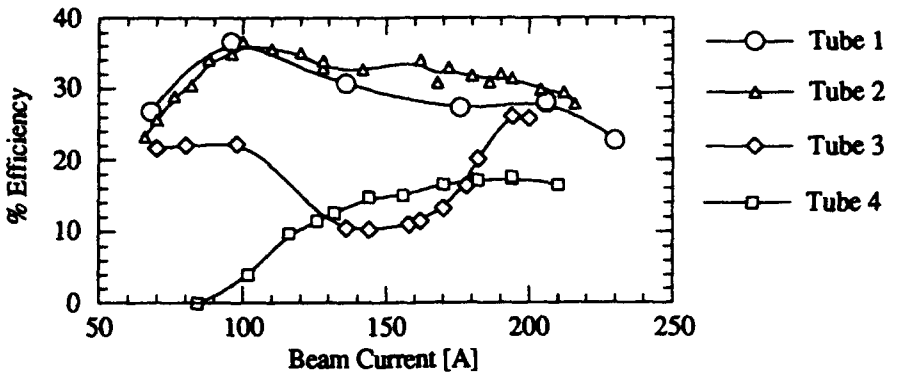


Figure 8. Dependence of efficiency on beam current for Tubes 1-4, at beam voltage 425 kV.

The original design study of the three-cavity gyroklystron predicted an output power of 30 MW when operating at 500 kV, 160 A and α=1.5. We were quite surprised to achieve 23 MW with 425 kV, 200 A and an α of only 0.72. Assuming constant axial momentum, the perpendicular efficiency is related to the total efficiency by [6].

$$\eta_{\perp} = \frac{2(1 - 1/\gamma_0)}{\beta_{\perp 0}^2} \eta_{total}$$

This gives perpendicular efficiency of 80% at the operating point. Moreover, at a beam current of 188 A, where $\alpha = 0.62$, the perpendicular efficiency was 94%. We believe that efficiencies this high are unlikely considering the velocity spread (predicted by the code EGUN) was 8%. Because the tube was optimized at lower magnetic field, and thus lower α, than predicted, we believe that the energy extraction mechanism was like that of a Cyclotron Auto-Resonance Maser (CARM).

In the CARM regime the energy extraction process operates as follows. As the electron loses its energy to the transverse electric field its orbit is reduced, however, the interaction between the axial velocity and the transverse magnetic field puts the electron back into orbit, and more energy can be extracted. In this process the total energy loss rate is proportional to the reduction in axial momentum, thus the perpendicular mechanism is kept in resonance, hence the term auto-resonance.

In the four examples presented above we showed the tubes had more that one regime of operation and that the regime was determined by the magnetic field profile used. We have also shown that with certain field profiles the tube operates quite well with little or no interaction in the output cavity. Although our diagnostics do not allow us to pinpoint the location of the interaction, we suspect that the high efficiencies observed are due to a CARM like interaction in the 20 cm region just past the output cavity.

V. References

[1] S. Tantawi, W. Main, P.E. Latham, G. Nusinovich, W. Lawson, C.D. Striffler, and V.L. Granatstein, "High Power X-Band Amplification from an Overmoded Three-Cavity Gyroklystron with a Tunable Penultimate Cavity," IEEE Trans. Plasma Sci., **20** (1992).

[2] W. Lawson, J.P. Calame, B. Hogan, P.E. Latham, M.E. Read V.L. Granatstein, M.E. Reiser and C.D. Striffler, "Efficient Operation of a High-Power X-Band Gyroklystron," Phys. Rev. Lett. **67**, 520 (1991).

[3] This conference, paper OD-1.

[4] K. Chu, V.L. Granatstein, P.E. Latham, W. Lawson, C.D. Striffler, "A 30-MW Gyroklystron-Amplifier Design for High Energy Linear Accelerators," IEEE Trans. Plasma Sci., **13**, 424 (1985).

[5] This conference, paper PE-02.

[6] T.M. Tran et al., "Optimization of Gyroklystron Efficiencies," Phys. Fluids, 29, 1274 (1986).

THEORETICAL INVESTIGATION OF ANOMALOUSLY HIGH EFFICIENCY IN A THREE CAVITY GYROKLYSTRON AMPLIFIER

P.E. Latham, U.-V. Koc, W. Main, and S.G. Tantawi
Laboratory for Plasma Research
University of Maryland, College Park, MD 20742

Abstract

The University of Maryland's three cavity gyroklystron amplifier operating at a frequency of 10 GHz, voltage of 425 kV, current of 160 A, and pitch angle ($v_\perp/v_z$) near .82, has demonstrated an efficiency of 35%. Our simulations using fixed field profiles predict a significantly lower efficiency, primarily because of the small pitch angle in the experiment. We will be investigating two methods of improving the efficiency in our simulations: beam-wave interaction after the output cavity, and modification of the first two cavity Qs due to beam loading. Results of our nonlinear code will be given for both cases.

I. Introduction

Recent three cavity gyroklystron amplifier experiments at the University of Maryland[1,2] have achieved an efficiency near 35% with a pitch angle, $\alpha = v_\perp/v_z$, around 0.82. The pitch angle was calculated using an an electrostatic gun code,[3] so the value 0.82 is only an estimate. However, even when we let α increase by 30%, our theoretical simulations using fixed field profiles and the nominal beam and cavity parameters have not been able to achieve such a high efficiency. In this paper we consider two effects which may raise the efficiency: (i) interaction of the electromagnetic radiation with the beam after the output cavity, and (ii) modification of the cavity Qs due to beam loading. In the remainder of this paper we discuss how these affect efficiency.

II. The experiment

The three cavity gyroklystron amplifier experiment performed at the University of Maryland has been discussed in detail elsewhere[1,2]; we give only a brief description here. A schematic of the experiment is shown in Fig. 1, with the beam and circuit parameters given in Table I. The magnetic field, also shown in Fig. 1, has an average taper of about -.04 kG/cm. The frequency of the second cavity was tunable over a range of 100 MHz; this tuning played an important role in achieving the high experimental efficiency. The first two cavities were loaded with lossy dielectrics, so their quality factors were due to dissipation. The quality factor of the output cavity was primarily diffractive.

In this configuration the peak experimental efficiency was 35% with a gain of 36 dB. This efficiency is quite high; in general the maximum efficiency in a gyroklystron amplifier is[4]

$$\eta_{\max} = \frac{\beta_{\perp 0}^2}{\beta_{\perp 0}^2 + \beta_{z0}^2} \frac{\omega}{s\Omega_{c0}} \frac{\gamma_0 + 1}{2\gamma_0} \quad . \tag{1}$$

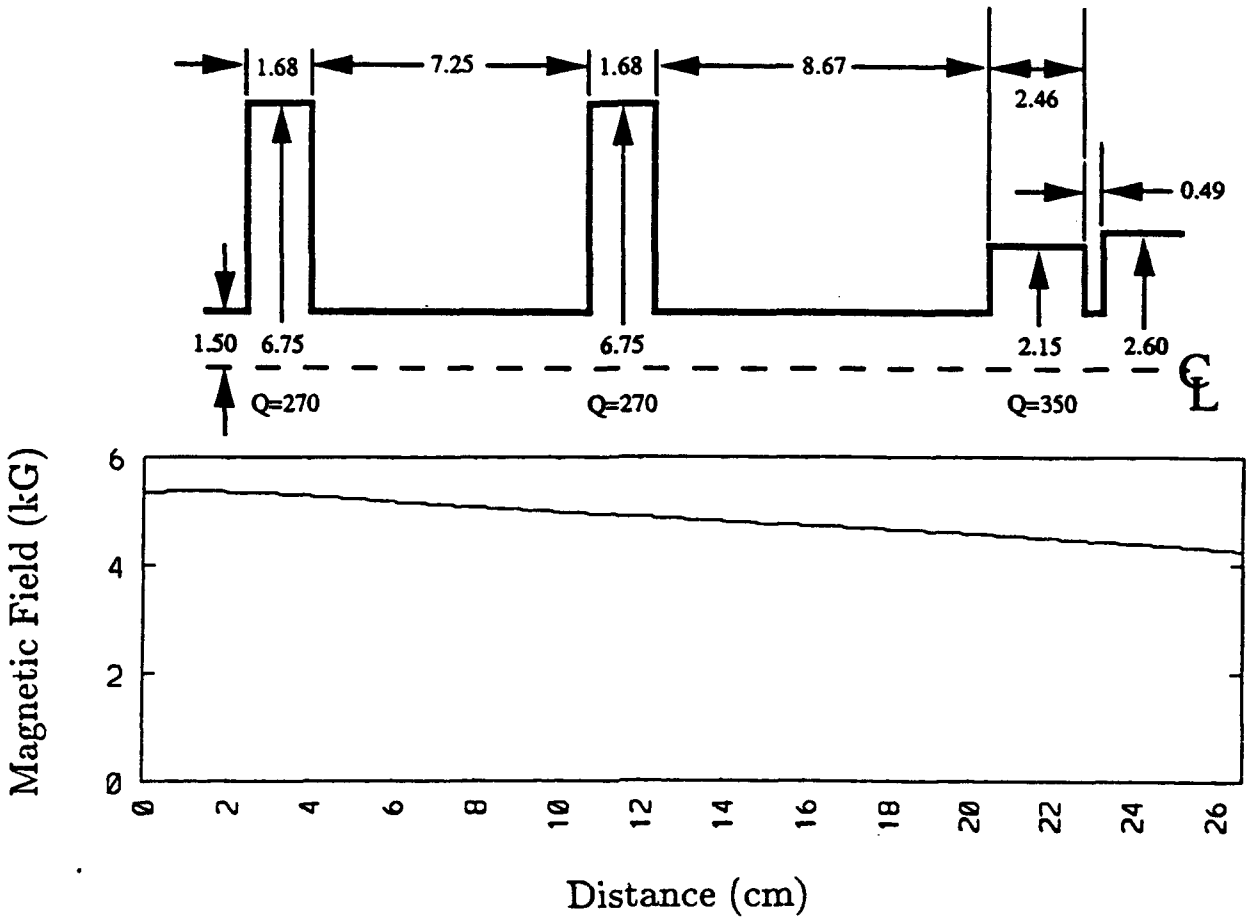


Figure 1: The three cavity circuit, including the magnetic field. All distances are in cm.

Using the experimental value of 5.34 kG for the magnetic field at the beginning of the input cavity and the computed value of 0.94 for the pitch angle, we find that $\eta_{max} = 44\%$. (Because the magnetic field was tapered, $\alpha = .94$ at the beginning of the input cavity corresponds to $\alpha = .82$ at the output cavity.) The experimental efficiency of 35% is 80% of the maximum – an exceptionally high value, considering that there was an axial velocity spread of 6.5%. At this value of α, our fixed field profile nonlinear code predicts an efficiency of about 21% if we use the nominal cold cavities quality factors. If we let α increase by, say, 30%, then the corresponding η_{max} goes up to 53% and the experimental efficiency is only 66% of this value. However, even with this large value of α our nonlinear code predicts and efficiency of only 31%.

III. Post-cavity interaction

In our theoretical analysis, we assumed that the field profiles in the cavities were not altered by the electron beam; the only effect of the beam was to shift the frequency. This

Table 1: Three cavity parameters.

Beam voltage	425 kV
Beam current	160 A
Axial velocity spread ($\delta v_z/v_z$)	6.5%
Frequency	9.85 GHz
Mode	$TE_{m=0}$
Experimental efficiency	35%
Experimental gain	36 dB

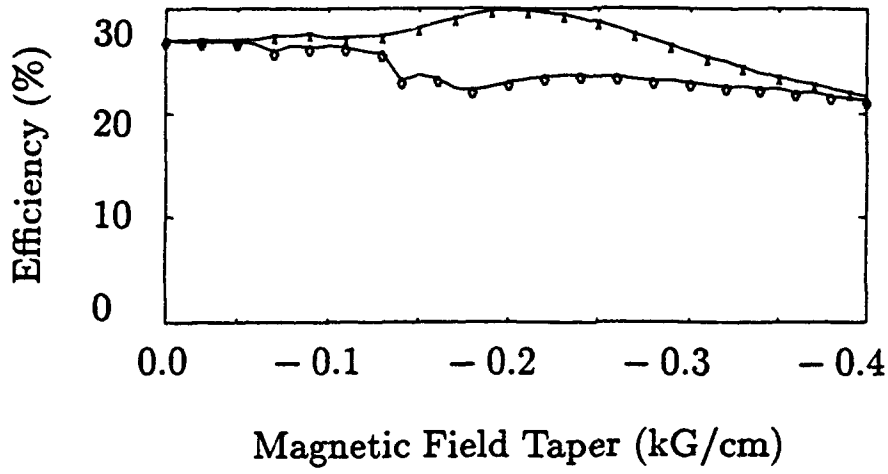


Figure 2: Efficiency versus magnetic field taper. The lower curve (O) is the efficiency at the end of the cavity. The upper curve (X) is the maximum efficiency in the drift section after the cavity.

assumption is certainly violated after the output cavity, where the field amplitude can grow or decay as the electrons exchange energy with the wave. To estimate the effect of this energy exchange on the efficiency, we used a simple model consisting of a closed cavity followed by a waveguide. The cavity supports, in general, the TE_{mnl} mode, the waveguide supports the TE_{mn} mode, and the device operates at the sth harmonic. The indices m, n and l stand for the azimuthal, radial and axial mode numbers. In our analysis we used the TE_{011} mode operating at the first harmonic. To model the beam bunching that occurs in the first two cavities, we followed the usual prescription and let the gyrophase ψ have the initial condition $\psi = \psi_0 + q \sin \psi_0$ where ψ_0 is uniformly distributed between 0 and 2π. The bunching parameter, q, was typically around 1.5.

We did an extensive parameter search (we varied the pitch angle, magnetic field and its taper, the length of the first cavity and the bunching parameter), and we did indeed find that at *some* parameter values a significant interaction after the output cavity is indeed possible. However, at the experimental parameter values the post-cavity interaction was relatively

Table 2: Post-output cavity interaction parameters.

Beam voltage	425 kV
Beam current	160 A
Axial velocity spread ($\delta v_z/v_z$)	0
Initial pitch angle ($v_\perp/v_z$)	0.82
Frequency	9.85 GHz
Initial magnetic field	4.5 kG
Cavity mode	TE_{011}
Cavity radius	2.0 cm
Waveguide mode	TE_{01}
Waveguide radius	2.6 cm

weak. Figure 2 shows a typical plot of efficiency versus magnetic field taper for the cavity and drift tube parameters shown in Table II. There is little difference between the efficiency at the end of the cavity (the lower curve in Fig. 2) and the peak efficiency in the drift tube (the upper curve). Moreover, the largest efficiency enhancement occurs a a taper of -0.20 kG/cm, much steeper than the experimental value of -0.04 kG/cm. These results suggest that a post-cavity interaction cannot account for the enhanced efficiency in the experiment. However, there is some experimental evidence suggesting that a post-cavity interaction can be important at steep magnetic field tapers,[2] although those experiments do suggest that such an interaction is not *necessary* for high efficiency. This is somewhat consistent with the results presented in Fig. 2, which indicate a stronger post-cavity interaction as the magnetic field gradient steepens. A more sophisticated model will be needed to resolve this issue.

IV. Modification of the cavity Qs due to beam loading

In simple gyrotron cavities in which the cavity quality factor is much greater than the minimum diffractive Q, it is a good approximation to assume that the beam profile is not significantly altered by the electron beam. The cavities used in the University of Maryland experiment, however, are relatively complicated: they all have sharp edges, and the first two are loaded with lossy dielectrics and can support more than one propagating radial mode at the operating azimuthal mode number $m = 0$. Moreover, our nonlinear code assumes the cavity walls are perfectly conducting. To achieve the correct resonant frequency, we had to increase the cavity radius well beyond that of the experimental cavities, as shown in Fig. 3. Because of this, in the cavities that we used for theoretical modeling the start oscillation current was twice as high as it was in the experimental cavities. Also, in the first two cavities it may be possible for the beam to pull the radiation into the beam tunnel, away from the dielectrics. This could significantly raise their quality factors. Such an effect is extremely

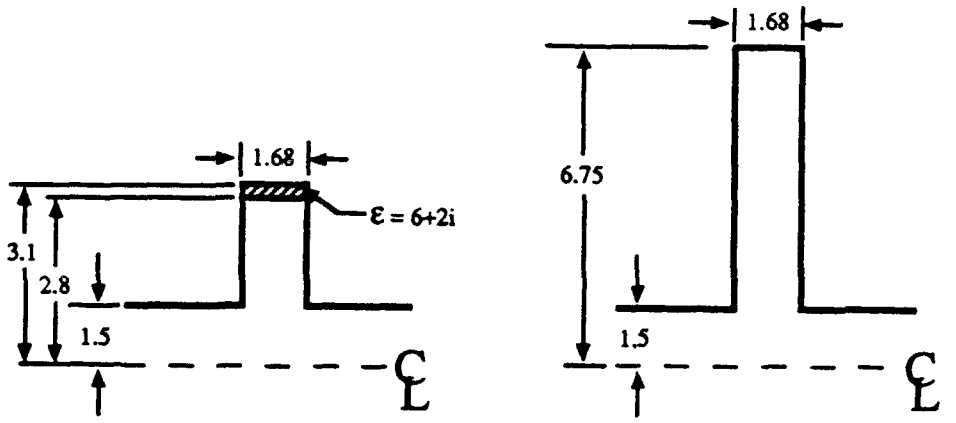


Figure 3: The cavity used in the experiment (left) and the cavity used in our numerical modeling (right).

difficult to model analytically; instead, we decided to take a phenomenological approach. We modeled the circuit without regard to the cavity Qs.

Shown in Fig. 4 is a plot of efficiency versus $\alpha/\alpha_{\text{nominal}}$ where α_{nominal} corresponds to the predicted value of 0.82 in the output cavity. The lower curve corresponds to the experimental parameters: the input power was 20 kW and the first, second and third cavity Qs were 270, 270 and 350, respectively. Even out to a pitch angle 30% above its nominal value, the efficiency was only 31%. For the upper curve, we dropped the restriction on input power and the second cavity Q, although we still demanded that the third cavity Q be 350. Along this curve, both the first and second cavity Qs were around 1000, an increase of almost 4 over their cold cavity values. For a pitch angle 25% over the value predicted from the gun code, the experimental and theoretical efficiencies match.

V. Summary and conclusions

To eliminate the discrepancy between theory and the University of Maryland three cavity experiment, we looked at both modification of the field profiles after the output cavity and modification of the quality factors in the first two cavities. Both of these effects tended to increase the efficiency, although modifying the cavity Qs led to a larger increase in efficiency than the post-cavity interaction. Even with an increase in the cavity Q by a factor of nearly 4, we needed to increase the pitch angle by 25% to agree with the experiment.

Although we can make the experimental and theoretical efficiencies fairly close, we have to adjust a number of parameters to do this. The validity of the theoretical results, then, hinges on two questions: can the beam really increase the Qs by a factor of 4 in the first two cavities, and can the gun code predictions for the pitch angle be too small by 25%? We are

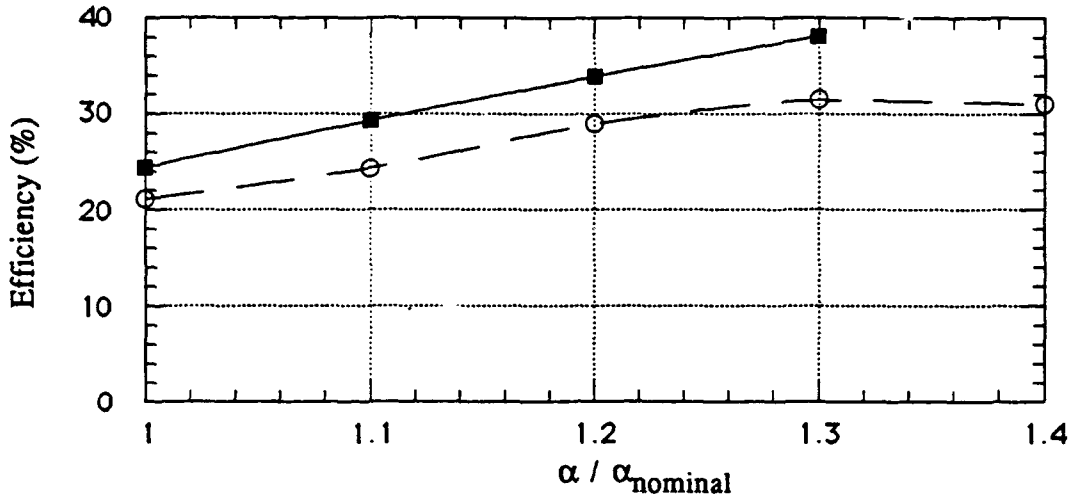


Figure 4: Efficiency versus $\alpha/\alpha_{\text{nominal}}$ where α_{nominal} corresponds to the predicted value of 0.82 in the output cavity. For the lower curve (circles) the Qs were fixed at their cold cavity values. For the upper curve (squares) the Qs of the first and second cavity were allowed to increase.

currently investigating ways to model these effects both theoretically and experimentally. In addition, we will be working on more more realistic modeling of the post-output cavity region to see if it can yield a stronger interaction than we have seen with our simple model.

Acknowledgements

This work was supported by the United States Department of Energy.

References

1. S.G. Tantawi *et.al.*, To be published in *IEEE Trans. Plasma Sci.* **20**, (1992).
2. W. Main *et.al.*, these proceedings.
3. W.B. Herrmannsfeldt, SLAC Report No. 226, 1979 (unpublished).
4. P.E. Latham *et.al.*, "High Efficiency, Low Magnetic Field Gyroklystron Amplifiers," these proceedings.

High Efficiency, Low Magnetic Field Gyroklystron Amplifiers

P.E. Latham, G.S. Nusinovich and B. Levush

Laboratory for Plasma Research
University of Maryland
College Park, MD 20742 USA

Abstract

The possibility of operating a gyroklystron amplifier at high efficiency and low magnetic field is considered. Two devices are discussed: a two cavity second harmonic TE_{02} gyroklystron amplifier operating at 19.7 GHz with subharmonic bunching, and a fundamental mode TE_{01} gyrotwistron at 16 GHz. The nonlinear efficiency is given for both devices.

I. Introduction.

For accelerator applications of gyroklystrons, which require a large number of tubes, reducing the applied magnetic field of the gyroklystron is of critical importance. The resonance condition for gyrotrons is

$$\omega - s\Omega_c - k_z v_z \simeq 0 \tag{1}$$

where ω is the operating frequency, s is the harmonic number, $\Omega_c = qB_0/m_0c\gamma$ is the relativistic cyclotron frequency, k_z is the axial wavenumber, v_z is the z-component of the beam velocity, q and m_0 are the electron charge and mass, B_0 is the applied magnetic field, c is the speed of light and γ is the relativistic factor. According to Eq. (1) there are two ways to reduce the magnetic field: (i) operate at a harmonic of the cyclotron frequency ($s > 1$), and (ii) operate at the fundamental but with high k_z. Harmonic operation has obvious appeal, as it allows for significant reduction in the magnetic field with little decrease in the efficiency,[1] at least for weakly relativistic devices. At high voltages, however, the large Larmor radius makes it difficult to fit the beam into a cutoff drift tube, and it becomes more attractive to operate at Doppler upshifted frequencies. In the remainder of this paper we discuss harmonic and Doppler upshifted gyroklystron amplifiers.

II. Opening remarks

A conventional gyroklystron amplifier[2] consists of two or more cavities separated by drift sections (see Fig. 1). To achieve stable operation, there must be no radiation in the drift section. The simplest way to achieve this is to make the drift tube radius small enough that the radiation is cutoff. If we demand that the drift tube radius be n_L Larmor radii thick but still small enough to cutoff the radiation in the operating mode, we arrive at the condition

$$\beta_{\perp 0}\frac{\omega}{\Omega_{c0}} < \frac{x_{mn}}{n_L[1+\mathrm{Im}\{k_z c/\omega\}^2]^{1/2}} \tag{2}$$

where $\beta_{\perp 0} = v_{\perp 0}/c$ is the perpendicular component of the beam velocity normalized to the speed of light and x_{mn} follows from $J'_m(x_{mn}) = 0$ (J_m is the mth order Bessel function, m

is the azimuthal mode number and n is the radial mode number). Typically, $n_\perp \sim 3-5$. Equation (2) tells us that if we want to operate in a low order mode, both $\beta_{\perp 0}$ and ω/Ω_{c0} should be as small as possible. However, high efficiency is achieved in the opposite limit: for the averaged equations of motion (i.e. only a single harmonic present), there is a conserved quantity I given by

$$I = \frac{\gamma}{\gamma_0} - \frac{\beta_{\perp 0}^2}{2}\frac{\omega}{s\Omega_{c0}}\frac{P_\perp^2}{P_{\perp 0}^2} \tag{3}$$

where $P_\perp$ is the perpendicular component of the canonical angular momentum. Equation (3) can be derived by noting that the averaged Hamiltonian depends only on the combination of coordinates $s\psi - \omega t$ where ψ is the gyrophase. Thus, the appropriate linear combination of conjugate momenta is conserved. That combination appears on the right hand side of Eq. (3). Using this conserved quantity, it is straightforward to show that the maximum single particle efficiency is given by

$$\eta_{\max} = \frac{\beta_{\perp 0}^2}{\beta_{\perp 0}^2 + \beta_{z0}^2}\frac{\omega}{s\Omega_{c0}}\frac{\gamma_0 + 1}{2\gamma_0} \quad . \tag{4}$$

Equation (4) indicates that high efficiency occurs when $\beta_{\perp 0}$ is large (which translates into large α_0), and when $s\Omega_{c0}/\omega$ is small (which corresponds to a large Doppler upshift). In fact, interpretation of Eq. (4) is slightly more subtle: if we demand that the resonance condition, Eq. (1), be approximately satisfied, then for a given k_z there is an optimal value of $\beta_{\perp 0}$ which maximizes η_{max}. For reasonable values of fast wave devices, however, the largest η_{max} is generally obtained at high $\beta_{\perp 0}$ and small Ω_{c0}. Because of Eq. (2), both of these trends make it difficult to operate in a low order mode with the drift tube cutoff. There are two ways to get around this: (i) operate in a higher order mode, and (ii) operate in a low order mode but drop the condition that the radiation be cutoff in the drift tube. If we choose the first option, we can operate at harmonics of the cyclotron frequency; if we choose the second, we are forced into the gyrotwistron configuration. A discussion of the relative merits of each device is the subject of the next two sections.

III. Harmonic gyroklystron amplifiers operating at higher order modes.

To satisfy Eq. (2) at high voltage and pitch angle and low magnetic field, x_{mn} must be reasonably large. Thus, either m or n must increase. Both of these have their problems: if m is increased, the beam-wave coupling decreases (the coupling is proportional to $J_{m-s}^2(k_\perp r_g)$ where $k_\perp$ is the perpendicular wavenumber and r_g is the guiding center radius). Although higher order azimuthal mode numbers favor higher harmonics, which in turn lead to lower magnetic fields, x_{mn} is not that large until m is about 6, at which point the beam-wave coupling at the third harmonic and below is small. If, on the other hand, n is increased, the wave can mode convert to a lower order radial mode at the boundaries of the cavities and then propagate into the drift sections.

We considered the problem of weak coupling the more serious of the two, and thus only looked at increasing the radial mode number. To minimize mode conversion, it is

necessary to smoothly taper the cavity walls. In addition, the cavity can't be too long or the start current of competing modes will be low. Consequently, the difference between the drift tube radius and the cavity radius must be small, which in turn implies that the cavity must operate near cutoff with ω close to Ω_{c0}. This reduces somewhat the maximum achievable efficiency (see Eq. (4)). However, there is still the possibility of increasing α_0 while satisfying Eq. (2), so this is potentially a relatively high efficiency device.

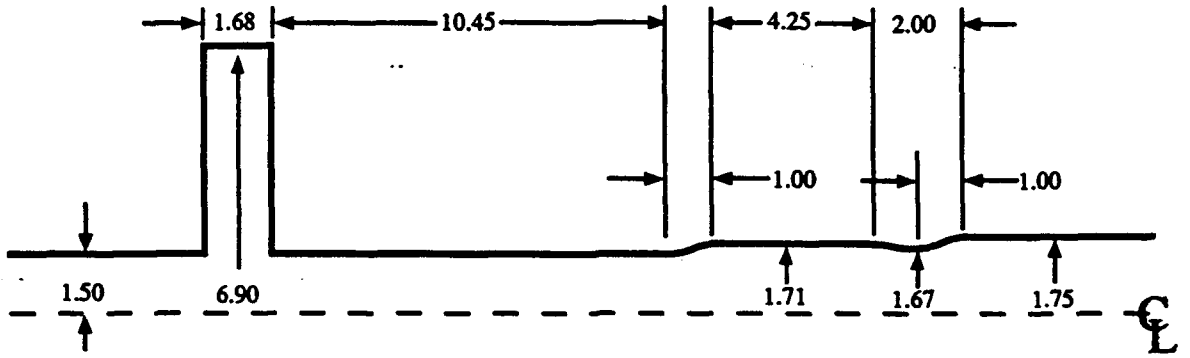


Fig. 1. Second harmonic gyroklystron. All dimensions are in cm. Tapers are sinusoidal.

We have designed a proof-of-principle experiment operating in the TE_{02} mode at 19.7 GHz. The circuit is shown in Fig. 1, with the operating parameters given in Table I. The input cavity operates at 9.85 GHz in the fundamental cyclotron harmonic. In modeling the input cavity, we used the cold cavity fields assuming perfectly conducting walls; in practice, the input cavity is loaded with lossy dielectric to reduce its quality factor. Thus, in Table I we include neither the Q of the first cavity nor the gain of the device. The quality factor of the second cavity is purely diffractive.

Table I — Second Harmonic Gyrotron Parameters

Beam voltage		425 kV
Beam current		160 A
Pitch angle ($v_{\perp 0}/v_{z0}$)		1
Velocity spread ($\delta v_z/v_{z0}$)		10%
Magnetic field		5.66 kG
Input cavity:	frequency	9.85 GHz
	mode	$TE_{m=0}$
	cyclotron harmonic	1
Output cavity:	frequency	19.7 GHz
	Q	744
	mode	TE_{02}
	cyclotron harmonic	2
Efficiency		25%

This experiment is scheduled to go on line in June of 1992. While it has the advantage of being relatively conventional and similar to the current University of Maryland experiment,[3] it clearly suffers from two drawbacks: its efficiency is low (about 25%); and

the output cavity is long (over 6 cm including the tapers), which makes it susceptible to mode competition. However, positive experimental results from this device would give us confidence in our modeling and allow us to design future devices with larger pitch angle.

IV. The gyrotwistron configuration.

Another option for low magnetic field operation is to drop the condition that the radiation be cutoff in the drift section and instead operate in the gyrotwistron configuration, as shown in Fig. 2 (See Ref. 4 and references therein for a general discussion of gyrotwistrons). In this configuration, there is an input cavity, a drift section filled with lossy dielectric, and an output waveguide. The purpose of the drift section is to allow the beam to bunch without significant interaction with the electromagnetic radiation. Because all the radiation is in the forward direction there is no need to have the drift tube cutoff.

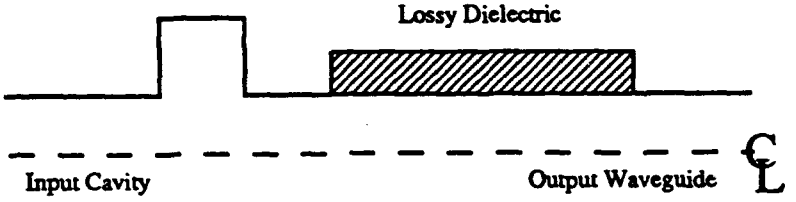


Fig. 2. Gyrotwistron configuration.

In the drift section we impose a real and imaginary axial wavenumber k_z, and let the perpendicular structure be that of a perfectly conducting waveguide with perpendicular wavenumber given by $k_\perp = [\omega^2/c^2 - \mathrm{Re}\{k_z\}^2]^{1/2}$. In the output section we assume perfectly conducting walls, so k_z is purely real and a function only of the radius. We fix the frequency, and in both the drift section and output waveguide we let the field amplitude evolve in z. Instead of simulating the input cavity numerically, we let the particles have an initial distribution (at the start of the drift tube) given by

$$\begin{aligned} \psi &= \psi_0 \quad \in [0, 2\pi] \\ u_\perp &= u_{\perp 0} + \frac{q}{L_d \psi_0'} \sin(\psi_0) \\ u_z &= u_{z0} \end{aligned}$$

where ψ is the gyrophase, $u_\perp$ is the normalized perpendicular momentum, L_d is the drift tube length and ψ_0' is the value of $d\psi/dz$ evaluated at the beginning of the drift tube. Letting the initial value of u_z be independent of phase is consistent with an input cavity operating near cutoff; future modeling will use more realistic assumptions. With these initial values, at the end of the drift tube the particles will have a phase distribution corresponding to a bunching parameter equal to q.

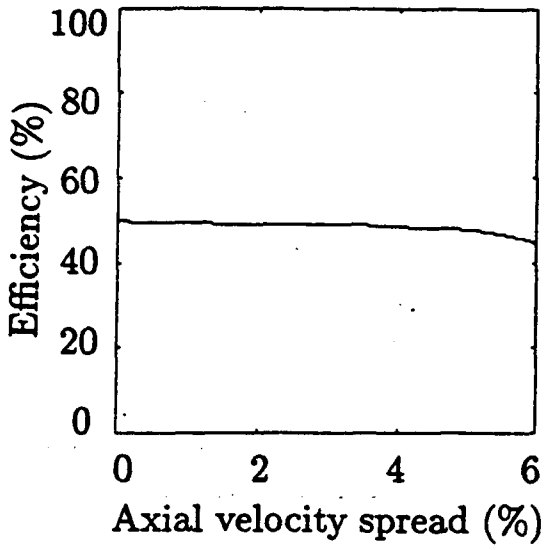


Fig. 3. Efficiency vs. $\delta v_z/v_{z0}$.

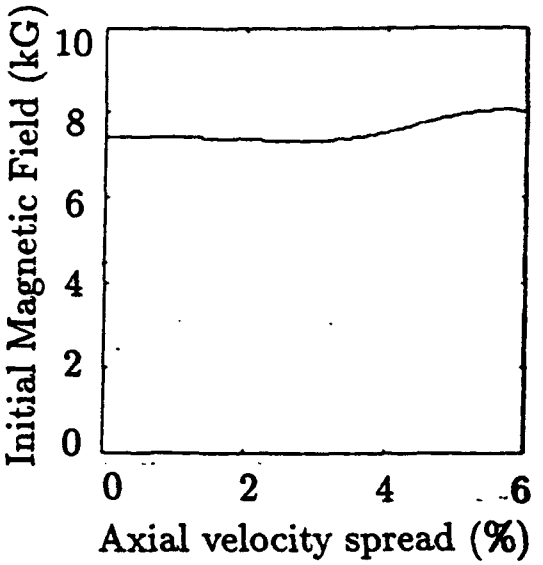


Fig. 4. Initial magnetic field vs. $\delta v_z/v_{z0}$.

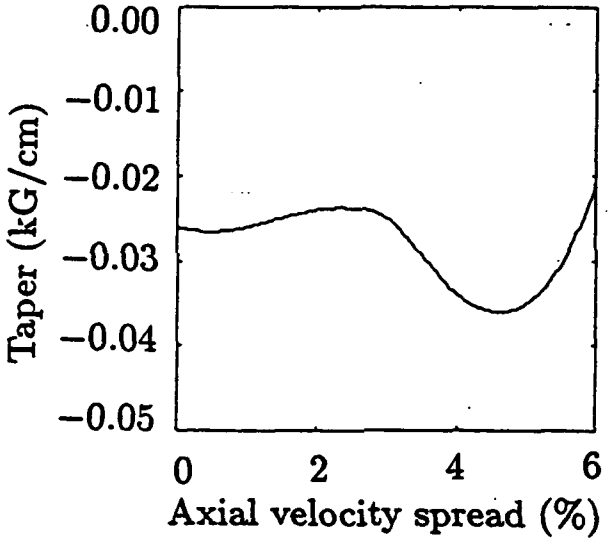


Fig. 5. Magnetic field taper vs. $\delta v_z/v_{z0}$.

The parameters for the device we simulated are listed in Table II. The voltage, current and pitch angle are the same as in Table I and the magnetic field can have a linear taper. Preliminary results are encouraging: as shown in Fig. 3, efficiency is on the order of 45-50%, more or less independent of axial velocity spread out to a spread of 6%. However, the device is relatively long: the overall length, including the lossy drift section, varies between 100 and 200 cm. We suspect that the length can be decreased significantly by using a nonlinear rather than linear taper. The peak magnetic field and taper are plotted in Figs. 4 and 5. These plots were created by optimizing efficiency with respect to magnetic field and magnetic field taper, but we did not perform a complete exploration of the parameter

space. Thus, there is no guarantee that we found the global maximum; a more detailed analysis could yield slightly different results.

Table II — Gyrotwistron Parameters

Frequency		16 GHz
Mode		TE_{01}
Lossy drift section:	length	10 cm
	Re$\{k_z c/\omega\}$	0.900
	Im $\{k_z c/\omega\}$	0.025
Output waveguide:	radius	1.5 cm
	Re $\{k_z c/\omega\}$	0.648
	Im $\{k_z c/\omega\}$	0.0

We also looked at the sensitivity of phase to changes in the pitch angle and beam voltage. We found that the phase changed about 20 degree per percent change in pitch angle and about 40 degrees per percent change in beam voltage, with a weak dependence on velocity spread. This is comparable to conventional multi-cavity gyroklystron amplifiers operating at similar voltages.[5] As in Ref. 6 we were able to almost eliminate the phase noise by simultaneously adjusting the beam voltage and the pitch angle. For our parameters, the phase shift caused by a 1% increase in beam voltage can be compensated by a 2% decrease in pitch angle. Such an adjustment could in principle be done with an appropriate active divider circuit on the magnetron injection gun.[7]

V. Summary

We have examined a second harmonic gyroklystron amplifier operating in the TE_{02} mode near cutoff, and a fundamental mode TE_{01} gyrotwistron. The second harmonic device achieved an efficiency of 25%; the gyrotwistron efficiency was around 45%. Because of its higher efficiency, the gyrotwistron appears more promising. However, further investigation needs to be done. In particular, the magnetic field and the overall length of the device need to be reduced. Both of these goals could probably be accomplished by using a nonlinear magnetic field taper; this will be the main thrust of our future research.

Acknowledgements.

This work was supported by the United States Department of Energy.

References

1. V.I. Belousov, et al, *Elektronnaya Tekhnika*, Se. 1, Elektronika SVCh,**9**, 41 (1978).
2. R.S. Symons and H. Jory, *Advances in Electronics and Electron Physics*, **55**, (1981).
3. W. Lawson, et al, *Phys. Rev. Lett.* **67**, 520 (1991).
4. G.S. Nusinovich and H. Li, *Phys. Fluids B* **4**, 1058 (1992).
5. K.R. Chu, et al, *IEEE Trans. Plasma Sci.*, **PS-13**, 424, (1985).
6. W.L. Menninger, et al, *Phys. Fluids B* **4**, 1077 (1992).
7. W. Lawson, private communication.

MODE-PRIMED OPERATION OF AN 85 GHZ QUASIOPTICAL GYROKLYSTRON

R. P. Fischer, A. W. Fliflet, and W. M. Manheimer
Beam Physics Branch
Plasma Physics Division
U.S. Naval Research Laboratory
Washington, D.C. 20375-5000

Abstract

The quasioptical gyrotron (QOG) is currently under development at the U.S. Naval Research Laboratory as a high power source of millimeter-wave radiation. A quasioptical gyroklystron configuration has recently been realized by the addition of an open-mirror prebunching resonator driven by an 85 GHz, 1.5 kW extended interaction oscillator (EIO). The experiment is designed to operate at a voltage of 70 kV and beam currents of 5-15 A. The experiment is currently in progress, and results are presented for EIO mode priming and depressed collector operation at powers up to 100 kW. A technique for increasing the efficiency by adjusting the electron beam parameters on the rise of the voltage pulse is also described.

Introduction

High-power millimeter-wave gyrotrons are being developed for a number of applications including the heating of fusion plasmas and high frequency radar. The QOG[1], an alternative to conventional cavity gyrotrons, is a promising millimeter-wave source which has produced 600 kW pulsed power at a frequency of 120 GHz and an efficiency of 8%, with a peak efficiency of 12% at lower power[2]. The addition of a simple, single-stage depressed collector raised the peak efficiency to 16%[3]. The QOG is widely tunable, has low ohmic heating densities at the resonator mirrors, and the inherent separation of the radiation and electron beams simplifies both radiation output coupling and the use of a depressed collector for spent electron beam energy recovery. A new experiment is underway which uses an external millimeter-wave source to prebunch the electron beam in an upstream open resonator. This experiment is currently investigating mode priming, efficiency enhancement, and phaselocking in a quasioptical gyroklystron configuration.

The term *mode priming* refers to using an external source to select one of several modes during the growth of the rf fields in the output resonator. The EIO can be used to prebunch the electron beam at a frequency which will preferentially excite one of several modes in the output resonator during the rise of the voltage pulse. If this mode is stable with respect to decay into sidebands, it can grow and nonlinearly suppress neighboring modes. Thus, mode priming will result in a more highly detuned mode with higher efficiency than the free-running oscillator case. It should be stressed that the external pulse is used only during the build-up of fields and does not contribute to the stability of the steady state. The final equilibrium is determined by the nonlinear interaction of the longitudinal modes in the output resonator. Some of the results of the present study should prove useful to other highly overmoded devices where mode competition is a problem, such as conventional cavity gyrotrons and free electron lasers.

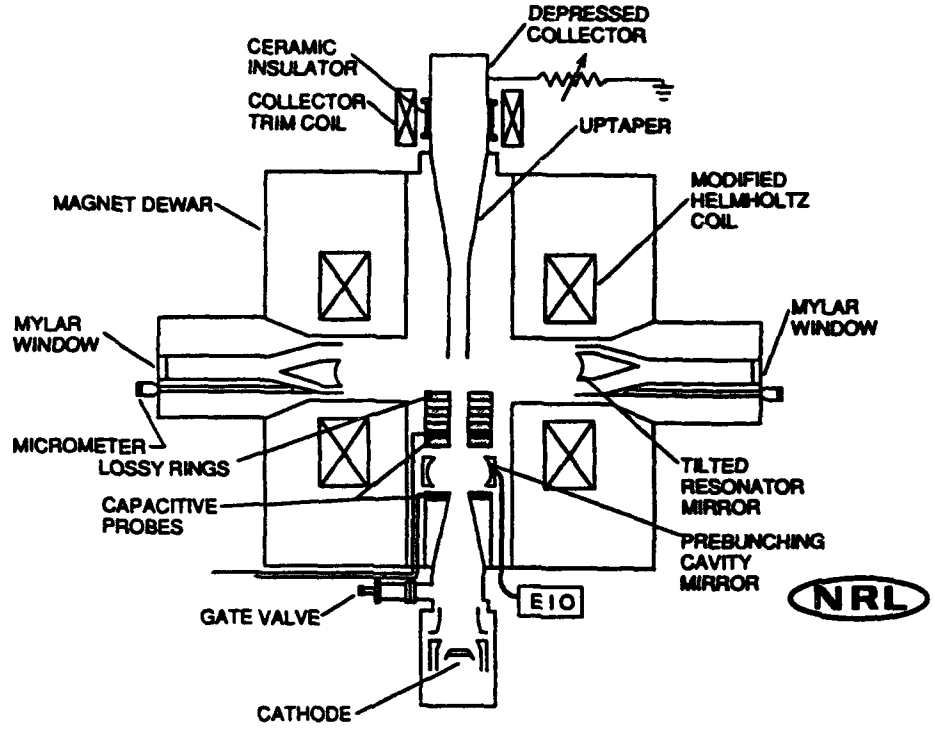


Figure 1: Schematic diagram of the quasioptical gyroklystron experiment.

Experimental Set-up

A schematic diagram of the quasioptical gyroklystron experiment is shown in Figure 1. The magnetic field is produced by a pair of modified Helmholtz coils in a cold-bore superconducting magnet with a crossbore. The magnetron injection gun (80 kV, 50 A) is mounted to a flange on the bottom of the magnet dewar and produces an annular electron beam in the fringing field of the coils. The pitch ratio of the beam electrons ($\alpha = v_\perp / v_\parallel$) is controlled by changing the voltage applied to the intermediate anode of the electron gun via a resistive divider. The collector is located outside the magnet dewar and is electrically isolated from the rest of the experiment. This allows for depressed collector experiments by adding different resistances between the collector and ground. A trim coil is used so that nearly all of the beam current reaches the collector and is not intercepted by the uptaper.

The main resonator, located in the crossbore, comprises a pair of 5.5 cm-diameter mirrors with 38.7 cm radii of curvature. The resonator axis is tilted by $\sim 2^\circ$ relative to the plane perpendicular to the electron beam. Tilting the resonator axis allows each electron to interact with both even and odd longitudinal modes in the output resonator, which is predicted to increase the efficiency and region of stable, single-mode operation[4]. The output resonator mirror holders are mounted on precision micrometers so that the separation and alignment can be varied from outside the magnet dewar. A continuously tunable output resonator is

particularly important in a gyroklystron experiment where the electrons should be bunched at the resonant frequency of the output resonator.

The drift tube is composed of alternating copper and ceramic rings to load spurious gyrotron oscillations in the high magnetic field region. A pair of capacitive probes are installed in the drift tube before and after the prebunching resonator. These probes are used to determine the average α of the beam by measuring the longitudinal charge density. The drift tube is interrupted for 5 cm to allow for the prebunching resonator, which is formed by a pair of 3.1 cm diameter mirrors with radii of curvature 20 cm. The EIO signal is coupled into the prebuncher through a 1.8 mm diameter coupling hole in one of the mirrors. The other mirror also has a coupling hole to monitor millimeter waves in the input resonator. The coupling aperture excites the TEM_{00} mode in the prebuncher with a total Q of 2000. The low-Q prebunching resonator is required to prevent oscillations in the input resonator, since strong oscillations will introduce a large energy spread on the beam and spoil the interaction in the output resonator. The input and detected signals are transmitted using standard WR-10 rectangular waveguide through vacuum windows mounted near the electron gun. The external source is a 1.5 kW, 85 GHz EIO with ± 1 GHz tuning and a variable pulse width up to 2 μsec. The voltage pulse produced by the gyrotron modulator has a 13 μsec flat top, although it can be shortened to 2 μsec by removing elements from the pulse forming network. The 13 μsec pulse length is used for all of the work presented here.

Experimental Results

A new region of operation of the gyroklystron which has recently been demonstrated is mode priming. The output mirror separation is adjusted so that the two resonators have nearly the same frequency. Typical operating currents are about 5 A so that the prebuncher does not oscillate, with a measured beam pitch ratio of $\alpha = 1.9$. The rf pulse is displayed on the oscilloscope and the frequency is measured continuously using a heterodyne technique and band-pass filters. The gyrotron operates in a series of longitudinal modes with frequency separation $\Delta f = c/2L \sim 700$ MHz, where L is the mirror separation. The output of the gyrotron is single-moded, and the frequency detuning and efficiency increase with increasing cathode voltage. As the voltage is increased past the maximum value for a particular longitudinal mode, mode skipping occurs between the desired mode and a lower frequency, less-detuned mode. The output pulse skips from one mode to another on a pulse-to-pulse basis, determined by the noise present in the output resonator during the rise of the voltage pulse. A further increase in voltage results in 100% of the pulses occurring in the low frequency, low efficiency mode.

The EIO is used to prime the desired high-frequency mode near a cathode voltage where mode skipping begins. The EIO signal is injected on the rise of the voltage pulse to prebunch the electron beam. This bunched beam preferentially excites the 85.55 GHz mode, since the prebunching is much stronger than the noise present at the frequency of the competing mode.

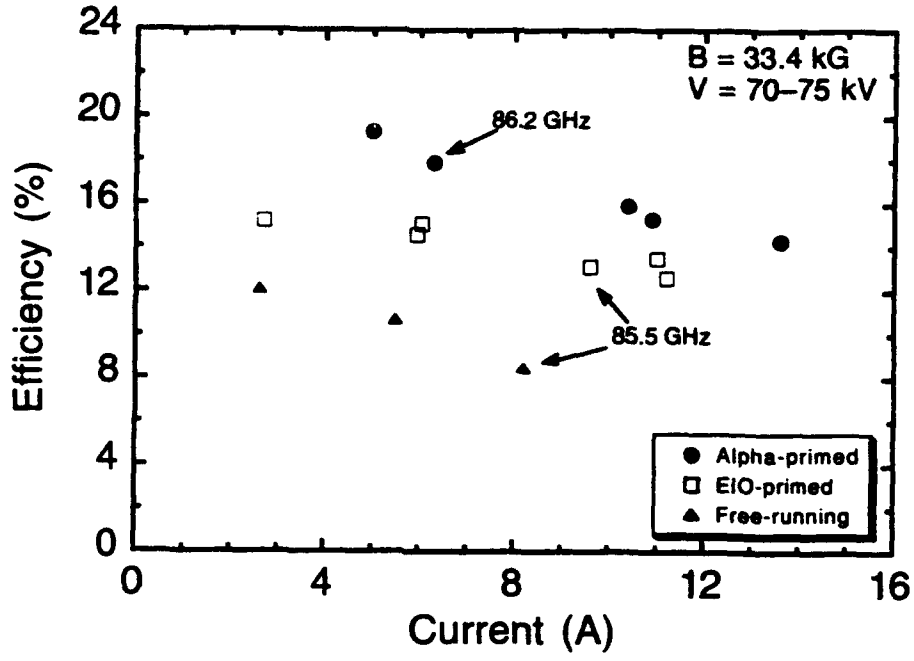


Figure 2: Efficiency versus beam current for the gyroklystron for three regimes of operation.

Now, 100% of the pulses occur in the desired mode, and the cathode voltage may be increased, which increases the detuning, to further increase the efficiency over the free-running oscillator value. The 2 μsec EIO pulse is used only during the rise of the 13 μsec gyrotron pulse, and has no effect on mode selection if it occurs too early or after the flat-top has been reached.

The limit to EIO mode priming occurs when mode competition becomes a problem. Here the 85.5 GHz mode grows to saturation but is unable to suppress the competing mode at lower frequency. This 84.8 GHz mode takes over later in the 13 μsec pulse and causes the efficiency to drop due to the lower frequency detuning. This behavior is in contrast to the free running oscillator, where mode skipping occurs when the voltage maximum is surpassed for a particular mode.

A comparison of free-running and mode-primed operation is shown in Figure 2, where the efficiency is plotted as a function of beam current. Typical free-running oscillator efficiencies are on the order of 10%, while the mode-primed data are approximately 15%. These results demonstrate the benefit of increased voltage and increased detuning by using the EIO to seed the desired mode during the rise of the voltage pulse. The trend of falling efficiencies at higher currents is due to the need to reduce the electron beam α so that the prebuncher does not oscillate.

Another set of data points are plotted in Figure 2 denoted as alpha primed. These are

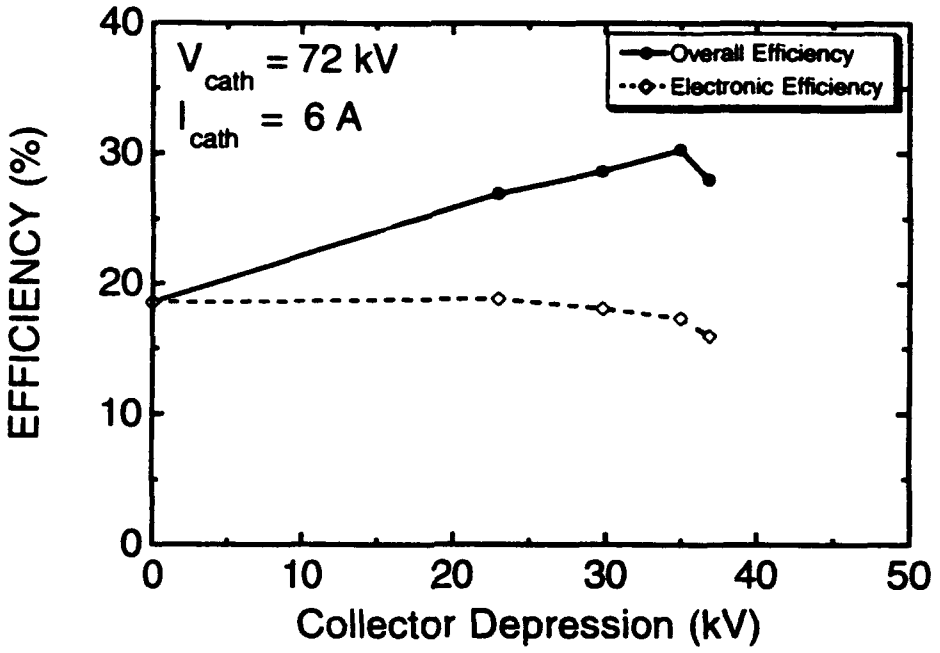


Figure 3: Efficiency versus collector voltage depression for the gyroklystron.

obtained by making α large during the rise of the voltage pulse by adjusting the capacitance in the intermediate anode circuit. Previously, α reached its maximum value on the flat-top of the voltage pulse, whereas in alpha priming it occurs during the rise at lower voltage. This excites a high frequency mode since $\omega \cong \Omega/\gamma$, where γ is the relativistic mass factor. This mode is highly detuned during the flat-top of the pulse and effectively suppresses competing modes. The limit for alpha priming is similar to that for EIO mode priming: competition from a low-frequency mode later in the pulse. This highly-detuned mode is obtained by varying the electron beam parameters on the rise of the voltage pulse and does not require any prebunching using the EIO.

The overall efficiency of the quasioptical gyroklystron can be further increased by depressing the collector. This is accomplished by adding different resistances between collector and ground. The performance of the gyroklystron is shown in Figure 3 as a function of collector voltage depression. The gyrotron is operated in the alpha-primed regime with an electronic efficiency of 19% at a current of 6 A and 72 kV beam voltage. The maximum efficiency obtained is 30% for a collector depression of 35 kV, which corresponds to a collector efficiency of 50%. If the depression is increased further, electrons begin reflecting from the collector and rapidly degrade the oscillation in the main resonator. This work demonstrates that relatively high overall efficiencies can be obtained for high values of α and electronic efficiency.

Conclusions

An 85 GHz quasioptical gyroklystron has been designed, assembled, and is currently under test. The EIO has been used to mode prime the gyroklystron during the build-up of fields during the rise of the voltage pulse, resulting in 16% electronic efficiency. Mode priming allows for higher detunings and higher efficiencies over the free-running oscillator case. A new technique is described called alpha priming, where the α of the beam electrons is made large during the rise of the voltage pulse. This excites an even more highly detuned mode with peak electronic efficiencies of 19%. A depressed collector has been added to further increase the total efficiency to over 30%. It is anticipated that future experiments with higher beam currents would result in even higher efficiencies since the present experiment is not optimized to run at 6 A. Phase-locking studies are presently being performed where the gyrotron is phase locked to the EIO via prebunching the electron beam.

Acknowledgements

This work was supported by the Office of Fusion Energy of the U.S. Department of Energy and by the Office of Naval Research.

References

[1] P. Sprangle, J. L. Vomvoridis, and W. M. Manheimer, "Theory of the quasioptical electron cyclotron maser," *Phys. Rev. A*, vol. 23, no. 6, pp. 3127-3138, June 1981.

[2] T.A. Hargreaves, A.W. Fliflet, R.P. Fischer, M.L. Barsanti, W.M. Manheimer, B. Levush, and T.M. Antonsen, Jr, "Tilted resonator experiments on a quasioptical gyrotron," NRL Memorandum Report 6887, Sept. 16, 1991.

[3] T.A. Hargreaves, A.W. Fliflet, R.P. Fischer, and M.L. Barsanti, "Depressed collector experiments on a quasioptical gyrotron," *Phys. Fluids B*, vol. 3, no. 11, pp.3171-3176, Nov. 1991.

[4] T.M. Antonsen, Jr, B. Levush, and W.M. Manheimer, "Stable single mode operation of a quasioptical gyrotron," *Phys. Fluids B*, vol. 2, no. 2, p. 419, 1990.

LARGE ORBIT GYROKLYSTRON DEVELOPMENT AT LOS ALAMOS

R. M. Stringfield, R. M. Wheat, D. J. Brown, M. V. Fazio, J. Kinross-Wright, B. E. Carlsten, G. Rodenz, R. J. Faehl, R. F. Hoeberling

Los Alamos National Laboratory, Los Alamos, New Mexico, 87545

ABSTRACT

We have designed and are testing a large orbit gyroklystron amplifier for 1.3 GHz operation in 70 ns pulses. The ultimate power output goal is 500 MW with a gain in excess of 20 dB. This initial investigation is intended to lay the groundwork for operation at 11.4 GHz for particle accelerator applications, and also at frequencies of up to 35 GHz for other uses. Computational design has been performed with the resonant cavity code MAFIA and the particle in cell codes MERLIN and ISIS. Experimental measurements of the resonator modes were correlated with computational and analytical predictions. Electron beam optics through a magnetic cusp was also studied with ISIS and MERLIN, and verified experimentally, to develop a suitable electron beam trajectory from the diode into the resonator region. Performance tests of a single stage device have just begun. The device is intended in its final form to use two resonators separated by an electron beam drift pipe.

Introduction

A large orbit gyrotron (gyroklystron) (LOG) amplifier operating at 1.3 GHz is being developed to operate at powers of up to 500 MW for 70 ns pulses. While this initial investigation is being performed at 1.3 GHz, this device can be scaled to higher frequencies in a straight forward fashion. LOG oscillators have operated at 15 GHz and higher frequencies with comparable performance to that at lower frequencies. Amplifier operation has been examined theoretically and experimentally, but less extensively [1-4].

These devices produce microwaves by the interaction of a helically rotating electron beam with the oscillating fields of a resonant cavity structure. The beam is formed by injecting a hollow, non-rotating beam, born in an axial magnetic field, through a magnetic cusp positioned at the anode plane. An annular slot is cut into the mild steel cusp plate to allow the beam to pass into the downstream resonator. In the cusp, a portion of the axial beam energy is converted to rotational energy. Typical ratios of rotational velocity to axial velocity (defined as alpha) are in the range of 1.5 to 2.5. The electron beam entering the resonator has an energy of 500-700 keV, a current of 1-2 kA, and a radius of 5-8 cm. The device, shown in Figure 1, employs a cylindrical resonator with three vanes in the wall spaced equally in azimuth.

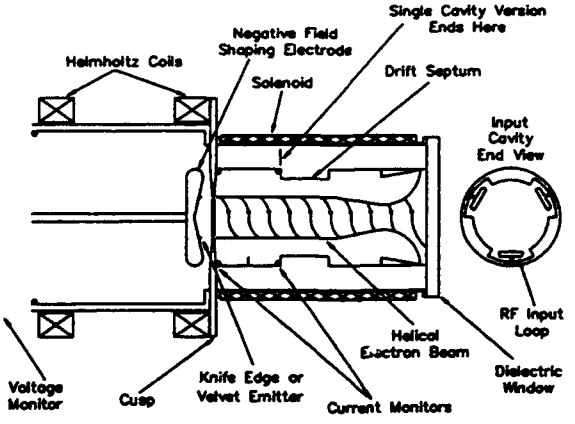


Figure 1. Large orbit gyrotron and gyroklystron geometry. Two resonator stages are shown, although single stage operation also will be investigated.

Two approaches to the amplifier are being considered: a single resonator device and a staged two resonator device. Both approaches will use cylindrical resonators of the type describe above. The vane structure is used to evoke coupling of the rotating electron beam with the TE(0,1,n) resonant cavity mode of the cylindrical structure by modifying the normally circular electric field pattern of the mode into a scalloped pattern, similar to the TE(3,1,n) mode, but near the lower TE(0,1,n) frequency for a non-vaned cylindrical wall with an intermediate radius. The single stage device has a closed boundary on the end of the cylinder where the beam enters. The other end is open, and serves as the beam exit and rf output port. Rf is fed into the cavity using two loops, one in each of two of the vanes at the axial midplane. The standing wave pattern of the cavity will couple to the rotating beam, provided the beam angular velocity is in synchronism, in such a way that an azimuthal density perturbation will grow on the beam with three density maxima around the azimuth. The magnitude of the density variation will grow as the beam propagates down the length of the resonator, influenced both by the applied oscillating fields, and the space charge self fields of the beam that drive the negative mass instability. The instability will grow as the electron beam propagates through the system. Feedback from the beam instability drives the cavity fields to greater amplitude.

The two stage device has two such resonators, which allow the processes of bunch inception, growth, and rf power extraction to be performed in separated regions, enabling freer optimization of each process with less coupling among them. The first cavity accepts rf input through a loop coupler, and is similar in design to the single stage resonator, except that the downstream end is closed off by an annular metallic plate. The central opening forms the entrance to a cylindrical, non-vaned electron beam drift pipe. The pipe is intended to serve the role of an rf isolating sever between the first and second cavities, and also as a region in which the beam bunching can grow by the negative mass instability, independent of applied microwave fields. An optimum drift pipe length will be determined experimentally to maximize azimuthal beam bunching. A second, output resonator designed to be strongly coupled to the beam will be place downstream of the drift pipe at the point of optimum beam bunching to extract rf energy. Mode converters suitable for transforming the TE01 circular waveguide mode of the output resonator into TE10 rectangular waveguide mode have been thoroughly studied since the 1950's. [5,6].

LOG Amplifier Design and Testing

Work performed to date has consisted of theory and experiments to improve the electron beam injection through the cusp and propagation through the resonator, and computational modelling, design, fabrication, and cold test of the 1.3 GHz LOG resonators. Experimental tests of the single stage amplifier with injected electron beam have just begun.

Computational Electron Beam Diode Studies

This investigation was motivated by the desire to inject as much current into the resonator as possible, while maintaining stable beam placement in the interaction space of the microwave circuit. Particle-in-cell computer modelling was performed using the 2 dimensional versions of ISIS and MERLIN to survey alternative configurations. Measured magnetic field profiles of the experimental configuration were used in the calculations. Parameters varied in the survey included the negative electrode shape, the radius and width of the electron emission annulus on the negative electrode, the width of the annular slot in the anode that allows the beam to pass through the cusp into the resonator, and the spacing between the anode and cathode.

Preliminary studies were performed with a computational technique known as synthesis. This technique steps the particles backward in position and time from the final state of the system (beam current,

position, and velocity components), to determine the initial conditions (emission electrode position, shape, and potential) which lead to them, and a satisfactory trajectory through the device.

An acceptable synthetically generated diode configuration, shown in Figure 2, consists of a cathode emission annulus with a diameter of 14-14.2 cm, situated on a conical equi-potential surface at an angle of 67.5 degrees with respect to the symmetry axis. The distance between the emission annulus and the anode was 2.2 cm, yielding an cathode electric field of 300 kV/cm at a voltage of 650 kV. The annular opening at the anode through which the beam passes into the resonator drift section has a mean diameter of 12.5 cm and is 1 cm wide.

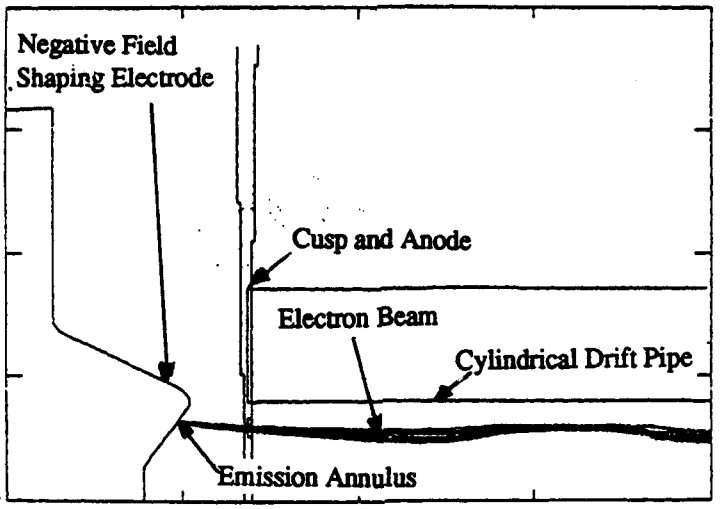


Figure 2. Particle-in-cell computer model of the baseline design of a suitable electron beam diode and transport geometry.

The synthetic computation was the starting point for conventional calculations of beam dynamics moving forward in time. A conventional run using the diode and drift pipe parameters found from the synthetic calculations agreed with the synthetic calculation prediction. All of the current emitted from the cathode, up to a maximum of 2.7 kA, passed through the cusp and drifted with little radial oscillation in the resonator region. Three aspects of these initial conditions given us by the synthetic prediction (the emitted current, the inter-electrode separation, and emission annulus width) were varied in subsequent studies to assess the performance degradations which might result from accommodating experimentally achievable conditions, such as a wider cathode emission annulus and a greater inter-electrode separation. Increasing the cathode emission annulus width from the initial case of 1 mm to 5 mm and the electrode gap to 3 cm from the earlier 2.2 cm reduced the transmitted current to 1.8 kA out of an emitted current of 3 kA. An electrode gap of 3.8 cm reduced the propagated current to 1.5 kA out of an emitted 3.5 kA. Alpha, the ratio of azimuthal velocity to axial velocity, ranges from 2 near the cusp, to 4 farther downstream, where the rotating beam piles up due to an increased electrostatic potential depression farther in the tube.

Experimental Diode Results

Diode hardware was built with the guidance of the computer modelling. The experimental diode geometry is shown in Figure 1. A cathode electric field shaping surface, angled at 67.5 degrees with the axis of symmetry, was fabricated with a rounded outer radius to minimize unwanted emission from the outer edge of the electrode. Emission was evoked from an annular region of the angled surface either by mounting a knife edged ring or a belt of velvet on the surface as an explosive emission emitter. The diameter of the emitting ring

was varied from 11.4 to 14 cm. Plasma motion of a few cm/microsecond from the cathode modified the effective radius, annular width, and emission surface position somewhat from the initial conditions.

Rogowski current monitors were positioned in the diode, immediately downstream of the cusp in the drift region, and at the end of the drift pipe, 30 cm downstream of the cusp. The voltage monitor was situated about 60 cm behind the diode in an oil insulated region, electrically separated from the diode by 1.6 microhenries of inductance. The drift pipe had no vane structure for these diode experiments, to simulate the conditions of the computer model.

Alpha, the ratio of rotational velocity to axial velocity of the electron beam, was measured by a technique suggested by Professor William Destler [8]. By interposing a quartz plate in the beam path downstream of the cusp, a pattern of the electron deposition at the plate location can be seen in luminosity of the quartz. By attaching a metal rectangle upright on the upstream side of the quartz at the radius of the beam, a shadow is cast on the quartz by the metal obstruction. The ratio of the length of the shadow to the height of the obstruction is a determination of alpha.

Alpha was measured in this manner for a 1.75 kA beam emitted from a velvet surface having a mean diameter of 14.2 cm and a width of 0.5 cm. Alpha was measured to be in the range of 1.5 to 2.0 for a magnetic field of 400 gauss, and in the range of 2.0 to 2.5 with a magnetic field strength of 500 gauss. This set of conditions most closely matched those found by the computer modelling to provide good beam transport.

The results using the knife edge emitters provided similar current transmission, but not at the emission radius of the computer model. The discrepancy may be due to the emission occurring not in the flat surface of the field shaper, but instead, above it a height of 6 mm. Proper current transmission with the knife edge occurred with a knife edge emission ring diameter of 12.8 cm at a field of 500 gauss on the cathode emission surface.

Using a knife edge emitter with a diameter of 12.4 cm, a magnetic field of 300 to 400 gauss, and a diode voltage of 700 kV, 3 kA was transported past the cusp with an alpha of 1.5. Waveforms for this case are shown in Figure 3. These lower magnetic field conditions are those anticipated for the 1.3 GHz amplifier experiments. The computer study did not include these parameters in its investigation, but rather had used values of magnetic field of 500 gauss at the cathode, based upon the needs of an amplifier designed for higher frequency.

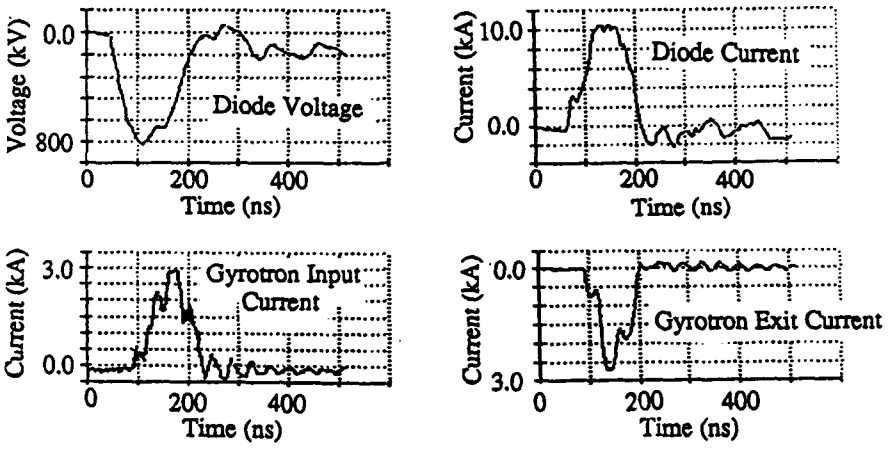


Figure 3. Waveforms for the diode voltage, diode current, current immediately downstream of the cusp, and 30 cm downstream. The magnetic field at the cathode was 330 gauss.

Studies of the Resonant Cavity Modes

An extensive study of the cavity modes of the resonant structure for this device has been performed using the electromagnetic field solving code MAFIA, analytic modelling,and cold test measurements of structures performed with a vector network analyzer. The modes found with MAFIA were in general agreement with an analytical approximation of the cavity as a smooth walled cylinder. Cold test measurements were consistent with both MAFIA and the analytic calculations. Figure 4 shows the frequencies measured with a network analyzer connected to magnetic loop probes in the cavity, oriented to couple to the TE(0,1,n) modes. The peak of interest, the TE(0,1,0.5) mode, oscillates at 1,280 Hz. Figure 5 shows the MAFIA calculated electric field pattern for this mode at 1277 MHz, showing good agreement with the cold test measurement. As a one stage device, the cavity has a Q of 45. As a two stage device, the first stage Q will be much higher, of the order of several hundred, but has not been established. The output cavity Q of the two stage device will be similar to that of the single stage resonator, in the range of 25 to 100.

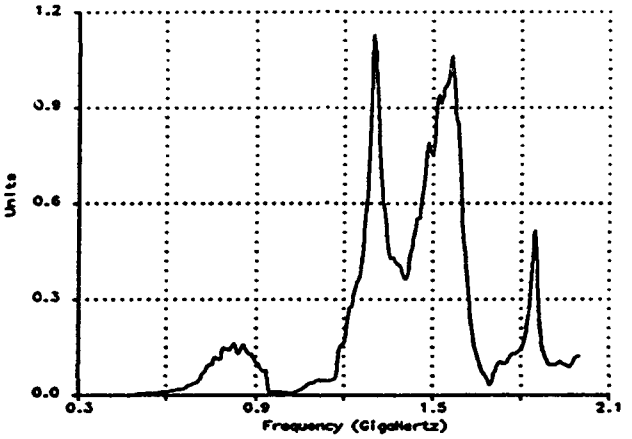


Figure 4. Linear plot of relative signal amplitude vs frequency in the resonant cavity of the single stage device. One cylinder end is open. Strong resonance is seen at the desired frequency of 1280 MHz.

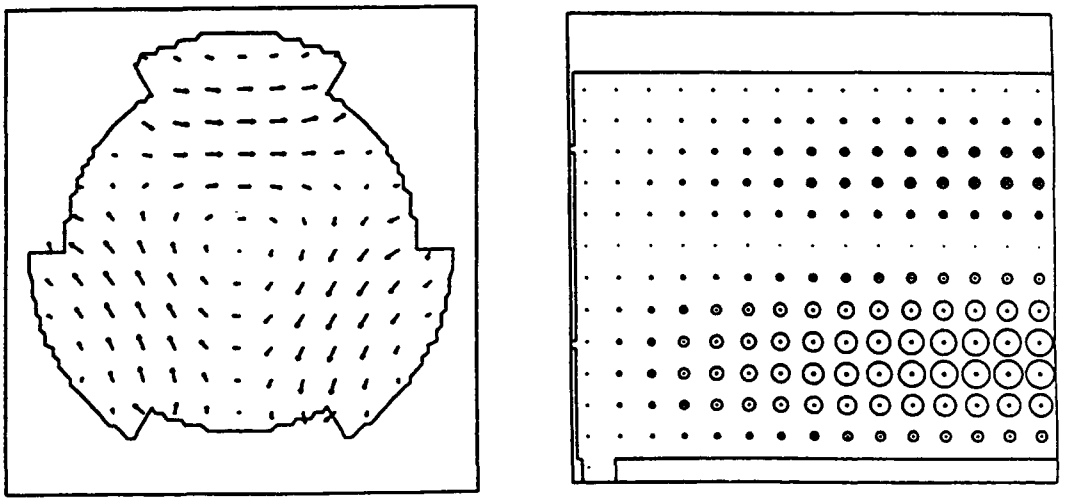


Figure 5. MAFIA electric field map for the single open ended resonator resonating at 1277 MHz.

Experimental Plans

Experiments to measure amplifier operation recently have begun. The experimental configuration consists of the diode, cusp and magnetic field coils, downstream resonator section, and a dielectric vacuum window for radiating the microwavesinto an anechoic volume downstream of the vacuum chamber. A 1 kW 1.3 GHz source provides rf input drive to the resonator in these initial studies. Up to 20 MW is available as input drive but will require device modifications for aperture coupling to accommodate the power. Presently, magnetic loops are situated at the base of two of the vanes for cavity input drive. A loop in the third vane is used to monitor the standing wave field in the cavity. A standard gain horn is positioned in the anechoic volume downstream of the open resonator end to monitor the radiated power in the far field.

We intend to evaluate amplifier performance by comparing the radiated microwave power in three different circumstances. First, the radiated power due to the 1 kW input drive alone will be measured. Second, the radiated power with no input drive, but with the electron beam injected, will be measured. Finally, the radiated power when both input rf drive and injected electron beam are present in the resonator will be measured. Amplifier performance will be attributed to the added power produced when both the electron beam and the input rf drive are present. The total power will be measured in initial experiments by performing a spatial scan of the radiated power density in the far field of the radiating aperture and integrating over the radiated area.

Summary

The study and construction of a large orbit gyrotron and two stage gyroklystron amplifier are underway. Modelling and experiments have been performed to design these devices. Experiments are ongoing to measure and optimize the performance of the single stage device, in preparation for subsequent two stage operation.

Acknowledgements

The authors would like to express their appreciation to Mrs. Yolanda Martinez, Mr. Donald Holcomb, Mr. Richard Lovato, and Mr. Paul Haddock, for their assistance and support during this effort. The contributions of Professor W. W. Destler in inspiring this work and in sharing his experience with LOG devices has been of great value to this effort. This work has been supported by the Los Alamos National Laboratory Independent Research and Development Program, sponsored by the U. S. Department of Energy.

1. W. W. Destler, et al, "High-power microwave generation from large-orbit devices," IEEE Trans. on Plasma Science **PS-16** (2), April 1988, p71.
2. Y. Y. Lau and L. R. Barnett, "Theory of a low magnetic field gyrotron (gyromagnetron)," Int. J. of Infrared and Millimeter Waves **3** (5), 1982, p. 619.
3. J. Y. Choe, K. Boulais, V. Ayres, W. Namkung, and H. Uhm, "Preliminary study of cusptron amplifier," Microwave and Particle Beam Sources and Directed Energy Concepts, SPIE **1061** (1989) p. 132.
4. K. R. Chu, et al, "Theory, design, and operation of large-orbit high harmonic gyroklystron amplifiers," IEEE Trans. on Plasma Science **PS-13** (6), December 1985, p 435.
5. S. S. Saad, et al, "Analysis and design of a circular TE01 Mode Transducer," Microwaves, Optics, and Acoustics **1** (2), p. 58.
6. S. E. Miller, "Coupled wave theory and waveguide applications," Bell System Journal, May 1954, p. 661.
7. Prof. W. W. Destler, private communication.

THE NRL 11.4 GHZ MAGNICON AMPLIFIER EXPERIMENT

S.H. Gold, C.A. Sullivan, B. Hafizi,† W.M. Manheimer, and W.M. Black
Plasma Physics Division, Naval Research Laboratory
Washington, DC 20375–5000

Abstract

We present a progress report on a program to develop a high–power X–band magnicon amplifier for accelerator applications. The goal of the program is to generate 50 MW at 11.4 GHz with 50% efficiency, using a 200 A, 500 keV electron beam produced by a cold–cathode diode on the NRL Long–Pulse Accelerator Facility. The initial experiment, designed to study the gain from the first (driven) deflection cavity to a second (passive) deflection cavity, has recently begun.

I. Introduction

The magnicon [1–3] is a "scanning beam" microwave amplifier tube related to the gyrocon [4]. Scanning beam devices modulate the insertion point of the electron beam into the output cavity in synchronism with the phase of a rotating rf wave. This synchronism creates the potential for an extremely efficient interaction in the output cavity, since every electron will in principle experience identical decelerating rf fields. In the magnicon, the output interaction is gyrotron–like, and requires a beam with substantial transverse momentum about the applied axial magnetic field. The transverse momentum is produced by spinning up the electron beam in a sequence of deflection cavities, the first of them driven by an external rf source. The deflection cavities employ a mode that rotates at the same angular velocity as the mode in the output cavity. As a result, the beam entering the output cavity is fully phase modulated. The optimum magnetic field in the deflection cavities is twice the cyclotron resonant value at the drive frequency, while the output cavity operates as a first harmonic cyclotron device. These twin constraints lead naturally to the design of a second-harmonic amplifier, in which the deflection cavities operate at half the frequency of the output cavity. The overall design concept is shown in Fig. 1.

In this paper, we discuss a preliminary experiment, employing only two 5.7 GHz deflection cavities, the first driven by an external source. We are performing parametric studies of the gain between these two cavities, preparatory to the design of a complete deflection system that will spin up an electron beam to high α for injection into an 11.4 GHz output cavity, where α is the ratio of perpendicular to parallel velocity.

---

† Permanent address: Icarus Research, Bethesda, MD 20814.

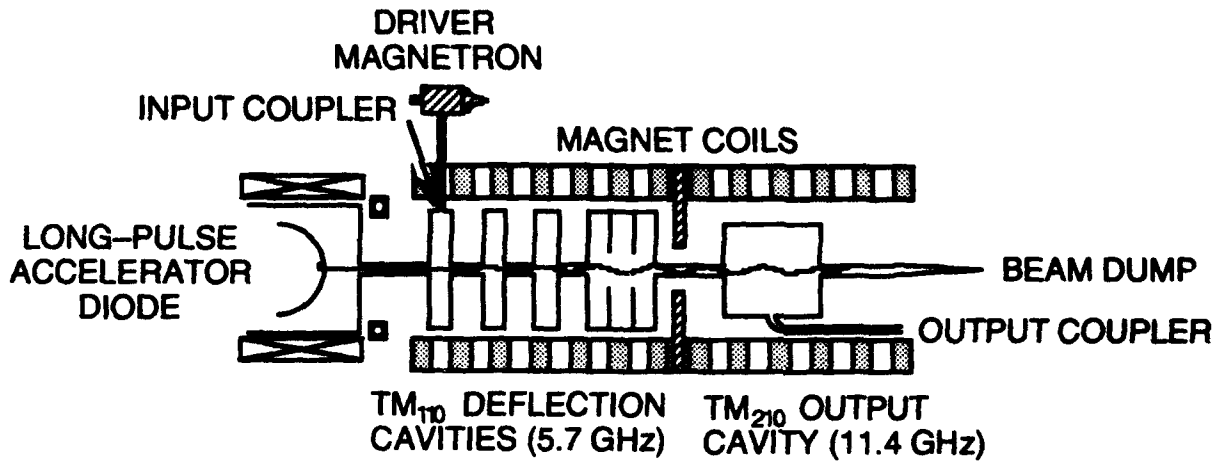


Fig. 1. NRL 11.4 GHz magnicon amplifier concept

II. Apparatus

The first two–deflection–cavity magnicon gain experiment is under way on the NRL Long–Pulse Accelerator Facility [5]. It is shown schematically in Fig. 2. It employs a field emission diode that was designed via the Herrmannsfeldt Code [6] to produce a high quality solid electron beam with minimum diameter and minimum velocity spread. The diode design is shown in Fig. 2. The measured beam parameters are ~200 A at 500 kV, with a beam diameter of ~5 mm at a final magnetic field of 8.1 kG. The Herrmannsfeldt Code predicts a mean α of ~.025. The propagated current is measured by a Faraday cup, and beam cross sections are measured using witness plates.

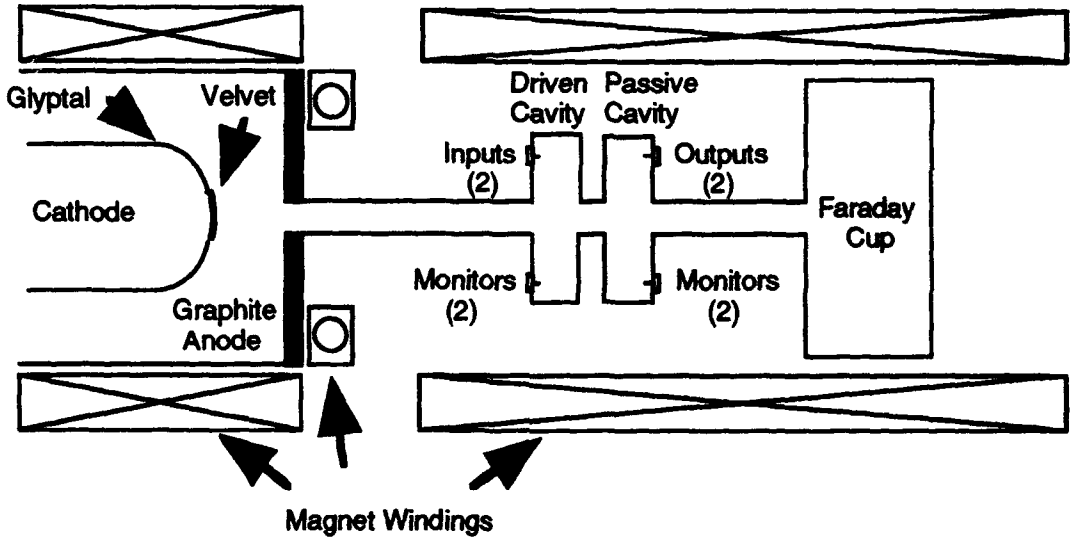


Fig. 2. Schematic of two–deflection–cavity gain experiment

A schematic of a single TM_{110}–mode deflection cavity is given in Fig. 3. There are four coupling ports spaced at 90° intervals in one end–wall of the cavity. Two adjacent pins are "long," for use in driving the cavity in each linear polarization, and the remaining pins are "short," in order to sample the cavity fields without significantly loading the cavity. The design value of the cavity quality factor, Q, is 1000, in each linear polarization, where the primary loading factor is the coupling pins. All the pins are coupled through type "N" connectors to external coaxial cables. The microwave cavities are fabricated from stainless steel, with a copper coating on interior surfaces to increase the ohmic Q. The design of both cavities is identical. The first cavity is driven by a tunable C–band magnetron at ~5.7 GHz.

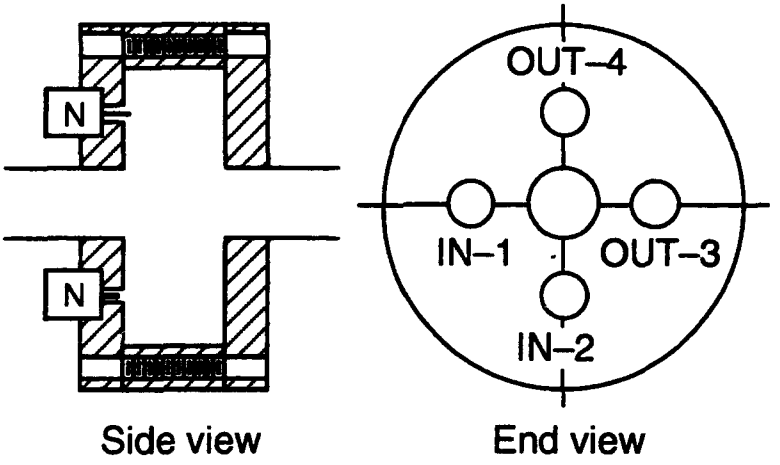


Fig. 3. Schematic of magnicon deflection cavity

The magnicon is designed to employ a circularly–polarized signal in the first cavity, and should generate a circularly–polarized signal in the second deflection cavity. The circularly polarized signals will be generated, and detected, using 3 dB hybrid couplers to drive (or sample) adjacent pins with a $\pi/2$ phase difference. However, the initial experiments are under way without 3 dB hybrids, and employ a linearly polarized signal in the driven cavity. The coupling port in the orthogonal linear polarization is terminated in a matched load, in order to maintain the design Q value. All of the coupling and sampling ports of each cavity are fully calibrated.

III. Magnicon theory and simulation

The linear theory of the magnetized deflection cavities was first presented by Karliner, *et al.* [1], and is developed in detail by Hafizi, *et al.* [7]. The linear theory has been evaluated for a single on–axis electron, with no initial transverse momentum, and without

finite beam radius and finite velocity spreads. Furthermore, it assumes that the electron energy is not changed by transit through the deflection cavities. In order to consider the use of more realistic beam parameters, such as are predicted by the diode simulation discussed above, and to model the variation of beam kinetic energy in the deflection cavities, a numerical simulation code for the deflection cavities was developed [7]. It is a self–consistent steady–state code that propagates particles through the TM_{110} fields of the first (driven) deflection cavity, through a drift space, and then through successive deflection cavities, followed by drift spaces. The rf field amplitudes are made (by iteration) self–consistent with the finite value of cavity Q and with the energy lost by the electron beam in transit through each cavity. The rf phase in each of the passive cavities is assumed to be the optimum phase to extract electron beam energy from an initially on–axis electron, since this should be a good approximation to the phase that is driven by a finite electron beam.

IV. Results

In the first experimental test of microwave gain and beam frequency–pulling effects, the first deflection cavity was driven by a tunable C–band magnetron in a linearly–polarized TM_{110} mode through a single coupling pin. A sampling pin was used to diagnose the linearly–polarized signal in the driven cavity. The remaining pins of the first cavity lead to matched loads. The signal in the second cavity was measured, in either linear polarization, by means of the sampling pins, with the larger coupling pins terminated to preserve the Q of 1000 seen in the cold tests.

In the first set of measurements, the magnetron frequency was varied to directly measure the intercavity gain and bandwidth, and to observe the frequency pulling effect of the beam on the cold cavity resonant frequency. A signal gain of ~6 dB was observed, into a single linear polarization of the output cavity, with a comparable signal in the orthogonal polarization, for a total gain of 9 dB. Theory suggests that only one circular polarization is effective in driving the interaction. Correcting for this as well leads to an apparent gain of ~12 dB, compared to ~13 dB predicted by theory and simulation. In addition, a frequency detuning of the first cavity is observed, due to the presence of the beam. This detuning is approximately –0.2%, in good agreement with the predictions of theory.

V. Discussion

This first two–cavity gain experiment has demonstrated gain between a driven and a passive deflection cavity relevant to a future magnicon device. This gain is being studied as a function of macroscopic beam parameters (current, voltage) and magnetic field. The initial results compare well to predictions of theory. For the present experiment, a measurement of

intercavity rf gain can be used to infer the amount of coherently phased transverse momentum (beam α) that has been produced. However, the driven α is still small, and cannot be directly measured without the addition of further gain cavities. In future experiments, additional deflection cavities will be employed, in order to study the coherent spin–up of the electron beam to high α for injection into a magnicon output cavity. The effect of velocity spread on the gain in the present experiment is predicted to be small. However, it will affect the quality of the final high α electron beam delivered to the output cavity. The real test of the final multicavity deflection system will be to produce a high α electron beam without excessive spreads in α or in gyrophase, and without employing excessively large rf electric fields in the final deflection cavity.

VI. Summary

The NRL X–band magnicon amplifier experiment has begun its initial experimental operation. The first experiments are examining only the deflection cavities, and are intended to measure the gain and beam loading in a pair of deflection cavities, the first driven and the second passive. The initial results show an apparent gain of ~12 dB between a driven and a passive deflection cavity, accompanied by a frequency shift of approximately –0.2%, in good agreement with the predictions of theory and numerical simulation.

Acknowledgments

This work was supported by the U.S. Department of Energy, under Interagency Agreement No. DE–AI05–91ER40638, and by the Office of Naval Research.

References

[1] M.. Karliner, E.V. Kozyrev, I.G. Makarov, O.A. Nezhevenko, G.N. Ostreiko, B.Z. Persov, and G.V. Serdobintsev, "The Magnicon—An Advanced Version of the Gyrocon," *Nucl. Instrum. Methods Phys. Res.*, vol. A269, pp. 459–473, 1988.

[2] O.A. Nezhevenko, "The Magnicon: A New RF Power Source for Accelerators," in *Conference Record—1991 IEEE Particle Accelerator Conference*, edited by L. Lizama and J. Chew [IEEE, New York, 1991], p. 2933–2942.

[3] W.M. Manheimer, "Theory and Conceptual Design of a High–Power Highly Efficient Magnicon at 10 and 20 GHz," *IEEE Trans. Plasma Sci.*, vol. 18, pp. 632–645, 1990.

[4] G.I. Budker, M.M. Karliner, I.G. Makarov, S.N. Morosov, O.A. Nezhevenko, G.N. Ostreiko, and I.A. Shekhtman, "The Gyrocon—An efficient relativistic high–power vhf generator," *Part. Accel.*, vol. 10, pp. 41–59, 1979.

[5] N.C. Jaitly, M. Coleman, S. Eckhouse, A. Ramrus, S.H. Gold, R.B. McCowan, and C.A. Sullivan,"1 MV Long Pulse Generator with Low Ripple and Low Droop," in *Digest of Technical Papers—Eighth IEEE International Pulsed Power Conference*, edited by K. Prestwich and R. White (IEEE, New York, 1991), pp. 161–165.

[6] W.B. Herrmannsfeldt, "Electron Trajectory Program," Stanford Linear Accelerator Report No. 226, 1979.

[7] B. Hafizi, Y. Seo, S.H. Gold, W.M. Manheimer, and P. Sprangle, "Analysis of the Deflection System for a Magnetic–Field–Immersed Magnicon Amplifier," *IEEE Trans. Plasma Sci.*, in press.

HIGH PERFORMANCE 33.2 GHZ GYROKLYSTRON

J. D. McNally, M. P. Bobys, D. B. McDermott, and N. C. Luhmann, Jr.

Department of Electrical Engineering
University of California, Los Angeles 90024

Abstract

The design for a high performance, 33.2 GHz three-cavity gyroklystron has been completed. The design modifies Varian's pioneering 28 GHz gyroklystron in order to suppress oscillation and yield higher gain and efficiency. Modifications include an additional buncher cavity, lower beam α, and a slight increase in frequency. Self-consistent simulation for an axial velocity spread of 7% and α=1.5 predicts an output power of 250 kW with a saturated gain of 52 dB and an efficiency of 39%. An investigation of penultimate cavity detuning showed no improvement in efficiency for the above velocity spread. A synchronously tuned gyroklystron is currently being constructed.

I. Introduction

Applications for high power sources in the millimeter to submillimeter wave region include radar, communications, high-gradient linear accelerators, and electron cyclotron heating (ECH) of fusion plasmas. Gyro-devices have emerged as a prime candidate for high power sources in this region. The gyroklystron circuit resembles a linear klystron except that the beam-wave interaction can be extended over many wavelengths. In the driver cavity of a gyroklystron, a weak rf field modulates the electrons' energy which initiates phase bunching. Because of the weak field, linear analysis may be used to accurately describe this region. The electrons continue to inertially bunch in phase as they traverse the drift tube. Additional bunching cavities can be added to increase the gain and/or efficiency. In these cavities, the field generated by the modulated beam current serves to further modulate the electrons' velocity. Finally the output cavity is designed to generate high power. The output cavity is generally partially closed at one end and tapered at the other end to facilitate the removal of the microwave energy. Nonlinear analysis is usually required in the penultimate and output cavities. The electron beam will be generated by a magnetron injection gun (MIG)[1] which is routinely used in gyro-devices because it gives a beam with a fairly low velocity spread and a high percentage of transverse velocity.

Other gyroklystron experiments have been constructed using MIG beams. Varian designed a 28 GHz gyroklystron for ECH applications with a circular TE_{01} input cavity and a circular

TE_{02} output cavity. Severe oscillation problems were encountered, but after some redesign an output power of 50 kW was obtained[2]. Efficiency remained under 10%. More recently NRL built a 4.5 GHz three-cavity gyroklystron with TE_{10} rectangular cavity modes and achieved an output power of 50 kW with an efficiency of 21%[3]. The University of Maryland has recently tested their high power 9.87 GHz two-cavity gyroklystron with TE_{01} circular cavity modes and obtained an output power of 20 MW with an efficiency of 31%[4].

II. Design of a Three-Cavity, 33.2 GHz Gyroklystron

The purpose of this experiment is to improve Varian's gyroklystron, which was tested in 1977. An additional buncher cavity has been added to increase gain and the design was completed with a lower α for better stability. The drift tube will be loaded with a thin ceramic tube with a lossy inner coating as used in the recent and successful gyro-TWT experiment at NTHU[5]. The frequency has been increased to 33.2 GHz and the magnetic field was optimized for the new frequency.

A self-consistent computer code[6] written by K. R. Chu for the University of Maryland's high power gyroklystron was used to optimize parameters for the new design. The code can perform either a linear or nonlinear analysis of each cavity. Additionally, it allows for beam loading of the cavities, beam velocity spread, and a radial guiding center spread. The code was used to successfully predict the results of the University of Maryland gyroklystron and UCLA's fifth harmonic, large-orbit gyroklystron[7]. As shown in Figure 1, the code was also used to simulate Varian's experiment. For an ideal beam, our code predicts a saturated output power of 280 kW, which agrees with Varian's computations[2]. For 10% axial velocity spread, however, our code finds that the efficiency falls to 10%, which agrees quite well with Varian's experimental results of an output power of 50 kW. Since Varian's gun code predicted an axial velocity spread of 11%, velocity spread does appear to have contributed considerably to their gyroklystron not performing to design specifications. Because axial velocity spread scales with α^2, our proposed gyroklystron will use a lower α of 1.5 in order to reduce the effects of velocity spread.

The parameters of the new design along with simulation results can be seen in Table I. For an ideal beam, the code predicts an optimum output power of 300 kW, 54 dB saturated gain, and 46% efficiency. Using a more realistic axial velocity spread of 7%, the output power is predicted to reach 250 kW with an efficiency of 39% and a saturated gain of 52 dB, which does not include the 3 dB loss associated with exciting the driver cavity in linear polarization.

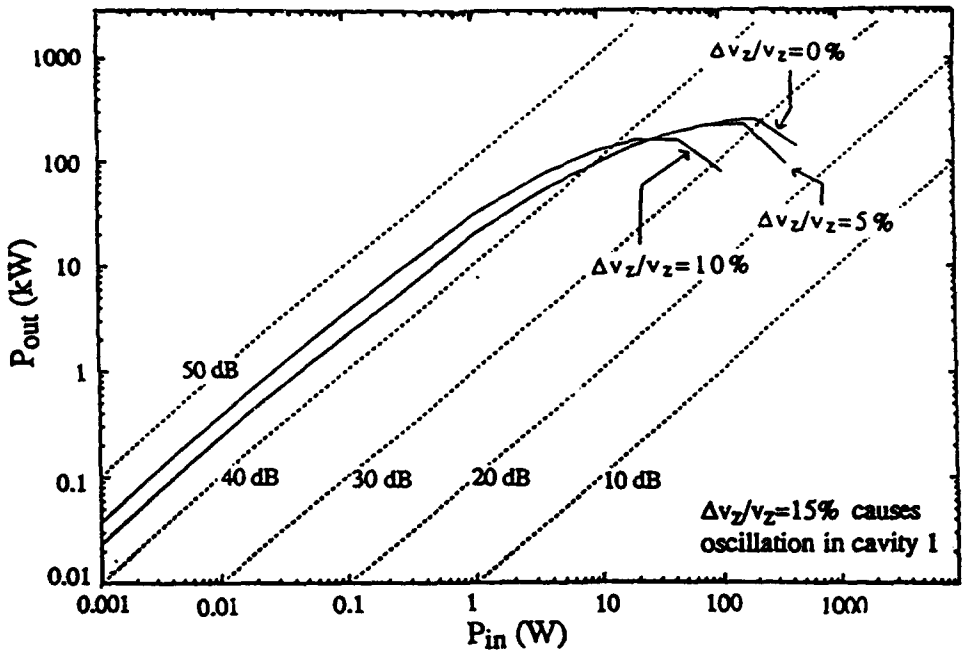


Figure 1. Simulation results for Varian's 28 GHz gyroklystron for several values of axial velocity spread. (V=80 kV, I=8 A, α=2, TE_{01} buncher cavity with L=1.5λ and Q=500, TE_{02} catcher cavity with L=2λ and Q=200, L_{drift}=5λ.)

Table I. Design Parameters of the Three-Cavity 33.2 GHz Gyroklystron

Beam Parameters			
Voltage	80 kV		
Current	8 A		
B-field	12.4 kG		
α	1.5		
$\Delta v_z/v_z$	7%		
Cavity Parameters			
	1	2	3
L_{cav}/λ	2.0	2.0	2.0
Q	300	300	550
TE mode	01	01	02
L_{drift}/λ	3.0	3.0	
Frequency	-33.2 GHz-		
Simulation Results			
Power	250-300 kW		
Saturated Gain	52-54 dB		
Efficiency	39-46%		

Figure 2 shows the predicted nonlinear gain characteristics for several values of velocity spread. Since the driver cavity will be excited in linear polarization, the device will saturate for an input power of approximately 6 W.

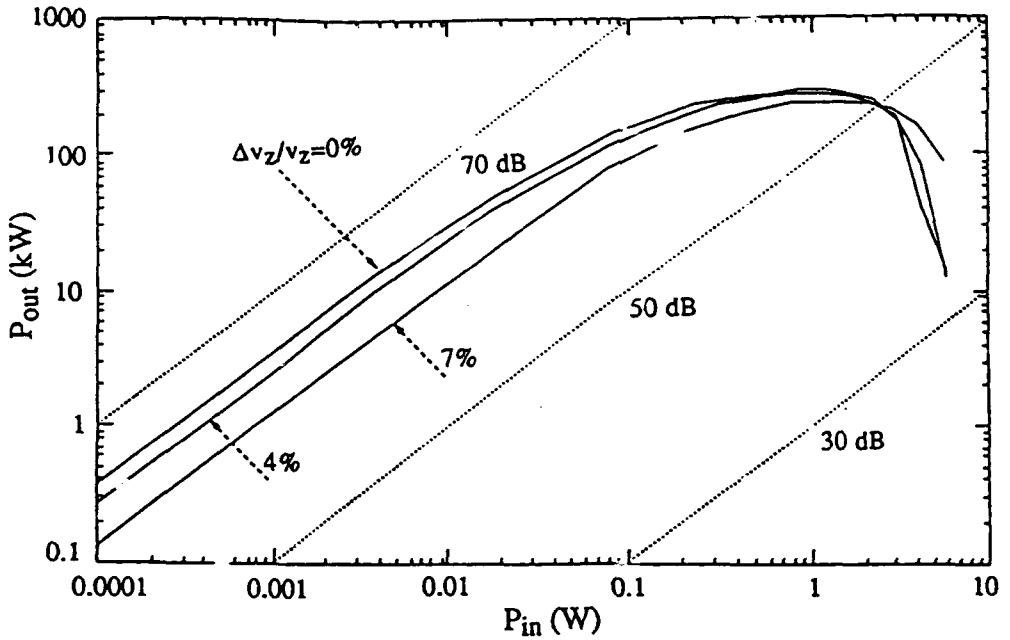


Figure 2. Gain characteristics of the proposed three-cavity 33.2 GHz gyroklystron described in Table I.

Similar to the linear klystron, a gyroklystron's efficiency may be enhanced by properly detuning the bunching cavities so as to enhance the electron bunching. For the gyroklystron, in contrast to the linear klystron, it is desirable to have the leading phase electrons accelerated and the lagging phase electrons decelerated. This can be accomplished by detuning the cavity frequency downward. It can be seen in Figure 3 that for zero velocity spread, a significant enhancement of the efficiency is predicted at the expense of gain. This loss in gain could be compensated by the addition of more bunching cavities. However, when a velocity spread of 7% was included, the increase in efficiency was negligible and the gain was still greatly reduced. For this reason, detuning of the penultimate cavity is not planned.

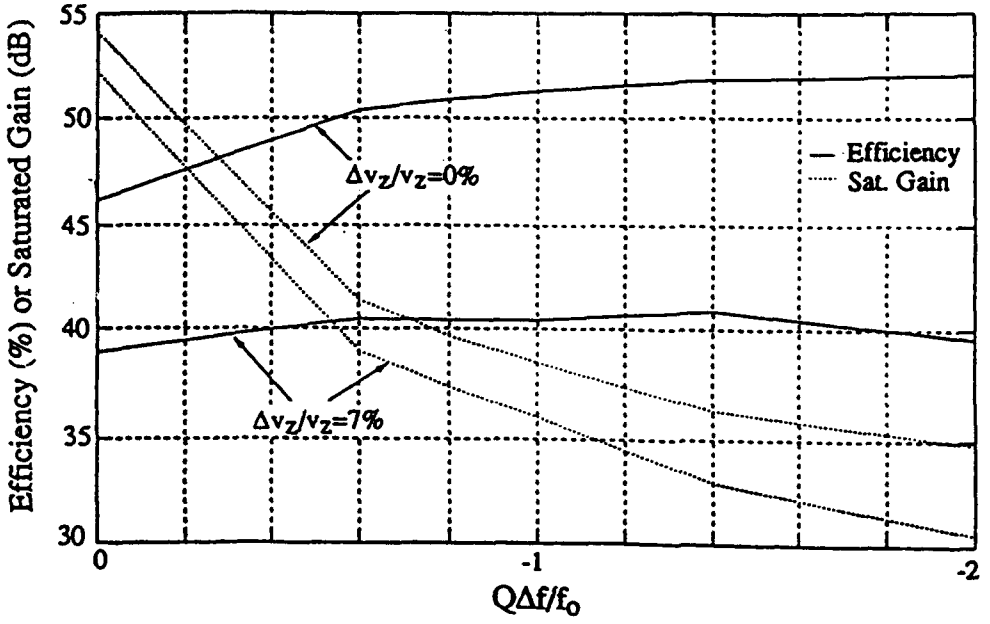


Figure 3. Efficiency and saturated gain in the proposed three-cavity 33.2 GHz (Table I) as a function of penultimate cavity detuning.

The diffraction coupled output cavity was designed using a computer code written by Dr. K. R. Chu. Given the physical dimensions of the tapered cavity and the choice of TE_{mnl} operating mode, the code predicts the field distribution in the cavity, the cavity's Q, and the resonant frequency. It can also account for wall loss in the cavity. The output cavity will operate in the TE_{021} mode with a length of 2λ as in the Varian experiment. The cavity was designed to have a Q of 550 and a resonant frequency of 33.2 GHz.

III. Experimental Configuration

The electron beam will be produced by a 28 GHz gyrotron MIG donated by Varian Associates. A 32.9-33.5 GHz tunable, 50 kW magnetron will provide the input signal. A seven-coil superconducting solenoid with a 12 cm uniform region donated by Hughes Aircraft Co. will be used to generate the 12.4 kG field necessary in the interaction region. All three cavities are 2λ long and are connected by 3λ long drift tubes. The driver and buncher cavity will operate in the TE_{01} mode and the output cavity operates in the TE_{02} mode so as to be relevant for eventual cw operation.

IV. Summary

The design of a 33.2 GHz, three-cavity gyroklystron has been completed and construction has begun. All major components for the gyroklystron have been obtained. Computer simulation of the final design predicts an output power of 250 kW with an efficiency of 39% using an electron beam with a 7% axial velocity spread.

V. Acknowledgments

The authors would like to thank Professor K. R. Chu of NTHU for supplying the gyroklystron simulation code and tapered cavity simulation code. This work has been supported by ARO through contract DAAL03-91-C-0190 and by RADC (ATRI) through Contract F30602-91-C-0020.

References

1. J. M. Baird and W. Lawson, "Magnetron Injection Gun (MIG) Design for Gyrotron Applications," Int. J. Electronics, 61, pp. 953-67, (1986).

2. H. R. Jory, F. Friedlander, S. J. Hegji, J. F. Shively, and R. S. Symons, "Gyrotrons for High Power Wave Generation,"Digest of Int. Electron Dev. Meeting, pp. 234-37, (1977).

3. W. M. Bollen, A. H. McCurdy, B. Arfin, R. K. Parker, and A. K. Ganguly, "Design and Performance of a Three-Cavity Gyroklystron Amplifier," IEEE Trans. on Plasma Sci., 13, pp. 417-23, (1985).

4. W. Lawson, J. P. Calame, B. Hogan, P. E. Latham, M. E. Read, V. L. Granatstein, M. Reiser, and C. D. Striffler, "Efficient Operation of a High-Power, X-Band Gyroklystron," Phys. Rev. Lett., 67, p.520, (1991).

5. K. R. Chu, L. R. Barnett, W. K. Lau, L. H. Chang, and C. S. Lou, "Recent Developments in Millimeter Wave Gyro-TWT Research at NTHU," Digest of Int. Electron Dev. Meeting, pp. 699-702, (1990).

6. K. R. Chu, V. L. Granatstein, P. E. Latham, W. Lawson, and C. D. Striffler, "30-MW Gyroklystron Amplifier Design for High Energy Linear Accelerators," IEEE Trans. on Plasma Sci., 13, p. 424, (1985).

7. K. R. Chu, D. S. Furuno, N. C. Luhmann, Jr., D. B. McDermott, P. Vitello, and K. Ko, "Theory, Design and Operation of Large-Orbit High-Harmonic Gyroklystron Amplifiers," IEEE Trans. on Plasma Sci., 13, pp. 435-43, (1985).

HARMONIC GYRO-TWT AMPLIFIER FOR HIGH POWER

Q. S. Wang, D. B. McDermott, N. C. Luhmann, Jr. and A. T. Lin
University of California, Los Angeles
C. S. Kou and K. R. Chu
National Tsing Hua University, Taiwan, ROC

Abstract

An extremely high power, second harmonic TE_{21} gyrotron traveling wave amplifier (gyro-TWT) utilizing a MIG beam will be described. Based on a marginal stability procedure [1], a second harmonic gyro-TWT using a 100 kV, 25 A MIG beam with $\alpha = 1$ and $\Delta v_z/v_z = 5\%$ has been designed, where the total interaction tube is comprised of three sections separated by absorbing severs. The length of each section is shorter than the length at which the device will spontaneously oscillate, which is determined through a combination of analytical theory and multi-mode PIC code simulation. The number of sections is chosen to yield the desired gain. An output power of 500 kW, efficiency of 21 % and bandwidth of 7 % have been obtained through self-consistent nonlinear simulations for the designed amplifier.

I. Introduction

Harmonic gyro-TWT's offer the same features of reasonably strong interaction and high efficiency as conventional fundamental gyro-TWT's, but require a substantially weaker magnetic field and have the potential to stably generate much higher levels of power. Since the harmonic interaction is in general considerably weaker than the fundamental interaction, the threshold value of beam current for the onset of oscillation is increased significantly. This allows the beam current and therefore the output power to be extremely high. Although an axis-encircling beam offers the strongest interaction for the operating TE_{21} mode, a more conventional annular beam emitted from a MIG gun can also be employed.

As depicted in Fig. 1, the dispersion diagram for a second harmonic gyro-TWT amplifier operating in the TE_{21} mode reveals that in addition to the absolute oscillations near cutoff, harmonic gyrotron backward wave oscillations (gyro-BWO) can also be excited at the intersections of the beam resonance lines and the waveguide modes in the negative wavenumber region. Only the strongest competing gyro-BWO modes ($TE_{11}^{(2)}$, $TE_{21}^{(3)}$, etc.) are shown in Fig. 1, where the superscript refers to the relevant cyclotron harmonic number. These gyro-BWO modes compete with the desired operating mode (TE_{21}) and can greatly degrade the performance of the amplifier. Very important to the stability of the $TE_{21}^{(2)}$ amplifier is that fundamental emission is suppressed since the fundamental cyclotron resonance line is well below the lowest order waveguide mode.

A recent linear theory has shown that there exists a starting oscillation length for each gyro-BWO mode, beyond which an rf wave will be excited from noise and propagate counter to the electron axial flow direction [2]. In light of this, a gyro-BWO will be stabilized if the interaction length is shorter than its starting oscillation length and stable amplification is then possible.

A marginal stability design criterion has been introduced recently [1] to fully explore the power handling capability of harmonic gyro-TWT's employing axis-encircling electron beams. However, since the techniques for forming such a high current beam (e.g., using a cusp gun.) are currently undergoing development [3] and have not yet demonstrated the requisite parameters, an annular

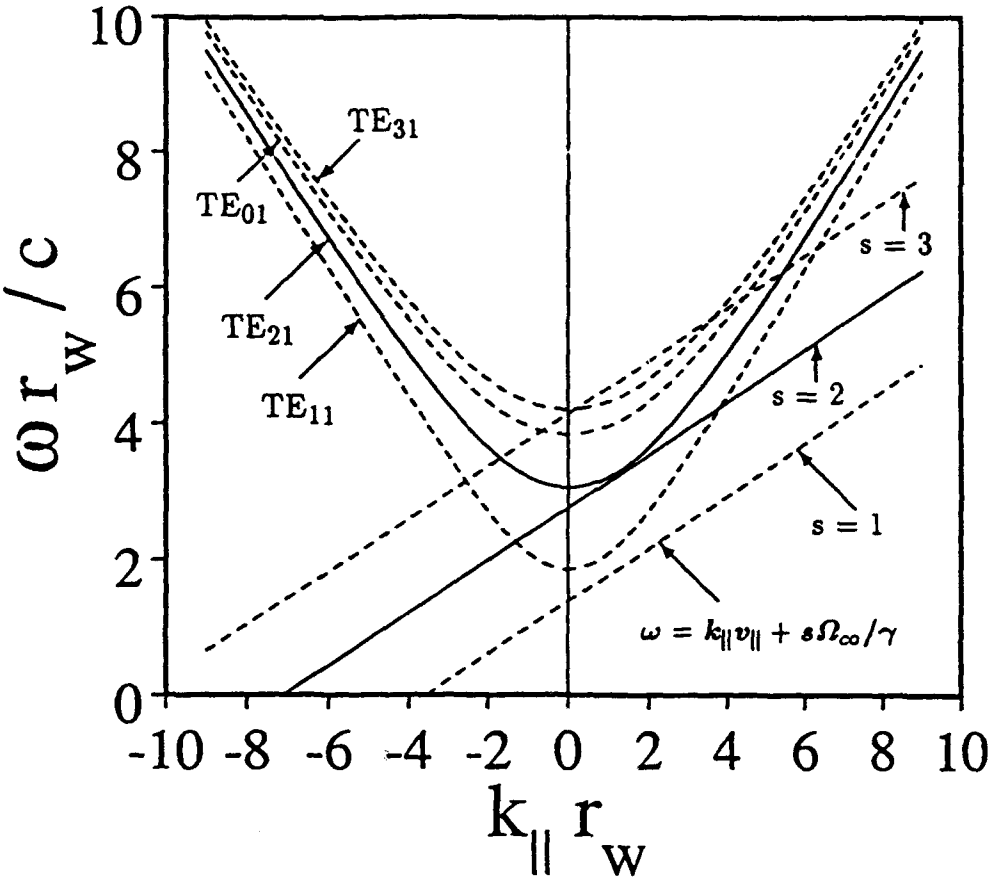


Figure 1: Uncoupled dispersion relation of operating mode (intersection of unbroken curves) and likely oscillating modes (intersections of broken curves with negative $k_{||}$) for $TE_{21}^{(2)}$ gyro-TWT amplifier (100 kV, $\alpha = 1$, $B_0 = 0.98B_g$).

beam formed by well developed MIG techniques is utilized in the high power gyro-TWT design presented below.

II. High-Power Second-Harmonic Gyro-TWT Design

To realize a stable as well as a high gain gyro-TWT amplifier, the MIG gun should produce a beam which interacts with the operating mode most strongly. This can be determined quantitatively by examining the coupling strength for each mode. For the $TE_{mn}^{(s)}$ interaction, the coupling strength is described by the coupling function $H_{sm}(k_{mn}r_c, k_{mn}r_L)$ defined as [2] [4],

$$H_{sm}(x,y) = J_{s-m}^2(x)J_s'^2(y)$$

where r_c and r_L are the electron guiding center radius and Larmor radius, respectively, and $k_{mn} = x_{mn}/r_w$ and x_{mn} is the nth root such that $J_m'(k_{mn}r_w) = 0$ is satisfied at the waveguide wall radius, r_w. Physically, H_{sm} can be viewed as the effective sth harmonic component of the TE_{mn} mode's electric field seen by the electrons and its contour plots are depicted in Fig. 2 for a 100 kV beam with $\alpha = 1$.

A properly placed beam will then maximize the value of H_{sm} for the operating mode (H_{22} in the case shown), while minimizing the H_{sm}'s for all the other modes. It is clear from the figure

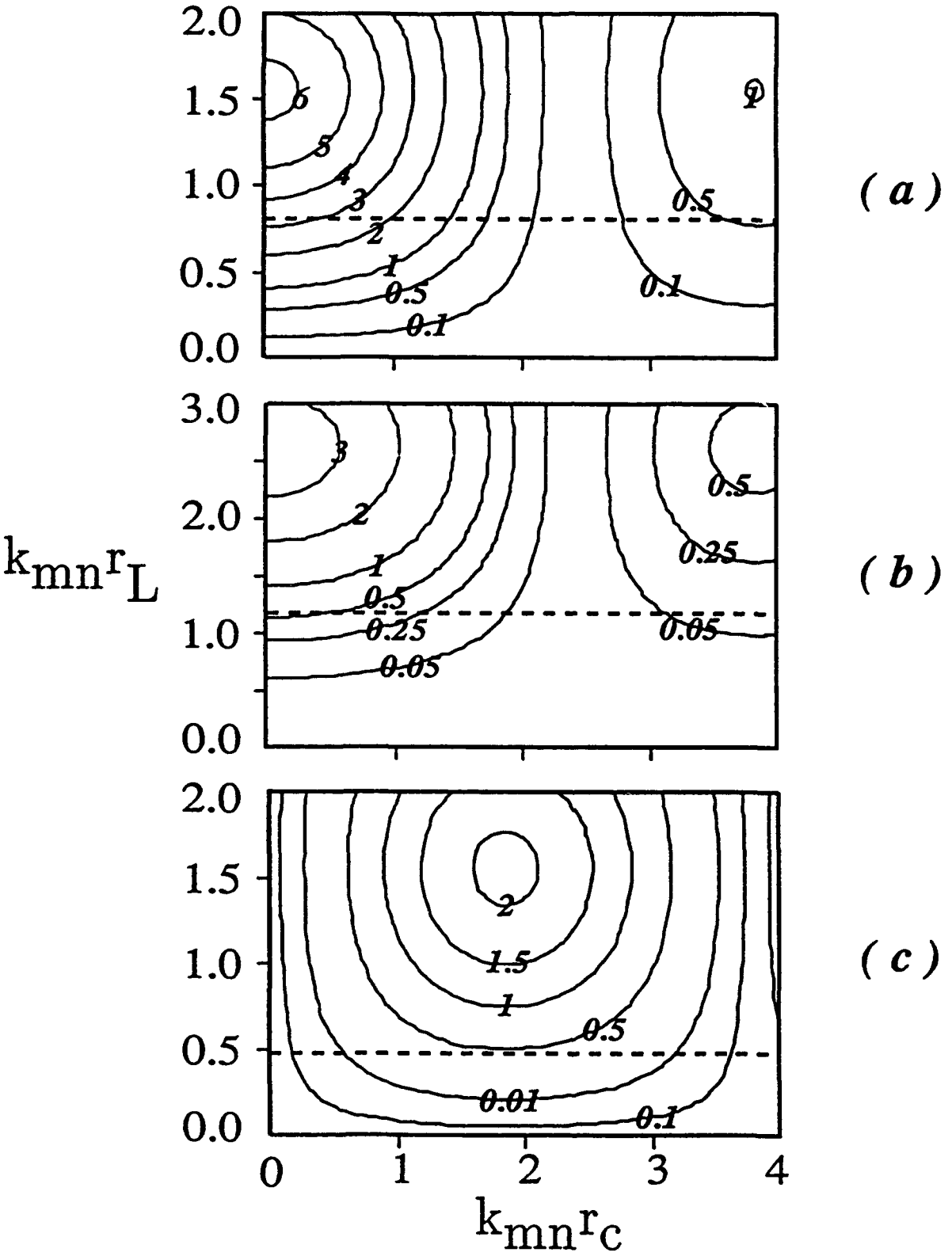


Figure 2: Contour plot for coupling functions (a) H_{22}, (b) H_{33} and (c) H_{21}. Absolute value of H_{sm} has been magnified by 100. Dashed line corresponds to 100 kV, $\alpha = 1$ and $B_0/B_g = 0.98$.

Table I : Second Harmonic 35 GHz Gyro-TWT Amplifier Design

Beam Voltage	100	kV
Beam Current	25	A
Magnetic Field	6.4	kG
Center Frequency	35	GHz
Mode	TE_{21}	
Cyclotron Harmonic	2nd	
Circuit Radius	0.44	cm
r_c/r_w	0.4	
α	1.0	
B/B_g	0.98	
$\Delta v_\parallel/v_\parallel$	5 %	
Number of Stages	3	
Section Length	11.5	cm
Sever Length	3	cm
Circuit Length	40.5	cm
Simulation Results :		
Output Power	533	kW
Saturated Gain	54	dB
Efficiency	21.3 %	
Constant Drive Bandwidth	6 %	
Saturated Bandwidth	7.4 %	

that the coupling with the operating $TE_{21}^{(2)}$ mode is strongest for an axis-encircling beam ($r_c = 0$). However, the unavailability of such a beam at high levels of current and low velocity spread forces one to resort to other beam geometries such as an annular beam formed from a MIG gun. Moreover, an axis-encircling beam can also couple relatively strongly to various $TE_{mn}^{(m)}$ gyro-BWO modes as well. Although the interaction strength for the operating $TE_{21}^{(2)}$ mode is weaker for a MIG beam ($r_c \neq 0$), as indicated by a reduced value of H_{22}, it is reduced even more for the most threatening gyro-BWO mode ($TE_{31}^{(3)}$). As a result, the net effect is an increase in the ratio of H_{22} / H_{33} and less severe competition from $TE_{31}^{(3)}$ mode oscillation can be expected. Therefore, a harmonic gyro-TWT utilizing a MIG beam can exhibit a performance comparable with or even better than one using an axis-encircling beam.

As found in the recent linear and nonlinear theories for the $TE_{21}^{(2)}$ gyro-TWT in Refs. [2] and [5], an amplifier can be made completely stable to all types of spontaneous oscillations by limiting its interaction tubes to lengths shorter than the smallest oscillation threshold length. It was found for the high-power second-harmonic gyro-TWT design listed in Table I that the $TE_{31}^{(3)}$ starting oscillation length is 12 cm. The length of the interaction tube has been taken to be 11.5 cm. Since the gain will be low for such a short interaction length, a device with three stages was designed to achieve reasonably high gain.

The performance of the gyro-TWT given in Table I was simulated with a nonlinear, self-consistent, multi-stage numerical simulation code. The code is a general three-dimensional particle tracing code using a slow time-scale formulation and includes the effects of particle axial velocity spread, guiding center motion and spread, axial magnetic field tapering and the attenuating severs

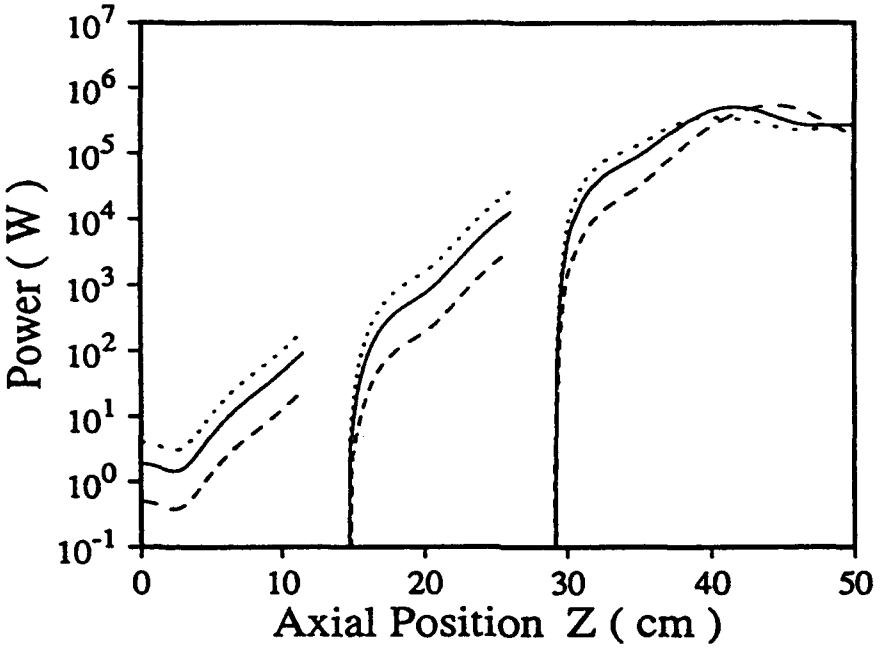


Figure 3: Predicted spatial power profile of 35 GHz wave in proposed three stage $TE_{21}^{(2)}$ gyro-TWT (Table I) for input powers of 0.5 W (dashed curve), 1.9 W (solid curve) and 4 W (dotted curve).

in a smooth wall circular waveguide [5]. The power evolution in the proposed three-stage $TE_{21}^{(2)}$ gyro-TWT obtained from nonlinear simulation is shown in Fig. 3. The maximum output power at the exit of the amplifier is 533 kW. As expected, the gain for a single section with a length of 11.5 cm is only 14 to 20 dB. The saturated bandwidth of the three-stage, second harmonic gyro-TWT is plotted in Fig. 4 for several values of beam axial velocity spread. In obtaining the saturated bandwidth for the fixed device length, the input signal frequency had been swept and input power varied such that a maximum output power appears at the exit of the device at each signal frequency. The beam axial velocity spread degrades the performance of the multi-stage gyro-TWT greatly by reducing both the output power level and the bandwidth. While the saturated bandwidth is 13% for an ideal cold beam, it drops to 7.5% for a beam with an axial velocity spread of 5%. For the case of 5% axial velocity spread, a peak output power of 533 kW is predicted at 34.5 GHz, which is far in excess of the power levels achieved by state-of-the-art fundamental gyro-TWT's. At 34.5 GHz, the peak efficiency and gain are 21.3% and 54 dB, respectively.

III. ACKNOWLEDGMENT

This work was supported by AFOSR under Grant 91-0382 and ARO under Contract DAAL03-91-G-0190.

References

[1] A. T. Lin, K. R. Chu, C. C. Lin, C. S. Kou, D. B. McDermott and N. C. Luhmann, Jr.,

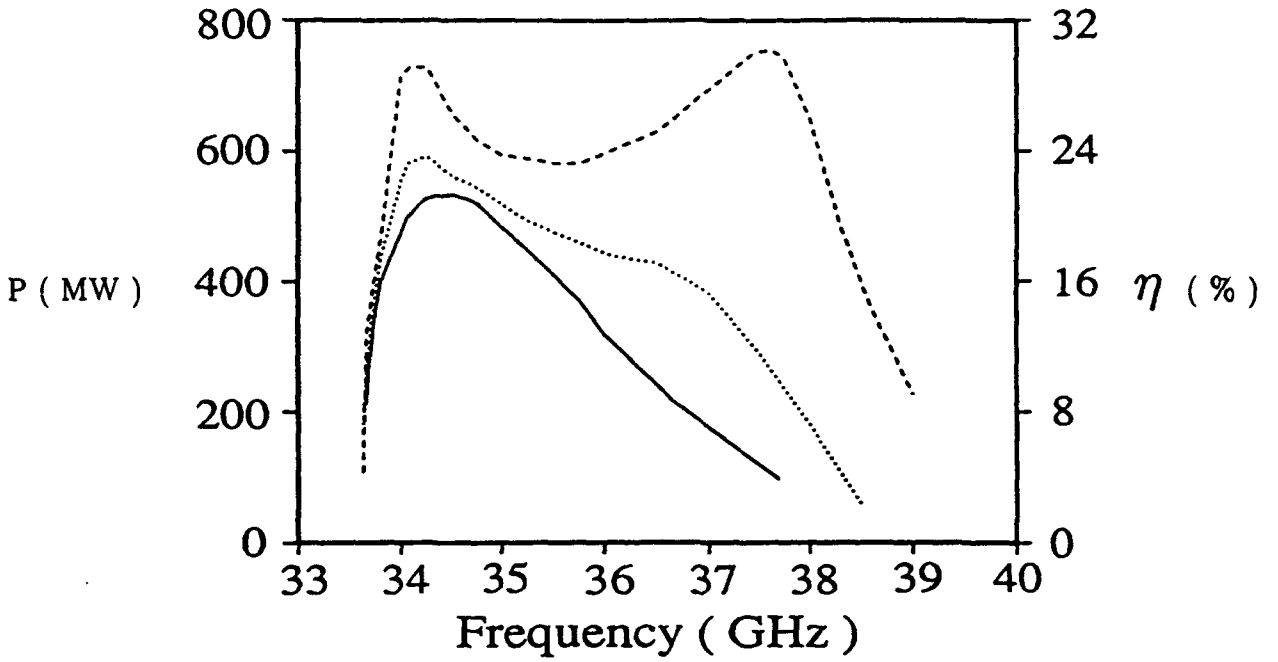


Figure 4: Saturated bandwidth of proposed three stage $TE_{21}^{(2)}$ gyro-TWT (Table I) for axial velocity spreads of 0% (dashed curve), 3% (dotted curve) and 5% (solid curve).

"Marginal Stability Design Criterion for Gyro-TWT's and Comparison of Fundamental with Second Harmonic Operation", to be published, *Int. J. Electronics*, 1992.

[2] C. S. Kou, Q. S. Wang, D. B. McDermott, A. T. Lin, K. R. Chu and N. C. Luhmann, Jr., "High Power Harmonic Gyro-TWT's: I. Linear Theory and Oscillation Study", *IEEE Trans. Plasma Science*, 20, no. 3, June 1992.

[3] G. P. Scheitrum, R. S. Symons and R. B. True, "Low velocity spread axis encircling electron beam forming system", *Tech. Digest, IEEE Int. Electron Devices Meeting, Washington, D.C.* pp. 743-746, 1989.

[4] K. R. Chu, "Theory of electron cyclotron maser interaction in a cavity at the harmonic frequencies" *Phys. Fluids*, 21, no. 12, pp. 2354-2364, 1978.

[5] Q. S. Wang, D. B. McDermott, C. S. Kou, A. T. Lin, K. R. Chu and N. C. Luhmann, Jr., "High Power Harmonic Gyro-TWT's: II. Nonlinear Theory and Design", *IEEE Trans. Plasma Science*, 20, no. 3, June 1992.

STABILITY AND NONLINEAR DYNAMICS OF GYROTRONS AT CYCLOTRON HARMONICS *

G. P. Saraph, G. S. Nusinovich, T. M. Antonsen, Jr., and B. Levush
Laboratory for Plasma Research
University of Maryland, College Park, MD 20742 U.S.A.

Gyrotrons operating at higher harmonics of the cyclotron frequency can overcome the frequency limitations caused by achievable strength of the magnetic field. However, the excitation of modes at the fundamental frequency exhibit a major problem for stable operation of harmonic gyrotron at high power with high efficiency. Therefore the issues of stability of gyrotron operation at the cyclotron harmonics and nonlinear dynamics of mode interaction are of great importance. The results of our stability analysis and multimode simulation are presented here.

A detailed nonlinear theory of steady state single mode operation at cyclotron harmonics has been presented before [1,2], which takes into account beam-wave coupling and nonlinear gain function at cyclotron harmonics. A set of equations describing low gain regime interaciton of modes resonant at different cyclotron harmonics was studied in [3]. The multifrequency time-dependent nonlinear analysis presented here is based on our previous gyrotron studies [4-7] and beam-wave interaction at the cyclotron harmonics formulated in [8,9].

The equations of motion of the particle in the guiding center variables are transformed into the frame of reference rotating with the frequency $\omega = \omega_1/s_1$, where ω_1 is the frequency of the operating mode resonant with the s_1th harmonic of electron cyclotron frequency (Ω_0/γ). The transit time of particles, T_p, is assumed to be much smaller than the cavity decay time (slow time scale), $\tau_s = Q/\omega$, where Q is the quality factor of the cavity. The axial field profiles are assumed to be gaussian and the field amplitudes of the individual modes are assumed to evolve in the slow time scale. The evolution of mode amplitudes is determined by computing the overlap integral of the beam current with each mode eigenfunction and averaging over the entrance times and entrance gyrophases. The results of the numerical analysis for the gyrotron operating at the second harmonic are presented here.

The results are expressed in terms of the normalized length μ, cyclotron resonance

mismatch or detuning of the operating mode δ, relative detuning of the parasite (mode 2) δ_1, mode amplitude for $TE_{\ell,p}$ mode $e_{\ell,p}$ and beam current $\hat{I}$. These normalized parameters are defined as follows:

$$\mu = \frac{T_p \Omega_0}{\gamma_0} \cdot \beta_{\perp 0}^2,$$

$$\delta = T_p \cdot \left(\frac{\omega_1}{s_1} - \frac{\Omega_0}{\gamma_0}(1 - \frac{\beta_{zo}^2}{2}(u_{\|}^2 - 1)) \right),$$

$$\delta_1 = \left(\omega_2 - \frac{s_2}{s_1}\omega_1 \right) T_p,$$

$$e_{\ell,p}(\tau) = \frac{2qE_{\ell,p}(\tau)}{m\gamma_0} \frac{T_p}{v_\perp} \frac{J_{\ell+p}(k_{\ell,p} r_b)}{(s-1)!} \left(\frac{k_{\ell,p}\gamma_0 v_{\perp 0}}{2\Omega_0} \right)^{s-1},$$

$$\hat{I} = 2\left(\frac{2}{\pi}\right)^{1/2} \frac{I}{I_a} \cdot \frac{s_1 \omega_1 Q_1 T_p}{(s_1 - 1)!} \cdot h_1^2 \left(\frac{k_{\ell,p}\gamma_0 v_{\perp 0}}{2\Omega_0} \right)^{2(s_1-1)},$$

where Alfvén Current

$$I_a = \frac{mc^3 \beta_z \gamma_0}{q},$$

Beam Coupling (with mode 1)

$$h_1^2 = h_{\ell_1 p_1}^2 = \frac{J_{\ell+s}^2(k_{\ell,p} r_b)}{(k_{\ell,p}^2 r_w^2 - \ell_1^2) \cdot J_{\ell_1}^2(k_{\ell_1 p_1} r_w)},$$

where r_b, r_w are beam and wall radii, respectively, and $v_{\perp 0} = c\beta_{\perp 0}$ is the perpendicular velocity at the entrance and $u_{\|} = (\gamma v_z / \gamma_0 v_{z0})$ is the normalized axial momentum.

In the equilibrium state analysis under the assumption of steady state single mode operation, the results obtained are consistent with the earlier studies of the harmonic gyrotron [2,10,11]. The level curves of the perpendicular efficiency $\eta_\perp$ and equilibrium current $\hat{I}$ in the parameter space $e - \delta$ for the steady state operation at the second harmonic for $\mu = 7.5$ are shown in Figs. 1a and 1b. This analysis helps in choosing the operating parameters of the device.

Stable single mode operation of the gyrotron at the second harmonic has been experimentally demonstrated before [12-15]. It has been observed that the mode competition due to parasites at the fundamental cyclotron harmonic is very important in determining the regime of stable single mode operation. In the stability analysis we determine the region of parameter space in which a preexisting large amplitude operating mode at the second harmonic is able to suppress competing parasitic mode at the fundamental harmonic.

Depending upon the relative detuning δ_1 of the parasite the stable region changes. It is found that in the regions of high efficiency ($\eta_\perp > 0.4$) the parasites with positive values of detuning between 0.2 to 1.5 are likely to have positive gain. The stability boundaries in the presence of one of such parasites at $\delta_1 = 0.5$ are shown in Fig. 2 for different values of r_2. The parameter r_2 is the product of the relative coupling of the parasite with the electron beam and the relative quality factor of the cavity for the parasite and is given by

$$r_2 = r_{coupl_2} \cdot r_{q_2} = \frac{h_2^2}{h_1^2} \cdot \frac{s_1 Q_2}{s_2 Q_1}.$$

As the value of the parameter r_2 is increased the region of stable operation shrinks in size, which is consistent with the earlier studies [16].

It is important to find out from the time dependent analysis whether this equilibrium state in the stability analysis can be reached starting from very low field amplitudes. The nonlinear dynamics of mode evolution for a single mode operating at the second harmonic is shown in Fig. 3. The mode amplitude grows exponentially in the beginning corresponding to linear gain and when the amplitude reaches to approximately 0.3, then it enters a nonlinear regime in which gain increases significantly due to phase bunching of electrons in the RF field of the synchronously rotating multipole [17,18]. Correspondingly, the mode at the second harmonic tends to form two electron phase bunches which are π radians apart in gyrophase.

In a harmonic gyrotron various types of mode interactions can take place and it can govern what is the ultimate equilibrium state of the device [3]. The numerical results of nonlinear mode interaction between the operating mode at the second harmonic and the parasite at the fundamental cyclotron frequency are presented in Fig. 4 for $\hat{I} = 10.0$. For small initial mode amplitudes we start from an unstable region in which the linear gain of the fundamental harmonic mode is much higher and therefore it starts off first. This mode can be considered to be a synchronously rotating dipole and it tends to form a single electron bunch and the mode at the second harmonic can extract gain out of this bunching. The nonlinear gain of the operating mode kicks in strongly and as its amplitude increases it starts influencing the phase bunching. The nature of the phase bunching due to second harmonic mode discussed above leads to appearance of two bunches in gyrophase π radians apart which tend to kill the gain at the fundamental harmonic. Thus the parasite

is suppressed and stable single mode operation is achieved at the second harmonic with the perpendicular efficiency of 0.287. It is important to reemphasize that the nonlinear mode interaction in this case is of constructive nature and it helps to switch on the operating mode at the second harmonic faster.

This nonlinear effect is even more prominent when we are oeprating below the start oscillation current I_{st} of the operating mode and, hence, this mode can not start without a significant priming signal. Figure 5 shows the nonlinear dynamics of mode interaction for $\hat{I} = 4.8$ (lower than $\hat{I}_{st} = 5.0$) and all other parameters are kept the same as the results in Fig. 4. The negative slope of the operating mode amplitude in the logarithmic scale indicates that without the help of parasite at the fundamental harmonic, the operating mode could never start. The stable single mode operation in this case has the perpendicular efficiency of 0.417. Thus we can achieve a significantly higher efficiency while operating at a lower value of current. Figure 5 shows that the mode at the second harmonic could start with the shot noise level corresponding to $e = 10^{-4}$. Whereas when the simulation is performed with only one second harmonic mode, it is necessary to inject a signal corresponding to a normalized amplitude of 0.1.

The operating current chosen in the above case is just below the start oscillation current. However, the regions of highest efficiency for the second harmonic mode are deep into the region of hard excitation ($\hat{I} < \hat{I}_{st}$) as can be seen from Fig. 1. These regions cannot be accessed without a priming signal at the second harmonic frequency even in the presence of the mode at the fundamental frequency. With the nonlinear effect demonstrated here the power of such a priming signal can be reduced by two orders of magnitude. The detialed investigation of this phenomenon would be presented in our future studies.

In summary, we have determined the parameter space for stable single mode operation at the second harmonic. The nonlinear dynamics of mode evolution and mode interaction for a harmonic gyrotron is presented. A new nonlinear effect in which the parasite at the fundamental harmonic helps excite the operating mode at the second harmonic has been demonstrated.

References

1. K. R. Chu, Phys. Fluids **21**, 12, 2354-2364 (1978).

2. B. G. Danly and R. J. Temkin, Phys. Fluids **29**, 561-562 (1986).
3. M. A. Moiseev and G. S. Nusinovich, Radiophys. Quantum Electron. **17**, 11, 1305-1311 (1974).
4. T. M. Antonsen, Jr., W. M. Manheimer, and B. Levush, Int. J. Electron. **61**, 6, 823-854 (1986).
5. B. Levush and T. M. Antonsen, Jr., IEEE Trans. Plasma Science **18**, 3, 260-272 (1990).
6. G. P. Saraph, T. M. Antonsen, Jr., B. Levush, and G. I. Lin, to be published in IEEE Trans. Plasma Sci., **20**, 3, (1992).
7. S. Y. Cai, T. M. Antonsen, Jr., G. Saraph, and B. Levush, to be published in Int. J. Electron.
8. G. N. Rapoport, A. K. Nemak, and V. A. Zhurakhovskiy, Radio Eng. Electron. Phys. **12**, 4, 587-595 (1967).
9. M. K. Haldar and A. H. Beck, Electron. Lett. **15**, 16, 487-489 (1979).
10. A. V. Gaponov, V. A. Flyogin, A. L. Goldenberg, G. S. Nusinovich, et. al. Int. J. Electron **51**, 4, 277-302 (1981).
11. G. S. Nusinovich, to be published in Int. J. Electron. **72**, 5-6 (1992).
12. N. I. Zaytsev, T. B. Pankratova, M. I. Petelin, and V. A. Flyagin, Radio Eng. Electron. Phys. **19**, 5, 103-107 (1974).
13. V. Y. Zapevalov, G. S. Korablev, and S. E. Tsimring, Radioteck. Elektronika **22**, 86-94 (1977).
14. H. Guo, IEEE Trans. on Plasma Science **18**, 3, 326-333 (1990).
15. S. Spira-Hakkarainen, K. E. Kreischer, and R. J. Temkin, IEEE Trans. Plasma Science, **18**, 3, 334-342 (1990).
16. I. G. Zarnitsyna and G. S. Nusinovich, Radiophys. Quantum Electron. **20**, 3, 313-317 (1977).
17. J. L. Hirshfield and V. L. Granatstein, IEEE Trans. MTT, **MTT-25**, 6, 522-527 (1977).
18. V. A. Flyagin, A. V. Gaponov, M. I. Petelin, and V. K. Yulapatov, IEEE Trans. MTT, **MTT-25**, 6, 514 (1977).

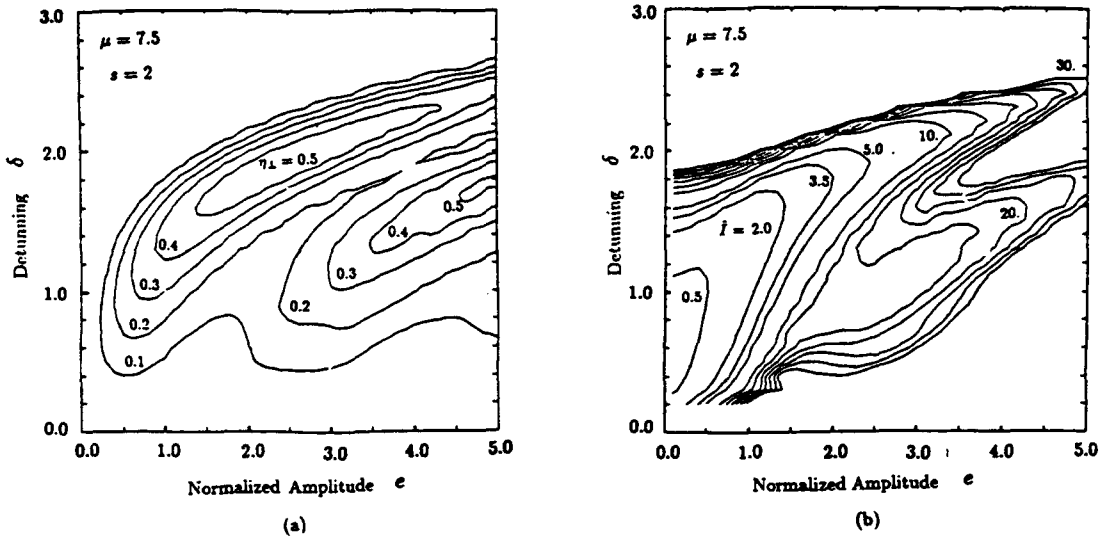


Fig.1 Level curves of (a) perpendicular efficiency $\eta_\perp$ and (b) normalized equilibrium current $\hat{I}$ plotted in the e - δ plane for $\mu = 7.5$.

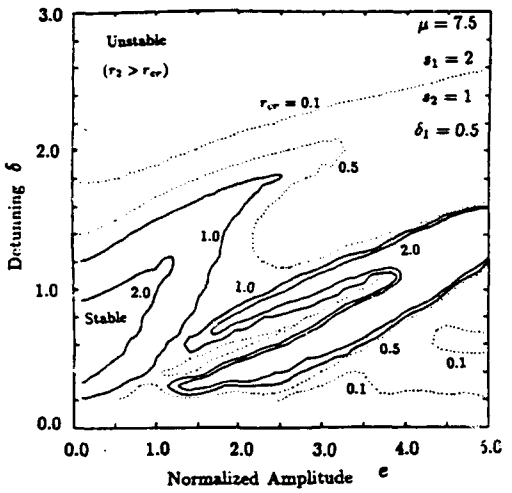


Fig.2 Level curves of critical coupling ratio ($r_{cr} = 0.1, 0.5, 1.0, 2.0$) of the small amplitude parasitic mode at the fundamental cyclotron frequency in the presence of a large amplitude (e) operating mode at the second harmonic frequency. The level curve corresponding to $r_2 = r_{cr}$ is the stability boundary.

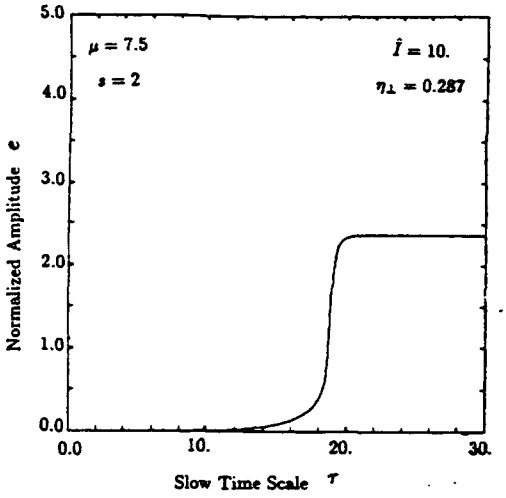


Fig.3 The evolution of normalized mode amplitude e with the slow time variable $\tau = t/\tau_s$ for a single mode operating at the second harmonic frequency for the normalized beam current $\hat{I} = 10.0$.

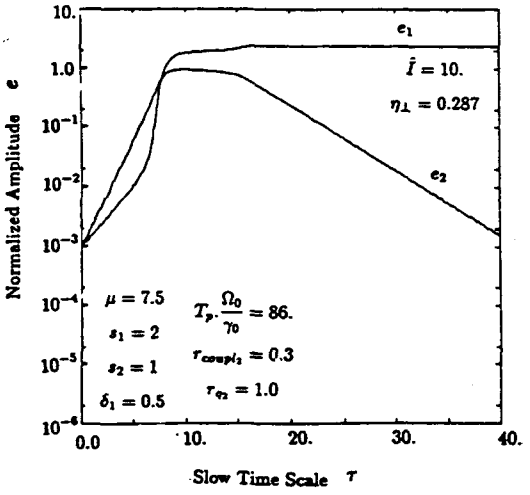


Fig.4 The evolution of normalized mode amplitudes e_1 and e_2 with the slow time variable $\tau = t/\tau_s$ indicating nonlinear mode interaction for the normalized beam current $\hat{I} = 10.0$. The normalized parameters chosen here correspond to gyrotron operating at the second harmoic in $TE_{0,1}$ mode at $30GHz$ with the beam voltage of $30kV, \alpha = 2.0$ and beam current $10Amp$ for cavity $Q = 1115$. At steady state the perpendicular efficiency is 0.287.

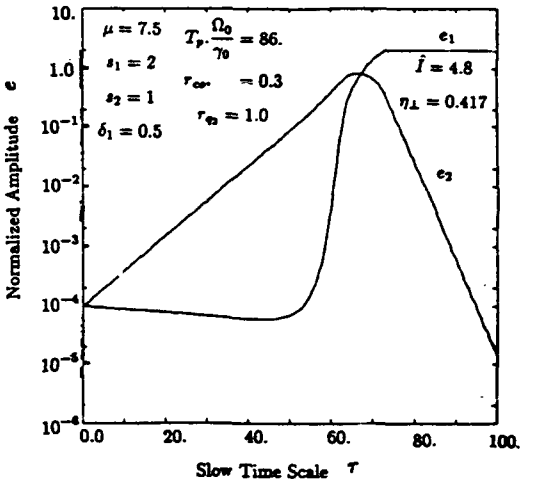


Fig.5 The evolution of normalized mode amplitudes e_1 and e_2 with the slow time variable $\tau = t/\tau_s$ indicating nonlinear mode interaction for the normalized beam current $\hat{I} = 4.8$, which is below the start oscillation current. The normalized parameters chosen here correspond to gyrotron operating at the second harmoic in $TE_{0,1}$ mode at $30GHz$ with the beam voltage of $30kV, \alpha = 2.0$ and beam current $4.8Amp$ for cavity $Q = 1115$. At steady state the perpendicular efficiency is 0.417.

*work supported by DOE and AFOSR.

PROSPECTS FOR DEVELOPMENT OF POWERFUL, HIGHLY EFFICIENT, RELATIVISTIC GYRODEVICES

G.S. Nusinovich and V.L. Granatstein
Laboratory for Plasma Research
University of Maryland, College Park, MD 20742 U.S.A.

1. Introduction

For various applications the required parameters of sources of powerful microwave radiation lie far beyond the capabilities of existing tubes. This provokes an interest in reconsidering basic principles of relevant microwave sources in order to search for alternative concepts in their development.

One of the most promising devices in the short-wavelength region of microwaves is the cyclotron resonance maser (CRM).[1,2] During the last decade, two important varieties of CRMs have been distinguished, namely, gyrotrons,[1] which operate at frequencies close to cut-off, and cyclotron autoresonance masers (CARMs)[3], which operate at frequencies far from cut-off.

The smallness of the axial wavenumber ($k_z = \frac{\omega}{v_{ph}} \ll k = \frac{\omega}{c}$) in gyrotrons makes these devices relatively insensitive to the electron axial velocity spread, since the Doppler term $k_z v_z$ in the cyclotron resonance condition

$$|\omega - k_z v_z - n\Omega_c| \ll \Omega_c \tag{1}$$

is small (in Eq. (1) v_z is an electron axial velocity, Ω_c is an electron cyclotron frequency, n is the number of the resonant cyclotron harmonic). This is an essential advantage of gyrotrons. However, at large operating voltages, these devices when they have axial uniformity lose efficiency because the energy dependence of the electron cyclotron frequency $\Omega_c = \frac{eH_0c}{W}$ leads to a disturbance of the cyclotron resonance condition given by Eq. (1) after a relatively small change in an electron energy.

On the other hand, in CARMs, the closeness of k_z to k leads to an almost complete compensation of the cyclotron frequency shift in Eq. (1) by the change in the energy dependent Doppler term $k_z v_z(W)$. Due to this CARMs can be considered at high operating voltages as highly efficient, frequency tunable sources of microwave radiation, capable of

operation with the large Doppler frequency up-shift, which are, however, sensitive to the electron velocity spread.

Between these two limiting cases ($k_z \ll k$-gyrotron, effective at small voltage, $V_b \ll m_0c^2/e$; and $|k_z - k| \ll k$-CARM, effective at large voltages, $V_b \gg m_0c^2/e$) there is a wide range of CRM operation at arbitrary voltages ($V_b \sim m_0c^2/e$) and arbitrary axial wavenumbers, that will be considered below.

2. Electron Beam–Electromagnetic Wave Interaction

When electrons gyrate in an external magnetic field $\vec{B}_0$ and interact with the TE-wave propagating in the direction of $\vec{B}_0$ with a phase velocity $v_{ph} = \omega/k_z$ the electron energy W and axial momentum p_z are varied in the process of interaction according to the autoresonance integral[4]

$$v_{ph}p_z - W = \text{const.}$$

This equation being combined with the general relation between electron energy and momentum $W^2 = m_0^2c^4 + c^2p^2$ permits one to define the normalized axial wavenumber[5], which is optimal for maximum transfer of energy from the electrons to the wave; viz.

$$(k_z/k)^2_{\text{opt}} = \frac{\gamma_0 + 1}{(\gamma_0 - 1)(\alpha^2 + 1)}. \tag{2}$$

Equation (2) shows how to adjust the waveguide to the given electron beam in order to withdraw all the kinetic energy of the electrons. As follows from Eq. (2), when the initial pitch-ratio of the electrons, $\alpha = p_{\perp 0}/p_{z0}$, satisfies the relation $\alpha^2 < 2/(\gamma_0 - 1)$, the maximum electron efficiency can be realized only if electrons interact with a slow electromagnetic wave. Note that an effective interaction between relativistic electrons and the optimally oriented electromagnetic wave in a constant external magnetic field takes place in a relatively small number of electron orbits. This makes it inevitable that for such systems particle-in-cell simulations must be used instead of a conventional approach based on consideration of average equations.

Besides the use of the variation in the Doppler term for maintenance of the cyclotron resonance between an electromagnetic wave and relativistic electrons, it is also possible to profile for this purpose the axial distribution of the external magnetic field. The idea

is to trap charged particles in the electromagnetic wave, and then, to vary parameters of the system in order to maintain resonance between the wave and decelerating particles. It was discussed with respect to linear beam devices in Refs. 7 and 8 and with respect to free electron lasers in Refs. 9 and 10. With respect to relativistic gyrotrons, this idea was considered in Ref. 11. Recently, it was shown[12] that the same method can be used in CRMs, in which relativistic electrons interact at arbitrary cyclotron harmonics with the electromagnetic waves propagating at arbitrary axial wavenumbers.

Note, that a phase prebunching of electrons leads to an increase in the number of trapped particles and enhances the efficiency of such devices. This idea is illustrated in Fig. 1,[12] where the coefficient of trapping C_T is given as a function of the phase of the synchronous electron, i.e. an electron that does not change its phase in the interaction space, for different values of the bunching parameter, X defined in Ref. 12. Electron phase at the input of the interaction space is here equal to $(n_2/n_1)\cdot(\theta_0 - X\sin\theta_0)$ where the $n_{1,2}$ are resonance cyclotron harmonic numbers in the prebunching cavity and output section, respectively, and θ_0 is the initial gyrophase. Figure 1a corresponds to the fundamental resonance ($n_1 = n_2 = 1$); Fig. 1b, to the initial modulation at the first harmonic and bunch deceleration at the second harmonic. In the latter case particles will be trapped by two potential wells formed by the electromagnetic wave; the ratio of particles trapped in the first well to those in the second one, N_1/N_2 is shown in Fig. 1c.

We have carried out a numerical study of the interaction of one macrobunch with the electromagnetic wave at the first two cyclotron harmonics.[12] Results are presented in Fig. 2, where ζ is the normalized axial coordinate (normalization is given in Ref. 12), solid lines show the efficiency of interaction η; dash-dotted lines show the axial distribution of the normalized external magnetic field μ; dashed lines illustrate the axial dependence of the product MK (M is the effective mass and K is the coefficient of elasticity of the electron bunch oscillating in the potential well). With decrease in MK the swing of the electron synchrotron oscillations grows and, therefore, a portion of the particles can leave the region of synchronous interaction with the wave. The results are given for $\gamma_0 = 2$, (a) $n = 1,\ \alpha = 0.5,\ k_z/k = 0.9$, (b) $n = 1,\ \alpha = 1,\ k_z/k = 0.5$, (also shown is η for $k_z/k = 0.9$), (c) $n = 2,\ \alpha = 0.5,\ k_z/k = 0.9$, (d) $n = 2,\ \alpha = 1,\ k_z/k = 0.5$ (also shown are orbital and

axial components of the electron momentum).

3. Discussion

When the axial phase velocity of the wave is properly adjusted to the beam voltage and the electron pitch-ratio, the efficiency of relativistic CRMs may be high ($\gtrsim$50%). The method of optimizing efficiency based on a partial compensation of the shift in the relativistic electron cyclotron frequency by the change in the Doppler term can be, in principle, accompanied by a corresponding profiling of the external magnetic field and/or the wave phase velocity in a slightly irregular waveguide.

These methods can be used in such relativistic CRMs as relativistic gyrotrons,[3] gyroklystrons,[13] gyro-traveling-wave-tubes (gyro-TWTs)[14] and gyrotwistrons.[15] The most important point is their sensitivity to a spread in electron parameters. As the beam voltage grows, the operation becomes more sensitive. However, at relatively low voltages such devices are quite tolerant to electron velocity spread. For example, as is shown in Ref. 14, the electron efficiency of the gyro-TWT at 300 kV beam voltage can be on the order of 35% even with a 15% spread in electron orbital velocities.

Acknowledgement

This work has been supported by the U.S. Department of Energy.

References

1. V.A. Flyagin, A.V. Gaponov, M.I. Petelin, and V.K. Yulpatov, IEEE-MTT **25**, No. 6, p. 514 (1977).
2. J.L. Hirshfield and V.L. Granatstein, ibid, p. 522.
3. V.L. Bratman, et al. Int. J. Electronics, **51**, No. 4, p. 541 (1981).
4. A.A. Kolomensky and A.N. Lebedev, DAN SSSR, **145** p. 1259 (1962); V. Ya. Davydovsky, Zh. Eksp. Teor. Fiz. **43**, p. 886 (1962).
5. N.S. Ginzburg, I.G. Zarnitsyna, and G.S. Nusinovich, Radiophys. and Quantum Electronic **24**, p. 331 (1981).
6. A.W. Fliflet, Int. J. Electronics, **61**, No. 6, p. 1049 (1986).
7. J. Meeker and J.E. Rowe, IRE Trans. ED, **ED-9**, p. 257 (1962).
8. E.D. Belyavsky, Radio Eng. and Electron. Phys. **16**, p. 186 (1971).
9. N.M. Kroll, P.L. Morton, and M.N. Rosenbluth, IEEE-QE **QE-17**, p. 1436 (1981).
10. P. Sprangle, C.M. Tang, and W.M. Manheimer, Phys. Rev. A. **21**, p. 302 (1980).
11. N.S. Ginzburg, Radiophys.and Quantum Electron. **30**, p. 865 (1987).

12. G.S. Nusinovich, Phys. Fluids B 4, No. 1, (1992).
13. W. Lawson et al., Phys. Rev. Lett. 67, p. 520 (1991).
14. G.S. Nusinovich and H. Li, IEEE PS 20, No. 3 (1992).
15. G.S. Nusinovich and H. Li, Phys. Fluids B 4, p. 1058 (1992).

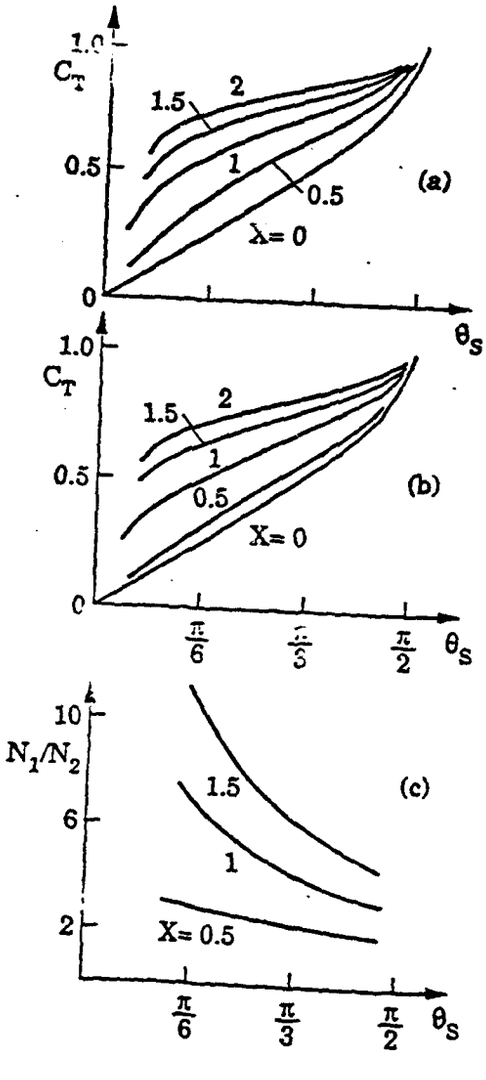


Fig. 1. Coefficient of particle trapping in a prebunched electron beam.

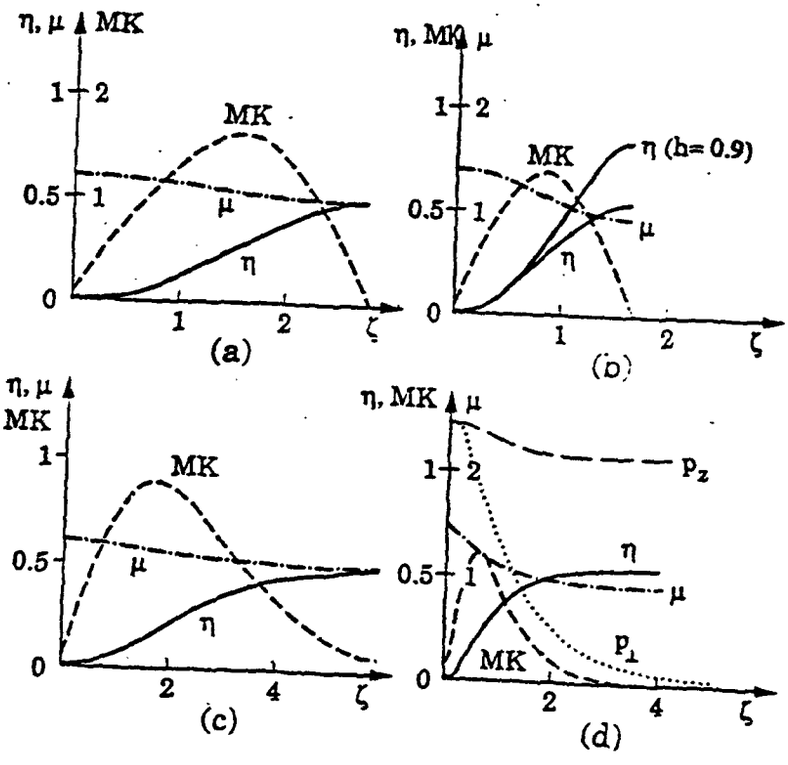


Fig. 2. Axial dependences of the efficiency, η (solid lines), the normalized external magnetic field, μ (dash-dotted lines), and the parameter MK (dashed lines) responsible for the swing of electron synchrotron oscillations.

DEPRESSED COLLECTORS FOR MILLIMETER WAVE GYROTRONS*

A. Singh and V. L. Granatstein
Laboratory for Plasma Research
University of Maryland, College Park, MD 20742 U.S.A.

Abstract

The main issues relating to design of depressed collectors for millimeter wave gyrotrons are discussed. A flow diagram is presented and the interlinking steps are outlined. Design studies are given for two kinds of gyrotrons on which severe constraints on the maximum radii of the collectors had been imposed; namely, for a cavity type and a quasi-optical gyrotron. A collector efficiency of the order of 70 percent is shown to be feasible for either case using careful tailoring of magnetic field profiles. A code has been developed to assist in doing this. A general approach toward initial placement of collectors has been indicated.

Basic Approaches and Techniques

Gyrotrons operating at millimeter wavelengths require very high magnetic field in the interaction region, especially when operating at the fundamental of the electron cyclotron frequency, which is the cyclotron harmonic most commonly used. In the collector region, in order to be able to perform energy sorting of the spent beam, it is necessary to go to very low values of magnetic field.[1,2] Energy sorting is needed so as to collect different energy components of the spent beam on electrodes at different depressed potentials so as to maximize collector efficiency. When the force due to the electrostatic field of the depressed collectors is larger than that due to the magnetic field, the energy sorting can be done more readily.

As the ratio by which the magnetic field has to diminish from cavity to collector region is very large for millimeter wave gyrotrons, purely adiabatic transitions would make for excessively large radii of collectors.[2] It is necessary to have a judicious combination of adiabatic and non-adiabatic transitions.[3]

Adiabatic reduction in magnetic field results in a reduction of the transverse component of motion. The corresponding enhancement of the energy component in longitudinal motion facilitates energy recovery by an axisymmetric electrostatic field. In special cases,

*Sponsored in part by the Department of Energy.

such as in a large-orbit gyrotron, the transfer of energy from transverse to longitudinal components of motion can be achieved by using a non-adiabatic transition without incurring the penalty of an increase in radius.[4] In general, non-adiabatic transitions result in beam heating, i.e. increasing the spread of transverse energy of motion. However, beam heating can be minimized by choosing an optimum profile for the magnetic field, as discussed in Ref. 3. That reference presents results of simulations of trajectories using a single particle code for the cases of step or staircase transitions as well as for peaks and troughs in profile. Non-adiabatic transitions can also be put to use in energy sorting. When flux lines bend sharply as a result of such a transition, the slower electrons tend to follow the bend more closely than their more energetic counterparts.

The above issues are addressed in the first series of steps outlined in the flow diagram for design as given in Fig. 1. In order to facilitate obtaining the desired magnetic field configuration vis-a-viz the geometry of the collectors and the potentials on them, we have devised a code, referred to as "contour-graphics" in Fig. 1. It takes arrays of data generated by running unit currents through the coils that will control the field along with the magnetic yoke and pole pieces. The actual current values can be inserted and the resultant magnetic flux lines seen almost in real time along with the outlines of the collector electrodes. In this way a configuration is obtained for which, as the next step, the electron trajectories are simulated using a code such as EGUN. Their starting energies are derived from a code simulating the process of interaction in the rf cavity. The procedure is iterated to eliminate the premature return of some electrons before reaching a depressed collector and to minimize the effects of secondary electrons. Trajectories of the latter are plotted by restarting them at points of impact of primaries after introducing the statistics of secondary emission from the material of the collector.

Case Studies for Cavity and Quasi-Optical Gyrotrons

We have used the design techniques described above for cavity type and quasi-optical gyrotrons. In the former case, the path of the spent beam has to be separated from that of the millimeter wave output, in order that there be little rf field in the collector region. If the beam proceeds axially the rf needs to be extracted radially by a coupler such as a

Vlasov coupler. The magnetic field profile and the trajectories in the collector region in such a case are shown in Fig. 2. In tailoring the profile, it was observed that too rapid a decrease in B-field results in collection of almost all beamlets on the nearest and least depressed potential. On the other hand, too slow a decrease results in the return of some trajectories.[1] It is estimated that a collector efficiency of greater than 70% is achievable.

In the case of radial extraction of the beam, the beamlets have a greater tendency to return before collection, because the radial component of velocity interacting with the axial component of magnetic field generates an azimuthal component of velocity. However, by precise tailoring of the magnetic field along the lines discussed above, it was possible to get a configuration with an estimated collector efficiency of 70%. This is shown in Fig. 3.

In the case of a quasi-optical gyrotron (QOG) the paths of the spent beam and the rf output are naturally separated. We did a design study for a QOG which was being developed at the Naval Research Laboratory. In this case there were very severe restrictions on the maximum radius of the collectors. A design giving a 70% collector efficiency could be obtained in which the maximum radius of collectors was restricted to 15 cm. The energy sorting was done by a combination of electrostatic forces and bends in the magnetic flux lines.[5]

A General Approach to Avoid Return of Electrons Before Collection

If at any point in the collector region all that remains of the initial energy of a beamlet is in transverse motion, then the beamlet would return before getting collected. It is possible to get an overview of this problem by using basic laws of electron motion in an electromagnetic field having azimuthal symmetry.

In such a case, the Hamiltonian is independent of the azimuthal coordinate, and the canonical angular momentum is a constant with time. Thus

$$p_\theta = \gamma m_0 r^2 \dot{\theta} + qrA_\theta = C \tag{1}$$

or

$$r\dot{\theta} = \frac{1}{\gamma m_0}\left(\frac{C}{r} - qA_\theta\right), \tag{2}$$

where $\gamma = (1 - v^2/c^2)^{1/2}$. As $v_r^2 + v_\theta^2 + v_z^2 = v^2$, we can write

$$v_r^2 + v_z^2 = v^2 - \frac{1}{\gamma^2 m_0^2}\left(\frac{C}{r} - qA_\theta\right)^2. \tag{3}$$

The left-hand side must be positive in regions that can be reached by particles. Thus,

$$v^2 \geq \frac{1}{\gamma^2 m_0^2}\left(\frac{C}{r} - qA_\theta\right)^2. \tag{4}$$

For mildly relativistic particles, the boundary line between accessible and inaccessible regions can thus be defined by the equation

$$2q^{1/2}\left[\frac{V_s - V_{\text{equip}(r,z)}}{m_0}\right]^{1/2} = \frac{1}{\gamma m_0}\left[\frac{C}{r} - qA_\theta(r,z)\right], \tag{5}$$

where qV_s represents the initial energy of the particle, and qV_{equip} represents the energy delivered to the electrostatic field up to any given equipotential reached by the particles. Equation (5) has bean solved for cases analogous to the case of the cavity gyrotron with axially streaming spent beam and an assumed electrostatic potential distribution. An example of a graph showing the boundary line dividing the region accessible to electrons from that which is inaccessible is shown in Fig. 5 for an assumed magnetic field profile, and an assumed depressed potential varying linearly with axial and radial coordinates. A similar initial exercise in a new case starting with physically realizable estimates of overall trends of the fields can help to define the initial geometry of collectors, by putting them in the accessible region.

Conclusions

The main problems encountered in the design of multiple depressed collectors for millimeter wave gyrotrons have been presented along with techniques for resolving them. The magnetic field configurations have to be precisely tailored. Controlled non-adiabaticity allows the radius of the collectors to be kept within reasonable limits without excessive beam heating. A computer code has been developed to facilitate the precise design of magnetic fields. Examples have been presented for the cases of cavity gyrotrons with axial and radially extracted spent beams and for quasi-optical gyrotrons. An estimated collector efficiency of 70% is seen to be feasible in all of these cases. An analysis has been given for defining the regions which are accessible to electrons in the spent beam, so as to put collector electrodes there only.

References

1. A. Singh, G. Hazel, V.L. Granatstein, and G. Saraph, "Magnetic field profiles in depressed collector regions for small orbit gyrotrons and axial or radially extracted spent beams," to be published in Int. J. Electronics.

2.1. M.E. Read, A.J. Dudas, W. Lawson, and A. Singh, IEEE Trans. **ED17**, 1579-1589 (1990).

3. A. Singh, V.L. Granatstein, C. Casey, and W.W. Destler, Int. J. Electronics **70**, 1143-1154 (1991).

4. A. Singh, W.W. Destler, V.L. Granatstein, and W.R. Hix, Int. J. Electronics **72**, 827-840 (1992).

5. A. Singh, V.L. Granatstein, G. Hazel, and J.M. Cooperstein, Int. J. Infrared and Millimeter Waves **12**, 323-334 (1991).

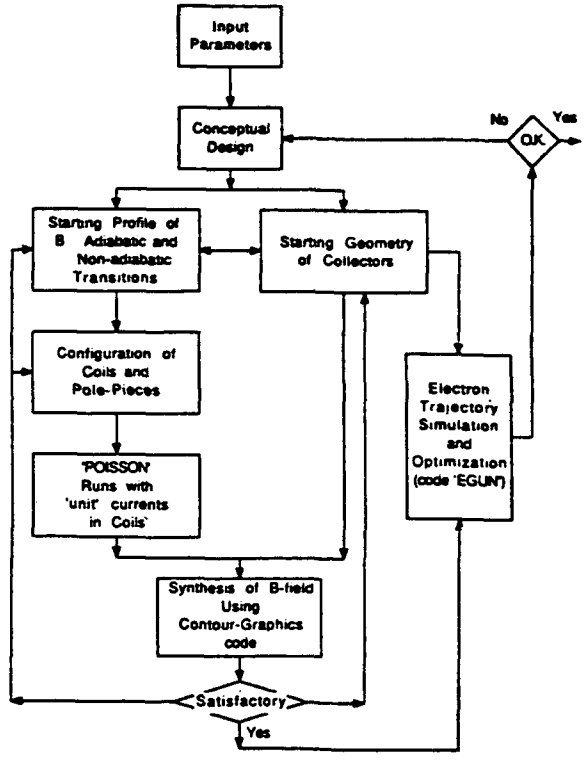


Fig. 1. Flow diagram for design of multiple depressed collectors.

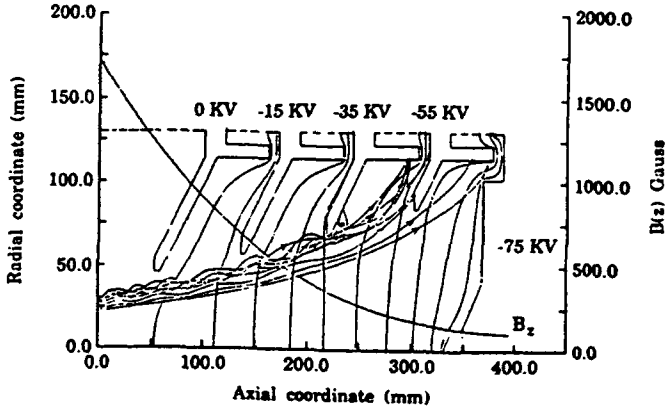


Fig. 2. Electron trajectories in collector region of a cavity gyrotron with axially streaming spent beam.

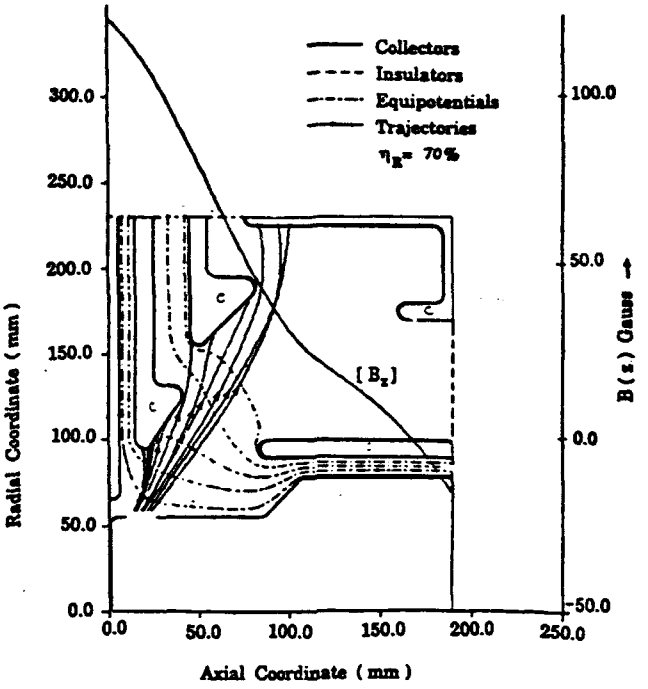


Fig. 3. Trajectories in collector region of a cavity gyrotron with a radially extracted beam.

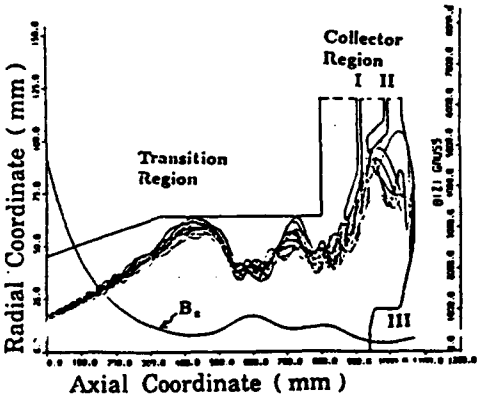


Fig. 4. Trajectories for a quasi-optical gyrotron. The profile of magnetic field is precisely adjusted to accommodate the collector region in a radius of 12.5 cm, while giving energy sorting and a collector efficiency of 70%.

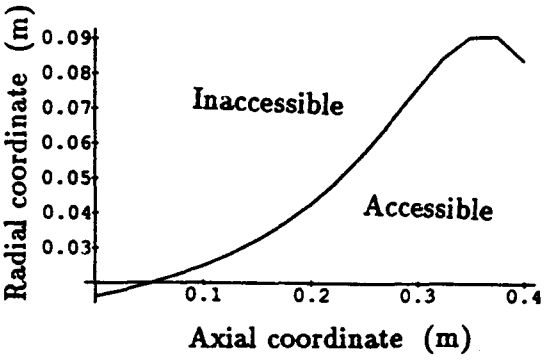


Fig. 5. An example of initially defining accessible and inaccessible areas for electrons in collector region.

Acknowledgements: Discussions with Professors C.D. Striffler, W. Lawson, and M. Reiser were very valuable. Our student collaborators at various stages were: D. Goutos, W.R. Hix, G. Hazel, G. Saraph, J. Cooperstein, and A.M. Darwish.

COHERENT FAST WAVE RADIATION FROM SPATIOTEMPORALLY MODULATED GYRATING RELATIVISTIC ELECTRON BEAMS

J. L. Hirshfield

Omega-P, Inc., 2008 Yale Station, New Haven, CT 06517; and
Physics Department, Yale University, New Haven, CT 06511

and

A. K. Ganguly

Code 6841, Naval Research Laboratory, Washington, D.C. 20375

Generation of radiation is described at a harmonic of the rotation frequency for a spatiotemporally modulated gyrating electron beam. Cumulative energy flow into the wave occurs when its group velocity matches the beam's axial velocity. Fifth harmonic wave growth at 94 GHz in a cylindrical waveguide is shown to be relatively free of mode competition for a device employing a 150 kV, 6.7 A beam. Non-linear simulations show a saturated efficiency of 56% for a linear magnetic field taper in this device. The saturated efficiency only drops to 50% for an axial velocity spread of 10%.

Introduction

Continuing demand exists for efficient rf sources as drivers for next-generation $e^- - e^+$ colliders, as amplifiers for advanced radars, and as power sources for plasma heating and control. This paper gives new results on the detailed evaluation of a harmonic conversion process for the generation of rf power proposed in 1991.[1] In this process, spatiotemporally-coherent gyrating motion is imposed on an electron beam during cyclotron autoresonance acceleration,[2] and energy flows cumulatively from the beam into a fast guided wave at a harmonic of the accelerator frequency. The initial work on the process was limited to a first-order analysis for radiation into TE_{0m} modes in a rectangular waveguide. Subsequent work[3] extended the first-order analysis to radiation into TE_{lm} modes of both rectangular and square waveguides. That work showed that, while modes at undesired harmonics would compete with the design mode in rectangular waveguides, mode competition may not be a significant issue for circularily-polarized TE_{0m} modes in square waveguides, since square guides have a lower mode density than rectangular guides.

The present work extends the analysis to cylindrical waveguides, where the mode spectral density is essentially identical to that for square waveguides. The first-order interaction for an axisymmetric distribution of beam guiding centers can be shown to be absent for all TM modes and for all TE modes except those whose azimuthal mode index equals the working harmonic.[4] This further helps to insulate the interaction against mode competition. Preliminary results of a non-linear particle simulation study of the interaction are also given that show, as an example, a fifth harmonic interaction at 94 GHz with high efficiency, and furthermore show that the efficiency will fall but slowly as beam axial velocity spread is increased.

These results, and extensions thereof, can be used to set the required specifications for beams from cyclotron autoresonance accelerators to power efficient 50 MW sources in the 10 - 30 GHz regime for future colliders, at the 100 kW level at 94 GHz for future radars, and at the MW-level at 140 and 280 GHz for plasma heating and control.

First-Order Analysis

We summarize here results of our analysis for the cumulative power flow P(L) from the beam into the fields of a TE_{lm} mode in a cylindrical waveguide after the beam and wave have traveled together a distance L along the waveguide, where

$$dP(z,t)/dz = -\int_0^R dr\, r \int_0^{2\pi} d\phi\ \mathbf{J}(r, \phi, z, t) \cdot \mathbf{E}(r, \phi, z, t) \qquad (1)$$

In this equation R is the waveguide radius, r and ϕ are polar coordinates with respect to the waveguide axis along which a uniform magnetic field B_o is imposed; **J** is the instantaneous current density of the beam; and **E** is the rf electric field. For a TE_{lm} mode, $P(z) = \pi R^2 g_{mn}(k_\perp R)E_o^2(z)/2Z_{TE}$, where $k_\perp R = s_{mn}$, the n-th zero of $J_m'(s)$; $g_{mn} = J_m^2(s_{mn})(1 - m^2/s_{mn}^2)$; $Z_{TE} = 120\pi(\omega/k_z c)$ ohms; and $E_o(z)$ is the slowly varying amplitude of the field. The current density for a spatiotemporally coherent beam is

$$\mathbf{J}(r,\phi,z;t) = -e\int_{-\infty}^{\infty} du \int_0^{\infty} dw\, w \int_0^{2\pi} d\theta \left[\hat{e}_\theta \frac{w}{\gamma} + \hat{e}_z \frac{u}{\gamma}\right] \times \delta(\theta - \theta_o + \xi z - pt)\, f_o(w,u,r,\phi,\theta), \qquad (2)$$

where w and u are the magnitudes of the momentum components (divided by the electron rest mass) across and along the axis; θ is the gyration angle; f_o is the electron distribution function; p is the radian frequency of orbit temporal rotation; and $\xi = \gamma(p - \Omega)/u$ is the pitch number for orbit spatial variation, with $\Omega = eB_o/m\gamma$.

Expansion of the fields in terms of the electron's center and angle of gyration r_g and ϕ_g, and limitation to beams with axisymmetric distributions of guiding centers, i.e. with $f_o = N_o F_o(u,w) G_o(r_g)$, leads to[4]

$$E_o(L) - E_o(0) = -\frac{Z_{TE} L}{g_{mn}} \left(\frac{R_b}{R}\right)^2 N_o e\, H(k_\perp R_b) \int du \int dw\, \frac{w^2}{\gamma} F_o(u,w)$$
$$\times J_m'\left(\frac{k_\perp w}{\Omega\gamma}\right) \frac{1}{\zeta_1} \int_{\zeta_2 - \zeta_1}^{\zeta_2} \frac{d\zeta}{\zeta} \left[\sin(m\theta_o + \zeta) - \sin(m\theta_o)\right], \qquad (3)$$

where $E_o(0)$ is the input value; $H(k_\perp R_b) = (2/R_b^2) \int_0^{R_b} dr_g r_g J_o(k_\perp r_g) G_o(r_g)$ with R_b the outer guiding center radius; $\zeta_1 = (\omega - mp)\gamma L/u$ and $\zeta_2 = (k_z - m\zeta)L$. Eq. 3 is seen to embody spreads in both guiding center and momentum. For a cold beam with no spread in guiding centers the rhs of Eq. 3 is $(120/R^2 g_{mn}\beta_z)(W/U) I_o L J_m'(k_\perp \rho)$, where I_o is the dc beam current, ρ is the gyration radius, and $\beta_z = u/c\gamma$. With no input signal, we thus find for a cold beam

$$P(L) = \frac{60\, L^2}{R^2 g_{mn} \beta_z} \left(\frac{W}{U}\right)^2 I_o^2 J_m'^2(k_\perp \rho) \text{ watts.} \qquad (4)$$

As an example, we consider a 5-th harmonic interaction at 94 GHz between TE_{51} mode fields and a 150 kV, 6.67 A electron beam with W/U = 2.0. For $B_o = 7.983$ kG and R = 0.340 cm, $\zeta_1 = \zeta_2 = 0$, the beam axial velocity equals the wave group velocity, and wave growth is cumulative. We then find the rf power to evolve as $P(L) = 20.1L^2$ kW, reaching 100 kW in an interaction length of 2.23 cm. Table I gives the rate at which power would grow in competing modes at other harmonics, based on an evaluation of Eq. (3) with the consequent mismatch between the axial beam velocity and the competing mode's group velocity. The Table shows that, while the initial wave growth rates are comparable for all harmonics that can propagate, all but the design mode TE_{51} evolve to insignificant levels, due to phase interference from the aforementioned

mismatch.

harmonic	5	4	3	2	1	1
mode	TE_{51}	TE_{42}	TE_{31}	TE_{21}	TE_{11}	TE_{12}
$P(L)/L^2$, $L\rightarrow 0$	2.01(4)	1.98(4)	3.05(4)	4.65(4)	5.54(4)	6.96(4)
P(L=5cm)	2.00(5)*	3.20(1)	8.46(2)	1.87(2)	1.86(2)	2.26(3)

Table 1. Wave growth into all propagating modes. Figures in parentheses are powers of 10. *Result based on non-linear simulation; see below.

When a finite spread in centers of gyration is present, wave growth is reduced from the values given above. For example, if the distribution of guiding centers is uniform, one finds that the factor $H(k_\perp R_b)$ falls to 0.707 for $k_\perp R_b = 1.6$. For the TE_{51} example given above this reduces the linear growth to half that for a beam with no spread for $R_b = 0.085$ cm, corresponding to about 25% of the waveguide radius. For a finite spread in axial momentum, analysis of Eq. (3) shows that the linear growth falls to half that for a cold beam when $\delta u/u = 7.7/k_z L$. For the above TE_{51} example with $L = 5$ cm, this gives $\delta u/u = 0.28$.

Nonlinear Simulation

Nonlinear analysis is needed to provide an estimate of the efficiency and influence of beam thermal effects. The non-linear equations describing the evolution of the fields and particle trajectories have been published elsewhere.[5] A slow time scale formulation in three dimensions first developed to describe steady-state operation of a gyrotron amplifier is used. Only a single frequency excitation is assumed to propagate, and Maxwell's equations and the Lorentz equation can thus be averaged over a wave period. Electron trajectories are taken to be a fast Larmor rotation about a slowly varying guiding center drift. These assumptions result in two simplifications in the numerical calculations that increase the step size, relative to the particle-in-cell procedure: (i) fast oscillations are absent; and (ii) only those electrons need be tracked that enter the interaction within one period. An infinitesimally thin, monoenergetic beam is taken to enter the interaction waveguide with a gyration angle $\theta = \theta_0 - \xi z + pt$, as in Eq. (2). Axial velocity spread is introduced through a pitch-angle distribution for f_0. The initial wave amplitude is taken at the noise level. Numerical results are shown for the 94 GHz, 5-th harmonic example discussed above.

Results are shown in Fig. 1 for a cold beam, i.e. a monoenergetic beam with no spread in pitch angle. For a uniform magnetic field $B_{gr} = 7.983$ kG, the efficiency saturates at an interaction length of 2.92 cm at 9.62%. This occurs since the beam particles, behaving as a macro-bunch, all slip out of synchronism with the wave due to energy depletion. Tapering the magnetic field allows the macro-bunch to remain in synchronism, as is shown also in Fig. 1 for the case of a linear taper: $B = B_{gr}$ for $z < 0.5R$, and $B = B_{gr}\left[1 - 0.003(z - 0.5R)/R\right]$ for $z > 0.5R$. (These are values which maximized the efficiency for a linear taper.) In this case the saturated efficiency increases to 55.7% at an interaction length of 18.6 cm. Fig 2 shows the effect of a spread in axial velocity for the tapered case: as $\delta u/u$ increases from 0 to 10%, the efficiency drops from 55.7% to 49.7%; at $\delta u/u = 20\%$, the efficiency drops more rapidly to 32.4%. Fig. 2 also shows the interaction lengths at saturation. Other runs not shown here with non-linear field tapers show even higher efficiency and similar insensitivity to axial velocity spread.

Conclusions

Harmonic conversion from a spatiotemporally modulated gyrating relativistic electron beam into modes of a cylindrical waveguide has been described. First-order wave growth from a beam with an axisymmetric distribution of guiding centers is absent for all TM modes, and for TE modes whose azimuthal index does not equal the working harmonic number. As an example, 5-th harmonic wave growth for the TE_{51} mode of a cylindrical waveguide at 94 GHz from a 150 kV, 6.7 A beam was considered. This conceptual device was shown to be relatively free of competition from interactions in all other modes that can interact with the beam. For this example, a saturated efficiency of 56% was found for a linearly tapered magnetic field. For short interaction lengths, the simulated non-linear efficiency agrees with the analytically derived first-order theoretical value of $2L^2$ %, where L is the interaction length in cm. The saturated efficiency falls only to 50% for a 10% axial velocity spread. These results confirm earlier expectations that electrons behave in this interaction as a macro-bunch, and thus remain in phase as they give up a substantial portion of their transverse energy to the wave. One can thus conceive of highly efficient moderate-to-high power radiation sources with low distributed wall losses, direct waveguide output coupling, and simple depressed beam collectors for advanced millimeter wave radars, tokamak plasma heating and control, and cm-wavelength drivers for next-generation $e^- - e^+$ colliders.

This research was sponsored by the Office of Naval Technology and the Office of Naval Research.

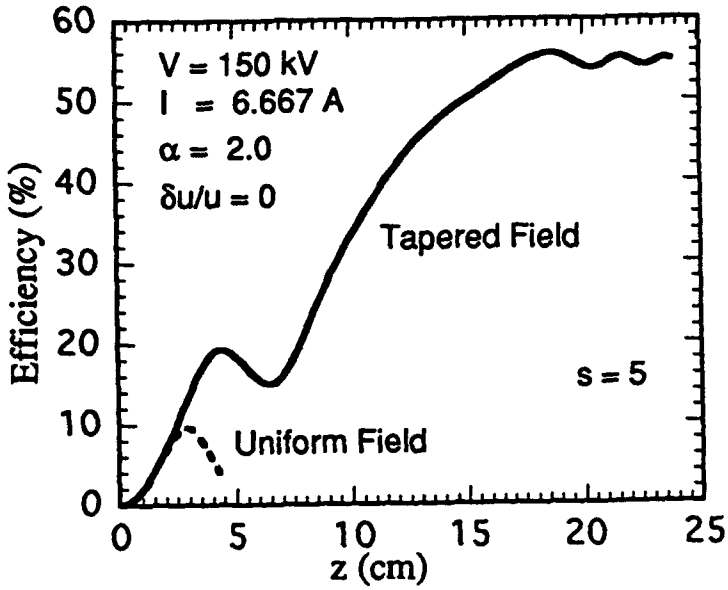


Fig. 1. Efficiency *vs* axial interaction length at 94 GHz for a 5-th harmonic converter. Dashed curve: uniform B-field; solid curve: linearly tapered B-field.

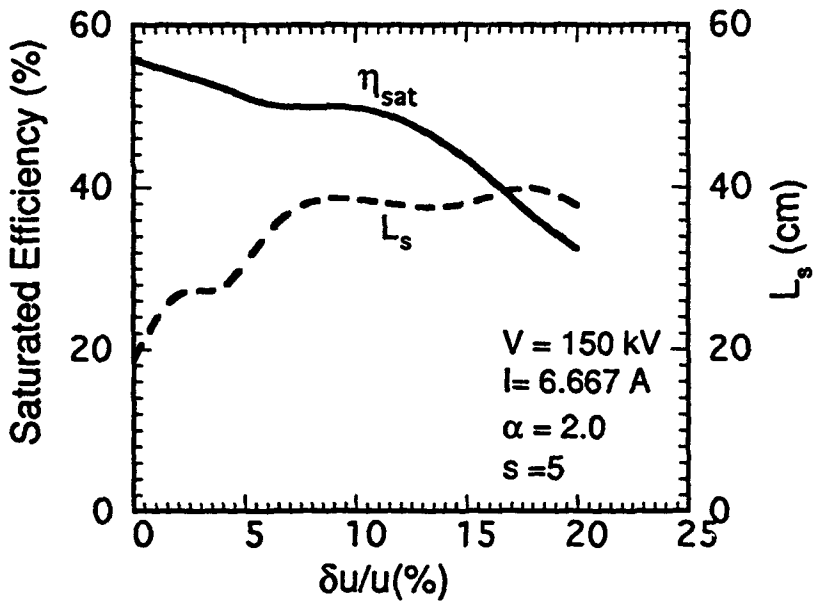


Fig. 2. Saturated efficiency *vs* axial velocity spread at 94 GHz for a 5-th harmonic converter with linearly tapered B-field. Solid curve: saturated efficiency; dashed curve: length for saturation.

---

1. J. L. Hirshfield, Phys. Rev. A **44**, 6845 (1991).
2. P. Shpitalnik, et al, J. Appl. Phys. **70**, 1101 (1991); **71**, 1583 (1992).
3. J. L. Hirshfield, submitted for publication.
4. J. L. Hirshfield and A. K. Ganguly, to be published.
5. A. K. Ganguly, S. Ahn and S. Y. Park, Int. J. Electronics **53**, 641 (1982); **65**, 597 (1988); **67**, 261 (1989).

Cyclotron Autoresonance Masers: Recent Experiments and Projects

V.L. Bratman, G.G. Denisov,
and S.V. Samsonov

Institute of Applied Physics,
Russian Academy of Sciences,
46 Uljanov Street, 603600 Nizhny Novgorod, Russia

Introduction

The cyclotron autoresonance maser (CARM) [1-3] is one of the promising modifications of free-electron masers (FEM) operated at the millimeter and submillimeter waves. In this range CARM requires particle energies significantly lower than for the ubitron, and magnetic fields smaller than those for the gyrotron. The CARM is considered as a possible source of coherent millimeter wavelength radiation with large average (continuous) power for plasma heating in controlled fusion devices.

The CARM, as well as the gyrotron, is a modification of the cyclotron resonance maser, i.e. it is a device which uses stimulated radiation of electrons moving along helical trajectories in a homogeneous magnetic field. Unlike in the gyrotron, electrons in CARM interact with an electromagnetic wave $\exp i\,(hz - \omega t)$ propagating not across but nearly along their translation velocities. So, it is evident from the condition of electron resonance with the wave $\omega - hv_{\|} \simeq \omega_H$ that due to the Doppler effect the wave frequency in CARM at relativistic translation velocities of electrons $v_{\|}$ greatly exceeds the frequency of particle oscillations (here it is the cyclotron frequency ω_H): $\omega \sim \gamma^2 \omega_H$ where $\gamma = \mathcal{E}/mc^2$ is a relativistic factor of electrons.

Another consequence of the quasi-longitudinal propagation of the wave in CARM is partial autoresonance compensation of the variation of the cyclotron frequency $\Delta\omega_H$ by the Doppler shift $\Delta(hv_{\|})$. By virtue of this compensation the electrons resonantly interact with the wave even at considerable variations of their energies and CARM efficiency at large enough rotational velocities of particles $\beta_{\perp} \sim \gamma^{-1}$ can be some tens per cent. It is due to the same reason that CARM is characterized by small sensitivity to particle energy spread $\delta\gamma_0$. But like other FEL's and FEM's, CARM is very sensitive to the spread in the pitch angles of particles. Thus, so as to

attain high electron efficiency in CARM, the electron-optical system must produce an electron beam with a sufficiently great rotational velocity of particles $\beta_{\perp 0} \sim \gamma_0^{-1}$ at small spread $\delta\beta_\perp$.

Another problem that is essential in the realization of an efficient CARM is the suppression of the parasitic mode excitation. The gyrotron and backward waves are usually most difficult to suppress. In principle, this problem can be solved by using as an operating mode a lower mode of a regular waveguide in the regime of tangential dispersion characteristics of the wave and of the beam or in a regime close to it. In a number of cases it appears more natural to employ higher modes, although this requires, generally speaking, the development of effective methods for suppressing low-frequency generation.

Experimental Investigations of CARMs

Early experiments demonstrated the short-wave properties of CARM. For relatively low energies of 350-600 keV and magnetic fields of 10-20 kOe, the chosen modes: $H_{1,1}$, $H_{2,1}$ and $H_{4,1}$ of cylindric resonators with Bragg mirrors were excited selectively at the wavelengths ranging from 4.5 mm to 2.4 mm with the output power on the order of 10 MW.

A high amplification coefficient in the absence of parasitic generation was obtained in the joint experiment of the Institute of Applied Physics of the Russian Academy of Sciences (IAP) and the Institute of High-Current Electronics on the first CARM-TWT [4]. The experiment was performed on the high-current direct-action accelerator "Sinus-6" employing an electron beam having the energy of 500 keV, current 0.5 kA and pulse duration 25 ns. The $H_{1,1}$-mode of a circular waveguide in the regime of tangential dispersion characteristics of the wave and the beam was used as an operating mode. The amplified external signal with the wavelength of 8.2 mm was injected into the operating waveguide by means of a directional coupler. The amplification amounted to 30 dB with the maximum output power 10 MW and efficiency 4 %. Similar results were obtained in the investigation of the CARM-TWT in MIT [5].

New experimental investigations of CARM-generators are now carried out on the accelerator "Sinus-6" in IAP and on the LIA- unit in the Joint Institute of Nuclear Research (JINR). These investigations are aimed at pro-

ducing the efficiencies that will be much higher than in early experiments. For this purpose improved kickers are used to provide greater rotational velocities $\beta_{\perp_0} \approx \gamma_0^{-1}$ with smaller spread and the spread influence is decreased by shortening the length of the interaction space down to $N \sim 5$–7.

Experiments performed at the accelerator "Sinus-6" employed a thin tubular electron beam having the energy of 500 keV and current 500 A that was produced in a co-axial diode with magnetic insulation. The beam acquired rotational velocity $\beta_{\perp_0} \leq 0.5$ in the kicker in the form of two coils that were co-axial to the beam, had opposite directions of current and were placed inside and outside the beam at a distance $\frac{1}{2}L_H$ from one another, where L_H is the Larmore step of electrons. The higher $H_{5,1}$-mode of a cylindrical Bragg resonator 24-mm in diameter was used as the operating mode. High efficiency of gyrotron generation at the $H_{3,1}$-mode excited when the magnetic field was lower than the operating value testifies indirectly to a high quality of the electron beam: the radiation power was 80 MW with the efficiency 30% at the wavelength 19 mm. The radiation power at the operating $H_{5,1}$-mode with the 8-mm wavelength was 20 MW with the efficiency 8% .

In the joint experiment of the IAP and JINR that was carried out at the LIA-unit in Dubna a thin solid electron beam having the energy 1-1.2 MeV and current 300-500 A produced in a co-axial diode with magnetic insulation was used. The beam acquired the rotational velocity $\beta_{\perp_0} \leq 0.3$ in the kicker in the form of two rectilinear currents of opposite directions which were located perpendicular to the beam on its both sides at a distance $\frac{1}{2}L_H$ from one another. The lower $H_{1,1}$-mode of a cylindrical Bragg resonator 10 mm in diameter was used as the operating mode.

Two generation regimes were realized in the experiment. In the first regime, the electron energy was 1.2 MW and the magnetic field 10 kOe. Correspondingly, the dispersion characteristics of the beam and the wave intersected in two points. With great enough reflection coefficients and short length of the interaction space the operating mode with the wavelength of 4.4 mm was excited. However, besides that mode a rather powerful radiation at close frequencies was also observed all through the band of cyclotron resonance $\Delta f \sim 20\%$ and did not disappear even without Bragg mirrors. The radiation power at the operating wavelength was 50 MW with efficiency 8% .

In the second regime, the electron energy was 1.0 MeV and the magnetic field, 7 kOe. The dispersion characteristics of the electron beam and of the wave did not intersect (the characteristic of the beam was slightly lower than the tangential point). In that case the power of parasitic radiation was much lower and the radiation efficiency at the 6-mm wave corresponding to high-Q oscillation of Bragg resonator was higher: the radiation power amounted to 30 MW with efficiency 10%.

Prospects and projects

At present only CARM with nanosecond electron beams produced by means of explosive emission have been realized (the only exception is CARM with 8-mm Bragg resonator employing thermoemitter, that was elaborated in MIT). The CARMs described above generate single-pulse radiation of about 0.1-1 J. When passing over from the single-pulse to the pulse-periodic regime with the repetition frequency of about 1 kHz that is the maximal attainable magnitude at present, we can expect that the CARM of interest will produce a kilowatt average power. Generation of significantly higher power will need considerable advance in the technology of powerful high voltage modulators and emitter operating with the high repetition frequency or in a continuous regime. On the basis of such electron sources the CARM varieties considered above could provide a rather high average power with acceptable level of heating of the walls of electrodynamic system caused by ohmic losses. Thus, the CARM-generator operated at the lower $H_{1,1}$-mode at the wavelength 4.4 mm with average radiation power 5 MW the thermal load would not exceed 1 kW/cm . This power can be increased by an order of magnitude if a smooth waveguide is replaced by a corrugated waveguide with the operating $HE_{1,1}$-mode having a small field at the wall, and if quasi-optical reflectors are used instead of Bragg mirrors. Estimations show that such a CARM with the electron energy $\mathcal{E} \sim 1$ MeV may be realized also at the 1-2 mm waves with the average power 5-10 MW for relatively low magnetic fields of 20-40 kOe. Similar results may be also obtained in CRM-TWT having a relatively low-energy beam $\mathcal{E} \sim$ 0.3-0.5 MeV and a high magnetic field $H \sim$ 50-100 kOe.

At present the developing a special installation for investigations of CARM on the short-wave part of the millimeter wavelength band is close

to the completion at the IAP. This set-up will include thermal emission injectors and cryomagnets. Along with that, experiments on realization of a CARM generator with the wavelength 8 mm including a thermoemitter and pulsed magnetic field have been started at the "Saturn" installation. In the course of this experiment a hollow cylindrical electron beam with helical trajectories of the particles is produced in a magnetron injection gun similar to those used in gyrotrons. The energy of electrons is up to 300 keV, current, 20-30 A, and current pulse duration, 5 μs. As an operating the axially symmetrical $H_{0,1}$ mode of a cavity with circular cross-section is used. To avoid parasitic low-frequency generation, the cavity section within the interaction space is tapered with a low angle of the order of 1°. This measure not only raises the start-up currents of the parasitic modes, but leads to favorable distribution of the phase velocity of the operating wave as well as increases the efficiency by 1.6 times. At the collector end of the cavity the traditional Bragg reflector with reflectivity 0.8 is used, and at the cathode end, the short reflector using resonance reflection from the subsidiary resonator of the wave connected with the eigenmode of this resonator (in this case, with the $H_{0,2}$ mode). The cathode reflector assures the wave reflectivity close to unity. Calculations show that when the quality of the electron beam is sufficiently high, the generator efficiency is close to 30% , and output power is about 1.5 MW.

References

1. Petelin, M.I, 1974, On the theory of ultrarelativistic cyclotron self-resonance masers. Izv. Vyssh. ucheb. Zaved. Radiofiz., 17 902-908; also in Radiophys. Quantum Electron., 17, 686-690.

2. Bratman, V.L., Ginzburg, N.S., Nusinovich, G.S., Petelin, M.I., and Yulpatov, V.K., 1979, Cyclotron and synchrotron masers. Relativistic HF Electronics, Vol. 1, edited. by A.V. Gaponov-Grekhov (Gorky, U.S.S.R.: Institute of Applied Physics), pp. 157-216.

3. Bratman, V.L., Denisov, G.G., Ginzburg, N.S., and Petelin, M.I., 1983, FEL's with Bragg reflection resonators. Cyclotron autoresonance masers versus ubitrons. I.E.E.E. J. Quantum Electron., 19, 282-296.

4. Bratman, V.L., Gubanov, V.P., Denisov, G.G., Korovin, S.D., Movshevich, B.Z., Polevin, S.D., Rostov, V.V., Smorgonsky, A.V., 1986. Coherent radiation of modulated high-current beam of relativistic electrons. 6 All-Union Symposium on High-Current Electronics, Novosibirsk, U.S.S.R., Symp. Digest , part 3, pp.6-8.

5. Bekefi, G., Di Rienzo, A., Leibovitch, C., and Danly, B.G., 1989, A 35 GHz Cyclotron Autoresonance Maser (CARM) Amplifier. Appl. Phys. Lett., 54, 1302-1304.

CYCLOTRON AUTORESONANCE MASER (CARM) AMPLIFIER EXPERIMENTS AT 17 GHZ[1]

W.L. Menninger, B.G. Danly, S. Alberti[2], C. Chen, D.L. Goodman[3],
E. Giguet[4], J.L. Rullier[5], J.S. Wurtele, R.J. Temkin
Plasma Fusion Center, Massachusetts Institute of Technology
Cambridge, MA 02139

Abstract

CARMs are attractive sources for applications such as electron cyclotron resonance heating of fusion plasmas and driving high-gradient RF linear accelerators. For applications such as accelerator drivers, amplifiers or locked-oscillators are required. A 17 GHz cyclotron autoresonance maser (CARM) amplifier experiment is presently underway at the MIT Plasma Fusion Center. This experiment uses an electron beam generated by the 500 kV injector on the SRL/MIT SNOMAD II induction accelerator. The present gun geometry produces a beam at 400 kV in a 50 ns pulse. The amplifier is designed to operate in the TE_{11} mode. To date, only second and third harmonic relativistic gyro-TWT modes have been seen. The power levels of these modes are $\sim$ 1 MW. We characterize these modes and discuss steps which we are taking in order to operate in the TE_{11} CARM mode.

A high power, 17 GHz CARM amplifier has numerous applications. An RF injection electron gun is currently being designed at MIT that has RF input requirements quite comparable to the CARM amplifier's predicted rf output (see elsewhere in these proceedings). A potential high degree of phase stability may allow the CARM amplifier to serve as a driver for future high gradient linear e^+e^- colliders.

I Introduction

The cyclotron autoresonance maser (CARM) is similar to a gyrotron, except that the electromagnetic wave propagates with a phase velocity close to the speed of light. The CARM typically employs relativistic electron beams with pitch angles, $\alpha_0 \equiv \beta_{\perp 0}/\beta_{\|0}$, smaller than those of the gyrotron. These features allow CARMs to operate at higher frequencies than gyrotrons for comparable magnetic guide field strengths. There have been numerous theoretical studies and simulations of CARMs[1,2,3,4,5,6]. Unlike gyrotrons and free-electron lasers, however, there have been very few experimental demonstrations of the CARM amplifier[7,8]. MIT currently

[1] Supported by the Department of Energy, Advanced Energy Projects Office, under contract DE-FG02-89ER14052. Additional support from Science Research Laboratory, Thomson Tubes Electroniques, DARPA, Varian Associates, LBL, Northstar Research, and LLNL is gratefully acknowledged.
[2] Supported by Swiss National Science Foundation, Fellowship Nr. 8220-30665
[3] Also with Science Research Laboratory, Somerville, MA
[4] Also with Thomson Tubes Electroniques, Vélizy, France
[5] Supported by CEA/CESTA, France

has two operating CARM experiments. The MIT CARM oscillator is discussed elsewhere in these proceedings. A 17 GHz MIT CARM amplifier experiment that is presently underway is discussed here.

II Design

We designed the 17 GHz CARM amplifier utilizing a 500 kV linear induction accelerator which generates a 500 A, 30 ns flat-top pulse. The CARM amplifier is designed to operate in the TE_{11} mode. A three period bifilar helical wiggler with a wiggler period of 9.21 cm and a field of up to 40 G is used to spin-up the electron beam, which is injected by a thermionic Pierce-type gun. The beam then travels through a region of adiabatic compression where the magnetic field increases to a strength suitable for extracting energy from the beam via the upshifted CRM resonance. A 17 GHz input signal is injected into the interaction region using a wire-mesh coupler. The signal copropagates with the beam in a 1.27 cm radius waveguide. The source of the signal is a magnetron. The amplified microwave radiation travels through an alumina-ceramic window matched at 17 GHz. Original designs predicted 23 MW of output power and 44 dB of gain for a beam pitch of $\alpha = 0.4$ and a guide field of $\sim$3 kG [9,10].

III Diagnostics

An important part of any maser experiment is accurate measurement of beam parameters. We use two diagnostics on our beam line that allow us to determine the beam current, position, and pitch. The first diagnostic, a B-dot probe, consists of four small wire loops. Each loop is in a plane of constant azimuthal angle, and the loops are placed around the beam line at 90° intervals. As the beam passes through the beam pipe, a voltage signal on each loop is generated that is proportional to dB_θ/dt, which is in turn proportional to dI/dt. By time-integrating the signals from the loops, we determine the total current in the beam. By comparing the relative signal strengths of the loops, we can determine the position of the beam. Calibrations show that we can predict the beam position to an accuracy of less than 1 mm.

The other diagnostic is a diamagnetic loop. This wire loop is in a plane of constant axial position, and it encircles the beam path. Ideally, a perfectly straight beam will generate no signal on such a loop, however, a beam with pitch, α, and Larmor radius, r_L, will generate a signal proportional to $dB_{z,\mathrm{self}}/dt$. Assume that the beam is pencil thin, follows a perfectly helical trajectory, and is infinitely long. If $V(t)$ is the time-dependent signal seen on the diamagnetic loop, then the time-integrated signal is

$$\int V(t)dt = \int \mathbf{B}_{\mathrm{self}} \cdot d\mathbf{A} = \int B_{z,\mathrm{self}} dA, \tag{1}$$

where

$$B_{z,\mathrm{self}} = \mu_0 n I = \mu_0 \frac{I}{\lambda_c}, \tag{2}$$

and λ_c is defined here as the axial distance through which an electron travels over a single cyclotron orbit. Substituting $\int dA = \pi r_L^2$ and converting λ_c to beam pitch: $\alpha = 2\pi r_L/\lambda_c$, the loop flux becomes

$$B_{z,\text{self}} A = \frac{\mu_0 I}{2} \alpha r_L. \tag{3}$$

The time-integrated diamagnetic loop signal divided by the total beam current is measured in volt-seconds per ampere. Let S be the normalized time-integrated diamagnetic loop signal strength:

$$S \equiv \frac{\int V(t)dt}{I} = \frac{\mu_0}{2} \alpha r_L \equiv \kappa \alpha r_L. \tag{4}$$

We measured the value of κ in a calibration to be 9.35×10^{-8} $\frac{\text{V}\cdot\text{s}}{\text{A}\cdot\text{m}}$. This compares to $\mu_0/2 = 6.28 \times 10^{-7}$ $\frac{\text{V}\cdot\text{s}}{\text{A}\cdot\text{m}}$. The smaller calibration value is likely due to an azimuthal wall current which reduces the self B_z field of the beam. From the Lorentz force law,

$$r_L = \frac{c\beta_\perp}{\Omega_c}, \tag{5}$$

and again converting to beam pitch, r_L is represented as

$$r_L = \frac{\alpha}{\sqrt{1+\alpha^2}} \left(\frac{c\beta}{\Omega_c}\right). \tag{6}$$

Letting $\Delta \equiv (S\Omega_c)/(c\beta\kappa)$ and simultaneously solving Eqs. 4 and 6, the solution for α is

$$\alpha = \frac{\Delta}{\sqrt{2}} \sqrt{1 + \sqrt{1 + \frac{4}{\Delta^2}}}. \tag{7}$$

Thus by knowing the beam energy and current and the axial guide field at the diamagnetic loop, we use the diamagnetic loop signal to calculate the beam pitch.

The values of α that are determined from the diamagnetic loop signal are quite inconsistent with theory. We have modeled beam transport through a bifilar helical wiggler with three independent codes. All of the codes agree to within ~20%; however, as shown in Fig. 1, the values of α derived from the diamagnetic loop signal are over three times larger than a single particle code predicts. The CARM oscillator experiment, using a completely different diagnostic (see elsewhere in these proceedings) has obtained similar results. There are several reasons α may be larger than theory predicts, including gun misalignment, larger than expected beam emittance, and errors in the calculation of α from the diamagnetic loop signal, but most of these explanations cannot account for a factor of three increase in α. This remains unexplained. While the values of α predicted from the diamagnetic loop signal do not match theory, they more accurately match the expected values of α based on the RF modes that have been excited in the CARM amplifier. This is discussed further in Section IV.

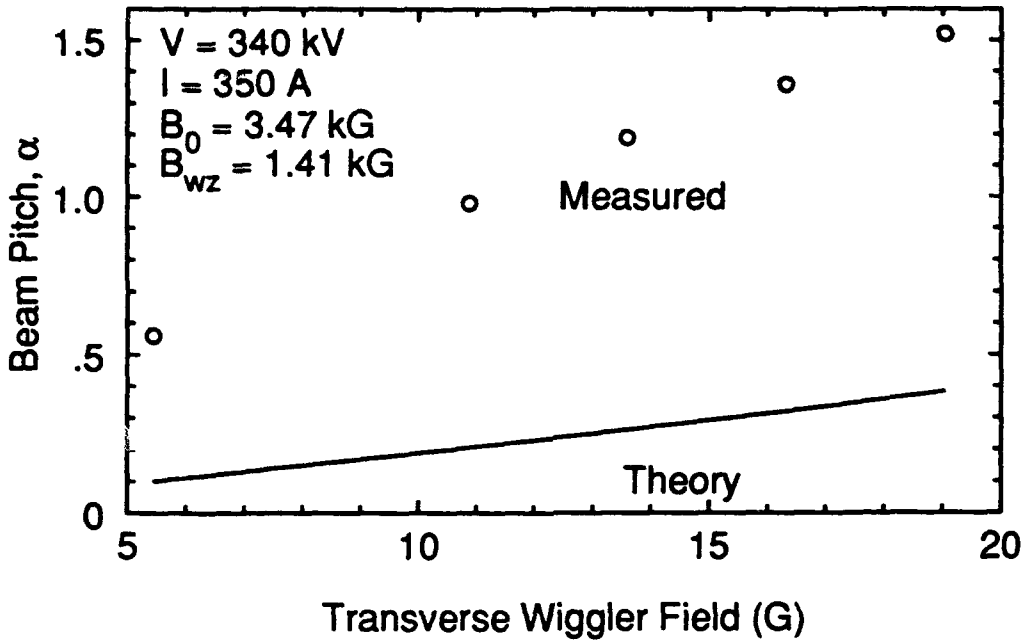


Figure 1: Beam pitch, α, vs. transverse wiggler field. The measured values were obtained using the signal from a diamagnetic loop. The theory values are derived from a single particle code.

IV RF Amplification

To date, the CARM amplifier has been run up to 350 kV. Typical voltage and current pulses are shown in Fig. 2. Breakdown problems presently occur above this voltage, but we anticipate eventually achieving the designed voltage of 500 kV. Having done scans in guide field from 2 kG to 3.75 kG and scans in wiggler field strength from 0 G to 30 G, we have seen two reproducible modes of significant power. Both of these modes were seen with 330 kV, 350 A pulses. The first mode is a ~1.5 MW (±3 dB) TE_{31} mode at 17 GHz. The power is calculated from a calibrated diode signal in the far field assuming a pure TE_{31} pattern. This mode is determined to be TE_{31} based primarily on a far-field scan of the output radiation, which is shown in Fig. 3. The guide field setting is 2.6 kG, indicating third harmonic operation. The beam pitch derived from the diamagnetic loop signal is $\alpha \sim 0.9$. A single particle code predicts $\alpha \sim 0.3$; however, based on the dispersion diagram for this mode and the power level measured, α is predicted to be > 0.5. The input power is not well determined, since the input signal is predominantly in the TE_{11} mode rather than the TE_{31} mode, but the lower bound on the gain for this TE_{31} mode is 22 dB.

The other significant mode is a ~0.5 MW TE_{21} mode at 16 GHz. Again, a far-field pattern is used to characterize this mode, which occurs at almost the same experimental settings as the TE_{31} mode described previously. The wiggler field was slightly higher, indicating a higher beam pitch. The lower bound on the gain for this mode is 18 dB.

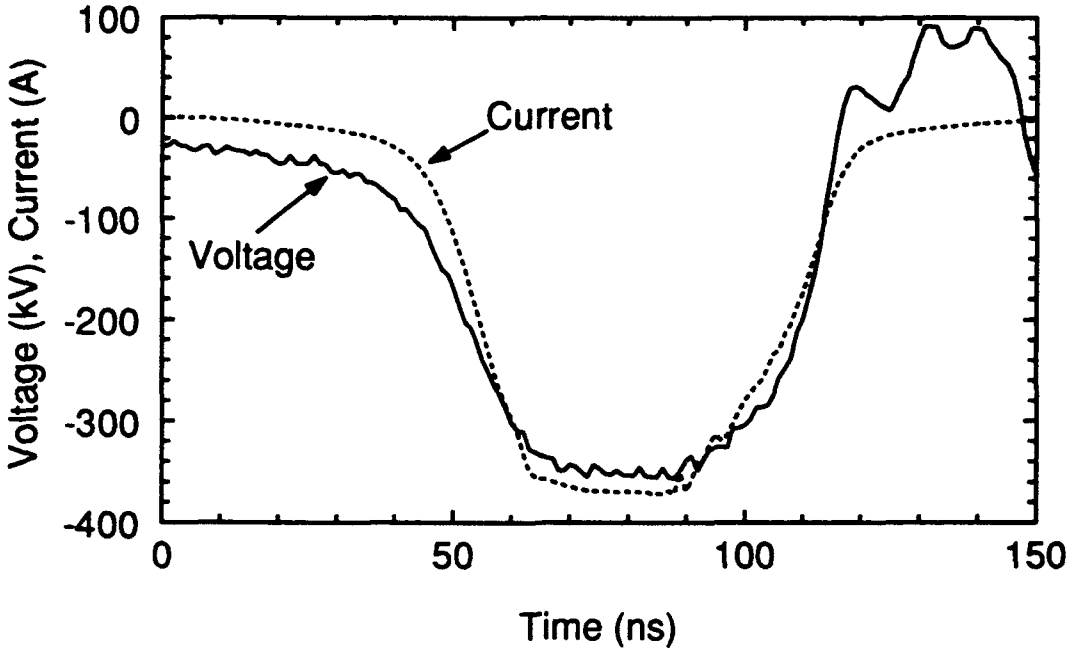


Figure 2: Typical SNOMAD-II voltage and current pulses.

The reason for the lack of TE_{11} gain seen to date is most likely poor beam quality. For the TE_{21} and TE_{31} power levels mentioned earlier, nonlinear simulations predict that the corresponding axial velocity spread in the electron beam is ~15%. If the beam axial velocity spread is similar in the parameter space where TE_{11} operation is expected, then no significant power would be expected since the TE_{11} CARM mode is much more upshifted than the TE_{21} and TE_{31} modes and is consequently more sensitive to axial velocity spread. In order to improve the beam quality, a study of the effects of the bifilar helical wiggler will be done this summer using a witness plate. This may also answer some of the questions about our higher than expected beam pitch measurements. The wire mesh rf coupler will also be replaced with a hole coupler which will not intercept the beam.

V Conclusions

The 17 GHz MIT CARM amplifier has thus far only operated as a gyro-TWT, producing significant power in the TE_{31} mode at third harmonic, and in the TE_{21} mode at second harmonic. Poor beam quality is the probable reason that no TE_{11} gain has been seen. Steps are being taking to improve the beam quality. The gun geometry is known to produce a high quality beam, so we are confident that beam quality issues can be overcome. Interaction efficiencies for CARMs with good quality beams are predicted to be in the 10-40% range, with higher efficiencies attainable by magnetic field tapering. A CARM amplifier that uses a wiggler to produce pitch in the beam is also predicted to have a very high degree of phase stability [6]. For these reasons, the CARM amplifier remains a promising source of high frequency radiation for future linear colliders.

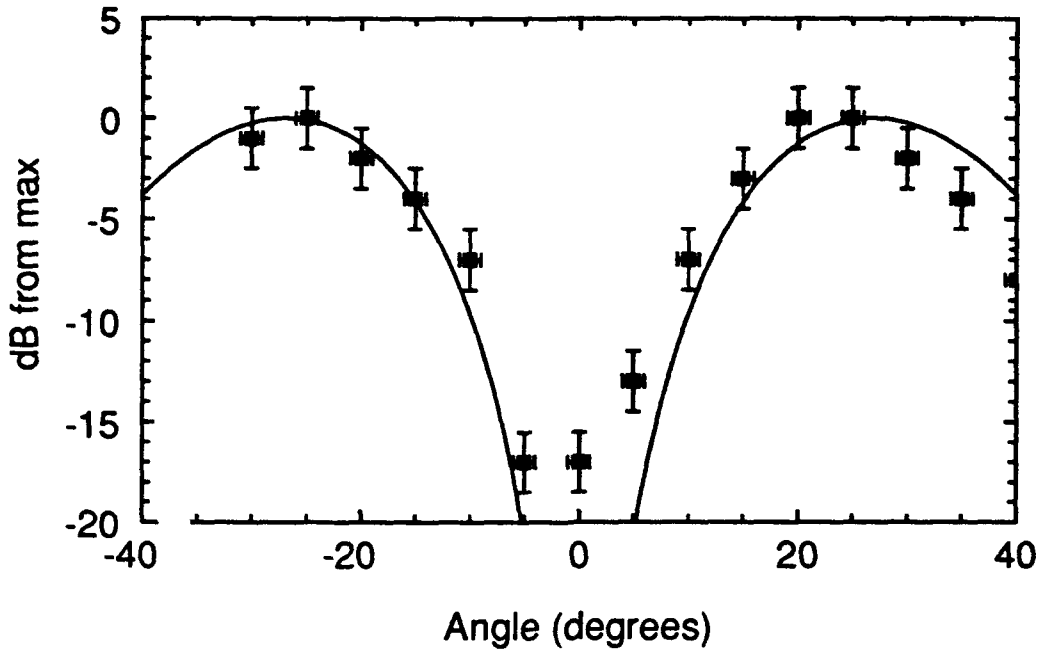


Figure 3: Far field scan, measured and theory, for the TE_{31} mode.

References

[1] V.L. Bratman, N.S.Ginzburg, G.S.Nusinovich, M.I.Petelin, and P.S.Strelkov. Relativistic gyrotrons and cyclotron autoresonance masers. *Int. J. Electron.*, 51:541–567, 1981.

[2] A.T. Lin. Doppler shift dominated cyclotron masers. *Int. J. Electron.*, 57:1097–1108, 1984.

[3] A.W. Fliflet. Linear and nonlinear theory of the Doppler shifted cyclotron resonance maser based in TE and TM waveguide modes. *Int. J. Electron.*, 61:1049, 1986.

[4] K.D. Pendergast, B.D. Danly, R.J. Temkin, and J.S. Wurtele. Self-consistent simulation of cyclotron autoresonance maser amplifiers. *IEEE Trans. Plasma Sci.*, PS-16:122–128, 1988.

[5] C. Chen and J.S. Wurtele. Multimode interactions in cyclotron autoresonance maser amplifiers. *Phys. Rev. Lett.*, 65(27):3389–3392, December 1990.

[6] W. L. Menninger, B. G. Danly, and R. J. Temkin. Autophase cyclotron autoresonant maser amplifiers. *Phys. Fluids B*, 4(5):1077–1080, 1992.

[7] G. Bekefi, A. DiRienzo, C. Leibovitch, and B.G. Danly. A 35 GHz cyclotron autoresonance maser (CARM) amplifier. *Appl. Phys. Lett.*, 54:1302–1304, 1989.

[8] V.L. Bratman. Cyclotron autoresonance masers. In *Proceedings of the Workshop on Strong Microwaves in Plasmas, Suzdal, USSR*, Institute of Applied Physics, Gorky, 1990, 1990.

[9] W.L. Menninger, B.G. Danly, C. Chen, K.D. Pendergast, R.J. Temkin, D.L. Goodman, and D. Birx. Cyclotron autoresonance maser (CARM) amplifiers for RF accelerator drivers. In *Proceedings of the 1991 Particle Accelerator Conference*, pages 754–756, IEEE, 1991.

[10] W.L. Menninger, B.G. Danly, C. Chen, D.L. Goodman, G. Gulotta, and R.J. Temkin. Short-pulse high-power 17 GHz CARM amplifier. In *International Conference on Infrared and Millimeter Waves*, 1991.

CYCLOTRON AUTORESONANCE MASER (CARM) OSCILLATOR EXPERIMENT AT 28 GHZ [1]

G. Gulotta, S. Alberti[2], B.G. Danly, T. Kimura, W.L. Menninger, J.L. Rullier[3], and R.J. Temkin
Plasma Fusion Center, Massachusetts Institute of Technology
Cambridge, MA 02139

Abstract

Experimental results on a long pulse, high frequency, cyclotron autoresonance maser oscillator (CARM) are reported. An electron gun produces a 1 μs, 450 kV, 80 A electron beam with good beam quality. A bifilar magnetic wiggler operated near the guide field resonance followed by an adiabatic compression of the guide field is used to impart transverse velocity ($\beta_\perp$) to the beam. A capacitive probe, located after the adiabatic compression, is used to measure the mean parallel velocity of the beam, and using energy conservation the beam pitch ($\alpha = \beta_\perp/\beta_{||}$) is derived. The measured α values are significantly higher than the theoretical values. The interaction region is defined by a Bragg resonator designed to oscillate in the TE_{11} mode at 27.8 GHz (diffractive quality factor $Q_D = 300$). A cold test measurement of the resonant frequency of the Bragg resonator is consistent with the designed frequency.

A rf power level of 1.9 MW (5.2% efficiency) has been measured in the TE_{11} mode at the designed frequency; however, significant mode competition is observed between TE_{11} mode and TM_{01} mode. Identification of these CARM modes is made by comparison of measured frequencies with cold test frequencies, uncoupled dispersion theory and measurement of the far field radiation pattern. Operation in the TE_{11} CARM mode occurred at a Doppler upshifted frequency of 2.9 times the relativistic cyclotron frequency.

I Introduction

A promising candidate for the efficient generation of coherent electromagnetic radiation in the millimeter and submillimeter regimes is the cyclotron autoresonance maser (CARM). A principal advantage of the CARM over the gyrotron is the large Doppler upshift of the operating frequency from the relativistic cyclotron frequency, which results from wave phase velocity close to unity. There have been numerous theoretical studies and simulation of CARMs for amplifier and oscillator configurations [1,2,3]. This paper reports experimental results on a long pulse (1 μs), 28 GHz, cyclotron autoresonance maser (CARM) oscillator. Preliminary experimental studies on this device at a frequency of 32 GHz were reported earlier [4]. Other experimental results on CARM oscillators have been reported[5,2].

[1] Supported by the Department of Energy, Advanced Energy Projects Office, under contract DE-FG02-89ER14052. Additional support from Thomson Tubes Electroniques and Ferretec, Inc. is gratefully acknowledged.
[2] Supported by Swiss National Science Foundation, Fellowship No.8220-30665
[3] Supported by CEA/CESTA, France

II Experimental Setup and Diagnostics

A schematic of the CARM oscillator setup is shown in Fig. 1. A high-voltage 2.5 μs

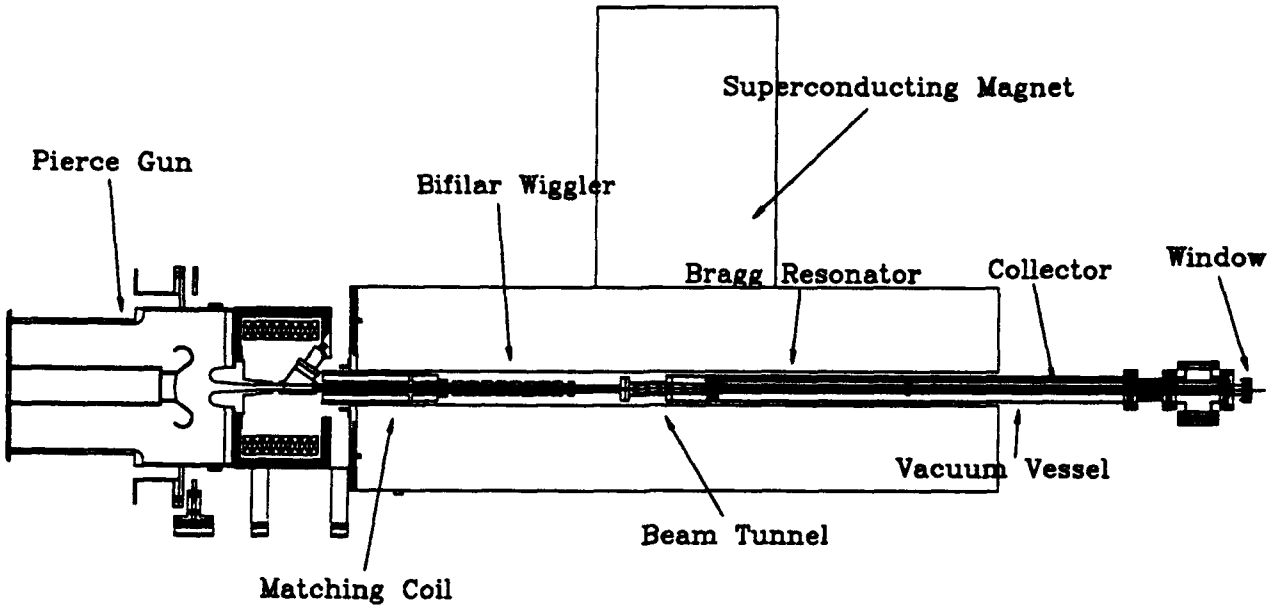


Figure 1: CARM oscillator schematic.

(1 μs flat-top) pulse modulator [6] provides the accelerating potential (450 kV) to a Thomson Tubes Electroniques (TTE) Pierce-type electron gun (0.27 μP) which emits a solid axi-centered electron beam into a uniform magnetic field (1.92 kG). At this perveance, the beam current corresponds to 80 A. From EGUN [7] simulations, the electron beam has a small emittance (normalized emittance 110 mm-mrad) as it enters a bifilar helical wiggler and resonantly interacts with a rotating transverse magnetic field which converts parallel momentum to perpendicular momentum. The wiggler has $N_w = 4$ periods with a helix pitch of $\lambda_w = 8.57$ cm. For a wiggler current of $I_w = 3$ A the perpendicular magnetic field is 14.5 G on the axis of a 1.1 cm radius beam duct. The guide field in the wiggler region is set to $B_{zw} = 1.92$ kG.

Upon exiting the wiggler region, the electron beam is adiabatically compressed into the high magnetic field region ($B_{z0} = 6.42$ kG) where the CARM interaction takes place. The two uniform axial magnetic field regions, that in the wiggler region and that in the interaction region, are provided by a superconducting magnet which allows the fields to be varied independently. The spent beam is collected after the Bragg resonator on the waveguide wall. To calculate the beam properties at the entrance of the interaction region we use the ray-tracing code EGUN from the cathode to the wiggler entrance and then a particle trajectory code TRAJ which was developed at MIT.

The resonator used in the experiment is a Bragg resonator which consists of a cylindrical waveguide section with corrugated wall reflectors at both ends. The rippled wall section defines a distributed feedback which under the Bragg conditions allows a constructive interference between

forward and backward propagating modes[8]. In this experiment the corrugated sections are built using alternating copper rings of equal axial length but different radii. A schematic of the Bragg resonator with the characteristic dimensions is shown in Fig. 2. Notice that the waveguide

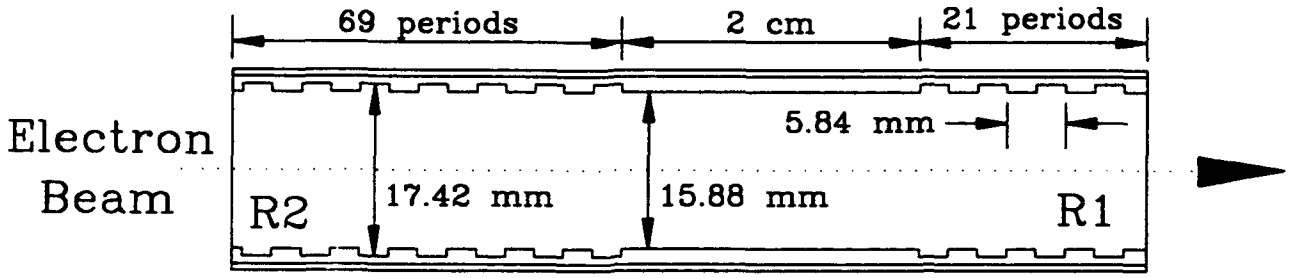


Figure 2: Schematic of the Bragg resonator, not to scale.

radius in the straight section has a radius corresponding to the minimum radius of the corrugated section. This avoids the high Q factors for modes near cutoff which would otherwise be obtained if the Bragg corrugations had a smaller diameter than the straight section diameter[4]. Since the corrugated section has an $m = 0$ structure, only modes with the same azimuthal index are coupled. The periodicity λ_b of the corrugation has been chosen in order to satisfy the Bragg resonant condition for the TE_{11} at 27.8 GHz. The resonant condition being: $k_b \simeq 2k_z$, with $k_b = 2\pi/\lambda_b$ and k_z being the Bragg and the axial wavenumbers, respectively. A cold cavity code, based on coupled mode equations [8] is used to compute the resonant frequencies and diffractive quality factors for a given mode.

A cold test measurement of the longitudinal resonant modes for the TE_{11} modes was performed with a network analyzer. Three different modes where observed at 27.2, 27.8 and 28.26 GHz. The measured frequencies are in good agreement with the frequencies predicted by the cold cavity code. The computed diffractive quality factors for these three modes are 390, 300 and 390, respectively. Only the mode at 27.8 GHz ($Q_D = 300$) is in the rejection band of the Bragg resonator. For the designed geometry, a TM_{01} mode with a quality factor of $Q_D = 20000$ is theoretically predicted in the rejection band.

In most experiments using the cyclotron resonance, a critical parameter is the beam α which is defined as $\alpha = \beta_\perp/\beta_{||}$. The present CARM experiment was designed for an α in the range of 0.6-0.8. In order to measure experimentally this parameter we make use of a capacitive probe [9] which is placed after the adiabatic compression. When the electron beam is present, the potential difference between the inner and outer capacitor plates, $\Delta\Phi$, is proportional to the ratio $I_b/\langle v_{||}\rangle$, where I_b is the transmitted beam current and $\langle v_{||}\rangle$ is the mean parallel velocity. The calibration of the probe has been made by measuring $\Delta\Phi$ versus beam voltage with no wiggler field ($\alpha = 0$). In this case, the relative variation of the measured signal, $\Delta\Phi$, is consistent with the theoretical value. When the wiggler field is set to the operating value, for a fixed beam voltage and beam current, the mean beam α is deduced by measuring the relative change of $\Delta\Phi$ from the case with no wiggler field.

The microwave circuit for the frequency and power measurements is based on a tunable frequency-locked band-pass filter (20-40 GHz, filter bandwidth Δf = 60 MHz) and a careful measurement of the attenuation factors of different microwave components. For the power measurement, the tunable frequency-locked band-pass filter (insertion loss −13 dB @ 27.8 GHz) was placed after both a calibrated TE_{11} low VSWR directional coupler (-60 dB ±0.5 dB @ 27.8 GHz) and a variable attenuator (0–60 dB ±0.1 dB) in order to insure that only one mode was detected by a calibrated diode. The overall accuracy of this power measurement is ±2 dB. Presently, power measurement is only possible for the TE_{11} mode because no calibration of the coupler attenuation is yet available for different transverse modes. The identification of the modes was also made through far field scans after the rf window.

III Experimental Results and Discussion

The capacitive probe diagnostic shows that for the experimental setting the beam pitch α is significantly larger than the value predicted by single particle theory. Within the accuracy of our measurement we measured an α_{exp} = 0.7(±0.2) when the value predicted by a single particle theory is α_{th} = 0.35. The physical mechanism which leads to higher α is not yet understood and further investigations are needed. As shown in Fig.3 the experimentally determined α is consistent with the uncoupled dispersion relation between the beam and the waveguide mode and the observed frequency for the CARM operation.

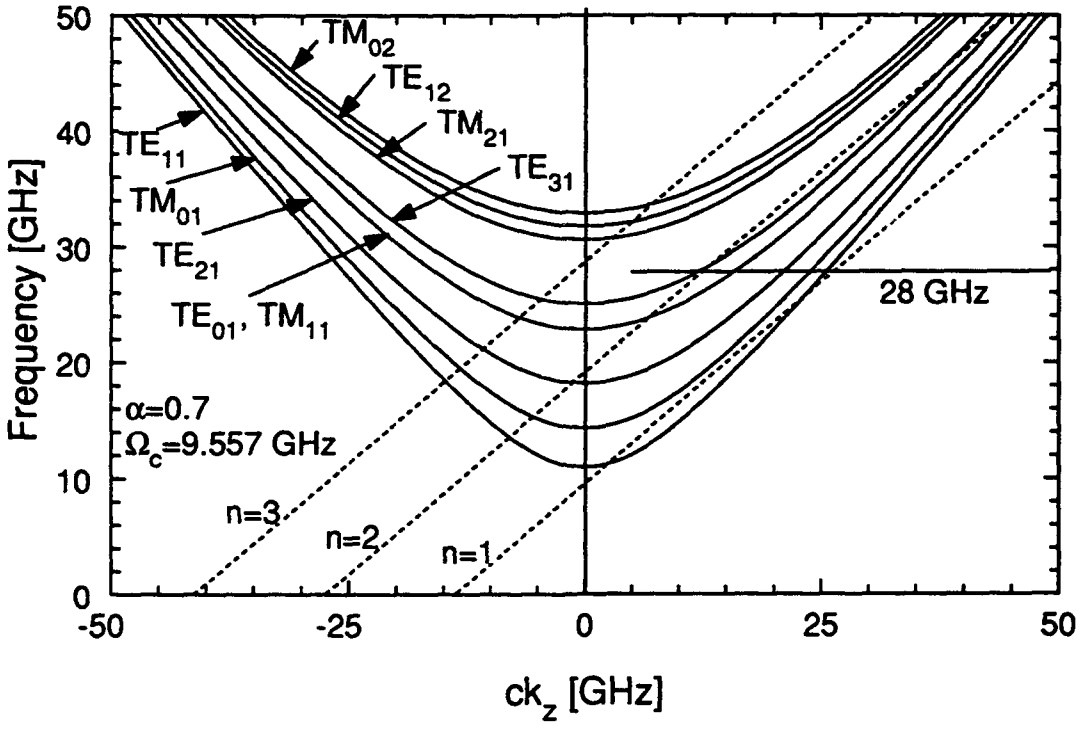


Figure 3: The dispersion diagram suggests several possible intersections of the fundamental beam line and the waveguide modes at observed frequencies with α = 0.7.

The measured rf signals have shown an important competition between the designed TE_{11} mode at 27.8 GHz and a TM_{01} mode at 29.6 GHz, the latter mode being dominant. These two frequencies are in very good agreement with the theoretical frequencies predicted by a cold resonator code. A typical trace of the rf signal is shown in Fig. 4.

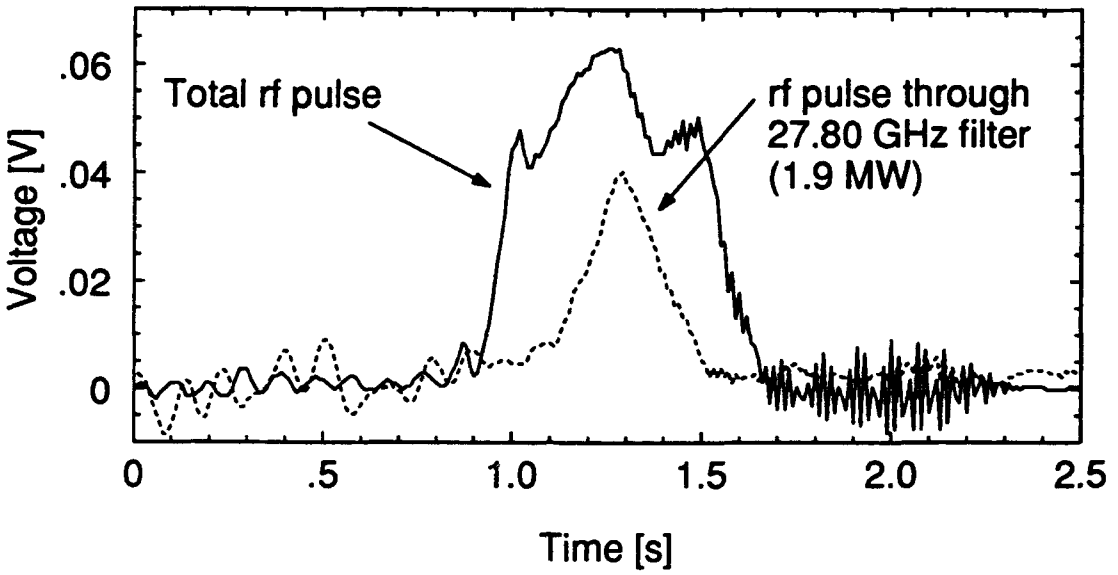


Figure 4: A typical rf pulse from the CARM oscillator.

From linear theory, the simultaneous excitation of the TE_{11} mode and the TM_{01} is only possible if the beam has an alpha spread of ± 0.1 around an average value of $\langle\alpha\rangle = 0.6$. Fig.5 shows a good agreement between the measured and calculated far field scan in the E_θ polarization for the TM_{01} mode.

The measured power for the TE_{11} mode corresponds to 1.9 MW with an accuracy of ± 2 dB due to the experimental technique. The efficiency corresponding to this rf power level is 5.2% (V_b = 450 kV, I_b = 80 A). Such efficiency is predicted by a single mode non-linear model if a parallel momentum spread of $\sigma_{p_z}/p_z = 6\%$ is assumed. Power is not reported for the TM_{01} mode because the coupler attenuation is not yet known for this mode. Nonidentified higher order modes were observed at lower power than the two dominant modes.

IV Conclusions

Operation of a long-pulse high-power CARM oscillator has been demonstrated. An rf power up to 1.9 MW has been measured in the designed TE_{11} mode at a frequency of 27.8 GHz. The corresponding efficiency is 5.2% (V_b = 450 kV, I_b = 80 A). Simultaneous emission of a TM_{01} mode was observed with the TE_{11} mode. An important spread in pitch angle α is the probable reason of the simultaneous excitation of these modes. Further theoretical and experimental investigations on the beam transport will be undertaken in order to explain the discrepancies between the measured and the theoretical beam pitch α. In order to eliminate the

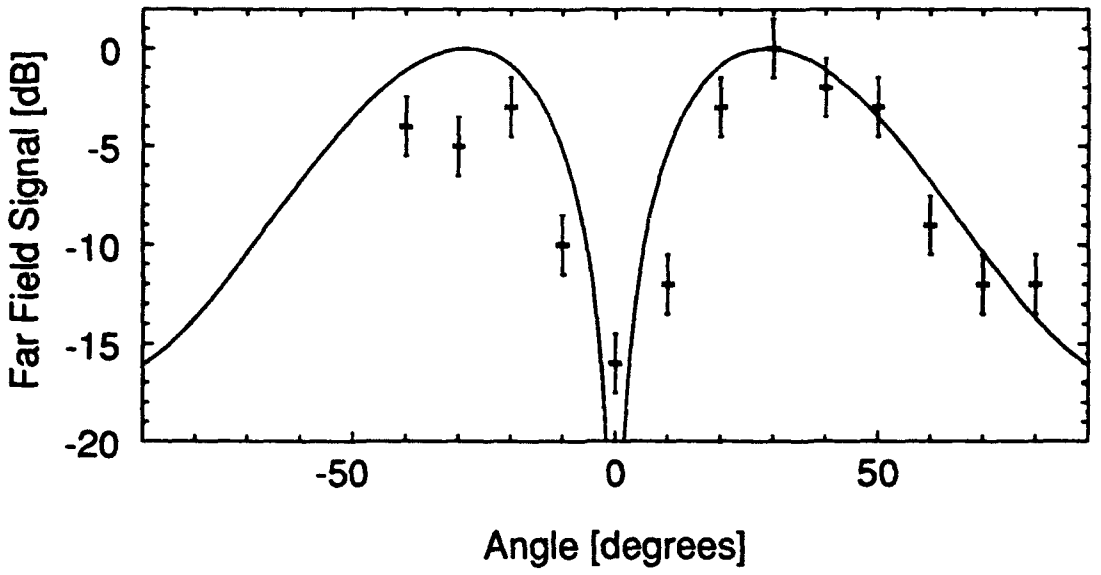


Figure 5: Far field scan of the TM_{01} mode, E_θ polarization, both theory and measured.

spurious oscillation in the TM_{01} mode, operation at the grazing condition will be studied, and a new Bragg resonator with an azimuthal structure ($m = 2$) in the corrugated sections may be implemented.

References

[1] A.W. Fliflet. Linear and nonlinear theory of the Doppler shifted cyclotron resonance maser based on TE and TM waveguide modes. *Int. J. Electron.*, 61:1049, 1986.

[2] V.L. Bratman. Cyclotron autoresonance masers. In *Proceedings of the Workshop on Strong Microwaves in Plasmas, Suzdal, USSR*, Institute of Applied Physics, Gorky, 1990, 1990.

[3] C. Chen, B.G. Danly, J.A. Davies, W.L. Menninger, J.S. Wurtele, and G. Zhang. CARM amplifier theory and simulation. *Nucl. Instr. Methods Phys. Res. A*, A304:593–600, 1991.

[4] K.D. Pendergast, B.G. Danly, and R.J. Temkin. Operation of a long-pulse CARM oscillator. *Nucl. Instr. Methods Phys. Res. A*, A304:121–126, 1991.

[5] J.G. Wang, R.M. Gilgenbach, J.J. Choi, C.A. Outten, and T.A. Spencer. Frequency-tunable, high-power microwave emission from cyclotron autoresonance maser oscillation and gyrotron interactions. *IEEE Trans. Plasma Sci.*, 17:906–908, 1989.

[6] W.J. Mulligan, G. Bekefi, S.C. Chen, B.G. Danly, and R.J. Temkin. A high-voltage modulator for high-power rf source research. *IEEE Trans. Electron Dev.*, 38:817–821, 1991.

[7] W.B. Herrmannsfeldt. *Electron Trajectory Program*. Technical Report SLAC-226, UC-28, Stanford Linear Accelerator Center, 1979.

[8] G.G. Denisov and M.G. Reznikov. Corrugated cylindrical resonators for short-wavelength relativistic microwave oscillators. *Iz. Vys. Uch. Zav. Rad.*, 25(5):562–569, 1989.

[9] W.C. Guss, T.L. Grimm, K.E. Kreisher, J.T. Polevoy, and R.J. Temkin. Velocity ratio measurements of a gyrotron electron beam. *Appl. Phys.*, 69:3789–3795, 1991.

THE ELECTRODYNAMICS OF A CO-AXIAL PLASMA SLOW-WAVE STRUCTURE OF A PLASMA CHERENKOV AMPLIFIER DRIVEN BY A HIGH-CURRENT REB IN FINITE MAGNETIC FIELD

I.A. Selivanov, A.G. Shkvarunets *, V.P. Tarakanov**

* Institute for General Physics of the Russian Academy of sciences, Vavilov Str., 38, Moscow, 117942

** The Moscow Technological Institute for Food Industry, Volokolamskoe Ave., 11, Moscow, 125080

Abstract. The experiment devoted to microwave transport ($\omega_0 = 7.8*10^{10}$ s^{-1} , P =100 W) down the co-axial plasma slow-wave structure in finite magnetic field (B = 0.02 - 2.5 T) is reported. The experimental results are treated in terms of the analytical and numerical ones obtained by using the following problem sets-up: 1. the general dispersion equation for the case of uniform plasma annulus with sharp boundaries; 2. the numerical solving of Maxwell equations for φ , z - components of electromagnetic field in the case of nonuniform radial plasma density profile; 3. the PIC - simulation for microwave transport down the co-axial plasma waveguide of finite length.

1. EXPERIMENTAL APPARATUS

The schematic diagram of our experimental apparatus is given in a Figure 1 . It consists of the following main parts: coaxial mode transformer (1); annular plasma column (2) and plasma source (3); the coaxial-transmission-line output and the coaxial emitting horn (4); the conical plasma collector (5); the hollow metallic tube which shields the part of plasma column (6). The system is located in an external longitudinal quasi-stationary magnetic field whose intensity could be changed up to 2 T. The source of the microwave M-band radiation transported down the coaxial plasma waveguide is a magnetron with the following parameters: the radiation wavelength - λ = 2.4 cm; the generation duration - τ =10 -100 μs; the radiation power - P =50 - 150 kW. The plasma annulus was produced due to the ionization of background gas (xenon under the pressure p =$2*10^{-3}$ torr) by an annular low-voltage electron beam (E=500 V, t =100 μs) with mean radius r_b = 0.9 cm and thickness δ_b = 0.08 cm. The plasma densities from the region from 10^{12} cm^{-3} up to 10^{14} cm^{-3} were achieved with the help of this source. The radial plasma density profile was a thin annular one with mean radius r_p = 0.9 cm. The thickness of the plasma annulus was 0.15 cm on a 0.3-level and 0.3 cm - on a 0.03-level. The azimuthal structure of the plasma annulus was measured using two probes which could be rotated azimuthally. These measurements determined that the local value of plasma density, at the fixed azimuthal position of the probe, had an amplitude modulation with the characteristic period of about 10 μs. The level of modulation was 30 % . Moreover, in this time interval, the azimuthal nonuniformity of plasma annulus was localized to about 20^o . That fact that the plasma annulus had a non-azimuthally symmetric density profile may lead to conversion between symmetric and non-symmetric modes of the partially-filled plasma waveguide. In order to prevent such a conversion, we've studied the basic characteristics of microwave transport of azimuthally symmetric modes under the conditions of short plasma annulus (4 - 5 cm in length) by shielding the part of plasma column by hollow metallic tube (6). Also we can identify the type of the excited mode by placing the cylindrical absorber (7) inside the plasma annulus. The question is that the most part of the microwave energy flux for the fast mode is concentrated near the system axis while for the slow mode - in the gap between plasma and metallic wall. Therefore, the absorber will affect on these mode transport in a quite different manners. The coaxial plasma

waveguide was excited by the fundamental TEM mode of coaxial waveguide. This mode was formed into the quasi-optical mode transformer.

2. THEORY

We've used three theoretical models in order to study in detail the dispersion characteristics of the coaxial plasma waveguide in finite magnetic field.

2.1. Radially Uniform Plasma Tube In Finite Magnetic Field (RUPT-model)

In the framework of this model we've obtained the general dispersion equation for the symmetric and non-symmetric normal modes by solving the Maxwell equations for the axial components (E_z and B_z) of electromagnetic field and taking into account the boundary conditions [1]. The plasma was considered to be cold and collisionless. The numerical analysis of this dispersion equation was conducted for the real experiment [2]. The dispersion curves are displayed on a Figure 2 for the following system parameters: $\Omega_e = 2.1\omega_0$, $\omega_p = 3\omega_0$, $\omega_0 = 7.8*10^{10}$ s^{-1}, R=1.8 cm, r_p =0.9 cm, δ_p =0.1 cm. The dash lines represent the following ones: $\omega = k_z c$ and $\omega = \omega_0$. The dashed area is so called "opaque region" within which the arguments of Bessel's functions determining the radial structure of electromagnetic field components are complex. Note that this term ("opaque region") isn't a correct one. As one has been shown in work [3], there exist the solutions of general equation laying into this re-gion. The numerical analysis showed that the mode excitation at the fixed frequency ω_0 depends on the ratio between plasma frequency ω_p and cyclotron frequency Ω_e. One can see from a Figure 2 that for a small plasma densities ($\omega_p < \omega_0$) , only the fast TM_{01} mode can be excited. As this takes place, the regime of efficient microwave transport down the plasma coaxial is a possibility as the mode excited has the high phase and group velocities. For an intermediate plasma densities ($\omega_0 < \omega_p < \omega_{01}$), both the fast and slow TM_{01} modes can be excited simultaneously. The analytical analysis showed [1] that the cut-off frequency ω_{01} for the fast TM_{01} mode can be estimated by using the following expression:

$$(\omega_{01})^2 = (\mu_{01}c/R)^2 + 2r_p\delta_p\omega_p^2 J_0^2(\mu_{01}r_p/R)\,(J_1(\mu_{01})R)^{-2} \quad (1).$$

In this plasma density region, the interference between two normal modes having the different phase velocities takes place. But in the framework of RUPT-model, the question of microwave transport efficiency can't be solved. It'll be discussed later. For a high plasma densities ($\omega_p > \omega_{01}$), only the slow TM_{01} mode can be excited. As this takes place, the regime of efficient microwave transport down the plasma coaxial is a possibility as the mode excited has the phase and group velocities near the speed of light c. The numerical calculations done for the other cyclotron frequencies $\Omega_e = 0.42\omega_0$ and $\Omega_e = \omega_0$ showed that the mode excitation pictures don't differ from the case described above. Also one should mention the following facts obtained from this analytical analysis. First, the frequency region where the volume normal modes exist are determined by the following inequalities [1]:

$$\omega < \min\{\omega_p , \Omega_e\} \text{ and } \max\{\omega_p , \Omega_e\} < \omega < \omega_h \quad (2),$$

where: ω_h - the upper hybrid frequency. And second, the spectra of the slow normal modes in the limit k_z goes to zero don't depend on the cyclotron frequency value.

2.2. Radially Nonuniform Plasma Tube In Finite Magnetic Field (RNPT-model)

In works [4,5], one has been made an attempt to take into account the influence of nonuniformity of radial density profile of the plasma annulus on the dispersion characteristics of the coaxial plasma waveguide. The plasma was considered just to be cold. The electron collision frequency ν_e was considered to be much smaller than the transport, plasma and cyclotron ones. The radial plasma density profile was taken in the following form:

$$n_p(r) = n_{pmax} \exp(-(r - r_p)^2/\delta_p^2) \qquad (3),$$

where: r_p =0.915 cm and δ_p =0.068 cm were measured experimentally [2]. The computational technique was in the Maxwell equations numerical solving for z- and φ-components of electromagnetic field. By giving the frequency ω, the authors obtained the functional dependences for complex axial wave number $k_z(\omega)$. The main results obtained in the framework of RNPT-model are the following:

1. For strong magnetic fields ($\Omega_e > \omega$), the numerical results obtained from a RUPT-model are actually the same that obtained from a RNPT-model.
2. For weak magnetic field ($\Omega_e < \omega$), $\mathrm{Re}k_z(\omega)$ calculated in the both models are much the same. However, when the following inequality:

$$\omega_{pmax}^2 > \omega^2 - \Omega_e^2 \quad (4),$$

is fulfilled, in the framework of RNPT-model there are the nonzero $\mathrm{Im}k_z(\omega)$ which characterize the damping rates for the fast and slow TM_{01} modes. This damping out is due to the resonance microwave absorption occuring into the plasma layers where the following condition:

$$\omega_p^2(r_{1,2}) = \omega^2 - \Omega_e^2 \quad (5),$$

is fulfilled. In this plasma layers the E_r component amplitude grows up indefinitely. This fact leads to microwave power damping out and electromagnetic wave transformation into the local plasma oscillations. The expression for damping rate is given as [4,5]:

$$\mathrm{Im}k_z(\omega) = \mathrm{const}\,\Sigma(d(\ln(n_p(r))/dr)^{-1} \quad (6).$$

Here the sum is done over all the plasma layers within which the condition (5) is fulfilled. One can see from (4)-(6) that the absorption rate decreases as the magnetic field intensity decreases, because of increase in plasma density gradient. In the case of radially uniform plasma tube having a sharp boundaries, the absorption rate equals to zero. The numerical calculations [4,5] showed that the damping out is 10 dB for the fast TM_{01} mode over the nonshielded plasma coaxial length of 6 cm and 30-40 dB for the slow TM_{01} mode over the same length. Note that this absorption takes place without the reflection of microwave power transported.

2.3. PIC-Simulation For Microwave Transport In An Intermediate Plasma Density Region

As one has been said in Section 2.1, for an intermediate plasma densities ($\omega_o < \omega_p < \omega_{01}$) both the fast and slow TM_{01} modes can be excited simultaneously. In this case the question of microwave transport efficiency can be solved only with the help of PIC-simulation for the excitation of the plasma coaxial by the monochromatic TEM wave. This PIC-simulation was done by solving the nonstationary initial-boundary electrodynamic problem. We've used the

computational code called CARAT [6]. We've assumed the linear approximation for plasma electrons. The magnetic field was considered to be infinite. The computational geometry was consistent with the experimental one [2 and Section 1]. The length of plasma coaxial which is not shielded by hollow metallic tube (see Fig.1) was 5-6.5 cm. The accuracy of our PIC-simulation was about 1-2%. We've used the spatial grid having 600 nodes over z-axis and 37 nodes over r-axis.This PIC-simulation showed that actually both the slow and fast TM_{01} modes are excited simultaneously for an intermediate plasma densities. As this takes place, the interference between these modes takes place. The resulting electromagnetic field structure is defined by the amplitudes, phase velocities and radial structures of the modes interfered. As the plasma density increases, the difference between the axial wave numbers of the modes interfered changes accordingly with the behaviour of dispersion curves for these modes (see Fig. 2). Hence, there exists the spatial "modulation" of the flux of microwave power transported down the plasma coaxial waveguide. For a particular plasma density, the amplitudes of these modes become very close and the difference between wave numbers goes to the minimum. In this case, the level of spatial "modulation" is maximal. Therefore, the level of microwave power emitted from the system depends on the length of plasma tube (l_p) which isn't shielded as well as on the plasma density n_p. In particular, for a fixed l_p there must be the specific value of plasma density for which the microwave power transported down the plasma coaxial won't be thrown into the output horn. Figure 3 shows the dependence of ratio between the Poynting's vector fluxes averaged in time for the output coaxial metallic horn and the quasi-optical mode transformer, respectively, on the plasma density for l_p =5 cm. Actually, this dependence is the dependence of transport coefficient k_{tr} on plasma density. One can see from this Figure that there exists the minimal value of k_{tr} corresponding to the plasma density $n_p = 1.9*10^{13}$ cm^{-3}.

3. EXPERIMENT (THE CASE OF LOW MICROWAVE POWER TRANSPORTED)

The experiments devoted to the study of electrodynamics of the coaxial plasma waveguide were conducted by transporting the low power microwave (λ = 2.4 cm, P = 100 W) down the plasma coaxial. The length of nonshielded plasma column was 4 cm. The experimental results can be divided into two following groups.

3.1. The Case For Strong Magnetic Fields

The dependences for k_{tr} (n_p) (the relative level of microwave power transported down the system) and $k_{ref}(n_p)$ (the relative level of microwave power reflected from the system) experimentally measured are pictured on a Figure 4 for strong magnetic field B=1.84 T (Ω_e =4.3ω_0). Figure 4.1 shows the dependences measured in the case of cylindrical microwave absorber was absent into the system. Figure 4.2 shows the dependences measured when the microwave absorber was placed into the plasma annulus. The solid lines note the dependences for $k_{tr}(n_p)$, the dash ones - for $k_{ref}(n_p)$. When the dependences shown on a Figure 4.1 are compared with that of a Figure 4.2 , it's apparent that the fast TM_{01} mode is excited inside the plasma coaxial for plasma densities $n_p < 4*10^{12}$ cm^{-3} (effective microwave transport). The slow TM_{01} mode is excited for plasma densities $n_p > 2*10^{13}$ cm^{-3} (effective microwave transport).

For an intermediate plasma densities $4*10^{12}$ cm^{-3} $< n_p < 2*10^{13}$ cm^{-3}, the transport coefficient decreases and reaches the minimum in the vicinity of plasma density what is in a good agreement with the theoretically obtained value for l_p= 5 cm (see Section 2.3). By decreasing the magnetic field, the microwave transport picture described above remains the same as long as the magnetic field intensity will reach the value of about 0.62 T ($\Omega_e \cong 0.62\omega_0$). After that the microwave transport nature changes completely.

3.2. The Case For Weak Magnetic Fields

The dependences for k_{tr} (n_p) and k_{ref}(n_p) experimentally measured are pictured on a Figure 5 for weak magnetic fields without the microwave absorber. Figure 5.1 shows the dependences measured for B= 0.52 T and Figure 5.2 - for B= 0.38 T . The solid lines note the dependences for k_{tr} (n_p), the dash ones - for k_{ref}(n_p). One can see from Figure 5.1 that the effective microwave transport takes place for plasma densities $n_p < 3*10^{11}$ cm^3 . Moreover, the reflection level is greater than the vacuum one by a factor 3.5. The experiment showed that the further decrease in magnetic field intensity resulted in the increase in reflection coefficient as long as magnetic field becomes 0.48 T ($\Omega_e = \omega_0$). After that the further decrease in magnetic field intensity didn't lead to the change in the value of reflection level. For magnetic fields B < 0.48 T, the reflection levels didn't change actually and were equal to the vacuum one. Also one can see from Figure 5.2 that the decrease in the magnetic field intensity results in the increase in the value of critical plasma density n_p^* starting with which the inefficient microwave transport takes place. Moreover, the placing of microwave absorber into the plasma annulus showed that only the fast TM_{01} mode was excited for weak magnetic fields. All the fact experimentally observed for weak magnetic field are in a good agreement with the results obtained in the framework of RNPT-model (see Section 2.2). Really, the inefficient microwave transport for plasma densities $n_p > n_p^*$ is dictated by the resonance microwave absorption into local plasma layers where (5) is fulfilled. Accordingly with (4)-(5), the critical plasma density value increases under the decrease in magnetic field intensity. Also, that fact that the damping rate for the fast mode is smaller nearly by a factor 3 than the corresponding value for the slow mode dictates the preferable excitation of the fast mode for weak magnetic fields. The shift in the strong magnetic field threshold may originate from our system drawbacks. The question is that there exists the region of inhomogeneous magnetic field in our system. In this region the minimal magnetic field is smaller than that in plasma co-axial by a factor of about 1.4. That fact that in this region there exists the background plasma may lead to the shift in the value of strong magnetic field threshold.The considerable reflections (for magnetic fields 0.48 T < B < 0.62 T) may originate from the electron cyclotron resonance into the plasma coaxial as well as into the background plasma region.

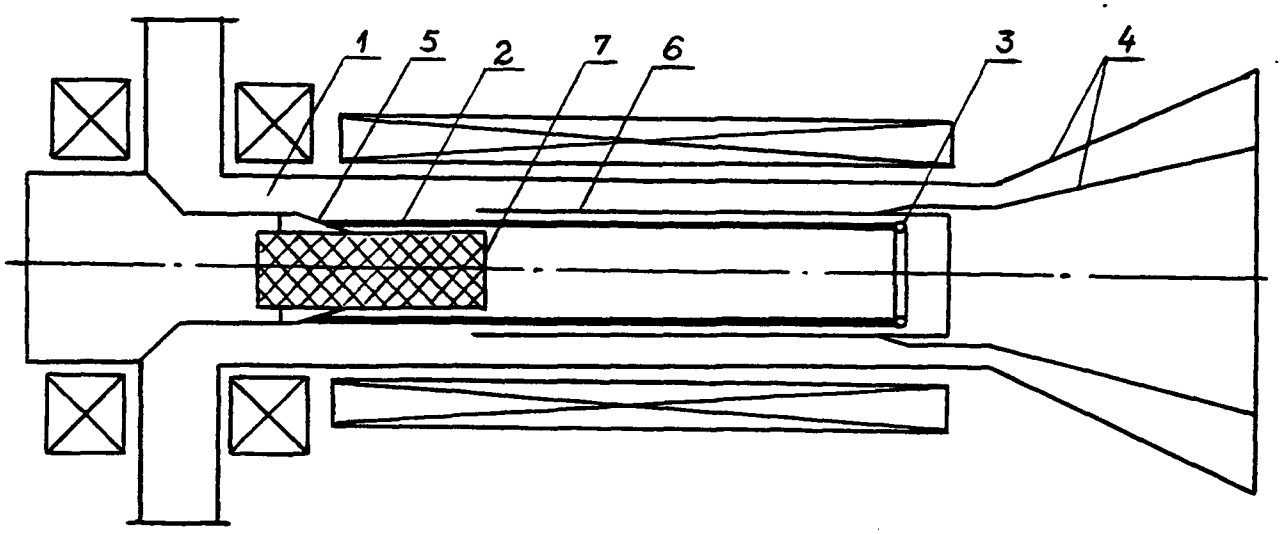
4. HIGH POWER MICROWAVE TRANSPORT IN THE REGIME OF EXCITATION THE SLOW TM_{01} MODE

The main aim of this work was to determine: 1. can be the coaxial plasma waveguide utilized as a slow-wave structure of a Plasma Cherenkov Amplifier driven by a high-current REB or not? 2. the system parameters under which only the slow TM_{01} mode having the high phase and group

velocities will be excited into the plasma co-axial. All the experimental and theoretical results described above made it clear that the coaxial plasma waveguide can be utilized as a slow-wave structure of a PCA when the system parameters fulfill the following conditions: $\omega_p > \omega_{01}$ and $\Omega_e > 1.4\ \omega_o$. We've conducted the experiment with high power microwave (P = 140 kW) . The system parameters were the following: B = 0.92 T , $n_p = 3*10^{13}$ cm^{-3} ($\omega_p \cong 3\omega_o$) , i.e. we've provided the regime of only the slow mode excitation. The length of plasma annulus nonshielded was 30 cm in order to give us a possibility to reach a high amplification rates in the following experiment with REB. We've carried out the high power microwave transport under the experiment conditions said above during the time interval of 2.8 μs. So, we've provided experimentally the high-power microwave transport down the co-axial plasma waveguide of 30 cm length under the condition of only the slow TM_{01} mode excitation. This fact allows us to advance to the experiment with REB devoted to the PCA operation. In accord with the nonlinear numerical calculation conducting nowadays by us, this PCA will have the output microwave power of about 100 MW for the input one of about 100 kW.

REFERENCES

1. M.V. Kuzelev, R.V. Romanov, I.A. Selivanov et al. The proceedings of the Institute for General Physics. 1992. V. 45. (to be published).
2. I.A. Selivanov, A.G. Shkvarunets. Fizika Plazmy. 1992. V. 18. (to be published).
3. I.N. Onitchenko, G.V. Sotnikov. Pre-print of Kharkov's Physical Techlological Institute N 88-24. 1986.
4. N.I. Karbushev, Yu.A. Kolosov, A.I. Polovkov. Fizika Plazmy. 1992. V. 18. N 1 . P. 31.
5. N.I. Karbushev, Yu.A. Kolosov, A.I. Polovkov et al. Fizika Plazmy. 1992. V. 18. (to be published).
6. P.V. Koteteshvili, P.V. Rybak, V.P. Tarakanov. Pre-print of the Institute for General Physics N 44. 1991.



1. The experimental apparatus scheme.

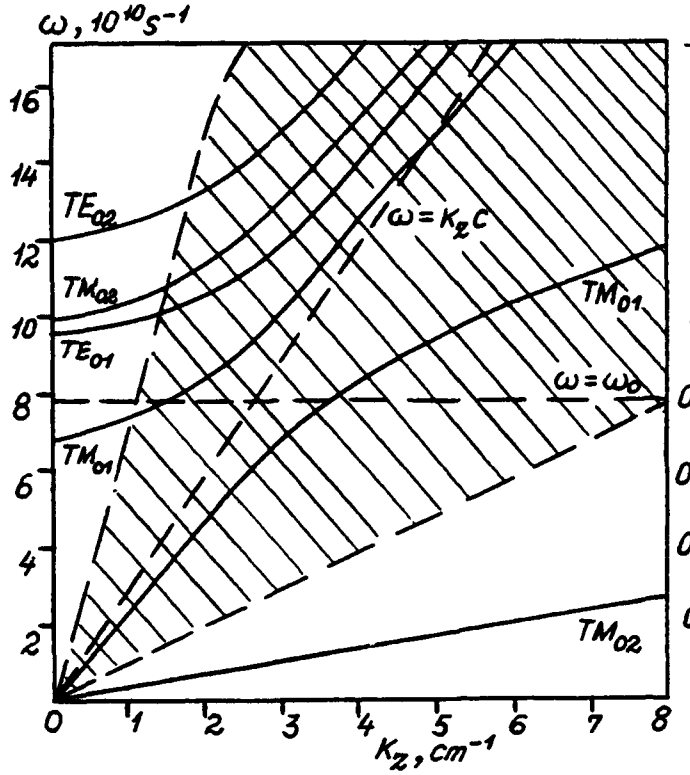


Fig. 2. The dispersion characteristics of the coaxial plasma waveguide for strong magnetic field $\Omega_e = 2.1\omega_0$, $\omega_p = 3\omega_0$.

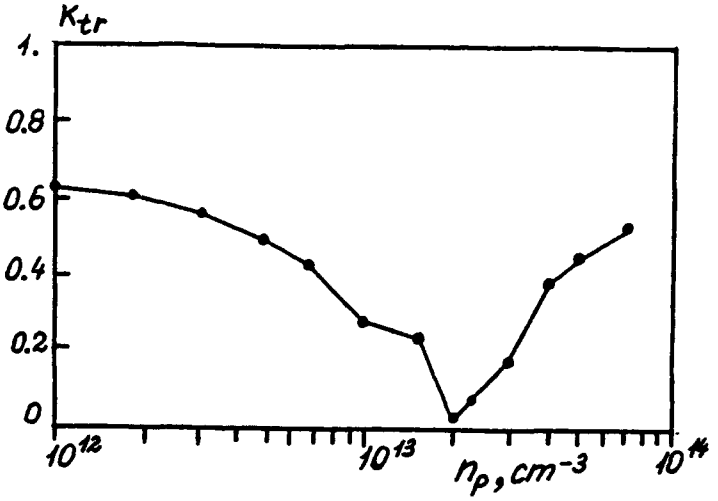
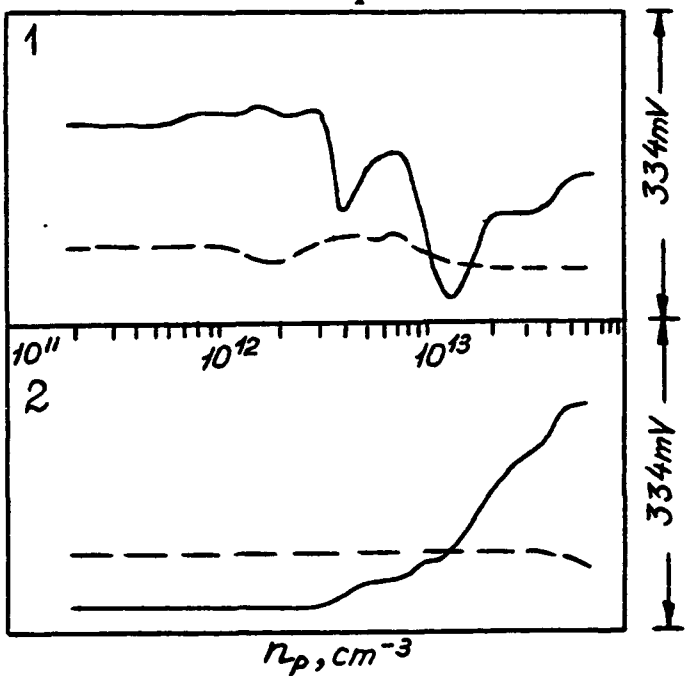


Fig. 3 . The dependence of transport co-efficient on plasma density n_p obtained with the help of PIC-simulation.



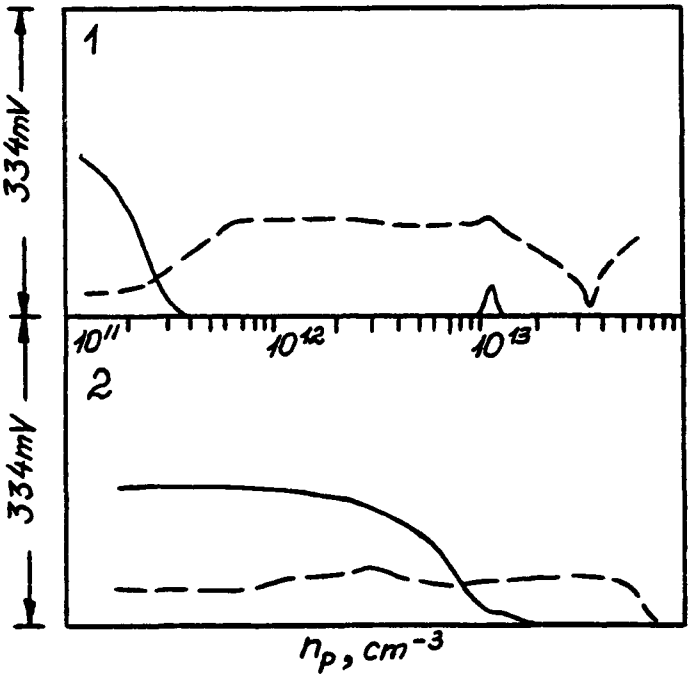


Fig. 4. The experimental dependences of the transport co-efficient k_{tr} (solid lines) and the reflection co-efficient k_{ref} (dash lines) on plasma density for strong magnetic field B =1.84 T: 1 - with the microwave absorber; 2 - without the microwave absorber.

Fig. 5. The experimental dependences of transport co-efficient k_{tr} (solid lines) and reflection co-efficient $k_{ref}(n_p)$ (dash lines) on plasma density for weak magnetic fields: 1 - B = 0.52; 2 - B = 0.38 T. Without the mivrowave absorber.

EXPERIMENTAL STUDY AND PIC-SIMULATION FOR THE PCM OPERATION

P.S. Strelkov, A.G. Shkvarunets*, V.P. Tarakanov**

* Institute for General Physics of the Russian Academy of Sciences, Vavilov Str., 38, Moscow, 117942, Russia

** The Moscow Technological Institute for Food Industry, Volokolamskoe Ave., 11, Moscow, 125080, Russia

Abstract. The results of computer simulation for the PCM and the PCA operations are reported. The plasma annulus is considered to be cold, collisionless media (r_p=0.9 cm, δ_p=0.1 cm, L_p=30 cm, R=1.8 cm) with dielectric constant $\varepsilon_p = (1 - \omega_p^2/\omega^2)$. The microwave power must be amplified by REB is generated by the M-band magnetron: λ =2.71 cm, P =150 kW. The hollow high-current REB (γ =2.2) is PIC-simulated for the case of its injection into the plasma annulus.

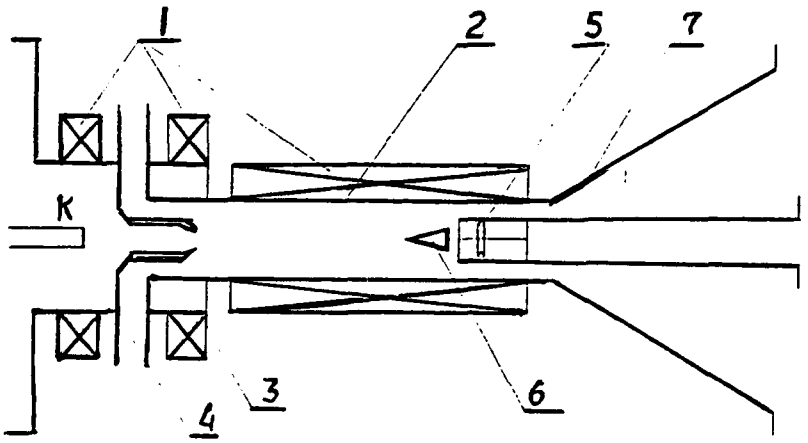
The electromagnetic fields are resulted from the numerical solving of Maxwell equations. This simulation sho-wed that there exists the microwave generation at the wavelength λ – 3 cm. Moreover, the generation wavelength decreases as the plasma density increases. The microwave power generated is of about tens megawatts for the REB current of 2 kA. The maximal efficiency is of about 5 %. The excitation of the co-axial plasma waveguide by the external wave with microwave power of 100 kW leads to the increase in the output microwave power within narrow region of plasma density. This takes place if the the input frequency is coincident with the one of wave inherently generated. Also we present the experiment for the PCM operation and the preliminary experiment devoted to the PCA operation.

The works [1,2,3] were devoted to the operation of PCM (Plasma Cherenkov Maser) driven by high-current REBs (Relativistic Electron Beams). In these works, the microwaves generated by REBs (λ – 3 cm) had the output power of several tens of megawatts. The REBs injected into the co-axial plasma waveguide had the following parameters: electron energies were of about 500 keV, beam currents were of about 1 kA. The further developments of these works are to realize clearly the mechanism of microwave amplification which takes place under the REB injection into the co-axial plasma waveguide and to make efforts to operate the PCA (Plasma Cherenkov Amplifier) driven by high-current REB.

In this report, the results of PIC-simulation for the interaction between high-current REB and the normal slow modes of the co-axial plasma waveguide are presented. This PIC-simulation was conducted by solving the non-stationary initial-boundary electrodynamic problem with the help of computer code called CARAT [4]. We've used the 2.5D axially-symmetric version of this code. The real experiment parameters allowed us to propose the linear approximation for plasma electrons. We've taken into account only the axial component of plasma current, because of the high leading magnetic field (B = 2 T).

The computational area which is consistent with the real experiment geometry is pictured on a Figure1. The waveguide walls are drawn by the solid and pointed lines, the plasma

region boundaries - by the dotted ones, the REB - by the points. Here, the radii of conducting boundaries of the waveguide structure are r_1 =1.8 cm, r_2 = 1.15 cm, r_3 = 1.45 cm, r_4 = 2.25 cm. The maximal REB radius is r = 0.55 cm, the REB thickness is Δ = 0.1 cm. The maximal plasma radius is r_p = 0.8 cm, the thickness of plasma annulus is Δ_p = 0.1 cm. The right region of the co-axial waveguide has the length of 18 cm. As usual, the plasma co-axial length was 30 cm. The boundary conditions providing the microwave output from the system was taken at the right and left system edges. The plasma is considered to be cold for the time moment t = 0. After that, REB having the linear pulse front of 0.5 ns is injected into the co-axial plasma waveguide from the left system edge. The electromagnetic perturbation which arises in the REB injection point runs away leftwards and rightwards. Depending on the REB current and the plasma density, the perturbation running right-wards grows up.



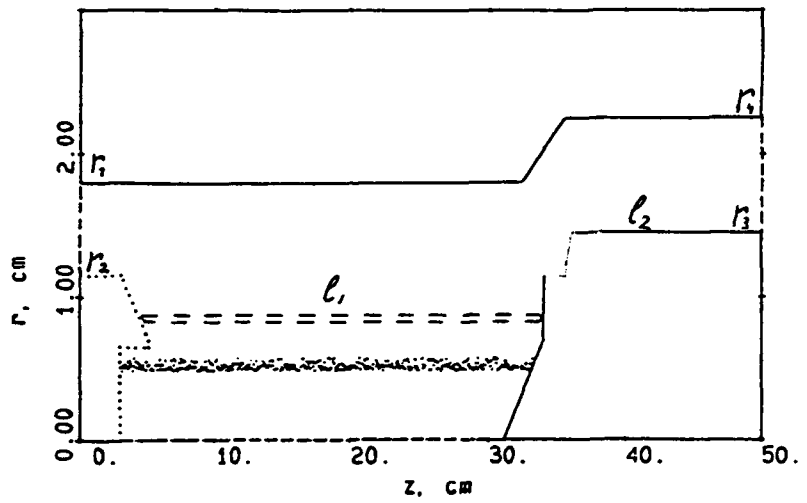


Fig. 1.

We've conducted PIC-simulation for the following sets of the system parameters: 1. the REB current - I_b = 2 kA, the electron energy - E_b = 0.6 MeV, the plasma densities - n_p = $3*10^{13}$, $2*10^{13}$, 10^{13} cm^{-3}; 2. the REB current I_b = 4 kA and the plasma density n_p = $3*10^{13}cm^{-3}$. The results obtained for the case of I_b = 2 kA and n_p =$3*10^{13}cm^{-3}$ are shown on a Figure 2. The top box is the phase plane picture for REB; the mid-position one is the dependence of E_r component of the wave on the axial coordinate z for r=1.7 cm and t= 2 ns; and the bottom one is the dependences of the REB and plasma currents on z for the same time moment. Note that the TEM wave with λ = 2.5 cm and power of 35 MW is radiated into the output co-axial waveguide for t = 2 ns. In this case, the efficiency is of about 3 %.

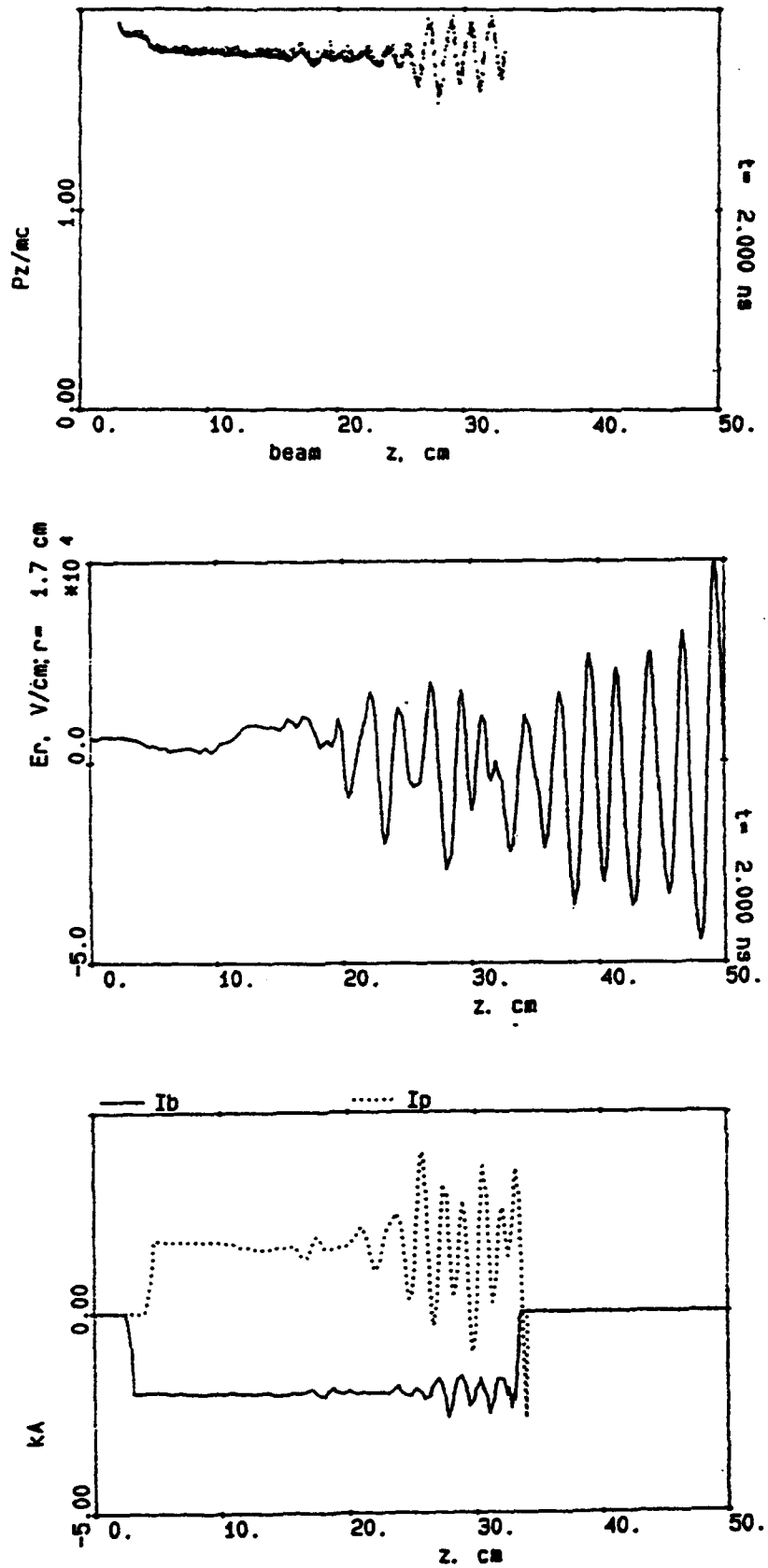

Pz/mc
1.00
0.00
0.
10.
20.
30.
40.
50.
beam z, cm
t= 2.000 ns
Er, V/cm; r= 1.7 cm
*10 4
0.0
-5.0
z, cm
Ib
Ip
kA
-5.00

Fig. 2.

It is of very importance that the feedback which is handled by the partial microwave reflection from the co-axial plasma waveguide edges didn't take place for the time moment t = 2 ns yet. As the time interval during which the wave travels over the co-axail plasma waveguide is of about 1.1 ns, there's the regime of microwave amplification over a single wave travel. The feedback is switched on for t > 2 ns what results in the modulation of the output microwave (the period modulation - 0.5 ns) and the decrease in the level of average microwave power by a factor of about 1.5. For the plasma density $n_p = 2*10^{13}$ cm^{-3}, there's the increase in the microwave wavelength from 2.5 cm up to 3 cm. In this case, also the output microwave power increased up to 60 MW. The further decrease in the plasma density up to $n_p = 10^{13}$ cm^{-3} leads to the increase in the radiation wavelength up to 4.5 cm and to the decrease in the level of the output microwave power up to 6 MW.

The experiments were conducted on the high-current electron accelerator "TEREK-3-2" with the following parameters: the charging diode voltage is of 650 keV, the REB currents are up to 25 kA, the pulse duration is of 100 ns. In conducting these experiments, the hollow REB having the electron energy of 650 keV and current of 2.2 or 8 kA is injected into the plasma annulus [3]. The experiment geometry is shown on a Figure 1. We've measured the microwave power with the help of four detector locally placed at the output window and connected with the rectangular waveguides with the cutt-off wavelengths of 4.6, 3.3, 2.6 and 1.9 cm. The co-efficient of the microwave power transition from the emitting horn into each of the receiving waveguide was $2.5*10^{-3}$. The leading magnetic field intensity was 2 T. The plasma density was changed in the region from 10^{12} cm^{-3} up to 10^{14} cm^{-3}. The experimentally measured dependences of the

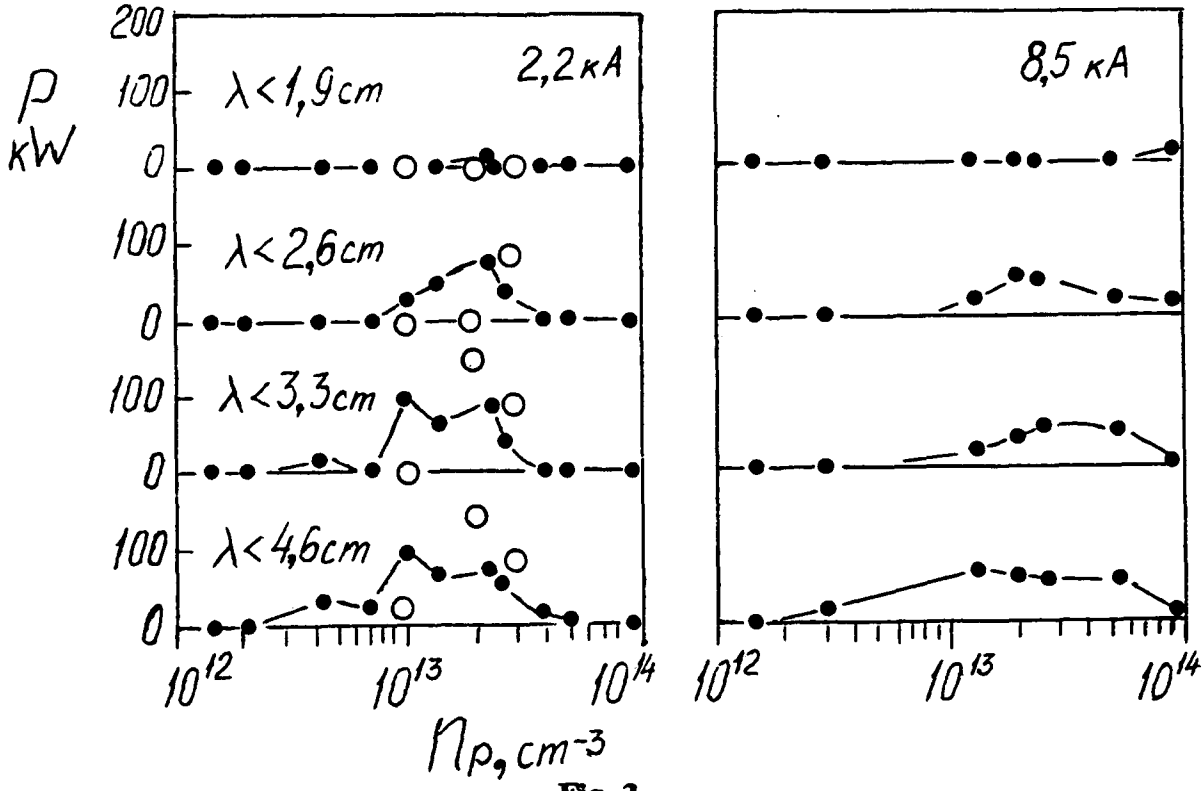


Fig. 3.

microwave power registered by these four detectors on the plasma density are pictured on a Figure 3 for two values of REB current I_b = 2.2 and 8.5 kA. The points represent the experiment, the circles - the PIC-simulation results. One can see from this Figure that there's a good agreement between the computational model and experiment for the case of REB current of 2.2 kA. In the case of REB current of 8.5 kA. the output microwave power decreases. That fact is in a fair agreement with the computational model.

The PIC-simulation conducted for the regime of external microwave amplification by REB showed the following. For the input microwave power of 100 kW, there's the increase in the output microwave power amplified in comparison with case the input microwave was absent. This increase takes place within narrow region of plasma densities when the inherent microwave frequency is coincident with the input one.

The good agreement between the results experimentally observed and the computational ones gives us an opportunity to optimize the PCM operation as well as to seek for the conditions under which PCA (Plasma Cherenkov Amplifier) will operate profitably.

That fact that the real amplification mechanism of the PCA operation is an amplification of the initial electromagnetic perturbation produced by REB under its injection into the co-axial plasma waveguide will offer considerable possibilities to generate the ultrashort superpower microwave pulses.

REFERENCES

1.M.V. Kuzelev, F.Kh. Mukhametzyanov, M.S. Rabinovitch et al. JETP. 1982.V. 83. N 10. P. 1358-1367.

2. I.A. Selivanov, P.S. Strelkov, A.V. Fedotov et al. Fizika Plazmy. 1989. V. 15. N 11. P. 1283-1289.

3. I.A. Selivanov, A.G. Shkvarunets. Fizika Plazmy. 1992. V. 18. (to be published).

4. P.V. Kotetishvili, P.V. Rybak, V.P. Tarakanov. Pre-print of the Institute for General Physics N 44. 1991.

INFLUENCE OF CATHODE PLASMA UPON THE RADIATION PULSE DURATION OF VACUUM MICROSECOND RELATIVISTIC MICROWAVE GENERATOR

O.T.Loza, P.S.Strelkov, S.N.Voronkov.
Institute for General Physics, Vavilova,38,Moscow,117942,Russia

Abstract. It was shown earlier, that microwave pulse duration in a relativistic microsecond generator is restricted in time by the electron beam radius enhancement. The method of fast magnetic decompression was proposed,that allows to stabilize the beam radius. This method was applied to the electron beam in a relativistic BWO and increased the microwave pulse duration.

Introduction

Utilization of high-current REB has culminated in drastic enhancement of microwave (MW) emission power. However, in 3-cm wavelength band at the power level of $10^8 \div 10^9$ W RF pulse duration does not usually exceed 100 ns. The only explanation of such an irreversible transfer is the production (or irreversible conversion of already existing) plasma in the vacuum microwave device.

To eliminate plasma in the electrodynamic system completely, we applied in [1] the spent beam bend as a whole and its settling on a collector well off the waveguide. In so doing the beam transportation was performing in a strong magnetic field, that allowed us to extract REB through comparatively narrow hole in the waveguide without disturbances of output RF emission structure.

High-current REBs are usually generated by cold emission cathodes. The motion of emitting plasma boundary at a speed of $v_\perp \sim 10^5 \div 10^6$ cm/s causes an increase in transverse REB dimension. In currently available MW devices in 3-cm wavelength band the beam diameter change of 1 mm (e.g. the pulse duration being more than 100 ns) may have a determining effect on the generator efficiency. As a possible method of control of average beam radius throughout pulse duration the proposed in [2] fast (e.g. essential during the pulse) reduction of magnetic field induction B on the emitting plasma boundary with radius r_e can be applied. If in doing so $B \cdot r_e^2 = const$, the beam diameter in the generator is tempo-

rally constant.

The objective of the present work was to eliminate, wherever possible, the reasons for RF generation break, and to attain these ends - to obtain a hollow microsecond REB with invariant current density profile over all the pulse duration.

Experiment

The investigations were conducted with REB parameters: voltage - 500 kV, current - 3.3 kA, pulse duration $\lesssim$ 1 μs.

The conceptual sketch of the experimental setup is shown in Fig. 1. Electron beam 1 is generated by cold emission cathode 2 in a magnetically insulated diode. In what follows we define graphite anode diaphragm 3 (connected with the body of the tube by means of shunt 4) and the interaction space 5. The downstream part of the device consists of the horn 6 with dielectric vacuum window 7 and the beam collector 8, disposed in the special chamber 9. The solenoid coils 10 provide quasi-steady-state magnetic field with the induction ~ 1 T. Besides, the additional loop 11 creates oppositely directed magnetic field in the diode with

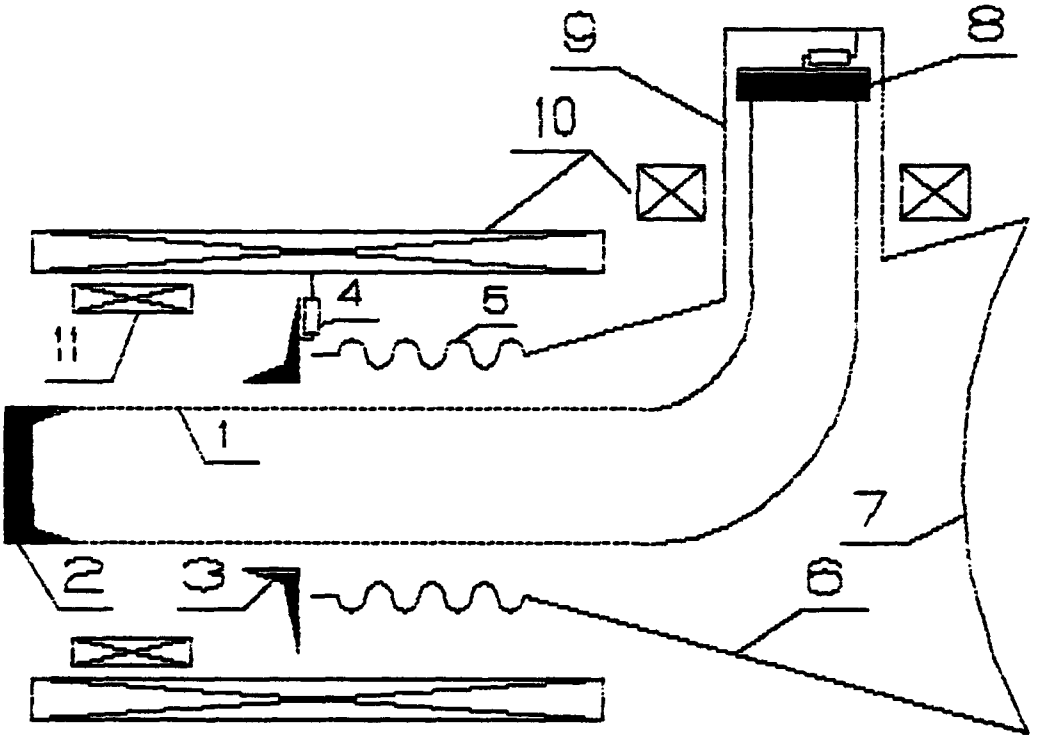


Fig.1.

pulse duration (half-period) 3.5 μs. As MW generator a relativistic BWO was used, rated at generation in 3-cm wavelength band on E_{02} mode with cyclotron mode selection [3].

REB radial profile was measured by collector receiver [4] installed in the upstream end of the carsinotron; the results are presented in Fig. 2. The bar graph shows the beam current distribution over the radius at different times without the correction loop 11. It is seen from Fig.2 that average beam radius enhances at a speed $v_\perp \sim 7 \cdot 10^5$ cm/s. The beam thickness increases in time from ~ 2 mm in the beginning of the pulse to ~ 4 mm on its completion.

MW power from the BWO was of the order of 50 MW. For this power level a suppression of electron discharge on the walls by electrostatic REB field takes place. In fact, the expression for the group wave velocity v_g being inserted into the results of [5] and taking into account twice amplitude of E-field in BWO because of the reflection in the entrance, for any axial-symmetric E-wave one can obtain:

$$P = I^2 \frac{4.75}{\beta \cdot \beta_g} , \qquad (1)$$

where P,MW - RF power; I,kA - REB current; β - beam electron velocity; β_g - RF wave group velocity (β and β_g - in the units of speed of light c). Here the corrections for rippled walls of BWO are not considered.

This formula determines the threshold power in a generator that being exceeded, the electric field in a generator may appear to provide electron emission. At the indicated REB conditions (500 kV, 3.3 kA, beam potential 100 kV, β_g=0.25 - measured experimentally) the threshold power P=280 MW, that corresponds to efficiency 17% (electron efficiency 21%). Even with regard to the corrections for rippling the emitting power 100 MW is not sufficient to provoke electron discharge on the walls.

The possibility to explain the observed restriction of the pulse duration only by MW discharge is ruled out again by the following: the magnetic field induction being diminished from the optimal value B=1.3·B_0 to the resonant one B_0, both the duration of RF pulse and its power decrease.

We applied a collimated X ray receiver for the control over the beam settling onto the surface. A signal from the anode diaphragm (not earlier than 500 ns after the pulse beginning) and that from the collector were recorded. Nowhere else a leakage of particles with current ≥ 1 A/cm was revealed.

Thus, the motion of cathode plasma can be stabilized by the correction of magnetic field during the pulse, collector plasma is removed from the waveguide, plasma on the anode diaphragm, in the horn and on the window escaped detection.

First, the dependence of the RF radiation parameters on the initial radius of the electron beam was investigated. To do this the moment of energizing the correction loop was chosen, the magnetic field in the diode area to be approximately invariable during the REB pulse. The additional field of the loop varied from shot to shot. The loop field induction being enhanced, the initial beam radius decreased. In response to this, time interval between the beginning of voltage pulse and that of RF radiation increased. Correlation of the loop field induction and operating time of the MW generator is shown in Fig. 3. The delay time is counted in response to the beginning of voltage, time scale coincides here and in the following figures.

In Fig.4 a,b oscillograms of RF pulses, corresponding to different ΔB in the diode are presented. These and other pulses are shown conventionally in Fig.3 as short lengths, the beginning and the end coinciding with generation process turning on and off due to different magnetic field ΔB in the diode. Connecting these lengths (dashed line in Fig. 3), one can obtain a generation area on the plane (ΔB,t). Inside this area RF radiation takes place, outside - the generator is switched off.

To yield magnetic field induction in different parts of the setup, a magnetic probe was used. The magnitude of

$$\Delta r = r_g - r_c \cdot \sqrt{\frac{B_c - \Delta B}{B_g}}, \qquad (2)$$

is presented along the right axis in Fig.3. It corresponds to the difference between the optimal beam radius in the generator and its initial radius due to that of cathode r_c, guiding magnetic

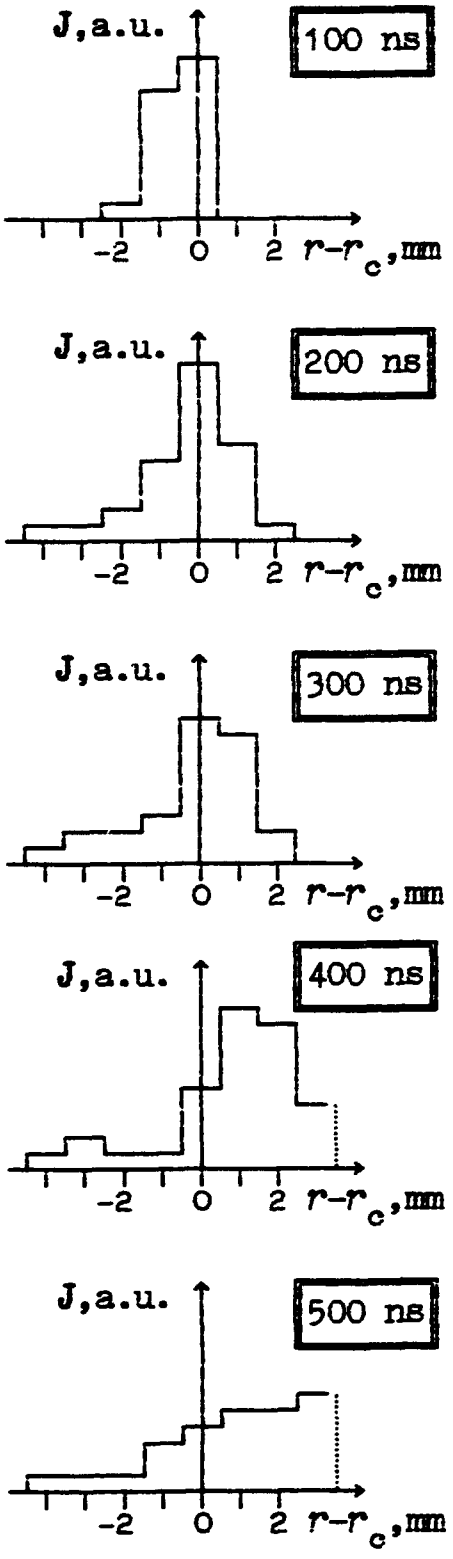


Fig.2.

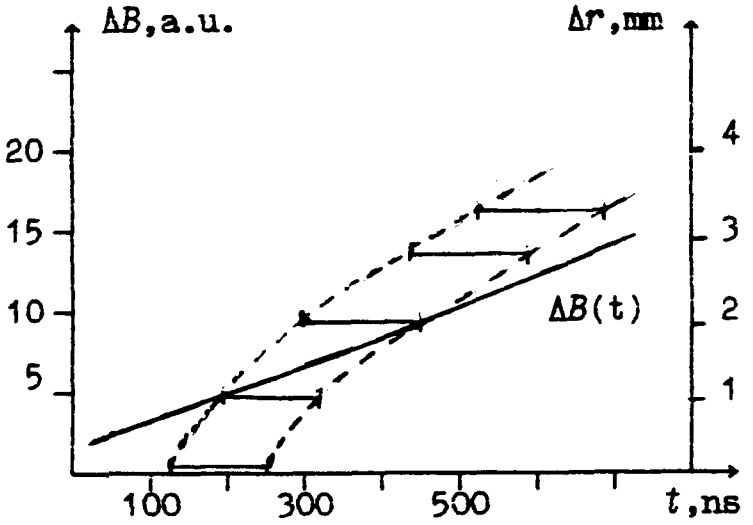


Fig.3.

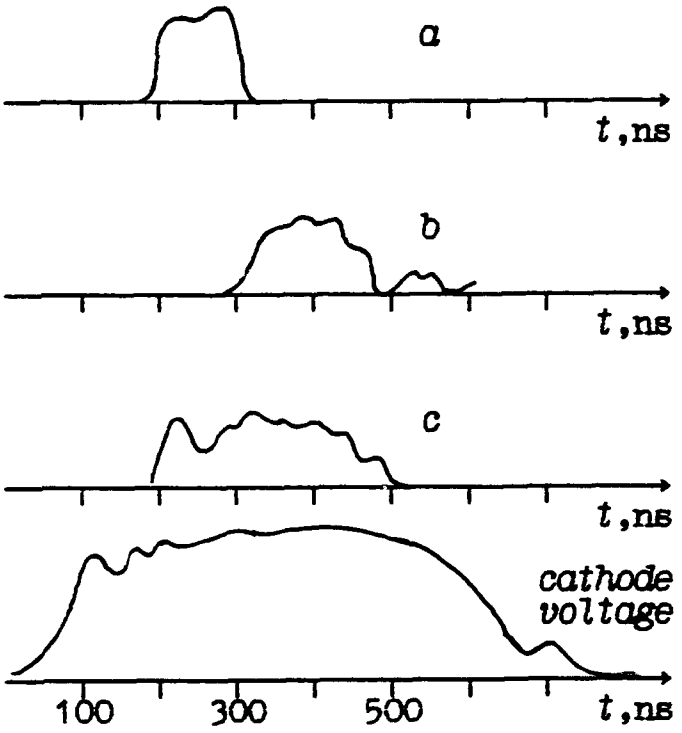


Fig.4.

field induction in the cathode area B_c and in the generator B_g and the loop field ΔB. From the figure we notice, that average velocity of the displacement of generation area corresponds to that of REB radial enhancement (Fig.2) that in its turn depends on the transverse motion of cathode plasma.

Let the loop be turned on, and the correction magnetic field in the diode increase according to the law $\Delta B(t)$. In Fig.4c RF pulse oscillogram is shown, the loop field being varied. It is seen that the duration of MW process coincides with the time of presence of the curve $\Delta B(t)$ in the generation area. RF pulses reduction in amplitude with a rise of delay time is connected, according to our mode of thought, with modifications in transverse structure of the hollow beam, that also affects RF pulse duration.

Conclusion

In this paper it was shown that the cathode plasma influence being partially compensated, MW generator operates in a quasi-steady mode. RF pulse duration, determined by residence time of the average REB radius in generation area, is equal to ~ 300 ns. RF power was ~ 50 MW (the efficiency was small because of inconsistency between the mode of operation - voltage and current - and BWO parameters). Besides, RF power grows smaller in the course of time because of modifications in transverse structure of the hollow beam.

1. Voronkov S.N., Loza O.T., P.S.Strelkov. Proc. of 8-th Int. conf. on High-Power Particle beams (BEAMS' 90),July 2-5, 1990, Novosibirsk, USSR, v.2, p.1147-1152.
2. Alexandrov A.F., Voronkov S.N., Galuzo S.Yu., et. al. Fizika plasmy, 1988, v.14, N11, p.1388-1392.
3. Abubakirov E.B., Belousov V.I., Varganov V.N., et. al. Pis'ma v Zh. Tekh. Fiz., 1983, v.9, N9, p.533-536.
4. Voronkov S.N., Loza O.T., Ravaev A.A., et. al. Fizika plasmy, 1988, v.14, N10, p. 1259-1262.
5. Belov N.E., Karbushev N.I., Rukhadze A.A. USSR IV Simp. on High-Current Electronics, Tomsk, 1982, v.1, p.293-296.

THE "HOSE TYPE" INSTABILITY OF REB AND MICROWAVE GENERATION IN A WAVEGUIDE

A.A.Ruchadze, P.V.Rybak, V.P.Tarakanov

General Physics Institute
Moscow, Russia

Abstract. *The results of the computer simulation of the relativistic electron beam (REB) injection into vacuum waveguide through a conductive foil without the guide magnetic field are presented. The beam current is lower than that limiting current for this waveguide. The intense generation of TM_{2n}-mode with $15\% - 25\%$ efficiency resulting from the formation of "hose type" instability is observed.*

Introduction

The effect of a neutralization of an electron beam charge by a waveguide butt–end conductive foils was described in [1,2], where the influence of that effect on REB dynamics during a time equal the passed time of a waveguide is studied. The first picture on fig.1 shows this dynamic in planar geometry. The cause of a beam focusing is the appearance of a positive image charge in the waveguide butt–end foils reducing of repulsive electric field nearby. But evidently at moving of the foils the beam charge neutralization relaxes and the beam starts to dilate. The stationary envelope equation is derived as follows [2]:

$$\frac{d^2x}{dz^2} = \frac{2\pi eI}{mu^3\gamma}\left[\frac{1}{\gamma^2} - \sum_{n=0}^{\infty}\frac{x}{a}\frac{sin^2(\beta_n x)}{(\beta_n x)^2}exp(-\beta_n z)\right] \qquad (1)$$

where I is beam current linear density, m and e are electron mass and charge respectivetly, c is the light velocity, γ is the relativistic factor, $u = const$ is the longitudinal velocity. This analytical result is in accordance with the simulation results[2].

In this paper we continue the consideration of the behavior of a high-current REB under the conditions of self focusing existence during time essentially exceeded that of the beam passing waveguide. Computer simulations

were implemented using the "Karat" 2- and 3-dimensional fully electromagnetic relativistic PIC code in about 20 hours on a $PC - 386$.

Simulations

Let's return to fig.1 where the time evolution of beam dynamics is shown. In this simulation we use the planar geometry. The waveguide thickness is $a = 10cm$, the length is $l = 30cm$. The beam current linear density is $I = 1kA/cm$ the beam energy is $W = 2MeV$. The electron beam is injected at the left butt-end foil end ($z = 0$). The external magnetic field is absent. One can see from this figure that the beam attained the "hose type" form. The instability has oscillation character and the beam oscillate up-down as the whole with some frequency while the electron trajectories are almost straight lines diverging like a fan from the injection point. In the neighborhood of that electrons get the transversal velocity.

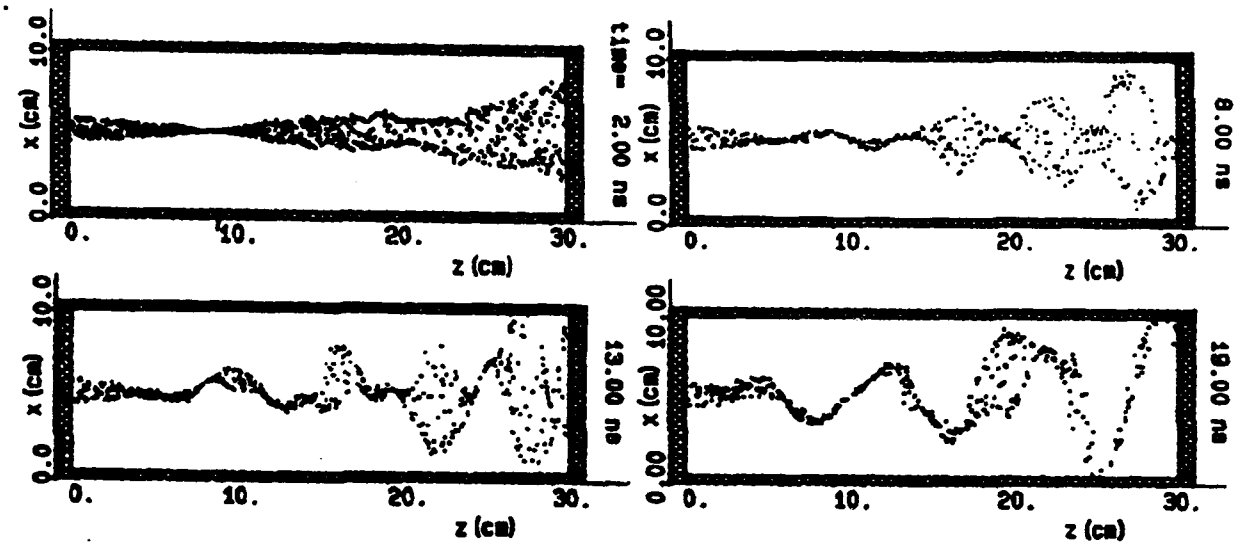


Figure 1: The time evolution of a beam in configuration space showing the beam focusing nearby the butt-end foil and development of hose instability.

The 3-dimensional simulation also shows the existence of this instability resulting in the beam spiral form (fig.2).

The analysis of spatial and time dependencies of electromagnetic fields show the generation of TM_{2n}-mode with $n \leq 2$. Fig.3a represents the E_z spectrum where the main frequency equal to $3.1HHz$ is near to frequency of TM_{20}-mode. Fig.3b shows the time dependence of radiation efficiency where

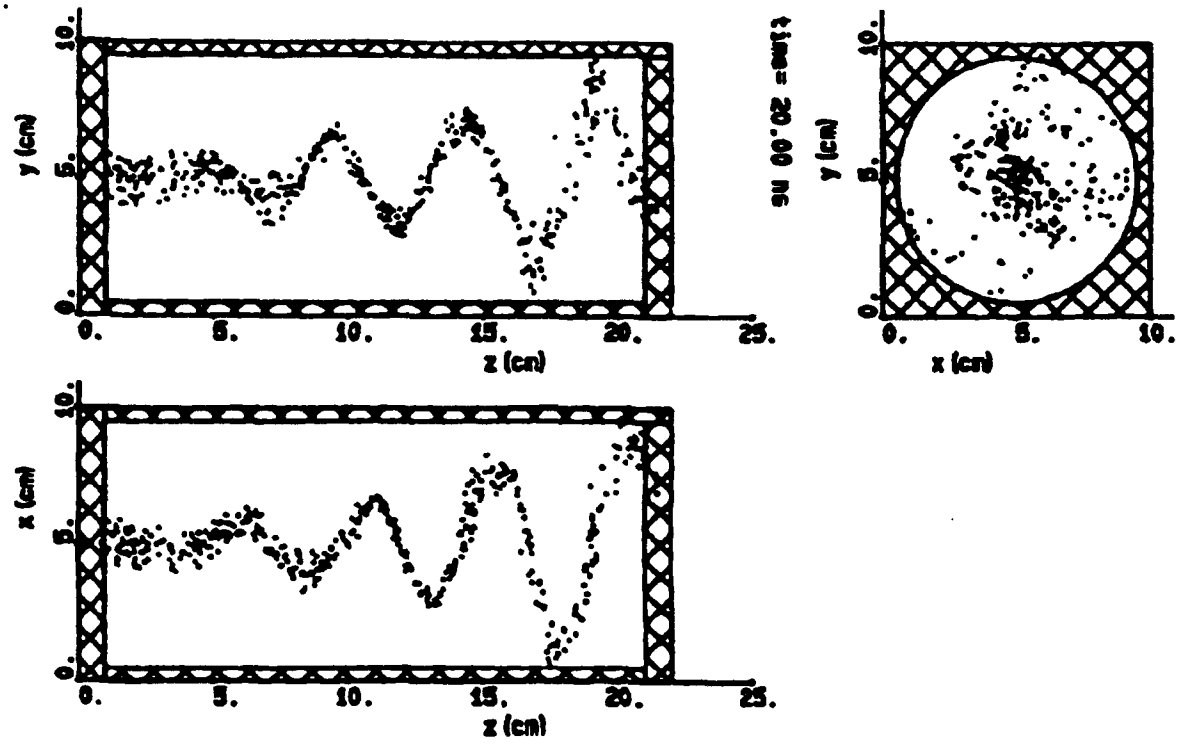


Figure 2: $3-D$ simulation of hose instability (beam energy is $2MeV$, current is $3kA$, time is $20ns$).

the efficiency was defined as the ratio of Pointing flux in right open waveguide end to initial beam power.

In the plane geometry the instability where current density more then $100 - 200A/cm$ is observed. This fact shows the threshold character of the instability. The threshold current density decreases when decrease the initial beam thickness and waveguide thickness.

Fig.4a shows efficiency and main frequency against beam linear current density. One can see a frequency slowly enhances with increasing of current density. Meanwhile the efficiency increases before some maximum and then fast gets to zero value.

Fig.4b shows the radiation efficiency and the main frequency dependences on waveguide thickness. One can see the frequency dependence as that for TM_{2n}-mode of waveguide. A rise of efficiency is explained by the fact that during increasing of the waveguide thickness the beam current leads to the space charge limit current of a vacuum waveguide. There isn't maximum in fig.4a because here the injection current $(0.5kA/cm)$ at $a = 20cm$ is much smaller than the space charge limit current.

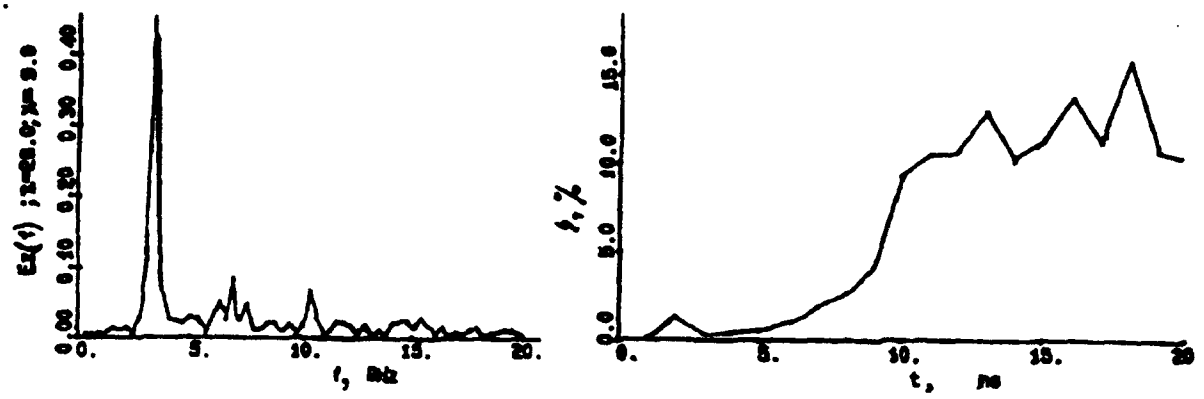


Figure 3: a) Spectrum of E_z at point $z = 28cm$, $x = 9$cm. b) Axial energy exchange between beam and electromagnetic wave vs disposition on XZ-plane.

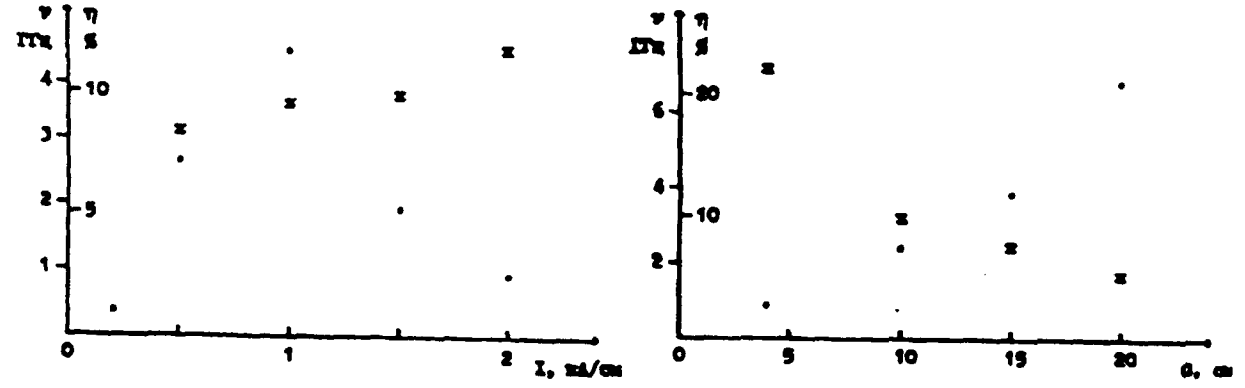


Figure 4: a) Frequency and efficiency vs beam current density. b) Frequency and efficiency vs waveguide thickness.

The decreasing of the beam-wave interaction region from $20cm$ to $10cm$ results in a rise of efficiency up 25%.

The instability was observed with energy greater $0.5MeV$.

For determine the excitation mechanism at $t = 0$ in waveguide the TM_{2n}-mode was excited. Then REB with different current was injected. Electron beam gets the "hose type" form and the beam energy transforms to electromagnetic energy.

Discussion and conclusions

The analysis of simulation results on generation and on interaction of beam with initially excited TM-mode show that in planar geometry unstable

mode is TM_{2n}–mode with $n \leq 2$. The electron trajectories are determined by an effect that in central disposed injection point the electrons declined by the H_y component of TM_{2n}-mode up–down with respect to the waveguide symmetry plane. The E_z component changes synchronously with the H_y component and therefore electrons always get in decelerating field.

To determine the energy exchange between the electron beam and microwave values $j_z E_z$ and $j_x E_x$ are monitored in the waveguide. These diagnostics show that energy is removed from the electron beam by E_z component. The spatial distribution of $j_z E_z$ is showed on fig.5.

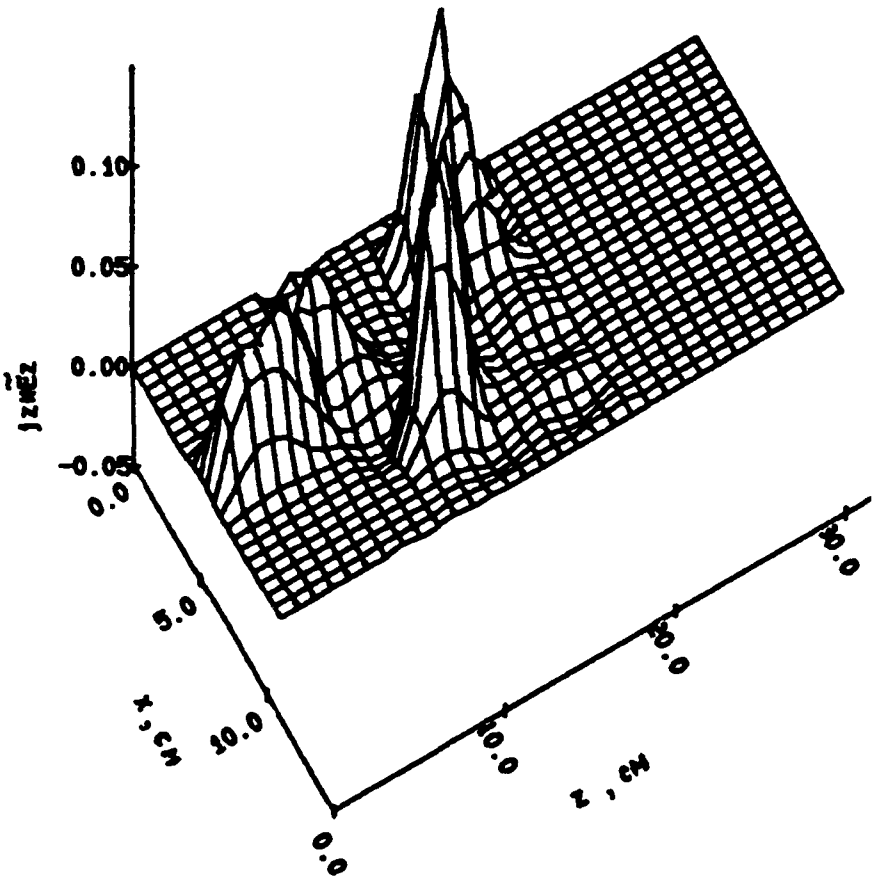


Figure 5: Axial energy exchange between beam and electromagnetic wave vs disposition on XZ–plane.

Only when the self–focusing of REB is observed the "hose type" instability is possible. The self focusing results in the brake radiation of TM–modes. In this way the nonzero initial conditions for development of the instability in the system are secured. The amplitude of the excited wave is equal to the field created by the beam that is partly neutralized by the image charge.

Assuming that $\Delta^2 << a^2 << L^2$ and $n \leq 2$ the equation for the frequency of the waveguide TM_{2n}-mode can be written as:

$$\omega = \left[\left(\frac{2\pi c}{a}\right)^2 + \frac{\alpha\omega_b^2}{\gamma^3}\right]^{1/2} \simeq \left(\frac{2\pi c}{a}\right)\left[1 + \frac{\alpha\omega_b^2 a^2}{8\pi^2 c^2 \gamma^3}\right] \tag{2}$$

where ω_b is the plasma frequency, $\alpha = \Delta/a$. This equation contains the linear dependence of radiation frequency on the beam density and the waveguide thickness.

To define of the generation efficiency the B_y–component of excited wave on the beam boundary and the current magnetic field of the REB was equated:

$$\frac{cB_y^2}{4\pi}\left[1 - 2\left(\frac{\Delta\pi}{a}\right)^2\right] = \frac{c}{4\pi}\left(\frac{4\pi e n_b u \Delta}{2c}\right)^2 \tag{3}$$

where n_b is the initial density of the beam electrons. Whereof the expression for the generation efficiency can be written as follows:

$$\eta = \frac{acB_y^2}{8\pi\Delta n_b mc^2 u(\gamma - 1)} = \frac{\omega_b^2 \Delta u a}{8c^3(\gamma - 1)}\left[1 + 2\left(\frac{\Delta\pi}{a}\right)^2\right] \tag{4}$$

The expression for the threshold beam current can be provided by using the eq.(1) and the condition that the focus's distant is not less than the waveguide length:

$$I_b > \frac{mu^3}{e}\frac{a}{\pi L^2}\gamma \tag{5}$$

Results of implemented analysis and numerical modeling are in good correspondence with each other.

References

1. R.Adler Particle Accelerators 1982 v.12,1, pp. 39–44.
2. Koteteshvili P.V., Rukhadze A.A., Rybak P.V., Tarakanov V.P. Proceedings XX ICPIG, Pisa, Italy 1991 v.3 pp. 721–722.

ON SOME PRACTICAL CONSIDERATION OF THE ELECTRON BEAM BREAKUP TRANSIT TIME OSCILLATOR

Thomas J. T. Kwan
Los Alamos National Laboratory
Los Alamos, NM 87545, USA

Abstract

The electron beam breakup transit time oscillator (BTO) makes use of the interaction between an electron beam and the azimuthally asymmetric transverse magnetic mode (TM_{110}) of a cavity to facilitate the exchange of energy between them. Linear theory has shown a large growth rate in the regime where space-charge effects can be ignored. In this study, we have investigated the non-ideal elements in the BTO and evaluated their effects accordingly. The practical issues under consideration are electron beam quality, energy, and space-charge potential. Our calculations indicate only a modest unfavorable scalings with respect to these parameters.

High-power microwave sources which depend on longitudinal bunching of the driving electron beam suffer from the decrease in efficiency in the regime of high beam energy. The general characteristic can be attributed to the increasing stiffness of the electron beam at higher energies. The electron beam-breakup transit-time oscillator (BTO) is a high-power microwave source which does not depend on axial bunching of the electron beam. The BTO makes use of the interaction between an electron beam and the asymuthally asymmetric transverse magnetic mode (TM_{110}) of a cavity to extract energy from the electron beam into the cavity mode. The electromagnetic cavity mode grows or damps depending on the transit time of the electron beam across the cavity. This characteristic offers a unique advantage over other microwave sources in efficiency and power scalings. Essentially, in this device the electron beam is deflected sideways by the finite transverse magnetic field of a cavity mode such as TM_{110} or TE_{112}. During the beam's transverse excursion, the electrons coherently exchange energy with the cavity mode according to $\underline{J}_\perp \cdot \underline{E}_\perp$ and to $J_z \underline{\nabla}_\perp E_z \cdot \underline{X}_\perp$. Here $\underline{X}_\perp$ is the transverse displacement of the electrons. The cavity mode grows or damps depending on the transit time, T=d/v, of the electron beam with axial velocity v traveling across the cavity of length d. Since the beam-wave interaction involves primarily the transverse deflections of the electrons, the growth rate of the process is expected to scale only as $1/\gamma$ where $(\gamma - 1)mc^2$ is the kinetic energy of the electron.

The linear analysis [1] has shown a large growth rate of the BTO in the regime where space-charge of the electron beam can be ignored. The analysis also assumes the electron beam to be monoenergetic and to have zero emittance. In this paper, we examine some practical issues and their impacts on the microwave generator. These will include finite emittance, beam energy scaling, and space-charge effects.

The linear growth rate of the interaction under the ideal situation is given by [1],

$$\frac{\omega_i d}{v} = \frac{\nu}{\gamma}(J_1'\chi_1)^{-2}[2(cos\frac{\omega d}{v} - 1) + \frac{\omega d}{v} sin \frac{wd}{v}]$$

where J_1', is the derivative of the Bessel function of the first kind evaluated at $\chi_1 = k_\perp R$, the first zero of J_1. R is the radius of the cavity. The transit time effects enter through the sine and cosine terms in the above expression. The numerical solution of the growth rate is shown in Fig. 1 as a function of the cavity length. There are regions of growth and damp for the cavity mode. In Fig. 1, the electron beam energy is taken to be 2.55 MeV and current 5 kA. The maximum growth rate occurs at the cavity length of 15.0 cm and it has a value of 0.25/ns. The frequency of the TM_{110} mode is 2.44 GHz, and the growth time is only about ten wave periods. We used the three dimensional particle-in-cell simulation code IVORY to model the interaction of TM_{110} mode and the electron beam. The electron beam had a small finite perpendicular momentum which corresponded to a normalized emittance of 0.2 rad-cm to counteract the self-pinching force experienced by the beam during its propagation through the cavity. The strong growth of the cavity was observed in the simulation, and it is shown in Fig. 2. The electron beam dynamics is shown in Fig. 3 which illustrates its transverse oscillation. Detailed comparison between theory and simulation had been presented elsewhere [1], and the agreement was very good.

We proceeded to use the simulation code IVORY to investigate some non-ideal issues in BTO. The effect of beam emittance on the interaction is studied by injecting an electron beam into the cavity with an increased emittance from 0.2 to 0.7 rad-cm. Three simulations were carried out to evaluate the impact on the growth rate and its dependence on the cavity length. The results are shown in Fig. 4 where the growth rate from the simulation are compared with the linear theory with zero emittance. The overall characteristics agree quite well, however, the growth rates are reduced by 40% due to the finite beam emittance.

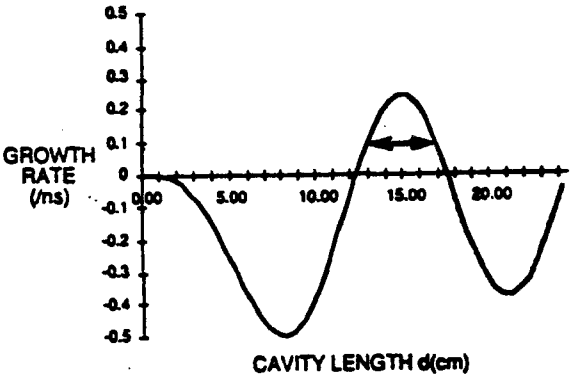


Figure 1. Numerical evaluation of the linear growth rate versus cavity length. The electron beam current and voltage are 5 kA and 2.56 MV, respectively. The radius of the cavity is 7.5 cm.

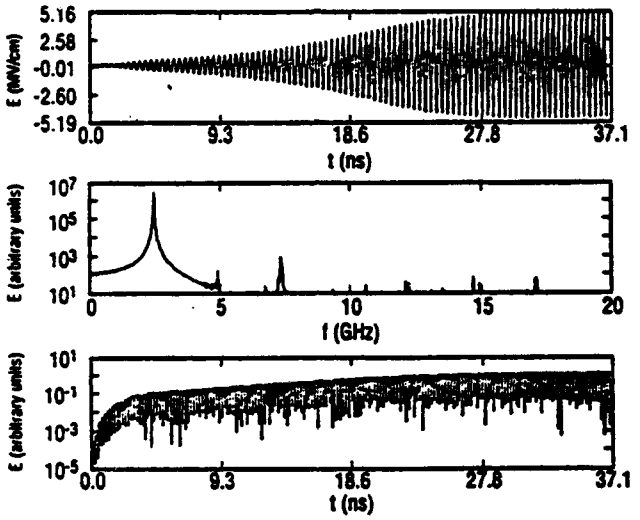


Figure 2. Computer simulation shows exponential growth of TM_{110} mode at a frequency of 2.44 GHz.

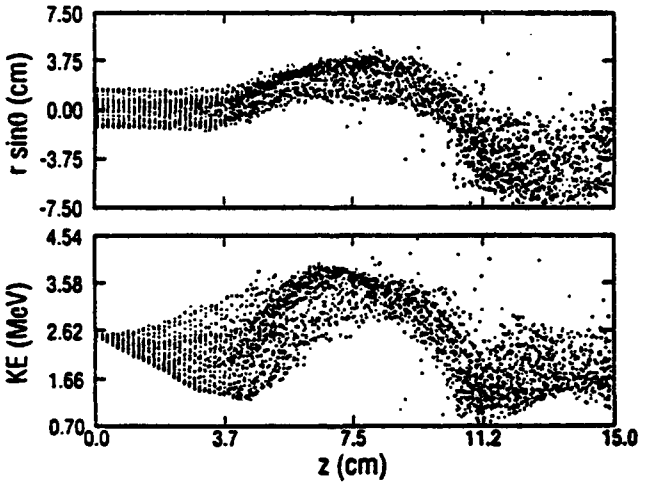


Figure 3. The electron beam exhibits transverse oscillation and simultaneous energy exchanges with the cavity mode.

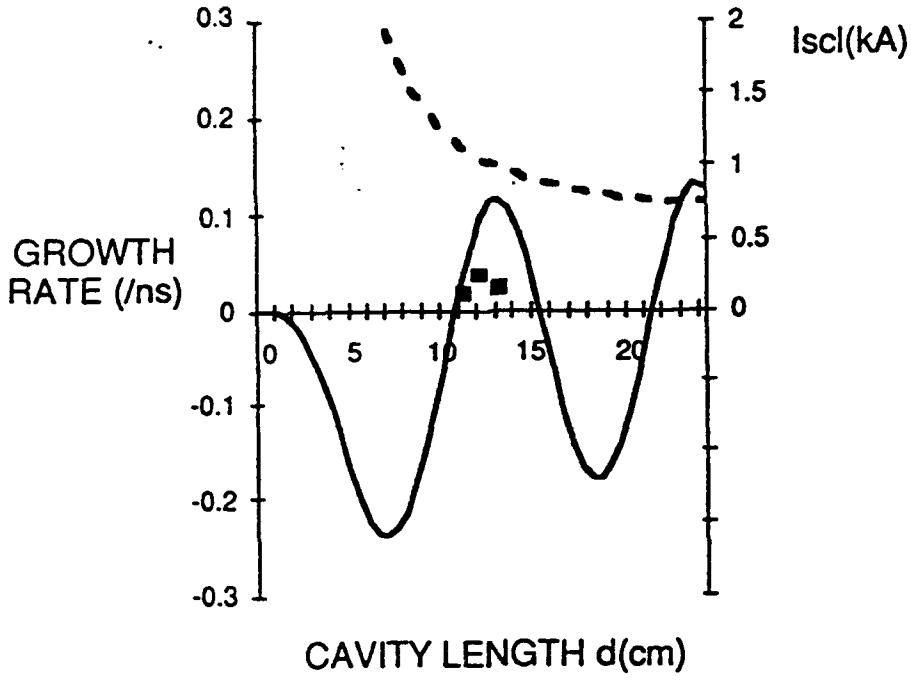


Figure 4. The growth rate from the simulation using electron beam with 0.7 rad-cm emittance shows a reduction of 40%. The electron beam energy and current are 0.51 MV and 0.8 kA, respectively.

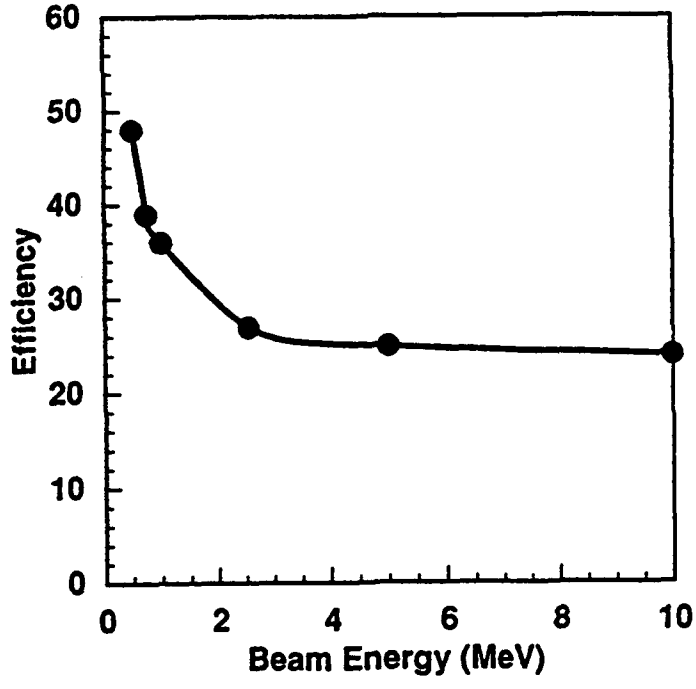


Figure 5. The efficiency has a favorable dependence on beam energy.

The fact that an increase of 3.5 times in emittance only caused approximately a factor of two reduction in growth rate supports a robust interaction of the BTO.

The second parameter varied in our simulation was the electron beam energy. In general, efficiency of high-power microwave generators declines with increases in energy of the driving electron beam. The simple explanation is that the electron beam becomes increasingly stiff and rigid with higher kinetic energy. Consequently, the coupling to electromagnetic perturbation becomes weaker. In the BTO, longitudinal bunching plays little role whereas transverse oscillation is primarily responsible for the energy exchange between the cavity mode and the electron beam. Numerical integration of single electron traversing through the cavity indicates a rather mild relation between efficiency and beam energy. The results are shown in Fig. 5. This energy dependence is significant for high-power operation where an energetic electron beam is used.

Another aspect important in the high-power regime is the beam current which should not exceed the space-charge limiting current to ensure its propagation through the cavity. However, it is often desirable to use high current electron beams to maximize available power. Under the assumption that space-charge effect can be ignored, the linear growth rate is directly proportional to the beam current. The space-charge of the electron beam can impact the interaction in the following way. The electron beam loses part of its kinetic energy due to the buildup of its self-field in the cavity. Consequently, its velocity will be reduced and, therefore, the transit time will be longer. For optimal growth, the cavity length has to be shortened. We studied three cases with increased beam current. The results of the growth rate as a function of electron beam current are shown in Fig. 6. The triangles are data obtained from simulations, and the squares are corresponding evaluations from the linear growth rate formula. The linear behavior is quite evident. However, the simulation results diverge from the linear theory as the beam current becomes a significant part of the space-charge limiting current. For the case where the beam current is 80% of the space-charge limiting current, the discrepancy is found to be almost a factor of two. On the other hand, the linear dependence still holds approximately.

Our study of the above practical issue in connection to the performance of the BTO

shows that the operation is quite robust in terms of linear growth rate and efficiency of energy exchange. The high growth rate facilitates high-power extraction of microwaves from the cavity. The extraction mechanism can be vertical (side extraction) or horizontal (axial extraction). The optimal configuration is currently under investigation.

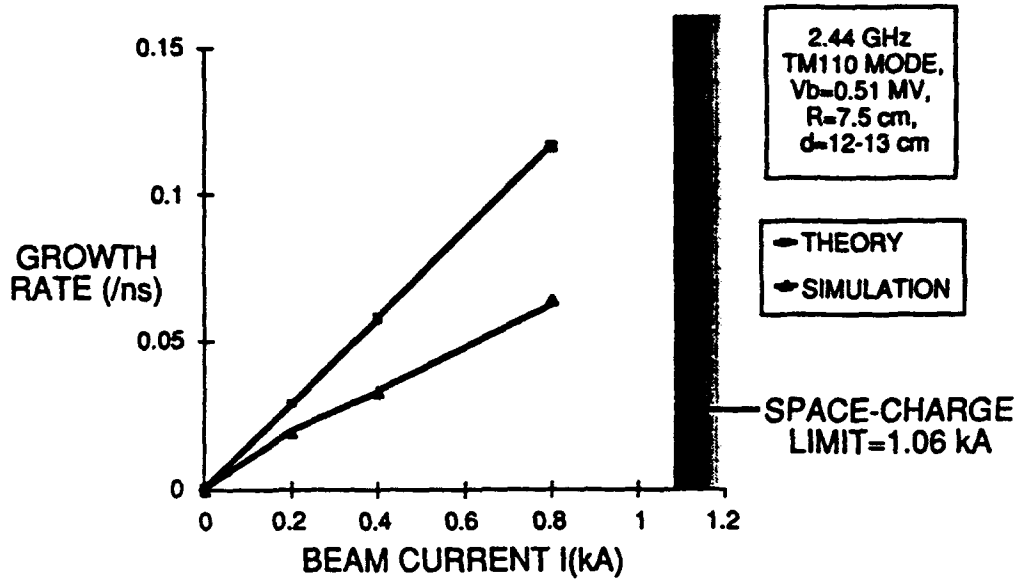


Figure 6. Linear behavior holds even when beam current becomes a significant part of the space-charge limiting current.

References:

1. Thomas J. T. Kwan, Michael A. Mostrom, and Brendan B. Godfrey, Phys. Rev. Lett., 66, 3221 (1991)

EXTERNAL QUASI-OPTICAL FEEDBACK SYSTEM FOR NARROWING RADIATION BAND

V.A.Bogachenkov, V.A.Papadichev, I.V.Sinilshikova, O.A.Smith

P.N.Lebedev Physical Institute, Academy of Sciences, 117924 Moscow, Russia

Abstract. Previous work has demonstrated the generation of powerful microwave radiation in the 0.7-6 mm wavelength range in a smooth cylindrical waveguide. In order to investigate the possibility of easy retuning, mode selection and narrowing the radiation band an external quasi-optical feedback system has been proposed. The results of cold measurements for this system are presented.

Intense microwave radiation in a free electron maser (FEM) regime in the interval 0.7-6 mm was registered in experiments on the high-current accelerator "ERG" at an electron beam energy of 0.8-1.1 MeV and voltage pulse duration of 100 ns [1,2]. An FEM scheme without selective feedback was used in the experiments. Radiation was achieved by the interaction of electron beam with modes of a cylindrical waveguide in a regime of amplification of noise in the presence of an undulator field. The broad spectrum can be explained by the possibility of simultaneous amplification of several modes in a smooth waveguide. The presence in the spectrum of more intense lines (λ = 1 mm and λ = 4 mm) can be explained as the greatest coupling of certain modes with the electron beam or as accidental feedback (possible reflection from structural joints).

To obtain radiation in a narrower band, it is necessary to provide selective feedback, for example, by means of a quasi-optical cavity .Usually, the Bragg mirrors are located within a vacuum chamber. One can change the cavity's parameters only by replacing one vacuum chamber by another.

In our experiment, one of the mirrors of the cavity consists of a cut-off constriction from which a mode with the required wavelength can be reflected. This constriction is located in the region of entrance of the electron beam into the region of interaction with the undulator field. The other mirror consists of a

diffraction grating (echelette) which is placed externally to the vacuum chamber at an angle to the incident radiation, providing selective reflection of radiation. This enables one to vary the wavelength and reflection coefficient during the RF-generation experiment, thereby optimizing them. A set of echelettes with a 40^0 blaze angle and spacings from 8.0 mm to 0.5 mm covers the range of radiation wavelengths from 8 mm to 0.34 mm. In systems of optical Bragg cavities the echelettes are placed in an autocollimation scheme, whereby the incident and diffraction angles are equal to each other. The greatest effect of reflection can be achieved if the incident and diffraction angles are equal to the blaze angle of the echelette. Thus, the intense spectrum created under such condition consists of modes with $\lambda = \lambda_m$; $1/2\ \lambda_m$; $1/3\ \lambda_m$;..., where λ_m corresponds to echelette spacing and incident angle of autocollimation regime.

Test-bed measurements using a generator operating in the 58.8 to 74.0 GHz frequency range for the TE_{11} electromagnetic mode are presented. An echelette with 8-mm spacings was tested. The scheme of measurements is shown in Fig. 1. The radiation from the radiator passed via a lens with a 420-mm focal length and was reflected from the echelette. The angle at which the echelette was placed relative to the incident radiation was chosen equal to the diffraction angle in the third order maximum of the spectrum, i.e. the measurements were performed in an autocollimation scheme. Of most interest was the radiation at a frequency of $f = 70$ GHz, i.e., the wavelength $\lambda = 4.28$ mm. For such a wavelength and selected echelette, the angle of incidence ψ coincides with the angle of diffraction φ at the maximum of the third order ($m = 3$) and is near 53^0. The angle of diffraction at the same incident angle of the second order maximum is 15^0. Measurements were performed for radiation directed at maxima $m = 3$, $m = 2$, and also at the zero-order maximum. The forms of the signals corresponding to the indicated cases are shown in Fig. 2. The line width of the signal reflected at the $m = 3$ maximum was $\Delta f/f = 3.14$ % and at the $m = 2$ maximum $\Delta f/f = 3.57$ %. Comparison of the amplitudes of the signals made it possible to determine what fraction of the in-

cident radiation is reflected back for m = 3 and what fraction for m = 2. These values are $P_{m=3} = 0.36P_{incid}$ and $P_{m=2} = 0.02\ P_{incid}$. For the zero-order maximum, $0.02\ P_{incid}$ is reflected.

Certain changes in elements of the experimental scheme as compared with those described in [1,2] have been made. First, by replacing the double pulse-forming line by a single one in accelerator "ERG", the voltage pulse length increased to ≈ 250 ns and the length of the flat part of the pulse increased, but the voltage amplitude decreased to 600-700 kV. Secondly, the double cylindrical cathode was replaced by a single tapered cone, the diameter of its emitting end being 2 mm. The graphite anode diaphragm is also in the form of a tapered cone with an output aperture of 2-mm diameter. Finally, in order to decrease the stray field of the undulator, which leads to considerably increasing the transverse velocity of cyclotron rotation of electrons [3], a new undulator was designed and constructed. It consists of a two-conductor winding, whereby the winding of the second conductor is one-half period less than the first. This significantly reduces the magnitude of the stray field and decreases the transverse velocity of the electrons acquired in the stray field of the undulator.

The methods of diagnostics of electron beam and microwave radiation have remained the same [1,2].

The experimental scheme is shown in Fig.1. Oscillograms of voltage and current pulses, as well as the pulse from the rf-detector, obtained in the absence of a cavity, are shown in Fig.3. The time-of-flight of the radiation in the cavity (back and forth) is ≈ 7 ns. During this time, the fluctuation of diode voltage is about a few percent.

References

[1] V.A.Bogachenkov, V.A.Papadichev, I.V.Sinilshikova, O.A.Smith. 8th Int.Conf. on High Particle Beams, Novosibirsk, 1990,pp. 1123-1128.
[2] V.A.Bogachenkov, V.A.Papadichev, I.V.Sinilshikova, O.A.Smith. Nucl. Instr.and Meth.in Phys.Res. A304 (1991) 104-106.
[3] V.A.Papadichev, O.A.Smith. 13th Int. Conf.on FEL,Santa Fe, USA, 1991.

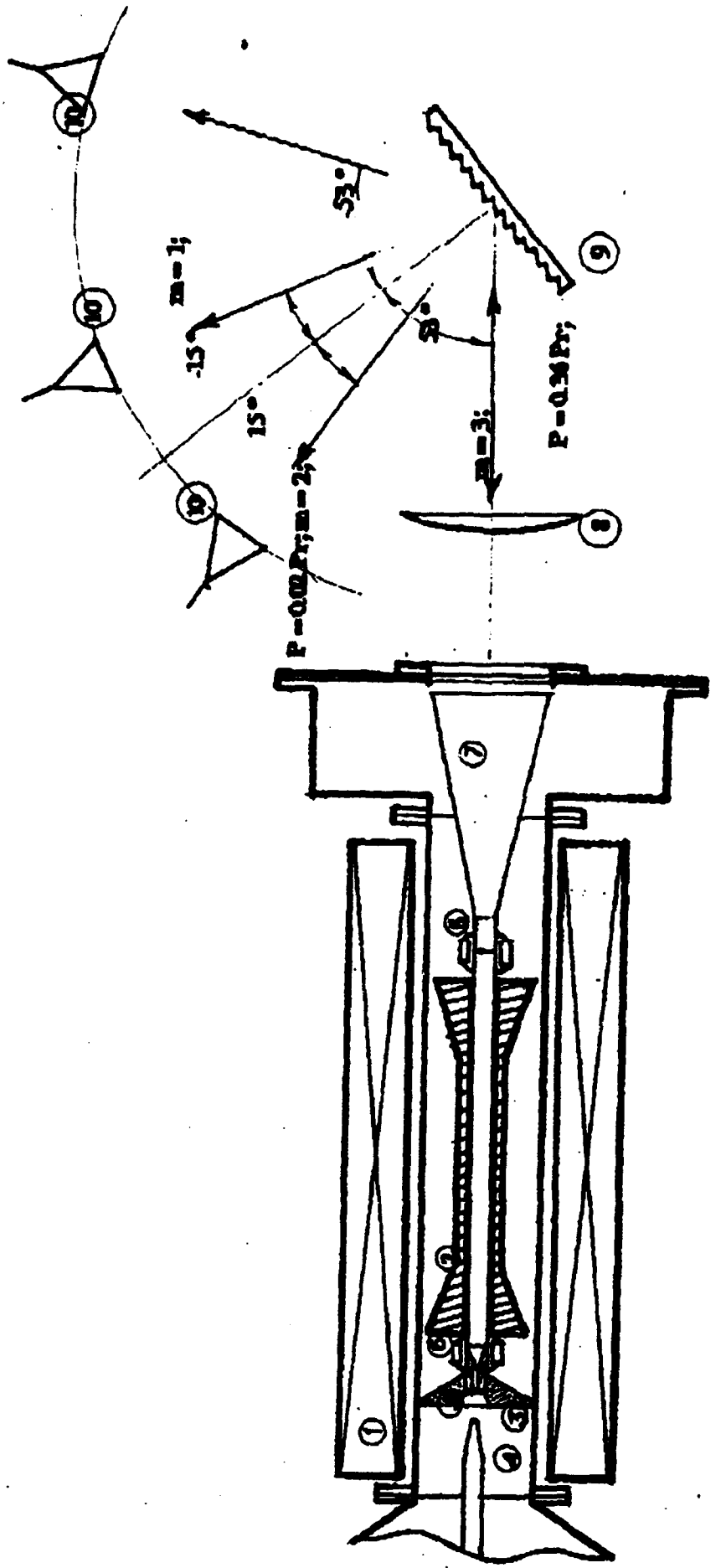


Fig.1. SCHEME OF THE EXPERIMENT.
1. Solenoid. 2. Ubéliator. 3. Constrictor. 4. Cathode. 5. Anode.
6. Current density. 7. Output horn. 8. Focusing lens. 9. Ubéliator.
10. Microwave detector with receiver horn.

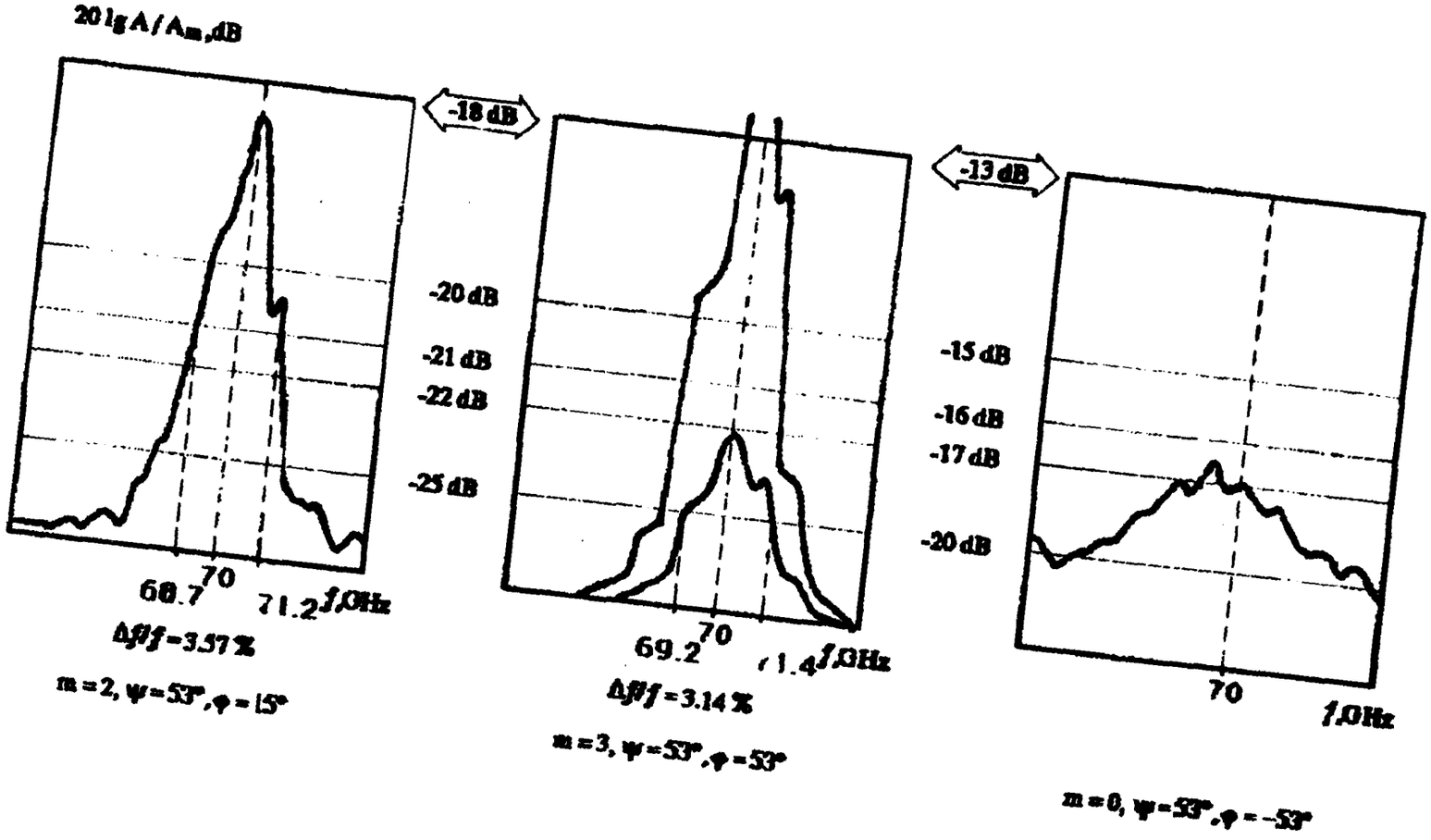


Fig 2. CURVES OF ECHELETTE REFLECTION AT MAXIMA OF VARIOUS ORDERS
ψ - Incident angle, φ - Diffraction angle

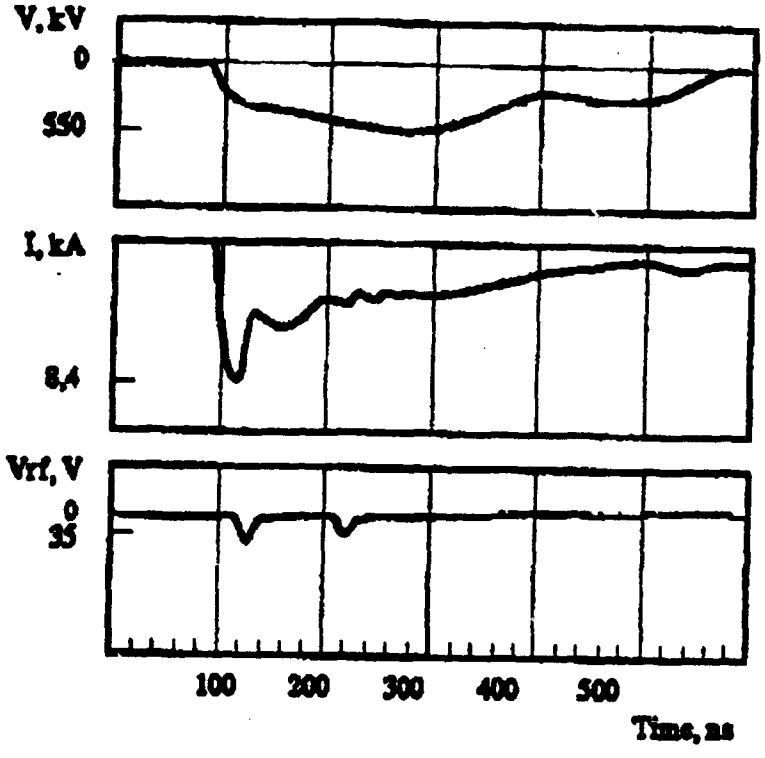


Fig. 3. TYPICAL WAVEFORMS OF DIODE VOLTAGE V, DIODE CURRENT I, MICROWAVE SIGNAL Vrf FOR Bz = 17,4 kG, B1 = 1,4 kG.

RELATIVISTIC MAGNETRONS: OPTIMIZATION OF PARAMETERS AND MODELLING OF PHASE LOCKING PROCESSES

D.V.Alexandrovich, S.V.Baranov, A.N.Didenko,*
N.M.Filipenko, G.P.Fomenko, A.S.Maidanovskii,
S.S.Novikov, V.V.Pozdeev, A.S.Sulakshin

Institute of Nuclear Physics,634050, P.O.Box25, Tomsk, Russia

* Tomsk State University,634010, Lenin av.,36, Tomsk, Russia

ABSTRACT

Calculations of microwave radiation power dependence upon magnetron parameters with a real voltage pulse shape being considered showed fairly good agreement with similar dependencies obtained experimentally.This allowed to choose magnetron optimal parameters in agreement with a high current accelerator as a power source.Next way to increase radiated power is to sum up powers of some pulse relativistic magnetrons. A scheme is based on the principle of nonsymmetry allowing a rather strong mismatch of magnetrons eigenfrequencies and being not so critical to a choice of connection line length. The strong coupling provides fast phase locking and high effeciency of the pulse powers addition.

An application of high-current linear induction accelerators for power supplying of magnetron generators [1,2] results in difficulties of their mutual compatibility both due to a small duration of produced voltage pulse and influence of geometry and magnetron diode operation conditions on accelerator electrical parameters.

Using a relativistic model of magnetron [3] we will take into account the detuning of a phase velocity $v_f = \beta_f c$ and velocity of electrons $v_e = \beta_e c = u_o/(d\,H_o)$($c$ -light velocity, u_o-anode voltage, H_o-magnetic field strength, d -anode-cathode gap).

Let's suppose that all microwave power is transmitted to a load

$$P = \eta I u_o \qquad (1)$$

where η -electron efficiency ,I -anode current.As in non-relativistic case [4] electron efficiency $\eta = 1 - 2\,R_L/d$,where $R_L = E_N^2 / (H_N^2 - E_N^2)$ -is Larmor radius in crossed-fields electric

$E_N = eE_o/mc^2$, $E_o = u_o/d$ and magnetic $H_N = eH_o/mc$ ones.

Magnetron anode current I depending on parameter of detuning $\alpha = 1 - \beta_f/\beta_e$ is formed by electrons from a region of favourable phases. But here electrons can reach anode just in case α meets the following condition :

$$A \ln\left(A + \sqrt{A^2 - 1} \right) - \sqrt{A^2 - 1} - ApR_L - sh(pR_L) \leqslant 0 , \quad (2)$$

where $p = 2\pi/(\lambda\beta\gamma)$ - transverse wave number , λ - wave length , $A = \alpha\gamma\, sh(pd)E_o/E$, E-effective amplitude of basic space harmonics of microwave field on anode surface. Calculating electrons drift velocity from a region of unfavourable phases into a region of favourable ones [3] ,in a space charge limited regime one can obtain the value of generated power

$$P(GW) = 8{,}7\, NL\, \frac{E}{E_o} E_N^2\, \frac{\beta [A_1 + ch(pR_L)] (d - 2R_L)}{8\pi\gamma\, sh(pd)(1 - \alpha\gamma^2)} , \quad (3)$$

where N - number of resonators of magnetron anode ,L - anode length,

$$A_1 = \begin{cases} A & \text{at } A > ch(pR_L), \\ ch(pR_L) & \text{at } A \leqslant ch(pR_L) . \end{cases}$$

Calculations of microwave power dependence upon a magnetic field value (Fig.1,curve 1) with a real pulse voltage shape being taken into account made according to formula (2,3) for six-vane magnetron of 10cm wavelength [2] showed a similar dependence obtained experimentally (Fig.1,curve 2).

So, obtained expression (3) ,in contrast to [3] allows to consider the real features of used high-current accelerator and more then that adjust an electro-dynamical system of magnetron to it. Volt-ampere characteristics calculated for various magnetic fields (Fig.2) allow to choose matched operation regime of magnetron and high-current accelerator what is necessary from the point of the total system effeciency increasing.One can calculate operating characterictics when magnetron power or efficiency values are constant.

It should be noted that while calculating relationship E/E_o

was choosen as arbitrary constant .Therefore a change of effective amplitude of a basic space harmonics during a pulse voltage and the influence of this change on a matched model of linear accellerator will be taken into account at further development.

It is clear that to create a microwave device with power level of 10^{11}- 10^{12} Wt order is practically an unsolved problem. The most real way to solve it is a coherent power addition of separate relativistic microwave generators. This was experimentally confirmed with 2 - 7 relativistic magnetrons [5]. A coherent powers addition for two magnetrons and reproducibility of phase differencies between separate generators in a system consisting of seven magnetrons have been demonstrated. However, a traditional approach to produce oscillators system with coherent powers addition used in these works has certain drawbacks: the necessity of frequency and amplitude parametrs identity of separate generators and a comparatively long time to establish a synchronous regime. Investigations carried out by us earlier allowed to put forward an idea of non-symmetrical powers addition systems [6] permitting to avoid these difficultes.

A generalized system of two oscillators [Fig.3] connected by circuit Y containing a common load is considered here theoretically. Without a concrete definition of connection line scheme one can describe it by means of the following ratios within the framework of general approach:

$$S_{11} = -S_{12}\exp(j\theta) \qquad S_{12} = s\exp(-j\gamma)$$
$$S_{22} = -S_{12}\exp(-j\gamma) \qquad (4)$$

Ratio (4) expresses a natural agreement of coherent operating oscillators at powers addition. Here θ is non-symmetry pararameter determining phase differences between oscillators at addition regime.

A module of wave transit coefficient S_{12} can change within 0 - 0,5. In this case a connection line provides a strong interaction of oscillators.

Investigation of synchronous regimes for two generators checked by the method of slow-changing amplitudes allowed to obtain the following general ratios:

$$\frac{d\varphi_i}{d\tau} = - \frac{\omega_o - \omega_i}{\omega_o} - \frac{K}{Q_i} \left[\sin \Theta - \frac{U_l(\tau-\tau_d)}{U_i(\tau)} \sin [\varphi_l(\tau-\tau_d)-\varphi_i(\tau)] \right], \quad (5)$$

where ω_i, ω_l, ω_o - natural and synchronous oscillations frequencies; τ - normalized time; U_i, U_l - amplitude of oscillations; τ_d - time of signal delay in connection line; Q - quality of oscillating systems of oscillators.

A distinguishing feature of (5) compared to expressions used for modelling in [5] is that normalized coupling K

$$K = -2s \frac{\cos\gamma - 2s\cos\Theta - j2s\sin\gamma}{1 + 4s\cos\Theta(s\cos\Theta - \cos\gamma)} \quad (6)$$

between oscillators due to non-symmetry ($\Theta \neq 0$) is significantly more than 1.

Due to it one may expect a signiticant increase of synchronising band and velocity of a phase-locking state establishing and decreasing demands to identity of oscillators in use.

Figures 4,5 represent results of numerical modelling of phase-locking process of symmetrical and non-symmetrical connection. The calculations were made for the following magnetrons parameters: ω_o= 2,95 GHz, length of connection line - 28 cm. Figures 4a and 4b demonstrate a process of phase-locking state establishing in symmetrical (4a) and non-symmetrical (4b) schemes at parameters of $Q\Delta f$ = 1200 , Δf - is the magnetrons frequencies mismatch.

Fig. 5 shows a synchronizing process for $Q\Delta f$ = 5000. As seen, non-symmetrical scheme is in phase-locking while a symmetrical one does not provide generators synchronization.

At present we have made experiments with semiconductor generators which results confirm the correctness mentioned above. The experiment on two relativistic magnetrons phase-locking with application of non-symmetrical connection line is prepared to perform.

References :

1. Alexandrovich D.V.et al.Proc.of 8th.Int.Conf. on High- Power Particles Beams (BEAMS'90), Novosibirsk 1990, v.2, p.1161.
2. Vasil'ev V.V. et al. Pis'ma Zh. Tekn. Fiz., 1987, v.13, N 12, p.762.
3. Nechaev V.E., Petelin M.I., Fuks M.I. Pis'ma Zh. Tekn. Fiz., 1977, v.3, N 15, p.763.
4. Vainshtein L.A., Solntsev V.A. Lectures on microwave electronics, Moscow : Sov. Radio, 1973.
5. Benford J. and Levine J. Proc. of 8th Int.Conf. on High-Power Particle Beams (BEAMS'90), Novosibirsk 1990, v.1, p.321.
6. Novikov S.S., Maidanovskii A.S., Radioteknika i Electronika, 1983, v.28, N 3, p.513.

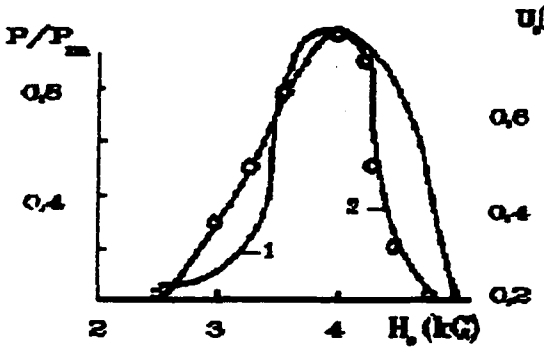


Fig.1 Microwave power versus magnetic field:
1 – calculation; 2 – experiment

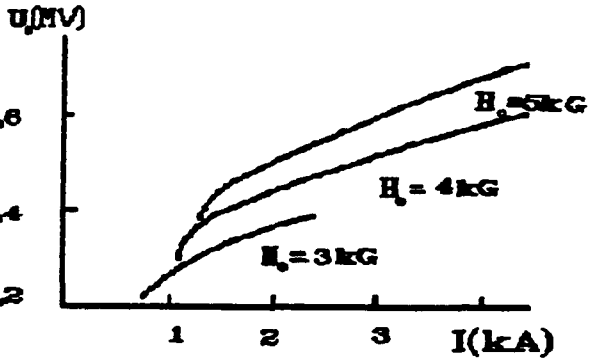


Fig.2 Volt – ampere characteristics

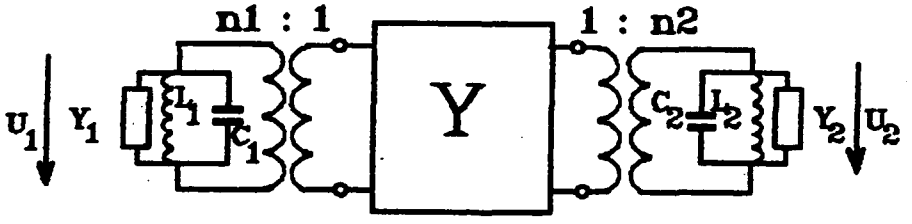


Fig.3 Generalized system of two oscillators

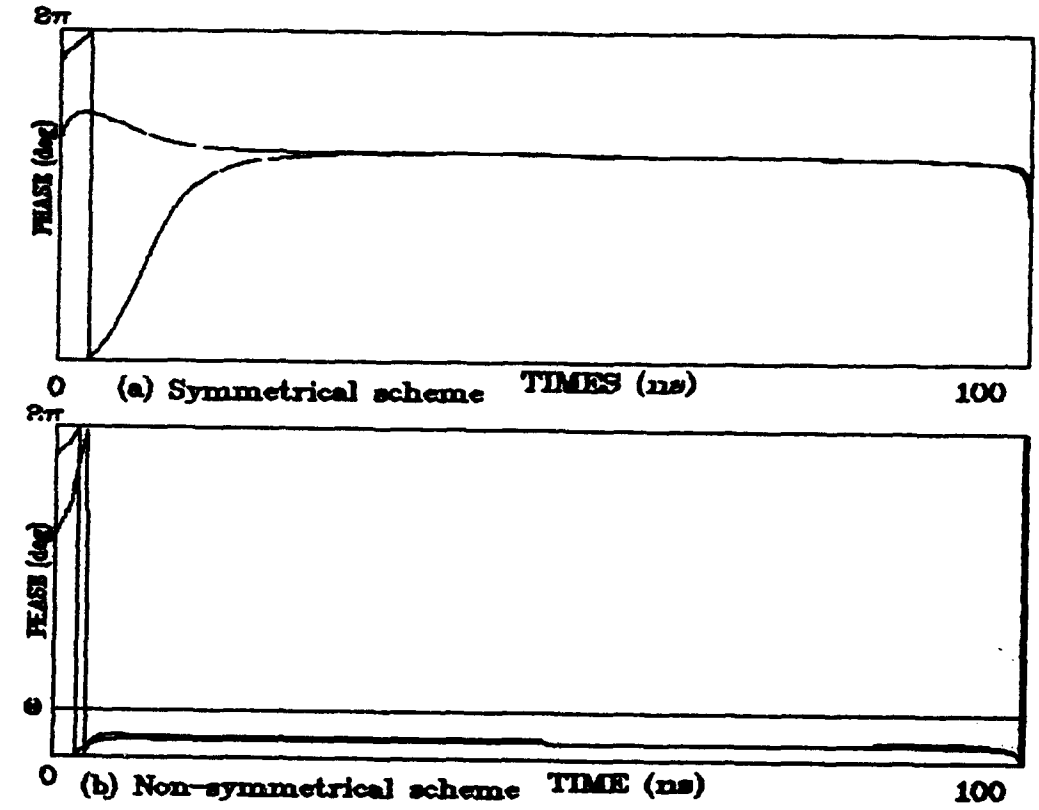


Fig. 4 Phase-locking process of two magnetrons for QΔf=1200

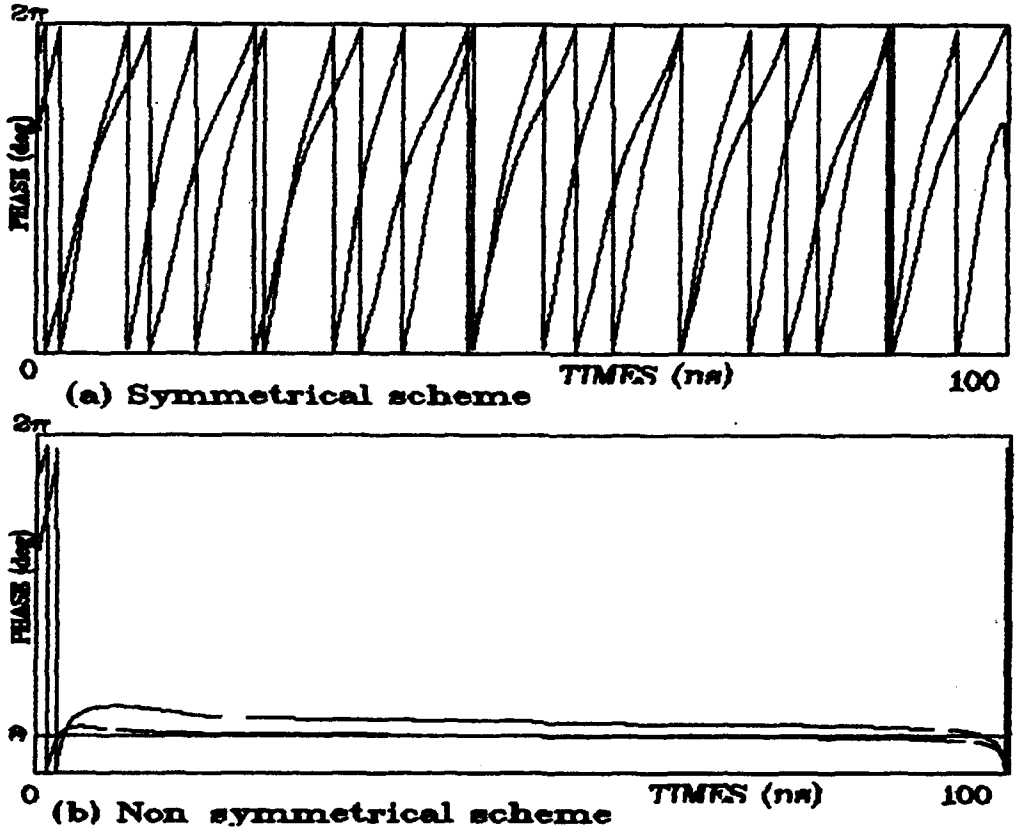


Fig.5 Phase-locking process of two magnetrons for QΔf=5000

THE NONUNIFORM-PHASE-VELOCITY RELATIVISTIC BWO

S.D. Korovin, S.D. Polevin, V.V. Rostov, and A.M.Roitman
Institute of High Current Electronics, Russian Academy of Sciences,
Siberian Devision, Tomsk

Abstract. The possibility of increasing the efficiency of a carcinotron by varying the phase velocity of the -1th space harmonic in the class of single-step functions has been studied both numerically and experimentally. The numerical simulation has shown that increasing the phase velocity along the interaction space improves the phase relationships between the HF current and electromagnetic field and increases the efficiency of energy exchange to 70 %. In the experiment carried out on the SINUS-K electron accelerator, a nonuniform-phase-velocity BWO operating with an efficiency of 45 % and microwave pulse power of 500 MW has been realised.

Introduction

The Cherenkov resonance condition for a BWO is satisfied for the -1th space harmonic of an electromagnetic wave propagating in a periodic waveguide to meet the injected beam electrons:

$$\omega + h v \cong \bar{h} v$$

where $\omega = 2\pi c/\lambda$, where c is the velocity of light, and λ is the radiation wavelength; h is the longitudinal propagation number of the wave zero space harmonic; $\bar{h} = 2\pi/d$, where d is the corrugation pitch; v is the electron velocity. The problem of increasing the efficiency of this type of device is related to the provision for most favorable conditions for energy exchange between the electron beam and the electromagnetic wave throughout the interaction space. This requirement can be met with the use of inhomogeneous electrodynamic systems by varying the amplitude and the phase velocity of the wave harmonic being in synchronism with the electrons [1,2]. It has earlier been shown theoretically [1,3] that the efficiency of a carcinotron with a nonuniform distributed coupling resistance can reach more than 50 %.

The present work investigated the effect of varying the phase velocity of the -1th harmonic of an electromagnetic wave ($v_\varphi = \omega /(\bar{h} - h)$) on the efficiency of the electron beam-electromagnetic wave interaction for the case of moderate relativistic electron energies (~ 500 keV).

Numerical Simulation of the BWO Operation

The BWO operation was simulated using a self-consistent set of equations describing the steady-state energy exchange between the electron beam and the electromagnetic wave excited by the beam [3,4] with due account for the longitudinal nonuniformity in phase velocity:

$$\begin{cases} \dfrac{da}{d\xi} = I \displaystyle\int_0^{2\pi} e^{i\theta}\, d\theta_o\,, & a(\xi_k) = 0 \\ \dfrac{d\omega}{d\xi} = Re\left\{\left(a - i\alpha \displaystyle\int_0^{2\pi} e^{i\theta}\, d\theta_o\right) e^{-i\theta}\right\}, & \omega(0) = 1 \\ \dfrac{d\theta}{d\xi} = 2\gamma_o^2 \left(\dfrac{\omega}{\sqrt{\omega^2 - \gamma_o^{-2}}} - \beta(\xi)^{-1}\right), & \theta_o \in (0, 2\pi) \end{cases}$$

where

$$a = \frac{2\gamma_o e}{mc^2 k} E, \qquad I = \frac{2\gamma_o^5 e}{\pi(\gamma_o^2 - 1)\, mc^2} JZ, \qquad \alpha = \frac{eJ}{\pi(\gamma_o^2 - 1)^{3/2}} \frac{4\gamma_o^2}{mc^3} T,$$

$$\omega = \frac{\gamma}{\gamma_o}, \qquad \xi = \frac{kz}{2\gamma_o^2}, \qquad \beta = \frac{k}{h}$$

where E is the synchroneous field amplitude, γ the relativistic factor, e and m the electron charge and mass, k the wave number, ξ_k is the total length of the electrodynamic system, Z the coupling resistance of the beam electrons with the -1th harmonic of the electromagnetic field, J the beam current, α the HF space charge parameter, where

$$T = \frac{I_o(pR_b)}{I_o(pR_o)} \left[I_o(pR_o)\ K_o(pR_b) - I_o(pR_b)\ K_o(pR_o)\right]$$

K_o and I_o are, respectively, the zero-order McDonald and modified Bessel functions, R_o the average waveguide radius, R_b the beam radius, p and h the transverse and longitudinal wave numbers of the synchroneous wave, respectively. It was assumed that the electrons are monoenergetic and have no transverse velocity component.

For a carcinotron with a nonuniform phase velocity, investigated was the simplest case of its single-step change throughout the interaction space:

$$\beta(\xi) = \beta(0) + \Delta\beta\ \ \varepsilon(\xi, \xi_c)$$

where $\Delta\beta$ and ξ_c are the amplitude and coordinate of the phase velocity jump, respectively.

The processes of bunching and energy exchange in a BWO are determined by the distribution of the synchroneous field along the electrodynamic system, such that its amplitude falls, with the coupling resistance being constant, along the direction

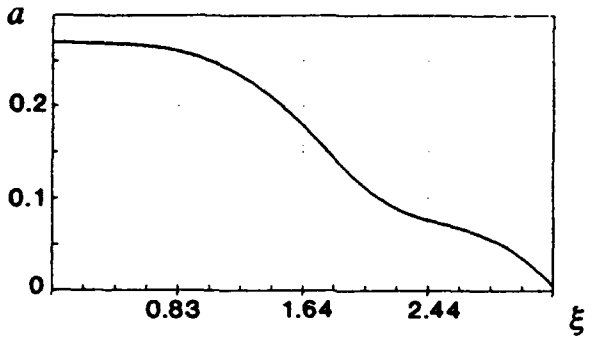


Fig.1. Field amplitude distribution in the homogeneous BWO
I = 0.0625, γ_0 =2.2, $\beta(\xi)$ = 0.77, α = 0.

of the electron beam propagation (Fig.1). Such a distribution of field does not conform to the conditions to be satisfied for the electrons could be properly bunched. Moreover, a portion of the beam electrons, having accelerated by a strong magnetic field during the initial stage of flight through the interaction space, fail to loose the acquired energy when flying through the decelerating phases of the field. The kinetic energy of these electrons, throughout the interaction space, turns out to be in excess of their initial energy (Fig.2a,b). This essentially limits the efficiency of a homogeneous carcinotron, which, for optimum modes, is about 15 % [4].

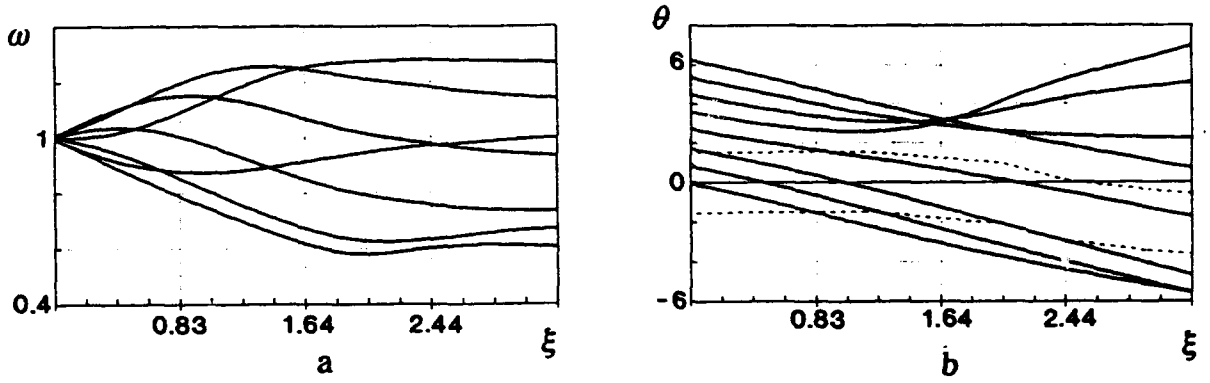


Fig.2. Reduced electron energy distribution (a) and relative electron phase distribution (b) in homogeneous BWC
I = 0.0625, γ_0 = 2.2, $\beta(\xi)$= 0.77, α = 0.

The energy exchange can be made more efficient by creating conditions which would simultaneously be favorable for electron bunching and provide for efficient decelerating of the majority of electrons which have fallen in the field accelerating phases at $\xi \simeq 0$.

This can be done by two ways: (1) to purposefully increase the synhcroneous harmonic amplitude to the end of the interaction stage so that the initially accelerated electrons would fall into the higher-amplitude decelerating phases of the field or (2) to increase the phase velocity of the synchroneous wave not changing

specially its field. This would lengthen the time during which the initially accelerated electrons stay in the decelerating field phases (Fig.3a,b) and hence increase the interaction space length.

In the both cases, the most favorable phase ratio of the HF current first harmonic and the microwave field is ensured (Fig.4).

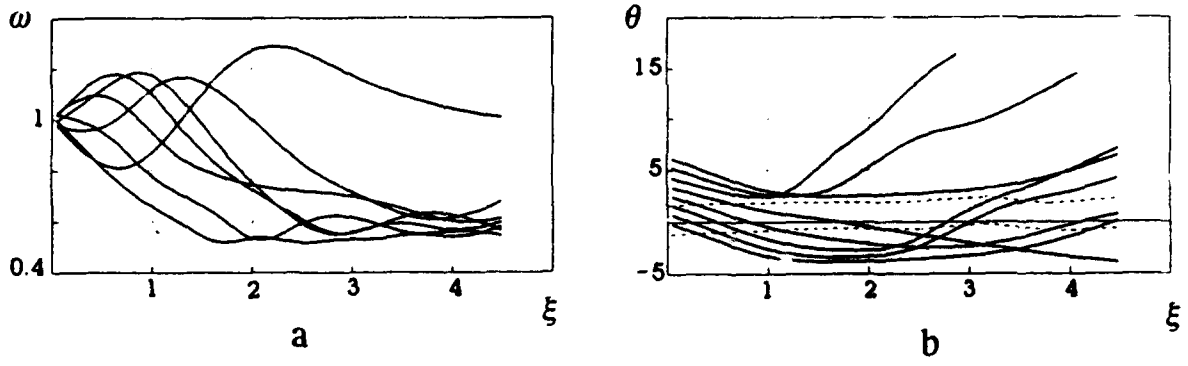


Fig.3. Reduced electron energy distribution (a) and relative electron phase distribution (b) in the nonuniform-phase-velocity BWO
I = 0.0625, γ_0 = 2.2, α=0.1, $\beta(0)$= 0.68, $\Delta\beta$ = 0.12, ξ_c = 1.01, η = 67%.

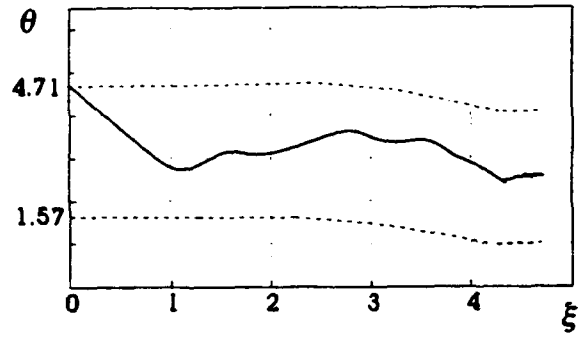


Fig.4. HF current first harmonic distribution in the nonuniform-phase-velocity BWO
I = 0.0625, γ_0 =2.2, α=0.1, $\beta(0)$= 0.68, $\Delta\beta$= 0.12, ξ_c= 1.01,

As it follows from calculations, the existence of favorable phasing of the HF current throughout a long interaction space increases the efficiency of the nonuniform phase velocity BWO to 70%. For the optimum regimes, the jump in phase velocity occurs within the first quarter of the corrugated electrodynamic system length and its amplitude is 10-20 % of the initial phase velocity. The initial difference between the e-beam velocity and the wave phase velocity turns out to be about factor 1.5-2 as large as for a homogeneous electrodynamic system. As the per-unit length of the first section is increased, the $\Delta\beta$ and $\beta(0)^{-1}$ values decreases thus decreasing the energy exchange efficiency, and for $\xi_c = \xi_k$ we have $\Delta\beta = 0$. The existence of the phase velocity jump increases the optimum length of the

interaction space by a factor of 1.2-1.6. The calculation has shown that a 10-15 % change in the value of one of the ξ_c, ξ_k, and $\Delta\beta$ from the parameter optimum value results in an upset in solving the time-independent BWO problem.

Experimental

The experiment was carried out on the SINUS-K accelerator [5] built at the Institute of High Current Electronics. The TM_{01}-type wave in a circular waveguide was chosen as a working wave. The carcinotron electrodynamic system consisted of a steck of stainless-steel rings and was set up so that its parameters agreed with the design values as well as possible. The phase velocity increase along the interaction space was provided for by varying the corrugation pitch, the corrugation height being varied so that the coupling resistance would remain constant. For the electron beam transportation a pulsed solenoid with a magnetic field strength up to 26 kOe was used.

In the experiment, the phase velocity jump was 10 % for the length ratio of the initial phase velocity section to the jumped phase velocity 1/3. According to the numerical simulation prediction, these parameters provide for an about 55 % BWO efficiency. The maximum pulsed power achieved in the experiment was 500 MW for a microwave length of 3.2 cm and a pulse duration 12 ns. With a cathode voltage of 400 kV and an electron beam current of 2.8 kA, the efficiency reached

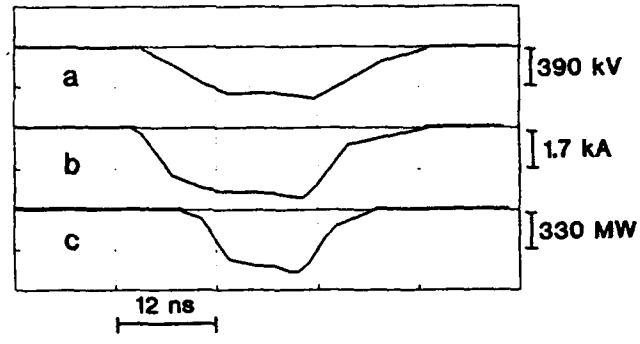


Fig.5. Cathode voltage (a), beam current (b) and microwave pulse envelope waveforms.

45% (Fig.5) It was noticed that, in order that the operation mode was an optimum with decreasing the cathode voltage, the amplitude jump had to be increased, which conforms the predictions of the numerical simulation. Estimates of the instantaneous spread of longitudinal electron energies, obtained in accordance with Ref.6, show that for the above experimental conditions it was not in excess of 0.5 %.

Thus, the reported experimental study has confirmed that the efficiency of a BWO can be increased by varying the phase velocity of the synchroneous wave. The obtained data together with the results of other recent BWO studies suggest

that a relativistic BWO with an efficiency of more than 50 % may have been realized in the nearest future.

REFERENCES

[1] Kovalev N.F., Petruhina B.I. Electron Technique, S.1, Microwave Electronics, 1977, N 7, pp.102-105.
[2] Ginzburg N.S. et al. -In: Relativistic Microwave Electronics, Gorky, 1988, pp.37-78.
[3] Kovalev N.F., Petruhina V.I., Smorgonsky A.V. Radiotechnique and Electronics, 1975, v.20, N 7, pp.1547-1550.
[4] Kovalev N.F. et al. - In: Relativistic Microwave Electronics, Gorky, 1979, pp.76-113.
[5] Bykov N.M. et al. PTE, 1991, N 2, pp.38-40.
[6] Korovin S.D., Pegel I.V. Zh.Tekhn.Fiz. (in publisht)

THE STATE OF ART OF INVESTIGATIONS OF RELATIVISTIC MULTIWAVE MICROWAVE GENERATORS

A.N.Bastrikov, S.P.Bugaev, I.A.Chernyavsky, M.P.Deichuli, P.A.Khryapov, V.I.Koshelev, V.V.Lopatin, N.S.Sochugov, K.N.Sukhushin, A.N.Zakharov

High Current Electronics Institute, Russian Academy of Sciences, Siberian Division, Tomsk

V.I.Kanavets, V.M.Pikunov, A.I.Slepkov

Moscow State University, Moscow, Russia

Abstract. To carry out experimental investigations of multiwave microwave generators, new electron guns have been constructed and hollow electron beams with the power up to 100 GW and 15 GW have been obtained on the "Gamma" and "Sinus-7M" accelerators, respectively. A 3-cm wavelength range multiwave Cerenkov generator (MWCG) with a 11-cm-diameter nanosecond electron beam has been studied in detail. First results of investigations of MWCG with a 35-cm-diameter beam have been obtained.

Introduction

One of the scientific trends in relativistic microwave electronics is development and investigation of super high-power (>1 GW) multiwave generators [1] . To date, main efforts are applied to a multiwave Cerenkov generator [2] due to its relative simplicity and high efficiency.

Investigations carried out previously [2] on the "Gamma" accelerator [3] with a 10 - 11-cm-diameter hollow electron beam and pulse duration t_p = 1000 ns have shown the duration of gigawatt radiation pulses to be essentially shorter than t_p. Experimental investigations of MWCG on the accelerator at $t_p \lesssim 100$ ns are necessary.

High MWCG efficiency is obtained at the linear current density of $\sim 0{,}5$ kA/cm. Therefore generation of $\sim 10^{10}$-W-power radiation pulses and their transporting from vacuum into atmosphere are related to the application of hollow beams with a diameter of tens of centimeters. The main is the problem of synchronization of the beam - electromagnetic field interacti-

on in an overmoded slow-wave structure with a large diameter.

Experimental Setups

To obtain large diameter hollow electron beams on the "Gamma" accelerator, a new electron gun was constructed. A 35 - 36-cm-diameter electron beam is formed in a coaxial diode with magnetic insulation, transported in the drift tube or slow-wave structure and deposited on the I80-cm-diameter conical collector. The collector is connected with a 380-cm-long vacuum chamber having the same diameter. Microwave radiation is transported from vacuum into atmosphere through a I8-cm-thick polyethylene window. To feed a solenoid, a capacitor bank with the stored energy up to 4 MJ is used. Magnetic field strength can vary in the limits of B = 4,5 - 22,5 kG. Duration of the voltage pulse applied to the electron gun from a Marx generator is varied by a crow-bar discharge switch and equals to t_p = 500 - I000 ns, the front of the voltage pulse being t_f = 200 ns. At the diode voltage U = 0,8 - I,7 MV beam current I_b = 20 - 70 kA.

Beams with the current I_b = 4 - I3 kA at t_p = 45 ns and t_f = 5 - 7 ns were obtained on the "Sinus-7M" accelerator at the voltage U = 600 - II00 kV. Beam diameter varied in the limits of I0 - II,6 cm and magnetic field B = 6 - I5 kG. The systems of beam formation and microwave radiation transporting from vacuum into atmosphere previously used in the experiments [2] on the "Gamma" accelerator are applied with the "Sinus-7M".

Experimental Results

In the experiments on generation of a 3-cm wavelength range radiation on the "Sinus-7M" accelerator diaphragmatic waveguides with the diameter D = I3 cm and period l = I,4 cm were used. Both one-sectional, with the length L = (I2 - 45)l, and two-sectional slow-wave structures with different lenghts of the first L_I, second L_2 sections and the drift tube L_{dr} be-

tween them were studued. Beam interaction with the field of the E_{01}-mode near the π-mode oscillations (λ_π = 3,25 cm) was used in the generators.

For a one-sectional structure the following main results have been obtained. The starting length of the generator L_{st} = = (I3 - I4)l. In the directivity diagram there is radiation with θ - and φ -polarizations. Correlation of powers for them is $P_\varphi \approx (0,3 - 0,5)P_\theta$. Microwave pulse and front durations are I5 - 35 ns and 5 - I2 ns, respectively. Wavelength λ (L = = I8l) decreases with the electron energy $\mathcal{E}$ rise that corresponds to the BWC-regime. At $\mathcal{E} > 700$ keV in a narrow-band ($\lesssim$I%) spectrum of the output radiation additional side maxima (satellites) appear (Fig. I). Radiation power dependence on the diode voltage has maximum that shifts to the lower U when the structure length is increased. With the uniform slow-wave structure the 500 - 800-MW powers were reached, the efficiency of generation calculated for the microwave radiation power in atmosphere being $\lesssim$ I0%.

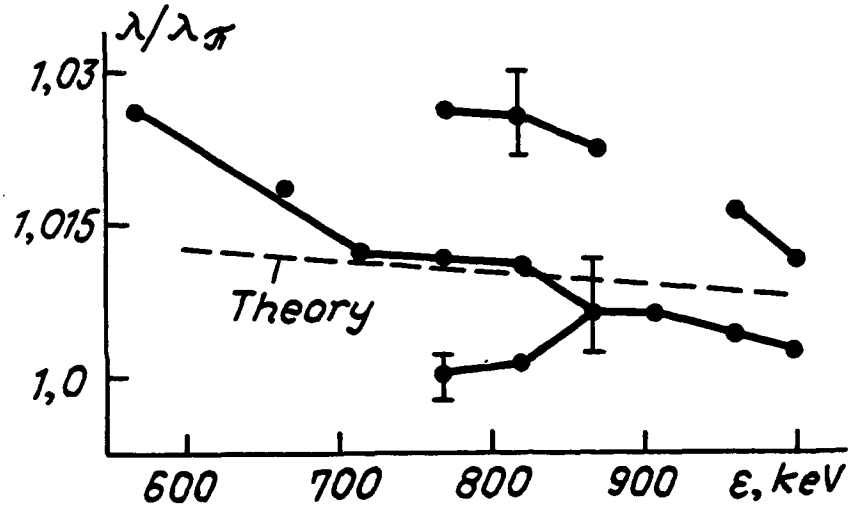


Fig. I

The following main results were obtained in the experiments with MWCG. Optimum lengths are $L_I \approx L_2 \approx 2L_{dr} \approx \approx L_{st}$. Radiation power dependence on the magnetic field has the maximum at B = = 9 - I0 kG. Directivity diagram and radiation power with θ -polarization essentially depend on the second section length and the beam radius. The character of radiation spectrum change with electron energy change is similar to the one obtained in a uniform structure with L = I8l. Satellites

are observed in the spectrum and they are suppressed when the beam radius is decreased. In an optimized generator it is possible to obtain a ~ 0,5-percent-wide radiation spectrum. Radiation spectra with θ - and φ -polarizations coincide with each other. MWCG studies carried out allowed to obtain microwave pulses with the power up to 2 GW, duration of 35 ns and front of 3 - 7 ns, the efficiency of generation calculated for the microwave radiation power in atmosphere being 20%.

In the experiments on the "Gamma" accelerator diaphragmatic waveguides with the diameter D = 38 cm and period l = I,45 cm were used. Voltage pulses with the amplitude of I,3 - I,6 MV and duration of 500 - 600 ns were applied to the diode. Beam current reached 60 - 70 kA. Radiation generation with the duration of $\lesssim$ 50 ns appeared on the voltage pulse front at U = 0,9 - I,2 MV, I_b = 30 - 40 kA. BWO-regime was experimentally realized near the π -mode oscillations of the E_{0I}-mode (λ_π = 3,I4 cm). Power correlation for the two polarizations was $P_\varphi \lesssim 0{,}2\, P_\theta$. Radiation wavelength depended on the slow-wave structure geometry and varied in the limits of λ = 3,I5 - 3,27 cm. Radiation spectrum width was ~ I%. In the first experiments with MWCG, microwave pulses with the power up to 3 GW were obtained, the efficiency of generation calculated for the microwave radiation power in atmosphere being $\lesssim$ I0%.

Numerical Simulation

To analyze physical processes in MWCG, linear and nonlinear theoretical models were developed. A linear stationary theory was created for the devices with axial symmetry and $D/\lambda \gtrsim$ I - - I0. By means of incomplete Galerkin method the initial equation system comes to the system of usual differential equations. Boundary-value problem is solved by means of modified method of directed ortogonalization. In a nonlinear nonstationary theory a slow-wave structure is replaced by the chain of fore-poles. Parameters necessary for calculations are determined on the basis of the preliminary analysis [4] .

Numerical simulation of microwave generators studied expe -

rimentally on the "Sinus-7M" accelerator was made. We start with consideration of the linear theory results. When solving the boundary-value problem for a uniform structure L = 181, the first three longitudinal resonances are well distinguished. Calculated starting length of the generator L_{st} = (12 - 13)l is in good agreement with the experimental one. Generation wavelength change (by maximum amplification) from the electron energy for the first longitudinal resonance (L = 181) is shown in Fig. 1 by a dashed line and corresponds to the BWO-regime. Fig. 2 presents longitudinal distributions of the E_z-field, alternating component of current $\tilde{j}$, Umov-Pointing flows: S_Σ = $= S^+ + S^-$ is the summary flow, S^+ and S^- are the flows of the proper waves running to the right and left, respectively. Calculations indicate the TWT-mechanism of interaction in the system. So, complicated interaction of the TWT-BWO-type is realized near the π -mode. In MWCG, interaction of the beam and field is more complicated. Change of λ from $\mathcal{E}$ in MWCG is analogous to the uniform structure. In the second section the main rise of S^+ and energy losses by electrons are realized.

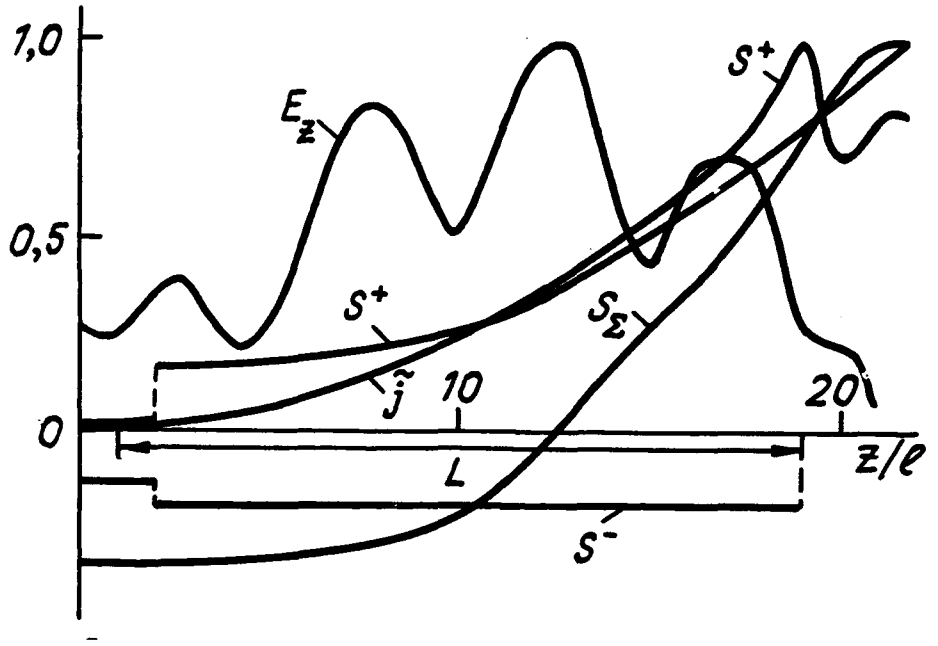


Fig. 2

Electron efficiency dependence on the time for a uniform structure L = 181 computed by the nonlinear nonstationary theory is presented in Fig. 3. The steepness of the output power rise is determined by the back-coupling delay time and beam and field interaction efficiency. Field structure settled in the system is

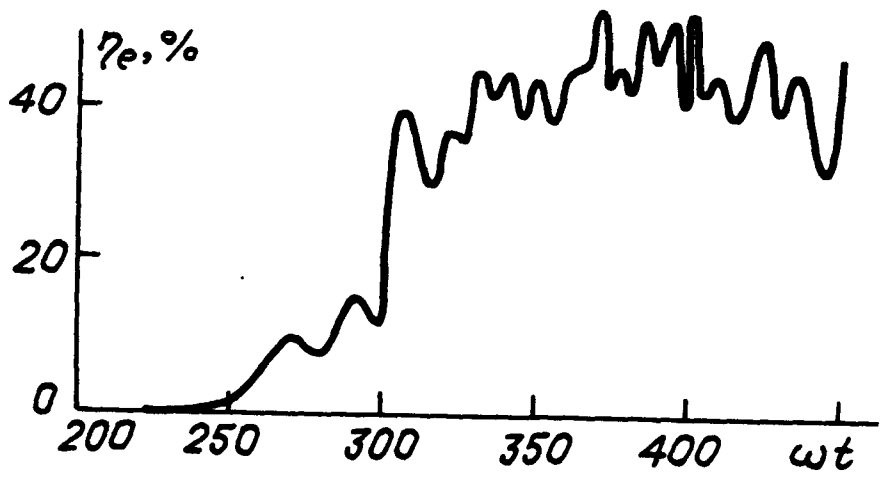


Fig. 3

close to the one of the first longitudinal generator mode. More complicated processes of oscillation rise are developed in MWCG. In the second section the field has a large amplitude that provides energy exchange of the beam and field with the efficiency up to 30%.

The authors thank A.I.Klimov and Yu.A.Andreev for many useful discussions and technical assistance in measurements.

References

I. Bugaev S.P., Kanavets V.I., Koshelev V.I., Cherepenin V.A. Relativistic Multiwave Microwave Generators. Novosibirsk: Nauka, I99I.
2. Bugaev S.P., Cherepenin V.A., Kanavets V.I. et al. IEEE Trans. Plasma Science, I990, v. I8, N 3, p. 525-536.
3. Bastrikov A.N., Bugaev S.P., Vorobjushko M.I. et al. Pribori i Tekhnika Eksperimenta, I989, N 2, p. 36-4I.
4. Kanavets V.I., Nifanov A.S., Slepkov A.I. Vestnik Moskovskogo Universiteta. Seria 3. Fizika. Astronomia, I990, v.3I, N 5, p. 34-4I.

Cherenkov microwave generator of high-current relativistic electron beams

N.F.Kovalev

Institute of Applied Physics,
Russian Academy of Sciences
Nizhny Novgorod, Russia

Numerous experimental investigations have shown that relativistic electron beams produced at strong-current accelerators with cold burst-emission injectors can be used for generation of powerful pulses of coherent radiation in the microwave band. The maximum output power is achieved in the Cherenkov-type generators; this is primarily due to the possibility to use simple electron-optical systems in them, which can produce most powerful electron beams used for generation.

It should be noted that it is very difficult to give a general and universal definition that would single out Cherenkov-type generators. For the sake of definiteness, to the generators of the Cherenkov type we assign here high-frequency sources whose operation is based on interaction of electromagnetic waves with waves of the spatial charge of the electron beam.

Fig. 1 shows a concept scheme of a Cherenkov generator with a strong-current electron beam. As electrodynamic systems such generators most frequently use smoothly corrugated waveguides and resonator cavities with high electric reliability, which do not change the value of the limit current of the electrons beam. Accordingly, it is convenient to choose as synchronous ones low-amplitude spatial harmonics of the operating waves; that would make the optical regime of interaction possible, as well as transportation of the high generated power. As a natural input or output in the source shown in Fig. 1, one can use short waveguide sections with smoothly changing corrugation, i.e., diffraction outputs of the energy.

Brillouin diagrams of the possible interaction types are presented in Fig. 2. The lower intersection exemplifies interaction of the electron beam with the backward wave under the conditions of Cherenkov synchronism, i.e., when the translation velocity of electrons equals to the phase velocity of the electromagnetic wave. This type of interaction is realized in carsinotrons: these devices are widely used for generation of pulses of coherent electromagnetic radiation with power of the order of

1GW in the short-wave part of the centimeter wavelength band, and of the order of several hundreds of megawatts in the millimeter band.

The Table gives the characteristic parameters for existing carsinotrons, and Fig. 3 shows the design of the device in more detail.

A carsinotron with a regular electrodynamic system cannot achieve very high efficiency: it is of the order of 15% in the ultrarelativistic limit. This fact is caused by unfavorable distribution of the high-frequency field, but can be remedied by passing over to irregular electrodynamic systems. The efficiency of carsinotrons with such systems can achieve more than 30% with no change in their basic properties: adaptability, duration of the transition process, and low response on the spread of initial energies of electrons in the beam.

The last line of the Table presents the parameters of the carsinotron with the cyclotron-resonance selection of modes. The essence of this concept is that at a certain value of the focusing magnetic field

$$B \approx 10.7\,\gamma\beta/d \quad \text{kOe}$$

($\gamma = (1-\beta^{2})^{-1/2}$, $\beta = v/c$, v is translation velocity of electrons, and , corrugation period) there arises resonance re-radiation of the operating wave into fast cyclotron waves of the electron beam. Intensity of this re-radiation depends on the transverse structure of the waves and the beam. This re-radiation can be always made sufficiently low for one of the highest wave types chosen as the operating one, and a thin-wall electron beam. In recent experiments at generators of this type with irregular electrodynamic systems the researchers achieved the power of the coherent radiation of the order of 3GW.

Two upper intersections in Fig. 2 exemplify Cherenkov radiation of passing electromagnetic waves by the electron beam. The lower intersection is characteristic for traveling wave tubes (TWTs), and the upper one, for free-electron lasers (FELs).

Realized varieties of experimental models of generators on such kind of interaction are grouped into four schemes shown in Fig. 4. The first two schemes are resonance TWTs. Within them, selective feedback is produced by Bragg reflectors: convertors shaped as smoothly corrugated waveguides. In the second scheme, the input reflector re-radiates the electromagnetic wave into two electron waves acting as the input signal for the TWT. In its essence, it is an under-excited autogenerator. Logical development of this idea is presented in the third scheme, where the input reflector works in the autooscillation regime. In all the three cases the output powers of the order of 1.5-2 GW and efficiencies about 20% were achieved within the 3 cm wavelength band.

The fourth scheme shows an amplifier. Realization of an accelerator on relativistic electron beams produced by burst-emission injectors is difficult primarily due to the limitations for the amplification set by the high noise level being, evidently, characteristic for such beams, and to the danger self-excitations caused by the necessity of high amplification coefficients. To remedy this problem we used the scheme with a regenerative BWO amplifier as the first cascade. The preliminary amplifier worked in a narrow band of the order of 1%, and that decreased the level of the noise signal and made great amplification possible. In the last experiments we achieved the amplification coefficient 60 dB, and output power of the order of 100 MW.

The second intersection in Fig. 2 shows the interaction regime realized in orotrons. This generator type is of great prospects for producing not very high powers (lower than 1 GW). One of its most important applications is its use as a section of sectioned generators; this case is illustrated in Fig. 4.

The experimental results described above belong to the 3cm band. All the three possible interaction types can be realized or have been realized already in the millimeter band. In the bands of shorter wavelengths, due to the surface character of the synchronous spatial harmonics, generators of the Cherenkov type are of less prospect than the devices based on the principle of electron oscillators.

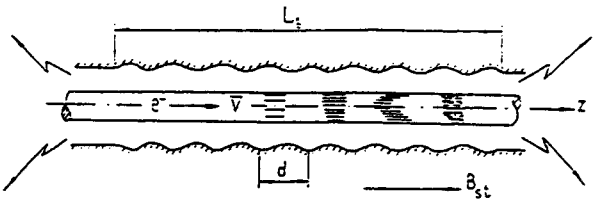


Fig. 1

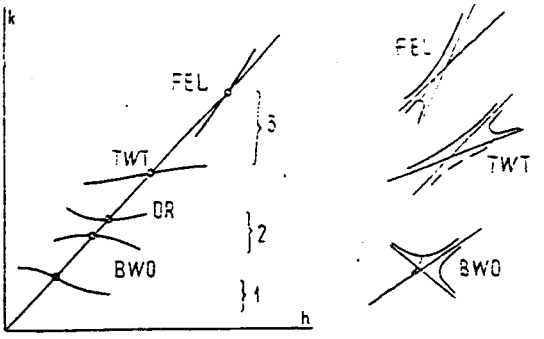


Fig. 2

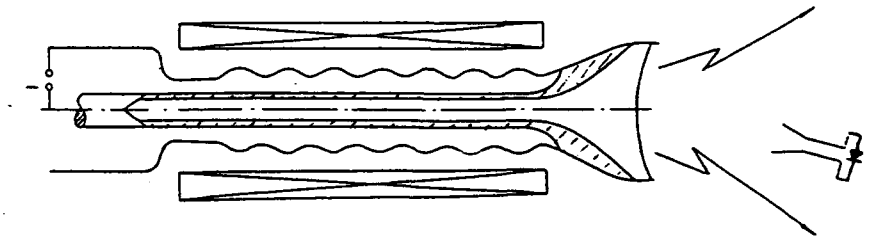


Fig. 3

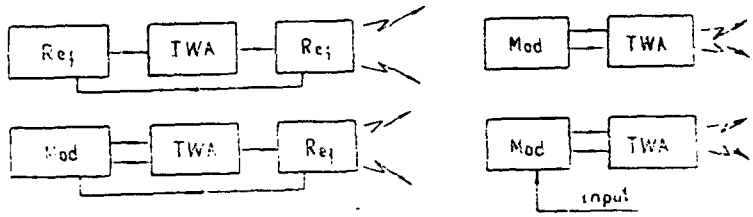


Fig. 4

n/n	Laboratory	Type wave	Ø cm	λ cm	U MV	I kA	τ_1 nS	$P_\sim$ MW	$\tau_\sim$ nS	η %
1	SRRPhI, PhI	E_{01}	3	3,1	0,6	4	15	350	10	15
2	IAPh	E_{01}	3	3,2	0,3	1,9	1500	50	400	10
3	IHC, IAPh	E_{01}	3	3,3	0,4	3	25	300	25	30
4	IAPh	H_{11}	1,9	2,9	0,5	3	20	120	20	10
5	IAPh	E_{02}	6	3	1,4	10	200	1400	50	10

MULTIWAVE RELATIVISTIC ELECTRON DEVICES: PROGRESS AND PROSPECTS

Vladimir A.Cherepenin

Instititute of Radioengineering and Electronics

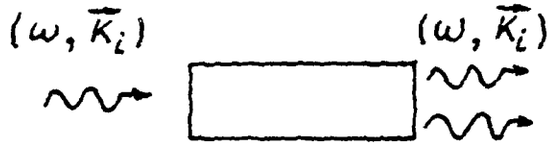
Mohovaya str., 11, GSP-3, 103907, Moscow, Russia

Abstract

During the last decade, attempts to use the properties of coherent eigen radiation of bunches of high-power relativistic electron streams have led to the multiwave conception of the beam-field interaction. In the multiwave electron devices an electron beam interacts simultaneously at a definite frequency with a number of modes, or waves, of electrodynamic structure within the syncronism band. The electron efficiency is shown to be higher in the multiwave regimes in comparison with the onewave ones. All types of multiwave devices are possible.

1. Conception of multiwave coherent radiation.

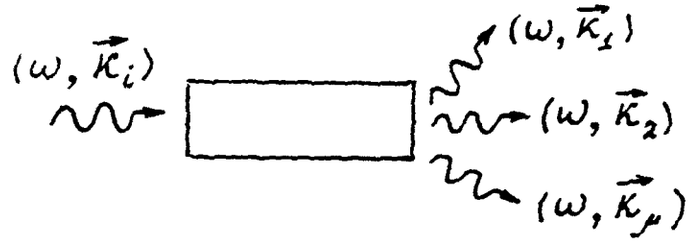
First of all we present basic definitions. If a electromagnetic wave with frequency ω and wavenumber $\mathbf{k_i}$ propagates into an active medium under a amplification candition one can obtaine at the output the wave with the same frequency ω, same wavenumber $\mathbf{k_i}$ and the same polarization as an input signal. This case shell call onewave interaction. It corresponds to the classical conception of unduced radiation, Fig.1a. However,in some cases it is possible to amplifity with the same $(\omega, \mathbf{k_i})$ also waves with the same frequency but varios directions of wavesnumbers $(\mathbf{k_1}, \mathbf{k_2}, ..., \mathbf{k_n})$. Such a case corresponds to the unduced Rayleigh scattering, Fig. 1b. If an active medium is a relativistic electron beam a multiwave interaction depends on eigen radiation of the electron bunchs. Polarization and angle distributions of radiating power depend on the electron energy, the lengh of interaction space and another reasons, for example, on number electromagnetic waves iside the synchronism band. Usualy, the spectrum is continuos for free space. All types of multiwave interaction are possible: synchrotron, undulator, normal and anormalous Doppler-effect, diffractional and cherenkov radition see Fig.2. Computer simulation of multiwave coherent radiation of relativistic electrons in a free space [1] showed the independence of distribution radiation on characteristies



onewave interaction

induced radiation

a)

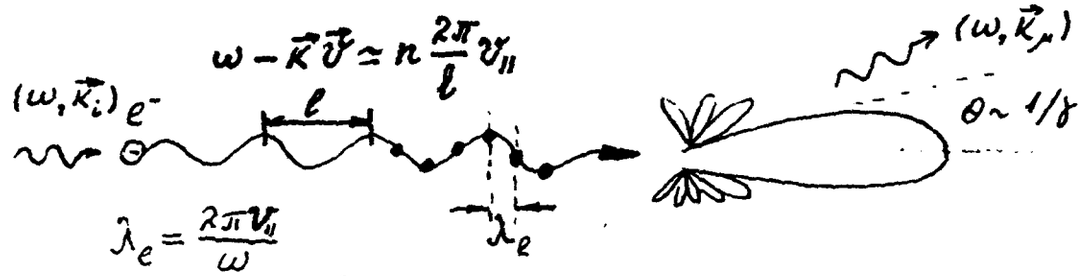


multiwave interaction

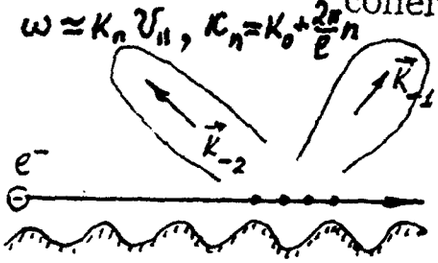
induced Rayleigh scattering

b)

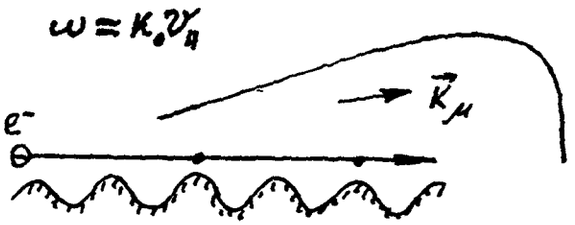
Fig.1.



coherent undulator radiation



coherent diffractional radiation



coherent Cherenkov radiation

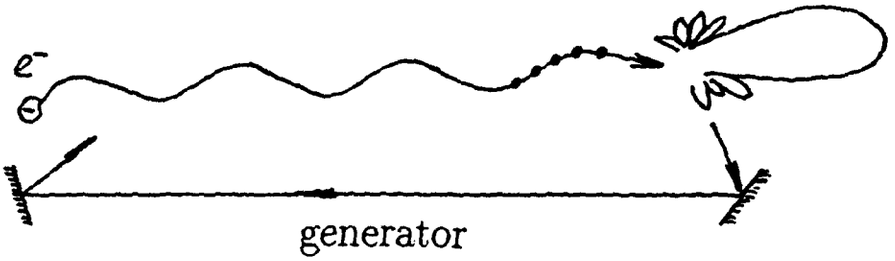
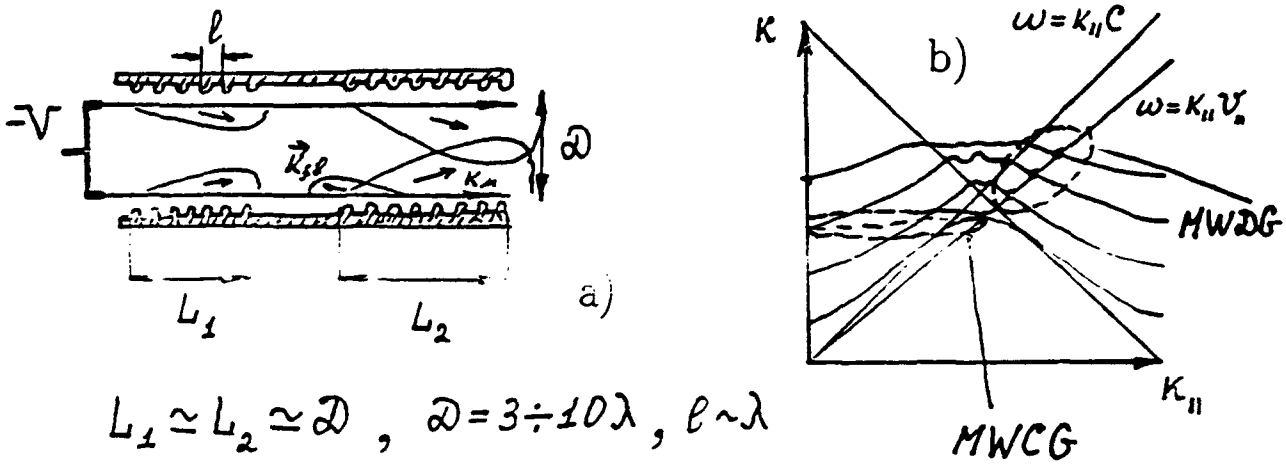


Fig.2.

of the input radiation enough high values of the electron beam current. In the optimal case an amplification is 40-50 dB. Efficiency of interaction in all multiwave cases is higher then in a onewave case . This fact has a simple interpretation: if electron bunches lose their energy and go out of synchronism with on wave, they can interact with another wave at definite frequency. Both multiwave amplifiers and oscillators (generators) are possible. In oscillators feedback has to be provided, Fig.2. In the case of multiwave oscillators one of siclobes can be used for such feedback while a main lobe can be radiated without reflections.

2. A design principles of multiwave relativistic electron tubes.

A design of high power devices depends on varios reasons. First of all, it depends on the quality of electron beams. Nowadays, it is possible to produce the good quality annular electron beams in high current accelerators. That is why the designs of real multiwave devices: multiwave cherenkov and diffractional generators (MWCG and MWDG) are based on the use of intense annular electron beams [2,3]. Usualy, it is twosectional devices and the diameter of the system is on the order lengh of the interaction space, Fig.3a. These dimensions can be as large as tens of wavelengths and at the same time, the period of the slow-wave structure can be on the order of the wavelength. These dimensions define a spectrum of wavenumbers $\mathbf{k_n}$ that may be synchronous with the electron beam. Usualy, multiwave cherenkov generators operate near cut-off, near lowest limit of electromagnetic waves not propagation in an infinitely long periodical structure, while a diffractional generators operatenear upper limit othe propagation bands, Fig.3b. Dispersion curves in Fig.3b give only an approximate picture of modes of the electrodinamic structure. Because of it is an inhomogeneously, in synchronism with the electron electron beam will be and another modes, for example, with another radial numbers ($\omega = const$). Therefore, in multiwave cherenkov and diffractional generators electron beam change a transverse structure of the electromagnetic field. In optimal case interaction in the second section is more intensive then in the first section. A share of the radiation go in the first section. It is a feedback. Computer sumulation confirm this phisical picture [2] .



$L_1 \simeq L_2 \simeq \mathcal{D}$, $\mathcal{D} = 3 \div 10\lambda$, $\ell \sim \lambda$

Fig.3.

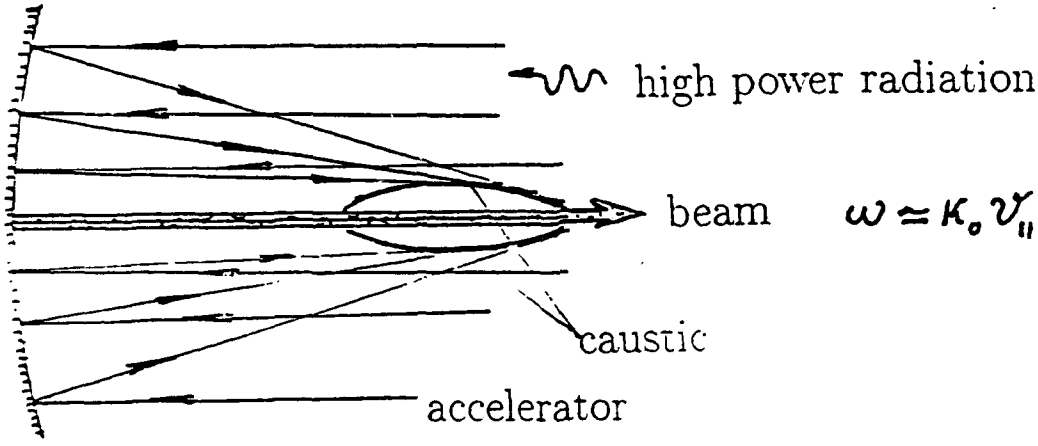


Fig.4.

3. Progress and prospects.

To-date is have been only multiwave cherenkov and diffractional generators [2,3]. In spite of good results it is only beginning, because is investigated not enough number of differenz devices. For example, it is interesting to fill a interaction space on plasma. A interesting way is a creation with help of the multiwave interaction a know type of accelerators. When waves with different **k** interfere in free space the caustic zones are arized. The phase speed in near caustic zone is slowly and smaller of the speed light. Therefore, cherenkov interaction is possible. At Fig.4 is an example of the accelerator. Computations show the possibi lity of effective conversion of electromagnetic waves energy into straightforward electron motion. For example, if the power initial electromagnetic field $\sim$ 1 TW and wavelengh $\sim$ 10 μm that acceleration rates of $\sim$ 1 GeV/m at acceleration lengh 0.1 m are easily accessible [4] .

References

1. V.A.Cherepenin, A.V.Korzhenevsky, International Journal of Infrared and Millimeter Waves, v.8, No.11, 1987, p.1411-1423.

2. S.P.Bugaev and al. IEEE Trans. on Plasma Science, v.18, No.3, 1990, p.518-524.

3. S.P.Bugaev ande al. ibid , p.525-536.

4. V.A.Cherepenin, M.G.Kurkin, Proc. 1989 URSI Intern. Simp. on Electromagnetic Theory, Stockholm, Sweden, p.357-359.

HIGH POWER X-BAND MICROWAVE AMPLIFIERS AND THEIR APPLICATION FOR PARTICLE ACCELERATION

T. J. Davis, J. D. Ivers, G. S. Kerslick, E. Kuang, J. A. Nation,
M. Oppenheim, and L. Schächter.

Laboratory of Plasma Studies & School of Electrical Engineering
Cornell University, Ithaca, NY 14853, USA

Abstract

We report results from experiments studying X-Band amplification in both cylindrical traveling wave tube (TWT) and coaxial drift tube geometries. In the TWT geometry 800-900 kV, 1-2 kA, 50-100 ns electron beams are injected into cylindrical guides containing slow wave structures. The amplifiers operate in the TM_{01} mode. With single stage ripple wall slow wave structures gains of order 30 dB have been obtained with output powers of 100 MW. Using a dielectric loaded TWT amplifier gains of 30 dB have also been measured, although at lower output powers of 35 MW. In the coaxial geometry a 9 cm diameter annular, 400 kV, 7 kA, 50 ns electron beam is injected through a 16 cm dielectrically loaded cavity, and an X-Band magnetron provides frequency locking of the interaction. The interaction processes involved in these devices have been studied analytically and also simulated with the MAGIC code. These studies show significant electron energy spreads result from the amplification process in the TWT devices. A magnetic spectrometer has been built to analyze the output energy spectrum of the accelerated electrons. Preliminary results from this experiment show evidence of a change in the electron distribution at the amplifier output when the r.f. power is present.

Introduction

In recent years we have developed a number of TWT X-Band amplifiers using ripple wall slow wave structures. Single stage devices have operated at output powers of 100 MW while severed two-stage amplifiers have been operated around 400 MW. At output powers above 70 MW sidebands have been observed and we are planning a number of experiments to address this issue. We are currently exploring the use of these high power sources for electron acceleration in both disc-loaded and dielectric structures. Since this application requires single frequency output we have been operating at power levels around 30 MW. At these power levels dielectric structures can be used for proof-of-principle experiments and scaled to higher powers by replacing them with equivalent periodic structures. In addition, an experiment is in progress using a large diameter coaxial geometry to increase the beam power available for r.f. generation as well as reduce the surface fields in the microwave structures. In the future we plan to increase the amplifier output in single frequency operation and consequently the accelerating field in these devices.

TWT Amplifiers

A schematic of the experiment is shown in Figure 1. A relativistic electron beam is injected into the drift tube along an axial guide field of 10 kG. Input microwave power of up to 100 kW is provided by an X-Band magnetron and fed in such a way as to couple to the TM_{01} mode in the cylindrical guide. The slow wave structure is a ripple wall waveguide with a measured TM_{01} passband of 8.5-9.8 GHz. The amplified signal is detected both in the far field and with a $\dot{B}_\theta$ probe located at the amplifier output. The signal is split and heterodyned with a local oscillator to measure the frequency. Gains of 35 dB at 9.28 GHz have been measured, corresponding to output powers of $\approx$ 100 MW. At these output powers sideband phenomena [1] have again been observed. At lower power levels the sidebands are not present. We have succeeded in producing an improved output pulse by adding a silicon carbide attenuator after the amplifier stage. The heterodyned signal from the $\dot{B}_\theta$ probe under these conditions is shown in Figure 2. These results indicate that reflections after the amplifier section, most likely from the output window, play a significant role in the amplification process. In earlier work [2] reflections due to the finite length of the amplifier itself were found to be a major influence on the passband characteristic of the device.

Analytic studies [3] and MAGIC simulations [4] of this experiment show that during the amplification process the particle distribution of the electron beam is spread with some particles accelerated and some decelerated. For an injected energy around 850 kV an energy spread between $1.7< \gamma <3.2$ can be expected at the output of the amplifier when the output r.f. power is 30 MW. We have developed an electron spectrometer to measure this change in electron distribution. The spectrometer consists of a small electromagnet producing a deflection field that can be varied to sample the electron distribution over an array of ten Faraday collectors. The current detected on each channel is integrated to give the total charge collected. For a 250 G deflection field the charge collected over a number of shots with and without r.f. power is shown in Figure 3. Higher channel number corresponds to increasing deflection and thus lower electron energy. These results show some evidence for a component of decelerated electrons when the r.f. power is present. We are currently working to improve the resolution of the spectrometer and plan to increase the amplifier output power to around 100 MW. This should increase the energy spread in the electron distribution to $1.5< \gamma <4.5$. An accelerator section has been constructed to take the high energy component of the distribution exiting the amplifier and accelerate these particles up to a γ of $\approx$ 10, with an average accelerating field of 5 MV/m.

Dielectric Amplifiers

In an experiment with a similar geometry and mode of operation the slow wave structure is provided by a dielectric loaded section of waveguide. The structure used in these experiments is 30 cm long with an outer radius equal to that of the guide tube, 1.6 cm, and an inner radius of 1.3 cm. The uniform radius section was 20 cm long and tapered sections at both ends of the device were each 5 cm long. The main advantages in such a device are the reduced level of reflections and the broader gain-bandwidth compared to a conducting ripple wall structure. Using a 1 MV, 1-2 kA annular electron beam the amplified r.f. power measured by a far field horn is shown in Figure 4. The heterodyned signal and its' FFT are shown in Figure 5. The gain-bandwidth for this ϵ=5 structure is shown in Figure 6. The output power level corresponding to a gain of 30 dB is $\approx$ 35 MW. This gain corresponds to 1.5 dB/cm in the uniform section, compared to a calculated Pierce gain of 1.2 dB/cm. Simulations of the experiment using the MAGIC code indicate that output power levels of more than 100 MW should be possible with a 60 cm structure.

In order to address the issue of power handling in such devices we are planning to explore the characteristics of longer structures, and the use of low loss dielectrics to reduce any breakdown problems associated with charge build-up.

Coaxial Source

We are also studying the feasibility of using a large diameter coaxial geometry to drive X-Band high power sources. The primary advantage of this geometry is the reduction of surface field levels, thus alleviating limits imposed by structure breakdown. Our experiment uses a 9 cm diameter 2 mm thick annular electron beam propagating between inner and outer drift tube conductors. The 400 kV, 6.5 kA beam is produced by a modified ETA module. The diode region and coaxial drift tube are immersed in a guiding magnetic field of 9 kG. The use of toroidal vacuum cavities to interact with the beam, effective at lower frequencies [5], becomes increasingly difficult at higher frequencies due to coupling to the drift tube TEM mode. Therefore, it is advantageous to increase the strength of the interaction by loading the coaxial cavities with a dielectric liner or a periodic structure. The conceptual design for such cavities is presented elsewhere in these proceedings [6]. We are currently experimenting with a 16 cm long cavity, which is loaded on both inner and outer conductors with 6 cm acrylic liners. The modes in this cavity arise due to the typical slow wave interaction [7] and the feedback from the cavity boundaries.

The interaction has been measured with a coupling slot directly on the cavity and

with $\dot{B}_\theta$ probes downstream of the cavity. Using a long section of waveguide as a dispersive medium, we identified the operating frequencies of the device with only the beam as the driving source. Figure 7 shows a dispersed $\dot{B}_\theta$ signal. Although seemingly broadband, the frequency content is due to interactions at three distinct resonances. By driving the cavity with an X–Band magnetron, we can lock the interaction to one resonance, as demonstrated by a dispersed signal from the same probe in Figure 8. A heterodyned waveform in Figure 9 also shows single frequency operation, as well as interaction over the entire effective beam pulse width.

Although the use of an external source greatly improves the frequency and phase content of the output r.f., it has not affected the magnitude of the output signals. A typical $\dot{B}_\theta$ level is 35 dB above that of the magnetron only. The actual power level in the device is difficult to measure due to reflections within the input coupler, although an optimized interaction in simulation has produced several hundred megawatts of radiation. Also, with the external drive source, the r.f. appears approximately 15 ns earlier in the beam pulse. The lack of amplitude variation and the reduced turn–on time of the device indicates that it behaves as a phased–locked oscillator rather than a long traveling wave tube. We are focusing our efforts on a power calibration of the system as well as the use of multiple cavities to enhance the output signals and provide further frequency selection.

Acknowledgements

This work supported by AFOSR and Department of Energy.

References

[1] D. Shiffler, J. D. Ivers, G. S. Kerslick, J. A. Nation and L. Schächter, *Appl. Phys. Lett.* **58**, 899, (1991).
[2] L. Schächter, J. A. Nation and G. S. Kerslick, *J. Appl. Phys.* **68**, 5874, (1990).
[3] D. Shiffler, J. A. Nation, L. Schächter, J. D. Ivers, and G. S. Kerslick, *J. Appl. Phys.* **70**, 106, (1991).
[4] L. Schächter, J. A. Nation and D. Shiffler, *J. Appl. Phys.* **70**, 114, (1991).
[5] J. Krall, M. Friedman, Y.Y. Lau, and V. Serlin, NRL Memorandum Report 6750, November 1990.
[6] L Schächter, T.J. Davis, and J.A. Nation,"A Proposed Extended Cavity For Coaxial Relativistic Klystrons," to be published in the proceedings of Beams '92.
[7] Eusebio P. Garate, Amnon Fisher, and William Main, IEEE Trans. Plasma Sci., **18**, 831, (1990).

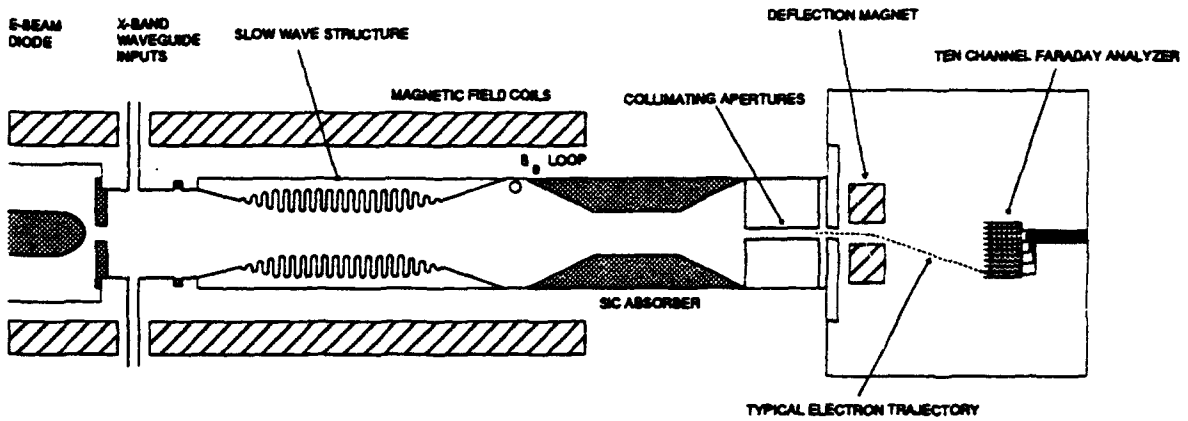


Figure 1. Schematic of the ripple wall TWT amplifier experiment

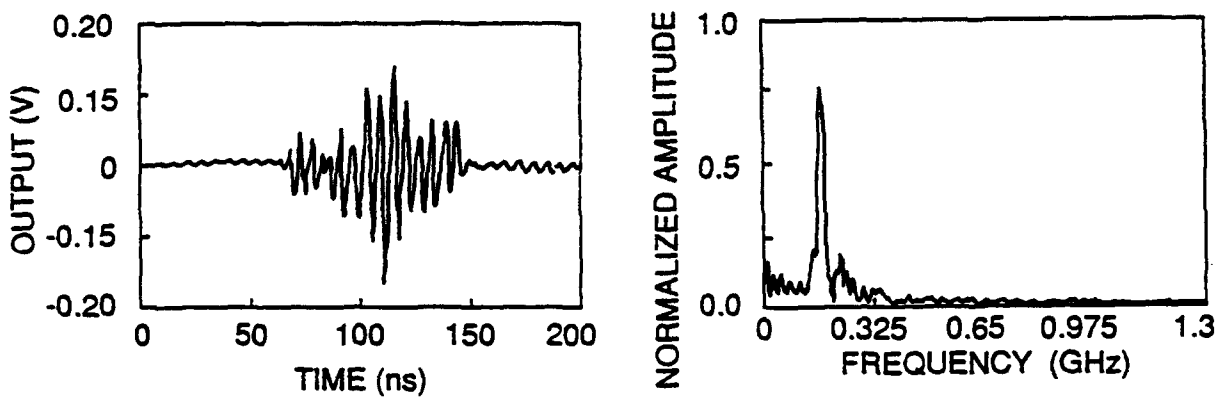


Figure 2. Heterodyned $\dot{B}_\theta$ probe signal at amplifier output (left) and FFT of this signal with local oscillator at 9.12 GHz. The peak in the FFT signal is at 165 MHz.

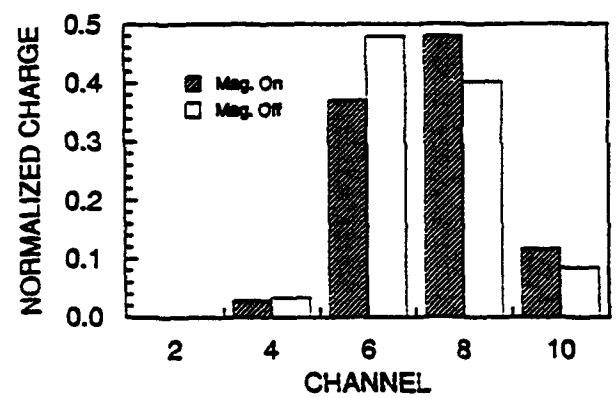


Figure 3. Charge collected on each spectrometer channel with r.f. power off (white) and with r.f. power on (shaded) for a 250 G deflection field.

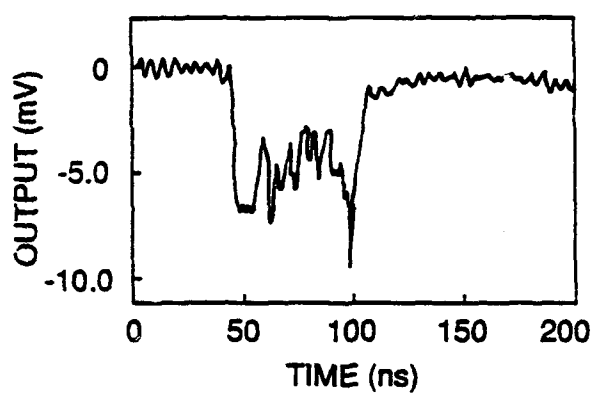


Figure 4. Crystal detector waveform measuring power at far field horn with the dielectric amplifier.

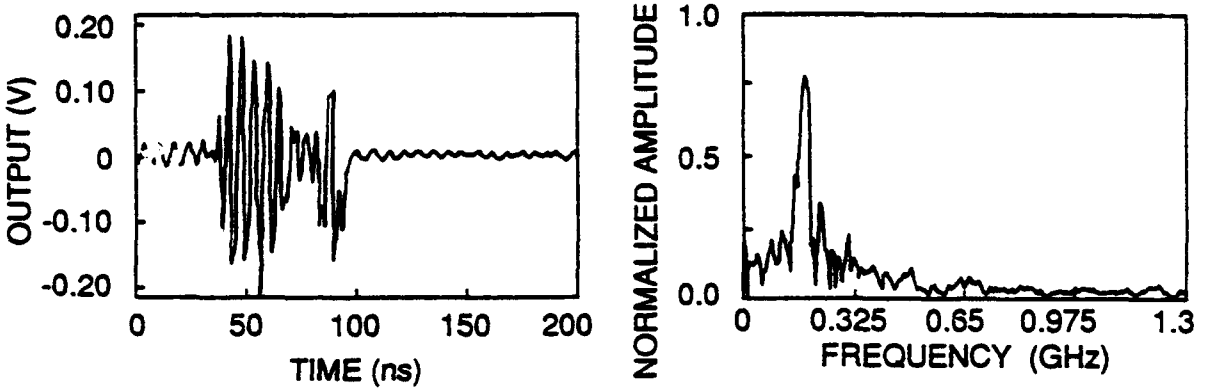


Figure 5. Heterodyned horn signal at amplifier output (left) and FFT of this signal with local oscillator at 9.04 GHz. The peak in the FFT signal is at 175 MHz.

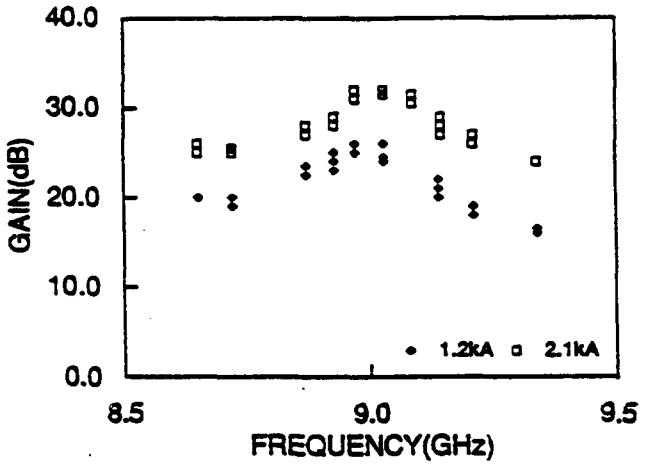


Figure 6. Gain-bandwidth of the dielectric TWT for two levels of electron beam current.

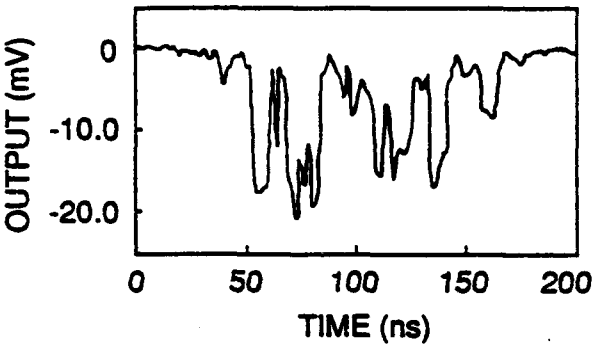


Figure 7. A typical dispersed $\dot{B}_\theta$ probe trace from the self-excited cavity showing coupling over several resonant frequencies.

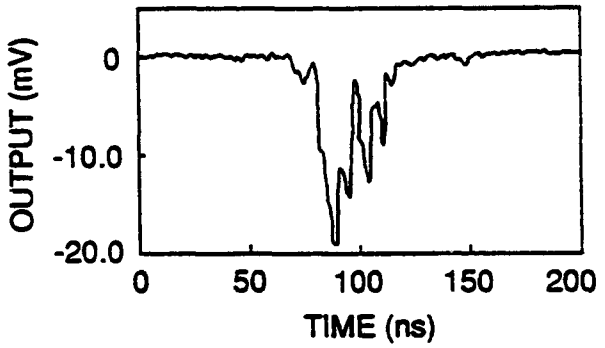


Figure 8. Dispersed signal from the same probe but with the external drive source turned on, showing selection of a single frequency.

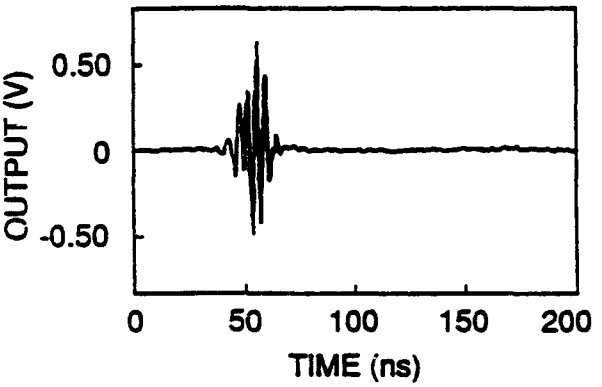


Figure 9. A heterodyned probe signal, also with the drive source on, demonstrating single frequency operation.

Recent Results from the University of Maryland Overmoded BWO and MWCG Program

D.K. Abe, T. Antonsen, Jr., Y. Carmel, B. Levush, and S.M. Miller

Laboratory for Plasma Research

University of Maryland, College Park, MD 20742

A. Bromborsky

U.S. Army Harry Diamond Laboratories

Adelphi, MD 20783

Two classes of overmoded HPM devices are under experimental investigation by the University of Maryland : overmoded backward wave oscillators (BWOs) and multiwave Čerenkov generators (MWCGs), shown schematically in Figs. 1 and 2. Both structures use an overmoded, cylindrically symmetric, periodically corrugated slow wave structure (SWS), immersed in a strong axial magnetic field. In the case of the MWCG, two sections of corrugated waveguide are separated a smooth walled drift section which is not cutoff to the RF radiation. Our interest in the MWCG is the result of pioneering work done at the Institute of High Current Electronics in Tomsk, which produced a record 7.5 GW of microwave power in air at a wavelength of $\sim$ 3 cm.[1] The University of Maryland experiments operate at lower power and frequency, with the goal of improving our physical understanding of the overmoded BWO and MWCG.

The microwave experiments all required a large diameter ($\sim$ 15 cm), thin (1.5 mm $\leq$ $\Delta_{beam} \leq$ 3 mm), annular electron beam propagating close to the waveguide wall for efficient beam-wave coupling and to maximize the beam power. Electron beam experiments in a long ($\sim$ 1 meter), smooth walled circular waveguide were conducted and produced annular cathode designs which could be operated over a wide range of average electric fields (75 kV/cm $\leq E_z \leq$ 600 kV/cm) with relatively uniform emission using a novel graphite/epoxy cathode coating.[2] Corresponding current densities ranged from 400 to 1600 A/cm^2. These large diameter beams were successfully propagated over a distance of $\sim$ 1 meter without appreciable beam spread or rotation. The dependence of beam

symmetry and uniformity on axial magnetic field strength was also studied; it was found that beams could be successfully generated and propagated without beam breakup or pinching over a wide range of magnetic field strengths (3 kG $\leq B_z \leq$ 14 kG). X-ray production at the electron beam collector was also studied extensively.

For the microwave experiments, the desired output frequency was in the range of 5 to 6 GHz. Both the overmoded BWO and MWCG slow wave structures were designed with the aid of linear backward wave oscillator theory. An SWS diameter of $D/\lambda_g \sim 3$ was chosen to maximize RF power flow in the structure within the mechanical constraints of the overall system. Both sinusoidal and semicircular corrugated structures were studied; the smooth shapes were chosen to minimize electric field enhancement. The mechanical design of the SWSs consisted of interlocking corrugated and/or smooth walled rings to allow for parameter studies of electrodynamic structure length.

The basic parameters for the microwave experiments are summarized in Table 1. Microwave radiation generated in the magnetized electrodynamic structure was propagated down a long ($\sim$ 6 meter), 29.2 cm diameter cylindrical waveguide and radiated into a large (20 m $\times$ 9 m $\times$ 15 m) anechoic chamber through a 1 meter diameter output horn and hemispherical radome. The radiated power density was measured in the anechoic chamber at distance of $\sim$ 10 meters from the source antenna using a 10 element monopole array with calibrated crystal detectors. Wave polarization was measured at a single spatial location (parallel to the experiment axis and a few degrees above the boresight) with a pair of cross-polarized standard gain horns. A dual heterodyne measurement technique was used to measure the frequency, using two microwave mixers and two local oscillators at offset frequencies. In some cases, the frequency was also measured directly with a 6 GHz oscilloscope.

There are a number of potential difficulties involved in making accurate measurements of the radiation pattern from a large diameter antenna; some simplifying assumptions had to made in order to integrate the measured power density pattern. There is the inherent problem of measuring a relatively high directivity pattern with a discrete array

Diode voltage	250 kV to 900 kV
Diode current	2.5 kA to 9 kA
Pulse duration	$\sim$ 80 ns
Magnetic field strength	0 to 14 kG
Pressure	10^{-6} to 10^{-5} torr
SWS R_{min}	7.99 cm
SWS R_{max}	8.89 cm
SWS period	2.15 cm

Table 1: Basic parameters for the microwave experiments

of antennas. The receiving antenna array sampled a 1-D slice of the total radiation pattern and asymmetries, which did not correspond to the expected symmetric TM_{01}^{o} pattern, were found in the measurement. These asymmetries may have been produced as a result of electron beam misalignment in the SWS, misalignment between the source and receiving antennas or passive mode conversion in the evacuated wave transmission system. A set of conservative estimates were made and the power density pattern was integrated accordingly – the resulting power estimates represent the *minimum* power produced by the experiment. Power in the azimuthal component of the electric field, which may account for as much as 50% of the total power, was not taken into account in this analysis.

Overmoded BWO experiments were conducted using the SWS structure described in Table 1. Structures with lengths of 35, 14, 10 and eight sinusoidal periods were investigated. Start oscillation currents were experimentally measured for the 10 and 14 period devices. The 35 period BWO was found to always start and the eight period structure never started oscillation with any of the experimentally attainable beam voltages and currents. A maximum output power of $\sim$ 320 MW was obtained with the 10 period BWO at a frequency of 5.483 GHz. The source power as a function of diode voltage for

all of the overmoded BWO structures is plotted in Fig. 3.

The corrugated input section of the MWCG should not oscillate on its own.[3] Based on the overmoded BWO experimental results, an MWCG was constructed with two corrugated sections of seven sinusoidal periods each connected by a variable length smooth walled drift section (L_d = 10, 15, 22.5 and 25 cm). A maximum output power of $\sim$ 105 MW was obtained for the structure with L_d = 10 cm at a frequency of 5.542 GHz. The source power as a function of voltage for all of the MWCG structures investigated is plotted in Fig. 4.

Both the overmoded BWO and the MWCG structures exhibited excellent frequency coherency. Fast fourier transforms of the heterodyne measurements reveal narrow frequency spectra, with $\Delta f/f < 0.5\%$ in many cases. The width of these spectra is on the same order as the finite width of the microwave pulse.

References

1. Bugaev, S.P., et al., "Relativistic Multiwave Čerenkov Generators," IEEE Trans. on Plasma Sci., **18**(3), June, 1990, pp. 525-536.

2. Lou, W.R., et al., "Experimental Studies of Explosive Emission Electron Beam Guns for High Power Microwave Devices," Bull. Am. Phys. Soc., **35**(9), 1990, p. 1937.

3. S.P. Bugaev and V.I. Kanavets, private conversation.

Fig. 1: Overmoded BWO schematic

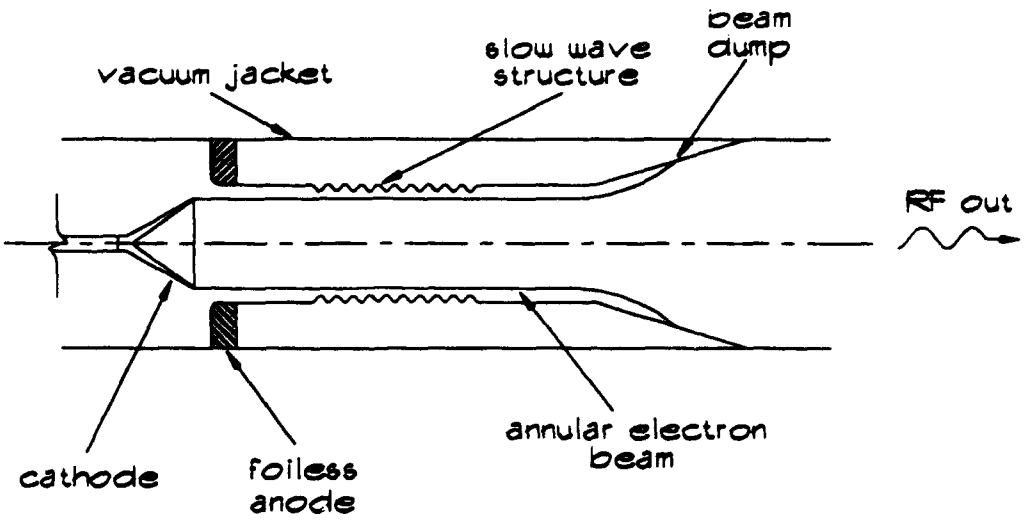
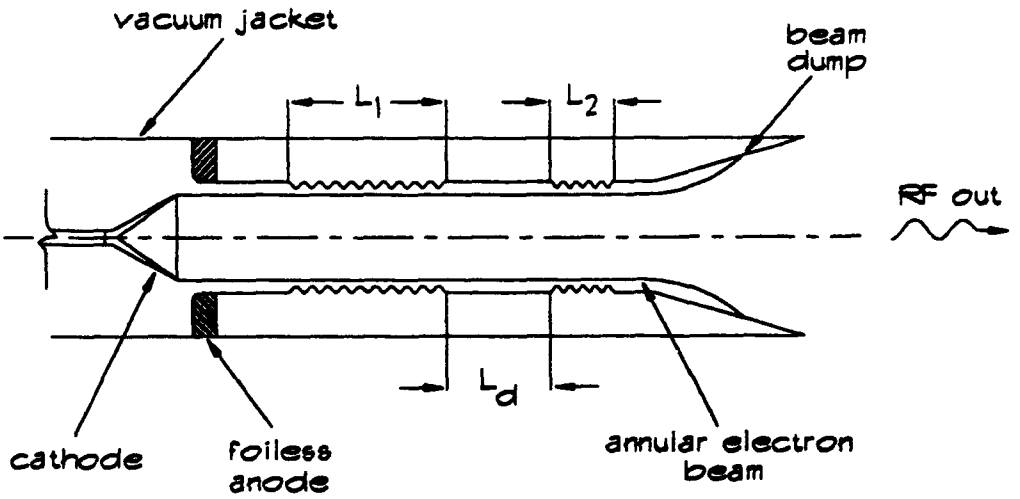


Fig. 2 : MWCG schematic



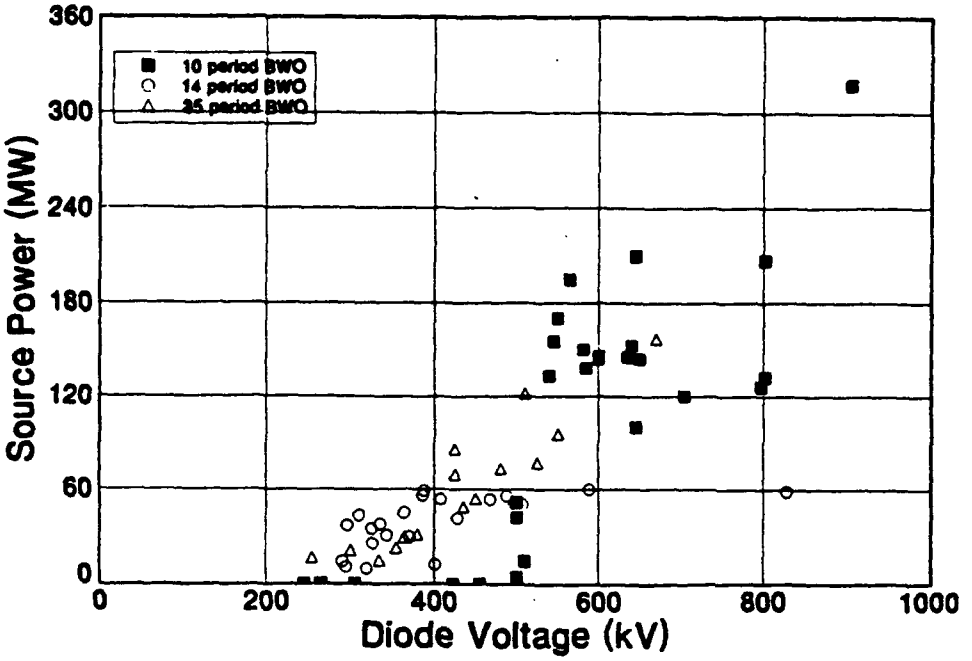


Fig. 3 : Radiated source power vs. diode voltage for BWO expm'ts

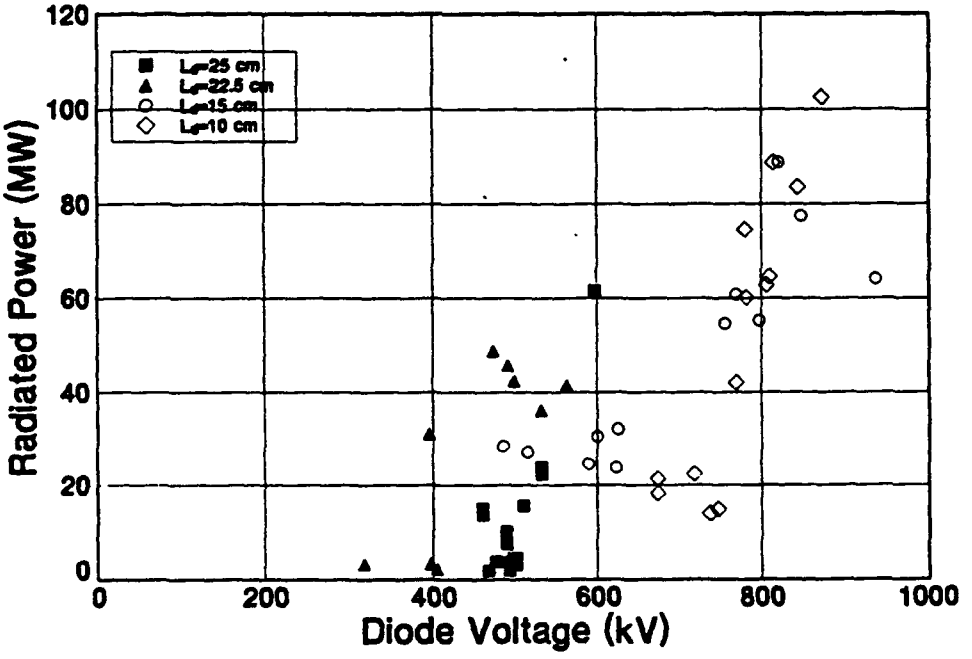


Fig. 4: Radiated source power vs. diode voltage for MWCG expm'ts

THEORY OF RELATIVISTIC BACKWARD WAVE OSCILLATORS OPERATING NEAR CUTOFF†

S. M. Miller, T. M. Antonsen Jr., B. Levush and A. Bromborsky‡

Laboratory for Plasma Research

University of Maryland, College Park, MD 20742 U.S.A.

§1 FORMULATION

Backward-Wave Oscillators utilize a high-current electron beam to produce high-power, coherent radiation in the centimeter and millimeter wavelength regime. Under certain voltage and beam current operating conditions, a Backward-Wave Oscillator (BWO) can operate near the upper edge of the transmission band where the group velocity of the electromagnetic wave goes to zero. In this regime, the cold structure dispersion relation can be approximated as a quadratic function of the wavenumber. A theoretical model similar to those presented in [1-3] has been developed to describe the operation of the device in this regime. We solve a self-consistent set of equations to describe the slow evolution of the envelope of the radiation field and the relativistic motion of the particles along a strong magnetic field. Included in the theoretical model are the effects of D.C. and A.C. space charge, and velocity spread in the beam. Numerical calculations of the starting current are performed and compared with an analytic expression for the starting current derived by assuming a fixed field profile.

In order to compare with experimental results, the effects of a time varying voltage and beam current pulse is included in the theoretical modeling. We consider two backward wave oscillators, an X-band BWO and a J-band BWO. We compare predictions of peak efficiencies and operating frequencies from the theoretical model with experimental results [4,5]. From studies performed on the X-band BWO, agreement is shown between experiment and theory. The earlier theory [6] was developed with the assumption that the interaction takes place far away from the zero group velocity point. However, at high voltages this assumption breaks down. The present model allows us to accurately model the behavior of the device at operating points near the upper edge of the transmission band.

In our model, we assume the interaction between the electron beam and the electromagnetic waves of the cold slow-wave structure are weak. Over a length equal to a period of the structure, the electromagnetic fields have a temporal and spatial dependence equal to the cold-structure fields. The effect of the beam is to cause the envelope of the electromagnetic fields to vary slowly in axial distance and time. In addition, the beam produces a small space-charge field. The electromagnetic fields in the structure are described as follows

$$\mathbf{E}(\mathbf{x},t) = [\frac{mc^2}{qL}a(z,t)\mathbf{E}_p(\mathbf{x}) + \mathbf{E}_p^{(1)}(\mathbf{x})]e^{i(k_0 z - w_0 t)} + c.c.$$

$$\mathbf{B}(\mathbf{x},t) = [\frac{mc^2}{qL}a(z,t)\mathbf{B}_p(\mathbf{x}) + \mathbf{B}_p^{(1)}(\mathbf{x})]e^{i(k_0 z - w_0 t)} + c.c.$$

where $a(z,t)$ is the slowly varying amplitude of the electromagnetic waves, $\mathbf{E}_p(\mathbf{x})$ and $\mathbf{B}_p(\mathbf{x})$ are the periodic eigenfunctions of the empty slow-wave structure and $\mathbf{E}_p^{(1)}(\mathbf{x})$ and $\mathbf{B}_p^{(1)}(\mathbf{x})$ are the first order space charge fields which are proportional to the beam density. The frequency and wavenumber at the "π" point (zero group velocity) are ω_0 and k_0 and L is the length of the structure. The slowly varying amplitude $a(z,t)$ satisfies the following equation

$$2\frac{\partial a}{\partial \tau} + i\frac{\partial^2 a}{\partial \xi^2} = -\widehat{I}\langle e^{-i\psi}\rangle_{\psi_0}$$

where the normalized length is $\xi = z/L$ and the normalized time is $\tau = \mid \frac{\partial \beta_g}{\partial kL} \mid \frac{ct}{L}$ where $\beta_g = v_g/c$ is the normalized group velocity. In addition we have introduced a normalized current defined as

$$\widehat{I} = 8\pi(\frac{I}{I_A})(\frac{L}{d})^2 \frac{C(r)}{\mid \frac{\partial \beta_g}{\partial kL} \mid}$$

where $I_A = mc^3/q = 1.7 \times 10^4 Amps$ and $C(r)$ is the coupling coefficient. The coupling coefficient is a measure of how well the electromagnetic fields of the cold structure couple to the electron beam. The coupling coefficient is defined as

$$C(r) = \frac{\mid \int_0^d \frac{dz}{z} E_{zp}(r,z) \mid^2}{\int_0^d \int_0^{r_w(z)} \frac{2\pi r dr dz}{d^3} \{\mid \mathbf{E}_p(r,z) \mid^2 + \mid \mathbf{B}_p(r,z) \mid^2\}}.$$

For our model we use the value of the coupling coefficient at the radius of the electron beam for the cold structure electromagnetic fields with frequency ω_0 and wavenumber k_0. We assume outgoing boundary conditions at both ends of the structure for the slowly varying envelope, namely

$$\frac{\partial a}{\partial \xi}(\xi = 0) = ik_b La(\xi = 0)$$

$$\frac{\partial a}{\partial \xi}(\xi = 1) = -ik_b La(\xi = 1)$$

where $k_b L$ is the boundary-condition parameter. For the two structures we analyzed, $k_b L = 0.53N$ for the $6GHz$ structure and $k_b L = 5.8N$ for the $6GHz$ structure where N is the number of periods of the structure. Large values of the boundary-condition parameter correspond to structures with large values of the reflection coefficients for all operating wavenumbers under consideration, whereas small values of the boundary-condition parameter correspond to structures with low reflection coefficients except when operating near the cutoff.

The electron beam is characterized by its phase $\psi = k_0 z - \omega_0 t$ and its energy $mc^2\gamma$ where $\gamma = (1 - v^2/c^2)^{1/2}$. Since the electron beam is assumed to be immersed in a strong axial magnetic field, only motion in the axial direction is considered. As the beam travels through the interaction region its phase and energy evolve according to

$$\frac{\partial \psi}{\partial \xi} = k_0 L - \frac{\omega_0 L}{c\beta_z}$$

$$\frac{\partial \gamma}{\partial \xi} = 2Re\left[[a(\xi, \tau) - i\frac{\bar{\omega}_p^2}{w_0}\langle e^{-i\psi}\rangle_{\psi_0}]e^{i\psi}\right]$$

where $\bar{\omega}_p$ is the space-charge parameter. To reduce the particle equations of motion to the above form, we consider interaction only with the synchronous spatial harmonic by averaging the axial electric field at the beam position over a period of the structure.

§2 STARTING CURRENT

Several authors have investigated conditions for self oscillation near the edge of the transmission band [8-10]. Using our model we calculate numerically the starting current for the X-band BWO and the J-band BWO. Fig. 1 shows the starting current calculation

for the X-band BWO based on the theory with $v_g \neq 0$ [6] compared with our model near cutoff. For voltages between $300kV - 400kV$ the two theories agree well. For voltages greater than $400kV$ the model with $v_g \neq 0$ breaks down. We derive an analytic expression for the starting current assuming a fixed field profile $a(\xi) = a_0 sin(n\Delta kL\xi)$ where $n\Delta k$ corresponds to the shift in axial wavenumber away from k_0 for $n = 1, 2, 3$. As shown in Fig. 1, the analytically calculated starting current agrees well with the starting current predicted by numerical calculation. Our numerical simulations show the slowly varying field profile is very nearly equal to the fixed field profile. Fig. 2 shows the analytic and numerical starting currents for three structure lengths for the J-band BWO. A discrepancy exists between the two curves because the actual slowly varying field profile differs from a sine wave as shown in the inset figures of Fig. 2 for the 16 period structure.

§3 NONLINEAR SIMULATIONS

To simulate BWO experiments, we assume a rising exponential for the beam current and voltage, namely

$$I(t) = I_p(1 - e^{(t+t_p)/t_r})^\rho$$

$$V(t) = V_p(1 - e^{(t+t_p)/t_r})$$

where t_r is the rise time and t_p, V_p and I_p are parameters chosen to best model the characteristics of the beam. We assume the Child-Langmuir law is approximately valid and let $\rho = 1.5$. To model the end of the pulse, we assume the voltage and current drop exponentially at some time $t = t_f$. In addition, we include the effects of D.C. space charge. When the electron beam enters the RF structure the beam slows down due to a build up of an electrostatic potential. This voltage depression reduces the electron beam energy. The reduction in the beam energy is calculated using the following formula [7]:

$$\Delta\gamma = 2\frac{I}{I_A}\ln\left(\frac{r_{av}}{r_b}\right)\left(1 - \frac{1}{(\gamma_0 - \Delta\gamma)^2}\right)^{-1/2}$$

where r_{av} is the average wall radius of the corrugated structure and r_b is the radius of the electron beam. Since the voltage and current are time dependent, the initial value of the relativistic factor γ_i is given by $\gamma_i = \gamma_0 - \Delta\gamma$ where $\gamma_0 = 1 + V(t)/mc^2$. Using our

modified code for a finite length current and voltage pulse we compare numerical simulation with experimental results [5,8]. Fig. 3 shows the comparison of the peak efficiency versus voltage for the $9GHz$ structure. Fig. 4 shows the comparison of the operating frequency versus voltage for the $6GHz$ structure. The peak theoretical efficiency versus voltage for the $6GHz$ structure is shown in Fig. 5.

§4 SUMMARY

We use the theoretical model for the operation of a BWO near the edge of the transmission band to calculate starting current for two structures. This model agrees well with the previous model formulated with non-zero group velocity assumptions for operating voltages where the cold structure dispersion makes a transition from a linear to a quadratic function of wavelength. After modifying the model near cutoff to include a time-dependent current and voltage, we simulate two BWO experiments and compared the predicted and measured results for peak efficiency and operating frequency.

References

[1] A. P. Kuznetsov and S. P. Kuznetsov, *Sov. Radiophys. and Electr.*, vol. 27, no. 12, pp. 1575-1583, Dec. 1984.

[2] L. V. Bulgakova and S. P. Kuznetsov, *Sov. Radiophys. and Electr.*, vol. 31, pp. 155-166, 1988.

[3] L. V. Bulgakova and S. P. Kuznetsov, *Sov. Radiophys. and Electr.*, vol. 31, pp. 452-460, 1988.

[4] B. Levush *et al.*, *IEEE Plasma Sc.*, vol. 20, no. 3, June, 1992.

[5] D. Abe *et al.*, private communication

[6] B. Levush *et al.*, *Phys. Fluids*, vol. B4, July, 1992

[7] T. M. Antonsen and B. Levush, *Int. J. Electr.*, vol. 61, pp. 871-880, 1986.

[8] E. A. Galst'yan, S. V. Gerasimov, and N. I. Karbushev, *Radiotekhnika i electronika*, no. 5, pp. 1061-1068, 1990.

[9] V. I. Kanavets, YU. D. Mozgovoy and A. I. Slepkov, *Radiotekhnika i electronika*, no. 6, pp. 1178-1186, 1986.

[10] N. P. Kravchenko, N. L. Romashin and V. A. Solntsev, *Radiotekhnika i electronika*, no. 6, pp. 1320-1324, 1987.

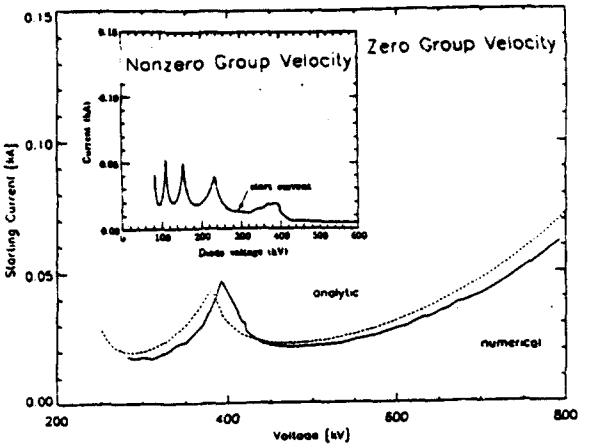


Fig. 1 Starting current versus voltage for X-band BWO with period length $d = 1.67cm$, number of periods $N = 8$, cutoff frequency $f_0 = 8.7395GHz$, average wall radius $r_w = 1.50cm$ and beam radius $r_b = 0.775cm$.

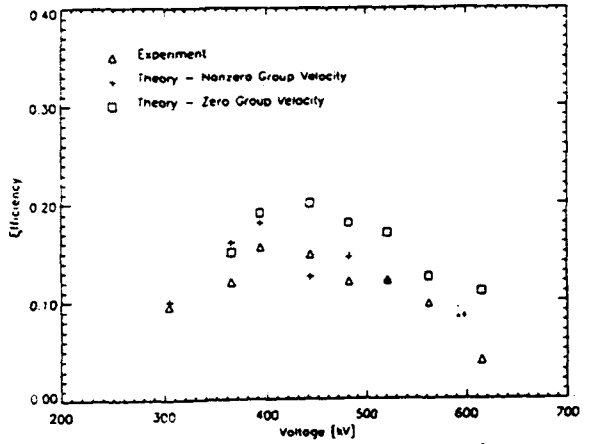


Fig. 3 Peak efficiency versus voltage for X-band BWO with period length $d = 1.67cm$, number of periods $N = 8$,cutoff frequency $f_0 = 8.7395GHz$, average wall radius $r_w = 1.50cm$ and beam radius $r_b = 0.775cm$.

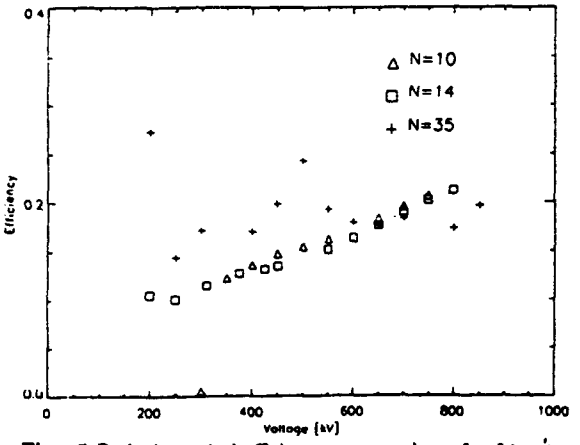


Fig. 5 Peak theoretical efficiency versus voltage for J-band BWO with period length $d = 2.15cm$, number of periods $N = 10, 14, 35$, cutoff frequency $f_0 = 5.8488GHz$, average wall radius $r_w = 8.44cm$ and beam radius $r_b = 7.375cm$.

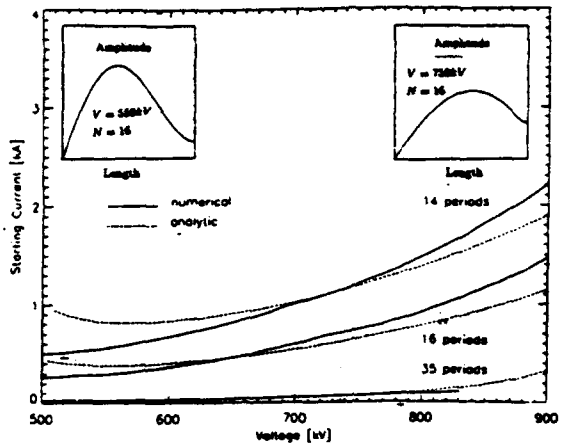


Fig. 2 Starting current versus voltage for J-band BWO with period length $d = 2.15cm$, number of periods $N = 14, 16, 35$, cutoff frequency $f_0 = 5.8488GHz$, beam radius $r_b = 7.375cm$ and average wall radius $r_w = 8.44cm$. Profiles in the upper left and right corners are the normalized slowly varying amplitude versus normalized length.

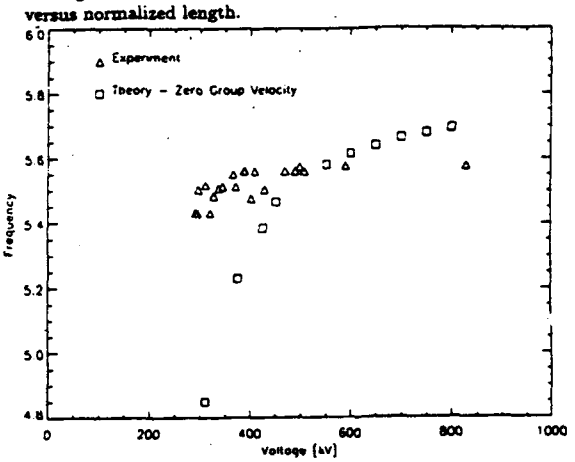


Fig. 4 Operating frequency versus voltage for J-band BWO with period length $d = 2.15cm$, number of periods $N = 14$, cutoff frequency $f_0 = 5.8488GHz$, beam radius $r_b = 7.375cm$ and average wall radius $r_w = 8.44cm$.

† Work partially supported by Harry Diamond Laboratories and AFOSR

‡ Harry Diamond Laboratories, Adelphi, MD 20783

THEORY OF RELATIVISTIC BACKWARD WAVE OSCILLATORS OPERATING NEAR CYCLOTRON RESONANCE[1]

A. Vlasov[2],G.Nusinovich,B.Levush, A.Bromborsky[3]
Laboratory for Plasma Research
University of Maryland, College Park, MD 20742 U.S.A.

Abstract

A linear and nonlinear, time dependent self-consistent theory for relativistic backward wave oscillator is developed. In this theory the transverse motion of the electrons is taken into account. Analytical and numerical analysis of the model equations near the cyclotron resonance gives a good estimate for the power drop due to the cyclotron absorption observed in many experiments and predicts an increase in the power under some conditions.

Introduction

Relativistic backward wave oscillator (BWO) is based on an interaction between high current relativistic electron beam and a slow electromagnetic wave under condition of Cherenkov synchronism

$$\omega \approx k_z v_z, \tag{1}$$

were v_z is the axial velocity of electrons. As a rule, the intense electron beam used in relativistic BWOs are guided by strong homogeneous external magnetic field. Therefore in addition to Cherenkov synchronism for some frequencies cyclotron resonance condition is satisfied:

$$\omega - k_z v_z \simeq \frac{n\Omega}{\gamma}, \tag{2}$$

where Ω is the electron cyclotron frequency, γ is the relativistic factor, and n is the harmonic number. We will restrict ourselfs to the case with $n = 1$. The existence of this resonance is responsible for the cyclotron absorption phenomema, which is commonly observed in BWOs [1-3]. In addition, the effect of cyclotron absorption is used for mode selection [4], since modes with frequencies satisfying (2) have larger starting currents.

[1]supported by HDL and AFOSR
[2]Permanent address: Moscow State University. Russia
[3]Harry Diamond Laboratory

The existing theory which describes the combined Cherenkov- cyclotron interaction in BWOs is limited to the stationary regime and uses a fixed axial profile for the RF field [5]. In this paper we extend our previous nonstationary, selfconsistent theory with infinite magnetic field [6] by taking into account the transverse motion of the electron beam.

Basic formulation

The theoretical model which we used to describe the operation of the BWO is based on the model published in Ref. [6]. We extend this model by taking unto account the cyclotron motion of the electrons. To do so we solved 3D equations for relativistic particles:

$$\frac{d\mathbf{p}}{dt} = -e(\mathbf{E} + \beta \times \mathbf{B}), \frac{d\mathbf{r}}{dt} = \mathbf{v}, \tag{3}$$

in which fields $\mathbf{E}$, $\mathbf{B}$ contain not only high frequency electromagnetic field but also the external magnetic field $\mathbf{B_0}$.

The synchronous conditions (1)-(2) are fullfield simultaneously if the electron cyclotron frequency Ω satisfies the condition:

$$\frac{n\Omega}{\gamma} \simeq v_z \frac{2\pi}{d}(m_{ch} - m_{cy}), \tag{4}$$

where m_{ch} is number of spatial harmonic satisfied to Cherencov synchronous conditions,m_{cy} is number of spatial harmonic satisfied to cyclotron resonance condition. Therefore, only the synchronous spatial harmonics, 0 and -1, of the RF field are taken into account in Eq. (3).

Starting current

The starting current is the minimum beam current required to start oscillations from noise in the RF structure. The expression for the stating current in our notation taken the form

$$I_{st} = \frac{I_A}{4\pi}(\frac{d}{L})^3 \frac{\gamma_i^3 \beta_{zi}^2}{k_* d} \frac{\mid \beta_g(\omega_*) \mid}{C(r_b, \omega_*)} \tilde{I}_{st}(R, B_z), \tag{5}$$

where I_A is Alfven's vacuum current, β_{zi} is the initial normalized axial velocity of the injected beam. The resonant frequency, ω_*, appearing in Eq. (4), is defined as the intersection of the dispersion curve $\omega(k)$ of the cold structure and the electron beam Doppler line $\omega = k_{\|} v_{zi}$.

This also determines the resonance wave number $k_* = \omega_*/v_{zi}$ and the group velocity $\beta_g(\omega_*)$. The coupling coeffitient $C(r = r_b)$ is the measure of strength of the axial electric field component which couples with the beam, r_b is the beam position. The quantity $\tilde{I}_{st}$ is a dimentionless number which we refer to as the "universal" starting current.

When reflections of the electromagnetic wave are included, Eq.(4) remains valid: however the "universal" starting current now depends on the magnitude of the combined reflection coefficient, R. This dependence was studied in detail in Ref. [6]. Similary, when the effect of finite magnetic field is included, Eq. (4) remains valid, while in general the dependence at the "universal" starting current on the magnetic field is determined via a numerical solution of the nonlinear equations in the linear regime. In the case of high reflection $R \simeq 1$ (high Q resonator). the axial profile of the RF field is practically constant, which yields an anlytical expression for the "universal" starting current

$$\tilde{I}_{st} = 7.41(1-R)\frac{1}{1 - MF_2(\psi_2)}, \tag{6}$$

where absorbption function

$$F_2(\psi_2) = (\sin(\psi_2/2)/\psi_2/2)^2,$$

$$\psi_2 = (1 - \frac{B_z}{B_{z,res}})(\frac{1}{\beta_{zi}} - \frac{k_{\|q}}{k})kL, k = \frac{\omega}{c},$$

the resononce magnetic field is defined as

$$B_{z,res} = \frac{mc^2}{\mid e \mid}\gamma_i k(\frac{1}{\beta_{zi}} - \frac{k_{\|q}}{k}),$$

$$M = 3.7\frac{\beta_{zi}^2}{k_* L}\frac{\gamma_i^2}{\mid a_{s,f} \mid^2}(\frac{J_1(k_{\perp q} r_b)}{I_0(k_{\perp q} r_b)})^2(\frac{k_{\|q}}{k} - \beta_{zi})^2\frac{1}{1 - \frac{k_{\|q}}{k}\beta_{zi}},$$

where J_1 is the ordinary Bessel function and I_0 is modified Bessel function, $k_{\|q}, k_{\perp q}$ are parallel and perpendicular wavenumbers of resonator's mode with longitudial number q respectivelly, $a_{s,f}$ is ratio between synchronous and fundamental spatial harmonics amplitudes.

The dependence of normalized starting current versus focusing magnetic field magnitude is presented at fig. 1 for different values of coeffitient M. When the electron beam orbital velocity is small the cyclotron absorption effect manifest itself in BWO's operation only when magnetic field is close to the rasonance value. In general, the cyclotron absorption effect

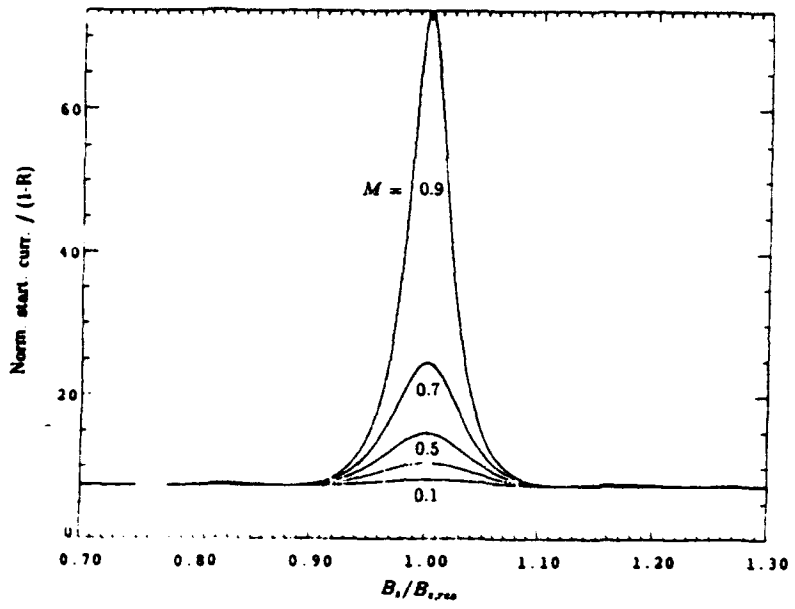


Figure 1: Normalized starting current versus magnetic field

leads to an increase in the starting current and correspondently, to the delay in establishment of stationary regime. If the ratio between the amplitude of the fundamental and the synchronous spatial harmonics is large ($M \geq 1$), there will be a range of magnetic guide fields for which RF oscillations will not start, for any value of electron beam current. This leads to total suppresion of Cherenkov interaction.

Nonlinear theory

The nonlinear dynamics of BWOs when described by a model with finite magnetic field becomes more complicated, than in the case when the model with the infinite magnetic field is used.

Results of the numerical calculations indicate that four typical regions of BWO's operation in the plane of parameters M and $B_z/B_{z,res}$ exist, see fig. 2.

In the region **A** the 1-D electron motion model ($B_z \rightarrow \infty$) predicts the same output power and efficiency as 3-D electron motion model (B_z is finite). Note, that for magnetic field near the resonance value the time required to reach the stationary regime with this efficiency is longer, than one would predict from the 1-D model. In addition, in this region appearance of the overbunching (automodulation) effect, transition from single frequency regime to multifrequency regime, is predicted to occur by the two models at the same ratio

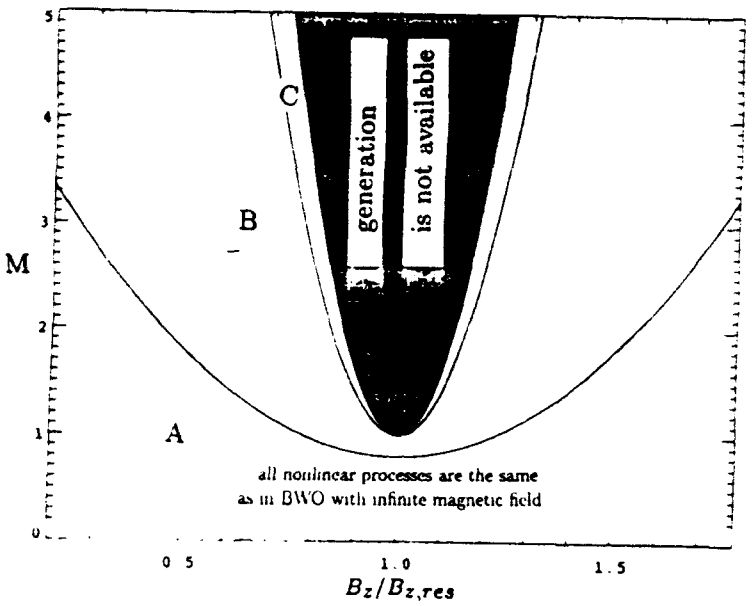


Figure 2: BWO's operation regions

of the beam current to the starting current, I/I_{st} [6]. In the region **B** the output power and efficiency yielded by the 1-D model is different from those predicted by the 3-D model. A typical behaviour of the efficiency versus magnetic field is shown in fig. 3. The efficiency curves are given for the fixed ratio I/I_{st} and different values of the ratio $q = E_z^{fund}/E_z^{synch}$ (of course the starting current here is a function of the same ratio). The cyclotron absorption effect manifest itself in the dip of the efficiency near the resonance magnetic field, which was observed in a number of expeiments [1-3]. The model also predicts an increase in the efficiency at magnetic fields which are slightly greater than the resonance value. Both of these effects depend strongly on the ration q. Note that the predictions of the 1-D model and the 3-D model for the transition from the single frequency to multi-frequency regimes are similar. In the region **C**, the 3-D model predicts phenomena which have not been observed when the 1-D model is used. More information about these phenomena will be published at a later date. Finally, the shaded region indicates the parameter space where no oscillation in BWOs are possible.

Conclusion

The results obtained in our investigations demonstrate a wide range of physical phenomena that can be observed in BWOs operating near the cyclotron resonance. The important

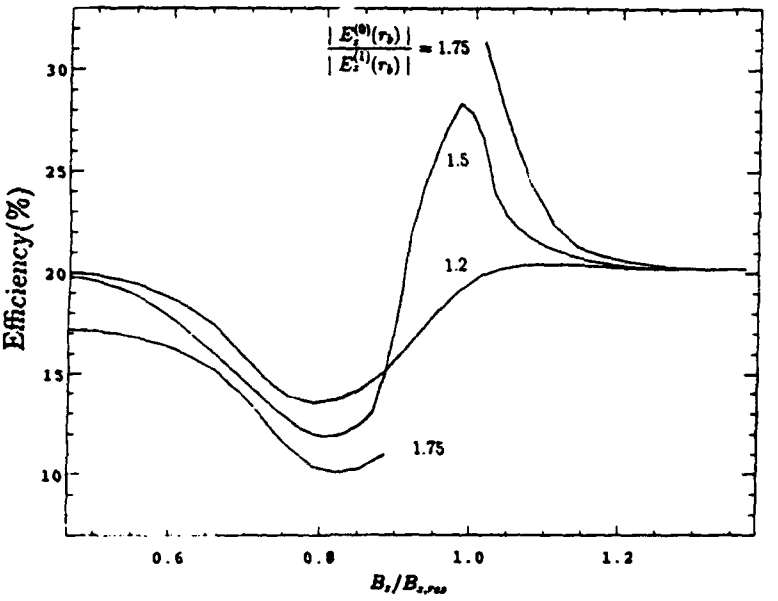


Figure 3: BWO's electron efficiency

result of these investigations is the possibility to increase the efficiency of BWO operation when the magnetic field slightly exceeds the resonant value and the ratio of synchronous space harmonics is above 1.5. The increase in starting currents caused by the cyclotron absorption shifts the region of efficient operation to larger value of the electron beam current. This effect allows one to increase the level of radiated microwave power.

References

1. R.A.Kesh, at all. IEEE Trans on plasma science, **PS-13**, 559-562,(1985). 2. S.P.Bugaev, at all. IEEE Trans on plasma science, **PS-18**, 525-536,(1990). 3. Y.Carmel, at all. Phys. Fluid B **4(7)**, (1992). 4. E.B.Abubakirov, at all. Sov. Tech. Phys. Lett., **9**, 230-231, (1983). 5. E.B.Abubakirov, at all Sov. J. Comm. Tech. Electr.,**34**, 129-136, (1989). 6. B.Levush et all IEEE Trans on Plasma Sc. **20**, 3,(1992). 7. N. Ginzburg, et al., Sov. Radiophys. and Electronics, **21**, 728 (1979).

DIELECTRIC CHERENKOV MASER AS A POWERFUL AMPLIFIER WITH SUPERWIDE BANDWIDTH

A.S.Shlapakovskii, K.A.Chirko

Institute of Nuclear Physics, 634050, Box-25, Tomsk, Russia

ABSTRACT

An important feature of dielectric Cherenkov masers (DCM), distinguishing them from other FEL kinds is emphasized.So far practically all DCM experiments were carried out with rather thin dielectric liners or films. Meanwhile, when the coefficient of waveguide filling by the dielectric is not small, the beam wave coupling doesn't depend on frequency, and, hence, superwide bandwidth is possible. The value of bandwidth is significantly determined also by the current and velocity of electron beam.

In this context DCM dispersion relations have been analysed analitically in simplest of total waveguide filling and numerically,for a hollow beam in a waveguide with dielectric liner. It hasbeen shown that maximum value of bandwidth is achieved at a certain optimal value of the beam current for fixed velocity (and vice versa). Numerical results demonstrate the -3 dB bandwidth of 40-50% at a peak gain of 40 dB for usual electron energies (300-600 keV) and beam currents (1-10 kA).Also, an effect of discontinous gain disappearance at a lower boundary of the band has been found.

INTRODUCTION

Investigations of DCM have been developed in direction of more short wavelength generation [1-3] and direct ion of very high power microwave generation [4-6]. A simplicity of dielectric slow-wave structures is a very attractive feature of DCM.In this report we point out another important DCM feature. It is a potential for amplifier superwide-bandwidth operation under certain parameters of the wavequide and electron beam.

A superwide bandwidth is a characteristic of Cherenkov TWT-amplifiers with a smooth slow-wave supporting structure as usual helix for non-relativistic phase velocities. Just a smooth system has a very weak dispersion in a wide frequency range that is necessary for the wide-bandwidth operation in the first place When the phase velocity is relativistic, such type of dispersion may be provided by dielectric waveguides with materials of not

too large dielectric constant.But the wavequide geometry is significant here. If the dielectric liner or film is thin in comparison with transverse size of the system, the wave field is evanescent and the beam-wave coupling exponentially decreases with frequency increase, hence, wide-bandwidth operation is impossible. It is possible in another case, when the wavequide filling with the dielectric is not small and the transverse size of va - cuum channel in which electron beam propagates is less than the operation wavelength.

It is important to determine what values of the bandwidth can be achieved in DCM amplifier and how do these values depend on the beam current and energy.

In the next sections we consider DCM dispersion relations for two configurations: 1) in the simplest model of total wave - quide filling both the dielectric and cold magnetized beam [7], allowing one to obtain analytical solution, and 2) in the model of infinitely thin hollow beam in the circular wavequide with dielectric liner [8,9], which is closed to real experimental conditions.

MODEL OF TOTAL FILLING

The dispersion relation in this idealized model had been analysed earlier in original works concerning DCM (see,for example, [7]). Here we emphasize that it is possible to obtain analitical solution for the bandwidth.

So the solution of equation

$$\omega^2 - \frac{c^2(p^2+k^2)}{\varepsilon} - \frac{\Omega_b^2\,(\omega^2 - \frac{c^2k^2}{\varepsilon})}{\varepsilon\gamma^3(\omega-ku)^2} = 0, \qquad (1)$$

where ω is the frequency, k, p are longitudinal and transverse wavenumbers, ε is the dielectric constant, $u=\beta c$ is the electron velocity, $\gamma = (1-\beta^2)^{-1/2}$, Ω_b is the beam plasma frequency, is written in the form

$$k = \frac{\omega}{u}(1+\delta), \quad \delta << 1. \qquad (2)$$

With new variables

$$\tilde{\delta} = \delta \frac{\varepsilon\gamma^3 p u^2}{2\Omega_b^2}, \quad x = \frac{\varepsilon\gamma^3 p u^4}{4\Omega_b^2 \omega^2}, \quad \zeta = \frac{(\varepsilon\beta^2 - 1)\varepsilon\gamma^3 p u^2}{4\Omega_b^2} \qquad (3)$$

one can obtain from Eq.(1), the cubic equation for $\tilde{\delta}$

$$\tilde{\delta}^3 + \tilde{\delta}^2 (x - \zeta) - \tilde{\delta} x + \zeta x = 0. \qquad (4)$$

The demand to Eq.(4) to have imaginary roots leads to the inequality

$$\Delta (x > 0) < 0,$$

$$\Delta = x^3\left(\frac{1}{4} - \zeta\right) + x^2(1-5\zeta+3\zeta^2) - x(3\zeta^3+2\zeta^2) + \zeta^4 \qquad (5)$$

Analising (5) and taking (3) into account one can easily write some expressions for the bandwidth. In single-particle operation regime ($\zeta >> 1$) an amplification occurs in the frequency range

$$0 < \omega < \omega_s = \frac{pu}{\varepsilon\beta^2 - 1}, \qquad (6)$$

where ω is the synchronous frequensy of the electromagnetic mode with the beam. The maximum bandwidth is achieved at $\zeta = 1/4$ when

$$0 < \omega < 11\ \omega_s. \qquad (7)$$

At last, in the collective operation regime ($\zeta << 1$) an amplification takes place for frequencies

$$\frac{\omega_s}{\zeta} - 2\omega_s < \omega < \frac{\omega_s}{\zeta} + 2\omega_s. \qquad (8)$$

It is shown now that absolute value of bandwidth increases with electron velocity comes nearer the Cherenkov threshold, and at fixed velocity it achieves maximum at a certain optimal magnetude of the beam current. As to the relative bandwidth value it decreases when velocity approach to threshold and current is large ($\Delta\omega/\omega = 2\sqrt{2\zeta}$, if $\zeta << 1$). It follows from (5) that for $\zeta \geq 1/4$ the relative bandwidth value does not already depend on ζ. Note, however, that the long wavelength part of the bandwidth corresponds to growing of potential perturbation in the beam, and the maximum of $Im\ k(\omega)$ dependence in the single-particle regime becomes more and more sharp with

the current decrease so that -3 dB bandwidth will reduce with ζ increasing. Hence the relative bandwidth also achieves maximum at a certain optimal value of ζ, i.e.,the optimal current magnetude for fixed velocity and vice versa. If the beam velocity is near the Cherenkov threshold, the current value corresponding to maximum bandwidth is small.

It follows even from (8) that the bandwidth of DCM amplifier may be very wide (for example, 100% at ζ = 1/8). However, only numerical calculations of -3 dB bandwidth in the more natural model are interesting practically.

A HOLLOW BEAM IN PARTIALE-FILLED WAVEGUIDE

The dispersion relation for thin hollow magnetized beam of radius r_b propagating within the circular wavequide of radius b loaded by dielectric liner of inner and outer radii a and b [8,9] may be written as

$$[(\omega-ku)^2 - 2J\frac{c^2q^2}{\beta\gamma^3} I_o(qr_b)K_o(qr_b)]\,[p\frac{I_1(qa)}{I_0(qa)} - \varepsilon qF] =$$

$$= 2J\frac{c^2q^2}{\beta\gamma^3} I_o^2(qr_b)\frac{K_o(qa)}{I_o(qa)}\,[p\frac{K_1(qa)}{K_o(qa)} + \varepsilon qF]. \qquad (9)$$

Here J is the beam current normalized on 17 kA,

$$q^2 = k^2 - \frac{\omega^2}{c^2}, \quad p^2 = \varepsilon\frac{\omega^2}{c^2} - k^2,$$

$$F = \frac{j_1(pa)\;Y_o(pb) - j_o(pb)Y_1(pa)}{j_o(pa)\;Y_o(pb) - j_o(pb)Y_o(pa)}, \quad j_{o,1}, Y_{o,1}, I_{o,1},$$

$K_{o,1}$ are Bessel functionus. Some results of the Eq.(9) numerical solution for various parameters are presented in Fig.1-3 in the form of spatial growth rate vs frequency dependences.

All the curves in Figs.1-3 have been obtained for the dielectric liner of ε=2, and inner to outer radius relation a/b =0,5. Beam characteristics (current,radius and energy) have been varied.Fig.1 cleary demonstrates the significant bandwidth dependence on the beam current.Its change from 1 to 2 kA results in the bandwidth becomes much more narrow. Concerte values of -3 dB

bandwidth depend on the peak gain magnetude. One can easily show that for large gain magnetude

$$\frac{\Delta\,(\mathrm{Jm}\,k)}{(\mathrm{Jm}\,k)_m} = \frac{10\,\ln 2\,\lg e}{G\,(\mathrm{dB}) + \alpha} = \frac{3}{G\,(\mathrm{dB}) + \alpha}\,, \qquad (10)$$

where $\Delta\,(\mathrm{Jm}\,k)$ stands for difference between the maximal spatial growth rate $(\mathrm{Jm}\,k)_m$ and the value of growth rate corresponding of -3 dB power level, and $\alpha \in (6.0, 9.5)$ (9.5 in the singlepar - ticle operation regime, and 6.0 in collective one). It is seen from Eq.(10) that, for instance, when G = 40 dB -3 dB bandwidth at the beam current of 1 kA and the rest parameters of Fiq.1 is of $\simeq$ 20%.

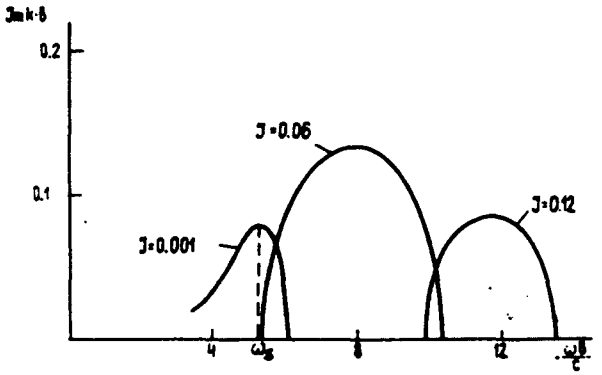


Fig.1. Spatial growth rate vs frequency dependences for various beam currents. $\varepsilon = 2$, a/b = = 0.5, $r_b/b = 0.4$, $\gamma = 1.6$.

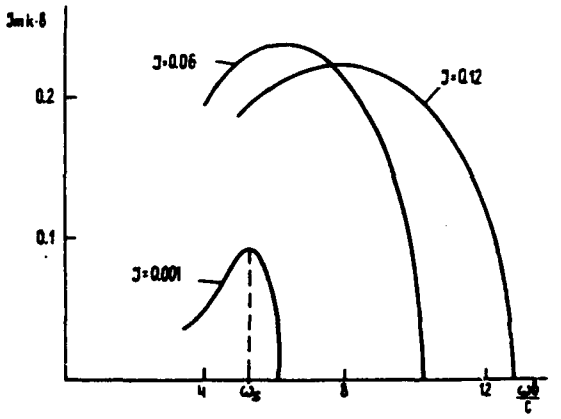


Fig.2 The same as in Fig.1. r_b / b = 0,45.

Comparing Fig.1 and Fig.2 one see the great expansion of the amplification band when the gap between the beam and dielectric surface reduces. At smaller.gap the bandwidth for 2 kA current is more wide than for 1 kA,it will decrease for higher current level.If we put peak gain of 40 dB, Eq.(10) and corresponding curve in Fig.2 (J = 0.12) give us -3 dB bandwidth of about 50% .At the wavequide radius b= 4 cm we have an amplifier operating in the X-band with [illegible] length of $\simeq$ 95 cm and beam - dielectric gap of 2 mm.

The comparison of Fig.3 and Fig.1 shows that the increase of beam energy at fixed its radius also leads to relative band -

width increase. It is significant here that the maximum of bandwidth is achieved at considerably higher current level.Among all curves presented in Fig.3 the curve with J = 0,6 (10 kA) corresponds to the widest bandwidth and it is of 40% at 40 dB peak gain. An X-band amplifier comes out at b = = 2 cm,so that we have the gap of 2 mm,and the length of $\simeq$ 30 cm.

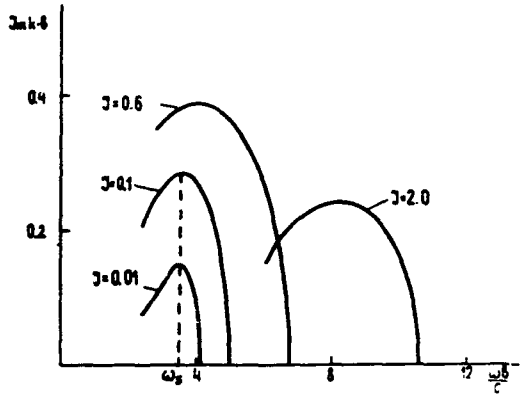


Fig.3. The same as in Fig.1. γ = 2,2.

DISCONTINUOUS GAIN DISAPPEARANCE

Now pay attention to the fact that all the curves in Figs. 2,3 are torn off to the left, i.e .discontinuous gain disappearance occurs at the lower boundary of the band. Nature of this effect is not clear for us so far, and its manifestations dependences on parameters of beam and waveguide are worth of special investigation. For presented curves the effect found does not influence on -3 dB bandwidth value, but if the degree of waveguide filling with dielectric is slightly more (a/b=0,4) the gain disappearance occurs at the peak gain frequency, so that amplifier characteristics turns out to be nonsymmetric and the bandwidth becomes twice narrower.

REFERENCES

1. E.Garate ,R.Cook, P.Heim et al., J.Appl.Phys. 58 (1985) 627.
2. E.Garate, S.Moustaizis, J.Buzzi et al., Appl. Phys. Lett.48 (1986) 1326.
3. J.Walsh, C.Shaughnessy, R.Layman et al., Nucl. Inst. and Meth. A272 (1988) 132.
4. A.Didenko, A.Borisov, G.Fomenko et al. Pis'ma Zh. Tekh. Fiz. 9 (1983) 60.
5. W.Main, R.Cherry and E.Garate, Appl.Phys.Lett. 55(1989)1498.
6. W.Main, R.Cherry and E.Garate, IEEE Trans. PS-18 (1990) 507.
7. J.Walsh, T.Marshall, M.Mross and S.Schlesinger, IEEE Trans. MTT-25 (1977) 561.
8. D.Lemons and L.Thode, Phys. Rev. Lett. 56 (1986) 2684.
9. G.Fomenko and A.Shlapakovski, Zh.Tekh.Fiz. 59 (1989) 121.

EXPERIMENTAL STUDY OF A PLASMA-FILLED BACKWARD WAVE OSCILLATOR

X. Zhai, E. Garate, R. Probaska, A. Fisher, G. Benford

Physics Department, University of California, Irvine, CA 92717

Abstract

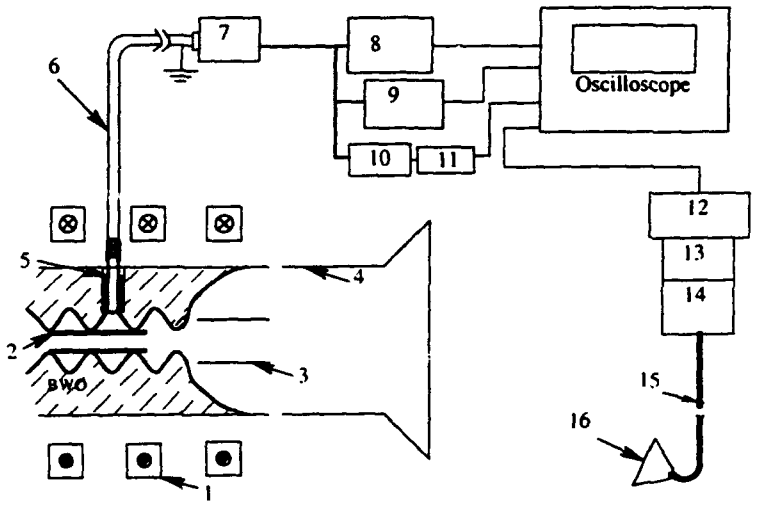
We present experimental studies of a plasma-filled X-band backward wave oscillator (BWO). Depending on the background gas pressure, microwave frequency upshifts of up to 1 GHz appeared along with an enhancement by a factor of 7 in the total microwave power emission. The bandwidth of the microwave emission increased from $\leq$0.5 GHz to 2 GHz when the BWO was working at the RF power enhancement pressure region. The RF power enhancement appeared over a much wider pressure range in a high beam current case (10-100 mT for 3 kA) as compared to a lower beam case (80-115 mT for 1.6 kA). The plasma-filled BWO has higher power output compared to the vacuum BWO over a broader region of magnetic guide field strength. Trivelpiece-Gould modes (T-G modes) are observed with frequencies up to the background plasma frequency in a plasma-filled BWO. Mode competition between the Trivelpiece-Gould modes and the X-band TM_{01} mode prevailed when the background plasma density was below $6x10^{11}$ cm^{-3}. At a critical background plasma density of $n_{cr} \cong 8x10^{11}$ cm^{-3} power enhancement appeared in both X-band and the T-G modes, with mode collaboration. Power enhancement of the S-band in this mode collaboration region reached up to 8 dB. Electric fields measured by Stark-effect method were as high as 34 kV/cm while BWO power level was 80 MW. These electric fields lasted throughout the high power microwave pulse.

Introduction

Intense relativistic electron beam excitation of slow wave structures has been an active subject since the possibility was first confirmed by Nation[1] in 1972. Many vacuum slow wave devices have been studied [2-6] since, with conversion efficiency of beam kinetic energy into microwaves as high as 30%. Using current pulse power technology, vacuum backward wave oscillators (BWOs) can emit microwave power as high as 1 GW[7-9]. Injecting plasma into the slow wave structure[10,11] enhances power emission by factors of 3 to 8. Introducing plasma into the BWO increased power output and efficiency. However, some of the basic mechanisms of the system are still not well understood. All previous plasma-filled BWO experiments concentrated on producing higher power microwaves, higher efficiency and longer pulse. The goals of this work were to study the effect background plasma had on the microwave frequency and bandwidth of the output radiation in a high power plasma filled BWO; to study the plasma modes (Trivelpiece-Gould modes) in the plasma-filled BWO and their effect on the BWO waveguide mode (TM_{01}); and to measure the electric field in the plasma-filled BWO using light emission from the background plasma via the Stark shift.

Experimental Setup

In our experiment (Fig. 1), a Marx capacitor bank generates a 650 kV, 2 kA voltage pulse with 500 ns pulse duration. The electron beam was produced by field emission from a graphite cathode. The beam is annular with 1.8 cm diameter and 2 mm thickness, and is injected into the BWO along a guiding magnetic field of 6-16 kG. Our plasma was produced by background helium ionization by the beam. The BWO is a cylindrical waveguide with a periodically varying wall radius, R(z), sinusoidally rippled about the mean radius, R_0, such that $R(z)=R_0+h\cos(k_0 z)$, $k_0=2p/z_0$, where h=0.45 cm is the ripple amplitude, z_0=1.67 cm is the period and R_0=1.45 cm. An X-band horn placed 2 m away received the RF generated by the BWO. The RF was guided by waveguide to a screen room, where the RF was split and detected by an X-band crystal detector and an X-band 8-channel spectrometer which covered frequencies 8.2<f<12.4 GHz. Each channel covered about 500 MHz. There was an observation window on the 9th ripple of the BWO for the electric field measurement. Two optical lenses collected photons from the center of the BWO then focused the photons onto two optical fibers, which guided the light to two spectrometers in the screen room[12]. One spectrometer "looked" at the helium allowed line λ=501.56 nm and the other one "looked" at the forbidden line λ=663.20nm. Both spectrometers had reciprocal linear dispersion of 0.7nm/mm. The allowed and forbidden photons were then recorded by two fast photomulitipliers. Electric fields in the system can be calculated by the ratio of the allowed line and the forbidden line intensity[13]. The observation window on the BWO was also used for the T-G modes measurement. A coaxial cable extended through one window into the BWO with the center conductor acting as a microwave antenna. Microwaves went through more than 30 meters of RG-9 cable, then were measured by a crystal detector, or by an 8 channel S-band (2.6 GHz<f<3.9 GHz) and J-band (5.85 GHz<f<8.2 GHz) microwave spectrometer. Each channel of the S-band spectrometer covered approximately 160 MHz bandwidth with the J-band channels covering approximately 294 MHz bandwidth. We measured frequencies between 3.9 GHz and 5.85 GHz with high pass filters, since a C-band spectrometer was not available to us. Frequency resolved measurements below 2.6 GHz were not made due to a lack of diagnostic equipment. In the X, J and S-band spectrometers the filters had 50 dB stopband insertion loss with 0.9 dB passband insertion loss. The plasma density was measured by a heterodyne microwave interferometer. In order to avoid strong X-band TM_{01} radiation and to not modify the oscillator, we replaced our BWO with a stainless steel tube of 10 mm radius, keeping anode and cathode geometry the same. Since the X-band radiation consistently arrived 140 ns (± 10 ns) into the beam pulse, we could correlate the microwave signal with the plasma density measurement at the turn on of the



1. B field coils
2. Electron beam
3. Beam dump
4. Drift chamber
5. Antenna
6. 30 m RG-9 cable
7. S-band waveguide
8. S-band rf spectrometer
9. J-band rf spectrometer
10. High pass filter
11. Detector
12. X-band detector
13. X-band bandpass filter
14. Attenator
15. 20 m X-band waveguide
16. X-band recivibg horn

Fig. 1 Experimental setup

microwaves, this method likely underestimates the plasma density during the RF pulse, because of plasma production in the background helium due to the high RF field.

Experimental Results

Our vacuum BWO efficiency of converting beam kinetic energy into RF radiation was about 5%. Depending on the beam current, the RF power output was between 30 MW to 100 MW in vacuum with a frequency of 8.3 GHz. The RF pulse duration was 50~150 ns depending on the RF power output level, As the RF power output increased the RF pulse duration decreased. As we added helium to the BWO, we observed a power increase, frequency upshift and bandwidth increase in the RF output. At low gas pressure (under 10 mT) and beam current of 3 kA only channel 1 (center frequency, f_c=8.46 GHz) and 2 (f_c=8.99 GHz) of the X-band spectrometer detected microwave signal and the signal in channel 1 was 1.5 ~2 times larger. However, in the pressure region where the enhancement in RF power was observed (between 50 mT to 80 mT), signals appeared in the first four channels of the spectrometer and channel 3 gave the maximum output. This indicted a frequency upshift of 1 GHz. Fig. 2(b) shows a shot taken at 60 mT with 3 kA beam current. If we sum the signal output from all channels of the spectrometer in Fig. 2(b) and compare to the signal in Fig. 2 (a), it is more than 7 times larger. Comparison also indicated the bandwidth of the microwave emission increased from ≤0.5 GHz in vacuum to 2 GHz. We observed similar frequency upshift and bandwidth increase for the 1.6 kA beam case as well. Microwave emission bandwidth as a function of the background helium pressure is shown in Fig. 3. The percentage bandwidth $\Delta f/f_0$ changed from ≤5% in vacuum to 25% at the pressure which gave maximum power enhancement. The RF power output as a function of the background helium

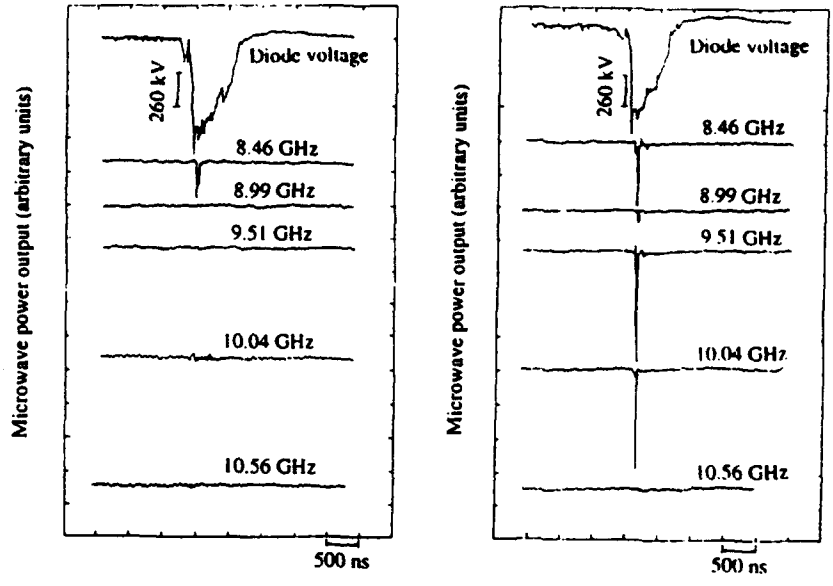


Fig. 2 Beam voltage and RF signal output from the RF spectrometer. (a) vacuum, (b) with plasma

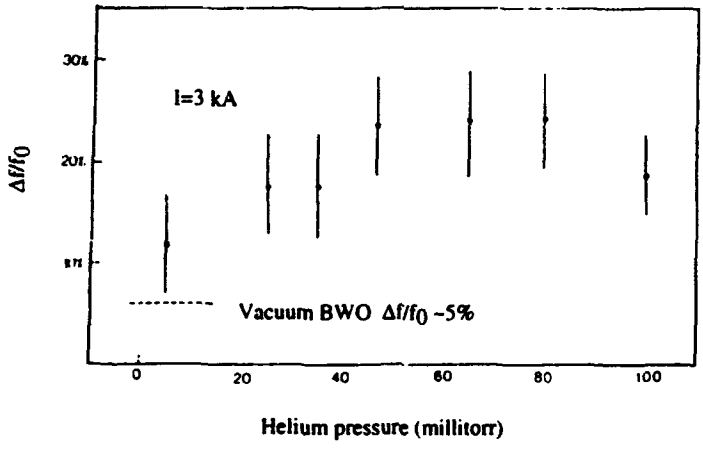


Fig. 3 RF output bandwidth vs background gas pressure

pressure was measured for two different beam currents (1.6 and 3 kA). It is interesting to note that in the 3 kA case,) we observed RF power enhancement over a wider pressure range (10 ~100 mT, while in the 1.6 kA case the RF power enhancement appeared only in a narrow pressure range (80 ~ 100 mT).

Using the antenna placed in the BWO, we detected broadband low frequency microwave radiation up to the plasma frequency of the background plasma. This broadband low frequency emission appeared only with plasma present in the BWO, at frequencies below the cutoff frequency of the plasma-filled BWO and lower than f_p. Power and pulse duration depended on n_p. When the background helium pressure was lower than 70 mT ($n_p<4x10^{11}$ cm^{-3}, $f_p<5.7$ GHz), no RF signal was detected in the J-band spectrometer. RF signals appeared in every channel of the S-band spectrometer with about the same amplitude and pulse duration. The T-G mode emission (f<5.7 GHz) showed correlation with the X-band TM_{01} mode emission. As in Fig.4 T-G mode power emission always dropped when the TM_{01} mode peaked. This mode competition appeared every shot for about 100 shots when $n_p<4x10^{11}cm^{-3}$. As plasma density rose to $4x10^{11}$ cm^{-3} the TM_{01} mode power output showed no change. However, the T-G mode emission power gradually increased by a factor of 2 over a plasma density change of 2 to $4x10^{11}$ cm^{-3} (4 GHz $<f_p<$5.7 GHz). As the pressure reached 100 mT (n_p~$7x10^{11}$ cm^{-3}, f_p=7.5 GHz), RF signals appeared in the first 7 channels (8th channel overlapped with the X-band TM_{01} emission) of the J-band spectrometer and every channel of the S-band spectrometer. The S and J-band spectrometer signals had a pulse duration of ~100 ns. RF signals in J-band had smaller amplitude compared with that of the S-band. However, the coupling efficiency of the antenna as a function of the frequency and the presence of the S-band waveguide (Fig. 1) prevent determination of a quantitative difference in S and J-band signals.

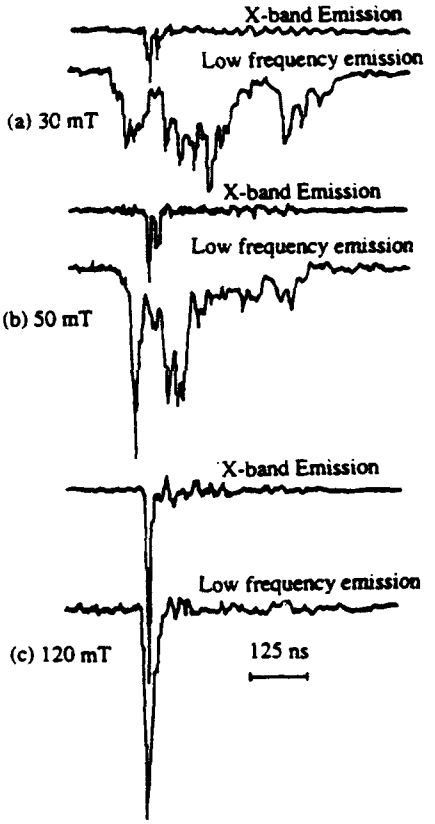


Fig. 4 Oscilloscope traces of the X-band (8.2-10.2 GHz, measured by X-band crystal detector) and the T-G modes (measured by a crystal detector) microwave signals (2 GHz<f<5.7 GHz).

As the background helium pressure reached 120 mT ($n_p=n_{cr}$~$8x10^{11}$ cm^{-3}) a simultaneous peak in the TM_{01} mode and the T-G modes (both S and J-band) was observed. A sudden enhancement appeared in the S-band T-G mode peak power of up to 8 dB. The J-band RF signal amplitude increased with the S-band RF but no more than 3 dB. The X-band TM_{01} mode emission increased for $6x10^{11}$ $cm^{-3}<n_p<8x10^{11}$ cm^{-3} and peaked at n_{cr}. Power enhancement was typically a factor of 3 at n_{cr}, but up to a factor of 6 in some shots. Given the error in the plasma density measurement, the background plasma density could be as high as n_p~$9.5x10^{11}$ cm^{-3} (f_p~8.8 GHz) when the TM_{01} mode and T-G modes power emission are enhanced. This could indicate the possibility that part of the enhanced X-band signal was a result of T-G mode radiation. Although the absolute T-G modes power emission was not calibrated, we found that the power carried by the T-G modes emission (in J-band) was at least 27 dB less

than the X-band TM_{01} mode. For plasma density $n_p > 8 \times 10^{11}$ cm^{-3}, power emission in the TM_{01} mode gradually decreased, and the T-G modes pulse became much shorter (~50 ns) but their amplitude kept increasing (both S and J-band). When the pressure reached 170 mT the J and S-band power emission was 2-3 times larger than that for 120 mT.

Using a spectroscopic method to measure the electric field distribution in a relatively high noise level system is very efficient and convenient. We choose the four energy-level system (3^1P, 3^1D, 2^1P, 2^1S) of helium I for the spectroscopic measurement. Transitions from 3^1P to 2^1S (λ_A=501.56 nm) and from 3^1D to 2^1P (λ=667.80 nm) are allowed, and the transition from 3^1P to 2^1P is forbidden (l_F=663.20 nm) in the electric dipole approximation. In a perturbing electric field, energy levels 3^1D and 2^1P are mixed, under this condition, it is possible to see photons from the forbidden line. The perturbing electric field strength can be calculated by the forbidden (λ_F=663.20 nm) and allowed (λ_A=501.56 nm) line intensity ratio I_F/I_A,, (Ref. 13):

$$E = 305.8\left(\frac{I_F}{I_A}\right)^{0.54} \text{kV/cm}, \qquad (1)$$

We increased the diode A-K gap reducing the beam current to ~1 kA to get a longer microwave pulse. We counted photon numbers in each time interval for both the forbidden and allowed lines in each shot, then averaged over ~100 shots. The ratio of the average photon numbers in the forbidden and allowed lines was used to calculate the electric field using equation (1).

Fig. 5 shows the results of the electric field measurement in the plasma-filled BWO when the RF was enhanced by the background plasma by a factor of 2 over its vacuum counterpart. The measured RF power was 80 MW$\pm$10 MW and the RF pulse duration (FWHM) was ~60 ns. Fig. 5 shows the electric fields lasted only as long as the microwave pulse, peaking at 34 kV/cm, then dropped to ~12 kV/cm. To estimate how much microwave power this field strength implies, assume a smooth wall tube with radius of the average radius of the BWO, R_0=1.9 cm. Assuming a TM_{01} mode propagating along the axis, and the average electric field of the RF equal to our measured value $\bar{E} = \sqrt{< E^2 >}$ =34 kV/cm, then we get a power of S=17$\pm$10 MW, with the uncertainty due to the error in electric field measurement (photon number fluctuation from shot to shot). This 34 kV/cm electric field is lower than we expected from the direct RF power measurement, since it gives a power flux lower than the measured X-band power of 80 MW$\pm$10 MW. The electric field of the electron beam charge is not important here, since the plasma density was 8×10^{11} cm^{-3} and the beam density was 5×10^{11} cm^{-3}, so the beam was charge neutralized. However, this calculation assumes a smooth tube with a TM_{01} mode propagating axially with average electric field

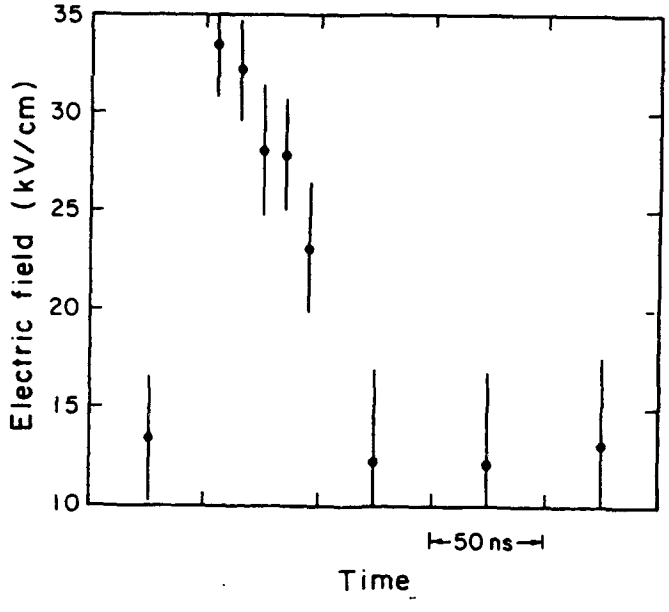


Fig. 5 Electric field vs time when the BWO RF power was enhanced by the background plasma.

the same as our measured fields. The real situation differs greatly from this, since the BWO RF electric field is strong near the wall. Our optical system focused in the BWO center when we measure E. Since we collect most of our photons from the center of the BWO our measured E field is much lower than the peak electric field. This may explain why the estimated microwave power is much lower than the measured RF power. To do an accurate power calculation requires knowing $\vec{E}(\vec{r})$ in the plasma filled BWO, a very complex calculation. (see Ref. 14)

In conclusion, we measured the average electric field strength as a function of time on our BWO axis, where the relativistic electron beam, high power microwaves and plasma interact. While the microwave power output was enhanced by the background plasma, the electric field peaked at 34 kV/cm and lasted only as long as the high power RF pulse (~80 MW), about 50 ns. We measured the T-G modes with frequencies up to the background plasma frequency in our plasma-filled BWO. This could be the "dense spectrum" of plasma waves as discussed in Ref. 15. At a critical plasma density the T-G modes and the BWO TM_{01} mode output power were simultaneously enhanced. The T-G mode measurement and the electric field measurement, to the best of our knowledge, have not been done previously for a device of the kind.

We thank Dr. K. Kato, David Sar and General Dynamics, Pomona Division, for the use of their equipment. This work was supported by AFOSR under contract # 90-0255.

References

1. J. A. Nation, Appl. Phys. Lett 17, 491 (1970).
2. Y. Carmel, J. Ivers, R. E. Kriel, and J. Nation, phys. Rev. Lett. 33, 1278 (1974)
3. M. Friedman, Appl. Phys. Lett 26,376 (1975).
4. V. I. Belousov, V. V. Bunkin, A. V. Gaponov-Grekhov, et al., Sov. Tech. Phys. Lett. 4, 584 (1978).
5. V. S. Ivanov, N. F. Kovalev, S. I. Krementsov, and M. D. Raizer, Sov. Tech. phys. Lett. 4,329 (1978).
6. Yu. V. Tkach, Ya. B. Fainberg, N. P.Gadetskii, et al., Ukr. Fiz. Zh. 23, 1902 (1978).
7. V. S. Ivanov, S. I. Krementsov, V. A. Kutsenko, M. D. Raizer, and A. A. Ruchadze, Proceedings of the International Topical Conference on High Power Electron and Ion Beams, Vol. II, Novosibirsk 679 (1979).
8. Yu. F. Bondar', S. I. Zavorotnyi, A. L. Ipatov, N. I. Karbushev, N. F. Kovalev, O. T. Loza, G. P. Mkheidze, and L. E' Tsopp, Sov. J. Plasma Phys. 9(2) 223, (1983).
9. V. S. Ivanov, S. I. Krementsov, V. A. Kutsenko, M. D. Raizer, A. A. Rukhadze, and A. V. Fedotov, Sov. Phys. Tech. Phys. 26 (5),580 (1980).
10. A. A. Kolomenskii, E. G. Krastelev, G. O. Meskhi, and B. N. yablokov. Second Symoposium on Collective Acceleration Methods, Dubna, 160, (1976) [in Russian].
11. Y. Carmel, K. Minami, R. A. Kehs, W. W. Destler, V. L. Granatstein, D. Abe, and W. L. Lou, Phys. Rev. Lett. 62,(20) 2389 (1989).
12. A. Dovrat and G. Benford, Phys. Fluids B1 (12), 2488 (1989).
13. K. Kawasaki, T. Usui and T. Oda, J. phys. Soc. Jpn. 51, 3666 (1982)
14. Minami, Y. Carmel, V. L. Granatstein, W. W. Destler, W. R. Lou, D. K. Abe, R. A. Kehs, M. M. Ali, T. Hosokawa, K, Ogura and T. Watanabe, IEEE Transations on Plasma Science. 18, 537 (1990).
15. W. R. Lou, Y. Carmel, W. W. Destler, and V. L. Granatstein, Phys. Rev. Lett. Oct, 28 (1991).

PASOTRON™ HIGH-ENERGY MICROWAVE SOURCE*

J.M. Butler, D.M. Goebel, R.W. Schumacher, J. Hyman,
J. Santoru, R.M. Watkins, R.J. Harvey, F.A. Dolezal

Hughes Research Laboratories
3011 Malibu Canyon Road, Malibu, CA 90265

R.L. Eisenhart and A.J. Schneider

Hughes Missile Systems Group
8433 Fallbrook Avenue, Canoga Park, CA

Abstract

A unique, high-energy microwave source, called PASOTRON for Plasma-Assisted Slow-wave Oscillator has been developed. Similar to the Backward Wave Oscillator (BWO), the PASOTRON spontaneously generates microwave radiation by efficiently converting electron beam energy into electromagnetic radiation. The PASOTRON, however, utilizes a novel E-gun and plasma-filled slow-wave structure (SWS) to produce and propagate very long, high-power beam pulses which require no axial magnetic fields for transport. The long electron beam pulses are obtained from a Hughes Hollow-Cathode Plasma (HCP) E-gun, which employs a low-pressure glow discharge to provide a stable, high current-density electron source. Electrons from this source are accelerated through a multi-aperture array to produce a large area, high-current beam consisting initially of many individual beamlets. Since the device is operated in the ion focused regime, the plasma filling the SWS, space-charge neutralizes the beam, and the Bennett self-pinch compresses the beamlets and increases the beam's current density . Experimental results from a PASOTRON tube designed to operate in a TM_{01} mode at C-band frequencies when driven by a 50-to-100-kV, 50-to-250 A electron beam are reported. Results show output power is in the 1-to-4 MW range, for rf pulselengths up to 100 μsec, corresponding to an integrated energy per pulse of up to 300 J. Calculations show the E-beam to microwave-radiation power-conversion efficiency is ~20%. Instantaneous bandwidth measurements further reveal that for the duration of the long rf pulse the PASOTRON's oscillation center frequency maintains a narrow line < 3 MHz.

* Work supported by Hughes Internal Research and Development funds

Experimental Apparatus

The Plasma-Assisted Slow-wave Oscillator (PASOTRON™) is a long-pulse (>100 μsec), high-power (>1 MW) microwave source which was invented[1] and developed[2] at Hughes Research Laboratories. Based on an innovative combination of conventional slow-

wave technology and novel plasma-assisted beam generation and propagation techniques, the PASOTRON has demonstrated that high-power, long rf pulses can be produced from a simple, compact system which requires no external magnetic fields. As shown in the diagram of Fig. 1, a non-conventional, electron-beam generator known as Hughes' Hollow-Cathode-Plasma Electron-gun (HCP E-gun) is employed to produce long, high-power beam pulses. A low-pressure glow discharge is generated inside a hollow cathode via a low-voltage (<5 kV) discharge pulser to create a stable electron source. The anode of the discharge simultaneously functions as the cathode of a high-perveance, multi-aperture, two-grid electron accelerator. Electrons generated within the hollow cathode are extracted and accelerated by a dc high-voltage applied between the grids to produce a large area, high-current density beam consisting initially of many individual beamlets. The injection voltage of the electron beam is controlled by the dc voltage level, while the beam current, pulsewidth, and pulse repetition frequency are independently controlled by the discharge pulser.

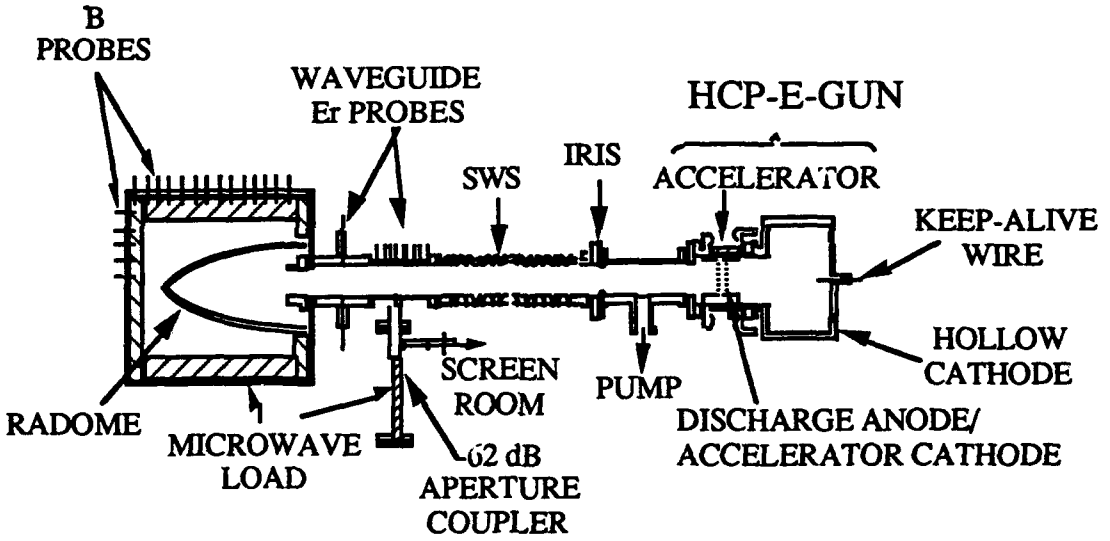


Fig. 1. Overview of experimental PASOTRON apparatus.

The individual electron beamlets are focused electrostatically by the electrode aperatures, and injected into a gas-filled drift-section. The beam electrons ionize the low-pressure gas to create a low- density background plasma. The beam-generated plasma neutralizes the beam's radial-space-charge forces which are normally responsible for beam expansion; thereby eliminating the need for an axial magnetic field. In the absence of space-charge forces and an external-magnetic field, the beam's self-magnetic field causes the overall beam radius to compress and merge the individual beamlets via the Bennett Pinch Effect[3].

The electron beam travels through the plasma-filled drift section and enters a slow-wave structure(SWS). The SWS, composed of a hollow, cylindrical waveguide with a sinusoidally-varying wall radius, provides a set of periodically-dispersive, electromagnetic-wave modes having regions in which the phase velocity is less than the speed of light as shown in the dispersion diagram[4] of Fig. 2. The electron beam provides an energy source within the structure which can drive unstable interactions. The frequency and wavenumber at which these instabilities occur are shown in Fig. 2 for conditions of matching phase velocity represented by the intersections of the beam line with the structure modes. Of course, the plasma filling the SWS can influence the dispersive properties of the structure modes[5], and hence the operating frequency of the system. However, experimental investigations of the C-band PASOTRON have indicated that the background-plasma density does not significantly influence the dispersive characteristics of the C-band SWS's modes.

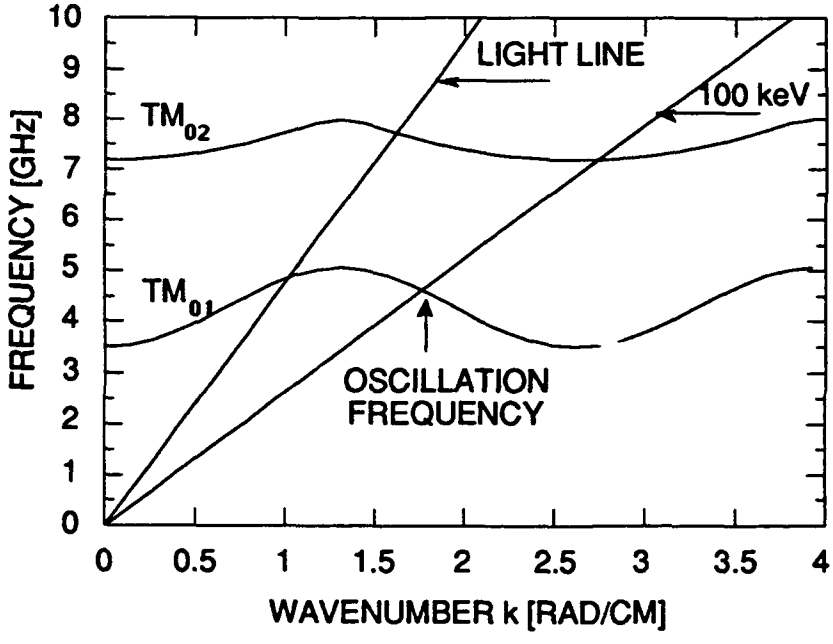


Fig. 2 Dispersion diagram of the C-band PASOTRON system's SWS having an average radius of 3.25 cm, a ripple depth of 0.715 cm, and a period of 2.4 cm.

The dispersion diagram of the PASOTRON's C-band SWS in Fig. 2 shows the intersection of the beam with the structure's TM_{01} mode occurs where the structure mode has a negative group velocity $d\omega/dk<0$. This results in a transfer of beam energy to the electromagnetic-wave field in a direction which is backward or anti-parallel to the beam

velocity. Devices which spontaneously generate radiation in this manner are commonly referred to as Backward Wave Oscillators (BWO's). As shown in Fig. 1, a reflective iris is positioned upstream of the SWS to re-direct the reverse power flow back through the structure to the forward output horn. The microwave radiation is coupled out of the system through a slightly diverging section of cut-off C-band waveguide positioned within a ceramic enclosure which functions as an rf window and vacuum-air interface. The electron beam is terminated in the tip of the enclosure while the rf is transmitted through the interface and terminated in a microwave load.

Diagnostic instruments for microwave analysis were designed, built and calibrated for operation in the C-band frequency range of 3-to-6 GHz. The rf signal exiting the SWS is monitored with a hole coupler having an average coupling coefficient of -62 dB. The sampled signal from the coupler is further attenuated and either sent to a calibrated detector with its output viewed on an oscilloscope for peak power and pulse width measurements, or sent to a spectrum analyzer operated as a tuned receiver with its vertical output sent to an oscilloscope for frequency and bandwidth analysis. A linear array of eleven E_r probes and an azimuthal array of eight E_r probes are positioned downstream of the hole coupler and are respectively used for VSWR and mode analysis. Rf measurements are also performed outside of vacuum where twenty-four dB/dt loop probes are placed along the length of the microwave load to determine the radiation pattern.

Experimental Results

Typical operation of the PASOTRON is shown in Fig. 3, where the upper and lower traces represent respectively the electron-beam current monitor and microwave power from a calibrated detector monitoring the downstream hole coupler. In this example a 93-kV, 110-A electron beam having a 100-μsec pulse width generated a 90-μsec-long rf pulse. The average rf power was 1.3 MW, which gives an energy per rf-pulse of ~120 Joules. The radiation frequency was found to be 4.355 GHz, and was maintained within a 3 MHz bandwidth. The operating mode was determined by simultaneously monitoring the outputs of the eight azimuthal E_r probes, which are shown in Fig.4a. In this example we observe all eight probes have similar amplitude and shape. This is indicative of a TM_{01} cylindrical waveguide mode's radial-electric field pattern which is azimuthally symmetric.



MICROWAVE
DETECTOR OUTPUT

BEAM CURRENT
50 [A/div]

TIME [20 μsec/div]

Fig.3 Diagnostic waveforms of beam current pulse and calibrated microwave detector monitoring downstream hole coupler.

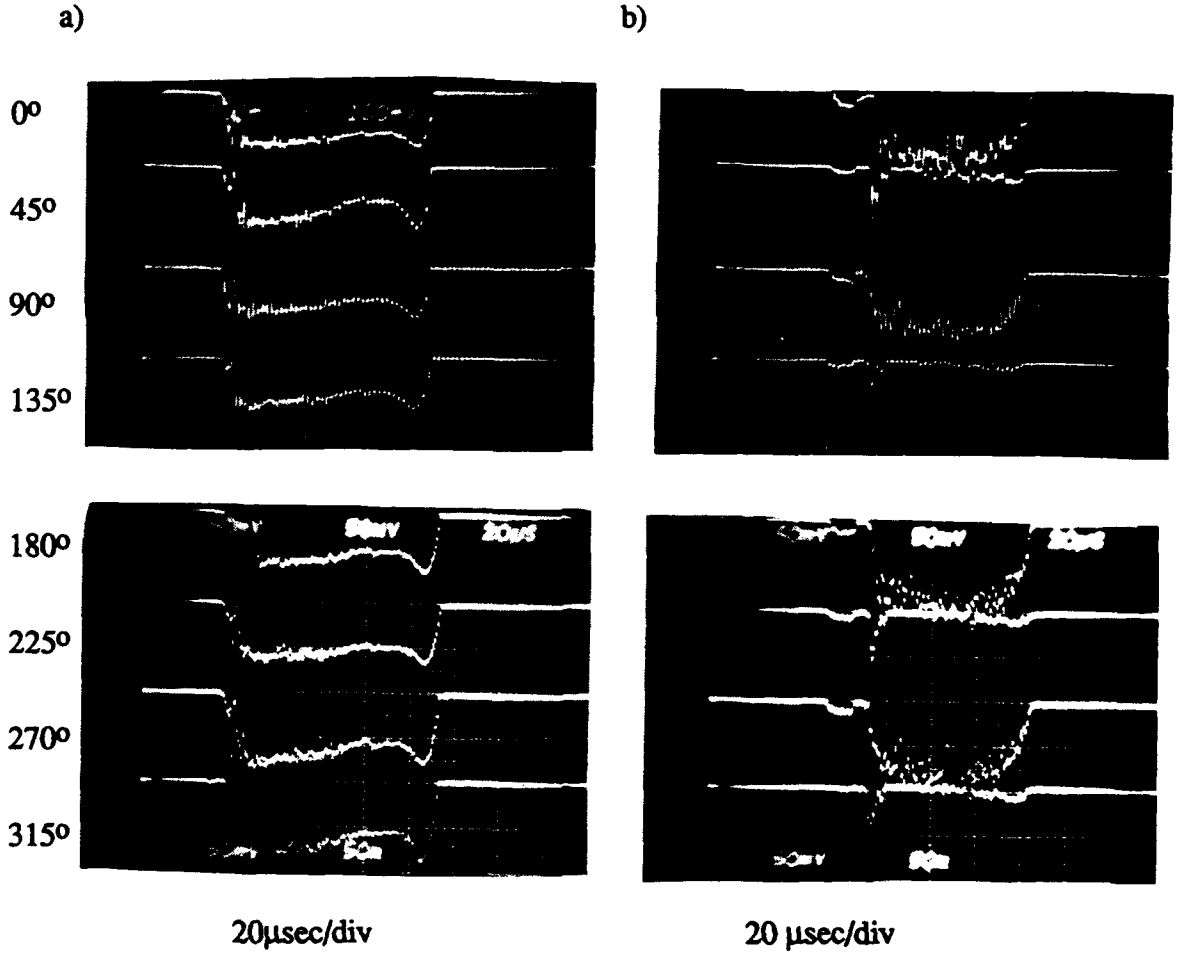


Fig. 4 Voltage response of eight calibrated microwave detectors monitoring azimuthal array probes. a) TM_{01} mode operation: V_b=93 kV, I_b=110 A, f_o=4.355 GHz and b)TE_{21} mode operation: V_b=75 kV, I_b=50 A, f_o=5.161 GHz.

The C-band PASOTRON operates in a TM_{01} mode for beam voltages of 55-to-65 kV and 80-to-100 kV. However, for beam voltages in the range of 65-to-80 kV, the mode and frequency of the system is observed to shift. When the SWS is driven with a 75-kV, 50-A electron beam, the PASOTRON generates TE mode radiation maintained within a <3 MHz bandwidth at a frequency of 5.161 GHz. This is shown in Fig. 4b were we observe the amplitude of the azimuthal probes is not maintained at a consistent level, but alternates between minimum and maximum values at periodic intervals of 45°. This behavior is indicative of a non-rotating TE_{21} cylindrical waveguide mode.

Excitation of TE mode radiation has previously been observed in magnetically confined BWO experiments[6,7] however its generation has always been attributed to excitation of beam-cyclotron waves. Since no magnetic field is employed in the PASOTRON, excitation and coupling to cyclotron waves does not explain the generation mechanism. We suggest that the existence of this mode is attributed to hydrodynamic beam-plasma instabilities and transverse electron trajectories associated with beam propagation in the ion-focused regime. Further investigations studying the motion of the electron beam and its stability during TE and TM mode operation are presently underway.

Acknowledgments

The authors would like to thank Paul Sumner and Don Mize for their assistance in the construction and operation of the experimental apparatus.

References

1. R.W. Schumacher, et al., U.S. Patent #4912367, March 1990.

2. D.M. Goebel, R.W. Schumacher, J.M. Butler, J. Hyman Jr., J. Santoru, R.M. Watkins, R.J. Harvey, F.A. Dolezal, R.L. Eisenhart, and A.J. Schneider, Proc. of SPIE, Vol. 1629, 119 (1992).

2. N. A. Krall and A. W. Trivelpiece, " Principles of Plasma Physics," (McGraw Hill, New York, 1973) p 495.

3. BWOPLT a numerical linear dispersion relation solver. Developed J. A. Swegle in 1985, and upgraded J. M. Butler in 1988.

4. Y. Carmel, K. Minami, W. Lou, R.A. Kehs W. W. Destler, V. L. Granastein, D.K. Abe and J. Rodgers, IEEE Trans. Plasma. Sci., **18**(3), 497 (1990).

5. R. A. Kehs, A. Bromborsky, B. G. Ruth, S. E. Graybill, W. W. Destler, Y. C. Carmel, and M. C. Wang, Harry Diamond Laboratories, Adelphi, MD, preprint no. **HDL-PP-NWR-85-1** (1985).

6. G. G. Denisov, A. V. Smorgonsky, V. P. Gubanov, S. D. Korovin, V. V. Rostovr, and M. I. Yaladin, Int. J. Infrared Mil. Waves, **5**, 1389 (1985).

THEORY OF THE INTERACTION OF ELECTRON BEAMS WITH THE WAVES IN PLASMA FILLED WAVEGUIDES

N.I. Karbushev, Yu.A. Kolosov, Ye.I. Ostrenskiy,
A.I. Polovkov and A.D. Shatkus
Moscow Radiotechnical Institute
113519, Moscow, Russia
L.A. Mitin and I.L. Volokitenkova
All-Russia Electrotechnical Institute
111250,Moscow, Russia
V.A. Balakirev and G.V. Sotnikov
Kharkov Physical-Technical Institute
320208, Kharkov, Ukrain

The interaction of electron beams with electromagnetic waves in plasma filled waveguides is investigated theoretically. It is shown that plasma can considerably improve the characteristics of vacuum microwave devices and allow to reach the higher amplification, efficiency and output power.

Plasma filled waveguides are very interesting for the amplification and generation of powerful microwave radiation by electron beams [1-4]. It is expected that the better characteristics can be reached in plasma microwave devices than in vacuum those. In this paper some theoretical results on the characteristics of electromagnetic waves in plasma filled waveguides and the interaction of electron beams with them are presented.

Waves of corrugated and dielectric waveguides with radially inhomogeneous plasma filling

The extraction of radiation from the interior of plasma is one of the basic problems [5,6]. In connection with this new slowing structures of hybrid type were proposed to use in electron microwave devices [7,8]. They consist of a plasma filled periodic or smooth slowing structures. At the great enough density of plasma in the case of partial filling of the structure volume structure and plasma waves can be mixed and form new waves which combine the properties of the structure and plasma those

[9,10]. The main feature of hybrid waves is an increased value of the amplitude of the longitudinal electric field inside the plasma and the great value of the current of the electromagnetic energy outside the plasma. The structure may be of any type, for example, the chain of coupled cavities [9], the corrugated waveguide [10], dielectric liner in a circular veguide [11], spiral [12], a waveguide with slits [13], diaphragmed waveguide etc.

Hybrid waves may be considered as a product of coupling of plasma and structure waves. In the case of weak coupling the dispersion relation for hybrid waves can be written in the following form [10]:

$$[(k-k_0) - (\omega-\omega_0)/v_p][(k-k_0) - (\omega-\omega_0)/v_s] = \pm (\Delta k)^2, \quad (1)$$

where ω and k are the frequency and the wave number, v_p and v_s are the group velocities of plasma and structure waves in the absence of their coupling $\Delta k \to 0$, ω_0 and k_0 determine the point of the intersection oı their dispersion curves, and Δk characterizes the strength of coupling. It follows from (1) that hybrid waves are formed in the range of frequencies $|\omega - \omega_0| \leq 2\,\Delta k\,|v_p v_s|\,|v_p - v_s|^{-1}$. If the directions of the propagation of coupled waves coincide and the sign in the right-hand side of (1) is "+" curves become splitted and hybrid waves propagate in the same direction. When the directions of the propagation of coupled waves are opposite and the sign in the right-hand side of (1) is "-", a new stop-band is formed on the boundaries of which hybrid waves have zero group velocities. In the case of strong coupling of plasma and structure waves the problem of calculation of dispersion characteristics of hybrid waves is more complicated and various numerical methods should be used. In Fig. 1 the dispersion curves of hybrid waves in plasma filled corrugated waveguide (a), dielectric waveguide (b) and chain of coupled cavities (c) are shown, d is the periods of structures.These results were obtained under the assumptions that: (i) the plasma density is proportional to the function $\cos^2(\pi r/2r_p)$, where r_p is the plasma radius less than the radius of the waveguide or the drift tube, (ii) the guiding axial

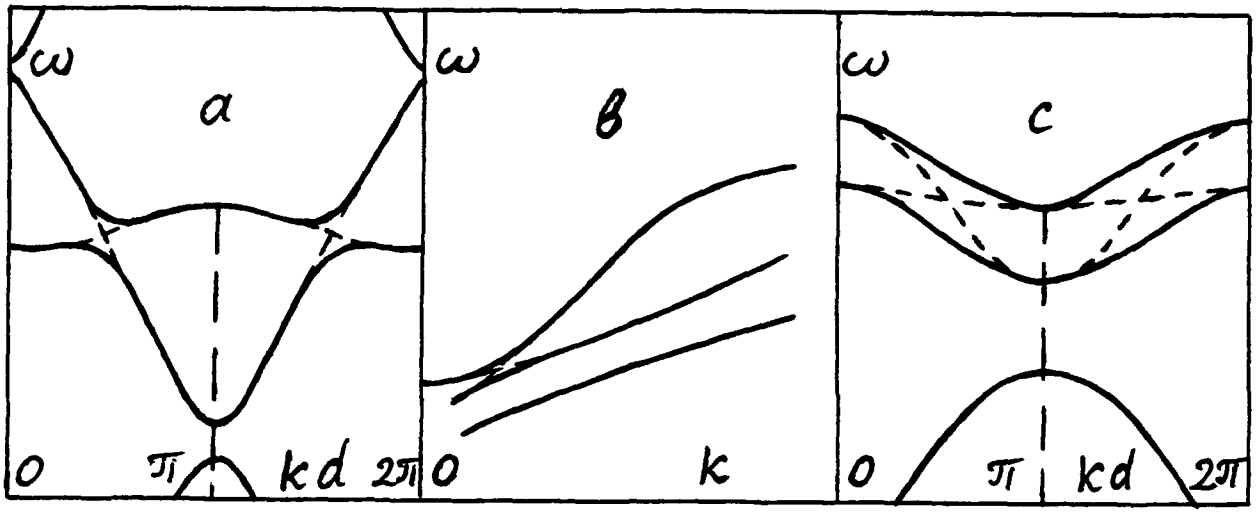


Fig.1: The dispersion curves of hybrid waves

magnetic field is finite but the cyclotron frequency is greater than ω, (iii) the maximum plasma frequency is greater than the characteristic frequency of an empty waveguide. At the lower plasma densities [14] or in the case of complete filling of the waveguide with plasma [15] hybrid waves are not formed. In the range of frequencies greater than the cyclotron frequency a strong resonance absorption of waves in the transition slab in radially inhomogeneous plasma arises[16].

Linear theory of amplification and excitation of waves in hybrid plasma electron devices

The interaction of an electron beam with hybrid waves in the linear approximation is described by the dispersion equation in which the contribution of the beam is accounted. If the electron beam propagates inside the plasma or near to it coupling of a beam with plasma wave is ever strong. Because of this the presence of plasma can lead to increasing of growth rates.

In an analytic form the dispersion equation for hybrid waves with an electron beam may be written analog to (1), namely [10]

$$[(k-k_0) - (\omega-\omega_0)/v_p + \alpha^3\omega\omega_b^2(\omega-ku)^{-2}]\times \times[(k-k_0) - (\omega-\omega_0)/v_s] = \pm (\Delta k)^2, \quad (2)$$

where the square of Lengmuir frequency of a beam ω_b^2 is proportional to its current, the coefficient α^3 characterizes

coupling of a beam with the plasma wave, u - the velocity of beam electrons. If the inequality

$$\alpha(\omega\omega_b^2)^{1/3} \gg \Delta k\, u \qquad (3)$$

is fulfilled an electron beam interacts simultaneously with both hybrid waves.

When the inverse to (3) inequality is fulfilled an electron beam interacts only with one of hybrid waves. The dependencies of the growth rates of forward hybrid waves on frequency detuning $\omega-\omega_0$ are plotted in Fig.2. At great detuning the values of growth rates tend to those of plasma and structure waves uncoupled. The coefficients of power amplification of forward hybrid waves by an electron beam is proportional to the function $\exp(2\mathrm{Im}kz)$, where z is the axial coordinate. But in the case of backward hybrid waves or hybrid waves with zero group velocities the imaginary part of the wave number does not determine the coefficient of amplification. It can be find only in the case of accounting of several interfering normal waves and boundary conditions on the ends of structures.

In the presence of feedback (external or internal) the electromagnetic radiation can be generated. The linear theory allows to determine the starting conditions of generation. For generation of forward waves their reflections on the ends of the structure are needed. The generation of backward waves or the waves with zero group velocities can be reached in the absence of reflections.

Nonlinear theory of the interaction of an electron beam with hybrid waves of a periodic structure with plasma

The efficiency of the interaction of an electron beam with hybrid waves and the power of the microwave radiation can be found in frames of nonlinear theory.In the case of the amplification of forward waves the stationary nonlinear equations are like the ordinary TWT equations [17]. The difference is only in two hybrid waves interacting with the beam. Such situation is analog to that in the multiwave nonlinear theory [18,19]. Because of this the process of the amplification is accompanied by

nonregular changing of amplitudes of waves along the axis and less compact bunching of beam electrons. But the efficiency of the interaction can be increased.

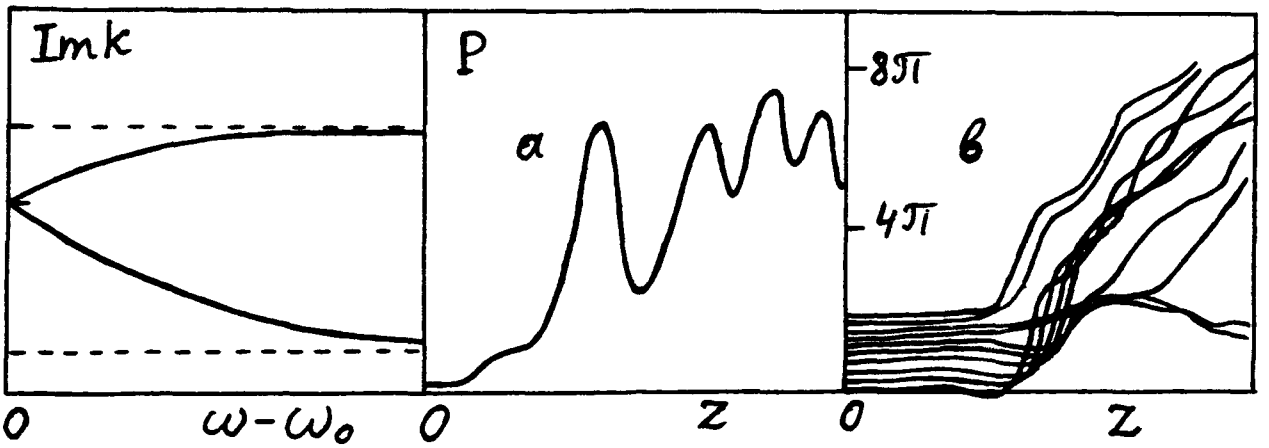


Fig.2: The dependencies of the growth rates on frequency detuning

Fig.3: The dependence of the radiation power on the length (a) and phase trajectories (b)

In Fig.3 the results of numerical computation of the amplification of the microwave radiation power outside plasma (a) in a chain of coupled cavities and phase trajectories of beam electrons (b) are presented. They illustrate effects said upper.

The nonlinear theory of the interaction of electron beams with backward hybrid waves or the waves with zero group velocities is more complicated and should be preferably nonstationary.

Amplification of slow and fast waves of a plasma waveguide by an electron beam in the multiwave nonlinear theory

When plasma occupies the small part of the cross-section of the smooth waveguide, like, for example, in the experiment [2], two waves, fast and slow can possess the phase velocities very close to the speed of light [20]. If the electron beam is relativistic and intense it can interact with both these waves. Such situation is analog to the multiwave nonlinear theory of interaction [18,19] and to the hybrid plasma microwave devices. The difference is that the phase velocity of the fast wave is ever more than the speed of light and therefore than the velocity

of beam electrons. Nevertheless, this wave also can be amplified by an electron beam because of the presence of the slow wave with the phase velocity less than the speed of light. Such mechanism of beam-plasma interaction may result in the increased efficiency.

[1] Ya.B. Fainberg, Fizika Plasmy 11, 1391 (1985).
[2] I.A. Selivanov, P.S. Strelkov, A.V. Fedotov, A.G. Shkvarunets, Fizika Plasmy 15, 1283 (1989).
[3] Y. Carmel, K. Minami, W. Lou et al., IEEE Trans. on Plasma Sci. 18, 497 (1990).
[4] V.L. Granatstein, T.M. Antonsen, Jr., S.Bidwell et al., Proc. of the 8th Int. Conf. "Beams'90" 1, 295 (1990).
[5] G.A. Bernashevskiy, Ye.V. Bogdanov, V.Ya. Kislov, Z.S. Chernov, Plazmennyye i Electronnyye Usiliteli i Generatory SVCh (Moscow, Soviet radio, 1965).
[6] D.I. Trubetskov, L.A. Pishchik, Fizika Plasmy 15, 342 (1980)
[7] G.I. Batskikh, K.G. Gureyev, N.I. Karbushev, A.I. Lisitsyn, Proc. of the 8th Int. Conf. "Beams'90" 2, 1173 (1990).
[8] Ya.B. Fainberg, Yu.P. Bliokh, L.A. Mitin et al., Doklady AN UkrSSR, no 11, 76 (1990).
[9] V.I Kanavets, N.I. Karbushev, Ye.I. Ostrenskiy, A.I. Slepkov, Radioternika i Electronika 35, 2574 (1990)
[10] N.I. Karbushev, Izvestiya Vuzov, Radiofizika 34, no.7 (1991)
[11] H. Kosai, E.P. Garate, A. Fisher, IEEE Trans. on Plasma Sci. 18, 1002 (1990)
[12] B.M. Bulgakov, V.P. Shestopalov, L.A. Shishkin, I.P. Yakimenko, Zh. Tekh. Fiz. 30, 840 (1960)
[13] G.N. Gestrina, Izv. Vuzov, Radiofizika 31, 1502 (1988)
[14] M.M. Ali, K. Minami, S. Amano et al., J. Phys. Soc. of Japan 60, 2655 (1991)
[15] K. Minami, Y. Carmel, V.L. Granatstein et al., IEEE Trans. on Plasma Sci. 18, 537 (1990)
[16] N.I. Karbushev, Yu.A. Kolosov, A.I. Polovkov, Fizika Plasmy 18, 54 (1992)
[17] A.I. Rogashkova, M.B. Tseytlin, Elektronnaya Tekhnika, Ser. 1, Elektronika SVCh, no. 7, 3 (1967)
[18] V.A. Balakirev, Ye.A. Galst'yan, N.I. Karbushev et al., In.:Relyativistskaya Vysokochastotnaya Elektronika (Ed. by A.V. Gaponov-Grekhov, Gorky, Inst. of Appl. Phys.) no. 6, 127 (1990)
[19] Ye.A. Galst'yan, N.I. Karbushev, Fizika Plasmy 16, 1109 (1990)
[20] J.S. DeGroot, R.A. Stone, K. Mizuno et al., IEEE Trans. on Plasma Sci.16, 206 (1988)

RESEARCH ON A 1.3 GHz ANNULAR ELECTRON BEAM POWERED MULTI-GIGAWATT MICROWAVE AMPLIFIER

Kyle J. Hendricks, Walter R. Fayne, Lester A. Bowers, Charles E. Davis

Microwave Sources Branch (PL/WSR)
Phillips Laboratory
Kirtland AFB, NM 87117-6008

Michael D. Haworth and Robert C. Platt

SAIC
Albuquerque, New Mexico

Raymond W. Lemke and M. Collins Clark

Division 124
Sandia National Laboratory
Albuquerque, NM 87185

ABSTRACT

We have been conducting experiments and computer simulations of annular electron beam powered microwave devices. This work includes the generation of an annular electron beam using the IMP pulser (500 kV, 5 Ω, 300 ns), the modulation of this beam by the Single Cavity Double Gap Modulator and a two cavity klystron-like amplifier, and the extraction or radiation of the microwave power via a Vlasov antenna. We have conducted experiments with two different geometries, one with the annular beam inside the microwave circuit and one with the microwave circuit inside the annular beam. We will present results of computer simulations from the 2-D code **MAGIC** and experiments for both geometries. We will also present results of simulations and experiments on injecting a magnetron signal into the two cavity klystron-like amplifier via RG-220 50 Ω cable. The **MAGIC** simulations of the amplifier are compared with the code Superfish to verify that the antenna model of **MAGIC** establishes the proper mode in the cavity.

Introduction

The efforts throughout the past ten years to develop and design high power or high energy microwave sources have been somewhat successful. Work on Multi-Wave Diffraction/Cerenkov Generators[1] and the Relativistic Klystron Amplifier (RKA)[2] have produced 1 kJ microwave pulses. Work has also been progressing on Backward Wave Oscillator/Traveling Wave Tube Amplifier[3] combinations. The

focus of that research has been to impose an rf signal on an electron beam traveling in an external axial magnetic field, followed by the efficient extraction of the amplified rf signal. We have been pursuing a similar program to modulate a "long pulse" annular electron beam. The goal is to develop design tools into computer simulations which agree with experimental results.

Our initial program has been an investigation into self-oscillation circuits patterned after re-entrant klystron cavities, and an amplifier concept patterned after the RKA. Our experiments are conducted on the IMP pulser (500 kV, 5 Ω, 300 ns). This pulser has the potential to generate a 50 GW electron beam, however we restrict our experiments to a 2 to 6 GW electron beam (400 kV, 5 to 16 kA). We have been simulating these devices with the PIC code MAGIC[4]. The electric field generated by the antenna model of MAGIC is compared with the mode patterns computed with SUPERFISH[5]. The modulation coefficient of the electron beam current as computed by MAGIC agrees quite well with the coefficient determined by the trajectory code RKA, however the final verification of simulation results must remain agreement with experiment.

Device Geometries

Our work has been limited to three geometries (Fig. 1). The two oscillator geometries were selected to allow a self-consistent mode to be established on the two modulating gaps. This mode had an electric field null at the axial mid-point of the cavity due to placement of inductive standoffs used to support the inner cavity wall. The cavities used in both oscillator geometries were simulated with SUPERFISH (Fig. 2) and then cold tested to verify the simulation results. The problem found with geometry a) (Fig. 1) was that the self-oscillation occurred at about 1.5 GHz rather than 1.3 GHz which indicates that the self-oscillation was in a TM_{01} rather than a mode where the beam carried the rf and the signal propagated through the outer cavity. Geometry b) (Fig. 1) was never employed in an rf extraction experiment. We monitored the E_r field in the modulating cavity, and found agreement with the SUPERFISH rf mode. The frequency observed also agreed with the SUPERFISH simulations.

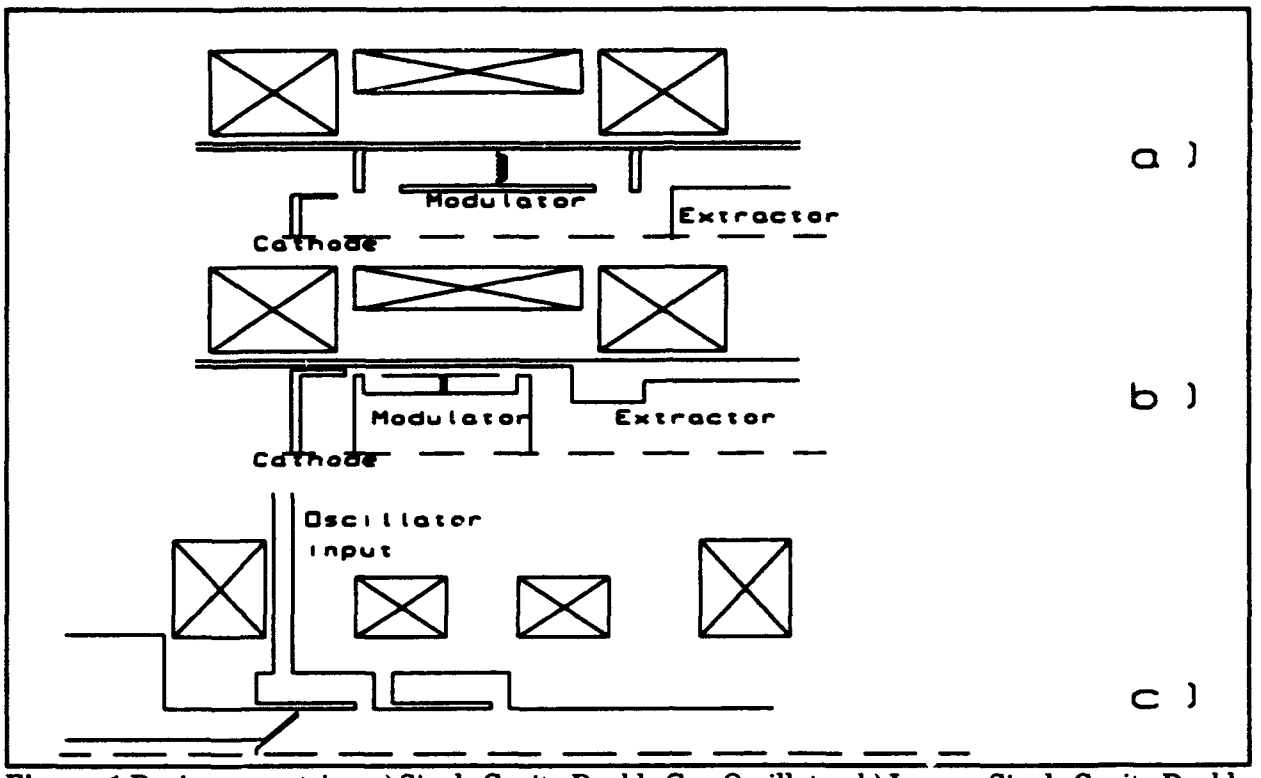


Figure 1 Device geometries: a) Single Cavity Double Gap Oscillator, b) Inverse Single Cavity Double Gap Oscillator, c) Annular Beam Amplifier.

Geometry c) (Fig. 1) has also been successfully modeled by SUPERFISH, however a beam instability with a lower frequency (~ 380 MHz) than desired was found in MAGIC simulations which has a tendency to grow faster than the desired frequency (~ 1300 Mhz). This results from our choice of using $3\lambda/4$ rather than $\lambda/4$ cavities. When using the $\lambda/4$ cavities in our MAGIC simulations we have been able to generate the proper mode in the cavity with the antenna model. We have focused our attention on the rf voltage in the first gap rather than trying to calibrate the Magic antenna amplitude to our external oscillator. Amplification of the rf signal was observed in the simulations. This has been indicated by the modulation of the electron beam current at several axial points following the first gap (Fig. 3). The computed results for the modulation coefficient as the beam drifts past the second gap toward the extractor are shown in figure 4. Given that the current modulation is of order 70% indicates that we should ideally obtain approximately 35% of the beam power as rf power with a perfect extractor. Extractors may be designed to be nearly 100% efficient at a single frequency thus we expect 30 to 35% conversion.

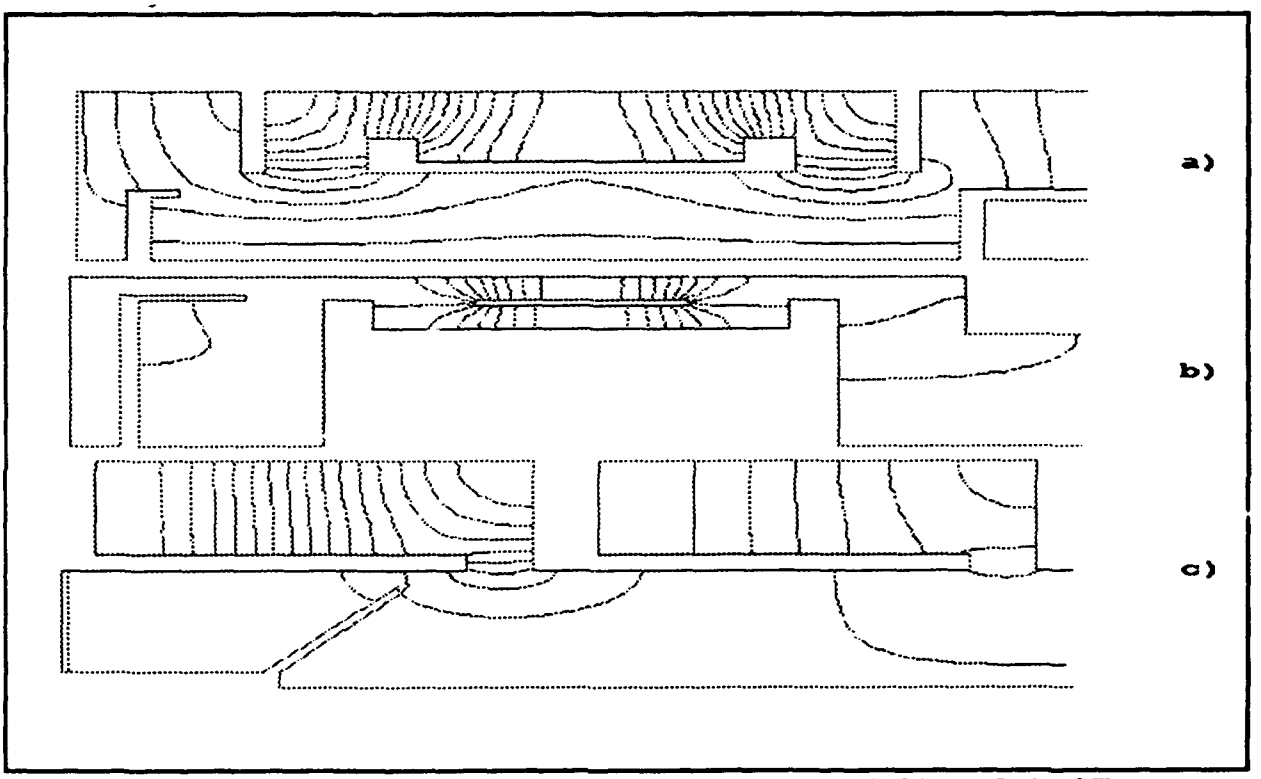


Figure 2 SUPERFISH simulation results for geometry a), b), and c) of Fig. 1.

RESULTS

We have had limited success with the self-oscillating geometries. We have been able to experimentally verify that the oscillator cavities will provide a self-consistent mode which agrees with the SUPERFISH results. We then began an amplifier experiment and have had success coupling power from an external oscillator via coaxial cable and using a magnetic coupling loop with a single stub tuner to excite our modulating cavity. We believe we are seeing evidence of "electrostatic insulation" in our simulations. Electric fields in the idler gap exceed 100 kV/cm, well beyond the level where field emission is typically observed. Good agreement between the computed and measured beam modulation coefficient indicates that our efficiency should be sufficient to generate of order 1 kJ of rf energy in a single pulse.

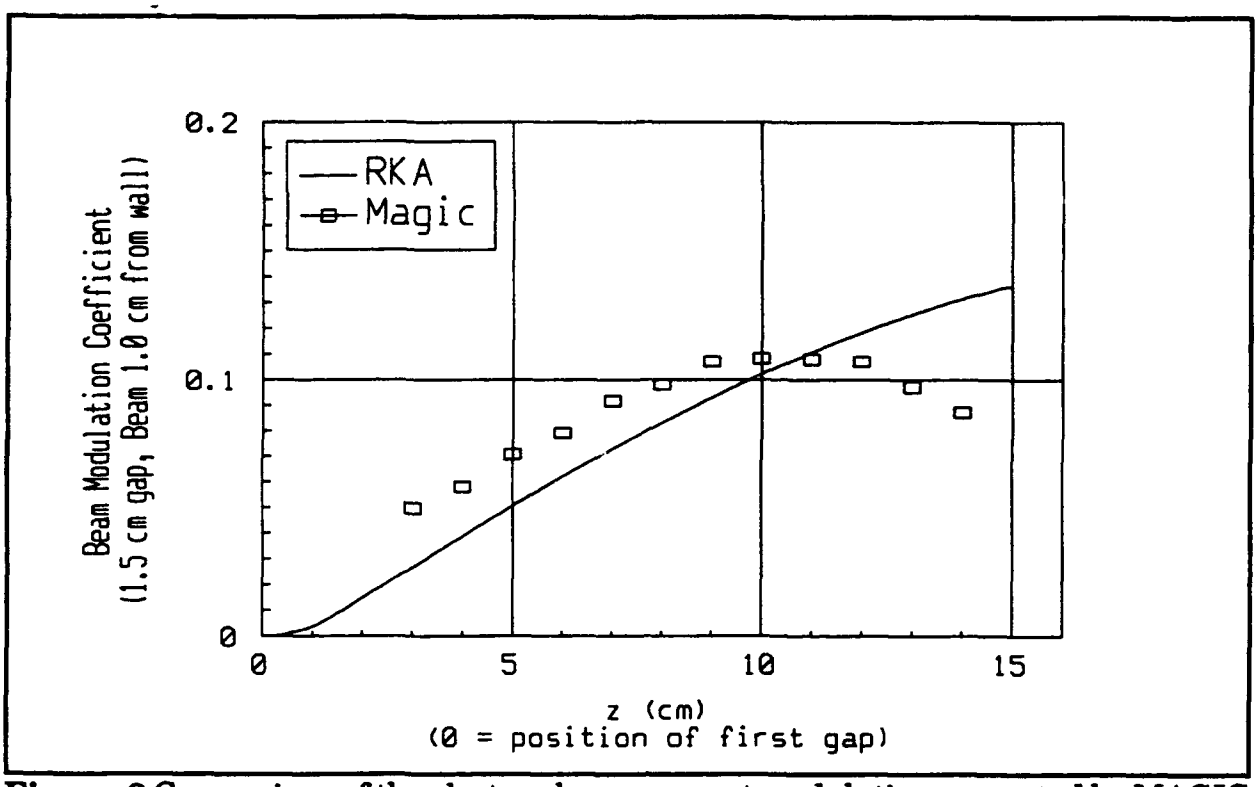


Figure 3 Comparison of the electron beam current modulation computed by MAGIC and RKA. Problem parameters: V_B= 350 kV, I_B= 10 kA, V_{gap1}= 56 kV.

Future Plans

In the short term we plan to field an amplifier experiment capable of operation with a 400 kV and 16 kA electron beam. This required fabrication of a stainless steel vacuum vessel and a pulsed magnet capable of providing 6 to 12 kG of axial field. These experiments will begin in the summer of 1992. Following the initial experiments with pulse lengths of 300 ns we plan to move our experiments to a pulser with a 500 ns pulse and then move to 1 μsec electron beam pulses. We also plan to look into replacing the rf circuit of the klystron with other modulating structures capable of higher power handling or providing other modes for extraction to the antenna.

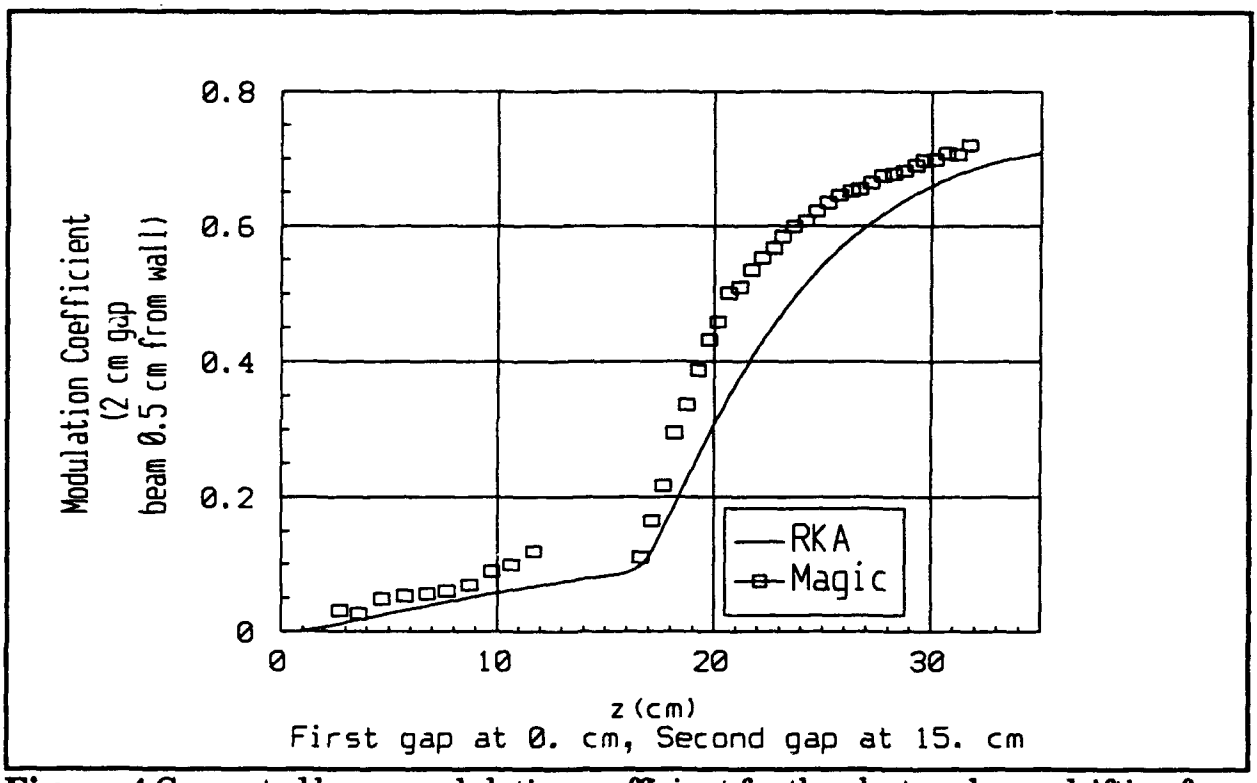


Figure 4 Computed beam modulation coefficient for the electron beam drifting from the second gap. Parameters: V_B=400 kV, I_B=16 kA, V_{gap1}=40 kV, V_{gap2}=280 kV.

REFERENCES

1. S.P. Bugaev, V.A. Cherepenin, V.I. Kanavets, A.I. Klimov, A.D. Kopenkin, V.I. Koshelev, V.A. Popov, and A.I. Slepkov, "Relativistic Multiwave Cerenkov Generators", IEEE Trans. on Plasma Science, 18(3), June 1990, p.525-536

2. M. Friedman, V. Serlin, Y.Y. Lau, J. Krall, "Relativistic Klystron Amplifier I: High-Power Operation", SPIE Vol. 1407/Intense Microwave and Particle Beams II (Jan. 1991), p.2-7

3. D. Shiffler, J.A. Nation, L. Schlachter, J.D. Ivers, and G.S. Kerslick, "A High-Power two stage traveling-wave tube amplifier", J. Appl. Phys., 70(1), 1 July, 1991, p.106-113

4. B.L. Goplen, L. Ludeking, J. McDonald, G. Warren, and R. Worl, The MAGIC Users Manual, MRC/WDC-R-216

5. User's Guide and Reference Manual for the POISSON/SUPERFISH Group of Codes, Los Alamos Accelerator Code Group, LANL, LA-UR-87-115 and LA-UR-87-126

APPLICATION OF HIGH-CURRENT ACCELERATORS WITH INDUCTORS, BASED ON DISTRIBUTED PARAMETERS LINES FOR GENERATION OF HIGH-POWER MICROWAVE PULSES.

A.I. Pavlovskii, V.D. Selemir, V.V. Ivanov, I.V. Konovalov, I.G. Prikhod'ko, V.G. Suvorov, K.V. Shibalko, V.G. Kornilov, V.Y. Vatrunin, V.S. Zhdanov

(Experimental Physics Research Institute, Arzamas-16, Nizhni Novgorod region, 607200, Russia)

Considerable increase of accelerating voltage in comparison with the charging one along with high quality of electron beam to be formed, is obtained using in microwave generators accelerating module from inductors, based on lines with distributed parameters.

Electron beam, formed in a magnetic field in the range from 4 kG to 20 kG (pulse duration 20 ns, current 15 kA and electron energy 3 MeV) interacted with rippled (ripple period of 16 mm) waveguide, generates high power microwave pulse in the frequency range of 10 GHz with an amplitude of several gigawatt.

Application of high-current accelerators, with inductors, based on distributed parameters lines, in Cherenkov generators, allows to increase microwave power and advance them into more short wave region.

In the field of power relativistic electronics the considerable progress has been achieved in solving the problem of high power microwave pulses generation. Tens of gigawatt generation levels have been realized [1, 2]. The particular interest in this direction is connected with investigations of coherent microwave Cherenkov generators [3, 4], electromagnetic flux of which presents large opportunities for its transformation and transportation in various conditions.

These facilities in centimetre and millimetre wave range are called to take the position, corresponding to that, occupied by a laser among generators of light radiation.

Up to now single or double shaping line accelerators of direct action have been used as electron-beam generators, applying in relativistic microwave electronics. In connection with the efforts of shaping coherent microwave of millimetre and submillimetre ranges the interest has grown to the beams, generated in linear inductive accelerators [5, 6]. Linear inductive accelerators on the basis of lines with distributed parameters [7], combining the opportunity of acceleration energy change, when varying scales of accelerating system, with high-current property, inherent to direct discharge of law impedance lines, represent serious opportunities for increasing electron beam power, along with preserving angular and energetic particle dispersion, acceptable to microwave electronics

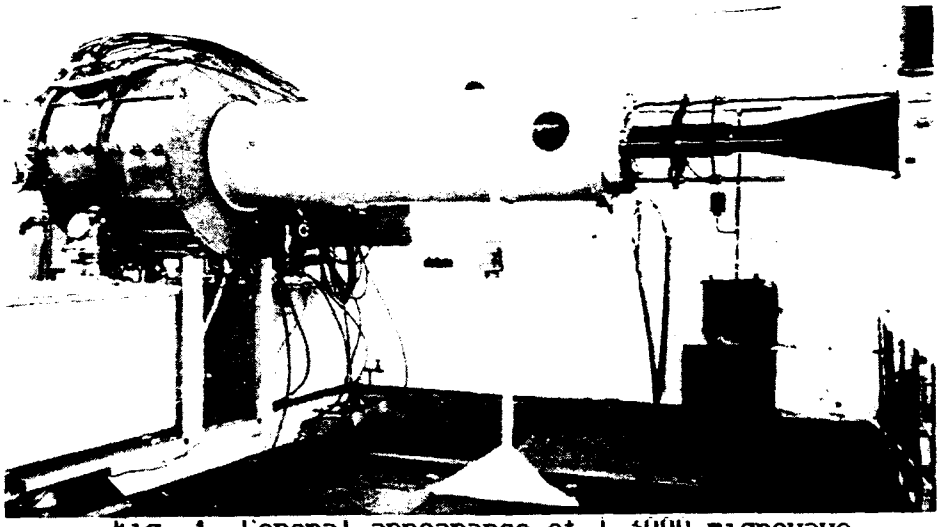


Fig. 1. General appearance of I-3000-microwave facility.

The paper is devoted to application of inductors LIA, based on radial lines, as a part of high power generators of coherent radiation. As an electron beam generator we used accelerator I-3000 [8, 9] (Fig.1), created on the basis of two accelerating module of the LIA-10 facility [10].

One of the methods of voltage increase, generating by a series of inductors, is connecting to their output the transmission line with high wave resistance.

The load (electron beam) is switched on at the moment when the second accelerating voltage of 2 duration comes to the transmission line output of c electric length. The generator output voltage with optimization of transmission line wave resistance may rise up to the value of 1.85Uo at R/Wo = 10, where Uo is output voltage of series of inductors, Wo is their output resistance, R is load resistance.

I-3000 accelerator is implemented on the basis of two module and vacuum transmission line (W = 43 Ohm) of 2 m length. The line is formed by grounded electrode (1) with the inner diameter of 510 mm and cantilever high voltage electrode (2) 240 mm in diameter.

Fig.2 also shows the circuit of microwave generator of Cherenkov type [4]. Electron beam, emittered by a cathode (3), passing through electrodynamic microwave structure (5), interacts with its spatial field harmonics and generates high power microwave pulse at the output. To let electromagnetic energy flux out into atmosphere we used tapered horn (6) and vacuum window (7) made of polyethylene or teflon with an aperture of 300 mm.

Electron beam shaping is implemented in coaxial diode with magnetic insulation. Magnetic system of a generator consists of two solenoids: the main one (8) and adjusting (9). The diode system structure, where the cathode profile and tapered anode profile coincide with the magnetic field line, is implemented by special calculations with consequent experimental finishing. With mag-

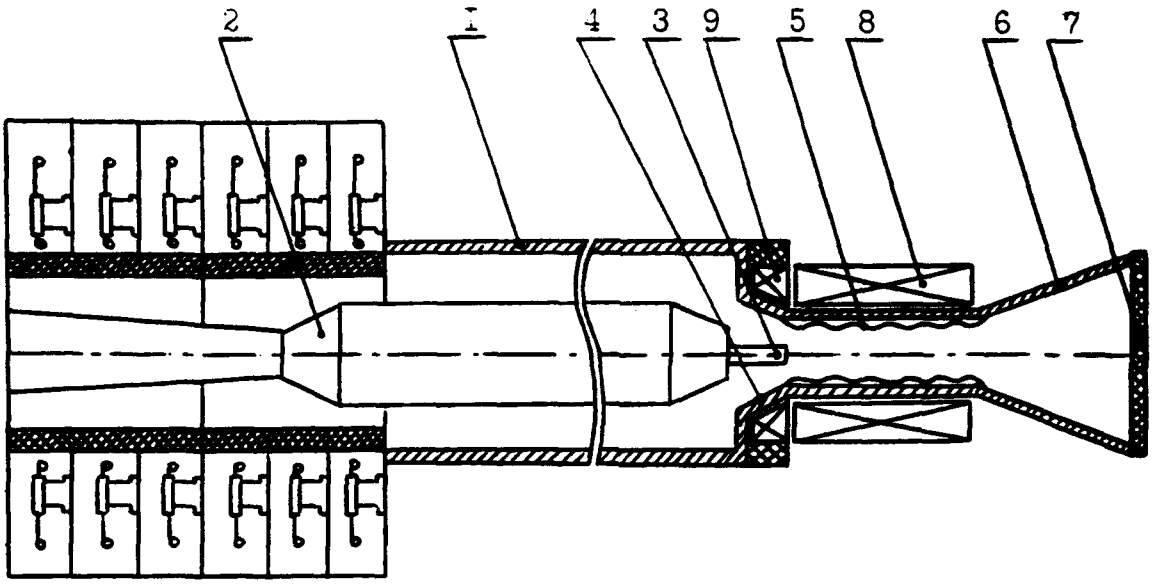


Fig.2. Structural circuit of high power microwave generator I-3000-microwave.

1 - grounded electrode, 2 - inner electrode, 3 - cathode, 4 - tapered anode, 5 - electrodynamic structure, 6 - horn, 7 - output window, 8, 9 - the main and adjusting solenoids.

netic field from 4 to 20 kG given configuration of electrodes and force lines ensures diode magnetic insulation at the first pulse (having positive polarity of cathode) and high quality electron beam generation (law angular and spatial dispersion) at the second pulse of accelerating voltage. Fig.3 illustrates magnetic field distribution at the generator axis.

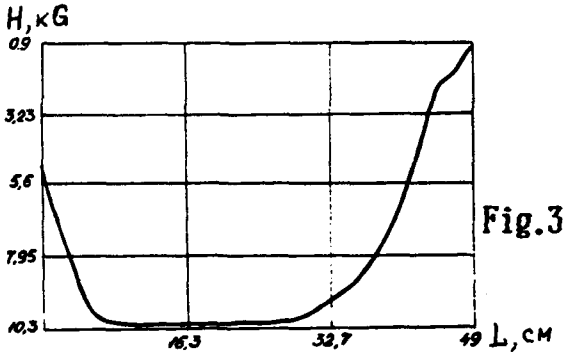


Fig.3. Magnetic field at the generator axis. The position of cathode edge is marked by a cross.

Damage-pattern of the beam in a cylindrical drift region at the distance of 20 cm from cathode edge is shown in Fig.4. Beam diameter of 35 mm coincides with the diameter of a the hollow cylindrical cathode. The beam width is 1.5 mm, the radial shift being not more than 1 mm.

Boundary energy of electrons at the drift region terminal has been measured

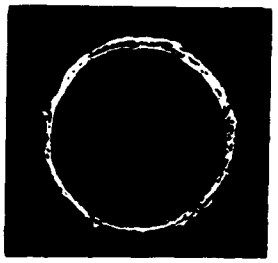


Fig.4. The damage-pattern of electron beam, formed in a diode.

by a spectrometer with torroidal dispersing field [12]. It occurs to be 3 MeV in the case when pulse voltage Marx-generator was charged to 90 kV. Beam current amplitude, measured by self-integrating Rogowski coil at the drift region input, is 15 kA. When the distance between cathode edge and electrodynamic structure input increases, the accelerator I-3000 generates series of two pulses with a time interval of 45 ns. Their amplitudes are 12 and 10 kA, pulse width at full duration is 20 ns. Electrodynamic structure represents sinusoidally rippled (ripple period of 16 mm) cylindrical waveguide 59 mm in diameter, having cylindrical input and output, made of stainless steel. Inner surface to ensure electrical strength is polished.

Calculations of interaction between electron beam and electrodynamic structure, carried out on the basis of specifying dispersion characteristics of rippled waveguide, taking into account electron beam [13, 14] and gain factor [15], showed, that the mode of travelling wave tube with distributed along the structure length back coupling was realized in a generator. Starting current of excitation of electromagnetic field with space characteristics, similar to E_{01} mode of a round cylindrical waveguide, is 8 kA. Optimum depth of ripple is 6 mm.

Generation frequency is 9.5 GHz. In our experiments of microwaves, formed by the generator, were recorded by a set of detectors, based on carrier mobility change in semiconductors in electric field [16]. The set was placed in a wave region of horn antenna at a distance of 9 m from facility output window. Typical microwave power in a single shot is presented in Fig.5. Pulse width at full duration of 20 ns practically coincides with current pulse duration of generated electron beam, which testifies about high gain factor of electrodynamic structure and qualitatively matches with calculation results.

Power integration performed on the basis of the directivity diagram and taking into account radial an angular polarization gives the power value of microwaves, let out into atmosphere to be 3 GW. Increase of pulse-voltage generator charging voltage of I-3000 facility and correspondingly, increase of beam power leads to shortening of pulse duration, according to pulse width at full duration, up to 10 ns (Fig.6) and is accompanied by breakdown phenomena at the horn output window and at the electrodynamic structure output.

When forming in electron diode two electron fluxes with a time interval of 45 ns, two pulses of microwaves are shaped at microwave generator output, ha-

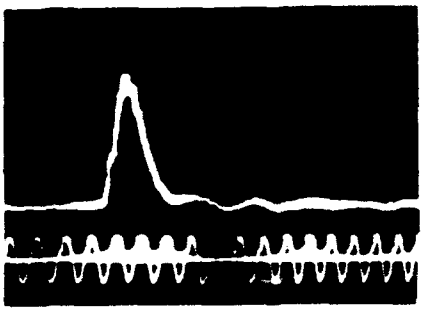


Fig.5. Typical microwave power in a single shot, obtained by semiconductor detector, based on "hot carriers". Time marks are 10 ns.

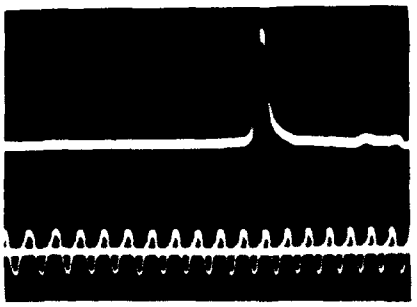


Fig.6. Microwave power output pulse with increased electron beam power. Time marks are 10 ns.

ving durations of 20 ns and 15 ns (Fig.7).

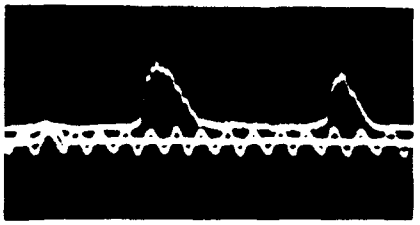


Fig.7. Oscillogram, demonstrating generation of two microwave pulses. Time marks are 10 ns.

Measurements of microwaves by tuned filters showed, that practically all microwave energy is in the frequency range from 9.5 to 10 GHz, which satisfactory coincides with calculation data. Additional information about monochromatism degree of microwaves is obtained when investigating luminous annular discharge with periodic structure, appearing in atmosphere, when waves are reflected by flat metallic mirror, perpendicular to radiation direction. Fig.8 shows the picture of integral discharge glow. Typical diameter of luminous area is 20 cm. Analysis of microwave breakdown picture allows to determine the length of microwave, according to the distance between annular discharges. The corresponding measurements lead to the values from 3.0 to 3.2 cm, which matches with data, measured by tuned filters. Both monochromatism and coherence of generating radiation have been testified by axial discharge symmetry, its azimuthal uniformity and appearance of interference picture, arising due to superposition of the opposite elements of wave field, when microwave was reflected at the angle of 45 .

Thus, first experiments to use accelerators with inductors, based on radial

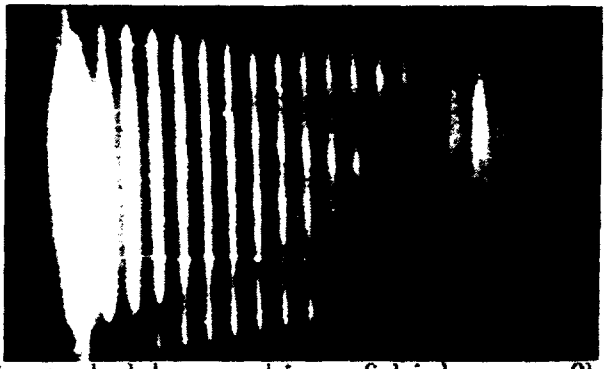


Fig.8. Integral glow of microwave discharge in atmosphere, appearing in standing wave loops. Typical diameter of luminous area is 20 cm.

lines, led to creation of high power Cherenkov generator, having microwave power of 3 GW let out into atmosphere. The opportunities, given by LIA, to increase the energy of accelerated particles, are prosperous for mastering of millimetre and submillimetre radiation wave length ranges, under high currents, typical of LIA, based on lines with distributed parameters.

References.

1. S.P. Bugaev, V.I. Kanavets, V.I. Klimov et al.
   Radiotekhnika i Elektronika.-1987.-T.32.vyp.7.-s.1488-1498.
2. A. Bromborsky, F. Agee, M. Bollen et al.
   "On the path to terawatt: high power microwave experiments at Aurora" SPIE, v.873. Microwave and Particle Beam Sources and Propagation (1988) pp 51-61.
3. J.A. Nation. Appl. Phys. Lett.-1970.vol.17.N11.pp 491-494.
4. N.F. Kovalev, M.I. Petelin, M.D. Rajzer et al.
   Pis'ma v Zh. Eksperim. i Teoret. Fiziki.-1973.T.18,vyp.4. -s.232-235.
5. V.I. Aver'yanov, O.V. Arkhipov, V.L. Bratman et al.
   Zh. Tekh. Fiz. 1987, T.57,N5.s.1213-1217.
6. D. Hopkins, A.C. Paul, A.M. Sessler, and J. Wurtele
   Phys. Rev. Lett. V.54.N9.pp 889-893.
7. A.I. Pavlovskii, V.S. Bosamykin.
   Atomnaya Energiya - 1974, T.37, vyp.3, s. 228-232.
8. A.I. Pavlovskii, V.S. Bosamykin, V.D. Selemir et al.
   "Linear Inductive Accelerators for Microwave Generators" in VII Conference on Relativistic Microwave Electronics. Tomsk. Russia. 1991.
9. V.S. Bosamykin, V.S. Gordeev, A.I. Pavlovskii et al. "Pulsed Power Electron Accelerators with the Forming Systems Based on Stepped Transmission Lines" in 9-th International Conference on High Power Particle Beams.
10. A.I. Pavlovskii, V.S. Bosamykin, V.A. Savchenko et al.
    Dokl. AN SSSR, 1980, T.250, N5, s. 1118-1122.
11. V.D. Selemir, V.V. Ivanov, I.V. Konovalov et al.
    "High Power Microwave Generator I-3000-Microwave", in VII Conference on Relativistic Microwave Electronics. Tomsk. Russia. 1991.
12. N.V.Minashkin, V.D. Selemir, N.V. Stepanov. Authors certificat N1681658.SU.
13. V.I. Kurilko, V.N. Kucherov, A.O.Ostrovskii, Y.V. Tkach.
    Zh. Tekh. Fiz. 1979, T.49,N12.s.2569-2575.
14. J.A. Swegle, J.W.Poukey, G.T. Leiteste.
    Phys. Fluids. 1985, v.28, N9, pp 2882-2894.
15. A.A. Rukhadze, L.S. Bogdankevich, S.E. Rosinskii, V.T. Rukhlin. "High Current Relativistic Electron Beams Physics". M:Atomizdat, 1980, in Russian.
16. M.D. Raizer, L.E. Tsopp.
    Radiotekhnika i Elektronika.-1975-T.20.vyp.8.-s.1691-1697

EFFECT OF INTENSE SPACE CHARGE IN RELATIVISTIC KLYSTRON AMPLIFIERS*

B. E. Carlsten, R. J. Faehl, M. V. Fazio, T. J. Kwan,
D. G. Rickel, R. D. Ryne, and R. M. Stringfield

Los Alamos National Laboratory, MS H825
Los Alamos, New Mexico 87544

Abstract

We discuss basic Relativistic Klystron Amplifier (RKA) physics. We show that, for pulse lengths of one microsecond or longer in the intense space-charge regime, the maximum power extraction from the beam does not coincide with the maximum harmonic bunching. We also discuss the beam-cavity interaction model and present experimental and theoretical single cavity modulation results. Finally, we discuss alternatives to the basic RKA design that enhance beam to microwave power conversion efficiency, particularly at high frequency.

Introduction

We will review basic Relativistic Klystron Amplifier (RKA) theory, with emphasis on the effects resulting from intense space charge. In addition, we will include numerical simulations done with a self-consistent particle-in-cell (PIC) code to demonstrate certain effects. We will see that some of the effects are beneficial; for example the intense space charge aids the bunching process and the generation of large harmonic currents. However, other effects are harmful and the potential depression from the space charge is responsible for an overall limit on the extraction efficiency.

For a given injection voltage V_{inj}, as the beam current I_b is increased, the beam's potential energy must also increase, thereby reducing its kinetic energy. As a result, there is a trade off between harmonic current and extraction of kinetic energy, providing a distinct optimum operating condition. If the space charge is too high, the potential energy fields can contain most of the initial beam energy. For sufficiently short pulse lengths, the potential energy can be reconverted to kinetic energy and extracted if the beam is allowed to intercept a conducting wall in the output cavity. For pulse lengths longer than the time required for the plasma generated to expand into the output gap, this interception is not feasible. Although this time depends on the plasma velocity, it is typically less than one microsecond. One possible solution, which maintains large harmonic current and short drifts but prevents large amounts of the beam energy from being partitioned into the potential fields, is to post accelerate the beam after bunching. Additionally, the large higher (second and above) harmonic currents which are generated by bunching the intense beam allow harmonic extraction that scales favorably to higher frequencies.

We will cover three topics in this paper. First, we will review intense-beam physics and describe the partitioning of injection energy into kinetic and potential parts. We will also show how beam harmonic-current generation depends on the space charge. Next we will analyze the beam-interaction model for the drive cavity, and compare experimental and theoretical reflected power results. In the final section, we will discuss alternatives to the basic RKA design, including the harmonic extraction and post acceleration modifications.

RKA Microwave and Beam Physics

In this section we will first review microwave power definitions. We will see that maximizing the overall extraction efficiency requires both large harmonic currents and a small potential depression of the beam. We will then analyze the beam potential depression in terms of how much excess energy it has under bunched conditions. Finally, we will see how the generation of harmonic current depends on the space charge.

In Fig. 1, we see a schematic of an RKA. An annular, intense (5 kA), mildly relativistic (500 keV) electron beam passes through three cavities. The first cavity is externally driven and impresses an axial momentum variation on the initially uniform beam. This momentum variation causes variations in the

* Work supported and funded jointly by the DoD Office of Munitions and the DOE Defense Programs through the joint DoD/DOE Munitions Technology Development Program, and by the Army Harry Diamond Laboratories and Missile Command.

beam's axial density. We can describe the beam current in terms of its Fourier components

$$I(t,z) = I_o + I_1(z)\cos(\omega t + \phi_1) + I_2(z)\cos(2\omega t + \phi_2) + \ \ldots \tag{1}$$

The product $\frac{1}{2}I_1V_o$ is often referred to as the beam rf power, where V_o is the beam kinetic voltage. The second cavity is driven by the harmonic current, and is modeled in Fig. 2 (without the external load). We see that the cavity's gap voltage is given by

$$V_{gap} = Z_{cav}I_{ind} \tag{2}$$

where Z_{cav} is the cavity impedance and I_{ind}, the induced current, is the harmonic current times a coupling factor close to one. The idler cavity rf fields further modulate the beam momentum and provide harmonic current at the output cavity close to the DC beam current. The output cavity is tuned resonantly, so the rf fields induced in it decelerate the beam. Ramo's theorem[1] gives the microwave power that is extracted from the beam,

$$P(t) = \int_V \vec{J}(\vec{r},t)\cdot\vec{E}(\vec{r},t)dV \tag{3}$$

where $\vec{J}$ is the beam current density and $\vec{E}$ is the rf electric field. We see from Eq. (3) that only the beam's kinetic energy can be extracted; and since $E \sim e^{j\omega t}$, we can only extract power from the fundamental harmonic component. To have the highest microwave power, we must simultaneously maximize I_1 and extract the maximum kinetic energy from the beam.

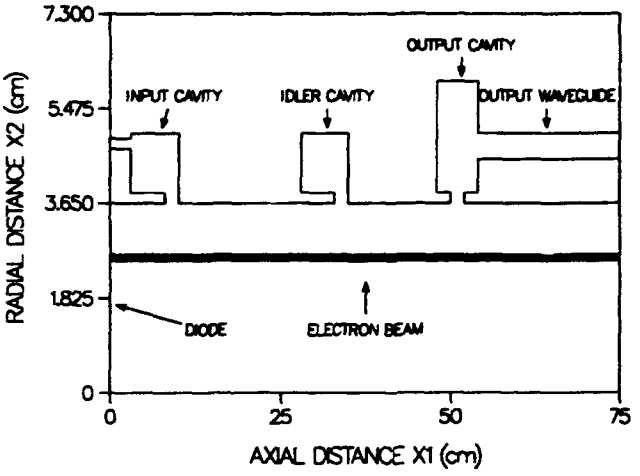


Figure 1. Nominal 500-kV, 5-kA RKA with pipe radius 3.65 cm.

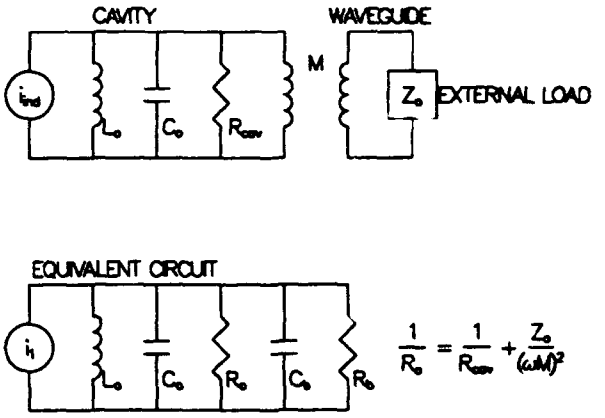


Figure 2. Beam-cavity interaction model.

The maximum extraction power is largely dominated by the space-charge physics. The beam voltage that can be extracted is calculated by subtracting the minimum voltage required to transport the bunched beam (including the increased potential energy requirement) from the space-charge depressed kinetic voltage of the bunched beam.

For a given injection diode voltage, the voltage associated with an annular beam's kinetic energy is less since some potential energy is required to set up the Coulomb fields within the cylindrical pipe. The largest permissible current at a radius r_b with initial gamma γ_{inj}, injected into a conducting cylinder of radius r_w is given by[2]

$$I_{max} = \frac{2\pi\epsilon_o m_o c^3}{e}\frac{\left(\gamma_{inj}^{\frac{2}{3}} - 1\right)^{\frac{3}{2}}}{\log\frac{r_w}{r_b}} \ . \tag{4}$$

If the beam current is near the threshold current I_{max} and is increased slightly, a significant reduction in the beam's kinetic energy (and velocity) is possible. The growth of the bunch is aided by this nonlinear slowing of the beam as the bunch is formed.[3] In Fig. 3 we see the partitioning of the total energy into kinetic and potential energy parts as a function of the injection gamma, γ_{inj}, and $\frac{I_o}{I_{max}}$.

A more useful version of Eq. (4) for space-charge-limited current can tell us the maximum amount of kinetic energy we can extract. Solving for the minimum potential and kinetic energy we get

$$\gamma_{min}^{\frac{2}{3}} = \left(\frac{PE+KE}{m_0c^2}+1\right)^{\frac{2}{3}} = \left(\frac{I_{peak}}{8.5\text{kA}}\log\frac{r_w}{r_b}\right)^{\frac{2}{3}}+1 \quad . \tag{5}$$

For a given peak current, I_{peak}, the difference between γ_{inj} and γ_{min} is the available kinetic energy for conversion to microwaves. The potential energy in the Coulomb fields is basically lost. The maximum power extraction is one-half the product of the harmonic current and the difference between the injection voltage and the minimum beam energy (in volts). In a previous paper[4] we tabulated available kinetic energy as a function of beam current and radius for an injection voltage of 500 kV. The potential depression can lead to small values of available kinetic energy. For example, a 3.2-cm-radius beam bunched to 10 kA in a 3.65-cm-radius pipe only has an excess of 250 keV.

The growth of the beam harmonic current can either be space-charge dominated or ballistic, depending on the current, the ratio of the wall radius to the beam radius, and the modulation voltage. Ballistic motion is well known for the short-gap, nonrelativistic limit.[1] For a relativistic beam without space charge, the harmonic current in the limit of small gap voltages is

$$I_1 = 2I_0J_1(\chi)$$

where

$$\chi = \frac{MV_{gap}e}{m_0c^2\gamma(\gamma^2-1)}\frac{\omega}{v_0}z \quad . \tag{6}$$

The harmonic current has a maximum of 1.164 I_0 at $\chi = 1.84$. As the current is increased, the bunching becomes dominated by the space charge. The current modulation in the small-signal space-charge regime is well known.[3]

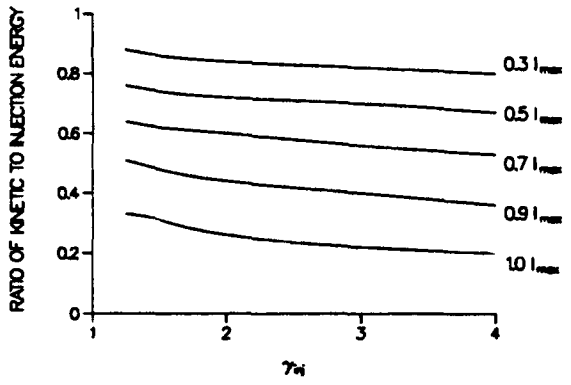


Figure 3. Partitioning of injection energy for different injection energies and beam currents.

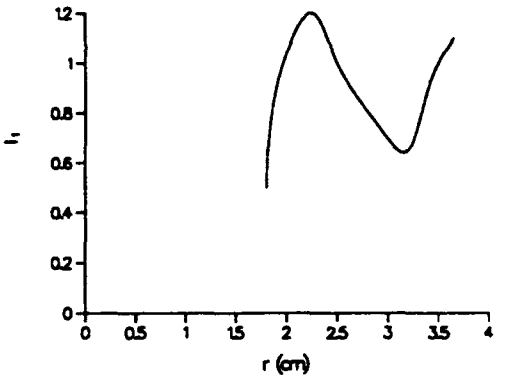


Figure 4. Maximum current modulation as a function of beam radius.

For moderate space charge, increasing the beam DC current will decrease the maximum harmonic content possible. However, for currents close to the space-charge limit, increasing the beam DC current tends to increase the relative harmonic content for large-signal bunching because of the nonlinear slowing of the beam as it bunches. From Eqs. (4) and (5) we see that reducing the beam radius is equivalent to increasing the space charge. In Fig. 4, we plot the maximum current modulation for a 5-kA, 500-keV beam for different beam radii in a 3.65-cm radius pipe.

We see this tradeoff between harmonic current and kinetic energy in the next series of plots, with the beam bunched to 100% fundamental harmonic current ($I_1 = I_0$) in a 1.3 GHz RKA. In Fig. 5, we see the beam profile and longitudinal phase space at a snapshot in time for $r_b = 3.2$ cm. The axial momentum $\gamma\beta_z$ for each particle followed is plotted. The bunch before extraction has $\gamma\beta_z \sim 1.0$, or only about 200 keV of kinetic energy. In Fig. 6, we see the bunch after extraction, with $\gamma\beta_z \sim 0.5$. Because the extraction also slowed the beam, 60 keV of the lost kinetic energy went into the potential energy fields of the beam, and only 90 keV was extracted. This increase in the potential fields results in the low output power of 0.4 GW (18%

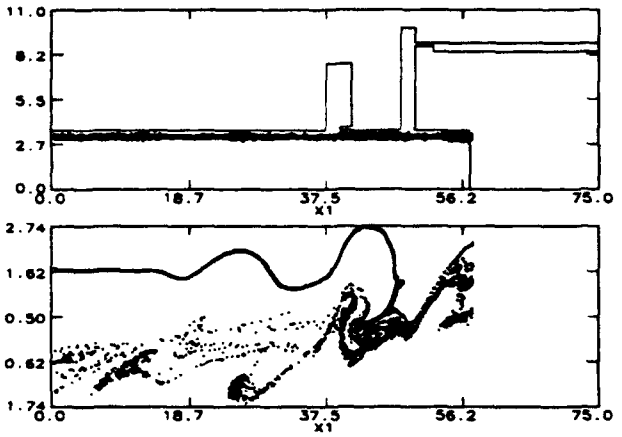


Figure 5. RKA geometry and axial momentum $\gamma\beta_z$ at a snapshot in time with bunch before output cavity, for 100% harmonic current and r_b=3.2 cm.

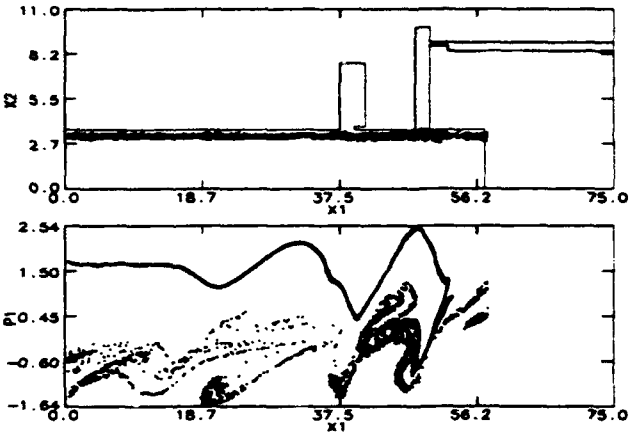


Figure 6. RKA geometry and axial momentum $\gamma\beta_z$ at a snapshot in time with bunch after output cavity, for 100% harmonic current and r_b=3.2 cm.

extraction). Note the shape of the output cavity leads to a low $\frac{R}{Q}$ in order to maintain reasonable cavity resonance while preventing too large an output gap voltage. For this beam radius, the maximum extraction would occur for 70% harmonic current and is only 25%.

Beam Loaded Cavity Model

In this section, we present our small-signal cavity model. We will show that it correctly describes the unloaded and loaded cavity matches.

In the cavity model illustrated in Fig. 2, β is defined as the usual coupling coefficient

$$\beta = \frac{\omega^2 M^2 Q_o^2}{Z_o Z_{cav}}$$

where Z_o is the input waveguide characteristic impedance, Q_o is the cavity unloaded Q, and M is the mutual inductance of the coupling. When the cavity is driven by the external waveguide, the reflected power is given by

$$P_{refl} = \left(\frac{1-\beta}{1+\beta}\right)^2 \quad .$$

The unloaded cavity impedance is calculated by SUPERFISH to be R_{cav}=1.56 (10^5) Ω and the beam impedance is given by

$$R_b = \frac{\gamma(\gamma^2-1)m_o c^2}{I_o} R_o(r) 1.70(10^{-2}) \quad . \tag{7}$$

$R_o(r)$ is shown in Fig. 7 for this 1.3 GHz cavity.[5] The beam capacitance is negligible (it detunes the cavity less than 3 MHz). R_o depends on r because of the large beam pipe radius, which leads to both transit time variations and radial variations in the integrated axial electric field.

In Fig. 8 we see an experimental reflected power profile during an actual pulse. We have a good match for about a microsecond, despite the ragged nature of the beam current and voltage profiles.

The cavity is initially overcoupled; the unloaded coupling $\beta_{no\ beam}$ = 38.2 In Fig. 9 we show the calculated reflected power profile, using a beam radius of 2.8 cm and the actual experimental current and voltage profiles.

RKA Design Modifications

The advantage of the intense-beam regime for the RKA is that it provides for significant nonlinear bunching within only a relatively short distance. The disadvantage is that the potential depression, which provides for the bunching, also limits the beam energy available for extraction, as has been discussed earlier. This limitation becomes worse as the RKA is designed for higher frequencies. If the device is scaled directly

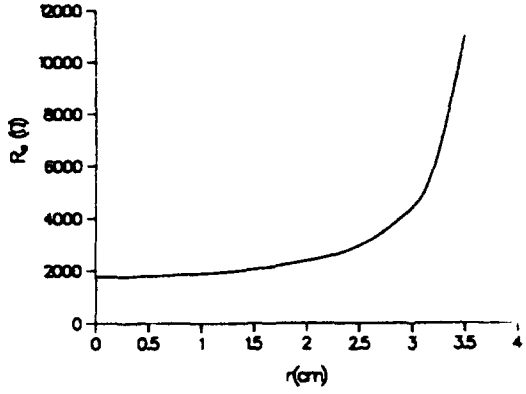


Figure 7. Beam impedance R_o versus radial position.

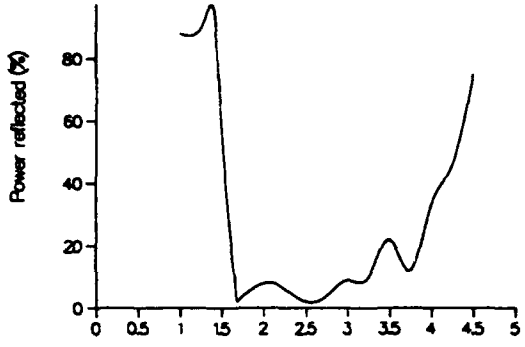


Figure 8. Experimental input-cavity reflected power.

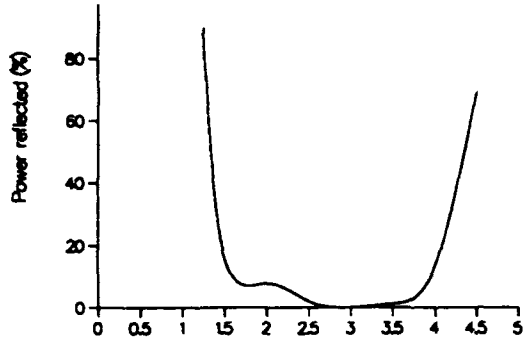


Figure 9. Theoretical input-cavity reflected power.

to the higher frequency, to keep the beam current below the threshold current, the current is reduced as the inverse square of the frequency. This leads to a rapid dropoff in device power. In this section, we will outline two modifications to the standard RKA that can potentially increase its frequency and efficiency range.

The first modification is to modulate the beam at a lower frequency and then extract power at the desired frequency, while maintaining the larger beam-pipe radius corresponding to the cutoff of the lower frequency. This approach is possible because the large nonlinear bunching provides large second and higher harmonic currents. In Fig. 10 we plot the beam current as a function of time at the output cavity, and in Fig. 11 we plot the Fourier spectrum of the beam current. We see that the harmonic current is relatively flat over the first few harmonics. In principle, we could also design input and idler cavities at the higher frequency,[6] but since the desired frequency is above cutoff, it is hard to isolate the cavities. A single cavity is easier to isolate, and if necessary, tailoring of the magnetic field is possible to alter the beam radius. In Fig. 12 we see the mode of a cavity in a tube above cutoff, but its fields are partially isolated by severe undercoupling to the beam-pipe waveguide modes.



Figure 10. Beam current as a function of time at the output cavity. Current units are 1.35 kA.

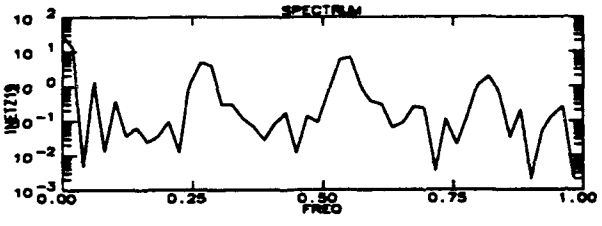


Figure 11. Fourier spectrum of beam current at output cavity. Time units are seconds multiplied by the speed of light.

The second modification uses post acceleration of the beam after bunching to solve the problem of the large potential depression of the beam. Certain RKA designs address this problem by operating in the tenuous limit, such as the 3.0-MeV, 1-kA LLNL-SLAC device.[7] However, these devices require long drift regions to generate significant harmonic current because of the relativistic correction to the ballistic bunching distance. In addition, the low space charge prevents large harmonic currents. These devices are typically

only 20% efficient. By post accelerating the bunched beam, we can preserve the large nonlinear harmonic currents and short bunching distances without losing any of the new beam power to potential depression. In fact, as the bunch is accelerated, its velocity increases and its potential-energy requirements actually decrease. The extraction efficiency of the post accelerated power, limited to one-half the harmonic current multiplied by the post accelerated voltage, can exceed 50% in this regime. In Fig. 13 we show the beam profile and longitudinal phase space at a snapshot in time for a post accelerated beam, with 100% harmonic current. The post accelerating cavity can be inductively tuned to maintain high harmonic current.[4] Note the decreased energy spread of the accelerated bunch. In principle, several alternating post acceleration units and output cavities can be used for maximizing the overall extraction efficiency.

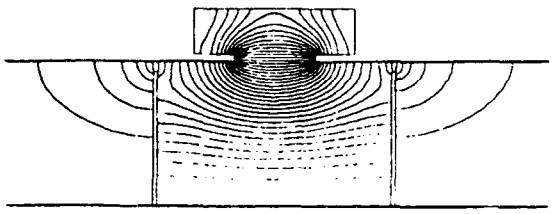


Figure 12. Isolated higher frequency cavity mode, undercoupled to waveguide modes.

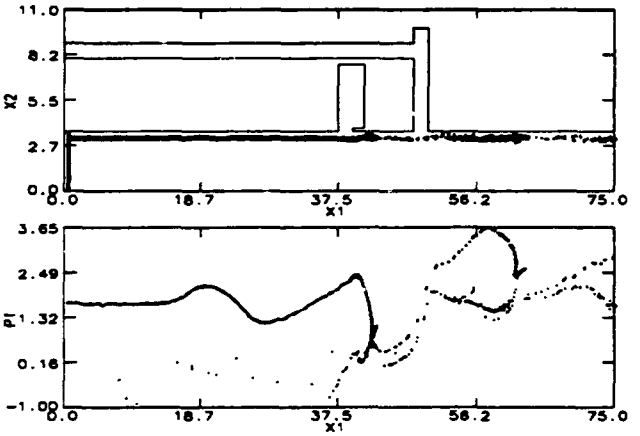


Figure 13. RKA geometry and axial momentum $\gamma\beta_z$ at a snapshot in time with post acceleration.

These two modifications can be used together to provide a two-beam microwave power source for higher-frequency, higher-power accelerators, such as the next linear collider.[8]

Conclusion

We have reviewed basic RKA microwave and intense-beam physics. We have shown the relationship between harmonic current and potential depression. The tradeoff for a 5-kA, 500-keV electron beam leads to a limit of about 35% extraction efficiency at 1.3 GHz for microsecond-long pulses. We have also presented our cavity model, which agrees well with experimental data on reflected power. Finally, we have discussed modifications to the RKA design that allow extraction at higher frequencies and with higher efficiencies. These modifications use the inherent bunching capability of the intense-beam regime but remove the extraction efficiency limitation arising from the large potential-energy requirement.

References

1. J. W. Gewartowski and H. A. Watson, Principles of Electron Tubes, D. Van Nostrand Co., Inc., Princeton (1965).

2. R. B. Miller, An Introduction to the Physics of Intense Charge Particle Beams, Plenum, New York, 85 (1982).

3. M. Friedman, J. Krall, Y. Y. Lau, and V. Serlin,"Externally Modulated Intense Relativistic Electron Beams," J. Appl. Phys., 64 (7), 3353 (1988).

4. B. E. Carlsten, M. V. Fazio, R. J. Faehl, T. J. Kwan, D. G. Rickel, and R. M. Stringfield,"Theory and modeling of a relativistic klystron amplifier with high space charge for microsecond applications," Proc. 1992 SPIE Intense Microwave and Particle Beams III, SPIE Vol. 1629, 57 (1992).

5. R. D. Ryne, *private communication.*

6. M. Friedman and V. Serlin,"Present and Future Developments of High Power Relativistic Klystron Amplifiers," Proc. 1992 SPIE Intense Microwave and Particle Beams III, SPIE Vol. 1629, 2 (1992).

7. G. Westenskow, J. Boyd, T. Houck, D. Rogers, and R. Ryne, "A Chopper Driven 11.4 GHz Traveling-Wave RF Generator," Proc. 1991 IEEE Part. Accel. Conf., IEEE Catalog No. 91CH3038-7, 646 (1991).

8. A. Mondelli, "Linear e^+-e^- Colliders Above 1 TeV (CM)," Proc. 1991 IEEE Part. Accel. Conf., IEEE Catalog No. 91CH3038-7, 3261 (1991).

A PROPOSED EXTENDED CAVITY FOR COAXIAL RELATIVISTIC KLYSTRONS

L. Schächter, T.J. Davis, and J.A. Nation

Laboratory of Plasma Studies & School of Electrical Engineering

Cornell University, Ithaca, NY 14853, USA

Abstract

The quality factor of a coaxial klystron cavity is relatively low due to the coupling to the TEM mode which can propagate in the annular channel. This leads to low efficiency, especially at high frequency, e.g., X-band. To mitigate this effect we replace the usual cavity with an extended length, active cavity. The cavity consists of either a coaxial structure partially loaded with dielectric material or with a periodic structure. The interaction of the electrons is with the TM_{01} mode within the cavity, which extends over several wavelengths. Outside the loaded section only the TEM mode can exist. At the boundaries the TM_{01} mode and the TEM mode are coupled therefore part of the power gained by the former mode is transferred to the TEM mode in the channel. One of the advantages of this system is the fact that the interaction length is larger than the wavelength, the local electric field intensity lower and therefore the breakdown probability is reduced. A theoretical analysis of the device is discussed including analytical and simulation work. Typical results for a 7 kA, 400 kV beam show an equivalent gain of 1 dB/cm can be expected at 9 GHz.

Introduction

Among high power microwave sources the relativistic klystrons have attracted significant attention recently. At SLAC a relativistic version of the conventional klystron has been built and tested [1]. This device consists of a waveguide loaded with "pill-box" cavities which operate at $11.4GHz$ ($1MV$ and $1kA$ pencil beam). The ouput RF reported was $290MW$. The other successful experiment was performed at NRL [2] . In this experiment, a relatively large waveguide was loaded with two coaxial cavities both tuned at the same frequency, $1.3GHz$. An annular beam ($500kV$, $16kA$ and $100ns$) propagates in the close vicinity of the waveguide's wall. For an input RF power, in the first cavity, of about $100kW$, the output power reported was of order of $3GW$. A similar experiment with a longer electron pulse ($1\mu s$) was performed at Los Alamos [3]. The advantage of the SLAC experiment is the higher frequency which makes it favorable for acceleration applications; but it suffers from pulse shortening and vacuum breakdown near the cavity gaps. On the other hand, in the NRL experiment, the so called "electrostatic insulation" near the gaps of the cavities seems to eliminate the breakdown problem. Furthermore, the space charge effect and the proximity to the limiting current cause an efficient current bunching which leads to increased RF generation. However these two effects have only been demonstrated so far at $1.3GHz$

and partially at $3.5GHz$; scaling the device to higher frequencies (X-band and beyond) may not be straightforward in the same configuration. The problem is that the power carried by the electron beam and the operating RF frequency for a single mode, impose conflicting requirements on the radius of the structure. It is however possible to release the constraint which forbids modes to propagate in the drift tube. In this case, one has two possibilities: (1) a multi mode waveguide or (2) coaxial structure which can be designed to have (dominantly) only the TEM mode. In either case, the quality factor Q of any cavity becomes small, and as a result, the bunching process is inefficient. Here we present a possible solution of these conflicting requirements. The essence of our suggestion is to increase the quality factor using the interaction process in an extended cavity which is a short section of a slow wave structure. At this stage of "proof of principle" we consider a dielectrically loaded structure since it provides the main features of a slow wave structure and it is easier to analyze, design and manufacture. For very high power levels however one should resort to metallic periodic structures.

Analytical Work

We consider a section of a slow wave structure in which the electrons interact with a TM mode along several wavelengths - see Fig.1. The dispersion relation was calculated analytically for an infinitely long structure. The structure's parameters were designed such that the first symmetric TM mode, at $9GHz$, is synchronous with a $400kV$ electron. This implies that $R_{ext} = 5.56cm$, $R_{int} = 3.18cm$, $R_{d,int} = 3.75cm$ and $R_{d,ext} = 4.95cm$; $\epsilon = 2.6$. Fig. 2 illustrates the wavenumbers of the first 5 modes; the evanescent modes are illustrated since they play a crucial role in the reflection process at the both ends of the cavity. When considering the full electromagnetic problem we assumed that only the TEM mode exists in the coaxial channel and the first 9 modes in the extended cavity were used for matching the boundary conditions at the two ends (the TEM mode and 8 symmetric transverse magnetic modes). The transmission and reflection coefficients as a wave is injected into the coaxial channel, in the absence of the beam, have been calculated analytically. In Figure 3 the former is illustrated versus the frequency for $L = 16.5cm$, $\rho_{ext} = 4.85cm$ and $\rho_{int} = 3.85cm$.

Electrons injected into a structure generate spontaneous radiation which preferentially leaves the system at the frequencies near the constructive interference peaks (e.g. Ref. 4-6) illustrated in Fig.3. If one of the peaks is located close to the resonance frequency ($V_{ph} = V_{electron}$), then the noise at that frequency is dominant and so is the stimulated emission when a wave is launched. The length of the structure for the transmission coefficient illustrated in Fig.3 was chosen such that the peak in the transmission

(approximately) coincide with the resonant frequency. The bunching process in such a cavity is illustrated in Fig. 4 where we present the phase space at $t = 64ns$ when the other relevant parameters are: pulse length $80nsec$, the initial amplitude of the electric field is $5MV/m$ and the current is $7kA$. In this regime the system is well above the threshold condition. The quasi-analytic calculation in this case is based on a set of equations which has been developed in Ref. 7. The first electrons entering the cavity are not bunched (we ignore the effect of the pulse front). The unbunched electrons enter at $z = 0$; they are gradually getting bunched. The bunching amplitude starts from zero at $z = 0$ and it reaches "spatial steady state" value after about 30% of the interaction region. This value is determined by the amplitude of the electric field (E_z) in the cavity. As the intensity of the field increases in time, it takes the electrons more space to reach this level. The interaction along this extended cavity causes an effective bunching of the beam.

Simulations

Many of the analytical results have been confirmed using the particle–in–cell code MAGIC. The code is fully electromagnetic and assumes only azimuthal symmetry. The simulation beam parameters, structure dimensions, and diagnostic methods all match those of the analytic analysis and the experimental program. The drift tube is terminated by absorbing boundaries to eliminate any feedback from the substantial drift tube radiation. By simply launching a beam through the extended length cavity (no input RF), we can obtain the structure resonances and compare them to simple analytic predictions. Fig. 5 shows the FFT of a magnetic field diagnostic located just downstream of the cavity at the outer drift tube wall. The diagnostic thus measures radiation coupled from the cavity as well as space charge fields from the beam. The resolution of the FFT is 10 MHz, and demonstrates the sharp and separated resonances arising from the different axial cavity modes. These sharp resonances are obtained for a cold beam with no variation in voltage and current over time; real beams, whose waveforms vary with the driving voltage pulse, will broaden the resonances. By neglecting the coaxial channel the resonant frequency is calculated analytically to be 9.06 GHz for a 16 cm long cavity. The simulation resonance of 8.92 GHz thus represents a frequency shift of about 140 MHz due to the presence of the cavity apertures and also indicates some beam loading.

An external drive source provides us with a better selection ability of modes in the cavity. This can be modeled in MAGIC easily with a section of coaxial line coupled to a slot in the cavity wall. A schematic of this, together with a typical beam trajectory

plot, is shown in Fig. 6. A portion of the 100 kW power launched in the coaxial line is coupled through the slot and drives the selected cavity resonance, and thus provides a rather simple and effective model of a real coupler. By selecting the input frequency to match the 8.9 GHz mode, the same magnetic field diagnostic shows a drastically improved output spectrum. A substantial amount of power in the cavity is also coupled out through the slot, and is calculated to be above 50 MW.

The use of a drive source does not alter the magnitude of the output signals, only the frequency content. This could be due to a saturation mechanism, as may be indicated by the strong phase space variation of the particles in Fig. 7. Note that the momentum spectrum shown in Fig. 4 is averaged over a cycle and only the envelope is comparable with that in Fig. 7. It may be necessary to decrease the length of the cavity or arrange multiple cavities in ways to increase the magnitude and quality of the output radiation. However, simulations also measure a decrease in total beam power of over 600 MW over the 16 cm interaction length, and thus the focus of our program is developing the most efficient conversion and coupling methods to make this a useful device.

Experiment

The experimental program is described in elsewhere in these proceedings [8]. We have been able to measure the frequency and separation of the cavity resonances, and by the use of an X-band magnetron, drive the chosen resonance to improve the quality of the output spectrum. We are currently calibrating the system to obtain a measure of the output RF power. We have also observed a shortening of the RF build-up time of about $15nsec$ when the magnetron was turned on.

Summary

In conclusion, we have introduced the concept of the extended cavity which incorporates in one device the advantages of a traveling wave tube and a relativistic klystron. A coaxial single stage cavity loaded with a dielectric material was analyzed. The dispersion relation was obtained analytically and so were the expressions for the reflection and transmission. The phase-space picture in the interaction region indicates that the bunching of the beam is efficient. Both particle in cell code (MAGIC) and preliminary experiments confirm the designed parameters using the analytical theory.

Acknowledgements

This work is supported by the U.S. Department of Energy. The MAGIC code was obtained from Mission Research Corporation.

References

[1] M.A. Allen et.al; Phys. Rev. Lett. **63**(22) (1989).

[2] M. Friedman, J. Krall, Y.Y. Lau and V. Serlin; J. Appl. Phys **64**(7), 3353(1988).

[3] M.V. Fazio *et. al.*; "Intense Microwave and Particle Beams III" SPIE Proceedings, Vol. 1629 ,20-24 January Los Angeles 1992.

[4] L. Schachter, J.A. Nation and G. Kerslick, J. Appl. Phys. **68**, 5874(1990).

[5] D.A. Shiffler *et. al.*, J. Appl. Phys. **70**(1), 106(1991).

[6] L. Schachter, J.A. Nation and D.A. Shiffler;J. Appl. Phys. **70**(1), 114(1991).

[7] L. Schachter and J.A. Nation; to be published in Physical Review A.

[8] T.J. Davis *et. al.*, see these proceedings of Beams '92.

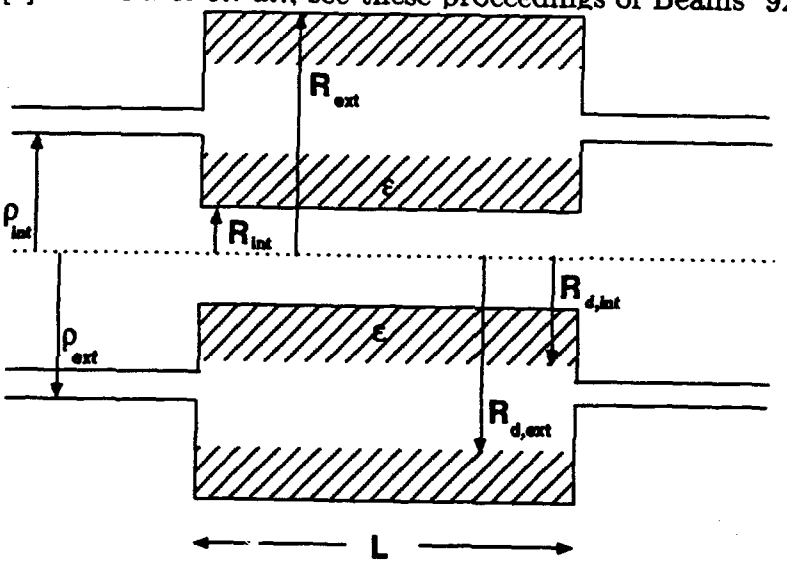


Fig. 1:Schematic showing the coaxial extended cavity system. At the operating frequency, only the TEM and the first TM_{01} mode can propagate in the cavity whereas in the coaxial channel the TEM mode alone propagates.

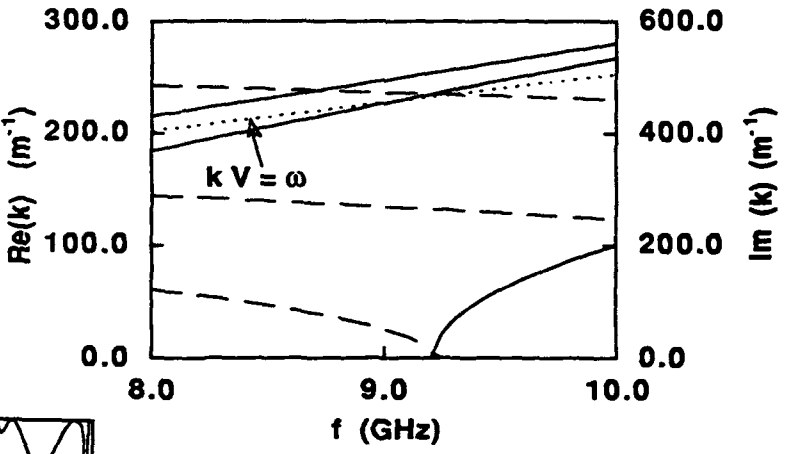


Fig. 2: The dispersion relation for an infinite section of a dielectrically loaded coaxial line. Three of the evanescent waves are also plotted (dashed line); they play an important role matching the boundary conditions at the two ends of the cavity.

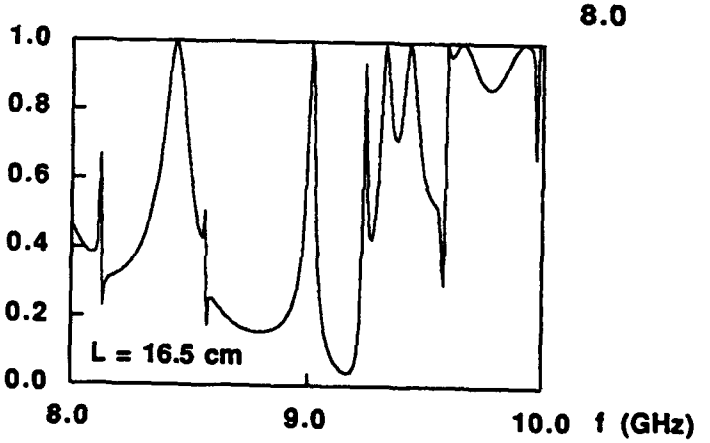


Fig. 3: The absolute value of the transmission coefficient, $|\tau|$, as a function of the frequency .

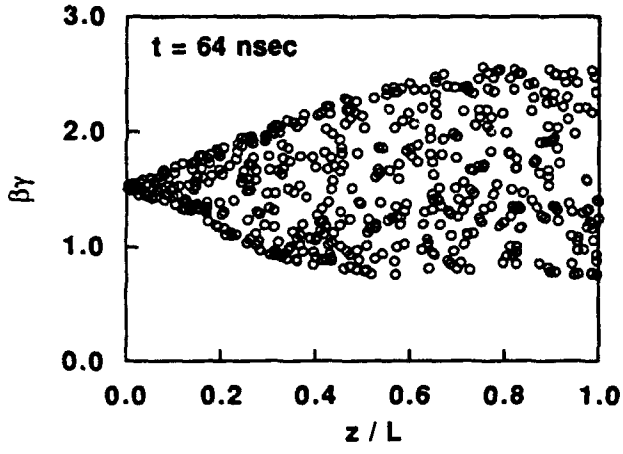


Fig. 4: The phase space distribution in the interaction region at $64nsec$. The increase in the momentum distribution is evident.

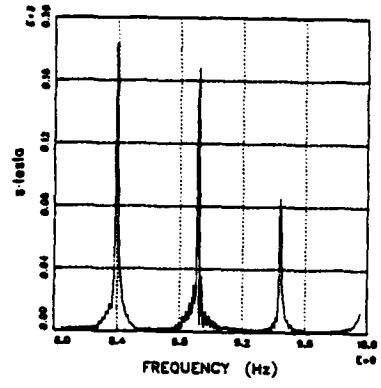


Fig. 5: Simulation FFT of magnetic field diagnostic downstream of the cavity, showing sharply defined and separated resonances due to constructive interference at various frequencies.

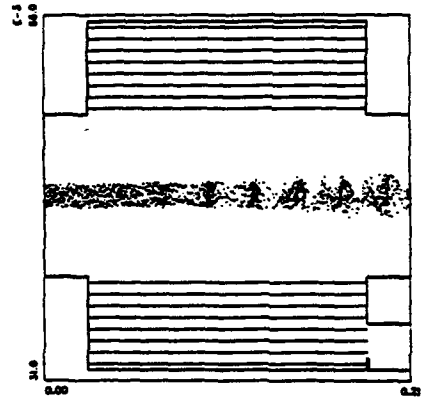


Fig. 6: Geometry of slotted cavity with beam trajectory in a typical simulation.

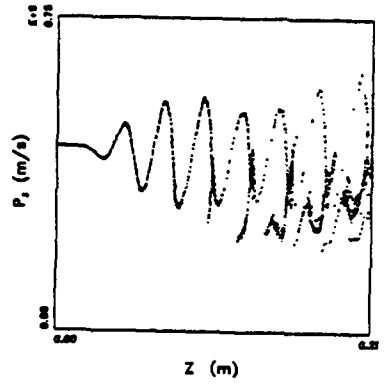


Fig. 7: Phase space plot of electrons through the interaction region.

RELATIVISTIC HIGH POWER KLYSTRONS

A.N.Sandalov, V.M.Pikunov, V.E.Rodiakin, A.A.Stogov
Physics Department, Moscow State University
Moscow, 119899 Russia

Abstract

The design and the first testing of relativistic klystrons amplifier (RKA) with the efficiency of 40-50% for realization on intense electron beams with beam energy 400 keV are presented.

Theoretical investigations of RKA have been made by 1D, 1.5D and 2.5D PIC codes. The self-field structure of relativistic electron bunch is numerically studies from these codes.

Theory and Modeling

A high beam voltage gives significant changes of nonlinear bunching process in electron beams. There is nonsymmetrical velocity modulation for accelerated and decelerated particles when its come through idler cavities [1]. The high beam voltage increases the total device length, and made more complicated electron beam transmission line and up grade the influence of 2D bunching effects.

An important relativistic effect connected with the relativistic electrons velocity in RKA, is an excitation of rotational space-charge fields for that div $\vec{E}_c$ = div $\vec{H}_c$ = 0. Rotational fields ($\vec{E}_c$, $\vec{H}_c$) with potential Coulomb fields E_q (rotE_q = 0) that are analogous for rested charges, create wake fields of electron beams. Fig.1 presents the results of calculations of homogeneously charged "charge groups" wake fields. We assume that the particle is a disk with radius r and thickness D, and it moves through the RKA drift tube with the kinetic electron energy equal to V = 1 MeV [2]. Similar "charge groups" are very often used in computer simulation of nonlinear electron-wave interaction phenomena at RKA.

On fig.1a equipotential lines φ of Coulomb field excited by electron bunch are presented. On the fig.1b force lines of Coulomb field $E_q = -grad\ \varphi$ are presented. The location of force lines of potential part of wakefield is independent of

bunch movement velocity and is similar to the rest charge force lines picture. The E_q localization region is determined by the Coulomb forces action radius $r_q = r_T/\mu_{01}$, where r_T - drift tube radius, μ_{01} - 1-st root of Bessel function $J_0(\mu_{01})=0$. As against to E_q, rotational field have both electrical $\{E_{cr},0,E_{cz}\}$ and magnetic $\{0,H_\varphi,0\}$ components. On the fig.1c electrical component of rotational field force lines and on fig. 1d - magnetic field lines levels are presented. The graph of rotational field depends on charge movement velocity, however, the radius of localization remains equal to r_q. Bunch force lines of total electric field $E=E_q+E_c$ are shown on fig.1e. Radius of E field localization depends on electron's movement velocity and is equal r_q/γ, i.e. decreases in γ times in comparison with the radius of space charge Coulomb forces influence ($\gamma=1+V$ [MeV]/0.511 - relativistic Lorentz factor). Fig.1f and 1g present a distribution of longitudinal and radial components of electric field from longitudinal coordinate.

The maximum of E_r amplitudes depending on bunch thickness and for the infinitely thin bunch exceeds a E_{qr} amplitude value for rested bunch in γ times. The increasing of bunch movement velocity goes to the decreasing of field E_z amplitude in comparison with E_{qz}.

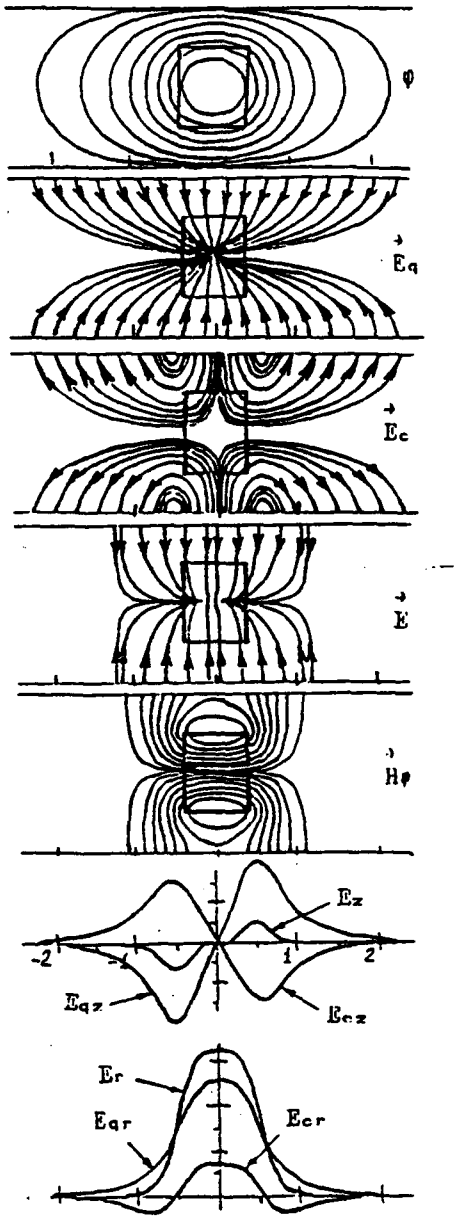


Fig.1. Relativistic bunch wakefield distribution.

The energy, which is concentrate in longitudinal, radial and azimuthal components of electric and magnetic fields of wakefield for infinitely thin bunch are: $W_z^{(e)}=\frac{1}{2\gamma}W_0$, $W_r^{(e)}=\frac{\gamma}{2}W_0$, $W_\varphi^{(h)}=\frac{\gamma^2-1}{2\gamma}W_0$, where W_0- energy of rest disk Coulomb field. The infinitely thin disk wakefield the total energy exceeds the Coulomb field ones in γ times.

The pointed out features of relativistic particles electromagnetic fields play a significant role in an electron bunching process and must been taken into account in investigation of relativistic powerful klystron amplifiers.

The most complicated RKA problem is energy beam extraction. The single-gap output structure gives to a significant RF pulse duration shortening , which is connected with RF breakdown due to large energy concentration in output section. The overcoming of these difficulties is possible by means of distributed output structure , as double or four-gap coupled cavity (fig.2a,b). For X band the periodical super dimensional waveguide with distributed RF extraction system may be used. Besides the damping of parasitic oscillations by absorbers is an important too and we suggest the "Samovar" output structure which is shown on fig.2c [3].

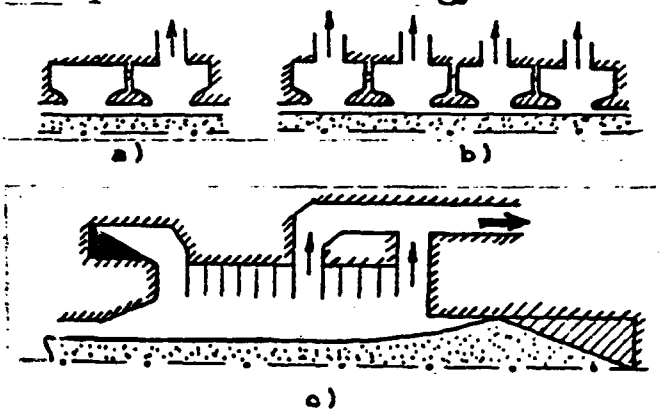


Fig.2. Output structures.

The high efficiency RKA comes only under careful analysis of nonlinear interaction phenomena of all klystron parts: electron gun, linear and nonlinear bunchers, output structure and collector. For these purposes the computer codes "Klystron" [4], "Arsenal" [5] and "Multiwaves" [6] were performed at MSU. "Klystron" based on 1-1.5D disk-ring model of electron beam and is used as the first step of klystron design [3]. The 2.5D PIC code "Arsenal" allows to analyze klystrons, containing thermionic and field-emission electron guns, linear and nonlinear bunchers,

distributed output structures, conventional and depressed collectors. This code is based on the self-consistent analysis of charged particles dynamics in electromagnetic fields, representation of electron beam by "charge groups" and modified Galerkin's method for Maxwell equations solution [7]. The computer code "Multiwaves" helps to investigate the dispersion characteristics of electromagnetic and electron waves, electromagnetic fields structures, RF breakdown phenomena and self-excitation of parasitic oscillations of different output structures.

All that technic was used for MSU relativistic klystrons design.

Testing and experimental results

Three RKA have been designed and fabricated at MSU (table I.).

Tab. I. Relativistic klystrons design parameters

	KMT-1	KMT-2	KMT-3
Beam Voltage, kV	400	400	400
Beam Current, A	700	300	200
Microperveance	2,77	1,18	0,79
Voltage Pulse Duration, μsec	1,5	1,5	0,12
Beam Diameter, mm	15	10	6
Drift Tube Diameter, mm	25	25(15)	8
Total length, cm	92	91	28
Efficiency, %	25	50	50
Frequency, GHz	2,85	2,85	9,4
Cathode Type	f.e.	f.e.	d.e.
Focusing	solenoid	solenoid	solenoid

The klystron KMT-1 was designed for beam voltage 1 MV and beam current 500 A and had four bunching and two output cavities

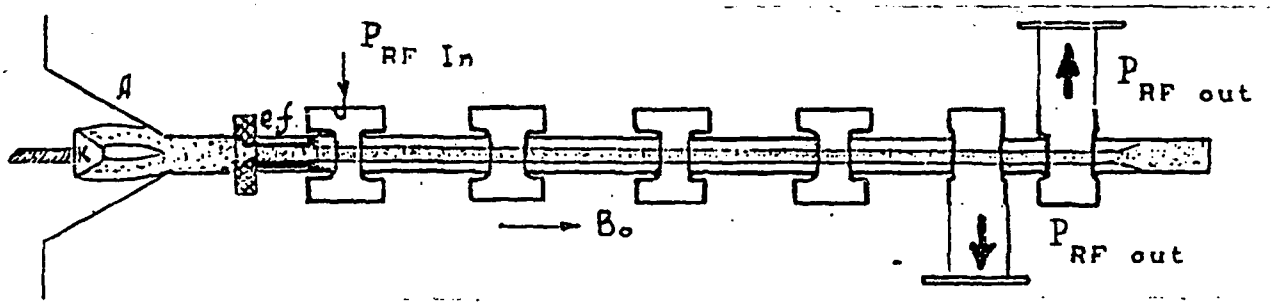


Fig.3. Diagram of KMT-1 relativistic klystron.

(fig.3). Bunching cavities are toroidal, output ones - two pieces

of waveguide 72×34 mm with reduction capacity in the center of cavity and connection with output waveguide through inductive iris diaphragm. KMT-1 klystron was tested on HCA "Luch" (INP TPU, Tomsk) in 1985 [8]. There was obtained RF power amplification 26 dB. The experiments of KMT-1 were carried out at the beam voltage 400 kV and beam current 700 A. The typical oscillograms of beam voltage , magnetron drive power - and output RF power pulses are shown on the fig.4. The transverse structure of electron beam, formed by conical coaxial diode, for different value of guiding magnetic field 2,5; 10 and 15 kGs was studied. The current density was determined by the current difference, which are coming on Faradey Cup placed behind the anode diaphragm with different hole radius. Discontinuity of current density distribution was 50% for r ≤ 4 mm. For r ≥ 4 mm there were observed layer structure of electron beam, which has weak dependence from magnetic field value.

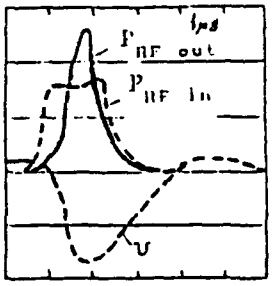


Fig.4.

Obtained dependencies of beam current from guiding magnetic field value for the holes of anode diaphragm 6, 8 and 10 mm have the similar character. For H ≥ 10 kGs the beam current practically had no changes. For improving beam quality we tested emittance filter (ef) as pipe with 8mm diameter and length 120 mm with anode diaphragm 8mm. It was observed, that it play important role for H ≤ 1 kGs only. For higher magnetic field electron beam became magnetized and influence of emittance filter is negligible.

Analogous tests were made for diode with flat cathode with 10 mm diameter. In this case the emittance filter act in all range of focusing magnetic fields, decreasing beam current twice. For the high efficiency RKA one of the possibility may be using of multi-beam electron gun [9].

The experiments on the klystron KMT-1 have shown, that obtained electron beam parameters are non-optimal for this klystron construction. Besides the restriction of output RF power was observed, which is probably comes from RF breakdown in the output cavity and also high beam loading in input cavity be found.

So a new version of klystron - KMT-2 (fig.5) was fabricated.

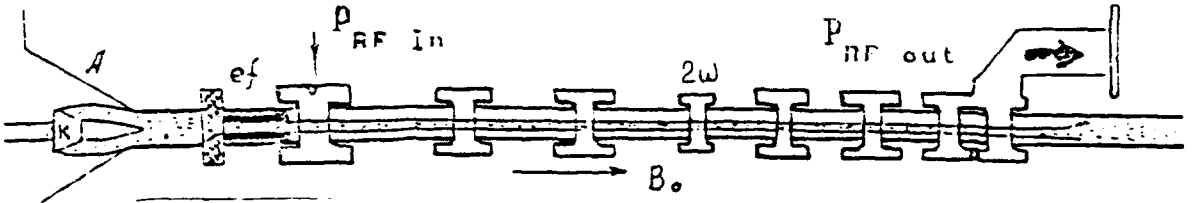


Fig.5.Diagram of KMT-2 relativistic klystron.

KMT-2 has six bunching cavities, one of which is second harmonic cavity. For decreasing of RF breakdown probability output system of KMT-2 was made as double-gap cavity.

The RKA X band KMT-3 (fig.6) was made for testing on the

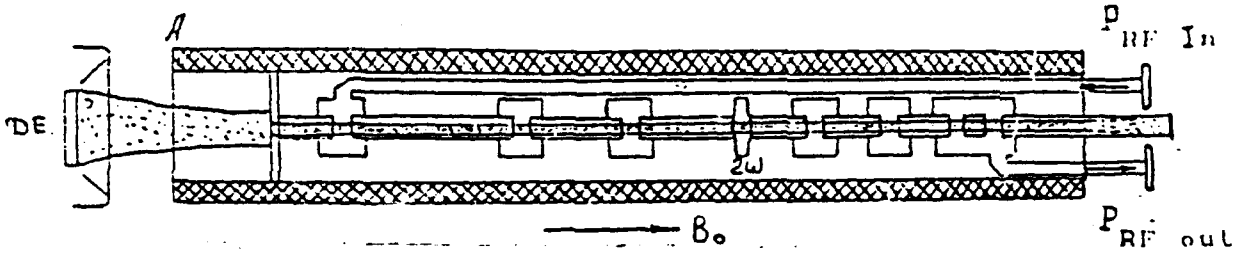


Fig.6. Diagram of KMT-3 relativistic klystron

LIA with dielectric emitter (d.e.)[10]. KMT-2 and KMT-3 relativistic klystrons will be tested this autumn.

Acknowledgment

The authors are thankful to Dr. A.P.Arzin, Dr. Yu.G.Shtein and Dr. A.S.Sulakshin for great help in carrying out experiments on the HCA "Luch" .

References

1. Sandalov A.N., Terebilov A.V.// Radio Engineering and Electron Physics. V.27, N.9, 1983. Sandalov A.N., Terebilov A.V., Vasiliev E.I. Proc Beams'86, Kobe, 1986,p.566.
2. Pikunov V.M., Rodiakin V.E., Sandalov A.N. All-Union school on "Microwave and Physics Application", 1991.
3. Sandalov A.N., Pikunov V.M. LC-91, Protvino, september 1991.
4. Sandalov A.N. in book: Generators and amplifiers on relativistic electron beams // MSU, 1987, p.28.
5. Rodiakin V.E., Sandalov A.N. // in book: Voprosy electronnoi tekhniki. Saratov, 1988, p.28.
6. Luzianin D.B., Pikunov V.M. // Radio Engineering and Electron Physics. V.36, N.1, 1991.
7. Pikunov V.M., Rodiakin V.E., Sandalov A.N. All-Union school on "Microwave and Physics Application", 1991.
8. Sandalov A.N., Stogov A.A., Shtein Yu.G.//The 10th All-Union Conf. on microwave electronics., 1986.
9. Artiukh I.G., Sandalov A.N., Sulakshin A.S. et al// Obzory po electronnoi tekhnike. s.1, v.17(1490), 1989, 70p.
10. Isakov P.Ya., Tomskikh O.N., Furman E.G.//7th All-Union simp. of high current electronics, Tomsk, 1988, v.2, p.127.

A NONLINEAR THEORY OF ENERGY AND CURRENT MODULATION IN RELATIVISTIC KLYSTRON AMPLIFIERS

Han S. Uhm
Naval Surface Warfare Center
10901 New Hampshire Ave., White Oak
Silver Spring, Maryland 20903-5000

A self-consistent nonlinear theory of the energy and current modulation in a relativistic electron beam propagating through a klystron amplifier is developed. A closed integro-differential equation for the beam current is obtained, assuming that the beam current is a function of time t and propagation distance z. Properties of the current and energy modulation are investigated from this integro-differential equation for a broad range of system parameters. Magnitudes of the energy and current modulation are determined in terms of the gap voltage, the cavity frequency, geometric configuration, the beam intensity and initial kinetic energy of the beam. The modulation amplitude increases, reaches peak and decreases slowly, as the beam propagates through the amplifier.

When a segment of an electron beam pulse passes through the opening of a microwave cavity, this beam segment gains or loses energy, depending on the sign of the gap voltage appeared on the cavity opening. The gap voltage originates from the externally driven microwaves. This one-time energy gain (or loss) in a single cavity klystron increases (or decreases) this segment velocity, modulating the beam current in the downstream region. The current modulation developed in the downstream initiates to generate a self-electric potential, which propagates with the beam, and further influences the beam energy and current. This self-electric field depends strongly on the geometric configuration and on the beam intensity.

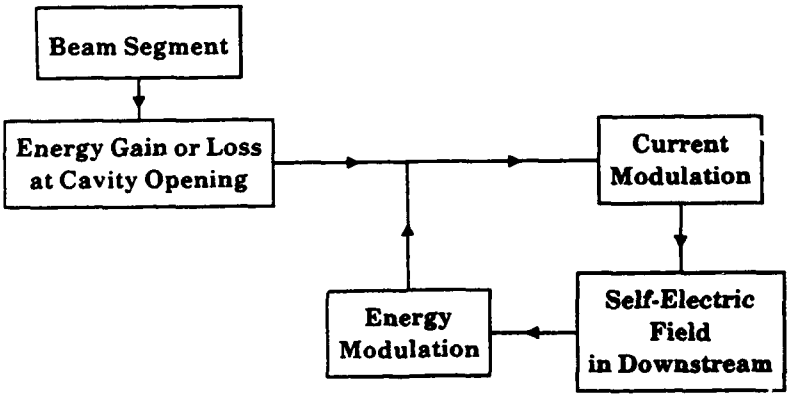


Fig. 1. A block diagram of self-consistent nonlinear theory.

Shown in Fig. 1 is a block diagram of the nonlinear theory developed in this article. The closed loop in the diagram represents self consistence, which ensures a fully self-consistent nonlinear theory.

The axial electric field appearing at the opening of a microwave cavity is a function of time and of geometrical configuration. When a segment of an electron beam pulse passes through the cavity opening, this beam segment gains or loses energy, according to the sign of the gap voltage appeared on the opening. The energy gain $\Delta\gamma mc^2$ of the segment, which passes the cavity opening at time $t = t_0$, is thus given by

$$\Delta\gamma = -e\frac{\Delta\phi}{mc^2}\sin\theta, \tag{1}$$

where $\Delta\phi$ is the maximum gap voltage at the opening, the parameter $\theta = \omega t_0$, ω is the cavity resonance frequency, c is the speed of light in vacuum, and -e and m are the charge and rest-mass of electrons, respectively. In obtaining Eq. (1), we assume that the time profile of the gap voltage is sin θ.

Any charge and current deviations from their equilibrium values will generate the axial component $E_z(r,z,t)$ of the perturbed electric field in the downstream. This perturbed electric field is related to the charge density $\rho(r,z,t)$ and the axial component $J_z(r,z,t)$ of the current density by

$$\begin{aligned}\frac{1}{r}\frac{\partial}{\partial r}\left(r\frac{\partial}{\partial r}E_z\right) + \frac{\partial^2}{\partial z^2}E_z - \frac{1}{c^2}\frac{\partial^2}{\partial t^2}E_z \\ = \frac{4\pi}{c^2}\frac{\partial}{\partial t}J_z + 4\pi\frac{\partial}{\partial z}\rho,\end{aligned} \tag{2}$$

where r is the radial coordinate from the axis of symmetry. The propagation distance z is related to the present time t and the time t_0 by

$$z = \int_{t_0}^{t} c\beta(t')\,dt', \tag{3}$$

where βc is the instantaneous velocity of the beam segment labeled by t_0. Thus, eliminating the variable t in favor of t_0, all of the physical quantities are described in terms of r, z, and θ. In this context, we approximately find

$$\frac{\partial J_z}{\partial t} = \omega\left(\frac{\partial J_z}{\partial\theta}\right)_z = -\beta^2 c^2\frac{\partial\rho}{\partial z}. \tag{4}$$

Therefore, the electric field in Eq. (2) is expressed as

$$\frac{1}{r}\frac{\partial}{\partial r}\left(r\frac{\partial}{\partial r}E_z\right) + \frac{1}{\gamma^2}\frac{\partial^2}{\partial z^2}E_z = -\frac{4\pi\omega}{\beta^2\gamma^2c^2}\left(\frac{\partial}{\partial\theta}J_z\right)_z. \tag{5}$$

Assuming that the radial variation of the axial electric field dominates its axial variation, which is common in the relativistic klystron application, we can neglect the term proportional to $(\partial^2/\partial z^2)$ in Eq. (5). For convenience in the subsequent analysis, we define the instantaneous normalized-beam current $F(z,\theta)$ by

$$F(z,\theta) = \frac{2\pi}{I_b}\int_{R_0}^{R_c} rJ_z(r,z,\theta)\,dr, \tag{6}$$

where R_c is the drift tube radius in the downstream region and R_0 is the inner cylinder radius in the case when the beam propagates through coaxial cylindrical conductors. In order to find the axial electric field $E_z(r,z,\theta)$, we solve Eq. (5) for either a solid beam or a hollow beam. After carrying out a straightforward algebra, we find the average axial electric field $E(z,\theta)$

$$E(z,\theta) = 2G(a)I_b\frac{\omega}{\beta^2\gamma^2c^2}\left(\frac{\partial F}{\partial\theta}\right)_z, \tag{7}$$

which exerts on beam electrons. In Eq. (7), G(a) is the geometric factor of the configuration, i.e.,

$$G = \begin{cases} \ln(R_c/a) + 0.25, & \textit{solid beam,} \\ \ln(R_c/a), & \textit{hollow beam,} \\ \ln\left(\dfrac{R_c}{a}\right)\dfrac{\ln\left(\frac{a}{R_0}\right)}{\ln\left(\frac{R_c}{R_0}\right)}, & \textit{for coaxial cylinders,} \end{cases} \tag{8}$$

where a is the beam radius. Here, the first two geometrical factors are for an electron beam propagating through a drift tube and the last one is the geometric factor of a beam propagating through a coaxial cylindrical conductor.

Velocity modulation of the beam segment labeled by t_0 is obtained from

$$m\beta c\frac{d}{dz}(\gamma\beta c) = -eE, \tag{9}$$

with the boundary condition

$$\gamma_0(\theta) = \gamma_b - \frac{e\Delta\phi}{mc^2}\sin\theta, \tag{10}$$

where E is the average axial electric field in Eq. (7) and γ_b is the initial relativistic mass factor of electrons before they pass through the cavity opening. Substituting Eq. (7) into Eq. (9) and making an approximation that the instantaneous velocity βc in the average electric field E in Eq. (7) is reasonably close to the initial beam velocity $V_b = \beta_b c$, we obtain the relativistic mass factor $\gamma(z,\theta)$

$$K = \frac{\gamma-1}{\gamma_b-1} = 1 - \frac{\epsilon}{\gamma_b-1}\sin\theta + \frac{S}{\gamma_b^2(\gamma_b-1)}\int_0^\zeta d\zeta'(\partial F/\partial\theta)_{\zeta'}, \tag{11}$$

where the integration along ζ for a specified beam segment θ is carried out in a straightforward manner. In Eq. (11), $\zeta = \omega z/V_b$, $\epsilon = e\Delta\phi/mc^2$, $S = 2\nu G(a)$ and $\nu = -eI_b/m\beta_b c^3$ is the Budker's parameter.

The instantaneous velocity $\beta(\zeta,\theta)c$ of the beam segment θ is expressed as

$$\frac{\beta_b}{\beta} = 1 + \frac{\gamma_b - \gamma}{\gamma_b(\gamma_b^2-1)}, \tag{12}$$

where $\beta_b c$ is the beam velocity at the injection point. Making use of the velocity definition $dz/dt = \beta c$ and the definition $\varphi = \omega t$, we obtain the relation

$$\varphi - \theta = \int_0^\zeta (\beta_b/\beta)\, d\zeta, \tag{13}$$

where $\zeta = \omega z/\beta_b c$. The beam current at the cavity entrance located at $z = 0$ is a constant value of I_b. Remember that the beam segment t_0 passed the cavity opening of $z = 0$ at time $t = t_0$. When this segment arrives at z in time t, it is stretched by a factor of dt/dt_0. Thus, the beam current of the segment t_0 at z is proportional to the factor of $d\theta/d\varphi$. In other words, the normalized current $F(\zeta,\theta)$ is proportional to $d\theta/d\varphi$ i.e., $F \approx d\theta/d\varphi$. The ratio F of the current $I(\zeta,\theta)$ to the input current I_b is therefore expressed as

$$F(\zeta,\theta) = \frac{I(\zeta,\theta)}{I_b} = \frac{N(\zeta)}{|d\varphi/d\theta|}, \tag{14}$$

where the normalization constant N is defined by

$$\frac{2\pi}{N(\zeta)} = \int_0^{2\pi} |d\theta/d\phi| d\theta. \tag{15}$$

The normalization constant $N(\zeta)$ ensures the charge conservation. Substituting Eqs. (11)-(13) into Eq. (14) finally gives

$$\frac{N(\zeta)}{F(\zeta,\theta)} = \left|1 + \frac{\epsilon}{\gamma_b(\gamma_b^2-1)}\zeta\cos\theta - \frac{S}{\gamma_b^3(\gamma_b^2-1)} \cdot \int_0^{\zeta} dy \int_0^{y} dx \frac{\partial^2}{\partial\theta^2} F(x,\theta)\right|, \tag{16}$$

with initial condition $F(0,\theta) = 1$. Equations (11) and (16) are main results of the nonlinear theory in the article. Once the normalization current $F(\zeta,\theta)$ in Eq. (16) is determined in terms of the time t_0 and the propagation distance z, the energy modulation in Eq. (11) is calculated from the current modulation. The current modulation in Eq. (16) is a partial integro-differential equation with independent variables ζ and θ. For specified values of the physical parameters ϵ and S ,and the injection energy (γ_b), this integro-differential equation can be solved by a numerical method.

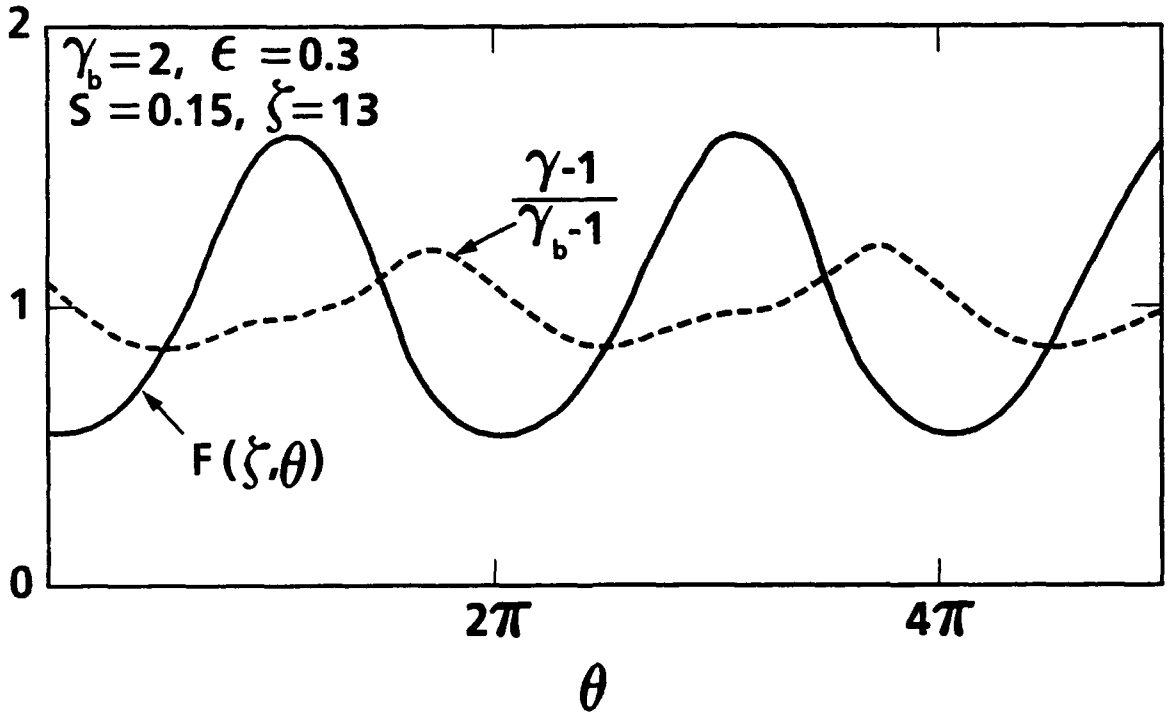


Fig. 2. Plots of normalized current, $F(\zeta,\theta)$ (solid line), and normalized kinetic energy, $(\gamma-1)/(\gamma_b-1)$ (broken line), versus the normalized time θ obtained from Eqs. (11), (15), and (16) for $\gamma_b = 2$, $\epsilon = 0.3$, $S = 0.15$, and $\zeta = 13$.

A typical example of energy and current modulations calculated from Eqs. (11), (15) and (16) is presented in Fig. 2, where the normalized current, $F(\zeta,\theta)$ (solid line), and the normalized kinetic energy, $(\gamma-1)/(\gamma_b-1)$ (broken line), are plotted versus the normalized time θ for $\gamma_b = 2$, $\epsilon = 0.3$, $S = 0.15$ and $\zeta = 13$. As expected, the maximum I_{max} and minimum I_{min} currents in these parameters occur around $\theta = (2n-1)\pi$ and $\theta = 2n\pi$, respectively, where $n = 1, 2, \ldots$ are integers. The time profile of kinetic energy (broken line in Fig. 2) is significantly distorted from a typical sinusoidal wave form. It is useful in the subsequent analysis to define the current difference $\Delta I = I_{max} - I_{min}$. Shown in Fig. 3 is a plot of the normalized current difference $\Delta I/2I_b$ versus the propagation distance ζ for the parameters identical to Fig. 2. The current modulation increases linearly at beginning, saturates around $\zeta = 15$ and then slowly decreases to zero as the propagation distance increases.

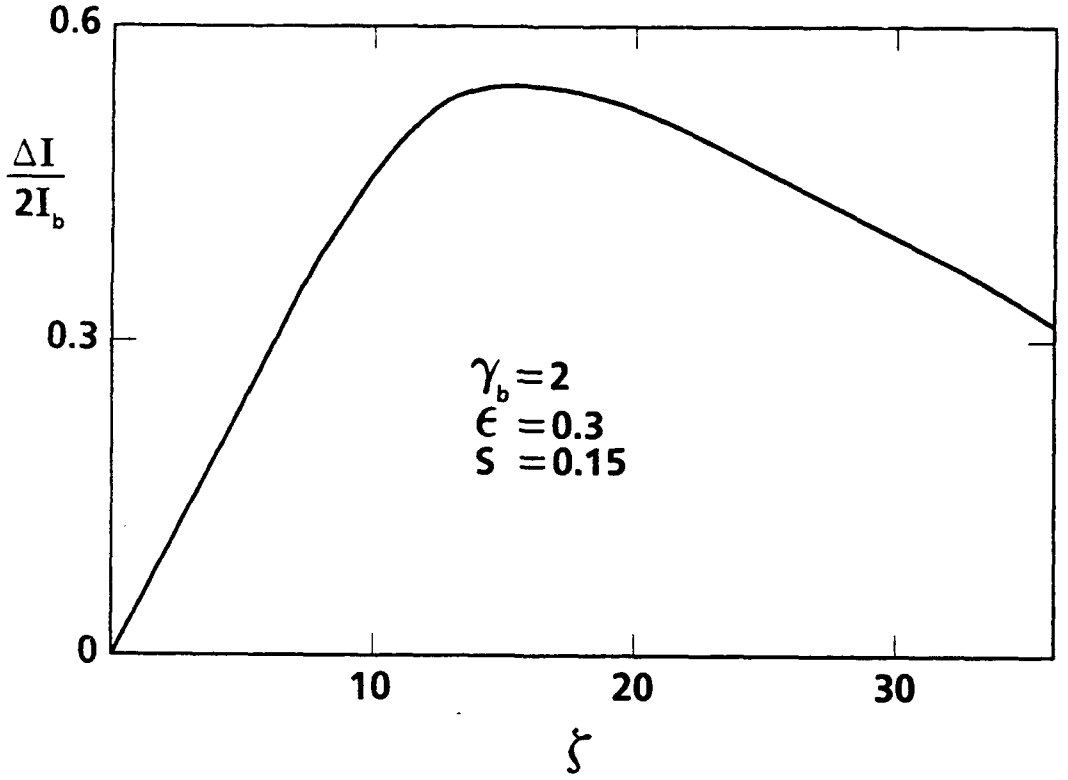


Fig. 3. Plot of normalized current difference $\Delta I/2I_b$ versus propagation distance ζ for the parameters identical to Fig. 2. Here, ΔI is the current difference between its maximum and minimum values, i.e., $\Delta I = I_{max} - I_{min}$.

Acknowledgment: This research was supported in part by the Independent Research Fund at NSWCWODET and in part by IST/SDIO, managed by the Harry Diamond Laboratories.

THE TIME ENERGY COMPRESSION OF PULSE MICROWAVE VIRCATOR RADIATION

P.Yu.Chumerin, G.V.Melnikov, S.A.Novikov, S.V.Razin,
Yu.G.Yushkov, A.G.Zcherlitsin
Institute of Nuclear Physics. 634050. Tomsk. RF
A.N.Didenko
Moscow Institute of Engeneering and Physics.115409.Moscow.RF

ABSTRACT

The microwave pulse energy compression method supplies power amplitication factor of about numbers of tens. It is probable to yield microwave pulses of $10 - 10^3$ W power and 1 ns width in L and S-bands by utilizing relativistic generators as exiting sources. This report covers the first experimental data of the time energy compression of the output pulse radiation of the relativistic virtual cathode triode and cycletron resonance vircator.

Application of high-power microwave nano-and picosecond pulses is of interest in various spheres of science and technology, in particular, for high distance resolution radiolocation of low scattering efficiency targets. It is known that pulse power upper levels of nanosecond pulse width microwave radiation were gained in relativistic generators which were fed with voltage sources of high current accelerators.

The required voltage and current up to 10^5-10^6V and 10^5 A respectively are obstacles for creation of reliable microwave generators with low weight and demention parameters. So these generators largely remain as laboratory sets and are restricted for wide useful application. Moreover generation of most short pulses have limitation in the capacity for exitation of relativistic tubes in very short times especially where the pulse width is comparable with the cycle of high frequency oscillations.

All this explains an interest for obtaining nano- and picosecond microwave pulses of 10^9-10^{10} W peak power by storaging the output energy of relativistic generator in high Q-value resonant cavities and then by its subsequent rapid dumping [1].

Due to the time energy compression the resonant cavity output power get amplified in $\frac{2Q_L}{w_o t_o}$, here Q_L is loaded quality factor, w_o - cycle frequency, t_o - output microwave width. The power level in question may be attained by application the compression method to pulses of relativistic generators of 10^6-10^8 W peak power and pulse width exceeding 10^{-8} s.

This paper covers experimental data of the time microwave energy compression with the relativistic virtual cathode triod or the cycletron resonance vircator being used as a gene - rator for exitation. These demonstration experiments were preceded by investigations of rapid exitation of resonant cavities, their electric strength, different mode operation and different types of compression device curcuits.

The experiments of electric strength of single-mode resonant structure showed that an increase of critical field strength due to rising the gas pressure over 10 atm became uneffective and caused great technological problems [2]. The results allow that output power level of storage cavities made of pattern copper waveguides and exited by microwave pulsewidth over 10^{-6} s may be about 10^9 - 4 10^9 W in L-wavelength band, 10^8--10^9 W in S-band and 10^6-10^7 W in X-band. Considerable increase of critical field strength level and output peak power are attained with the times of resonant exitation of about 10^{-8}-10^{-7} s. In this the output power of the device may be increased about an order with compare to the operation regime of long pulsewidth exitation. Decreasing of power amplification factor is compensated by an increase of exiting microwave power.

Limitation of output power bound up with electric strength may be overcome by some special circuits. One of them represented the S-band device in which the series energy compression and the pattern issued magnetron were used. It had power of $P_g = 10^6$ W and pulsewidth $t_p = 3 \cdot 10^{-6}$ s as magnetron parame - ters, P_{01} = 21 MW and t_p = 30 ns for output parameters of the first step, P_{o2} = 312 MW and t_{p2} = 1,5 ns for the second one,

P_o = 630 MW and t_p = o.4 ns for the third and the last [3]. It is assential the third step was a coaxial resonator simulating rapid switching and minimum dispersion.

The other way to get super high power pulses is the utilizing number of sources coherently and the adding their radiation in the common load [4]. The two storage cavities were exitied by the magnetron pulses of 10^6 W and $3 \cdot 10^{-6}$ s through the 3 dB coupler. The simultanuous switching to the energy dumping regime is acheaved by applying to the sparkle gaps the trigger pulses of 10 kV and rising time 5 ns. The output peak power of each compression device was $5 \cdot 10^7$ W and 10^8 W as summed up at the common load. Some increase of total pulse width was defined by jitterring of switch operation in both cavities. These results cause a proposal that the compression of relativistic generator radiation will help to solve the problem to acheave microwave pulses with the length of about (1-10) cycles of field oscillations and the peak power exceeding 10^9 W. The possibility of the operation of coherent multiple cavity system makes feasible the development of super high power sources based upon utilizing phase locked relativistic generators.

The fist relativistic tube was the virtual cathode triode used as a exiting generator 5 . The scheme and the main results are presented on fig. 1. The triod pulse was of $3.5 \cdot 10^8$W power and of $(2.7\text{-}3) \cdot 10^9$ H frequency bandwidth. The part of the triod microwave power fell on the horn antenna and then was guided to the storage cavity. Maximum input cavity power was $2 \cdot 10^7$ W. The storage cavity had the double T-type coupling, $Q_L = 4 \cdot 10^3$ and operated on TE_{10} mode with 2.83 GH resonant frequency.

The cavity volume was filled with SF_6 and N_2 mixture up to 16 atm pressure to keep its electric strength. The microwave pulses had $4.6 \cdot 10^{-9}$ width at 0.5 amplitude level $4 \cdot 10^8$ W peak power. The power gain was 13 dB. The disadvantage of this scheme was the low efficiency $\simeq$ 1 % caused by difficulties to exite the one-mode cavity as the exiting triod had multy-mode radia-

tion.

Therefore the vircator generating one-mode oscillations was used in following. The scheme of the experimental setting is presented on fig. 2. The energy source had output voltage of 950 kV, current of 20 kA and voltage pulse length 80 ns. the vircator had output microwave power of 1÷2 MW, pulsewidth 50÷÷80 ns and the frequency 3.33 GH with magnetic field strength H_o = 4 kG. Radiation had one operating mode of TE_{11} type. The radiation frequency was monitored by the injected electron beam density value. In this set the matching of the generator and the storage cavity benefit from single mode vircator operation and frequency tuning possibility.

The coaxial cavity comprising the T-coaxial coupling and the shorting capasity for a switching gas gap was utilized to gain 10^{-9} s pulse width. It had Q_L = 500, was filled by the air of atmosphere pressure and operated with spontaneous discharge of the gap. The gained microwave pulses were attenuated and controlled by the high bandwidth oscilloscope. The pulses had pulse width of 3 ns at 0.1 amplitude level and the power of 5÷10 MW. The power amplification factor was 5-9.

Thus carried out experiments showed the power amplification of either triod or vircator of 10 without an increase of the primary feeding energy source.

The advantages of the method covered in this report are technical simpisity and capacity for reaching the pulse width up to one cycle of oscillation.

1. A.N.Didenko, Yu.G.Yushkov. High power microwave pulses of nanosecond width. Moscow. 1984.
2. S.A.Novikov. P.Yu.Chumerin, Yu.G.Yushkov. Proceedings of the High-Frequency Breakdown Workshorp. Tartu. Estonia, 1989, p. 93.
3. A.N.Didenko, S.A.Novikov, S.V.Razin. P.Yu.Chumerin, Yu.G. Yushkov. - Reports of the Academy of Science. v. 321, No 3, 518 (1991).
4. S.A.Novikov. S.V.Razin, P.Yu.Chumerin, Yu.G.Yushkov. Sov. Technical Physics Letters. v. 16, No 20, 46 (1990).
5. A.N.Didenko, A.G.Zcherlitsin, G.V.Melnikov, S.V.Razin, Yu.G.Yushkov, P.Yu.Chumerin. Reports of the Academy of Science. v. 309, No 5, 1117 (1989).

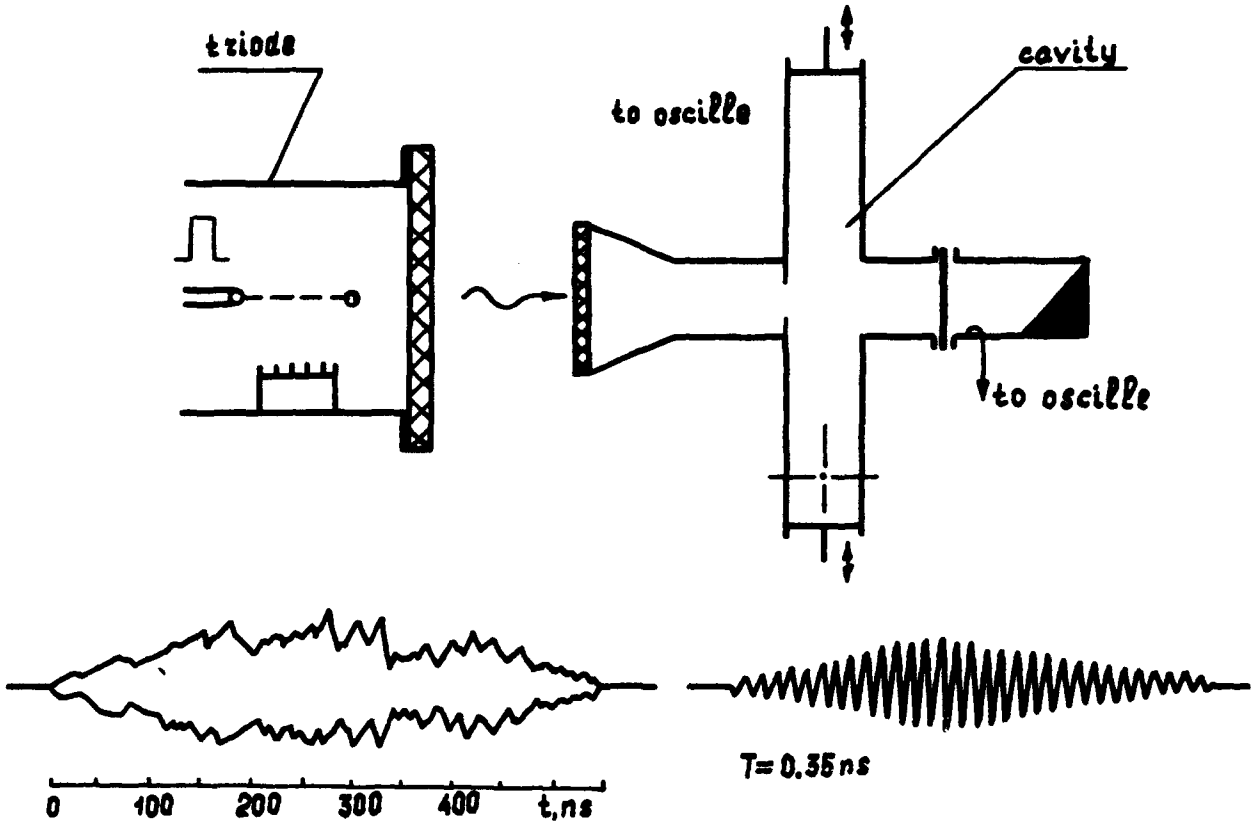


Fig.1. The scheme for the time compression of pulse triode microwaves

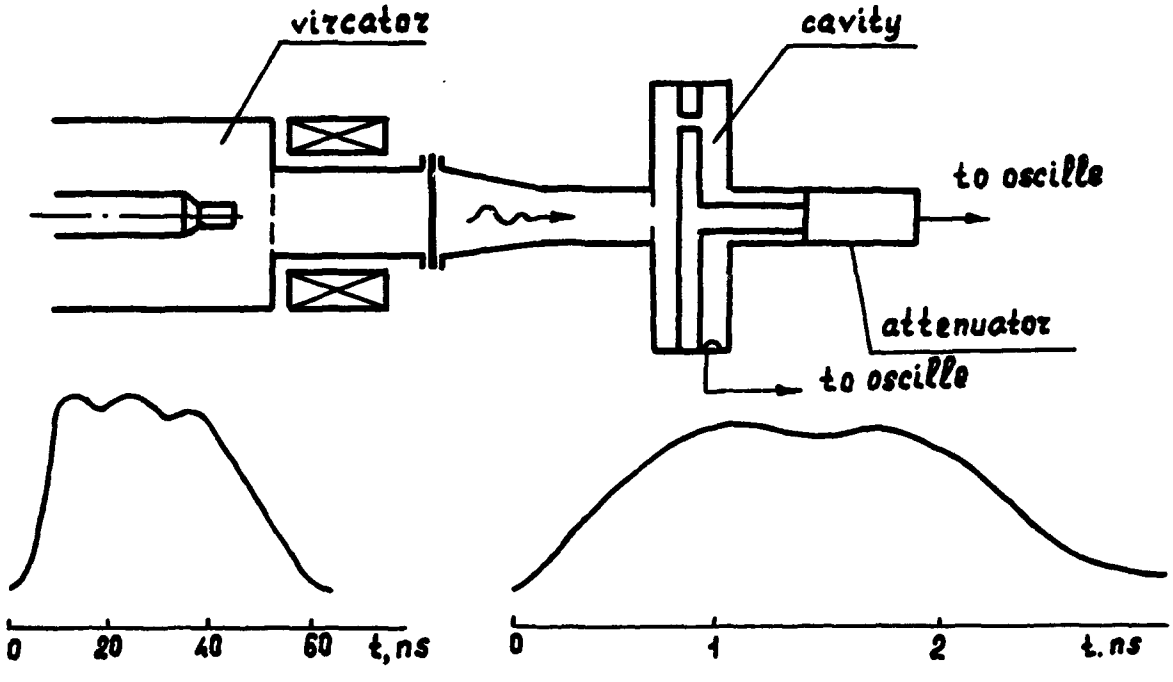


Fig.2. The scheme for the time compression of output vircator radiation

FREQUENCY CONTROL OF VIRCATORS MICROWAVE RADIATION

A.N.Didenko

Moskow Engineering and Physical Institute, 115409,Moskow Russia

M.Yu.Antoshkin, G.P.Fomenko, V.P.Grigoryev, T.V.Koval, G.V.Melnikov, V.I.Tsvetkov, A.G.Zherlitsin

Institute of Nuclear Physics of Tomsk Polytechnical University 634050, Box-25, Tomsk, Russia

A b s t r a c t

Possibility of frequency control in vircators by means of beam parameters, magnetic field and external microwave signal has been studied. The conditions have been found when generated frequency doesn't depend on magnetic field B but radiation power has resonant dependence on B. It has been shown that some vircator can operate at two frequencies simultaneously.

Generation of electromagnetic oscillations in virtual cathode systems draws attention due to absence of current limitation in these systems because of space charge field available in familiar vacuum generators, a possibility for propagating into a region of great powers and enhance of radiation efficiency. The ability for generating electromagnetic oscillations when electron beam currents are higher than vacuum limit current and conditions of a virtual cathode formation are carried out is a distinguished feature of a virtual cathode systems (VC). Therefore one can produce new powerful high-current relativistic devices on the basis of virtual cathode systems. These devices may embrace the cantimeter and millimeter wavelength ranges and have such advantages as frequency retuning, formation of durable electromagnetic pulses, structural simplicity and small size (it's possible not to have the focusing magnetic fields and its power sources).

The first investigations on generating in these systems [1-5] showed a possibility for producing powerful high frequency pulses and stimulated a research of dependencies of basic radiation characteristics upon electrical and geometric parameters of various generating devices and make the generation mechanism clear.

According to available results devices with VC can be divided into two groups.

1. High frequency devices with VC where electrons only oscillates between a real cathode and VC. These devices are called triodes with VC (or reflex triodes with VC)[2-4].

2. High frequency devices with VC where parallel with oscillatory movement of electrons between real and virtual cathodes there is a flow of electrons passing through VC into a drift space. These devices are called vircators [1,5,6].

Numerous vircators modifications differ in cathode and anode geometry, electrodynamical systems, radiation output mechanism as well as a magnetic field availability or its absence.

One of the most important problems in all VC systems is to define a radiation frequency and establish a frequency control technique.

Radiation frequency ω in VC systems is determined by VC oscillations frequency ($\omega = \Omega + \delta\omega$) which is close to frequency of nonlinear oscillations of electrons in a potential well Ω. As ω and Ω frequencies depend upon beam parameters, therefore there is a possibility to control a radiation frequency by changing an accelerating voltage, a gap of cathode - anode spacing, by changing a density of injected flow[2-4,7,8] as well as by varying its non-uniformity profile of cross - section. As numerical calculations showed that the highest frequency of VC oscillations corresponds to distribution of solid beam density with maximum in the centre [9].

The experiment performed [10] demonstrated that the changing of a beam profile from solid to annular correspends to frequency changing from 2.94 GHz to 2.5 GHz.

Fig.1 shows an experimental dependence of radiation frequency of annular beam upon its density obtained in reditron. According to experimental data the electrons density was changed by external magnetic field.

When an interaction of cyclotron wave with l harmonics of VC oscillation occurs under conditions of parameter resonance, radiation power is of resonance character depending

upon a magnetic field [11]. Maximum radiations occur at

$$B_{o_\ell} \sim |\ell + 1|\Omega \quad , \quad \ell = \pm 2, \pm 3, \ldots$$

Here a radiation frequency depends upon a magnetic field $\omega \sim \Omega \sim n_e^{1/2}$. For beams density with a weak dependence upon B we have $\omega \approx \Omega$ = const. A radiation power depends as well upon a value of a transverse pulse which is produced by a longitudinal gradient of magnetic field.

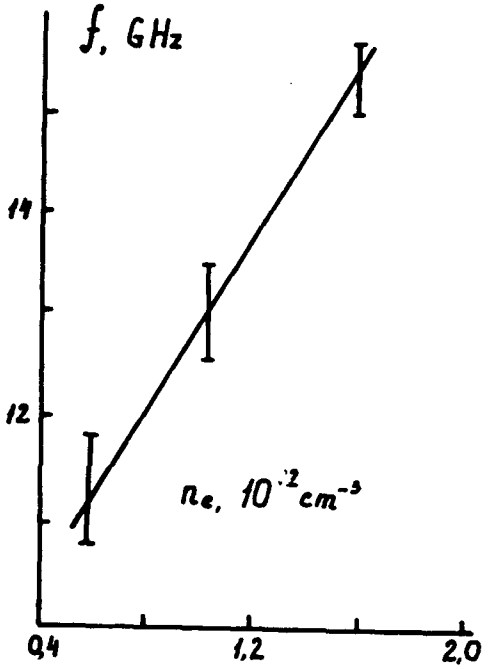


Fig.1. Radiation frequency dependence upon electron density in a flow. Parameters of an experiment: U = 0.8 MV; I = 30 kA; P = 0.3 GW.

Experimentally maximum relative longitudinal gradient was $B/B_{max} = 0.2 \cdot \Delta z \ \ cm^{-1}$ [8]. The highest power has been observed at B_o field which depends upon parameters of injected beam. B_o field increases with the increasing of electrons density. Results of experimental investigations are given in the Table 1.

Table 1

Beam radius (cm)	V (MV)	I (kA)	B (kG)	f (GHz)
20	1,2	9	0,6	2,6
20	1,2	20	1,8	2,86
10	1,2	9	2,8	3,4
10	1,2	20	6,0	5,45

One of the features of VC systems is two frequency generation regime which can be realized for two reasons [12,13].
a) In triode systems where is a drift space produced by a collector under the same potential as anode, a two frequency generation regime is realized due to switchin on two-beam interaction. This method is carried out when flowing current is

higher than threshold one for a two-beam instability and it is characterized by a generation of oscillations at close frequ - encies. Fig.2 demonstrates radiation frequency characteristics

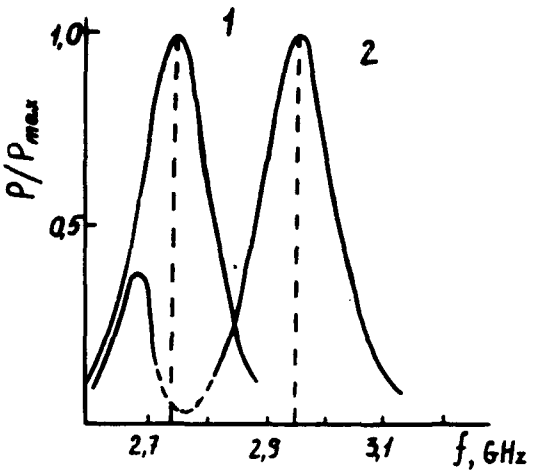


Fig.2. Radiation frequency characteristics.
1 - without collector,
2 - collector is 8 cm away from anode.

in triode systems with a collector and without it, produced in the experiment [12].

b) Another reasos for two frequency generation regime to occur can be a potential well asymmetry what is characteristic of vircators with magneto-insulated diode. In so doing, frequen -

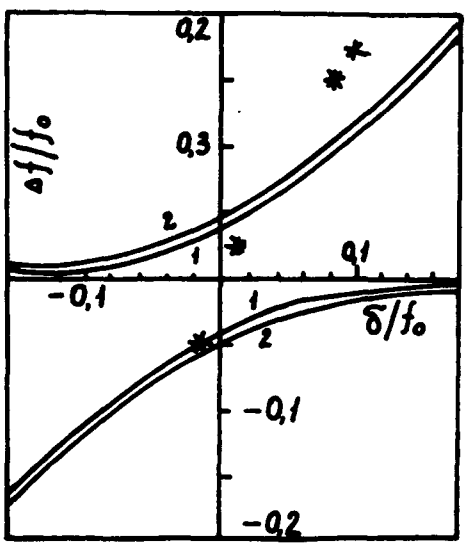


Fig.3. Dependence of $\Delta f/f_0$ upon untuning δ/f_0.
1 - $|Ed/V| = 1/60$;
2 - $|Ed/V| = 1/30$;
* - experimental points.

cies of excited oscillations can differ several times. The expe - riment [13] demonstrates short wave radiation in range of 2.5 - - 2.8 cm with power $P_1 \sim 10^8$ W and long wave radiation in range of 5-7 cm with power $P_2 \sim 10^6$ W. A short wave radiation is connected with virtual cathode formation in drift tube and it occurs at frequency determined by parameters of injected beam. Long wave radiation in such systems is connected with the second cathode formation in a region of electron flow formation and depends

significantly upon parameters of a reflected beam and reso - nance system. This dependence enables to control radiation parameters and provide oscillations generation in the range of wave lengths you need in. In particular, a real cathode being transferred over a distance less than τ_D (τ_D is Debay radius with reduction considered) from a drift tube, one can obtain one-frequency generation regime at high frequency.

Radiation frequency control in VC system can be carried out by external signal filling at frequency close to radia - tion one.

It is possible due to frequency dependence of oscillating electrons upon amplitude of oscillations [12]. Frequency retuning in a triode with VC is carried out by varying frequency untuning δ between an external signal f_g and frequency of electron oscillations f_o as well as by varying voltage level of an external signal E

$$\Delta f = \frac{1}{2}\left\{ \delta \pm \left[\delta^2 + \frac{3}{4}\left(\gamma_o - 1\right) \left|\frac{d \cdot E}{V}\right| \frac{f_o^2}{f_g} \right]^{1/2} \right\} .$$

Here d is diode gap. Fig.3 shows dependence of a frequency change upon untuning and level of an external signal including experimental parameters region.

REFERENCES

1. A.N.Didenko, A.G.Zherlitsin, V.I.Zelentsov, G.P.Fomenko, Yu.G.Shtein, Yu.G.Yushkov. Proc. Int. Top. Conf. on Electron Beam Research and Technology. Albuquerque, 1975, v.2, p.424.
2. R.A.Mahaffey, P.Sprangle, J.Goldek and C.A.Kapetanakos. Phys. Rev. Lett. 39.843 (1977).
3. H.E.Brandt, A.Bromborsky, H.B.Burks and R.A.Keks. Proc. 2nd Int. Top. Conf. on High Power Electron and Ion Beam Research and Technology (Cornell University, Itha - ca, N 4, 1977), p.649.
4. A.N.Didenko, Ya.E.Krasik, S.F.Perelygin and G.P.Fomenko. Pis'ma Zh. Tekh. Fiz. 5, 321 (1979).
5. J.M.Buzzi, H.J.Doucet, H.Lamain, C.Roulle, J.Delvaux and J.C.Jouys. Le Journal de Physique Lettres, 39, 1 (1978).

6. S.C.Burkhart, R.D.Scarpetty, R.L.Lundberg. J.Appl. Phys., 58, 28 (1985).

7. A.G.Zherlitsin, S.I.Kyznetsov, G.V.Melnikov, G.P.Fomenko. Zh. Tekh. Fiz., 56, 1384 (1986).

8. A.G.Zherlitsin, G.V.Melnikov, G.P.Fomenko, V.I.Tsvetkov. Fiz. Plaz., 16, 100 (1990).

9. V.P.Grigoryev, T.V.Koval, N.I.Sablin. Proc. XIY Int. Symp. on Discharges and Electrical Insulation in Vacuum (Santa Fe, New Mexico, USA, 1990), p. 704.

10. A.N.Didenko, A.P.Arzin, A.G.Zherlitsin et al. Rel. High-Frequency Electr. Iss., p. 104 (1984).

11. V.P.Grigoryev, T.V.Koval et al. Radiotechn. and Electr. N 9, 312 (1992), p. 116.

12. A.N.Didenko, G.P.Fomenko, V.P.Grogoryev, T.V.Koval, S.I.Kuznetsov, A.G.Zherlitsin and G.V.Meinikov. Proc. YII Int. Conf. on High Power Particles "Beams 88" (Karlsruhe, FRG, 1988), v.2, p. 1402.

13. V.P.Grigoryev, A.G.Zherlitsin and T.V.Koval. Fisika plasmy, N 11, (1990), p. 1353.

NUMERICAL SIMULATION AND EXPERIMENT STUDY OF VIRCATOR

Wang Zhixiong,Chen Yanqiao
Chen Yusheng,Fan Ruyu

Northwest Institute of Nuclear Technology

Abstract

A $2\frac{1}{2}$ dimensional,fully electromagnetic,relativistic CIC particle simulation code has been developed to simulate the virtual cathode oscillations and the HPM generations. Solid electron beams are used both in the simulations and the experiments.The microwave radiations whose average power is of the order of GW have been observed.The simulations are in agreement with the experiments.

1.Introduction

There are many ways for the generation of the high power microwave(HPM).An important and simple one is Vircator.This types of devices are strongly nonlinear so that it is difficult trying to make any purely theoretical analyses.However,many phenomena of such devices have been revealed through a series of particle simulations and experiments[1-10].In this paper we will focus on the simulations and experiments that we have carried out.

2. The Simulation Model

The simulation arrangement is shown in Fig.1.A cylindrical waveguide which is of radius Rw and of semi-infinite length along oz-directon is evacuated inside.A monoenergetic relativistic electron beam,inner radius Ri, outer radius Ro, is injected symmetrically into the waveguide from the left end.The initial velocity which is parallel to the waveguide axis is V_0 and the initial density is N_0 under laboratory reference frame.An axial magnetic field B_0 which is homogeneous in space and time is exerted externally.A board located at L is used to absorb the transmitting electrons, but is transparent to the eletromagnetic fields. Its dielectric and magnetic permittivities are the same as vacuum.

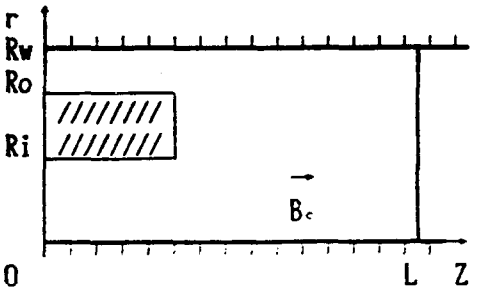


Fig.1 The simulation arrangement

For a solid electron beam,the limited current is[7]

$$I_1 = 17kA\frac{(\gamma_0^{2/3}-1)^{3/2}}{G(Rw,Ro)}\,g(\gamma_0,G(Rw,Ro)) \tag{1}$$

$$G(Rw,Ro)=1+2\ln(Rw/Ro) \tag{2}$$

$$g(\gamma_0,G(Rw,Ro))=\gamma_0^{2/3}\left(\left[\gamma_0^{2/3}+G(Rw,Ro)\right]^2-\gamma_0^{2/3}\right)^{1/2}-G(Rw,Ro))^{-1} \tag{3}$$

The electromagnetic fields satisfy Maxwell's equations:

$$\frac{\partial \vec{B}}{\partial t} = -\nabla\times\vec{E} \qquad \nabla\cdot\vec{B}=0 \tag{4}$$

$$\frac{\partial \vec{E}}{\partial t} = C^2\,\nabla\times\vec{B}-\vec{J}/\varepsilon_0 \qquad \nabla\cdot\vec{E}=0 \tag{5}$$

The perfectly conducting boundary conditions are imposed upon the left end and lateral wall of the waveguide,but the right end remains open;the fields are reflected on the axis;initially,there are no charges and fields inside the waveguide.

The cold,collisionless equation for the electrons is:

$$\frac{d(\gamma\vec{v})}{dt} = \frac{e}{Me}(\vec{E} + \vec{v} \times \vec{B}) \qquad (6)$$

The electrons that go beyond the wall and the board are omitted; the waveguide axis reflects the electrons passing through it. Those electrons which return from the virtual cathode region and bump into the left end are also neglected in order to eliminate the effects of the reflective electrons.

The CIC method is employed in the simulation and the longitudinal Lorentz contract of the finite size electrons is taken into account.The equations (4)-(6) are solved by finite difference through the combination of the cylindrical coordinates and the temporary Cartesian coordinates.

3. The Simulation Results

Solid electron beams are injected into the waveguide and the results are as follows:

(a)The electron densities are much larger than the initial density in the virtual cathode region, Fig.2.If $Ro >> \frac{\sqrt{\gamma_o(\gamma_o-1)}}{\sqrt{\gamma_o+1}}\frac{C}{\omega p}$,the virtual cathode will be formed about $t=2\gamma_o/\omega p$ and its axial distance is aproximitely $\frac{\sqrt{\gamma_o(\gamma_o-1)}}{\sqrt{\gamma_o+1}}\frac{C}{\omega p}$—[11].Where ωp is electron plasma frequency.

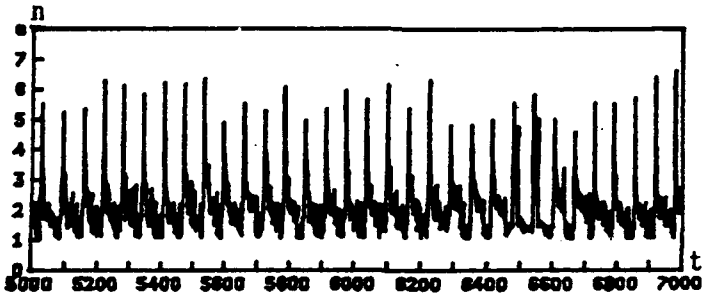


Fig.2 The density vs time at a fixed space point

(b)The velocities of the transmitting electrons are modulated by the microwave fields,Fig.3.When Larmor frequency $\Omega > 5\omega p$,the radial spread of the beam is negligible,Fig.4.



Fig.3 The phase space plot of the electrons

(c)The transmitting current oscillates with time,Fig.5.The average is larger than that calculated from the formula (1). The electrons near the beam edge easily penetrate the virtual cathode region and contribute a large portion of the transmitting current.

(d)The virtual cathode oscillates with a definite period, Fig.2.The bounds of the angular frequency ωv are $\omega p/\sqrt{\gamma_o} < \omega v < \omega p\sqrt{Nmax/N_o}$ .Where Nmax is the maximum electron density in the space. ωv slightly dependens on the B_o and increases a bit with the increase of the field B_o .It fits the formula $(I_o/I_1)^{1/4}$,where I_o is the injecting beam current.

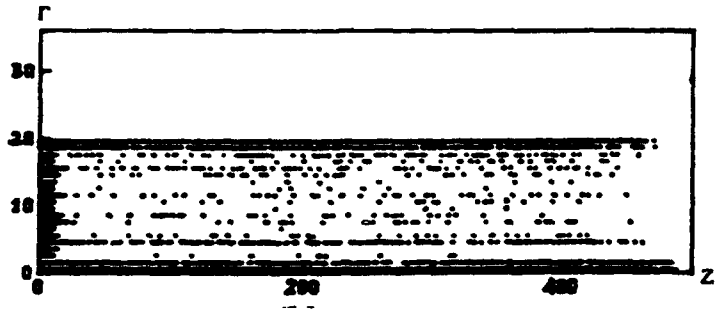


Fig.4 The cross section plot of the electrons

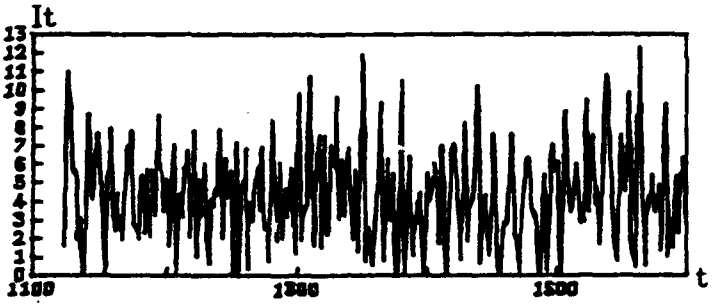


Fig.5 The transmitting current vs time

(e)The microwave radiations have been observed,Fig.6. The amplitude of the component Eθ is far smaller than that of the component Ez,Fig.6-7. Hence,the TMon models are primarily important. The spectrum of the Eθ also indicates the monochromatic excitation of the microwave further, Fig.8.

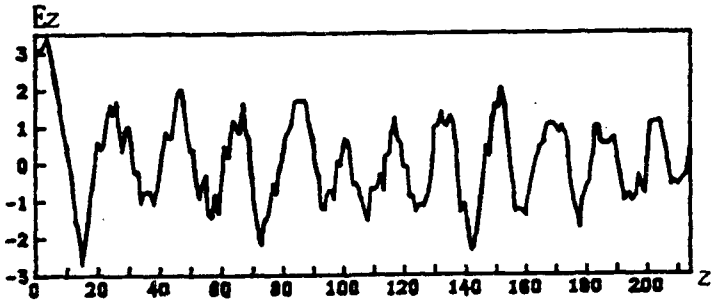


Fig.6 Ez vs z

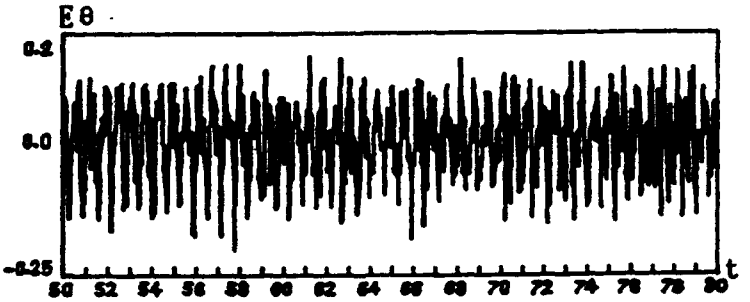


Fig.7 Eθ vs t

(f)The average power is of the order of GW and in direct proportion to J_0^2, where J_0 is the injecting current dencity.The field B_0 is in favor of the microwave excitation.

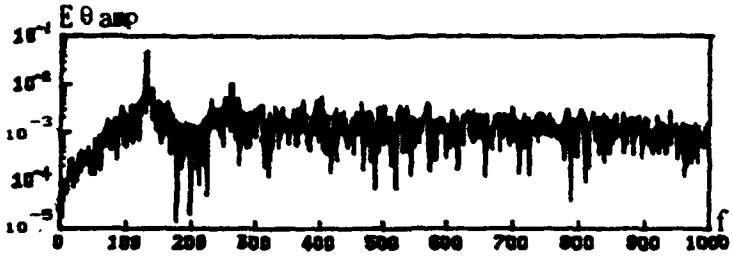


Fig.8 The frequency spectrum of the Eθ

4. The Experiments

The virtual cathode oscillations have also been investigated in the experiments with intense relativistic electron beam generator—Flash-II operating at diode voltages 0.8~1.2MV and beam currents 300~400kA. A diagnostic system including an E-field probe and a calorimeter has been designed to measure the microwave envelope and record the energy deposit. Fig.9 is a typical time response of the thermistor in the calorimeter to a single microwave pulse. The maximum output voltage is 20mV which corresponds to 30J energy deposit on the calorimeter. The duration of the microwave pulse is about 20ns. Therefore, the average power is 1.5GW. This is no discrepancy to our simulations.

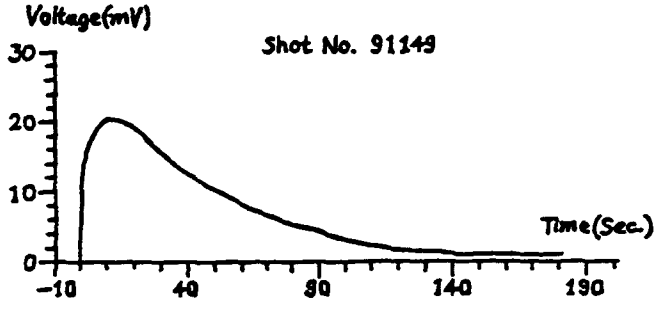


Fig.9 The time response of the thermistor

5. The End

The HPM which is almost monochromatic has been obtained both in the simulations and experiments. The output power is $\propto J_0^2$ so that it is extremely sensetive to the slight change of the J_0. Under the solid beam cases, a large portion of field energy exists in the form of Coulomb's energy which is longitudinal and exchanges with the kinetic energy of the electrons. Thus, the efficiency is usually low. It can be expected that a thin annular beam will be more effective than a solid one. The guide field B_0 plays an important role in improving the beam quality and the microwave power.

References

[1]H.Sze, et al., Phys.Fluids29, 3873(1986).
[2]R.A.Mahaffey, et al., Phys.Rev.Lett.39, 843(1977).
[3]T.J.T.Kwan, Phys.Rev.Lett.57, 1895(1986).
[4]T.J.T.Kwan and L.E.Thode, Phys.Fluids27, 1570(1984).
[5]T.J.T.Kwan, Phys.Fluids27, 228(1984).
[6]Abraham Kadish, et al., Phys.Fluids29, 4192(1986).
[7]Lester E.Thode, et al., Phys.Fluids22, 747(1979).
[8]Wee-yong Woo, Phys.Fluids30, 239(1987).
[9]H.A.Davis, et al., Phys.Rev.Lett.55, 2293(1985).
[10]S.C.Burkhart, et al., J.Appl.Phys.58, 28(1985).
[11]J.W.Poukey and N.Rostoker, Plasma Phys.13, 897(1971).

EXPERIMENTAL STUDY OF VIRTUAL CATHODE OSCILLATOR IN UNIFORM MAGNETIC FIELD

K.G. Kostov, N.A. Nikolov, I.P. Spasovsky and
R. Atanassov

Sofia University
Dept. of General Physics
5, Blvd. J. Bouchier
Sofia 1126, Bulgaria

Abstract. High-frequency high-power microwave radiations by a virtual cathode oscillator have been obtained. We performed experiments using 350 kV, 7 kA, 30 ns electron beam. A virtual cathode forms when the magnetized relativistic electron beam is injected into circular waveguide. The microwave generation exists in wide range of magnetic field magnitudes (2 kGs-40 kGs). The measured peak microwave power is about 15 MW at frequency region of 11-17 GHz. The radiation frequency has not depend on the magnetic field intensity. A nonsymmetric TM mode is observed. The sources of the microwave emission are both the reflexing electrons and the oscillating virtual cathode.

The virtual cathode oscillators (vircators) are among the most promising generators in the centimeter region with output power up to several gigawatts. The virtual cathode is formed when the beam current into a drift tube exceeds the space-charge limited current. Some of the electrons reflex from the virtual cathode and others passe through it in the forward direction. The electrons reflexing between real and virtual cathodes bunch in phase[1] (as they are relativistic) and radiate microwaves. In this case the radiation frequency equals the electron bounce frequency between the real and virtual cathodes. In other hand, the virtual cathode oscillates[2] in space and time with a characteristic frequency ranging from ω_p^b to $\sqrt{2\pi}\omega_p^b$. Here $\omega_p^b=(4\pi e^2 n/m\gamma)^{1/2}$ is the plasma frequency of the beam, n is the electron number density, γ is the Lorentz factor, e is the electron charge and m is the electron rest mass. The oscillation frequency increases when the ratio of the beam current to the space-charge limited current

increases. The steady-state oscillations of the virtual cathode leads to strong excitation of some waveguide modes. These two nonlinear oscillation processes have been separately observed in the numerical simulations[3] and in the experiments[4,5]. Generally, both mechanisms take place, but usually one of them dominates[5]. The competition between them leads to an incoherent, multimode, and inefficient broad-band microwave radiation[6].

Unlike the past experiments[7-10] we report an experimental finding[11] of a steady microwave generation by virtual cathode oscillator when a guide magnetic field is applied.

The experimental set-up is shown in Fig. 1.

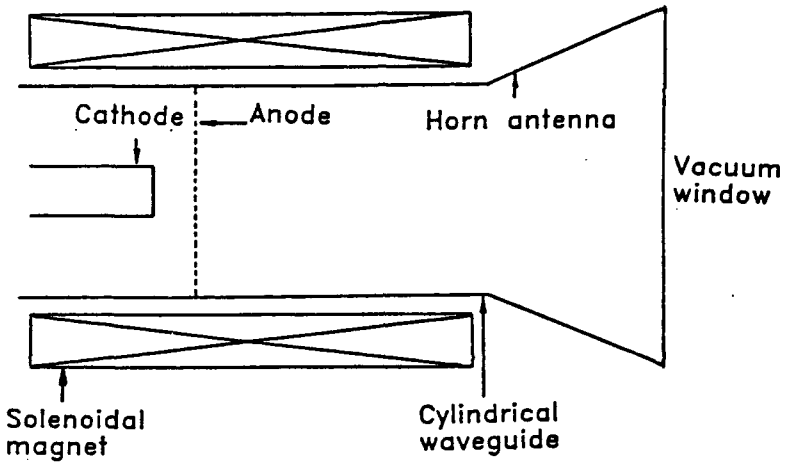


Fig. 1. Schematic experimental set-up.

A 30 ns negative voltage pulse from a 28 Ω oil-filled Blumleine pulse-forming line was applied to the diode of the virtual cathode oscillator. The beam electrons were emitted through cold plasma emission from a 1.8-cm-diam graphite cathode with a flat front surface centered inside a 5.6-cm-diam drift tube. A 0.5-mil-thick stainless-steel mesh (with 70 percent transparency) used as anode was positioned 0.4 cm from the cathode. The maximum diode voltage was 370 kV with the peak diode current of 7 kA measured by a Rogowsky coil. The diode and the drift tube have been immersed in a pulse solenoidal magnetic field which enables a variation from 0 to 40 kGs. The injected current has been about three times larger than the space-charge limited current and the virtual cathode is formed downstream the

anode. The microwave radiation propagates along the 45-cm-long drift tube. It was followed by a conical antenna with 12-cm-diam vacuum window for microwave extraction. A residual gas pressure was approximately 2×10^{-4} Torr.

The radiation field was measured at the output window by open end of standard rectangular waveguide as receiver. Its signals were transmitted through an attenuator to a calibrated fast-response-time semiconductor detector. Radiation power was evaluated integrating radiation radial profiles obtained by partial measuring of the radiation power from shot to shot. Typical waveforms of the diode voltage, the diode current and the microwave pulse are shown in Fig. 2.

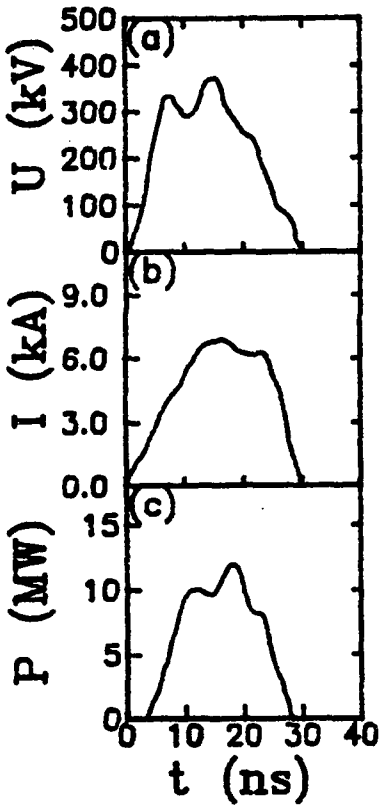


Fig. 2. Time history of (a) diode voltage,(b) diode current and (c) microwave emission.

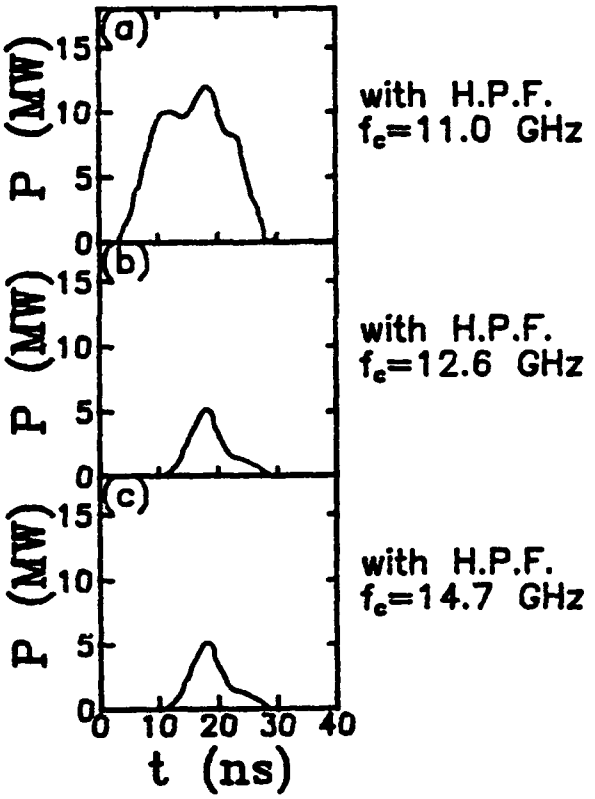


Fig. 3. The frequency region of the radiation for Fig. 2 experimental conditions.

The experimental parameters of this shot were 0.4 cm gap spacing, 370 kV maximum voltage, 7 kA maximum current and magnetic field of 20 kGs. The comparison of the microwave signal with the diode current shows that the microwave pulse occurs

several nanoseconds later, at the time when the beam current reaches the space-charge limited current of the output waveguide.

The frequency region of the microwave emission was investigated with set of high-pass filters, the result of which is shown in Fig. 3. For more accurate frequency measurement in the interval 7.5-12.5 GHz a bandpass filter with 5.7% bandwidth was used as well. A well-defined peak in microwave radiation spectrum was found, centered at 12 ± 0.6 GHz near the higher end of X band. The bigger part of the output power 10 ± 5 MW corresponds to this frequency (see Fig. 3a,b). A smaller peak appears above 14.7 GHz as it can be seen on Fig. 3c.

Following the computer simulations[3,6], the experiments[4,5] and also taking in to account our estimations of the electron bounce and the beam plasma frequencies we suggest that the reflexing electrons are the source of the low-frequency (12 ± 0.6 GHz) radiation component whereas the high-frequency component (among 14.7 GHz and 17.6 GHz) comes from the virtual cathode.

The radiation frequency was studied as a function of the external magnetic field (Fig. 4). The microwave frequency was found to be approximately independent on the magnetic field.

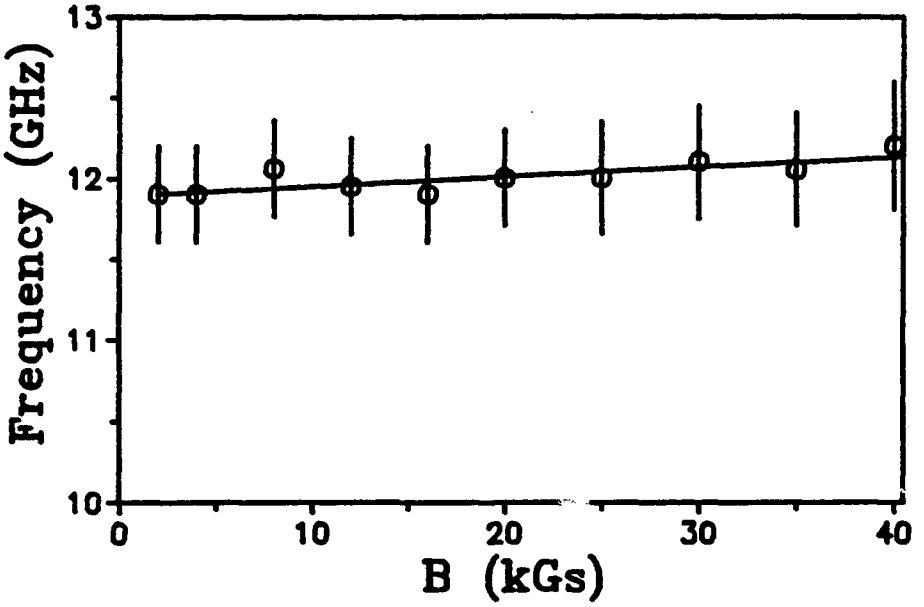


Fig. 4. Radiation frequency as a function of the applied magnetic field intensity.

An output power of level of about 10 MW was obtained in the

interval from 2 kGs to 40 kGs (Fig. 5). The maximum microwave power of 15 ± 7 MW with about 1% efficiency was obtained. No microwave emission is measured at B ≤ 2 kGs and a reduction in the microwave generation was observed above 20 kGs.

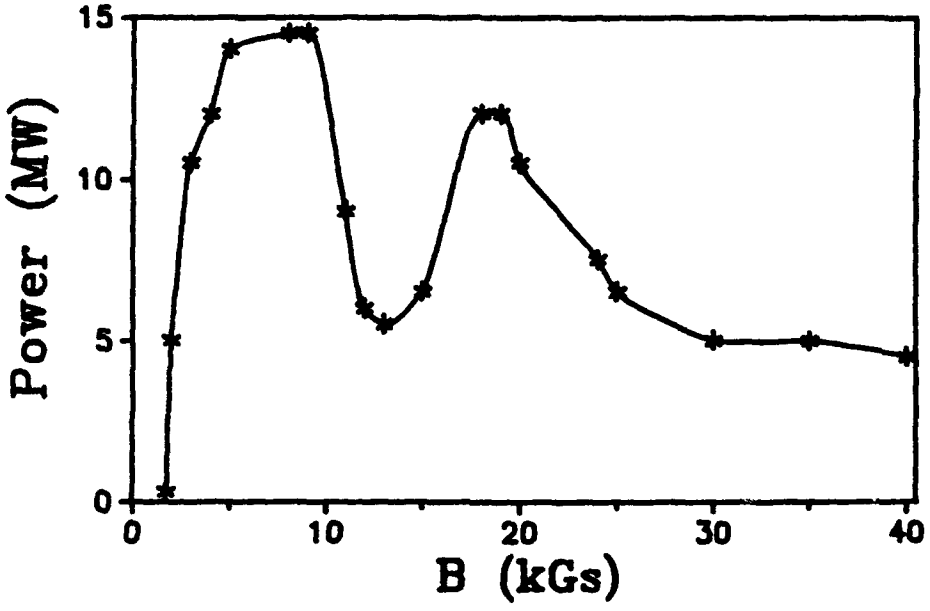


Fig. 5. Dependence of microwave power on the external magnetic field.

Gas break-down of an argon filled panel and radiation profiles were used for mode identification. The radiation pattern has been found to be asymmetric with a significant radial polarization. The specific for TM_{11} mode radial and azimuthal variations of the output power (see Fig. 6) are well seen.

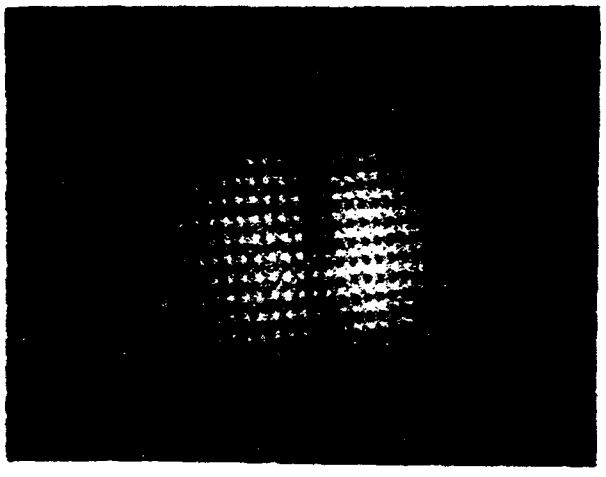


Fig. 6. Microwave induced gas breakdown at B = 22 kGs demonstrating TM_{11} mode.

As a summary, an output power of 10 ± 5 MW at (12 ± 0.6) GHz and 5 ± 2 MW between 14.7 GHz and 17.6 GHz was obtained in a single shot. The low and high frequency components are emitted by the reflexing electrons and the oscillating virtual cathode, respectively. Our results show that the applied magnetic field (up to 40 kGs) does not suppress the microwave generation and also does not change the radiation frequency. Unlike the previous vircator experiments an excitation of cyllindrical TM mode with azimuthal variation was observed.

REFERENCES

1. R. Mahaffey, P. Sprangle, J. Golden and C. Kapetanakos, Phys. Rev. Lett. 39, 843 (1977)
2. T. Kwan, Phys. Fluids 27, 228 (1984)
3. S. Burkhart, R. Scarpetti and R. Lundberg, J. Appl. Phys. 58, 28 (1985)
4. H. Davis, R. Bartsch, L. Thode, E. Sherwood and R. Stringfied, Phys. Rev. Lett. 55, 2293 (1985)
5. M. Haworth, R. Adler, B. Anderson, M Connaughton, W. Dungan, J. Enns, J. Metz, P. Pelletier, R. Platt, J. Polaco, R. Rupp, L. Thode and D. Voss, Appl. Phys. Lett. 59, 408 (1991)
6. L. Thode, in *High-power Microwave Sources* edited by V. Granatstein and I. Alexeff (Artech House, Boston 1987) chap. 14
7. J. Buzzi, H. Doucet, H. Lamain, C. Rouille, J. Delvaux and J. Jouys, Le Journal de Physique Letters, 39, 1 (1978)
8. H. Davis, R. Bartsch, L. Thode, E. Sherwood and R. Stringfied, Los Alamos National Laboratory, private communication
9. R. Scarpetti and S. Burkhart, IEEE Trans. Plasma Sci. 13, 506 (1985)
10. H. Sze, J. Benford, W. Woo and B. Harteneck, Phys. Fluids, 29, 3873 (1986)
11. K. Kostov, N. Nikolov, I. Spassovsky and V. Spassov, Appl. Phys. Lett.,60, May (1992)

Contributed Free Electron Laser Papers

NONLINEAR SIMULATION OF A HIGH-POWER COLLECTIVE FREE-ELECTRON LASER

H.P. Freund† and A.K. Ganguly
Naval Research Laboratory, Washington, D.C. 20375

ABSTRACT

A comparison is described between the 3-D simulation code ARACHNE and a recent 33.4 GHz collective FEL amplifier experiment at MIT. The experiment demonstrated power levels of 61 MW (≈ 27% efficiency) without recourse to tapered magnetic fields using a 750 keV/300 A electron beam with an axial energy spread of 1.5% propagating through a cylindrical drift tube in the presence of a helical wiggler [$B_w \leq 1.8$ kG, $\lambda_w = 3.18$ cm] and a guide magnetic field [$B_0 \leq 12$ kG]. The maximum power was observed when the wiggler and guide fields were antiparallel. ARACHNE is in substantial agreement with the experiment and shows peak power levels of 60 MW.

I. INTRODUCTION

Free-Electron Laser (FEL) experiments have used electron beams produced by every accelerator type. High energy/low current accelerators are employed at infrared or shorter wavelengths, and the maximum efficiencies achieved are of the order of 4% using tapered wiggler designs.[1,2] In contrast, low energy/high current electron beams are employed at longer wavelengths in the microwave or millimeter wave regime. In the past, the optimal performance demonstrated in this regime is represented by efficiencies of the order of approximately 12% for a uniform wiggler configuration,[3,4] and approximately 35% for the case of a tapered wiggler.[5]

The present paper is concerned with the theoretical description of a recent uniform wiggler experiment conducted by Conde and Bekefi[6,7] at MIT which demonstrated a peak efficiency of approximately 27% at 33.4 GHz. The above-mentioned tapered wiggler experiment achieved a 35% efficiency at the same frequency using a 3.5 MeV/850 A electron beam in conjunction with a planar wiggler.[5] In contrast, the MIT experiment employed a 750 keV/300 A beam in conjunction with a helical wiggler/axial guide field configuration. A novel feature of this experiment is that the peak efficiency occurred when the wiggler and axial guide magnetic fields were directed anti-parallel. This reversed-field geometry is a previously untried configuration.

For convenience, we refer to the 3-D nonlinear simulation code used to analyze this experiment as ARACHNE. This code was first developed to treat FEL amplifiers in the high-gain Compton regime.[8-12] However, ARACHNE was extended to treat the collective Raman regime[13] and has been benchmarked, with good results, against earlier FEL experiments[14,15,16]

II. EXPERIMENTAL DESCRIPTION

The experiment[6,7] is an amplifier in which the electron beam is injected into a cylindrical waveguide with a radius of 0.51 cm in the presence of both a helical wiggler and an axial guide

field. The interaction is with the TE_{11} mode at 33.39 GHz, which is the frequency of the drive magnetron. The magnetron produces ≈ 17 kW (±10%) in a linear polarization corresponding to 8.5 kW in the circular polarization capable of interacting with the helical wiggler geometry.

The beam energy was 750(±50) keV, and beam quality was controlled by scraping the beam with a shaped graphite anode.[17] The beam radius was 0.25 cm [the anode aperture radius], and the axial energy spread was $\Delta\gamma_z/\gamma_0 \approx 1.5\%$. The current at the wiggler entrance was 300(±30) A. However, the propagating current varied with the orientation and magnitude of the guide field. The current generally increased with increases in the guide field, except when the Larmor and wiggler periods were comparable. For a parallel orientation, an orbital instability prevents propagation of the beam. In the field-reversed case, the increase in the propagation current leveled off when the Larmor and wiggler periods were comparable [i.e., the *anti-resonance*]. The anti-resonant effect is important for beams big enough that electrons far from the axis experience a varying wiggler field which results in an anti-resonant enhancement in orbital perturbations.[18]

The bifilar helical wiggler had a period of $\lambda_w = 3.18$ cm, a length of $50\lambda_w$, and a six wiggler period adiabatic entry taper. The wiggler amplitude was continuously adjustable up to an amplitude of ≈ 1.8 kG. The guide field could be adjusted up to a maximum amplitude of ≈ 12 kG.

The peak efficiency occurred for the field-reversed configuration at a power of 61 MW [for an efficiency of 27%] for wiggler and axial field magnitudes of ≈ 1.47 kG and 10.92 kG respectively. The propagation current for these fields was near the maximum of 300 A. The output power for the field-reversed configuration also showed a sharp decrease in the vicinity of the anti-resonance, dropping by more than three orders of magnitude. The power observed when the guide field was parallel to the wiggler [≈ 4 MW] was much less than for the field-reversed configuration.

III. THE THEORETICAL COMPARISON

We summarize the essential properties of the formulation, and refer the interested reader to the original papers[8-13] for a complete discussion. ARACHNE is a 3-D slow-time-scale description of an FEL amplifier. Single frequency propagation is assumed and Maxwell's equations are averaged over a wave period. This results in two numerical simplifications: (1) the fast-time-scale oscillation disappears and only the slow-time-scale growth (or damping) of the wave need be resolved, and (2) only a *beamlet* of electrons entering the wiggler within one wave period needs to be included. Run times are 5-10 minutes on a Cray-2 supercomputer.

The electromagnetic field is represented as a superposition of the propagating TE and TM modes of the vacuum waveguide. The space-charge field is represented as a superposition of the Gould-Trivelpiece modes for a completely filled waveguide.[19] Since both the fluctuating electromagnetic and electrostatic fields are at the same frequency, the dynamical equations for both

cases can be averaged over the wave period in order to obtain the equations for the slow variations.

Electron dynamics are treated by integration of the 3-D Lorentz force equations in the complete set of electrostatic, magnetostatic, and electromagnetic fields. The generality of this formulation of the orbits is crucial, and permits ARACHNE to describe the primary wiggler oscillation, Larmor effects due to the presence of the axial field, and Betatron oscillations and guiding-center drifts due to the wiggler inhomogenieties. This is the critical requirement in the simulation of the field-reversed configuration near the anti-resonance.

The initial conditions describe the beam upon entry into the wiggler, and the effect of an axial energy spread is included by means of a pitch angle spread. The wiggler field model is 3-D and includes an adiabatic entry taper, and ARACHNE describes the injection of the beam. This has a practical advantage, since it is easier to determine the beam characteristics prior to injection. The initial conditions imposed on the TE and TM modes are that the initial amplitude of each mode is chosen to reflect the injected power into the system, and the initial wavenumber corresponds to the vacuum value appropriate to the mode. Initialization of the Gould-Trivelpiece modes is accomplished by evaluation of the appropriate initial phase averages of the beam.

ARACHNE self-consistently integrates the dynamical equations for the field amplitudes and phases in conjunction with the Lorentz force equations for the electrons. Since the complete Lorentz force equations are used, this permits the self-consistent description of the injection of the beam into the wiggler, the bulk wiggler motion, Larmor motion, wiggler inhomogenieties [i.e., Betatron motion, guiding-center drifts, velocity shear effects, orbital instabilities, and etc.], and harmonic interactions. Of the greatest significance to the current experiment, however, is the implicit inclusion of the anti-resonance phenomena in the reversed-field configuration.

The experiment has operated with the guide field oriented both parallel and anti-parallel with the wiggler, and we shall limit the discussion here to the field-reversed orientation. A more complete discussion of the comparison is given in ref. 20. We use the actual experimental parameters in ARACHNE; specifically, a waveguide radius of $R_g = 0.51$ cm, a wiggler period of $\lambda_w = 3.18$ cm, a wiggler entry taper of $N_w = 6$ wiggler periods, and a beam energy and initial radius of 750 keV and 0.25 cm. In all cases, we use the measured beam current for the given values of the guide field. The initial power of the TE_{11} mode is chosen to be 8.5 kW. The only Gould-Trivelpiece modes which interact in this case have an azimuthal mode number of $l = 0$, and only the lowest order radial mode is required to give reasonable agreement with the experiment.

The first case we consider is that of a field-reversed configuration in which the nominal experimental magnetic field parameters were an axial field magnitude of 10.92 kG and a wiggler field of 1.47 kG. The transmitted current for these field parameters was 300 A [±10%], and the

axial energy spread of the beam is assumed to be 1.5% as indicated in the experiment. These parameters represent the case of the peak power observed in the experiment of 61 MW.

The comparison of the experiment and ARACHNE is shown in Fig. 1 where we plot the evolution of the power, and in which the dots represent the measured power in the experiment. As shown in the figure, ARACHNE was used for two sets of parameters. One corresponds to the nominal experimental values, and the second corresponds to the upper limits on the current, wiggler field, and input power due to the experimental uncertainties of 330 A, 1.55 kG and 10 kW respectively. As is evident, the agreement between the experimental measurements and ARACHNE is good, and the virtually all the data points fall between these two curves. The saturated power for these two choices of the current, wiggler field, and input power differ only marginally and are close to the 61 MW measured in the experiment. The principal difference is in the saturation length which is due to a small discrepancy in the growth rates for these two cases.

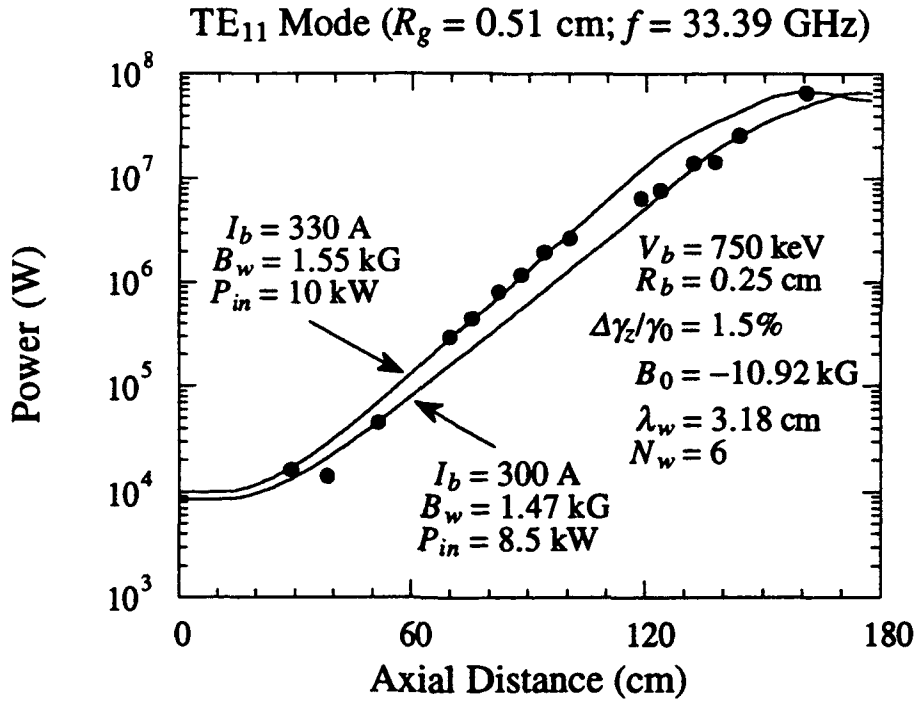


Fig. 1 The evolution of the power with axial position as determined with ARACHNE and from the experiment (dots) for a field-reversed configuration.

The interaction efficiency in this case is approximately 27% and is comparable to that expected on the basis of phase trapping arguments. The phase trapping efficiency is estimated by the energy lost as the axial electron velocity decreases by an amount $\Delta v_z = 2(v_z - v_{ph})$, where $v_{ph} = \omega/(k + k_w)$, (ω,k) are the angular frequency and wavenumber of the electromagnetic wave, and k_w is the wiggler wavenumber. The inclusion of Raman effects in this estimate is implicitly

accomplished by the choice of the appropriate frequency and wavenumber ARACHNE includes Raman effects, and results in $k/k_w \approx 2.980$ [in vacuum $k/k_w \approx 2.985$]. In addition, $v_z/c \approx 0.911$ hence, the estimate of the phase trapping efficiency is approximately 34%.

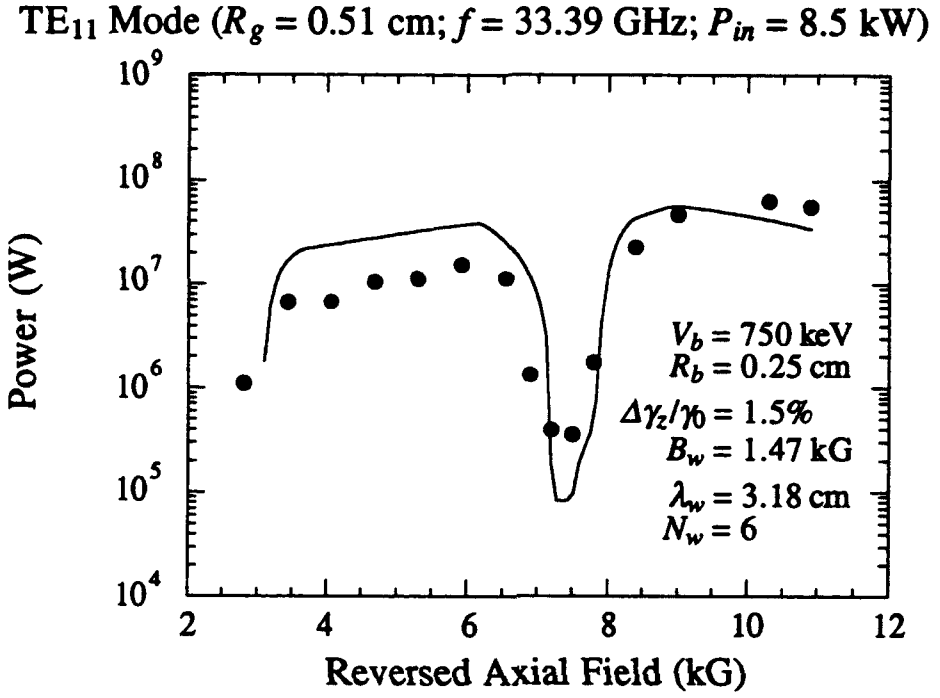


Fig. 2 The variation in the output power versus the magnitude of the reversed axial field as measured in the experiment (dots) over an interaction length of 150 cm and with ARACHNE.

The variation in the output power over an interaction length of 150 cm as a function of the magnitude of the reversed magnetic field is shown in Fig. 2. Again, the dots represent the experimentally measured power and the curve is the result from ARACHNE. The current used in the simulation for each value of the axial field corresponds to the measured current.[6,7] Agreement between the experiment and theory is good across the entire range studied. Of particular note, however, is the sharp decrease in the output power in the vicinity of the anti-resonance at axial field magnitudes between approximately 7-8.5 kG.

The source of this anti-resonant decrease in the interaction efficiency is the irregularity introduced in the electron trajectories by the transverse wiggler inhomogeniety. For this particular example, the radius of the wiggler-induced motion [i.e., the radius of the helical steady-state trajectory] is approximately 0.04 cm. However, the beam radius is 0.25 cm in the experiment. As a consequence, the electrons at the outer regions of the beam are quite sensitive to the wiggler inhomogeniety, and experience a sinusoidally varying wiggler field during the course of their trajectories. The effect of this sinusoidal variation is to act as an anti-resonant harmonic driver to

the electron orbits which distorts the wiggler motion and degrades the interaction. These effects are implicitly included in the ARACHNE formulation, and are discussed in detail in ref. 20.

IV. SUMMARY AND DISCUSSION

We have presented a detailed comparison showing substantial agreement between a high power FEL amplifier experiment using a combined helical wiggler/axial guide magnetic field configuration and a 3-D nonlinear formulation of the FEL in the collective Raman regime (ARACHNE). Two significant new results are represented by this comparison. The first is the near-30% efficiency with a uniform-wiggler design. While efficiencies of this magnitude are expected on the basis of both simple phase-trapping arguments and detailed numerical simulations, this is the first time such efficiencies have been demonstrated in the laboratory. The second, is the existence of the anti-resonant degradation in the operating efficiency. This had been previously unsuspected, and the experimental demonstration of the effect has been instrumental in pointing the way toward a theoretical reexamination of the orbital dynamics in this regime.

ACKNOWLEDGMENTS

This work was supported by ONR and the ONT. We would like to thank G. Bekefi and M.E. Conde for providing us with the experimental data.

REFERENCES

†Permanent Address: Science Applications International Corp., McLean, VA 22102.
[1]R.W. Warren *et al.*, IEEE J. Quantum Electron. **QE-19**, 391 (1983).
[2]J.A. Edighoffer *et al.*, Phys. Rev. Lett. **52**, 344 (1984).
[3]R.M. Phillips, IRE Trans. Electron Dev. **ED-7**, 231 (1960).
[4]J. Fajans, G. Bekefi, Y.Z. Yin, and B. Lax, Phys. Rev. Lett. **53**, 246 (1984).
[5]T.J. Orzechowski *et al.*, Phys. Rev. Lett. **57**, 2172 (1986).
[6]M.E. Conde and G. Bekefi, Phys. Rev. Lett. **67**, 3082 (1991).
[7]M.E. Conde and G. Bekefi, IEEE Trans. Plasma Sci. (this issue).
[8]A.K. Ganguly and H.P. Freund, Phys. Rev. A **32**, 2275 (1985) .
[9]H.P. Freund and A.K. Ganguly, Phys. Rev. A **33**, 1060 (1986).
[10]H.P. Freund and A.K. Ganguly, Phys. Rev. A **34**, 1242 (1986).
[11]H.P. Freund and A.K. Ganguly, J. Quantum Electron. **QE-23**, 1657 (1987).
[12]A.K. Ganguly and H.P. Freund, IEEE Trans. Plasma Sci. **16**, 167 (1988).
[13]A.K. Ganguly and H.P. Freund, Phys. Fluids **31**, 387 (1988).
[14]J. Fajans *et al.*, Phys. Rev. Lett. **57**, 579 (1986).
[15]D.A. Kirkpatrick *et al.*, Phys. Fluids **B1**, 1511 (1989).
[16]D.E. Pershing *et al.*, Nucl. Instr Meth. **A304**, 127 (1991).
[17]R.K. Parker *et al.*, Phys. Rev. Lett. **48**, 238 (1982).
[18]K.R. Chu and A.T. Lin, Phys. Rev. Lett. **67**, 3235 (1991).
[19]N.A. Krall and A.W. Trivelpiece, *Principles of Plasma Physics* (McGraw-Hill, New York, 1973), p. 202.
[20]H.P. Freund and A.K. Ganguly, IEEE Trans. Plasma Science (in press).

ANALYSIS OF THE ELECTRON DYNAMICS IN A RAMAN FREE ELECTRON LASER WITH REVERSED AXIAL GUIDE MAGNETIC FIELD

G. Spindler and G. Renz
Institut für Technische Physik, German Aerospace Research Establishment
W-7000 Stuttgart 80, Germany

M.E. Conde and G. Bekefi
Plasma Fusion Center, Massachusetts Institute of Technology
Cambridge, MA 02139 USA

Numerical simulations of the electron dynamics in a combined helical wiggler and reversed guide field arrangement, currently being under investigation at the MIT Plasma Fusion Center, are presented. The paper focuses on the unexpected breakdown of the FEL amplifier performance for a specific value of the reversed guide field, corresponding to the positive value at magnetoresonance. As an outgrowth, the theoretical possibility of higher harmonics generation in the presence of a reversed guide field is highlighted.

Introduction

High-current free electron lasers operating in the Raman and strong-pump regimes generally need a strong magnetic guide field in combination with a helical wiggler; e.g. [1]. In the experiments performed so far, the cyclotron rotation of the beam electrons introduced by the guide field has always been in the same direction as the rotation imposed by the helical wiggler field. As a consequence, if the wiggler-induced frequency of the electrons equals the cyclotron frequency, the transverse motion is resonantly enhanced, leading to a dramatic exchange of energy between the longitudinal and transverse degrees of freedom (magnetoresonance).

Recent experimental studies of a 33.3 GHz FEL amplifier with a helical wiggler have demonstrated performance with very high efficiency (around 30%) and power output (around 60 MW), if the direction of the guide field is *reversed* [2]. Operation in the conventional group I and group II modes respectively yields 9%, 6 MW and 2%, 4 MW. There is, however, unexpected evidence for a breakdown of the power output for a value of the reversed guide field, corresponding to the positive value at magnetoresonance. In this study, we address this effect by means of single-particle computations of the electron dynamics in the external fields and the resulting spontaneous emission. In completion of this paper, the simulation of *higher harmonics* under reversed guide field conditions is reported.

Computation of the Electron Dynamics

Our code comprises a realizable wiggler field, with a radial dependence given by the modified Bessel functions; e.g. [3]. The mean magnetic and electrostatic self-fields of the electron beam can be considered. A more detailed discussion of the properties of the dynamical problem can be found in [4]. In Fig. 1, the orbit of

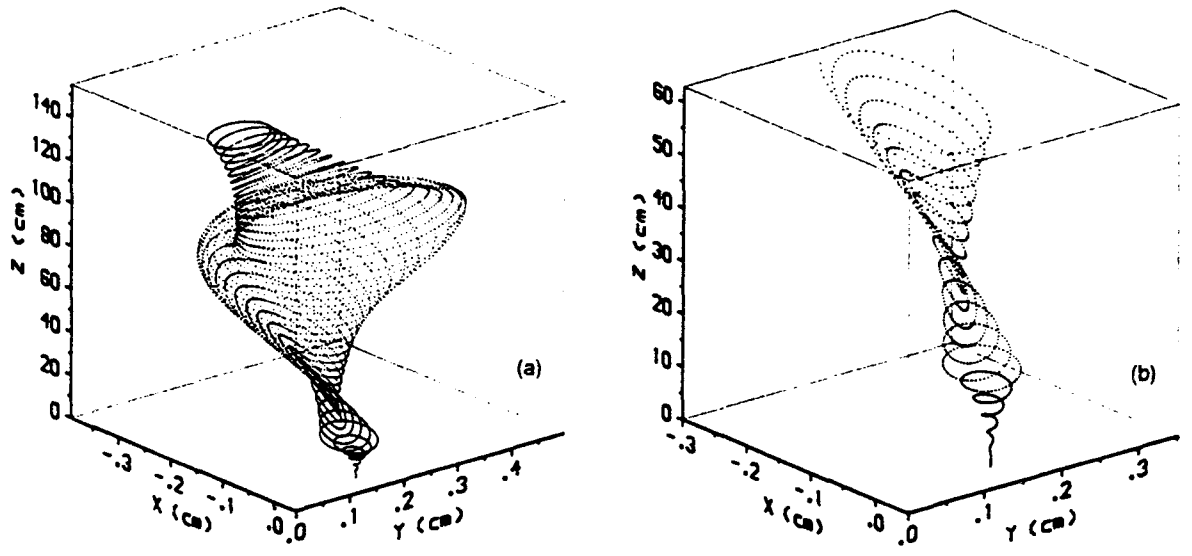


Fig. 1. Electron orbit in combined helical wiggler and reversed guide field, for parameters leading to a breakdown of amplification in the experiment. In Fig. 1b, the part of the orbit containing the first change of the direction of revolution has been blown up.

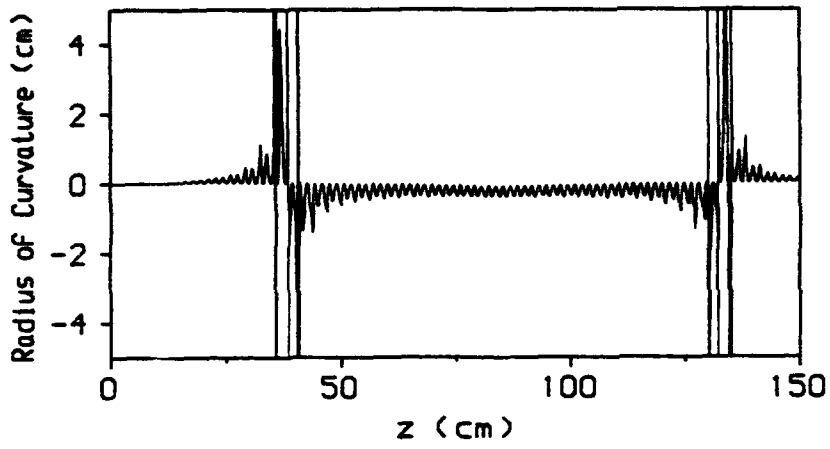


Fig. 2. Radius of curvature of the electron orbit in the transverse (x-y) plane versus the axial position in the wiggler.

an off-axis electron (transverse start position: $x_0 = 0.00$ cm, $y_0 = 0.15$ cm) for the reversed guide field arrangement is shown for parameters, marking the breakdown of amplification in the experiment [2]; i.e., $B_w = 1470$ G (wiggler field on axis), $B_0 = -7525$ G (reversed guide field), $\lambda_w = 3.18$ cm (wiggler period) and $\gamma = 2.47$ (750 keV beam energy). The beam self-fields have been suppressed (case of weak electron current) as they do not alter the essential characteristics of the trajectory. Figure 2 reflects the radius of curvature of the orbit in the transverse (x-y) plane as a function of the axial position in the wiggler. The electron enters the wiggler via an adiabatic entrance consisting of 6 periods, its direction of revolution being imposed by the wiggler field. The transverse velocity grows beyond the value given by the well-known steady-state orbit theories [5], [6]. Triggered by a *change* of the direction of revolution (cf. Figs. 1b, 2), the orbit strongly expands in the transverse plane; i.e., energy of the axial motion is transformed into energy of the transverse degrees of freedom. The electron orbit contracts again and, after a second change of the direction of revolution, nearly reaches its original state just behind the adiabatic entrance. After that, the same process starts again.

A possible explanation for this behavior might be given in terms of a theory recently introduced in [7]: An off-axis electron orbit in velocity space can be decomposed into positive and *negative* harmonics of the fundamental wiggler-induced frequency $(2\pi/\lambda_w)\, v_z$. This is due to the transverse dependence of the realizable helical wiggler field. Hence, in accordance with [7], we infer that our orbit is governed by the influence of the negative harmonic n = -1, resonantly enhanced by the reversed guide field. A numerical experiment, with an ideal wiggler in combination with a relatively weak ($\approx$ 1%) ideal wiggler having the same period but reversed direction of rotation, qualitatively reproduces the orbit shown in Fig. 1, and thus, lends support to our conclusions.

Spontaneous Emission

The spectrum of spontaneous emission for a guide field $B_0 = -10900$ G is presented in Fig. 3a. We have, according to [2], very high amplifier performance in this case. The numerical calculation has been done for the TE_{11} mode of a circular waveguide with an internal radius of 0.51 cm (cutoff frequency $\approx$ 17.2 GHz). The corresponding orbit of the electron in velocity space is well described by the

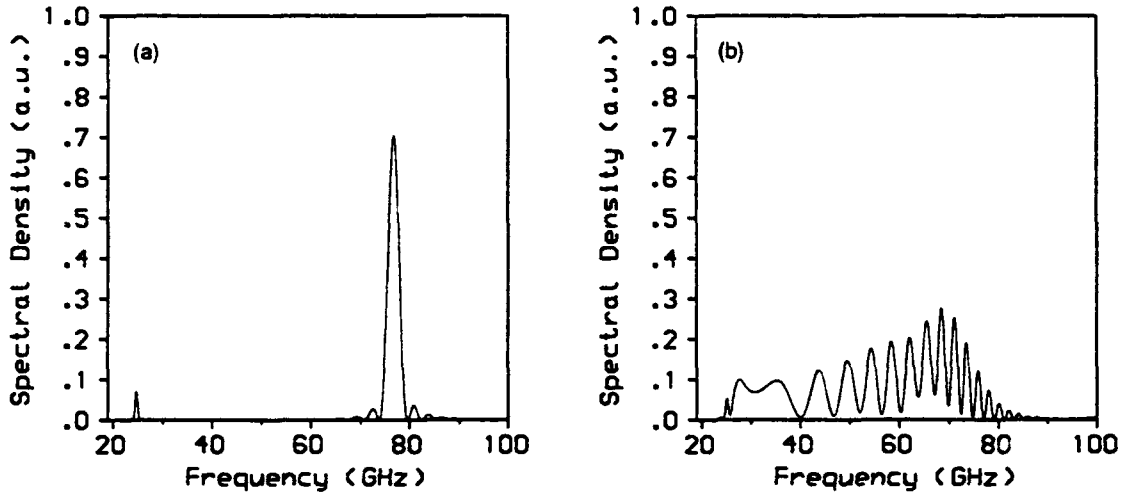


Fig. 3. Spontaneous emission, computed for two values of the reversed guide field: (a) $B_0 = -10900$ G, high amplifier performance and (b) $B_0 = -7525$ G, failure of amplification.

theories of [5] and [6]. The self-fields of the electron beam ($I_b \approx 300$ A) have been included in the simulation of the electron dynamics in this case. The line near 30 GHz is to be amplified; whereas the strong line at approx. 80 GHz is not expected to interfere with the amplification process as a *superradiant* mode. The spectrum of spontaneous emission, created by the resonant orbit for $B_0 = -7525$ G (cf. Fig. 1), is shown in Fig. 3b. The very broad and irregular spectrum predicts a degradation of the amplifier operation, and hence, might provide an explanation for the observed failure of the experiment.

Higher Harmonics Generation

To complete this paper, we briefly address the possibility of the generation of *higher harmonics* in the off-axis field of a helical wiggler [7]. As an example, adjusting the reversed guide field in our experiment to a value necessary to resonantly support the *third* negative harmonic (n = -3) of the fundamental wiggler-induced frequency, the simulation predicts a spectrum of spontaneous emission for free space conditions, as shown in Fig. 4a.

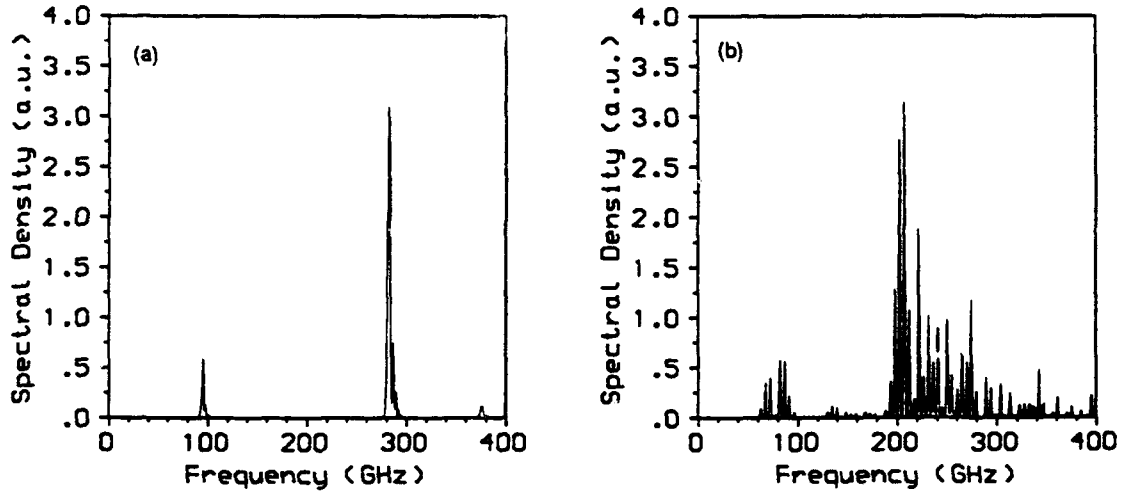


Fig. 4. Generation of the third harmonic in the spectrum of spontaneous emission: (a) reversed guide field, (b) conventional orientation of the guide field.

Here, the transverse start position of the test-electron has been given by $x_0 = 0.00$ cm, $y_0 = 0.60$ cm; i.e., an annular beam of medium diameter is required in order to experimentally verify this spectrum. Further, to obtain a fairly narrow line, the (axial) energy spread of the electron beam should be below 1%. The spectrum for a guide field with conventional (positive) orientation, but with the same absolute value, is depicted in Fig. 4b. In this case, the noisy character of the spontaneous emission does not promise FEL performance on the third harmonic. It should be noted, in this context, that all spectra presented in this paper have the *same*, but arbitrary units of spectral density.

Conclusions

In this paper, we numerically analysed the electron dynamics in a free electron laser with combined helical wiggler and reversed guide field. Upon starting the electron off axis, and adjusting the reversed guide field to resonantly stimulate negative harmonics of the fundamental wiggler-induced frequency in the electron orbit (in velocity space), higher harmonics (up to the third) in the spectrum of spontaneous emission have been demonstrated. Owing to a relatively strong resonant coupling between the longitudinal and transverse degrees of freedom, in the case of the first negative harmonic ($n = -1$), the spectrum appears to be very broad and irregular. The consequence could be a degradation of the FEL amplifier performance which is, in fact, observed in the MIT experiment.

References

[1] C.W. Roberson and P. Sprangle, Phys. Fluids B **1**, 3 (1989)
[2] M.E. Conde and G. Bekefi, Phys. Rev. Lett. **67**, 3082 (1991)
[3] J.P. Blewett and R. Chasman, J. Appl. Phys. **48**, 2692 (1977)
[4] G. Spindler and G. Renz, Phys. Fluids B **3**, 3517 (1991)
[5] L. Friedland, Phys. Fluids **23**, 2376 (1980)
[6] H.P. Freund and A.K. Ganguly, IEEE J. Quantum Electron. **QE-21**, 1073 (1985)
[7] K.R. Chu and A.T. Lin, Phys. Rev. Lett. **67**, 3235 (1991)

HELICAL SMALL PERIOD WIGGLER FOR THE RAMAN FREE ELECTRON LASER OF SIOFM

Ming Chang Wang, Bibo Feng, Zhijiang Wang
Zaitong Lu, and Lifen Zhang
Shanghai Institute of Optics and Fine Mechanics
Academia Sinica, P.O.Box 800211,Shanghai 201800,China

ABSTRACT

The small period wigglers in recent years have been attracted by developing a compact free electron laser (FEL) device. A new small period wiggler configuration constructed by the bifilar helical sheets with ferro-magnetic cores for the Raman FEL of Shanghai Institute of Optics and Fine Mechanics (SIOFM) is developed, and the performance characteristics of the wiggler with 10 mm period and 600 mm length are measured. It is similar to the bifilar helical wires wiggler, but in this configuration, there are the copper sheets instead of the wires, some ferro-magnetic laminations between the copper sheets have been inserted in order to enhance the wiggler field. The field as high as 1500 G has been obtained with a large gap of 16 mm.

1. Introduction

A wiggler is an important element of free electron lasers (FEL's), which couples the electron beam to optical wave. In order to achieve the shortest possible wavelength with given electron energies, the wigglers with small periods have to be considered. In recent years, the small period wigglers have been attracted by developing a compact FEL.

In a FEL, the wavelength of the optical beam λ is related to the wiggler period λw and the energy of the electron beam $E = \gamma mc^2$ by $\lambda \approx \lambda w / \beta(1 + \beta) \gamma^2$, where $\beta = v/c$ and $\gamma = (1 - \beta^2)^{-1/2}$ are the dimensionless parameters of the electrons velocity and energy.

Many designs and experiments of small-period wigglers have been performed recently[1]. The development of the helical wigglers is somewhat behind the linear wigglers, although the former is more efficient for FEL's. Proposals have been made to construct a helical wiggler from permanent magnets[2], and to design an iron-core electromagnet with helical geometry[3].

The experiments of a high gain Raman FEL oscillator with a Bragg reflection resonator have been made in SIOFM[4]. The 14 MW peak power at 7.7 mm wavelength with a 500 KeV/800 A electron beam of 60 ns pulse duration was obtained.

This work invistigates a new wiggler configuration constructed by bifilar helical sheets with ferro-magnetic cores for the Raman FEL of SIOFM. A peak field of 1.5 kilogauss for relatively large gap to period ratios, gap/λw =1.6, is achieved.

It is feasible to make a Raman FEL with this type of wiggler operating in the range of millimeters and submillimeters in low electron energy (500 KeV).

2. Design considerations

The configuration of new wiggler is showed in Fig. 1. It is similar to the bifilar helical wires wiggler, but in this configuration, there are the copper sheets instead of the wires. In order to enhance the wiggler fields, the conducting sheets of copper are wound through a stack of helical ferro-magnetic cores in alternating directions. The helical cores are insulated standard transformer laminations, which have been inserted between the copper sheets.

Because of the magnetic materials, the wiggler fields are increased largely, so the wiggler periods can be reduced to several millimeters and the comparative strong wiggler fields have been obtained. At one end, two helical coppers connect each other; at the other end, there are the current input and output poles. A current is passed through the copper sheet to produce a periodic magnetic field.

In Fig. 1, r_i and r_o are the internal radius and external radius of the helical copper sheets, respectively; h_1 and h_2 are the thickness

of the helical copper sheets and the ferro-magnetic laminations, respectively. The field from the bifilar helical wires has been calculated[4] and its components are

$$B_r = 2B_w[I_0(k_w r) - \frac{I_1(k_w r)}{k_w r}] \sin(\vartheta - k_w z)$$

$$B_\vartheta = \frac{2B_w I_1(k_w r)}{k_w r} \cos(\vartheta - k_w z) \qquad (1)$$

$$B_z = -2B_w I_1(k_w r) \cos(\vartheta - k_w z)$$

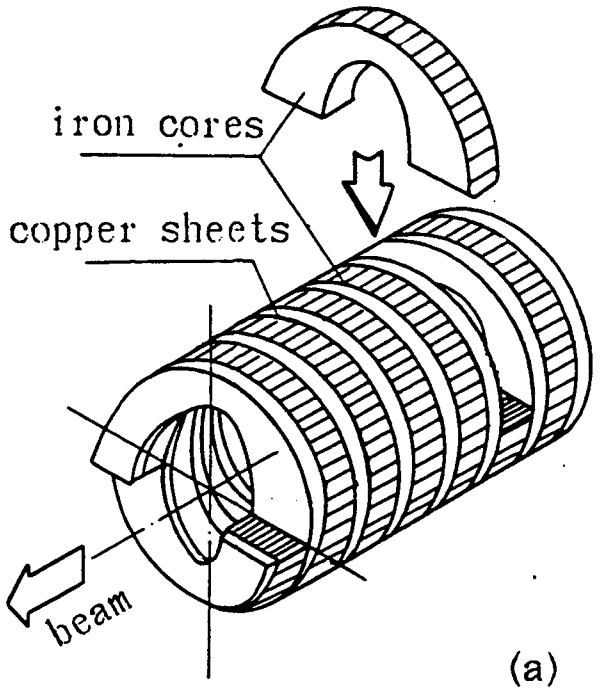
where Io , I1 are Bessel functions of imaginary arguments, and Bw , the transverse field amplitude along the wiggler axis, is given approximately by

$$B_w = \frac{8\pi I}{10\lambda_w} [\frac{2\pi r}{\lambda_w} k_0(\frac{2\pi r}{\lambda_w}) - k_1(\frac{2\pi r}{\lambda_w})] \qquad (2)$$

where r is the radius of helical wires, I is the current of wiggler, and ko, k1 are modified Bessel functions. The bifilar helical sheets wiggler can be considered as a superposition of many bifilar helical wires, it also produces the periodic, circular polarization fields inside the wiggler. From (2), the transverse field amplitude on the axis can be derived as follows

$$B_w = \frac{8\pi I}{10\lambda_w (r_o - r_i)} \int_{r_i}^{r_o} dr \, [\frac{2\pi r}{\lambda_w} k_0(\frac{2\pi r}{\lambda_w}) - k_1(\frac{2\pi r}{\lambda_w})] \qquad (3)$$

By inserting some magnetic cores between the copper sheets, the transverse field can be increased. The field distribution will be changed, but the periodicity of the wiggler fields is not varied.



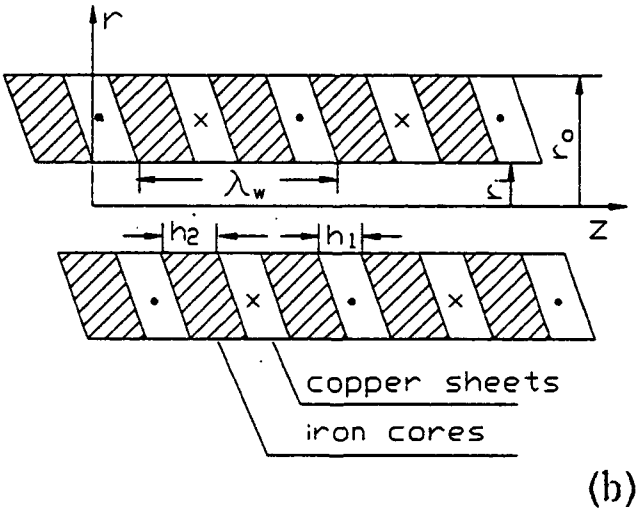


Fig. 1 Configuration of the helical small period wiggler with ferro-magnetic cores. (a), Schematic of the wiggler; (b), Cross section of the wiggler along z-axis.

3. Experimental results

A small period wiggler with number of periods of 60 has been constructed, and its field characteristics are measured.

The wiggler period λw =10 mm; the internal radius and external radius of the helical sheets are 8 mm and 15 mm, respectively; The thickness of copper sheets and iron-cores are 1.5 mm and 3.5 mm, respectively. The resistance between the two copper-sheet poles is about 100 mΩ, and the pulse current of wiggler is supplied by a capacitor bank. The relation of capacitor voltage Vo with the current I is approximately I ≈ 13 Vo (Ampere) according to the experience of experiments. The wiggler along the axis was measured with an induction coil and a Miller integrator.

Fig. 2 shows the measured wiggler field versus capacitor voltage Vo , with magnetic iron cores (top line) and without iron cores (bottom line). The wiggler field increases when the magnetic cores are added and can be varied continuously by varying the current in the sheets. The saturation of the magnetic materials is a reason to limit the wiggler to produce much strong transvese fields.

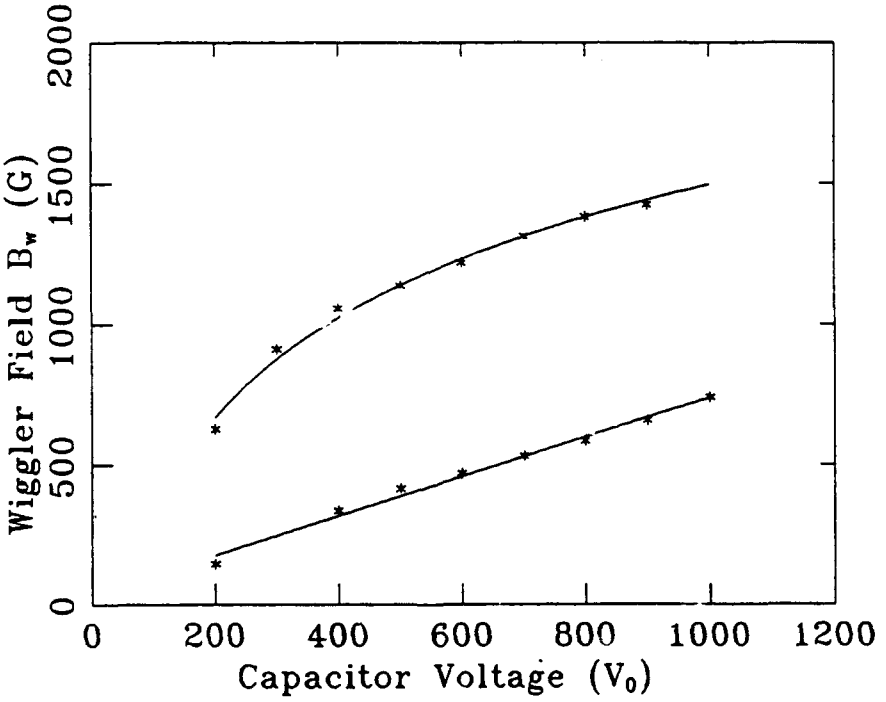


Fig.2 Wiggler field Bw vs. capacitor voltage Vo . with iron cores (top line), without iron cores (bottom line).

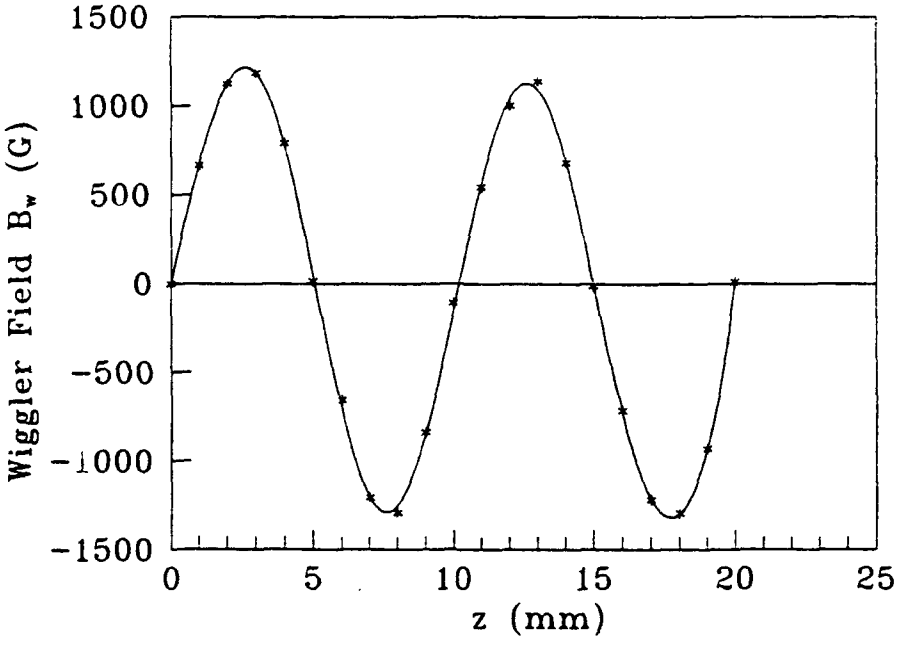


Fig.3 Measured values of the wiggler fields along z-axis, capacitor voltage is 800 V.

The periodicity of the wiggler field along the z-axis has been measured and is shown in Fig. 3. The periodic nature of the field is readily seen, and the variation in maximum field amplitude can be attributed to probe positioning errors, small irregularities in copper sheets fabrication, and end effects.

We assume the guided field of Bo = 3 KG, and the wiggler field of Bw = 1000 G, the computer simulation for SIOFM FEL indicates that, the output power of 20 MW at wavelength of 1.72 mm, the maximum efficiency of 5.05 % will be expected.

Table I lists the parameter values of the SIOFM FEL. It is especially simple and inexpensive to fabricate this type of wiggler, even make a tapered one. The experiment of FEL with the small-periods wiggler at SIOFM is undertaken.

In conclusion, the wiggler gap in our configuration is large enough so that a strong cylindrical beam can be used to produce high power radiation. Numerous applications in the millimeter wave, mid- and far-IR range could benefit from a compact, moderate power, tunable coherent source based on small period wigglers.

Table I. Parameter Values of the SIOFM FEL

Accelerator		
Beam voltage	V	500 KV
Beam current	I	800 A
Beam radius	r_e	3 mm
Pulse duration		60 ns
Wiggler		
Wiggler period	λ_w	10 mm
Wiggler length	L	600 mm
Wiggler field	B_w	1000 G
Internal radius	r_i	8 mm
External radius	r_o	15 mm
Thickness of copper-sheets	h_1	1.5 mm
Thickness of iron-cores	h_2	3.5 mm
Radiation wave (expected)		
Wavelength	λ_s	1.7 mm
Output power	P_o	20 MW
Efficiency	η	5.05 %

References

1. V.L. Granatstein, et al, **A.P.L.**, 47, (1985)643.
2. M.S. Curtin, **Nucl.Instr. and Meth.**, A 250(1986)110.
3. J. Vetrovec, **Nucl.Instr. and Meth.**, A 296(1990)563.
4. M.C. Wang, et al, **Nucl.Instr. and Meth.**, A 304(1991)116.
5. J.P. Blewewtt, and R. Chasman, **J.A.P.**, 48, 7(1977)2692.

DEVELOPMENT OF A HIGH POWER MILLIMETER WAVE FREE-ELECTRON LASER AMPLIFIER

S. W. Bidwell, Z. X. Zhang, T. M. Antonsen, Jr., W. W. Destler,
V. L. Granatstein, B. Levush, J. Rodgers,
Laboratory for Plasma Research
University of Maryland, College Park, MD 20742, U.S.A.

and

H. P. Freund
Science Applications International Corporation, McLean, VA 22102, U.S.A

Abstract

Progress on the development of a high-average-power millimeter wave free-electron laser amplifier is reported. Successful sheet electron beam propagation has been observed through a 54 cm long wiggler magnet. One hundred percent transport efficiency is reported with a 15 A, 0.1 cm × 2.0 cm, sheet electron beam through $B_w = 5.1$ kG, $\lambda_w = 0.96$ cm, planar electromagnet wiggler. Preliminary success with a novel, yet simple, method of side focusing using offset poles is reported. Status of development on a 94 GHz, 180 kW, pulsed amplifier is discussed with results from numerical simulation.

Introduction

There is considerable interest in the magnetic fusion community for high-average-power millimeter wave sources for use in electron cyclotron resonance applications. These applications include bulk plasma heating, temperature profile control, reactor startup assist, and diagnostics. Depending on the fusion device the frequencies of interest range from 150 GHz to 600 GHz. For plasma heating CW power levels exceeding 1 MW are required. The method under investigation at the University of Maryland is a sheet electron beam, planar wiggler magnet, free-electron laser (FEL) amplifier.

A short period wiggler magnet and sheet electron beam are distinctive features of the Maryland effort.[1] The decision to employ a short period ($\lambda_w \sim 1$ cm) wiggler magnet is motivated by the desire to operate at conventional power supply voltages. Operation at voltages below 1 MV will allow for smaller and less costly modulators. Wiggler fabrication and magnet performance become more difficult at smaller periods but are not prohibitive at periods of $\lambda_w \sim 1$ cm. The sheet electron beam is chosen for its several advantages over the more conventional pencil beam. These advantages include large total beam currents and narrow interaction regions permitting high magnetic wiggler fields. The current density is held constant while the total current is increased through the wide dimension of the beam.

This paper is divided into two sections: II. Sheet Electron Beam Propagation and III. A FEL Amplifier at Millimeter Wave Frequencies. The first section will elaborate on extensive efforts to

propagate a sheet electron beam stably and confined through an amplifier relevant length of wiggler magnet. The second section discusses the effort to develop a 94 GHz linear gain amplifier as well as higher power and higher frequency devices.

II. Sheet Electron Beam Propagation

As with any high power tube much consideration must be given to stable and confined beam transport. The beam power, as high as 25 MW in some of our designs, must be transported free of interference with any material structure to avoid catastrophic damage. In the sheet configuration the beam is transported through a wide aspect ratio wiggler channel. Depending on the design this channel may have a narrow dimension of only a few millimeters and a wide dimension of several centimeters.

Previous experiments have shown stable and confined sheet beam propagation through a 10 period, $\lambda_w = 1$ cm, wiggler.[2] For practical amplifiers interaction lengths approaching one meter are necessary. To study transport in amplifier relevant lengths we have constructed a 54 cm long, 56.5 periods, $\lambda_w = 0.96$ cm, wiggler magnet. This magnet is also intended for linear gain amplification experiments at 94 GHz to be discussed shortly.

Sheet beam generation is accomplished, in our configuration, with a field emission diode and an anode with a machined slit aperture. The slit (~ 0.1 cm $\times$ 2.0 cm) within the anode serves to scrape the beam providing a high quality sheet beam to the interaction region. Beams with typical currents $I_b \leq 30$ A and current densities $J_b \approx 75$ A/cm^2 emerge from the slit.

Our efforts have involved the propagation of sheet electron beams through the wiggler interaction region without the benefit of an imposed axial guide magnetic field. Axial guide magnetic fields are compatible with a sheet beam configuration since under the influence of an axial magnetic field and its self electric field the sheet beam experiences an $\mathbf{E} \times \mathbf{B}$ velocity drift. This drift generates a velocity shear across the narrow dimension of the beam and a curling motion (diocotron instability) at the beam wide ends. It is therefore necessary to propagate the sheet beam under the influence of the wiggler magnetic fields exclusively.

Beam confinement within the narrow y dimension of the channel is excellent. The narrow dimension focusing is provided by the $F_y \sim v_x B_z$ Lorentz force component in which the axial magnetic field B_z is antisymmetric about the center of the channel. Additional considerations become necessary as the interaction length is increased. For example, with increased magnet length any deflection experienced by the beam as it enters the wiggler will manifest itself through

beam interception with the side walls at a later axial position. This deflection may result from a number of reasons including: a poor entrance taper, a misalignment of the interaction region with the beam forming structure, beam space charge, and stray magnetic fields influencing the beam before it enters the wiggler magnet.

In order to cope with these potential influences, a mechanism of wide (x) dimension focusing – also known as wiggle plane or side focusing – is needed. We choose an offset pole technique of side focusing. Physically, this technique is implemented by staggering each laminated steel pole some distance δx in the wide dimension. Beam electrons with trajectories off center, near the offset region, will experience a nonzero net flux density over several periods of travel. (Ideally those electrons traveling in the central region of the wiggler will experience zero net flux over several periods). It is intended that this nonzero net flux density, experienced by those electrons traveling near the wiggler edge, will reflect the beam electron back toward the central axis of the channel.

Results with the offset technique are encouraging. Since the wiggler is an electromagnet the alternating fields can be reversed simply by exchanging the two current feeds. Under this reversed polarity one would expect wiggler side defocusing. (Focusing in the narrow dimension should be unaffected). Defocusing is expected since the net flux experienced by the wayward electron is of the opposite polarity. This net flux should deflect the electron out the side of the wiggler. For the proper polarity for side focusing results indicate nearly 100% beam transport while, for the reversed polarity – side defocusing, transport is only 40%.

We have found the entrance taper to the wiggler magnet to be critical for overall transport. By electrically shorting the first few wiggler periods we produce a field entrance taper approximating:

$$B_{taper}(z) = B_w \sin^2(k_w z/4N).$$

The tapering is accomplished over the first $N = 3$ periods, with $B_w = 5.1$ kG, and $k_w = 2\pi/\lambda_w$ representing the wiggler wavenumber.

Sheet electron beam transport results are shown in Fig. 1. Current as monitored by a Faraday cup is indicated by closed circles (wiggler entrance) and by open circles (wiggler exit). Each data point represents a distinct measurement – simultaneous measurement on a single shot of entrance and exit current is not yet possible with our diagnostics. Allowing for shot-to-shot variation note that transport is nearly 100% for sheet beams up to 2.0 cm in width. As the beam is made wider the edges are outside of the focusing region of the magnet and that portion of the beam is therefore lost. Offset pole focusing, with an offset of $\delta x = 2.5$ mm, is used for these propagation results.

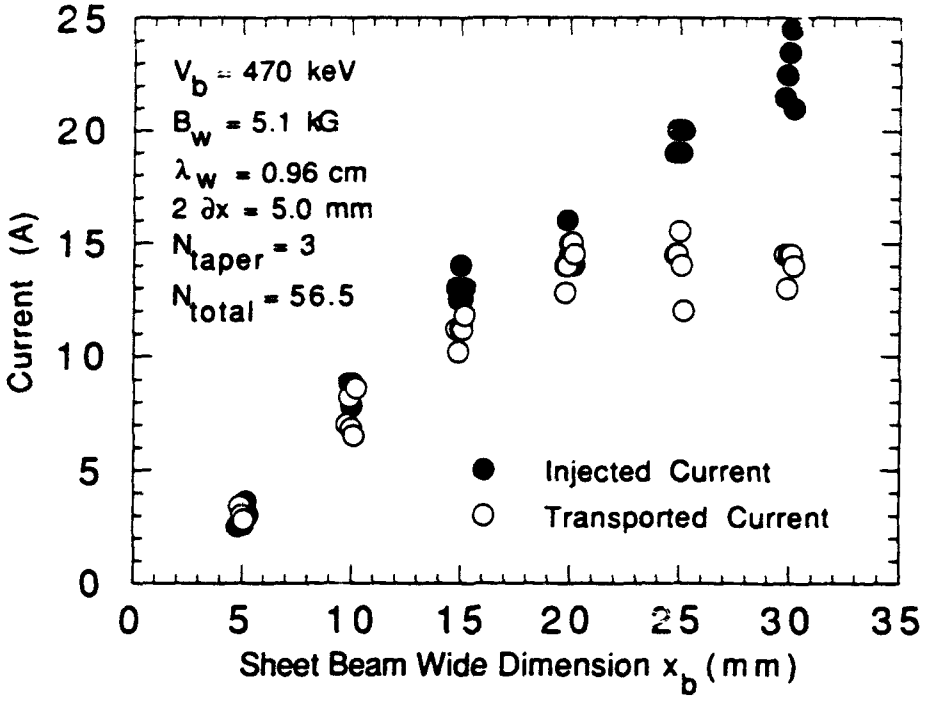


FIG. 1. Sheet electron beam propagation results through 54 cm long wiggler magnet. Injected current, measured at beam aperturing entrance slit, is represented by closed circles. Transported current, measured at exit of 56.5 period magnet, is represented by open circles.

III. A FEL Amplifier at Millimeter Wave Frequencies

Previous experimental work has shown the feasibility of high power microwave free-electron laser amplifiers.[3] Whereas most FELs operate at very high beam energies, the goal of our work is to remain at modest voltages $\gamma < 3$ and use a short period wiggler magnet $\lambda_w \approx 1$ cm.

Table I. shows three amplifier designs. The first column of Table I. indicates the parameters for the linear gain amplifier currently being developed. This amplifier will operate at 94 GHz using the $\lambda_w = 0.96$ cm wiggler at magnetic fields of $B_w = 5.1$ kG. The parameters found in this table are obtained from a 1D universal formulation[4] and verified by a 3D numerical code. A saturated power of 180 kW after 90 cm of interaction length is indicated in the first column. This assumes a cold electron beam; with a thermal spread $\Delta\gamma_z/\gamma_0 = 0.5\%$, one can expect the saturated power to decrease to 120 kW and the saturation length to increase to 100 cm.

TABLE I. Design parameters for three millimeter wave free-electron laser amplifiers.

	1 cm Wiggler	Future Exp.	Design Goal
frequency (GHz)	94	94	150
V_{beam} (MV)	0.47	0.65	0.86
I_{beam} (A)	10	30	30
S_{beam} (cm^2)	0.1 x 2.0	0.1 x 3.0	0.1 x 3.0
$B_{w,0}$ (kG)	5.1	7.0	7.0
λ_w (cm)	0.96	1.5	1.5
$a_{w,0}$	0.46	.98	.98
S_{wg} (cm^2)	0.32 x 4.0	0.75 x 4.0	0.75 x 4.0
P_{sat} (kW)	180●	610▪	620†
z_{sat} (cm)	90	41	63
Gain (dB/cm)	0.47	0.44	0.44
L_{taper} (cm)	110	45	66
P_{out} (MW)	0.5	4.2	5.0
η (%)	11	21	19
$< P_{wall} >_t$ (W/cm^2)	71	39	23

input power: ● 10 W, ▪ 10 kW, † 1 kW

A future experiment is indicated in the second column of Table I. A larger wiggler period λ_w = 1.5 cm and higher beam energy V_b = 650 keV is employed. Attaining the increased wiggler field of 7.0 kG should pose no difficulty. Higher powers P_{out} = 4.2 MW might be achieved by tapering the wiggler magnet (either field magnitude or wiggler period) after saturation of the interaction. Tapering has the additional advantage of enhancing the electronic efficiency of the interaction (η = 21% for this example). In keeping with the goal of a compact design overall length of the interaction region would not exceed one meter. An eventual design goal, as proposed for electron cyclotron resonance applications, is illustrated in the third column. It would operate at 150 GHz with 5.0 MW of millimeter wave power.

Results of a 3D numerical code as applied to the 94 GHz linear gain experiment (first column of Table I.) are presented in Fig. 2. The waveguide mode of interest TE_{01} is indicated along with the waveguide dimensions: a = 4.0 cm, b = 0.32 cm. The input power to the amplifier P_{in} = 10 W will be provided by a commercial klystron tube. Three simulation results are shown: (1) ideal beam and ideal wiggler, (2) ideal beam and real wiggler, and (3) real beam and real wiggler. Ideal beam

refers to a cold or zero temperature spread electron beam while ideal wiggler refers to a wiggler with no field errors. The "real beam" case is simulated with a temperature spread $\Delta\gamma_z/\gamma_0 = 0.5\%$. Experimentally measured wiggler peak-to-peak field fluctuations of 2.6% models the "real wiggler" case. Note that the influence of beam temperature is more detrimental than wiggler field errors to power gain. The relatively low power (1 kW to 4 kW) indicated in Fig. 2 is for a 54 cm long wiggler magnet. Additional wiggler length is required to achieve saturation power up to 180 kW.

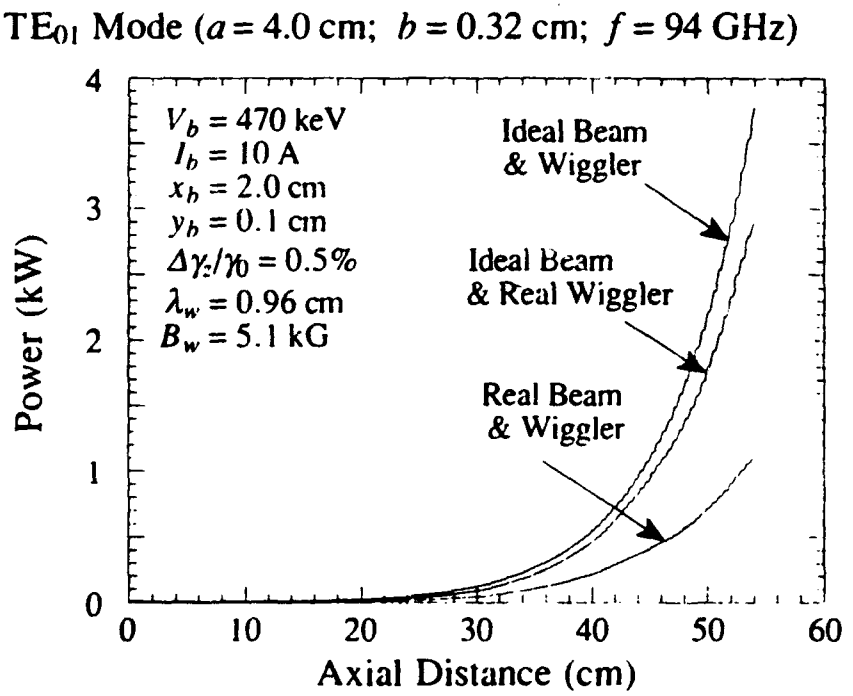


FIG. 2. Numerical simulation results showing power evolution for the linear gain amplifier with considerations of electron beam energy spread and wiggler field errors.

Acknowledgment

This work is supported by the United States Department of Energy, Office of Fusion Energy.

References

1. W. W. Destler, V. L. Granatstein, I. D. Mayergoyz, and Z. Segalov, J. Appl. Phys. **60** (2), 521 (1986).

2. D. J. Radack, J. H. Booske, Y. Carmel, and W. W. Destler, Appl. Phys. Lett. **55** (20), 2069 (1989).

3. T. J. Orzechowski, B. R. Anderson, J. C. Clark, W. M. Fawley, A. C. Paul, D. Prosnitz, E. T. Scharlemann, S. M. Yarema, D. B. Hopkins, A. M. Sessler, and J. S. Wurtele, Phys. Rev. Lett. **57** (17), 2172 (1986).

4. J. H. Booske, S. W. Bidwell, B. Levush, T. M. Antonsen, Jr., and V. L. Granatstein, J. Appl. Phys. **69** (11), 7503 (1991).

A Kind of Micro–FEL Device with Super–High Gain

Wu Ding

Institute of Applied Physics and Computational Mathematics
(P. O. Box 8009, Beijing 100088, China)

Abstract In this paper we have studied the gain characteristic of a FEL and found that there is a kind of micro–FEL device with super–high gain. This FEL device lies on the far infrared spectrum, it consists of a rf–linac with the electron beam of high brightness, a microwiggler and a capillary waveguide.

I. Introduction

The gain characteristic of a FEL have been discussed using a dimensionless current j in reference [1] and [2]. In this paper we try to perform a further study for the gain characteristic of a FEL using a dimensional gain parameter and find that a new FEL device which is worth exploring.

II. The gain characteristic of a FEL

The gain per unit length of a FEL is

$$g = \frac{1}{L} ln \frac{|a_s(L)|^2}{|a_s(0)|^2} \tag{1}$$

$$a_s = \frac{eE_s}{\sqrt{2} m_0 c \omega_s} \tag{2}$$

where L is the gain length; E_s, ω_s and c are the amplitude, the frequency and the speed in free space of the optical field; e and m_0 are the charge and the mass of the electron.

Define a gain parameter g_0, it relates with the gain per unit length of a FEL as follows

$$g = -\frac{1}{2} \frac{(g_0 L)^3}{L} F_L^2 \frac{d}{d\theta} \left(\frac{sin^2 \theta}{\theta^2} \right) \tag{3}$$

$$\theta = \frac{L}{2} \Delta K_s \tag{4}$$

$$\Delta K_s = K_w - K_s \left(\frac{1}{\beta_z^{(0)}} - 1 \right) \tag{5}$$

for low gain

$$g = \sqrt{3} g_0 F_L^{2/3} \left[1 - \left(\frac{\Delta K_s}{3 g_0 F_L^{2/3}} \right)^2 \right] \tag{6}$$

for high gain

where K_w and K_s are the wave numbers of the wiggler field and the optical field, respectively; $\beta_z^{(0)}$ is the dimensionless longitudinal velocity of the electron beam and F_L is the coupling factor of interaction of the electron beam and the optical beam.

In one dimension case, g_0 reads

$$g_0 = \left(\frac{\omega_b^2 a_w^2 K_w}{2 c^2 \gamma_0^3} \right)^{\frac{1}{3}}$$

$$= 2.71 \times 10^{-4} \left(\frac{\lambda_s(cm)}{\gamma_0} \right)^{\frac{1}{3}} \left(\frac{I(A)}{S_b(cm^2)} \right)^{\frac{1}{3}} \frac{B_w^{2/3}(G)}{\left(1 + a_w^2\right)^{\frac{1}{3}}} (cm^{-1}) \tag{7}$$

$$\lambda_s = \frac{\lambda_w}{2\gamma_0^2} \left(1 + a_w^2\right) \tag{8}$$

where B_w, λ_w and $a_w = \frac{eB_w}{\sqrt{2} m_0 c^2 K_w}$ are the amplitude, the period and the dimensionless amplitude of the wiggler field; I, S_b, γ_0 and ω_b are the current, transverse cross–section, relativistic factor and plasma frequency of electron beam, and λ_s is the wavelength of the FEL.

FELs can be divided into two kinds according to the scale of the gain parameter g_0 :

1. The first kind of FELs ($g_0 < 1cm^{-1}$)

The existing FELs belongs to this kind. It still divides into two classes which respond the low gain and high gain.

A. The low gain FELs ($g_0 L < 1$)

For this FELs, its gain curve versus the detuning is antisymmetry which shows in the expression (3).

B. The high gain FELs ($g_0 L > 1$)

In this FELs, there is a length z_0 (the original point of coordinates is at the entrance of the wiggler), it divides the system into two sections which correspond the low gain and the exponential growth, the later versus the detuning is symmetry which shows in the expression (6).

2. The second kind of FELs ($g_0 \geqslant 1cm^{-1}$)

This FELs does not exist at present. It has only the exponential

growth section and not the low gain section.

III. The gain of a capillary waveguide FEL

In the microwiggler with high field and small period, its full gap can reach 2 millimeters, thus, a waveguide is needed for the wavelength more than 50 micrometers of the FEL. In a waveguide FEL, the gain parameter g_0 has been derived[3], what corresponds the high frequency mode reads

$$g_0 = \left[\pi \frac{I}{I_A} \frac{1}{\Sigma_L} \frac{a_w^2 (1 + a_w^2)}{\left(\beta_z^{(0)}\right)^4 \gamma_0^5} \frac{\frac{\omega^+}{c}}{\left(1 - \left(\frac{\lambda_s^+}{\lambda_t}\right)^2\right)^{\frac{1}{2}}} \right]^{\frac{1}{3}} (cm^{-1}) \tag{9}$$

$$\Sigma_L = \begin{cases} \dfrac{ab}{4} & \textit{the rectangular guide } EB_{11} \textit{ mode} \\ \pi r_g^2 J_1^2(u_{01}) & \textit{the cylindrical guide } EB_{11} \textit{ mode} \end{cases} \tag{10}$$

$$\lambda_t = \begin{cases} \dfrac{2ab}{\sqrt{a^2 + b^2}} & \textit{the rectangular guide } EB_{11} \textit{ mode} \\ \dfrac{2\pi r_g}{u_{01}} & \textit{the cylindrical guide } EB_{11} \textit{ mode} \end{cases} \tag{11}$$

$$\frac{\omega^+}{c} = \beta_z^{(0)} \gamma_z^2 K_w \left[1 + \beta_z^{(0)} \left(1 - \left(\frac{\lambda_w}{\beta_z^{(0)} \gamma_z \lambda_t} \right)^2 \right)^{\frac{1}{2}} \right] \tag{12}$$

$$\lambda_s^+ = \frac{2\pi c}{\omega^+} \qquad \gamma_z = \frac{\gamma_0}{\sqrt{1 + a_w^2}} \tag{13}$$

where I_A is the Alfven current, Σ_L is the laser mode transverse cross–section, a,$b$and r_g are the transverse sizes of the rectangular and cylindrical guide, λ_t is the intercept wavelength of the guide; J_1 is the first–order Bessel function of the first kind; u_{01} is the first zero of the

zeroth–order Bessel function of the first kind J_0.

Using the formulas (9)–(13), we calculate g_0 for the FIR FEL, the results are listed in the table. The magnet field parameters used in the table come from the report of R.Warren in LANL [4]. The current and transverse cross–section of the electron beam are expected for the photocathode injector progress.

It is shown, from the table, that in the range of the wavelength $\lambda_s = 100\mu m - 1000\mu m$, g_0 can exceed $1cm^{-1}$ for the given parameters in the table.

IV. Discussion

From the table, we can design a kind of FIR micro–FEL device with super–high gain. Assume the wiggler length to be 10 centimeters, then the power may be amplified 10^4times when the laser and electron beam pass through the wiggler simultaneousely. However, we will face many challenges to realize this idea:

(1) the generation of the electron beam with the high current density (about $10^5 A / cm^2$);

(2) if more than 90% of electrons in such electron beam off–axis displacement in transport process is confined at less than $100\mu m$, then, the requirement for emittance and focus of the electron beam will be severe;

(3) when $\lambda_s / r_g \sim 1$, the high order guide modes may be excited;

(4) the capillary waveguide may be damaged by a high power laser.

Reference

[1] W.B.Colson, J.C.Gallardo and P.M.Bosco, Phys. Rev. A34, No 6, 4875 (1986);

[2] G.Dattoli, A. Torre, C.Centioli and M. Richetta. IEEE. J. of QE–25, No 11, 2327 (1989);

[3] W.Ding "Gain of a waveguide FEL" (to be published)

[4] R.Warren "Progress with the slotted–Tube pulsed Microwiggler" (submit to the 13th International Free–Electron Laser Conference, Aug. 25–30,1991, Santa Fe. NM. USA)

TABLE

λ_s (μm)	γ_0	I (A)	r_b (cm)	r_g (cm)	λ_w (cm)	B_w (T)	g_0 (cm^{-1})
50	9.6	200	0.025	0.1	0.3	5	0.766
100	6.9	200	0.025	0.1	0.3	5	1.08
204	5	200	0.025	0.1	0.3	5	1.51
350	4	20	0.025	0.1	0.3	5	1.94
814	3	200	0.025	0.1	0.3	5	2.73
1730	2.61	200	0.025	0.1	0.3	5	7.98

OPTICAL GUIDING AND SUPERRADIANCE EFFECTS IN FREE ELECTRON LASERS

N. S. Ginzburg
Institute of Applied Physics, Russian Academy of Science,
46 Uljanov Str., 603600 N. Novgorod, Russia

Efficiency enhancement in FEL under optical guiding condition and generation of short power electromagnetic pulse due to the superradiation processes are investigated

The paper is concerned with radiation of ensembles of electron-oscillators in free space (see also [1-8]). Processes of two types are investigated: 1) the amplification and canalization of radiation along the electron waveguide formed by high-current electron beams; 2) the superradiance of the short electron pulse (clusters) that are essentially moving active resonators.

1. *OPTICAL GUIDING EFFECTS.* Consider a two-dimensional FEL model. Assume that the oscillatory motion is imparted to the electrons passing through a plane undulator whose magnetic field is specified by the vector potential $\vec{A}_u = \mathrm{Re}\,[\vec{y}_0\, A_u\, e^{ih_u z}]$ where $h_u = 2\pi/d$ and d is the undulator period. The electrons are injected near the undulator axis (x=0). Let the electromagnetic field be a quasi-optical monochromatic beam $\vec{A}_s = \mathrm{Re}[\vec{y}_0 A_s(z,x) e^{i(\omega_s t - h_s z)}]$. The sheet electron beam - optical beam interaction under the conditions of combination synchronism, $\omega_s = (h_u + h_s)v_{\parallel}$, is described by the following set of equations

$$i\frac{\partial^2 a}{\partial X^2} + \frac{\partial a}{\partial Z} = 2i\delta(X)\,\frac{1}{\pi}\int_0^{2\pi} e^{-i\vartheta}\,d\vartheta_0\,, \qquad a(Z=0) = a_0(X),$$

$$\frac{\partial^2 \vartheta}{\partial Z^2} = \mathrm{Im}(e^{i\vartheta}), \qquad \vartheta(Z=0) = \vartheta_0 \in [0,2\pi], \qquad \frac{\partial\vartheta}{\partial Z}(Z=0) = -\Delta \qquad (1)$$

Here $Z = \omega/c\; zG$, $X = \omega/c\; x(2G)^{1/2}$, $a = \alpha_s\alpha_u G^2/2$, $\vartheta = \omega t - (h_u + h_s)z$, $\Delta = (c/v_{c0} - c/v_{\parallel 0})\,G^{-1}$ is the initial mismatch of the combination synchronism, v_{c0} is the phase velocity of the combination wave which corresponds to the electromagnetic wave propagated strictly along the z-axis, $G = 2^{-1/5}(\omega_p^2 b\,\alpha_u^2/8\omega c\gamma)^{2/5}$ is the gain

parameter taking into account diffractional effects, ω_p is the plasma frequency, $\alpha_{s,u} = eA_{s,u}/mc^2\gamma$, and $\delta(X)$ is the delta function. We investigate here the case of a thin electron beam, corresponding to a small Fresnel parameter $h_s b^2/L \ll 1$ where b is the electron beam width and $L_s \sim (h_s G)^{-1}$ is the characteristic length of the interaction space (reverse increment).

At the linear stage of interaction when plane wave is incident on the REB: $a_0(X)=\text{const}$, for $\Delta=0$ we obtain for an amplified and diffracted field

$$a(X,Z) = a_0\left[\Phi\left(\frac{\sqrt{i}|X|}{2\sqrt{Z}}\right) + \frac{1}{5}\sum_{n=1}^{5} e^{-ix_n|X| + i\Gamma_n Z}\left(1 - \Phi\left(\frac{\sqrt{i}|X|}{2\sqrt{Z}} - x_n\sqrt{iZ}\right)\right)\right]$$

where Φ is probability integral, while $x_n = e^{i[\pi/5 + 2\pi(n-1)/5]}$ and $\Gamma_n = x_n^2$ are the transverse and longitudinal wave numbers of the eigenmodes in a system unbounded in z-direction. Among these waves there is only one wave ($n=5$) that is amplified in the longitudinal direction, $\mathrm{Im}\Gamma<0$, is damped in the transverse

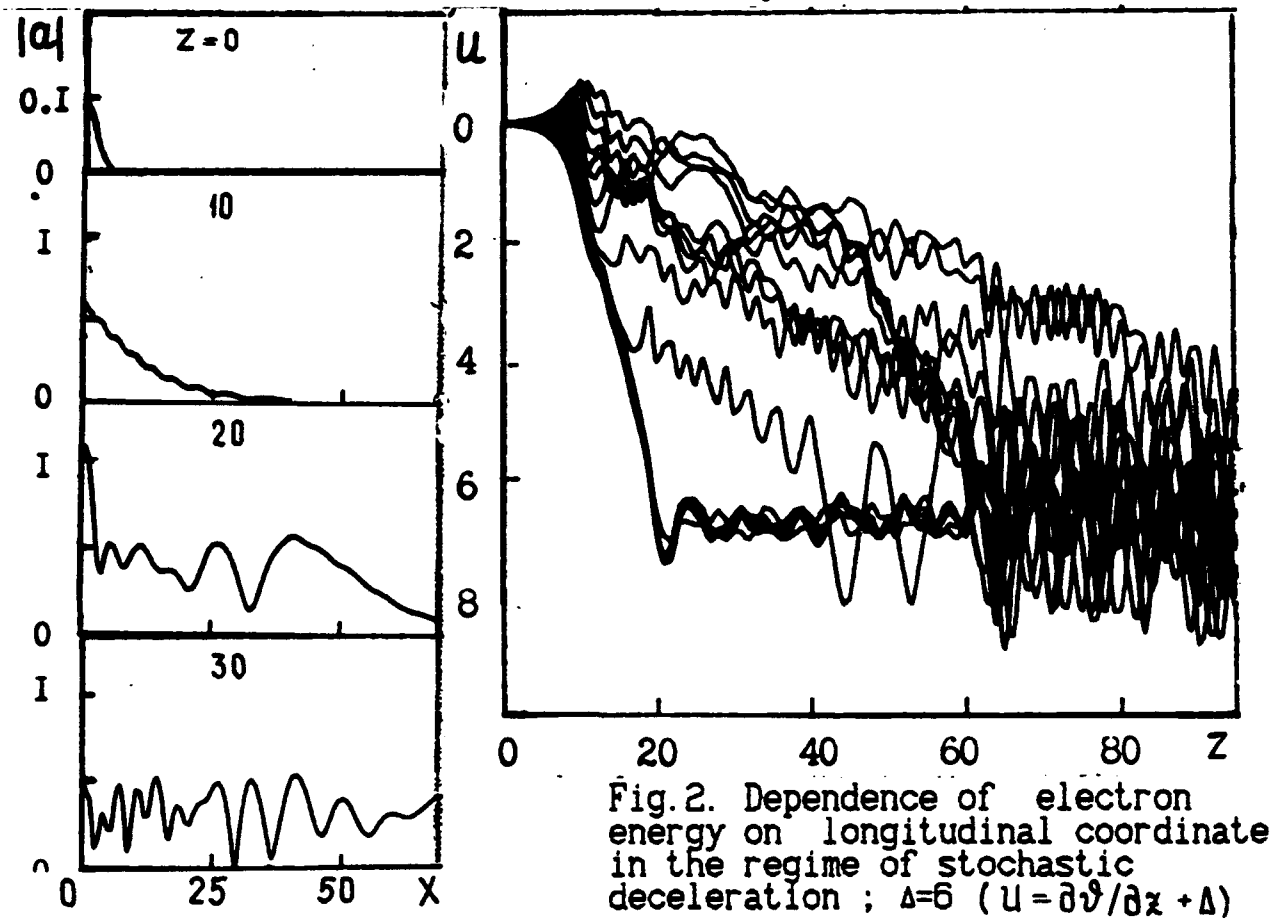


Fig.2. Dependence of electron energy on longitudinal coordinate in the regime of stochastic deceleration ; $\Delta=6$ ($U = \partial\vartheta/\partial\chi + \Delta$)

Fig.1 Evolution of the transverse profile of the wave beam; $\Delta=6$

direction, Im $\varkappa < 0$, and has an energy flux propagating towards external space Re$\varkappa > 0$. For extended interaction length the field structure is determined by the excitation of this wave:

$$a(X,Z) \xrightarrow{Z>>1} 2/5\, a_0 e^{-i\varkappa_s|X|+i\Gamma_s Z}$$

Computer simulation of Eqs (1) confirms the radiation canalization at the linear stage. However, at the nonlinear stage, when the EM field amplitude in the axial region is saturated, diffractional effects lead to the wave beam broadeing and emission of EM energy to the external space (Fig.1).

Because EM waves are radiated at different angles ψ different phases velocities of the combination wave ($v_c = \omega_s/(h \pm \omega_s/c \cos\psi)$ correspond to each wave. Consequently, if $\Delta \gg 1$ and the initial electron velocity $v_\parallel$ greatly exceeds the phase velocity of the slowest component of the combination field $v_{c0}=v_c(\psi=0)$, then the regime of stochastic deceleration occurs (Fig.2). In this regime electrons interact with different component of the combination field until their mean velocity reaches the value v_{c0}. In this way a considerable enhancement in extraction efficiency (more than 50% [4]) can be achieved.

2. *SUPERRADIANCE EFFECTS.* The radiation by electron cluster moving through an undulator field can serve as an example of spontaneous coherent emission (or Dicke superradiance [9]) in system of classical oscillators. It is assumed that the size of the cluster is large at the scale of the wavelength but small at the scale of the undulator length, so the lifetime of an electron in undulator field can be assumed infinite. As a result, non-threshold instability occurs that leads to a bunching of the particles and subsequent coherent emission by them. While the frequency of the emission in the co-moving frame of reference K', will be the same in various directions and will approximately equal the electron oscillation frequency, the frequency in the laboratory frame of reference K, will depend on the observation angle, because of Doppler effect. Thus this emission simultaneously exhibits the properties of stimulated processes (coherence) and spontaneous processes (anisotropy, multiplicity of frequency, and absence of threshold).

Here we wish to examine the nonlinear stage of superradiance

effect on the basis of 1D model. We assume that cluster is a layer of width b along z direction, while it is infinite along the x- and y - directions. We analyze situation in the co-moving K' frame, in which the undulator field transforms into the field of EM pump wave given by the vector-potential: $\vec{A}_u'=\mathrm{Re}[\vec{y}_o A_u' e^{i(\omega_u' t' + h_u' z')}]$, where $h_u'=\gamma h_u$, $\omega_u'=\gamma c h_u$, $\gamma = (1-v_{\parallel 0}^2/c^2)$. The field emitted (scattered) by the layer can be written as two waves, travelling in the $\pm z'$ directions: $\vec{A}_s'=\mathrm{Re}[\vec{y}_0 A_s'^{\pm}(z',t')e^{i(\omega_s' t' \mp h_s' z')}]$. Here $h_s'=\omega_s'/c$ and ω_s' is carrier frequency (below we set $\omega_s'=\omega_u'$). The combined effects of these fields on the electrons give rise to the average ponderomotive force, which is responsible for the bunching of particles

$$F_p = -\frac{e^2}{4 m \omega_u'^2}\frac{\partial}{\partial z'}\mathrm{Re}\left[A_u' A_s'^{*} e^{i(h_s'+h_u')z'} + A_u' A_s'^{-} e^{i(h_s'-h_u')z'}\right].$$

For numerical simulation of the superradiance processes, we partition the layer into N planes (macroelectrons) at the coordinates $z_n'(t', z_{0n}')$, where z_{0n}' are the initial coordinates of the macroelectrons. These macroelectrons interact with each other via ponderomotive force and the repulsive Coulomb force (we supposed that the unperturbed static electron charge is compensated by the ion background). In Lagrangian variables, the equation of motion the macroelectrons can be written [8]

$$d^2 Z_n'/d\tau'^2 = F_p^n + F_c^n \quad , \quad Z_n'|_{\tau=0} = 2B/N\,(\,n - N/2\,) \qquad (2)$$

where

$$F_p^n = q^2\alpha_i^2 B / 8N_0\left[-\sum_m^{N^+}\mu_+\cos(Z_n' - Z_m') + \sum_m^{N^-}\mu_-\cos(Z_n' - Z_m')\right] ,$$

$$F_c^n = q^2 B/2N_0\left[N^+ - N^- - N_i^+ + N_i^-\right] .$$

Here $\tau=\omega_i t$, $Z'=(\omega_i/c)z$, $B=(\omega_i/c)b$, $q=\omega_p'/\omega_i' < 1$, $\mu_\pm = (h_s' \pm h_i')c/\omega_i'$, $N^\pm(n)$ is the number of electrons with coordinates larger (smaller) than Z_n'; and $N_i^\pm$ is the same number for the ion background. The amplitudes of the waves emitted by electrons are given by

$$a_s'^{\pm}(Z',\tau') = iq^2\alpha_u' B/4N\sum_m^{N\mp} e^{-i\mu_\pm[Z'-Z_m']} .$$

Figure 3 shows the profile along the longitudinal coordinate of the ponderomotive force which one macroelectron exerts on the others. In contrast with the repulsive Coulomb force (shown by dashes lines), this force is attractive in the near zone. This behavior of interaction force should case instability and breakup of the layer into coherently emitted bunch.

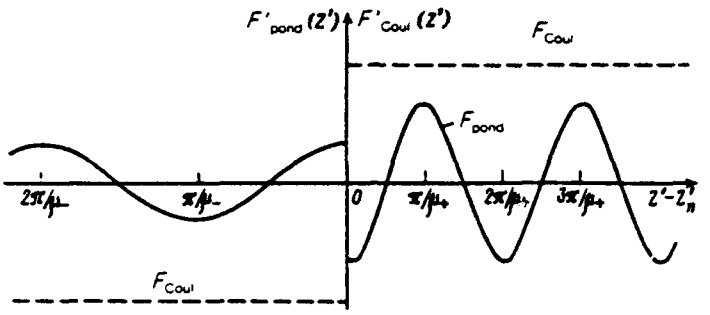


Fig.3. Dependence on the longitudinal coordinate of the ponderomotive force which one macroelectron exerts on the others.

For initial stage of the process ($\tau' \simeq 10$-40), this effect is clear from Fig.4.a which shows the time evolution of the coordinate of the electrons. For the relativistic ($\gamma \gg 1$) motion of the layer (in the laboratory frame), when $h'_s \simeq h'_u$ and $\mu_+ \gg \mu_-$, the motion of the electrons is governed by that component of the ponderomotive force which stems from the wave a'^*_s; the wave propagating opposite the pump wave (in the direction of translational motion in frame K). Correspondingly, the electrons became bunched so that the amplitude of this wave is substantially larger than that at the initial time (Fig.3b). In the case of ideal bunching, the maximum amplitude of this wave is determined by $a'^*_s = iq\alpha'^2_u B'/4$. The peak field amplitude in Fig.4b is smaller than this value by a factor of about 2.7. So at a certain time $\tau' \simeq 15$ the emission of the particles reaches a high degree of coherence. After a long time, the particles in the layer undergo pronounced mixing, and the amplitude a'^*_s falls off.

Consider in conclusion, the characteristic features of the superradiance in the laboratory frame K. While the frequency of the waves emitted by the layer in the $\pm z'$-direction are the same in the co-moving frame, in the laboratory frame these frequencies become quite different as $v \to c$: $\omega^+/\omega^- \simeq 2\gamma^2 \gg 1$.

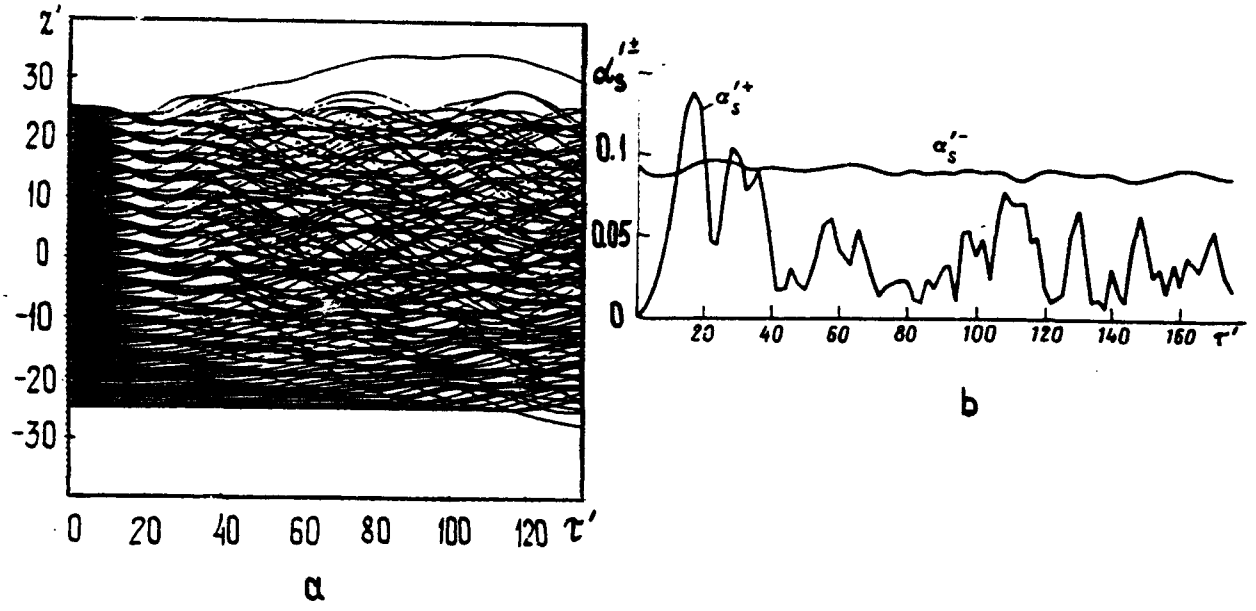


Fig. 4. (a) Time evolution (a) of the electron coordinates, (b) emitted waves amplitudes; q=0.04, α_u'=0.8, μ_+ =2, μ_-=0.1, B = 50.

Correspondingly, when we take into account the conservation of the number of photons, we conclude that power radiated along positive z-direction is much higher than that radiated in opposite direction

$$P^+/P^- = \omega^+/\omega^- \quad P'^+/P'^- \propto 2\gamma^2$$

Thus in the laboratory frame, most of the energy of superradiance is concentrated in the short-wave component and the effect discussed here may be regarded as a promising method for producing coherent emission, especially in the ranges where no efficient reflectors are available.

References

1. C.M. Tang, P. Sprangle, Phys. of Quant. Electr. 1982, v.9, p.627.
2. E.T. Sharlemann e.l Phys.Rev.Lett. 54 (1985) 1925.
3. G.T. Moore ,Opt. Comm.52 (1985) 46.
4. N.S. Ginzburg e.l. Optics Comm.70 (1989) 218; 76 (1990) 69.
5. R.H. Bonifacio e.l..Comm.68 (1988) 369.
6. N.S Ginzburg, Pis'ma v ZhTF 14 (1988) 440.
7. N.S. Ginzburg, A.S. Sergeev,. JETF 72 (1991) 243
8. N.S. Ginzburg, A.S. Sergeev, JETF Lett.54 (1991) 450.
9. R.H. Dicke, Phys.Rev.,93 (1954) 99.

NONLINEAR ANALYSIS OF A GRATING FREE-ELECTRON LASER

B. Hafizi†, P. Sprangle, P. Serafim‡ and A. Fisher
Beam Physics Branch, Plasma Physics Division
Naval Research Laboratory, Washington D.C. 20375

Abstract

A nonlinear model of a grating free-electron laser is formulated that includes the effects of self-field forces, beam emittance, energy spread and gyromotion in a guide field. We compare the efficiency of an infinitely-thin beam, a finite-thickness beam with laminar flow and a finite-thickness beam with full transverse motion. For a thick beam, the effect of electron gyration about the beam axis is to enhance the efficiency as compared to that for a beam with laminar flow.

At the Naval Research Laboratory a grating free-electron laser (FEL) experiment is underway whose ultimate goal is the generation of high-power radiation in the near-IR windows in the atmosphere. A key element of this experiment is the use of state-of-the-art, high-brightness electron beams obtained from novel cathode materials and designs. A schematic of the experimental set-up is shown in Fig. 1.[1,2]

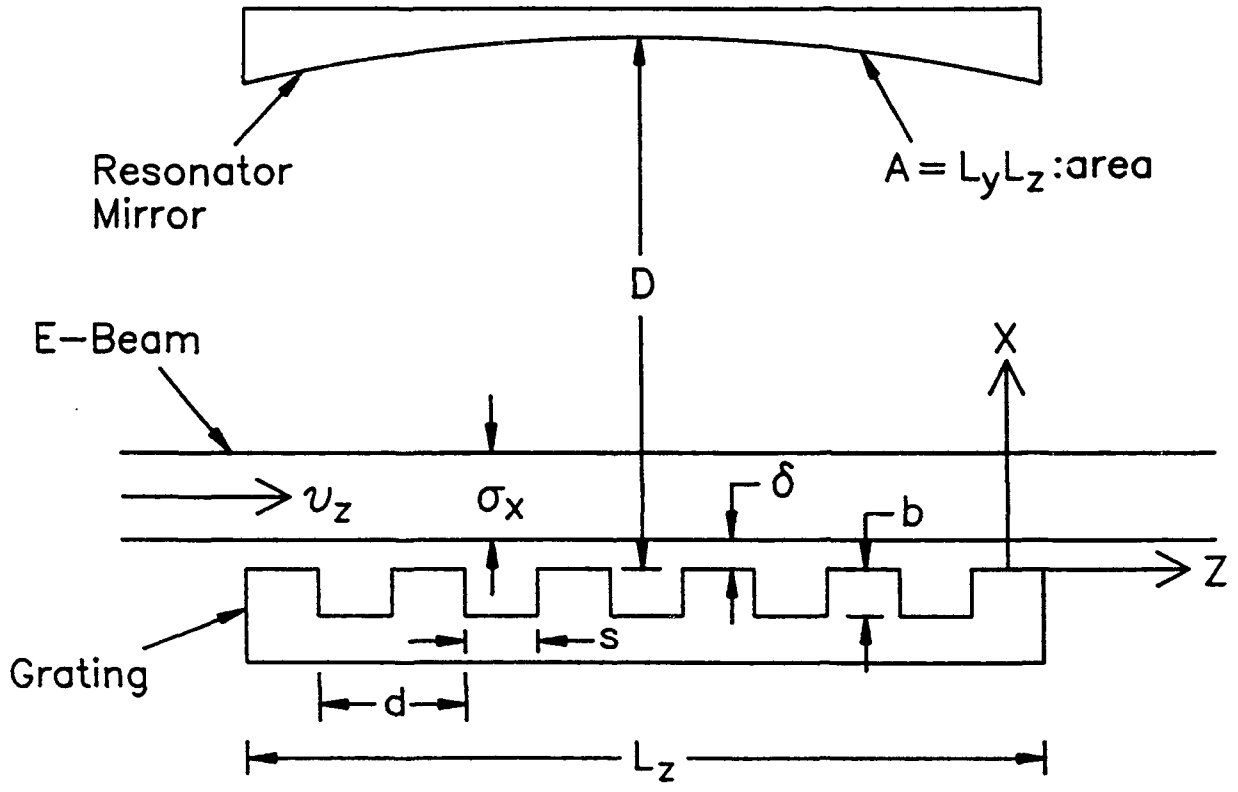


Figure 1: Schematic of an open resonator configuration for a grating FEL oscillator.

Resonator Field

$\mathcal{E}_z(x,z,t) = E_z(x,z)\exp(-i\omega t) + c.c.$ represents the z component of the electric field, $\omega = 2\pi\, c/\lambda$ is the frequency, λ is the wavelength,

$$E_z(x,z) = E_0 \sin[k_x(D-x)] + \sum_{n=1}^{\infty} E_n \cos(2\pi\, n\, z/d)\, \sinh[k_n(D-x)],$$

d is the grating pitch, D is the resonator spacing, E_0 is the amplitude of the fundamental spatial harmonic, $k_x = \omega/c$, E_n is the amplitude of the nth spatial harmonic and $k_n = \left[(2\pi n/d)^2 - (\omega/c)^2\right]^{1/2}$. Only the $n = 1$ harmonic is resonant with the electrons; i.e., $\lambda/d \approx 1/\beta_z$, where $\beta_z = v_z/c$ is the ratio of the axial velocity to the speed of light.

Trajectories and Beam Emittance

Defining $\psi_j = 2\pi z_j/d - \omega t$, the equations of motion of the jth electron, of charge $-|e|$ and rest mass m, are given by

$$\frac{d\psi_j}{dt} = 2\pi c\beta_{zj}/d - \omega, \tag{1}$$

$$\frac{d\gamma_j}{dt} = -\frac{|e|E_1\beta_{zj}}{2mc} \sinh\left[k_1\left(D - x_j\right)\right] \exp\left(i\psi_j\right) + c.c., \tag{2}$$

$$x = \xi\left(\frac{\epsilon v_z}{\Omega}\right)^{1/2} \cos\left(\Omega t + \theta\right), \tag{3}$$

where $0 \le \xi \le 1$ and $0 \le \theta \le 2\pi$ may be chosen to represent any desired distribution of electrons, $\Omega_0 = |e|B_0/\gamma mc$ is the gyrofrequency in the axial guide magnetic field, B_0, $\gamma = (1 - v^2/c^2)^{-1/2}$, $\Omega^2 = \Omega_0^2 - \Omega_b^2$, $\Omega_b = (4\pi n_b|e|^2/\gamma\gamma_z^2 m)^{1/2}$ is the plasma frequency, n_b is the beam density, $\gamma_z = (1 - v_z^2/c^2)^{-1/2}$ and ϵ is the (unnormalized) emittance of the matched strip beam of half-width $X_b = (\epsilon v_z/\Omega)^{1/2}$.

Equations (1)-(3) form a closed system. Setting $v_x = v_y = 0$ and $\gamma = \gamma_z$, Eqs. (1) and (2) can be combined into a single 'pendulum' equation for ψ_j:

$$\frac{d^2\psi_j}{dt^2} = -\frac{\pi|e|E_1}{\gamma_{zj}^3 md} \sinh[k_1(D - x_j)] \exp(i\psi_j) + c.c. \tag{4}$$

Efficiency : Numerical Simulations and Analytical Estimates

The efficiency η is the fraction of the beam energy that is converted into electromagnetic energy. An upper bound for η is obtained by considering the maximum tolerable spread in the detuning $\Theta \equiv (\omega/v_z - 2\pi/d)L_z/2$ over the interaction length L_z:

$$\eta = \frac{\lambda}{L_z} \frac{(\gamma_z^2 - 1)^{3/2}}{\gamma_z - 1}. \tag{5}$$

i) Infinitely-Thin Beam

Figure 2 (a) shows the efficiency as a function of the amplitude of the fundamental spatial harmonic for a cold, infinitely thin beam (taking $X_b \to 0$ in Table I). The efficiency according to Eq. (5) is 0.72%, which is to be compared with the code result of 0.63%, optimized with respect to Θ.

Equation (4) indicates that the motion of the electrons is in the form of synchrotron oscillations. The maximum efficiency is obtained when, in the beam frame, the initial velocity is reversed. The reversal is attained after a time $\sim \pi/\Omega_{syn0}$, where Ω_{syn0} is the synchrotron frequency:

$$\Omega_{syn0} = \left\{ \frac{2\pi|e|E_1}{\gamma_z^3 md} \sinh[k_1(D - X_0)] \right\}^{1/2}, \tag{6}$$

where X_0 is the x coordinate of the beam centroid. The optimal Θ corresponds to an ω such that the electrons at X_0 undergo $\sim 1/2$ of a synchrotron oscillation in a distance L_z.

ii) Finite-Thickness Beam

Case (a) Electron Beam with Laminar Flow

Figure 2 (b) shows the efficiency for a finite-thickness beam with electron gyration suppressed in the numerical code. The peak efficiency of 0.36% is smaller than that for the infinitely-thin beam in Fig. 2 (a).

For a thick beam the synchrotron frequency varies according to the x coordinate of the electrons. Consequently the inner electrons experience a field that is larger than the optimal value and they execute more than 1/2 of a synchrotron oscillation. The outer electrons experience a smaller field than the optimal value and do not complete 1/2 of a synchrotron motion. The frequency Ω_{syn0} is greater than the mean synchrotron frequency of electrons located at $x > X_0$ by $F_+ = \Omega_{syn0}/ < \Omega_{syn} >$, where

$$\Omega_{syn} = \left\{ \frac{2\pi|e|E_1}{\gamma_z^3 md} \sinh[k_1(D - x)] \right\}^{1/2}, \tag{7}$$

is the synchrotron frequency of electrons at a distance x from the grating surface, and $<>$ indicates an average over $X_0 \le x \le 2X_b$. F_+ is the amount by which the extraction from the electrons at $x > X_0$ is reduced. For electrons at $x < X_0$ the extraction is reduced by $F_- = < \Omega_{syn} > /\Omega_{syn0}$, where $< \Omega_{syn} >$ is the average, over $0 < x < X_0$, of the frequency in Eq. (7). Considering both groups, the efficiency is expected to be reduced, relative to

the infinitely-thin beam case, by $F \equiv (F_+ + F_-)/2$. Inserting the appropriate values, we find $F = 1.8$. This is fairly close to the value of $0.63/0.36 = 1.7$ for the ratio of the peak efficiencies in Figs. 2 (a) and 2 (b).

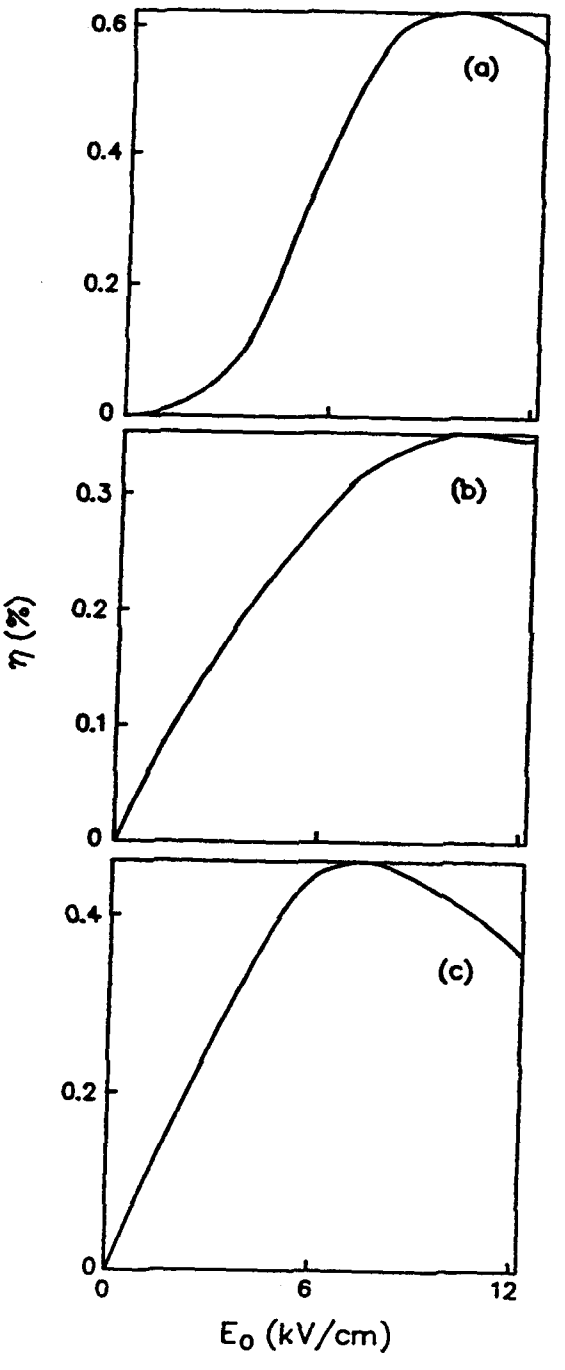


Figure 2: Efficiency, η, versus amplitude of fundamental spatial harmonic, E_0, for $\lambda = 100\,\mu m$ radiation using a $100\,kV$ beam. Beam axis is $25\,\mu m$ above grating surface. (a) Infinitely-thin beam. (b) Finite-thickness beam with laminar flow ($X_b = 25\,\mu m$). (c) Finite-thickness beam with full transverse motion ($X_b = 25\,\mu m$).

Case (b) Electron Beam with Full Transverse Motion

Figure 2 (c) shows the efficiency for a warm, finite-thickness electron beam. The peak efficiency, $\eta = 0.46\%$, is observed to be smaller than the peak efficiency for the infinitely-thin beam example in Fig. 2 (a) *but higher than that for a thick beam with laminar flow*, Fig. 2(b).

As a consequence of their gyromotion the electrons rotate about the beam axis and sample the transverse profile of the electric field as they cross the interaction region. From Eqs. (1)-(3), assuming $\Omega/\Omega_{syn0} \gg 1$, we obtain

$$\frac{d^2\Psi_j}{dt^2} = -\frac{\pi|e|E_1}{dm\Gamma_{zj}^3} I_0(k_1\xi X_b)\sinh[k_1(D-X_0)]\exp(i\Psi_j) + \mathcal{O}(E_1^2) + c.c.,$$

where Ψ_j and Γ_j are the slowly-varying parts of ψ_j and γ_j, respectively and I_0 is the modified Bessel function of the first kind of order 0. For the beam as a whole, the efficiency is expected to be reduced by $< I_0^{1/2}(k_1\xi X_b) >$ relative to that for an infinitely-thin beam. Inserting the appropriate values, we find $< I_0^{1/2}(k_1\xi X_b) >= 1.24$, which is close to the ratio of the peak efficiencies in Figs. 2 (a) and 2 (c), i.e., $0.63/0.46 = 1.37$.

Table I: Design parameters for a grating FEL Oscillator operating at 100 μm using a 100 kV electron beam.

Wavelength λ	100	μm
Voltage	100	kV
Current	125	mA
Output Power	57.5	W
Gain/Pass	4	%
Efficiency η	0.46	%
Interaction Length L_z	2	cm
Guide Magnetic Field B_0	3	T
Beam Thickness $2X_b$	50	μm
Beam-Grating Gap δ	0	μm
Grating Pitch d	55	μm
Groove Width s	27.5	μm
Groove Depth b	27.5	μm
Resonator Spacing D	1	cm
Resonator Cross-Sectional Area A	1	cm^2
Resonator Quality Factor	6×10^4	

Conclusion

We have studied the efficiency of the grating FEL in detail for three examples. The example of the infinitely-thin beam is found to have the highest efficiency and the example of a thick beam with laminar flow is found to have the smallest efficiency. We have found the remarkable result that for a thick beam, gyration of the electrons about the beam axis leads to an enhancement of the efficiency as compared to the case with laminar flow. This is due to the fact that electron gyration tends to effectively reduce the variation of the slow-wave electric field normal to the grating surface.

Acknowledgment

The authors are grateful to Drs. A. W. Fliflet, S. H. Gold, W. M. Manheimer and J. E. Walsh for valuable discussions. This work was supported by the Defense Sciences Office at DARPA and by the Office of Naval Research.

† Icarus Research, 7113 Exfair Rd., Bethesda, MD 20814
‡ Northeastern University, Boston, MA 02115

References

1. S. J. Smith and E. M. Purcell, Phys. Rev. 92, 1069 (1953).
2. F. S. Rusin and G. D. Bogomolov, JETP Lett. 4, 160 (1966).

EUPHROSYNE A PULSED ELECTRON GENERATOR FOR FEL APPLICATION

C. BONNAFOND, J. BARDY, H. BOTTOLLIER-CURTET, A. DEVIN,
J. GARDELLE, G. GERMAIN, J. LABROUCHE, J. LAUNSPACH,
P. LE TAILLANDIER, J. de MASCUREAU

Centre d'Etudes Scientifiques et Techniques d'Aquitaine
Commissariat à l'Energie Atomique,
B.P. n° 2 - 33114 LE BARP (France)

1. INTRODUCTION

At CESTA, the 35 GHz experiment ONDINE I is in progress. The studies focus on intense electron beam creation with the Euphrosyne generator and its propagation to the wiggler by mean of a transmission line. The generator consists in a Marx generator, a pulse forming line and a diode using both thermoionic and cold cathodes. The diode has been adapted to the forming line at 36 Ω in order to narrow the energetic spectrum. A full characterization of the beam has been achieved by measuring the position, the size with Cerenkov detectors, the energetic spectrum and the transverse emittance at different points of the transmission line. Calculations has been done by using envelope and particle codes to perform the propagation of the beam. Good agreement has been achieved. Typically, 1 kA at 1.5 MeV is obtained.

In the frame of a preliminary superradiant experiment using a bifilar helical wiggler, we have measured an amplification of the spontaneous emission up to 1 MW in the Ka band and .2 MW in the 33-36 GHz band.

II - GENERATOR

The pulsed generator Euphrosyne Fig.1 is a classical intense relativistic electron beam device. It consists in a Marx generator with 20 stages (150 nF, 150 kV per capacitor), a 36 Ω oil pulse forming line (blumlein) and a field emission diode without magnetic guiding field. The diode uses a graphite hemispherical cold cathode with a curvature radius ρ = 55 mm and a planar electron transparent graphite anode (mesh) with an anode-cathode gap spacing of 30 mm. This diode delivers an electron beam between 1.5 and 3.0 MV with a 50 to 100 kA current.

However an FEL experiment needs some further developments firstly to reduce beam instability as well as to improve shot to shot reproductibility and secondly to increase flat top pulse voltage for higher gain emission.

The first point has been achieved by using a spark-gap switch between the blumlein and the diode to suppress the prepulse voltage. Thus we obtained, for 100 consecutive shots 76, 56 and 45 shots for respectively ± 10%, ± 5% and ± 3% current variation for fixed operating conditions without changing the mesh anode.

The second point has been solved by matching the diode impedance to the blumlein one with a liquid resistive impedance of 75 Ω parallel with the diode. Typically we obtained a flat top pulse voltage duration of 15 ns with $\Delta V/V$ = 4%. Moreover a hole aperture with a diameter ϕ = 10 mm downstream the anode limits the beam current at around 1 kA in order to remove the outer hot electrons.

III - ONDINE I Experiment

One of the goal of this electron device is to deliver an electron beam for the ONDINE I FEL experiment at 35 GHz (**Fig.2**). It uses a beam transmission line and a helical wiggler immersed in a solenoid magnetic field with an 8 period liquid shunt adiabatic entrance. It can be operated in the amplifier mode using a magnetron microwave source, with the following parameters :

Microwave input		Bifilar helical wiggler	
Frequency :	34.85 GHz	Period :	12 cm
Power :	100 kW	Length :	3 m
Pulse duration :	800 ns	adiabatic entrance :8 periods	
Mode :	TEII rotating	Max wiggler field :	2 kG
Wave-guide radius :	30 mm	Max solenoid field :	10 kG

a) Beam characterization

A full characterization of the beam has been performed using resistive shunts for voltage, Rogowski coil and Faraday cup for current measurement.

Energetic spectrum has been measured by mean of a permanent compact magnetic analyzer with 180° deflection using a calibrated electron film (Kodak SO 163) as detector in the focal plane. Energy resolution has been estimated to 4%. **Fig.3** shows a typical microdensitomer time integrated trace of the developed Kodak film with a peak at 1.54 MeV.

Position and spot size of the beam have been established by taking time integrated photographs of a Cerenkov emitter which consists in a 5 mm thick fused silica window.

Transverse beam emittance has been measured by using the pepper-pot technique. The beam is screened by a plate which contains regularly spaced identical holes (diameter = 0.4 mm) in the two transverse directions. The emerging beamlets travel a drift length L = 100 mm and strike a silica window for electron-photon conversion. **Fig.4** presents experimental emittance diagrams measured at different locations in the beam transport line with interpolated elliptical curves. The emittance decrease (1200 => 970 π.mm.mrad) is due in part to the loss of low energetic electrons in the first solenoid lens BB1, matched for higher energies but also to the loss of too divergent electron trajectories.

Twiss parameters has been estimated to perform beam propagation between the diode and the wiggler by mean of a transport code. We can compare in **Fig.5.** The beam radius computed from an envelope equation to the radius measured from the Cerenkov emission at different positions. The agreement is found to be good and this allows us to optimize the injection of the electron beam into the wiggler with the following typical parameters :

I = 1 kA ; E = 1.54 MeV ; diameter = 10 mm ; ϵ = 950 π mm.mrad

We have also checked the beam trajectory inside the wiggler with a silica window mounted on a shuttle.

b) Preliminary results

In the superradiant configuration 1.2 MW is obtained in the 22.48 GHz band and 200 kW in the 33-36 GHz band. **Fig.6** is a variation of the output power versus the wiggler field for a fixed solenoid field at 2.4 MeV in order to keep an optimal transport efficiency. The efficiency is rather poor due in part to the growth of the transverse emittance induced by the gradient of the solenoid field. Additional work is being done to improve beam emittance and understand this gradient effect.

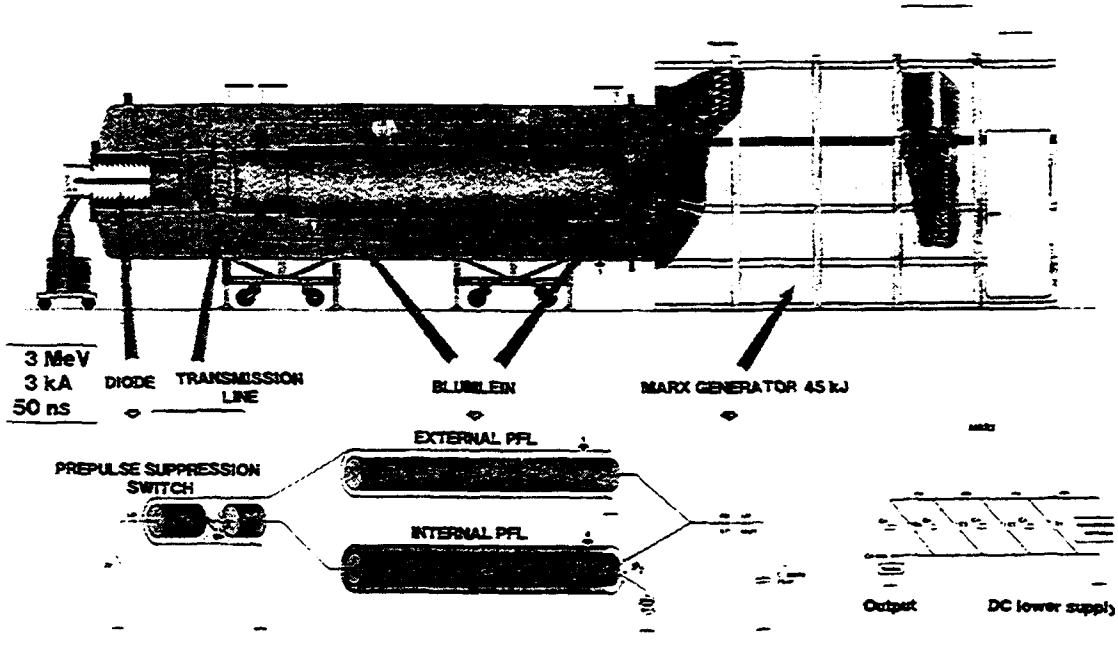


FIGURE 1 : EUPHROSYNE - A PULSED POWER ACCELERATOR

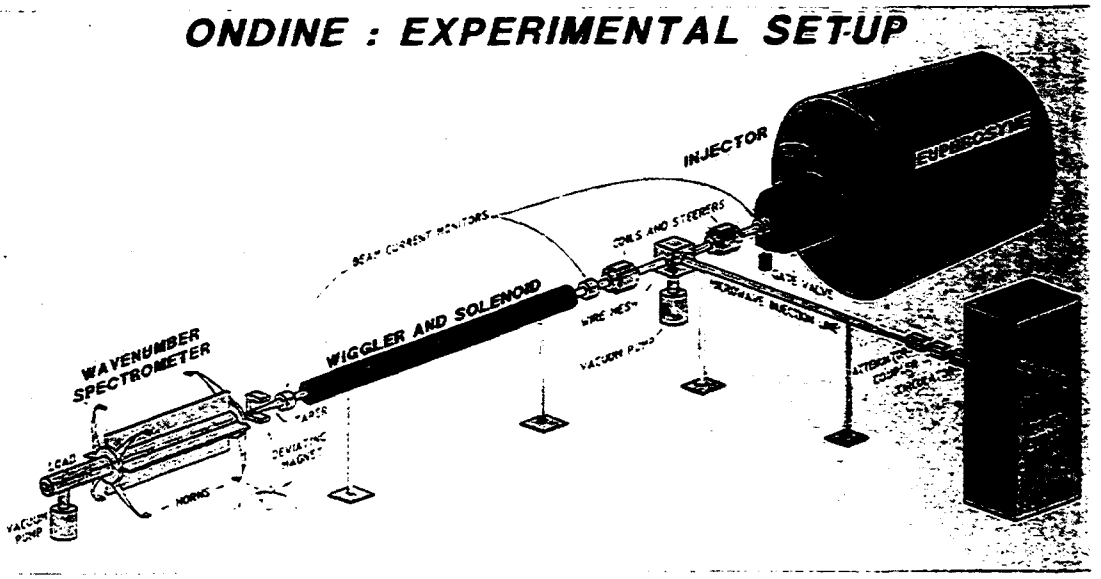


FIGURE 2 : ONDINE - EXPERIMENTAL SET-UP

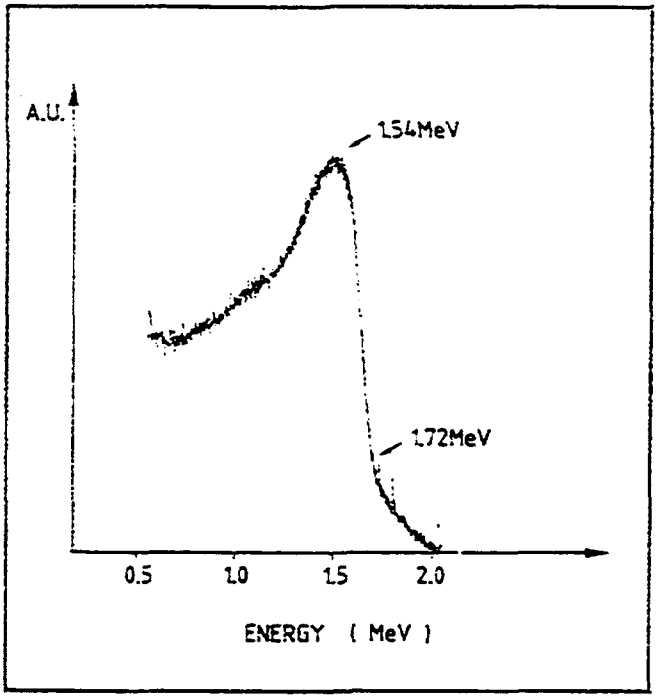
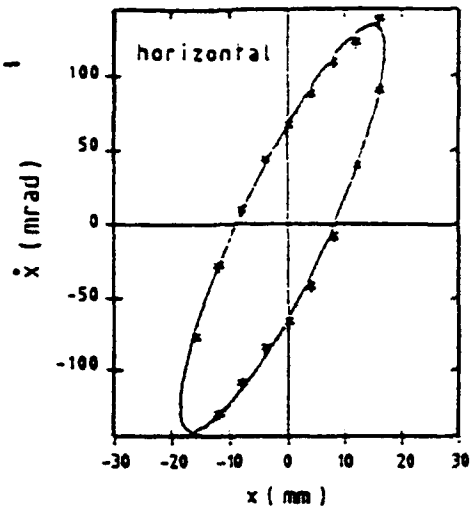
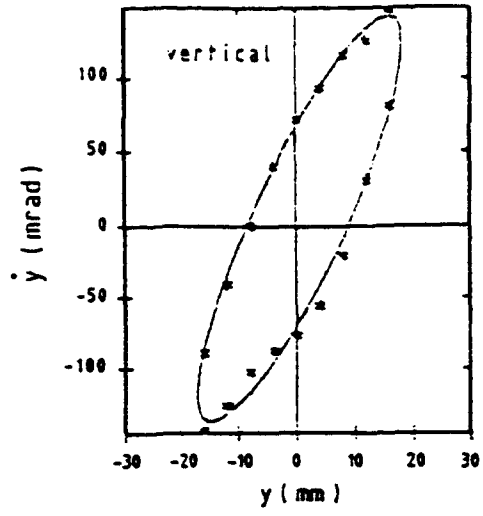


FIGURE 3 : TYPICAL EXPERIMENTAL ENERGY SPECTRUM

-a-

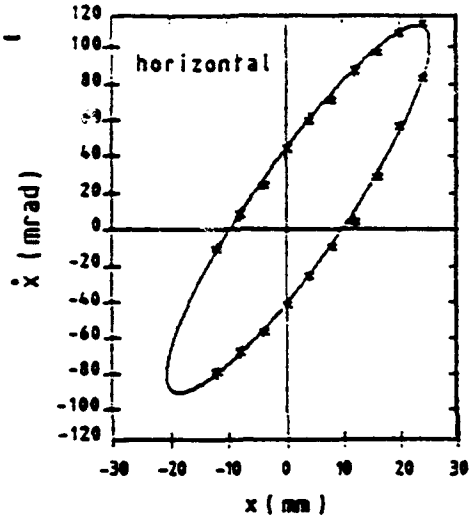


Emittance = 1176π.mm.mrad
(α,β,γ) = (-1.85, 0.27, 16.24)

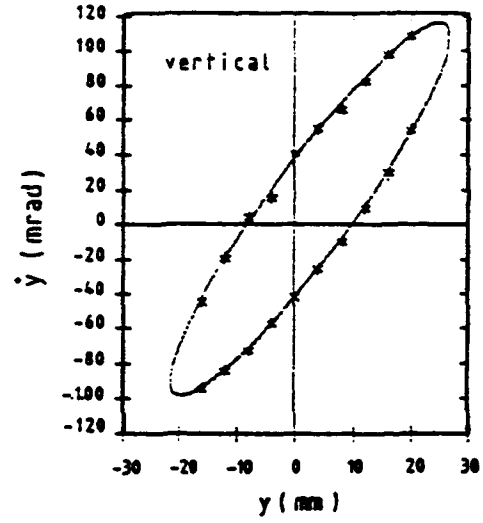


Emittance = 1225π.mm.mrad
(α,β,γ) = (-1.76, 0.25, 16.1)

-b-



Emittance = 988π.mm.mrad
(α,β,γ) = (-2.13, 0.54, 10.31)



Emittance = 966π.mm.mrad
(α,β,γ) = (-2.48, 0.60, 11.94)

FIGURE 4 : Experimental emittance diagrams (*) and interpolated elliptical curves (-) $\gamma X^2 + \beta \dot{X}^2 + 2\alpha X\dot{X} = \varepsilon$ with (α, β, γ) the Twiss parameters measured at point 1 (-a-) and 3 (-b-) in the transmision line.

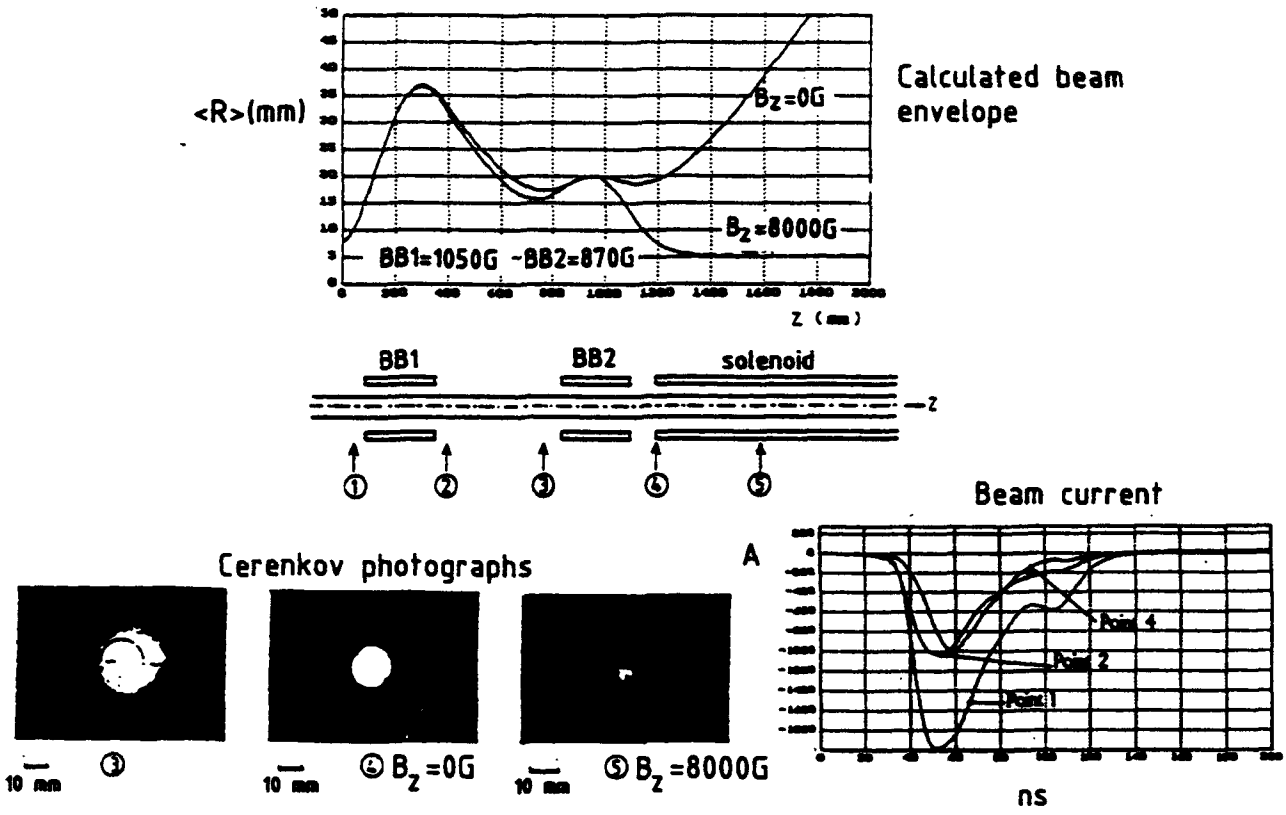


FIGURE 5 : Calculated beam envelope and experimental beam size and current at different locations.

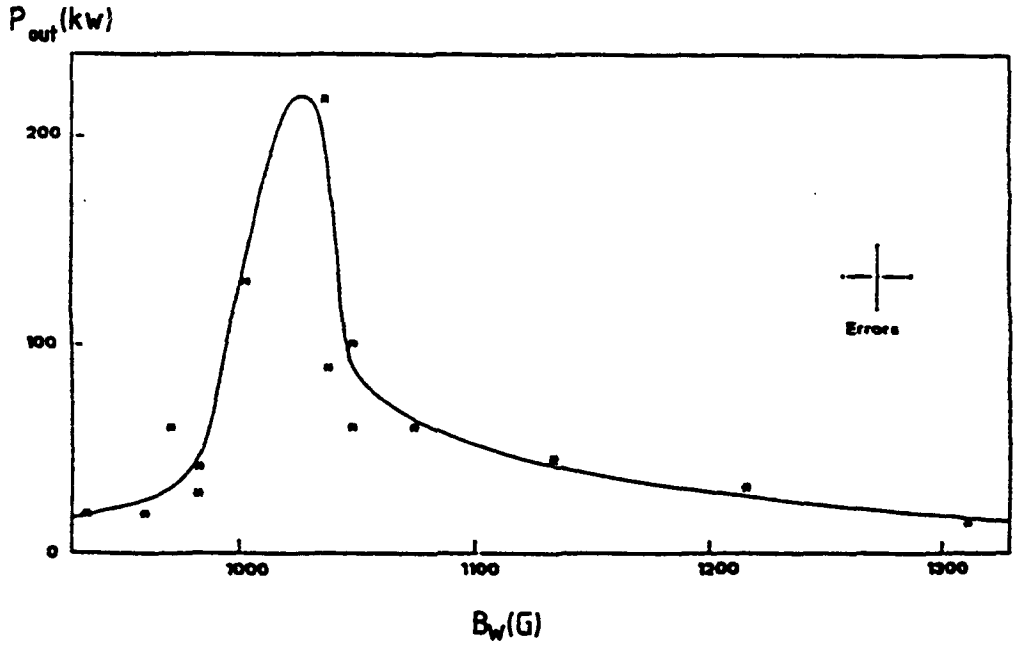


FIGURE 6 : Microwave power filtered 33 - 36 GHz with respect to Wiggler field with :

E = 2.4 MeV ; I = 350 A ; B_z = 8500 G

FEL Project for Industrial Applications in Japan

K. Imasaki, S. Sato, Y. Miyauchi, T. Keishi, A. Kobayashi, A. Koga,
E. Nishimura, K. Saeki, I Bessho, M. Okano, S. Abe, A. Nagai, T. Tomimasu

FEL Research Institute
2-7-4 Kyo-machi-bori, Nishi-ku, Osaka 550
Japan

Abstract

FEL project for industrial application was started in Japan. The purpose of this project is to generate FEL from FIR to UV and use it to investigate industrial applications. FEL Engineering Corporation is founded to perform this project.

1. Introduction

FEL has advantages as high average power, tunability of wide wavelength and long life. From these points of view, feasibility of FEL applications to industry has been discussed in Japan. [1] FEL Research Institute (FELI) was founded to develop FEL technology and to investigate application issues of the FEL by 12 private companies, 1 foundation and Japan Key Technology Center at the end of PY90. Main purpose of FELI is to develop FEL technology, to obtain oscillation from FIR to UV region and to investigate this application.

In this paper we present scheme of project and status of FELI. In section 2, concept and plan of the projects are described. Facilities and accelerator system, and FEL system under designing is briefly noted in section 3. Application of FEL to industry which we have considered is presented in section 4.

2. Scheme and Plan of Project

Purposes of the project are to develop the RF-linac FEL technology, to obtain oscillation from 20um ~ 0.35um with sufficient output average power and to use this for the investigation of the industrial applications.

Time table is shown in Fig. 1. We start designing of the system, and the investigation of the components such as the high bright injector, the wiggler, the resonator, the optical components from March 1991, end of PY90 in Japan. We will complete a construction of the FEL facility in PY 93 for the 1st phase. In this phase, we will construct the low energy RF linac of the energy of 40 ~ 80MeV with the conventional thermionic electron injector with the subharmonic buncher. In the 2nd phase the RF linac of 170MeV will be completed and we

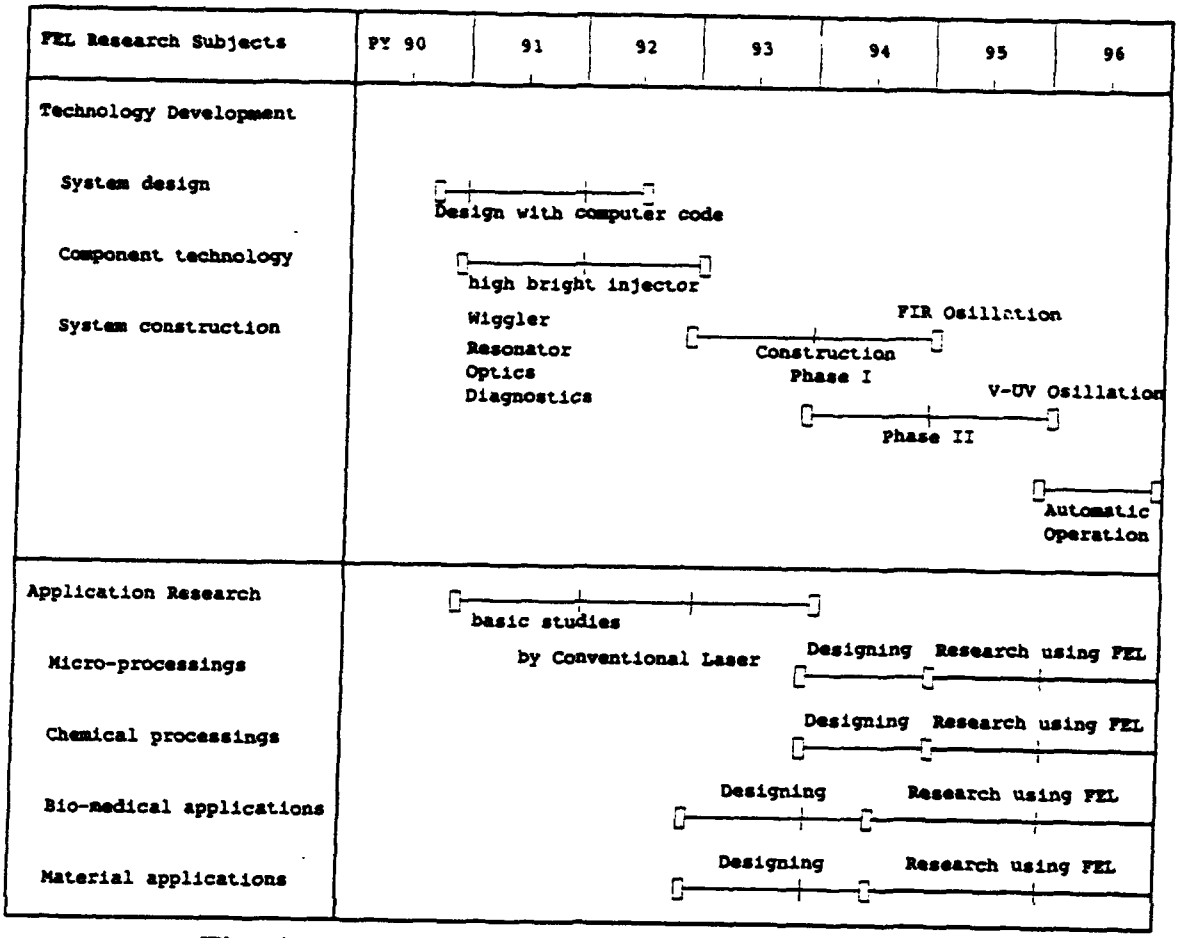


Fig. 1 Time schedule of project

Tab. 1 Designing parameters of accelerator

Accelerator	Phase I	Phase II
RF frequency	2856MHz	
Energy	20~80MeV	170MeV
Current Peak	20A	80A
Pulse		
Micropulse	10ps	2~5ps
Macropulse	15μsec	25μsec
Repetition Rate		
Micro	476MHz	89.25MHz
Macro	50pps	50pps
Emittance	πmm mrad	0.3πmm mrad
Beam power	6.6kw	3.2kw
Beam radius	2mmϕ	2mmϕ
Energy Spread	±0.5	±0.2
Tube	2π/3	
Injector	Pierce Gun + SHB RF Gun + Photo cathode	

expect the generation of FEL in the UV range. To achieve this, to develop a high bright beam source with RF gun with laser cathode is required.

The FEL applications to the industry as the micro processings, the chemical processings, the bio-medical applications and the material applications are considered to study in this project. The most interesting point of FEL application to these items is the tunability of laser wavelength in IR to UV region. We can expect more efficient, more purified, faster processing.

Each companies and foundation which are funding this project have their own technology and program of the basic research to support this project, such as the laser cathode technology, the wiggler, the diagnostics, the control system, the optical component, the simulation code development and so on.

3. Facility and system design

The total length of the designed accelerator system is about 80m. There are three outlet of the beam, the first outlet for FIR experiments, the second one to NIR experiments. The third one corresponds to FIR, NIR and V-UV FEL respectively. The application experiments will be performed on upper floor.

A current design is to use S band RF linac for accelerator. The parameters are shown in Table 1. The most important issue is to obtain high bright electron beam. We will use usual thermionic cathode with sub harmonic buncher for FIR and NIR FEL and RF gun with photo cathode for NIR and V-UV FEL injector respectively. Magnetic compressor among the accelerator tube chain is set to reduce energy spread. The beam transport through the accelerator system thewiggler has been designed to achieve a double chromatic and isochronous beam.

Using 3 D FEL code, FUELNDES, gains for several cases in the designed FEL system are estimated. [2] The typical run parameters which are determined by accelerator and wiggler technologies and results are shown in Table 2.

From the small signal gain and spontaneous emission power, we can evaluate the number of round trip time for each case without nonlinear processes. On the other hand, cavity length is determined by the damage threshold of the end mirror of the resonance cavity and intracavity power, P_n.

From the power saturation, minimum macro pulse requirement can be derived. The ring resonator are considerable to achieve larger number of the round trip to obtain a stable output power in hte UV region. Parameters of designed accelerator meets these requirements.

Table 2. Simulation Parameters and Results

	Phase I		Phase II
Typical Wavelength	17μm	1μm	0.3μm
Beam Energy	20MeV	85MeV	170MeV
Beam Current	20A	80A	80A
Energy Spread	1%	1%	0.5%
Emittance	πmm mrad	0.184πmm mrad	0.10πmm mrad
Wiggler λ_w N_w B_O	3cm 30 0.45T	3cm 30 0.45T	3cm 50 0.45T
Laser radius and Beam radius at Wiggler Center	1.56mm 0.67mm	0.38mm 0.3mm	0.29mm 0.28mm
Code Parameters Particle Number Mode	441 × 8 (each π/4) (0.0)~(2.2) even mode only		
Small signal Gun	64.7%	21%	24.7%
Saturation Power and round trip time till saturation	120MW ~200	19GW ~300	2.8GW ~300

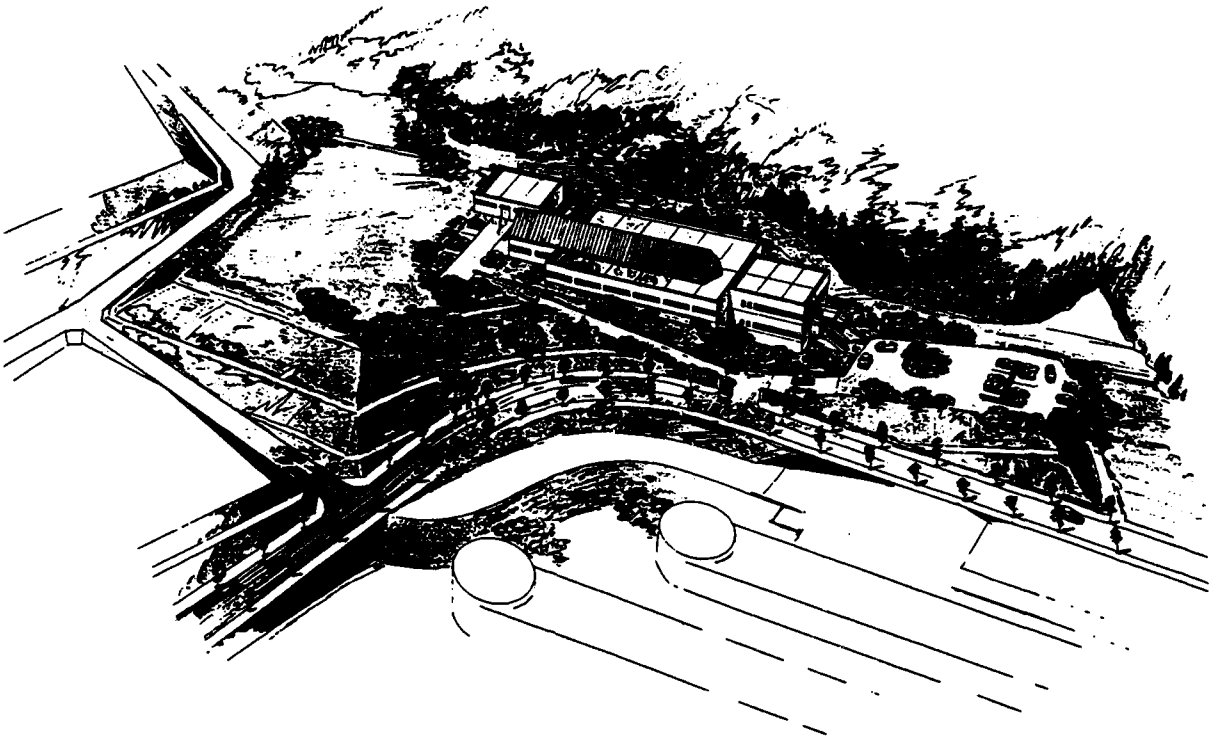


Fig. 2 A bird-eye-view of FELI facility

Table 3. Industrial Applications

Infrared Region
Solid state physics research Material research Medical applications Laser computer tomography Bio physics Molecular-chemistry Isotope Separation
Visible-UV Region
Chemical processing Refining and Purifying of valuable materials Partitioning of Nuclear waste Isotope separation Micro-processing Spectroscopy

Such large number of the round trip will make a restriction of the mirror alignment concerning the accuracy of the tilting angles. The beam trajectory control in the wiggler is also essential to achieve the gain obtained from the simulation.

Bird's eye view picture of FELI facility is shown in Fig. 2 which will be completed in PY93. The accelerators and the FEL system are set in the underground level. The experiments for applications are performed on the upper floors. The site of the facility is located in Kansai science city.

4. Industrial Applications

Industrial applications which is planned to investigate in FELI are listed in Table 3. The most important points of FEL application is its wide tunability. We can tune the wavelength of FEL where the conventional laser has not been exist.

In far-infrared region, FEL will be a unique light source of solid physics research. The medical and biological applications are most conventional war update in near-infrared region. In addition to this, FEL is very attractive for laser computer tomographies in the region of 1 ~ 5um because there are many bio-molecular resonance lines. We may observe the aiming molecules distribution of human body in situ.

In visible-UV FEL, well tuned light may promote a chemical reaction for refining, purifying and partitioning of valuable material of rare metal, nuclear fuel and waste, fine chemicals and so on. Especially in the deep UV region, there is no conventional tunable laser, so FEL will be a unique light source. .

Reference

1) K. Imasaki: J IEE Jpn, 109, 903 (1989)

2) S. Kuruma, K. Mima: OQD 89-15, IEE Japan, 69 (1989)

A FREE ELECTRON LASER AT P.N.LEBEDEV INSTITUTE

Accelerator Physics Laboratory Staff

P.N. Lebedev Physics Institute
117924, Leninsky Prosp. 53, Moscow, Russia

A free electron laser for IR spectroscopic research is now under construction on the basis of a specially designed RF linac. A goal of the project is obtaining IR radiation of 1 kW power in a 200 μs macropulse at wavelengths λ exceeding 10 μm. An approximately twofold tuning of the frequency can be achieved by varying the undulator field, while submillimeter wavelengths (up to 200 μm) can be obtained by increasing the undulator period and/or decreasing the electron energy.

A self excitation mode of FEL operation requires positive feedback in an optical cavity and is possible with rather low micropulse electron currents (about 1 A). We can hardly increase the number of undulator periods for that would lead to unacceptable requirements for beam quality and would decrease the FEL efficiency. An amplification regime with the same restriction as to the number of undulator periods requires much larger currents. Still, bearing in mind the importance of large gain regimes for advanced FELs, we intend to achieve currents sufficient for $G > 1$ at least at the far end of our spectral band.

The abovementioned requirements must be compatible with small longitudinal and transverse emittances ϵ of the beam. A tolerable energy spread of the order of N^{-1} requires minimization of the accelerating field frequency (down to 150 MHz) and of the micropulse duration (down to $0.1-0.2\ ns$). The former means employment of a standing wave structure, the latter — a controlled short pulse photoinjector.

Since the average power required for spectroscopy is rather low and all transient times of intrinsic FEL processes do not exceed ten microseconds, a low repetition-rate regime with $150 - 200\ \mu s$ macropulses is quite acceptable. A set of the FEL parameters based on the abovementioned considerations is listed in Table 1.

Table 1. Main parameters of the FEL

Radiation wavelength	$10 - 200\ \mu m$
Operative tuning	twofold
Micro/macropulse duration	$200\ ps/200\ \mu s$
Repetition rate micro/macro	50 MHz/1 Hz
Starting current in a microbunch	3 A
One pass gain	5%
Output radiation power micro/macro	100 kW/1 kW
Internal radiation power micro/macro	5 MW/50 kW
Undulator period (minimal)	2.5 cm
Number of periods	50
Deflection parameter	1
Optical cavity length	3(6) m
Optical losses/pass	3%

Photoinjector

To get a 200 μs train of 200 ps electron bunches with a micropulse current up to 100 A a special photoemission laser-controlled gun was designed. It consists of a coaxial $\lambda/4$ cavity, the capacitive part of which is a diode gap. The cathode is illuminated by a train of 200 ps UV laser pulse which follow with 50 MHz frequency and are synchronized with the accelerating field. Preference was given to metallic photocathodes that are stable in the atmosphere. A Cu + 10% BaO cathode provides a $1.7 \cdot 10^{-3}$ quantum yield [1] for the fourth harmonic of a Nd laser (Fig. 1) and requires a light energy of less than 1 mJ/micropulse, which is not too much to create serious heating problems. For the master laser oscillator, long ($\approx$ 1.5 ms) pumping was used together with active mode synchronization, acousto-optical modulators and an almost half-confocal optical cavity to provide 150 MHz intermode beating. For that scheme, a rather low-frequency ($\leq$ 0.1 MHz) amplitude modulation was observed, as is shown in Fig. 2 (upper trace) with 5 μs time resolution and 200 μs total duration. The modulation is probably due to competing modes that are initially randomly phased. To minimize their number a negative optical feedback was used. Due to a quasisteady pumping, 1% feedback was found to be sufficient when a photodiode 3 V signal was applied directly to an electrooptical modulator with $U = 200\ V$.

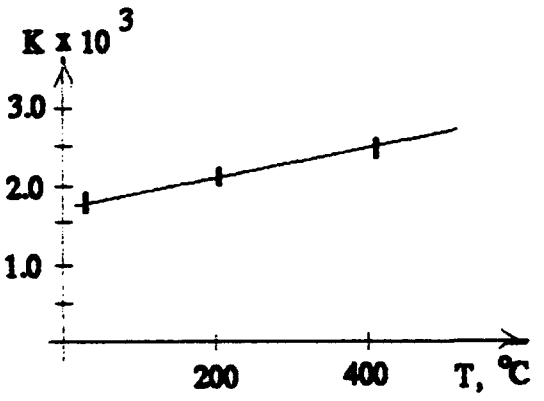


Fig. 1

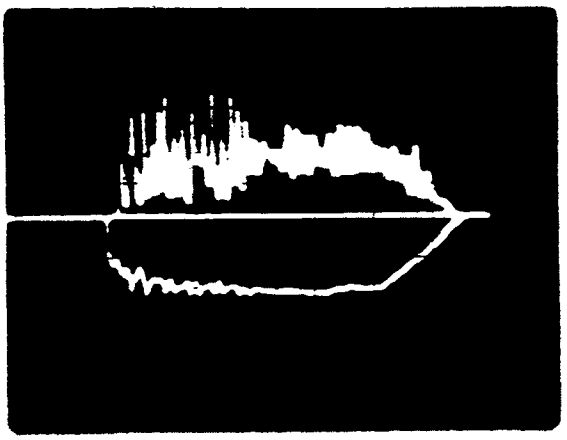


Fig. 2

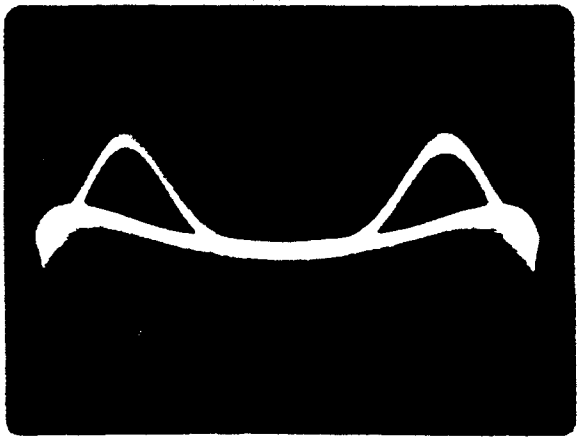


Fig. 3

The envelope of the micropulsesin the feedback regime is represented by the bottom trace in Fig. 2, while the superimposed pulses over the whole macropulse are shown in Fig. 3 with 1 ns time resolution (sinusoidal 75 MHz sweep). When using integral optical feedback, one can hope to obtain almost the same energy in the macropulse as in a free generation regime.

Particle dynamics

Three computer codes were used to optimize particle motion in the linac: electromagnetic 2.5-D code KARAT [2], electro- and magnetostatic code SAM [3] and code ENV to compute transversal motion envelopes. Code KARAT was oriented mainly on features of short bunch dynamics in the photoinjector and possible deviations from the Child-Langmuir law.

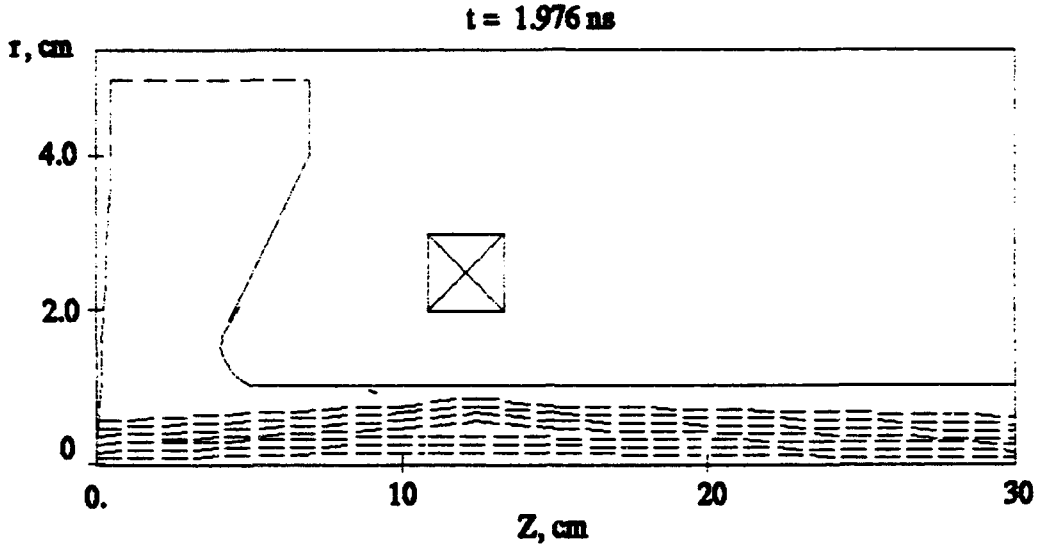


Fig. 4

The configuration of electrodes can be seen in Fig. 4. The accelerating voltage was usually 250 kV with the restriction of 100 kV/cm for the electric field on the surfaces. General current dependences on the effective gap and on the accelerating voltage were found to be analogous to the C.-L. law for pulse duration ≥ 0.1 ns.

For currents $\geq$100 A, tails of the current pulses were observed after the light pulses ended. They are probably due to inertia of a rather dense virtual cathode. A decrease of the emission current to 50 A combined with selected variation of the cathode surface angle yielded 100% bunch propagation with no visible tails. Fig. 4 shows the propagation of such a bunch through an optimized short magnetic coil, the focussing field being equal to 600 G. Computations of further beam transport based on the SAM code showed a transverse emittance of 0.1–0.15 mm.rad at the input of the main cavities.

Accelerating structure

A chain of independently phased rf-cavities chosen for the accelerating structure permits additional control flexibility when varying currents to be accelerated. The initial stage of the structure in Fig. 5 consists of three independently fed cavities. The first (with the photocathode), is excited up to 250 kV with a power of about 30 kW. The maximal field strength at the axis of the following cylindical cavities is 110 kV/cm, which is about 80% of the Kilpatric criterion [4]. Measurements on the assembled system yielded a Q-factor

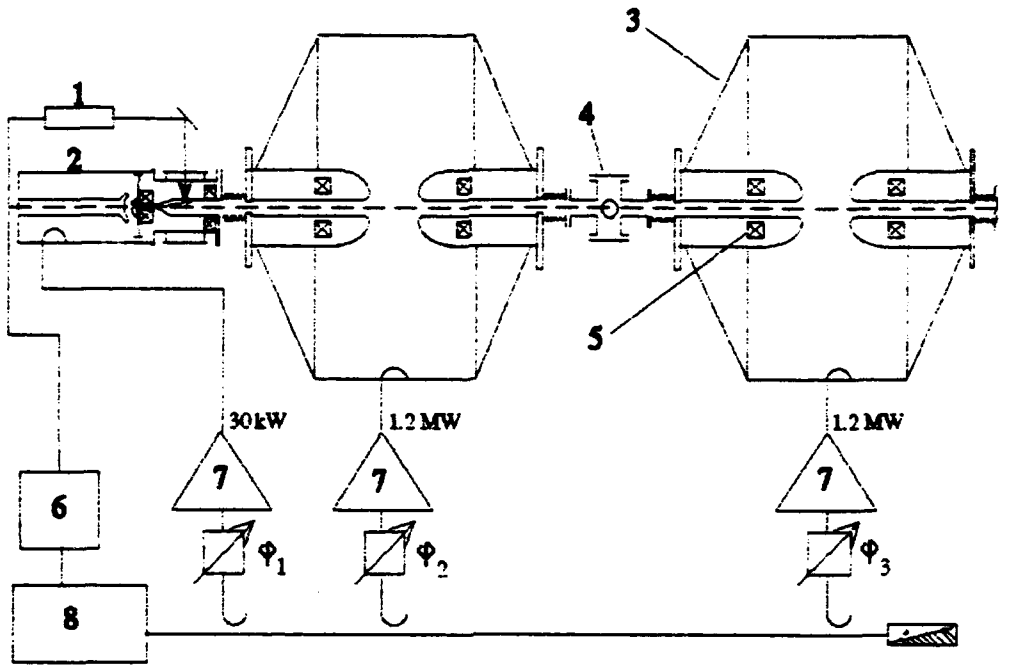


Fig.5. The scheme of the accelerating structure and RF-systems:
1–laser, 2–coaxial cavity e-gun, 3–cylindrical cavities, 4–diagnostic port,
5–focusing coils, 6–synchronization unit, 7–power amplifiers, 8–master generator

larger than $2 \cdot 10^4$ and a shunt impedance of 3.4 MOhm. Thus, the designed energy gain ($\approx$2 MeV/cavity) can be obtained with an input power of less than 1 MW. The master oscillator now uses a quartz 75 MHz cavity and a transistor amplifier-frequency doubler. The frequency instability is less than 10^{-7}, and the output signal power 1.5 W. We plan to change it in the future for a autogenerator with self-tuning of frequency, a synchronization system with an illuminating laser.

The distribution channel of excitation signals has a set of directed couplers and phase-shifters of mechanical and electronic types. The weak coupling with power stages permits using the same channel for measurements of relative phase shift at various points of the system.

The channels of excitation of main cavities include preamplification stages and a 1.2 MW power stage based on a triode. Accelerating field stabilization is provided by proper choice of power stage regimes of operation, power supply stabilization and phase feedback in oscillator channels. In the future certain features of bunch induced fields are to be investigated experimentally. In particular, relatively sharp changes of boundary conditions at the drift tube entrance and exit cause rather powerful coherent transient radiation, which leads to additional energy losses and to complicated interaction of the bunch and wake fields. Certain features of beam loading at the main harmonic are to be investigated as well as their partial compensation by means of fine cavity detuning.

Undulators

The energy of our electron linear accelerator will be increased gradually by adding new cavities and power supplies. To cover a wider spectral range one needs various undulators of different periods l and deflection parameters K. It is possible also to use higher harmonics generation applying microundulators ($3 - 10$ mm period) with deflection parameter $K = 1.5 - 2$.

A plane undulator with a period of 4.8 cm was constructed to cover millimeter and, partially, submillimeter ranges. It is of an electromagnetic type with negative and positive iron yokes being placed on different sides of the undulator. The main advantage of such a design is a simple geometry and common windings for each set of positive and negative field magnets. The unpleasant price for this simplicity is large stray fluxes between adjacent positive and negative poles, leading to early saturation of yokes and allowing only moderate $K = 0.5 - 0.7$ with an air gap between upper and lower poles of 1.6 cm. A possible way to increase the deflection parameter up to $K = 2$ is to insert permanent magnets (PM) between positive and negative poles, with PM flux reducing the stray and iron saturation [5]. A scheme of the undulator is presented in Fig. 6.

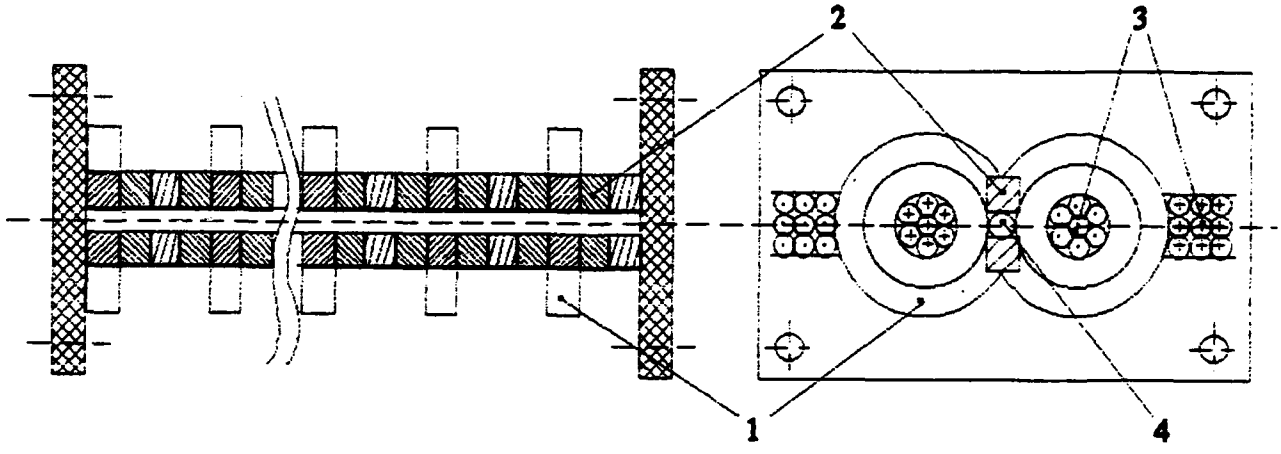


Fig.6. The plane undulator scheme:
1–C-shaped yokes, 2–permanent magnets, 3–coils, 4–undulator aperture,

To obtain infrared radiation in the range $10 - 100$ μ at electron energies of 5–7 MeV, one should use microundulators with a 3–10 mm period. Keeping this in mind, several pulsed helical undulators (with periods of 5 mm, 8 mm and 10 mm) were constructed and tested. The 8 mm period undulator with an adiabatic entry has a $0.3 - 0.4$ T maximal transverse field on axis ($K \leq 0.3$) and allows rather low repetition rates ($< 0.1Hz$) [6]. A water cooled, 10 mm period undulator was tested with fields up to 2 T ($K = 2$) capable to sustain 10–15 Hz repetition rates with about a 100 μs pulse duration. To generate FEL radiation in higher harmonics [7] with high field ($K = 2$) two types of undulators were studied and modelled

with the aim to attain high repetition rates. One is superferric (l = 8 mm), and the other — a pulsed electromagnetic undulator with iron.

First beam experiments at the initial 3-cavity structure are planned for the fall of the year.

References

1. A.Airapetov, G.Gevorgian et al. "Photoemitters and pulsed ferroelectric electron emitters with high current density", Proc. Int. Conf. "Beams-90", v.**2**, p.921. Novosibirsk, 1990.
2. P.Kotetishvili, V.Rybak, V.Tarakhanov, "KARAT — the instrument of a computational experiment in electrodynamics", Inst. for Gen. Phys. preprint No 44. Moscow, 1991.
3. M.Tiunov et al. "SAM — an interactive code for electron guns design", Inst. Nucl. Phys. prep. N 87-35. Novosibirsk, 1987.
4. M.Kilpatrik, "Criterion for vacuum sparking designed to include both RF and DC", Rev. Sci. Instr., v.**28**, p.824, 1957.
5. K.Halbach, "Concepts for insertion devices that will produce high-quality SR", Proc. Int.Conf. on X-ray and VUV SR Instrumentation; Nucl. Instr. & Meth. **A246**, pp.77-81, 1986.
6. V.A.Papadichev and O.A.Smith, "Helical microundulators of P.N.Lebedev Physical Institute", to be published Proc. 13th Int. FEL Conf., Santa Fe, USA.
7. R.W.Warren, et al. "Lasing on the third harmonic", Proc. 11th Int. FEL Conf., Naples, USA, Nucl. Instr. & Meth. in Phys. Res. **A296**, N 1-3 p.84-88, 1990, 12 Int. FEL Conf., Paris , Nucl. Instr. and Meth. in Phys. Res. **A304**, p.512, 1991.

FREE-ELECTRON LASER - FEL - BASED ON MSU RM-100 RACE-TRACK MICROTRON

Grishin V.K., Ishkhanov B.S., Sandalov A.N., Shvedunov V.I.
Nuclear Physics Institute, Physics Department
Moscow State University

The race-track microtron RM-100 MSU, the first stage of which has recently come into operation, is designed to accelerate electrons with variable energy of 7-180 MeV at a high quality of the beam: the homogeneity of energy is 10^{-4}, the beam emittance is not higher than 0.01 mm*mrad. Fig.1 shows the MSU RM-100 set-up.

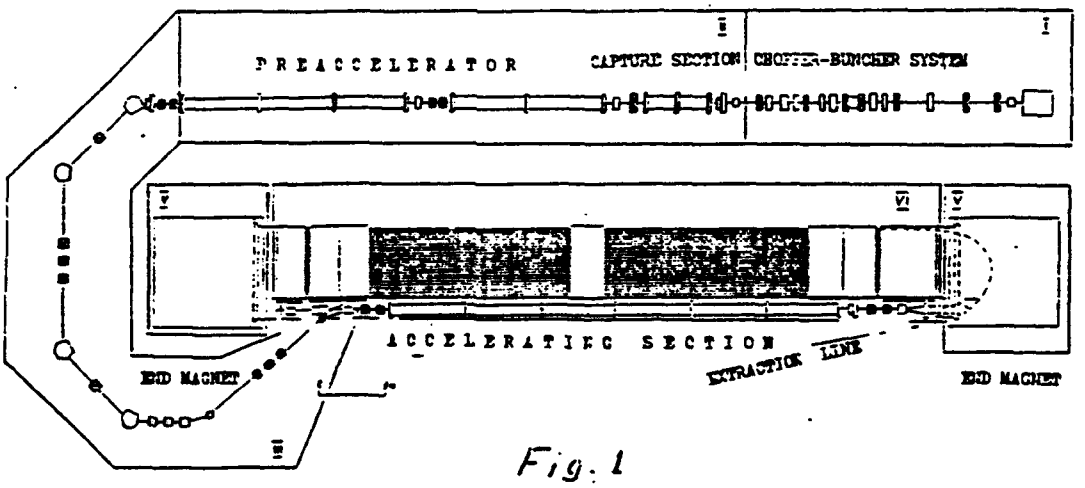


Fig. 1

The beam current is a conti-sequence of electron pulses with duration of 3-4 ps, repetition frequency of 2.45 GHz and the

average current of 100 mkA. A special operation mode of the acceleration is provided with duty cycle decreased by 100-300 times and the amplitude of current pulses increased up to 1-10 A.

The high quality of the beam makes it possible to use it as a microwave source. One of the considered schemes is a conventional FEL with magnetic undulator its electromagnetic radiation being in the range of 200-0.2 mkm. Fig.2 and Fig.3 show the possible schemes of MSU RM-100 FEL for low and high beam energy respectively.

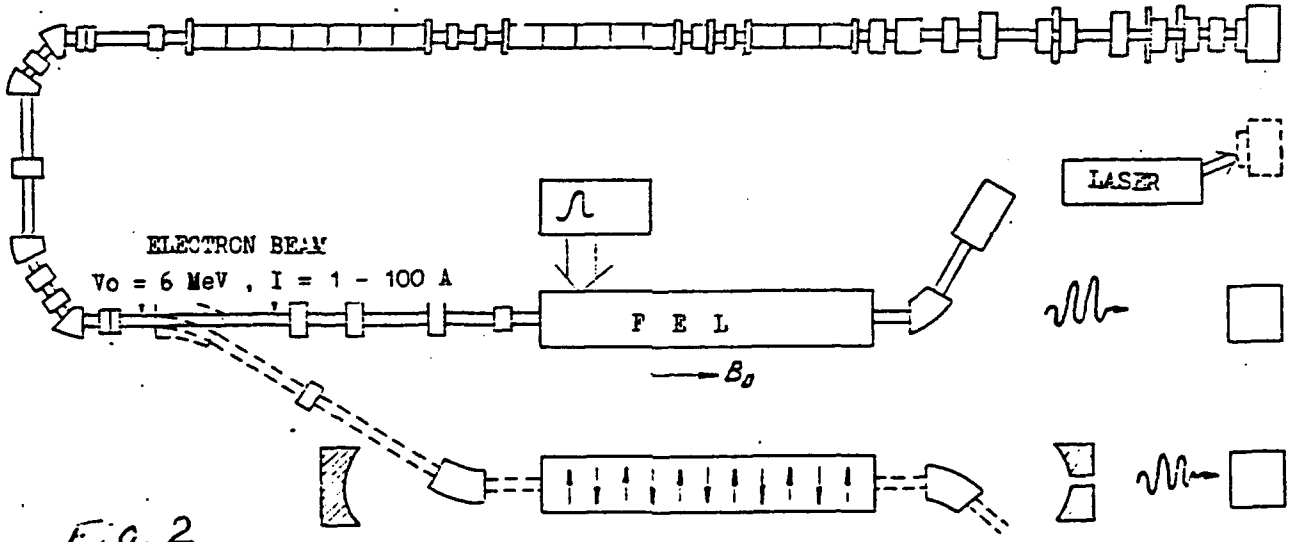


Fig. 2

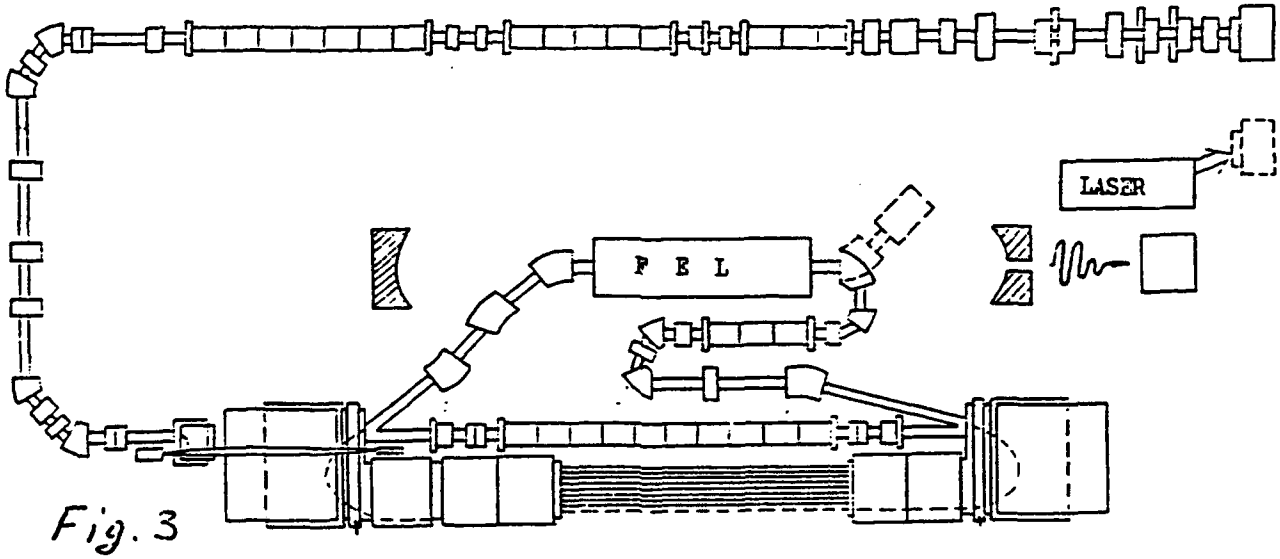


Fig. 3

Preliminary estimates of the possible FEL parameters were reported at the "Beam-90". These estimates were made for the so-called single-particle amplification mode (single-particle interaction of electrons with the radiation) at which the power of the radiation is proportional to the beam current. In this mode the peak values of the electron current are relatively small and there is no rearrangement of the particle density.

In this single-particle mode the RM-100 MU is suitable for building FEL with the following parameters [1-3]:

Parameters of FEL based on the RM-100(single-particle mode)

Wave-length range of laser radiation	170-1mm
Pulse duration	3 ps
Repetition frequency	2.45 GHz
Peak current.	1-3 A
Beam diameter, 2 a	0.2 cm
Amplification at pass	10-3 %
Undulator parameters:	
Period, λ_o	2.5 cm
Number of periods, N	100
Undulate factor, K	

The inevitable disturbances leave no hope that even more

intricate technology (inhomogeneous undulator, N = 300-350) would permit to move in this mode into the range of shorter wavelengths (λ = 1mkm corresponds only to the beam energy of 60-80 MeV).

Therefore we studied another mode of collective amplification in FEL based on the RM-100 MSU. Additional possibilities emerge here due to the guided radiation effect [4,5] which arise in the intense beams. In the RM-100 this effect may be achieved at peak currents I_b~3-10 A due to the high beam quality. The maximum tolerated divergence of the FEL beam is of the order of $1/\gamma(2N)^{1/2}$mrad [1] (γ is the Lorentz factor of the beam). Low emittance of the beam in the RM-100 permits (in principle) to satisfy the above restrictions on the beam divergence by decreasing its diameter at γ>100-200 down to <0.01 cm. The minimal diffraction limit of the laser beam at the above parameters of the set-up is $10^{-2}cm^2$, and its quenching (following the electron beam quenching) can be achieved only by the guided radiation.

The estimate of the efficiency of the collective amplification is based on the analysis of the dispersion equation, stemming from the equation for the transverse distribution of the radiation amplitude

$$E(r,z) = E_s(r)\exp(-i\omega t + ikz),$$

where r and z are transverse and longitudinal coordinates relative to the beam direction:

$$\frac{1}{r}\frac{d}{dr}\left(r\frac{dE_s}{dr}\right) + \left(\frac{\omega^2}{c^2} - k^2 - \frac{2I_b\omega^2\beta_1^2\rho(r)}{I_o a^2\gamma^3(\omega - v(k+k_o))^2}\right)E_s = 0$$

where I_b is the peak beam current, $\beta_\perp$ is the transverse particle velocity determined by factor K, $\rho(r)$ describes the transverse distribution of the beam density: $\rho(0)=1; \rho(r>a) \to 0$; I_c = 17 kA, at the boundary condition $E_s(r>a) \to 0$.

The guided radiation effect and the subsequent collective amplification are described by

$$G = \frac{1}{3} \exp X \quad ; \qquad X = \frac{N \lambda_0 Re\nu \, I\mu\nu}{2\pi \gamma^2 a^2}$$

where $\nu^2 = \left(\frac{\omega^2}{c^2} - k^2 \right) a^2$ follows from the wave equation.

The analysis of the FEL parameters gives the following results.

Amplification increment $X_{1,10}$ (for current I_b = 1,10 A, a=0.02cm)

E, MeV	25	78	108	168
γ	50	156	216	336
λ, mkm	10	1.02	0.54	0.32
X_1	1.4	< 1	<1	<1
X_{10}	3.6	1.6	1.4	1.2

The X > 1 values indicate the gain of the set-up which proves that RM-100 MSU can be used for producing very short-wave radiation. In principle the accelerator parameters permit a stronger quenching of the beam (a < 0.01 cm). Besides, the repulsing of the beam particles by their own fields is not significant yet and therefore the obtained estimates inspire one with a certain optimism.

1.Marshall T.C. Free-Electron Laser ,Macmillan Publishing Company.

2.Pellegrini C. The free electron laser. IEEE Trans.Nucl.Sci.1979, N 5-6,p.3791.

3.Grishin V.K.,Daremskaij L. Korotkowolnowoe izluchenie in FEL na base RM-100 MSU..M.,1991.

4.Scharlemann E.T.,Sessler A.M., Wurtele J.S. Optical quiding in a free electron laser, Nucl.Inst.and Meth.in Phys.Rev.,A,1995.v.239,N 1-2,p.19-28.

5.Spangle P.,Ting A. et al. Guided radiation beams in free-electron laser,Nucl.Inst.and Meth. in Phys.Rev.A,1988,v.272, n !-2, p.536-542.

HIGH CURRENT CERENCOV FREE ELECTRON LASER-CFEL AT FAR INFRARED WAVELENGTHS

Grishin V.K.,Cricket C.M.,Lenski I.F.
Institute of Nuclear Physics,Moscow State University
Moscow, 119899 Russia

At present the so-called cerencov free electron laser -CFEL- is given much experimental and theoretical attention to [1-3]. In CFEL the electron beam propagates near the dielectric surface and excites a slow electromagnetic wave with the phase velocity that is somewhat less then beam's one: $v_{ph}= \beta_{ph}c= \omega/kc \quad v_0= \beta_0 c$ where v_0 is beam velocity,and transfer its kinetic energy to the radiation.

CFEL-systems with dielectric layers are structurally sufficiently simple andarepromising devicesforexcitation of electromagnetic radiation at millimeter and submillimeter wavelengths with smooth tuning by means of varying the electron energy. Of course now we consider using of low-energy relativities electron beams, since the radiation wavelength increases very rapidly with the growing energy of a relativistic beam as follows from the approximation $\lambda_0 = 2\pi\Delta\gamma_0(\varepsilon\beta_o^2-1)/\varepsilon\beta_o$,where Δ is the dielectric thickness, ε is the permittivity of the layer, $v_o= \beta_o c$ and γ_o are the velocity and the Loren factor of the beam. We shall discuss the efficiency of a modified version of this scheme including elements of gas plasma.

The field in the short wavelength radiation CFEL is concentrated near the dielectric surface within a layer of one

wavelength thick. It is quite natural therefore to press the beam against the dielectric surface as strongly as possible in order to make the field-beam interaction more intense. This, in turn, would cause intense gas plasma creation near the surface which can change crucially the electrodynamic properties of the system. The most significant change takes place if the magnitude of the plasma frequency exceeds that of the field oscillation . In this case the field amplitude varies rather slowly in the vicinity of the dielectric and as a result the efficiency of the field -beam interaction increases.

Consider a cylindrical configuration with R and Z being the waveguide radius and the axis, the thickness of the ε-layer being Δ and the radius b of the thick tube beam. In the dielectric-beam space there is intense gas plasma. The axial component of its dielectric permittivity tensor $\varepsilon_{zz} = \varepsilon_{pp} < 0$. The beam and the plasma are magnetized longitudinally. We take into account the interaction of the beam with the symmetrical E-mode only.

The joint treatment of the Maxwell equations, the boundary conditions and the linearized motion equations lead to the dispersion relation which determines the spectrum of wave number k at a fixed frequency of the system ω ($E_z = \exp(-i\omega t+ikz)$; $kb \gg 1$; in the Compton approximation) :

$$D_0 = \frac{\varepsilon}{\gamma_{ph}\sqrt{\varepsilon\beta^2-1}}\,(1+(tg\chi_1\delta)/\alpha)(ctg\,\chi_2\Delta) + (tg\chi_1\delta)/\alpha - 1 =$$

$$= \frac{2\,k\,Q\,I_b}{I_0 b\,\beta^2\gamma^3(\omega-kv_0)^2} \quad ; \quad Q=1-\frac{\varepsilon}{\alpha\,\gamma_{ph}\sqrt{\varepsilon\,\beta^2-1}}\,(tg\chi_1\delta)(ctg\chi_2\Delta)$$

where $\beta_{ph}= \omega/kc$, $\gamma_{ph}=1/\sqrt{1-\beta^2}$, $\chi_1^2= - k^2\alpha_1^2/\gamma^2$, $\alpha^2=-\varepsilon_p$, $\chi_2^2= \varepsilon\omega^2/c^2 -k^2$, $\delta =R-b-\Delta$.

At $\alpha \to i$ (no plasma, tg $\to$th) this relation transforms into the dispersion equation for a dielectric waveguide with the beam in the shortwave limit. Under this condition a typical factor $\exp(-2k\delta/\gamma)$ appears in the right-hand side of the equation and its value becomes very small already at $\delta= 2\pi/k$. On the contrary, at $\alpha>0$ the situation qualitatively changes since the drop of the field amplitude in the plasma layer decreases significantly, and the Q-factor becomes of the order of unity. Therefore the efficiency of the beam-field interaction increases substantially.

The dispersion properties of the cold system are determined by the $D_0=0$ equation under the resonance condition $\beta_{ph}= \beta_0$. At $\delta=0$ (like at $\alpha \to i$) this equation describes oscillations $k_0=k_0(\omega)$ of the plasmaless waveguide with the beam slipping along of dielectric. At $\delta>0$ the equation manifests an important feature: up to $\delta \cong 3\Delta$ (at $0<\alpha<1$) the wavelength remains practically constantand appears to be close to that in the plasma less waveguide (see the relation at the beginning).

Ultimate efficiency of the radiation excitation can be estimated in the following way. The accompanying wave travelling along the Z-axis becomes amplified to such extent that it captures the beam particles (it is the major mechanism of nonlinear saturation which restricts the excitation of electromagnetic radiation in sufficiently extended systems). After that the wave and the beam come into synchronization on averag e , and the amplification

stops (this occurs at a length of 20-40 cm for typical parameter values). The level of capturing determines the ultimate beam energy transfer into the electromagnetic flux.

From this fact and from the requirement of the balance of the energy and momentum fluxes in the system it is possible to estimate the ultimate efficiency coefficient E_f of the device (for details see [4]):

$$E_f = \frac{\Pi_E}{\Pi_0} = \frac{\gamma_0(\beta_0 - \beta)}{(\gamma_0 - 1)(cG_E/\Pi_E - 1)}$$

where $\Pi_{E,0}$ are the energy flues of the original beam and of the radiation, G_E is the momentum flux of the radiation, $v=\beta c$ is the velocity of the wave and the beam at the moment of capture. To fulfill the resonance conditions at the initial moment one must put $k=k_o \beta_o/\beta$. In our calculations we put $\beta= \beta_o - \delta_\beta$, where $\delta_\beta \beta_o \mathrm{Im}\delta_k / 3^{1/3} k_o$where the value of $\mathrm{Im}\delta_k$ follows from the dispersion equation.We have made estimates for the existing device of the Physics department of MSU with the following parameter values:
$\gamma_o=1.4$, $R=0.5$, $\Delta=0.1$, $\varepsilon=3.4$ ($\lambda=0.59$ cm).

	δ/Δ	I_b= 50 A	I_b= 500 A
	0	3.9%	7.8%
E_f	1	2.6%	5.2%
	3	2.5%	> 5%

For comparison the efficiency value is less then 1% for the plasmaless case at $\delta = \Delta$.

It is necessary to remark that in the CFEL-scheme different collective amplification and nonlinear saturation regimes - Copmton, Raman (with the subsequent capture of particles) and frequency detuning can be already implemented at the beam currents as low as hundreds of A [4]. But the indicated estimate should conserve its validity in the plasma-dielecric CFEL because of more intense beam-wave coupling.

The role of plasma formation in the submillimeter range is equally significant. But in this case the plasma density must amount to $10^{14} cm^{-3}$ and therefore a more detailed analysis is needed.

1.Fetch K.L.,Busby K.O.,Laymon R.W. et al. Cerencov radiation in dielectric-lined waveguides, Appl.Phys.Lett.,1981.v.38,p.601-603.

2.Garate E.,Walsh J.,Shaughnessy C. et al.Cerencov free electron laser operation from 375 to 1000 mkm, Nucl.Inst and Meth.in Phys. Rev.,1987,v.A259,p.125-127.

3.Ciocci F.,Patt G. et al. Status of the ENEA-Dartmouth far infrared Cerenkov laser experiment,ibid,p.128-132.

4.Lenski I.F.,Doct. tesis,MSU,1991.

Contributed Advanced Accelerator Papers

Model of Cavity Coupling for Beam Breakup Control

D. G. Colombant and Y. Y. Lau

Beam Physics Branch, Plasma Physics Division
Naval Research Laboratory
Washington, DC 20375-5000

D. Chernin

SAIC, McLean, VA 22102

ABSTRACT

The coupling of the accelerating cavities to dummy cavities was recently found to reduce beam breakup growth. This paper analyzes a more sophisticated model, that includes the time delay between coupled cavities and covers the possibilities of wave cutoff and resonance in the coupling path. A dispersion relation is obtained. We show that the peak spatial exponentiation rate of the dominant BBU mode is reduced by as much as a factor of two, and this reduction is insensitive to the coupling path length. Other modes are destabilized, however, but they have lower growth rates, in general.

I. INTRODUCTION

The presence of coupled cavities has been shown to reduce beam breakup growth in both linear and recirculating accelerators.[1] This growth reduction is a result of the sharing of the energy of the deflecting mode between a dummy (bleeding) cavity with the main (accelerating) cavity to which the former is coupled. This preliminary conclusion is based on a crude model that uses a mutual inductance to describe the coupling.[2] Such a model fails to account for the time delay that necessarily occurs when the electromagnetic signal travels back and forth along the coupling path. This deficiency was drawn to our attention by G. Caporaso,[3] who proposed a model that may account for such a delay. The present paper reports our findings based on this model. Independently, researchers at the University of Michigan[4] also addressed the effects of time delay that results from the finite length of the cables that couple the main cavities with the bleeding cavities.

II. A MODEL FOR CAVITY COUPLING

Consider a linac geometry, where an electron beam passes through a sequence of accelerating cavities along the z-axis [Fig. 1]. Each main cavity is coupled to a dummy cavity which acts as an energy storage for the deflecting mode that is excited in the main cavities by the beam. The coupling path, which is finite, is in the x-direction [Fig. 1].

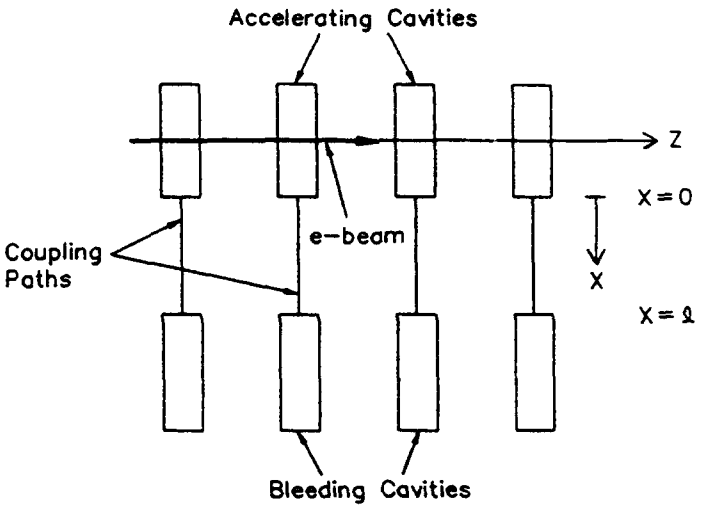


Fig. 1 Coupling between the accelerating (main) cavities and the bleeding (dummy) cavities.

A mechanical model was proposed by Caporaso[3] that describes the coupling between the cavities. In this model [Fig. 2], both the dummy cavity and the main cavity are modelled by a damped oscillating spring, whose natural frequency ω_o and quality factor Q coincide with those of the BBU mode under consideration. The two springs are assumed to be identical, and are attached to the two ends of the coupling path, at x = 0 and at x = ℓ, [Fig. 2]. These end oscillators are coupled by the string under tension T, and along the string are suspended individual oscillators, each of which has a natural frequency ω_c.

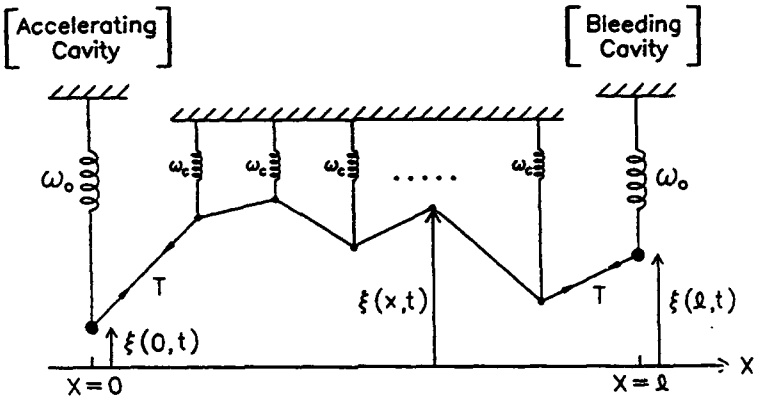


Fig. 2 A mechanical analog, proposed by Caporaso, that describes the coupling between an accelerating cavity and a bleeding cavity. This model includes the effects of time delay along the coupling path (x).

In the continuum limit, the transverse displacement of the string, $\xi(x,t)$, is governed by the partial differential equation:

$$\frac{\partial^2 \xi(x,t)}{\partial t^2} = u^2 \frac{\partial^2 \xi(x,t)}{\partial x^2} - \omega_c^2 \xi(x,t) \qquad (1)$$

where $u = \sqrt{T/\rho}$ is the characteristic speed of propagation of disturbance on the string, with ρ being the mass per unit length of the string. Equation (1) has a simple interpretation when $\omega_c \to 0$. The $\omega_c^2 \xi$ term in Eq. (1) represents the restoring force exerted by the individual springs that are attached along the coupling path [Fig. 2].

Note that Eq. (1) includes time delays in the signal as it propagates along the string (coupling path). Note also that signals with frequency $\omega < \omega_c$ cannot propagate in the x-direction, according to Eq. (1). Thus, cutoff phenomena may also be modelled by this equation.

Let $A(t) \equiv \xi(0,t)$ and $D(t) \equiv \xi(\ell,t)$ be the respective displacements of the end oscillators at $x = 0$ and at $x = \ell$, [Fig. 2]. The governing equations for these end oscillators are

$$L\,A(t) = \alpha \left.\frac{\partial \xi(x,t)}{\partial x}\right|_{x=0} \qquad (2)$$

$$L\,D(t) = -\alpha \left.\frac{\partial \xi(x,t)}{\partial x}\right|_{x=\ell} \qquad (3)$$

where

$$L = \frac{\partial^2}{\partial t^2} + \frac{\omega_o}{Q}\frac{\partial}{\partial t} + \omega_o^2 \qquad (4)$$

is the familiar operator for damped oscillators. The right-hand sides in Eqs. (2) and (3) represent the forces acting on these end oscillators by the string. These forces are proportional to the tension, represented through α, and to the slopes, $\partial\xi/\partial x$, of the string at $x = 0$ and at $x = \ell$ [Fig. 2]. From Eqs. (2) and (3), the coupling between the accelerating cavity [A(t)] and the dummy cavity [D(t)] is measured by α, whereas $\xi(x,t)$ includes the effects of time delay as it is governed by the wave equation (1).

III. CONTINUUM DESCRIPTION OF BBU

The above building blocks for cavity coupling may be used to investigate the BBU evolution via a continuum description of the model shown in Fig. 1. Let $y(z,t)$ be the transverse displacement of a beam at the axial position z at time t. Let $A(z,t)$ and $D(z,t)$ be, respectively, the deflecting mode amplitude of the accelerating cavity and of the dummy cavity at position z at time t. Since only the deflecting mode $A(z,t)$ in the main cavities would act on the beam, the force law for the beam reads

$$\left(\frac{\partial}{\partial t} + v\,\frac{\partial}{\partial z}\right) \gamma \left(\frac{\partial}{\partial t} + v\,\frac{\partial}{\partial z}\right) y(z,t) + \gamma\,\omega_\beta^2 y(z,t) = A(z,t) \qquad (5)$$

where v is the beam's coasting velocity, γ is the relativistic mass factor and ω_β is the betatron frequency measuring the focal strength. The main cavities are acted on by the beam, and by the dummy cavity. Thus, the governing equation for $A(z,t)$ reads

$$L\,A(z,t) = 2\,\gamma\,\omega_o^4\,\varepsilon\,y(z,t) + \alpha\,\frac{\partial \xi(x,z,t)}{\partial x}\bigg|_{x\,=\,0} \qquad (6)$$

where L is defined by Eq. (4), ε is the BBU coupling constant[5,6] which is proportional to the beam current and to the transverse shunt impedance, and the last term in (6) models the coupling described by Eq. (2). Similarly, one can write an equation for the deflecting mode amplitude $D(z,t)$ of the dummy cavity [cf. Eq. (3)] and for the disturbance $\xi(x,z,t)$ on the coupling path (at axial position z) [cf. Eq. (1)] where we replace u by c, the speed of light.

Assuming a modal solution of the form $\exp(j\omega t - jkz)$ where ω is the frequency, and k is the wavenumber whose positive imaginary part gives the BBU spatial growth rate, we obtain

$$\xi(x,z,t) = \left[\bar{C}_1\,e^{jpx} + \bar{C}_2\,e^{-jpx}\right] e^{j\omega t - jkz} \qquad (7)$$

where

$$p^2 \equiv \frac{\omega^2}{c^2} - \frac{\omega_c^2}{c^2}. \qquad (8)$$

Similarly, we assume

$$\begin{bmatrix} y(z,t) \\ A(z,t) \\ D(z,t) \end{bmatrix} = \begin{bmatrix} \bar{Y} \\ \bar{A} \\ \bar{D} \end{bmatrix} e^{j\omega t - jkz} \tag{9}$$

where $\bar{Y}$, $\bar{A}$, $\bar{D}$ are constants. To obtain the dispersion relation $D(\omega,k) = 0$, we substitute the solutions (7) and (9) into the previous set of equations. Five equations relate the five unknowns $\bar{C}_1$, $\bar{C}_2$, $\bar{Y}$, $\bar{A}$, $\bar{D}$. For a nontrivial solution to exist, a dispersion relation is derived.[7] This dispersion relation accounts for phase delay (through l) and coupling strength (through α).

IV. NUMERICAL RESULTS

We have obtained the normalized spatial growth rate $\bar{k}_i \equiv \mathrm{Im}(kc/\omega_o)$ as a function of the normalized frequency $\bar{\omega} \equiv \omega/\omega_o$, according to the dispersion relation. Of particular interest is the dependence on the normalized coupling length $\bar{\ell} \equiv \omega_o \ell/c$. The following set of parameters has been used: $\varepsilon = 1.42 \times 10^{-4}$, $\omega_\beta/\omega_o = 1.181$, $\bar{\ell} \simeq \bar{\ell}_o \equiv 43.6$. These numbers are within the range of the University of Michigan experiments.[4] We introduce a dimensionless coupling constant κ to model the coupling coefficient between a bleeding cavity and the accelerating cavity. Specifically, we assign $\kappa \equiv 0.182\ (\alpha/c\omega_o)^{1/2}$, and postulate that κ may range from zero (no coupling) to 0.1. We arbitrarily assign $\omega_c/\omega_o = 0.8$.

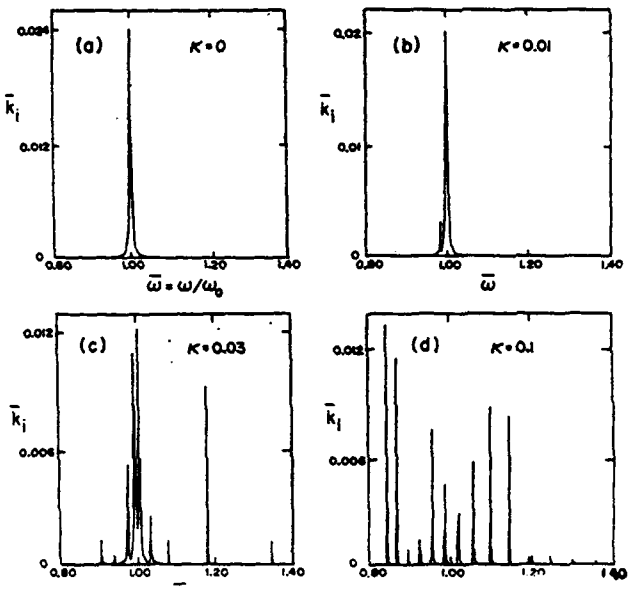


Fig. 3 The normalized spatial exponentiation rate $\bar{k}_i$ as a function of the normalized frequency $\bar{\omega}$.

Using the above set of parameters, the numerical results follow. In Fig. 3, we show $\bar{k}_i$ as a function of $\bar{\omega}$ for Q = 200 and for various coupling coefficients κ. For $\kappa = 0$ (no coupling), we see that $\bar{k}_i$ reaches a maximum value of 0.024 for $\bar{\omega} \equiv \omega/\omega_o = 1$. The peak in $\bar{k}_i$ is very sharp because of the large value of Q. As κ increases, two things happen: the maximum value of $\bar{k}_i$ decreases from 0.02 for $\kappa = 0.01$, to 0.0125 for $\kappa = 0.03$ and $\kappa = 0.1$; that is, the maximum spatial growth goes down by a factor of 2 over this range of κ. The second important feature is that the number of unstable modes increases as κ increases but except for the case of $\kappa = 0.1$, the growth rate of these modes does not exceed that of $\bar{\omega} = 1$.

Note that Fig. 3 already shows the insensitivity of BBU growth to the coupling path length ℓ. As the frequency ($\bar{\omega}$) is varied along the abscissa in Fig. 3, the coupling path length, measured in units of wavelength, also varies. No extra resonance is observed, for example, in Fig. 3b. We have also re-performed the calculation in Fig. 3, changing only $\bar{\ell} = 7 \times 2\pi$, a multiple integer of 2π (instead of $\bar{\ell} = 43.6$), while keeping all other parameters the same. The results are very similar to those shown in Fig. 3. The amplitude of the growth rate hardly changes but the distribution of the unstable modes is slightly different for the larger values of κ. The sensitivity of the results to the variation in coupling length is minimal.

ACKNOWLEDGMENT

We are indebted to George Caporaso for suggesting to us the mode coupling model. Useful discussions with R. Gilgenbach, R. Bosch and S. Putnam are gratefully acknowledged. This work was supported by SDIO/IST/ONR, and by DARPA under ARPA Order No. 7781.

REFERENCES

1. D.G. Colombant, Y. Y. Lau and D. Chernin, Part. Accel. 35, 193 (1991); Nucl. Instrum. Methods A31, 1 (1992).
2. See, e.g., H. J. Reich, P. F. Ordung, H. L. Krauss and J. G. Skalnik, Microwave Theory and Techniques, Van Nostrand, N. Y. (1953), p. 539.
3. G. Caporaso, private communications (1991).
4. R. A. Bosch and R. M. Gilgenbach, private communications (1991).
5. Y. Y. Lau, Phys. Rev. Lett. 63, 1141 (1989); Y. Y. Lau and D. G. Colombant in Advanced Accelerator Concepts, AIP Conf. Proceedings 193, p. 244 (1989).
6. R. A. Bosch and R. M. Gilgenbach, Appl. Phys. Lett. 58, 699 (1991); R. A. Bosch, P. R. Menge and R. M. Gilgenbach, J. Appl. Phys. 71, (April 1, 1992).
7. D.G. Colombant and Y.Y. Lau, SPIE Proceedings, Vol. 1629 (1992),p.538.

EXPERIMENTS ON THE EXCITATION AND COUPLED-CAVITY SUPPRESSION OF BEAM-BREAKUP-INSTABILITY IN LONG-PULSE ELECTRON BEAM TRANSPORT

R. M. GILGENBACH, P. R. MENGE, M. T. WALTER,
C. H. CHING, J. FOSTER, and P.L.G. VENTZEK
Intense Energy Beam Interaction Laboratory
Nuclear Engineering Department
University of Michigan
Ann Arbor, MI 48109-2104

Abstract

Experiments have been performed to excite and suppress the beam breakup (BBU) instability in long pulse electron beam transport through RF cavity systems. Electron beams are generated by the Michigan Electron Long Beam Accelerator (MELBA) at parameters: V=0.7-0.8 MV, I_{diode} = 1-10 kA, $I_{injected}$ = 100-400 A, and pulselength= 0.5-1 μs. The transport system consists of a solenoidal magnetic field with 10 RF cavities. The TM_{110} mode BBU resonance frequency of the cavities is 2.5 GHz and the cavity Q is adjusted to about 200-300. Each cavity has a small coupling loop oriented to detect the RF field in the TM_{110} mode. The cavities are separated by 6.5 cm-long sections of tubing which are cutoff to the RF frequency. The BBU instability is primed by a kW level microwave signal injected into the first cavity from a magnetron. Growth of the RF is measured between the second cavity and the last cavity. Strong growth (2-5 dB per cavity) is only observed when the RF priming signal is tuned to the exact TM_{110} mode resonance frequency ($\Delta f/f_o << 1\%$). Experiments to test techniques for suppression of the BBU instability are also being performed. The primary BBU suppression technique being investigated is cavity cross-coupling, in which 7 out of 10 internal beam-cavities are connected by cables to 7 identical cavities located externally to the e-beam. These are the first experiments which have shown a consistent reduction (about -6 dB average) in BBU microwave growth when external cavities are coupled to the internal cavity system.

Introduction

The beam breakup instability is the most serious instability which limits the pulselength and current of electron accelerators.[1] Beam breakup instability can also be a problem in multi-cavity klystrons. During the past several years a great deal of theoretical research has advanced the knowledge of the BBU[1-5]. Very few experiments to-date have systematically excited the BBU in high current, long-pulse electron beams. Experiments at the University of Michigan have the goal of exciting the beam breakup instability on a few (ten) cavity system and measuring the scaling of BBU growth.[6,7] Suppression techniques for the BBU are also being investigated, particularly coupled-cavities.[8,9] These experiments are made possible by an accelerator which operates at long-pulse and high current; the Michigan Electron Long Beam Accelerator[10], MELBA, operates at diode parameters of 0.7-0.8 MV, 1-10 kA, and pulselength of 0.5-1 μs. The parameters of this electron beam transport experiment are in a unique regime[2], intermediate between previous weak focusing[1] and strong focusing[3,4] regimes.

Experimental Configuration

The experimental configuration for the beam breakup instability growth measurement is depicted in Figure 1. The experiment is driven by the MELBA accelerator,[10] which is based on a Marx generator with an Abramyan type compensation stage, which flattens the voltage over pulselengths of about 1 μs. Pulselengths on MELBA can be set by an adjustable crowbar switch between 0.3-1 μs and are typically set at about 0.5 μs for these experiments. A velvet button cathode is installed on the hemispherical end of the cathode stalk. A graphite aperture defines the 2-cm injected beam diameter and yields extracted currents of 40-400 A. The anode cathode gap is about 10.2 cm. Diode magnetic field (≈0.8 kG) is generated by large coils pulsed by a capacitor bank. The transport chamber is a stainless steel tube wound with pulsed solenoidal magnetic field coils. Typical solenoidal magnetic fields of 3-4 kG were employed.

Inside the chamber is an array of ten brass pillbox microwave cavities with radius of 6.9 cm and length of 2.0 cm. The TM_{110} mode resonant frequency of each cavity is set at 2.5075 GHz ± 0.0026 GHz. In order to lower the cavity Qs to values of about 200-300, each cavity was loaded with a small ring of microwave absorber. Smaller radius (1.9 cm) copper tubes of length 6.5 cm connect the cavities and prevent electromagnetic crosstalk (-26 dB), which would lead to the regenerative BBU instability.

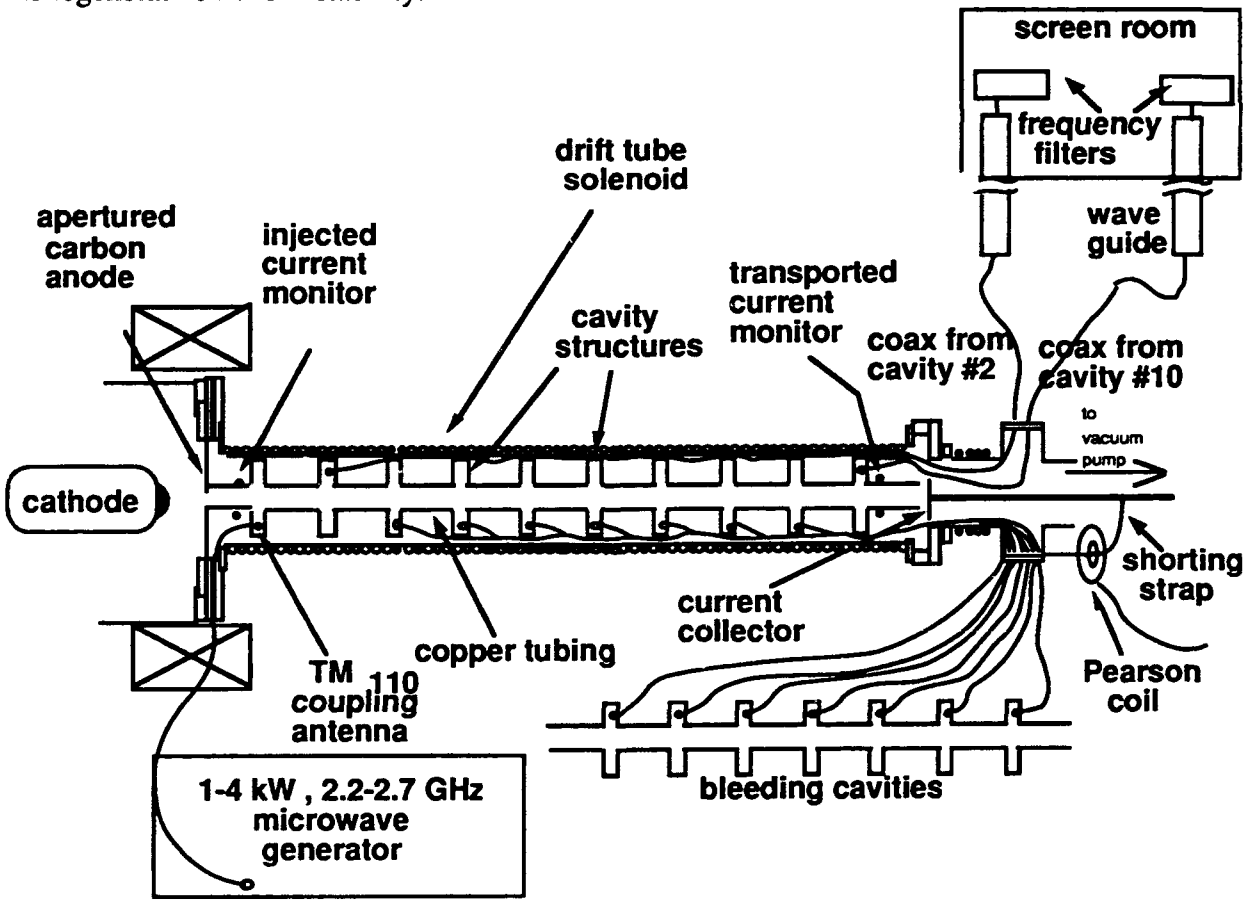


Figure 1. Experimental Configuration

Each cavity contains a small coupling loop designed to detect the TM_{110} mode for cold-testing and e-beam experiments. The coupling loop in the first cavity is utilized for priming the TM_{110} mode with the signal from a kW level microwave pulse generator. Coupling loops in the second and tenth cavities are used to measure the growth of beam-breakup-instability -generated microwaves as the electron beam coasts through the cavity system. Microwave signals are coupled out of the chamber by coaxial cable and transmitted to the Faraday cage by waveguide. In the Faraday cage, the signals are filtered to extract the BBU signal at the TM_{110} mode resonance frequency of 2.5075 ± 0.0115 GHz and signals are attenuated for measurement on crystal detectors. For coupled-cavity BBU growth experiments, a set of equal-length (16λ) coaxial cables connects seven internal cavities to seven identical external cavities. For baseline BBU growth measurements, the coaxial cables are disconnected between internal and external cavities.

Electron beam current is measured at a number of points in the transport experiment. Cathode stalk current in the diode is measured by a B-dot loop in the MELBA oil tank, behind the insulators. Extracted current is monitored by a Rogowski coil in the flange after the anode. Injected current is measured by a Rogowski coil before the first cavity and exit current is detected by a Rogowski coil after the last cavity. Exiting current is also measured by a current collector which is grounded by a strap which passes through a Pearson current transformer.

Experimental Results

In order to compare the BBU growth for the uncoupled-cavity baseline case to the coupled-cavity case, a typical experimental run alternated between several shots for each case. Microwave priming was applied to the first cavity for several microseconds before the e-beam pulse. The solenoidal magnetic field was about 3.4 kG. Experimental data signals for microwave priming of the beam-breakup-instability for the baseline case (no external coupled cavities) are presented in Figure 2. The voltage flattop was reached after about 200 ns, at which time the electron beam current was nearly flat. In Figure 2, the baseline (uncoupled-cavity) microwave growth is about 36 dB between the second cavity signal and the tenth cavity signal. Injected electron beam current was typically about 200-300 A; 75-90% of this current was transported through the 10 cavity system.

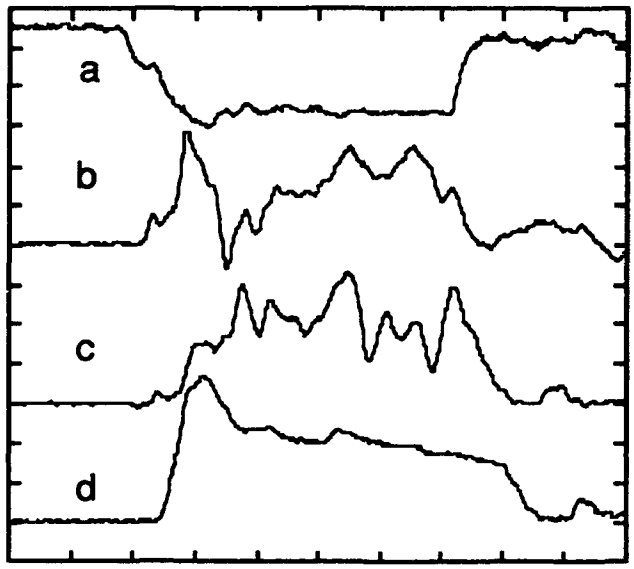


Figure 2. Uncoupled cavity data. (a) Diode voltage (310 kV/div). (b) 2nd cavity 2.5 GHz diode detector signal (50 mV/div). (c) 10th cavity diode detector signal (50 mV/div). (d) Transported current (92 A/div) from a different shot. The applied magnetic field is 3.4 kG.

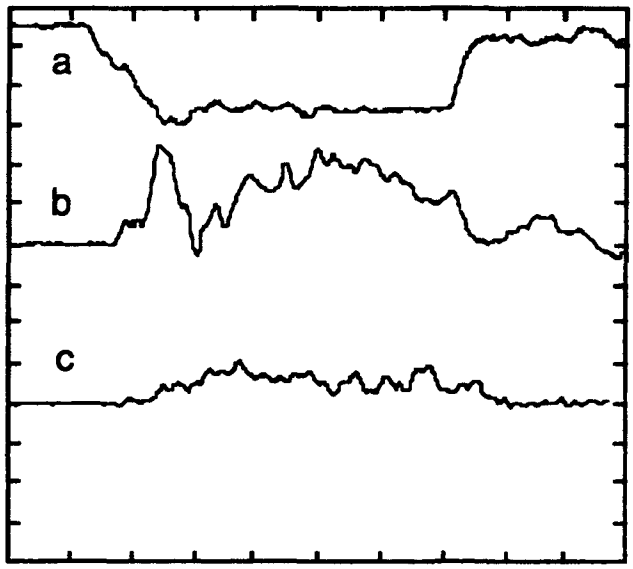


Figure 3. Coupled cavity data. (a) Diode voltage (310 kV/div). (b) 2nd cavity 2.5 GHz diode detector signal (50 mV/div). (c) 10th cavity diode detector signal (50 mV/div). The applied magnetic field is 3.4 kG.

For comparison, data from a coupled cavity shot is presented in Figure 3; in this case, the microwave growth between the two signals is much lower, about 25 dB. A summary of beam-breakup-instability microwave growth data from some 40 shots is presented in Figure 4. The data show a consistent reduction of BBU growth from about 36 dB average ($\sigma = \pm$ 1.5 dB) for the uncoupled case to about 30 dB average ($\sigma = \pm$ 2.4 dB) for the coupled-cavity case. Thus, for the present seven cavity system, we measure an average BBU growth reduction of about 6 dB due to coupled-cavities. Variations of BBU signal amplitudes may be due to varying current amplitudes and other differences between shots. Figure 5 presents the transported current for each pulse of Figure 4. A correlation can be seen between the BBU growth data of Figure 4 and the transported current data of Figure 5.

Theoretical research[9] by Colombant and Lau predicts that the growth rate for the beam breakup instability can be reduced by up to a factor of two, depending upon the coupling strength. The physical mechanism for coupled cavity reduction of beam-breakup-instability growth is believed to be TM_{110} mode energy-sharing between internal and external cavities.

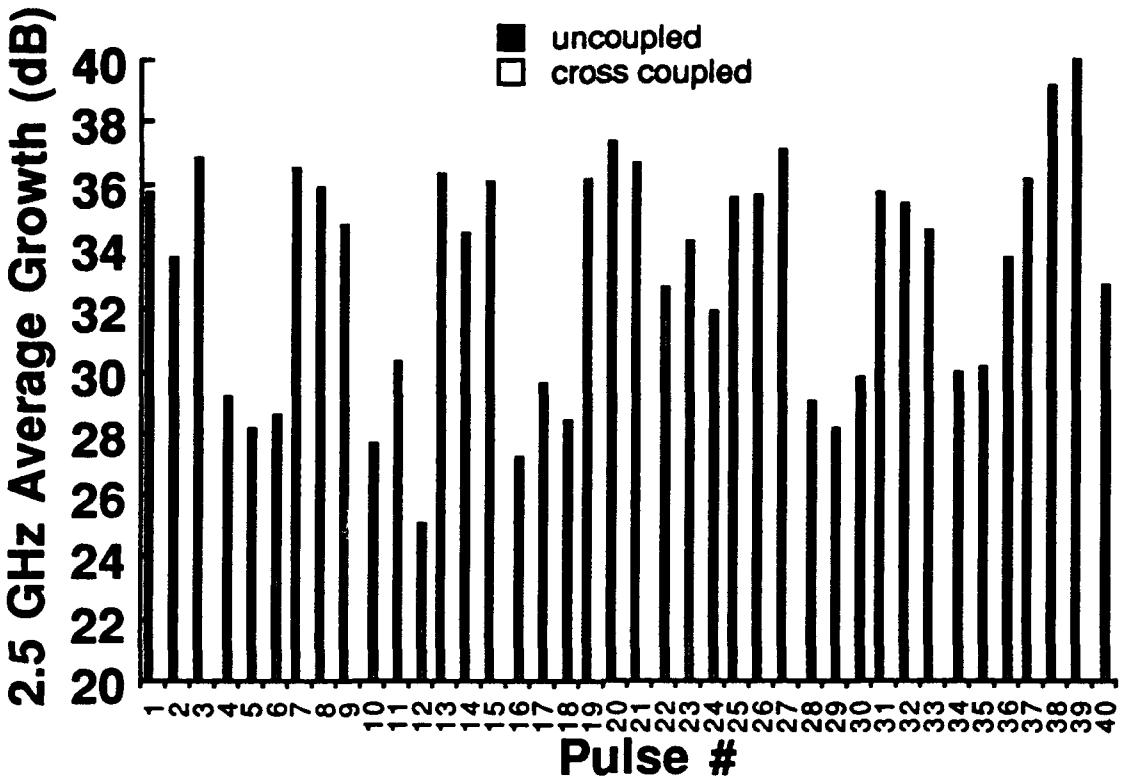


Figure 4. Column graph showing the growth in decibels of the 2.5 GHz microwaves for electron beam pulses in which the cavities were uncoupled (black columns) or cross coupled (open columns).

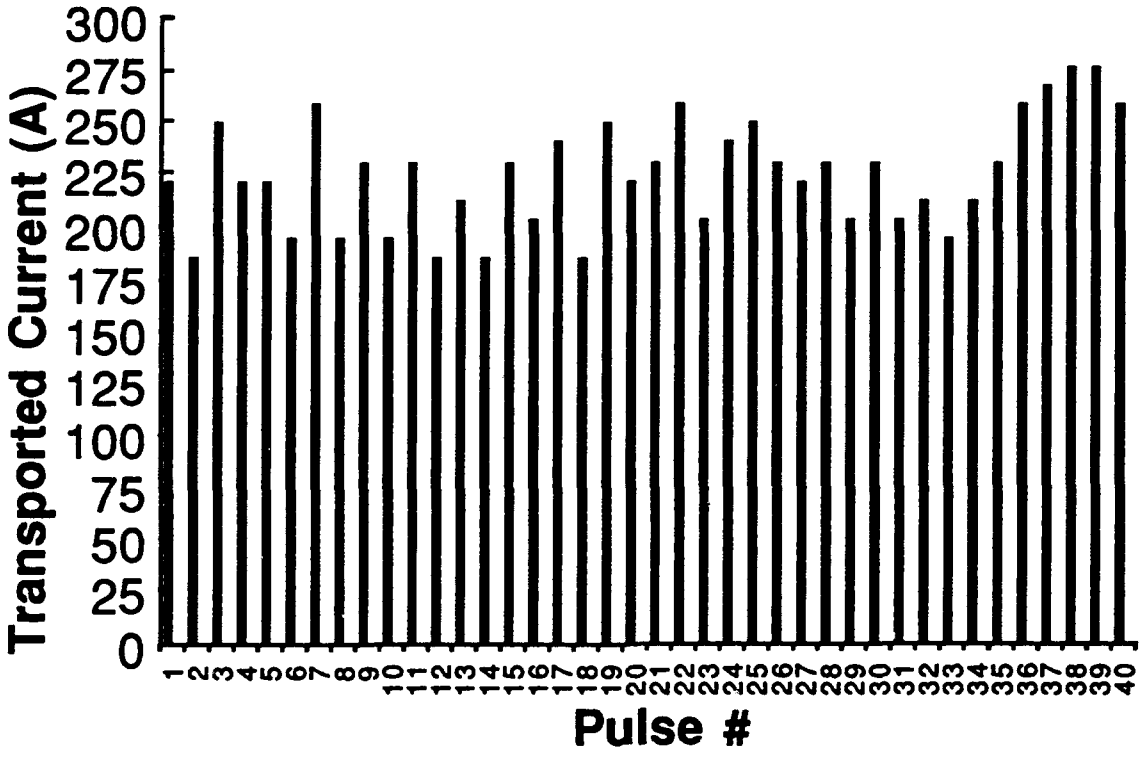


Figure 5. Column graph showing the amount of transported current for each electron beam pulse.

Acknowledgement

We appreciate valuable interactions with Y. Y. Lau. This research was supported by SDIO-IST through an ONR contract.

References

1) W. K. Panofsky and M. Bander, Rev. Sci. Instrum. **39**, 206 (1968)
2) Y. Y. Lau, Phys. Rev. Lett. **63** 1141 (1989)
3) K. Neil and R. K. Cooper, Part. Accel. **1**, 111 (1970)
4) K. Neil, L. S. Hall, and R. K. Cooper, Part. Accel. **9**, 213 (1970)
5) R. A. Bosch, P. R. Menge, and R. M. Gilgenbach, J. Appl. Phys. **71** 3091 (1992)
6) R. M. Gilgenbach, P. R. Menge, R. A. Bosch, J. J. Choi, C. H. Ching, and T.A Spencer, Conference Record of the 1991 Particle Accelerator Conference, IEEE Cat. No. 91CH3038-7
7) P.R. Menge, R. M. Gilgenbach, R.A. Bosch, C.H. Ching, T.A. Spencer, and M. Walter, in Intense Microwave and Particle Beams III, edited by H. Brandt, SPIE Vol. 1629, p 529, (1992)
8) D.G. Colombant, Y.Y. Lau, and D. Chernin, Part. Accel. **35** no. 4 Vol. 2, (1991)
9) D. G. Colombant and Y. Y. Lau, in Intense Microwave and Particle Beams III, edited by H. Brandt, SPIE Vol. 1629, p 538, (1992)
10) R. M. Gilgenbach, et al., in Digest of the 5th IEEE Pulsed Power Conference, p126 (IEEE, New York, NY, 1985)

ELECTRON FLOW IN POSITIVE-POLARITY MULTIGAP INDUCTIVE ACCELERATORS*

B.W. Church and *R.N. Sudan*
Laboratory of Plasma Studies, Cornell University, Ithaca, N.Y. 14853

Abstract

We study the electron flow in multi-gap inductive accelerators, such as Hermes III operating in positive polarity by numerical simulation and modeling. The objective of this work is to determine the operating principles such that an optimally efficient design of the Hermes-type machine can be achieved for intense ion beam generation. We employ a 2-D fully electromagnetic particle in cell code, MASK†, to represent the electrons emitted in the accelerating gaps and their dynamics. Because the electrons emitted in different gaps have different energies and canonical momenta, the simple theory of magnetic insulation[1] has to be extended to such multi-component electron flows.

In order to understand the effects of load impedance on the electron flows in the multi-gap accelerator and on the coupling of power to the load, MASK has been used to simulate an accelerator with a small number of gaps for various load impedances. For load impedances below the self-limited impedance Z_{SL} of the last segment of the accelerator, the electron flow in both segments is well insulated. The overall current efficiency is over 90% and is insensitive to the load impedance Z_L for $Z_L < Z_{SL}$. Beyond Z_{SL}, the current efficiency decreases rapidly with increasing load impedance. Because of this rapid decrease in efficiency, the power delivered to the load also falls off rapidly as load impedance is increased. To better understand these results, a simple theoretical model for multi-component electron flows has been developed to predict the distribution of electron flows. The model will be compared with existing multi-component models[2] and simulations.

For both high and low impedance loads the electron flow from the leading edge of each cathode is unsteady, producing an intermittent train of diamagnetic electron vortices. These vortices are not circular but elongated with an aspect ratio near one half. The center of each vortex $\mathbf{E} \times \mathbf{B}$ drifts along with the local electron flow. In each vortex, electrons $\mathbf{E} \times \mathbf{B}$ drift about the vortex center along the potential contours of the vortex's self-electric field in a reference frame moving with the vortex center. These vortices were compared to a self-consistent solution of a cylindrically symmetric fluid model which showed good agreement with data observed from the runs.

Introduction

Inductive multi-gap positive polarity accelerators are potentially an optimal power supply ($\geq 10^{13}W$) for light ion beam inertial confinement fusion. Both the 4-gap machine HELIA[3] and the 20-gap machine Hermes-III, have been coupled to high impedance extraction ion diodes to demonstrate the feasibility of positive polarity operation. In addition, a 10 segment machine SABRE Much experimental work[4] has been done to characterize single cathode MITL's. Early theoretical work established one-dimensional MITL equilibria[5, 6] and a general theory for the adiabatic evolution of the electron distribution function in an MITL[7]. To engage theory with experiment a robust simple theory of the MITL voltage-current relation was also developed[1]. Recently, with the development of positive polarity inductive adders, the problem of multi-component electron flows has been addressed through simulation and modeling[2].

To investigate the load impedance dependence of electron flows a two-gap MITL adder has been simulated for load impedances from 5 to 12 Ω. A simple layered flow model has been constructed based on the physical

*Research supported by Sandia National Laboratory, under contract no. 63-4881 and by ONR grant N00014-89-J-1770.

principles of Mendel's simple MITL model. This model, along with the locally emitted flow (LEF) model, was employed to construct an equivalent circuit model that reproduced the results observed in simulation.

In addition, the electron flow was observed to be unsteady when the load impedance was sufficiently low, such that the launched electron current exceeds the equilibrium current[8]. The unsteady electron flow formed vortices that were distinct from the electron sheath attached to the cathode and that $E \times B$ drifted along with the electron flow. Past work on electron vortices has focused on rotating electron beams[9] and low-density nonneutral plasmas[10, 11] where collisionless skin depth $\lambda = c/\omega_{pe}$ is much larger than the size of the vortex. In contrast, here λ is on the order of the vortex size and thus the vortices are both relativistic and diamagnetic. We have found an analytic self-consistent description of a cylindrical vortex and compared the solution favorably with the vortices observed in simulation.

Modeling of Multi-Gap Positive Polarity MITL Adder

The voltage current relation predicted by the simple constant-density model of magnetic insulation[1] has proved robust at matching observations from both simulation and experiment on single component electron flows. It matches the parabolic potential profile of an electron sheath with constant density at the Brillouin limit[12] to the linear potential profile of the vacuum between the sheath and the anode. The slope of the vacuum potential, the electric field, is determined by the magnetic field above and below the sheath and thus by the currents in the anode and cathode. The locally emitted flow (LEF) model[2] has been successful at predicting MITL voltage as a function of measured currents in multi-component electron flows. The LEF model is an adaptation of the simple model to multi-component flows.

The simple MITL model predicts for the MITL voltage

$$V_{MITL}(I_1, I_2) = Z_0\sqrt{I_1^2 - I_2^2} - \frac{mc^2}{2e}\left(\frac{I_2^2}{I_1^2} - 1\right) \quad . \tag{1}$$

For the simple model $I_1 = I_a$ and $I_2 = I_c$, where I_a is the anode current and I_c is the cathode current. For the LEF in an MITL with no loss to the anode, I_a of the ith MITL section is replaced by the cathode current of the upstream MITL section, such that $I_1 = I_{c_{i-1}}$ and $I_2 = I_{c_i}$.

Replacing I_a by $I_{c_{i-1}}$ essentially has the effect of ignoring the contribution of the space charge of the launched electron flow on the anode voltage while retaining the effect of its current on the pressure balance of the underlying electron flow. This remains a good approximation as long as the launched electron sheath remains close to the anode. Rosenthal has shown[2] that the launched electrons stay close to the anode. Because the launched electron sheath is close to the anode, it does not greatly alter the anode voltage. The anode voltage is then largely determined by the locally emitted electrons.

It is possible to extend this picture to multiple electron layers separated by vacuum regions between the cathode and the anode. This is denoted as the layered flow (LF) model. The boundaries and the potentials at each electron layer are found self-consistently to match the potential and electric field at the vacuum/electron-layer boundaries. An example is shown in Fig. 1. The electric field in the vacuum regions between the electron layers is determined from the currents in the electron flows above and below the region using pressure balance. When the difference in these currents is small the electric field required by pressure balance is highly sensitive to small errors in the currents, and the resultant voltage drop across the sheath-vacuum pair is not robust to small errors in the measured currents.

Both models have been used to construct an equilibrium circuit model for the simulated two segment MITL positive polarity adder and for other multi-gap configurations. The power feed transmission lines are

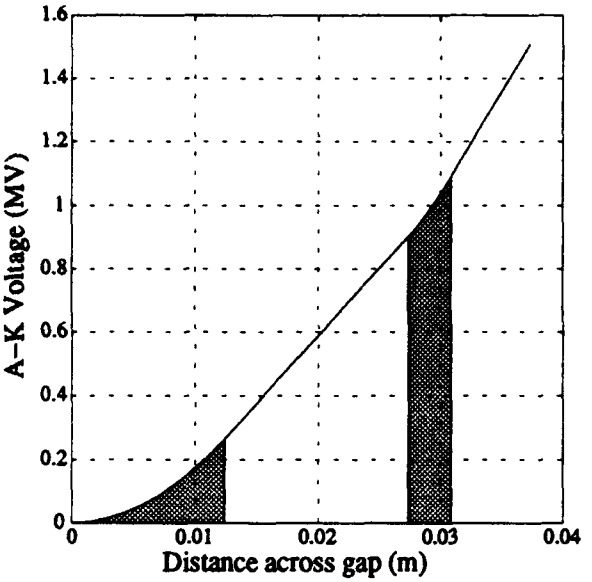


Figure 1: Voltage across anode-cathode gap for constant density layered flow model for $I_a = .24$ MA $I_{c_1} = .19$ MA $I_{c_2} = .14$ $Z_1 = 7.2\,\Omega$ $Z_2 = 12.4$ Ω. The grey regions denote the electron layers.

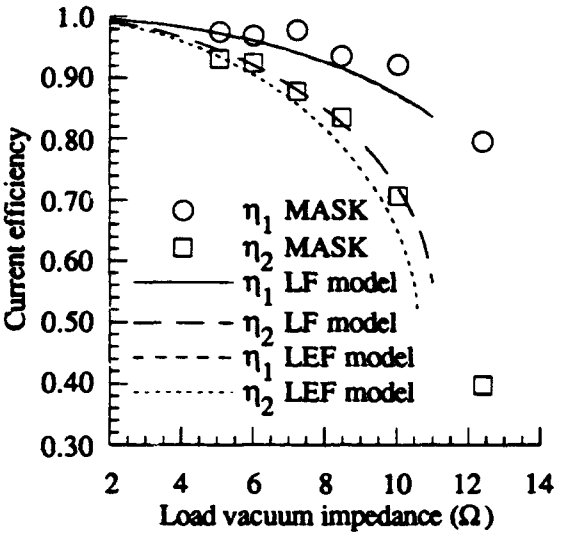


Figure 2: Comparison of MASK simulation with circuit models. The open circles and squares are the current efficiencies measured for the first and second MITL sections respectively. The curves are the efficiencies predicted by the circuit models.

modeled as linear circuits. The load circuit was modeled as a self-limited MITL segment. A set of nonlinear algebraic equations are obtained that describe the interaction of the power supplies, MITL sections and load circuit. These equations are solved numerically to find the operating point of the system. Because the voltage across the input ports in the simulation was fixed, the load voltage $V_{load} = V_{s_1} + V_{s_2}$. The simulation load was approximated in the circuit model by a self-limited MITL (ignoring the launched flow in the load), in which the anode current I_a is the mimimum current for the given operating voltage V_{load}[13]. Once I_a has been found from the load voltage-current relation, the cathode currents I_{c_1} and I_{c_2} can be found by matching $V_{s_1} = V_{MITL}(I_a, I_{c_1})$ using the simple MITL model and $V_{s_1} + V_{s_2} = V_{LF}(I_{c_1}, I_{c_2}, I_a)$ or $V_{s_1} + V_{s_2} = V_{MITL}(I_{c_1}, I_{c_2})$ using the LEF model.

To compare the circuit model with the simulation define the current efficiency of the ith MITL segment $\eta_i = I_{c_i}/I_a$. The current efficiencies measured from the MASK simulations are plotted in Fig. 2 along with η_i from the circuit model as a function of the vacuum impedance of the self-limited load. The circuit model shows better agreement with the simulation for the LF model than LEF. The sharp drop in η_2 occurs because as the load impedance is increased, less I_a is drawn by the load and I_{c_1} approaches the self-limited current of the second segment. Beyond this impedance I_{c_1} is below the self limited current and equation (1) cannot be satisfied.

Diamagnetic Electron Vortices

The unsteady electron flow at the head of each MITL section was found to intermittently form electron vortices that were distinct from the MITL electron sheath flow. These vortices form when ever excess electron current is present in the MITL[8]. Once formed the vortices drift axially along with the underlying sheath flow until they exit the system in the load. A vortex consists of a distinct group of electrons undergoing $E \times B$

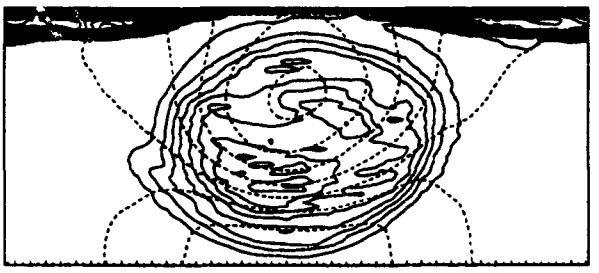


Figure 3: Contours of constant density (solid lines) and rB_θ for a typical vortex. Electro-magnetic fluctuations and particle noise have been removed via a co-moving average.

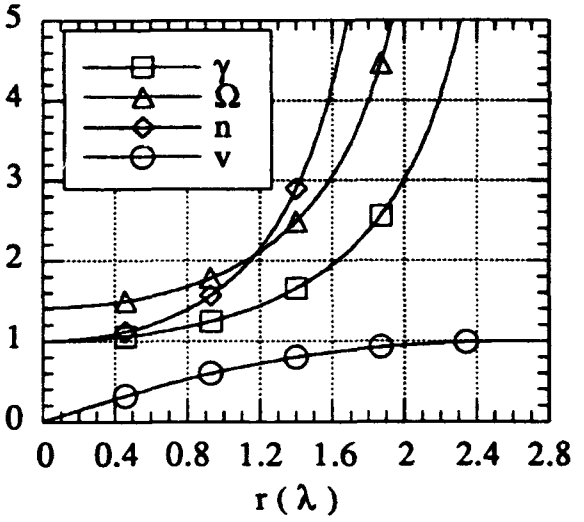


Figure 4: Solution of vortex equation (4), Eqns.(5) and (6) plotted as a function of radius.

motion about the center of the vortex. Because electrons at the outer edge of the vortex are relativistic, the relativistic change in the electron momentum and centripetal acceleration, as well as diamagnetism must be accounted for in the equilibrium model. The contours of constant density and rB_θ for a typical electron vortex are shown in Fig. 3.

The quasi-static equilibrium of a two-dimensional cold relativistic electron fluid is described by[14, 15]

$$\nabla^2\gamma = \frac{\gamma}{\sqrt{\gamma^2-1}}|\nabla\Omega| \ , \ \ \Omega = \nabla\cdot(\sqrt{\gamma^2-1}\frac{\nabla\Omega}{|\nabla\Omega|}), \tag{2}$$

where $\gamma = 1/\sqrt{1-v^2}$ and the orientation of the coordinate system is chosen such that the magnetic field $\Omega(r,\theta)\hat{\mathbf{z}}$ is oriented along the vortex axis and the velocity $\mathbf{v} = v_r(r,\theta)\hat{\mathbf{r}} + v_\theta(r,\theta)\hat{\theta}$ is perpendicular to $\hat{\mathbf{z}}$. The density at the vortex center is defined to be n_0. The velocity $\mathbf{v}$ is normalized to c, the electron cyclotron frequency Ω to $\omega_{pe} = \sqrt{4\pi e^2 n_0/m_e}$, ϕ to $e/m_e c^2$, and r to $\lambda = c/\omega_{pe}$.

In the limit that the vortex is cylindrically symmetric (ie. $\frac{\partial}{\partial\theta} = 0$ and $v = v_\theta(r)$), the set of PDEs (2), can be reduced to the set of ODE's,

$$\gamma'' + \frac{1}{r}\gamma' = \frac{\gamma}{\sqrt{\gamma^2-1}}|\Omega'| \ , \ \ \Omega = \frac{1}{r}\sqrt{\gamma^2-1} + \frac{\gamma\gamma'}{\gamma^2-1}, \tag{3}$$

where the prime denotes a total derivative with respect to r. These equations may be combined into the single nonlinear equation for γ,

$$\gamma'' + \frac{\gamma'}{r} - \frac{\gamma(\gamma^2-1)}{r^2} = \frac{\gamma|\gamma'|^2}{1-\gamma^2}, \tag{4}$$

which has the solution

$$\gamma = \frac{8+r^2}{8-r^2} \ . \tag{5}$$

The resultant magnetic field, density, and velocity are given by

$$\Omega = \frac{64\sqrt{2}}{(8-r^2)^2} \ , \ \ n = \frac{64(8+r^2)}{(8-r^2)^3} \ , \ \ v = \frac{4\sqrt{2}r}{8+r^2} \ . \tag{6}$$

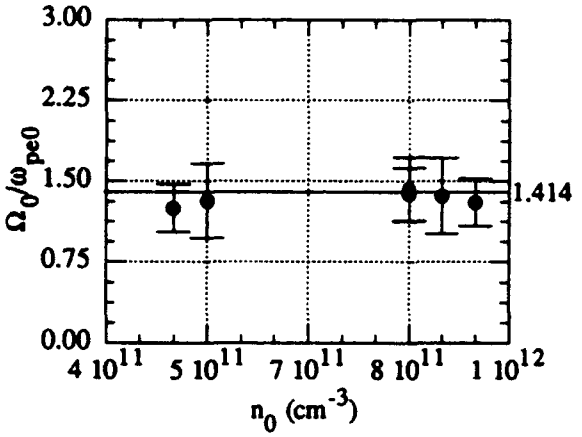


Figure 5: Vortex cyclotron frequency Ω normalized by ω_{pe} as predicted by the model is $\sqrt{2}$ and is independent of density.

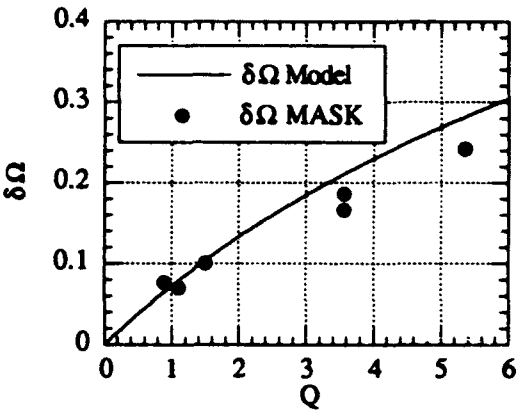


Figure 6: Vortex diamagnetism $\delta\Omega$ plotted as a function of Q.

These quantities are plotted in Fig. 4. The maximum radius for a vortex is $2\sqrt{2}$. At this radius γ, n, and Ω become infinite while v approaches one.

To compare this model with the vortices observed in simulation note that the model predicts that at the vortex center ($r = 0$) cyclotron frequency $\Omega = \sqrt{2}\ \omega_{pe0}$. In Fig. 5 the observed cyclotron frequency Ω_0 normalized to the plasma frequency is plotted against measured density at the vortex center and the agreement between the predicted and the observed value is within 10%.

The net diamagnetism of a vortex, $\delta\Omega$, defined as

$$\delta\Omega \equiv \frac{\Omega(R) - \Omega(0)}{\Omega(R)} = \frac{R^2(16 - R^2)}{64} \quad , \tag{7}$$

where R is the outer radius of the vortex, can be expressed as a function of the total charge per unit length in z, Q by

$$\delta\Omega(Q) = \frac{1}{Q^2}(Q^2 - 8\pi Q + 4\pi\sqrt{32\pi Q + 64\pi^2} - 32\pi^2) \quad , \tag{8}$$

which relates the two global quantities $\delta\Omega$ and Q that can be measured from the observed vortices. Equation (8) is plotted as the continuous line in Fig. 6. The data from the simulation is represented by the circles.

Conclusions

The LF model has been developed based upon the constant density simple MITL and locally emitted flow models. The model has been used in an equivalent circuit for the equilibrium state of a two gap MITL adder. The circuit model accurately reproduced the current efficiencies measured from particle-in-cell simulations of the system. The circuit model may be useful for optimizing the design of a positive polarity MITL adder. In addition a new self-consistent one-dimensional insulated electron flow solution has been found that describes the quasi-static equilibrium of diamagnetic electron vortices produced in the simulations.

†MASK was provided by Adam Drobot of Science Applications International Inc.

References

[1] C. W. Mendel Jr., D. B. Seidel, and S. E. Rosenthal. A simple theory of magnetic insulation from basic physical considerations. *Lasers and Particle Beams*, 1(3):310–320, 1983.

[2] S. E. Rosenthal. Characterization of electron flow in negative- and positive-polarity linear-induction accelerators. *IEEE Transactions on Plasma Science*, 19(5), October 1991.

[3] D. L. Hanson, M. E. Cueneo, P. F. McKay, R. C. Coats, and S. E. Rosenthal. Ion coupling efficiency for an extraction applied-B diode on the HELIA linear induction adder in positive polarity. *IEEE Transactions on Plasma Science*, 19(5), October 1991.

[4] J. P. Van Devender. Long self-magnetically insulated power transport experiments. *Journal of Applied Physics*, 50(6), 1979.

[5] R. V. Lovelace and E. Ott. Theory of magnetic insulation. *The Physics of Fluids*, 17(6), June 1974.

[6] J. M. Creedon. Relativistic Brillouin flow in the high ν/γ diode. *Journal of Applied Physics*, 46(7), July 1975.

[7] C. W. Mendel Jr., S. A. Slutz, and D. B. Seidel. A general theory of magnetically insulated electron flow. *The Physics of Fluids*, 26(12), 1983.

[8] C. W. Mendel Jr. and S. E. Rosenthal. Relativistic electron flow in charge cells. In *Bulletin of the American Physical Society*, volume 34, page 2020, 1989. Paper 4S16.

[9] A. J. Theiss, R. A. Mahaffey, and A. W. Trivelpiece. Rigid-rotor equilibria of nonneutral plasmas. *Physical Review Letters*, 35(21), November 1975.

[10] D. J. Heinzen, J. J. Bollinger, F. L. Moore, W. M. Itano, and D. J. Wineland. Rotational equilibria and low order modes of a nonneutral ion plasma. *Physical Review Letters*, 66(16), 1982.

[11] C.F. Driscoll and K.S. Fine. Experiments on vortex dynamics in pure electron plasmas. *Physics of Fluids B*, 2(6), 1990.

[12] L. Brillioun. A theorem of Larmor and its importance for electrons in magnetic fields. *Physical Review*, 67(7), 1945.

[13] D. B. Seidel. Magic simulations of the self-limited impedance of magnetically insulated transmission lines. In *Particle Beam Fusion progress report January 1983 through June 1983*, page 27. Sandia National Laboratories, 1984. SAND83-1547.

[14] R. N. Sudan. Intense particle beams in laboratory and in space. In *Bulletin of the American Physical Society*, volume 34, page 2111, 1989. Paper 7RV.

[15] B. W. Church, D. W. Longcope, C. K. Ng, and R. N. Sudan. Two dimensional electron flow in pulsed power transmission lines and plasma opening switches. In *Thirteenth International Conference on Plasma Physics and Controlled Nuclear Fusion Research*, pages 143–151, Washington D.C., October 1990. IAEA-CN-53/B-III-2.

SIMULATIONS OF MULTISTAGE INTENSE ION BEAM ACCELERATION[1]

S. A. Slutz and J. W. Poukey

Sandia National Laboratories, Albuquerque, N. M. 87125Abstract

An analytic theory for magnetically insulated, multistage acceleration of high intensity ion beams, where the diamagnetic effect due to electron flow is important, has been presented by Slutz and Desjarlais [J. Appl. Phys. 67, 6705 (1990)]. The theory predicts the existence of two limiting voltages called $V_1(W)$ and $V_2(W)$, which are both functions of the injection energy qW of ions entering the accelerating gap. As the voltage approaches $V_1(W)$, unlimited beam-current density can penetrate the gap without the formation of a virtual anode because the dynamic gap goes to zero. Unlimited beam current density can penetrate an accelerating gap above $V_2(W)$, although a virtual anode is formed. It was found that the behavior of these limiting voltages is strongly dependent on the electron density profile.

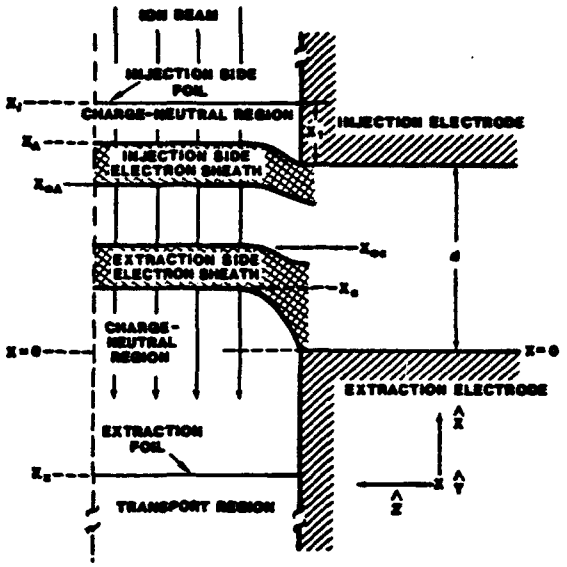
We have investigated the behavior of these limiting voltages numerically using the 2-D particle-in-cell (PIC) code MAGIC. Results of these simulations are consistent with the superinsulated analytic results. This is not surprising, since the ignored coordinate eliminates instabilities known to be important from studies of single stage magnetically insulated ion diodes. To investigate the effect of these instabilities we have simulated the problem with the 3-D PIC code QUICKSILVER, which indicates behavior that is consistent with the saturated model.

I. Introduction

High intensity light ion beams generated by magnetically insulated diodes are being developed to drive inertial confinement fusion (ICF)[1]. These diodes are driven by a high-power electrical pulse at the output of a pulsed power generator. The application of a strong magnetic field transverse to the anode-cathode gap inhibits electron flow across the gap as long as the diode voltage is below the critical value V_c given by the expression $eB_0d/mc=[(1+eV_c/mc^2)^2+1]^{1/2}$, where B_0 is the applied magnetic field, e/m is the charge to mass ratio of an electron, c is the speed of light and d is the anode-cathode gap. In response to the magnetic force, electrons drift primarily in the ExB direction. This results in diamagnetic electron currents that distort the initial applied magnetic field. Of particular importance are the magnetic flux surfaces coincident with the electrodes., labelled x_a and x_c in Fig.1. These surfaces define virtual-electrodes, due to the high electron conductivity along magnetic field lines. Note that $x_1=x_A=x_{*A}=d$ in a single stage diode and there is only a virtual cathode on the extraction side. It has been shown[2], in single-stage magnetically insulated diodes, that the dynamic gap $g=d-x_c$ goes to zero (and consequently the extracted ion current goes to infinity) at the limiting voltage V_*. The value of V_* depends weakly on the distribution of the electrons within the gap. If the electrons are confined to a thin sheath at the virtual-cathode (superinsulated model), as might be expected in the absence of electromagnetic fluctuations, $V_*=0.75V_c$. If the electrons are assumed to form a uniform density sheath extending from the virtual-cathode to the anode (saturated model), as would be expected when electro-

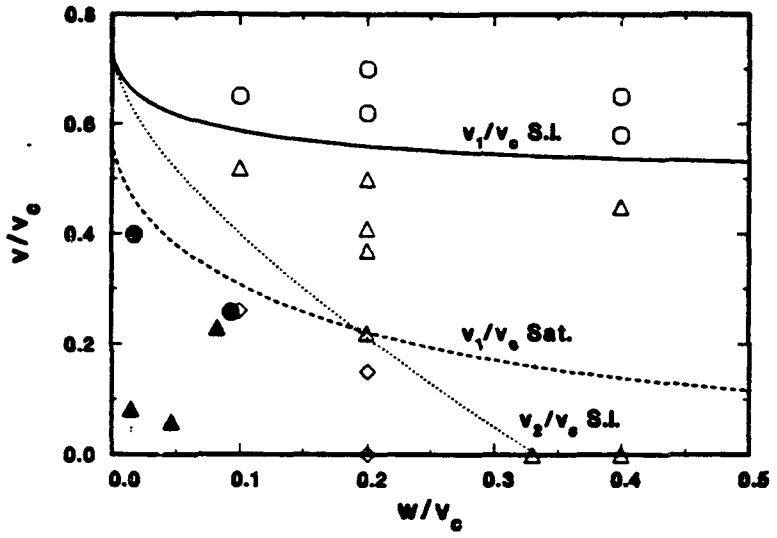
1. This work supported by U. S. Dept. Of Energy under Contract No. DE-ACO4-76-DP00789

magnetic fluctuations are present, $V_*=0.6V_c$. This theory has been quite successful in explaining the operating behavior of single-stage diodes.



1) A schematic of an accelerating stage of a multistage accelerator. Beam passes through the injection foil, is accelerated in the region between x_a and x_c, and exits through the extraction foil.

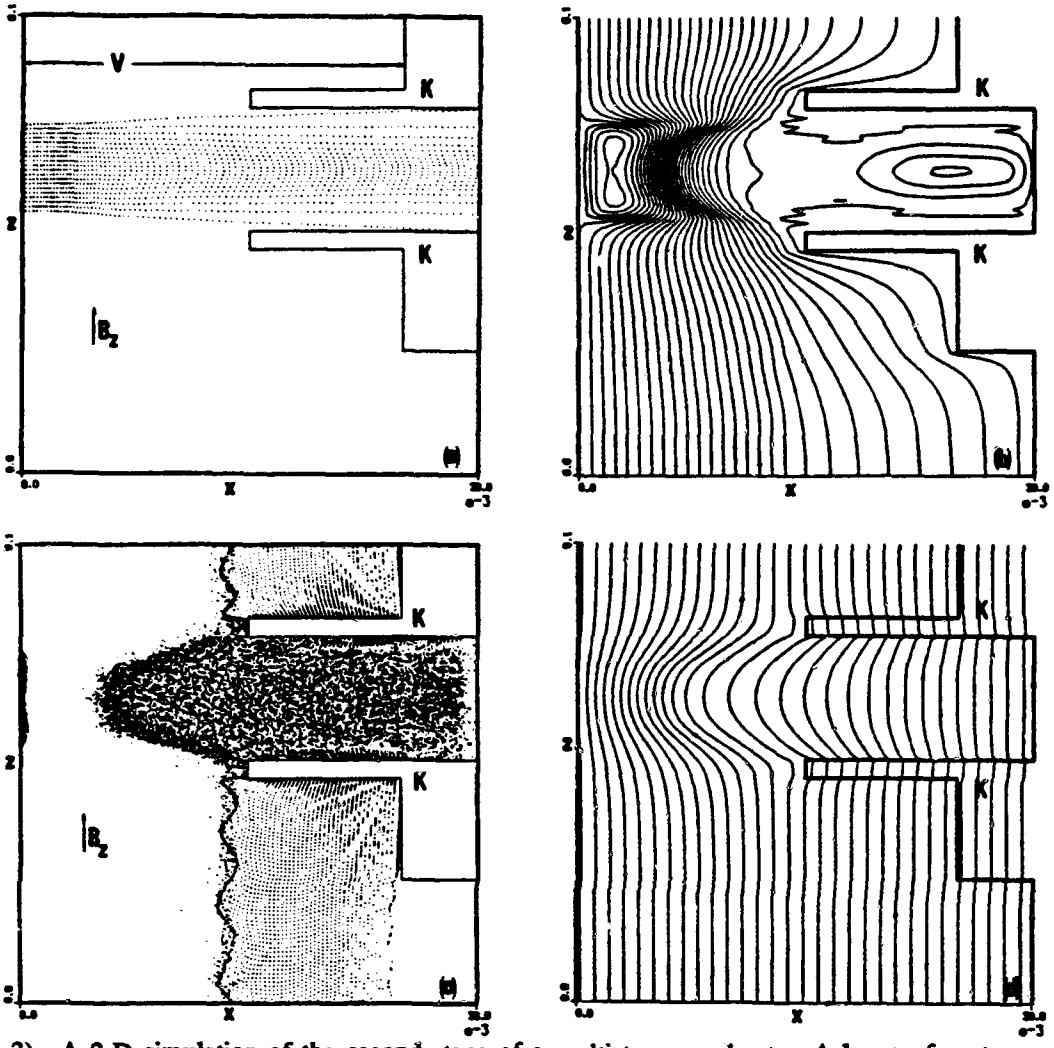
Recently, this work was extended to include multistage ion acceleration[3]. The multistage theory predicts the existence of two limiting current densities J_1 and J_2, which are functions of the injected beam energy, qW. In response to the beam space charge a sufficiently large injection current, $J>J_1$, will cause the formation of a virtual anode, i.e. the electric field is reversed at the injection side. This field reversal causes an electron sheath to be formed on the injection side of the acceleration gap. As long as $J<J_2$, a steady-state solution exists in which 100% of the injected current will be transmitted through the accelerating gap. Above J_2, some of the injected beam will be reflected. The multistage theory also predicts the existence of two corresponding limiting voltages, V_1 and V_2. As the voltage approaches V_1, J_1 goes to infinity. This is because the dynamic gap, $g=x_a-x_c$, goes to zero. The formation of a virtual anode should inhibit the extraction of unwanted ion current from the injection foil and thus it is desirable to operate with $V<V_1$. Similarly, J_2 goes to infinity, as the diode voltage approaches V_2. In contrast to single-stage theory these limiting voltages are strongly dependent of the distribution of the electrons, as can be seen in Fig. 2. Note that in the limit W goes to infinity, $V_1/V_c=0.5$ for superinsulated and $V_1/V_c=0.0$ for the saturated model. Thus it would not be possible to form a virtual anode to inhibit ion emission at each stage and obtain final ion beam energies significantly in excess of the critical voltage on each stage of a multistage accelerator if the saturated model is the correct solution. No such problem exists assuming that the superinsulated model is correct. An even more dramatic difference occurs for V_2, since $V_2=0$ for the saturated model. Clearly it is important to determine the functional behavior of these two limiting voltages. We have investigated the behavior of these limiting voltages numerically using both 2-D and 3-D PIC codes. The results of the 2-D simulations are presented in section II and the 3-D results are presented in section III.



2) The limiting voltages are plotted as a function of W/V_c. The solid and dotted lines are V_1 and V_2 as calculated from the superinsulated model. The dashed line is V_1 as calculated from the saturated model. The symbols represent the operating points of the simulations. The open symbols are the 2-D MAGIC simulations and the filled symbols are the 3-D QUICKSILVER simulations: circles for no virtual anode, triangles for a virtual anode but 100% transmission, and diamonds for beam reflection

II. 2-D PIC Simulations

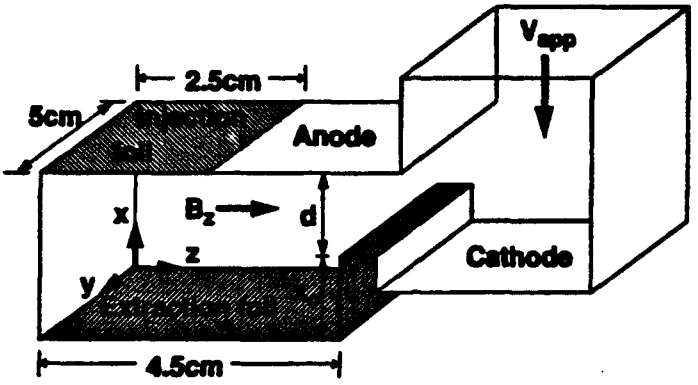
The 2-D simulations were performed using the fully electromagnetic particle-in-cell code MAGIC[4]. An acceleration stage was modelled in planar geometry with the applied magnetic field in the z-direction and the accelerating field in the x-direction. A cold beam of protons with an energy 0.8 MeV was injected into the simulations with various injected current densities, J_i, acceleration voltages, V, and magnetic field strengths. The results are summarized in Fig. 2. The open circles indicate that the beam was transmitted without the formation of a virtual anode despite the fact that the injected current was considerably in excess of J_{10} (the monopolar limiting current density). Note that all of the circles lie above the V_1 superinsulated curve. The open triangles indicate that a virtual anode was formed but that 100% of the beam was transmitted through the gap even though the injected current was considerably in excess of J_{20}. Note that all of these symbols lie between the superinsulated V_1 and V_2 curves, and that many of these lie above that saturated V_1 curve. The open diamonds indicate that the injected ion beam was reflected by the virtual anode. Clearly this behavior is inconsistent with the saturated model, since V_2=0 in saturated model, but is completely consistent with the superinsulated model. That the 2-D simulations should agree with the superinsulated model is not particularly surprising. The ignored y-coordinate is in the direction of the electron flow, which is also the direction of unstable wave propagation as predicted by theory[5,6], and observed in 3-D simulations[7] of single stage diodes. In the absence of electromagnetic field fluctuations, both the canonical momentum and the energy of the electrons should be conserved. The conservation of electron canonical momentum and energy plus the assumption of laminar electron orbits ($v=ExB/B^2$) leads to the so called Brillouin model[8]. It is well known that the electron sheath becomes very thin in this model when $eV_c>mc^2$. Figure 3 shows the particles and fields taken from a simulation that developed a virtual anode but 100% of the beam was transmitted through the accelerating gap.



3) A 2-D simulation of the second stage of a multistage accelerator. A beam of protons with W=0.8 MeV and J_i=1.2 kA/cm^2 is injected from the left. The acceleration voltage is 1.5 MV and the applied magnetic field is 1 T (V_c=3.94 MV). 100% of the beam is transmitted with some spreading as in (a) the ion map. A plot of the equipotential surfaces (b) shows a virtual anode, which results in both injection and extraction side electron sheaths as can be seen in the electron map (c). The applied magnetic field plotted in (d) shows a significant displacement of the virtual cathode toward the anode.

III. 3-D PIC Simulations

To test the importance of instabilities the electron drift direction must be included. We have performed simulations of the second stage of a multistage accelerator using the three dimensional, fully relativistic, particle-in-cell code QUICKSILVER[9]. A planar geometry was used in the simulations as shown in Fig. 4. An ion beam is injected through the shaded area (injection foil) passing through the accelerating gap and exiting through the extraction foil. A uniform B_z=2.5 T is applied to magnetically insulate the gap, V_c=12 MV.



4) The simulation geometry and coordinate system, d=1.7cm, and x_0=0.5cm.

The shaded areas on both anode and cathode sides were modelled as space-charge-limited emitters of electrons. Power is fed in from the upper right transmission line as a TEM wave with an open circuit voltage starting at zero and linearly rising to a fixed 20 MV in 1 ns. The effective impedance of the source is the vacuum impedance of the input port, Z_{eff}=226 ohms. Thus the injected ion current determines the accelerating voltage. In all of the simulations that we have performed, electromagnetic instabilities develop in a manner very similar to that seen in single stage simulations, i.e. the high frequency diocotron instability dominates initially and then a transition occurs to a low frequency ion mode[7]. The divergence introduced to the ion beam passing through the accelerating stage is modest during the diocotron phase, but grows to be quite large after the transition to the ion mode. In addition to generating ion divergence, the electromagnetic fluctuations allow the electrons to migrate across the magnetic field lines and thus the electron sheaths that form on both sides of the accelerating gap (when $J>J_1$) eventually coalesce. Since this process takes several nanoseconds, the injected current must be started at low current densities and gradually increased to obtain behavior other than observed in the 2-D simulations. We found that ramping the current density from zero to the full value in 5 ns was sufficiently gradual, whereas a 1 ns ramp was not.

In addition to ramping the injected current density, it was convenient to vary the injected beam energy with time. In this manner a single simulation swept out a path in W,V space. Symbols denoting various operating points of these simulations have been plotted on Fig. 2. A. solid circle indicates that the beam passed through the gap without the formation of a virtual anode (or an injection side charge-neutral region), while the solid triangle indicates that a virtual anode was formed and 100% of the beam was transmitted. Notice that there are solid circles below the saturated V_2 curve. This super-saturated behavior is due to the electron distribution that actually increases toward the anode. This behavior has been seen previously in 3-D simulations of single stage diodes. The operating points with very small values of W/V_c and V/V_c are particularly interesting. The fact that 100% of the beam was transmitted indicates that V_2 is very small as predicted by the saturated model. Our results clearly indicate that the

saturated model is best for predicting the behavior of a multistage accelerator as long as the beam pulse length is more than a few nanoseconds.

As we have mentioned the low value of V_1 as calculated from the saturated model indicates that it is not possible to maintain the condition $J>J_1$, which is necessary for the formation of a virtual anode, and accelerate the beam to energies much in excess of V_c. However, the very low value of V_2 (or more specifically W_0 which is the value of W where $V_2=0$) is a requirement of an alternative two stage scheme called the *Double Diode*[10]. In this scheme the second stage impedance is controlled by the injection of beam current from the first stage. The effective impedance of the second stage can be held to a low value by injecting a current equal to the short circuit current, I_{sc2} of the pulsed power generator driving the second stage. The discontinuation of this injected current forces the second stage to act as a single stage diode extracting ions off the injection foil which has been ionized by the injected beam. The low impedance phase can be used to store energy inductively in the circuit driving the second stage. This energy is then extracted after the primary beam is turned off. Thus the two stages act together as an opening switch. Note that the falling impedance behavior that has plagued single stage diode operation provides a means of disrupting the primary beam quite suddenly. This beam must pass through the injection foil which requires a certain minimum energy. When the first stage voltage falls below this value, the beam will not pass through the foil. Consider the importance of W_0. The power in the first stage beam must be greater than W_0I_{sc2}. Since a single stage diode must operate below V_* power in the second stage must be less than $V_*I_{sc2}/2$. A figure of merit for this device is the ratio, R, of the power delivered to a beam by the second stage over the beam power required to control the second stage impedance, thus $R=V_*/2W_0$. The analytic saturated model predicts $R=\infty$, while our simulations indicate that $W_0/V_c<.1$ and thus $R>3$. Clearly it is important to determine experimentally the values of both $V_1(W)$, $V_2(W)$ and in particular W_0.

Acknowledgments: We gratefully acknowledge many helpful discussions and encouragement from Dr. T. R. Lockner.

References

1 J. P. VanDevender and D. L. Cook, Science **232**, 831 (1986).

2 M. P. Desjarlais, Phys. Rev. Lett. **59**, 2295 (1987). and M. P. Desjarlais, Phys. Fluids B **1**, 1709 (1989).

3 S. A. Slutz, and M. P. Desjarlais, J. Appl. Phys. **67**, 6705 (1990).

4 B. Goplen, R. E. Clark, J. McDonald, and W. M. Bollen, "Users Manual for Magic", Report No. MRC/WDC-R-068 (Mission Research Corp., Washington. DC, 1983.

5 C. L Chang, D. P. Chernin, A. T. Drobot, E. Ott, and T. M Antonsen, Jr., Phys. Fluids **29**, 1258 (1986).

6 S. A. Slutz, and W. A. Johnson, Phys, Fluids B (1992).

7 M. P. Desjarlais, T. D. Pointon, D. B. Seidel, R. S. Coats, M. L. Kiefer, J. P. Quintenz, and S. A. Slutz, Phys. Rev. Lett. **67**, 3094 (1991).

8 T. M. Antonsen, Jr. and E. Ott, Phys. Fluids **19**, 52 (1976).

9 D. B. Seidel, M. L. Kiefer, R. S. Coats, T. D. Pointon, J. P. Quintenz, and W. A. Johnson, in *Computational Physics*, edited by A. Tenner (World Scientific, Singapore, 1991), pp. 475-482.

10 S. A. Slutz, *Particle Beam Fusion Progress Report January 1985 Through June 1985*, SAND86-0015,p. 31.

Prospects of Cyclotron Resonance Laser Acceleration†

Chiping Chen
Plasma Fusion Center
Massachusetts Institute of Technology
Cambridge, Massachusetts 02139

ABSTRACT

The cyclotron resonance laser (CRL) accelerator is a novel concept of accelerating continuous charged-particle beams to moderately or highly relativistic energies. This paper discusses the prospects and limitations of this concept. In particular, a three-dimensional, self-consistent theory is used to analyze the nonlinear interaction of an electron beam with an intense traveling electromagnetic wave in such an accelerator. The parameter regimes of experimental interest are identified on the basis of scaling calculations. The results of simulation modelling of a multi-megavolt electron CRL accelerator are presented. The possibility of building continuous-wave (CW) CRL accelerators is discussed.

I. INTRODUCTION

There has been growing theoretical and experimental interest recently in the cyclotron resonance laser (CRL) accelerator [1]-[7], an advanced accelerator concept of producing charged-particle beams to moderately or highly relativistic energies using an intense coherent electromagnetic wave and a guide magnetic field configuration (Fig. 1). This novel accelerator has the following advantages over conventional radio-frequency (RF) accelerators: i) acceleration of continuous beams without microbunches, ii) use of oscillators, not necessarily amplifiers, as driver, iii) use of smooth-wall structures to avoid breakdown problems, and iv) high duty factor of acceleration. It is compact in comparison with electrostatic accelerators which are bulky but capable of accelerating continuous charged-particle beams. In addition to these intriguing features, there is a variety of potential applications of CRL accelerators. These include: i) production of high-average-power charged-particle beams for material and chemical research, ii) X-ray generation, and iii) coherent millimeter wave generation, to mention a few examples. Proof-of-principle CRL accelerator experiments [2],[5],[7] so far have had limited success and demonstrated the acceleration of electrons up to ~ 0.5 MeV in the microwave regime. This paper discusses the prospects and limitations of this concept.

---

†Research supported by the Department of Energy High Energy Physics Division under Contract No. DE-AC02-90ER40465.

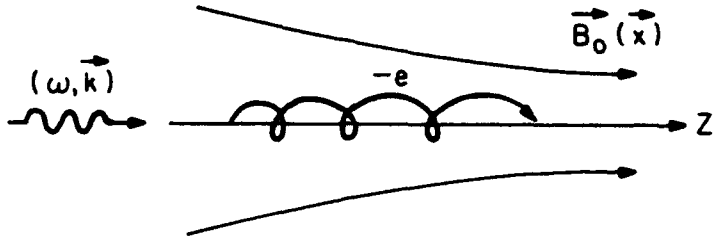


Figure 1: Schematic of a CRL accelerator.

II. SCALING PROPERTIES

Our earlier studies [8],[9] have shown that electron CRL accelerators with optimal magnetic taper possess the following scaling properties

$$G \equiv \frac{\gamma_f - \gamma_i}{\gamma_i - 1} \propto \frac{1}{(\beta_{ph} - 1)^{0.5}} \quad \text{(independent of } a) \,, \tag{1}$$

$$k_{\|} z_m \propto \frac{1}{a(\beta_{ph} - 1)^{0.6}} \,, \tag{2}$$

$$\frac{B_{0z}(z_m)}{B_{0z}(0)} = 2 - 3 \,, \tag{3}$$

$$\text{accelerating gradient} \;\propto a \quad \text{(for a fixed } \beta_{ph}) \,. \tag{4}$$

In Eqs. (1)-(4), $\gamma_i mc^2$ and $\gamma_f mc^2$ are the average initial and final energies of the beam electrons, respectively, z_m is the maximum accelerating distance, $B_{0z}(z)$ is the magnetic field profile on the z axis, a is the normalized wave amplitude, and $\beta_{ph} - 1 \equiv \omega/ck_{\|} - 1$ is a measure of wave dispersion, where m is the electron rest mass, $\omega = 2\pi f$ and $k_{\|}$ are the frequency and axial wave number of the driving electromagnetic wave, respectively, and c is a speed of light in vacuum.

In the microwave regime, the normalized wave amplitude and the dispersion parameter are given by

$$a = 1.7 \times 10^{-4} \left(\frac{[\text{cm}]}{r_w}\right) \left(\frac{[\text{GHz}]}{f}\right) \left(\frac{P}{[\text{W}]}\right)^{1/2} \,, \tag{5}$$

$$\beta_{ph} - 1 = 40 \times \left(\frac{[\text{cm}^2]}{r_w^2}\right) \left(\frac{[\text{GHz}^2]}{f^2}\right) \,, \tag{6}$$

where $|\beta_{ph} - 1| \ll 1$ and the lowest-order transverse-electric (TE) cylindrical waveguide mode, TE_{11}, have been assumed, f and P are the frequency and power (or integrated

axial Poynting flux) of the wave, respectively, and r_w is the waveguide radius. For microwave electron CRL accelerators, high energy gain, $G = 10 - 100$, and moderately high accelerating gradient, 1-10 MeV/m, can be achieved with presently available high-power microwave sources, (assuming the initial electron kinetic energy $(\gamma_i - 1)mc^2 \sim$ 100 keV). With a proper resonant cavity, a sizable wave amplitude ($a > 0.1$) can be achieved at a moderate input RF power level ($P \sim 1$ MW). This shows prospects for the production of high-average-power (> 100 kW), relativistic (> 1 MeV) electron beams using continuous-wave CRL accelerators. Potential applications of high-average-power beams were mentioned in the Introduction.

In the optical regime, the normalized wave amplitude and the dispersion parameter are given by

$$a = 6 \times 10^{-6} \frac{\lambda}{[\mathrm{cm}]} \left(\frac{\text{Laser Intensity}}{[\mathrm{W/cm^2}]} \right)^{1/2} , \tag{7}$$

$$\beta_{ph} - 1 \approx \frac{\lambda^2}{2r_0^2} , \tag{8}$$

respectively. Here, $\lambda = 2\pi/k_{\|}$ is the laser wavelength and r_0 is the characteristic laser beam radius. For example, a 1 μm, 10^{16} W/cm^2 Nd:glass-based laser yields a respectable wave amplitude, $a = 0.06$, and a small dispersion parameter, $\beta_{ph} - 1 \sim 10^{-8}$ (assuming $r_0 = 0.5$ cm). With presently available high-intensity lasers, accelerating gradient up to ~ 100 MeV/m may be achieved. However, the pulse length of such an ultra-intense laser is short (typically of order 1 ps), which posses limitations on the optical CRL accelerator concept in practice.

III. MODELLING OF A MULTI-MEGAVOLT CRL ACCELERATOR

The scaling calculations in Sec. II have revealed that microwave CRL accelerators are most attractive from a practical point of view. The underlying self-consistent equations of motion describing the wave-beam interaction in the microwave CRL accelerator, which are identical to those describing the cyclotron autoresonance maser (CARM) [10]-[14], have been derived and presented elsewhere [12],[13]. The scaling relations (1)-(4) and the self-consistent CRL accelerator equations in reference [9] are readily applicable for design modelling of CRL accelerators.

As an example, we discuss a moderately high-current, multi-megavolt electron CRL accelerator powered by a pulsed 20 MW, 11.4 GHz RF source, (such as an X-band relativistic klystron amplifier). In this design study, the electron beam current is chosen to be sufficiently large so that the effects of changes in both the wave amplitude and the axial wave number due to the *inverse* CARM interaction can be examined. Figure 2 summarizes the design simulations which yield the electron energy gain $G = 30$, for

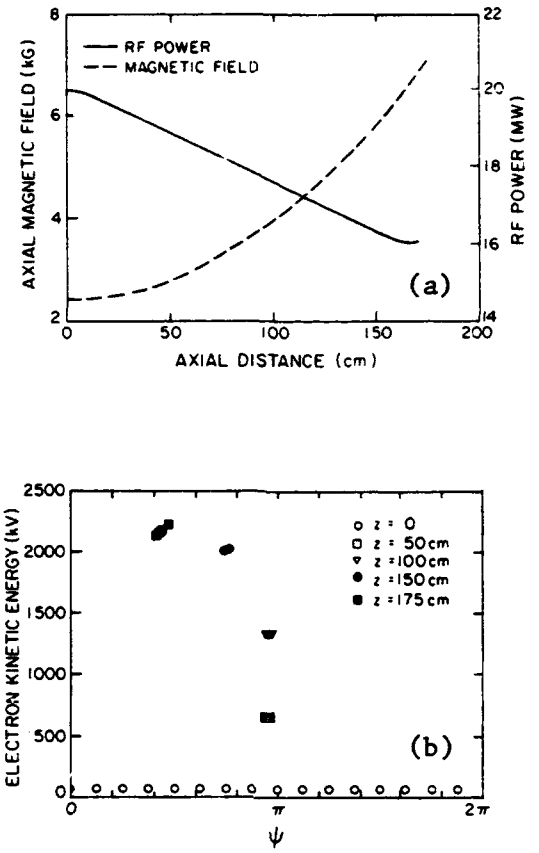


Figure 2: (a) Axial magnetic field and RF power as a function of the accelerating distance for an X-band CRL accelerator. (b) Phase space of beam electrons at several axial positions.

Table I. Parameters for a Proposed 2.3 MeV CRL Accelerator

Parameter	Symbol [Unit]	Value
Beam Current	I_b [A]	2
Initial Beam Voltage	V_i [kV]	75
Final Beam Voltage	V_f [kV]	2300
Acceleration Distance	z_m [cm]	170
Initial Axial Magnetic Field	$B_{0z}(0)$ [kG]	2.43
Final Axial Magnetic Field	$B_{0z}(z_m)$ [kG]	7.0
RF Frequency	f [GHz]	11.4
RF Power	P [MW]	20
Operating Mode		TE_{11}
Waveguide Radius	r_w [cm]	3.9

the beam current $I_b = 2$ A and the initial beam voltage $V_i = 75$ kV. The effects of time-independent space-charge are not included in the simulation. The parameters of this proposed 2.3 MeV CRL accelerator are given in Table I. For a TE_{11} mode and the waveguide radius $r_w = 3.9$ cm, the normalized amplitude is $a = 0.017$ and the dispersion parameter is $\beta_{ph} - 1 = 0.02$, as evaluated from Eqs. (5) and (6).

The optimal axial magnetic field B_{0z} and RF power are plotted in Fig. 2(a) as a function of the accelerating distance z. The axial magnetic field exhibits approximately a quadratic dependence on the distance z. It increases no more than three-fold throughout the entire accelerating distance. Significant RF power is converted into electron beam power, corresponding to 20% efficiency.

Figure 2(b) shows the phase space of the electrons, where the vertical axis is the electron kinetic energy and the horizontal axis is the electron gyrophase with respect to the phase of the RF field. In Fig. 2(b), only sixteen macroparticles are plotted at a given axial distance z. The initial energy (or axial momentum) spread is assumed to be negligibly small, and the final energy spread from the simulation is $\sigma_\gamma/\langle\gamma\rangle = 0.9\%$, where $\sigma_\gamma = (\langle\gamma^2\rangle - \langle\gamma\rangle^2)^{1/2}$.

IV. SUMMARY

The prospects and limitations of cyclotron resonance laser (CRL) accelerators have been discussed. Based on our scaling calculations and presently available intense lasers and microwave sources, microwave CRL accelerators have been identified as a practical concept in either pulse or continuous-wave (CW) operation, while optical CRL accelerators are so far of only theoretical interest. A multi-megavolt microwave electron CRL accelerator experiment has been proposed.

References

[1] C.S. Roberts and S.J. Buchsbaum, Phys. Rev. **135**, 381 (1964).

[2] H.R. Jory and A.W. Trivelpiece, J. Appl. Phys. **39**, 3053 (1967).

[3] P. Sprangle, L. Vlahos, and C.M. Tang, IEEE Trans. Nuclear Sci. **NS-30**, 3177 (1983).

[4] K.S. Golovanevsky, IEEE Trans. Plasma Sci. **PS-10**, 120 (1982).

[5] D.B. McDermott, D.S. Furuno, and N.C. Luhmann, Jr., J. Appl. Phys. **58**, 4501 (1985).

[6] A. Loeb and L. Friedland, Phys. Rev. **A33**, 1828 (1986).

[7] R. Shpitalnik, C. Cohen, F. Dothan, and L. Friedland, J. Appl. Phys. **70**, 1101 (1991).

[8] C. Chen, Phys. Fluids **B3**, 2933 (1991).

[9] C. Chen, submitted for publication, Phys. Rev. **A** (1992).

[10] V.L. Bratman, N.S. Ginsburg, G.S. Nusinovich, M.I. Petelin, and P.S. Strelkov, Int. J. Electron. **51**, 541 (1981).

[11] C. Chen and J.S. Wurtele, Phys. Rev. Lett. **65**, 3389 (1990).

[12] C. Chen and J.S. Wurtele, Phys. Fluids **B3**, 2133 (1991).

[13] H.P. Freund and C. Chen, Int. J. Electron., in press (1992).

[14] A.C. DiRienzo, G. Bekefi, C. Chen, and J.S. Wurtele, Phys. Fluids **B3**, 1755 (1991).

NUMERICAL SIMULATIONS OF DENSITY CHANNEL GUIDING AND RELATIVISTIC OPTICAL GUIDING OF LASER PULSES IN A PLASMA

J. Krall, G. Joyce, P. Sprangle and E. Esarey
Beam Physics Branch, Plasma Physics Division
Naval Research Laboratory, 4555 Overlook Avenue, SW
Washington, DC 20375-5000

In the laser wakefield accelerator, a short (τ_L < 1 ps), high power (P > 10^{12} W) laser pulse propagates in plasma to generate a large amplitude (E > 1 GV/m) wakefield. We present an axisymmetric nonlinear fluid model that allows simulation of laser pulse propagation through a plasma on the plasma time scale. We find that a laser pulse will propagate through a plasma for many vacuum diffraction lengths if either of two conditions are met: 1) an appropriately shaped plasma density channel can be obtained or 2) an ultra-high power tailored laser pulse can be created.

I. INTRODUCTION

In the laser wakefield accelerator (LWFA) concept[1], an intense laser pulse drives a plasma wave which, in turn, accelerates a trailing electron bunch. The problem of laser pulse propagation in a plasma over long distances must be solved in order to demonstrate the viability of this concept. By long distances, we mean $z >> Z_R$, where

$$Z_R = \frac{k}{2} r_{L,0}^2 \qquad (1)$$

is the vacuum diffraction length, or Rayleigh length, of the laser pulse, k is the laser wavenumber and $r_{L,0}$ is the initial spotsize of the laser pulse.

For high intensity laser pulses, which are characterized by $a_0 \gtrsim 1$, where $a_0 = eA_0/mc^2$ is the normalized amplitude of the laser vector potential field, m is the electron mass, c is the speed of light in vacuum and e, assumed positive, is the elementary charge, plasma wakefields can be obtained with amplitudes at or near the nonrelativistic wavebreaking field:

$$E_{WB} \equiv mc\omega_p/e \ , \qquad (2)$$

where $\omega_p = (4\pi n_0 e^2/m)^{1/2}$ and n_0 is the plasma density. For example, with $n_0 = 10^{18}$ cm^{-3}, $E_{WB} \approx$ 100 GeV/m.

We have shown, via numerical simulation, that laser diffraction in a plasma can be overcome by either of two methods: plasma channel guiding or relativistic optical guiding of a tailored pulse.[2] In this paper, we describe the numerical model by which these results were obtained and give a further

example. Because we make use of the fact that the plasma evolves on a slow time scale relative to that corresponding to the laser frequency, $\omega_p << \omega \approx kc$, the resulting code has tremendous advantages over conventional particle simulations, which must resolve the fast laser frequency.

II. MODEL EQUATIONS FOR NUMERICAL SOLUTION

Model equations giving the axisymmetric plasma response to a given laser field in the quasi-static approximation have been recently derived.[2] In deriving these equations, a coordinate transformation was made from (r,z,t) to $(r,\zeta=z-ct,\tau=t)$. The laser pulse moves in the positive z direction such that the front of the laser pulse remains at $\zeta = 0$ in these coordinates. The physical region of interest extends from $\zeta = 0$, where the plasma is unperturbed, to $\zeta < 0$. In the quasi-static approximation, it is assumed that the scale length over which the laser field evolves is long compared to the laser pulse length ($Z_R >> L_{laser}$). In this limit derivatives with respect to τ are dropped relative to derivatives with respect to ζ in the plasma fluid equations, but not in the wave equation. The model equations, after averaging over the laser frequency, to leading order in the small parameters $1/kr_L$ and ω_p/ω, are given by

$$(\nabla_\perp^2 + \frac{\partial^2}{\partial\zeta^2})\phi_s = k_p^2[\gamma_s\rho_s - \rho^{(0)}] , \tag{3}$$

$$\nabla_\perp^2\psi_s - k_p^2\rho_s\psi_s = k_p^2[\gamma_s - \rho^{(0)}] , \tag{4}$$

$$\nabla_\perp^2\underline{a}_{\perp,s} = k_p^2\rho_s\underline{u}_{\perp,s} - \nabla_\perp\frac{\partial\phi_s}{\partial\zeta} , \tag{5}$$

and

$$\frac{\partial\underline{u}_{\perp,s}}{\partial\zeta} = \frac{\partial\underline{a}_{\perp,s}}{\partial\zeta} + \nabla_\perp(\gamma_s - \phi_s) , \tag{6}$$

where the Coulomb gauge has been used and the subscript s indicates quantities associated with the slow time-scale plasma response: $\phi_s = e\Phi_s/mc^2$ is the normalized electrostatic potential, $\psi_s = \phi_s - a_{z,s}$, $\underline{a}_s$ is the normalized vector potential, $\underline{u}_s = \underline{v}_s/c$ is the normalized plasma electron fluid velocity, $\rho_s = n/\gamma_s n_0$, n is the plasma electron number density and n_0 is the unperturbed density at $r = 0$. The definitions $\rho^{(0)} = \rho_s(\zeta=0)$ and $k_p = \omega_p/c$ are also used. In this model, the plasma ions are assumed to

be immobile. The laser field enters through the relativistic factor for the plasma electrons:

$$\gamma_s = 1 + \frac{\underline{u}_{\perp,s}^2 + \hat{\underline{a}}_f \cdot \hat{\underline{a}}_f^*/2 + \psi_s^2}{2(1 + \psi_s)} , \tag{7}$$

where $\underline{a}_f$, which varies on a fast time-scale, is the normalized vector potential of the laser pulse and $\hat{\underline{a}}_f$ is the slowly varying laser amplitude. This form of the γ_s equation assumes a linearly polarized laser field. For circular polarization, the factor of 1/2 in the second term of the numerator above is dropped. The laser field, which is assumed to have a phase velocity, $v_{ph} = c$, is updated via a reduced wave equation:

$$(\nabla_\perp^2 + \frac{2ik}{c}\frac{\partial}{\partial \tau})\hat{\underline{a}}_f = k_p^2 \rho_s \hat{\underline{a}}_f . \tag{8}$$

Equations (3-7) are numerically intractable in the sense that it is not clear which equation should be solved first, second, etc. or if an iterative method of solving the equations can be expected to converge on a meaningful solution. We avoid this numerical quagmire by recasting the problem into a single equation for the quantity ψ_s. From Eqs. (3), (4) and the gauge condition, we have

$$\frac{\partial^2 \psi_s}{\partial \zeta^2} = \left(\frac{\gamma_s - \psi_s - 1}{\psi_s + 1}\right)(k_p^2 \rho^{(0)} + \nabla_\perp^2 \psi_s) - \nabla^2 a_{z,s} . \tag{9}$$

From Eq. (6) and the gauge condition we can write $\nabla^2(a_{z,s})$ in terms of ψ_s and $\underline{u}_{\perp,s}$:

$$\nabla^2 a_{z,s} = \nabla_\perp^2(\gamma_s - \psi_s) - \frac{\partial}{\partial \zeta}(\nabla_\perp \cdot \underline{u}_{\perp,s}) . \tag{10}$$

From Eqs. (3) and (5) we write $\underline{u}_{\perp,s}$ in terms of ψ_s:

$$\underline{u}_{\perp,s} = \frac{1}{k_p^2 \rho_s}\frac{\partial}{\partial \zeta}(\nabla_\perp \psi_s) . \tag{11}$$

For completeness, we point out that Eq. (4) can be recast as an equation for ρ_s in terms of ψ_s:

$$\rho_s = \frac{1}{1 + \psi_s}(\rho^{(0)} + \frac{1}{k_p^2}\nabla_\perp^2 \psi_s) . \tag{12}$$

The ψ_s equation can be written in the following form:

$$\left[1 - \frac{\nabla_\perp^2}{k_p^2 \rho_s} + \left(\frac{\nabla_\perp \rho_s}{k_p^2 \rho_s^2}\right)\cdot\nabla_\perp\right]\frac{\partial^2 \psi_s}{\partial \zeta^2}$$

$$= \left[1 - \frac{\nabla_\perp^2}{k_p^2 \rho_s} + \left(\frac{\nabla_\perp \rho_s}{k_p^2 \rho_s^2}\right)\cdot\nabla_\perp\right]\left[\left(\frac{\gamma_s - \psi_s - 1}{1 + \psi_s}\right)\left(k_p^2 \rho^{(0)} + \nabla_\perp^2 \psi_s\right)\right]$$

$$+ \nabla_\perp \cdot \left\{\left[\frac{1}{k_p^2}\frac{\partial}{\partial \zeta}\left(\frac{1}{\rho_s}\right)\right]\left[\frac{\partial}{\partial \zeta}\nabla_\perp \psi_s\right] + \frac{1}{\rho_s}(\gamma_s - \psi_s - 1)\nabla_\perp \rho_s\right\} . \qquad (13)$$

Equation (13) can be integrated numerically in ζ in a straightforward manner by starting at the $\zeta = 0$ boundary, where the plasma is unperturbed and where we assume $\psi_s = \nabla_\perp \psi_s = \nabla_\perp^2 \psi_s = \partial \psi_s / \partial \zeta = 0$. Radial boundary conditions are dictated by axisymmetry at $r = 0$ and by the imposition of a metallic wall at $r = r_w >> r_{L,0}$. In doing the integration, Eqs. (7), (11) and (12) are also used.

III. SIMULATION RESULTS

As an example, we consider a tailored laser pulse with modest energy and power (i.e., within the bounds of present technology). A tailored pulse is one in which the laser spotsize is tapered from a large value to a small value over the length of the laser pulse while keeping the laser power constant throughout the pulse and equal to the critical power[3] for relativistic optical guiding. This condition is met when

$$a_0(\zeta) r_{L,0}(\zeta) = 0.9\ \lambda_p . \qquad (14)$$

Figure 1 shows the laser intensity $|\hat{a}_f|^2$ and laser spotsize r_L for a tailored pulse with $a_{0,peak} = 0.9$ and $r_{L,0,min} = \lambda_p$ tapered over a length of $2\lambda_p$. With $n_0 = 1.24 \times 10^{18}$ cm^{-3} ($\lambda_p = 30$ μm) and laser wavelength $\lambda = 1$ μm, the laser power is $\simeq 16$ TW and the pulse energy is $\simeq 3$ J. Figure 2 shows the laser intensity and spotsize at $c\tau = 36\, Z_R = 10.2$ cm. The pulse is distorted but largely intact. Figure 3, a plot of the axial electric field at $c\tau = 36\, Z_R$, shows a peak accelerating gradient of 15 GV/m. Because the pulse has expanded somewhat, this is smaller than the average value of 18 GV/m over the length of the simulation. This indicates that electrons with energy in excess of 1.8 GeV could be

produced in a single accelerating stage. Figure 4 shows the laser spotsize at the point of peak laser intensity plotted versus τ. For comparison, the curve corresponding to vacuum expansion of the laser pulse is also shown.

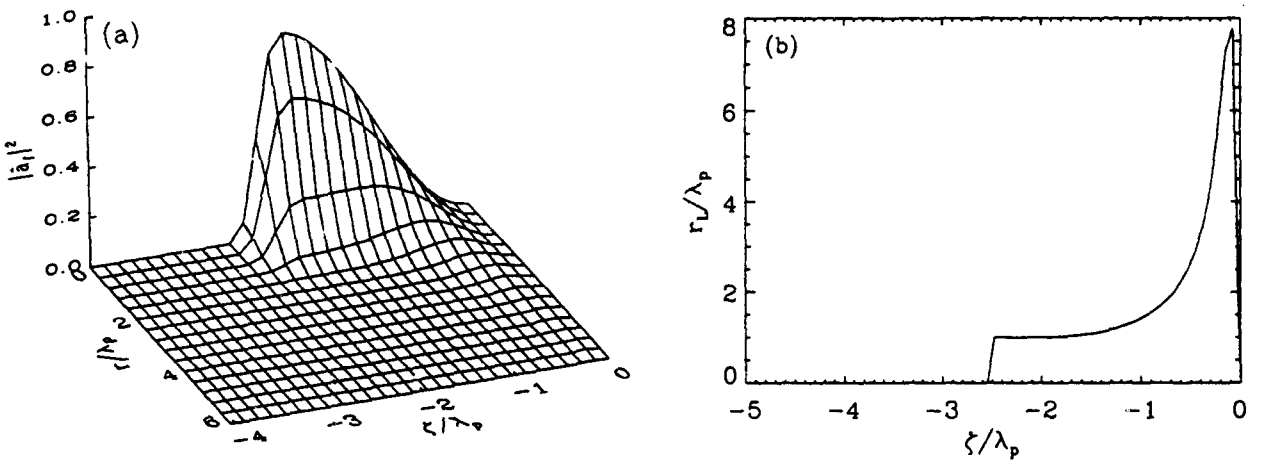


Fig. 1 Plots showing (a) laser intensity $|\hat{a}_f|^2$ and (b) laser spotsize r_L at $\tau = 0$.

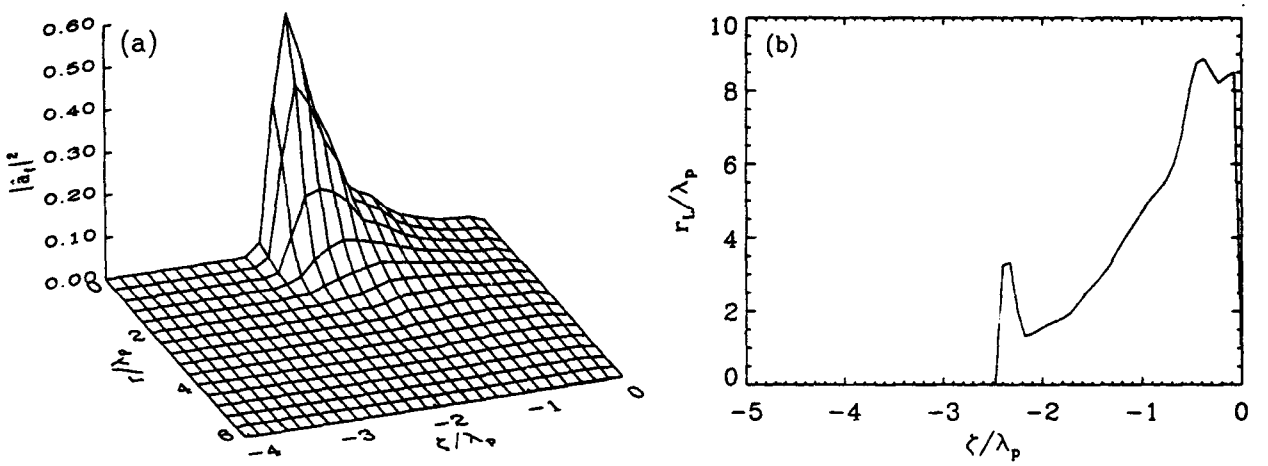


Fig. 2 Plots showing (a) laser intensity $|\hat{a}_f|^2$ and (b) laser spotsize r_L at $c\tau = 36\, Z_R$.

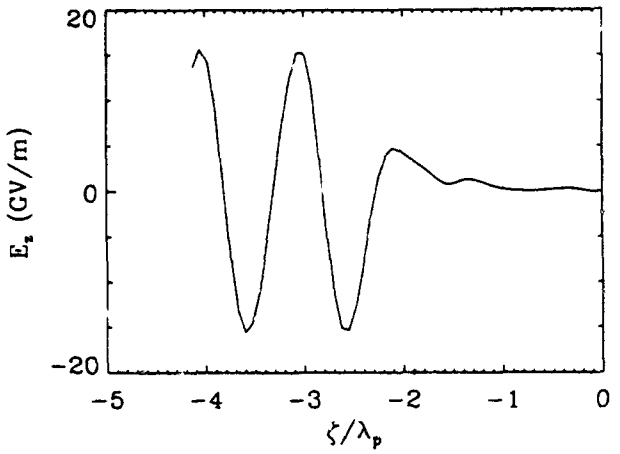


Fig. 3 Axial electric field E_z versus ζ at $c\tau = 36\, Z_R$.

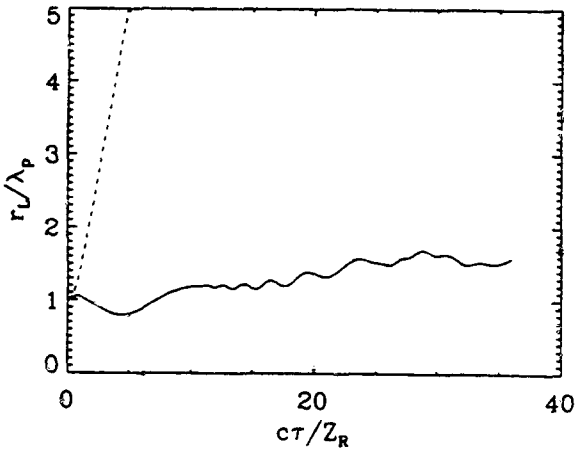


Fig. 4 Laser spotsize r_L, at point of peak intensity in the pulse, versus time (solid line) and vacuum diffraction curve (dashed line).

IV. CONCLUSIONS

We have presented an axisymmetric nonlinear fluid model that allows us to simulate laser pulse propagation through a plasma on the plasma time scale, $\omega_p << \omega$. Using this code, we have demonstrated that a "tailored" pulse can propagate for distances in excess of 36 vacuum diffraction lengths with only minimal distortion. We have also performed simulations of plasma density channel guiding over equally large distances with even less distortion of the laser pulse. We conclude that a laser pulse will propagate through a plasma for many vacuum diffraction lengths if either of two conditions are met: 1) an appropriately shaped plasma density channel can be obtained or 2) an ultra-high power tailored laser pulse can be created.

ACKNOWLEDGMENTS

This work was supported by the U. S. Department of Energy and the Office of Naval Research.

References

1. T. Tajima and J. M. Dawson, Phys. Rev. Lett. 43, 267 (1979).; L. M. Gorbunov and V.I. Kirsanov, Sov. Phys. JETP 66, 290 (1987); P. Sprangle, E. Esarey, A. Ting and G. Joyce, Appl. Phys. Lett. 53, 2146 (1988); E. Esarey, A. Ting, P. Sprangle and G. Joyce, Comments Plasma Phys. Controlled Fusion 12, 191 (1989).
2. P. Sprangle, E. Esarey, J. Krall and G. Joyce, submitted to Phys. Rev. Lett.
3. G. Schmidt and W. Horton, Comments Plasma Phys. Controlled Fusion 9, 85 (1985); G. Z. Sun, E. Ott, Y. C. Lee, and P. Guzdar, Phys. Fluids 30, 526 (1987); P. Sprangle, C. M. Tang, and E. Esarey, IEEE Trans. Plasma Sci. PS-15, 145 (1987); E. Esarey, A. Ting, and P. Sprangle, Appl. Phys. Lett. 53, 1266 (1988).

Two-beam virtual cathode accelerator

William Peter

Department of Physics
Ben-Gurion University
Beersheva, Israel

Abstract

A proposed method to control the motion of a virtual cathode is investigated. Applications to collective ion acceleration and microwave generation are indicated. If two counterstreaming relativistic electron beams of current I are injected into a drift tube of space-charge-limiting current $I_L = 2I$, it is shown that one beam can induce a moving virtual cathode in the other beam. By dynamically varying the current injected into the drift tube region, the virtual cathode can undergo controlled motion. For short drift tubes, the virtual cathodes on each end are strongly-coupled and undergo coherent large-amplitude spatial oscillations within the drift tube.

I. Introduction

Can the motion of a virtual cathode be controlled so it can be made to propagate up or down a drift tube? Can the oscillations of two opposing virtual cathodes be strongly-coupled and what would the resulting power level and spectrum look like? There have been a number of well-analyzed studies on controlling the motion of virtual cathodes by injecting relativistic electron beams (REB) into a gas-filled drift tube. The results up to the present do not seem to be especially impressive [1]. In practice, determining any uniform translational motion of the electrostatic well formed by the beam head has been difficult [2]. Numerical simulations (except for those reported by the Maryland group [3, 4]) have in general not observed virtual cathode motion [5]. A possible reason for this may be due to the fact that the ion currents necessary for the propagation may be prohibitively large [6].

A concept for controlling the motion of virtual cathodes is currently being investigated both experimentally and theoretically at the General Physics Institute in Moscow. This scheme is similar to a concept first investigated at UC Irvine and involves propagating the beam through a drift tube discontinuity. This concept is illustrated as follows: Consider an REB with radius r_b and kinetic energy $(\gamma_0 - 1)mc^2$ injected into a drift tube of radius R (Fig. 1). The space-charge-limit current can be described by the interpolation formula [7]

$$I_l = \frac{(\gamma_0^{2/3} - 1)^{3/2}(mc^3/e)}{1 + 2\ln R/r_b} \tag{1}$$

This formula assumes that the ends of the drift tube of length L are sufficiently far apart to approximate an infinitely long drift tube and is equivalent to requiring the condition $L > 2.58(R/r_b)^{0.133}$ [8].

Specifically, the drift tube discontinuity method involves propagating the beam through two drift tubes of different radii. The first drift tube has radius r_1 where $r_1 < r_2$ and r_2 is the radius of the adjacent drift tube. The magnitude of the radii are adjusted so that the beam cannot form a virtual cathode in the first tube, but forms a virtual cathode in the second tube. That is, if the space-charge limit current in the first drift tube is I_1, and the limit current in the larger drift tube current is I_2, then the beam current satisfies $I_2 < I < I_1$ and also $I > (I_1 + I_2)/2$. When the beam reaches the larger-radius tube with limit current I_2 it will form a virtual cathode. As the reflected particles from the beam enter the first drift tube, however, there is enough charge for another virtual cathode to form in the smaller-radius guide.

In Fig. 1 is shown a schematic diagram of the drift-tube discontinuity experiment being conducted at the General Physics Institute in Moscow [9] with an annular relativistic electron beam. There is a strong applied magnetic field of 25 kG, the beam energy is approximately 430 keV, and the current is approximately 10 kA. In the Moscow experiment, the injected current was increased up to the value when the total space charge of the injected beam together with that reflected from the first virtual cathode exceeds the limiting current I_1 [9]. The barrier reflecting the particles starts to move towards the injection plane, leaving a high-density, low-velocity, and highly thermal plasma behind it (between the discontinuity and the barrier). The high-density, low-velocity plasma between the two virtual cathodes emerges because of the balance of momentum flux "pressures". It is a stable configuration, and has been labeled by the Moscow group the "squeezed-beam" state [9].

Preliminary theory and simulations at Moscow suggests that a 200 kV barrier can move 10 cm at a velocity between 0.1 and 0.3 c. Simulations done at Ben-Gurion University suggest that the virtual cathode would have difficulty in moving past the discontinuity in

the drift-tubes. These simulations observe that the particles are seen to hit the drift tube wall in the vicinity of the discontinuity. This result is in agreement with early experiments at UC Irvine which showed that the beam in the large tube expanded in a few nanoseconds and the electrons hit the smaller drift tube wall. In addition, control of the UCI virtual cathode was difficult, and could only be maintained in a gas density gradient imbedded in a strong magnetic field [1]. In the Moscow experiments, evidence that some portion of the electrons were reaching the walls was also found [9].

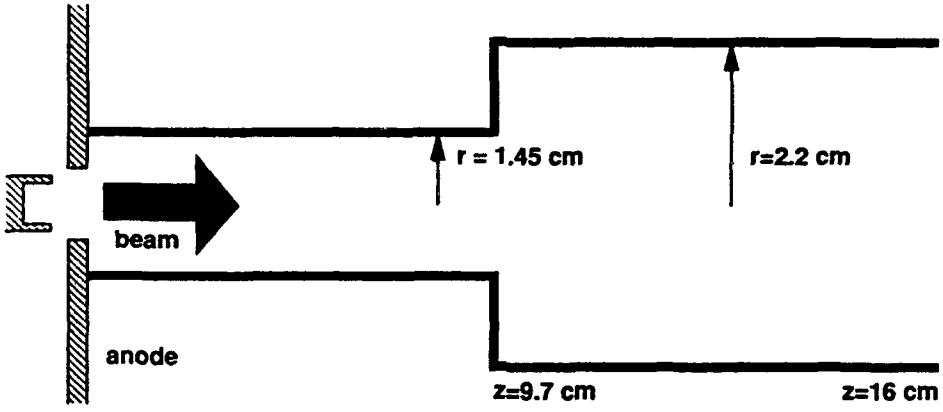


Fig. 1. Schematic drawing of the annular REB and drift tube discontinuity experiment at the General Physics Institute, Moscow.

One way to solve the electron loss problem would be to smooth out the discontinuity by using a conical drift tube [10]. In this paper, a concept is proposed which relies on the direct injection of a second, counterstreaming electron beam. This does not have the disadvantage of requiring a discontinuous corner surface and also has the advantage of allowing for more control of the back-flowing current. It is discussed in the next section.

Two-Beam Configuration

Instead of relying on a virtual cathode to reflect electrons, it is also possible to directly inject a counterstreaming relativistic electron beam. Consider the following: A REB of radius r_b is injected into a uniform drift tube of radius R. The current of the beam, I_1, is at least one-half of the space-charge limiting current in the drift tube, I_L. If now another beam of current I_2 is injected into the other side of the drift tube, a few questions arise: (1) Is it possible for the space charge of the counterstreaming REB to induce a virtual cathode in the first beam? (2) Let the beams have identical current, say $I = I_1 = I_2 = I_l/2$. Will one,

two, or zero virtual cathodes form? This question arises because the configuration is now *symmetric*, yet the sum of both currents is larger than the limiting current. (3) By varying the injected current will it be possible to move the virtual cathodes? (4) Do these results depend on the drift tube length L, i.e., the communication between both ends of the drift tube?

Preliminary 2-1/2 dimensional, fully electromagnetic and relativistic particle-in-cell simulations have been conducted on a configuration consisting of a small pillbox-like drift tube of length 1.4 cm and radius 1.4 cm, i.e., $L = R$. Two solid relativistic electron beams of radius $r_b = (2/3)R$ are injected from either end. The beam energy was 150 keV, and there was an applied axial guide field of 11.5 kG. Because of the dimensions of the drift tube region, the space-charge limit current equation for a finite-length drift tube, and not Eq.(1), must be used [8].

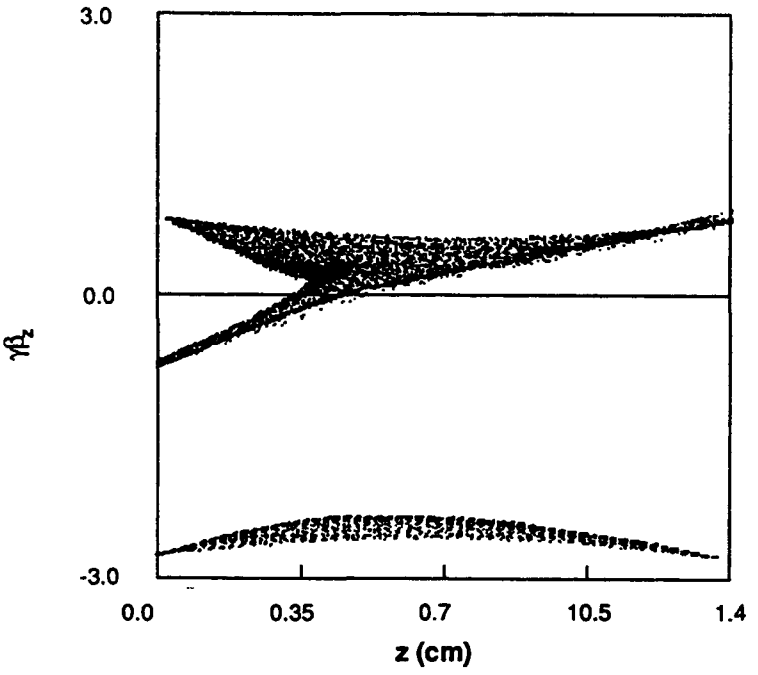


Fig. 2. Phase space plot showing a high-energy counterstreaming REB (bottom of figure) inducing a virtual cathode in a lower-energy REB (middle of figure). The position of the virtual cathode is controllable.

From the simulations, the space-charge limiting current was found to be approximately I_l =2.7 kA. This was the current for which one electron beam was found to form a virtual cathode. If two REBs were injected with a little more than half the current, i.e., $I \approx I_l/2$, such that the total current was now slightly more than than I_l, *two* virtual cathodes were

observed to form. For different energies, the beam with smaller energy formed a virtual cathode. For short drift tubes, the virtual cathodes are closely coupled, and the potential minimum position within the diode oscillated significantly within the drift tube, giving rise to high-power microwave radiation. virtual cathodes were strongly coupled, even when the counterstreaming beams had differing currents.

Applications

Collective ion acceleration by means of the propagation of an electron beam into a gas-filled drift tube was first reported by Graybill and Uglum in 1970 [12]. In most experiments the proton energy is 2-3 times that of the electrons, though sometimes larger proton energies have been obtained. The potential well model of Poukey and Rostoker [13] which depends on the formation of a moving well in which ambient ions are trapped and accelerated is a popular explanation for the experiments. However, experiments have never shown ion energies more than a few times the initial beam energy except in the Luce geometry, and movement of the potential well has never been demonstrated. The phenomenon observed here may be a way to move a virtual cathode in a controlled fashion for collective accelerator purposes, or to use the moving barrier as a piston to sweep up the ions [11].

Microwave generation from virtual cathodes [16] is an important application for the present investigation. One possibility would be to investigate the power and spectral output of the oscillating two virtual cathode configuration which has been simulated. One significant difference between this configuration and the usual single virtual cathode configuration is the unusually large spatial amplitude of the virtual cathode position. Another possibility is the development of a moving virtual-cathode plasma mirror, or a "photon compressor." Because of the large charge density within a virtual cathode, it may be possible to upshift incident photons by means of the relativistic Doppler effect over and above that which is possible for REBs. This is especially important since containment of the photons for high frequencies $\omega > \omega_p$ is poor because the small Thompson scattering cross section.

Conclusions

In this investigation we have observed the motion of a moving potential well in 2-1/2 dimensional, fully relativistic and electromagnetic particle-in-cell simulations. The presence of a counterstreaming beam of different energy can induce a virtual cathode in an opposite beam. If the two beams have the same energy, two virtual cathodes will form. In short drift tubes, the virtual cathodes are closely coupled and undergo large-amplitude spatial oscillations. In addition, a high-density state of plasma described in the literature as a

"squeezed-beam" state appears to have been observed between the two counterstreaming beams.

Acknowledgments

I would like to thank Amnon Fisher of the Naval Research Laboratory, Alex Fedotov of the General Physics Institute in Moscow, and Rick Mako of FM Technologies for useful conversations. This work was partially supported by the Israeli Ministry of Science.

References

[1] F. Mako, Ph.D. thesis., Univ. of Calif., Irvine, 1979 (unpublished).

[2] R. Stringfield, private communication.

[3] R. L. Yao and C. D. Striffler, J. Appl. Phys. **67** 1651 (1990).

[4] C. R. Chang and M. Reiser, J. Appl. Phys. **61** 1658 (1990).

[5] W. Peter, R. J. Faehl, C. Snell, and M. E. Jones, IEEE Trans. Nuc. Sci. **NS-32**, 3506 (1985).

[6] R. J. Faehl and W. Peter, IEEE Trans. Nuc. Sci. **NS-32**, 3500 (1985).

[7] L. A. Bogdankevich and A. A. Rukhadze, Sov. Phys. Uspekhi **14**, 163 (1971).

[8] R. B. Miller, Air Force Weapons Laboratory Technical Report AFWL-DYS-TN-75-113, 1975 and R. B. Miller and D. C. Straw, J. Appl. Phys. bf 47, 1897 (1976).

[9] A. V. Fedotov, private communication.

[10] A. Fisher, private communication.

[11] A. V. Fedotov et al., XXth Int. Conf. on Phenomena in Ionized Gases, Pisa,1991, v.3, p. 611.

[12] S. E. Graybill and J. R. Uglum, J. of Applied Physics **41**, 236 (1970).

[13] J. W. Poukey and N. Rostoker, Plasma Physics **13**, 897 (1971).

[14] See, for example, L. E. Thode, in High-power microwave sources (ed. by V. L. Granatstein and I. Alexeff), (Artech House, Boston, 1987), p. 507 or D. J. Sullivan, J. E. Walsh, and E. A. Coutsias, *ibid*, p. 441.

EXPERIMENTAL STUDIES OF BEAM ACCELERATION WITH A SHORT PULSE X-BAND ELECTRON CYCLOTRON MASER

Keiichi Kamada, Tatsuki Kanazawa[a], Mitsunori Sakamoto[b], Noboru Matsumura[c], Fumiyasu Tamagawa, Ritoku Ando and Masaru Masuzaki.
Department of Physics, Faculty of Science, Kanazawa University
Kanazawa 920, JAPAN

Sunao Kawasaki
Department of Physics, Faculty of Science, Saitama University
Saitama 338, JAPAN

Abstract

An experiment of the Two-Beam Acceleration is reported. An intense short microwave pulse of X-band generated with an IREB on a gyro-BWO was utilized. A matter of main concern is whether the radiation could really serve as the power source for acceleration of another electron beam even with its short pulse duration (a few ns). The microwave fed to the series of cavities where a 50 keV electron beam was injected. A part of the beam particles got the energy of 5 keV. The result is explained in the framework of the ordinary theory of the rf accelerating structures and shows that the TBA scheme will be operated successfully with appropriate choice of the parameters.

Introduction

In the last decade, the electron cyclotron resonance maser (ECRM) has been the subject of considerable interests as a new high-power millimeter wave tube. As high power sources of the coherent radiation, the studies of intense relativistic electron beams (IREBs) have been also rapidly developed. A gyro backward-wave oscillator (gyro-BWO) is one of the expected devices among the ECRM configurations, because it has advantageous characteristics: simple structure, wide tunability by changing the axial magnetic field, and above all the intrinsic feedback mechanism of the related absolute instability. Nevertheless, there have been a few theoretical and much less experimental reports[1]. We have carried out an experiment in this regime and found the microwave burst of TE_{01}

---

a) Deceased in May, 1991.
b) Present address: Toshiba corporation,Otawara Tochigi 329-26, Japan
c) Present address: Hitachi corporation, Tsuchiura Ibaraki 300, Japan

mode in X-band, identified to be due to the gyro-BWO at the second cyclotron harmonic. The frequency of the radiation was tunable in the range of 8-12 GHz and duration of the radiation was extremely short (a few ns)[2].

On the other hand, the concept of the Two-Beam Acceleration (TBA) is one of the most promising applications of the high-power coherent radiation source . The requirements for the power source applied to the TBA are to realize considerably high power level and high repetition rate[3]. The rf pulse width of the power source should be short to satisfy the requirements. We report here the result of a preliminary experiment on the TBA. The gyro-BWO was combined with the accelerating structures of a test electron beam having relatively low particle energy to investigate 1) how the ECRM could be adopted for TBA, and 2) the dynamics of the acceleration in a series of cavities driven with the short rf pulse.

Experimental Arrangement

The schematic of the experiment is shown in Fig.1. An IREB (600 keV,10 kA, 10 ns) was generated with the PI 105A and injected into an X-band slotted rectangular waveguide immersed in a quasi-steady axial magnetic field (Bz). The beam was produced at a field emission diode consisting of a hollow cylindrical cathode (10 mm in diam., 1 mm thick) and a carbon anode with a 11 mm diam. aperture. The magnetic field at the diode was about 1 kG and the beam got a perpendicular velocity component at entering the higher field of Bz. The beam intensity decreased down to about 200 A after passing through the transient region, while it remained nearly constant over the whole length of the constant Bz of 0.8 m waveguide. The beam hit the wall at the end of the magnetic field. The microwave radiated inside the waveguide propagated backwards, being amplified with the intrinsic absolute instability, and was reflected at the point of beam entrance back into the waveguide so that the power was extracted in the forward direction and was monitored at the entrance and the exit of the 100 m X-band dispersive line by crystal detectors.

The microwave was fed through the input hole into a series of cavities forming a traveling wave accelerator structure (9.4 GHz, 3 wavelengths, $\pi/2$ mode). As no design but a hole to lead the microwave to the cavities was made, the power led to the cavities was low compared with the total power of the radiation. A test electron beam of 50 keV, 1 mA and 1 μs duration was injected through a 1 mm diam.

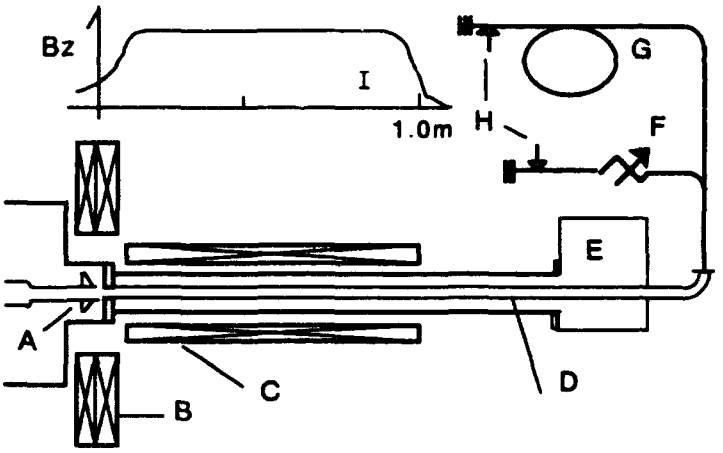


Fig.1 Schematic of the experiment . A: diode. B: diode coil . C: Bz coil. D: X-band rectangular waveguide. E: The cavities were set here when TBA experiment was carried out. F: variable attenuator. G: X-band 100 m dispersive line. H: crystal detectors. I: the shape of Bz field .

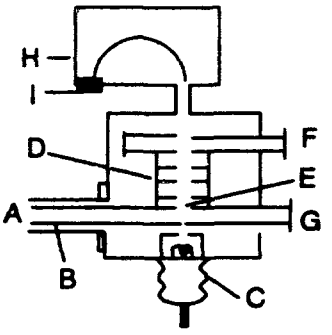


Fig. 2 Schematic of the TBA setup. A: to the gyro-BWO. B:X-band waveguide. C:50kV electron gun. D: cylindrical cavities. Precise structure is not shown. E: input hole. F,G: to 100 m dispersive line. H:magnetic analyzer. I: photomultiplier..

aperture into the cavities to investigate the coupling between the microwave and the cavities. Figure 2 shows the setup of the TBA experiment schematically. The energy of the test particles was analyzed by a magnetic analyzer placed behind the cavities. The resolution of the analyzer was less than 0.1 keV.

Gyro-BWO Radiation

The frequency of the microwave extracted at the end of the device was analyzed by the time elapse of the microwave pulse in the 100 m standard X-band waveguide. Typical examples of the waveforms detected after the dispersive line are shown in Fig. 3 for various applied field Bz. The dependence of the evaluated frequency at the peak intensity of the waveform on Bz is shown in Fig.4. Comparing the result with the dispersion diagram (Fig. 5) of the beam wave and waveguide modes, it was identified that the principal mode of the radiation was due to a backward wave interaction of a fast electron cyclotron second harmonic with an eigenmode TE_{01} of the waveguide. A solid line in Fig.4 indicates their intersections. The waveform also contains some discrete narrow peaks of the width about 0.2 GHz, suggesting certain subsidiary mechanisms involved. The waveform detected at the entrance of the dispersive line also suggested the presence of narrow peaks with a duration of less than 4 ns (the limit of the

oscilloscope resolution). Total power of the radiation was roughly estimated to be a hundred kW.

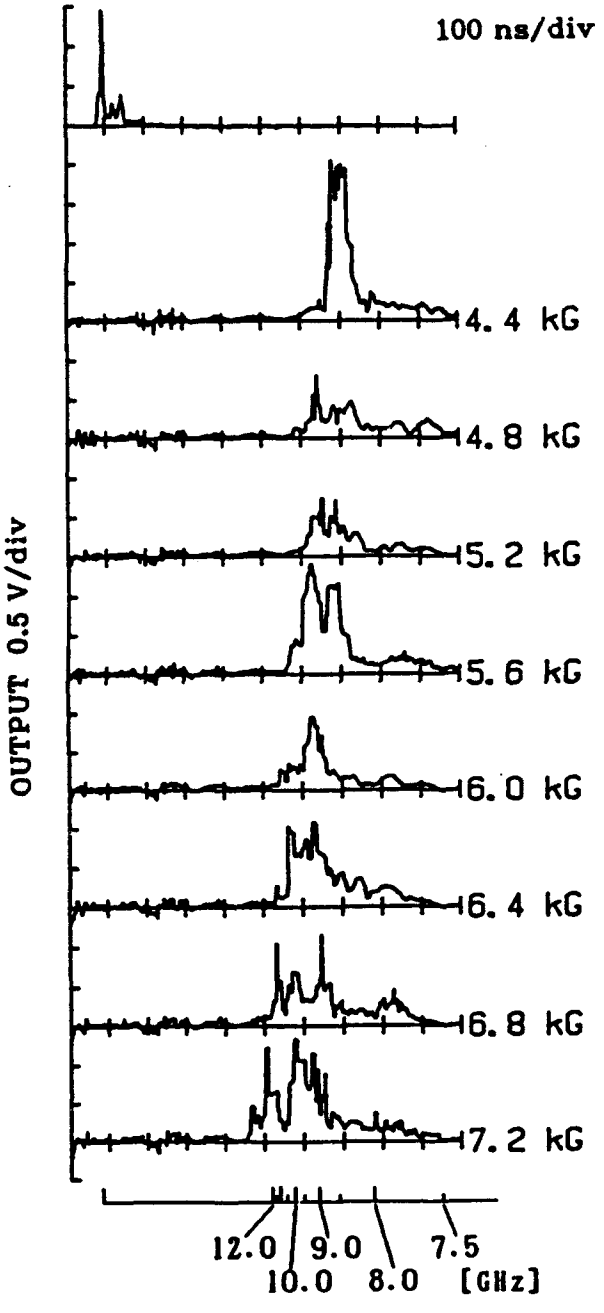


Fig.3 Typical pulse forms of the radiation by the gyro-BWO. detected at the entrance (Top) and the exit of the 100 m dispersive line for different Bz.

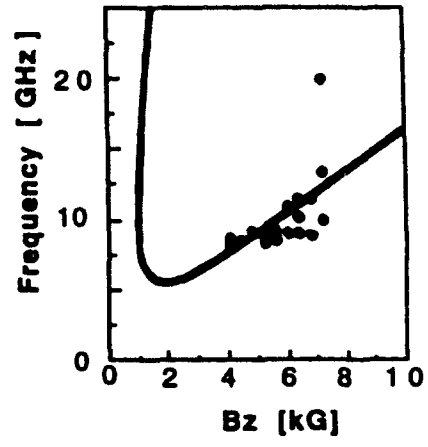


Fig.4 Dependence of frequency on Bz. Closed circle : evaluated frequency at the peak intensity of the signal. Solid line : intersections of dispersion diagram shown in Fig.5.

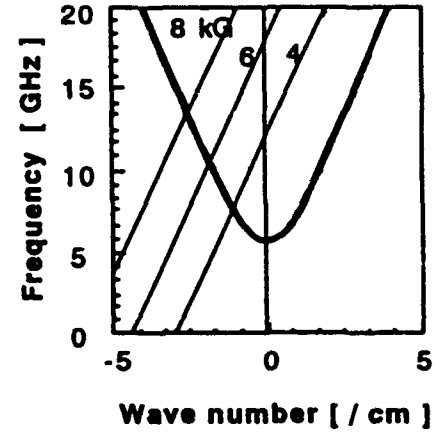


Fig. 5 Dispersion diagram. Hyperbolic line : TE_{01} eigenmode of the waveguide. 3 straight lines: fast electron cyclotron second harmonics at Bz=4,6,8 kG.

Beam Acceleration with the Radiation by Gyro-BWO

The waveform of the radiation by gyro-BWO passing through the cavities is shown in Fig.6. Narrow peaks of 8.6, 8.8 and 9.36 GHz with the width of less than 0.1 GHz are observed. The offset from designed frequency of 9.4 GHz is attributed to an error of the machining. The presence of the multiple frequencies could be due to different resonance modes of the cavities. These results are consistent with the characteristics of the cavities tested by a Gunn diode oscillator.

The microwave pulse of a few ns duration was led into the cavities when the test electron beam was flowing through them. The energy distributions of the beam observed at the end of the cavities with or without the microwave feed are shown in Fig.7. The beam particles were accelerated or decelerated depending on their phases with the microwave by about 5 keV at maximum. The effect of the microwave on the beam energy was clearly observed near the beam energy of 57 keV. The microwave of 9.36 GHz would principally contribute to the beam acceleration. The power of the microwave introduced into the cavities was estimated to be 1 kW due to a mismatching between the structure and the microwave input.

As the group velocity of the microwave energy flow is evaluated to be a little too small to fill the cavities over whole length during the short period of the microwave pulse, the acceleration efficiency cannot be high. Energy gain through

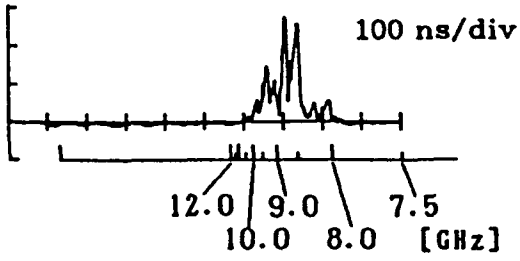


Fig.6 The pulse form of radiation through the cavities at Bz=5.6 kG detected at the exit of 100 m line.

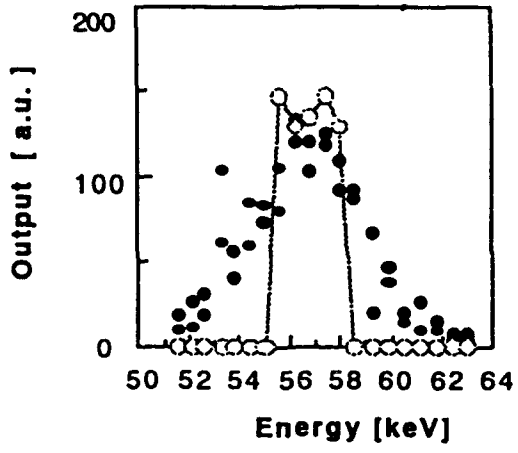


Fig. 7 The energy distributions of the beam with or without the microwave. Connected open circle : without microwave. Closed circle : with microwave.

the cavities calculated with the ordinary formula[4] is 11.5 keV/kW for the estimated Q value of 1450 and the shunt impedance of 28 MΩ. Considering the experimental error, the results could be consistent with the theory. An appropriate choice of the parameters of the cavities will improve the situation.

Conclusions

Two-Beam Acceleration by the radiation of the gyro-BWO generated with an IREB in Raman regime was demonstrated experimentally. Ordinary traveling wave accelerator would be useful if an effective input coupling with the gyro-BWO radiation is realized and the design of the cavities makes possible high gradient accelerating field.

Acknowledgement

The authors thank to Mr. Keiichi Mukai and Mr. Yuuji Nozaki for their technical supports.

References

1) J.Wachtel and E.Wachtel, Appl. Phys. Lett, 37,1059 (1980)
S.Y.Park et al., Int. J. Electrons, 57,1109 (1984)
A. K.Ganguly and S.Ahm, Appl. Phys. Lett.,54, 514 (1989)
S.Y.Park et al.,IEEE Trans. on Plasma Sci., 18,321 (1990).
2) S.Kawasaki et al.,Appl. Phys. Lett. , 52 , 757 (1988)
3) D.H.Hopkins et al., IEEE Trans.on Nuclear Sci.NS-32, 3476 (1985)
4) G.L.Ginzton et al., Rev. of Sci. Inst.,19, 89 (1948)

COLLECTIVE ACCELERATION OF LIGHT ION BEAMS IN KALI-200

T. Vijayan, P. Roychowdhury, and S. K. Iyyengar

Particle Beam Generation and Diagnostics Section
Neutron Physics Division, Bhabha Atomic Research Centre
Bombay 400 085, INDIA

Abstract

Collective acceleration of light ion beams has been studied by injecting a REB of 250keV, 5kA, 60ns into a short dielectric tube in vacuum situated inside a conducting tube. The ion energies obtained by using this moderately intense beam, are around 1-3MeV per nucleon with total currents reaching about tens of Amperes.

1. Introduction

Collective acceleration of ions by intense relativistic electron beams (REB) shows great promise for producing light and heavy ion beams of high energies[1] and currents.[2] This method has hence been investigated in various schemes,[3-6] both theoretically and experimentally. Destler et al[5] apply a laser produced target-plasma for accelerating metal ions of multiply charged states, while Masuzaki et al[6] use a rail-gun plasma for the same purpose. Enhancement of ion acceleration has been predicted in a multiple ion injection scheme.[3,4] In the present work, we investigate collective acceleration of light ion beams by injecting a REB (250keV, 5kA, 60ns), into a short dielectric-tube situated inside a conducting tube in vacuum.

2. Theory

For conditions of charge neutralization of REB by ions, its space-charge limiting current I_i in vacuum, is given as

$$I_i = I_i^{\bullet}/(1-f_e) \qquad (1)$$

where, the neutralization factor f_e is defined as the ratio of ion charge density to electron density, $I_i^{\bullet}$ is the limiting

current when $f_e=0$,

$$I_1^* = (4\pi\epsilon_0 m_0 c^3/e)(\Gamma_e^{2/3}-1)^{3/2}/[1+2\ln(r_d/r_b)] \quad (2)$$

ϵ_0 is permittivity of free space, m_0 is the electron rest mass, c is speed of light, $\Gamma_e=(1-\beta_e^2)^{-1/2}$, $\beta_e=v_e/c$; v_e and e are electron velocity and charge; r_d and r_b are the drift tube and beam radii respectively. The maximum electron current that can be propagated with full charge neutralization in vacuum, is however limited by the self-magnetic field and is given by the Alfven limit as

$$I_A = (4\pi\epsilon_0 m_0 c^3/e)\beta_e\Gamma_e \quad (3)$$

An IREB propagating in vacuum [given by Eq.(1)] provides the intense field needed for collective ion acceleration.

3. Experimental Set-up

The experiments of collective ion acceleration using REB reported here were performed on the Kilo Ampere Linear Injector (KALI-200) in BARC having parameters 250kV, 10kA, 80ns full width and about 200J energy. In the experimental set-up schematically shown in Fig.1, the REB diode with planar geometry has a graphite cathode of 5cm diameter and a copper-mesh anode of 60 per cent transparency located about 8mm downstream of cathode plane. A dielectric tube (DT) of 5cm dia., 1.25mm thickness, and length s, is co axially positioned downstream on anode inside a conducting drift tube of r_d=7.5cm for injecting ions. After an acceleration

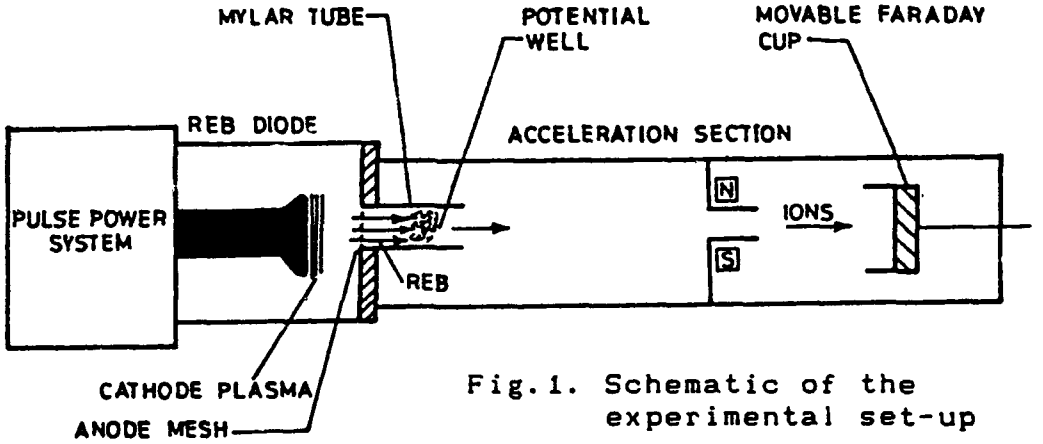


Fig.1. Schematic of the experimental set-up

distance L from anode, the ions are separated from electrons, by applying a transverse magnetic field of ~0.6kG provided by magnet NS. Two copper diaphragms with 5cm apertures are positioned before and after NS to remove stray electrons. The diagnostics employed include Faraday cups (FC) for monitoring the electron and ion currents, a $CuSO_4$ resistive divider for measuring the diode voltage, ion range-energy in aluminum foil, time-of-flight (TOF), and nuclear track detectors. The REB diode, the ion acceleration channel, and the diagnostics chamber are maintained at a vacuum of 3×10^{-5}Torr and the measurement devices have coaxial geometry.

4. Experimental Results and Discussions.

A. Ion injection and acceleration.

The REB current in diode as measured by a fixed FC is around 8kA. Of this, typically about 5kA passes through the anode mesh and DT to the propagation region. I_1^* for r_b=2.5cm, 250keV beam estimated from Eq.(2) is about 0.93kA. The present REB with current being much larger than I_1^*, forms a deep potential well (PW) inside DT. The PW is formed at a time when I exceeds I_1^* in the rising part of beam which is typically around 10ns from start of beam. During this, some of the electrons striking DT dislodge ions which are trapped into the PW. These ions provide the neutralization of space charge and f_e tends to one. In this situation, electrons in later part of REB face force neutralization for conditions of

$$F_r = (el_e r/2\pi\epsilon_o r_b^2 \beta_e c)(1-\beta_e^2-f_e) = 0 \qquad (4)$$

that is, when f_e equals $(1-\beta^2)$. This allows the electrons to move downstream dragging the ions along. In this mechanism, electrons are slowed down close to the ion velocity, while the ions are accelerated by the net space charge field in the axial direction.

B. Geometry optimization.

In a typical experiment using a mylar tube of s=5cm as DT, the waveforms of propagated current in absence of magnet NS, as

measured by a movable Faraday cup at various axial distances, are illustrated in Fig.2. The propagated currents have been obtained for various s (2.5-25cm), and they too are plotted and compared in Fig.2. As seen, the propagated current is large even for long distance in case of s=5cm as compared to the other s cases. Hence, s=5cm has been used in the ion acceleration experiments reported here.

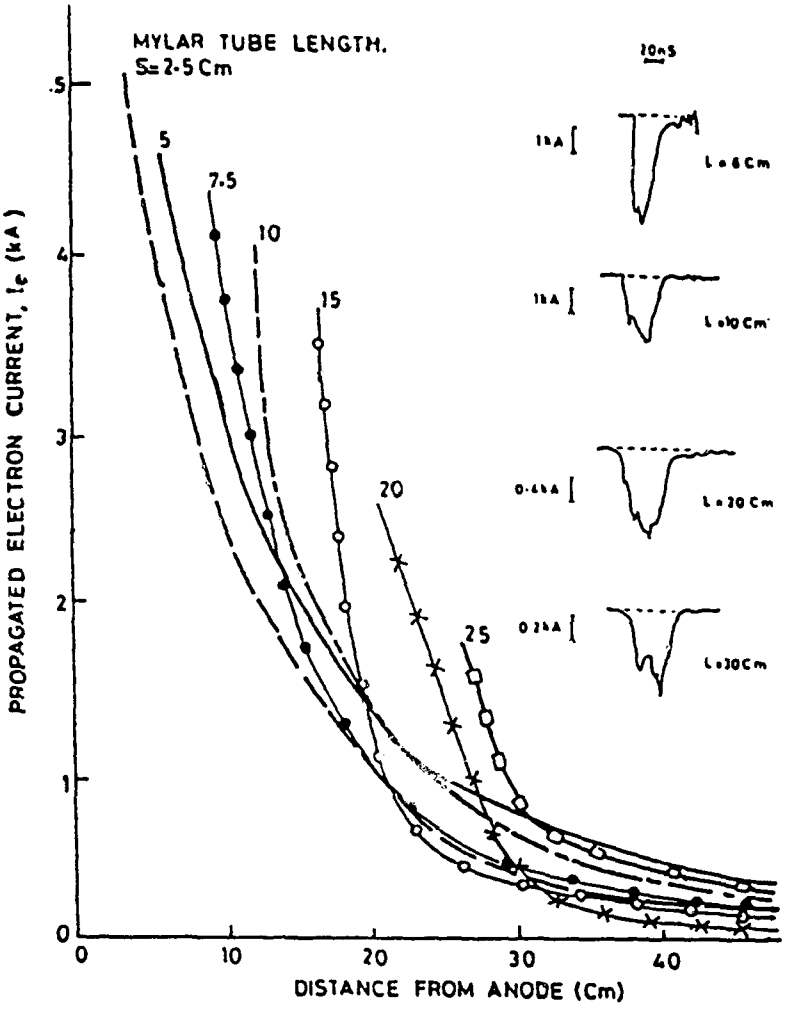


Fig.2. Propagated current with distance for various lengths (s) of mylar tube. The waveforms shown are at the distances indicated for s=5cm.

C. Ion beam characterization.

The magnet NS has been now located in position as in Fig.1. For the mylar tube of s=5cm, the variation of ion current (I_i) with axial distance, measured by movable ion Faraday cup (IFC) for various L, are plotted in Fig.3. The waveforms of the ion current in immediate downstream of NS for these L cases are also illustrated in Fig.3. As seen, this I_i is more than 4A for L=20cm, with pulse duration (τ_i) around 100ns. As compared to this, I_i is about 0.6A for L=

71cm, with τ_i increased to ~250ns. Moreover as seen from the plots, I_i at a given distance is higher with larger L.

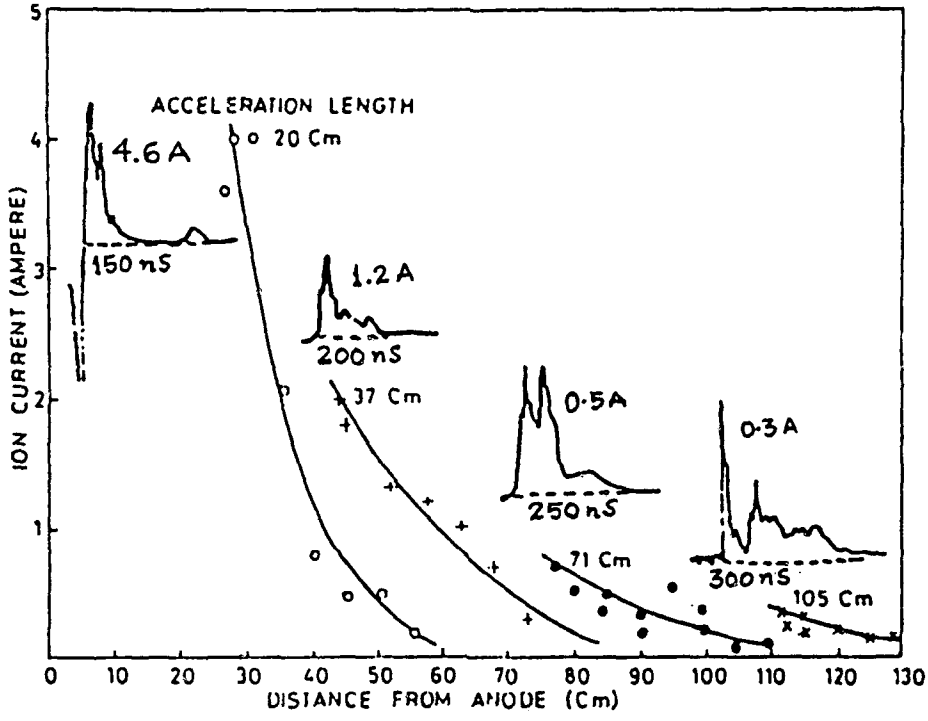


Fig.3. Variation of ion current with distance for different acceleration lengths.

Peak energies of 1, 15, and 21MeV respectively for hydrogen, carbon, and oxygen ions have been interpreted for L=71cm, from range energy penetration studies in aluminum foil. The ion current determined by IFC in range energy measurements using various foil thickness are plotted in Fig.4 along with typical waveforms. They show that the above peak energy component is about 0.05A, 20ns. For L=20cm, the peak energies are about half as compared to the L=71 cm case. The signature of ions after passing through Al foils has been obtained on CR-39 track detector. Also, the ion energies have been confirmed in time-of-flight studies.

By using a teflon tube of identical geometry as above, the energies of carbon and fluorine ions obtained for L=71cm are

about 10MeV and 17MeV respectively with amplitude about same as in the mylar tube case, but with smaller pulse width ~160ns.

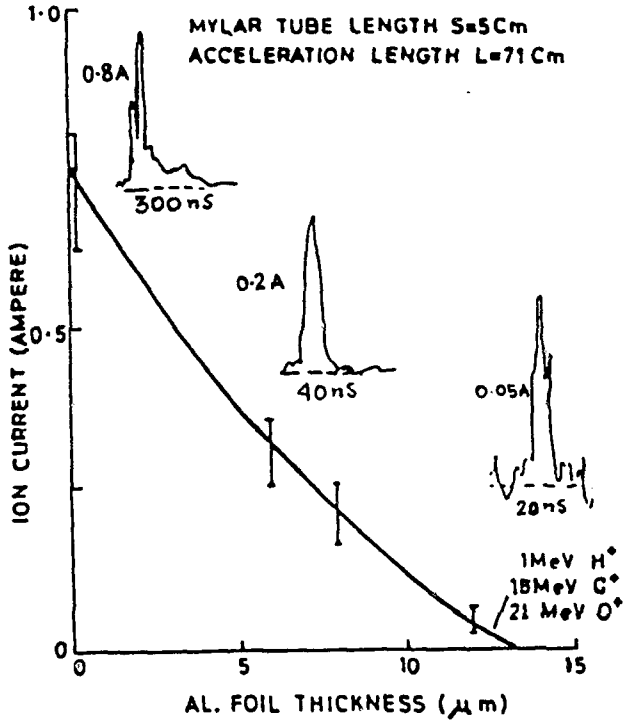


Fig.4. Results of range-energy measurements in aluminum.

By using a converging anode geometry of the REB diode, I_i has been significantly increased to 20-30A with peak energies of protons and oxygen raised to 2 and 45MeV respectively.

Conclusions

Light ion beams of significantly high currents and energies have been accelerated by using a moderately intense relativistic electron beam of 250keV, 5kA, 60ns in the Kilo Ampere Linear Injector.

Acknowledgments

We are thankful to Drs. S. S. Kapoor, M. Srinivasan, and P.H.Ron, for encouragement and discussions; and A. R. Chindarkar, G. Venugopala Rao, S. N. Acharya, and J. A. Gokhale, for assistance.

References

[1] L. E. Floyd, W. W. Destler, M. Reiser, and H.M. Shin, J. Appl. Phys. 52, 693 (1981).
[2] . N. Boyer, W. W. Destler, and H. Kim, IEEE Trans. Nucl. Sci. NS-24, 1625 (1977).
[3] T. Vijayan, S. K. Iyyengar, and V. K. Rohatgi, Bull. APS 31 (9) 1464 (1986).
[4] T. Vijayan, S. K. Iyyengar, and V. K. Rohatgi, Indian J. Phys. 63A, 61 (1989).
[5] W. W. Destler, P. G. O'Shea, and M. Reiser, Phys. Fluids, 27, 1897 (1984).
[6] M. Masuzaki, Jap. J. Appl. Phys. 21, L326 (1982).

MODELING HIGH-POWER RF ACCELERATOR CAVITIES WITH SPICE

Stanley Humphries, Jr.
Department of Electrical and Computer Engineering
University of New Mexico
Albuquerque, New Mexico 87131

ABSTRACT

The dynamical interactions between RF accelerator cavities and high-power beams can be treated on personal computers using a lumped circuit element model and the SPICE circuit analysis code. Applications include studies of wake potentials, two-beam accelerators, microwave sources, and transverse mode damping. This report describes the construction of analogs for TM_{mn0} modes and the creation of SPICE input for cylindrical cavities. The models were used to study continuous generation of kA electron beam pulses from a vacuum cavity driven by a high-power RF source.

A. INTRODUCTION

This paper describes theoretical work in support of a program on the generation of pulsed electron beams with RF cavities[1]. Peak currents in the kA range are possible using large low-frequency cavities with high stored energy. Inclusion of dielectrics raises the current generation capability by reducing the frequency, increasing the stored energy, and lowering the cavity impedance. One motivation for the work is recent research on high power RF sources in the FM range for accelerator applications. Large triodes[2] and scanned beam devices[3] have the potential ability to generate power in the frequency range 25-250 MHz at levels from 0.1 to 1 GW for extended macropulses. There two possible methods to generate intense electron beams. The first, the Phermex[4] mode, is to excite a high-Q cavity over an extended period with conventional RF sources and then to extract the energy in a single micropulse. Extraction may be a single event, or the cavity may be recharged to generate a periodic beam. The second method, possible with new high-power sources, is continuous extraction of a train of micropulses.

The two modes of beam extraction were investigated with the SPICE[5] circuit simulation code. This paper reports only results for steady-state beam excitation. SPICE provides a simple and versatile tool to derive dynamic solutions for realistic accelerator cavity geometries on small computer systems. Other

potential applications include calculation of cavity waveforms with strong beam loading, determination of resonant frequencies and Q values for longitudinal and transverse modes with wall and dielectric losses, and direct calculation of wake potentials[6]. Section B reviews the physical basis of a finite element representation of a resonant cavity. Section C covers steady-state generation of high current beams including effects of multiple power feeds.

B. SPICE MODELS OF MN0 MODES

SPICE can handle both AC and transient analyses with a variety of electronic components. The present work addresses only TM_{mn0} modes in cylindrical structures. The approximation is that electric field lines point predominantly in the axial direction. A corollary is that the electric field magnitude is almost constant in the axial direction - then we can represent electrical fields by voltages $V(r,\theta) = \int E_z(r,\theta,z)\, dz$. Reference 7 gives a detailed derivation of lumped element parameters. To summarize, we can represent the cavity by two conducting plates with a variable spacing $D(r,\theta)$ in the z-direction. A cylindrical mesh with spacings Δr and $\Delta\theta$ divides the cavity cross section. A short circuit condition (zero voltage) on the peripheral elements defines the outer wall at radius R. Figure 1 shows the lumped circuit model of an element. The radial index has the range $1 \leq i \leq n$, where $n = R/\Delta r$. Similarly, the azimuthal index varies over $1 \leq j \leq m$, where $m = 2\pi/\Delta\theta$.

For a smoothly varying function $D(r,\theta)$, the capacitance between plates averaged over an element centered at (r_i,θ_i) is

$$C[i,j] = \epsilon\, (i-\tfrac{1}{2})\Delta r^2 \Delta\theta / D(r_i,\theta_i), \qquad [1]$$

where ϵ is the dielectric constant of an isotropic fill medium. To calculate inductances associated with the element, we resolve current flow along the plates into components in the positive and negative x and y directions. The letters *a* through *d* denote the four directions (Fig. 1). Calculation of the field energy associated with the current gives the inductances as

$$L_a[i,j] = L_c[i,j] = \mu_o r_i \Delta\theta D(r_i,\theta_i)/2\Delta r, \text{ and} \qquad [2]$$

$$L_b[i,j] = L_d[i,j] = \mu_o \Delta r D(r_i,\theta_i)/2r_i\Delta\theta. \qquad [3]$$

Reference 7 derives values for the circuit resistors to describe power loss in the walls of a cylindrical cavity and dielectric losses.

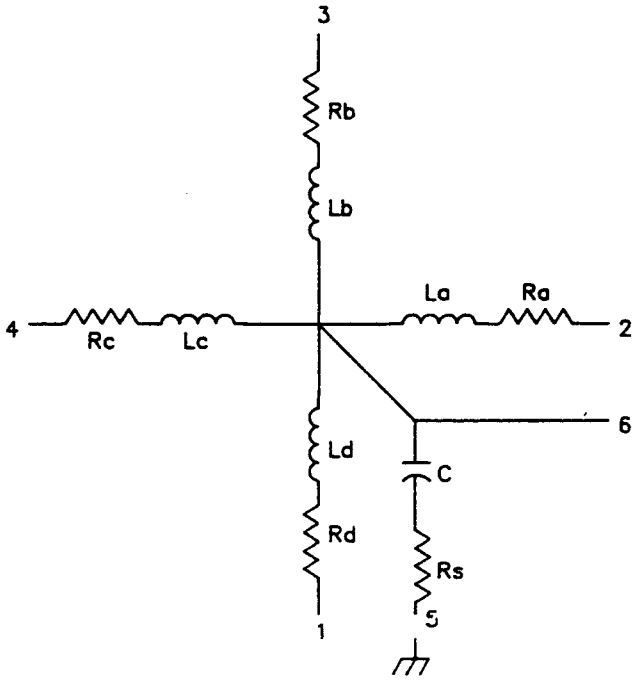
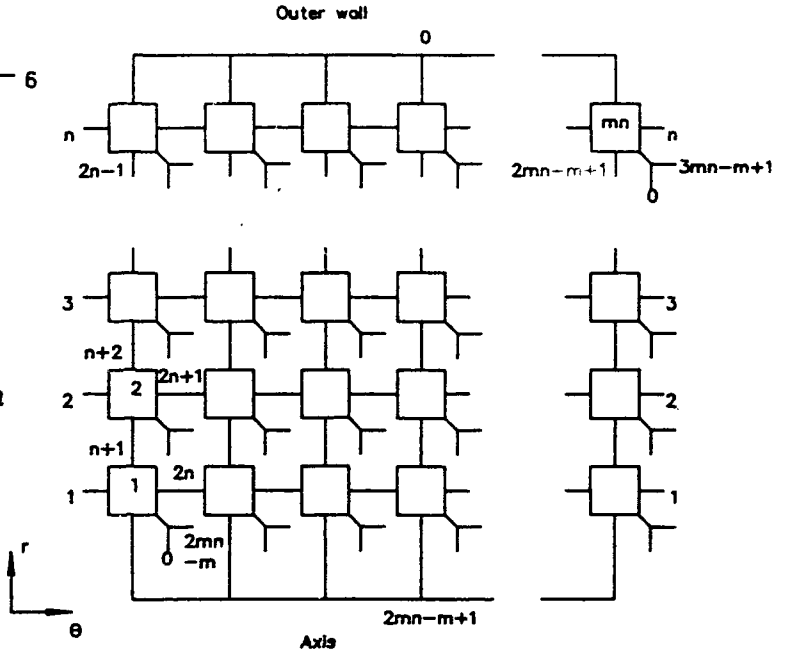


Figure 1. Circuit model of a single element.

Figure 2. Global node index conventions for cylindrical cavities.



We can define each element as a subcircuit in SPICE. For cylindrical cavities there are mn subcircuits plus additional elements to represent the on-axis beam and drive connections. Figure 2 shows the global layout of elements for a cylindrical cavity. In the radial direction, all nodes at the bottom connect to a point representing the axis - all nodes at the top short to ground at the outer wall. In the θ direction, nodes on the right-hand side connect to nodes on the left-hand side to impress a periodic boundary condition. A pre-processor program automatically created the extended SPICE text input for element subcircuits and their global node connections.

Comparisons with SUPERFISH[9] confirmed the performance of the lumped element model with a realistic cavity geometry. Figure 3 shows a large acceleration cavity with drift tube shields and a rounded outer wall. The structure had outer radius R = 1.2 m and a width on axis of D(0) = 0.8 m. The SUPERFISH calculation gave a resonant frequency of 86.07 MHz. The lumped element model gave a resonant frequency of 93.45, about 8.5 per cent higher.

C. LIMITS ON STEADY-STATE BEAM CURRENT IN A VACUUM CAVITY

With the development of new high-power RF sources in the FM band[2,3] it is feasible to excite large cavities continuously to high field levels over extended macropulses. This suggests the steady-state generation of kiloampere beams. If high-power RF sources are available, the main issue is the limit on beam power set by the cavity dynamics. We can express such a limit in terms of the effective Q factor of the beam $Q_{beam} = 2\pi f_o U_c / \langle P_{beam} \rangle$. In the expression, f_o is the accelerating mode frequency, U_c is the electromagnetic mode energy stored in the cavity, and $\langle P_{beam} \rangle$ is the time-averaged power extracted by the beam. The quantity Q_{beam} is approximately equal to 2π times the ratio of the stored RF energy to the energy extracted per RF period. SPICE runs were used to determine lower limits on Q_{beam}. The calculations showed surprisingly high power transfer capability even with a single RF drive loop. Good solutions were obtained with values of Q_{beam} as low as 20.

The calculations used the baseline vacuum cavity geometry of Fig. 3. In order to include effects of drive asymmetry, the cavity model had 80 elements with n = 20 and m = 8. The RF drives were represented as harmonic voltage sources in parallel with the capacitors of outer elements. With the connection at a radius of 1.0 m in the 1.2 m radius cavity (i = 17 for n = 20) and a driving voltage of 350 kV, the peak on-axis voltage was 3.0 MV. Runs were made with drives at one and two points (diametrically opposed). For comparison, results were also obtained for an infinite number of drives using a cavity model with n = 20 and m = 1.

The on-axis beam current was a series of micropulses separated by an RF period. For the AC analysis, the current was resolved into Fourier components. The beam was modeled by an ideal harmonic current source connected across the axis. The first set of runs used an ideal cavity drive with azimuthal symmetry (n=20, m=1). The cavity response was calculated for different amplitudes of the fundamental mode component of beam current. The frequency for minimum generator current defined the resonance condition - the value was constant at 93.468 MHz over the beam current range 0.0 to 1000.0 A. Table 1 summarizes the results. All entries are AC quantities at the resonant frequency. The table also shows beam power versus drive power. The fifth and sixth columns are the time-averaged power to the beam and from the generator. The last column is the difference in the powers. This quantity represents losses to wall and is almost independent of beam current.

TABLE 1

Beam current (A)	On-axis voltage (MV)	Generator voltage phase (degree)	Generator current (A)	Beam power (MW)	Drive power (MW)	Cavity losses (MW)
10.000	2.958	0.2115	99.13	14.79	17.35	2.56
50.000	2.958	0.9917	437.2	73.95	76.51	2.56
100.000	2.956	1.966	859.7	147.8	150.4	2.56
200.000	2.951	3.912	1705.0	295.1	292.7	2.60
500.000	2.916	9.677	4240.0	729.0	731.5	2.44
1000.000	2.781	19.92	8465.0	1391.0	1393.0	2.25

Table 1 shows that the cavity is an effective resonant transformer, even up to high beam power levels. The on-axis voltage remained close to 3 MV across the full range. At high current levels, it was necessary to introduce a phase shift in the driving voltage to maintain resonance. This shift was responsible for the drop in the mode voltage. The maximum tabulated value of AC current, 1000 A, corresponds to a micropulse with approximately 2 kA peak current. With an average beam power of 1.4 GW the effective Q factor was $Q_{beam} \cong 20$. At this level, power loss to the cavity walls was only about 0.16 per cent of the total power transfer.

The next set of runs investigated the effects of driving the cavity at discrete points. With a single drive point, we expect reduction of the on-axis voltage from the ideal drive cavity case because of power flow constriction. Furthermore, the azimuthal asymmetry leads to the generation of a dipole magnetic field on axis that may affect beam transport. We can calculate the approximate dipole magnetic from Faraday's law and a measurement of voltages at diametrically opposed points. For voltage probe points at a radius of $r_p = 0.54$ and a cavity voltage of 3 MV, we find that a voltage difference between points of 7.4 corresponds to a 1 milliradian deflection of a 3 MeV electron beam.

TABLE 2

Beam current (A)	Generator phase (degrees)	Generator current (A)	Cavity voltage (MV)
10.0	1.089	86.00	2.957
100.0	10.79	846.5	2.905
200.0	21.98	1692.0	2.749
300.0	34.05	2537.0	2.451
400.0	48.44	3381.0	1.738
500.0	69.09	4226.0	1.056

Table 2 shows results for different beam loading with a single point drive. It was again necessary to adjust the drive phase to maintain resonance as the beam loading increased. The required phase shift was smaller than the ideal drive case. This effect limited the maximum practical current to about 300 A. At this level of beam current, the probe voltages at r = 0.54 m were 1.584 MV on the side nearest the drive and 1.579 MV on the opposite side. The voltage difference of 5 kV implied a beam deflection less than 1 milliradian. The integral of dipole magnetic field was $\int B_x dz \cong 7.8 \times 10^{-6}$ tesla-m. In comparison, the field integral at the beam position for a bare drive wire carrying 2.5 kA is 4.1×10^{-4} tesla-m, about 50 times higher. The result illustrates the effectiveness of the cavity as a power flow equalization device. At high power levels, we can view a resonant cavity as a transmission structure for waves launched from the drive point. At resonance, reflection of waves from the walls and superposition at the axis equalizes power flow in azimuth. The calculations confirm that a large vacuum cavity can be an effective resonant transformer for kA electron beam generation, even with an offset drive. This work was supported by the Office of Naval Research.

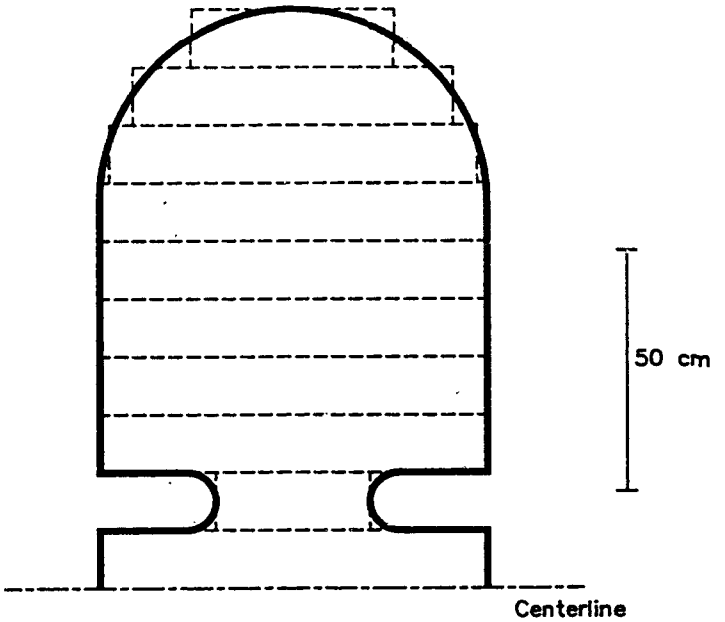


Figure 3. Geometry of test cavity, showing outline of 10 element lumped element approximation.

REFERENCES

1. S. Humphries, Jr., **Studies of High-gradient, High-average-power Electron Linac** (Univ. New Mexico, 1990), unpub.
2. R.J. Adler, *et.al.*, "Pulse Power Switching with Large Vacuum Triodes," **Proc. 1991 Pulsed Power Conf.**, to be published.
3. S. Humphries, Jr., *et.al.* Proc. SPIE **1407**, 512 (1991).
4. D. Venable, *et.al.*, **PHERMEX - a Pulsed High-energy Radiographic Machine**, (LANL, LA-3241, 1967).
5. A. Vladimirescu, *et.al.*, **SPICE Users' Guide** (U. of Cal. Berkeley, 1981), unpublished.
6. P.B. Wilson, "Wake Fields and Wake Potentials", in **Physics of Particle Accelerators** (Amer. Inst. Physics, New York, 1989), 525.
7. S. Humphries, Jr., **SPICE Models of RF Accelerator Cavity Dynamics**, (Univ. New Mexico, 1992), unpub.
8. K. Halbach and R.F. Holsinger, Part. Accel. 7, 213 (1976).

SUPERFISH POST-PROCESSOR FOR IBM-PC COMPATIBLE COMPUTERS

Stanley Humphries, Jr.
Department of Electrical and Computer Engineering
University of New Mexico
Albuquerque, New Mexico 87131

ABSTRACT

The SUPERFISH program calculates the fields of resonant modes in accelerating cavities and other structures. A new version for 386 and 486 personal computers achieves the functionality of the standard Cray version and has significantly expanded post-analysis capabilities.

A. INTRODUCTION

This paper describes the extended capabilities of the SUPERFISH[1] program in a version for MS-DOS 386 and 486 computers with emphasis on PROBE, a new post-processing program. PROBE supports interactive field calculations with second order accuracy at all points in the computational mesh. SUPERFISH, developed by K. Halbach and R. Holsinger[2], determines the fields of resonant modes in structures by solving the two-dimensional homogeneous Helmholtz equation. Reference 1 describes the numerical methods used. SUPERFISH solves problems in cylindrical coordinates with azimuthal symmetry - the main application is to the design of accelerator cavities. The program also describes Cartesian systems (variations in x and y and infinite extent in z) with applications to cavity magnetrons, RFQ accelerators and the cutoff modes of metal and dielectric waveguides. SUPERFISH uses a conformal triangular mesh with variable resolution for high accuracy and minimum computational time.

Public domain versions of SUPERFISH have long been available for VAX and CRAY computers[1]. A public domain version for IBM-PC standard computers was released several years ago by J. Coleman of Brookhaven National Laboratory. This package could handle only 4000 mesh points because of limitations of the Microsoft Fortran compiler. The present generation of fast 386 and 486 computers are ideally suited to the code - with advanced compilers and extended memory, PCs can equal the mesh point capability of the standard Cray version.

The version of SUPERFISH described in this report is marketed as an extension of the EMP 2.0 static field package[3] that includes the POISSON and PANDIRA programs. The package is not simply a recompilation of the mainframe programs - it features a a complete revamping of input and output capabilities. The goal was to make the programs instantly understandable to individual PC users with no access to a computer support group. Advances beyond the mainframe version include the following.

- A custom menu and interface program make it possible to generate input boundary information direct from the popular AUTOCAD[4] program.
- AUTOMESH (with its Fortran NAMELIST statements) has been replaced by the program VENTURE. The new program has a free-form input parser and easily-remembered data commands.
- INSTRUCT is a "pop-up" reference manual activated by a software interrupt from any text program. INSTRUCT gives comprehensive information on boundary input, electrical characteristics, and program control.
- Error messages have been expanded and translated into plain English. A step-by-step instruction manual with a library of examples supplements the advanced technical documentation from Los Alamos[1].
- The utility QCALC finds power losses on surfaces and the Q factor of a resonant structure. QCALC, which uses subroutines from the LANL code SFOUT, has highly streamlined input and output conventions.
- The post-processing program PROBE supports analysis of RF mode solutions in an interactive graphics environment. PROBE greatly exceeds the linear dump routines of the mainframe version. Differences include second order field calculations, preservation of accuracy across dielectric boundaries, and energy calculations organized by region.

The performance of SUPERFISH on a PC is good enough for serious design calculations. For example, Figure 1 shows a simulation of a two-cavity disk and washer structure with a large mesh (6072 points). SUPERFISH made three iterations to proceed from the starting frequency of 1.3300 GHz to the final value of 1.3387 GHz. The elapsed time on a 33 MHz 486 machine was 22 minutes.

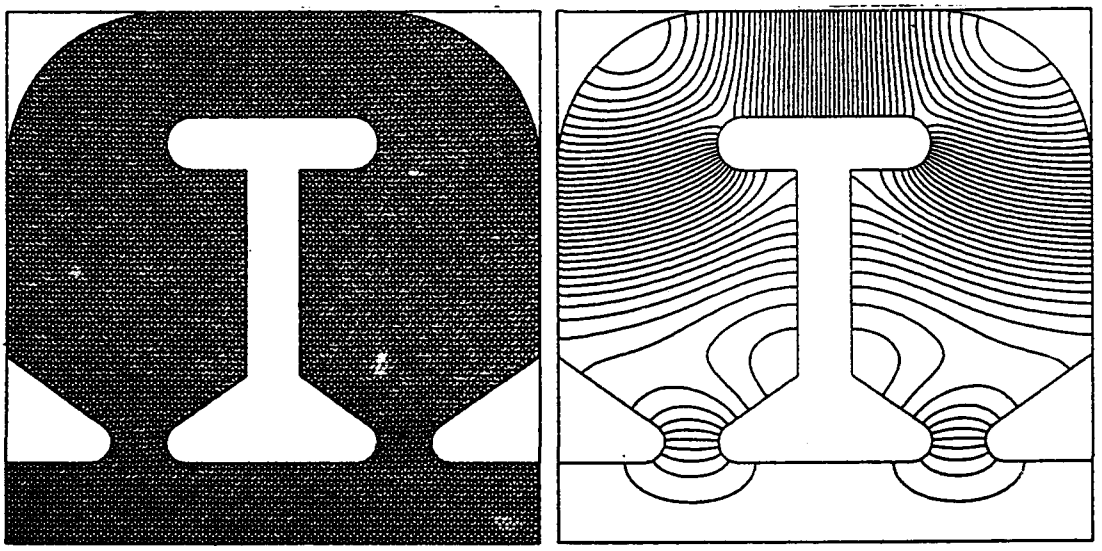


Figure 1. SUPERFISH calculation, π mode of a 2-cavity disk-and-washer structure. a) Triangular mesh. b) Electric field lines.

B. FIELD EXPRESSIONS IN SUPERFISH

SUPERFISH finds TM and TE modes of Cartesian and cylindrical structures. The program generates values for the mode generating function on an irregular triangular mesh. For the four types of problems, the generating function is: H_z (rectangular TE modes), E_z (rectangular TM modes), rH_θ (cylindrical TM modes) and rE_θ (cylindrical TE modes). The solution method in SUPERFISH is the same for the four choices - the solution type is determined by a symmetry flag and the boundary conditions of the generating function at metal surfaces. Derivatives of the generating function give the other field components. Figure 1a shows a typical computational mesh - note that the triangles conform to the boundaries and do not lie in a specific geometric pattern. The generating function has values at each triangle vertex, while values of the dielectric constant and magnetic permeability apply to the areas inside the triangles. SUPERFISH indentifies a mesh triangle by the indices of the leftmost vertex (K,L) and a flag that specifies whether the triangle is "up" or "down" with respect to the point.

We shall concentrate on TM modes in cylindrical geometry to illustrate field expressions. This is the common choice for acceleration cavities. In regions with constant and isotropic ϵ_r or μ_r, the Maxwell equations can be combined to give the Helmholtz equations

$$\nabla^2\mathbf{E} - (\epsilon\mu)\ \partial^2\mathbf{E}/\partial t^2 = 0, \text{ and} \qquad [1]$$

$$\nabla^2\mathbf{H} - (\epsilon\mu)\ \partial^2\mathbf{H}/\partial t^2 = 0. \qquad [2]$$

In cylindrical coordinates, TM modes have $H_z = 0$ and $E_z <> 0$. The transverse field components allowed by azimuthal symmetry are H_θ and E_r. The Neumann boundary condition holds for H_θ on a metal surface,

$$\nabla_n H_\theta = 0. \qquad [3]$$

Equation 3 states that the vector sun of radial and axial electric fields is zero on the wall. The generating function is determined from Eq. 3 and the equation

$$\frac{1}{r}\frac{\partial}{\partial r}\left(r\frac{\partial H_\theta}{\partial r}\right) + \frac{\partial^2 H_\theta}{\partial z^2} + \epsilon\mu\omega^2\frac{\partial^2 H_\theta}{\partial t^2} = 0. \qquad [4]$$

SUPERFISH searches for a value of ω that satisfies both Eqs. 3 and 4 and then makes a data file of the stream function rH_θ. Because Eq. 4 is homogeneous, the absolute values of rH_θ are arbitrary - multiplying them by a constant gives another valid solution. SUPERFISH sets the generating function equal to 1.0 at a special point on the computational mesh called the *drive point*.

The transverse electric fields are related to the stream function by

$$E_r = -\frac{1}{\epsilon\omega}\frac{1}{r}\frac{\partial}{\partial z}(rH_\theta), \quad E_z = \frac{1}{\epsilon\omega}\frac{1}{r}\frac{\partial}{\partial r}(rH_\theta). \qquad [5]$$

Eqs. 5 imply that electric field lines lie on contours of the stream function, rH_θ. Note also that for a uniform interval in the stream function, the separation between contour lines is proportional to $r|E|$ rather than $|E|$ as in rectangular problems. Figure 1*b* shows field lines defined by contours of stream function for the π mode of the disk-and-washer structure.

C. FEATURES OF PROBE

PROBE is an interactive post-processing program that uses the binary data files from SUPERFISH. Figure 2 shows a reproduction of the colored screen display. The program uses three windows for graphs, numerical output, and commands. Positions are be specified within the graphics window by a mouse pointer or from the keyboard. Regarding the PLOT commands, PROBE can generate mesh plots or field line plots, zoom in on key areas, or add reference grids. The program can also generate standardized plot files for export to hardcopy devices. The DUMP routines are simple ASCII file listings of the generating function and transverse fields for triangles in the current graphics view.

The keystone of PROBE is a new routine to interpolate the generating function and to find derivatives with second order accuracy. The challenge is to deal with the irregular triangular mesh and field discontinuities at dielectric and ferrite boundaries. For a given position (x_o,y_o), PROBE performs the following sequence of operations. The first step is to search for the triangle that contains the target point. To find if a point is "in" a triangle, PROBE checks the point position relative to the three lines coincident with the triangle sides. The program has options for a FAST or FULL search. The FAST search locates the approximate mesh coordinates (K,L) of the target triangle by

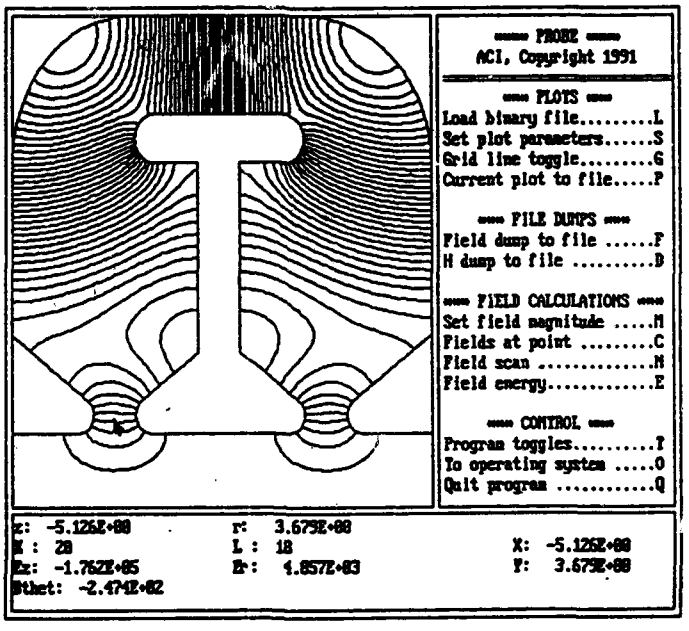


Figure 2. Screen display of PROBE program showing mouse icon and field calculation.

checking values along the solution edges and then searching in the vicinity. The FULL search checks all mesh triangles until a match is found - it has a 100 per cent success rate for valid points. Both routines return the (K,L) coordinates of the target triangle and set the up-down flag. These quantities yield the material number (dielectric, ferrite or air) from a masked value of the SUPERFISH data array INDEX(K,L). The next step is to call the main subroutine POINTFIT that has several operations. The first, FILLPOINTS, fills arrays with from 6 to 20 values of X (x or z, Y (y or r) and A (vector potential or stream function). The routine checks up to twenty vertices near the target triangle. There are two criteria to accept a point.

1. The point is not inside a metal structure or outside the problem dimensions. This means that near a sharp metal boundary, PROBE collects nearby points only in the air (or dielectric) region.
2. PROBE checks the six triangles adjacent to the point to ensure that at least one triangle has the same material number as the target triangle. In this way, PROBE accumulates only points on one side of a dielectric or ferrite boundary.

If there are enough valid points, the program calls a least-squares routine that fits a function of the form

$$A(x,y) = A_o + A_1(x-x_o) + A_2(y-y_o) + A_3(x-x_o)^2 + A_4(x-x_o)(y-y_o) + A_5(y-y_o)^2, \qquad [6]$$

where (x_o,y_o) is the target point. Using coefficients calculated from values at the collected points, the program solves six simultaneous linear equations using LU decomposition[5] to find the coefficients. The routine returns the interpolated value of the generating function and its first and second derivatives. The accuracy for field calculations is typically a few parts in 10^4. The final step is to convert the relative generating function and gradients to dimensioned field quantities. PROBE automatically adjusts factors for the four types of mode geometries.

PROBE calculates fields at a point or along a scan line at any orientation. Results are displayed on the screen and also recorded in an ASCII file that maintains a history of the analysis session. Figure 3 is an example of a scan, a axial sweep of Fig. 1*b* from -10 cm to 10 cm at r = 2.5 cm (just inside the drift tube inner radius). The **E** command (field energy) of PROBE calculates global field energy for a chosen normalization and also lists field energy by region. Given the peak electric field energy in a dielectric region (U_e), power losses can be computed from the formula

$$P_e = (\epsilon''/\epsilon')2\pi f U_e. \qquad [7]$$

In Eq. 7, the quantity f is the mode frequency, while ϵ' and ϵ'' are the real and imaginary parts of the dielectric constant. The **E** command also locates the triangle with the highest value of electric field within the current graphics window view.

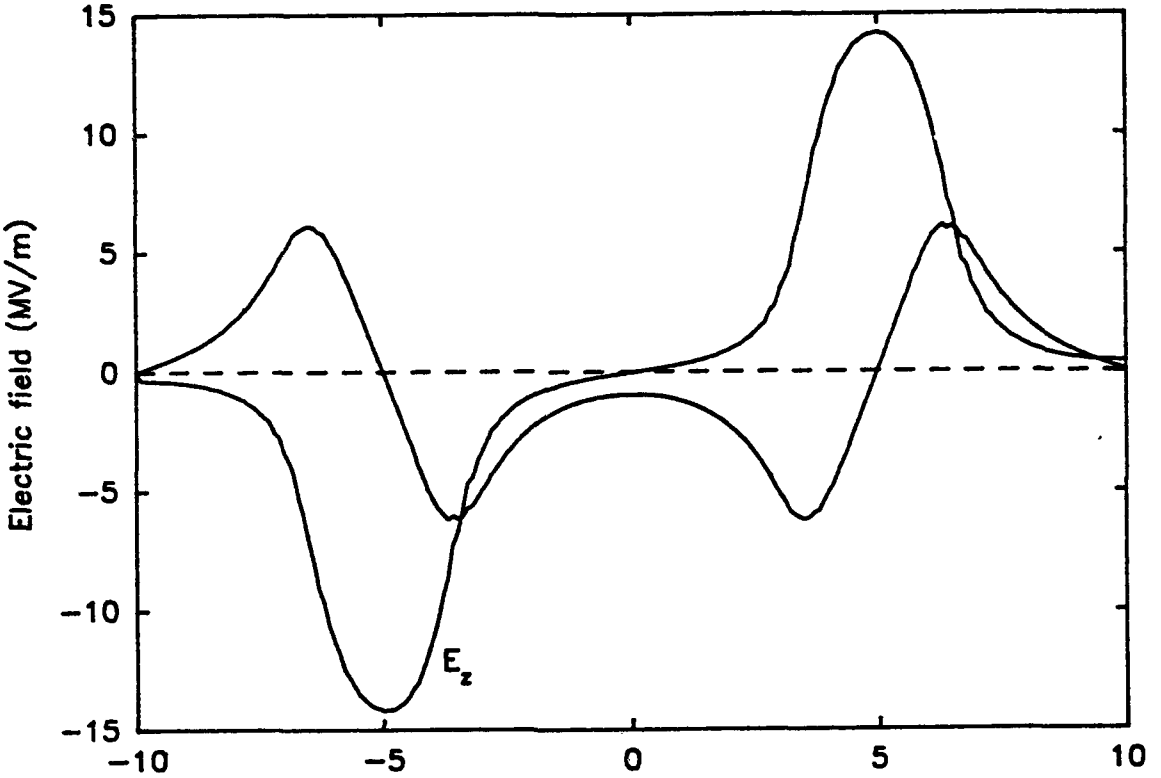


Figure 3. Scan of radial and axial electric fields generated by PROBE for the example of Fig. 1. Data abstracted from history file and plotted with Sigmaplot[6] 4.0.

D. PLANNED EXTENSIONS

The field calculation method of PROBE has been added to VISION, the static-field post-analysis program of EMP 2.0. The initial triangle search occupies the most time. Therefore, the process is fast for computations of nearby points. This capability suggests extending the capabilities of SUPERFISH and EMP 2.0 to include particle tracking. The codes have potential advantages over ray tracing codes that use a square mesh. The conformal triangular mesh gives high speed and good accuracy, especially for field emission problems. For static field solutions, it is possible to combine numerical calculations of magnetic and electric fields in a tracking session, even with different meshes. Finally, SUPERFISH solutions can be used to find orbits in electromagnetic fields. TRAK, a extension module for EMP 2.0, is currently under development. When complete, the program will handle space-charge-limited emission with a new fast algorithm that converges quickly, even with complex recirculating particle orbits. This work was supported, in part, by the Office of Naval Research.

1. **Reference Manual for the Poisson/Superfish Group of Codes** (Los Alamos National Laboratory, LA-UR-87-126, 1987).
2. K. Halbach and R.F. Holsinger, Part. Acc. 7 (1976), 213.
3. Copyright, Field Precision Co., Albuquerque, New Mexico.
4. Copyright, Autodesk Inc., Sausalito, California.
5. See, for instance, W.H. Press, *et.al.* (ed), **Numerical Recipes** (Cambridge Press, 1986), Sect. 2.3.
6. Copyright, Jandel Scientific, Corte Madera, California.

SIMULATION STUDIES OF BEAM QUALITY IN HIGH-GRADIENT ACCELERATORS

Glenn Joyce and Jonathan Krall
Beam Physics Branch, Plasma Physics Division
Naval Research Laboratory, Washington, DC 20375-5000

Abstract

We use particle simulation techniques to model an idealized induction accelerator geometry. We study the effect of high accelerating gradients on the transverse dynamics of the electron beam. Under these conditions, the significant measure of beam quality is emittance. The model includes the gap fields, but neglects the effect of the gap geometry on the self-fields of the electron beam. The results show that high gradient induction gaps can cause non-linear radial perturbations of the beam. If high enough energies are reached, these perturbations do not adversely affect the beam emittance.

I. INTRODUCTION

Beam quality is an important consideration in the development and application of high-gradient ($E_z \geq 100$ MeV/m) accelerators. In particular, a short wavelength (λ~1 micron) free electron laser (FEL) presents very stringent requirements on beam emittance and longitudinal energy spread [1]. For the case of the FEL, a simple measure of the optimum beam emittance can be derived from the requirement that the beam and the laser maintain maximum overlap as they co-propagate. From the envelope equation of an emittance dominated electron beam without external focusing and from the envelope equation of a Gaussian radiation beam in vacuum, one can show that maximum geometrical overlap is obtained when

$$\epsilon = \lambda/\pi, \tag{1}$$

where the emittance is in units of length and radians. Note that while Eq. (1) does not describe many cases of interest, such as those in which the electron beam is focussed or those in which the radiation beam does not undergo vacuum diffraction, as with optical guiding [2], it does provide a useful estimate of the optimum emittance for a given FEL wavelength.

An additional criterion for acceptable beam quality in an FEL is obtained from the requirement that the longitudinal thermal temperature of the beam be significantly less than the reduction in the mean velocity of the beam by the FEL interaction, Δv. This can be written as

$$\Delta\gamma_z/\gamma < \eta \sim 2\gamma_z^2 \Delta v/c, \tag{2}$$

where $\Delta\gamma_z$ is the longitudinal spread in $\gamma_z = [1 - (v_z/c)^2]^{-1/2}$, v_z is the mean axial velocity of

the beam, γ is the usual relativistic factor for the beam, η is a measure the FEL efficiency, and c is the speed of light in vacuum. The FEL interaction requires $\Delta v << 1$, but the exact value of Δv depends on the FEL regime of interest.

In this study we use particle simulation techniques to model a highly idealized induction accelerator geometry. The "accelerator" consists simply of a metallic pipe, an axial magnetic guide field, and externally imposed accelerating fields corresponding to one or more accelerating gaps. Because the gap fields are time independent, each particle will experience the same change in voltage. As a result, the gaps will not cause a longitudinal velocity spread in the beam. The study will be concerned solely with the effect of high accelerating gradients on the transverse dynamics of the electron beam. Under these conditions, the significant measure of beam quality is emittance.

In section II of this paper we describe our numerical model. In section III, we present simulations of both a single accelerating gap and of a series of accelerating gaps for various gap voltages and acceleration lengths. We discuss our findings in section IV.

II. NUMERICAL MODEL

We model beam transport through one or more induction gaps using the SST particle simulation code.[3] This is a fully electromagnetic, fully relativistic 2-d (r,θ) code that accurately models the transverse dynamics of an electron beam propagating in a metallic pipe under the assumption $\partial/\partial\zeta = 0$ where $\zeta = ct - z$. In making this approximation, we assume that the beam length is long compared to the pipe radius and that the beam remains unbunched. The induction gaps are modeled by external fields that are determined via a simple electrostatic calculation for which the pipe radius, gap width and gap voltage are specified. Thus our model includes the gap fields, but neglects the effect of the gap geometry on the self-fields of the electron beam. We use an emittance definition which was developed for beams with coupled x-y motion:[4]

$$\epsilon_{xy} = 4|\Sigma|^{1/4}, \tag{3}$$

where the elements of the Σ matrix are given by

$$\Sigma_{ij} = \langle u_i u_j \rangle - \langle u_i \rangle \langle u_j \rangle. \tag{4}$$

Here, "< >" signifies an average over the beam particles and i,j = 1,2,3,4 with $u_1 = x$, $u_2 = dx/dz$, $u_3 = y$ and $u_4 = dy/dz$. The normalized emittance is $\varepsilon_n = \beta\gamma\epsilon_{xy}$. In the limit that the x and y motion of the beam particles are uncoupled, one can show that $\varepsilon_{XY} = (\varepsilon_X \varepsilon_Y)^{1/2}$, where

$$\epsilon_x = 4[\Sigma_{11}\Sigma_{22} - \Sigma_{12}^2]^{1/2} \tag{5}$$

and

$$\epsilon_y = 4[\Sigma_{33}\Sigma_{44} - \Sigma_{34}^2]^{1/2}. \quad (6)$$

III. SIMULATION RESULTS

We consider acceleration of a beam by one or more gaps with varying gap voltage and beam current. The beam propagates within a r_w = 3 cm metallic pipe and is guided by a B_z = 4 kG magnetic field throughout. The initial beam parameters are $\gamma = 2$, $\epsilon_n \approx 2 \times 10^{-2}$ cm-rad, $r_b \approx 0.15$ cm and beam current I_b ranging from 400 to 1000 A. The beam, which is initially in equilibrium with the axial magnetic field, has Gaussian transverse spatial and velocity profiles. The equilibrium beam radius and emittance varied slightly with current.

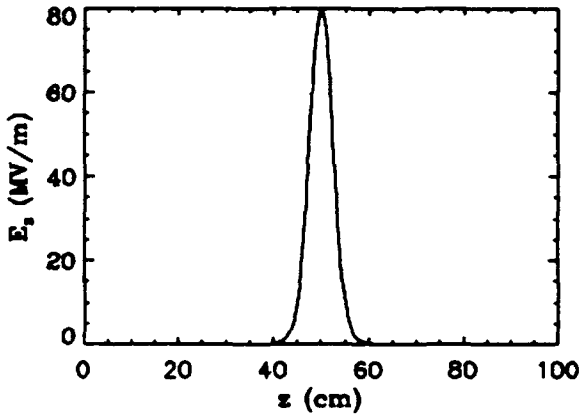


Figure 1. Axial field E_z vs. z for V_g = 5MV.

In one series of simulations, we considered the emittance growth due to the perturbation on the beam from a single high-voltage accelerating gap. For these simulations, we used I_b = 400, 600, 800 and 1000 A and gap voltages V_g = 5, 10, 15 and 20 MV. In all cases we the gap width is 5 cm and the gap radius is equal to the 3 cm pipe radius. The axial electric field for a V_g = 5 MV gap is shown in Fig. 1.

In each simulation, we propagate the beam through the gap, where the radial electric fields near the gap perturb the beam. We then follow the beam for five radial oscillation periods. For example, the rms beam radius (lower curve) and normalized emittance (upper curve) of an I_b = 1000 A beam are plotted in Fig. 2 for a case with V_g = 5 MV as in Fig. 1. After five envelope oscillations the emittance increase is $\Delta\epsilon$ = 11 %.

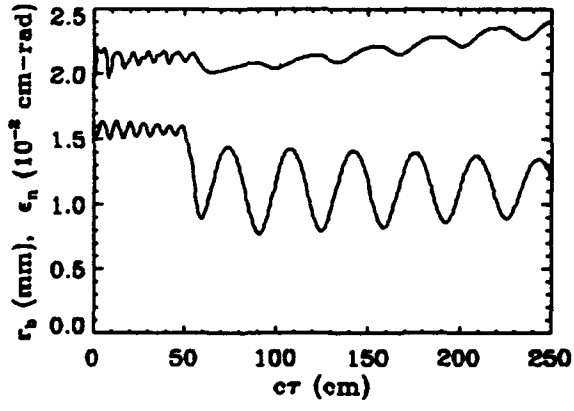


Figure 2. Emittance (upper curve) and beam radius (lower curve) vs. time for V_g = 5MV.

The changes of emittance due to the beam acceleration for this series of runs are summarized in Fig. 3. It is interesting to note that at each setting of I_b, we found the lowest emittance growth at V_g = 20 MV, our highest applied voltage. This suggests that if one can accelerate the beam fast enough, the effects of the space charge potential of the beam will be so small that the beam will experience only linear radial focusing forces. In this case, the envelope oscillations will be highly coherent and will not allow the phase-mixing of particle orbits that is necessary for emittance growth. Such coherent oscillations are easily removed

via magnetic focusing elements. In a simulation at I_b = 1000 A, V_g = 20 MV, for example, we found that we could use a series of simple solenoidal focusing coils to remove the coherent oscillations without causing additional emittance growth.

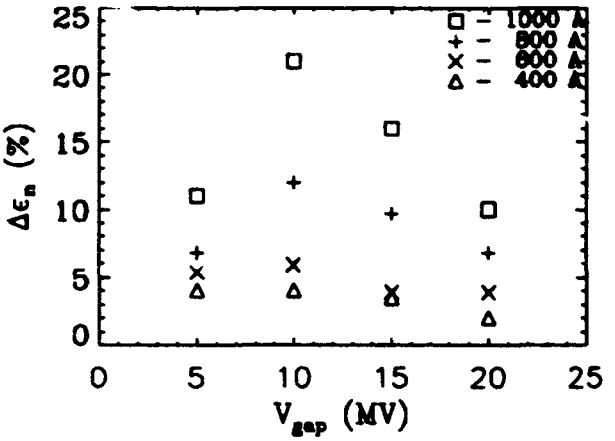


Figure 3. Emittance growth $\Delta\varepsilon_n$ as a function of gap voltage V_g and beam current.

Of additional interest when considering a hypothetical induction accelerator is the effect on emittance of a series of induction gaps. Here we model several 100 MV accelerator configurations with 5 - 20 gaps each spaced 20 cm apart. The four configurations we simulated had 5 gaps with V_g = 20 MV (acceleration length, L_a = 100 cm), 7 gaps with V_g =14.33 MV (L_a = 140 cm), 10 gaps with V_g = 10 MV (L_a = 200 cm) and 20 gaps with V_g = 5 MV (L_a = 400 cm), respectively. In each case we used I_b = 1000 A.

The results for this set of runs are summarized in Fig. 4. The initial and final emittances are essentially equal in all cases, and only a slight variation in the final emittance was observed as a function of the number of gaps. In each run, the emittance remained constant once the 100 MeV energy level was reached, despite the induced envelope oscillations. We believe that the slight variation in the final emittance level is entirely attributable to the radial oscillations that occurred between the initial radial perturbation and the point at which the beam energy becomes high enough that these oscillations become coherent.

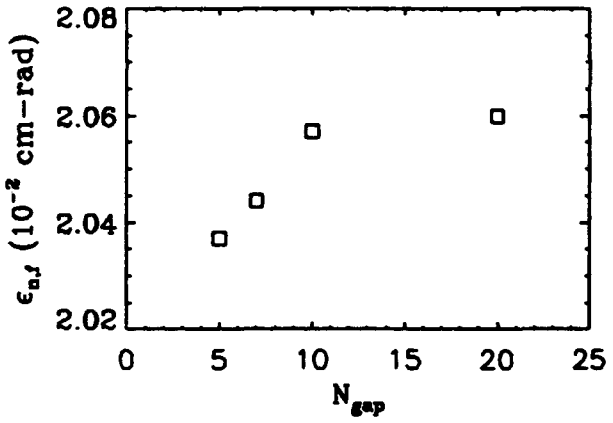


Figure 4. Final beam emittance as a function of the number of equally spaced gaps.

IV. CONCLUSIONS AND COMMENTS

Our results show that use of high gradient induction gaps or, by inference, any high-gradient accelerating structure, will almost certainly cause significant radial perturbations of the beam. In many of our cases, these perturbations were highly nonlinear. The results also suggest that if high enough energies are reached, these perturbations will not adversely effect the beam emittance.

To illustrate what we mean by "high enough energy," we consider the envelope equation for a beam in the presence of an axial magnetic field[5,6]

$$\frac{\partial^2 r_b}{\partial z^2}+\frac{\Omega_z^2}{4\beta^2c^2\gamma^2}r_b-\frac{2\nu}{\beta^2\gamma^3 r_b}-\frac{\epsilon_n^2+(P_\theta/m_ec^2)}{\beta^2\gamma^2 r_b^3}=0, \tag{7}$$

where $\Omega_z = eB_z/m_ec$ is the nonrelativistic cyclotron frequency, m_e is the electron mass, e is the elementary charge (assumed positive), $\gamma = (1 - \beta^2)^{-1/2}$ is the usual relativistic factor for the beam, $P_\theta = e\psi/2\pi$, ψ is the magnetic flux linking the cathode, $\upsilon = I_b[kA]/17\beta$ is Budker's parameter and ϵ_n has units of length and radians. In deriving Eq. (7) it was assumed that the focusing and defocusing forces on an electron in the beam are linearly proportional to its radius. In such cases radial oscillations of the beam are coherent and emittance is preserved. In a nonuniform beam, the space charge forces are no longer linear and phase mixing can occur. This is avoided when the second term above may be neglected relative to the third:

$$\nu/\gamma \ll (\epsilon_n/r_b)^2, \tag{8}$$

where we are considering $P_\theta = 0$ (field-free cathode). The actual level of emittance growth is difficult to predict as it depends upon the details of the radial beam profile and the strength of the radial perturbation.

ACKNOWLEDGMENTS

The authors would like to thank John Petillo of Science Applications International Corporation for his assistance. This work was supported by ONR/SDIO/IST.

References

1. C. W. Roberson and P. Sprangle, Phys. Fluids B 1, 3 (1989).
2. P. Sprangle and C. M. Tang, Appl. Phys. Lett. 39, 677 (1981).
3. J. Krall, G. Joyce and S. Slinker, Proc. 14th Intl. Conference on the Numerical Simulation of Plasmas (Annapolis, MD) (1991).
4. D. Chernin, Part. Accel. 24, 29 (1988).
5. E. P. Lee and R. K. Cooper. Part. Accel. 7, 83 (1976).
6. J. D. Lawson, The Physics of Charged Particle Beams (Oxford U. P., London, 1977).

CLIA—A COMPACT LINEAR INDUCTION ACCELERATOR SYSTEM

S. Ashby, D. Drury, P. Sincerny, L. Thompson
Physics International Company
Olin Corporation Aerospace Division
San Leandro, CA

L. Schlitt
Leland Schlitt Consulting Services
Livermore, CA

Abstract

CLIA (Compact Linear Induction Accelerator) is a 750 kV, 10 kA, 60 ns, 200 Hz pulse generator that has been designed, constructed, and operated at Physics International. The CLIA system consists of (from the load back to the mains) a ten-cell linear induction voltage adder, ten magnetically switched water insulated pulse forming lines (PFL's), a two-stage Magnetic Compression Unit (MCU), and thyratron-switched Intermediate Energy Store (IES), and Command Resonant Charge (CRC) units.

This system was conceived to drive repetitive e-beam loads for various types of repetitive testing. A linear induction accelerator system was used because it allows all pulse compression to be done at moderate voltage (40 to 150 kV) and then uses the accelerator structure to add parallel voltage pulses into a single high voltage output (750 kV). Nowhere except at the load does a voltage of higher than 150 kV appear. This allows the switching to be done at moderate voltage and the use of hydrogen thyratrons and magnetic switches is possible.

This generator has been in operation at Physics International for over a year and has achieved all its design goals. The design and operational characteristics of the accelerator will be described in this paper.

The CLIA Modulator

The modulator that drives the CLIA system is shown schematically in Figure 1. The first two stages of pulse compression raise the voltage from 40 kV to 75 kV and compress the time scale from dc to 4 μs using two EEV thyratrons. The first is used in a command resonant charge (CRC) configuration and the second as an intermediate energy store (IES) to allow the first thyratron time to recover. The second tube has a magnetic switch in series to aid its recovery characteristics. This thyratron modulator system was developed to test high average power thyratrons previously[1] and was converted to drive the CLIA system. These modifications included adding 250 feet of RG/218 cable between the CRC switch and CRC inductor to physically locate the CRC and IES sections of the modulator in different area of the facility. We needed the output of CLIA to be near the other microwave sources and did not want to move the large 300 kW dc supply and its ac power. This cable, after being properly terminated with snubbers, has caused no problems. The thyratron switched portion of the system has been very reliable at the 200 kW average power level.

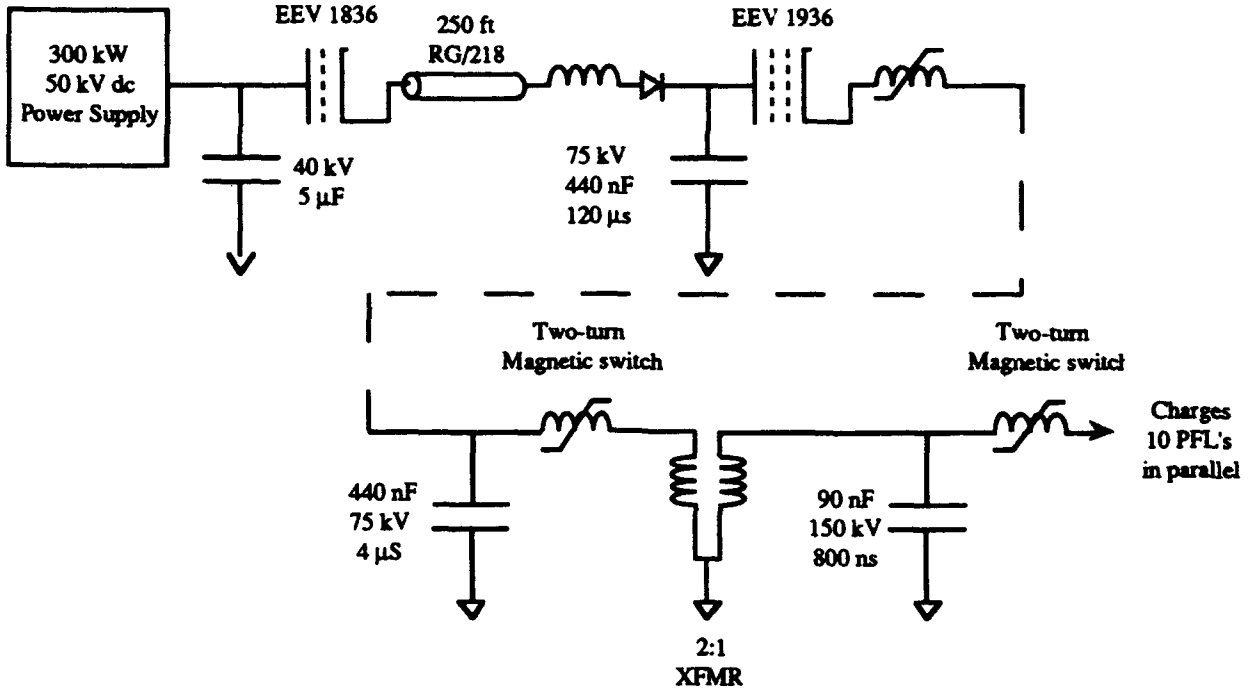


Figure 1. The CLIA System Modulator.

The second two stages of pulse compression in the CLIA modulator are magnetically switched. Figure 2 shows the assembled magnetic compression unit, composed of two capacitive storage sections, two magnetic switches, and a 2:1 inverting pulse transformer. The energy from the IES is supplied to the magnetic compression unit on four cables which allow the IES to sit outside of the concrete shielded test cell. The magnetic compression unit resides immediately next to the CLIA accelerator inside the cell. The magnetic compression unit is compact, combining the two pulse compression stages and pulse transformer into two cylinders, each less than 75 cm in diameter and 150 cm long.

The magnetic compression unit has worked very well. One modification has been performed to lessen the probability of breakdown in the water capacitor section. This water capacitor was designed as a parallel combination of 19 coaxial capacitors, each with a OD/ID ratio of 2 to take advantage of the well-known polarity effect in water. Significantly more voltage reversal is present in the water capacitor than was anticipated in the design, however, causing the inner conductor to be positive with respect to the outer conductor. This reversal is due in part to mismatches in the system (the capacitance of the water capacitor is sized for future extension of the pulse length to 100 ns) and, in part, to the use of low impedance loads on the front of the system. The radial dimensions of the water capacitor were increased by a factor of two with no change to the electrical design to ensure that this was a very conservative redesign, and there have been no problems with breakdown in over 20,000 pulses since.



Figure 2. The CLIA Magnetic Compression Unit.

The other components in the magnetic compression unit have performed extremely well. When the water capacitor was replaced, all of the magnetic cores were inspected and no signs of breakdown were observed. The first stage of pulse compression, composed of nine individual tubular capacitors arrayed on a 14-inch bolt circle with a 24-inch long, two-turn coaxial magnetic switch in the center has performed without a fault at full design levels. The transformer is a 2:1 inverting design involving convolutes to achieve a minimum leakage inductance and minimum mass of magnetic material while still running at conservative stress levels. It has also performed well with no observed faults. The second stage output switch is similar in design to the first stage switch, a two-turn coaxial design. It also has performed flawlessly.

The CLIA PFL's and Accelerator

The output of the second stage switch charges the PFL's via 10 high voltage cables, one per PFL. The 6.8 Ω, water-insulated coaxial PFL's are charged in 150 to 200 ns and switched out by an oil-insulated coaxial magnetic output switch. Each PFL drives one cell of the accelerator structure. The output switches are the one area of the system that has taken the most effort to get to work reliably. The initial design used 25 μm 2605CO Metglas insulated with 3.5 μm Mylar to achieve high packing fraction, low stray inductance switches. However, during initial testing using a single shot Marx generator to drive the PFL's and accelerator structure, these cores began to experience breakdown due to punch-through of the Mylar insulation. This was generally worse on the core closest to the PFL, which sees more voltage before switchout, but breakdowns were

present in the other cores as well. This effect is believed to be similar to the breakdowns observed by others[2] and due to surface roughness in the Metglas material. The interlaminar voltage in the CLIA output switch was approximately 65 volts. This problem was solved by replacing the cores in the output switch with ones wound with paper insulation (12 μm) and using double layers of insulation in the core nearer to the PFL. While this reduces the packing fraction achievable, these cores have performed extremely well since with no evidence of dielectric failure.

The accelerator cores were fabricated using the same methods as the initial output switches, i.e. 25 μm 2605CO with 3.5 μm Mylar insulation. The interlamination voltage is significantly less in the cores than in the output switches We have had no obvious problems with breakdown in them. We cannot be absolutely sure that they are not breaking down because it is difficult to see the cores upon dissembly due to the design of the mandrel. It is also not obvious how breakdowns in the accelerator cores would be evident in the operation of the accelerator.

The CLIA accelerator structure has been described previously.[3] It is a 10 cell, oil- and vacuum-insulated linear induction adder structure that is approximately one meter long. The output end is a 3.75-inch-diameter cathode stalk in a 7.5-inch-diameter bore accelerator. Loads that have been tested on the output of CLIA are described in a companion paper.[4] The PFL's and accelerator are shown in Figure 3.

Magnetic Switch Parameters

The system was brought on line initially in sections. First the accelerator and the PFL's were tested both in single pulse and double pulse mode with a fast Marx generator to measure the required parameters for the modulator to drive the system successfully. Then the second stage switch and water capacitor were inserted between the Marx and the PFL's. Again the efficiency of operation was investigated and the design of the first stage of the magnetic compression unit was finalized. The first stage was then installed and the thyratron modulator was attached to the magnetic compression unit for final testing.

At each stage of testing, comparisons between the experimental data and a computer circuit model were performed to update the model to reflect measured performance of the system, specifically the Metglas BH characteristics. We have developed a sophisticated model for the behavior of magnetic materials, including different models for different thicknesses of material and a rate dependent BH curve that varies the loss depending on voltage across the core. Through this process of adjusting the model to match the data, we have developed an accurate model of the CLIA system. This model can also be used as a tool to predict the performance of other magnetically switched systems.

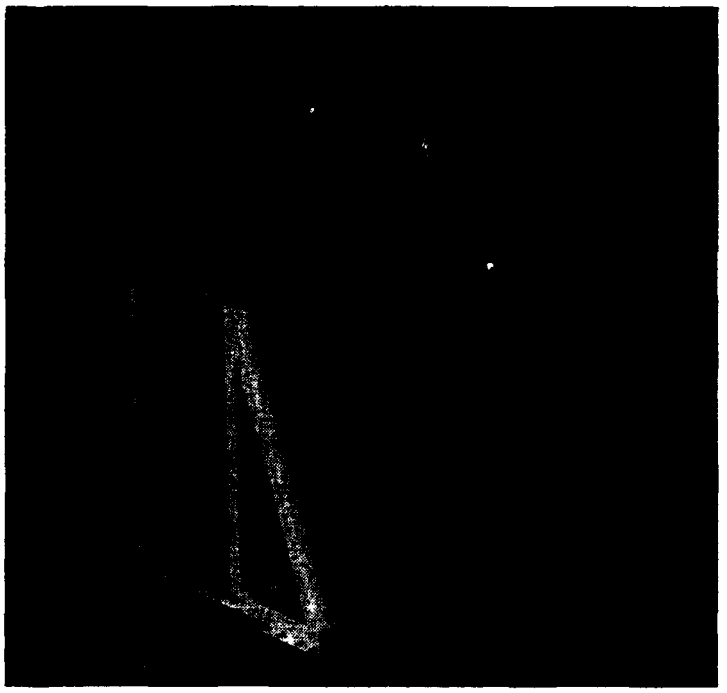


Figure 3. The CLIA Accelerator and PFLs.

The CLIA system uses various thicknesses of Metglas 2605CO material throughout. As the speed of saturation increases, thinner material is used to maintain a low loss system. Table I shows the characteristics of the various switch, transformer, and accelerator cores.

	Nominal Thickness μm	Insulation	Core ID cm	Core OD cm	Turns	Cores	Total Metglas kg
Accelerator	25	3.5 μm Mylar	22	39	1	10	240
Output Switch	25	12 μm paper	5	13	1	4 by 10	107
2nd Stage Switch	33	12 μm paper	11	20	2	6	30
Transformer	33	12 μm paper	22	37	2:1	6	101
1st Stage Switch	40	8 μm paper	9	18	2	9	48

Table I. Metglas core data for CLIA

Reset

In order to provide the highest possible flux swing, magnetic cores must be reset by passing a current through them opposite to the pulsed current before voltage is applied. There are two basic methods of providing this current, pulsed and dc. For the CLIA system, we chose a dc reset scheme for its simplicity. Two connection points were necessary for the CLIA system because there is a transformer with paths to ground between two magnetic switches. A connection immediately after the second thyratron switch provides current to reset the magnetic assist switch,

the first stage MCU switch, and the primary of the transformer. A second connection at the point between the water capacitor and the second stage switch provides current to reset the secondary of the transformer, the second stage switch, the PFL output switches, and the accelerator cores. This reset circuit must provide current to 11 different paths to ground. Thin-wall stainless-steel tubing was used to make some of the components in this region of the modulator. This ensures that sufficient voltage is developed to reset each core in each of the parallel paths when the other cores have all been reset.

During testing, various reset current levels were used at various voltage and repetition rates. If insufficient current was used to reset the accelerator cores, an interesting effect was observed. The output pulse would gently degrade pulse-by-pulse over the span of about 50 pulses until it disappeared. The effect of insufficient reset was not immediate on the next pulse but was a cumulative effect over many pulses. Our higher power runs used reset currents of 500 A dc at the second location (about 50 amperes per core) and about 50 A-dc at the first.

Summary of Operation and Future Work

The full CLIA system has been in operation for over a year and has experienced very few problems. It has been used primarily as a 100-Hz, 1-second burst generator to test a variety of front end loads. Some longer runs have been performed, such as a 50 second run at 100 Hz. We have also run the system at 250 Hz for 1 second. To test the reset scheme and load recovery, we have run at 1 kHz for three to five pulses. At this 1 ms separation between pulses, the dc power supply could not recharge the filter bank and the second and third pulses were much lower in amplitude, but we saw no unusual effects from the high repetition rate. In general, the system has performed very well.

The next step is to extend the pulse length of CLIA to 100 ns from the 60 ns at which it presently runs. This will require only a change to the output switches and PFLs since the rest of the system has been designed with this eventual extension of the pulse length in mind.

Acknowledgements

The authors would like to thank Steve Hogue and Ron Shaw for their expertise in assembling and operating the CLIA system. Thanks are also due R. Hitchcock and S. Ball for their technical work in the early stages of the program.

References:

1. T. Warren, *et al.*, "High-Power Testing of the EEV CX1936 and CX1937 Thyratrons," Nineteenth Power Modulator Symposium, June 1990, San Diego, CA, p 302.
2. H. C. Harjes, *et al.*, "Investigations into the Design of Multi-terawatt Magnetic Switches," Sixth IEEE Pulsed Power Conference, June 1987, Arlington, VA, p 540.
3. S. Ashby, *et al.*, "CLIA- A Compact Linear Induction Accelerator," Nineteenth Power Modulator Symposium, June 1990, San Diego, CA, p 137.
4. N. Aiello, *et al.*, "High Power Microwave Generation at High Repetition Rates" (this conference).

THE LELIA INDUCTION INJECTOR : FIRST RESULTS

J.BARDY, P. ANTHOUARD, P. EYHARTS, P. EYL, M. THEVENOT,
A. ROQUES, D. VILLATE

Centre d'Etudes Scientifiques et Techniques d'Aquitaine
Commissariat à l'Energie Atomique,
B.P. n° 2 - 33114 LE BARP (France)

1. INTRODUCTION

LELIA is an induction accelerator designed and built at CESTA for FEL applications.

The objective of this program is to produce a high- brightness and high-average-power electron beam [1]. An injector (1.5 MeV, 1.5 kA, 50 ns flat top pulse) is now under test. It uses an Osmium dispenser cathode and ten induction cells driven by a high voltage pulse generator (150 kV, 60 ns, 2 Ω) [2]. It is able to work at high repetition rate (1 KHz).

Initial operation began in June last year. Beam characteristics have been measured and compared with numerical simulations.

New beam diagnostics (B.Loop, emittancemeter, energy spectrometer ...) have been developed.

A twelve cells accelerating module is also being built taking into account guiding and stability problems.

The stretched-wire technique is used for magnetic alignement of the focusing coils.

The PALAS computer code has been written to calculate the transverse impedance of the accelerating cell.

We plan to have an accelerator working in a few months at 3 MeV energy level.

In this paper, we present first results and discuss future development.

2. INJECTOR DESIGN AND ENGINEERING

2.1. Induction cells

LELIA injector consists of ten induction cells (fig. 1).

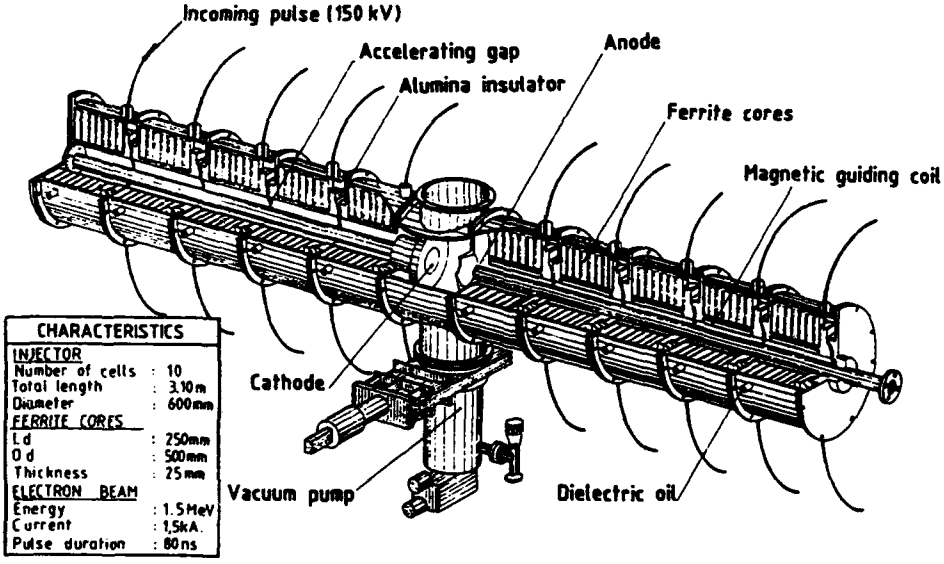


Figure 1 : LELIA injector

Each cell comprises seven TDK PE 11 B ferrite cores (250 mm I.D., 500 mm O.D. and 25.4 mm thick) housed in a non magnetic stainless steel body. Oil is used as dielectric and cooling fluid surrounding the ferrites.

The beam pipe diameter is about 185 mm and the accelerating gap is 8 mm wide. A pure alumina insulator brazed on the cell provides the vacuum oil interface. This technology eliminates any possibility of cathode poisoning by hydrocarbons.

The gap shape is curved to prevent induced breakdown by shielding insulator from electron beam ; it has been designed with FLUX-2D electrostatic code in order to limit electric stress to 200 kV/cm.

For beam transport, cells located in front of the cathode are provided with a solenoid capable of producing a 2 kG axial magnetic field; wrapped around the solenoid is a printed circuit correction coil.

Injector cells are assembled using flanges specially designed to allow a mechanical alignment better than 1 mm. The vacuum tightness is ensured by a metal gasket consisting of a slotted tubular aluminum ring backed up with a spring.

The high voltage pulse is applied to each cell on two opposite sides by two 100 Ω coaxial cables.

2.2. Electron gun

The electron gun is a triode configuration consisting of cathode, intermediate electrode and anode ; it has been optimized using FLUX-2D, SLAC and TETHYS numerical codes.

The cathode is a 85 mm osmium coated dispenser cathode surrounded by a focusing electrode ; it is mounted on a metal stalk and placed at the middle of the injector. The distance between cathode and intermediate electrode can be adjusted from 25 to 75 mm without breaking vacuum in the injector.

The anode pipe, 92 mm in diameter, is located 50 mm from the intermediate electrode.

2.3. Vacuum system

The vacuum inside the injector is ensured by two 4500 l/s cryogenic pumps associated with a turbomolecular pump for rough vacuum.

In operation (with cathode hot) the pressure was easily maintained at 10^{-3} torr and no presence of hydrocarbons was detected by mass spectrometer. This vacuum quality indicates that our mechanical choices are very effective and consistent with the use of a dispenser cathode.

3. EXPERIMENTAL RESULTS

Injector assembly began by the end of 1990 ; three months later, a first electrical characterization performed with a cable pulser allowed to :

- test electrical individual response of each induction cell up to 180 kV without any breakdown.

- observe voltage addition across the injector thanks to a 1000 Ohms resistive load placed between anode and cathode stalks.

Then, mechanical and magnetic alignments were checked using the stretched wire technique.

3.1. Cathode current

After a step by step cathode heating (thermal activation of the baryum and calcium oxides) up to 1200 °C, with an I.R. camera monitoring of the cathode surface temperature, the first electrical tests began using our cable pulser. Single shot operation under 100 to 350 kV accelerating voltage allowed to observe first cathode emission; 1 Hz burst operation completed this electrical activation and an experimental curve plotting cathode current I_k versus heating temperature Θ_k established the efficiency of this process : a knee determines the transition between emission limited and space charge limited operation, where temperature inhomogneities present less influence.

Electrical voltage testing grew up to 800 kV with the cable pulser, then to 1900 kV with the MAG generator and a second curve $I_k(\Theta_k)$ was constructed at 1.3 MV accelerating voltage (Fig 2).

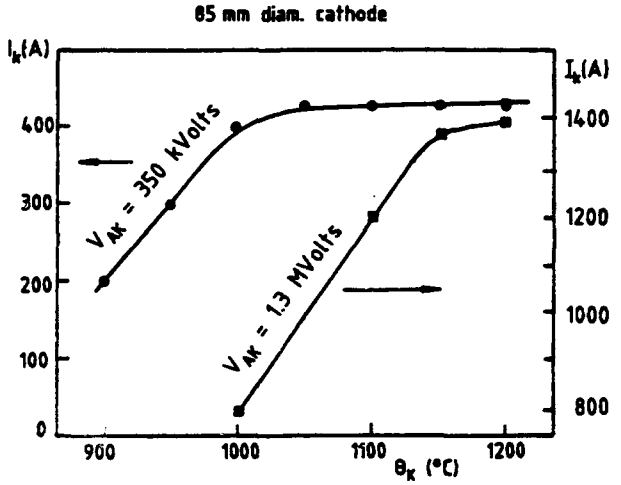


Figure 2 : Cathode formation Emitted current versus temperature

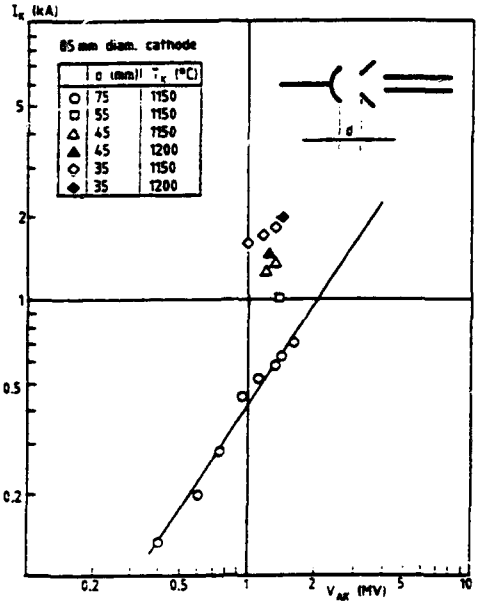


Figure 3 : Cathode current vs accelerating voltage

Fixing Θ_k = 1150° C and D = 110 mm for anode cathode spacing, a curve I_k versus V_{AK} drawn in logarithmic coordinates gave a straight line with a slope 1.3 very close to those predicted for space charge limited operation governed by Child's law $I_k = kV^{3/2}$ (Fig 3).

3.2. Injector current

The current I_k emitted from the cathode must be transported through the anode stalk along 1.5 m before being effectively extracted from the injector. Current probes integrated into the intermediate electrode and in the beam pipe at the injector output allow a comparison between I_k and injector current I_s ; the ratio I_s/I_k depends closely on magnetic guiding and electrode geometry. As predicted by PIC code TETHYS, anode internal diameter is too narrow and a part of the beam is lost on anode wall (fig.4) ; a compromise is to be found: a large anode cathode spacing D allows an efficient transport (I_s/I_k > 90 %) but the cathode emission current decreases when D grows up. By now, maximum emission current I_k has been 2.6 kA, at the lowest anode cathode spacing, but the highest current extracted from the injector has been 1.4 kA, obtained with D = 105 mm. Magnetic guiding and ratio I_s/I_k predicted by numerical codes have been in good agreement with experimental results. A new anode has been designed and will be tested in a near future.

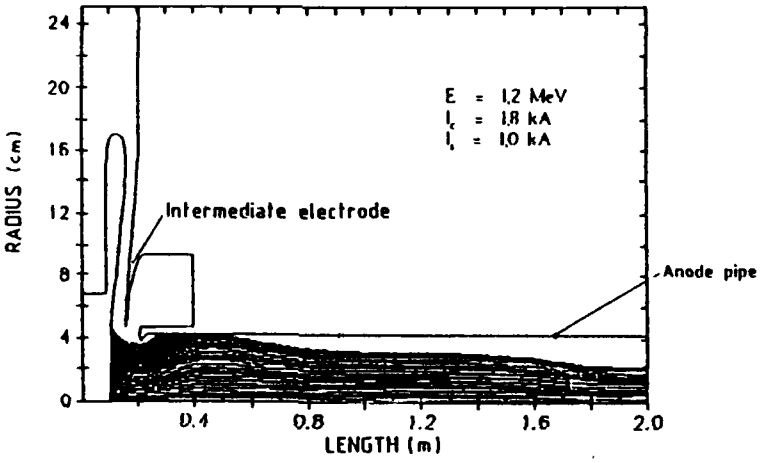


Figure 4 **LELIA INJECTOR**
Electron beam trajectories (TETHYS code)

3.3. Energy spectrum

A magnetic spectrometer placed at the injector output characterized the electron beam; reproducibility has been demonstrated at 1.1 MeV peak electron density (and 1.2 MeV maximum energy) ; Fig 5 shows a typical spectrum: the accelerating voltage quality is characterized by the half width of the peak on the high energy side. The maximum peak energy has been measured at 1.36 MeV.

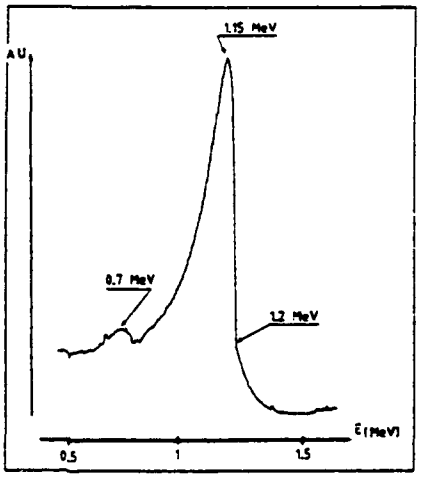


Figure 5 : LELIA injector: energy spectrum

3.4. Emittance. Brightness

Measurements have been performed at 1.3 MV accelerating voltage and 1 kA beam current using pepper pot technique. The measured emittance ϵ was close to 200 π.mm.mrad on the two axis, leading to a normalized brightness Bn = 5 10^8 A/m^2.rad^2.

3.5. Beam stability

Beam centroïd position is measured with four "B loop" probes; these measurements have indicated a good stability, all the more so that correction coils have not still been used : peak to peak amplitude of the beam centroïd motion was around 2 mm on each transverse axis over approximately 25 ns, indicating a relativaly low corkscrew instability.

4. ACCELERATING MODULE

A twelve induction cell accelerating module is under construction and will operate simultaneously with the injector by the end of 1992. Accelerator cell differs from the injector one in several points.

4.1. High voltage design

Gap shape has been design thanks to FLUX 2D numerical code in order to limit electric field to 200 kV/cm on metallic surfaces and 50 kV/cm along the alumine surface.

4.2. Cell transverse impedance

The B.B.U. instability results in high frequency transverse oscillation of the electron beam.

Growth factor depends on transverse impedance which is a function of gap geometry and materials ; in particular, ferrite torroïds may play a useful damping role.

The PALAS numerical code [3] was used to calculate the transverse impedance of our accelerator cell (fig. 6) ; first results were compared with AMOS calculations on pill box and LELIA injector prototype cell [4].

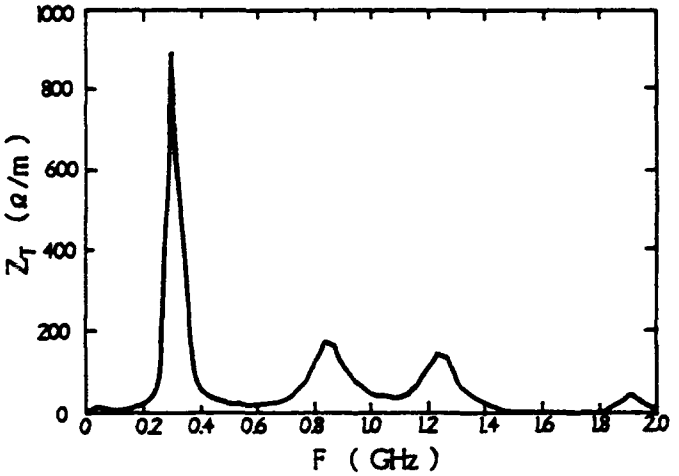


Fig. 6 Transverse impedance of accelerating cells.

An experimental method is under development at CESTA in order to measure induction cell transverse impedance.

5. CONCLUSION

First results on LELIA Induction Injector have demonstrated a 1.3 MeV, 1kA single shot operation with a high brightness beam. An important work is still necessary to improve higher repetition rate and higher voltage operation of the cells.

A 12 induction cell accelerating module is under construction and will be assembled and tested by the end of 1992 to reach 3 MeV energy level.

Meanwhile, our ONDINE F.E.L. experiment at 35 GHz is under assembly ; coupling with LELIA Injector is expected before June 1992.

6. REFERENCES

[1] Ph. Eyharts, J. Bardy, Ph. Anthouard, P. Eyl, M. Thevenot

LELIA : An Induction Linac developed for FEL Application.
Proceedings of the 1991 PAC, May 6-9, 1991,San Francisco, Ca Volume 5, p.3204-3206.

[2] M. Thevenot, P. Eyl, Ph. Anthouard.

Magnetic Compressor Studies for FEL Applications at the "Centre d'Etudes Scientifiques et Techniques d'Aquitaine".
90 International Magnetic Pulse Compression Workshop, February 12-14,1990, Granlibakken Lake Tahoe, California.

[3] A. Aregba, P. Lacoste

Le Code PALAS
CISI Ingénierie
CEA-CESTA/ LE BARP - FRANCE

[4] J.F. de FORD

AMOS simulation of CESTA prototype induction cell. Beam Research Program (LLNL), August 1990 - Private communication.

HIGH-CURRENT LINEAR ACCELERATOR

A.G. Mosgovoy

P.N. Lebedev Physical Institute
117924, Leninsky Prosp. 53, Moscow, Russia

Abstract

A pulsed linear accelerator for an energy of tens of MeV and beam current of tens of kA and pulse duration of tens of nanoseconds is described. The accelerating section, located in a common tank and joined by drift chambers, are fed by cables from a single source — a powerful pulse-forming line. Synchronisation is achieved by proper choice of cable lengths.

The construction of high-current linear accelerators for an energy of tens of MeV and pulse current of tens of kA is a timely task. For this purpose, induction or radial-line accelerators are used. Each has its advantages and disadvantages. In induction machines, ferromagnetic cores, constituting a considerable part of the overall cost of the facility, are used. A radial-line accelerator because of the low impedance of the line itself has a stored energy that is very large and, moreover, requires strict synchronisation in the operation of the multi-spark switches in every sector.

In many laboratories, there exists a high-current accelerator with low-ohmic pulse-forming line and a voltage of the order of one megavolt, current-hundreds of kiloamperes, and pulse duration of several tens of nanoseconds. If for physical experiments a beam with an energy of the order of 10 MeV and current of several kiloamperes (in particular, for experiments with FEL) is required, an accelerator-adder using a low-ohm generator appears promising. One such device is a cable transformer, where to a powerful high-voltage pulse source there are connected in parallel several cables, the outputs of which are connected in series via inductive coupling. In this manner voltages are added. But here too the maximum voltage will be limited by the electrical strength of the various elements, particularly the vacuum chamber insulator.

It was proposed in [1] to excite a radial line from the central part of a bipolar pulse with accelerated beam at the second half-wave. To obtain a pulse duration of several tens of nanoseconds, it is desirable to fill the line with a liquid having a high ε, e.g., water. But this leads to a decrease in the characteristic impedance of the line by a factor of $\sqrt{\varepsilon}$.

The scheme of the accelerator is shown in Fig.1. In such a scheme, a radial line is transformed to the limit and constitutes a practically symmetrical dipole, each arm of which is a drift chamber of the beam. The characteristic impedance of such a dipole can be estimated by means of

$$Z = \frac{120}{\sqrt{\varepsilon}} \cdot (\ln \frac{l}{2r} - 0.69)$$

where l is the length of a dipole and r is its outer radius. This characteristic impedance determines the losses of energy removed by the electromagnetic field. To obtain high values

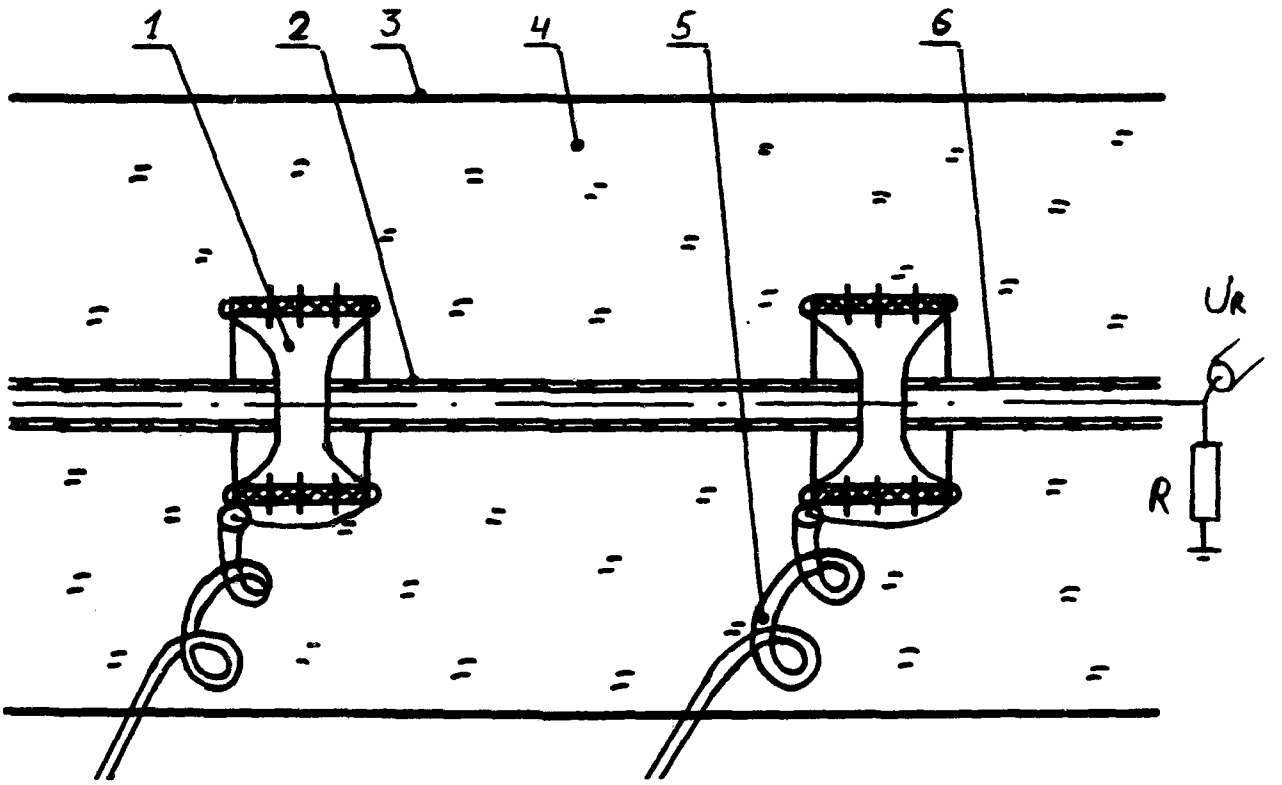


Fig.1. The scheme of the accelerator:
(1)–accelerating sections with a high-voltage sectionalised insulator,
(2)–drift chamber, (3)–accelerator tank, (4)–liquid dielectric,
(5)–high-voltage cables, (6)–thin-layer solenoid.

of Z (20–25 Ohm), it is necessary to select drift chambers with small values of r (1–2 cm), and use two high-voltage cables with a characteristic impedance of $\rho = 25$ Ohm, which permits transfer to the beam of about 50% of supplied power.

The high-voltage cable for feeding the sections should form a spiral having an inductance $L \approx 3\rho\tau$ in order to decrease the shunting effect of the cable jacket. The thin-layer solenoid (6) creates a longitudinal magnetic field providing beam transport.

The accelerator functions in the following manner. From a powerful high-voltage generator, a voltage pulse of duration $\tau = 20 - 50\ ns$ is fed by cables to every accelerating section (1). The length of the cables are selected in such a manner so that the instant of beam arrival at the accelerating section coincides with the instant of appearance of voltage at the cable output, i.e., synchronization is achieved by properly increasing the lengths of the cable feeders.To match a cable with the load, it is necessary to satisfy the condition

$$\rho = \frac{Z \cdot R}{Z + R}$$

where R is the equivalent resistance of the beam. Then, the voltage at the accelerating section is equal in amplitude to the pulse of voltage in the cable. The maximum pulse

duration will be limited by the diameter of the cylindrical tank and the distance between accelerating sections. For a given pulse duration τ, the tank diameter D and the drift chamber length l can be determined from the simple, evident relation

$$D \approx c \cdot \tau / \sqrt{\epsilon}, \qquad l = 0.5 \cdot D.$$

Pulse duration and impedance of the section may be increased $\sqrt{\mu}$ times by using ferromagnetic cores, but in this case the proposed scheme becomes similar to a usual induction accelerator.

The maximum rate of acceleration can reach 1 MV/m if one can obtain a sufficiently flexible cable withstanding 500 kV pulses. Such a cable, having an outer diameter of 30 mm, was successfully tested at an amplitude of 300 kV and 1 μs pulse duration.

Experimental confirmation of the realization of the proposed scheme was obtained on a model of the accelerator. In a cylindrical tank of 1-m diameter and 1.2-m length, filled with de-ionized water, there were placed two accelerator sections, fed by two cables from a single generator. A pulse of 30 ns duration was applied to the accelerating gaps. The beam was simulated by a conductor passed through the drift chamber, one end of which was at ground potential and the other loaded by a resistor R. The voltage from the load was measured by means of an oscilloscope. In Fig. 2 are shown two oscillograms: (a) the voltage on R when feeding one section and (b) the voltage on R when simultaneously feeding two sections. Thus, applying voltage to both sections leads to doubling the voltage on the load and the duration of this pulse is equal to the duration of that applied.

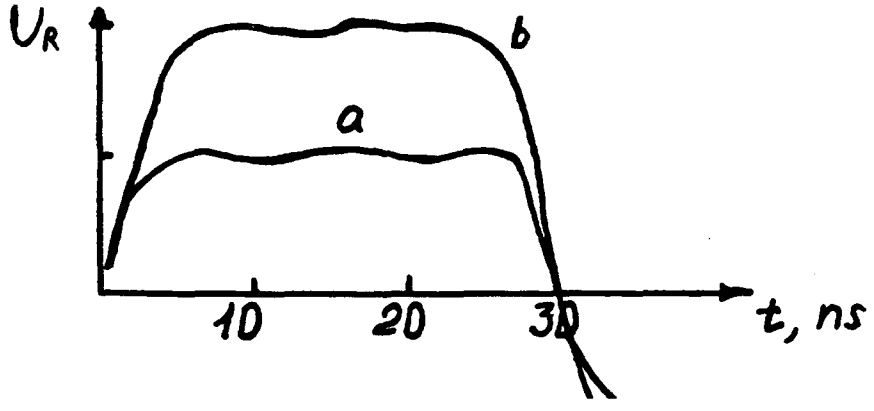


Fig.2. The voltage on R vs time when feeding:
(a) – one section, (b) – two sections.

The proposed scheme may be preferable to others when a quick and cheap method of obtaining a beam whose quality need not be very high. Moreover, it is of interest for use in summing voltages on magnetic insulation transmision lines.

References

1. Smith J. Rev. Sci. Instrum., vol. 50, No 6, p. 714-718.

RECENT ADVANCES IN INDUCTION ACCELERATION AND POSTACCELERATION OF HIGH-CURRENT BEAMS AT TOMSK NUCLEAR PHYSICS INSTITUTE

V.V.Vasiljev, I.B.Ivanov, G.G.Kanaev, O.N.Tomskikh, Yu.P.Usov, E.G.Furman

Nuclear Physics Institute of Tomsk Polytechnical University,634050,Tomsk,P.O.Box 25,RUSSIA

In Tomsk Nuclear Physics Institute (NPI) work on designing high power electron beam accelerators has been going on since 1970[1]. Since 1975 NPI has been working also on the development of the cell base of linear induction accelerators (LIA) and creation of installations for research and industry. The main advantage and the principle difference of LIAs from direct accelerators consists in the possibility to decrease the size of the device and the absence of limitations on the maximum energy of accelerated particles[2].

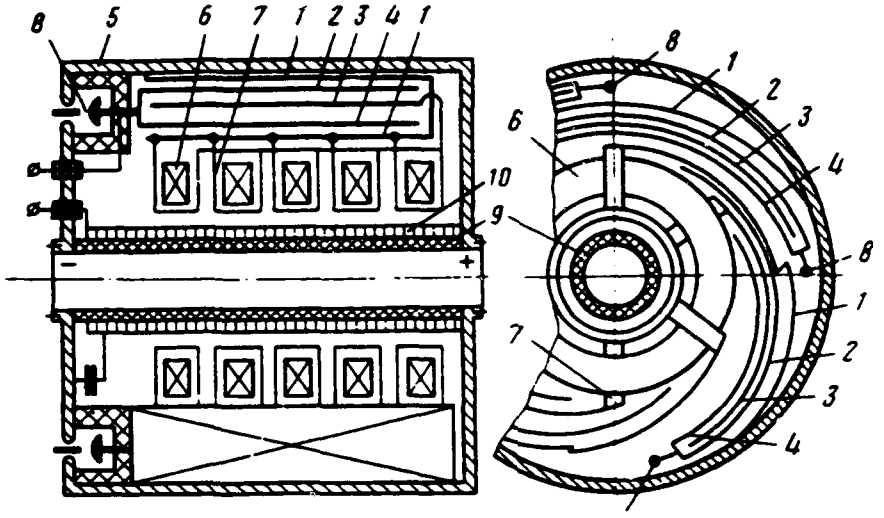


Fig. 1. LIAs module: 1-4 DFL electrodes; 5- module body; 6 - ferromagnetic core; 7 - toroidal coil; 8 - multi-channel spark gaps; 9- insulator; 10 - demagnetize and focusing coil.

The NPI's LIAs are based on the novel module structure, fig.1. The module combines a ferromegnetic induction system, a pulse generator on the base of low impedance strip pulse-forming double line (DFL) with solid insulation and high current multi-channel spark gaps or magnetic switches, joined systems of demagnetization and formation of axial focusing magnetic field.

The ferromagnetic induction system of LIA module is formed from 7 to 20 inductors. The toroidal coil serves to load the strip DFL with the impedance of fractions of Ohm[3]. The strip DFL is broken into a number of (2 to 8) parallel lines. The live electrodes of the lines are connected with multi-channel spark gas switch. The lines go above the inductors following the spiral. All the high voltage elements of the system are submerged into transformer oil. For pulse charging due to low conductivity layers the growth of the electrical field strength on the margins of strip DFL is virtually eliminated as compared to the unifirm. By this we reach the working field strength in the insulation nearly 40 kV/mm, which provides the energy storage in the lines competing with the best pulse capaci - tors known.

For DFL charging voltages of 60 to 70 kV the multi-channel spark switch commutes the current of the order of megaampers. In order to distribute the current into the channels evenly (their number varying for different arrangements from 18 to 24)[4], use is made of the forced current division by means of an anode divider. The latter is made up of ferromagnetic cores with a common shortcircuited coil. The usage of the anode di - vider allowed us to decrease the switch time jitter in the channels up to 0.5 ns.

A new type of controlled cathode[5] was used in NPI's LIAs. Its operation is based on the following principle: the electron charge needed for the formation of pulse electron beam is stored on the surface of the dielectric emitter (DE) during the DFL charge time. The charge is retained by the coulomb forces of the positive charge of the opposite metallic coating of DE. When a voltage accelerating pulse is applied to the cathode-anode gap the electrons stored on the DE surface are extracted to form the electron beam. Since the electrons are bound to the DE surface only by the electric fields near the cathode and the electron traps, the output electron energy from the cathode is as low as 1 eV. As to the Q-factor of the electron beam formed, the emitter is as efficient as thermocathode, mo-

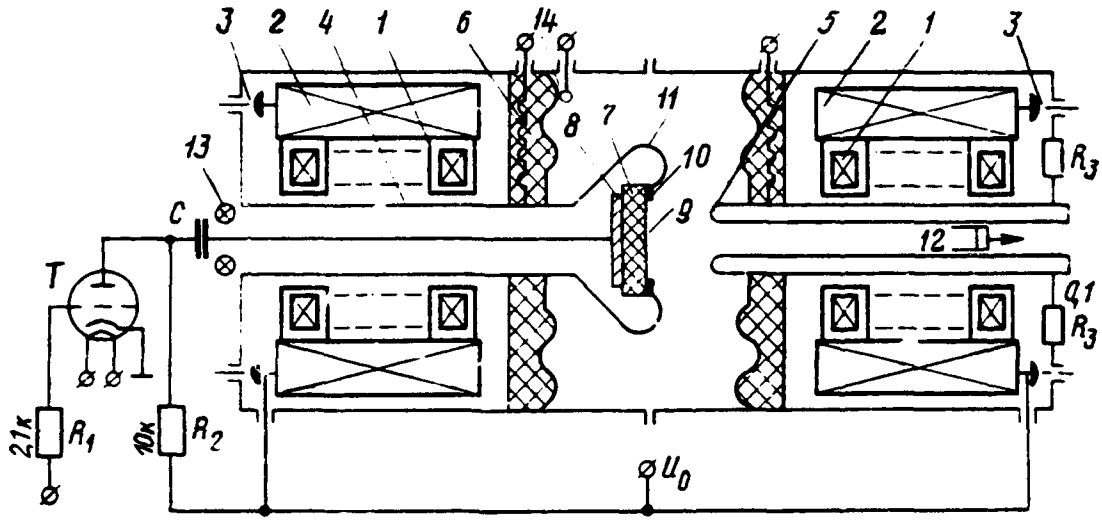


Fig. 2. Scheme of DE testing. 1 - ferromagnetic core; 2 - DFL; 3 - multi-channel spark gaps; 4 - cathode holder; 5 - drift tube; 6-demagnetizing coil; 7 - ceramics disk; 8 - mettallic coating; 9 - DE; 10 - toroidal electrode; 11 - focusing electrode; 12 - Faraday-cup; 13 - Rogowski-coil; 14 - B-loop.

reover it requires neither high vacuum nor heating. The emitter was tested on the LIA injector, whose schematics is drawn in fig. 2. The injector consists of two parts: the cathode and anode sections. The emitter is a disc made of ceramics ($\mathcal{E}$ = = 1300) with metallic coating. Upon switching the pulse gene - rator the charging of DFL is begun. A voltage is simultaneously applied to the DE coating through R_2C. When the electric field strength reaches its critical value, on the sharp margin of the toroidal electrode there appears spontaneous emissive current, ensuring the charge to be stored on the DE surface. The extraction of the accumulated charge and the formation of the beam occurs upon switching the gap and applying the accelerating voltage pulse. For the accelerating voltage of 400 kV, the beam current was 1.5 kA. The magnetic field was 1500 gs in the drift tube, 150 gs on the anode and 20 gs on the cathode. The beam was formed from the cathode 80 mm in diameter, then it was compressed in the growing magnetic field up to 15 mm and was transported to the distance of 1 m without any losses.

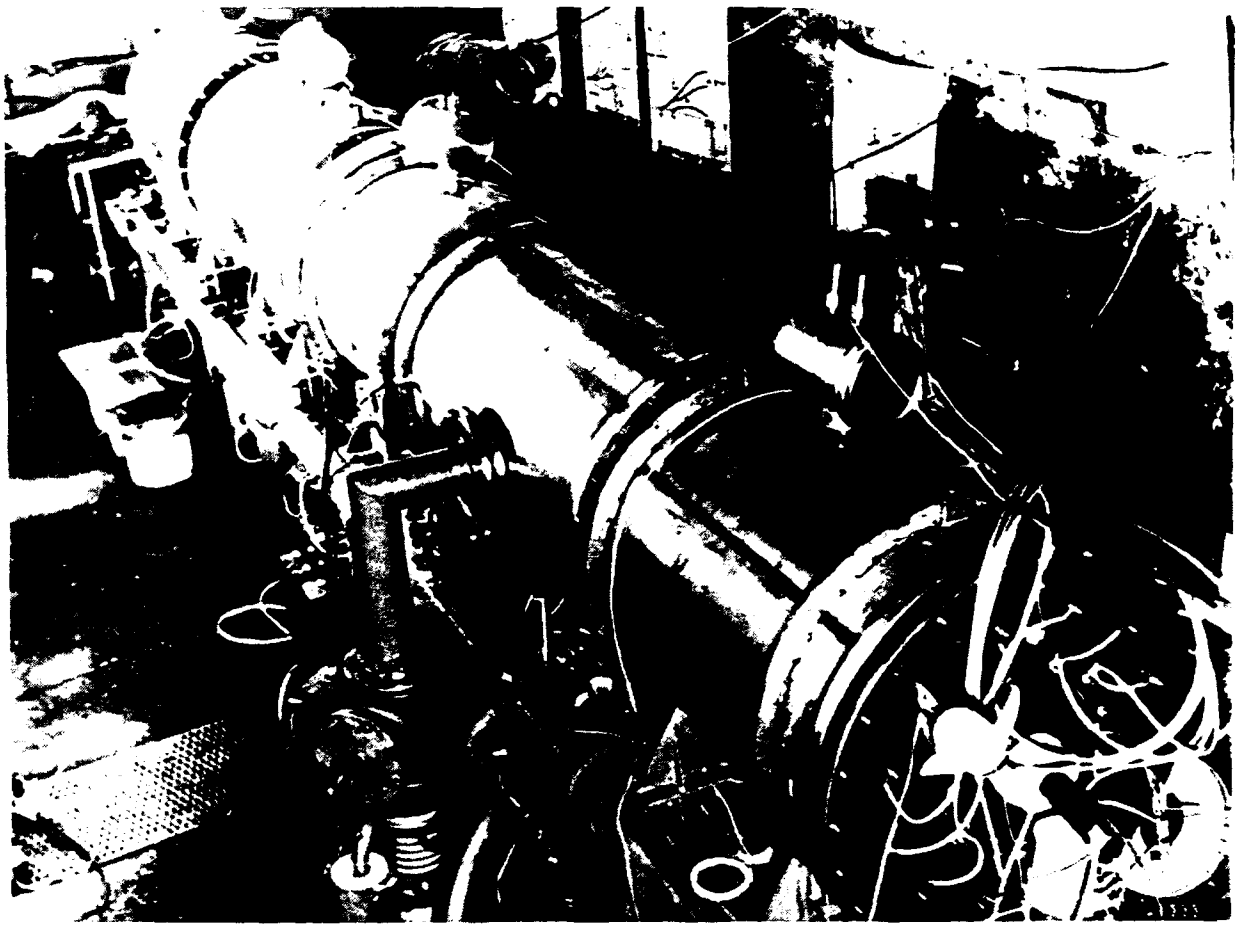


Fig. 3. LIA 4/2, 4 MV, 2 kA, 80 ns.

The density of the current from DE was 30 A/cm^2 which is not the limit.

LIA 4/2 (4 MV, 2 kA) is one of the most powerful accelerators of its kind constructed in NPI, fig. 3. The initial part of the accelerator is made up of two injecting and two accelerating sections and serves to form the beam with the current of 2 kA, the energy of 4 MeV, the pulse duration at half width of 80 ns. A characteristic feature of the accelerator is the usage of magnetic switches (MS) to commutate DFL, which makes it possible to form beam séries at a frequency of 3.3 kHz with the pulse repetition rate of 10 Hz fig. 4. MS is placed, similarly to the spark gap, at the end of the section and it has approximately the same size and therefore the same inductivity. To ensure the minimum charge time of DFL, use was made of magnetic pulse generators (MPG). Each pair of the sections is char-

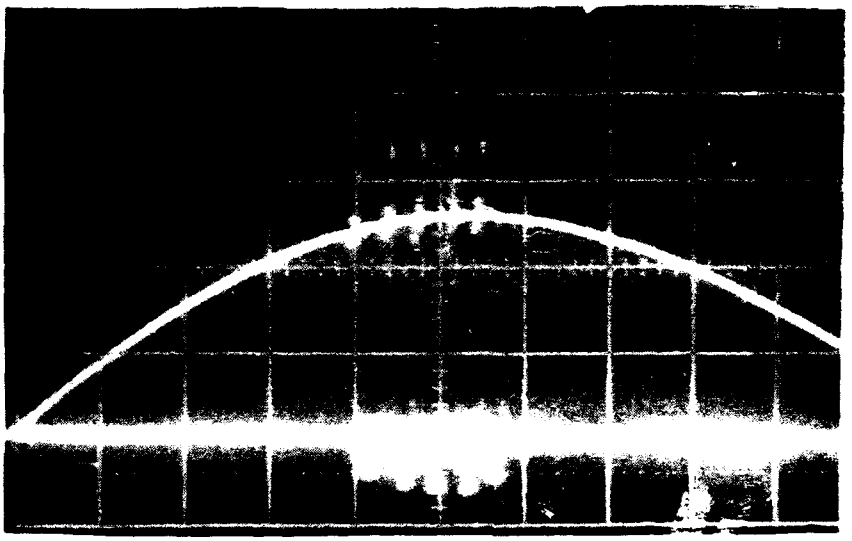


Fig. 4. Oscillograms of the focusing current and the beam series at a frequency of 3.3 kHz.

ged by a single MPG consisting of three compression stages.

In the above accelerator the phase locking of the accelerating modules is done by an electron beam injected from the controlled DE. This provides the operation mode of the accelerator when the inductivity of the circuit "switch - DFL" does not affect the front edge and temporal parameters of the beam, but is determined only by the electric line length and the impedance of the load, i.e. the electron beam.

The additional phase-locking of MPGs working concurrently is done by the anode divider similar to the ones used in multi - channel switches.

Employment of the induction sections of LIA expands the performance feasibilities of high current accelerators of direct action by transforming the accelerating voltage pulse into low- or high-impedance modes. Work has been carried out in NPI to study the performance of a direct action accelerator with an induction section operating in the mode of multiplying the voltage on the matched load Z with the transformation coefficient $K_V = 2$ and amplifying the current with $K_C = 2$ to 3, fig. 5.The induction section works similarly to the autoconnected trans - former. The direction of toroidal coils wrapping is chosen such that in the case of voltage multiplication the electromotive force induced in the coils is added to the generator's voltage, and in the case of current amplification the current induced is added to the generator's current.

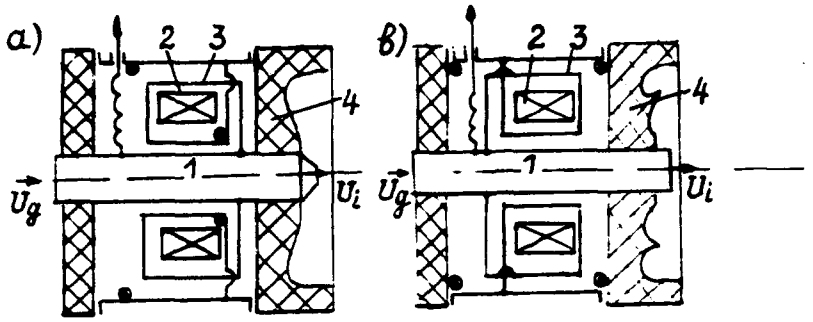


Fig. 5. An induction section operating in the mode of amplitying the current a) and in the mode of multiplying the voltage b) 1 - cathodeholder, 2 - induction section, 3 - toroidal coil, 4 - insulator.

The primary accelerating voltage pulse of the VERA-accelerator had the following parameters: the voltage amplitude U_g = 350 - -650 kV, the pulse duration T = = 80 ns, the generators impedance ρ = 8 Ohm. To vary the magnetic flux in the induction section in a wider range the ferromagnetic cores had been preliminary overmagnetized.

The results of the tests are shown in the table 1, where U_i, I_s is the output idle voltage and shortcircuited current, Δ I is the magnetization current, P is the maximum power, η is the efficiency, $Z = \rho K_v^2$ in voltage mode and $Z = \rho/K_c^2$ - in current mode.

Table 1.

Mode	U_g,kV	U_i,kV	I_s,kA	Z,Ohm	Δ I,kA	P·10^{10},W	η
K_v = 2	350	630	20	32	2 ÷ 3	1.1÷1.2	0.9
K_v = 2	450	750	28	32	3 ÷ 5	0.8-1	0.7
K = 1	640	640	80	8	-	1,3	1
K_c = 2	640	310	150	2	2 ÷ 3	1.1÷1.2	0.95
K_c = 3	640	200	210	0.9	5 ÷ 7	5÷7	0.9

REFERENCES

1. Didenko A.N."High power electron beams..." M.,Atomiz.,1977.
2. Vasiljev V.V. et al. PTE, No 5, 223, 1988.
3. Furman E.G. PTE, No 5, 26, 1987.
4. Furman E.G., Vasiljev V.V. PTE, No 1, 111, 1988.
5. Tomskikh O.N., Furman E.G. PTE, No 5, 136, 1991.

A 3. 4 MeV Linear Induction Accelerator

Cheng Nianan, Zhang Shouyun, and Tao Zucong

China Academy of Engineering Physics
P. O. Box 501 Chengdu, Sichuan 610003, China

ABSTRACT

A 3. 4 MeV linear induction accelerator has been built for use in free electron laser (FEL) research. This machine consists of a 1 MeV injector followed by eight accelerating induction cells. Each accelerating cell adds 300 kV to the electron beam. Eectron beam with the brightness of 2. 0 X 10^8 A/(m-rad)^2 has been produced. The beam current is 2. 0 kA and its radius is 2. 0 cm. The beam pulse length is 90 ns. The experiments ofthe self amplified spontaneous emission free electron laser (SASE-FEL) are being performed.

Introduction

A 3. 4 MeV linear induction accelerator (LIA) was built for free electron laser (FEL) research. This accelerator submits an electron beam with a prerequisite parameters for SG-1 FEL facility. An electron beam of 1. 5 kA with brightness better than 5×10^7 A/(m-rad)^2 was required[1]. This accelerator was designed in 1988 and finished in mid 1991. Using this machine a first round of self amplified spontaneous emission (SASE) FEL experiment is being conducted. This report will describe the construction of the accelerator, its operation characteristics and initial tests of FEL research.

construction of the accelerator

A 3. 4 MeV LIA is dipicted in Fig. 1. It is mounted in a two— floor hall. The upper part is the beam accelerating cell and the lower part is the pulse power system (Fig. 2). This accelerator consists of a 4 cell injector followd by 8 accelerating cells. The injector has a cathode stalk to sum up the voltage of 4 cells to a single field emission diode. The diode configuration was designed by numerical simulation. Using a velvet cathode and tungsten mesh anode, it has produced a beam current of 3 kA with a brightness of 2. 0×10^8 A/(m-rad)^2[2]. Each accelerating cell contains 14

ferrite rings with a magnetic characteristics of $B_s > 0.38T$ and $B_r > 2.8T$. It produces an electric pulse of 60 ns (flat top) and 300kV. In each cell there is a magnetic solenoide for beam transportation. The pulse power system consists of 2 Marx generators, 12 water Blumleins and a 3-stage switching system. Each Marx generator charges 6 water Blumleins. For keeping time synchronization a 3-stage coaxil gas switching system was developed to drive 12 blumlein switches. Fig. 3 is the block diagram of the switching system.

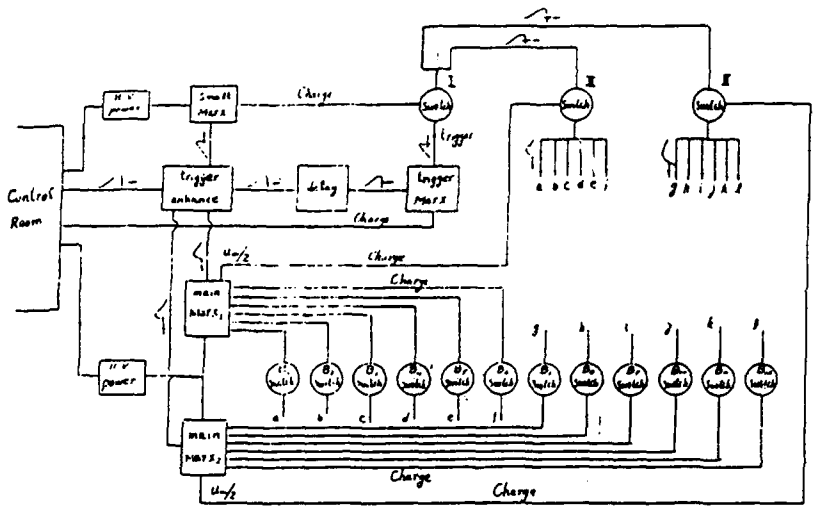


Fig. 3 Block diagram of control system

Operation characteristics

For a stable accelerator operation three points must be well-disposed:

(1) Precise alignment of the magnetic field over the length of the accelerator is an important factor for stable beam transport. The machine axis was defined accurately with help of a H_e-N_e laser.

(2) By properly regulating the magnetic field in each cell the electron beam produced by injector has been accelerated through the rest 8 cells to a final energy of 3.4 MeV without serious loss its peak current and brightness.

(3) Difficulties in maintaining stable operation and precise synchronization of 12 Blumlein switches cause some energy vari— ation of the beam. Properly adjusting the mixed gas (SF_6-N_2) pressure in each switch the jitter for each switch can keep within 2 ns.

Now the machine is routinely operated with a beam parameters listed in table 1.

Table 1 Present operating parameters

Beam energy W_e	3. 4 MeV
Beam current I	2. 0 kA
Beam brightness B_n	1.1×10^8 A/(m-rad)^2
Energy spread $\Delta\gamma/\gamma$	3. 7%
Burst length τ	90 ns (FWHM)

Voltage and beam current are measured with capacitive probes and resistive current monitors respectively. A magnetic analyzer measures energy spread of the beam and a pepper pot plate is used to determine the brightness of beam.

Initial tests on FEL research

A first round of self amplified spontaneous emission free electron laser experiment is conducted using this accelerator. SG-1 FEL facility consists of 3. 4 MeV LIA, beam modulation section and wiggler interaction region as shown in Fig. 4. In the beam modulation section there are an emittance selector, an energy selector and

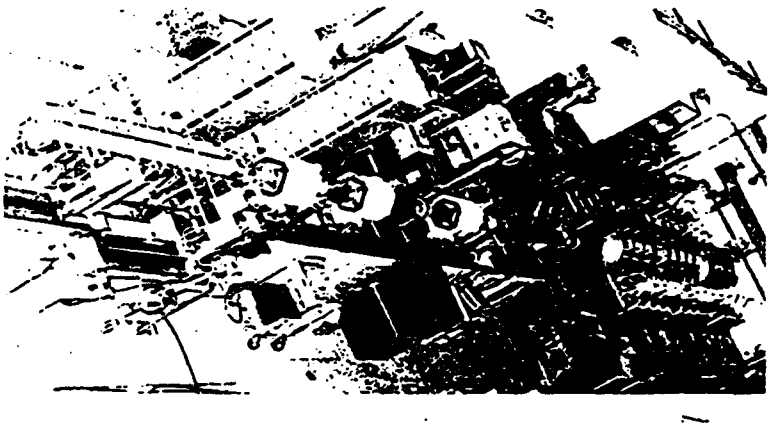


Fig. 4 Photograph of SG-1 FEL facility

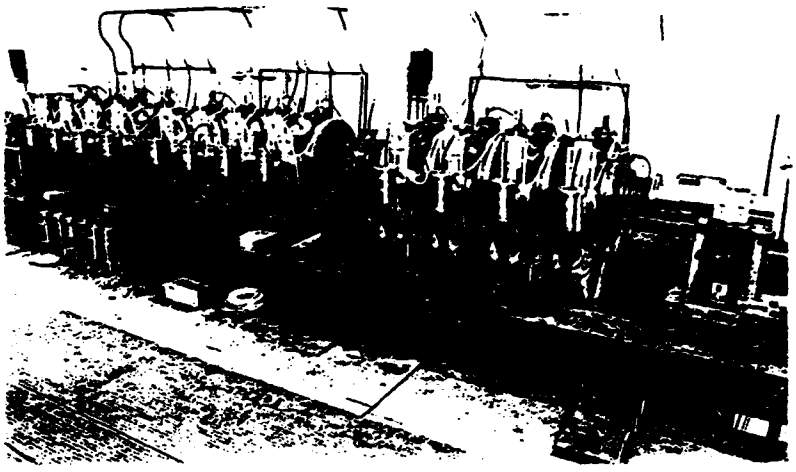


Fig. 1 Photograph of 3. 4 MeV LIA

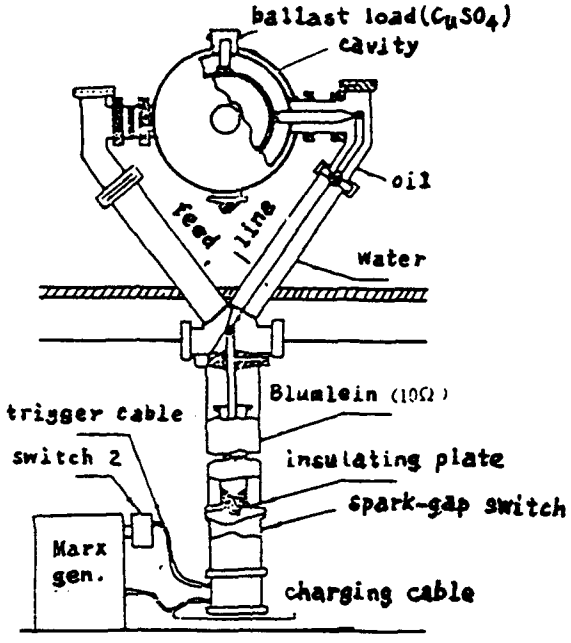


Fig. 2 Schematic of pulse power system

three pairs of quadrapole magnet to adjust the beam into the wiggler. The electromagnetic wiggler has a parabolic inner surface to confine the beam in two directions. The output microwave signal is detected by band filter diodes. The experimental parameters and initial results are listed in table 2. The obtained microwave of 700 mW and 35.5—36.0 GHz is confirmed as a SASE FEL output both experimentally and theoretically.

Table 2 Experimental parameters and initial results

Electron beam (into wiggler)	Wiggler	Wave guide	Output signal
We~3 MeV	L_w=2.64 m	a=9.8 cm	P=700 mW
I_b~100 A	λ_w=11 cm	b=2.9 cm	f=35.5-36.5GHz
τ=50 ns	B_w=2.6 kG	Mode: H_{01}	τ=30 ns

References

[1] Hui Zhongxi, High Power and Particle Beams, Vol. 2, No. 3, 257, (1991) (in chinese).

[2] Zhang Shouyun et. al., Proceedings of the IEEE Pulsed Power Conference, Monterey, CA, 1989, p47.

BEAM MATCHING INTO THE DARHT LINAC*

T. P. Hughes, Mission Research Corporation, Albuquerque, NM
D. C. Moir and R. L. Carlson, Los Alamos National Laboratory, Los Alamos, NM

Abstract

The DARHT (Dual-Axis Radiographic Hydro-Test) Facility is a large flash x-ray radiography facility to be built at Los Alamos National Laboratory (LANL). Prototyping of the beam injector and first block of eight accelerating cells is being carried out at the Intermediate Test Stand (ITS) at LANL. We have carried out numerical calculations using particle-in-cell and envelope codes to model initial beam transport experiments. The results agree reasonably well with experimental measurements of transported current and beam spot-size.

1. Introduction

The proposed DARHT facility [1] consists of two linear induction accelerators each of which produces a 3 kA, 16–20 MV electron beam pulse with a 60 ns flat-top. Each linac has 64 (eight blocks of eight) accelerating cells, where a cell consists of a solenoid with cosine-wound trim coils and a 250 kV accelerating gap [2]. The prototype assembled at the Intermediate Test Stand (ITS) has a 3 kA, 4 MV injector and eight accelerating cells. Experiments are being carried out to match the beam from the injector onto the transport solenoids, and to measure focused beam spot-size after the eight cells. In this paper, we compare results from these experiments to particle-in-cell simulations of the diode and extraction region, and to an envelope model of the transport through the cells.

2. Beam Extraction Experiments

A series of experiments was carried out measuring beam current transported to the first accelerating cell as a function of the extraction magnet strength (see Fig. 1). A flat 3" diameter velvet cathode was used, with an AK gap of 19.84 ± 0.05 cm. The diode voltage was 3.43 ± 0.05 MV. Beam current measurements were made at three locations: 26 (Beam Position Monitor 1), 84.2 (BPM2) and 243.6 cm (BPM3) from the cathode surface.

We modeled the injector with the particle-in-cell code ISIS. In the simulation code, the cathode diameter was 3.1", the AK gap was 20 cm, and the voltage was 3.42 MV. The beam current was calculated at 26, 84, and 243.5 cm from the cathode surface.

---

*Work performed under the auspices of the U.S. Department of Energy.

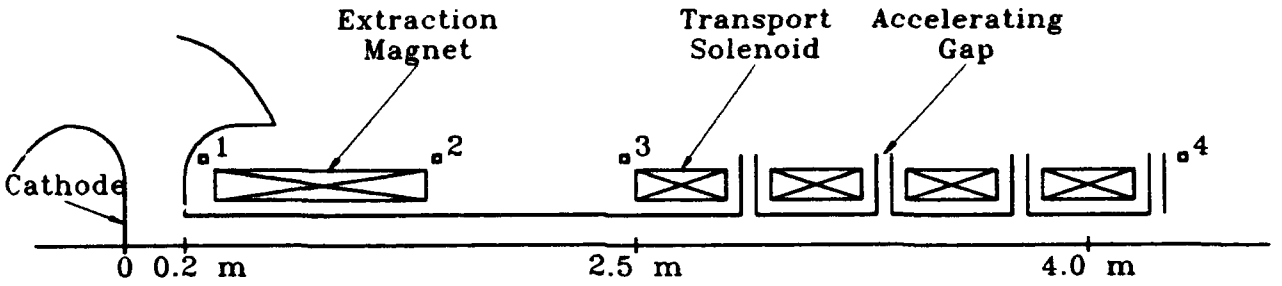


Figure 1. Schematic of ITS configuration, showing diode, extraction magnet, and four (of eight) accelerating cells. Beam current monitors are labeled 1, 2, 3 and 4. Gaps use ferrite isolation cores.

The current emitted off the cathode was 3.03 kA in the simulation vs. 3.5 kA in the experiment. This rather large discrepancy is not understood at present. The simulation current is reproduced by the electron gun code SPEED [3]. There may be emission from the electrode near the velvet, which is not allowed to emit in the codes. In any case the "extra" current in the experiment is lost before BPM3 (Fig. 1).

The transported fraction of the emitted current as a function of the current in the extraction solenoid (calibrated at 3.4 gauss/amp on axis at center of magnet) is shown in Fig. 2. We see that there is reasonable quantitative agreement between simulation and experiment.

3. Matching Onto Transport Solenoids

The REX machine [4], which is quite similar to the ITS injector, has been configured to do off-line beam transport experiments with 8 DARHT-type solenoids (minus the ferrite cores and accelerating gaps). Unfortunately, due to problems with the high-voltage insulator, experiments have been delayed. Since the distance from the cathode to the end of the last solenoid is about 6 m, a PIC simulation of the full transport region would be impractical. Fortunately, we can use a simple envelope model and expect to get accurate results. This is because the beam radius is large enough that emittance has a negligible effect on the envelope. The criterion for this is

$$a^2 \gg \frac{\gamma \epsilon_L^2}{2\nu} \tag{1}$$

where a is the beam edge radius, ϵ_L is the normalized Lapostolle emittance, and ν is Budker's parameter [$\approx I_b$ (kA)/17]. For typical ITS injection parameters [$\gamma = 9$, $\epsilon_L =$ 0.1 cm-rad, $\nu = 0.176$ (3 kA)] the RHS is about 0.25 cm^2, so that a beam with an edge

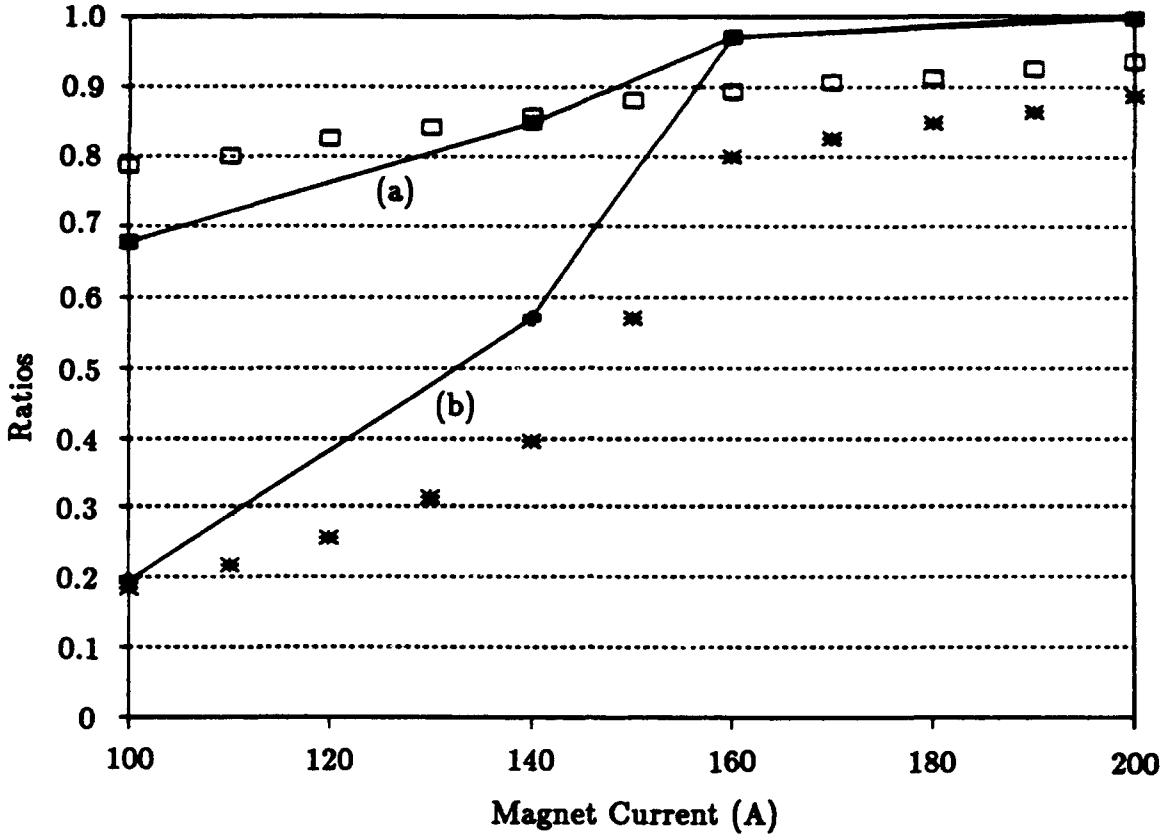


Figure 2. Ratios of beam current at (a) BPM2 and (b) BPM3 to beam current at BPM1, plotted vs. magnet current. Points connected by solid lines are from ISIS simulations. Unconnected points are experimental data.

radius of a few cm easily satisfies the criterion. Thus, if the emittance increases during the transport, an effect that the envelope equation by itself cannot model, the effect on beam matching will be small. Since the envelope equation is a second-order differential equation, a radius a and slope da/dz are needed as initial conditions. We obtain this data from an ISIS simulation of the diode, shown in Fig. 3. Since the envelope equation cannot model the AK gap, we take the initial values at a point 30 cm from the cathode surface, where the beam has reached full voltage. Fortunately, this point is in the fringe field at the entrance to the extraction magnet, so that the beam has not yet been significantly affected by the magnet. The edge radius to be input to the envelope code is set equal to $\sqrt{2}r_{rms}$, where r_{rms} is the RMS radius obtained from ISIS. The slope da/dz is adjusted to do a one-parameter fit to ISIS data at downstream locations. A good fit out to 250 cm (the length of the simulation) can be obtained. The axial magnetic field used in the envelope code is the same as that used in ISIS.

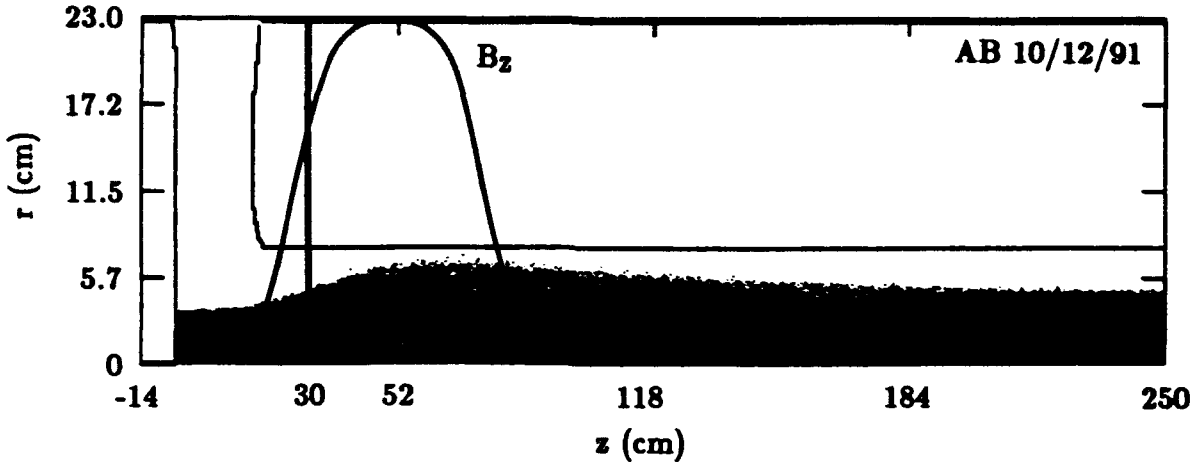


Figure 3. REX diode simulation of 4 MV, 3 kA beam showing particle positions and axial magnetic field profile. Magnet strength corresponds to a current of about 185 A.

Having modeled the beam envelope through the anode magnet, we now add the transport solenoids downstream. In the REX experiment, the accelerating gaps will not be powered, so the beam transport is at constant energy. The experiment will have 8 solenoids, but we have gone out to 16 with the envelope code. This is to ensure that the magnet settings obtained are useful for transporting the beam beyond 8 solenoids. The downstream solenoids are adjusted until a reasonably constant radius is achieved. The result at 4 MV is shown in Fig. 4, and we see that a good match into the solenoids can be obtained.

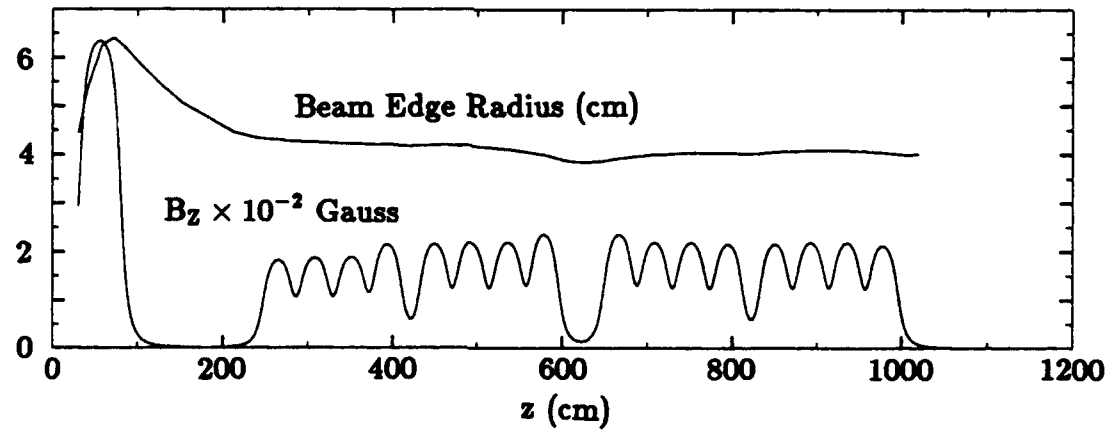


Figure 4. Beam edge radius and axial magnetic field profile for a well-matched 4 MV, 3 kA beam.

We have also carried out this procedure at 3.5 MV and 3 MV. In each case, a good match into the transport fields was obtainable.

4. Focal Spot Measurements

The primary figure-of-merit for the ITS beam is the spot-size obtained in a 50 cm final-focusing distance. The beam is allowed to expand to the drift-tube radius ($\approx$ 7.5 cm) and is focused onto a scintillator which is viewed by a streak camera. We have used the envelope code to model this measurement. Figure 5 shows predicted and measured spot-sizes as functions of current in the final-focus solenoid (3.19 gauss/amp) for the magnet configuration in Fig. 6. We have assumed a normalized Lapostolle emittance of 0.12 cm-rad in the envelope code [4]. The experimental values are estimates of the beam edge radius from streak photographs, and it is not clear at this point whether the discrepancies in Fig. 6 arise from this procedure or from some other source. A more exact comparison using data from a scanning densitometer is being carried out.

5. Acknowledgments

We thank Lee Builta and Roger Shurter for technical support.

References

1. M. Burns, P. Allison, D. Moir, G. Caporaso, and Y. J. Chen, these proceedings.

2. M. Burns, K. Chellis, C. Mockler, T. Tucker, G. Velasquez, and R. Van Maren, Proc. IEEE 1991 Part. Accel. Conference, p. 2110.

3. SPEED was written by J. Boers, Thunderbird Simulations.

4. T. P. Hughes, R. L. Carlson and D. C. Moir, J. Appl. Phys. 68, 2562 (1990).

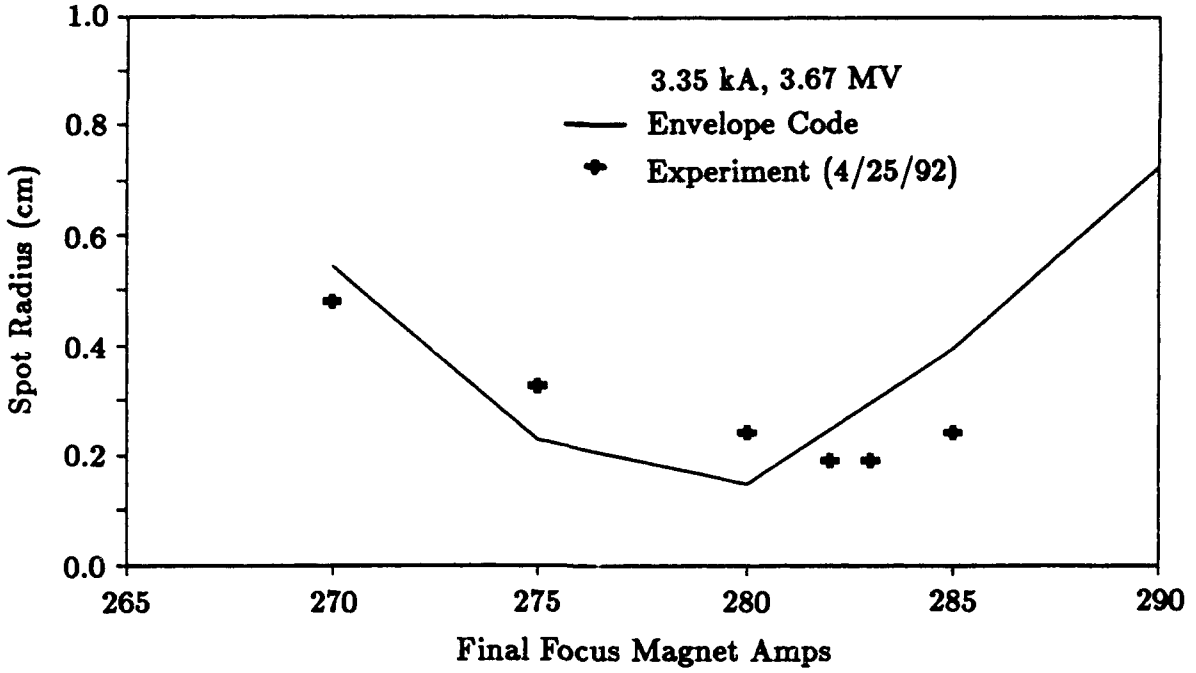


Figure 5. Spot-size vs. final-focus solenoid current at 50 cm from center of final-focus magnet.

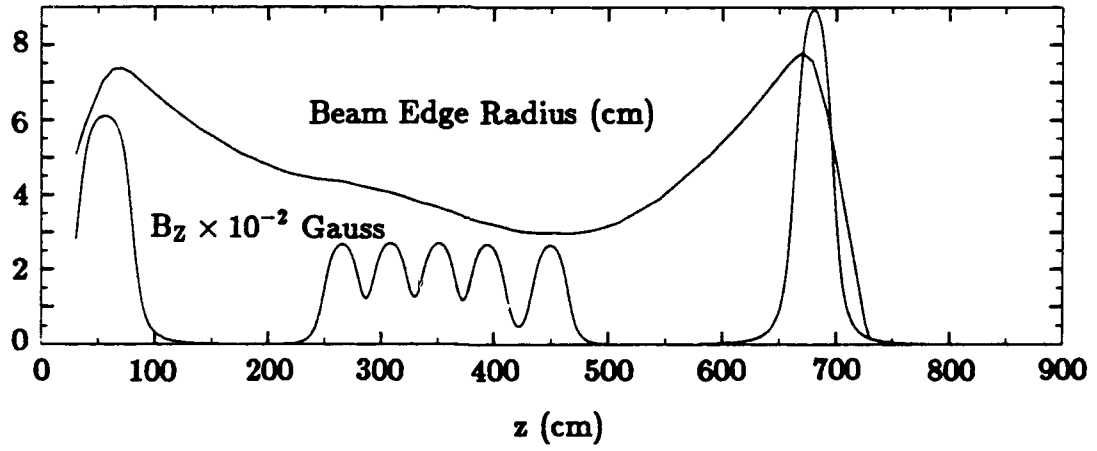


Figure 6. Axial magnetic field and beam envelope radius for spot-size measurements. Final-focus magnet strength used gives minimum spot. Beam parameters: 3.35 kA, 3.67 MV.

HITMI: Experiments with an Electron-Beam Driven Vacuum Linear Induction Accelerator

Carl Ekdahl, *Los Alamos National Laboratory*
Stanley Humphries, Jr., *University of New Mexico*
Bill Rix, *Maxwell Laboratories, Inc.*
Charles Warn, *EG&G Energy Measurements, Inc.*

We executed experiments with a single-stage vacuum accelerating cavity driven by injection of an annular 1-MA, 10^{14}-A/s, 1.5-MeV electron beam. We successfully accelerated a co-injected load beam through the magnetically insulated 50-MV/m gap (average gradient of >5 MeV/m). The load beam was transported through the accelerator with a passive grid system.

I. INTRODUCTION

The HITMI (High-Temperature diode, Magnetically Insulated) experiments were performed to test a novel linear-induction accelerator concept that uses vacuum diodes to power each stage. It has immediate application as a relatively simple means for increasing the voltage of existing diode machines, and future application for multi-stage accelerators. The experiments used a single acceleration stage to demonstrate drive efficiency, non-magnetic beam transport, and magnetic insulation of the acceleration gap.

HITMI is a vacuum accelerator – it uses magnetic insulation rather than dielectric materials. One of the most challenging problems in application of pulse power to the acceleration of charged particles is the transmission of high power density across dielectric-vacuum interfaces without breakdown (flashover). HITMI does away with the interface entirely — it uses vacuum diodes as its primary pulse-power source, and it uses only magnetic insulation.

The demonstration experiments used a coaxial, annular drive diode (actually a triode).

Electrons emitted from the pulse-power driven cathode are accelerated through a foil into the drive diode ("inverse diode") region, where they are collected by an anode isolated from ground by a coaxial inductor.

The distribution of electrons injected from a high ν/γ diode is very nearly a Maxwellian if the injection foil is thick enough to withstand continuous service without frequent replacement. As illustrated in Fig. 1, the injected distribution initially contains only forward velocities, but is rapidly thermalized as electrons are reflected back to the cathode by the accumulating space-charge. A steady state results with the space-charge producing a potential well between the cathode and anode. Electrons in the injected distribution with energies less than $\mid \Phi_m \mid$ are reflected back to the cathode. Electrons in the high-energy tail of the distribution pass through the well and are collected by the anode at a potential determined self-consistently by the external circuit. The potential distribution in the gap is arrived at by solving the Poisson equation, $\partial^2\Phi/\partial x^2 = en(\Phi)/\epsilon_o$, where the electron density is parametrically dependent on x through $\Phi(x)$. The density, $n(\Phi)$, is derived from the distribution, which in Region I includes both passing and reflected electrons, while in Re-

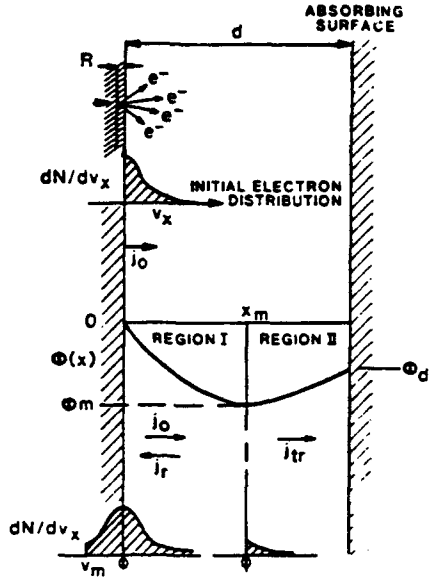


Figure 1: Drive diode physics model.

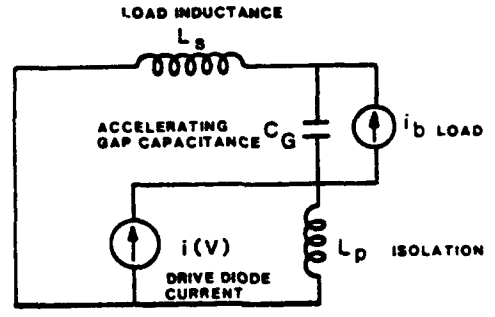


Figure 2: Simple lumped element circuit model of a single acceleration stage of the HITMI accelerator.

gion II includes only passing electrons. This problem was first solved more than 50 years ago[9, 10, 11] for a nonrelativistic thermal distribution of electrons. More recently, this problem has been solved for a Maxwellian distribution including the effects of relativity.[12]

The current return path from anode to cathode of each drive diode encloses a large coaxial volume that provides the inductive isolation for the fast-rising power pulse. A simple circuit model of the operation of a single cavity is shown in Fig. 2, in which all circuit elements are treated as lumped elements. Ignoring for the moment the load beam, one sees that the maximum open circuit voltage is $L_p di/dt = \Phi_a$, where $i = j_{tr}A$ is the anode current from the drive diode. Now consider the circuit with the load beam present. If $L_p \gg L_s$ most of the open circuit diode voltage can be applied to the accelerating gap, and if the gap capacitance, C_g, is low, most of the diode current not shunted through the isolation inductor is available for the load beam. The HITMI geometry insures that $L_p \gg L_s$, because the flux linking area for L_p is largest near the axis, where B_θ is large, while the largest area for L_s is far from the axis, where B_θ is small.

The beam is transported through the HITMI accelerator by a system of transverse grids that partially short out the beam space-charge fields. In principal, the emittance-dominated beam current that can be transported by this method is limited only by the injector, because in equilibrium the beam current is $I = 8.5(\epsilon_n/a)^2\gamma^{-1}(1/\gamma^2 - f_e)^{-1}$ kA, which can be made arbitrarily large for any γ, radius a, or emittance ϵ_n by adjusting the space-charge neutralization fraction f_e. This passive, non-magnetic transport system eliminates the usual bulky B-field magnets — which in turn makes a compact high-gradient, high-current accelerator feasible.

II. CAVITY EXPERIMENTS

We conducted experiments at Maxwell Laboratories to demonstrate that high-voltage pulse-power could be generated and transmit-

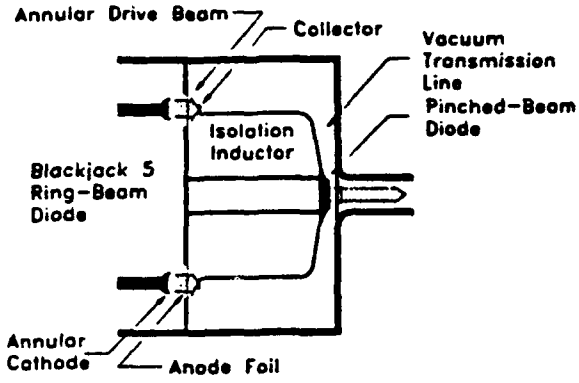


Figure 3: Diagram of the HITMI pinched-beam diode experiment.

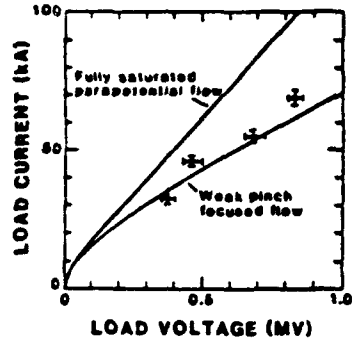


Figure 4: Current-voltage characteristic for the pinched-beam diode driven by an inductively isolated electron diode.

ted using the HITMI geometry. We used a simple, coaxial geometry by injecting the annular 1-MA, 10^{14}-A/s electron beam from the Maxwell Laboratories Blackjack-5 generator into a diode that energized a single-stage HITMI-geometry cavity. In the first experiments on Blackjack-5 we simply used a pinched-beam diode as a load, while in later experiments we accelerated a load beam.

Blackjack-5 is a five-stage pulse compression water transmission line driven by a 1.5 MJ Marx generator. For the HITMI experiments the pulse from the water-line was transferred through a plasma-erosion opening switch (PEOS) into a 25-cm diameter annular ring cathode. The emitted electrons were injected through a thin anode foil into the HITMI drive diode, where the space-charge limited current was collected, and returned to ground through the coaxial isolation inductor (Fig. 3). The injected electron distribution had a maximum kinetic energy of 1-1.5 MeV, and a current in excess of 1 MA. The distribution was very hot as a result of the high self-magnetic field; the mean angular spread was in excess of 90° FWHM. The PEOS provided a risetime of ~10 ns, producing $di_o/dt > 10^{14}$ A/s injected into the HITMI diode.

We determined the pinched-beam diode voltage from measurements of the beam electron energy with a magnetic spectrometer. Using simultaneous measurements of the beam current with B-dot loops we derived the I-V characteristic for the pinched-beam diode (Fig. 4). Also shown are the I-V characteristics predicted by Goldstein's focused-flow theory [1], for which $I_{ff} = 8.5(R/d)\gamma^{1/2}\ln(\gamma + (\gamma^2 - 1)^{1/2})$ kA, and by Creedon's parapotential-flow model [2], ($I_p = \gamma^{1/2} I_{ff}$). The I-V data are more in keeping with focused-flow, rather than parapotential-flow. This result is somewhat surprising, because the parapotential model accurately predicts the I-V characteristic of conventional pulse-power driven pinched-beam diodes. The HITMI result is likely due to the reaction of the space-charge limited flow in the drive diode to variations in the load parameters. There is no equivalent feedback effect for a pinched-beam driven by a conventional fixed-impedance pulsed-power generator.

On the other hand, feedback effects did not prevent the generation and transmission of

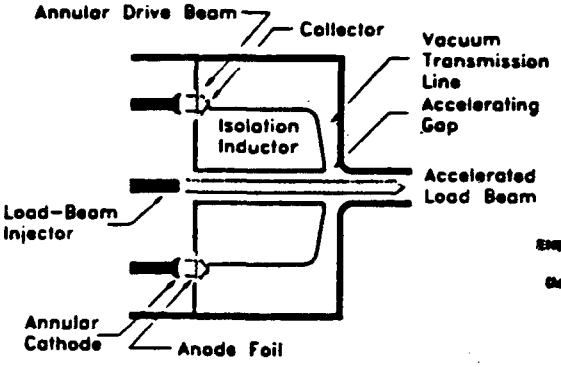


Figure 5: Diagram of the HITMI-2 single-stage accelerator experiment.

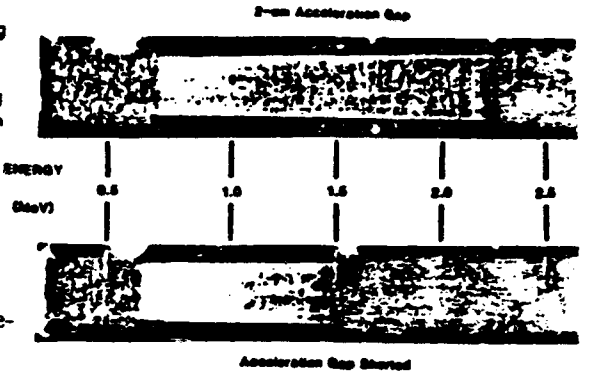


Figure 6: Films exposed in HITMI-2 spectrometer comparing the energy of a beam accelerated by the single stage with the energy of a beam transported through the accelerator with the gap shorted.

power with peak voltage a substantial fraction of the energy of the injected electron distribution. This result was an essential landmark to pass on the HITMI development road.

We next used the vacuum-diode-generated power to accelerate a coaxially injected load beam in the HITMI-2 experiment on Blackjack-5. (Fig. 5).

For this single-stage accelerator experiment the load beam was injected from a cathode on axis that was energized by the Blackjack-5 power-pulse in synchronism with the annular drive beam. The ~20-kA load beam was transported to the accelerating gap with a system of transverse grids, and from the gap to the magnetic spectrometer with another system of grids. In Fig. 6 we show the raw spectrometer film data for two shots, one of which had the 2-cm accelerating gap shorted with a copper ring. There is clear evidence for acceleration of the load beam. In Table 1 we list the results for all of the shots on which the spectrometer was used. The first column in this table is the injected load-beam energy inferred from Blackjack-5 diagnostics, the second column is the accelerated load-beam energy measured with the spectrometer, and the

shot	E_{inj} (MeV)	E_{spect} (MeV)	ΔE (MeV)	ΔE_{acc} (MeV)
2881	0.6	2.25	1.45	1.10
2888	1.1	2.23	1.13	0.78
2889	0.9	2.25	1.35	1.00
2890	1.4	2.65	1.25	0.90
2891	0.9	2.40	1.50	1.15
2894 (short)	1.2	1.55	0.35	0.00

Table 1: Summary of spectrometer measurements of HITMI-2 accelerated beam energies.

third column is the difference between the first two. The difference ΔE should be zero for the shot with the gap shorted; that it is not indicates a systematic error in the Blackjack-5 diagnostics, which is corrected for in the last column — the energy imparted to the load beam by the accelerating gap.

The average energy gained by the load beam in these experiments was 1 MeV. Dividing by the total cell length (18-cm inductor plus 2-cm gap) gives an average gradient of 5-MV/m — greater than any other induction accelerator. The gap itself was stressed to 50 MV/m — impossible were it not for magnetic insulation.

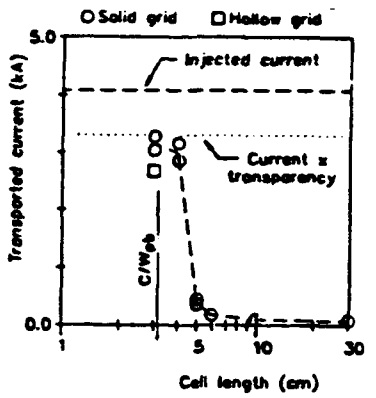


Figure 7: Results of transverse-grid beam transport experiments at UNM with a 300-keV, 4-kA beam.

III. BEAM TRANSPORT EXPERIMENTS

The load beam was transported through the HITMI-2 accelerator with the a passive grid system. This method is based on the principle that for a high-γ beam, the repulsive space-charge electric field is almost balanced by magnetic pinching. As a consequence, introduction of widely spaced transverse foils or grids to cancel a small fraction of the beam electric fields can modify the force balance to yield equilibium.

The current that can be transported by an emittance dominated beam using this method is limited only by the injector, because the beam brightness in equilibrium, $B \propto I/\pi^2\epsilon^2$, derived from beam envelope theory is inversely proportional to $[\beta^2(1-f_m)-(1-f_e)]$, which can be made arbitrarily small for any β by adjusting the average space-charge and current neutralization factors, f_e and f_m.

In experiments at the University of New Mexico[4] a 5-kA, 400-keV beam was transported using transverse grids. The transport of solid cylindrical beams was in excellent agreement with predictions. On the other hand, transport of hollow beams was characterized by the appearance of a strong magnetic filamentation instability that places constraints on the achievable brightness in high-current annular beams. [5]

Experiments were performed by injecting a solid 4.6-kA beam into a 30-cm long transport system subdivided into equal-length cells using high-transparency (98%) transverse grids. The total current transported through this system is shown in Fig. 7 as a function of cell length. Transported current was almost negligible for long cell lengths, but increased dramatically as the cell size was reduced to a size near the collisionless skin depth, c/ω_{pb}, which is consistent with theoretical predictions for the longitudinal space-charge limit.[3]

Emittance growth during beam capture and transport was less than 50%, and the beam was centered in the transport tube to within 1 mm, which is more accurate than the alignment of the experiment, because the beam was centered by wall image currents.[6]

To scale these results into the fully relativistic, high ν/γ beam parameter range in preparation for HITMI-2 we executed further grid transport experiments on accelerators at LANL and at the Naval Research Laboratory.

The Los Alamos experiments used the 1.5-MeV, 30-kA beam produced by the Viper accelerator. More than 90% of the injected current was transported through a 24-cm long system with 6 cells, compared with less than 20% for the same length system with no cells. In these experiments the beam had a ν/γ greater than 0.4 — the highest ν/γ beam ever transported with a passive system.

The experiments at NRL used the 4-MeV, 60-kA beam produced by the SuperIbex accelerator. This was a a 48-cm long experiment with sixteen 3-cm long cells. Because of a diode mismatch only ~70% transport was achieved on the high-current ($\nu/\gamma > 0.4$) shots, but we achieved almost 100% transport in experiments with a lower current (30 kA). [7]

IV. CONCLUSIONS

A vacuum-induction linac powered by electron diodes has, for the first time, been demonstrated in laboratory experiments. Moreover, the average acceleration gradient in this accelerator was higher than any other induction linac. For these experiments, a passive beam transport system was developed to handle high-power, high ν/γ beams.

V. ACKNOWLEDGEMENTS

The authors thank G. Craig, J. Denavit, M. Garcia, and C. Snell for stimulating discussions concerning vacuum diode physics. We are grateful to P. Walsh for design and assembly of the HITMI vacuum system. We are deeply indebted to R. Hooker, J. Garcia, J. Allen, D. Bartram, E. Horton and the personnel of the P-14 Anchor system, who valiantly trooped around the country getting these experiments done and the data recorded. We thank G. Quayle, C. Wright and the Blackjack 5 support crew for their expert technical assistance on the HITMI experiment. We are also grateful to C. Warn's colleagues at EG&G/LVO for the fabrication of much of the diagnostic hardware used in these experiments.

References

[1] S. A. Goldstein, R. C. Davidson, J. G. Siambis, and R. Lee, *Phys. Rev. Letters* **33**, 1471(1974).

[2] J. M. Creedon, *J. Appl. Physics* **46**, 2946(1975).

[3] J. W. Poukey, *Sandia National Laboratories Report SAND85-2670*, 1986.

[4] S. Humphries, Jr. and Carl Ekdahl, *J. Appl. Phys.* **63**, 583(1988).

[5] S. Humphries, Jr. and Carl Ekdahl, *Particle Accelerators* **24**, 147(1989).

[6] S. Humphries, Jr., Carl Ekdahl, and D. M. Woodall, *Appl. Phys. Lett.* **54**, 2195(1989).

[7] J. A. Antoniades, R. A. Meger, T. A. Peyser, M. C. Myers, S. Humphries, and C. A. Ekdahl, *Proc. 7th IEEE Pulsed Power Conference, Monterey, 1989.*

[8] J. P. VanDevender, *J. Appl. Phys.* **50**, 3928(1979) and references therein.

[9] B. Epstein, *Ber. d. Deut. phys. Ges.* **21**, 85(1919).

[10] T. C. Fry, *Phys. Rev.* **17**, 441(1921).

[11] I. Langmuir, *Phys. Rev.* **21**, 95(1923).

[12] J. Denavit and C. D. Craig, *LLNL Report UCRL-50021-83*, (1984)

[13] R. V. Lovelace and E. Ott, *Phys. Fluids* **17**, 1263(1974).

Contributed Beam Applications Papers

FOCUSING AND PROPAGATION OF PROTON BEAM AS DRIVER OF ICF

Keishiro Niu
Teikyo University of Technology
Uruido, Ichihara, Chiba 290-01, Japan

ABSTRACT

It is the aim of this paper to design a fusion power plant whose electric output power is 1GW, and to find a way for breaking through fusion technically and energy-economically. Proton beams, whose total energy is 12MJ, pulse width is 30ns and beam number is 6, are chosen here as the energy driver. Because of low quality of proton beams, the target should be indirect driven and its radius should be large. The target with the radius of 3.7mm is the spherical cryogenic hollow one, which has double shells and five layers. The reactor has double solid walls. The inner wall rotates around the axis to induce a centrifugal acceleration. Flibe as the coolant protects the solid walls from damage and breeds tritium. The key technology of this power plant is for beam focusing and beam propagation. To suppress the beam divergence by the electrostatic force due to unneutralized proton charge, the simultaneous electron beam launching is proposed. When the excess electron beam current is -50kA, the induced magnetic field in the azimuthal direction confines the beam in the radius of 5mm, provided that the beam path is covered by the metal guide whose radius is 1cm.

INTRODUCTION

PBFA-II in Sandia National Laboratory has been started to be used for beam-target interaction experiment.[1,2] Ion beam has a preferable stopping range in the target. It is expected that fuel compression and fuel heating will be done efficiently by using light ion beam as energy driver in the near future. Light ion beam has a high energy conversion rate from electric energy to beam kinetic energy. Especially in the case of proton beam, the conversion rate with more than 30% is achieved. From the point of view of ion source, proton is easily supplied. If the ion source includes other ion species beside proton, proton is extracted from the ion source first than other species. Always proton hits target first. No preheat of target occurs by other ion species.

Being taken the facts described above into consideration, proton beam is chosen here as energy driver. The optimum particle energy of proton for ICF is 4MeV.[3] In order to launch a large amount of beam energy such as 12MJ to the target, the beam current becomes strong, and the local divergence angle remains not small. Thus the beam focusing and beam propagation is a most important issues for proton beam. In this paper, the simultaneous electron beam launching with the proton beam launching is proposed. The electron beam carries a excess current of 50kA. This current induced the azimuthal magnetic field, which confines the beam in a small radius. In order to strengthen the beam confinement effect by the magnetic field, beam path is proposed to be covered by a metal guide.

Figure 1 shows the power plant schematically. There are 36 modules of power supply systems numbered by 1 in Fig.1. Each system stores 1.3MJ of electric energy. Since the plant is operated with the frequency of one Hertz, the input electric power to the plant is 46.8MW. As the electric output power from the plant is expected to be 1GW, the net power amplification factor of the plant is about 20. Six modules of power supply system are combined to extract one proton beam. The target at the center of reactor cavity numbered by 2 in Fig.1 is irradiated by six proton beams with the total beam energy of 12MJ. The target releases the fusion thermal energy of 3GJ. The target cavity consists of double solid walls. An electric motor numbered by 3 rotates the inner solid wall of reactor cavity. By the action of centrifuge due to rotation, the coolant, flibe, with the thickness of 50cm flows along the inner solid wall of reactor cavity. This molten salt, flibe, absorbs the fusion thermal energy, especially the neutron kinetic energy, and protects the solid wall from damage. From the reactor cavity 2, the coolant, flibe, and the reactor gas, argon, flow down to chamber 4, where unburned deuterium in the argon gas is separated. In the next chamber 5, unburned tritium and breeded tritium are separated from argon gas and flibe, respectively. From the chamber 6, flibe and argon gas are sent back to the reactor cavity, after heat exchange is carried out from flibe to another molten salt,

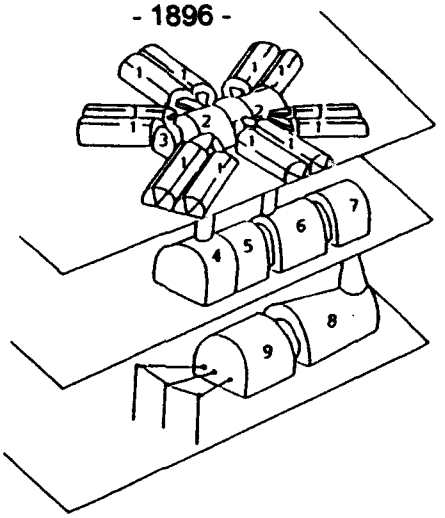


Fig. 1. Overview of power plant.

$NaF\text{-}BF_3$. The heat exchanger from $NaF\text{-}BF_3$ to water steam is in the chamber 7. A steam turbine and an electric power generator are located in chambers 8 and 9.

POWER SUPPLY SYSTEM

Table 1. Parameters of power supply system.

Marx Generator	36 modules
Charging Voltage	200kV
Capacitance of a Bank	1.7μ F
Number of Capacitor Banks	40
Stored Energy	1.3MJ
Output Voltage	8MV
Cylindrical Intermediate Storage Capacitor	36 modules
Insulator	Water
Inner (Anode) Radius	3m
Outer (Cathode) Radius	4m
Length	2.3m
Charging Time	103ns
Pulse Forming Line	36 modules
Input Voltage	8MV
Output Voltage	4MV
Length	0.67m
Pulse Width	30ns

The power supply system numbered by 1 in Fig. 1 consists of Marx generator, intermediate storage capacitance, laser trigger gap switch and pulse forming line. The pulse power is sent from pulse forming line to diode through magnetically insulated transmission line. The parameters of Marx generator, intermediate storage capacitor and pulse forming line are summarized in Table 1. The total stored energy in the Marx generators of 36 modules is 46.8MJ. The total energy of six proton beams is expected to be 12MJ. The energy conversion rate to beam kinetic energy is 26%. The proton beams with 12MJ should have high quality, that is, the incident angles at the target surface is within 30 degrees and the spread of particle energies is less than 10%.[4] The proton particles which exceeds the limits described above are inefficient for fuel implosion and are excluded from 12MJ. If the argument is confined in the plasma part apart from reactor, the main facilities for proton beam fusion is capacitor banks. The cost to construct these power supply systems is less by one or two orders of magnitude in comparison with other fusion machines such as Tokamak or glass laser. When the power plant of proton beam fusion is operated with the frequency of 1 Hertz, the plant must have a quick charging system. However the cost to construct increases only twice.

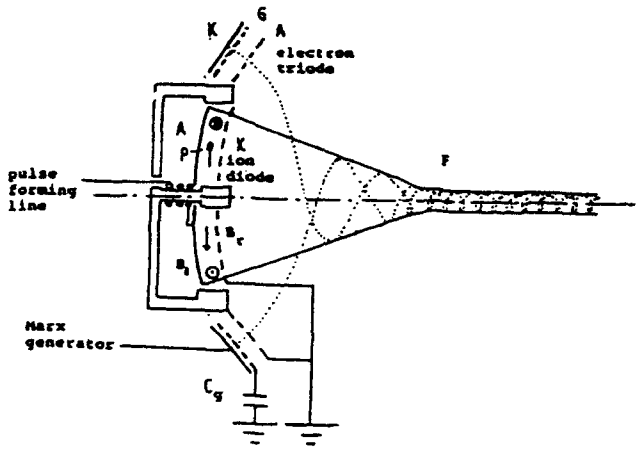


Fig. 2. The side view of diode and triode.

BEAM FOCUSING AND BEAM PROPAGATION

The side view of the diode to extract proton beam of 16.60MA and triode to extract electron beam of -16.65MA is shown in Fig. 3. Because the proton beam propagates with the high speed of 1/10 of light speed, proton charges at the leading part of the beam is not neutralized by electrons in the background plasma, and induces a strong electrostatic field, which causes the beam divergence during the propagation.[5,6] In order to delete this electrostatic field, it is proposed to launch simultaneously the electron beam from the triode with proton beam as is shown in Fig. 2.

Since the electron mass is much smaller than proton mass, the stored energy in banks to extract electron current of -16.65MA is order of 5kJ only. At the center axis, the diode has the magnetic coil, which induces the radial magnetic field of $B_r = 2.77 \times 10^{-4}$T. By the Lorentz force due to this field, the proton particle rotates around the axis with the average velocity $v_\theta = 2.77 \times 10^4$m/s during propagation. This proton rotation induces the axial magnetic field B_z, which stabilizes the beam propagation.

The number density of electron beam during propagation is controlled by grid voltage in triode. When the charging voltage to grid of triode is lower than -168kV, more number of electrons from triode than proton from the diode is extracted. Excess electrons soon run away from the proton beam, forming the negative radial electrostatic field, which shrinks the radius of propagating proton beam. The electron propagation velocity is decided by the anode voltage of triode. When the anode voltage of triode is -6.20kV, the electron propagation velocity is a little larger than that of proton with particle energy of 4MeV. Thus the net current of the combined beam with proton and electron is -50kA. That is, the beam is electron-current-rich and induces a negative azimuthal magnetic field, which confine the beam in a small radius. If the beam path is covered by a metal guide, the effect on beam confinement by the azimuthal magnetic field is strengthened. Thus the circumstance of beam propagation proposed here is similar to the plasma in Tokamak. The net electron current of -50kA induces the azimuthal magnetic field (poloidal field) whose intensity is -30T on the beam surface, whose radius is 5mm, surrounded by the metal guide, whose radius is 6mm. Rotation of proton particles around the propagation axis produces the axial magnetic field (toroidal field), which stabilizes the beam propagation. Although the metal tube expands radially by the magnetic pressure, the tube remains unmoved during a short period of beam propagation (beam pulse width is 30ns and beam propagation time in reactor is 100ns).

SIMULATION OF BEAM PROPAGATION

Focusing and propagation of proton beam is simulated. The equation of motion for a super particle (proton of electron) is

$$M\frac{d^2\mathbf{r}}{dt^2} = Q(\mathbf{E} + \mathbf{v} \times \mathbf{B}) \tag{1}$$

where M is the mass, Q the charge, $\mathbf{v}$ the velocity, $\mathbf{E}$ the electric field, $\mathbf{B}$ the magnetic field, $\mathbf{r}$ the space coordinate and t the time. The Maxwell equations for the electric field $\mathbf{E}$ and the magnetic field $\mathbf{B}$ is in the

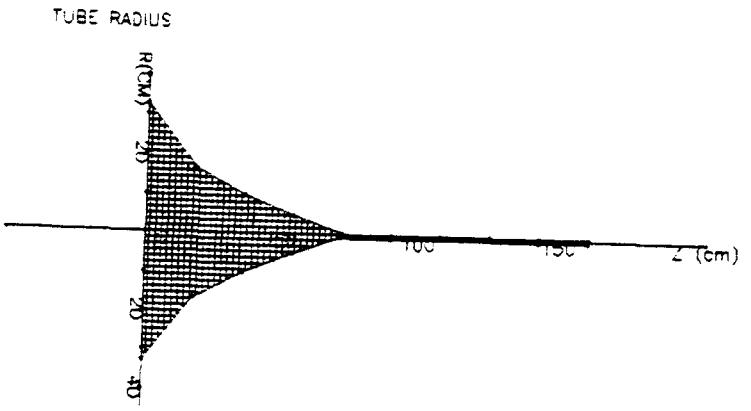


Fig. 3. Side view of metal guide.

following integral forms.

$$\mathbf{A}(\mathbf{r},t) = \frac{\mu}{4\pi}\int d^3\mathbf{r}'\frac{\mathbf{j}(\mathbf{r}',t')}{|\,\mathbf{r}-\mathbf{r}'\,|} \quad (2), \qquad \phi(\mathbf{r},t) = \frac{1}{4\pi\epsilon}\int d^3\mathbf{r}'\frac{\rho(\mathbf{r}',t')}{|\,\mathbf{r}-\mathbf{r}'\,|} \tag{3}$$

$$\mathbf{E}(\mathbf{r},t) = -\frac{\partial\mathbf{A}(\mathbf{r},t)}{\partial t} - \nabla\phi(\mathbf{r},t) \quad (4), \qquad \mathbf{B}(\mathbf{r},t) = \nabla\times\mathbf{A}(\mathbf{r},t) \tag{5}$$

where $\mathbf{A}$ is the vector potential, ϕ the scaler potential, $\mathbf{j}$ the current density, ρ the charge density, μ the magnetic permeability in vacuum and ϵ is the dielectric constant in vacuum. The simulation code is 2-dimensional in space. Here the axis-symmetry of the phenomena is assumed to be realized. Rotation motions of protons and electrons are neglected.

Other large assumption is done for the charge, $\rho = 0$ hence $\phi = 0$, in order to simplify the calculation. That is, the beam motion is charge free and no electrostatic field appears. In stead of (1), the equation of motion for MHD super particle

$$M\frac{d^2\mathbf{r}}{dt^2} = \mathbf{J}\times\mathbf{B} \quad (1'), \qquad \mathbf{J} = Q(\mathbf{v} - \frac{\mathbf{E}\times\mathbf{B}}{B^2}) \tag{6}$$

is used, where the current J is given by (6) because electrons do drift motion. In stead of (4), the electric field $\mathbf{E}$ is given by

$$\mathbf{E} = \frac{1}{Q}(\nabla\times\frac{\mathbf{B}}{\mu})\times\mathbf{B} - \mathbf{v}\times\mathbf{B} \tag{4'}$$

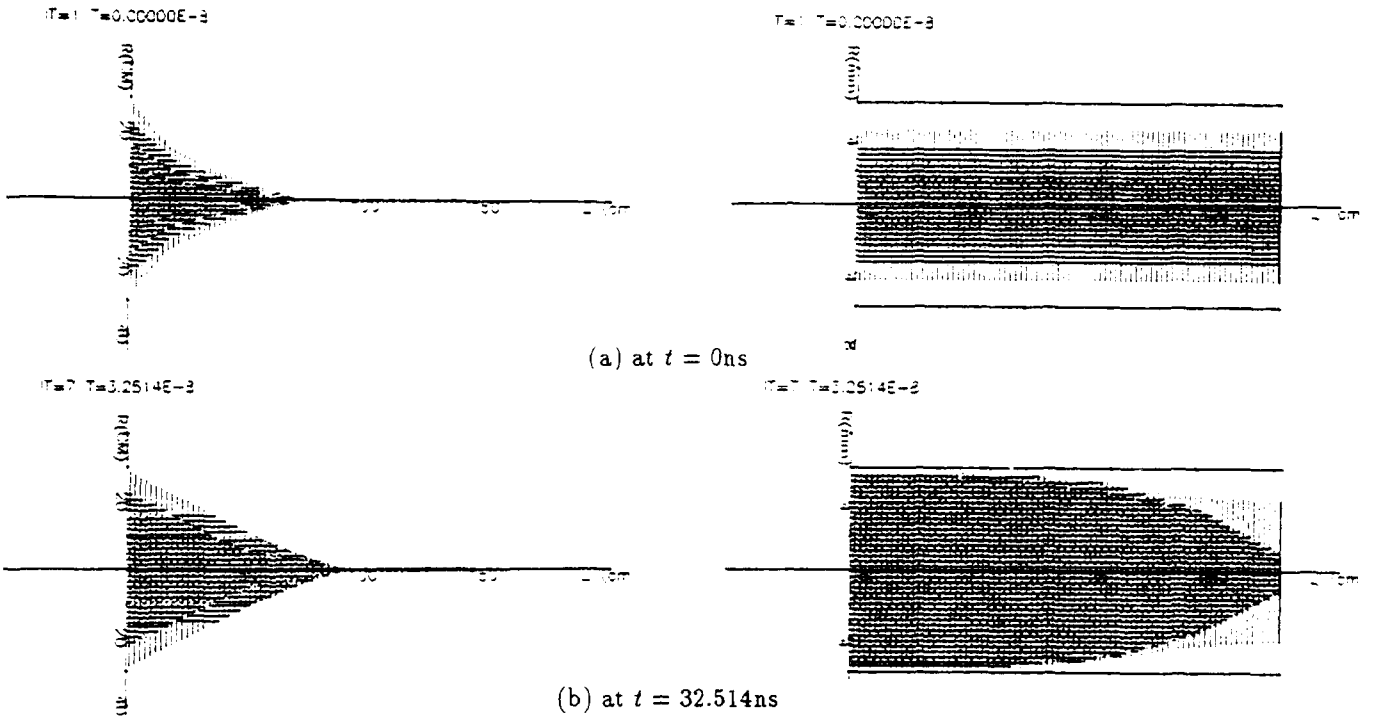
Figure 3 shows the side view of the metal guide for beam path. The radius of the narrow straight part is 6mm. Figure 4 shows the beam profile. The panel (a) is for $t = 0$s. The right shows the extended beam profile in the straight part. The panel (b) is for $t = 3.2514\times10^{-8}$s. Between the beam and the metal guide at the straight part, B_{theta} reaches -283.9T, which confines the beam without touching the metal guide.

INDIRECT DRIVEN TARGET

Since spherical symmetric beam irradiation on target surface is not expected in the case of proton beam, target should be indirect driven one and target should have a large radius.[7] Indirect driven target is effective for nonuniform beam irradiation. Recently, an analysis has been given for indirect driven reactor target[8], besides the small target.[9~11]

The vacuum radiation gap with the thickness of 2mm in the indirect driven target plays a role on radiation mixing. Although the target is irradiated by 6 proton beams in our case, there are energy unbalance among beams. Instead of direct driven target, indirect driven target is inevitably adopted in proton beam fusion. Our target is a cryogenic spherical hollow target, which has double shells and five layers.

The total radius of the target is $r_t = 8.716$mm while the total thickness of shells is $\delta = 3.216$mm. The aspect ratio of this target is $A = 2.71$. The target is irradiated by the six proton beams, whose beam energy



(a) at $t = 0$ns

(b) at $t = 32.514$ns

Fig. 4. Profile of propagating beam.

is 12MJ, whose pulse width is 30ns and whose particle energy is 4MeV. Eighty percent of beam energy deposits in the radiator layer. The temperature of radiator layer increases from 8K to 1.61keV and the radiator layer emits soft x-rays. Twelve percent of x-ray energy escapes through the tamper layer to the outside. Meanwhile, the radiation layer expands in the radiation gap, and radiator temperature decreases to 600eV. The radiation gap is filled by soft x-rays, whose initial radiation temperature is 600eV. The outer surface of aluminum layer absorbs x-rays and the temperature goes up to 600eV. Soon the aluminum surface expands in the radiation gap. This expansion decrease aluminum, radiation and lead-radiator temperatures to 200eV. The inward radiation intensity across the radiation gap from lead radiator to aluminum absorber is $I_{r_a} = 4.06 \times 10^{13}\mathrm{W/cm^2}$ at $T = 200$eV. By the expansion of radiator and absorber, the radiation gap closes 12.4ns after the start of beam irradiation. When the thickness of radiation gap is small, the radiation mixing is not enough and the radiation temperature in the radiation gap is not uniform. But the thickness of radiation gap is too large, then the energy loss due to expansion of radiator and absorber becomes large and causes the decrease in radiation temperature. There is the optimum value for the thickness of radiation gap. The thickness of 2mm is the optimum. The outer surface of aluminum absorber becomes hot and transparent for x-rays. The propagation velocity of transparent region is $v_{Al} = 5.42 \times 10^3\mathrm{m/s}$. Thus $\tau_{Al} = 40$ns after the start of beam irradiation, whole the aluminum layer becomes transparent for x-rays. This transparent time $\tau_{AL} = 40$ns is longer than the beam pulse width $\tau_b = 30$ns. The pressure of aluminum pusher (absorber) reaches 10^{12}Pa at $T_{Al} = 200$eV. This pusher pressure accelerates the solid DT fuel toward the target center. At the 3ns after the acceleration, the implosion velocity of the DT fuel arrive at $u = 3 \times 10^5\mathrm{m/s}$. With this velocity, the Mach number of fuel is $M = 12.8$. The supersonic flow of fuel in the decreasing cross-section inside the void of target compresses the fuel adiabatically.[1]2 Finally the fuel has the density $\rho_f = 220\rho_s$ (solid density), the temperature $T_f = 4$kev and the fusion parameter $< \rho_f R >= 35\mathrm{kg/m^2}$. The burn fraction of fuel arrives at 35%. Thus a target yields the fusion output thermal energy of 3GJ.

FUSION REACTOR

The cylindrical reactor cavity is surrounded by double solid walls. The outer wall is fixed on the ground while the inner wall rotates around the cylinder axis. If the radius of inner wall is 5m and the wall rates one revolution per second, the acceleration of the wall surface due to the centrifuge is 20 times the acceleration due to the gravity. From the inlets at the cylinder axis, molten salt, flibe, flows into the reactor cavity and

flow down along the inner solid wall by the action of centrifuge even under the ceiling part. The outer solid wall has six holes, through which proton beams are launched. The inner solid wall has six metal beam guides, which are connected with the target located at the reactor center. For the repetitive frequency of power plant is one Herz and the rotation of inner solid wall is one revolution per second, The synchronized six proton beams are launched when the holes on outer and inner walls overlap. The target releases the fusion thermal energy of 3GJ. The flibe layer whose thickness is 50cm absorbs the fusion energy including energetic neutrons and increases its temperature to 750°C. Flibe is chemically stable and handy as the coolant for proton beam fusion reactor. On the other hand, the operation temperature of flibe should be more than 500°C, in order to flow in the reactor with a high mobility. The generator 9 in Fig. 1 generates the electric power of 1GW.

The target yields 10^{21} neutrons with 14MeV. The number of neutrons impinging into flibe layer with the particle energy of 14MeV is 10^{21}. The number of neutrons which leak out from the flibe layer to the inner solid wall with the particle energies more than 10keV is 10^{18}. The latter reduces by three order of magnitude from former. The life time of the inner solid wall with thickness of 1/4 inch is estimated to be 420 years with respect to the swelling by this leaking out neutrons.

When the thickness of flibe layer is 50cm, the volume of flibe in a reactor is $314m^3$. The total mass of this flibe is 600 tons, among which the lithium mass is 200 tone. The total lithium mass on the earth is estimated to be 1.8×10^{10} tons. By using this lithium, we can construct 9×10^7 proton beam fusion reactors. This is the enough number of fusion reactors for the human beings.
The main part of tritium breezing comes from ^6Li. Flibe is the mixture of LiF and BeF_2 with the mol fraction of 2:1. The concentration of ^6Li in the natural lithium is only 2.5%. If ^6Li is little enriched in the flibe, the tritium breezing ratio exceeds unity in our proton beam fusion reactor.

SUMMARY

This paper wants to show the high possibility of proton beam as energy driver of inertial confinement fusion, although the beam quality in the case of proton beam is much lower than others at present. In this paper, a new method is proposed for focusing and propagation of intense proton beam. For the long term research for fusion, proton beam seems to have a high ability to break through fusion technically and economically. Of course, there are many subject for proton beam fusion. The life times of capacitor banks and gap switch, for instance, fro repetitive usage remains uncertain. In order to solve these problem, however, proton beam fusion does not included fatal defect.

REFERENCES

1. D. L. Cook, Bulletin of American Phys. Soc. **36**, 2480 (1991).
2. T. Mehlhorn et al., Abstract of 10th Int. Workshop on Laser Interaction (Monterey), 45 (1991)
3. K. Niu, H. Takeda and T. Aoki, Laser and Particle Beams **6**, 149 (1988).
4. M. Tamba, N. Nagata S. Kawata and K. Niu, Laser and Particle Beams **1**, 121 (1983).
5. T. Kaneda and K. Niu, Laser and Particle Beams **7**, 207 (1989).
6. K. Niu, P. Mulser and L. Drska, Laser and Particle Beams **9**, 149 (1991).
7. K. Niu, T. Aoki, T. Sasagawa and Y. Tanaka, Laser and Particle Beams **9**, 283 (1991).
8. N. A. Tahir and C. Deutsch, Abstract of 10th Int. Workshop on Laser Interaction (Monterey), 71 (1991).
9. M. Murakami and J. Meyer-ter-Vehn. Nuclear Fusion **31**, 1315 (1991).
10. M. Murakami and J. Meyer-ter-Vehn. Nuclear Fusion **31**, 1331 (1991).
11. N. A. Tahir and R. C. Arnols. Phys. Fluids **B3**, 1717 (1991).
12. K. Niu and T. Aoki, Fluid Dyn. Res. **4**, 195 (1988).
13. K. Niu and S Kawata, Fusion Tech. **11** 365 (1987).

LIBRA-LiTE, A BALLISTIC FOCUS LIGHT ION INERTIAL CONFINEMENT FUSION REACTOR

R.R. Peterson, D. Bruggink, R.L. Engelstad, G.L. Kulcinski,
E.G. Lovell, J.J. MacFarlane, E.A. Mogahed, G.A. Moses, S. Rutledge,
M.E. Sawan, I.N. Sviatoslavsky, G. Sviatoslavsky, and L.J. Wittenberg
Fusion Technology Institute
University of Wisconsin, Madison, WI 53706

Abstract

Ballistic propagation of ions in a light ion Inertial Confinement Fusion (ICF) reactor has potential advantages over propagation using plasma channels, but it requires that focusing magnets be close to the target. Ballistic transport is simpler and potentially more efficient, but limits on the ion microdivergence make a small focal spot and a large focal length simultaneously impossible. Target ignition requires a beam intensity above some minimum value, assumed to be 127 TW/cm^2. To achieve this intensity, one adjusts the total beam energy, the positions of the focusing magnets, the microdivergence of the ion beam, and the time of flight bunching of the beam. LIBRA-LiTE is a 1000 MWe power plant design consistent with ballistic ion focusing, where these parameters have been optimized.

Introduction

LIBRA-LiTE [1-3] is a 1000 MWe power plant conceptual design using light ion beam driven inertial fusion. A schematic picture of the LIBRA-LiTE target chamber is shown in Fig. 1. LIBRA-LiTE differs from the LIBRA design [4] in the electrical power level, the ion transport system, and the target chamber design. The general parameters are shown for both designs in Table I. Both designs use 127 TW/cm^2 of 30 MeV Li ions to drive the fusion target. Both designs use liquid metal first surface protection. The same liquid metal is used as breeding blanket material when confined in porous woven INPORT [5] units. LIBRA uses lithium-lead eutectic, LIBRA-LiTE, lithium. LIBRA uses plasma channels to propagate the ion beams, while LIBRA-LiTE uses ballistic propagation with focusing magnets near to the target. The LIBRA concept required electrical insulation magnets to prevent breakdown between the channels and the chamber structures. Finally, the target chamber roof was fabric wetted with liquid metal in LIBRA, but is a dry dome in LIBRA-LiTE. The LIBRA-LiTE roof of the target chamber is a large dome that is far enough away from the target that it needs no liquid metal coating for protection from target x rays and that neutron damage occurs slowly enough for the roof to be, along with the target chamber walls, a lifetime component. The target chamber and the 30 driver modules fit in a single large building.

Light Ion Driver and Beam Propagation

The pulsed power portion of the driver is essentially the same in LIBRA-LiTE as in LIBRA. Thirty modules with inductive voltage adders driven by magnetically switched water lines and step-up transformers provide roughly 30 MV, 40 ns shaped pulses on 30 diodes at a rate of 3.9 Hz. The number of modules has been increased from the 18 of LIBRA to provide better symmetry and more credible target performance. The pulses are carefully ramped in voltage to provide time-of-flight bunching of the beam. The total energy provided to all driver modules is 26.6 MJ, of which 6 MJ reach the target for a net driver and transport efficiency of 22.6%. We have assumed that the pulsed power efficiency is the same as in LIBRA, or 37.6%, that the ion production efficiency is 80%, and that the ion propagation efficiency is 75%. The last two efficiencies are consistent with LMF parameters [6].

Ballistic propagation of ions in a light ion fusion reactor has potential advantages over propagation using plasma channels, but it requires that focusing magnets be close to the target. Ballistic transport is simpler than channel transport and avoids the problem of electrical breakdown between the plasma channels and the target chamber structure. However, to keep the focusing magnets required for ballistic transport as far as possible from the target, the focal spot at the target is large, which leads to a large required driver energy. Target ignition requires a beam intensity above some minimum value, which we have taken to be 127 TW/cm^2. To achieve this intensity, one adjusts the total beam energy, the positions of the focusing magnets, the microdivergence of the ion beam, and the time of flight bunching of the beam.

We have used the SCATBALL computer code to verify the ability of the ion beam transport system to provide the proper target conditions. SCATBALL is a computer code written at the University of Wisconsin to study the passage of a ballistically focused ion beam through a gas. The code calculates the envelope of the beam as a function of position. It includes the effects of initial microdivergence, scattering by a background gas and a foil (if one is present), and magnets. The envelope calculation is based on an analytic formulation [7]. SCATBALL also calculates the heating of the background gas by the ion beam. Heating of the background gas by the beam is an important issue because the gas must have a high conductivity for the beam to be stable. We have performed calculations for 30 MeV Li ions and a 1 torr background gas of Li vapor with no foils intersecting the beam. This calculation predicts that the conductivity of the gas becomes sufficiently high.

Because the electrical resistance of any solid conductor in the focusing magnet would increase rapidly due to radiation effects, flowing lithium was selected as a conductor [8]. The magnet needs a center bore radius of 9 cm and a length average magnetic field product of 60 T-cm. The magnet is a 50 cm long five-turn solendoid. The current density in the present design is 10.1 MA/m^2, leading to a power loss of 2.1 MW per magnet. Nuclear heating, MHD effects on the flow, and

front surface heating have all been assessed. We estimate that the magnets will survive 1 calendar year.

Target Chamber Analysis

The target microexplosion releases x rays, neutrons and ion debris that deposit in the target chamber vapors and structures. We have assumed that the energy partitioning and the emitted spectra are the same as for the ion beam target designed by Bangerter [9]. The x rays deposit in the liquid Li film on the INPORTs and the magnets. A portion of the Li film is rapidly vaporized by the x rays and the debris ions are deposited in that vapor and in the original Li vapor in the target chamber.

To analyze the behavior of the target chamber gases and vapors, we have used the CONRAD computer code [10]. CONRAD is a one-dimensional Lagrangian radiation-hydrodynamics computer code. Radiation transport is calculated with 20 group radiation diffusion and time-dependent target x-ray and ion deposition is included. The code includes calculation of vaporization and recondensation of materials from an outer wall and heat transfer through the wall. CONRAD simulations have been carried out for vaporization over materials from the surface of the INPORTs and the focusing magnets. The simulations have shown that a shock wave is launched in the vaporized Li that leads to a very high peak pressure imposed on the remaining liquid at the vapor/liquid interface. The peak pressure is several GPa, which is certainly high enough to force a shock into the liquid. We have not yet considered the propagation of the shock in the liquid. The impulses on the INPORTs and magnets will be used to consider the mechanical response of these structures and to allow the design of structures with acceptable lifetimes.

Neutronics analysis has been performed for LIBRA-LiTE by performing several one-dimensional spherical geometry calculations. The discrete ordinates code ONEDANT [11] was utilized along with 30 neutron-12 gamma group cross section data based on the ENDF/B-V evaluation. A point source is used at the center of the chamber emitting neutrons and gamma photons with the LIBRA target spectrum [4]. The target spectrum takes into account neutron multiplication, spectrum softening and gamma generation resulting from the interaction of the fusion neutrons with the dense target material. The results were normalized to a 600 MJ yield and a repetition rate of 3.9 Hz.

Conclusion

We have designed and analyzed the LIBRA-LiTE ballistic ion propagation power plant. We have extended the life of the focusing magnets but using a liquid lithium conductor and by placing them

as far as possible from the target. The placement of the magnets requires low diode microdivergence and a high beam bunching ratio to avoid a very high driver energy. We have done neutronic and vaporization analysis for the target chamber.

Acknowledgements

This work is supported by Kernforschungszentrum Karlsruhe and Sandia National Laboratories. The authors wish to express their gratitude to Dr. Vetter and Dr. Kessler and their colleagues at KfK for helpful discussions. Similarly, we must thank Dr. Cook, Dr. Olson, and their colleagues at SNL. Computer calculations were in part performed at the San Diego Supercomputer Center, which is supported by the National Science Foundation.

References

1. G.L. Kulcinski, et al., "LIBRA-LiTE: A 1000 MWe Reactor," J. Fusion Energy **10**, 339 (1991).

2. B. Badger, et al., "LIBRA–LiTE: A Commercial Light Ion Fusion Power Plant," University of Wisconsin Fusion Technology Institute Report UWFDM-880 (1991).

3. R.R. Peterson, et al., "LIBRA-LiTE, A Light Ion Inertial Confinement Fusion Reactor With Ballistic Ion Propagation," University of Wisconsin Fusion Technology Institute Report UWFDM-864 (1991). Also published in Proc. 14th IEEE/NPSS Symp. Fusion Engn., (Sept. 30 - Oct. 3, 1991, San Diego, CA), p. 1050.

4. B. Badger, et al., "LIBRA - A Light Ion Beam Fusion Conceptual Reactor Design," University of Wisconsin Fusion Technology Institute Report UWFDM-800 (1989).

5. G.L. Kulcinski, et al., "The INPORT Concept - An Improved Method to Protect ICF Reactor First Walls," J. Nucl. Materials **103 & 104**, 103 (1982).

6. J.J. Ramirez, et al. "A Light Ion Beam Driver for the Laboratory Microfusion Facility," Fusion Tech. **19 2A**, 664 (1991).

7. C.L. Olson, "Achromatic Magnetic Lens Systems for High Current Ion Beams," Proc. 1988 Linear Accelerator Conference, CEBAF Report 89-001 (1989) p. 34.

8. D.C. Steiner, R.C. Block, and B.K. Malaverya, "The Integral Blanket - Coil Concept Applied to the Poloidal Field and Blanket Systems of a Tokamak Reactor," Fusion Technology **7**, 66 (1985).

9. R.O. Bangerter, "Targets for Heavy Ion Fusion," Fusion Tech. **13**, 348 (1988).

10. R.R. Peterson, J.J. MacFarlane, and G.A. Moses, "CONRAD – A Combined Hydrodynamic–Condensation/Vaporization Computer Code," University of Wisconsin Fusion Technology Institute Report UWFDM-670 (1988).

11. R. O'Dell et al., "User's Manual for ONEDANT: A Code Package for One-Dimensional, Diffusion-Accelerated, Neutral Particle Transport," LA-9184-M, Los Alamos National Laboratory (1982).

Table I. LIBRA-LiTE and LIBRA Parameters

	LIBRA	LIBRA-LiTE
General		
Net Power (MWe)	331	1000
Rep Rate (Hz)	3	3.9
Thermal Power (MW)	1161	2710
Gross Thermal Eff. (%)	38	44
Gross Power (MWe)	441	1192
Recirculating Power Fraction (%)	25	16.1
ηG	18.8	18
Availability (%)	75	75
Cost of Electricity (mills/kWh)	97	43
Driver		
Pulsed Power Type	Helia	Helia
Number of Beams	18	30
Beam Ion	30 MeV Li	30 Mev Li
Transport Method	channel	ballistic
Transport Length from Magnet (m)	3.3	2.05
Peak In Current/Diode (MA)	0.3	0.313
Bunching Factor	4.0	11.8
Peak Power on Target (TW)	400	1588
Pulsed Power Efficiency (%)	37.6	37.6
Transport Efficiency (%)	62.5	60.0
Net Driver Efficiency (%)	23.5	22.6
Target		
Ion Energy on Target(MJ)	4	6
Target Radius (cm)	0.5	1.0
Target Gain	80	100
Target Yield (MJ)	320	600
X-ray and Ion Yield (MJ)	95.4	179
Neutron Yield (MJ)	217	407
Chamber and Blanket		
Coolant/Breeder	PbLi	Li
Distance to INPORTs (m)	3.0	3.45
Mass Vaporized/Shot (kg)	8	5.2
Peak Pressure on INPORTs (GPa)	100	4.6
Pressure Impulse on INPORTs (Pa-s)	125	103
Peak Pressure on Magnets (GPa)	100	7.3
Pressure Impulse on Magnets (Pa-s)	125	188
Tritium Breeding Ratio	1.4	1.4
Vessel Life (FPY)	30	30
INPORT Life (FPY)	1.5	2.2
Magnet Life (FPY)	1.5	.75

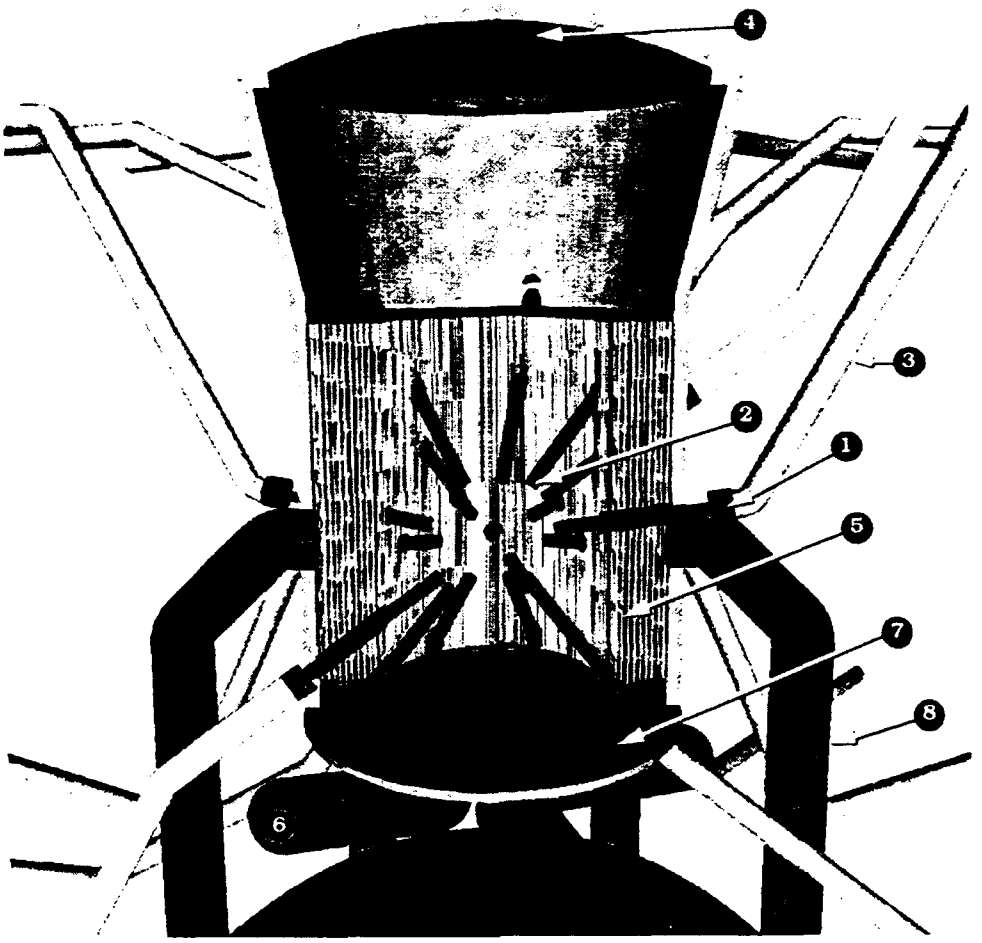


Figure 1. Schematic Picture of LIBRA-LiTE Target Chamber. (1) Diode, (2) Focusing Magnet, (3) Magnetically Insulated Transmission Line, (4) Chamber Roof, (5) INPORTs, (6) Heat Exchanger, (7) Bottom Plate, (8) Vacuum Line.

The choice of ballistic ion propagation in LIBRA-LiTE dictates some important features of the target chamber design. Ballistic propagation requires focusing magnets, each with a surface that faces and is near to the target microexplosion. Ballistic propagation also dictates that the gas density in the target chamber at the time of beam propagation be high enough to insure current and charge neutralization but low enough to not excessively scatter the beam. The focusing magnets in LIBRA-LiTE use liquid metal conductor in a metal case to avoid radiation damage to solid conductor. The tritium breeding blanket uses this same liquid metal, flowing in woven porous tubes. To protect solid surfaces from the target x rays, the blanket tubes and the focusing magnets are coated with this liquid metal. We have done neutronics calculations to determine the lifetime of the metallic case and the frequency at which it must be replaced. The optimum density for the gas in the target chamber has been determined with calculations with the SCATBALL code and has been found to be too low to absorb target x rays and ions before they reach the focusing magnets and INPORTs.

IONIZATION OF A HIGH ENERGY NEUTRAL BEAM PROPAGATING IN THE IONOSPHERE

Shu T. Lai

Phillips Laboratory/WSSI, Hanscom AFB, MA 01731

Abstract

By using modeled stripping ionization cross sections and standard atmospheric density models, we calculate stripping ionization probability of high energy (MeV) neutral beams propagating in the earth's atmosphere. Numerical results as functions of altitude, beam angle and beam energy are presented. We also consider Alfvén's critical ionization velocity (CIV) process as an alternate ionization pathway. If CIV occurs as the neutral beam propagates through the geoplasma across the ambient magnetic field, it may be an important pathway to rapid ionization halting the beam. We conclude that the parametric conditions are unfavorable for CIV to occur.

I. Introduction

When a high energy (MeV) neutral beam propagates in the earth's ionosphere, the beam particles interact with the particles and fields in the ionosphere. If the beam becomes ionized as a result of the interaction, the beam may be halted since the product beam ions gyrate around the ambient magnetic field lines. The cross-sections of electron impact ionization and charge transfer are insignificant at Mev energies. We do not consider nuclear reactions because they do not occur at energies below 30 MeV. Scattering dispersion of the beam can degrade beam energy but is unrelated to ionization. The dominant ionization process for a MeV neutral beam propagating in the ionosphere is probably stripping:

$$N + A \rightarrow N^{+} + A + e^{-} \qquad (1)$$

where N is a generic beam particle and M a generic atmospheric neutral particle or ion. Neutral particles are orders of magnitude more abundant than ions in the ionosphere.

II. Theoretical Model

Measurements of the cross sections σ of stripping of hydrogen H incident on various gases have been reported [1,2,3,4]. An empirical formula σ(E) of H is given in Ref.[5]:

$$\sigma(E) = \sigma_o \frac{(Za)^{\Omega}(E-I)^{\nu}}{J^{\Omega+\nu} + E^{\Omega+\nu}} \tag{2}$$

where $\sigma_o=10^{-16}$ cm^2, Ω=0.75, E is the energy (in keV) of the beam, Z, ν, J, and a are parameters of the ambient species, and I the beam ionization energy (in keV).

The density $I(z)$ of a neutral beam of energy E propagating from altitude z_o to altitude z is modeled simply as

$$I(E,z) = I(E,z_o) \exp\{-\int_{z_o}^{z} \sum_i [n_i(z)\sigma_i(E)]dz/\cos\theta\} \tag{3}$$

where θ is the angle between the beam and the vertical line (θ=180^o when the beam propagates downwards). We take the summation, i=1 to 5, over the 5 most abundant atmospheric species O, O_2, N_2, He, and H. The survivial probability $P(E,z)$ of the beam undergoing stripping is given by

$$P(E,z) = 1 - \frac{I(E,z)}{I(E,z_o)} \tag{4}$$

For atmospheric densities n_i(z), we use the Stein-Walker model [6] for simplicity.

III. Results

The survival probabilities of two downward propagating neutral H beams (2 and 250 MeV) are calculated (Fig.1). The higher energy beam can survive longer until it reaches about 110 km. where it is completely ionized. The survival probability of a 2 MeV beam propagating horizontally at various altitudes through various distances (1km to 1000 km) is also shown (Fig.2).

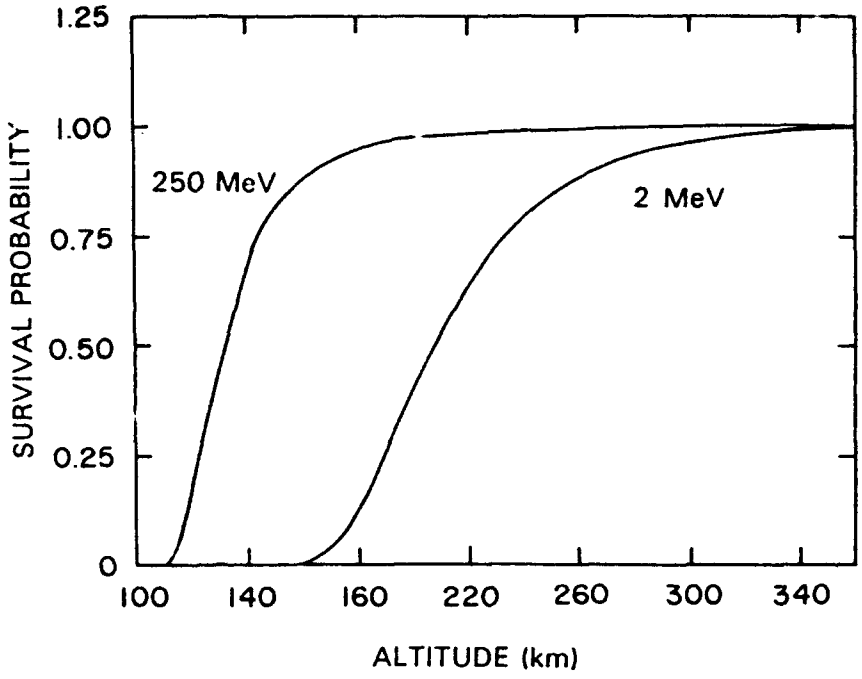


Figure 1. Survival probabilities of 2 MeV and 250 MeV neutral hydrogen beams propagating vertically downwards in the ionosphere.

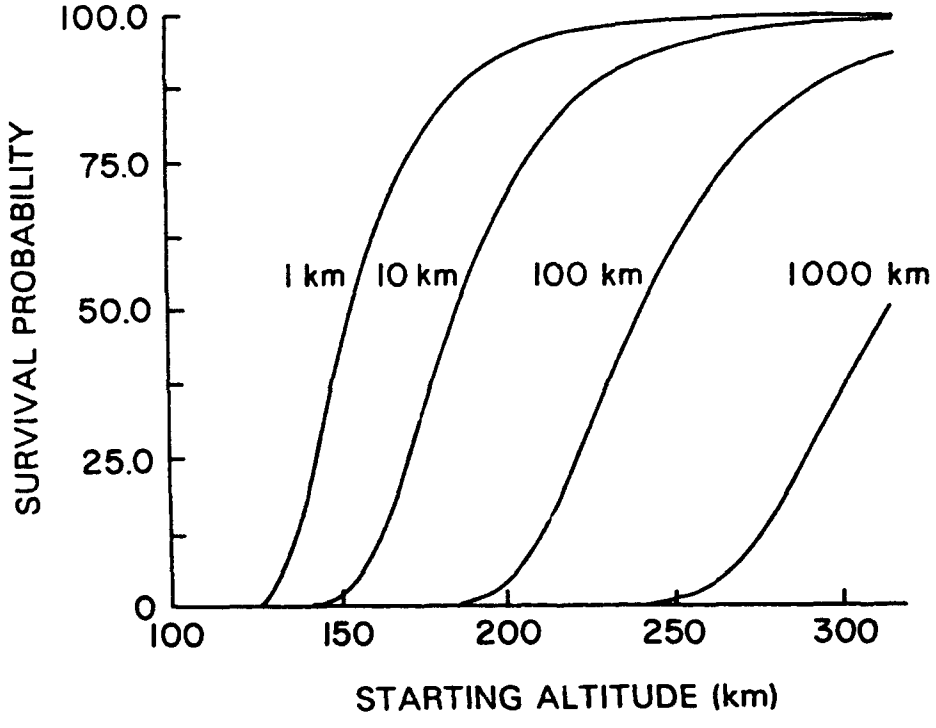


Figure 2. Survival probability of a 2 MeV neutral hydrogen beam propagating horizontally in the ionosphere.

IV. CIV Criteria

Alfvén's [7] critical ionization velocity (CIV) suggests that when a neutral gas and a magnetized plasma travel relative to each other with a velocity exceeding a critical velocity $V_c = \sqrt{(2e\phi/M)}$, rapid ionization occurs. M is the mass of a neutral particle and $e\phi$ the ionization energy. When an ion beam travels across the ambient magnetic field, beam-plasma interaction occurs. As a result, the electrons form a plateau tail distribution. Some electrons in the tail may be energetic enough to ionize. For a review of CIV, see, for example, Ref. [8].

Carini et al [9] questioned whether CIV can occur in MeV neutral beams. If CIV occurs, it could be a rapid path to ionization halting the neutral beam.

For CIV to occur, it is necessary [10] that an electron has to ionize at least once before it leaves the interaction region. This criterion requires $\tau\nu > 1$ where τ is the electron transit time and ν the ionization frequency. For a narrow low density beam, both τ and ν are small.

It is also necessary that the contact time τ_L of a neutral beam pulse with an ambient magnetic field line should be longer than the electron energization time τ_H [11].

$$\tau_L > \tau_H \tag{5}$$

For a MeV H beam pulse of length 1m, $\tau_L \sim 0.1\mu s$. Taking $\tau_H \sim 30/\omega_{LH}$ [12] where ω_{LH} is the lower hybrid frequency, one finds that in the ionosphere $\tau_H \sim 10ms$, which exceeds τ_L.

Electromagnetic modes may be excited when the beam velocity V exceeds V_s [13].

$$V_s = (1+\beta)^{1/2} V_A \tag{6}$$

where $\beta \sim nkT/B^2$ and V_A is the Alfvén velocity. These modes drain energy and may suppress CIV. Thus, for CIV to occur, the beam velocity criterion is

$$V_s > V > V_c \tag{7}$$

Since $\beta \sim 10^{-5}$ and $V_A(O) \sim 7x10^2$km/s in the ionosphere, it appears that CIV is unlikely because the beam velocity V (~10^4 km/s) exceeds V_s (~$7x10^2$ km/s).

References

[1] Toburen, L.H., Phys. Rev. A3, 216, (1973).

[2] Gilbody H.B. and M.B. Shah, Physica Scipta, 24, 712, (1981).

[3] Shah, M.B. and H.B. Gilbody, J. Phys. B14, 2361, (1981).

[4] Williams, I.D., J. Geddes and H.B. Gilbody, J. Phys. B17, 1547, (1984).

[5] Green A.E.S. and R.J. McNeal, J. Geophys. Res., 76, 133, (1971).

[6] Stein, J.A. and J. Walker, J. Atm. Sci., 22, 11, (1965).

[7] Alfvén, H., *On the Origin of the Solar System*, (Oxford University Press, Oxford, 1954).

[8] Goertz, C.K., S. Machida, and G. Lu, Adv. Space Res., 10, No.7, 33, (1990).

[9] Carini, P., G. Kalman, and P. Pulsifer, *Neutral Beam Propagation effects in the Upper Atmosphere*, AFGL-TR-85-0038, ADA-174896, Air Force Geophysics Laboratory, Hanscom AFB, MA (1985).

[10] Brenning, N., *Review of Impact Experiments on CIV*, TRITA-EPP-82-I4, Royal Institute of Technology, Stockolm, Sweden, (1982).

[11] Lai, S.T., W.J. McNeil, E. Murad, Geophys. Res. Lett., 17, No.6, 737, (1990).

[12] Tanaka M., and K. Papadopoulos, Phys. Fluids, 26, 1697, (1983).

[13] Papadopoulos, K., in *Proc. Workshop on Alfvén's Critical Velocity Effect*, G. Haerendel, ed., (Max Planck Institut für Extraterrestrische Physik, Garching, W. Germany, 1982), p.178.

LARGE AREA ELECTRON BEAM GENERATION AND PROPAGATION FOR KrF LASERS

C. J. Pawley, J. D. Sethian, S. P. Obenschain, and S. J. Czuchlewski†
Naval Research Laboratory
Plasma Physics Division
4555 Overlook Avenue SW
Washington, D.C., 20375

High energy KrF lasers have optical output apertures ranging from 10x10 cm^2 to 1x1 m^2. The electron beam must uniformly pump the entire aperture and the length of the laser amplifier. These electron beams are usually mildly relativistic (250 - 750 keV) and have moderate current densities (10 - 100 amps/cm^2). The NIKE system at NRL incorporates a 20x20 cm^2 aperture laser amplifier to drive a 60x60 cm^2 aperture final amplifier expected to deliver greater than 4 kJ of laser output. Design considerations, testing, and experimental data from the 20 cm amplifier are presented as well as an overview of some of the models used to understand the results. Particular attention is paid to obtaining a uniform electron beam with minimal small scale structure. Results of the electron beam uniformity and improved electron transmission efficiency to the gas for the 20 cm amplifier will be presented. The design of the 60 cm amplifier being constructed will also be presented.

KrF lasers are a primary candidate for laser fusion drivers because of a large number of advantages associated with this particular excimer[1,2]. KrF has a reasonable intrinsic efficiency (10%), large bandwidth (4 THz) and low nonlinear index of refraction. It is an ultraviolet laser (248 nm) which is required for a high fraction of absorption at the target pellet and good rocket efficiency. KrF is a gas laser, hence it can be operated at 10 to 100 Hz repetition rates with the use of gas cooling system.

KrF lasers require large output apertures for high energy because of the low saturated output intensity. Discharge amplifiers with 10x8 cm^2 gain regions can deliver 5 Joules in 30 nsec[3]. Amplifiers with 10x10 cm^2 or larger apertures require electron beam pumping provided by pulse power technology. To prevent optical distortion, the electron beams must uniformly pump the entire optical aperture over the extraction time without large lateral gradients. The parameters of the electron beam are determined by the optical requirements of the amplifier as it is designed into the optical chain. The desired output energy and gain determine the size of the electron beam, the energy, and the current density. Additionally, both the current and voltage waveforms of the electron beam should be constant during the time that light is being extracted from the amplifier, otherwise the optical beam's intensity and spatial distribution will vary in time because of the changing electron deposition profile. All of the energy in the rise and fall of the electron beam pulse is wasted energy. Laser fusion experiments require a short optical pulse (3-10 ns), which is too short a time to pump large KrF amplifiers. The long gain pulse (100-240 nsec) obtained from electron beam pumping must be extracted by a large number of contiguous short optical beams by angular multiplexing[4]. In order to minimize the number of optical beams, the electron beam energy should be delivered in as short a pulse as possible. The

inductance of the electron diode will limit the rise time, the current density will be limited to values where the effects of the self generated magnetic field can be compensated and the laser physics will limit how heavily the KrF medium can be pumped and extracted efficiently. All of these considerations must be integrated into the final design for each amplifier stage.

The NIKE system[5,6] uses a discharge oscillator and 4x4 cm^2 aperture discharge amplifiers to create 1-2 Joules in 4-5 nsec beams. These are then angularly multiplexed and fed to a 20x20 cm^2 aperture electron beam pumped amplifier ("the 20 cm amplifier") where the optical beams should reach 150J. That output is again divided and is amplified by a 60x60 cm^2 aperture electron beam pumped amplifier which should deliver 4 kJ of laser energy. This paper will examine the 20 cm amplifier electron beam design and performance. An overview for the 60 cm amplifier currently under construction will also be presented.

The 20 cm Amplifier

The 20 cm amplifier is shown schematically in Fig. 1. An eight stage Marx bank provides the intial pulse power. The erected capacitance is .05 microFarads and when fully charged reaches 800 kV. The output of the Marx is split by two balancing inductors and fed through rigid oil coax lines to two water pulse forming lines, one on each side of the laser. Each water line is a simple coaxial line with a total capacitance of .024 microFarads. The pulse impedence is 3.8 ohms with a round trip time of 180 nsec. The inductors are adjusted so that the two water lines reach peak charge at the same time with the same voltage to within 5%. The 1/4 cycle charging time is 1.0 μsec. The energy transfer from the Marx to the waterlines is 93%. At peak charge, the waterlines are discharged into the electron diodes by laser triggered spark gaps. An expanded view of one electron diode in figure 2 also shows the switch. The switch gap is 3 cm and uses a 70% SF_6 30% Argon mix as the insulating gas at 52 psig. A 4 nsec 266 nm trigger laser focuses 20 mJ of light 1 cm from the negative electrode on the waterline. The laser triggered gap closes with less than a $\pm$5 nsec jitter resulting in a very highly reproducible switch of 30 nH inductance. The cathode vacuum insulator and stalk structure have a low 35 nH inductance. The water line waveform at the switch, the gun voltage and current are shown in figure 3. There is a 135 nsec region where the current and voltage vary less than $\pm$5%. Optical power extraction will occur during this time. Standard operating conditions are: Marx erected voltage 640 kV, water line charge 615 kV, gun voltage 290 kV, and gun current 80 kA. A magnetic guide field is used on the 20 cm amplifier to improve electron beam deposition into the gas. The field is created by 2 racetrack coils in a modified helmholz configuration. The coils are 64 cm tall, 178 cm long, and mounted 43 cm apart. The maximum field in the center of the laser cell is 1.5 kG. For routine operation, high reliability is required. The 20 cm amplifier can fire 12 times an hour, 60 times a day with greater than 95% reliability.

The cathode emitter surface is a very smooth (32 finish or electropolish) stainless steel shaped shell with velveteen (50% cotton, 50% nylon) cloth pulled over it. There is no glue or epoxy underneath the velvet which might prevent electrical contact. The edges of the emitter have a parabolic profile tapering away from the anode screen to prevent emission past the beam edge without any enhancements or "halo" effects near the edge. The actual electron beam emitted is 21 cm tall by 80 cm long. The gap between the cathode emitter and the anode screen is 3 cm. A scenario for the emission buildup is that the higher

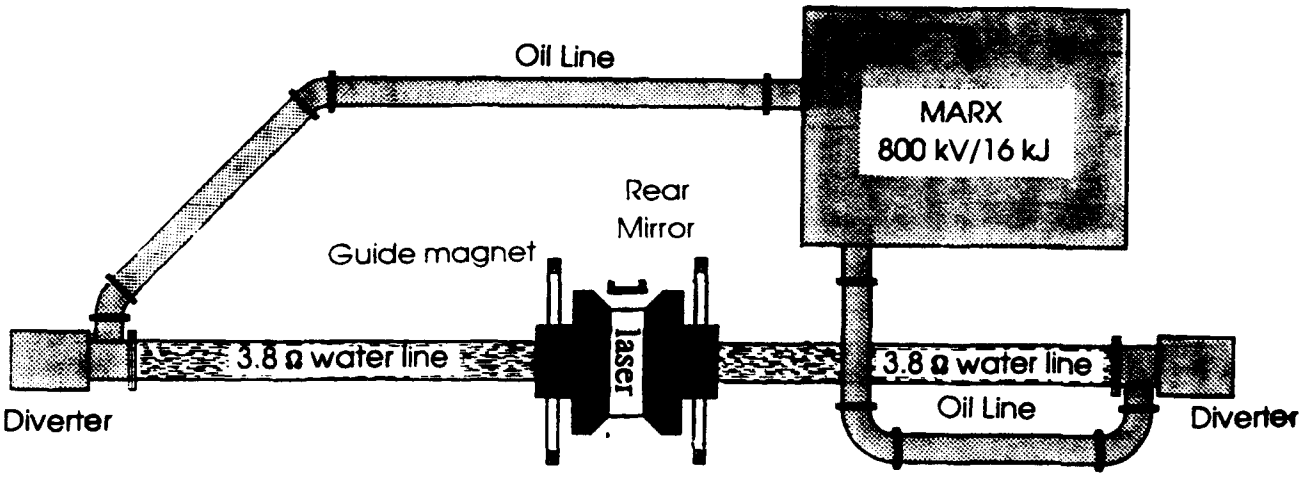


Figure 1. The 20 cm amplifier. Diverters protect the system in case of misfire.

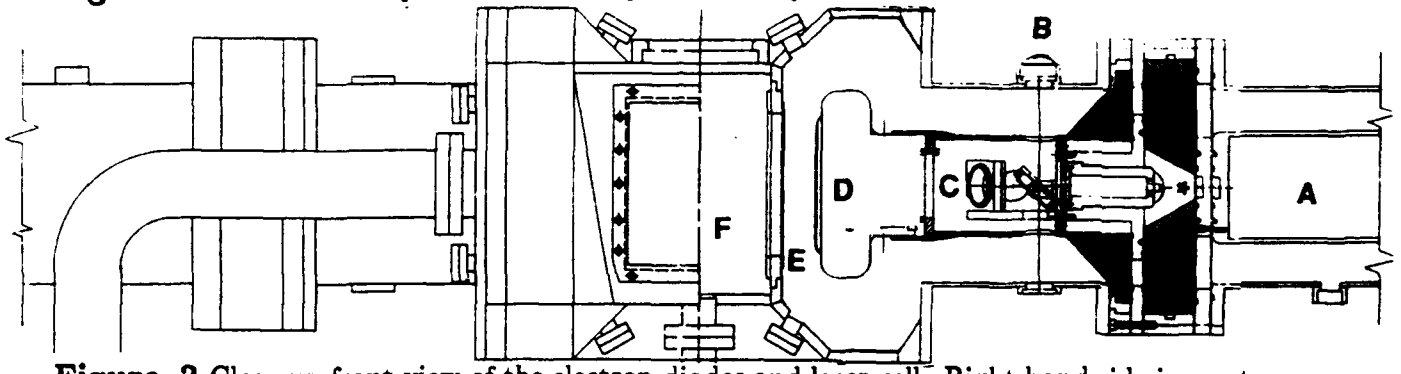


Figure 2. Close up front view of the electron diodes and laser cell. Right hand side is a cutaway view. The water line is A, trigger laser light enters through lens B reflects off of a 45° mirror and focuses at *, C is the cathode stalk and D is the cathode shell and emitter. E is the anode screen, hibachi and gas foil, and F is the laser cell.

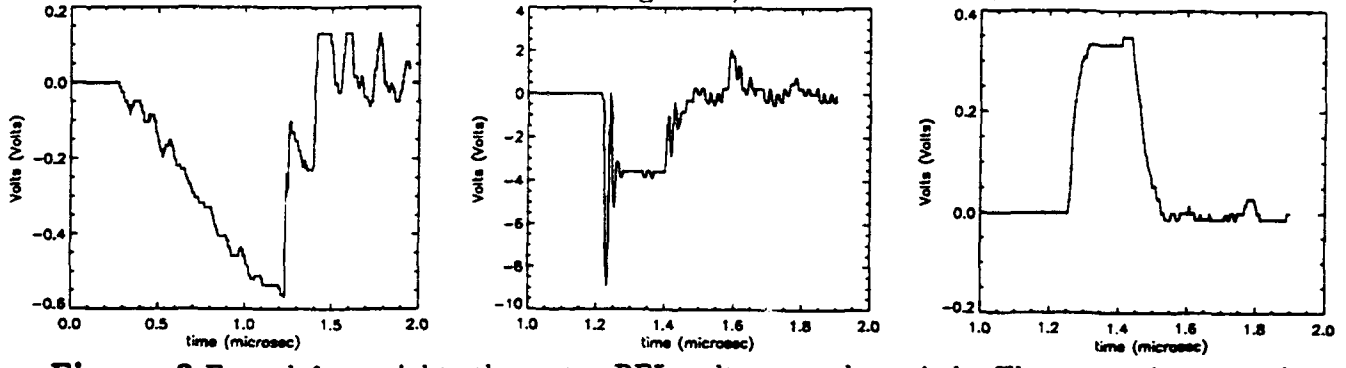


Figure 3. From left to right; the water PFL voltage at the switch, The gun voltage at the vacuum insulator, and the gun current through the cathode stalk. The flat portion of the gun voltage scales to 290 kV and the current to 80 kA.

average dielectric constant in the velveteen cloth region results in a partial exclusion of the electric field there. When the field exceeds the vacuum insulator holdoff of the velveteen fibers, the surface of the fibers flashes over, discharging the dielectric and creating a surface plasma. By stray electrons and ultraviolet light the discharge would spread, permeating the cloth with plasma, producing a plasma cathode. It has superior uniformity and slower closure to carbon felt or pin type cathodes[7]. The 20 cm cathode has a closure velocity of 1 cm/μsec or less after removing the effect of inductance from the data. We have obtained

several hundred shots on the velveteen with most damage due to arcs after the main pulse when the plasma closes the A-K gap. This damage can be minimized when the switches are triggered properly and the diodes are well matched to the water line impedance.

The electron beam created at the cathode is accelerated through an anode screen with an optical transparency of 82% calculated by wire to grid size ratio. A screen is used here because of its durability to after-pulse diode closures. The beam emerges into the hibachi structure. Figure 4 shows the structure as straight vertical bars 1.3 cm deep, .42 cm thick, and spaced 4 cm apart center to center. This results in nearly 90% optical transmission. The self generated magnetic field due to 80 kA of beam current is 500 gauss at the center of each edge of the electron beam. This field summed with the guide field results in slanted electron trajectories which increase the hibachi losses. For a 1.5 kG guide field, the transmission through the hibachi averaged over the entire beam is 80%. If the guide field is turned off, a strong instability develops between the anode screen and the gas foil, losing a significant amount of beam energy[8].

The cathode, anode screen, and hibachi are in vacuum. The lasing medium is 1100 Torr of argon, krypton, and fluorine laser gas mix. To separate gas from vacuum, a 50 μm thick sheet of polyamide plastic (Kapton) is clamped on top of the hibachi. The bars of the hibachi provide the required mechanical strength to support the pressure on the sheet, referred to as the gas foil. When the electrons strike the foil, 95% of the energy will go through and into the gas[9]. Approximately 17% of the electrons entering the gas will make a large angle collision with a gas atom and backscatter into the hibachi or the anode[10]. Multiplying the anode screen transmission by the average hibachi transmission and taking into account the foil and gas backscattering results in 52% of the electron beam which left the cathode emitter should significantly penetrate into the gas and deposit energy. This is much better than the average transmission of 30% typically reported[11,12,13].

To experimentally verify the cathode to gas transmission, several sizes of Faraday cups were used. These cups had a 5 μm thin polyethylene sheet enclosing the graphite cup. This way the plasma caused by the electron beam propagating through the gas would not short out the Faraday cup to ground. The polyethylene is so thin that very few high energy electrons would be stopped by it. Two cups were small enough to collect the beam from between two hibachi bars. A 7x7 cm^2 cup and a 10x10 cm^2 Faraday cup were used to average over several hibachi bars. The small cups gave 25 A/cm^2 and the large cups gave 22 A/cm^2. Taking the total area of the diode and the total current to be 80 kA, these results scaled to 48% with $\pm$6% error. Another experimental check is to measure the pressure rise of the gas due to the energy deposition. The raw pressure rise data is then corrected for fluorescence losses based on data from krypton and argon. Three independent sensors were used. They gave 3.7,3.8, and 4.0 psi rise. This averaged to 3.6 kJ deposited in the gas after correction for fluorescence. 3.6 kJ divided by the energy which left both diodes gives 42%. This is consistent with the Faraday cup result as some electrons will go all the way across the cell to the other diode and some electrons will scatter into the walls of the laser cell, and not deposit energy into the gas. An experimental plastic dosimetry media from GAF was used to produce a witness pattern of the entire beam. The images taken in the gas within .5 cm of the hibachi show the beam has a few 1-2 cm diameter hot spots in the beam, but is otherwise uniform. The hibachi losses visualized as beam

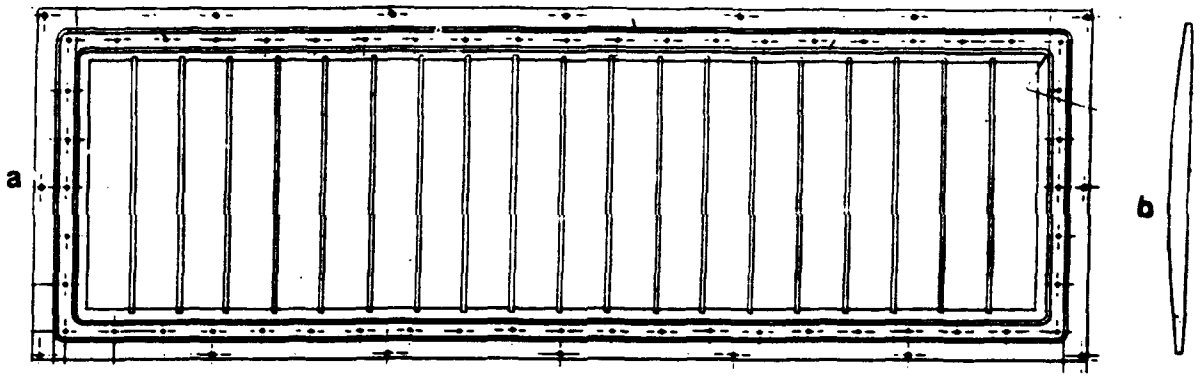


Figure 5.a. Beam view of the hibachi structure. b. tapered bar design to reduce beam slant losses on the 60 cm amplifier.

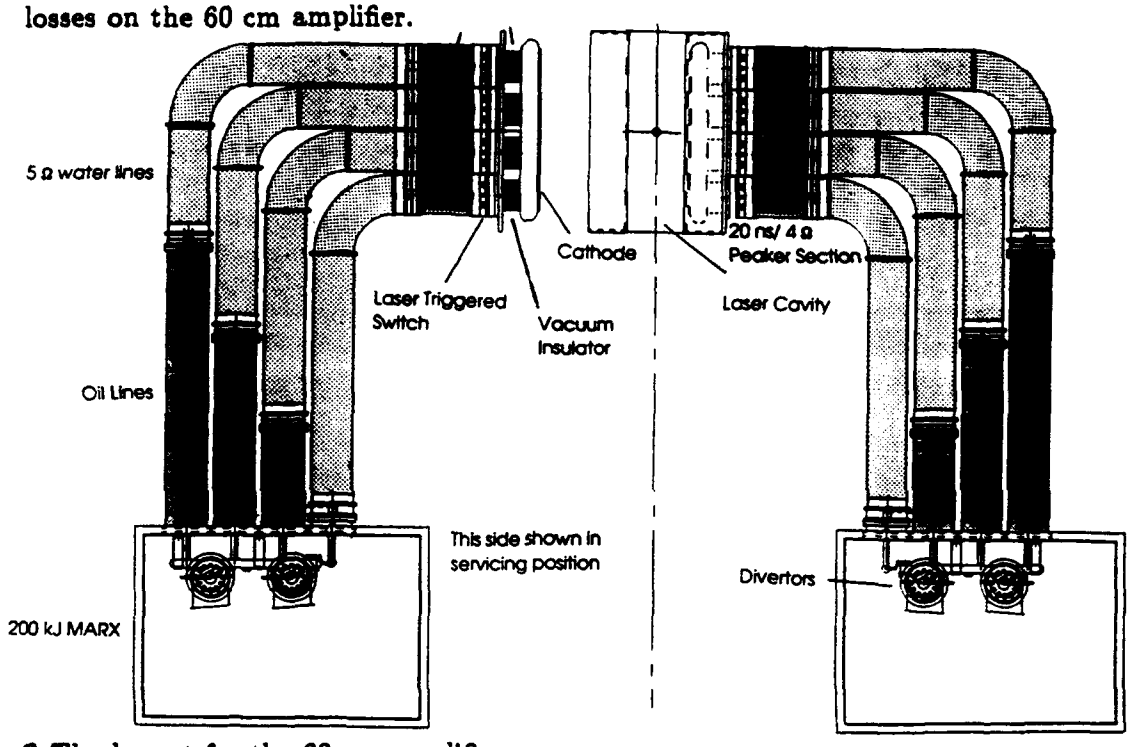


Figure 6. The layout for the 60 cm amplifier.

blockage on the media were approximately 80% as estimated. Calculations indicate that with the correct laser cell pressure a 10% uniformity across the laser aperture in the laser gain should occur with both the required stage gain and total energy output. Preliminary laser amplifier tests yielded the required performance, but more optimized extraction with better diagnostics are needed for more conclusive results.

The 60 cm Amplifier

Figure 6 shows the layout for the 60 cm amplifier. Each electron diode of the 60 cm amplifier has its own 12 stage 1.44 MV 240 kJ Marx bank. The Marx bank charges four water pulse forming lines which are bent in order to fit this amplifier into our facility. Simulations and scale tests have shown the bends will not distort the square top pulse or significantly increase the chance of breakdown. Each water pulse forming line has its own laser triggered switch and z-stack vacuum insulator which all connect to a single monlithic cathode shell and emitter. The cathode emitter edges do not require special care because

the edges of the beam are clipped at the anode screen. The electron beam is designed for 680 keV with 544 kA of current. The anode screen is tapered away from the cathode at the edges to reduce any emission from the cathode shell. To increase the deposition in the gas the 60 cm uses a 3.6 kG magnetic guide field and the hibachi bars are specially tapered (see Fig. 4 b) to reduce beam slant losses near the edges. 75μm Kapton or 25 μm metal foils will be used. A peaker section added to each water line is required to reduce the risetime to 70 nsec to produce a 240 nsec flat top pulse on the electron beam. If the 60 cm amplifier deposition efficiency matches that of the 20 cm amplifier, more than 80 kJ should be deposited into the lasing gas. This will allow 4 kJ of laser light to be extracted from the 60 cm amplifier.

Special thanks to Kent Gerber, John Bone and Warren Webster.
†Permanent address CLS-5, Los Alamos National Laboratory, Los Alamos, N.M. 87544.
This work supported by the U.S. Dept. of Energy

References

1. S. Obenschain, S. Bodner, R. Lehmberg, A. Mostovych, C. Pawley, M. Pronko, J. Sethian, J. Stamper, A. Deniz, T. Lehecka, and J. Shipman, Proc. of the Thirteenth Int. Conf. on Plasma Phy. and Cont. Nuc. Fusion Res., IAEA-CN-53\B-3-3, 1990
2. R. J. Jensen, L. A. Rosocha, and J. A. Sullivan, Proc. SPIE High Power and Solid State Lasers, 622, 70, 1986
3. H. Mizoguchi, A. Endoh, J. Jethwa, B. Rácz, F. P. Schäfer, Appl. Phys. B, 52, 195-199, 1991
4. L. A. Rosocha, J. A. Hanlon, J. McLeod, M. Kang, B. L. Kortegaard, M. D. Burrows, and P. S. Bowling, Fusion Technology, Vol. 11, No. 3, 497, 1987
5. S. P. Obenschain, S. E. Bodner, K. J. Kearney, R. H. Lehmberg, A. N. Mostovych, C. J. Pawley, M. S. Pronko, J. D. Sethian, J. A. Stamper, T. Lehecka, A. V. Deniz, Drivers for Inertial Confinement Fusion, vol. 2, IAEA, Dec. 1991
6. R. H. Lehmberg, T. Lehecka, A. V. Deniz, Drivers for Inertial Confinement Fusion, vol. 2, IAEA, Dec. 1991
7. Ken-ichi Ueda, Institute for Laser Science, UEC Tokyo, private communication
8. C. J. Pawley, T. Lehecka, S.P. Obenschain, J. Bone, V. A. Thomas, M. E. Jones, to be published.
9. J. E. Eninger, Dig. Tech. Papers, 3rd IEEE Pulsed Power Conf., 499, 1981
10. L. A. Rosocha, K. B. Reipe, Fusion Technology, Vol. 11, No. 3, 576, 1987
11. Y. Owadano, I. Okuda, M. Tanimoto, Y. Matsumoto, T. Kasai, M. Yano, Fusion Technology, Vol. 11, No. 3, 486, 1987
12. A. Endoh, M. Watanabe, S. Watanabe, Fusion Technology, Vol. 11, No. , 492, 1987
13. J.A. Sullivan, G. R. Allen, R. R. Berggren, S. J. Czuchlewski, D. B. Harris, M. E. Jones, B. J. Krohn, N. A. Kurnit, W. T. Leland, C. Mansfield, J. McLeod, A. W. McCown, J. H. Pendergrass, E. A. Rose, L. A. Rosocha, V. A. Thomas, Drivers for Inertial Confinement Fusion, vol. 2, IAEA, Dec. 1991

DEVELOPMENT OF A 100 JOULE LEVEL XeCl LASER PUMPED BY INTENSE RELATIVISTIC ELECTRON BEAM

J.R.Liu,R.F.Sun,A.C.Qiu,X.Yuan, Y.G.Gan,X.H.Wang,Y.M.Zhang,
X.Q.Zhao,S.Q.Ren,L.Nie,D.S.Yao,L.G.Wang,M.Zhang,Y.M.Wei,L.H.Wang
Northaest Institute of Nuclear Technology
P.O. Box 69, Xian, 710024, P.R. of China

ABSTRACT

A 100 J level XeCl laser pumped by an intense relativistic electron beam- FLASH II was constructed at Northwest Institute of Nuclear Technology in China. FLASH II is a low impedance REB accelerator. It consists of a 64 stage Marx generator, pulse forming line, field-distortion main switch,pulse transmission line,output lineand diode. The cathode of diode for laser pumping is a 15 x 60 cm long multi-point copper plate or graphite plane plate.The anode and pressure foils are both 25 micron Ti. The voltage of diode is measured to be 650-750 kv and the current 290-350 kA. The pump power density ranges between 1.5-2.0 MW/cm^3.

The aperture of laser cell is 20 x 20 cm and the effective excitation volume is 24 liters. We have obtained the laser output energy of 136 J with a parallel-plane resonator and 1.5 mrad divergence angle from an unstable resonator. The laser power is measured to be more than 10^9 W.

INTRODUCTION

The interaction of intense UV radiation with matter is an attractive field of research. A 100 J level XeCl laser pumped by an intense relativistic electron beam accelerator - FLASH II was developed in our Institute for the research of thermal and mechanical coupling of pulsed UV radiation to the materials.

Strcture and performance of the pulsed power system are described at the second section, followed by the laser resonator characteristics and the experimental results.

PULSED POWER SYSTEM

FLASH II is a low impedance relativistic electron beam accelerator which maximum storage energy of a 64 stage Marx generator is 224 KJ.[1] The water-dielectric coaxial line includes pulse forming line, main awitch, transmission line, prepulse switch and output line. The output pulse width of PFL is 80 ns and the characteristic impedance is 5Ω. The length of transmission line of 3.2Ω impedance is 1.34 m. The output line is a cone cylinder which actual length is 2.0 m and the impedance is 2Ω. The main -

switch is a water-dielectric field distortion switch and the prepulse switches are 8 gas switches filled with SF_6 in parallel. FLASH II was designed originally for generating electron beam for the effect to the materials, hence the diode is a 220 mm diameter plate which maximum voltage has been 1.3 MV and the current 650 KA. The electrical model of this accelerator is shown in Fig.1.

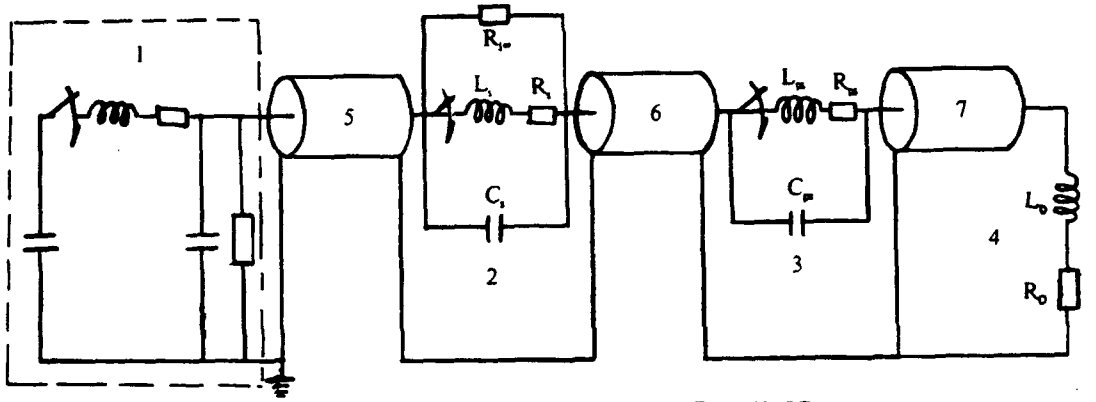


Fig.1 Electrical model of FLASH II
1. Marx generator 2.output switch 3.prepuls switch 4. diode
5. PFL 6.transmission line 7.output line

A large area rectangular (15 x 60 cm) diode was designed on the base of original diode chamber for excimer laser pumping. Two kinds of structure are used for the cathode, one is multi-point copper plate and another is a graphite plane plate. Titanium foil of 25 micron in thickness is used both as anode and pressure foil. Anode-cathode spacing is changed from 24-26.5 mm. The pressure foil is supported by hibachi structure which is 70 cm in length and 20 cm in width and has a geometrical transmission of 83 %.

The doide voltage is measured by a differential capacitor divider which is located at the end of output line. A Rogowski coil and a B-probe are used for diode current measurement. Typical waveforms of diode voltage and current are shown in fig.2(a) and 2(b). Measured diode parameters for different voltage level are shown

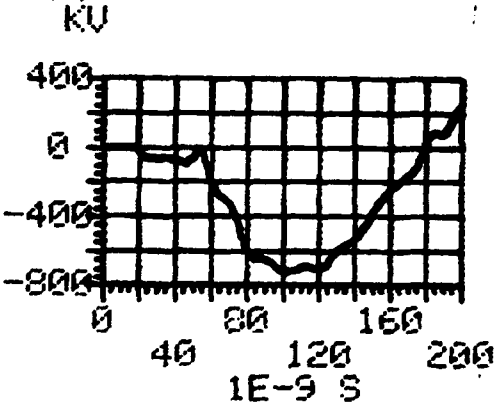


Fig.2(a) waveform of diode voltage

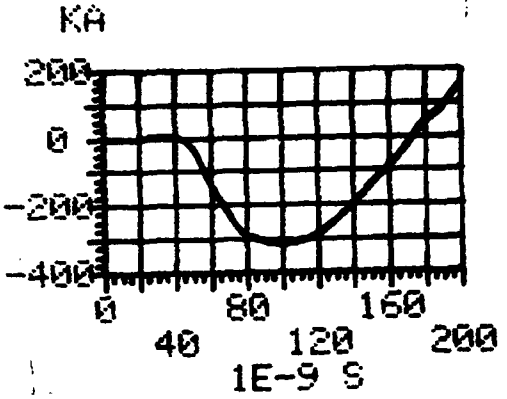


Fig.2(b) waveform of diode current

in table I. The parameters for 40 kv charge voltage are the average value for 22 shots using the multi-pin copper cathode and the data for 45 kv charge voltage are the average value for 124 shots using the graphite plane plate.

TABLE I

charge voltage	V (kv)	40	45
A - K gap	D (mm)	24	26.5
diode voltage	V_d (kv)	684.5	743.0
diode current	I_d (kA)	295.6	328.0
pulse width of I_d	T (ns)	83.6	83.7
total beam energy	E (kJ)	11.4	14.3
diode impedance	R (Ω)	2.25	2.24

A simulation code has been developed to calucating the deposition power density in laser gas.[2] According to the operation voltage of 650 kv - 750 kv and current of 290 - 350 kA, the deposition power density is estimated to be 1.5-2.0 MW/cm^3 when the gas pressure is 0.3 MP_a.

LASER EXPERIMENT

A. Laser Resonator and experimental device

Shown in fig.3 is the general view of XeCl laser pumped by FLASH II.

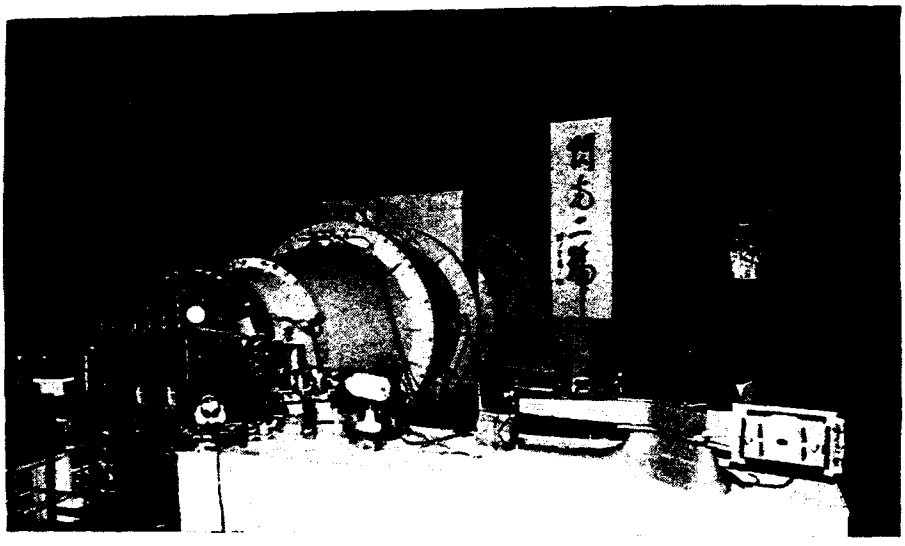


Fig.3 The general view of XeCl laser pumped by FLASH II

The schematic diagram of experimental device is shown in fig. 4. The laser cell has a 20 x 20 cm aperture and an effective excitation volume of 24 liters. The optical axis of laser chamber is at an angle of 7° to the normal of fused silca window coated by antireflection so that the reflection of the windows to the laser can be reduced. There are two kinds of optical resonators. The

parallal-plane resonator consists of a total reflector with 98 % reflectivity and a coupler with 30 % reflectivity. The positive confocal unstable resonator of 1.26m in length (M=3) and 1.5m in length (M=5) are used respectively. The damage threshold of all optical coatings to 308 nm laser are measured to be higher than 2.2J/cm^2. The partial pressure ratio of operation gas for XeCl laser is generally HCl:Xe:Ne=0.3%:2.7%:97% and the total pressure is 0.3MP$_a$ to 0.4MP$_a$.

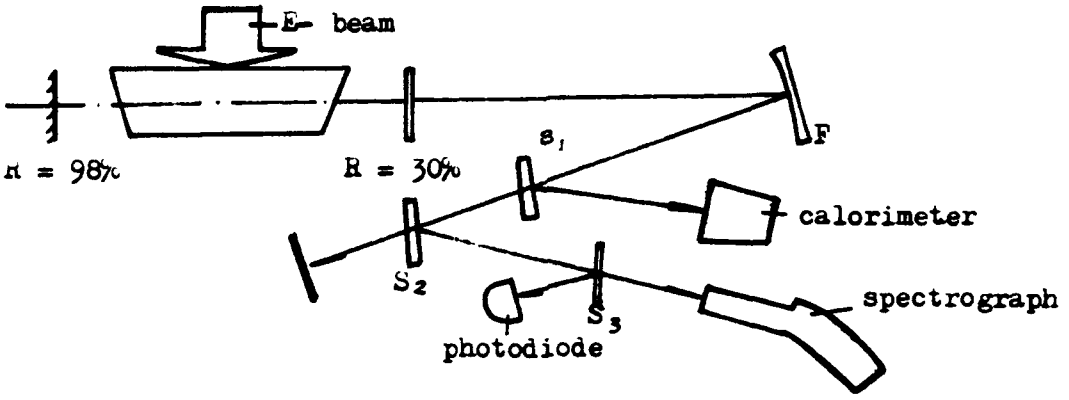


Fig.4 Schamatic diagram of laser experimental system

After reflecting by a concave mirror F and a quartz splitter S_1 the output laser energy is measured by a calorimeter. Laser waveform is monitored by a GD-40 photodiode. The laser beam passes through S_1, S_2 and produces burn pattern at the focal plane of mirror F so that we can estimate the divergence angle of the laser beam. The laser spectrum is observed by a quartz prism spectrograph.

B. Experimental Results

The maximum output energy of 136 J was obtained with parallel-plane

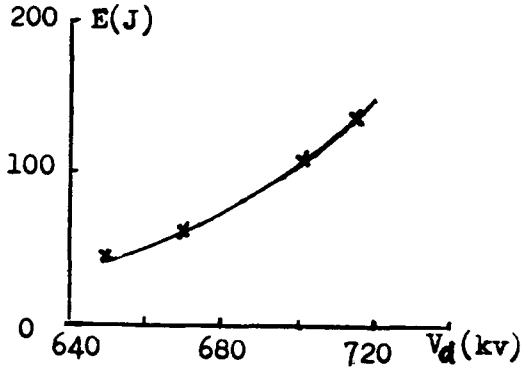


Fig.5 laser energy vs.diode voltage

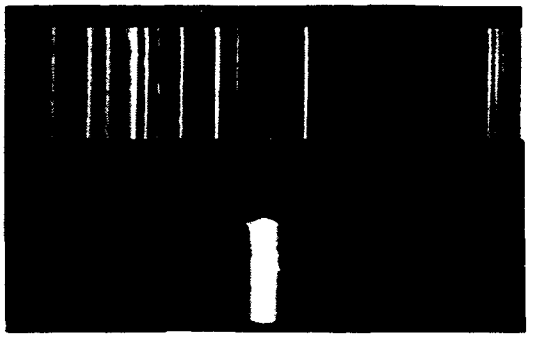


Fig.6 Typical XeCl laser spectrum, (middle) and fluorescence spectrum(lower).(the upper one is iron spectrum)

resonator in this experiment. Output laser energy versus diode voltage is shown in Fig.5. The maximum intrinsic efficiency is 3.5 % and the specific energy is 5.7 J/l. The typical XeCl laser spectrum and fluorescence spectrum are shown in Fig.6. Laser waveform and fluorescence waveform are shown in fig.7(a) and 7(b) respectively. The pulse width(FWHM) of laser is about 40 ns and that of fluorescence is about 60 ns. The delay time between laser and fluorescence is about 30 ns which is agreement with the gain built up time calculated by the kinetic model[2]. The laser power is calculated to be more than 10^9 W.

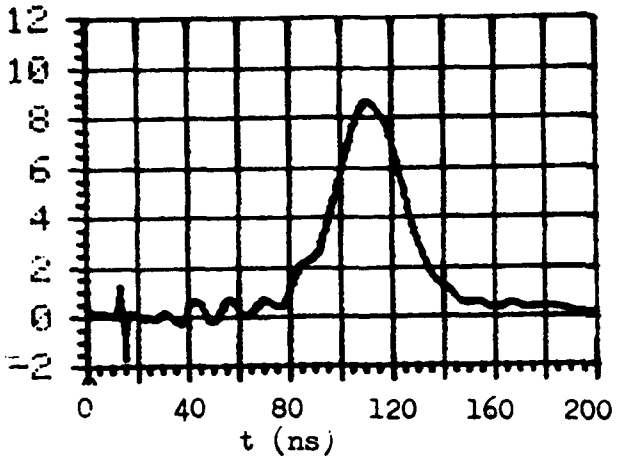


Fig. 7(a) laser waveform

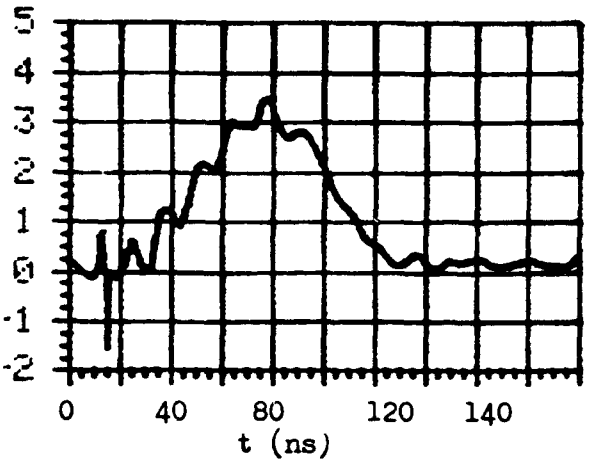


Fig.7(b) Fluorescence waveform

Shown in fig.8(a) and 8(b) are laser burn patterns at the focal plane with parallel-plane resonator and unstable resonator. The calculated divergence angle of 12.8 mrad for paeallel-plane resonator and 1.5 mrad for unstable resonator are obtained from the mearsured pattern.



Fig.8(a) Burn pattern for parallel plane resonator



Fig.8(b) Burn pattern for unstable resonator

SUMMARY

A 100 J level XeCl laser has been developed for the UV radiation research. Laser output energy of 136 J has been obtained with intrinsic efficiency of 3.5 % and power of more than 10^9 W. The divergence angle has been improved to be 1.5 mrad by using an unstable resonator.

REFERENCE

1. A.C.Qiu etal : High power laser and partical beams , Vol.3, No.3 P340,1991

2.Q.F.Tu etal: High power laser and partical beams, Vol.3, No.3, P356, 1991.

REB PUMPED SYSTEMS WITH MULTIPOLE MAGNETIC FIELD WALL SHIELDING

G.P. Mkheidze, A.A. Savin, F.B. Trintchouk

General Physics Institute
117942 Moscow, Vavilov st.38, Russia

Abstract Effective systems of REB injection have been proposed. Injection through multipole magnetic field allows to control spatial distribution of deposited energy and to reach high deposition efficiency (up to 90%).

The enhancement of efficiency of relativistic electron beam energy deposition into a gas is an important problem for the systems with beam plasma as an active medium. In this respect the system with wall shielding provided by the multipole magnetic field created by $N_m=2n$ conductors appears efficient. Such systems are good traps for the electrons injected into the "mouth" of the multipole magnetic field.

The examples of the systems with external (a) and internal (b) REB injection are shown in figure 1. Below we consider energy deposition in the external injection system only.

The code simulating electron beam propagation in the chamber filled with a noble gas in the presence of multipole magnetic field is based upon Monte-Carlo trajectory method. The electrons with energy E are injected from N_m points located between the conductors at a distance R_0=13 cm from the axis of the cylindrical chamber through δ=20 μm thick titanium foil into the volume containing argon at pressure P_0. The magnetic field in the point of injection is B_m. N_m, E, B_m and P_0 varied in the numerical experiments. Total efficiency of the system is determined

by the following parameters: the fraction of the energy absorbed by the gas $\eta_G = W_{dep}/W_d$ (ratio of REB ionization losses in gas to energy of the beam injected into the system) and the distribution of specific energy deposition $q(r)$ (divided by the energy W_b averaged over the chamber volume). Dependence of energy deposition efficiency η_G on magnetic field B_m is represented in the figure 2. The $\eta_G(B_m)$ curve spectacularly demonstrates efficiency of action of the multipole magnetic field, which limits losses of beam electrons on the walls. In increasing the number of conductors the magnetic field gradient in the mirror region grows and the field tends to keep closer to the chamber walls. This must be accompanied with diminishing losses of the beam injected into the chamber. On the other hand in increasing N_m the quantity of the losses channels also grows. Consequently one can expect the $\eta_G(N_m)$ curve to have a maximum. As is seen from figure 3, the efficiency remains high (>72%) over a wide range of N_m from 4 to 32 and reaches its maximum value of ≈ 0.86 at N_m=12.

The dependencies of energy deposition efficiency η_G on electrons energy E have maxima at E= 280 - 300 keV. η_G falls when E departs from these values in either direction.

The change in pressure P_0 leads to the change in integral electron track length λ. When $\lambda \gg R_b$, i.e. at low pressures, the number of collisions of an electron and the magnetic walls is large and consequently the probability of the electron's escape through the mirrors is high. At $\lambda \ll 2R_b$ the greater part of energy of the injected electrons is contributed to the gas. Figure 4 features curves $\eta_G(P_0)$ at N_m = 4, 12 and 24. Since the current in the conductors was held constant, the magnetic field B_m grew with the increase of the conductors number N_m. All three curves are characterized by fast growth of energy deposition efficiency with pressure increase up to 1.5 - 2.5 atm and

relatively weak dependence of η_G on P_0 at further pressure increase. One can see that optimal conditions are N_m=12 at P_0≈2.5 atm.

The energy deposition efficiency, while an important characteristic of the system, still does not determine its overall performance, which depends also on radial distribution of specific energy deposition. The change in N_m causes specific energy deposition profiles to change substantially (figure 5). The case of N_m=0 corresponds to absence of magnetic field (curve 1). The beam loses its energy primarily in the central region of the chamber (with effective radius of ≈4 - 5 cm) at N_m=4. As N_m increases the region of energy deposition becomes wider and at N_m=32 the FWHM radius of the $q(r)$ distribution is ≈ 11 - 12 cm. The beam energy losses distribution is rather homogeneous in the region with radius of ≈10-11 cm at N_m=12, which corresponds to maximal energy deposition efficiency. Thus it is possible to regulate the radius of effective beam losses energy by varying N_m. This is easy to do within certain limits by switching the direction of the current in the conductors.

The distributions of specific energy deposition for different values of pressure P_0 are shown in figure 6. The curves indicate that one can obtain various energy deposition configurations with maximum localization ranging from the central region to the periphery by means of varying P_0. A uniform energy deposition may be expected at pressures P_0=2 - 3 atm.

The calculations showed that the parameters N_m, P_0, E, B_m are of influence in obtaining the desired result: maximal η_G (up to ≈80%) in combination with uniformity of specific energy deposition $q(r)$.

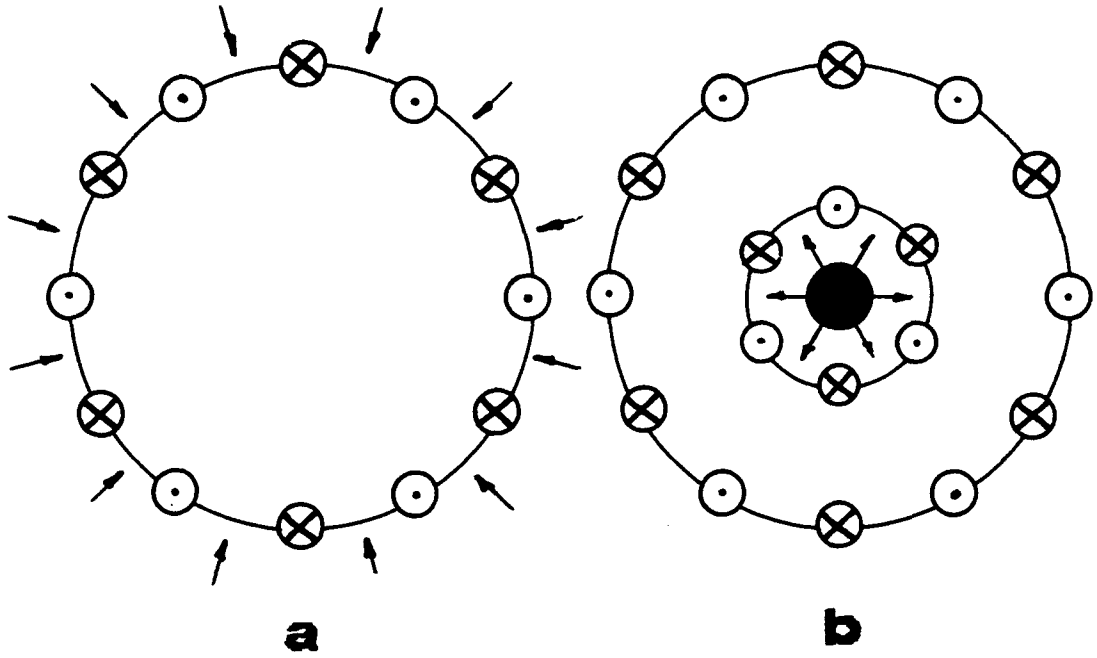


Fig. 1. Configurations with multipole magnetic field. a - external REB injection (N_m=12), b - internal REB injection.

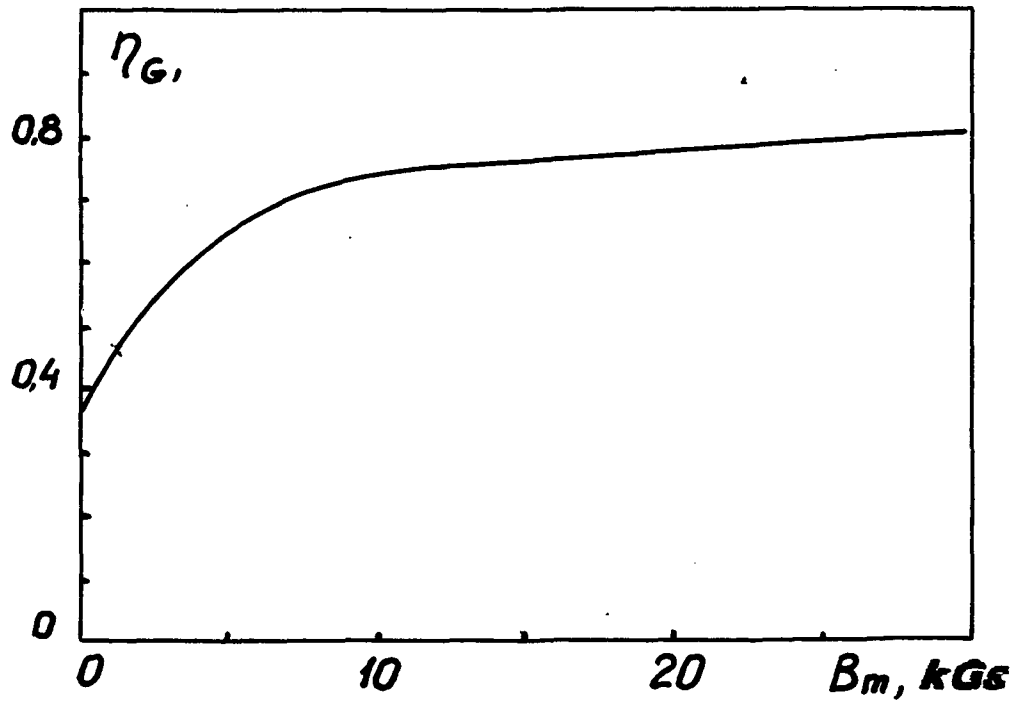


Fig. 2. Dependence of energy deposition efficiency η_G on magnetic field B_m (N_m=12, E=300 keV, P_0=1 atm).

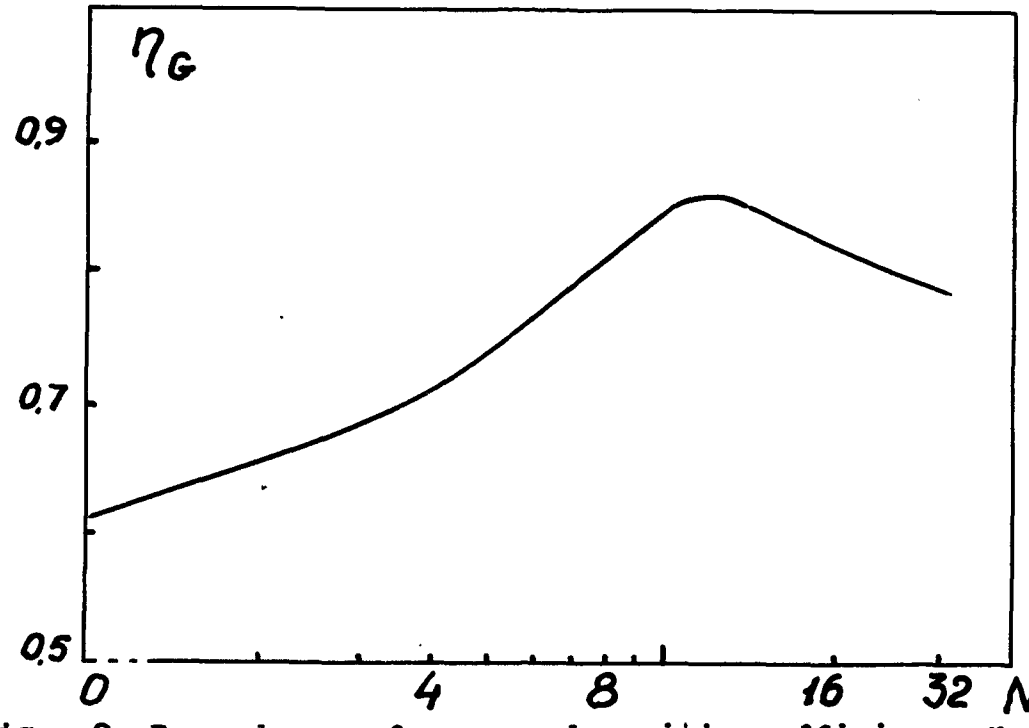


Fig. 3. Dependence of energy deposition efficiency η_G on number N_m of conductors (B_m=4.7 kGs, E=300 keV, P_o=2 atm).

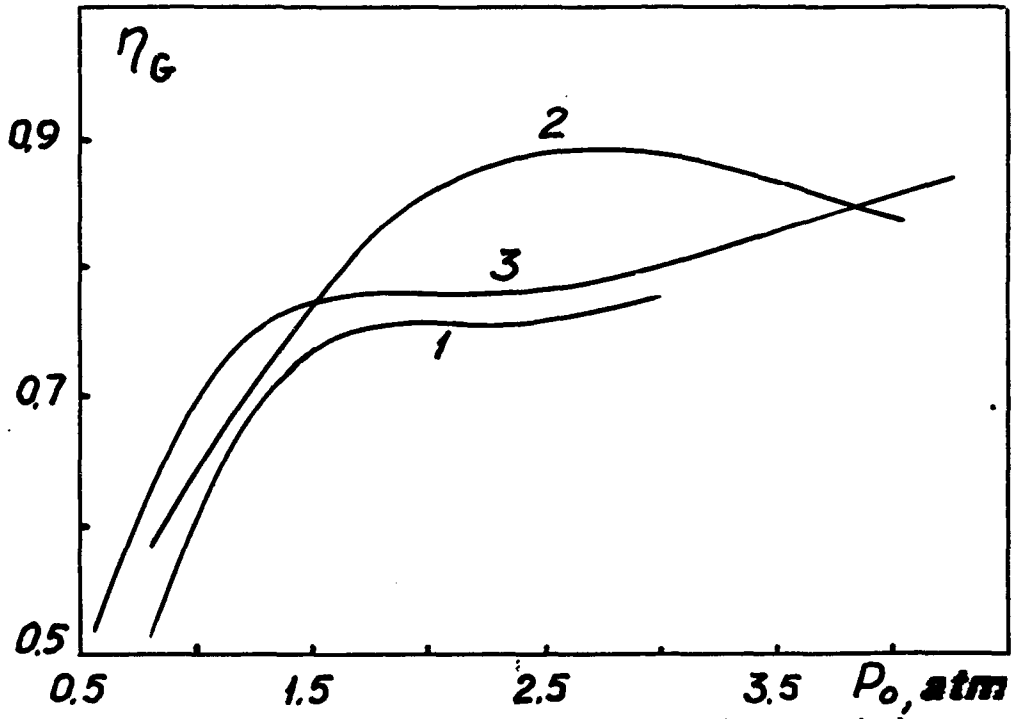


Fig. 4. Dependencies of energy deposition efficiency η_G on pressure P_o (I_m=50 kA, E=300 keV); **curve 1:** N_m=4; **curve 2:** N_m=12; **curve 3:** N_m=24.

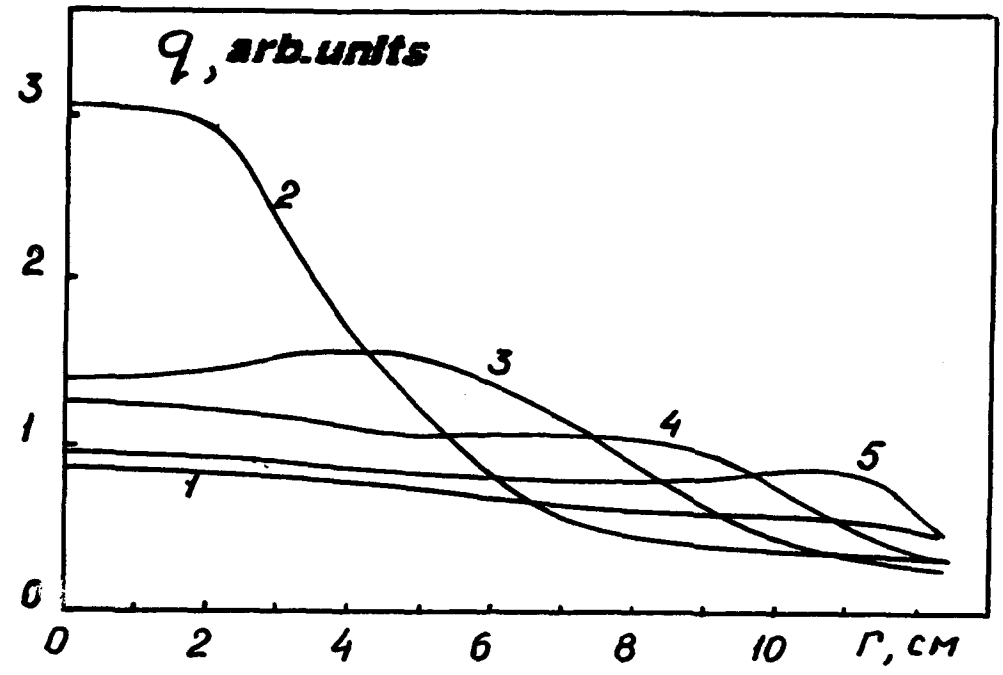


Fig. 5. Radial distribution of energy deposited in gas at various N_m; **curve 1:** N_m=0; **curve 2:** N_m=4; **curve 3:** N_m=8; **curve 4:** N_m=12; **curve 5:** N_m=32.

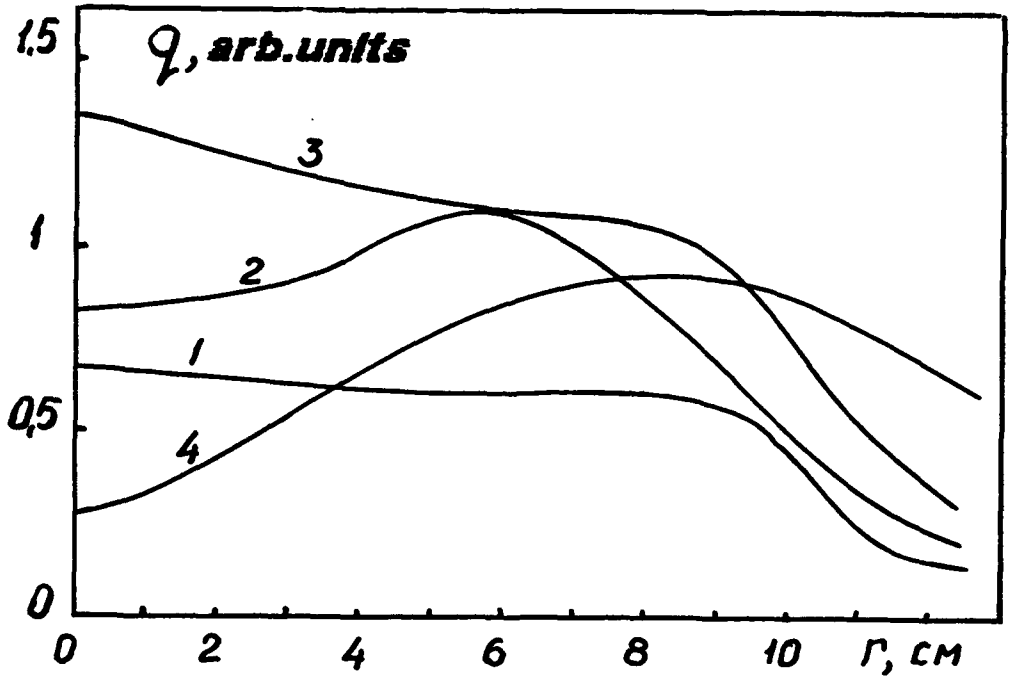


Fig. 6. Radial distribution of energy deposited in gas at various values of pressure; **curve 1:** P_o=0.5 atm; **curve 2:** 1 atm; **curve 3:** 2 atm; **curve 4:** 4 atm.

LARGE-APERTURE E-BEAM PUMPED EXCIMER LASERS FOR ICF

E.P.Bolshakov, V.A.Burtsev, M.A.Vasilevsky, V.M.Vodovosov,
V.V.Jeremkin, V.E.Kuznetsov, V.A.Ovsyannikov, O.P.Pechersky,
V.F.Prokopenko, R.F.Fidelskaya, K.I.Finkelstein, V.I.Chernobrovin,
V.I.Chetvertkov
D.V.Efremov Institute of Electrophisical Apparatus, 189631,
St.Petersburg, Russia
V.Yu.Baranov, A.P.Streltsov
I.V.Kurchatov Institute of Atomic Energy, 123182, Moscow

ABSTRACT. The design of an unified large-aperture final amplifier taken as a base of an excimer channel for laser drivers is described According to calculations it can yield in long pulse generation the laser output up to 20 kJ under using Ar-Kr-F_2 mixture at pressure P=1,4 atm. Also, the results, obtained at testing of the model excimer lasers pumped by contrary e-beams "Lira-1M" and "Lira-01" with 1 and 0,1 kJ output energy respectively are reported.

INTRODUCTION

Excimer lasers being capable of working in UV-range of spectrum with required pulse repetition rate are the main candidates as laser drivers for ICR. Efremov Institute in cooperation with Kurchatov Institute has performed the conceptual design of KrF laser channal with output energy up to 100 kJ at 3-5 ns pulse duration/1/. This design suggests the combined use of stackers and SMBS-compressors to solve the problem of laser pulse shortening to nanosecond level at microsecond pumping of active medium in powerful final amplifiers. The project was being worked out with using of unified large-aperture two-pass amplifiers, connected on parallel-consecutive scheme. The powerful amplifiers are supposed to be pumped through both sides of chambers by means of contrary e-beams in a guiding magnetic field to provide sufficiently uniform energy depossition.

In this report the results of more detailed designing of the unified final amplifier, including a high current diode, systems for high voltage pulse formation and coupling are presented. Besides, the preliminary test results of two excimer lasers "Lira-1M" and "Lira-01" are reported. These lasers are designed to obtain in a long pulse of generation, compared with the duration of e-beam pumping (500 ns) output energy 1 and 0,1 kJ correspondingly and intentended to verify physical ideas, engineering and designing solutions accepted in the project of the final laser amplifier.

CHOISE OF MAIN PARAMETERS FOR THE UNIFIED AMPLIFIER

Parameters of the final amplifier were defined by using of composite numerical simulation of e-beam pumping and generation processes with account of main physical phenomena /2,3/. Performed calculation showed existence of optimum for the total efficiency of laser channel η at the pumping pulse duration of $\tau \simeq 500$ ns, what corresponds the specific pumping power $p \simeq 0{,}2$ MW/c.cm at the specific energy deposition $w \simeq 0{,}1$ J/c.cm. The total efficiency of the laser line in this case can reach $\eta = 3{,}7$ % /3/.

Final calulations of geometrical dimensions of the chamber, total and partial pressures of active medium, specific energy and power of pumping, accelerating voltage and beam current were performed with account of the following limitations: the total pressure $P \leqslant 15$ atm, the current density on the foil $j_f \leqslant 25$ A/sq.cm, the accelerating voltage $U \leqslant 750$ kV. All the parameters of the final amplifier are presented in Table 1.

Table 1

Length of the chamber L, m	3,7
Chamber aperture HxD, m.m	1x1,1
Accelerating voltage U_d, kV	700
Diode current I_d, kA	1000
Cathode current density j_d , A/sq.cm	25
Current density after the foil j_g,	11,25
Stored energy per a single diode W_d, kJ	400
External magnetic field B, kG	2-3
Gas pressure P, atm	1,4
Efficiency of energy transfer into the diode η_d, %	85
Efficiency of transfer through the support structure η_s	45
Efficiency of energy transfer into gas η_g,%	90
Intrinsic efficiency η_{int}, %	6,2
Pumping pulse duration τ_p, ns	480
Specific pumping power p, MW/c.cm	0,14
Amplification factor G	13
Input beam energy E_{in}, kJ	1,55
Output beam energy E_{out}, kJ	20

The structural scheme of final amplifier is shown on Fig.1. Let us consider in more details the design of electron guns and its high voltage supply systems which compose large aperture electron accele-

raters for pumping of the final amplifier.

ELECTRON ACCELERATORS

Electron guns allow to obtain contrary e-beams 1,1x3,7 sq. m in cross-section. Explosive emission emitters are made from the strips of graphite material and positioned across the cathode with the pith being equal to one of the support structure. According to calculation performed with account of the electron trajectories in complex fields the total transparency of the structure $\eta_s \simeq 50$ % at $B/B_0 \geq 2$.

To provide the effective operation of cathodes the front duration of high voltage pulse should be not exceed 50 ns at 500ns plane part As a result of analysis of various versions the scheme, consisting of three parallelly disposed and synchronously operating complex forming modules was chosen (Fig.1). Analysis and calculations of the equivalent electric circuit showed that the pulsations on the top of accelerating voltage pulse do not exceed 0,64-0,7 MV (Fig.2).

MODEL EXCIMER LASER "LIRA-1M"

The peculiar feature of laserLira-1M" (the total view - Fig.3, the rated parameters - Table 2), created in Efremov Institute at 1990 is the construction of high voltage pulse forming systems on base of fast Marx generators with using of special low-inductive capacitors. Each of generators consists of 6 identical 5-stage branches, three of which are located above and the rest below the reverse current conductors. This allowed to minimize the total inductance of the circuit and to obtain experimentally the desired pulse duration of 0,45 μs.The parameters of the guns: $U_d \simeq 275$ kV, $I_d \simeq 75$ kV (Fig.4).

COMPACT EXCIMER LASERS

For thermonuclear investigations and other applications, especially for technological purposes it needs the compact exciter amplifiers and generators being capable of working in a pulse-periodical regime with accelerating voltage pulse form close to rectangular. From this point of view the wide possibilities are given by using of artificial single or double forming lines with paper-oil-film insulation. Similar double forming lines were used in compact 100 J exciмer laser "Lira-01", created in Efremov Institute (Fig.5). It has two explosive emission electron guns and one pulse power supply, connected by means of coaxial cables. Four-stage Marx generator is

swiched by rail spark gaps. At charging voltage of 75 kV it gives the pulse with amplitude of 300 kV, total duration of 500 ns, front duration of 100 ns on the load with resistance of 8 Om.

The design of 1kJ compact excimer laser "Lira-1" and the technical proposal on more powerful laser "Lira-10" were performed on the same principles. Thear parameters are presented also in Table 2.

Table 2

Parameters\Device name	LIRA-1M	LIRA-01	LIRA-1	LIRA-10
Laser output (KrF), kJ .	1	0,1	1	10
Chamber length, cm	150	100	150	300
Aperture, sq.cm	35x35	13x13	30x30	80x80
Pulse duration, ns	450	500	500	500
Repetition rate, Hz	10	20	10	10
.Pump.power,MW/c.cm	0,1	0,25	0,35	0,2
Ext.magn.field, T	0,16	0,05	0,16	0,3
Electron energy, keV	330	260	380	600
Curr.dens.in gas,A/sq.cm	12	10	18	15
Stored energy, kJ	13x2	4,9	32x2	200
Stored element/Capacity.,μF	C/0,2	FL/0,5	FL/0,5	FL/0,5
Charging voltage, kV	∓ 45	70	80	90
Stage/branch quantity	5/6	4/1	5/4	8/12
Insulating medium	Gas	Oil	Oil	Oil
Pumping pulse form	Aperiod.	Bell	Bell	Bell
Gas flow, c.m/s	8	1	8	45
Gas speed, m/s	13	6	13	16
Max.gas pressure,atm	1,5	1,5	1,5	1,5
Fan	Axial	Centrifugal many- streams		

REFERENCES

1. V.Yu.Baranov, V.A.Burtsev, M.A.Vasilevsky et.al. Design of an excimer laser channel for fusion: Preprint NIIEFA P-K-0859.- M: TSNIIatominform, 1990, 28 p.
2. M.I.Avramenko, V.A.Burtsev et al. Numerical investigations of electron energy deposition into gas medium of an excimer laser: Fusion Technology, May, 1991, p. 440-448.
3. V.A.Burtsev, A.G.Grad et al. Excimer lasers for inertial confinement fusion: lasma devices and operations, v.1, 1991, p. 213-226.

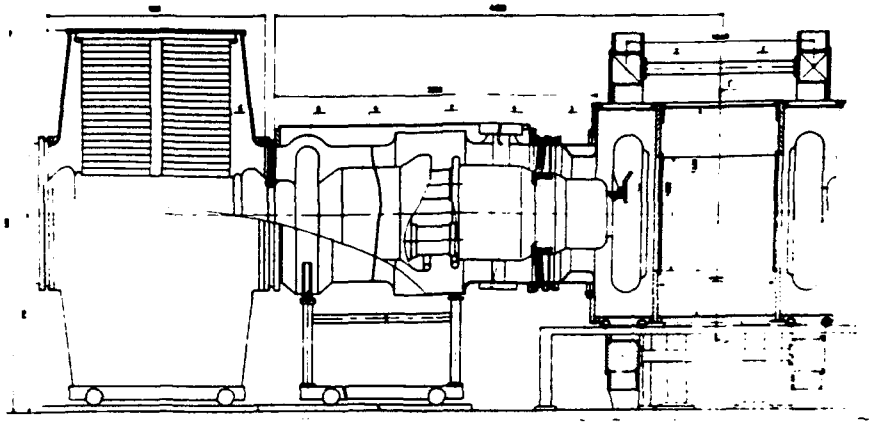
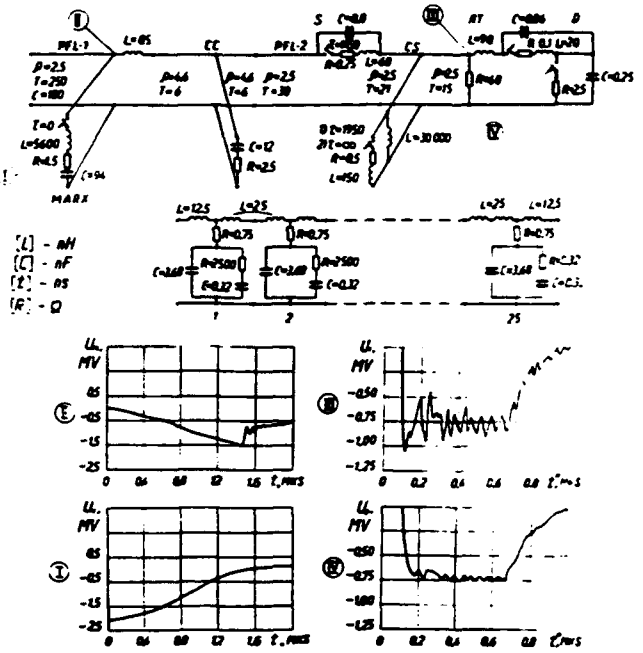


Fig.1.Final exoimer amplifier
1-chamber,
2-magnetic coils
3-diode
4-coaxial line
5-stripe line
6-accelerator tube
7-commutators
8-correc.element

Fig.2.Eqivalent scheme of the forming module and calculated oscillograms of voltage in different points



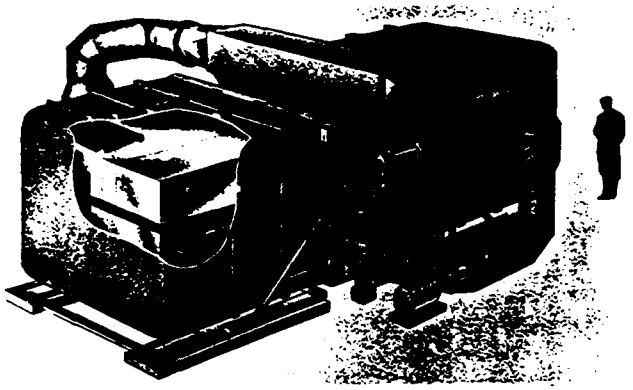


Fig.3.Exoimer laser "Lira-1M"

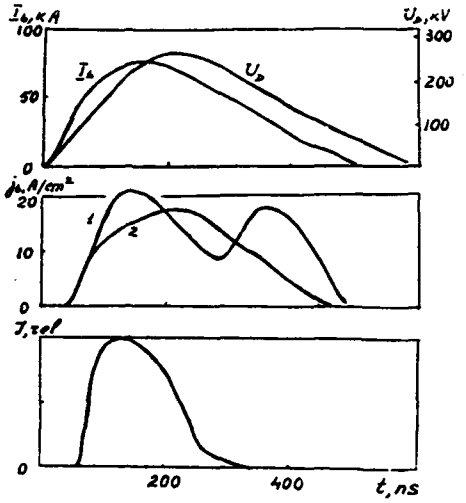


Fig.4.Oscillograms of diode voltage, current denoity on the edge(I) and in center (2) of beam, laser intenoity

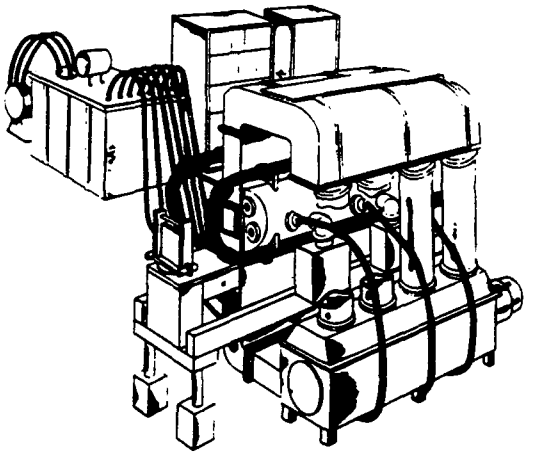


Fig.5.Excimer laser "Lira-01"

PULSE HEAT TREATMENT OF MATERIAL SURFACE BY HIGH-CURRENT ELECTRON BEAM

V.I.Engelko,A.V.Lazarenko,O.P.Pechersky

D. V. Efremov Scientific Research Institute
of Electrophysical Apparatus

Metallostroy St. Petersburg
189631 Russia

ABSTRACT. Results of the studies of high-current pulsed electron beam effect on a material surface are presented. An electron beam was produced in an accelerator with a multi-point explosion-emission cathode(60-180kV, 4-40μsec, 10-60J/cm^2). Modification of the surface properties was observed at the irradiation energy density, exceeding 22-25J/cm^2) and the depth of a modified layer in 10-50μm range. The hardness of a treated surface layer exceeded that of the base by a factor 2-5. The use of HEB treatment to obtain other possible surface modifications is also discussed.

High current pulse electron beams have energy, sufficient for heating of a surface of any material up to the melting point during a short period of time (10^{-9}-10^{-5}sec). In this case only a surface layer, thickness of which is comparable with an electron path length, is warmed thoroghly. After electron beam pulse termination a fast cooling of the surface layer takes place due to the heat removal deep into a sample being treated. Possibility of fast heating and cooling of the surface layer of the sample is the main peculiarity of pulse heat treatment of materials.

Laser, electron or ion beams as well as plasma flow are used for the pulse heat treatment. Each of the mentioned energy carriers has its advantages and disadvantages. In particular, high current electron beam (HEB) has the following advantages: depth of a layer being treated may be easily controlled by applied accelerating voltage from units up to hundreds of microns; preliminary preparation of a sample surface is not required; high current pulse accelerator has the highest efficiency of energy transfer from a source to a sample; it is possible to treat a part of the sample

surface area which is tens of square centimetres(hundreds centimetres,if necessary) for a single pulse; it is possible to treat samples of complicated geometry; treatment of samples may be performed both in vacuum and atmosphere.

High current pulse electron accelerators are simple in design, cheap,safe and reliable in operation.Already for many years D.V.Efremov Institute has been carried out studies,aimed at search and development of technological processes using heat treatment of material surfaces by a pulse high-current electron beam as well as works on designing of an experimental technological installation.At present production forms and records are available and this installation is under construction.

The choice of an electron beam parameters was based on the calculations of temperature distribution in a flat sample,that were carried out at the stages of heating and cooling.The optimum beam parameters were considered those,at which energy deposited in a sample did not run beyond an electron absorption layer during the whole pulse;an energy density was sufficient for melting of any material for a single pulse;depth of the treated layer had to be tens of microns.Fig.1 and 2 show the examples of the calculated temperature distributions at the heating stage and temperature gradient at the cooling stage for a steel 45 sample.The calculated data give us a cooling rate estimation:

$$\frac{dT}{dt} = 0.16 * 10^{10} \frac{\lambda \rho T_p}{c} E^{-3.3(keV)} 10^{2.3 \frac{T_k - T_o}{T_m - T_o}}$$

where λ is the heat-transfer coefficient,ρ is the material density,c is the heat capacity,T_o is the sample temperature,T_k is the peak value of the temperature distribution versus depth T(x) at the time t_k,T_m is the peak temperature when the cooling starts, T_p is the melting temperature,E is the electron energy.

Results of calculations allow to make a conclusion,that optimal parameters of an electron beam for technological studies are the following:electron energy is 100-300keV,pulse duration is $\tau \leq 10 \mu sec$,current density is 10-50A/cm^2,beam cross-section is 1-10cm^2,energy density on the sample is<150J/cm^2.In development of the industrial installation beam parameters should be defined more exactly taking into account the particular technological process.

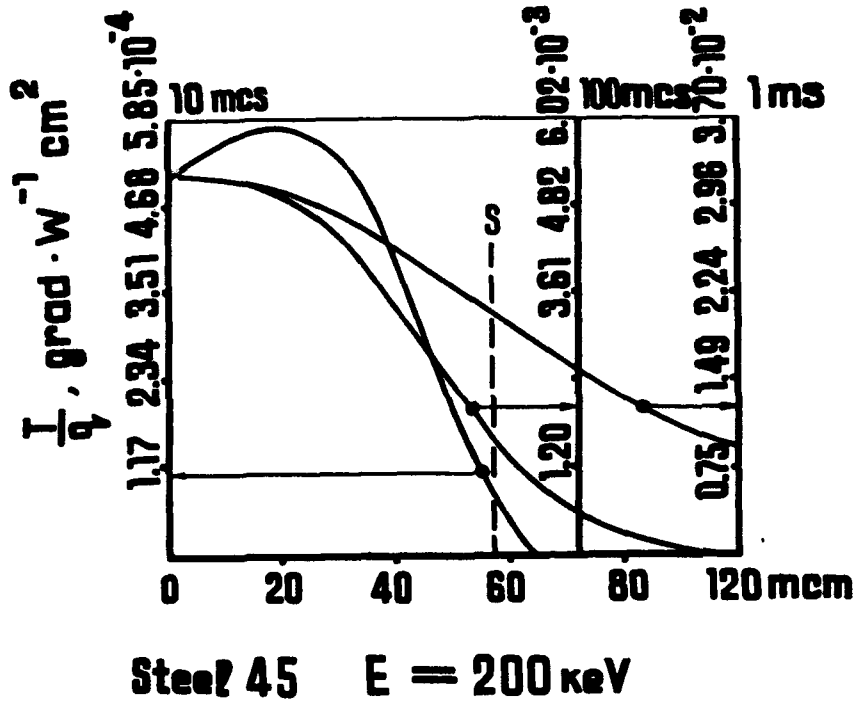
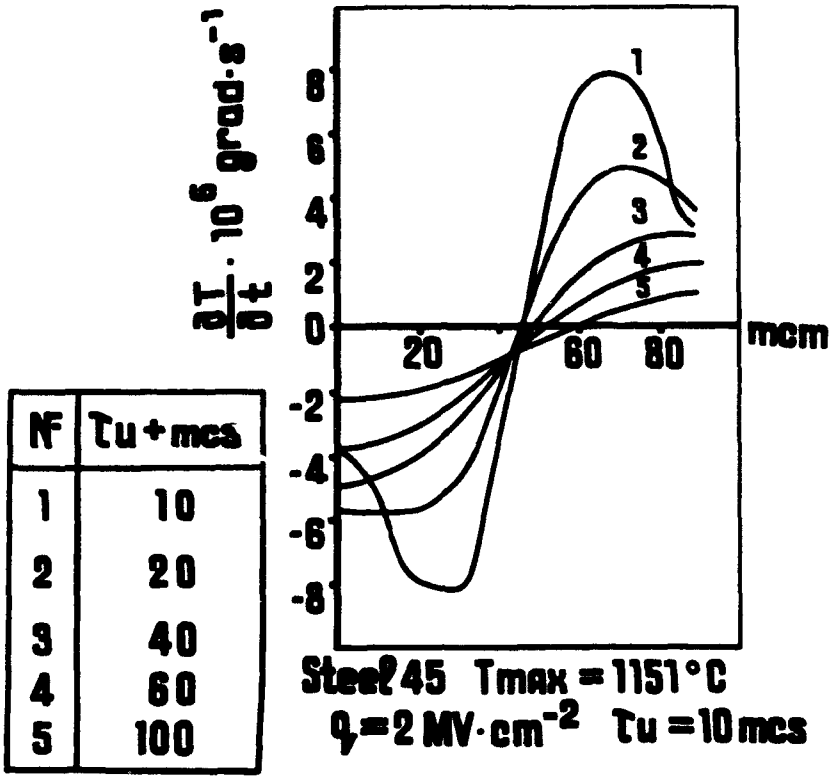


Fig.1 Calculated distribution of temperature in a surface layer depth at an electron beam current pulse duration of 10μsec,100μsec,1msec. Calculation has been performed for steel 45. The vertical axis shows a temperature with reference to density of beam power on the target surface. Arrows show the axes,on which it is necessary to read coordinates for each curve.

Electron beam parameters mentioned above show that the treatment of surface tens of square centimetres in area requirs an electron beam current of hundreds amperes. We obtain the electron beams with such currents using a multipoint explosion-emission cathode(MEC). These cathodes developed at D.V.Efremov Institute allow to obtain electron beams of various geometry with the beam current of hundreds or thousands amperes and pulse duration of tens or hundreds microseconds.

Omitting the details of the cathode design we may note that an MEC consists of a great number of points each of them being a bunch of carbon fibres 10μm in dia. The plasma which,is an electron emission sourse,is formed on the points in rather highly intensive electric field. MEC has a following advantages: no heating at all,operation in vacuum of 10^{-4}-10^{-5}Torr,resistance to leak-in an atmosphere,no poisoning with particle flows,formed as a result of



N	Tu+mcs
1	10
2	20
3	40
4	60
5	100

Fig. 2 Calculated distribution of a cooling-down rate in the surface layer of steel 45 under the influence of an electron beam of 200keV energy and 10μsec duration. The curves correspond to different moments of the time after termination of a pulse of an electron beam current: 1-10μsec, 2-20μsec, 3-40μsec, 4-60μsec, 5-100μsec.

evaporation of samples being treated. MEC may be of any geometry and area of emission surface.

One of the installation design version is shown in Fig. 3. The installation comprises a high-voltage pulse generator, an electron gun, a pulse length control device, magnetic lenses, a chamber for samples treatment, a pumping system and a control desk. The high-voltage pulse generator is made on the base of a pulse transformer A high-voltage pulse is transfered to the electron gun through a gas spark gap. The electron gun is designed as a triode. The use of a grid electrode allows to improve MEC operation, control beam current without change of the accelerating voltage and improve a beam focusing. An electron beam is extracted through the drift channel with two magnetic lenses into the treatment area.

A possibility to increase a material surface microhardness and

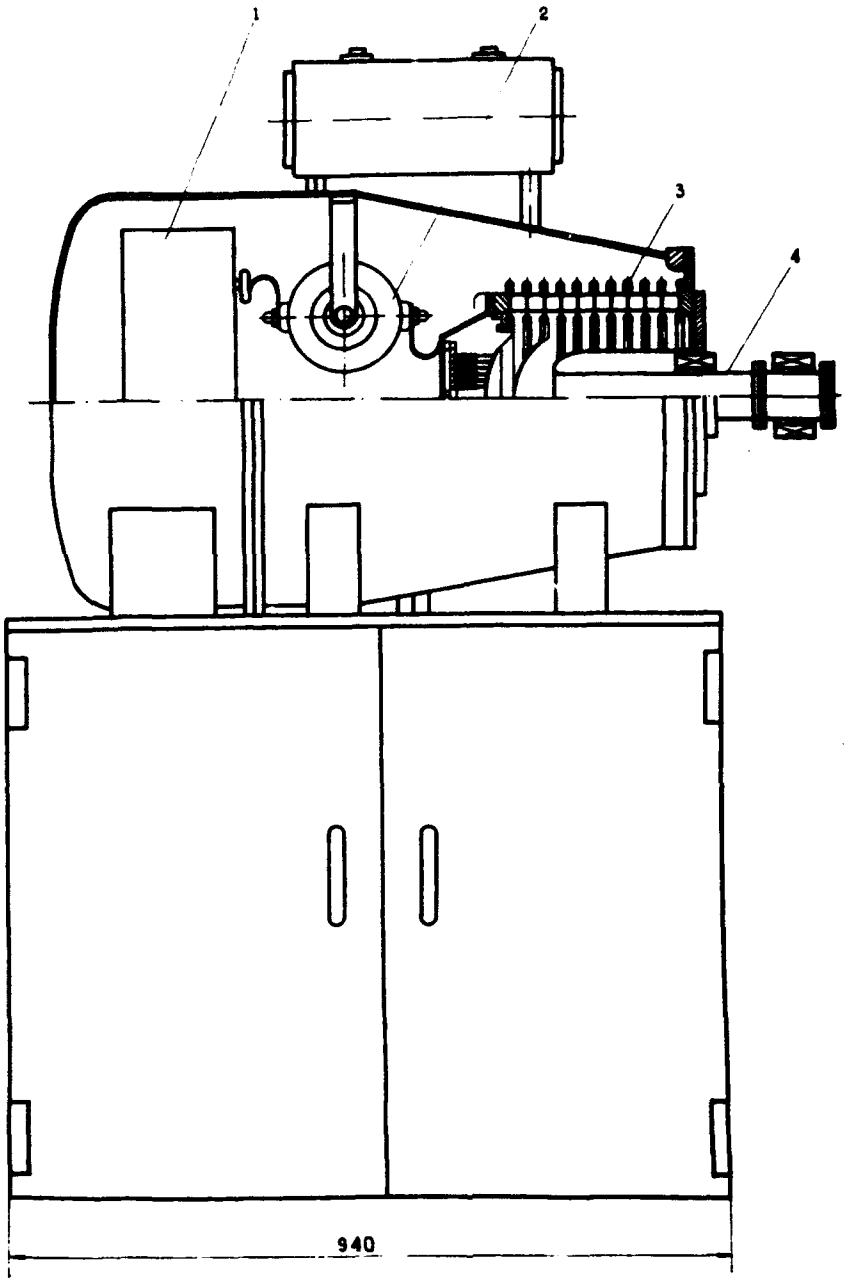


Fig.3 Design of high-current pulse accelerator.
1-pulse transformer,2-peaking spark gap,3-electron gun with multipoint cathode,4-drift channel.

wear resistance due to a HEB pulse heat treatment was studied on many metals and alloys,in particular,used in automobile production It was shown that there is a considerable microhardness increasing (by a factor of 2-5) and hence a wear resistance increase as a result of HEB treatment.The results of wear resistance tests of

automobile engine valves are shown in Fig.4. These tests were carried out at a special test bed, where not only the samples, treated by HEB, but also the samples with the surface strengthened

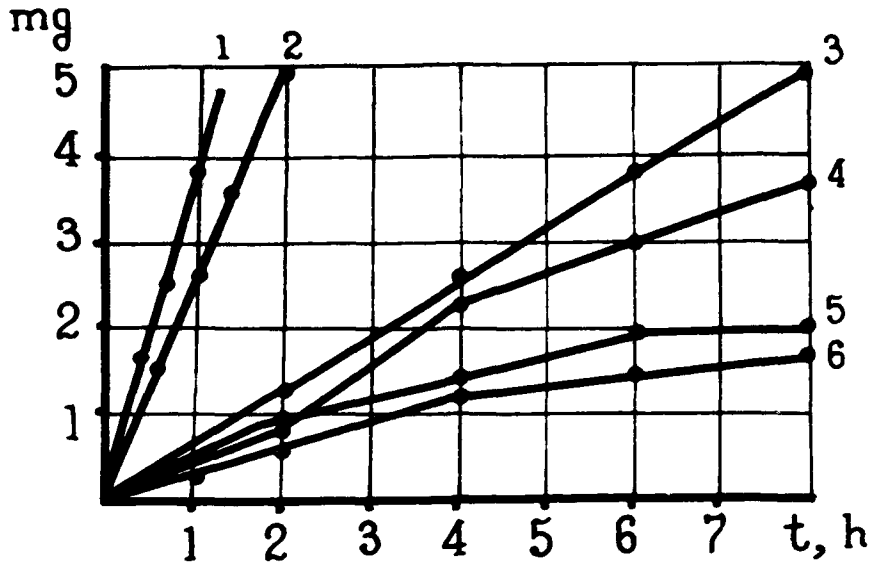


Fig.4 Valve mass lost at the tribological tests.
1-ion nitrogenized valve and brass sleeve; 2-chrome plated valve and brass sleeve; 3-chrome plated valve and cast iron sleeve; 4-liquid nitrogenized valve and cast iron sleeve; 5-ion nitrogenized valve and cast iron sleeve; 6-electron beam hardened valve and cast iron sleeve.

by the methods of ion nitride hardening, liquid nitride hardening, galvanic chromium plating were examined. There is an effect of a surface microforming as a result of an electron beam melting that possibly improves the performances of rubbing pairs (Fig.5). An influence of HEB treatment of a sample on its corrosion resistance was studied on stainless steel components. The stainless steel solubility in dry sulphuric acid (48%) was shown to decrease more than by a factor 10.

HEB influence on amorphous alloys, sputtered or other way deposited thin films, materials implanted by ions is a field for investigations. HEB treatment of amorphous alloys provides completly amorphous layers as well as copmlex structures consisting ofvarious crystalline and amorphous phases. A grain size is usually less than 1μm in such a layer. While melting a material surface with sputtered film, a base material surface is alloyed



Fig.5 Photomicrography of an automobile engine valve neck surface after a partial melting by an electron beam. The surface is of "orange peel" type. Scale is 1:30.

yed with film components. In this case the structures such as FePb are formed, that impossible to form by usual melting methods. An important advantage of HEB treatment of ion implanted structures are high rates of heating and cooling and, as a consequence, a lack of considerable thermal diffusion of implanted ions beyond a treated layer and lack of disintegration of metastable phases such a α-MoC_{1-x} in contrast to thermal annealing.

At present, the technology of pulse heat treatment of materials, applying a high-current electron beam is in the making. Nevertheless, an experience now available allows to expect its efficient and highly promising industrial applications in the nearest future.

DISSIPATION OF STRESS WAVE ENERGY AND STRUCTURUL MODIFICATION OF STEELS IRRADIATED BY A LOW-ENERGY HIGH-CURRENT ELECTRON BEAM

V.I.Itin, Yu.F.Ivanov, S.V.Lykov, G.A.Mesyats, G.E.Ozur, D.I.Proskurovsky, V.P.Rotshtein

Institute of High-Current Electronics, Academy of Sciences, Siberian Branch, 4,Academichesky Av.,634055, Tomsk, Russia

ABSTRACT. The results of investigation of the mechanism of hardening of previously hardened carbon steel (0.45 - 1.2 % C) by microsecond low - energy high-current electron beam are presented. It is shown that maximum hardening is reached beyond the thermal action zone and is caused by effect bipolar stress wave on martensite. Intense deformation processes initiated in region of penetration of this wave leads to the formation of strongly fragmented structure with high level of defectivity and anomalously high values of microhardness.

INTRODUCTION.

In recent studies [1-3] it has been found that irradiation of metals and alloys by the pulsed high-current electron beams of a moderate power density $q=10^7$-10^9 W/cm^2 results in intense deformation processes and significant hardening of the surface layers. These effects are caused by the action of a bipolar stress wave, which, in its turn, appears due to the effect of thermoelasticity. Durations of the compression and tension pulses of this wave are compared with the duration of electron beam. The propagation of bipolar stress waves in steels is accompanied by the formation of new structure states with a anomalously high microhardness [2,3].

This paper presents results of the studies on the influence of the stress wave parameters on the degree and type of the carbon steels (0.45-1.2% C) hardening. Some peculiarities phase and structure states within the zone of the beam action have also been studied. The electron beam used in these studies provided only small depth of the electrons penetration into a target. On the other hand the depth of the stress wave penetration many times exceeded the size of the beam thermal action zone. This circumstance allowed us to isolate and study the structure and phase transformations resulting mainly from the action of the stress waves.

EXPERIMENTAL DETAILS.

The electron beam was formed in a gun with the explosive-emission cathode and plasma anode [4], the average electron energy was 10-20 keV and the pulse duration was 0.7-0.8 μs and power density W = 2-6 J/cm^2. This made it possible to obtain different states of surface by the end of a pulse i.e., heating, melting or vaporization of the material. Stress waves were recorded by a piezoelectric detector with ~ 10^{-8} s time resolution. The detector was placed at the rear side of a target. In our experiments we have varied the number of pulses (N=1-300) and the time interval between pulses was 6 - 60 s. After the irradiation samples have been studied using the transmission electron microscopy (TEM), X-ray stuctural analysis, and measurements of microhardness.

Numerical calculations of thermal fields in the zone irradiated by a beam have been made based on the solution of one-dimensional nonstationary heat equation. The phase transition has been taken into account with the help of singular term added to the specific heat at the melting point. The heat source was constructed using the empirical depedences of the incident electrons' energy losses on the penetration depth according to diode voltage and current oscillogrammes.

RESULTS AND DISCUSSION.

As was shown by calculations and experimental data the irradiation results in melting of the surface layer whose thickness does not exceed 2 μm, at the thickness of the beam thermal action zone being less than 15 μm. These results are confirmed by the data of X-ray structural analysis and TEM, according to which the increased content of austenite characteristic to fast hardening from high temperatures is observed in layers up to 10 μm thickness.

Measurements of microhardness have shown that the formation of a hardened zone 200 to 300 μm thick and having two pronounced maximums is the result of such an irradiation (Fig.1,a). Four characteristic regions can be separated out within this zone, viz., the region of thermal action (I), the regions of maximum hardening (II and IV) and nonhardened region between them (III). It is well seen from this figure that total thickness of the hardened layer many times exceeds both the depth of the electron penetration into the target (~ 1 μm) and the size of the thermal action zone determined from calculations (~ 15 μm). As a consequence one can arrive at a conclusion that the mechanism of steel

hardening, as well as, the degree and character of the hardening are determined by the action of a bipolar stress wave. It should be noted that anomalously high microhardness values are observed only in the case when previously hardened samples of steel with the martensite structure are being irradiated. An increase of the number of pulses N results in the increase of microhardness values in both maximums and especially in the second one. Similarly anomalous hardening has been observed earlier when we irradiated steel samples with high-energy beem (200 keV, 60 ns,~ 10^8 W/cm^2). The degree of hardening, in this case, did not depend on previous thermal treatment of samples [5].

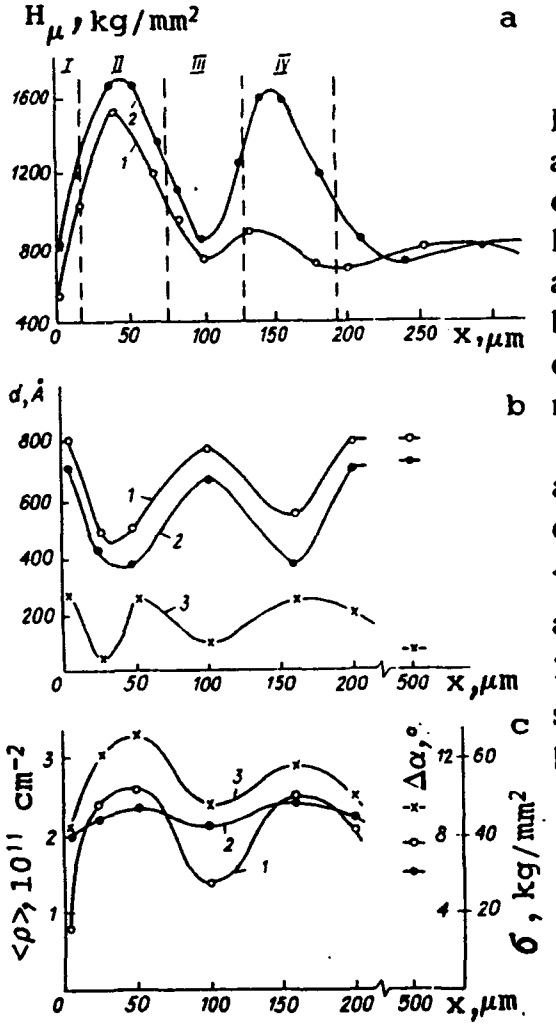


Fig.1.
a) Distribution of microhardness over the depth of the beam action zone of the hardened steel 45 at N = 1 (curve 1) and at N = 300 (curve 2);
b) Change of crystals' width (curve 1), diameter of fragments (curve 2) of the martensite phase, and of the cementite sizes (curve 3) with the depth of the beam action zone;
c) Change of scalar density of dislocations $\langle\rho\rangle$ (curve 1), azimutal component of the angle of complete disorientation $\Delta\alpha$ (curve 2), and of the amplitude of long-range stresses σ (curve 3) with the depth of the beam action zone for hardened steel 45 (W = 2.5 J/cm^2, N=300).

As follows from the analysis of experimental results the maximum hardening of martensite is reached at the action of a stress wave whose compression and tension pulses have close amplitudes which only slightly exceed the dinamic yield point of the material. It is also necessary that the tension pulse has maximum amplitude. Such a condition can occur is the surface temperature reaches the mel-

ting point by the end of pulse and the amplitude of the wave is 2 to 2.5 GPa. This regime can take place at the energy density W = 2.5 J/cm^2 (Fig.2).

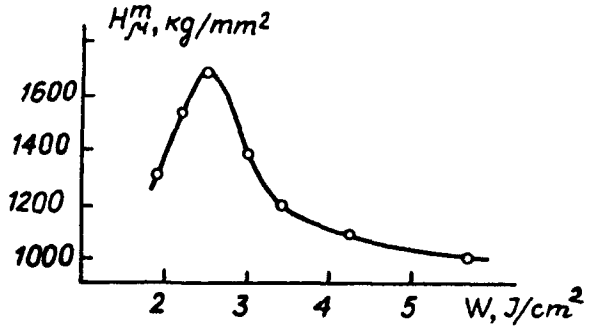


Fig.2.
Dependence of the maximum microhardness values H^m_μ in the region II on the energy density W (N=300).

Since for all steels under study we have obtained similar depth distributions of the microhardness a detailed TEM study only of the carbon steel (0.45 % C) has been undertaken. In the preliminarly hardened state this steel is a mixture of martensite, austenite (layer of austenite around the boundaries of the martensite crystals), and carbide (particles of plate cementite inside the martensite crystals) phases.

In the zone of direct thermal action of beam (I) most essential modifications of the phase and structural state of samples were observed on the surface. Under a single pulse irradiation the formation of a complex nanocrystal structure in the layer of 100 nm thickness occurs due to fast hardening from liquid state, the structure being composed of ferrite (α-Fe) and austenite (γ-Fe) grains. The thickness of the molten layer is, according to calculations, about 1 μm. The thickness of the zone with such a complicated structure and its phase composition change with increasing number of irradiation pulses. At N = 300 the thickness is about 200 nm and the layer is composed of γ-phase, and α and δ-ferrite. At the depth of 1 μm there takes place a growth of the austenite and cementite phases sizes and their volumetric fractions.

Essential modifications of the martensite phase defect structure are characteristic of the regions of maximum microhardness. Within the first maximum there are observed regions of martensite with enhanced parameters compared to these at the initial state independently of the number of pulses. Thus the scalar density of dislocations $\langle\rho\rangle$ reaches the values 3×10^{11} cm^{-2} (the initial one is 1.9×10^{11} cm^{-2}), the azimuthal component of the angle of complete disorientation $\Delta\alpha$ reaches 15-18° (the initial one is ~ 6°), the amplitude of the long-range fields of stress $\sigma \simeq 108$ kg/mm^2 (the initial one is 47 kg/mm^2). In addition,

these regions are characterized by a strong fragmentation (Fig.3,a), a complicated character of the structure bending (Fig. 3,c), as well as by an enhanced density of microtwins (Fig 3,d). According to our estimations the degree of deformation in the region of maximum hardening reaches 60 - 70 %. In the structure of martensite phase there are observed particles of cementite, both within the martensite fragments and at their boundaries. The volumetric fraction of the martensite with modified structure is about 18 - 20 % of steel structure at a single pulse irradiation, while reaching 70 - 80 % at N = 300. On the other side the values of $\langle\rho\rangle$ and $\Delta\alpha$ are being decreased to a certain extent. On the whole, the variations of the microstructure parameters observed within the limits of the modified zone (Fig.1) well correlate with the curve H_μ (x). Certain decrease of the dislocaton density in the nonhardened zone (III) compared to its initial value as well coagulation of the cementite phase at constant volumetric fraction of it in the regions of maximum microhardness should be noted.

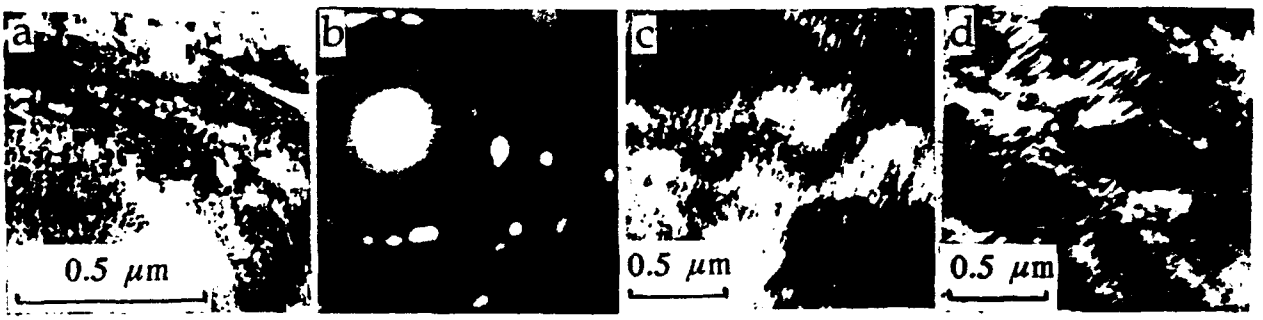


Fig.3. a,c,d,-TEM images of the martensite of previously hardened steel 45 in the region II; b- difraction pattern of (a); (W=2.5 J/cm^2, N=300).

The analysis of structural parameters (Fig. 1, b, c) shows that low-angle boundaries of fragments and crystals of martensite formed by the action of stress wave give the main contribution in common effect of hardening.

Analysis of the whole bulk of experimental data shows that very high degree of hardening and its periodic character are caused by specific features of the bipolar stress wave action on martensite, the action being alternative on the microseconds time scale. As was shown in [1,2] the stress wave attenuation is nonmonotonic. In the region of its propagation there were revealed narrow (~ 10 μm) intervals where an intense dissipation of the stress waves energy takes place. This process is accompanied by a step-wise decrease of the

compression pulse amplitude and practically vanishing amplitude of the tension pulse. As was shown in these experiments, despite of the relatively low amplitude of a bipolar stress wave the release of essential part of its energy in the localized regions results in strong tensile stresses within thin surface layers, which initiate intense deformation processes with no destruction of samples. This leads to the formation of a strongly fragmented structure of martensite with high level of defects and, as noted in [6], to redistribution of carbon atoms between the volume and boundaries of the fragments. As a result the concentration of carbon in defects can be sufficient for the formation of cementite phase. Just this factor determines the formation of a hardened zone with anomalously high values of microhardness. Besides, as a consequence of multiple action of the bipolar stress wave, which is in fact an alternating load of 10^{-6} s duration, there takes place an accumulation of anomalously large anisotropic deformation [7], that results in an additional hardening of the modified layer.

REFERENCES

1. S.V.Lykov, V.I.Itin, G.A.Mesyats, D.I.Proskurovsky and V.P.Rotstein, Dokl.Acad.Nauk USSR. 310(4), 858 (1990).

2. S.V.Lykov, I.M.Goncharenko, N.P.Kondratyuk, V.I.Itin, G.A.Mesyats, G.E.Ozur, D.I.Proskurovsky and V.P.Rotstein, In Proc. of 8-th Intern. Conf. on High-Power Particle Beams (BEAMS'90), Novosibirsk, USSR, World Scientific, Singapore, v.2, 1990, pp.721-726.

3. V.I.Itin, I.S.Kashinskaya, S.V.Lykov, G.E.Ozur, D.I.Proskurovsky and V.P.Rotstein, Pis'ma v Zh.T.Ph. 17(5), 89 (1991).

4. G.E.Ozur and D.I.Proskurovsky, Pis'ma v Zh.T.Ph. 14(5), 413 (1988).

5. V.I.Itin, B.A.Koval, N.N.Koval, S.V.Lykov, G.A.Mesyats, D.I.Proskurovsky, V.P.Rotstein, I.S.Chukhlantseva, Izv. Vyssh. Uchebn. Zaved., Fiz.6, 38 (1985).

6. V.M.Adeev, Yu.N.Ivaschenko, V.N.Minakov and V.I.Trefilov, in Structure and Chemical Inhomogenieties in Materials (Abstract of papers of 1-st All-Union Workshop, Kiev, (1990), pp.33-34.

7. V.E.Panin and T.F.Elsukova, in Synergetics and Fatigue Failure of Metals, Nauka, Moscow (1989), pp.113-138.

ACTION OF A NANOSECOND MEGAVOLT HIGH-CURRENT ELECTRON BEAM ON METALS AND ALLOYS

I.M.Goncharenko, A.M.Efremov, Yu.F.Ivanov, V.I.Itin,B.M.Koval'chuk, S.V.Lykov, A.B.Markov, V.P.Rotshtein,A.A.Tukhfatullin

Institute of High-Current Electronics,Acadamy of Sciences, Siberian Branch, 4, Academichesky Av., 634055, Tomsk, Russia

ABSTRACT. Using the X-ray structural and the transmission electron microscopy analyses specific features of the phase and structure transformations in armco-iron and steel 45 affected by a high-currentelectron beam of ~ 10^{11} W/cm^2 power density have been studied. It was revealed that hardening of steel with the martensite structure is of a through quasi-periodic character is caused by the action of a shock wave. The action of a shock wave results in formation of a thin (0.1 - 0.2 μm) layer on rear side of samples. The layer is composedof subgrains of α-ferrite of a regular hexagonal shape with thin layers of graphite on their boundaries.

INTRODUCTION

Action of high-current electron beams of a power density up to 10^{12} W/cm^2 on metals results in formation of a shock wave with the pressure at its front reaching several Mbar due to fast volume heating [1,2]. Propagation of the wave into a target is accompanied by intense deformation processes, including the splitting off destruction of the sample's rear surface [3]. This paper deals with the investigation of characteristic features of the phase and structure transformations of armco-iron and steel 45 under the irradiation by a beam of 10^{11} W/cm^2 power density.

EXPERIMENTAL DETAILS

Samples under study were irradiated by high-current electron beam with parameters: beam current 65 kA, the maximum energy of electrons up to 1.5 MeV and pulse duration at half maximum of 50 ns. For irradiation of samples only near axial portion of the beam 12 mm in diameter was used (the thickness of the samples was 5-10 mm). After the irradiation samples have been studied using the transmission electron microscopy (TEM), X-ray structural analysis, and

measurements of microhardness. Heat regime of a target has been found by solving the heat equation[4].

RESULTS AND DISCUSSION

Calculations of temperature fields of a samples and the experimental data have shown that the irradiation results in a volume explosion and evaporation of ~ 200 μm thickness surface layer. The amplitude of a shock wave estimated using the relation P=GE (where G is the Gruneisen parameter, E is the density of absorbed energy) was 500-700 kbar. The depth of a layer of molten material on the bottom of the crater was ~ 25 μm. The mean cooling rate of the layer was about 10^6 K/s and the mean rate of the crystallization front was about 0.5 m/s. Total depth of the thermal action zone did not exceed 150 μm.

In the case of armco-iron the irradiation results in formation of an extended zone of intense plastic deformation, just after the layer of fine-grained crystals hardened from the melt, with certain features of multiplet twinning. Thickness of the hardened zone is about 350 μm. The microhardness H_μ varies within this zone reaching at maxima the value of ~ 300 kg/mm^2 (the initial one ~ 120 kg/mm^2). The degree of deformation and the microhardness decrease with increasing depth into a sample due to the shock wave attenuation, while being increased near the rear surface of a sample where cracks and splitting off destruction have been observed. The latter effects are connected with the doubling of the wave amplitude because of its reflection from the free surface.

In the case of irradiation of nonhardened steel samples fast hardening from the melt yields a structure composed of a massive (packet) martensite and residual austenite. The microhardness of this structure is about 750 kg/mm^2. This zone is followed by a zone with the structure of annealed martensite gradually taking the initial structure.

Most interesting are the results obtained with pre-hardened steel samples having the martensite structure. The measurements have shown the hardening of this structure takes place at full depth of a sample with an explicit quasi-periodic behavior (Fig.1)

The X-ray analisys shown the cooling from the melt near surfase region (~ 25 μm) is composed of martensite and residual austenite (~ 12%).

The TEM have shown the structure of the region is the massive martensite (Fig.2,a) with the mean cross size d of crystals about 60 nm (initial one is ~

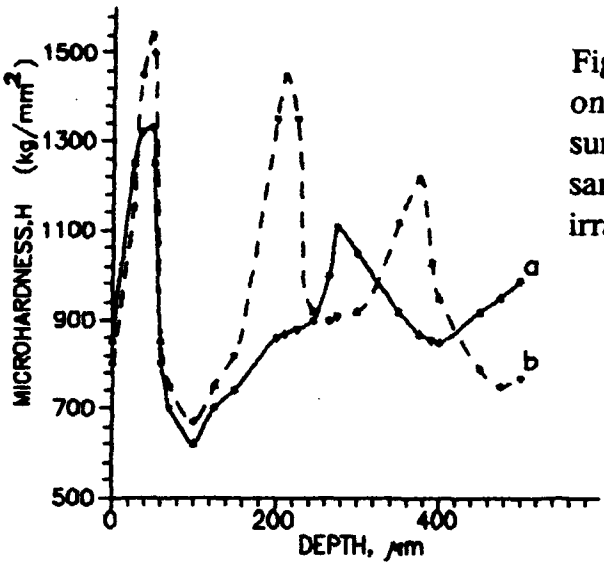


Fig.1 Dependence of microhardness on the distance to irradiative surface(a); to the rear surface(b) for a sample of pre-hardened steel 45 irradiated by a beam.

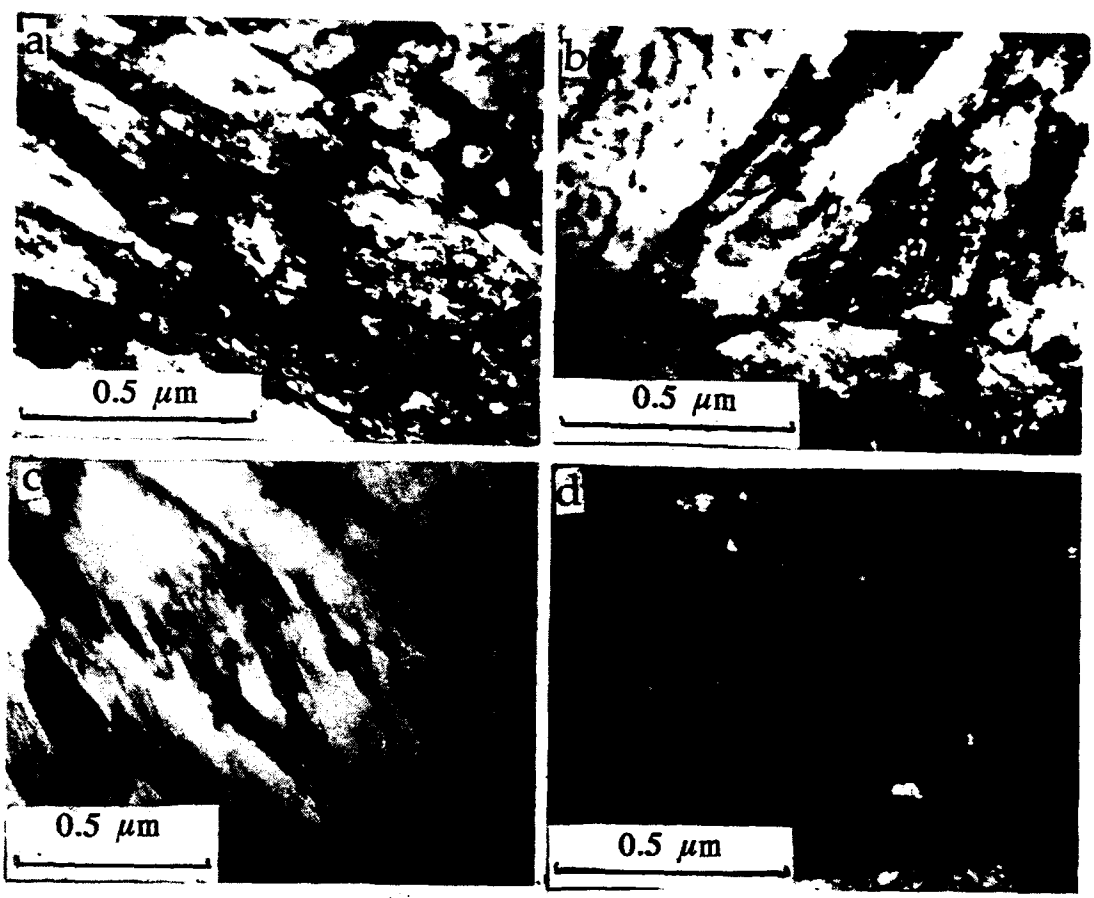


Fig.2 The TEM images of the structure of a pre-hardened sample of steel 45 after irradiation; d is the dark-field image (the distance from the surface is 5-10 mm).

200 nm). The values of the scalar density of dislocations $\langle\rho\rangle$ and of the azimuthal component of the complete disorientation angle $\Delta\alpha$ are ~ 10^{11} cm^{-2} and ~ 6°, respectively. Inside the martensite crystals and along their boundaries there are a lot of relatively large particles of cementite (Fig.2,b). Large amount of the cementite depositions and relatively low values of $\langle\rho\rangle$ and $\Delta\alpha$ show the annealing processes taking place in the region that is confirmed by heat regime calculations.

Within the regions of enhanced microhardness (Fig.1) the steel structure is the massive martensite (Fig.2,c) with the size of crystals d=62 nm. Inside these crystals there are dense dislocation grids where $\langle\rho\rangle$=4.8*10^{11} cm^{-2} (initial one is ~ 2*10^{11} cm^{-2}). The martensite crystals are fragmented with the mean size of fragments being ~ 50 nm. Quite frequently the packets with a noticeably higher values of $\langle\rho\rangle$ and $\Delta\alpha$ (~ 6*10^{11} cm^{-2} and ~ 14°, respectively) and more strong fragmentation are observed.

In the regions of enhanced microhardness there was also observed the presence of a residual austenite in the form of thin fillers located both inside the crystals in the form of disperse depositions and along the crystal boundaries in the form of thin films (Fig.2,d). We didn't yet manage to relate the presence of these phases to the nature of the anomalous hardening of steel and therefore our investigation only shows that the increase of microhardness at maxima of the $H_\mu(x)$ are mainly due to the substructural hardening of the material under the action of a shock wave [5].

According to X-ray analysis a ~ 40% increase of the γ-phase fraction in a ~ 10 μm thick layer near the rear surface occurs. Deformation of the γ-phase lattice in this layer is ~ 1.2*10^{-2} that corresponds to the increase of the carbon concentration in this phase up to ~ 2.3%.

The TEM of the rear surface (0.1-0.2 μm thick) are presented in Fig.3. It is quite clearly seen the structure of the surface layer is mainly formed by subgrains of a regular hexagonal shape (Fig.3,a,b) with the mean size of ~ 130 nm. The subgrains are surrounded by the second phase layers of ~ 35 nm cross size. Deciphering of the corresponding diffraction pattern (Fig.3,c) revealed the subgrains have a BCC lattice (α-ferrite) while the fillers are the graphite with the HCP lattice having the parameters a=0.254 nm and c= 1.004 nm.

Quite rarely there were observed lenticular formations (Fig 3,d) which evidently lie under the layer of subgrains. Deciphering of the corresponding iffraction pattern (Fig 3,e) has shown that this structure is the α-phase namely the low-temperature plate martensite that is characteristic of the hardened steels

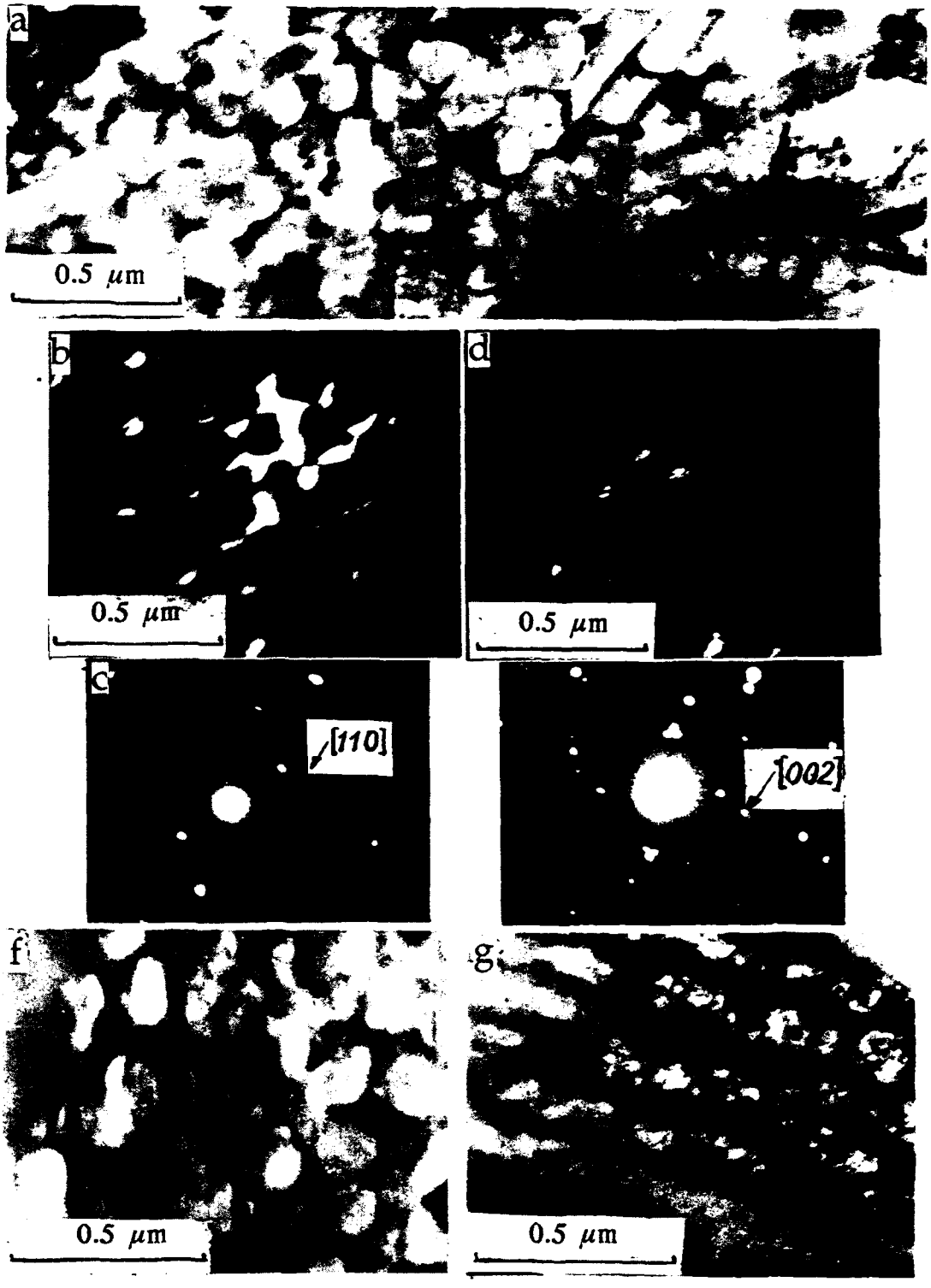


Fig.3 The TEM images of the structure of the rear surface layer of a sample of pre-hardened steel 45 irradiated by a beam; b and d are the dark-field images.

with high content of carbon. The presence of plates in this steel is also indicative of an enhanced, compared with the initial state, concentration of carbon near the rear surface of a sample.

Just under the surface layer there is a structure composed of a mixture of subgrains (mean size ~ 140 nm) of irregular oval shape (Fig.3,f) and a striped substructure (Fig.3,g). One can see from Fig.3,g a cellular-reticular dislocation structure. The distance between the strips (size of the dislocation cells) are practically identical to the size of the subgrain structure.

The regular shape of the subgrains (Fig.3,a,b) shows their similarity, to a certain degree, to Benar cells.The formation of such a dissipative structure is a specific response of the martensite on the action of a shock wave in a thin (~ 0.2 μm) layer near the rear surface of a sample. In this case the fillers of graphite at the boundaries of the subgrains are formed, by the analogy with the processes yielding the formation of the Benar cells in fluids, due to ascending diffusion of carbon from deep layers of the material to its surface.

REFERENCES:

1. Perry F.C., Widner M.M., J.Appl.Phys. 47, 127 · (1976).
2. Demidov B.A., Ivkin M.V., Petrov V.A., et.al. Zh.T.F, 50, 2205 (1980).
3. Uchaev A.Ya., Novikov S.A., Tsukerman V.A., et.al. Docl. Acad. Nauk USSR, 310, 3, 611 (1990).
4. Lykov S.V., et.al., in Proc. of BEAMS'90, Novosibirsk, USSR, World Scientific, Singapore, v.2, pp. 721-726 (1990).
5. Ivanov Yu.F., Itin V.I., Lykov S.V., et.al. Docl. Acad. Nauk USSR, 321, 6, 1192 (1991).
6. Ebeling W. Formation of Structures in Irreversible Processes. Mir, Moscow, (1979).

HIGH ENERGY ELECTRON BEAM MATERIALS PROCESSING

R. A. Stark, R. F. Schneider, E. E. Nolting, M. Skopec
Naval Surface Warfare Center, Dahlgren Division, White Oak Detachment
Silver Spring, Maryland, USA

J. C. Danko, C. D. Lundin, T. T. Meek
University of Tennessee
Knoxville, Tennessee, USA

ABSTRACT

High energy (≥1 Mev), pulsed electron beams are capable of rapid, in-depth energy deposition in materials. This feature should yield some significant advantages in the processing of materials. This report describes preliminary experiments using this technology for the joining via brazing of carbon-carbon and metal-matrix composites, and the bonding and sintering of ceramics. The experiments described are being conducted utilizing a high energy (1.5 - 3.0 MeV), high current (≤ 3kA), long pulse (0.2-2.0 μs) electron beam produced by the Naval Surface Warfare Center's Long Pulse Accelerator. Initial results and extensive numerical modeling indicate the advantages of using a beam delivering a train of much shorter pulses over a longer time. The deposition of energy over much longer times avoids large pressures which can cause material damage. Also, for brazing applications, some heating of the base materials by the braze during beam exposure is desirable.

I. Introduction

High energy (≥1 MeV), pulsed electron beams are capable of both rapid energy deposition and near instantaneous volumetric heating of materials. This penetration in depth is a unique advantage of these beams over lasers, lower energy (≤100 KeV) electron beams, and conventional heat sources (induction heating, flames and arcs), all of which are limited to surface deposition. In contrast to microwaves, high energy electron beams deliver a large fraction of their energy (as high as 95% for range thick materials) as heat in the target, and can be used with both conducting and non conducting materials. Furthermore, production of very high power beams (avg. powers ≥ 0.25 MW) is electrically efficient, with efficiency of approximately 50%. These feature can yield some significant advantages in the industrial processing of materials. Some of the potential applications include: the joining of metal-matrix and carbon-carbon composites, the joining and sintering of ceramics, shock hardening of metals, atmospheric thick section welding, surface hardening, annealing of electronic component substrates (e.g. diamond, silicon), and explosive welding of dissimilar

metals. The typical range of beam parameters for the applications that have been considered to date are 1 - 10 MeV electron energies, 0.1 to 10 kA currents, 10 - 10^4 ns pulse lengths, 0.1 - 5 kpps repetition rates, and 0.2 to 5 cm beam diameters. The lower energy limit is dictated by the requirement that the beam electrons should have a finite energy deposition range in the material and the upper energy bound is set to insure that the work piece does not undergo nuclear activation. Although currently no single accelerator is capable of operating throughout the parameter space cited above, the above parameters are within the state-of-the-art for accelerator technology.

Several applications of this technology are currently being investigated by the Naval Surface Warfare Center, White Oak Detachment (NSWC/WOD), with support from the materials science group at the University of Tennessee. These applications include the joining, via brazing, of carbon-carbon composites and metal matrix composites, and the sintering and joining of ceramics. Each of these applications use the high energy electron beam (HEEB) to deposit large specific energies (Joules/gram) quickly and in depth; the joining of materials also depends on the HEEB property to deposit energy preferentially to higher atomic number materials (the braze in this case). For the initial study, the beam is provided by NSWC/WOD's Long Pulse Accelerator (LPA). Exposed samples are being analyzed at the University of Tennessee, Knoxville.

The remainder of this paper is organized as follows: Section II details the brazing calculations and experiments performed to date, while Section III does the same for the joining and the sintering of ceramics. A summary is presented in Section IV.

II. Brazing Calculations and Experiments

An application of both commercial and military interest is the brazing of carbon-carbon and metal-matrix composites. The application of HEEB for this process is based upon the fundamental physics of electron beam energy deposition. At the low electron energies of interest here, energy deposition occurs primarily by collisions between beam electrons and atomic electrons. Thus the beam energy loss rate is proportional to the atomic number of the material. Therefore, it is possible to preferentially heat high atomic number foils or braze interlayer above their melt point while not significantly raising the temperature of the lower atomic number base materials.

The LPA is being used for the initial brazing experiments. While a single

pulse accelerator is not useful for industrial-type applications, it does have a fairly large parameter range for conducting exploratory material joining demonstration experiments of interest. The LPA can operate in the following parameter range: 2 – 3 MeV beam energy, 1 – 3 kA beam current, 150 – 1500 ns pulse length, and a minimum beam radius of 0.7 cm.

Samples for the demonstration of carbon–carbon bonding were composed of thin (0.03 to 0.05 mm) foils of various types of metals and alloys placed between two pieces of 3 mm thick composite. The transverse dimensions of the composite were 12 mm by 25 mm. In the experiments, the LPA beam was normally incident to the front surface. A magnetic lens was used to produce a beam diameter somewhat larger than the target to keep the energy fluence within acceptable levels.

Figure 1 displays an example of the preferred heating phenomenon obtained with the axisymmetric electron–photon Monte–Carlo transport code CYLTRAN[1]. The calculation illustrates the results of HEEB irradiation bonding with a platinum foil for the experimental configuration outlined above. As shown, a 0.05 mm platinum foil located between two – 3 mm thick carbon plates, can be heated to well above its melt temperature with the LPA beam. The differential heating that occurs between the high atomic number platinum (Z=78) and the low atomic number carbon (Z=6) is readily apparent. The relatively uniform temperature of the carbon plates occurs because the samples are range thin, i.e. the electrons pass completely through both plates. The calculation also predicts that melting in

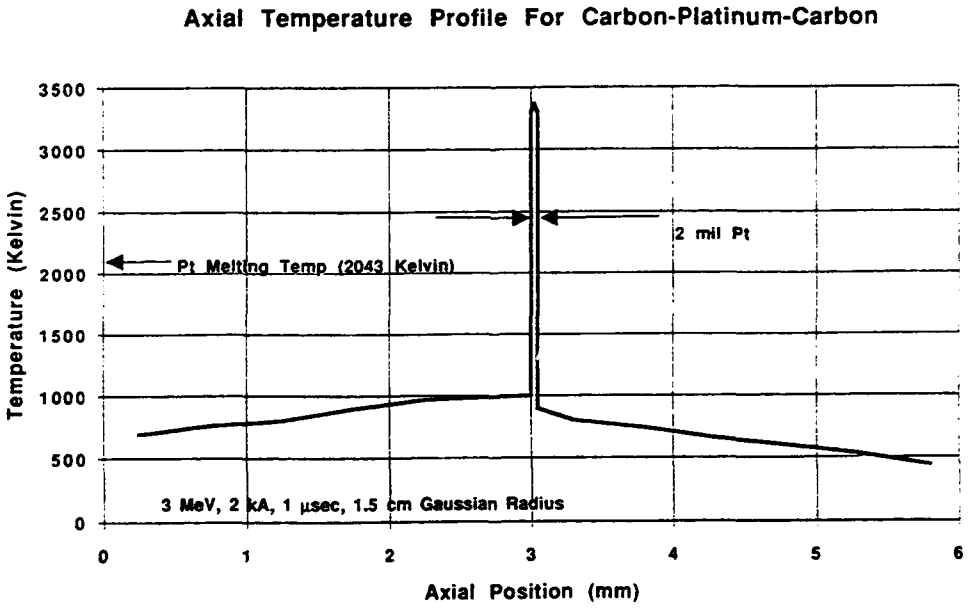


Figure 1. Axial temperature profile for carbon composite brazing with platinum

the platinum foil occurs over an approximately 2 cm diameter spot; this is surrounded by an annular mixed phase region of approximately 1 cm thickness.

Initial experiments with the LPA beam produced results generally consistent with the calculations. The exposure of the first platinum foil sample caused the carbon composite plates to separate rather than bond. This is believed to have been caused by a higher on-axis fluence than desired which lead to local vaporization of the platinum foil. Calculations and experiments were also performed for carbon composite bonding with tantalum and titanium foils. While these samples did not separate after exposure to the beam, the post-exposure evaluation at the University of Tennessee reveals that no bond was created. The reason for this lack of joining appears to be related to the duration of the molten braze material between the carbon plates, as outlined below.

One critical parameter that controls the quality of the bond is the temperature at the foil-composite interface. This contact temperature must be above the platinum foil melt point in order that wetting and carbide formation occur. Heat flow from the foil to the carbon-carbon composite (an excellent thermal conductor) rapidly reduces its surface temperature to a value between the peak foil temperature and the composite temperature. For the relatively long beam pulse of the LPA, this occurs even during the beam pulse. Though difficult to measure, the contact temperature may be estimated theoretically. A simple expression exists[2,3] for estimating the contact temperature just after exposure by the beam pulse, provided the characteristic time for cooling of the molten braze is much longer than the beam pulse and the thermodynamic quantities are relatively insensitive to temperature near the contact temperature. These are good approximations for pulse lengths shorter than 1 μs and braze thicknesses of 0.02 to 0.05 mm or larger, and for braze temperatures above melting. Under these restrictions, the contact temperature just after beam exposure, T_{ct}^0, is predicted to be

$$T_{ct}^0 = \frac{\sqrt{\rho_1 c_{p1} \kappa_1}\, T_1^0 + \sqrt{\rho_2 c_{p2} \kappa_2}\, T_2^0}{\sqrt{\rho_1 c_{p1} \kappa_1} + \sqrt{\rho_2 c_{p2} \kappa_2}} , \qquad (1)$$

where T^0 are the initial temperatures, ρ is the density, c_p denotes specific heat, and κ denotes thermal conductivity. The subscript "1" indicates values for the braze, and the subscript "2" indicates values for the adjacent carbon composite. From this value, the contact temperature gradually declines over the next several tens of microseconds for our interlayer materials and geometry.

Applying Equation (1) to our calculation for energy deposition for the brazing of carbon composites with a platinum foil, the relevant thermodynamics quantities are ρ_1=21.45 g/cm^3, c_{p1}=0.0425 cal/°K g, κ_1=1.0 W/cm °K, ρ_2=1.44 g/cm^3, c_{p2}=0.800 cal/°K g, κ_2=0.1195 W/cm °K, we find

$$T_{ct}^0 = 0.56\, T_1^0 + 0.44\, T_2^0 \quad . \tag{2}$$

The contact temperature on axis is then (T_1^0=3300 K, T_2^0=1000 K or 850 K) T_{ct}^0=2290 K or 2220 K, which is only slightly above 2043 K, the melting temperature of platinum. Similar calculations off axis reveal that the radius of the melt region at the interface is only 0.5 cm, in contrast to 1.0 cm in the interior of the foil.

These results show that the applicability of a single pulse HEEB to brazing is severely constrained. While the contact temperature must be above the melt temperature of the braze over a region suitable for bonding, the temperature in the interior of the braze must be below the vaporization temperature to avoid an explosive impulse. Since the radial beam profile is typically not uniform and scattering of electrons leads to further non uniformity, it is clear that heating with a single pulse HEEB is not a suitable method for brazing.

The above argument appears to account for the difficulty of bonding materials with the LPA. Several approaches are suggested which may circumvent this difficulty. The most straightforward and practical technique is to use a multipulse beam, which will deposit energy slowly enough to allow approximate heat equilibration between the braze and the adjacent region of the composite. Another approach possible for single pulse bonding is to use the greater flexibility gained by using alloy brazes. Alloys generally have a lower melting point than pure elements, but still have comparable vaporization temperatures. Experimental investigation of this approach is currently underway at NAVSWC/WOD's LPA.

III. Joining and Sintering of Ceramics

The ability of high energy electron beams to heat materials quickly and in depth make them potentially useful for the sintering and joining of ceramics. Because a large fraction (as high as 95% for range thick samples) of the energy of the beam is converted to thermal energy in the target, combined with heating rates much greater than thermal transport, the HEEB heat source should be much more efficient for sintering than conventional or microwave sources. Monte Carlo calculations[1] for the exposure of 50% density alumina samples with the LPA beam

indicates that the temperatures required for sintering, 1200 – 1800 °C (depending on grain size), are readily achievable. However, a beam source delivering a train of low intensity pulses may be required to minimize shock wave formation in the target which will arise if the energy deposition occurs too rapidly when heating with a single intense beam pulse. Experiments with both the sintering of alumina and joining of full density alumina are currently being conducted with the LPA and exposed samples will be evaluated at the University of Tennessee.

IV. Summary

In summary, the ability to rapidly heat materials to depths of centimeters or more makes high energy electron beams a unique heat source for material processing. Additional unique features are the deposition of a large fraction of the beam's energy as heat and the ability to selectively heat materials of high atomic number. Several applications of commercial and military interest have been identified that could benefit from this technology. At NSWC/WOD experiments are underway using the LPA to investigate some of these applications, namely the joining of carbon and metal matrix composites, and the sintering and joining of ceramics. The composite joining schemes all employ a higher atomic number interlayer to braze a lower atomic number base material. Exposed samples are then characterized at the University of Tennessee. Initial results and extensive numerical modeling indicate the advantages of using a beam delivering a train of much lower intensity pulses over a longer period: The deposition of energy over much longer times avoids generation of extremely large pressures which may cause materials failure. Also, for brazing applications, some heating of the base materials by the braze during beam exposure is desirable.

References

1. J. A. Halbleib, et al., "ITS version 3.0: the integrated TIGER series of coupled electron/photon Monte Carlo transport codes," SAND91-1634, March 1992.
2. T. S. Lovering, "Heat conduction in dissimilar rocks and the use of thermal models," Bull. Geo. Soc. Amer., V. 47, p67, Jan 31, 1936.
3. D. O. Ehrenburg, "Mathematical theory of heat flow in the earth's cru[illegible], Univ. Colo. Stud., V. 19, p. 327, 1932.

Acknowledgements

This research was supported by the Defense Advanced Research Projects Agency, under ARPA order 7792, amendment no. 7.

ENHANCEMENT OF METAL PROPERTIES BY IRRADIATION WITH INTENSE, HIGH-ENERGY ELECTRON BEAMS

Kenneth W. Struve
Mission Research Corporation
1720 Randolph Road, SE
Albuquerque, NM 87106-4245

Adrian C. Smith
Ballena Systems Corporation
1150 Ballena Blvd., Suite 210
Alameda, CA 94501

Eugene L. Neau
Sandia National Laboratories
P.O. Box 5800
Albuquerque, NM 87185

Abstract

There has been considerable interest in low energy (30–120 keV) electron beam surface treatment for both hardening and corrosion protection of steels and other alloys.[1] Techniques involve either melting the surface or raising the temperature to near melt and relying on self-quenching to rapidly cool the material below the critical transition temperature. With iron, for example, both carbon and carbides are dissolved in both the austenite (above 910 °C) and liquid phases. The rapid cooling to below 710 °C prevents growth of large ferric carbide (Fe_3C) or cementite crystals and thus produces a much harder surface. At sufficiently high cooling rates martensite or even amorphous compositions can be produced.[2] With previously used low-energy electron beams, only the top 10 to 100 μm of the material is directly heated by the electrons, although the heat affected zone may extend much further into the material. Recent accelerators have been developed in the high-current beam propagation program which have both high current density (>10 kA/cm^2), higher energy (up to 50 MeV), and high average beam power (150 kW). The advantage of using a high-energy machine is that the electron range is much greater. This leads to modifying bulk properties of the material and not just changing surface properties. For example, the range of 10 MeV electrons is nearly 1 cm in iron. The question that remains is whether it is possible to self-quench sufficiently fast when the material is heated to greater depths. We propose theory and experiments to study these effects. Theory will involve use of available PIC codes, such as ISIS, for electron deposition, and a radiation transport code, such as CYLTRAN, for radiation transport and deposition. These will provide input to thermal transport codes for determination of heat flow rates. Experiments will consist of irradiating samples with high power, high-energy beams and measuring the resulting materials changes.

I. Introduction

Electron beam irradiation of steel offers several unique capabilities. Material can be locally heated and thus selectively hardened. Surfaces can be melted, and through rapid self-quenching, be made amorphoric rather than crystalline. Beams can be easily focused to heat very localized regions. High-energy electrons can penetrate and heat steels to depths up to 1 cm and lighter materials to much greater depths.

A major problem in welding of carefully prepared steels is the loss of strength and hardness. Initial preparation of the steel may include hot forging, controlled-quenching or work hardening. When steel is welded the benefits of this preparation is lost. A high-energy, high-power electron beam provides a unique way to restore these properties. High-energy electrons heat a volume along a small path defined by the beam spot size, the repetition rate of the accelerator, and the material motion. Because only small volumes of material are heated, self-quenching can be effective.

II. High-Energy Electron Beam Features

A primary advantage of high-energy electron beams is greater electron range, as shown in Figure 1.[3] However, photoneutron production and resulting material activation above 10 MeV limit the usefulness of E-beam processing for most applications.

The ability to propagate an electron beam in air without a vacuum chamber is another important advantage. The scale lengths driving this requirement are the Nordsieck length and the betatron wavelength. The Nordsieck length is the length over which the beam expands a factor e due to air scattering. It is proportional to the net beam current in air,

$$L_N[\text{cm}] = 3.58\,\gamma\, I_{NET}(\text{kA}) \tag{1}$$

where γ is the usual relativistic energy factor. For example, a 1 kA, 10 MeV beam has a Nordsieck length of 72 cm. Beams with much lower currents will have Nordsieck lengths too short to be useful.

The betatron wavelength, is a measure of the growth length of the resistive hose instability. It is expressed as

$$\lambda_\beta = 2\,\pi\, a_b \sqrt{\frac{17\gamma\beta}{I_{NET}\,[\text{kA}]}} \tag{2}$$

where a_b is the beam radius. For a 1 kA, 10 MeV, 2.0 cm radius beam it is 240 cm.

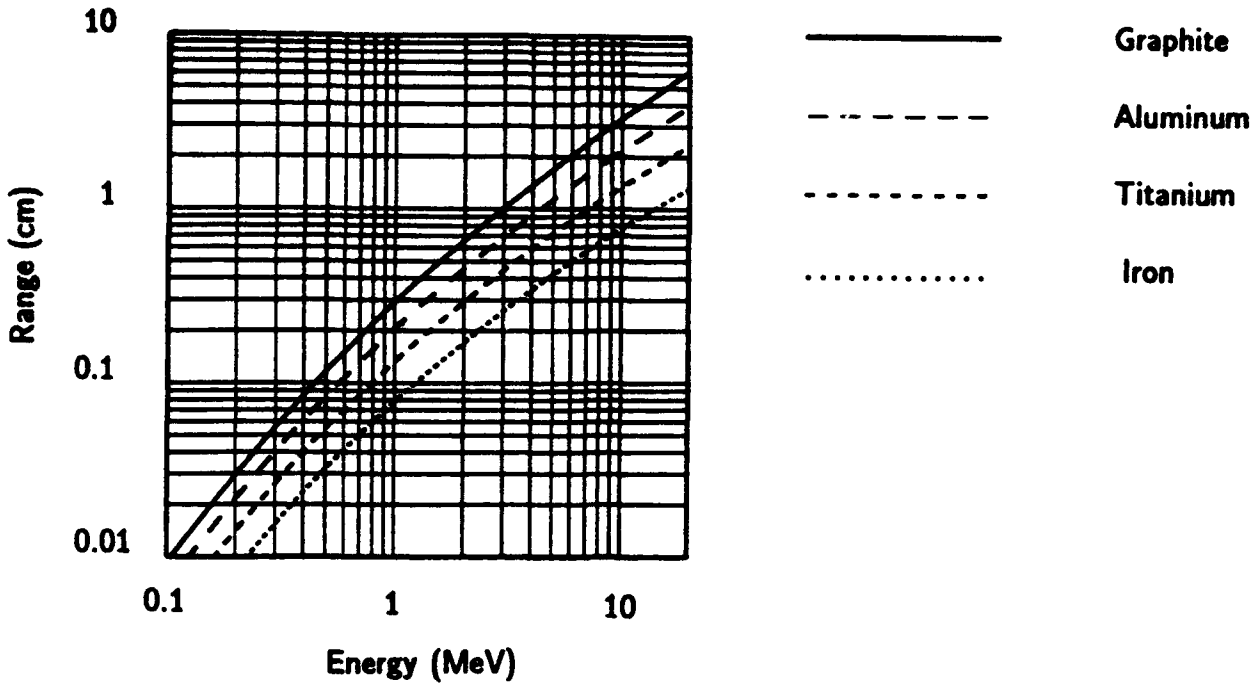


Figure 1. Electron range versus primary electron energy in several target materials.[3]

III. Hardening

Low energy electron beams have been used for surface hardening.[4]–[8] Two techniques are typically used, both of which use self-quenching for rapid cooling. One technique is to melt the metal, and rapidly cool to an amorphous phase that is very hard.[9]–[11] Another is to heat the steel to its austenitic phase and rapidly cool. Volumetric heating by a high-energy electron beam can be used to harden along a narrow path such as a weld seam, and over a broader area to temper. Self-quenching rates may not need be as high as those required for surface hardening, but with controlled cooling may restore properties lost in the original welding process.

Three allotropic forms of iron exist. The room temperature, or α–phase, is a body-centered cubic (bcc) crystal structure. The γ–phase, or austenitic iron, has a face-centered cubic (fcc) structure. At room temperatures steel is a mixture of α–iron and cementite, an iron carbide. The carbide adds hardness and toughness to the iron. The δ–iron phase exists only at elevated temperatures and is generally not important.

The material properties of steel are a strong function of the carbon content. At the eutectoid composition (0.8% carbon) and with slow cooling, a pearlite crystal structure forms. With hypoeutectoid compositions (less than 0.8% carbon) the pearlite exists in islands surrounded by ferrite. The size of the islands are related to the crystal size from

the austenitic phase. For hypereutectoid compositions the equilibrium crystal structure consists of islands of pearlite surrounded by iron carbide.

Upon cooling at faster rates, other crystal structures can develop. The diagram shown in Figure 2 is an isothermal transformation diagram of a typical carbon steel.[12] It shows the time for transformation from austenite to α−iron at each temperature. The left-hand curve is the time of onset of crystal growth, and the right-hand curve is the time for 100% formation. At the highest temperatures, the transformation is rather slow and the end result is pearlite. At lower temperatures there is a "knee" in the curves. In this region austenitic steel transforms to bainite, a somewhat harder and less ductile crystal structure. At the lowest temperatures, the transformation is to martensite, an extremely hard and brittle crystal structure. Martensite steels are formed by rapidly quenching the austenitic composition avoiding the "knee" of the curve. The brittleness of the martensite can be removed by tempering, which is to reheat to near the austenite transformation temperature to allow precipitation of some of the dissolved carbon.

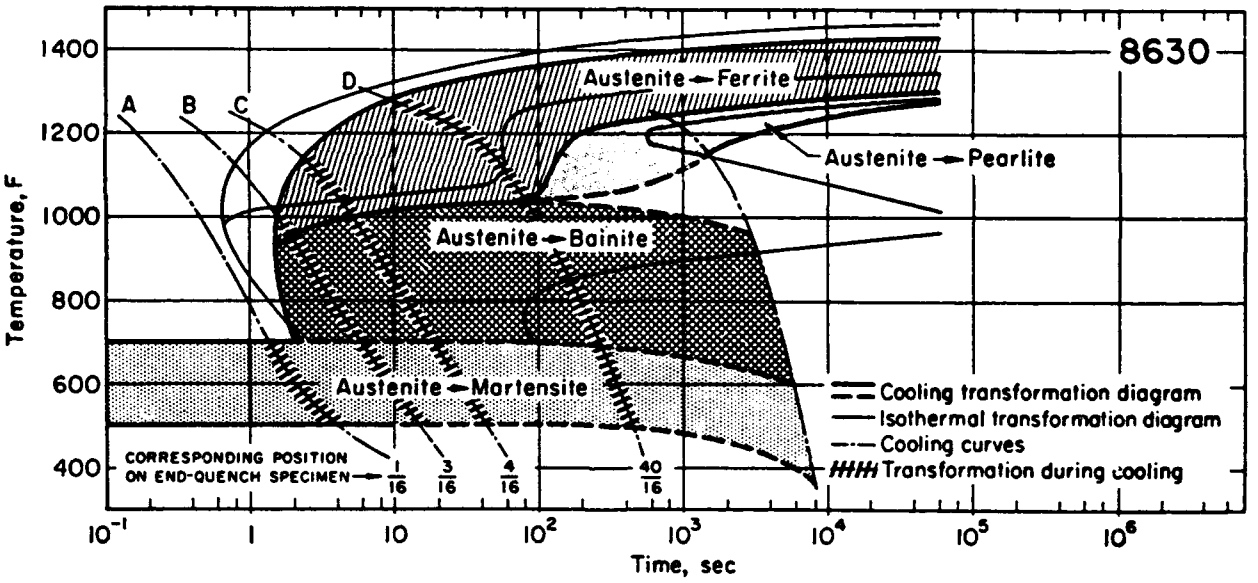


Figure 2. Transformation diagrams and cooling curves for 8630 steel, indicating the transformation of austenite to other constituents as a function of cooling rate.[12]

In addition to crystal structure, steel properties are also a strong function of the crystal size. Small crystals generally yield stronger, tougher, and harder materials. The size of the crystals at room temperature are directly related to the crystal size in the austenitic phase. Generally, the longer the material exists in the austenite phase the larger the crystals. Hot working of austenitic steel reduces crystal size. The grain size of the finished material is thus related to cooling time from the austenitic phase after the last hot

working. This effect provides a strong reason for quick reheating and quenching of welded areas and, thus, justifies a major potential advantage of the electron-beam technology.

IV. Theory and Experiments

Both theory and experiments are needed to answer questions about heat deposition and self-quenching rates. Electron beam scattering in the material reduces deposition depths. Preliminary calculations indicate a 4 mm heating depth for 10 MeV electrons.[13] For higher energies bremsstrahlung production could increase the heating depth. Self-quenching rates with volumetric heat deposition need to be calculated. Experience with surface layer heating indicate that cooling rates of 10^4 to 10^5 °K/sec are necessary.[4] There is also evidence that as the beam spot size becomes large heating depths are increased. Also important is a parametric study of the effect of heating rates, cooling rates, beam fluence, *etc.*, on hardening, tempering, and annealing.

Theoretical work needs to include three steps. (1) Realistic heat deposition calculations need to be determined using the CYLTRAN[14] and ISIS codes.[15] (2) Two-dimensional solutions to the heat transfer equation, $\partial T/\partial t = \alpha \nabla^2 T$, to determine the cooling rates. (3) Determination of optimal heating profiles for the desired results.

Experiments to verify these effects should be done with a high repetition-rate, high-current machine for which beam fluence and energy are well known. Beam energy of 1000 to 2000 J/g is needed to melt steel, but 500 J/g is sufficient to raise the temperature to austenitic temperatures. The RHEPP accelerator at Sandia, whose parameters are given in Table I, has sufficient energy to perform these experiments. Samples irradiated with a measured dose could then be post-analyzed for changes in hardness and crystal structure. Hardness testing can be done with a commercially available hardness tester.[16] Crystal size can be determined with an electron beam microscope. Slicing of irradiated samples would allow for measuring heat deposition contours to compare with the calculated contours.

V. Conclusions

High energy, high current electron beams offer many advantages for conditioning of steels over other techniques. The potential savings resulting from electron beam hardened welds could be substantial. The ability to selectively deposit energy volumetrically into a material is not matched by any other technique. This technique could have a potentially large effect on military applications. An even larger benefit is likely for commercial applications. The task remains to do the theory and experiment to develop and demonstrate its usefulness.

TABLE I. RHEPP beam parameters.

	May 1992	June 1992	June 1993
V(MV)	0.25	0.9	2.25
PRF(Hz)	0-500	120	0-120
I_b(kA)	2.5	25	25
τ_p(ns)	70	60	60
P_{out}(kW)	22	160	400

References

1. J. E. Jenkins, "Dynamic Electron Beam Hardening Cycles," Metal Progress, p. 38, July 1981.
2. B. G. Lewis and P. R. Strutt, "Practical Implications of Electron-Beam Surface Melting," Journal of Metals, p. 37, November 1982.
3. L. Pages, *et al.*, Atomic Data 4, pp. 1–127 (1972).
4. N. Taniguchi, *et al.*, Energy-Beam Processing of Materials, (Clarendon, Oxford, 1989).
5. D. R. Dreger, "Pinpoint Hardening by Electron Beam," Machine Design, p. 89, 26 October 1978.
6. G. Majni, *et al.*, "Electron Beam Induced Reactions in Metal/Si Systems," Vacuum **32**, p. 11 (1982).
7. A. Iwata, "Localized Transformation Hardening by Electron Beam," Proc. of the 5th Intern'l Conf. on Production Engineering, (Japan Soc. Prec. Engg., 1984) p. 496.
8. K. J. A. Mawella and R. W. K. Honeycombe, "Formation of Rapidly Quenched Surface Layers in Iron-Based Alloys Using Electron Beam," Proc. 4th Intern'l Conf. on Rapidly Quenched Metals, (Sendai, 1981) p. 185.
9. J. E. Jenkins, "Surface Modification by Electron Beam Glazing," Thin Solid Films **84**, p. 341 (1981).
10. H. W. Bergmann and B. L. Mordike, "Laser and Electron-Beam Melted Amorphous Layers," Journal of Materials Science **16**, p. 863 (1981).
11. B. G. Lewis and P. R. Strutt, "Practical Implications of Electron-Beam Surface Melting," Journal of Metals, p. 37 (1982).
12. Metals Handbook, Vol. 2, "Heat Treating, Cleaning, and Finishing," ed. by T. Lyman, 8th Edition, American Society for Metals, Metals Park, OH, p. 17 (1964).
13. F. Tsang, Idaho National Engineering Laboratory, private communication.
14. C. M. Snell, R. K. Keinigs, T. J. T. Kwan, and S. Caldwell, "CYLTRAN Enhanced Version (with Photon Link and Everything Else)," memo X-10(8-87)5, Group X-10, Los Alamos National Laboratory, 04 August 1987.
15. G. R. Gisler, M. E. Jones, and C. M. Snell, "ISIS: A New Code for PIC Plasma Simulation," Bull. Am. Phys. Soc. **29**, p. 1208 (1984).
16. Buehler, 41 Waukegan Road, Lake Bluff, IL 60044.

HIGH-RATE DEPOSITION OF THIN FILMS BY HIGH-POWER ION BEAM

I.F. Isakov, G.E. Remnev, and A.N. Zakutayev

Nuclear Physics Institute, 634050, Tomsk, Russia

Abstract

The results on the deposition of thin elemental and compound films by means of a high-power ion beam are presented. The TEMP accelerator (an ion energy of 300 keV, a current density of 100-150 A/cm^2 on a target, a pulse repetition rate of 0.3 Hz, a vacuum of 10^{-4} Torr) was used. The thin metallic (Cd, Zn and other) and stoichiometric Y_1-Ba_2-Cu_3-O_7-x films were obtained. The film growth rate was (0.3-1)·10^8 Å/s. The results show (i) the metallic films were continuous with very smooth surface morphology when they were examined by scanning electron microscopy, and (ii) transmission electron diffraction and transmission electron microscopy indicated small grain polycrystalline metallic films, and (iii) by Rutherford backward scattering and Auger electron spectroscopy it is shown that the stoichiometric Y_1-Ba_2-Cu_3-O_7-x films can be deposited at relatively low substrate temperature ~ 300-450°C.

Introduction

In recent years a new high-rate technique of thin-film vacuum deposition by means of a high-power ion beam (HPIB) named "Pulsed Ion Beam Evaporation (PIBE)" [1] is successfully advanced. By this method 10^{20} cm^{-3}, 1 eV ablation plasma generated through the beam-target interaction is used for the film deposition. The film growth rate achieves 10^8 Å/s. This ultra-high deposition rate allows to keep the film stochiometric composition and to produce the films with minimum contamination. Kinetic energy per particle is comparable to that achieved with nonthermal sputtering processes (~ eV), but the plasma density is much higher that obtained during normal thermal evaporation and nonthermal sputtering processes (10^{10} - 10^{13} cm^{-3}). The HPIB-ablated energetic particles have enough mobility to form polycristalline instead of amorphous phase at room temperature. In the present report the surface morphology, crystal structure of the metallic film were studied by scanning and transmission electron microscopy. Rutherford backward scattering and Auger electron spectroscopy were used to investigate the stoichiometry of Y_1-Ba_2-Cu_3-O_7-x films. Earlier [1] the Y_1-Ba_2-Cu_3-O_7-x were obtained by this method at higher power density of HPIB (1 MeV, 10.5 kA/cm^2, 10^9 W/cm^2, 40 ns). We show in the present report that the stoichiometric Y_1-Ba_2-Cu_3-O_7-x film can be obtained at lower power density of HPIB and at relatively low substrate temperature.

Deposition

The TEMP high-current ion accelerator [2] was used in the experiments. The feasibility of the use of the TEMP accelerator for thin metallic film deposition was considered earlier in the work [3]. The operation conditions of the accelerator were as follows: an ion energy of 300 keV, a pulse duration of 50 ns, a current density of 100-150 A/cm^2 on a target, a power density of (3-4.5)·10^7 W/cm^2, a pulse repetition rate of 0.3 Hz, the composition of the beam being 20 % of protons and 80 % of carbon ions. A diagram of the experimental system is shown schematically in Fig. 1.

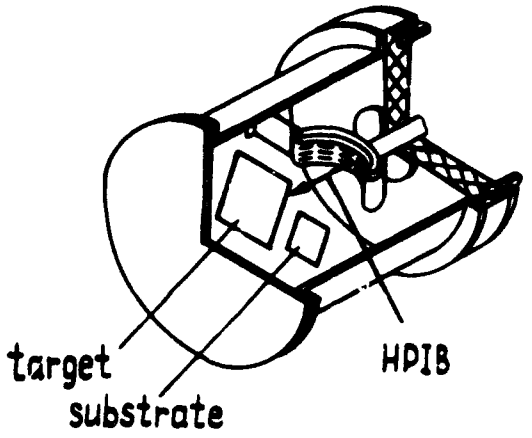
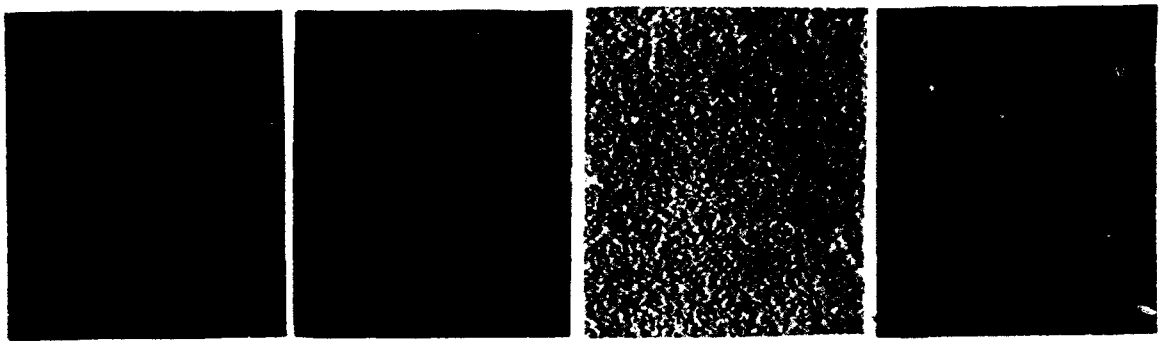


FIG. 1. Schematic diagram of the experimental system used to study the preparation of thin films.

The 20 cm^2 – transverse section ion beam was focussed onto a target at a 45° angle of incidence. The substrate was positioned at shallow angle to the target plane, at 2 and more cm distance. The base pressure in the deposition chamber was 10^{-4} Torr. The films were produced using a bunch of pulses. It should be noted that the area of the prepared films is comparable to the 20 cm^2 – transverse section of the HPIB, all the films being uniform in thickness.

RESULTS AND DISCUSSION

A. Film morphology



a) b) c) d)

0.1 μm

FIG. 2. Surface roughness of the metallic films observed by scanning electron microscopy. The films were deposited at 20°C on glass ceramics substrates:
(a) Cd film, 600 Å thick (two pulses);
(b) Pb film, 2500 Å thick (five pulses);
(c) Zn film, 1500 Å thick(five pulses);
(d) Cu (70 %) – Zn alloy film, 2500 Å thick (ten pulses).

Shown in Fig. 2 are scanning electron micrographs showing the surface morphology of Cd–, Zn– and Cu (70 %) – Zn films with different film thickness deposited at 20°C substrate temperature on glass ceramics. The film were produced using a bunch of pulses (up to 10). The

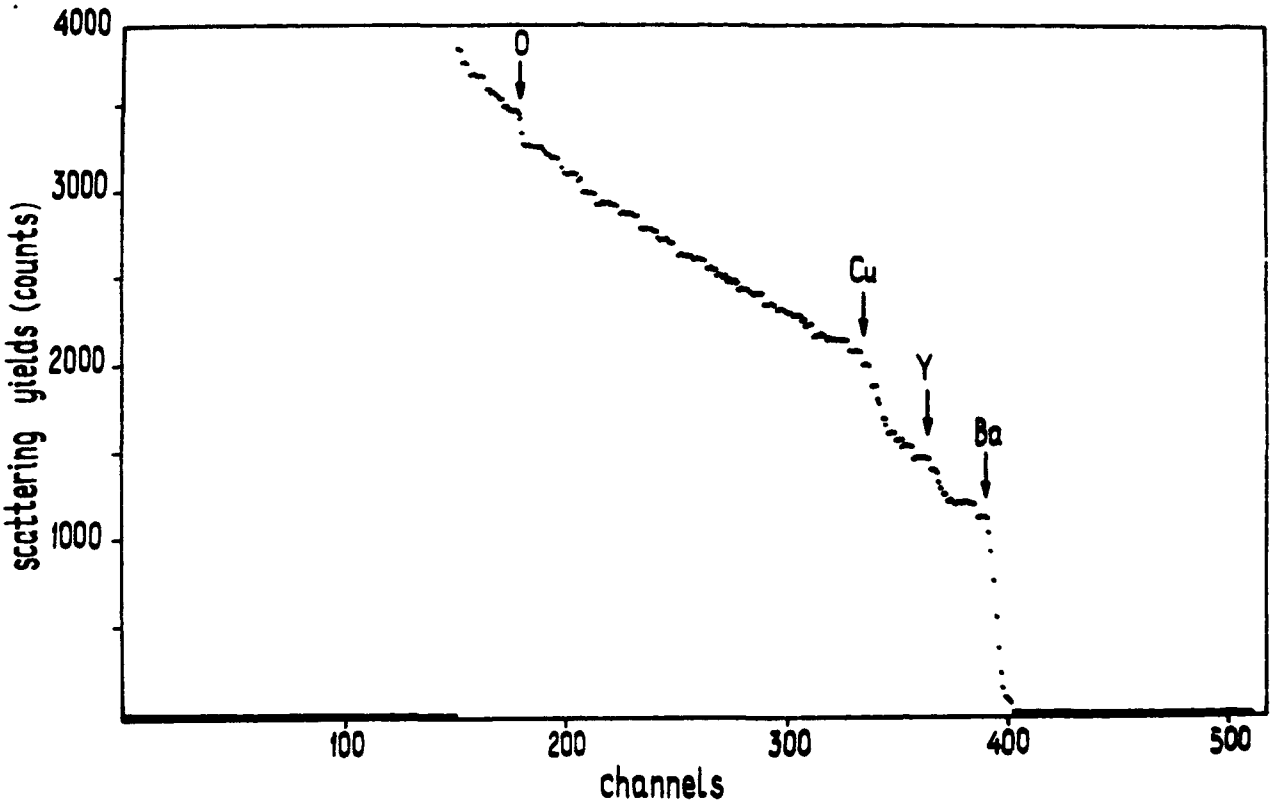


FIG. 4. Rutherford backscattering spectra of a Y_1-Ba_2-Cu_3-O_7-x film, 2 μm thick, deposited at 300°C on (100) $LiTaO_3$.The calculated Y-Ba-Cu composition is 0.97 : 2 : 3.03.

Fig. 5 shows Auger-profiles of elements distribution along the Y_1-Ba_2-Cu_3-O_7-x film depth. The growth conditions in this case were the same as Fig. 4. As seen from the figure the film has homogeneous linear profiles of elements distribution along the film depth.

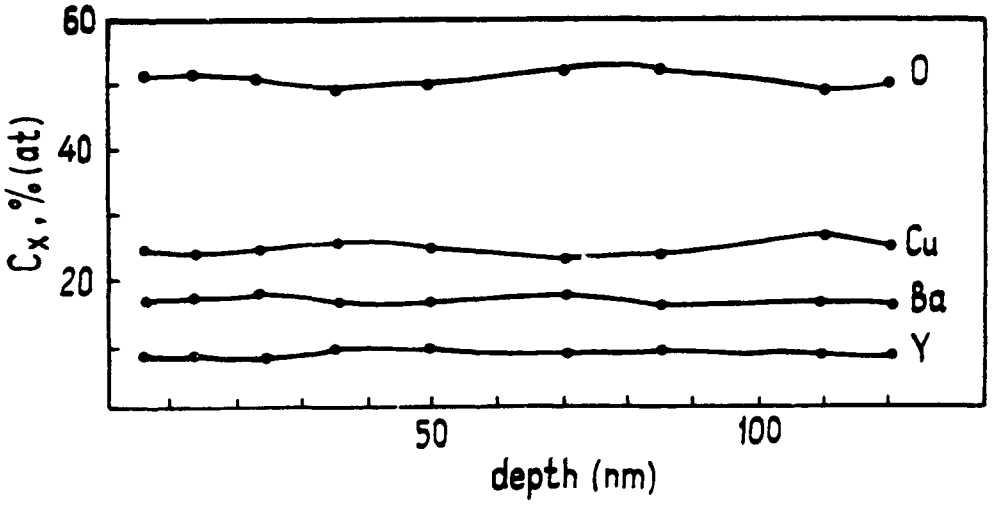
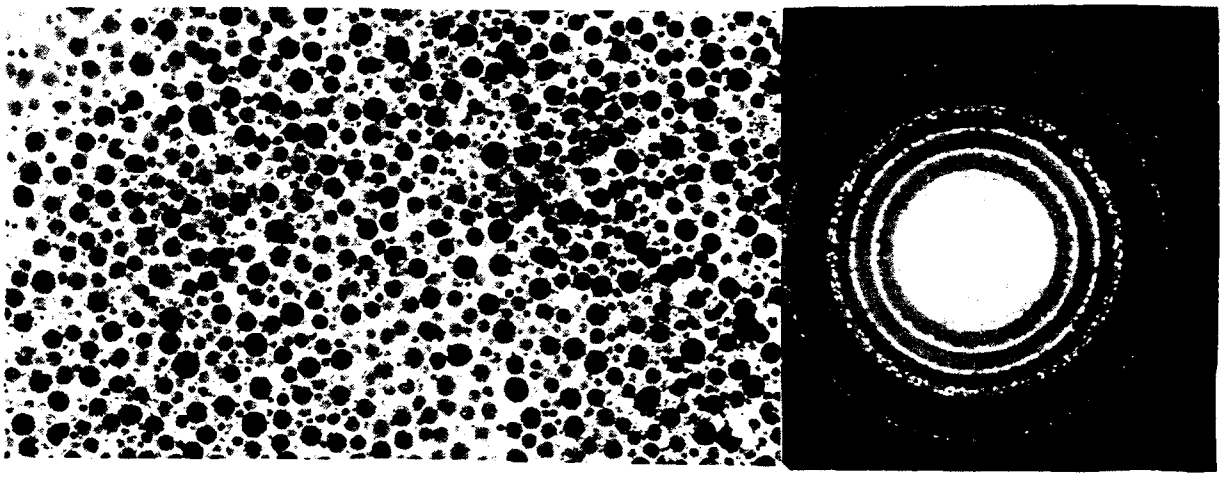


FIG. 5. Auger-profiles of components distribution along the Y_1-Ba_2-Cu_3-O_7-x film depth. The film was deposited at 300°C on (100) MgO.

deposited film depth was 200–300 Å/pulse for Cd-, Zn- and CuZn films, 500 Å/pulse for Pb. The film growth rate was $3 \cdot 10^7 - 10^8$ Å/s. All the films were continuous ones with the smooth-mirror surface without macrodefects (bound up with drop condensation)

B. Crystal structure of the films.

The crystal structure of the metallic films produced by this method was examined through transmission electron microscopy (TEM) and transmission electron diffraction (TED). In the case of TEM and TED observations, NaCl substrates were used, since it is covenience for sample preparation and also more stable for heating during deposition. Fig. 3 shows the TEM (a) and TED (b) patterns of a polycrystalline Zn film deposited at 20°C substrate temperature. The 600 Å – thick Zn film was obtained by two pulses. In the figure the average grain size of the polycrystalline film is estimated to be several hundred angstroms. The grains have an equilibrium round shape. The diffraction pattern shows no evidence of the broadbands which is characteristic of amorphous phases.



a) b)

0.1 μm

FIG. 3. (a) Transmission electron micrograph of polycrystalline Zn film, 600 Å thick (two pulses), deposited at 20°C on (001) NaCl. (b) Transmission electron diffraction from this film.

C. Y–Ba–Cu oxide films ctoichiometry

Rutherford backward scattering (RBS) and Auger electron spectroscopy (AES) were performed to investigate stoichiometry and profiles of elements distribution of the film deposited at relatively low substrate temperatures in the range of 300–450°C on (100) MgO, α–Al_2O_3 and (100) $LiTaO_3$. The target was a commercially prepared hot pressed and annealed at 950°C for 10 hours in O_2 stoichiometric Y–Ba–Cu oxide pellet (composition ratio = 1 : 2 : 3). Figure 4 shows RBS spectra of a Y_1–Ba_2–Cu_3–O_7–x film deposited at 300°C on (100) $LiTaO_3$ substrate. The 2 μm – thick film was obtained by 50 pulses (400 A/pulse). The calculated Y–Ba–Cu composition of the film is 0.97 : 2 : 3.03.

In the table the RBS and AES results are summarized, for more than twenty samples of such the films.

TABLE. Composition of Y–Ba–Cu oxide thin films deposited at 300–450 °C on (100) MgO , α–Al_2O_3 , (100) $LiTaO_3$ by PIBE

Investigation method	Elements ratio			
	Y	Ba	Cu	O
Rutherford backscattering	0.92 ÷ 1.18	2	2.98 ÷ 3.23	-
Auger electron spectroscopy	1	1.8 ÷ 2.2	2.8 ÷ 3.3	5.7 ÷ 6.3

The results show that the composition of the films is close to 1 : 2 : 3 (within experimental error), the stoichiometry of the films being similar to those of the target both before and after irradiation. Electrical properties of the Y_1–Ba_2–Cu_3–O_7–x films are not presented in the report. But it should be said that the films deposited on $LiTaO_3$ and MgO substrates showed a transition to the superconducting state at nitrogen temperatures at once after their deposition without an additional annealing in O_2 surroundings.

Conclusion

A high–power ion beam with the parameters (an ion energy of 300 keV, a pulse duration of 50 ns, a current density of 100–150 A/cm^2 on a target) was successfully used to deposit elemental and compound films. The result of SEM observations showed that the metallic films were continuous ones with very smooth surfaces without macrodefects. The TED and TEM pattern observations indicated that the metallic film deposited at room substrate temperature demonstrate a ring pattern indicating polycrystalline structure. In conclusion, we have shown that stichiometric Y_1–Ba_2–Cu_3–O_7–x films can be deposited on (100) MgO, α–Al_2O_3, (100) $LiTaO_3$ substrates at relatively low temperatures ~ 300–450°C by the technique of Pulsed Ion Beam Evaporation. These films had homogeneous linear profiles of elements distribution along the film depth. All the films were prepared on large areas comparable to the 20 cm^2 transverse section of the HPIB, the films being uniform in thickness.

Acknowledgments

The authours acknowledge the help of A.A. Yatis, I.A. Lapsker, Yu.P. Sharkeyev, V.G. Shulepov, V.N. Yanovskii for measurements on the thin films and E.V. Pashinskaya for taking figures.

References

[1] K. Masugata, et al., Proc. of 8th Intern. conf. on high–power perticle beams, 2, 1254 (1990).

[2] I.F. Isakov, et al. Vacuum, 42, No. 1/2/, 159–162 (1991).

[3] O.I. Goncharov, et al., Proc. of 8th Intern. conf. on high–power particle beams, 2, 1243 (1990).

Quick Preparation of Thin Films and Characteristics of Ablation Plasma produced by Ion-beam Evaporation

T. Sonegawa, X. D. Kang, H. Hoshino, M. Ohashi
Y. Shimotori*, S. Furuuchi*, K. Masugata and K. Yatsui
Laboratory of Beam Technology, Nagaoka Univarsity of Technology, Nagaoka, Niigata 940-21, Japan

ABSTRACT

An intense, pulsed, ligth-ion beam (LIB) can be used to produce high density "ablation" plasma when the LIB is irradiated on the solid targets. For this case, the LIB can be considered as theeffective heat source since the pulse width is short compared to thermal conduction time. Using the above plasma, we have succeeded in quick preparation of thin films by "ion-beam evaporation" (IBE) . Diamond-like carbon films have been successfully prepared on the silicon substrate kept at room temperature by using graphite target. furthermore, various films were made such as ZnS, ZnS:Mn, B, ITO, YBaCuO, $BaTiO_3$, BN, YSZ, apatite, and so on. The instantaneous deposition rate has been typically estimated on the order of several cm/s. The characteristics of the films prepared have been studied in detail.

In connection with the properties of the films studied above, several diagnostics have been carried out on the characteristics of the ablation plasma by time-resolved spectroscopic measurement by using Streak camera, where fully ionized, high-density plasma has been found to be produced.

INTRODUCTION

Recently, the applications of intense, pulsed, light-ion beam (LIB)[1] are interesting, particularly in materials science. If LIB is irradiated onto solid targets, a high density ($\sim 10^{20}$ cm^{-3}) "ablation" plasma will be produced with reasonably high temperature ($\sim$ a few eV). If such the plasma will be deposited on a substrate placed nereby, various thin films will be quickly prepared. Such a new deposition technique has been called "intense, pulsed, ion beam evaporation (IBE)" by the present

authors.[2,3] The features of IBE are summarized as follows:

1) The instantaneous deposition rate is very high (of the order of several cm/s).

2) Most atoms to be deposited are ions with energies of more than a few eV.

Using IBE, we have attempted to produce thin films of diamond by IBE using graphite target. Furthermore, various films have been preparated such as Zns:Mn, B, ITO, oxide superconductor (YBaCuO), $BaTiO_3$, boron nitride (BN), Yittria Stabilizsd Zirconia (YSZ), apatite, and so on.[2,3]

In the present paper, we mention the preparation of thin films of C, BN, YSZ and YBaCuO using IBE.

EXPERIMENT

Figure 1 shows the experimental arrangement of IBE. LIB is extracted from a magnetically-insulated diode (MID)[1], which is connected to a pulse-power machine, "ETIGO-II" (3 MV, 460 kA, 50 ns).[4] A flashboard (polyethylene) is stuck to the anode as an ion source. The cathode works as an one-turn theta-pinch coil, producing transverse magnetic field ($\sim$ 1 T). The gap length is 10 mm. The anode and cathode are shaped spherically, and the radii of the sphere are 160 mm and -150 mm, respectively. The beams are mainly composed of protons (> 80 %).[5] The vacuum chamber is pumped to $\sim 10^{-4}$ Torr.

The targets (normally, 35 mm in diameter, 5 mm thick) are placed at z = 140 mm from the anode in an angle of 45° with respect to the beam axis. The substrate is located in parallel with the target surface at ℓ (distance from target to substrate) = 30 or 40 mm. We do not need to heat the substrate during the deposition.

RESULTS AND DISCUSSION

a) Carbon target

Figure 2 shows a micrograph of scanning electron microscope (SEM) of the surface of the carbon film prepared on silicon substrate by one shot, where V_d (diode voltage) $\sim$ 1.5 MV and ℓ = 30 mm. The sample o the film is inclined by 60° with respect to the level surface in SEM. The upper

and the lower parts of SEM micrograph are the carbon film and the silicon surface, respectively. The carbon film has a surface covered by 1 μm or smaller grains like pebbles. The silicon surface is melted by being heated by deposition. Substrate temperature rises at 1400°C or greater, since melting point of silicon is about 1400°C. The average thickness of film is ~ 1 μm.

Figure 3 shows the oxygen-1s, carbon-1s and silicon-2p X-ray photoelectron spectroscopy (XPS) spectrum of the carbon film. The peak of oxygen-1s and carbon-1s appears at the binding energy of 532 eV and 285 eV, respectively, but that of silicon-2p do not appear. Hence, silicon atoms do no exist in the film surface. The intensity of oxygen-1s decreases with increasing etching time. It indicates that the surface of carbon films is covered by oxygen atoms. The spectrum of carbon-1s do not shift to 283 eV by chemical shift of SiC.[6] This result may correlate with the absence of silicon peak.

Figure 4 shows selected area diffraction (SAD) pattern by transmission electron microscope (TEM), where (a) and (b) correspond to graphite and silicon carbide, respectively. We find that silicon carbide is being made in the interface between film and substrate.

b) Boron nitride target

Figure 5 shows the infrared absorption spectra of BN film prepared on silicon substrate by five shots at V_d ~ 1.0 MV, ℓ = 40 mm. We see a strong absorption band near 1350 cm^{-1} and a weak one at 800 cm^{-1}. These peaks are due to hexagonal BN (h-BN). We cannot see the peak at 1050 cm^{-1} corresponding tocubic BN.

The atomic concentration in BN film was measured by XPS. Figure 6 shows oxygen-1s, nitrogen-1s and boron-1s spectra of BN target and BN film. The intensity of nitrogen-1s of BN film is smaller than that of target. Moreover, most of boron is B-B bond. These results suggest that nitrogen in the film is deficient, and that most of nitrogen are exhausted out from the film.

c) YSZ target

We have also prepared YSZ target on glass and silicon substrate, where ZrO_2-8 wt% Y_2O_3 and ZrO_2-20 wt% Y_2O_3 targets were used. The structures of these films were analyzed by X-ray diffraction (XRD), which is shown in

Fig. 7. In the former case, tetragonal (002) and (200) peaks were observed (cf. Fig. 7 (a), (b)). In the latter case, however, cubic (200) was observed (cf. Fig. 7 (c), (d)).

d) YBaCuO

Figure 8 shows resistivity vs. temperature of the film prepared by IBE on $SrTiO_3$ (100). We see clearly the superconductive film is prepared, where $T_{c\ onset} \sim 70$ K and $T_{c\ zero} \sim 15$ K.

Several diagnostics have been carried out on the characteristics of ablation plasma in connection with the perperties of the films prepared.[7)]

CONCLUDING REMARKS

(1) Carbon film is prepared on silicon substrate by IBE, where the deposition rate is ~ 1 μm/shot. Silicon carbide is present in the interface between film and substrate.

(2) H-BN film is obtained on silicon substrate by IBE. Nitrogen in this film are found to be deficient.

(3) YSZ film is obtained by ZrO_2-8 wt% Y_2O_3 and ZrO_2-20 wt% Y_2O_3 targets, where tetragonal and cubic YSZ are prepated, respectively.

(4) YBaCuO film is prepared on $SrTiO_3$ (100) substrate, which indicates the evidence of superconductive characteristics.

References

1) K. Yatsui et al.: Laser and Particle Beams 3, 119 (1985).
2) Y. Shimotori et al.: Jpn. J. Appl. Phys. 28, 468 (1989).
3) K. Yatsui: Laser and Particle Beams 7, 733 (1989).
4) A. Tokuchi et al.: Proc. 2nd Int'l Top. Symp. ICF Res. by High-Power Particle Beams, ed. K. Yatsui (Lab. of Beam Tech., Nagaoka Univ. of Tech., 430 (1986).
5) Y. Shimotori et al.: IPPJ-769 (2), 267 (1986).
6) D. N. Belton et al.: Appl. Phys. Lett. 54, 416 (1989).
7) K. Yatsui et al.: Proc. 3rd Int'l Conf. on Intense Ion-Beam Interaction with Matter, Albuquerque, USA (1990).

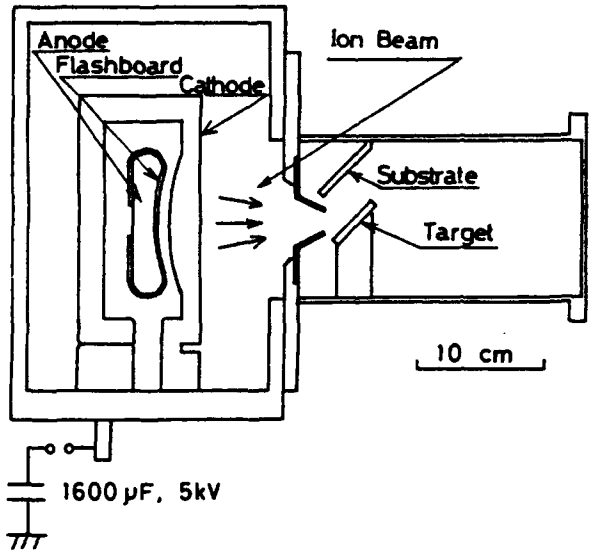


Fig. 1 Cross-sectional view of IBE system.

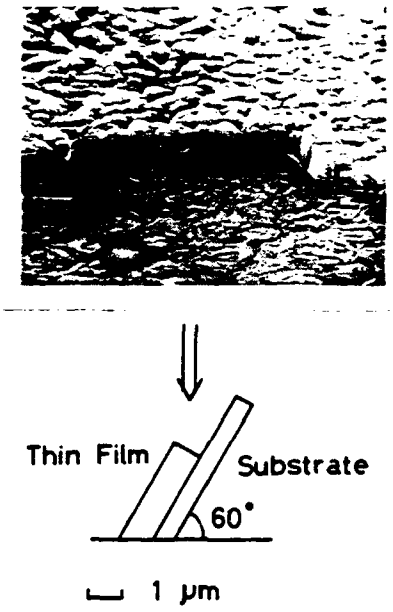


Fig. 2 SEM micrographs of the surface.

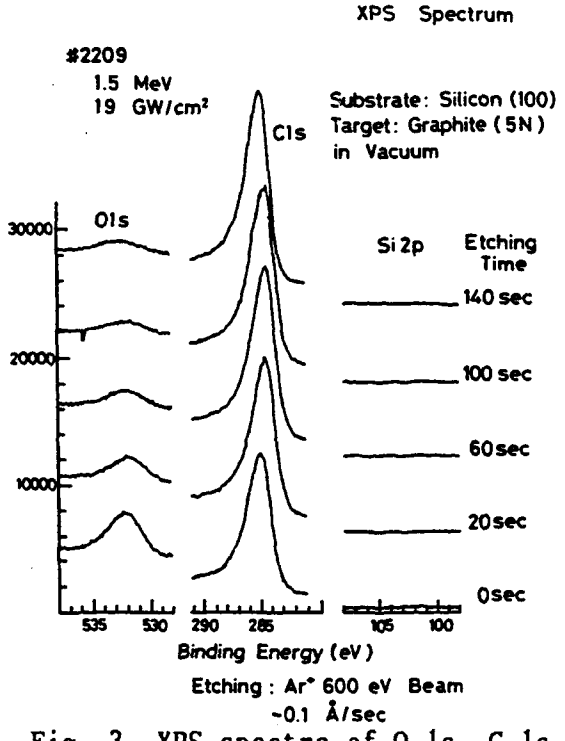


Fig. 3 XPS spectra of O-1s, C-1s and Si-2p region for different etching time of carbon film.

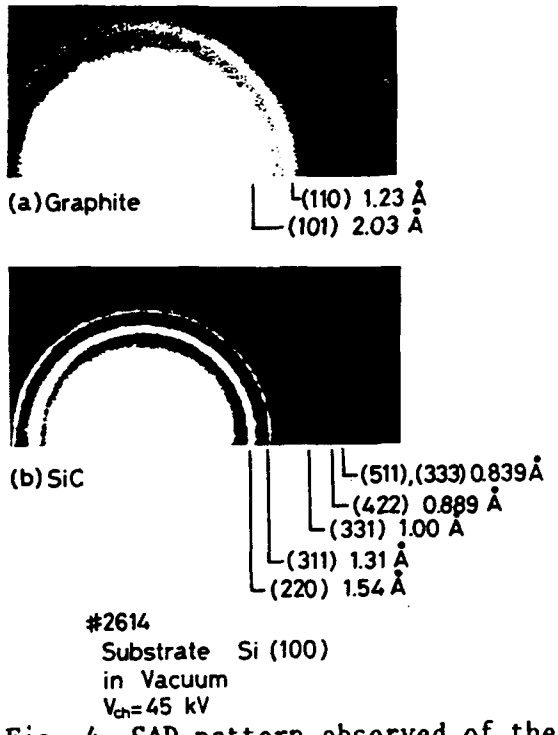


Fig. 4 SAD pattern observed of the carbon film; (a) graphite and (b) silicon carbide.

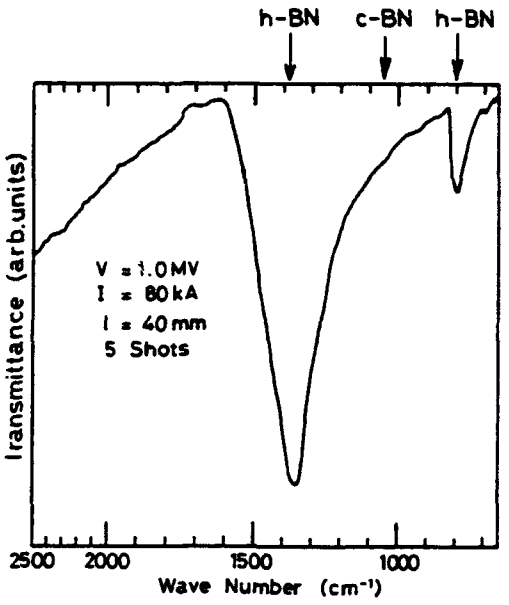


Fig. 5 IR absorption spectra of BN film.

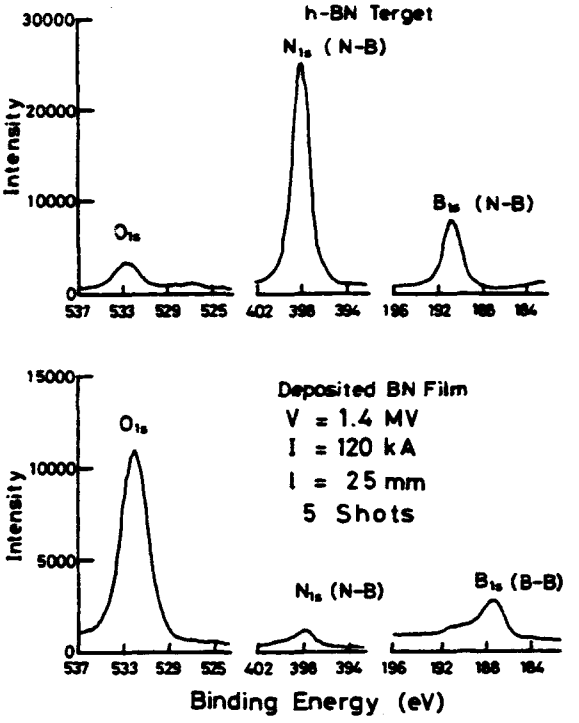


Fig. 6 XPS spectra of O-1s, N-1s and B-1s region for BN target and film.

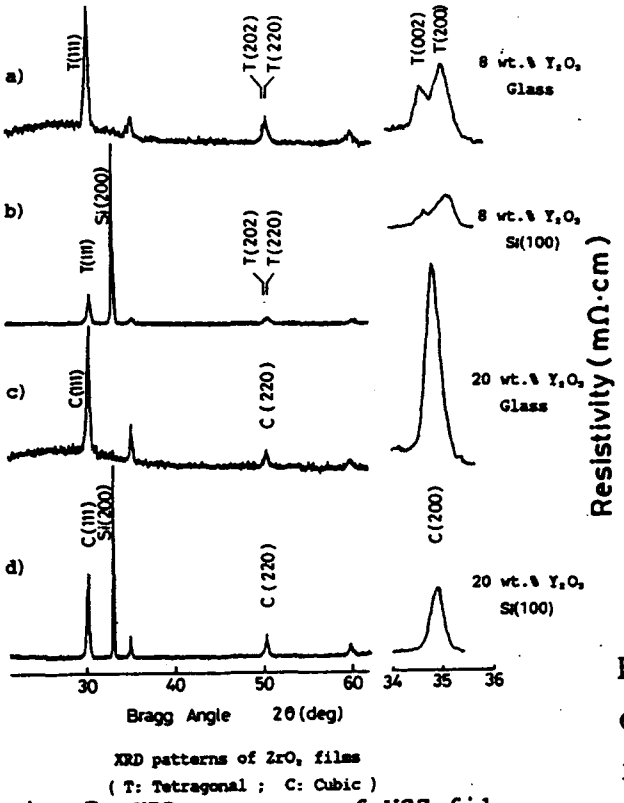


Fig. 7 XRD patterns of YSZ films deposited on a) glass and b) silicon substrate from ZrO_2-8 wt% Y_2O_3 target and on c) glass and d) silicon from ZrO_2-20 wt% Y_2O_3 .

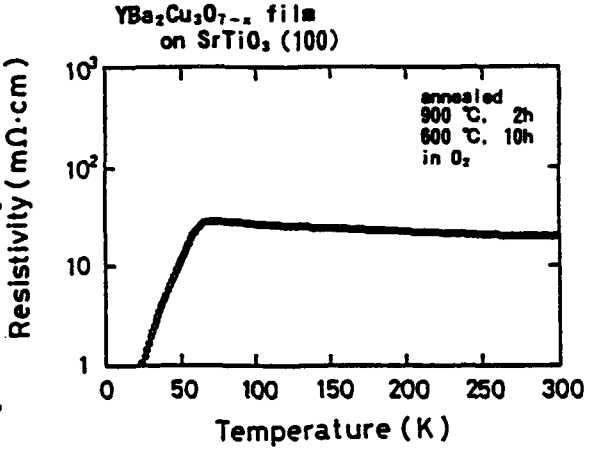


Fig. 8 Temperature dependence of electrical resistivity for YBaCuO film.

Contributed Plasma Discharge Papers

ELECTROTHERMAL PLASMA SOURCE AS A HIGH HEAT FLUX SIMULATOR FOR PLASMA-FACING COMPONENTS AND LAUNCH TECHNOLOGY STUDIES

M. Bourham, J. Gilligan, O. Hankins, W. Eddy and J. Hurley
Department of Nuclear Engineering, North Carolina State University
Raleigh, NC 27695-7909

ABSTRACT

An electrothermal plasma source "SIRENS" has been designed, constructed, and operated (over 450 shots) to produce high density (>10^{25} /m^3), low temperature (1-3 eV) plasma formed by the ablation of the insulator (Lexan, $C_{16}H_{14}O_3$) with currents of up to 100 kA and energies up 15 to kJ. Switchable capacitor modules allow for higher energy inputs (30 kJ) and longer pulse lengths (0.1 - 1.0 ms with pulse forming network). The plasma flows through a cylindrical barrel, situated along the axis of a pulsed magnet, which can produce a parallel magnetic field (up to 16 T) over 8 msec pulse length. The source heat flux (up to 90 GW/m^2 over 100 μsec pulse) and the diagnostics arrangements (electrical, magnetic, optical, heat flux, pressure, materials) are adequate for various applications (plasma-matter interaction; simulation of thermal quench phase of plasma disruption in fusion tokamaks; simulation of pulsed heat loading conditions of plasma-driven launchers; ablation-controlled arcs; plasma switchers). Different materials (metals, alloys, coated materials, insulators and graphite grades) have been exposed to the high heat flux in SIRENS, where comparative erosion behavior was obtained. Vapor shield phenomena has been characterized for different materials, and the energy transmission factor through the shielding layer is obtained. The magnetic field is produced parallel to the surface to cause a decrease in the turbulent energy transport through the vapor shield to provide further reduction of the surface erosion (magnetic vapor shield effect).

INTRODUCTION

The generated heat fluxes in plasma-driven launchers and large fusion tokamaks during hard plasma disruptions, exceed 10 GW/m^2 for a duration of 0.01 - 5 ms. Such high heat fluxes result in temperature rise of the material surface (launcher critical components, and tokamak plasma-facing components) to melting and vaporization, and thus produces material surface erosion [1-5]. Erosion (melting and vaporization) of these components is one of the factors that affects the efficiency of these devices, and decrease the lifetime [6,7]. Practical operation of such devices (plasma facing components for future large tokamaks like ITER, and rails and insulators of plasma-driven launchers) must withstand high heat loading with the minimum surface erosion so that the lifetime can be increased.

The plasma boundary layer, adjacent to the eroding surface, is characterized by large temperature and density gradients. The produced vapor due to ablation is injected into that boundary layer and thus the layer thickness increases and its temperature decreases, which results in less heat to the surface. Such boundary layer (vapor shield) helps to reduce the surface erosion by absorbing a fraction of the incident energy [3,8]. The heat flux q'' that reaches the surface is represented by $q''= f\,S$, where f is the energy transmission factor through the vapor layer, and S is the incident heat fluence. Absorbed energy appears as vapor shield internal energy which can be transported away from the localized area.

The plasma flow in plasma-driven launchers has Reynolds number of about 10^7, and consequently the viscous skin friction generates turbulence [9]. A strong applied magnetic field, parallel to the surface, can reduce transport coefficients across the field lines. Consequently, total melting and erosion are reduced due to reduction of the total energy transport through the plasma boundary layer [10]. The magnetic vapor shield mechanism naturally exists at the component surfaces of electromagnetic launchers due to rail currents (100 -1000 kA), which generate magnetic fields of 10 to 100 T. In the case of electrothermal launchers there is no self-induced magnetic field, and hence an external magnetic field must be applied. Reduced heat transfer, for increased applied magnetic fields, had been observed in turbulent flow of liquid metals through a channel [11,12].

Refractory and refractory-coated materials may help in reducing the erosion of rails, barrels and tokamaks plasma-facing components, while ablation of the insulators may be achieved by using high tensile insulating materials [6-8]. Different materials have been tested to understand their erosive behavior under typical operational conditions experienced in plasma-driven launchers and fusion disruption [13-15].

Experimental Device and Diagnostics

The electrothermal plasma source SIRENS [7,8] has been designed to simulate typical conditions of high heat flux deposition in plasma-driven launchers and fusion disruption. SIRENS produces low-temperature (1-3 eV) high-density (10^{25}-10^{26} /m^3) plasma formed by the ablation of a liner inside the main insulator (Lexan), with currents up to 100 kA. Material samples are shaped in tube-form, situated inside a stainless steel barrel connected to the source, and exposed to the plasma flow. Samples may also be exposed to the plasma at the source exit, where the plasma is incident normally or at an angle to the sample surface. The incident heat flux can be

varied between 2 to 90 GW/m^2 over a 100 μsec duration. The average plasma velocity is 10 - 12 km/s, which is well correlated to the predicted values obtained from the ZEUS code [16], and is in general agreement with previously reported results [17].

The magnetic field is produced by a pulsed 2 kA current over 8 msec, which produces an average magnetic field (with liquid nitrogen cooling) of 16-20 T at the barrel axis. An average axial magnetic field of 9 Tesla has been achieved without cooling. The electrical circuit of the magnet is floating and directly connected to the high voltage floating output of a slap-shot pulser, which is capable of providing a 2 kA pulsed current (at 2.45 kV charging voltage) with FWHM of 4 ms. A 70% charging cycle is capable of providing 1.6 kA into a 2mH, 0.5Ω inductive load. The plasma source is discharged at the top of the magnetic field pulse (4 msec after the setting of the magnetic field). Fig. 1 shows a schematic drawing of the electrothermal plasma source SIRENS. For multipurpose use of the device, different barrels are arranged with diagnostics access.

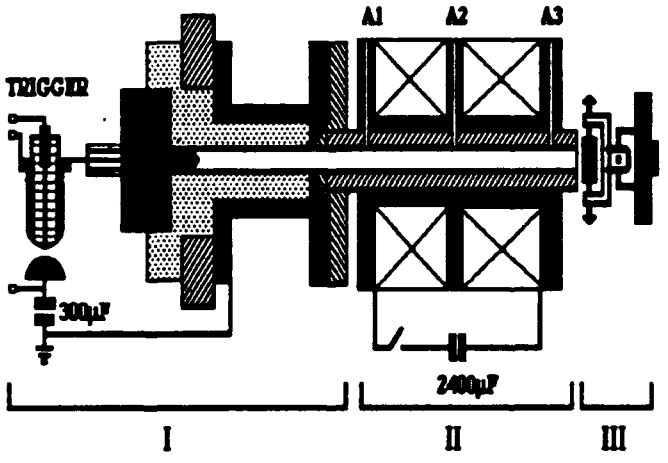


Fig.1 Schematic drawing of the SIRENS electrothermal plasma source. Capillary discharge source (Section I) , barrel with a high intensity pulsed magnet (section II), and pivot target holder (section III). Diagnostics could be accessed through A1, A2 and A3.

Fig. 2 (top) shows diagnostics arrangement for discharge and plasma currents (external and internal Rogowski coils), discharge potential (compensated capacitively-coupled potential divider), plasma velocity (phototransistors and a B-dot array), optical emission spectroscopy (fiber optics-to-optical multichannel analyzer), and heat flux (thermocouples). Fig 2 (bottom) shows the diagnostics arrangement for plasma resistance (conductivity probes), axial heat flux (thermocouples), and pressure and Drag forces (absolute pressure transducers). Signals are digitized via two 8-channel LeCroy waveform digitizers.

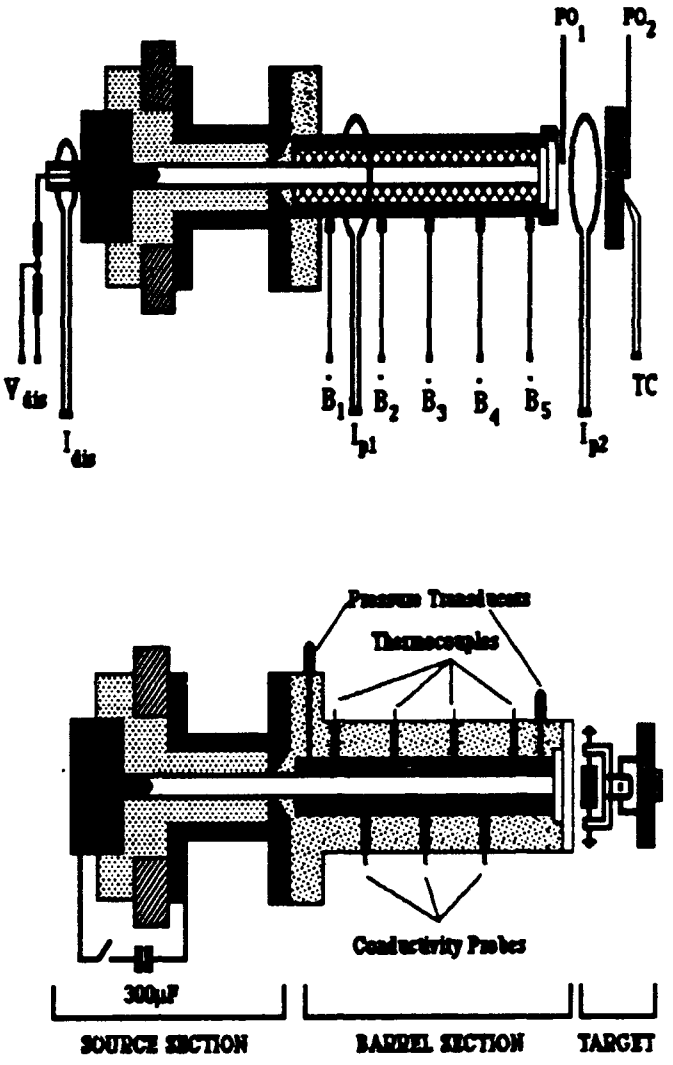
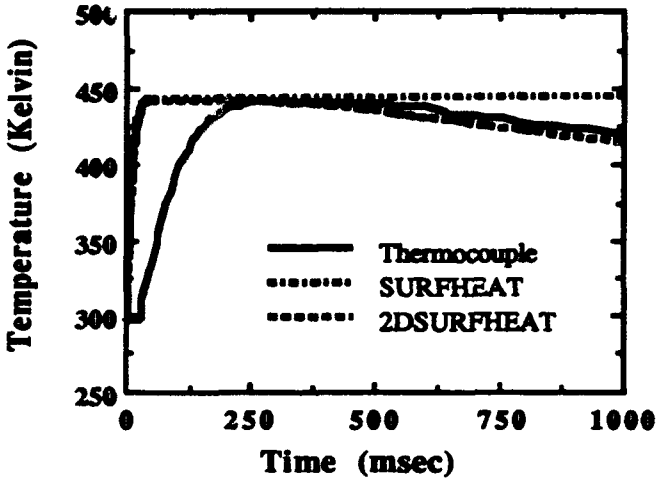


Fig.2 SIRENS multipurpose diagnostics arrangements. Top drawing shows B-dot array, Rogowski coils, fiber optics, discharge current and voltage measurements, and a thermocouple to measure the target temperature. Bottom drawing shows pressure transducers, conductivity probes, and thermocouples for heat flux measurements.

Measurement of the heat flux is evaluated from the temperature increase of the wall, and for a semi-infinite slab is equal to $(\Delta T/2)(\pi\rho Ck/\Delta t)^{1/2}$ where ρ, C and k are the wall material specific density, specific heat and thermal conductivity respectively. 1-D and 2-D, time dependent heat conduction codes (SURFHEAT and 2DSURFHEAT) read the temperature data file and compute the incident heat flux. Fig. 3 (top) shows the measured and calculated temperature histories. 2DSURFHEAT is a better match to the measured temperature history at longer times than that obtained using SURFHEAT. Fig.3 (bottom) shows better matching obtained from fast response thermocouples.



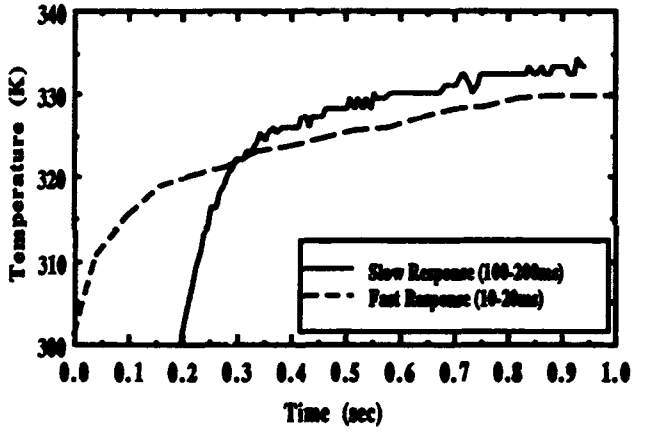


Fig. 3 Top graph show the measured and calculated temperature histories. Bottom graph shows a comparison between temperature histories obtained by slow and fast response thermocouples.

Measurement of the plasma temperature is evaluated from conductivity probes (plasma resistivity). SIRENS plasma tends to be weakly nonideal, and corrections to the ideal plasma transport, thermodynamic properties for resistivity and charge state must be included. A modified Coulomb logarithm $L = \ln (1 + 1.4\ \Lambda^2)^{1/2}$ has been introduced, and the modified plasma resistivity model was used to obtain the temperature [18,19]. Fig. 4 shows the plasma temperature, obtained from conductivity probes, compared to those obtained from heat flux and spectroscopic measurements [20].

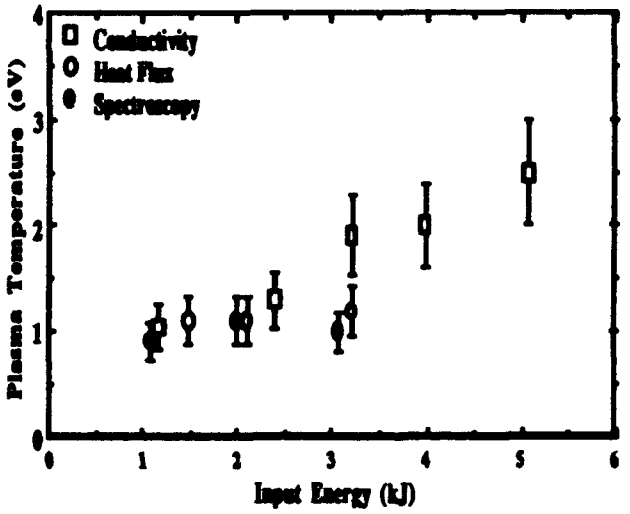


Fig. 4 Plasma temperature, obtained from conductivity probes, compared to those obtained from heat flux and optical emission spectroscopy measurements.

Surface Erosion of Plasma-Facing Components and Launchers Materials

Candidate plasma-facing components for launch technology and fusion reactors were tested under typical high heat loading conditions using the plasma source SIRENS. Incident heat fluxes were varied from 2 to 70 GW/m^2 over 100 μs, for input energies 1-8 kJ. Material samples were either tube-shaped or flat. Coated surfaces are prepared by different coating methods (sputtering, molten salt deposition, plasma spray, electroplating, etc.). Erosion thicknesses were calculated from weight loss measurements.

Fig. 5 shows the erosion thickness of tested materials (metals, alloys, refractory, coated materials, insulators and graphites), for an incident heat flux of 33 GW/m^2 (5 kJ input energy). It is clear that refractory materials, except titanium, have better erosion resistance than pure metals. Aluminum has the highest erosion, and melting is dominant. Pure copper and gunsteel have approximately equal erosion (about 64 and 58 μm respectively). Arc cast molybdenum (AC) withstands thermal shocks better than sintered molybdenum (S). Comparison of SEM micrographs indicated sharp deep cracks for sintered molybdenum, and smoother cracks for the arc cast. Tungsten has approximately no erosion below 20 GW/m^2, but surface coloration and microcracks were observed above 20 GW/m^2. Glidcop (copper-Aluminum oxide alloy) has the highest erosion among tested alloys (28μm), while tungsten-3% rhenium has approximately no erosion. HD-17 (90% W, 6% Ni, 4% Cu) stands in the middle (4.7 μm).

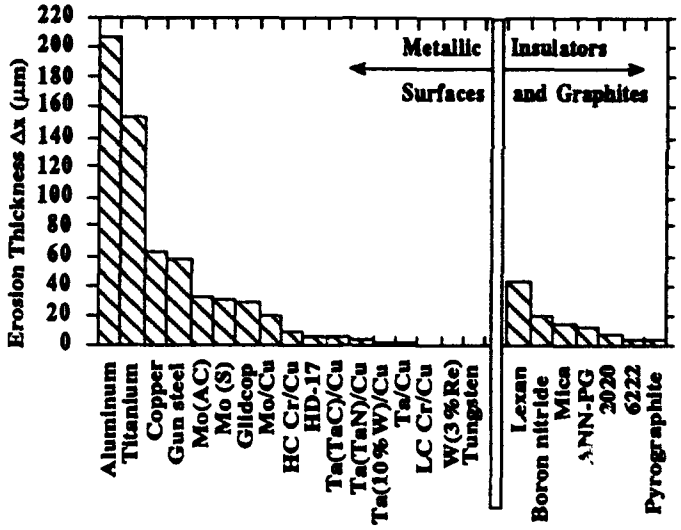


Fig. 5 Erosion thickness of metals, alloys, refractory, coated, insulators and graphite materials, exposed to 33 GW/m^2 over 100 μs duration (5 kJ input energy to plasma).

Coated surfaces have different erosion behavior than pure surfaces because of the amount of heat absorbed by the heat sink. Tantalum (Ta/Cu) and chromium (LC Cr/Cu) coatings on copper showed the lowest erosion, 0.8 and 0.5 μm respectively. Molybdenum coating on copper has ablative features with minimum microcracks, and approximately 40% less erosion than pure molybdenum. Surface melting is dominant at lower heat fluxes, while at higher heat fluxes vaporization is dominant.

For insulators and graphites, ablation of boron nitride and mica (glass-bonded) is less than Lexan (approximately 50% and 65% less, respectively). Boron nitride (BN) has an ablative-abrasive behavior when phase transformation from the hexagonal plate structure to the cubic diamond-like structure takes place under the influence of high pressure. Glass-bonded mica does not withstand higher heat fluxes due to melting of the glass-bond. Graphite grades (high density graphite GR6222 and molded dense electrographite GR2020) have the lowest ablation, but pyrolytic graphite tends to delaminate with increased heat fluxes [21].

The energy transmission factor, calculated from the ablation measurements and ZEUS-code calculations for the source fluence, takes the general empirical form $f = C_1 + C_2\, S^{-1/4}$, where S is the source fluence, and C_1 and C_2 are constants depending on the properties of the material. This factor varies from 75 to 90 % for pyrolytic graphite, and 20 to 35 % for insulators and isotropic graphites, and decreases to < 20% - 5% with the increase in the incident heat flux. Fig. 6 shows the energy transmission factor f through the vapor shield, for insulators and graphite grades, as a function of the incident heat flux.

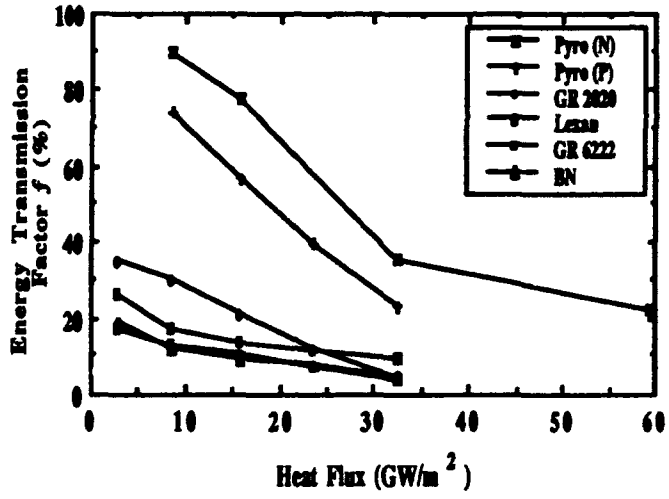


Fig. 6 Energy transmission factor f through the vapor shield, for insulators and graphite grades, as a function of the incident heat flux. For pyrographite, heat flux has been applied either normal (N) or parallel (P) to the direction of laminations.

With applied magnetic field, the empirical scaling law takes a modified form $f_{(B)} = F_1(B)\, S^{-1/4} + F_2(B)$, where $F_1(B)$ and $F_2(B)$ are quadratic functions of the magnetic field, S in W /m^2 and B in Tesla. Fig. 7 shows the normalized ablation thickness (ratio between ablation thicknesses with and without the magnetic field), where a reduction of 25-35% is obtained with an applied magnetic field of 6.25 T. Higher values of energy input require higher magnetic field, and it is apparent that a threshold for the onset of the magnetic vapor shield effect is necessary (above 5 T for Lexan), which means that the magnetic field at higher input energies should exceed 10 T.

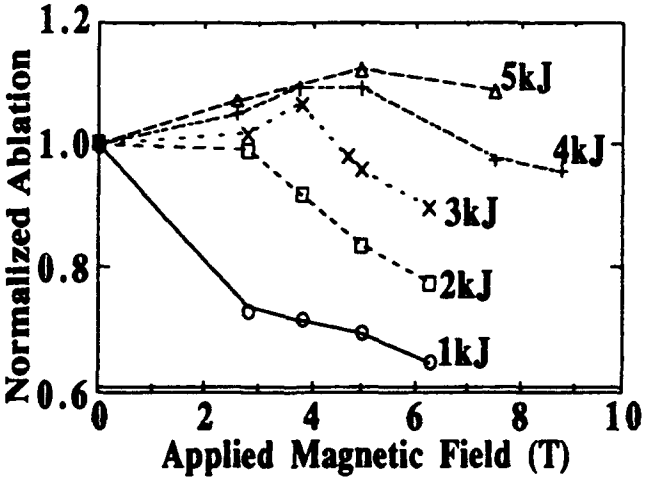


Fig. 7 Normalized ablation thickness for Lexan as a function of the applied magnetic field, at input energies from 1 to 5 kJ.

CONCLUSIONS

The electrothermal plasma source SIRENS, as an adjustable high heat flux source with multipurpose diagnostics arrangements, is an adequate device to experimentally simulate typical high heat loading conditions experienced in plasma-driven launch technology and plasma disruption in fusion tokamaks.

Vapor shield phenomena has been characterized for different insulators and graphite materials. The empirical scaling law for the energy transmission factor may, generally, be expressed by $f = C_1 + C_2 S^{-1/4}$; where S is the source fluence, and C_1 and C_2 are constants depending on the properties of the material. The energy transmission factor was found to vary from 20% to 5% as the heat flux increased.

With the magnetic field applied parallel to the ablating surface, the empirical scaling law is modified to include the magnetic field effect, where the constants C_1 and C_2 are replaced by quadratic functions of the magnetic field. Surface ablation is reduced by 25-35% at 6.25 T magnetic field. Higher values of energy inputs require a magnetic field above 5 T (threshold for the onset of the magnetic vapor shielding effect).

Refractory coatings have better erosion resistance with the better choice of the heat sink and the coating technique. Tungsten and tungsten alloys have approximately no erosion but crack formation may occur. Lexan has an approximately uniform ablation rate, while boron nitride has an ablative-abrasive feature. Graphite, in general, has uniformly low ablation. Pyrolytic graphite tends to delaminate and partial whole grain removal has been observed.

ACKNOWLEDGMENT

Work supported by the US Strategic Defense Command Contract DASG60-90-C-0028, US Army Research Office Contracts DAAL03-86-G-0157 and DAAL03-87-K-0103, US Watervliet Arsenal Contract DAAA22-91-M-4001, and partially by Varian Cross Field & Protector Products.

REFERENCES

[1] A. Bedford, "Rail damage in a small caliber rail-gun," IEEE Trans. on Magnetics, vol. 20, 348-351 (1984).

[2] J. Parker and W. Parson, "Experimental measurement of ablation effects in plasma armature railguns," IEEE Trans. on Magnetics, vol. 22, 1633 (1986).

[3] A. Hassanein, "Erosion and Redeposition of Divertor and Wall Materials During Abnormal Events," Fusion Technology, vol. 19, 1789 (1991).

[4] M. Bourham, O. Hankins, W. Eddy, J. Earnhart and J. Gilligan, "Experimental High Heat Load Surface Damage of Graphite and Refractory Materials," Proc. 14th IEEE Symp. Fusion Engineering, IEEE Cat. No. 91CH3035-3, vol.1, 381(1991).

[5] A. Sestero, "Protection of Walls from Hard Disruption in Large Tokamaks," Nuclear Fusion, vol.17, 115 (1977).

[6] F. Witherspoon, R. Burton and S. Goldstein,"Railgun experiments with Lexan insulators," IEEE Trans. on Plasma Science, vol. 17, 353 (1989).

[7] J. Gilligan, M. Bourham and O. Hankins,"Ablation and melting behavior of materials in electrothermal launchers," 28th JANNAF Combustion Meeting, Brooks Air Force Base, San Antonio, TX, paper I-18, 28 October - 1 November 1991.

[8] M. Bourham, O. Hankins, O. Auciello, J. Stock, B. Wehring, R. Mohanti and J. Gilligan,"Vapor shielding and erosion of surfaces exposed to high heat load in an electrothermal accelerator," IEEE Trans. on Plasma Science, vol.17, 386 (1989).

[9] D. Tidman, S. Goldstein and N. Winsor,"A rail gun plasma armature model," IEEE Trans. on Magnetics, vol.22, 1763 (1986).

[10] J. Gilligan and D. Hahn,"The magnetic vapor shield (MVS) mechanism for protection of high-heat flux components in high-field tokamaks," J.Nuclear Materials, vol.145-147, 391 (1987).

[11] K. Yu, D. Kovner, V. Nikolayenko and I. Panevin,"Experimental studies on the influence of a transverse magnetic field on convective heat transfer in turbulent channel flow of conducting fluid," 3rd All Union Congress on Theoretical and Applied Mechanics, Moscow, 162, 1968.

[12] E. Blums, Yu. Mikhailov and R. Ozols, "Heat and mass transfer in MHD flows," Singapore: World Scientific Publishing Co., 1987.

[13] J. Kolawole, R. Frierson, E. Clothiaux and C. Goodman,"Post-shot analysis of plasma/rail interaction in a small bore load driving EML," IEEE Trans. on Magnetics, vol.27, 386 (1991).

[14] J. Gilligan, M. Bourham, O. Hankins, S. Tallavarjula and R. Mohanti,"Studies to reduce material erosion in electrothermal launchers," IEEE Trans. on Magnetics, vol.27, 476 (1991).

[15] R. Stevenson, S. Rosenwasser and R. Washburn,"Development of advanced ceramic matrix composite insulators for electromagnetic railguns," IEEE Trans. on Magnetics, vol.27, 538 (1991).

[16] J. Gilligan and R. Mohanti, "Time dependent numerical simulation of ablation controlled arcs," IEEE Trans. on Plasma Science, vol. 18, 190 (1990).

[17] J. Upshaw, "Testing of coaxial railgun in high vacuum," IEEE Trans. on Magnetics, vol.22, 1779 (1986).

[18] R. Mohanti and J. Gilligan, "Electrical Conductivity and Thermodynamic Functions of Weakly Nonideal Plasmas," J. Appl. Phys. vol. 68, 5044 (1990).

[19] R. Mohanti, J. Gilligan and M. Bourham, "Time Dependent Simulation of Weakly Nonideal Plasmas in Electrothermal Launchers," Physics of Fluids B , vol. 3, 3046 (1991).

[20] O. Hankins, M. Bourham, J. Earnhart and J. Gilligan,"Visible Light Emission Measurements from a Dense Electrothermal Launcher Plasma," 6th Symp. on Electromagnetic Launch Technology, Austin, TX, April 28-30, 1992.

[21] H. Bolt, J. Linke, H. Nickel, E. Wallura, M. Akiba, M. Araki and M. Seki, "Performance of carbon materials under short and intense electron beam pulses in the JEBIS facility," Fusion Technology, vol. 20, 231 (1991).

Plasma Dynamics And Hotspots Studies From A Plasma Focus Device

C.C. Tzeng, C.K. Yeh, Y.J. Yu, Y.Y. Kuo
M. Wen, W.S. Hou, T.R. Yeh
Institute of Nuclear Energy Research
P.O. Box 3-4, Lung-Tan, Taiwan, ROC

The dynamics of the plasma (Ne, Ar) evolution and hotspots formation has been studied by a PIN detector, a time-resolved and time-integrated MCP soft X -ray pinhole camera, fast optical camera systems and a N_2-laser interferometry. Fast streak and framing photos reveal two well-defined compressions with $\sim$ 60 ns time seperation during the plasma evolution. Cosequently the soft X-ray emission which was monitored by MCP camera and PIN detector is observed to be mainly coming from the first compression. For both Ne and Ar gases, maximum electron densities of $> 5x10^{19}$ cm^{-3} are obtained $\sim$ 10 ns after the onset of the X-ray emission. The maximum electron densities of the hot spots estimated from the Bennet's relation are about 10^{21} cm^{-3} for Argon plasma.

INTRODUCTION

The dense plasma focus device is capable of producing high density, hot plasmas and generating intense radiations[1,2] as the plasma evolves. Plasma focus[3] was developed initially as a neutron source and becomes more attractive as a viable X-ray source for lithography[4] with submicron resolution. For latter application, the admixtures of heavy gases and hydrogen (deuterium) are served as the working gases, and the majority of the soft X-rays comes from a small, dense, hot and short-lived strongly emitting regions known as hotspots [5]. These plasma points are the pertinent characteristics of heavy ion plasmas, but not those of pure hydrogen (deuterium) plasmas when discharge current is below Pease-Braginski current[6]. Hotspots have been studied by several authors[7],[8,9], and many formation mechanisms have been proposed such as radiative collapse[10],[11] and electron beam interactions[12]. Nevertheless the physical properties of hotspots are still not yet clear.

In this paper, we report the results of an experimental study of the plasma dynamics and hotspots formation in a plasma focus discharge. Particular attention will be emphasized on the pinch phase and visible light together with soft X-ray emission are monitored throughout the experiments. The results presented here were obtained with pure Neon and Argon gases unless otherwise specified.

APPARATUS

The experiment was performed on a 16 μf/20 KV Mather type plasma focus device producing 200 KA maximum discharge current. The diameters of hollow copper anode and stainless steel cathode with a length of 89 mm are 22 and 50 mm respectively. The diagnostic set-up is shown schematically in Fig.1. Fast optical framing camera (IMACON-790)

and streak camera (Hamamatsu C979-01) were used to measure the radial and axial velocities of pinched plasmas respectively. The frame rate of $2x10^7$ f/sec with 10 ns

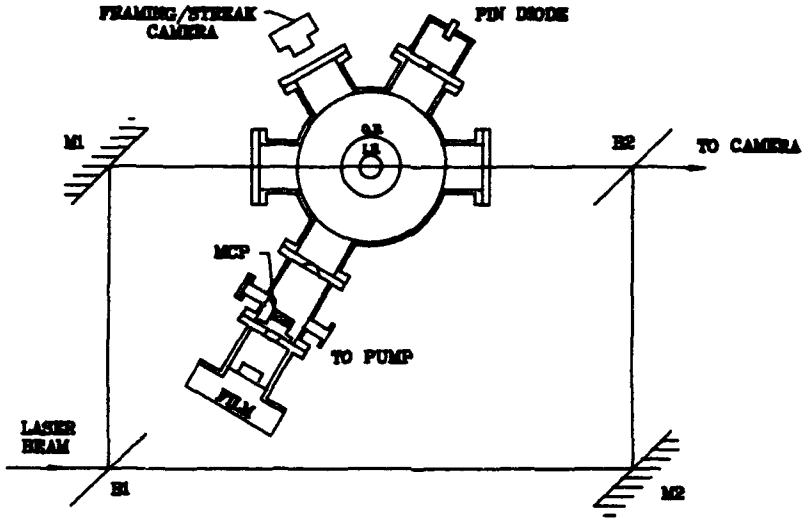


Fig.1 Schematic diagram of the diagnostic set-up

exposure time and the streak speed of 500 ns/15 mm with 0.3 mm slit parallel to the iner electrode were used in this experiment. The Mach-Zehnder interferometry contained a 600 μJ N_2-laser having coherent length of 5 cm and pulse width (FWHM) of 0.7 ns. The interferogram was recorded on polaroid film, type 665 with negative film.

The X-ray intensity was monitored by a silicon PIN diode covered with a 250-μm-thick beryllium (Be) foil. Soft X-ray MCP pinhole (400 μm ϕ) camera having 25μm Be foil in front was used to obtain either a time-resolved or a time-integrated soft X-ray image. This camera included the MCP and phsphor screen (Hamamatsu, F2225-11P) combination with effective diameter of 42 mm. A negative bias voltage of 1 KV was applied statically between two electrodes of the MCP. To get a time-resolved soft X-ray image, a gate pulse, as shown in Fig.2, is applied between the MCP and a phosphor screen [14,15]

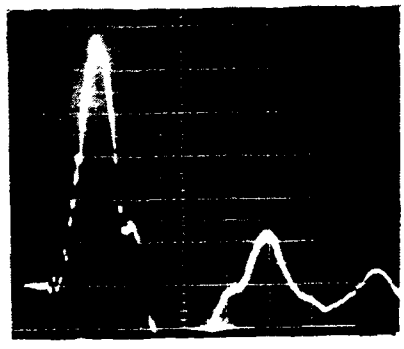


Fig.2 Waveform of the gate pulse (1 KV-10 ns/DIV)

to open the shutter, whereas a positive DC voltage of 4 KV is applied in order to obtain a time-integrated soft X-ray image. The visible image on the screen was recorded on polaroid Type 667 film. The shutter duration was experimentally estimated to be 8ns by varying the DC voltages of the gate pulse which begun to show a visible image at $\sim$ 4 KV.

RESULTS AND DISCUSSION

The capacitor bank was optimized at 18.6 KV and the corresponding filling pressure of Neon and Argon gases were 2 torr and 1 torr respectively. As shown in Fig.2 two compressions separated by ~ 50 ns are observed for both Neon and Argon plasmas. For

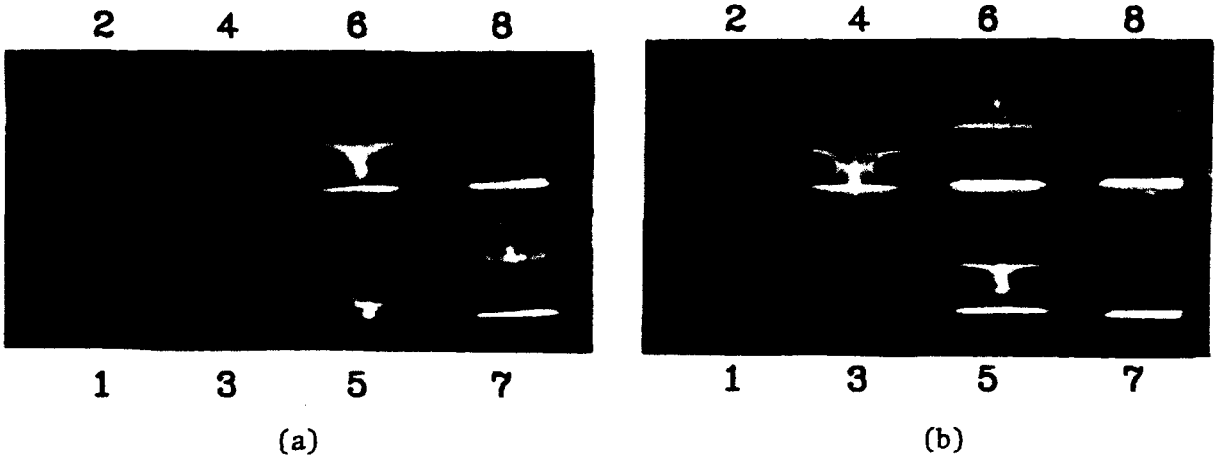


Fig.3 Framing photos for (a) Neon (b) Argon plasmas

Neon plasma, first compression occurs at the 5th frame and a plasma column of 2 mm in diameter is generated, while second compression at the 6th frame appears at ~ 5 mm awary from anode face and contains a bright spot of 3 mm in diameter. For Argon plasma, first and second compressions occur at 4th and 5th frames of Fig. 3(b) respectively. Similarly the axial streak photos, as shown in Fig.4, reveal again two separated compressions for both heavy ion plasmas. The Neon plasma has its first compression at 1 mm awary from anode face and lasts for ~ 15 ns, while second compression extends for ~ 70 ns. The

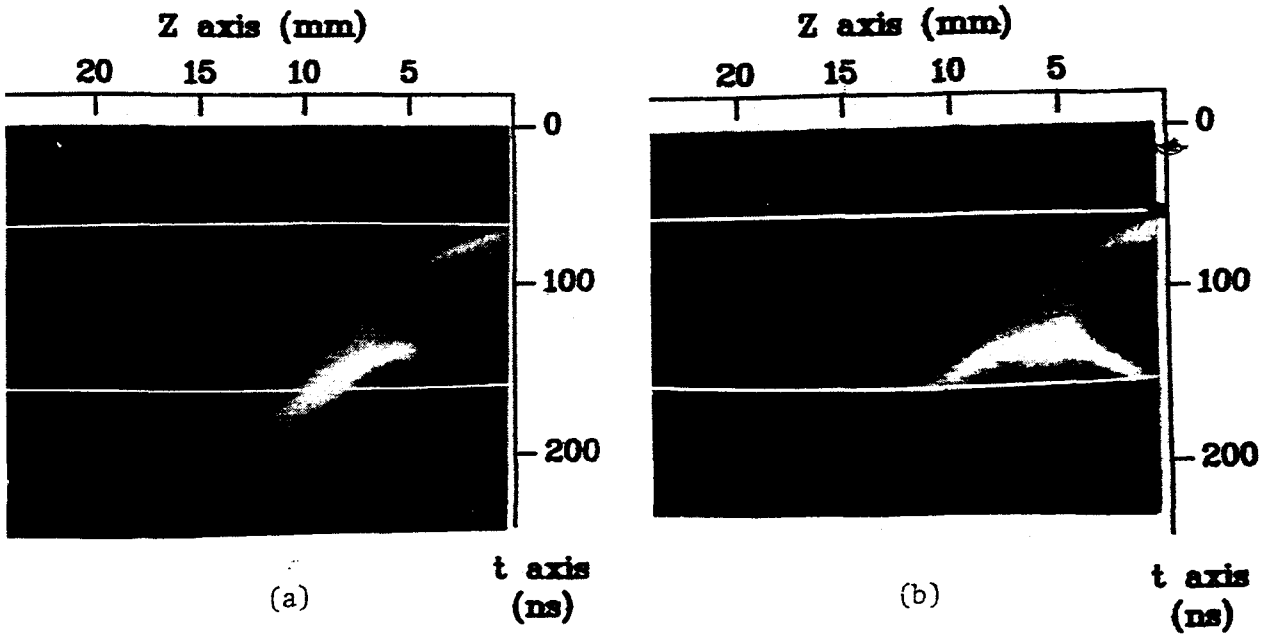


Fig.4 Axial streak photos for (a) Neon (b) Argon Plasmas

time separation between these two compressions is about 60 ns in consistence with the frame data. For Argon plasma, first and second compressions are observed at 1.3 mm and 5 mm respectively. The time separation between the two compression is nearly the same as that of Neon plasma. When second compression appears, the Argon plasma runs toward and away from the inner electrode face simultaneou-sly. Radial and axial velocities (Vr and Va respectively) of plasma compression are summarized in Table 1. The data of 5.0 torr deterium (D_2) with neutron yield

Table 1 Radial and axial plasma sheath velocities with different working gases

working gas / Velocity	Ne(2 torr)	Ar(1 torr)	D_2(5 torr)
Vr^{1st}(cm/μ sec)	12 ± 3	12 ± 3	13 ± 2
Vr^{2nd}(cm/μ sec)	5 ± 2	6 ± 2	-
Va^{1st}(cm/μsec)	33 ± 10	25 ± 10	57 ± 10
Va^{2nd}(cm/μ sec)	18 ± 3	18 ± 5	-

$3x10^8$ n/pulse are included for comparison, and no second compression is observed.

The time-integrated soft X-ray images with two well-separated regions for both heavy ion plasmas are shown in Fig.5. Typical data indicate that the X-ray

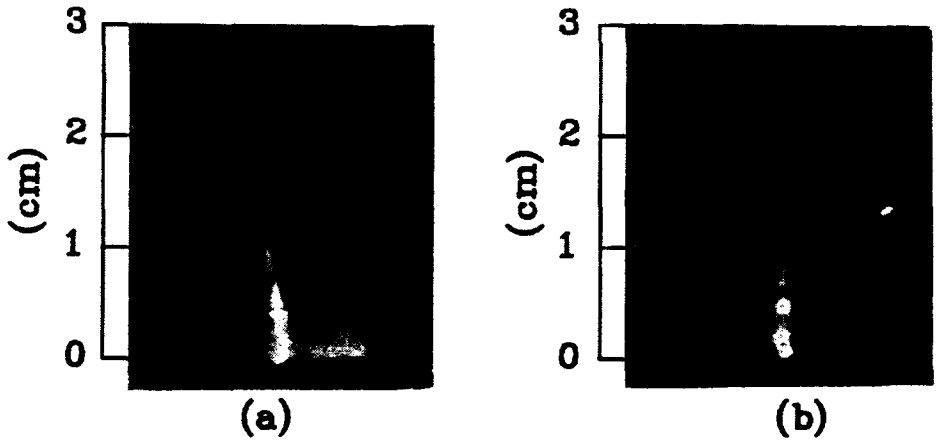


Fig.5 Time-integrated MCP X-ray pinhole photos for (a) Neon (b) Argon plasmas

images appear to be ~ 1.2 mm in diameter and 6-8 mm long for the lower region. The intensity of the upper region whose location is coincident to the 2nd compression (described earlier) is relative weaker. Noticed, however, the circle-like spots which is the pinhole image[11] are seen very often in Ar plasmas.

The plasma evolutions observed with the Mach-Zehnder interferometer and the time-resolved soft X-ray pinhole camera are shown in Fig.6 and Fig.7 for Neon and Argon plasma respectively. The first and second peaks of PIN signals in FIg.6(a) and 7(a) are directly related to first and second comporessions. In both figures, the (i)th frames are corresponding to the maximum compression which appears ~ 10 ns

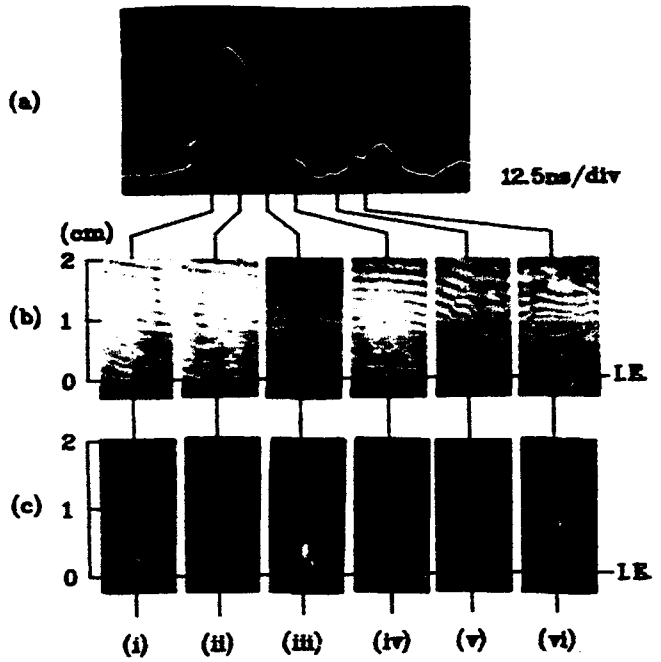


Fig.6 Time sequences of the X-ray emission from Neon plasmas
(a) PIN
(b) Laser interferoegrams
(c) MCP images

after the onset of the X-ray emissions. It follows with the maximum X-ray emission of the unstable phase (ii) and the disruption phase (iii). The 2nd compression, on the other

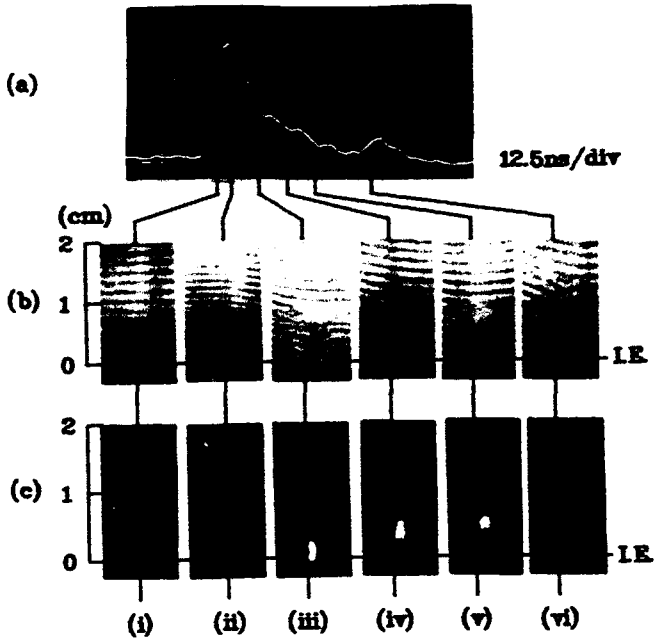


Fig.7 Time sequences of the X-ray emission from Argon plasma

hand, is indicated by the (vi)th frame where the X-ray images are rather weak to be visible typically. The (i)th interferograms at peak compression for both gases are smeared out at the dense plasma column, therefore, the maximum electron densities are beyond the high density limit[15] ($> 5\times10^{19}$ cm^{-3}) of the interferometer. Whereas the maximum electron densities at 2nd compressions are 7×10^{18} cm^{-3} typically for both plasmas. Noticed, however, the peak X-ray emission from PIN is inconsistent with the data from the MCP. This may be explained by the different sensitivities between this two detectors. As one knows[13] that the MCP is much more sensitive to the lower X-ray energy.

For figures 6 and 7, the MCP X-ray images show either dark columns (200 $\sim$ 300 m ϕ) or dark circles (various sizes) embedded in the bright images as shown in (i)-(iv). This is rather odd to observe, however, one might speculate the fast radiation cooling in the center region of the bright images. And therefore extreme large temperature gradients are anticipated during the plasma evolution. Nevertheless further studies are necessary in future.

As described elsewhere[5], hotspots appear after the lst compression and extend up to $\geq$ 50 ns. If the Bennet's relation is valid, the electron density (Ne) of the hotspots can be estimated[9] by $Ne = 3x10^{21}\ I^2/Te(2+Z)r^2$. By setting I=0.2 MA, Te = 200 eV[15], Z = 18 for Argon plasma, r = 50μm (obtained from time-integrated soft X-ray images with 100μm pin-hole) in the above equation, the maximum electron densities are estimated to be 10^{21} cm^{-3} for Argon hotspots, of the present case.

SUMMARY

The dynamics of the plasma evolution and hotspots formation has been studied both in visible and soft X-ray regions. Framing and streak photos show that two successive compressions are generated as the Neon and Argon plasmas evolve. The time separation between first and second compressions is about 60 ns, and the corresponding X-ray signals of first compression are about five times larger than those of second compression for both filling gases.

The maximum electron density which is beyond the high-density limit of the N_2-laser interferometer ($Ne > 5x10^{19}$ cm^{-3}) is obtained under the maximum compression phase for both heavy ion plasmas. The maximum electron densities of the hotspots reoughly estimated by the Bennet's relation are about 10^{21} cm^{-3} for Argon plasma.

REFERENCES

1. G. Decker, L. Flemming, H.J. Kaeppeler, T. Oppenlaender, G. Prob. P. Schilling, H. Schmidt, M. Shakhate and M. Trunk, Plasma Physics 22, 245 (1980).
2. G. Herziger, XVI Int. Conf. on Phenomena in Ionized Gases, 259 (1983).
3. J.W. Mather, Methods of Exp. Phys. B9, 187 (1971).
4. Y. Kato and S.H. Be, Appl. Phys. Lett. 48(11), 686 (1986).
5. P. Choi, et. al., Laser and Particle Beams, 8(3), 469 (1990).
6. Nino R. Pereira, Phys. Fluids B2(3), 677 (1990).
7. P. Choi, C.S. Wong and H. Herold, Laser and Particle Beams, Vol.7, 763 (1989).
8. J.M. Bayley, G. Decker, W. Kies, M. Maelzig, F. Mueller, P. Roewekamp, J. Westheide, and Y.V. Sidenikov, J. Appl. Phys. 69(2), 613 (1991).
9. K.N. Koshelev, V.I. Krauz, N.G. Reshetniak, R.G. Salukvadze, Yu V. Sidelnikov and E. Yu Khautiev, J. Phys. D : Appl. Phys. 21, 1827 (1988).
10. J.W. Shearer, Phys. Fluids, 19, 1426 (1976).
11. K.N. Koshelev and N.R. Pereira, J. Appl. Phys. 69(10), R21 (1991).
12. P. Choi, A.E. Dangor, C. Deeney & C.D. Challis, Rev. Sci. Instr. 57, 2162 (1986).
13. K. Hirano, T. Yamamoto, K. Shimoda,Y. Tagaya, Jap. J. Appl. Phys. 24, 1514 (1985).
14. K. Hirano, H. Nakajima, I. Kaneko, T. Yamamoto and K. Shimoda, Japanese J. Appl. Phys. 29, 779 (1990).
15. F. Venneri, K. Boulais, and Gerdin, Phys. Fluids B2(7), 1613 (1990).

DEUTERIUM-FIBER-INITIATED Z-PINCHES: SIMULATION COMPARED TO EXPERIMENT

Peter Sheehey[a], Irvin R. Lindemuth,
Ralph H. Lovberg[b], and Ronald A. Riley Jr.[b]
Los Alamos National Laboratory
Los Alamos, NM 87545

Deuterium-fiber-initiated Z-pinch experiments have been simulated using a two-dimensional resistive magnetohydrodynamic model[1,2] which includes many important experimental details, such as "cold-start" initial conditions, thermal conduction, radiation, actual discharge current vs. time, and grids of sufficient size and resolution to allow realistic development of the plasma. When the fiber becomes fully ionized (at a time depending on voltage ramp and fiber thickness), the simulations show rapidly developing m=0 instabilities drive intense non-uniform heating and rapid expansion of the plasma column. Diagnostics generated from the simulation results, such as shadowgrams and interferograms, are in good agreement with experiment[3]. Comparison of simulation-generated diagnostics with those from early experiments of this type suggests that shadowgram images of the plasma were misleading indicators of the stability and rate of expansion of the plasma column. Terms often left out of the fluid model, such as the Hall term and the viscous stress tensor, may be significant in the Z-pinch[4,5]. Progress will be reported on the addition of such terms to the simulation.

[a]Dept. of Physics, UCLA, Los Angeles, CA 90024
[b]Dept. of Physics, UC San Diego, La Jolla, CA 92093

1. Introduction

Deuterium-fiber-initiated Z-pinch experiments, with current peaks up to about 600 kA, reported very long-lived, compact plasmas showing little indication of disruption by m=0 "sausage" or m=1 "kink" instabilities[6–8]. Second-generation machines[3,9,10] have been designed to reach the Pease-Braginskii current (about 1.4 MA for deuterium)[11–13], in the hope that fusion conditions could be approached, if the earlier observed "anomalous stability" were to hold. Discharges at greater than half Pease-Braginskii current (700-900 kA)[3,9], however, have shown stronger indication of expansion and m=0 instability growth. We have computationally modelled low- and high-current deuterium-fiber-initiated experiments on the Los Alamos machines HDZP-I[7,8] and -II[3,8] in a very direct manner, and present here a comparison of our results with experiment.

For a significant fraction of its lifetime, a fiber-initiated Z-pinch plasma meets classical requirements for description as a magnetohydrodynamic (MHD) fluid (e.g., ion-ion collision time $\ll$ ion thermal transit time)[2,14]. Furthermore, the consistent (but so far unexplained) observation that three-dimensional behavior (e.g., growth of m=1 "kink" instabilities) is virtually absent in such experiments (diagnostic images are highly symmetric about the axis)[3,6–9] gives us some confidence in the results of MHD simulation in only two dimensions. This is fortunate, because the inclusion of vital experimental details discussed below would at present make full 3-d simulation prohibitively expensive.

Linear ideal MHD stability theory for a Z-pinch plasma in general predicts instability to "sausage" (m=0) and "kink" (m=1) modes[15]. However, the growth rate of such instabilities is dependent on radial pressure profiles of the plasma; indeed, "Kadomtsev" profiles exist which are m=0 stable. Any actual experiment is likely to move through several non-ideal regimes (such as resistive MHD), as density, temperature, etc., vary during the discharge; nonlinear effects, as well, are likely to be encountered.

Therefore, it is highly desirable to simulate such experiments starting from time zero (zero current, frozen fiber) if possible, in order for realistic plasma profiles to form and develop linearly/nonlinearly, as they will. Energy terms such as thermal conduction, Joule heating and radiation are clearly going to be important. And the plasma "surface" must be free to develop as if in vacuum, without the influence of an unrealistically confining or insufficiently resolved grid.

2. Method

The computations reported here are an extension of previous one-[16] and two-dimensional[1,2] deuterium-fiber-initiated Z-pinch modelling. An alternating-direction-implicit numerical method, utilizing Newton-Raphson-like iteration to deal with nonlinear quantities, is used to solve the two-dimensional (r,z) MHD equations for mass density, specific internal energy, azimuthal magnetic field, and perpendicular velocity (v_r, v_z)[17]. To obtain the equation of state (specific energy and pressure), the ionization level, the radiative energy loss, and the resistivity, we use the Los Alamos SESAME[18] tabulated atomic data base computer library. Thermal conductivity follows Braginskii[19].

Actual experimental current vs. time values provide the boundary condition for magnetic field at the outer radial wall. "Cold-start" initial conditions are a solid, cryogenic deuterium fiber, surrounded to about twice the fiber radius by a low density, "warm" halo plasma (density $10^{-3}\times$solid, temperature 1 eV), which provides an initial current conduction path. Our computed results are insensitive to the details of this halo plasma after a short-lived (10 nsec) transient, because of the small mass involved relative to the fiber-generated plasma; a similar insensitivity to the details of current initiation has been found in parallel work[20]. The surrounding vacuum is simulated by a cold, very low density region extending out to a zero-temperature, electrically insulating wall. The early fiber-ablation stage of the discharge necessitates relatively fine radial grid spacing, but because this stage can be followed by an explosive expansion of the heating plasma, the radial grid is checked at each timestep, and adjusted so that the outer boundary is always at least 150% of the radius within which 95% of the total axial current is contained.

Radial grids of ~100 points, more finely spaced near the axis to better resolve the fiber/plasma column, cover a radius as small as 1 mm, but ultimately as large as several cm, if rapid expansion is followed. Axial sections from 2 cm down to 0.25 mm, covered with uniformly spaced axial grids of 31 to 62 points, are respectively capable of resolving

the largest (X-ray "beads") and smallest (shadowgram "spicules") features observed in any of the experiments. Although the smallest, most finely resolved grids do show fine-scale instability growth starting earlier than the larger grids, saturation of shorter wavelengths results in larger grids ultimately showing faster expansion. Hence the timing of instability development and expansion may vary by as much as 20 nsec for different grid sizes, but this is comparable to experimental timing uncertainties (e.g., the relation between driving voltage, current, and diagnostic images in time).

3. Results

The low-current experiment HDZP-I (250 kA peak at 125 nsec) displayed plasmas "free from visible instabilities for typically 80 nsec into the current discharge, at which time the [m=0] instability growth times would be expected to be $\approx$1 nsec...m=1 modes are not observed."[7] Plasma columns also appeared relatively compact (radius $\leq 200\mu$m), based on shadowgrams[2,21] (Fig. 1(a)), which provide well time-resolved images (better than 0.2 nsec) without the complex temperature dependence of passive radiation emission.

Our simulations of HDZP-I discharges show significant expansion and m=0 instability development (Figs. 1(c), 1(d)) before the 15μm-radius fiber has become fully ionized, which occurs in the simulations at 40 to 50 nsec. Shadowgrams generated from simulation of HDZP-I[2] reasonably agree, in size and instability wavelength, with those from experiment (Figs. 1(a), 1(b)). The width of the shadowgrams tends to remain smaller than the effective diameter of the plasma column, in terms of mass (Fig. 1(c)) or current (Fig. 1(d)). Significant instability development in these outer regions (Figs. 1(c), 1(d)) may be reflected by only slight variations in the shadowgram (Fig. 1(b)). After the fiber is completely ionized, the simulation-generated shadowgrams expand and become more irregular, even disappearing at some points along the axis, again in agreement with experimental results. We interpret this as evidence of full development of the instability, such that line density (total number of particles per unit axial length) along the axis becomes very inconstant.

Simulations and observations of the Los Alamos high-current experiment HDZP-II (750 kA peak at 100 nsec)[2,3,8] resemble the higher-current, later phases of HDZP-I discharges. In the simulation of HDZP-II, higher current fully ionizes the fiber in 10 to 20 nsec. Instabilities develop rapidly, and drive intense nonuniform heating and rapid column expansion to radii on the order of cm, within 50 nsec. Only very early in the experiment is there enough density gradient to get a shadowgram at all, and this wide and irregular image resembles the late shadowgrams of HDZP-I. Later time plasma images were obtained using interferometric techniques[21]. These images, both experimental and simulated[2,3], also show the characteristic "island" pattern of deep m=0 development (Figs. 2(a), 2(b)); again, a repeat of what would be expected from late low-current simulations (Figs. 2(c), 2(d)).

Comparison of simulation and experimental results on HDZP-I and -II leads to the following conclusions: The "anomalous stability" reported for the low-current HDZP-I

experiments appears limited to the earlier, lower-current stages of the discharge. Increased instability and expansion noted in the later, higher-current stages is apparently related to the higher temperatures, lower densities, and higher effective Lundquist numbers encountered[22-24]. Such conditions are held back as long as some portion of the heat-sinking fiber persists. The presence of the cold core does seem to inhibit full nonlinear instability development, such as displayed in Figs. 2(c) and 2(d), which appears connected with the explosive expansion of higher-current discharges on HDZP-II. Re-connection of the outer parts of such m=0 lobes, and current jumping across them at progressively increasing scale lengths, may not only directly contribute to the physical expansion of the column, but may lead to instability heating which further drives expansion.

As temperatures rise and density drops (e.g., in narrow m=0 "necks"), the appropriateness of the fluid model breaks down, so late development of instabilities may well be driven by effects absent from the model. Improvements within the fluid model would be inclusion of separate ion and electron energy equations, and of terms usually ordered out on the basis of small Larmor radius (which may indeed not be small in the case of the Z-pinch[4,5]): the Hall and diamagnetic pressure terms in the Ohm's Law (magnetic field evolution) equation, viscous stress tensor terms, and accompanying terms in the energy equation. This work is now in progress. That the Hall term may have drastic effects on the important scales of an instability is graphically illustrated in a recent paper by Huba, et al[25]. Preliminary results with the Hall term included do show earlier short wavelength instability development in the coronal plasma. More sophisticated computational investigations, such as 3-d MHD, two-fluid, or full particle simulation, are likely to be affordable for no more than short sections of an experiment. We believe the use of realistic starting profiles, such as obtained with our presently developing 2-d model, is vital, in relating the results of any of these more sophisticated simulation approaches, to reality.

4. Conclusions

Detailed two-dimensional MHD simulations of deuterium-fiber Z-pinches have shown good agreement to the Los Alamos experiments HDZP-I and HDZP-II. Late in low-current and early in higher-current experiments, when the fiber has become fully ionized, m=0 instabilities develop rapidly, and drive intense nonuniform heating and rapid expansion of the plasma column, dropping densities orders of magnitude below the high densities desired for fusion conditions. We believe the "cold-start" approach taken here is vital to the realistic simulation of such experiments, due to the close tie between plasma profiles and stability. Whether or not the inclusion of finite-Larmor-radius, or other effects beyond the model used here, will prove stabilizing, is not known at this time; work is in progress. However, the agreement of the present results with experimental evidence suggests that some significant variations to the presently described high-current discharges on HDZP-II (in fiber thickness, plasma initiation, external fields, ramp time or level, etc.) may be

necessary, if the desired confinement to obtain fusion conditions is to be realized.

Acknowledgments

We would like to acknowledge the assistance of the HDZP-I/II experimental group: J. Hammel, D. Scudder, J. Shlachter, F. Venneri, et al; and stimulating discussions with N. Bobrova, S. Bogolyubskii, J. Chittenden, P. Choi, M. Coppins, J. Dawson, A. Glasser, M. Haines, S. Nedoseev, R. Nebel, A. Robson, P. Sasorov, J. Sethian, and V. Yankov.

References

1. I. R. Lindemuth, Phys. Rev. Lett. **65**, 179 (1990).
2. P. Sheehey, J. Hammel, I. Lindemuth, R. Lovberg, R. Riley Jr., D. Scudder, J. Shlachter, (LA-UR-92-747) submitted to Phys. Fluids B, March 1992.
3. D. W. Scudder, J. S. Shlachter, J. E. Hammel, F. Venneri, R. Chrien, R. Lovberg, R. Riley, in Physics of Alternative Magnetic Confinement Schemes, Proceedings of the Workshop Held at Varenna, Italy, 1990, ed. by S. Ortolani and E. Sindoni (SIF, Bologna, 1991), p. 519.
4. M. G. Haines, J. Phys. D **11**, 1709 (1978).
5. M. Coppins, D. J. Bond, and M. G. Haines, Phys. Fluids **27**, 2886 (1984).
6. J. D. Sethian, A. E. Robson, K. A. Gerber, and A. W. DeSilva, Phys. Rev. Lett. **59**, 892 (1987); **59**, 1790(E) (1987).
7. J. Hammel and D. Scudder, in Proceedings of the Fourteenth European Conference on Controlled Fusion and Plasma Physics, Madrid, Spain, 1987, ed. by F. Engelmann and J. L. Alvarez Rivas (EPS, Petit-Lancy, Switzerland, 1987), p. 450.
8. J. E. Hammel, in Dense Z-Pinches, ed. by N. R. Pereira, J. Davis, and N. Rostoker (American Institute of Physics, New York, 1989), p. 303.
9. J. Sethian, A. Robson, K. Gerber, and A. DeSilva, in Physics of Alternative Magnetic Confinement Schemes (Ref. 3), p. 511.
10. M. Haines, in Physics of Alternative Magnetic Confinement Schemes (Ref. 3), p. 277.
11. R. S. Pease, Proc. Phys. Soc. B **70**, 11 (1957).
12. S. I. Braginskii, Sov. Phys. JETP **6**, 494 (1958).
13. N. R. Pereira, Phys. Fluids B **2**, 677 (1990).
14. J. Freidberg, Ideal Magnetohydrodynamics (Plenum Press, New York, 1987), Ch. 2.
15. B. B. Kadomtsev, in Reviews of Plasma Physics, edited by M. A. Leontovich (Consultants Bureau, New York, 1966), Vol. 2, p. 165.
16. I. R. Lindemuth, G. H. McCall and R. A. Nebel, Phys. Rev. Lett. **62**, 264 (1989).
17. I. R. Lindemuth, UC Lawrence Livermore Laboratory Report UCRL-52492 (1979).
18. Los Alamos National Laboratory Report LA-10160-MS, ed. by K. S. Holian (1984).
19. S. I. Braginskii, in Reviews of Plasma Physics, edited by M. A. Leontovich (Consultants Bureau, New York, 1965), Vol. 1, p. 205.
20. N. A. Bobrova, T. L. Razinkova, and P. V. Sasorov, Institute of Theoretical and Experimental Physics, Moscow, B. Cheremushkinskaja, 25 (to be published).
21. F. C. Jahoda and G. A. Sawyer, in Methods of Experimental Physics Part B, edited by R. Lovberg and H. Griem (Academic Press, New York, 1971), Ch. 11.
22. I. D. Culverwell and M. Coppins, Phys. Fluids B **2**, 129 (1990).
23. A. Glasser, J. Hammel, H. Lewis, I. Lindemuth, R. Lovberg, G. McCall, R. Nebel, P. Rosenau, D. Scudder, P. Sheehey, and J. Shlachter, in Plasma Physics and Controlled Nuclear Fusion Research 1988 (IAEA Vienna, 1989), Vol. 2, p. 557.
24. F. L. Cochran and A. E. Robson, Phys. Fluids B **2**, 123 (1990).
25. J. D. Huba, J. G. Lyon, and A. B. Hassam, Phys. Rev. Lett. **59**, 2971 (1987).

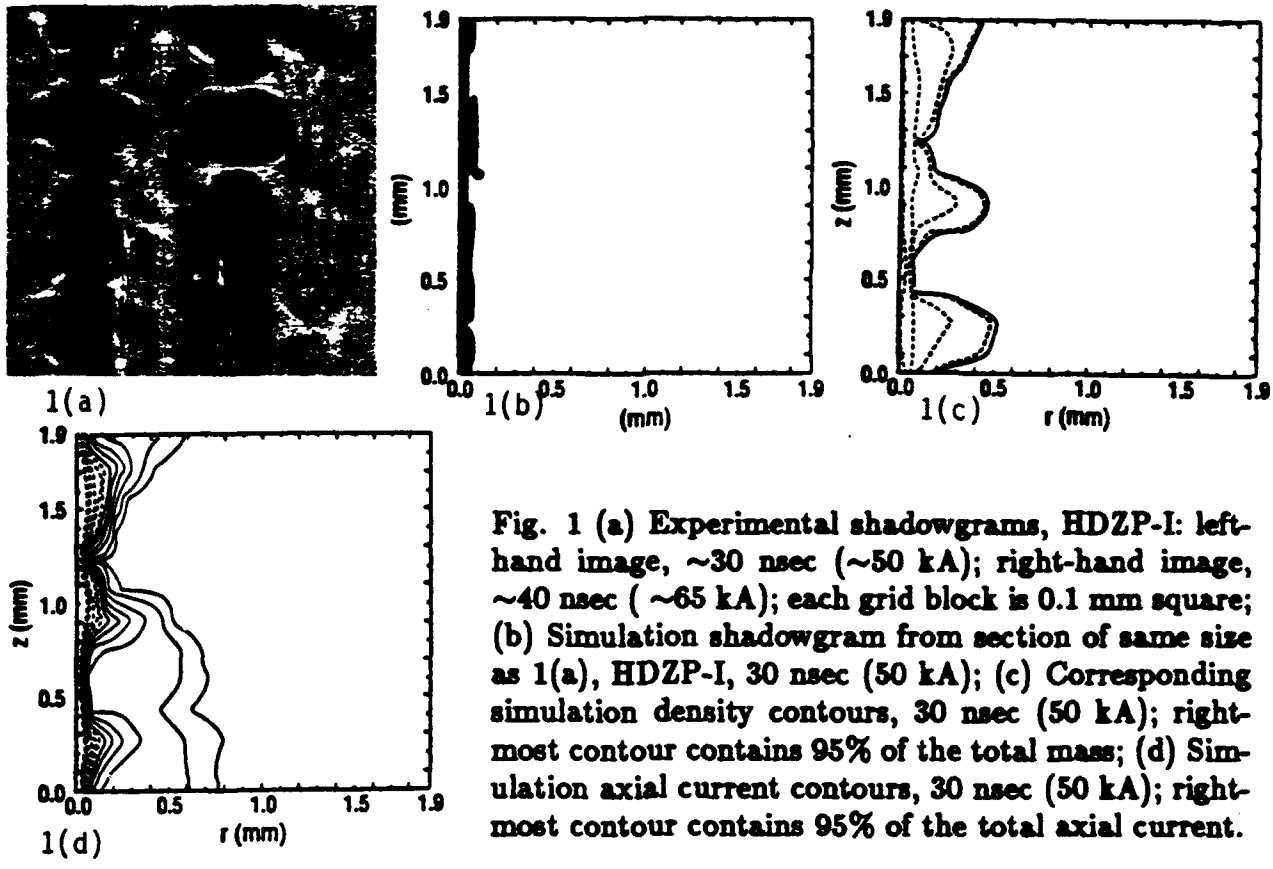


Fig. 1 (a) Experimental shadowgrams, HDZP-I: left-hand image, ~30 nsec (~50 kA); right-hand image, ~40 nsec (~65 kA); each grid block is 0.1 mm square; (b) Simulation shadowgram from section of same size as 1(a), HDZP-I, 30 nsec (50 kA); (c) Corresponding simulation density contours, 30 nsec (50 kA); right-most contour contains 95% of the total mass; (d) Simulation axial current contours, 30 nsec (50 kA); right-most contour contains 95% of the total axial current.

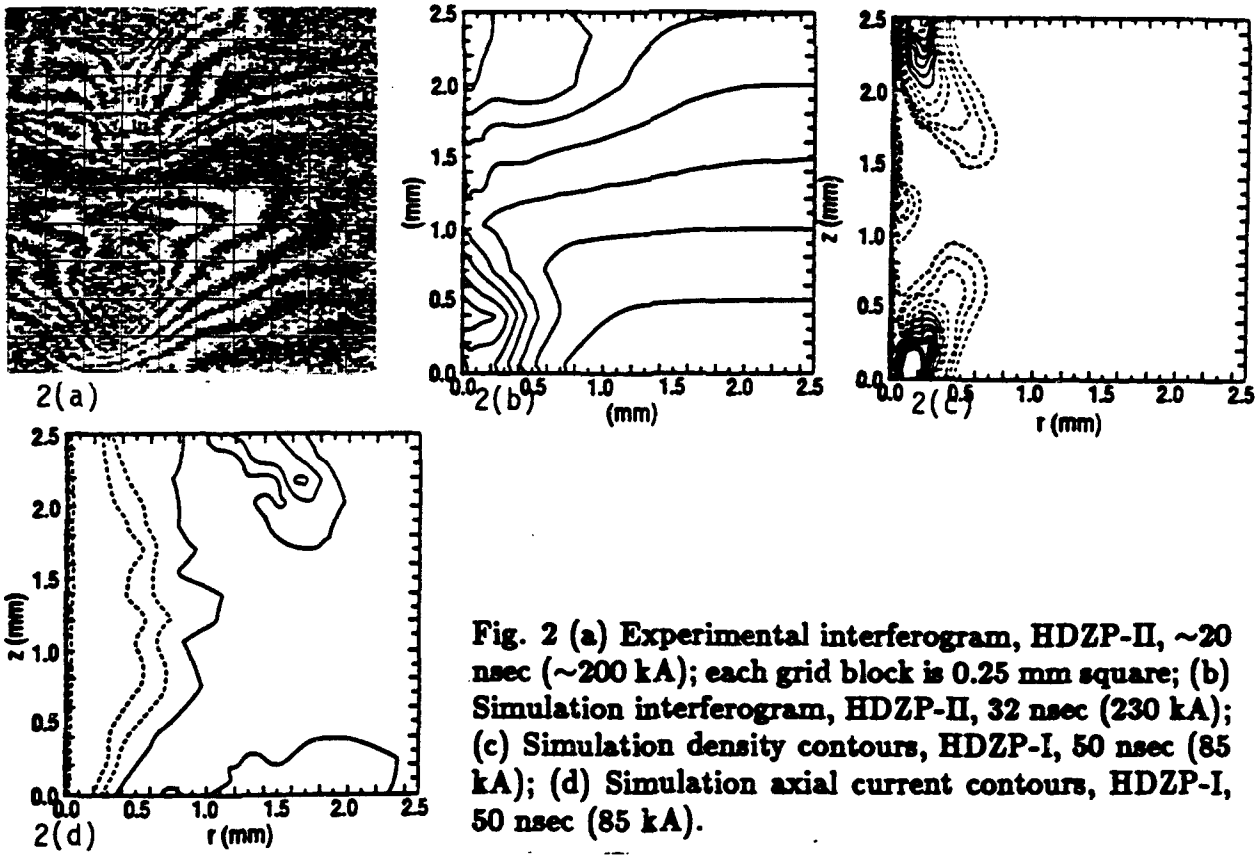


Fig. 2 (a) Experimental interferogram, HDZP-II, ~20 nsec (~200 kA); each grid block is 0.25 mm square; (b) Simulation interferogram, HDZP-II, 32 nsec (230 kA); (c) Simulation density contours, HDZP-I, 50 nsec (85 kA); (d) Simulation axial current contours, HDZP-I, 50 nsec (85 kA).

RADIATIVE COLLAPSE OF A DENSE PLASMA

H. U. Rahman

Institute of Geophysics and Planetary Physics

University of California, Riverside, California 92521

N. Rostoker and F. J. Wessel

Department of Physics

University of California, Irvine, California 92717

Radiative collapse of a dense θ pinch plasma driven by an annular Z-pinch is considered. A cryogenic fiber is coaxially located within the annular gas jet Z-pinch. The imploding Z-pinch traps an applied axial magnetic field and conserves the flux. The axial magnetic field increases due to the compression and has attained values in excess of 20 M-Gauss. If a fiber is placed on axis an azimuthal θ-current is induced with a rise time that is an order of magnitude shorter than the rise time of the Z-pinch current. Such a rise time could not be achieved with a simple Z-pinch because of the large inductance of the axial fiber-plasma. The implosion transfers the kinetic energy of the Z-pinch to the magnetic field and then to the θ-pinch. The terminal particle pressure of the θ-pinch exceeds the magnetic pressure so that the pinch then expands– the only confinement is inertial. It is possible to make an intense neutron source e.g. a yield of 4×10^{15} neutron/cm with a Z-pinch current of 10 M-Amperes; but break-even would require much larger currents. To reach break-even and beyond with a reasonable Z-pinch current, we propose to make use of radiative collapse. By seeding the cryogenic Hydrogen-like fiber with higher Z-material, the radiation would be substantially increased and the θ-pinch would cool and collapse thereby increasing the density. For example, a density of order 10^{24} cm^{-3} has been observed with a seeded plasma focus. The confinement time is determined by the temperature and would not decrease. Thus $n\tau \sim 10^{14}$ could be reached with a confinement time of .1 nanosec.

1. INTRODUCTION

Radiative collapse was first proposed by Pease[1] and Braginskii for Z-pinches of Hydrogen in a Bennett type equilibrium. Ohmic heating decreases with current I like $(1/I)$ and Bremstrahlung increases like I. If the current exceeds the value $I_c = 1.66$ M amps, the radiation dominates. If the current and magnetic pressure are maintained the plasma should be radiation cooled causing collapse. The collapse would cease when the absorption length becomes comparable with the plasma radius. The current required for radiative collapse can be much less for higher Z-plasmas such as Krypton,[2] or for hydrogen seeded with high Z-impurities.[3]

There is experimental evidence of radiative collapse for Z-pinches seeded[4] with high Z-impurities, vacuum sparks[5], and a plasma focus[6] seeded with high Z-impurities. In the latter case there are indications that in regions of very small size of the order of microns, densities of the order of $10^{24} cm^{-3}$ were attained, comparable to that achieved by implosions with the Nova laser at LLNL.

Recently there have been Z-pinch experiments of a solid fiber[7], or cryogenic deuterium fiber. The initial inductance of such fibers is large and the current rise time is at least 10's of nanoseconds. The plasma expands until the magnetic pressure is sufficiently large to contain the material pressure and the plasma eventually becomes unstable without achieving very high density. A solution to these problems is proposed that involves a Z-θ pinch[8] illustrated in Fig. 1. In this hybrid scheme an annular Z-pinch plasma implodes

an axial B_z-magnetic field compressing it to multi-megagauss fields with an order of magnitude shorter rise time than the Z-current. Coaxial with the Z-pinch is a solid fiber or straw which breaks down and forms a θ-pinch. The rise time of the current in the θ-pinch is a few nanoseconds and the Z-θ configuration is much more stable than a simple Z-pinch.

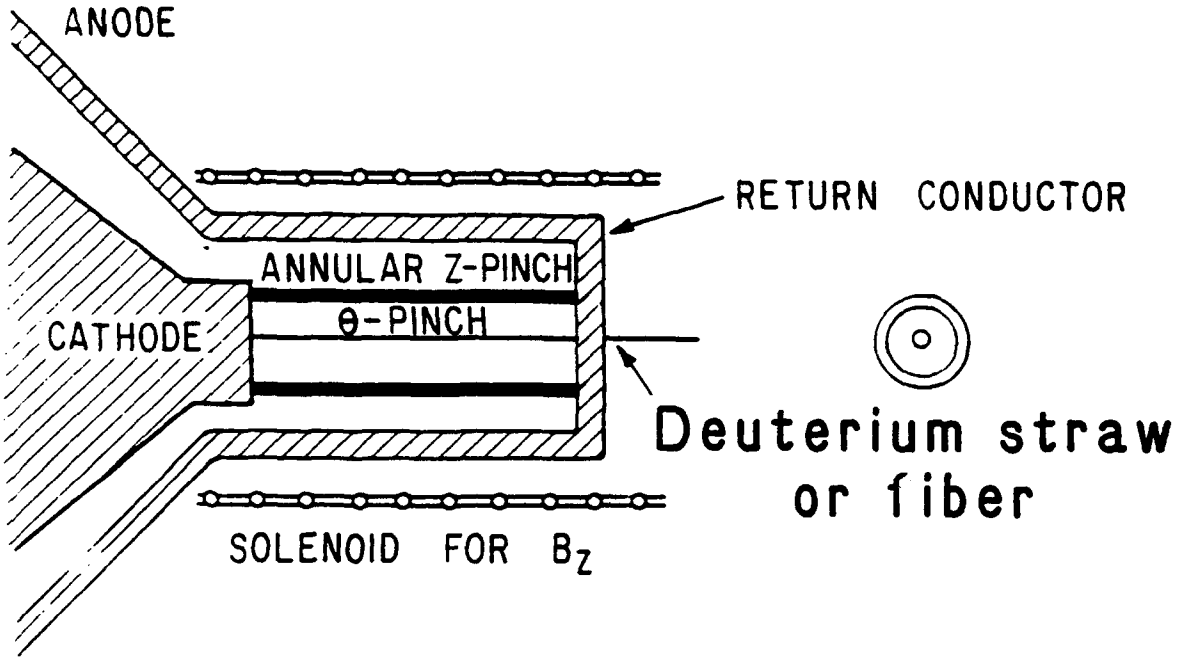


Figure 1. Z−θ PINCH

Key features of the Z-θ pinch have already been studied with small machines at UC-Irvine[9,10,11], and with large machines at Sandia Laboratories[12] and in the USSR[13]. The maximum axial fields reported are 1.6 MG (UCI), 2.5 MG (USSR) and 40 MG (Sandia).

Our results indicate that the θ-pinch plasma produced by the Z-θ pinch is sufficiently hot and dense to be a useful neutron source – without radiative collapse. Preliminary estimates indicate that with radiative collapse (which involves seeding a cryogenic filament with high Z elements) it should be possible to exceed break even.

2. Z-PINCH DYNAMICS WITH AN AXIAL B_z FIELD

To get some estimates consider a simple model for the dynamics of an imploding annular plasma shell where the thickness is neglected; this assumption is quite valid because the inclusion of a finite thickness has not changed the results significantly except in the final value of B_z field. The normalized equation of motion of the annulus for a sinusoidal current profile is

$$\frac{d^2R}{d\tau^2} = \frac{a}{R}\left\{-\sin^2\left(\frac{\pi\tau}{2}\right) + \frac{b}{R^2}\left(1 - R^4\right)\right\}, \tag{1}$$

where $R = r/r_0$, $\tau = t/t_0$, $a = {I_m}^2 {t_0}^2/100\, m\, {r_0}^2$ and $b = \left(5\, B_0\, r_0/I_m\right)^2$, m is the mass per unit length and r is the radius of the annulus.

Assuming parameters typical of UCI experiments, $I_m = 472KA$, $B_0 = 10KG$, $t_0 = 1\mu sec$, $m = 10^{-4} gm/cm$, and $b = 0.045$, the maximum compression ratio is about 200 and as a function of "a" has a broad maximum at $a = 4$. It is seen by solving Eqn. (1) that the rise time of $B_z(t)$ is about a factor of 20 less than the rise time of the current $I_z(t)$, or equivalently $B_\theta(t)$. The maximum value of B_z is greater than the maximum value of B_θ because the shell is decelerating when it reaches the minimum radius.

We can extrapolate these conditions to a larger machine like Sandia's Proto II or Saturn, Maxwell's Black Jack V, or Physics International's Pithon generator or other machines at NRL and LANL; by increasing I_m and B_0 each by a factor of 20 and reducing t_0 by a factor of 20, then a and b are the same. The result is that B_z increases to 20 MG on the time scale of a few 10's of nsecs. Recent flux compression experiments on Proto II have confirmed these expectations[12].

A magnetic field of such a high strength and fast rise can initiate a θ-pinch on the surface of a cryogenic fiber placed coaxial with the Z-pinch. Heating can be achieved by a combination of several different mechanisms, e.g. Ohmic heating, shock heating, adiabatic compression and anomalous heating. We now present our fusion estimates based upon simple Ohmic heating by using Spitzer resistivity and some numerical modeling of the adiabatic compression.

3. DYNAMICS OF θ-PINCH PLASMA WITH OHMIC HEATING

The induced θ-current is determined from Ampere's law where the profile for B_z can be obtained by solving the diffusion equation. For cylindrical geometry the current profile therefore is

$$J_\theta = \left(\frac{cB_{z0}}{2\pi a}\right)\left\{\frac{J_1(\xi_1 \tau)}{J_1(\xi_1)}\right\} e^{-\xi_1^2 \tau}, \tag{3}$$

where a is the radius of the inner plasma, $\tau = Dt/a^2$, $D = c^2\eta/4\pi$, J_1 is the first order Bessell function, $\xi_1^2 = 5.76$, and η is the resistivity of the newly formed θ-pinch plasma. Knowing the value of J_θ, one can easily estimate the ohmic heating as

$$W = \int \eta\, {J_\theta}^2\, 2\pi r\, dr\, dt = \frac{a^2\, B_{z0}^2}{2\xi_1^2} \cong \frac{B_{z0}^2}{8\pi}\, \text{area}\,(\text{erg cm}^{-1}). \tag{4}$$

If we ignore the losses due to radiation and other sources, then all the available magnetic energy will be utilized for heating purposes. The final temperature then depends on the final value of the magnetic field provided there is enough time available for field diffusion into the fiber plasma. The diffusion time can be obtained as, $\tau = (1/1.56)(a^2/D) = (4\pi a^2)/(56\, c^2\, \eta)$, which is inversely proportional to the resistivity and can be extremely short if we take into account the anomalous resistivity due to micro-instabilities. For classical Spitzer resistivity the time is on the order of a few nsecs in the regime suitable for thermonuclear fusion.

The maximum temperature can be obtained from the pressure balance equation, i.e. $T_{max} \cong B_{z0}^2/(8\pi n)$. Thermonuclear fusion conditions can be achieved if we use a DT cryogenic fiber of $20\mu m$ radius, maximum current for the Z-pinch of 5 to 10 MA with rise time of 50 to 100 nsec and initial axial field of 100 to 200 KG. With these initial conditions the final conditions are obtained as $B_f \approx 20$ MG, $T_f \approx 10$ KeV, $n_f \approx 10^{21} cm^{-3}$.

However, the confinement of the plasma would be inertial and for the above parameter would be about 1 nsec which is insufficient for breakeven. If radiative collapse takes place and the density reaches $10^{25} cm^{-3}$, breakeven requires $\tau \sim 10^{-2}$ nsec. The final radius must decrease by a factor of 10^{-2} and if the final temperature is the same, $\tau = r_f/r_i \sim 10^{-2}$ nsec.

4. NUMERICAL MODELING

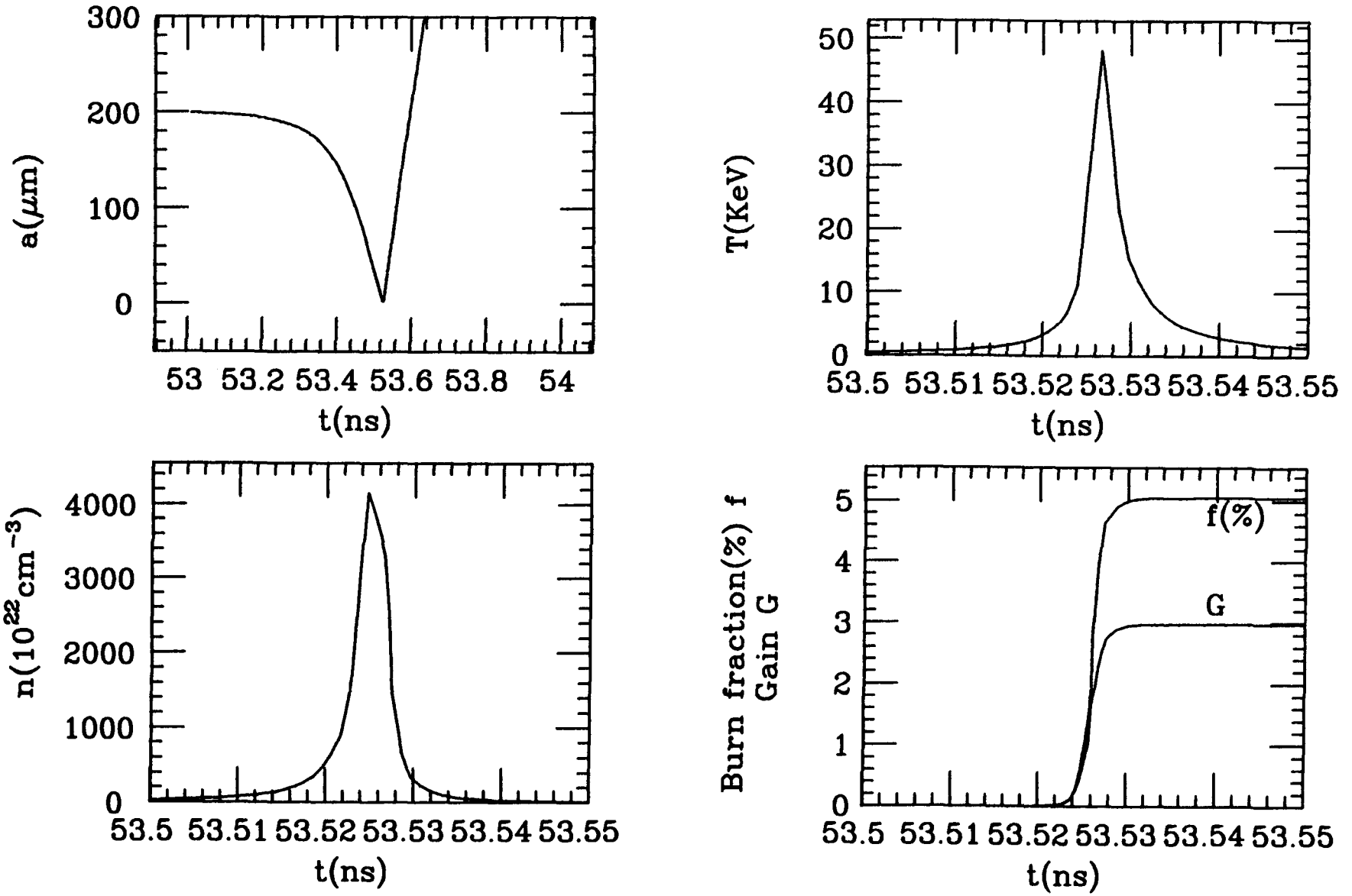
As a first approximation we perform the modelling of this configuration by using a zero-dimensional model of the θ-pinch plasma together with a thin shell model of the hollow Z-pinch with entrained magnetic field. The Ohmic heating is assumed to balance the radiative loss keeping the radius constant at initial value of 200μm, plasma density at 10^{22} cm^{-3} and temperature at 50 eV. Fig. 2 gives the results of the θ-pinch D-T plasma with a Z-pinch initial conditions I_m=10 MA, B_0=20 KG, t_0=50 nsec. The figure shows the plasma radius a, temperature T, density n, burn fraction f and the energy gain G as a function of time during the final stages of the collapse. The code also incorporates the heating due to α-particles produced by the fusion of D-T. The results show that adiabatic compression is the dominant source of heating during the final stages of compression. Final temperatures approaching 50 KeV were indicated while radiative losses were less than 40 eV during the implosion. The burn fraction $f = 2n_\alpha/n$ is on the order of 5% that corresponds to the neutron yield of 2×10^{17} per centimeter of the length. A gain of almost 3 is also observed which is way above the breakeven requirement. Eliminating the α-particle heating reduces the final temperature to 20 KeV and increases the density by a factor of two thus reducing both the G and f to 2.5 and 4% respectively. In conclusion the model shows that a careful control of the temperature at the early stages of collapse can easily lead to the breakeven and even beyond breakeven with the existing technology. The addition of the proper amount of impurities will provide a control in the rise of temperature by Ohmic heating thus keeping it to a desired temperature.

5. STABILITY ISSUES

The Rayleigh-Taylor instability occurs during the acceleration phase of the Z-pinch. Part of the B_θ magnetic field that accelerates the plasma and of the B_Z field produced by the external coil is trapped in the plasma and some in the space interior to the plasma. The B_θ and B_Z components and the resultant magnetic shear can stabilize the Rayleigh-Taylor instability. The stability during acceleration depends on details of the magnetic field distribution which involves magnetic diffusion. A complete analysis has never been carried out; however, in the UCI experiments we have noted, by means of the Mach-Zender interferometer, that the acceleration phase of a Z-pinch is more stable when there is a trapped B_Z-field.

After the acceleration phase, peak compression is attained which may be followed by one or more bounces. The plasma may settle down to a state that can be approximated as a conventional pinch equilibrium for which stability can be analyzed in the usual way by investigating small perturbations about a stationary state[15]. MHD analysis has been carried out for equilibria with general distributions $B_Z(r)$, $B_\theta(r)$ and $P(r)$ where P is pressure. The Z-θ pinch can be described by one of these distributions. It does not satisfy sufficient conditions for stability. In fact, it would always be unstable except in idealized cases. If the currents j_z for the outer pinch and j_θ for the inner θ-pinch are idealized surface currents, the configuration would be stable[16]. If the current penetrates the Z-pinch by diffusion to a depth δ then instability would be expected[17] with a growth rate of order $\gamma \cong (\delta/a)(C_A/a)$ where a is the pinch radius, and C_A/a is the characteristic growth time for an unstable pinch. C_A is the Alfvén wave velocity. These predictions are almost prehistoric for plasma physics, but they are in qualitative agreement with the observations at the UCI experiment where, the surface of the Z-pinch appears to be more unstable than the θ-pinch, but both

Fig. 2 Dynamics of θ-pinch



surfaces are much more stable than a conventional Z-pinch at maximum compression. The conclusion is that if there is little diffusion of the magnetic field in the Z-pinch, the Z-θ configuration should be fairly stable. This is also the requirement for trapping magnetic flux and obtaining very large magnetic fields. It should be noted that the θ-pinch stability is much less sensitive to magnetic field diffusion.

acknowledgments: We are grateful to Paul Ney for assisting us in computational analysis.

REFERENCES

1. S. I. Braginskii in Plasma Physics and the Problem of Controlled Thermonuclear Fusion, Pergamon Press (1961), p. 135; R. S. Pease, Proc. Phys. Soc. London B **70**, 11 (1957).
2. J. P. Apruzese and P. C. Kepple, Proc. 2nd Int. Conf. on High Density Pinches, Laguna Beach, April 26-29 (1989).
3. J. W. Shearer, Phys. Fluids **19**, 1426 (1976).
4. J. Bailey, Y. Ettinger, A. Fisher and N. Rostoker, Appl. Phys. Lett. **40**, 460 (1982); J. Appl. Phys. **60**, 1939 (1986).
5. E. Ya Gol'ts et al., Phys. Lett. A **115**, 114 (1986); Phys. Lett. A **119**, 359 (1987).
6. K. N. Koshelev et al., J. Phys. D - Appl. Phys. **21**, 1827 (1988) (printed in U.K.).
7. J. D. Sethian, A. E. Robsen, K. A. Gerber and A. W. DeSilva, proc. 2nd Int. Conf. on High Density Pinches; AIP Conf. Proc. (1989), p. 308. J. Hammel, p. 303.
8. H. U. Rahman, P. Ney, F. J. Wessel, A. Fisher and N. Rostoker, Proc. 2nd Int. Conf. on High Density Pinches, Laguna Beach, April 26-29 (1989), AIP Conf. Proc., p. 195. (This paper is enclosed as Appendix I.)
9. F. J. Wessel, F. S. Felber, N. C. Wild, H. U. Rahman, E. Ruden and A. Fisher, Appl. Phys. Lett. **48**, 1119(1986).
10. F. J. Wessel, N. C. Wild, A.Fisher, H. U. Rahman, A. Ron and F. S. Felber, Rev. Sci. Instrum. **57**, 2247(1986)
11. F. S. Felber, F. J. Wessel, N. C. Wild, H. U. Rahman, A. Fisher, C. M. Fowler, M. A. Liberman, A. L. Velikovich, J. Appl. Phys., **64**, 3831-3845(1988).
12. F. S. Felber, M. M. Malley, F. J. Wessel, M. K. Matzen, M. A. Palmer, R. B. Spielman, M. A. Liberman and A. L. Velikovich, Phys. Fluids, **31**, 2053, (1988).
13. N. A. Ratakhin, S. A. Sorokin, S. A. Chaikovsky, Proc. Seventh Int. Con. on High Power Particle Beams,Vol. II, 1204, (1988).
14. A radius compression rate of 50 has been reported by accelerating a plasma with a sheared magnetic field. C. Sovoken and S. Chaykayskii, Preprint #15, Institute of High Current Electronics, Tomsk (1991). Suppression of the R-T instability was first demonstrated by D. T. Albares, N. A. Krall and C. L. Oxley, Phys. Fluids **4**, 1031 (1961).
15. B. B. Kadomtsev, in Reviews of plasma physics, p. 153-199, Consultant Bureau, New York (1966).
16. M. N. Rosenbluth, Report LA 2030, Los Alamos, New Mexico (1959).
17. M. N. Rosenbluth, Proc. 2nd Int. Conf. on Peaceful Uses of Atomic Energy, Geneva (1958).

GOLD Z-PINCHES ON SATURN*

Rick B. Spielman
High Energy Plasma Physics Department
Sandia National Laboratories
Albuquerque, New Mexico 87185

Abstract

We will show data from gold z-pinch implosions on the Sandia Saturn accelerator at current levels of 10 MA. The x-ray yields and powers from these experiments have reached 600 kJ and 20 TW, respectively. These data differ dramatically from identical experiments using materials such as aluminum. The final pinch diameter, plasma temperature, overall radiation pulse width, and spectrum are also quite different than aluminum z-pinch results. The z-pinch load consists of a wire array 1.25 or 1.5 cm in diameter, 2-cm long with a variable number of wires (8-24). The total mass of the wire array is ~ 1 mg. Calculations suggest that the maximum kinetic energy which can be delivered to the the imploding load is ~ 350 kJ. The total x-ray output of 600 kJ was significantly larger than the kinetic energy stored in the pinch. This result implies a non-kinetic source of energy. An estimate of the Spitzer resistivity gave a pinch resistance which, when coupled with the current in the load, could explain the difference between the total x-ray yield and the kinetic energy in the plasma.

Introduction

Z Pinches efficiently couple the electrical energy of large accelerators such as Saturn into implosion kinetic energy, producing very hot, dense plasmas at stagnation, and generating intense bursts of soft x rays.[1-8] The initial condition required for z-pinch implosions can be established with annular gas puffs, annular foils, or cylindrical wire arrays. Gold z-pinches have higher radiation rates than lower Z radiators and and should provide x-ray powers comparable to the heating rates.

Experimental Configuration

Saturn[9] is a high-powered, state-of-the-art electrical generator capable of producing a peak power of 25 TW in a 40-ns FWHM pulse with a peak voltage of ~ 1.9 MV. The total electrical energy in the water transmission lines is 1.4 MJ. The 36 water-transmission lines are coupled to a 2-m diameter insulator stack assembly where 20 TW of electrical energy is fed into four, self-magnetically-insulated biconic

transmission lines (MITLs). The current in these four MITLs are added together using a double post-hole vacuum convolute and delivered to the load.[10] The current rises to 10 MA in approximately 40 ns.

A wire array load on Saturn consists of between 8 and 24 wires whose length is typically 2 cm. These wires are held by a fixture which supports and positions the wires azimuthally and radially. Eight stainless-steel current return posts, attached to the anode, support the anode side of the wire support fixture via conducting fingerstock. The cathode-side wire support is attached to the cathode via finger stock.We fabricated the wire support from graphite. The transition from the horizontal constant gap MITL to the wire array load is made at a diameter of 2.85 cm. The distance between the anode current return posts and the wires is 0.675 cm for a 1.5-cm diameter wire array. The minimum gap between the anode and the cathode at the base of the wire array is 0.6 cm.

Diagnostics

X-ray diagnostics included photoconducting detectors (PCDs), filtered and unfiltered bolometers, and time-resolved or time-integrated x-ray pinhole cameras. Three, filtered photoconducting detectors were used to get time histories of the keV radiation pulse. PCDs are capable of resolving pulses with a 2-ns rise time. We measured total and keV x-ray yields using nickel- and gold-foil resistive bolometers located 5.25 m from the source.[11] The bolometers have a time response of ~ 3 ns giving accurate, time-resolved information on the x-ray output from the plasma. The 1-μm thick nickel bolometer was fielded unfiltered, whereas the 1-μm-thick gold bolometer was typically filtered with 4-6 μm of beryllium and 1 μm of Parylene in order to measure only the x rays above 1 keV. On some shots a time-resolved x-ray pinhole camera was used to image the z-pinch radiation source. All of the electrical signals from the radiation and electrical diagnostics were recorded digitizers with a bandwidth of > 350 MHz.

Experiments and Data

We conducted two experiments using pure gold wires on 1.25-cm-diameter and 1.5-cm-diameter arrays. These shots utilized 24, 12.5-μm-diameter pure gold wires, the smallest diameter gold wires available at that time. The total mass of the array was 1.1 mg. The highest yield shot was the 1.25-cm diameter array, Saturn shot 937. The total x-ray yield and power are given in Fig. 1. The total x-ray yield was ~ 630 kJ and the peak x-ray power was ~ 20 TW. It is clear that the changes in wire number and array diameter had a significant impact on the x-ray yield and power. Saturn shot 940 used a 1.5-cm array diameter. The total x-ray yield and total x-ray power are shown in Fig. 2. In this case the total x-ray yield and power was lower than Shot 937. This may be due to the effective increase in the initial array nonuniformity (same number of wires with a greater circumference) giving a lower density stagnation and/or the fact that the mass was slightly too high to maintain the same implosion time. Time-

integrated x-ray pinhole camera image of the gold pinch from Shot 937 are shown in Fig. 3. The x-rays viewed by the camera have energies greater than 1 keV. The pinch diameter for the time-integrated image is ~ 500 μm.

It may be that the limitation on the power is the quality of the imploding plasma sheath. To a certain extent this final sheath quality is determined by the uniformity of the initial plasma. Wire arrays have a significant azimuthal nonuniformity because of the finite number of wires. Advanced loads such as foils and plasma jets might be able to improve the quality of the inital plasma. This may allow one to increase the initital diameter of the z pinch thus increasing the energy coupling, implosion velocity and hopefully increasing the peak x-ray power.

Z-pinch implosions can be modelled with a "0-dimensional" circuit model[12,13] in which the circuit parameters of the driver are included in the model and where the load dynamics are reflected in the values of the circuit parameters. Work is done on the system by the driver with the primary energy sink being the radially inward kinetic energy of the z pinch. Such a simple model does not include loss processes such as radiation or other dissipative mechanisms such as ohmic heating. The results from a typical calculation are given in Fig. 4. We used a driver impedance of 1/6 Ohm and a total inductance of 8.75 nH + load. The wire mass for this case is for 24, 0.5-mil Au wires 2-cm long. This calculation is inconsistent with the experimental data. This calculation suggests that the final kinetic energy found in the implosion is on the order of 250 kJ. If all of this kinetic energy is assumed to be converted to x-rays then the limit on x-ray yield would be the kinetic energy in the implosion. It is very difficult to change this value greatly without allowing the implosion to proceed to smaller diameter. In fact, a pinch diameter much less than 1 mm would be needed to obtain a kinetic energy comparable to the measured x-ray output. One possibility is that the final pinch diameter (position of actual current flow) is smaller that interpreted from the x-ray pinhole pictures. The second is through continued compression in a non-radial fashion. A third possibility is that there is an additional source of heating, most obviously ohmic heating.

A lower limit for resistive heating can be obtained using the Spitzer resistivity. The Spitzer resistivity is given by,

$$\eta = 5.2X10^{-3}\frac{\overline{Z}\ln\Lambda}{T^{3/2}} \text{ ohm-cm}$$

and, to first order, depends only on the $\overline{Z}$ (ionization level) and electron temperature of the plasma (ln Λ is a weakly varying function of plasma density and temperature). Resistive effects become more important with increasing plasma $\overline{Z}$ and this trend is consistent with our data. The discrepancy between

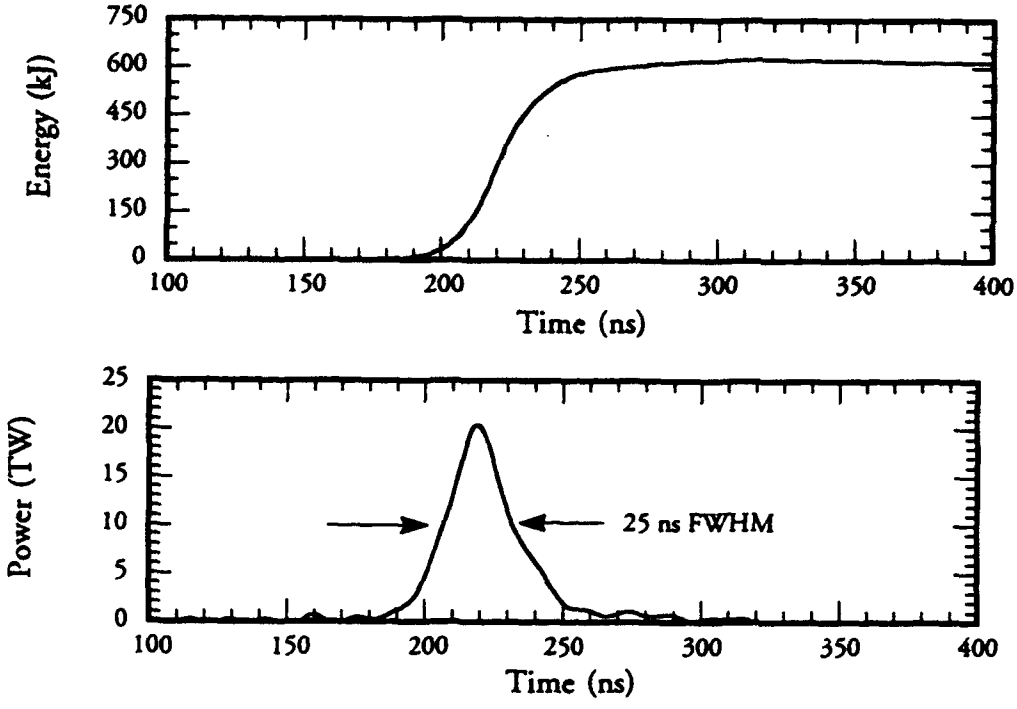


Figure 2. The total x-ray energy and power from a gold wire-array implosion, Saturn shot 937.

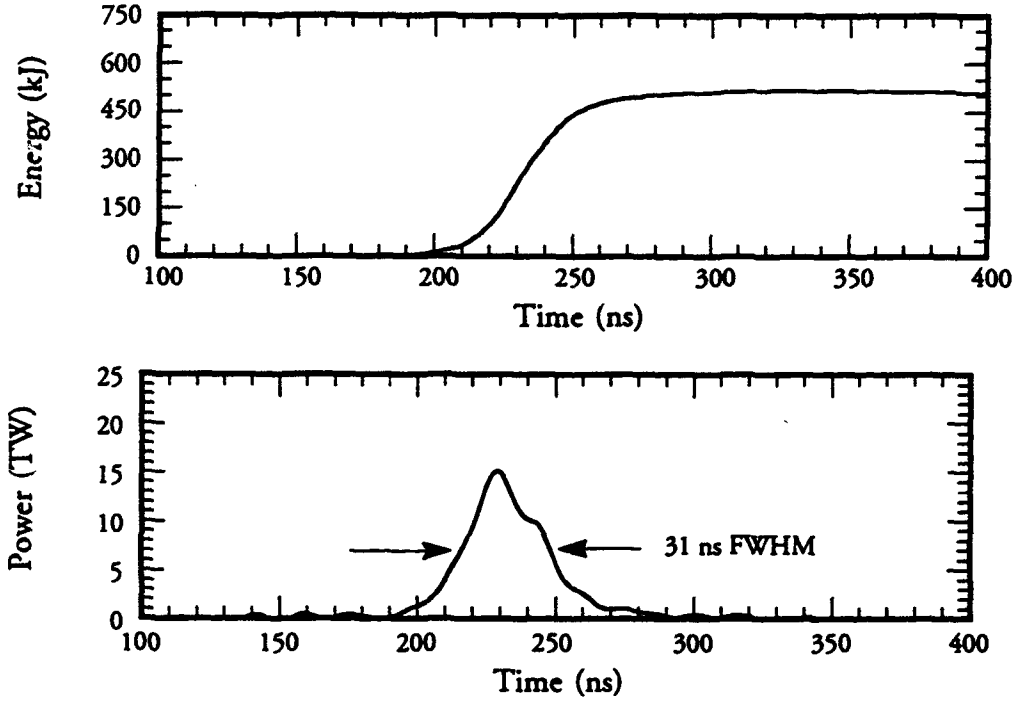


Figure 3. The total x-ray yield power from a gold wire-array implosion, Saturn shot 940.

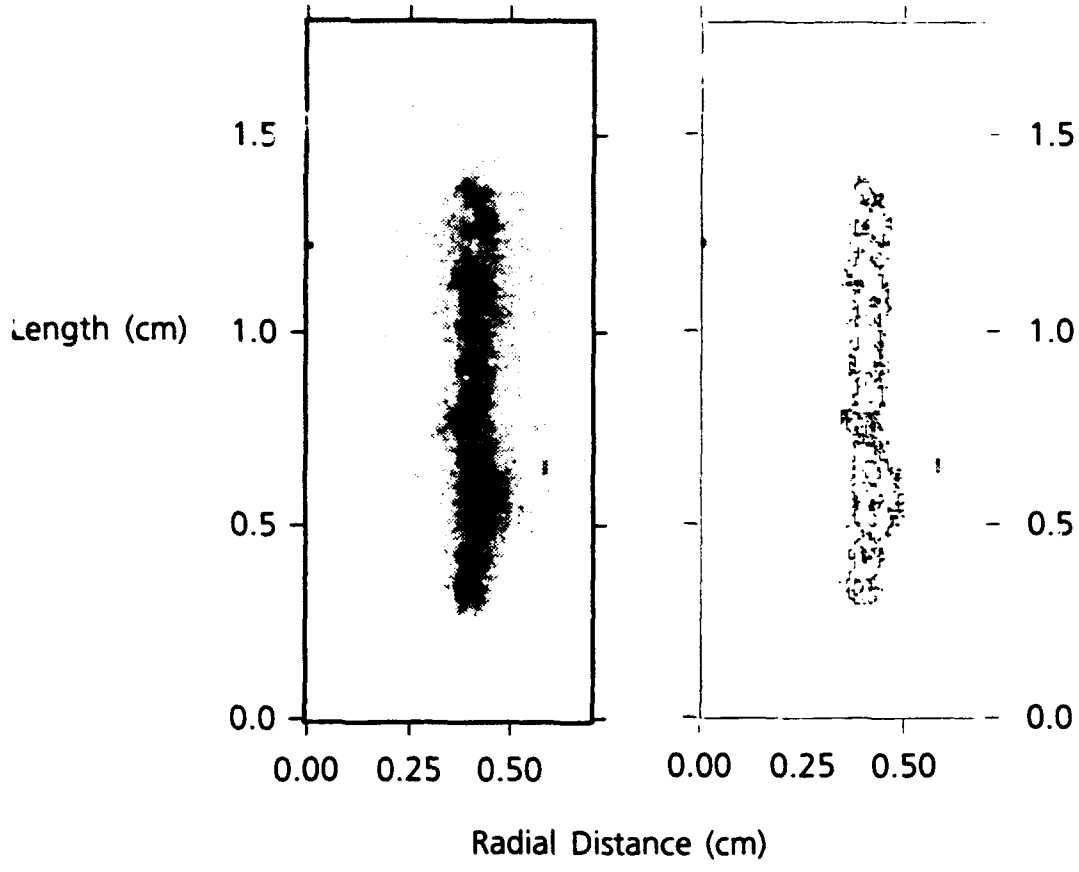


Figure 3. A time-integrated x-ray pinhole picture,Saturn shot 937. The diameter of the pinch is 500 μm and the viewed length is 1.2 cm. The features are close to the resolution of the camera. The right hand image is displayed in isodensity contours.

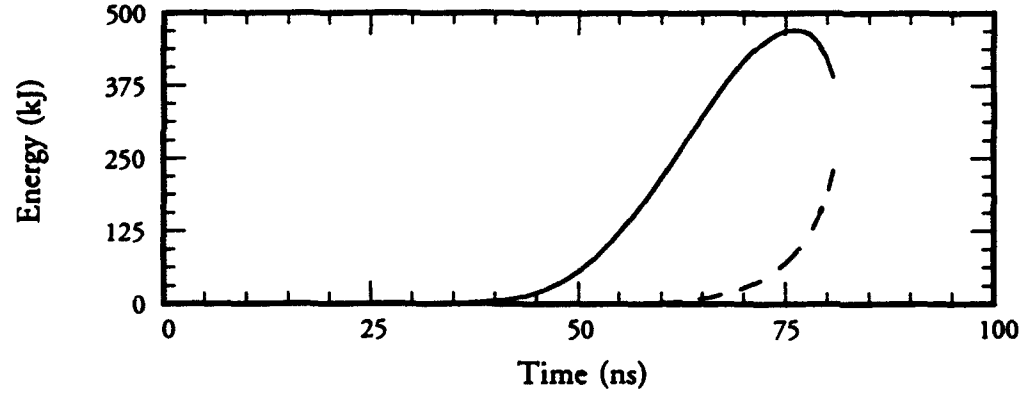


Figure 4 The pinch kinetic energy (dashed line) and the energy stored in the magnetic field (solid line) is plotted as a function of time.

the calculated kinetic energy and the measured x-ray yield increases with increasing pinch element Z. The peak resistive heating that would be expected assuming only Spitzer resistivity with Saturn pinch parameters is - 8 TW. The simple calculations assumed a 2-cm long plasma with a 1-mm diameter and a value of 6 for ln Λ. The temperature was an estimate based on energy balance. Plasma $\overline{Z}$ was obtained from reasonable estimates.

Conclusions

We have imploded gold wire arrays on Saturn. The coupling of machine energy to the implosion was very good with total x-ray yields of 400-600 kJ observed. It seems that the stagnation physics must include heating processes other than kinetic energy because x-ray yields exceed the kinetic energies calculated in "0-dimensional" models.

*We acknowledge the Saturn operations team, S. F. Lopez, J. S. McGurn, and L. Ruggles, Sandia National Laboratories and M. Vargas, Ewing Technical Design.

References

1C. Stallings, K. Nielsen and R. Schneider, Appl. Phys. Lett. 29, 404(1976).
[2]M. Gersten, J.E. Rauch, W. Clark, R.D. Richardson and G.M. Wilkinson, Appl. Phys. Lett. 39, 149(1981).
[3]W.L. Baker, M.C. Clark, J.H. Degnan, G.S. Kiuttu, C.R. McClenahan and R.E. Reinovsky, J. Appl. Physics 49, 4694(1978).
[4]C. Stallings, K. Childers, I. Roth and R. Schneider, Appl. Phys. Lett. 35, 524(1979).
[5]R.B. Spielman, D.L. Hanson, M.A. Palmer, M.K. Matzen, T.W. Hussey, and J.M. Peek, J. Appl. Phys. 57, 830(1985).
[6]P.G. Burkhalter, J. Shiloh, A. Fisher and R.D. Cowan, J. Appl. Phys. 50, 4532(1979).
[7]W. Clark, M. Gersten, D. Tanimoto, A. Kolb, J. Pearlman, J. Rauch, R. Richardson, J. Riordan, and M. Wilkinson, *Proceedings of the Fifth International Conference on High Power Particle Beams*, University of California, San Francisco, CA (1983).
[8]N.R. Pereira and J. Davis, J. Appl. Phys 64, R1(1988).
[9]D. D. Bloomquist, R. W. Stinnett, D. H. McDaniel, J. R. Lee, A. W. Sharpe, J. A. Halbleib, L. G. Schlitt, P. W. Spence, and P. Corcoran, Proc. of the Sixth IEEE Pulsed Power Conference, Arlington, VA edited by P. J. Turchi and B. H. Bernstein (IEEE, New York, 1987), p. 310.
[10]R. B. Spielman, P. Corcoran, J. Fockler, H. Kishi, and P. W. Spence, Proc. of the Seventh IEEE Pulsed Power Conference, Monterey, CA edited by B. H. Bernstein and J. P. Shannon (IEEE, New York, 1989), p. 445.
[11]D.L. Hanson, R.B. Spielman and J.P. Anthes, Bul. Am. Phys.Soc. 26, 910(1981) and L.P. Mix, E.J.T. Burns, D.L. Fehl, D.L. Hanson and D.J. Johnson, in Proc. of the Conf. on Low Energy X-ray Diag., Monterey, CA, AIP NY 75, 25(1981).
[12]P. J. Turchi and W. L. Baker, J. Appl. Phys. 44, 4936(1973).
[13]M. J. Clauser, L. Baker, D. H. McDaniel, R. W. Stinnett, and A. J. Toepfer, Magnetic Implosion of Plasmas with Short Pulse, High Power Generators, Sandia Report, SAND78-1387C.

DIFFERENT STABILIZATION PROCESSES IN Z-PINCH PLASMA EXPERIMENTAL APPROCH

B. Etlicher, A.S. Chuvatin,* L. Véron, F.J. Wessel,† C. Rouillé and S. Attelan
Laboratoire de Physique des Milieux Ionisés, Laboratoire du C.N.R.S.,
Ecole Polytechnique, 91128 Palaiseau, FRANCE

P. Choi
The Blackett Laboratory, Imperial College of Science, Technology and Medicine,
London SW7 2BZ, UK

ABSTRACT

We are investigating several methods to stabilize an aluminum vapor Z-pinch involving; applied axial magnetic fields, decreased z-current rise-time, and staged loads. The pinch is driven by a 2 Ω, 0.1 TW generator (~250 kA in ~50 ns) and is initiated in a plasma jet (3-mm diameter and 9-mm long) prepared by an exploded aluminum foil (5-mm thick). The axial-magnetic field is externally applied (B_{zo} ~ 50 G) or alternately, self-generated by a twisted discharge-return-current structure (B_{zo} <1 kG). The current risetime is decreased by a plasma opening switch (POS) located in the vacuum current feed, upstream of the pinch. The staged load involves a standard pinch imploded onto coaxial targets of conducting or nonconducting wires, i.e. plasma on wire (POW). Diagnostics include: framing/streak camera, filtered PIN XRDs, PET crystal spectrometer, multi-pinhole x-ray photos. Qualitatively, the stability improves with an axial field and the x-ray yield is greater with a self-generated field (twisted return-current structure). With a plasma load the POS reduces the prepulse, sharpens the current rise-time and improves the x-ray yield. Overall the POW configuration is associated with the best stability and highest radiation yields.

INTRODUCTION

In high-density pinched-plasma systems, stability is a principal concern associated with efficient transfer of driver energy into compressed plasma energy. Many pinch experiments emphasize the preparation of a uniform, initial-mass distribution aspiring for a well-behaved pinched-plasma column, for example in large-radius implosions. Unfortunately, large radius implosions often manifest instable final pinches. In wire-array and single-fiber discharges material ablation during current rise leads to inhomogeneities in the mass distribution which are preserved as the plasma later implodes. The use of applied axial magnetic fields stabilize the pinch yet adversely increase the

* I.V. Kurchatov Institute of Atomic Energy - Moscow, 123182
† University of California, Physics Department, Irvine, CA 92717

field energy at the expense of plasma energy. Another approach involves sharpening the load current rise-time with fast-opening switches. This decreases the acceleration time and hence, the time during which instabilities grow.

Injecting a preformed-plasma jet into the pinch-interelectrode space is a unique approach which inherently provides a uniform initial-mass distribution. With this technique pinches have been studied in both annular- and full-cylinder solid-jet configurations of aluminum at 0.1-1 TW[1,2]. Principal attributes include a pre-ionized, highly-collimated, radially and axially-homogenious plasma. In effect, the jet forms a plasma wire along the pinch axis of controllable diameter, mass, and atomic number. This configuration was recently modified to investigate discharge stabilization techniques using an axial-magnetic field[3], decreased-current rise-time[4], and staged loading[5]. The experimental flexibility for pinch systems and the implications for stability are noteworthy attributes and have provided interesting results, as described below.

GENERAL APPARATUS

The plasma jet is produced by a capacitor bank discharged through a 5 μm thick 3 mm wide aluminium-foil annulus (1.0 cm ID and 1.6 cm OD). The jet discharge is energized by two 4.24 μF capacitors charged to 13.5 kV and switched into a parallel plate-transmission line by a multichannel, dielectric-surface switch[6]; L~10 nH, $t_{1/4}$=650 ns, I_{max}=200 kA. The energy deposited in the foil is obtained by numerical integration of the foil discharge current-voltage trace and is approximately, E_{foil}~60 J; approximately 20 J to vaporization, and 40 J to ionize a 10^{19} cm^{-3} vapor to 1.5 eV. The mass/length between the pinch electrodes is estimated to be M/L=10 μg for a typical anode-cathode gap spacing 0.9 cm.

The jet is injected into the pinch-load region by a 4.5cm long collimating nozzle which terminates in a 3mm diameter aperture at the upstream face of the anode electrode, as shown in Fig.1. The load region is comprised of a multi-post discharge return-current structure, 3cm inner diameter, and the cathode and anode electrodes, 2 cm diameter, both fabricated from graphite. The cathode electrode was counterbored with a 1.5 cm diameter x 0.8 cm deep hole to prevent plasma density build-up and radial outflow in the load region when the aluminum jet stagnates.

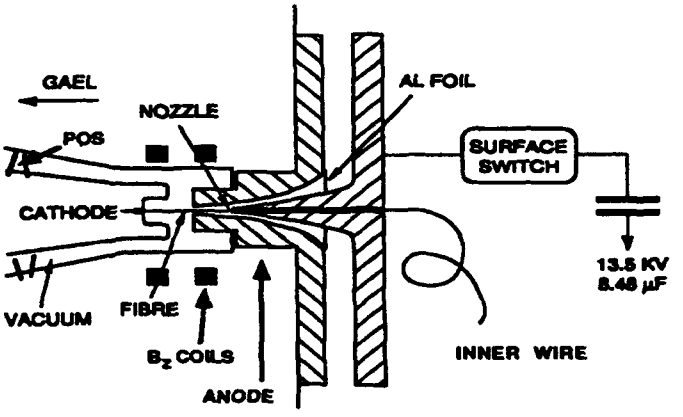


Fig.1 Schematic illustration of the load region, plasma-jet source, nozzle, and Al-foil system

The GAEL pulse-power generator[7] consists of a 12-stage Marx bank feeding a constant 2Ω tri-segment coaxial water-transmission line calculated to maximize energy transfer into the diode. The high-voltage pulse is applied directly to the cathode electrode via a conical-vacuum-feed transition (12-cm long). The line voltage and current were measured 12-cm upstream of the load region by a capacitive probe and B_θ probe, respectively. Another B_θ–probe, was located downstream of the pinch in the wall of the return-current structure, to measure the discharge current, I_L. The pinch x-ray emission was recorded by filtered BPX-65 silicon PIN photodiodes (-40 V bias). The filters were changed on various shots as identified below.

AXIAL MAGNETIC FIELD STABILIZATION

Typical time-correlated current (I_θ) and PXRD traces (12 μm Al-Mylar filter) are compared in Fig.2 for a normal shot where GAEL was fired into a standard aluminum plasma load. The prepulse current is approximately 75 kA and the flat-top main-current pulse is approximately 225 kA. Maximum x-ray power occurs at 105 ns into the discharge and has a 20 ns fwhm. Application of a 50 G axial magnetic field, using a Helmholtz coil, attenuated the PXRD x-ray emission fivefold, as confirmed by reduced intensity recorded on x-ray pinhole photographs and spectrograms (6-8 Å range).

Without the magnetic field, laser interferometry[2] revealed that the jet was initially divergent from the anode to cathode and underwent slight expansion during the prepulse. When the main current pulse arrived the divergent jet assembled into an axially uniform column which imploded from a 3 mm initial diameter to a 0.5 mm final diameter near maximum current with an implosion velocity of 10 cm/μs; final-compression ratio of 6:1. At the final compression stage, the ion density has an approximate value of, $n_{ion} = 3.3 \times 10^{19}$ cm^{-3} and electron temperature of Te = 300 eV (determined from spectroscopic line ratios of satellite lines).

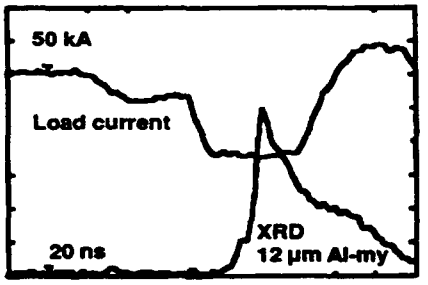
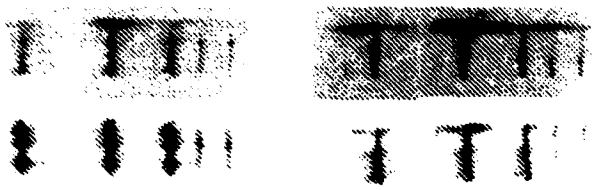


Fig.2 Typical current and PXRD signals on GAEL

Twisting the return-current structure (Fig.3) into a helix provides a self-generated axial field which tracks the discharge-current amplitude. Pinch discharges were compared for the straight (no-field) and twisted anode configurations. The time-dependent current waveforms were essentially the same, however an increase was noted in the PIN x-ray amplitude with the twisted-anode confi-



Fig.3 Return current anode



pinhole	9	8	7	6	5	4	3	2	1
dia. (μm)	400	100	20	20	400	50	100	100	100
filter	Ti	Be	Al	Al my	Al my	Ti	Be	Al my	Al my
thick (μm)	10.5	10	12	6	10,8	10,5	25	12	6

Fig.4 Comparison of multi-pinhole X-ray images for shots without (left) and with (right) twisted return current structure according to the filter / pinhole combination.

gura on. Qualitatively these results were confirmed by filtered, multi-pinhole x-ray image as shown in Fig.4 which compares two shots with and without the axial field. Both sets of data reveal axial modulations in the x-ray intensity contours, usually associated with instabilities.

It is uncertain what the magnetic field amplitude is during the pinch, since its value changes continuously during the current pulse and is assumed to diffuse into the on-axis plasma at some initial time. Using Spitzer conductivity, the diffusion time estimated early in the discharge is approximatively $\tau_{diff} \sim 8$ ns. Thus, it is reasonable that the initial magnetic-field intensity is established during the prepulse with a magnitude of the order of, $B_{zo} < 1$ kG, corresponding to a prepulse current $I < 50$ kA. Assuming flux conservation the final magnetic field can reach $B_{zf} = B_{zo}(r_o/r_f)^2 = 35$ kG. Of course the field could have been smaller than this, as the twisted structure provided possible evidence for breakdown which may have shorted-out the series circuit inductance of the twist at some time during the current pulse risetime.

POS EFFECT

Plasma parameters change with the delay between the plasma guns and generator[8]. The distance between the plasma guns and the cathode was 5 cm. Optimization for the prepulse suppression and the current rise increase has been done both in a 25 nH short-circuit diode and in the pinch configuration. Then the time delay between POS-triggering and Al-foil explosion was varied to obtain results shown on Fig.5. Though with the POS the load current prepulse was not completely suppressed, the current rise-time was increased by 37%. The peak XRD signal had a 20 ns duration and peaked for the optimum generator-jet delay near the end of the current pulse. Images obtained with the time-integrated pinhole photography show the qualitative difference for the shots with versus without the POS. The statistics obtained allows us to say that typi-

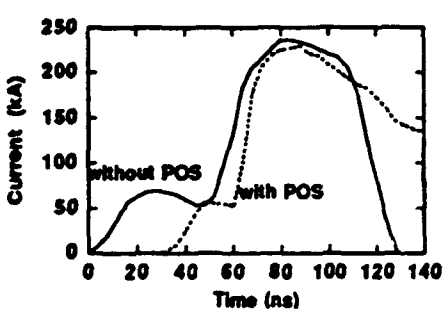


Fig.5 Prepulse reduction on GAEL

cally use of the POS for the prepulse suppression and the current rise-time sharpening lead to the appearance of plasma hot spots on pinhole images responsible for the higher energy x-ray radiation, while usually no strong difference in the pinch homogeneity was seen in comparison with shots without the POS. The data reveals that all XRD peak signals, which were considered to be responsible for the compression, were increased approximately by 50% for the case when the shape of the pulse was changed with use of the POS as well as maximum values of the prepulse produced by the generator and that one in the load after the suppression was decreased and delayed in time.

STAGED LOAD CONFIGURATION (POW)

A new configuration of dense Z-pinch based on a thin solid fiber embedded within a low density annular aluminium plasma is presented. Spatially resolved X-ray images reveal that energy supplied by the generator to the shell plasma is efficiently transferred to the fiber which is preionized by the shell radiation (Fig.6). The resultant plasma from the fiber is macroscopically stable and the m=0 instabilities observed with the fiber alone is suppressed. The first successful use of an intermediate plasma to couple energy from a pulsed power generator to a micron size plasma channel is demonstrated. High density plasma created by the passage of a high current through a thin metallic wire has long been studied extensively as a radiation source. The resultant exploding wire plasma is created from material ablated from the surface of the wire and is characterized by large scale non-uniformities along the whole length of the plasma.[9-11] The plasma is therefore of little use when an axially extended uniform plasma source is required. The new configuration involves the creation of a coaxial current carrying aluminium jet plasma over the thin wire [POW]. The aluminium jet plasma is designed to perform 3 distinct functions; a) to provide a plasma source of reasonable ionization to carry the bulk of the current at early time, b) to provide a source of radiation to photoionize the coaxial fiber on axis and c) to act as a temper to reduce the expansion of the coronal layer liberated from the fiber surface. The last task is made possible by creating the jet plasma in the form of a solid column, as distinct

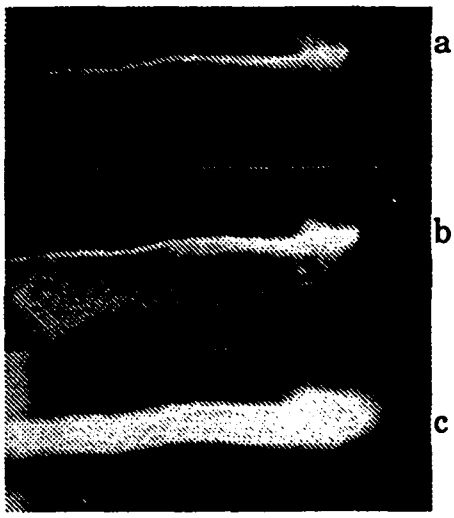


Fig.6 Time integrated X-ray pinhole photographs of a 9mm discharge from a 10 μm W fibre immersed in an Al jet plasma showing emission from (a) 400μm pinhole, 10.5 μm Ti filter, (b) 50μm pinhole, 10μm Be and (c) id. b with 25 μm Be.

from a hollow shell as used in the other double plasma scheme reported before. A range of sub-mm fibers of SiO_2, Al, Cu and W were used to investigate the characteristics of fiber pinches with and without the coaxial plasma jet. In the present study, the energy coupling to the fiber is found to vary as the mass of the Al plasma is changed by varying the delay between the initiation of the Al jet circuit and the firing of GAEL. In the absence of the fiber, this delay is optimized at 12 μs to achieve a pinch with best uniformity in emission in the 1-2 keV region. To obtain better energy coupling to the fiber the delay between the Al jet and the main discharge has to be reduced to below 8 μs, when a lower mass Al jet column would be formed around the fiber.

CONCLUSION

In summary, we have demonstrated the positive effect of an additional B_z and current rise on the pinch stabilization and x-ray yield. We have, also, proposed a new configuration of wire discharge with a concentric current carrying plasma as an intermediate energy coupling medium. This configuration has demonstrated the creation of a high temperature, stable pinch plasma with a length to diameter ratio in excess of 100 where the large scale m=0 instability is absent. It is the first demonstration that discharges created from a thin wire can behave completely different from that of an exploding wire plasma or standard Z-pinches.

REFERENCES

1 M. Gazaix, H.J. Doucet, B. Etlicher, J. P. Furtlehner, H. Lamain, and C. Rouille, J. Appl.Phys. **56** , p. 3209 (1984)

2 P. Audebert, H. Lamain, B. Dufour, C. Rouillé, B. Etlicher, Proc. 8th Intl. Conf. High Power Particle Beams, p. 423 (1990)

3 R.B. Baksht, I.M. Datsko, et al., J. Tech. Phys., **59**, 57, 1989

4 S.J. Stephanakis, at al., Appl. Phys. Lett. **48**, 829, (1986)

5 F.J. Wessel, B. Etlicher and P. Choi, to be published

6 J. M. Buzzi, H. J. Doucet, W. D. Jones, H. Lamain, and C. Rouille, Rev. Sci. Inst. **61**, 852, (1989)

7 J. Delvaux, H. Lamain, C. Rouille, H.J. Doucet, J. M. Buzzi, M. Gazaix, B. Etlicher, Proc. 4th Intl. Conf. High-Power Electron and Ion Beams, Palaiseau, France, p. 775 (1981)

8 L. Véron, R. Boivinet, C. Rouillé, B. Etlicher, C. Peugnet and B. Dufour, JAP **71**, 1992

9 S.M. Zakharov, G.V. Ivanankov, A.A. Kolomenskii, S.A. Pikuz and A.I. Samokhin, Sov. J. Plasma Phys., **9**, 271, (1983).

10 L.E. Aranchuk, et al., Sov. J. Plasma Phys., **12**, 765, (1986).

11 C. Stalling, K. Nielsen and R. Schneider, Appl. Phys. Lett., **29**, 404, (1976).

Work partially supported under contract ETCA/CEG 420/115/01

HIGH POWER IMPLODING PLASMA FOR THE X-RAY LASER

R.B.Baksht, I.M.Datsko, V.A.Kokshenev, A.A.Kim,
A.V.Luchinski, V.V.Loskutov, V.I.Oreshkin, A.G.Russkich
High Current Electronics Institute, Tomsk, 4, Akademichesky Ave.,
634055 Russia

The Al-Mg photoresonant X-ray laser scheme is investigated using collisional radiative model. It is shown that monochromatic pump powers of 10^9 Wt are obtainable within the 48 Å Al pump line. Experiments on Al-wire array implosion were carried out on the 1.2-1.5 MA GI-4 generator with a 1 cm separation between the plasma and the current return posts. The experimental output power in the region of λ =48 Å made up $(1\text{-}2)\cdot 10^9$ Wt/cm. The main K- and L-shell radiation yields from bright spots distributed 2-3 per cm. A simulation with the help of the collisional radiative model has demonstrated that the plasma temperature and density are 200 eV and 10^{20} cm^{-3}, respectively. Two schemes of the creating of the pumped plasma were suggested.

The possibility of using the radiation of fast Z-pinch (liner) for pumping the laser active medium is discussed in several works.[1, 2] One of the most attractive schemes of this type is that embodied in the Al-Mg laser,[3, 4] where the Al XI ion radiation by the $^2S_{1/2}$-$^2P_{1/2}$ transition provides for inverse population of the 4s-4l levels of the Mg IX ion. This scheme has the advantage that the wavelengths of the Al XI $^2S_{1/2}$-$^2P_{1/2}$ and Mg IX $^2S_0$-$^1P_1^o$ transitions are closely spaced (48.338 Å and 48.34 Å), respectively. Furthermore, according to the calculations described in [3, 4], the inverse population can be provided for with comparatively small radiation powers in the pumping line (10^9 W/cm throughout the liner length) which allows experimentation with this scheme at a comparatively low power level (on the order of 1 to 1.5 TW) of the driver. At the same time, the low gain ($\sim$ 1 cm^{-1}) offers some difficulties in the interpretation of the obtained experimental results. Moreover, the mentioned gain can only be reached when the Mg IX ions appear in the active medium

through photoionization in a plasma having a temperature of 10 to 20 eV. This specifies some requirements for the radiation pulse power as well as for the pulse duration which should be much shorter than the time needed for the production of necessary number of Mg IX ions. The paper describes the results of experiments with a wire-array pumping source.

Radiation Source

The experiment carried out on the GIT-4 generator with a POS[5] used Al wire-array liners of mass 160 to 420 μg/cm and initial diameter 0.5 to 1.4 cm (Fig. 1). Preliminary tests[6] have shown that the radiation intensity is a weak function of liner diameter within the 45 to 60 Å region containing the Al XI $^2S_{1/2}-^2P_{1/2}$ pumping line. Since a successful liner application as a pumping source requires that the liner-active medium separation would be a minimum, used in the further tests were liners of initial diameter d = 0.5 to 0.6 cm.

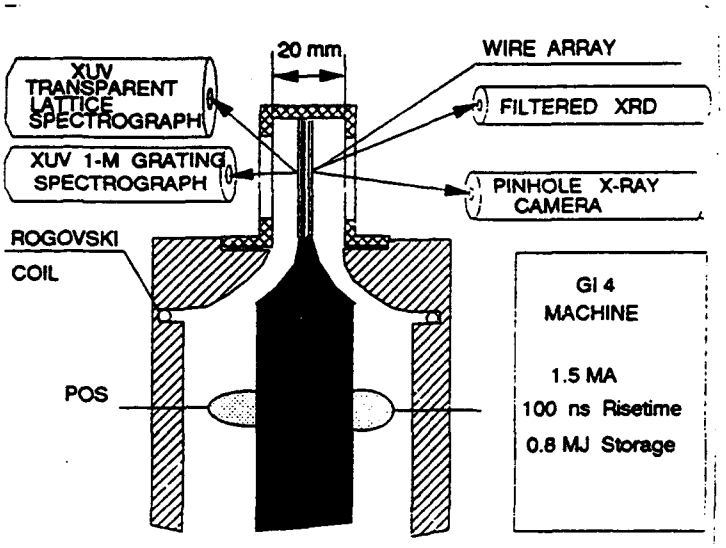


Fig. 1.

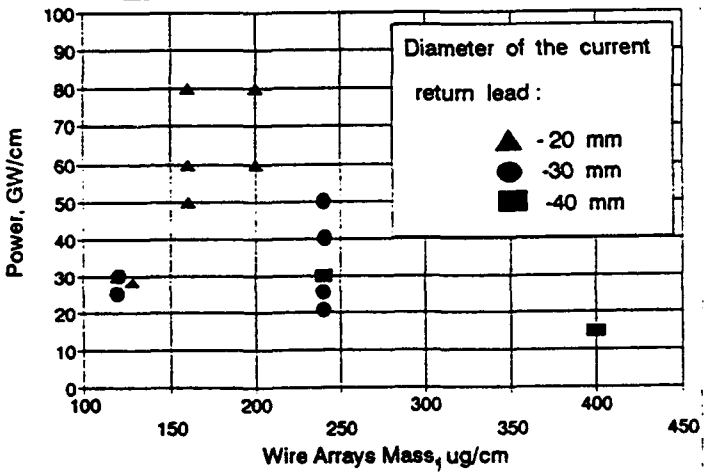


Fig. 2.

Figure 2 gives the power measured using the XRD as a function of liner mass for d_o=0.6 cm and I=1.4 MA. In this experiment we used a solid return current lead of diameter 40, 30, and 20 mm having windows to extract radiation. As follows from Fig. 2

the optimum mass from the viewpoint of the most intense radiation in the pumping line is 180 to 240 μg/cm. The increased data spread at d_{lead} = 20 mm and 30 mm is due to the enhanced erosion of the lead walls and the current post. The transmitting obscura grating used in spectral measurements allowed a spatial resolution along the plasma column axis so the radiation spectrum could be measured within and outside the "hot spots". Figure 3 gives the radiation spectrum measured for different regions of the plasma column: the "hot spot" region of length 1.6 mm (a) and a region of the same length with no "hot spot". The number of such "spots" is limited to two or three per centimeter, the spot diameter being of the order of 1 mm.

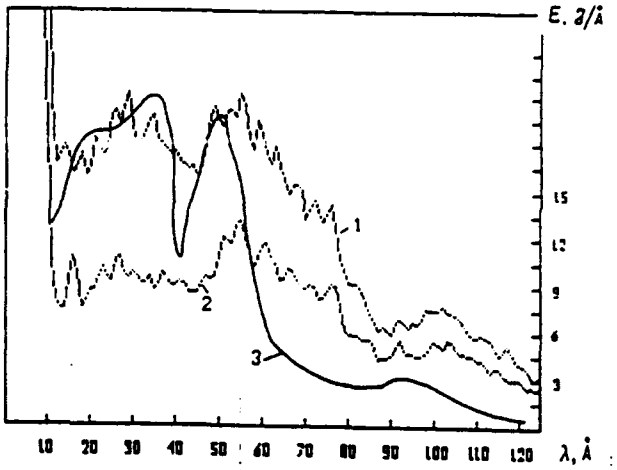


Fig. 3. Spectrum of the imploding plasma for Al wire array, 240 mg/cm, r_o=0.25cm, L_{wa}=3 cm, I=1.28 MA. 1. Radiation from bright spot, L=0.16cm 2. Radiation from cold region, L=0.16cm 3. Calculation results for I= 60 ns.

Spectral measurements have shown that for the 44 to 60 Å region containing several strong L-shell lines the power is $P^{exp}_{44-60} = 10^{10}$ W/cm, while the integrated liner radiation power is $P^{exp}_{13-20} = 4\ 10^{10}$ W/cm. In this case the liner current and mass were 1.4 MA and 240 μg/cm, respectively. The experimental liner radiation characteristics were compared to the predictions of a multi-level collision-radiation model[6]. The attempt to model the radiation by a homogeneous cylindrical column having a temperature ranging between 70 and 250 eV resulted in a significantly overestimated integral power: $P^{calc}_{13-100} = 10^{12}$ W/cm. In order to eliminate this discrepancy we supposed the plasma column to consist of intensely radiating "hot spots" and regions of comparatively cold (70 eV) plasma occurring intermittently. The hot spots were modeled by spheres of radius 0.5 mm confin-

ing a homogeneous plasma of temperature T_e = 200 eV and ion density 10^{20} cm^{-3}. Since the hot spots appear as a result of the sausage-type instability (necks), this demands that the model would take account of the dynamical effect of plasma motion in the compression-expansion process. The Doppler effect in this case leads to the increase in the equivalent line width of the radiating plasma by $\omega_0 \cdot v_0/(2c)$.

The spectral radiation flux at the sphere surface calculated in the above approximation for $v_0 = 3 \cdot 10^7$ cm/s is in satisfactory agreement with the hot-spot radiation energy (curve 3 in Fig. 3).

Taking into consideration the experimentally found hot spot number per unit length, we also obtained a satisfactory agreement with experimental results for integral radiation characteristics and for radiation intensities of some lines of the L shell: $P^{calc}_{13-120} = 5 \cdot 10^{10}$ W/cm and $P^{calc}_{line} = (1 \text{ to } 2) \cdot 10^9$ W/cm.

Active Medium

The understanding of the processes occuring at the interaction between the liner radiation and the pumped plasma was the principal goal of our preliminary studies. As follows from the calculations described in [3], the inverse population in the Al/Mg scheme can exist for $n_i \approx 2 \cdot 10^{18}$ cm^{-3} and T_e = 10 to 20 eV. In order to create an active medium with the mentioned parameters we used two schemes. In the first one plasma was generated by vaporizing a Mg target placed just behind the window of the reverse current . In the second scheme plasma was created using a Nd laser (3 J, 20 ns) focused into a 0.1 x 1 cm strip. In this case, optimization of the time lag between the laser pulse and the liner radiation significantly simplifies the task of producing the required Mg IX ion density. The total number of radiating Mg IX ions, however, is as low as 10^{16}, which is much smaller than the corresponding value calculated for the first case. For the first scheme we found both the Mg V lines and the OV, OVI lines in the spectrum.

Figure 4 demonstrates the simulation results for the conditions of the SNRT07 shot (1.42 MA, 160 μg/cm Al liner, d_{lead} = 30 mm). In the calculation we used the 1-D hydrodynamic model with account of the results of the stationary multi-level model. We took into account the magnetic field diffusion, the magnetic field was produced by the return current. We evaluated the plasma temperature with the help of the OV and OVI ion species, the temperature was equal 10-15 eV, which was less than the calculated one. The slight lines of the Mg VII and Mg VIII species were found also: $^1D_2 - {}^1D_2$ Mg VII 70.2 Å; $^4P - {}^4D$ Mg VIII 66.07 Å; $^4S^0 - {}^4P$ Mg VIII 76.8 Å. It's interesting to note, that for the quater radiation power of the W liner we could not find just the traces of the above transitions. This fact can be explained in the following way. The essential part of the W radiation is a result of the excited line transitions (line radiation). As for the Al radiation the continuum radiation power is comparable with the line radiation. As the result of this we have two additional processes. First the ionization rate increases due to the photoionization with the subsequent

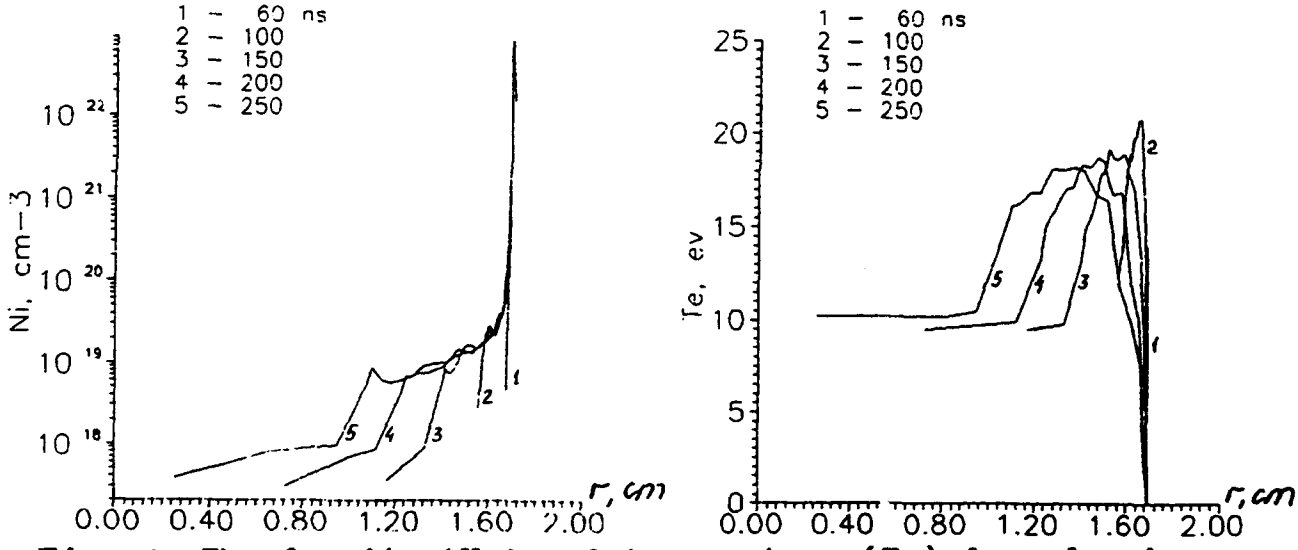


Fig. 4. The density (N_i) and temperature (T_e) dependencies as a function of the distance from the target surface.

ionization. Secondly, the line intensity also increases:

$$S_\nu = \frac{2h\nu^3}{c^2}\left(\frac{g_e N_{up}}{g_{up} N_e}\right)$$

where N_{up}, N_l, g_{up} and g_l are the population and the statistical weight of the upper and low levels, respectively. The increasing of the line intensity is more essential in our case. The $\frac{g_l N_{up}}{g_{up} N_l}$ values for the $2p^2\ {}^1S_0 - 2p3s\ {}^1P^o$ C-like magnesium Mg VIII are presented in Tabl. 1. In this case the calculations were fulfilled for the 1.5 cm liner target separation at T= 15 eV and $P_{44-120} = 5 \cdot 10^{10}$ Wt/cm. The data in the first line are taken with account of the photoexcitation and the second one without the photoexcitation. This effect leads to the fivefold increase of the line radiation when the plasma density is not large (10^{18} cm^{-3}). The certain discrepancy between the experimental and simulation results will be the research subject on the future.

Table 1.

Density, cm^{-3}	With photoexcitation	Without photoexcit.
10^{17}	$1.8 \cdot 10^{-5}$	$3.7 \cdot 10^{-6}$
10^{18}	$2.06 \cdot 10^{-5}$	$6.9 \cdot 10^{-6}$
10^{19}	$3.3 \cdot 10^{-5}$	$2.3 \cdot 10^{-5}$

The calculated $g_l N_{up} / g_{up} N_l$ values.

The second scheme experiments showed that the 1-GW Nd laser is not sufficient for the producing of the registered plasma.

Conclusion

For a current of 1.4 MA the plasma of an Al liner has a temperature of 200 eV and ion density of 10^{20} cm^{-3}, the radiation power in the pumping line being (2 to 3)$\cdot 10^9$ W/cm with a pulse length of 40 ns and the spectrum integrated power being (5 to 7)$\cdot 10^{10}$ W/cm.

1. Stephanakis et al. IEEE Trans. Plasma Sci.,1988, PS-10, 5, p.472-82.
2. Davis et al. ibid, p.482
3. Loskutov V.V., Oreshkin V.I. Pis'ma JETF, 1990, 52, p.1245-48 (1990).
4. Apruzece J.P., Buie M. JAP, 1991, 70, 4, 1975.
5. Bugaev S. et al. IEEE Trans. Plasma Sci., 1990, PS-18, 115.
6. Baksht R.B. et al. Phyzika Plasmi, in Russian, 1992, to be published.

MULTICHANNEL X-RAY SPECTRAL MEASUREMENT OF HOT PLASMA EVOLUTION IN NITROGEN-PUFF Z-PINCH

A. Krejčí, J. Rauš, V. Piffl

Institute of Plasma Physics, Czech. Acad. Sci.,
P.O.Box 17, 182 11 Praha 8, Czechoslovakia

A. V. Golubev

Ioffe Physical-Technical Institute, Acad. Sci. of Russia,
Polytekhnicheskaya 26, St.Petersburg, 194021, Russia

Yu. Ya. Platonov

Institute for Applied Physics, Acad. Sci. of Russia,
Nizhny Novgorod, Russia

E. Krouský, O. Renner

Institute of Physics, Czech. Acad. Sci.,
Na Slovance 2, 180 40 Praha 8, Czechoslovakia

Abstract. Soft x-ray emission from nitrogen plasma of gas-puff Z-pinch device (with energy input 4.3 kJ and current 160 kA) has been studied. Multilayer mirror polychromator with time-resolved registration by PIN diodes was installed and its relatively narrow spectral windows were aligned to the important parts of nitrogen spectrum between 390 and 710 eV. The T_e evolution (≈400 eV in hot spots) was measured from a slope of recomb. continuum of He-like N. The T_e of bulk plasma (≈100 eV) is compared with T_e calculated from yields of K-shell lines. Moreover, pinhole cameras were used for better understanding the radiation phase of the pinch. Time sequences of peaks in x-ray signals corresponding to a number of bright spots on photographs, are presented.

1. Introduction

Z-pinch plasma is, undoubtedly, quite complicated subject of research. It is too small to be investigated by a dipped probe, too dense (esp. inside the hot spots) to make good laser interferometry, and it is very short-living object which limits the choice of the applied techniques of measurement and/or the results obtained. Fortunately, Z-pinch plasma is also very intense pulse source of radiation. Our previous experiments with Ar and Ne allowed us to estimate plasma parameters [1]. Though it gave quite consistent data about the pinch, only time-integrated x-ray diagnostics (spectra and pinhole photographs) are not sufficient to study the Z-pinch nature. Advanced diagnostics, i.e.

spectrally or spatially resolved methods, joint with temporal resolution, have to be used. Therefore, after preliminary measurements with nitrogen [2], we installed such a diagnostic tool.

2. Experimental

A conventional small gas-puff Z-pinch device was operated in the regime with current 160 kA which promised to produce more He-like K-shell line radiation and less continuum radiation than in 200 kA regime [2]. About 1 cm^3 of nitrogen was injected in the form of a hollow shell (diameter and length 21 mm) between the electrodes and then imploded by the capacitor bank energy 4.3 kJ.

The absolute x-ray measurements were carried out by multichannel polychromator described in [3]. Each of 4 channels consisted from a submicron filter, multilayer mirror (MLM) and a PIN diode. The emitted spectral power density into 4π Sr is then

$$dP/dE = I_{PIN}\ 4\pi L^2/\overline{T}_F(E).\int R(E)dE.\overline{S}_{PIN}(E) \qquad [W/eV],$$

where $\overline{T}_F(E)$ is average filter transmission in the channel with energy interval ΔE, $\int R(E)dE$ is integrated reflection coefficient of MLM, $\overline{S}_{PIN}(E)$ is average PIN diode sensitivity within ΔE, L is source-to-MLM-to-detector distance, and I_{PIN} is detector current. A maximum error in the dP/dE determination is connected with the accuracy of the values T, R, S, L, and with an alignment of the channel. Here the total error of the dP/dE did not exceed 27 %.

The thickness 0.3 - 0.6 μm of used light-tight filters was sufficient to absorb a scattered low-energy component of x-rays. Filter transmissions as well as the reflectances of the dispersive elements (MLM) were calibrated by x-ray grazing incidence mo-

energy	392	430	500	540	573	650	704	930
filter	Ti	Sn	Sn	Fe	Cu	Cu	Cu	Al
T_F	0.16	0.21	0.25	0.09	0.05	0.10	0.18	0.20
$\int RdE$	0.67	0.41	1.85	1.80	3.03	2.16	4.70	1.29
$S_{CH}x10^{-3}$	0.65	0.6	4.02	1.53	1.53	2.38	9.84	3.4

Tab.I: Data of used polychromator channels - filter transmission T_F, reflection of MLM, and channel sensitivity S_{CH} [A.eV.cm^2/W].

nochromator in the range 270-940 eV (tab.I). The W-Si MLMs (R_{max}= 0.03-0.15, 2d = 72-78 Å, $\Delta E/E$ = 0.03-0.05) can be advantageously used in broad energy range owing to smooth spectral dependencies of scattering factors of W and Si up to K-edge of Si (1.84 keV). Silicon PIN diodes (dead layer 0.15 μm) have the time resolution 1.2 ns. The absolute calibration of their sensitivities (0.003 - - 0.013 A.cm^2/W) was carried out by photoionization quantometer [4]. The polychromator was placed 195 cm radially from the pinch.

3. Results from polychromator measurements

Four-channel polychromator was used in the experiment with different combinations of channels from tab. I. An attention was paid especially to the channel couples covering the basic K-shell lines (tab. II) or recombination continuum above the ionization potentials of He-like or H-like ion species. Signals acquired by the couple of 573/650 channels (fig.1) enabled us to calculate T_e evolution from the slope of the x-ray continuum (fig.2). A stable component of T_e (about 100 eV) corresponds to the bulk plasma,

ion	trans.	E/λ[eV/Å]	trans.	E/λ[eV/Å]	I [eV]
He-like	1s - 2p	431/28.8	1s - 3p	498/24.9	552
H-like	1s - 2p	500/24.8	1s - 3p	593/20.9	667

Tab.II: Principal data of nitrogen K-shell spectrum: main transitions, line energies and ionization potentials (after [5]).

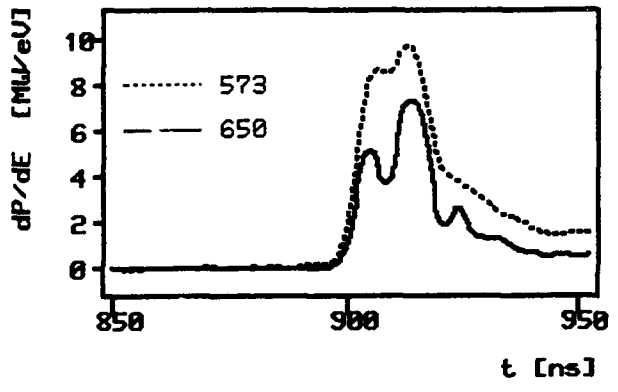


Fig.1: Power densities detected in channels aligned to energies 573 and 650 eV.

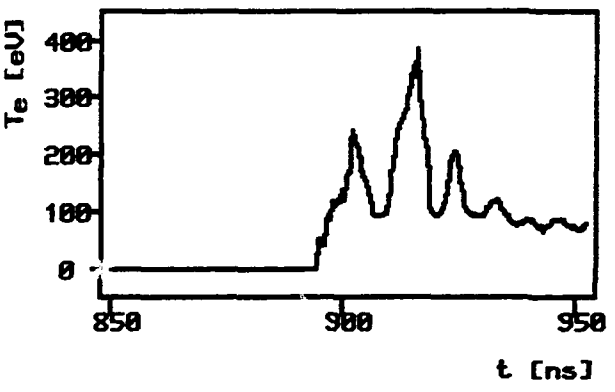


Fig.2: Time dependence of T_e calculated as a ratio of the power densities from fig.1.

which is a long-living formation in comparison with hot spot(s).

To better understand ionization and radiation in Z-pinch, an attempt was made to compare experimental results with theoretical ones from computer code RATION [6]. Evidently such a steady state model of hot dense plasma radiation can give a reliable estimate of plasma parameters just under the assumption that the tempera-

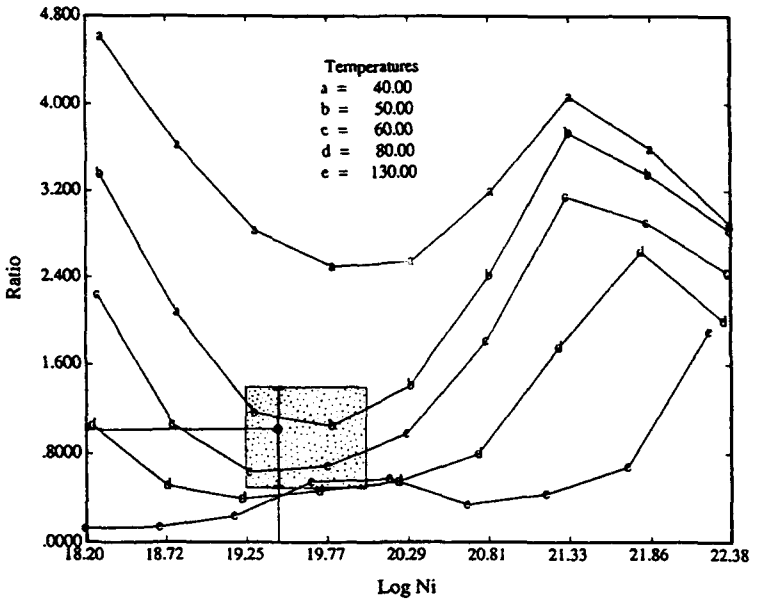


Fig.3: Ratio of total energies emitted in two pairs of important K-shell lines at 431 and 500 eV (see the text and tab. II) in dependence on N_i for different T_e. Experimental value of this ratio is taken from polychromator channels 430/500. A dotted area marks a range of ion densities N_i possible in our experiment.

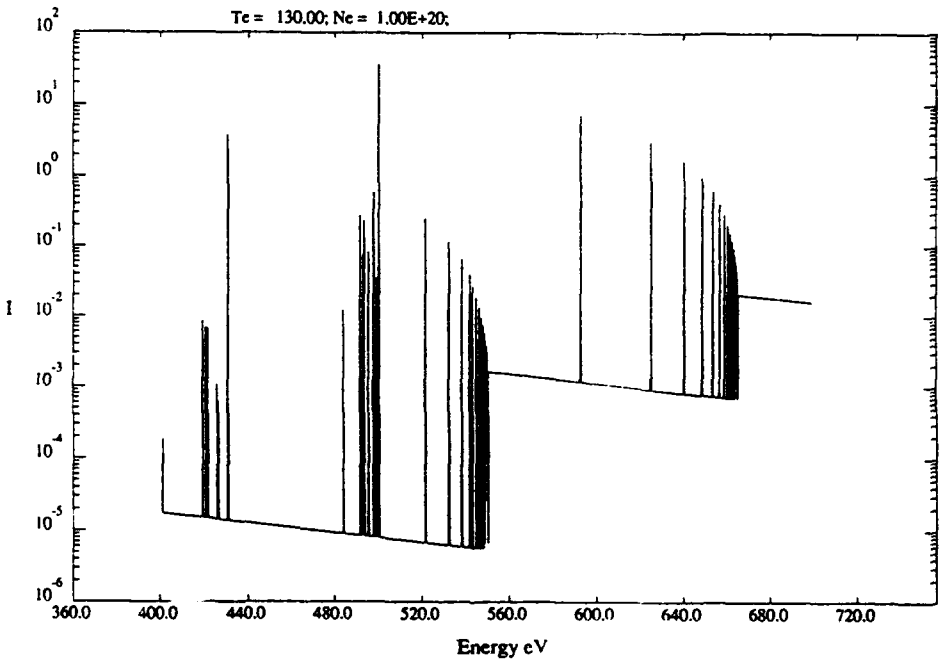


Fig.4: Nitrogen x-ray spectrum computed for steady state non-LTE conditions from [6] for plasma parameters taken from paper [2].

ture and density gradients are small during observed emission. Of course, the fulfillment of this condition in Z-pinch is rather limited. A ratio between the radiation yields in channels at 430 and 500 eV (covering He-like resonance and intercombination lines and both the lines close to 500 eV, respectively) was compared with the plot of different plasma parameters (fig.3). The experimental value of this ratio, tailored to a bulk ion density calculated from simple dynamics of Z-pinch plasma implosion indicates bulk plasma T_e somewhat lower ($\approx$ 50-60 eV) than mentioned above. This discrepancy may consist in unknown portion of continuum backing all the lines as well as in a deformed data in 650 eV channel due to a lot of merged lines of H-like 1s-np series. The simulated spectrum in fig.4 can give a rough image of the reality.

4. Pinhole photography

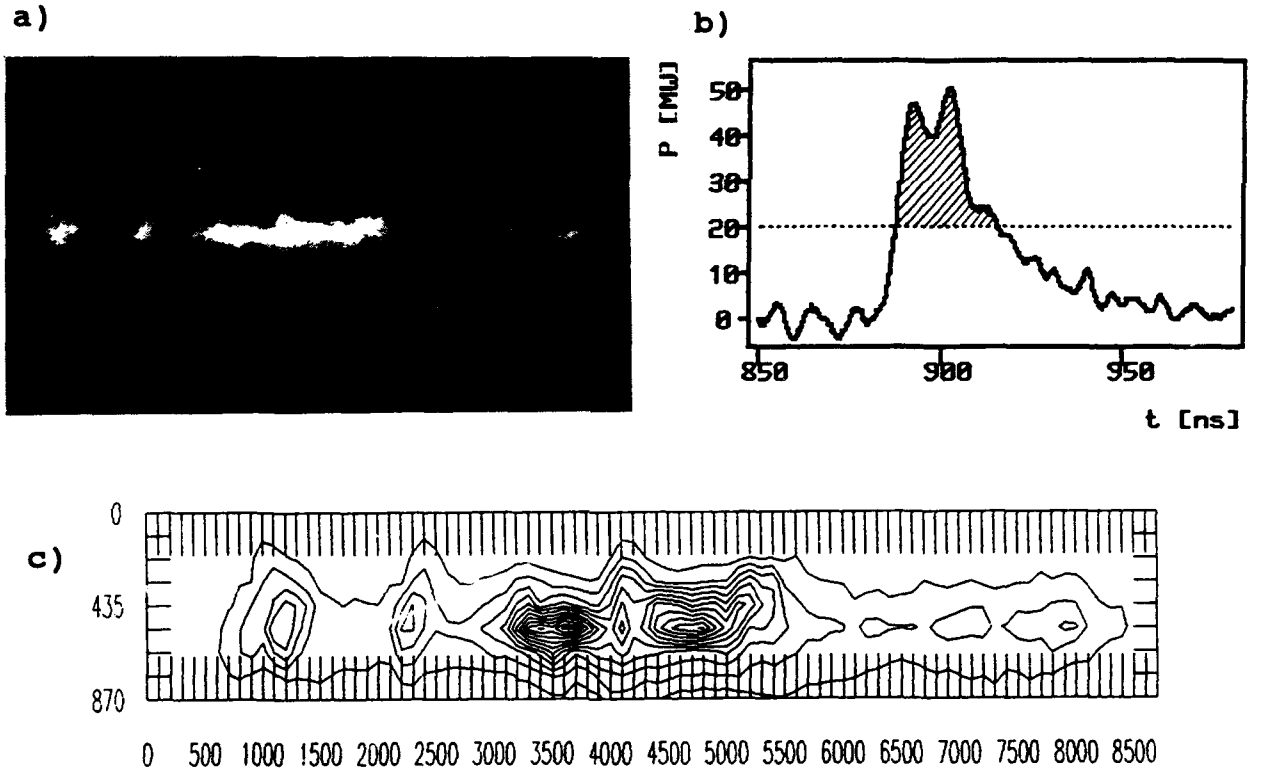


Fig.5: a) Enlarged pinhole photograph through 7.5 μm Be filter. b) X-ray intensity evolution in polychromator channel 430 eV during the same shot. The part of radiation responsible for the strong darkening of film by hot spots is hatched.
c) Contour plot of spots area as in a). Scale numbers are in μm; actual dimensions of the plasma formations are 0.65x smaller.

For independent x-ray measurements, 2 pinhole cameras (with entrance diameters 51 and 58 μm, different light-tight filters and x-ray film Agfa Structurix D 8) were placed 15 cm from pinch axis. Besides the "clouds" of bulk plasma there are also sharply bounded bright spots on the photographs. Their occurrence coincides with the shots providing the power densities from the polychromator channels higher than approx. 1.4 MW/eV. Also the number of the hot spots agrees well with a sequence of peaks in polychromator signals above this limit (fig.5 b).

5. Conclusion

The soft x-ray radiation carries rather detailed information about the plasma properties but a lot of ambiguities as well. In order to interprete the information properly, it is inevitable to analyse the radiation trying to decide what portion of it has an origin in the bulk or the hot spot plasma, in the continuum or the line emission. The value of bulk plasma T_e should be therefore precised by better alignment of polychromator channels to the parts of continuous spectrum without lines. The T_e found out during hot spots lifetime (fig.2) is lower than that in Ar [1] because the dimensions of bright plasma formations (fig. 5a) are much larger. To obtain full information about the appearance and evolution of hot spots, temporal resolution of the picture (e.g. x-ray streak camera, set of gated microchannel plates etc.) is desired to use simultaneously with the polychromator.

The authors would like to thank Drs. Pfeifer and Člupek for help with computation and one of them (OR) to Dr. Lee for providing an up-to-date version of code RATION.

References

[1] Krejčí A., Krouský E., Renner O.: *in* Dense Z-Pinches (eds. N. R. Pereira, J. Davis, N. Rostoker), AIP Conf. Proc. 195, AIP New York 1989, p.474; also Czech.J.Phys. 40(1990), 1244.
[2] Rauš J., Krejčí A., Piffl V.: this conference proceedings.
[3] Akhsakhalyan A. D. et al.: *in* Proc. SWLA-90, Nova Science Publishers, 1991.
[4] Bobashev S. V. et al.: Physica Scripta 43 (1991), 356.
[5] Kelly R. L.: Report No. 5922, Oak Ridge Nat. Lab., 1982.
[6] Lee R. W., Whitten B. L., Stout R. E.: J. Quant. Spectr. Rad. Trans. 32 (1984), 91.

INVESTIGATION OF INTENSE XUV EMISSION OF NITROGEN-PUFF Z-PINCH WITH SMALL ENERGY INPUT

J. Rauš, A. Krejčí, V. Piffl

Institute of Plasma Physics, Czech. Acad. Sci.,
P.O.Box 17, 182 11 Praha 8, Czechoslovakia

Abstract. Light elements like nitrogen or carbon are suggested as optimum working media for small Z-pinches (several kJ energy input). It is shown that such elements can be ionized up to K-shell ionization stages not only in hot-spots, but also in the bulk plasma. The yield of nitrogen K-shell radiation (about 10 J/shot) is therefore substantially higher than that of traditionaly used neon. Besides the pinch physics and radiation dynamics, such radiation could be of interest for applications in "water window" spectral region.

1. Introduction

In our previous experiments [1,2], a small linear Z-pinch device (present arrangement 5.4 μF, 4.3 kJ) with Ar or Ne plasmas starting from hollow gas-puffs was investigated as an intense pulsed source of XUV and soft x-rays [1)]. The total x-ray yield from the pinched bulk plasma (≈1 mm in diameter, $n_i > 10^{19} cm^{-3}$, $T_e \approx$ tens of eV) was dominated by VUV radiation. Typically it was about 250 J/200 ns for Ar and 100 J/100 ns for Ne. On the other hand, K-shell radiation was observed only from hot-spots (tens of μm in diameter, T_e up to 1 keV, $n_e \approx 10^{21} cm^{-3}$), and a higher emitted energy was measured for Ne (spectral range 0.9 - 1.4 keV): 0.6 J/shot, while for Ar (spectral range 3.0 - 4.4 keV) only 0.05 J/shot.

[1)] The x-ray regions are marked differently by many authors. In this paper we will use VUV for photon energies 10 - 100 eV, XUV for 0.1 - 1 keV and soft x-rays for 1 - 10 keV region. Moreover, let us label all radiation of electron transitions to the K-shells, i.e. both K-shell lines and recombination continuum, as "K-shell radiation" or "K-shell region". Similarly the "L-shell radiation".

Because the K-shell output has an inverse dependence on emitted photon energy, a higher intensity of this kind of radiation as well as a lower background in VUV region can be predicted for elements lighter than Ne (i.e. working gases like propane, CO_2, nitrogen). The K-shell region of nitrogen, for instance, ranges approx. 400 - 700 eV, while the L-shell region practically coincides with the VUV range. In addition, there is a substantially higher chance to ionize these elements, due to their lower ionization potentials, up to He-like or even H-like state also in the bulk plasma by the same energy input. This can lead to a stronger effect of VUV background suppression in favour of K-shell radiation. Of course, we assume similar plasma parameters as mentioned above. For a rough orientation in radiative properties of the elements in question see Tab. I and Fig. 1.

Tab. I: Energies of first two electron transitions and ionization potentials of nitrogen ions. Note: for neon all the mentioned energies concerning He- and H-like ions are approximately two times higher.

Nitrogen	Be-like	Li-like	He-like	H-like
E_1[eV] trans.	16 2s - 2p	10 2s - 2p	431 1s - 2p	500 1s - 2p
E_2[eV] trans.	50 2s - 3p	59 2s - 3p	498 1s - 3p	593 1s - 3p
I [eV]	77.5	97.9	552	667

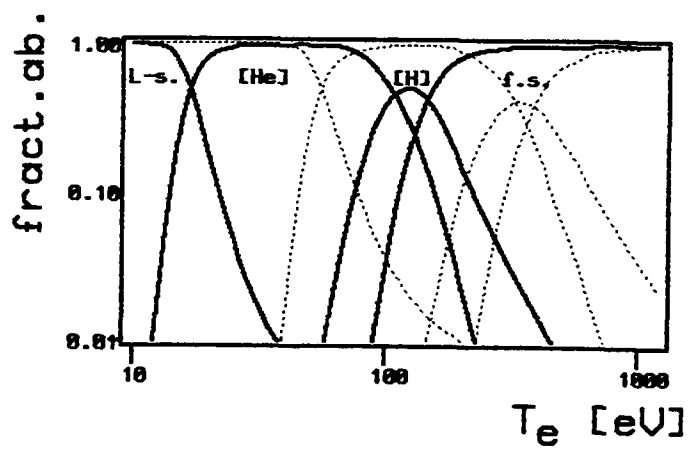


Fig. 1:
Calculated fractional abundances of L-shell (summed up), He-like, H-like, and fully stripped nitrogen ions in dependence on electron temperature. Dotted curves: the same for neon.

The purpose of this work was to obtain approximate information about the radiation of nitrogen Z-pinch as a basis for further investigation in this field.

2. Method, results and discussion

Four-channel system of vacuum X-ray diodes with metalic photocathodes (XRD) and spectral analysis by thin filters [3] were chosen as suitable tools for simple time-resolved radiation measurements in the whole spectral range of nitrogen-plasma intense emission, i.e. approx. 10-700 eV (see Tab. I). For individual spectral ranges different combinations of nitrocellulose (nt, 0.05-0.9 μm thick) and Al (1-3 layers of 0.75 μm foil) filters were used to achieve unambiguous spectral analysis. Spectral characteristics of the apparatus are shown in Fig 2. From the reduction of XRD signals by filters, some "effective" photon energies in individual spectral ranges were found out. This allowed us to derive time-dependent radiation intensities from the signal shapes and magnitudes. The reliability of results was improved comparing the experimental XRD signals with those calculated from the obtained intensities for all the filter-combinations used. The inaccuracy of absolute intensities determined by this procedure can be estimated to be a factor of 2-3.

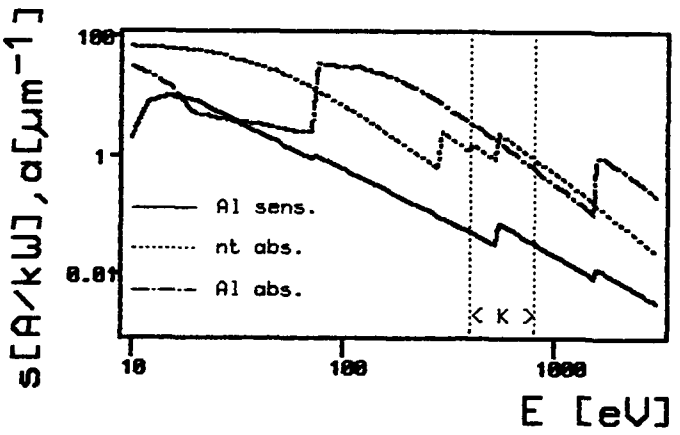


Fig. 2:
Spectral dependence of absorption coefficients of nitrocellulose (nt) and Al filters and of sensitivity of Al photocathode [4-6]. K-shell region of nitrogen plasma emission is marked.

The results reported here are taken from two Z-pinch regimes with current maximum 200 and 160 kA (risetime 1.2 μs), both starting from a hollow gas cylinder of length and diameter of 21 mm. Each regime was optimized by selecting suitable delay between gas

valve opening and discharge switching on (here about 340-350 μs). In both regimes the pinch occurred near the current maximum.

In the "200 kA" regime the shots were quite good reproducible (the shapes and magnitudes of XRD signals within accuracy ±10 %). In Fig. 3 the comparison of XRD signals without and with various filters is shown. It is evident that by using thicker filters the portion of K-shell radiation in signals, with characteristic temporal structure (short peak) corresponding to hot-spots gradually increases in comparison with VUV background radiation.

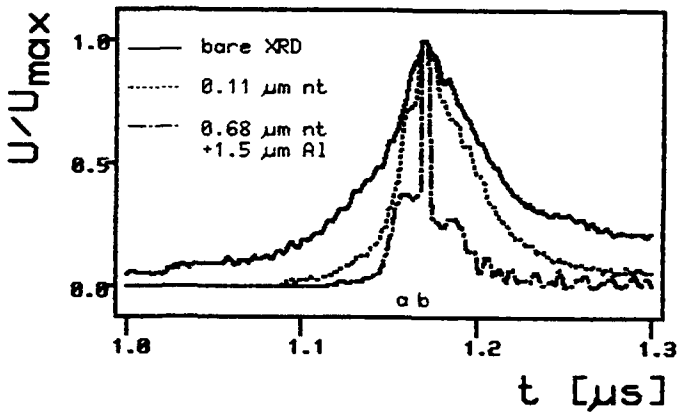


Fig. 3:

Typical XRD signals from nitrogen-puff Z-pinch: bare XRD (U_{max} = 50x4.4 V), channels with 0.11 μm nt (U_{max} = 22 V) and with 0.68 μm nt + 1.50 μm Al filters (U_{max} = 0.22 V).

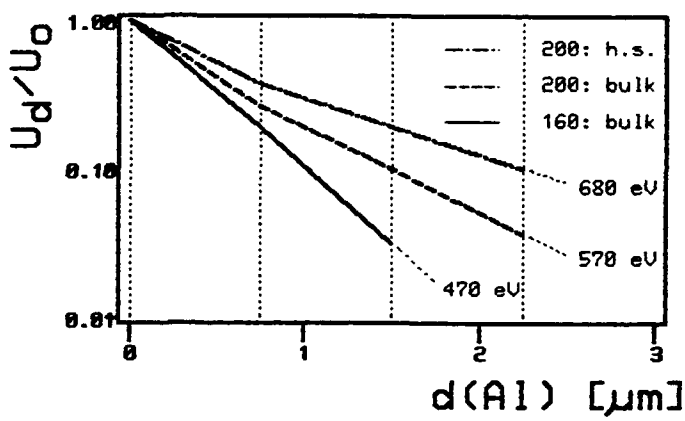


Fig. 4:

K-shell spectrum analysis by Al filters with 0.68 μm nt prefilter. Effective photon energies corresponding to the slopes are indicated.

In Fig. 4 the results of analysis of K-shell radiation by Al filters are demonstrated including 0.68 μm thick nt prefilter which is sufficient to suppress the L-shell radiation completely. The first maximum of K-shell radiation intensity (a in Fig. 3) is taken as a representative display of a bare bulk plasma not influenced by hot-spot radiation. At this instant the K-shell emission is evidently caused by a mixture of He-like and H-like nit-

rogen ions (cf. Fig. 4 with Tab. 1). The more rapid signal reduction by the first 0.75 μm Al layer can be interpreted as about 30 % of the intensity concentrated into the first resonant line of N [He] (430 eV); the rest between 500 and 600 eV is probably substantially influenced by recombination continuum in a narrow spectral interval above the ionization potential of N [He] (552 eV). The attenuation of mere hot-spot peak (i.e. after subtracting the main signal from the bulk, b in Fig. 3) seen from Fig. 4 shows a considerable amount of recombination continuum above the ionization potential of N [H] (667 eV), which indicates a non-negligible presence of fully stripped ions in hot-spot plasma.

The total energy output in K-shell region into 4π solid angle was about 12 J. Most of this amount was emitted from the bulk plasma in spectral range 400 - 600 eV during 50 ns pulse; the hot-spot radiation corresponds to about 1 J energy in spectral range 500 - 700 eV in a short (≈ 6 ns) peak.

Measurements with different sets of filters gave the "effective" photon energy of the dominant part of L-shell radiation between 50 and 70 eV. In this optimized regime only 20 % or less of the total intensity of L-shell radiation was indicated in the range of 2s - 2p resonant lines of L-shell ions. This is due to low abundance of these ions and/or collisional deexcitation which takes place at $n_e \geq 10^{18}$ cm^{-3} for such low-energy transitions [7]. From the comparison of radiation intensity attenuation by Al and nt filters follows that the emission between the L-absorption edge of Al (73 eV) and the first resonant transition of N [He] (430 eV) is not substantial. Total energy emitted in L-shell region was approx. 50 J in pulse duration (FWHM) about 100 ns.

The preliminary conclusions of spectral analysis enabled us to make following rough estimates of bulk-plasma parameters at maximum plasma compression, which could explain the observed time-dependent absolute radiation intensities. Ion density $n_i \geq 10^{19}$ cm^{-3} is composed of about 70 % of N [He], 20 % of N [H] and 10 % (probably in plasma periphery) of lower ionization stages

(i.e. electron density $n_e \approx 5\ n_i$). At a typical pinched plasma cross-section 1 mm^2, the imploded plasma mass is about 10 μg. To reach an expected Bennett equilibrium the thermal energy needed is about 60 J which is comparable to kinetic energy of the imploded plasma shell at calculated final velocity about 10^5m/s (the total plasma internal energy is higher because some 20 J is "stored" in multiply ionized ions). Under the assumption of fully termalized plasma it corresponds to temperature of about 130 eV.

The results reported above evoked a simple idea that the line emission of N [He] has to be a dominant part of K-shell radiation at slightly lower electron temperature (cf. Fig. 1). This was the reason to operate the Z-pinch at somewhat lower discharge currents, typically 160 kA. In this regime the shot reproducibility was worse and the radiation analysis cannot be as detailed as in the 200 kA regime. Nevertheless, typical results of analysis of bulk plasma radiation (shown also in Fig. 4) confirmed our expectation. This means that in this regime the recombination continuum at higher energies is strongly suppressed; this could be important from the point of view of radiation sources.

To conclude, the presented measurements serve us as preliminary ones to realize more detailed investigation of Z-pinch with light working media and small energy input (see [8]).

This work was partially supported by the Grant Agency of Czech. Acad. Sci. under contract No. 14301.

References

[1] Krejčí A.: Czech. J. Phys. 40 (1990), 182.
[2] Krejčí A., Krouský E., Renner O.: in Dense Z-Pinches (eds. N. R. Pereira, J. Davis, N. Rostoker), AIP Conf. Proc. 195, AIP New York 1989, p.474; also Czech.J.Phys. 40 (1990), 1244.
[3] Rauš J., Piffl V.: Czech. J. Phys. B 38 (1988), 1222.
[4] Day R.H. et al.: J. Appl. Phys. 52 (1981), 6965.
[5] Henke B.L.: At. Data Nucl. Data Tables 27 (1982), 1.
[6] Nitrocellulose filters calibration at the VEPP synchrotron in INP Novosibirsk (unpublished).
[7] De Michelis C., Mattioli M.: Nucl. Fusion 21 (1981),667.
[8] Krejčí A. et al.: this conference.

TIME RESOLVED INTERFEROMETRY OF PLASMA RADIATION SOURCE LOADS

prepared by
Edward J. Yadlowsky, Robert C. Hazelton, John J. Moschella, and Thomas B. Settersten
HY-Tech Research Corporation
Radford, VA 2414

Abstract

Models of imploding wire arrays usually assume an expansion and instantaneous ionization of the array material with the subsequent implosion proceeding as a distinct array of individual plasma elements or as a cylindrical shell. Experimental evidence indicates that precursor plasmas form and implode ahead of the array, x-ray pulse lengths are longer than 1D models predict, and part of the array mass is left behind. Interferometry with 10 to 1 magnification is used to probe the initial plasma formation processes. Results on Al and C loads indicate that neutral Al vapor cores or solid C cores persist for up to 400 to 600 ns into the current pulse, and that precursor plasma formation is possible. These results predict similar behavior for the first 40 to 60 ns on current generators with $\dot{I}$ per wire – 1.4 MA/μs.

Introduction

Wire arrays and annular gas puff loads are commonly used on plasma radiation sources to produce soft x-rays. Although 1D models simulate some features of the load implosion and x-ray emission process, such as the implosion velocity and implosion time, other features, such as the x-ray pulse length, are not that well predicted. The observed pulse lengths of 40 ns and 10 ns for wire arrays and gas puffs, respectively, are significantly longer than the 1 ns predicted by models.[1] Furthermore, agreement between the measured x-ray yields and the predicted values can be achieved only if a small fraction of the initial array mass is assumed to be radiating.[2] The difference between the properties of the array and gas puffed loads may be due to the method by which the plasma is initially formed, which is not properly taken into account in 1D simulation.

Bloomberg, et al [3] have modeled the initial evolution of single and multiple wire array loads. They found the wire to initially expand until skin currents formed to shield the interior, at which point a contraction set in and pinching ensued. The pinched wires then implode radially as individual entities. They estimated the plasma formation to require less than 1% of the generator energy required to take the wire to maximum expansion, and so ignored the initial vaporization stage in these fast rising high current discharges. However, Aranchuk, et al [4] find evidence for a residual solid copper core in their experiments on a high current generator delivering 0.5 MA in 120 ns and Aivozov, et al [5] found evidence for a precursor plasma assembling on axis before the wires in the array.

The work herein studies the dynamics of single and two wire arrays using interferometry and absorption/shadow photography. A long pulse (300 ns) dye laser is used in this study to obtain streaked interferograms and absorptiongrams for time resolved investigation of the dynamics of Al and C fiber loads. The results indicate that the initial current in exploded Al wires is carried in a plasma corona surrounding a neutral Al vapor core that persists for 400 ns or more. Discharges on carbon fiber loads occur in a plasma corona surrounding a solid carbon fiber which persists for 600 ns or more. There is evidence for separation of the plasma corona from the core of imploding wires which can lead to precursor formation, straggling in the implosion time of imploding arrays, and mass left at the original array position.

Experimental System

A 7.8 μF capacitor bank was connected to a coaxial electrode structure using a parallel plate transmission line and a rail gap switch. A ringing current waveform having a quarter period of 1.5 μs and a peak amplitude of 324 kA is obtained with a short circuit load.

The 25 μm diameter aluminum wire loads, and the 10 and 33 μm diameter carbon fiber loads, 1.8 cm long, can be loaded without breaking the vacuum. The wire or fiber is tacked to the stainless steel cathode tip by discharging a small capacitor through the load to insure good electrical contact.

The plasma is inserted into one arm of a Mach Zender interferometer. The light source for the interferometer was a flashlamp pumped dye laser delivering a 300 ns long pulse with a linewidth of 0.003 nm or less. A lens, placed after the reference and scene beams are recombined, serves to both magnify the image (4 to 1 and 10 to 1) and to collect and image rays which are deflected by index gradients in the plasma region. If the reference beam is blocked, then an absorptiongram is recorded by the camera, provided that the lens has properly corrected for all refractive effects and there is no significant reflection from the plasma. A shadowgram is obtained if the lens does not adequately compensate for refractive effects.

An image converter camera is used to obtain either streaked images of the plasma evolution at one axial position or a two dimensional 20 ns gated snapshot. The interference fringes were oriented parallel to the wire load for the streaked pictures and perpendicular to the load for the gated framing shots. Radial deflections of the interference fringes are a measure of the radial density profile at that axial position and time. The slit of the streak camera was positioned to view the mid point of the load region.

Results

The streaked interferogram and absorptiongram in Figs. 1 and 2 respectively, present the initial expansion phase of an Al wire load. At onset of current flow, the expanding wire is rendered as a dark object in the photograph either through absorption or refractive (Schlieren/shadow) effects. At later times, the laser radiation penetrates the center of the wire (some interference fringes are visible on the negative of Fig 1).

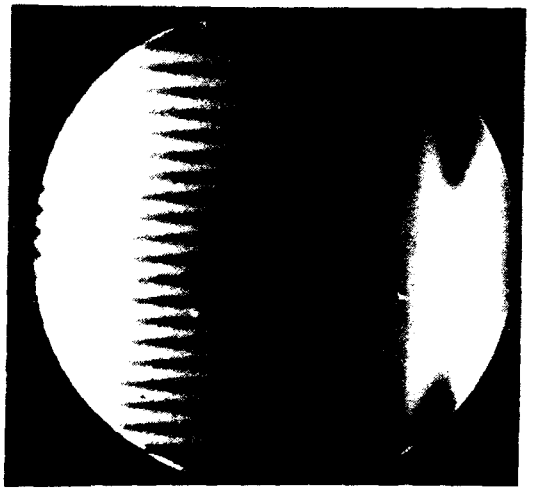


Fig. 1. Streaked interferogram of 25 μm Al wire. The 1 μs streak duration starts at the left. Current begins where wire explodes.Mag 17x.

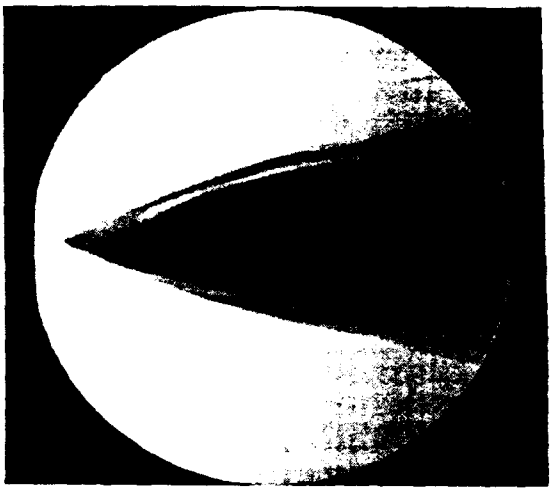


Fig. 2. A 300 ns duration streaked absorptiongram of Al wire. Mag 17x.

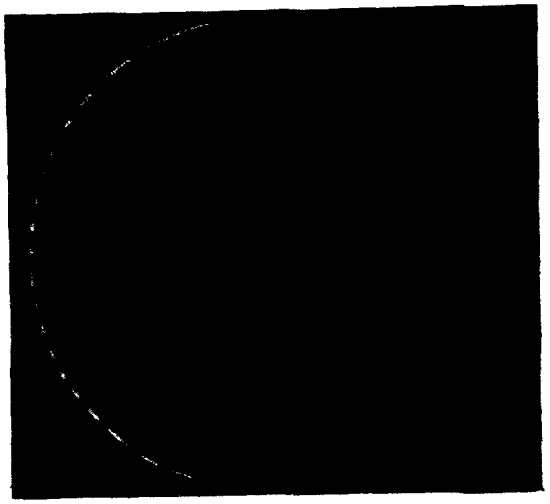


Fig. 3. Interferogram of Al wire 310 ns into current pulse. Mag = 17x.

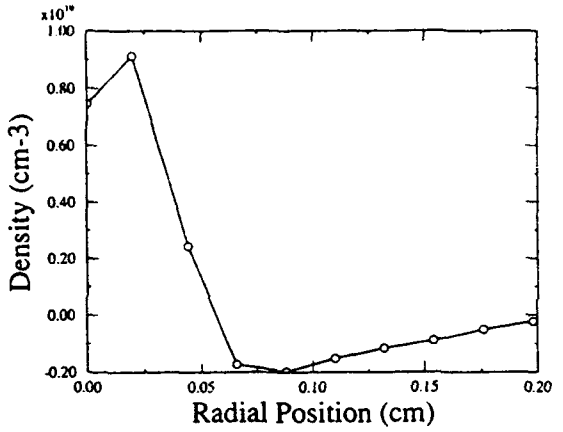


Fig. 4. Density distribution obtained by Abel inverting fringe shifts of Fig. 3. Density of neutral core is 10 times the value shown.

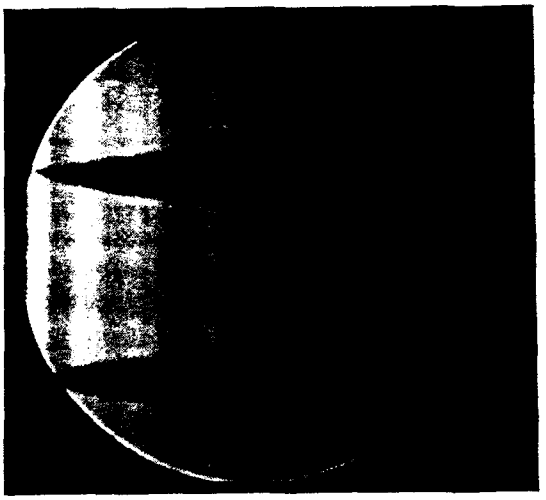


Fig. 5. A 300 ns duration streaked absorptiongram of 2 Al wires 0.35 cm apart. Mag = 6.8.

Figure 3 is a gated interferogram 310 ns into the current pulse, and Fig. 4 is the radial profile of the index obtained by Abel inverting the fringe shifts recorded in Fig. 3. The density profile can be obtained by relating the index to the local density. Since the fringe shifts indicate that the polarizability of the central core and outer shell have opposite polarity, it is natural to assume the core to be predominately neutral Al atoms surrounded by a tenuous plasma corona. Although the index of refraction for an Al vapor is not readily found in the literature, the polarizability of neutral gas (Ar, He, N_2) is approximately 1/10 that of electrons in a plasma having the same density.[6] Assuming a similar polarizability ratio for Al vapor is valid, the density profile in Fig. 4 is obtained if the positive portion of the graph is multiplied by a factor of 10. The bending of the fringes, external to the dark absorbing region of the streaked interferogram of Fig. 1, was measured at a number of times into the current pulse. An electron density profile in the shell was inferred, and the results integrated to give the line density of electrons in the corona. A linear dependence of the electron line density on time was observed during the laser pulse duration. Since the current is a linear ramp at this time, a net ionization rate proportional to dI/dt is implied by these measurements. A streaked absorptiongram of two Al wires 0.35 cm apart is shown in Fig. 5. The implosion velocity of the inside and outside edges of the expanding wire can be determined by measuring the position of the edges as a function of time. This analysis indicates the inside edges to be imploding faster than the outside edges, and can be interpreted to be the initial phase of plasma separation from the core and precursor formation.

A different discharge behavior is observed with carbon fiber loads. The 10 μ carbon fiber appears to be intact for the entire 300 ns duration of the streaked absorptiongram in Fig. 6 which begins 310 ns into the discharge pulse. There is oscillatory plasma behavior surrounding the fiber, with bright emission pulses evident at the pinch points, which does not seem to disturb the fiber itself. In some absorptiongrams a dark, well defined fiber is observed to suddenly disappear with no expansion phenomena characteristic of the Al wire loads visible. In some interferograms, distinct pieces of the carbon fiber are seen to be intact 2.7 μs into the current pulse. The pieces are randomly oriented and off-axis as if they were propelled by an explosion. Figure 7 shows the maximum fringe shift associated with the discharge on a 33 μm carbon load to be displaced from the fiber.

Further analysis of Fig. 2 is possible if the recorded image is truly a measure of the laser absorption by the exploding wire. Estimates of the laser beam deflection by the discharge were obtained by assuming the index profile in Fig. 4 can be approximated by two cylindrical lenses having the maximum index measured in both regions. The results indicate that all of the rays are collected and no shadow effects should be present. However, the picture does reveal a very narrow structure near the edges that could be due to shadow effects caused by strong radially index gradients associated with shock waves. Also the measured indices do not indicate that substantial reflection should occur.

With these caveats, the photographs were analyzed by scanning the negative with a microdensitometer at a number of times into the plasma expansion. An absorption coefficient was inferred using the manufacturers published sensitivity curves for the film and assuming a uniformly absorbing medium. The absorption coefficient was related to plasma parameters using theoretically calculated absorption coefficients obtained by J. Apruzese [7] for a range of densities (neutral and ion) and temperatures. Assuming the Al atoms were uniformly distributed over the measured cross section, temperatures in the range of 0.76 to 2.4 eV were inferred by linear interpolation between the calculated values. At a temperature of 2.4 the resistance of the core was estimated to be 0.9 Ω by assuming uniform current flow and a resistivity value given by the Spitzer expression.

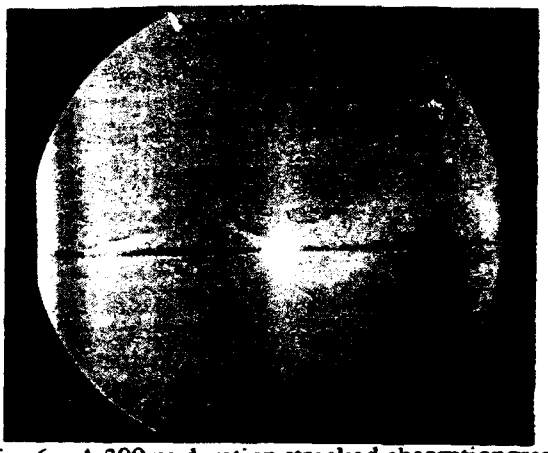


Fig. 6. A 300 ns duration streaked absorptiongram of 10 μm C fiber. Mag = 17x.

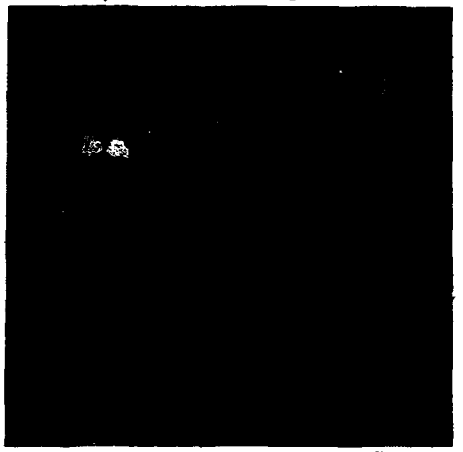


Fig. 7. Interferogram of 33 μm C fiber 465 ns into current pulse. Mag = 17 x.

Discussion of Results

The interferometer was set up with a 10 to 1 magnification and very narrow closely spaced fringes to minimize ambiguities in following a fringe through regions with large density gradients. In spite of those precautions, the density gradients and absorption effects conspired with a slight defocusing in the camera to make the task difficult. The sensitivity of the results to the relationship of fringes far from the column to those within the column was studied by assuming an exterior fringe could be connected to one of 3 adjacent interior fringes. The resulting density profile obtained by Abel inverting these 3 assumed fringe shift patterns went from a profile with a neutral core to one with a hollow center. Furthermore, the profile with the neutral core could account for 60% of the Al atoms in the initial wire whereas the hollow shell profile could only account for 23 % of them. These results, together with the interferograms obtained on other shots, all indicate that a neutral Al core exists up to 0.4 μs or more into the current pulse. A neutral core is visible with single wavelength interferometry only if the degree of ionization of the gas is less than the ratio of the gas to electron polarizability, which has been assumed to be 0.1. The degree of ionization that is predicted for the temperatures inferred from the absorption measurement (0.76 to 2.4 eV) and densities in the range of 2×10^{19} to 2×10^{20} is 100% or more at 2.4 eV, which is incompatible with the less than 10% ionization requirement. Although the value of 2.4 eV is not physically unreasonable, a refinement in the absorption measurement is required for self consistent agreement.

The resistance of the core (0.9 Ω), that is predicted using temperature values obtained from the absorption measurement is excessive, indicating that the corona is the primary current carrying channel. The 0.1 cm thick plasma shell observed in Fig. 4 would provide a 20 mΩ resistive path for the current if the corona temperature was 6 to 7 eV. A wider channel would be required for lower plasma temperatures (0.5 cm thick for a 2 eV plasma).

The results obtained here agree with some of the features predicted by Bloomberg et al.[3] After the current heats and vaporizes the core, the expansion continues because the core is too resistive to shield out the magnetic field. Their model can be used to estimate the corona temperature when expansion stops by requiring the skin depth to be equal to the plasma radius. However, the presence of neutral Al vapor 300 ns into the current pulse is definitely inconsistent with their hypothesis that the vapor is ionized almost instantaneously. Although dI/dt is less in this work than their calculations, it is not clear that this is the important distinction, if an $\dot{I}$ scaling is assumed to hold for the net ionization rate. The neutral core observed here at 300 ns would be expected to occur 30 ns into the current pulse from a generator delivering 2 MA pulse 100 ns long to a 12 wire array where the $\dot{I}$/wire is approximately 10% of the $\dot{I}$ in this study. There is other evidence for a neutral core. Aranchuk, et al [4] concluded that only 2 - 7 % of a wire mass is converted to a radiating plasma with the remainder a solid core when $\dot{I} \sim 4 \times 10^{12}$ A/S.

The precursor plasma formation, inferred from relative velocities of the inside and outside edges of the expanding wires in Fig. 8, is consistent with the observations of Aivozov et al.[5] Furthermore, this separation of the outer plasma layer from the inner core can explain why the x-ray pulse duration is longer

in a wire array than in gas puff plasmas. It could also result in leaving some of the initial mass behind explaining why only a fraction of the total mass can account for the radiated energy.[4]

The difference between the Al and C loads is probably due to the fact that carbon does not melt and vaporize as does Al. The discharge probably initiates as a surface breakdown similar to that occurring on insulators, with desorption and subsequent ionization of gases from the fiber surface providing the initial plasma channel for current flow. The fiber is then consumed by an ablation process, as modeled by Lindenmuth [9] for frozen deuterium fibers. Riordan, et al [10] observed m = 1 instabilities but no m = 0 instabilities with carbon arrays which also left a significant fraction of their mass at the initial array position. This observation is not surprising if the current path is primarily external to the fiber and further emphasizes the possibility of corona plasma separation from the core during implosion.

Conclusion

An interferometer with 10 to 1 magnification has been used to study the spatial structure in the z-pinch channel with resolution not previously reported. Different discharge characteristics are observed with C and Al loads which appear to be due to melting and vaporization properties of the load. With Al wire loads the outside surface of the vaporized and expanding wire is ionized to form a current channel with a neutral vapor core persisting for 400 ns or more. With C fibers, a plasma current channel is formed in desorbed gases and ablated surface layers of the fiber with a solid core persisting for 600 ns or more into the pulse. The initial precursor plasma formation in a two wire array has been observed. Finally, the potential of using laser absorption as a temperature diagnostic in the core of a z-pinch column has been indicated.

References

[1] C. Deeney, Private Communication.

[2] C. Deeney, T. Nash, R. R. Prasad, L. Warren, K. G. Whitney, J. W. Thornhill, and M. C. Coulter, "Role of the Implosion Kinetic Energy in Determining the Kilovolt X-ray Emission from Aluminum Wire-Array Implosion," Phys. Rev. A44, 6762 (1991).

[3] H. W. Bloomberg, M. Lampe, and D. G. Colombant, "Early Expansion in Exploding Multiple Wire Arrays," J. Appl. Phys. 51, 5277 (1980).

[4] L. E. Aranchuk, G. S. Bogolyubskii, G. S. Volkov, V. D. Korolev, Yu V. Koba, V. I Liksonov, A. A. Lukin, L. B. Nikandrov, O. V. Tel'kobskaya, M. V. Tilupov, A. S. Cherenko, V. Ya Tsarfin, and V. V. Yankov, "Radiatively Cooled Z-Pinch Produced by an Exploding Copper Wire," Sov. J. Plasma Phys. 12, 765 (1986).

[5] I. K. Aivozov, V. D. Vikarev, G. S. Volkov, L. B. Nikandrov, V. P. Smirnov, and V. Ya Tsarfin, "Formation of Axial Foreplasma Channel in the Initial Stage of the Compression of a Multiwire System by Megampere Currents (Experimental)," Sov. J. Plasma Phys. 14, 110 (1988).

[6] C. M. Vest, Holographic Interferometry, John Wiley & Sons, N.Y., 355, (1979).

[7] J. Apruzese, Private Communication

[8] I. R. Lindenmuth, G. H. McCall, and R. A. Nebel, "Fiber Ablation in the Solid-Deuterium Z-pinch," Phys. Rev. Lett. 62, 269 (1989).

[9] J. C. Riordan, J. S. Pearlman, M. Gersten, and J. E. Rauch, "Sub-Kilovolt X-ray Emission from Imploding Wire Plasmas," AIP Conf. Proc. No. 75, 35, (1981, Monterey).

Acknowledgements

The authors thank T. C. Towell and W. D. Cook for help with data taking and J. Apruzese for calculations of Al absorption coefficients.

MAGNETIC PICKUP LOOP ANALYSIS ON AN EXPLODING WIRE Z-PINCH

John J. Moschella and Edward J. Yadlowsky
HY-Tech Research Corporation
Radford, VA 24141

Abstract

Magnetic pickup loop signals obtained from an exploding wire z-pinch have been analyzed on the HY-Tech z-pinch. This machine can produce 300 kA at full charge rising in 1.5 μsec. By comparing the observed signals with a model of the driving circuit and stray elements, information on the dynamics of the load has been obtained. The load was modeled as an inductor, where the inductance is a function of the radius which varies with time. Streaked shadowgrams were used to monitor the wire radius for the first 300 nsec. It has been determined that an implosion occurs at least 0.3 μsec into the discharge and the duration of the implosion phase, according to the model, is near 50 nsec.

Introduction

Single wire z-pinches and wire arrays have been investigated as x-ray sources with applications to microlithography and x-ray microscopy. The dynamics of imploding arrays of aluminum wires, as well as single fibre pinches, have been extensively studied.[1-4] Issues such as implosion kinetic energy are important in determining the x-ray yield of the pinch. Therefore, diagnostics which allow us to determine the implosion dynamics can be useful in optimizing the x-ray yield for a given device. Using a z-pinch with single 25 μm aluminum wires, we have been successful in determining when pinching occurs as well as estimating the implosion time. Our z-pinch can produce approximately 300 kA at full charge rising in 1.5 μsec, and has been used to energize loads that are 2 cm in length. The diagnosis of the implosion involves observing the unintegrated signals from magnetic pickup loops close to the load and comparing them to a circuit model which takes into account variations in the load inductance. This technique works on our system because the load, at least initially, is a significant fraction of the total circuit inductance. The initial load impedance in our system is around 68 nH and the total inductance is 180 nH. Therefore, changes in the load radius, which change the inductance, can be observed on the magnetic loop signals. It is very important to note that the signatures of an imploding wire on a pickup loop could be easily missed if the loops were integrated. This technique may be applicable to other systems where the load inductance is a significant fraction of the total inductance.

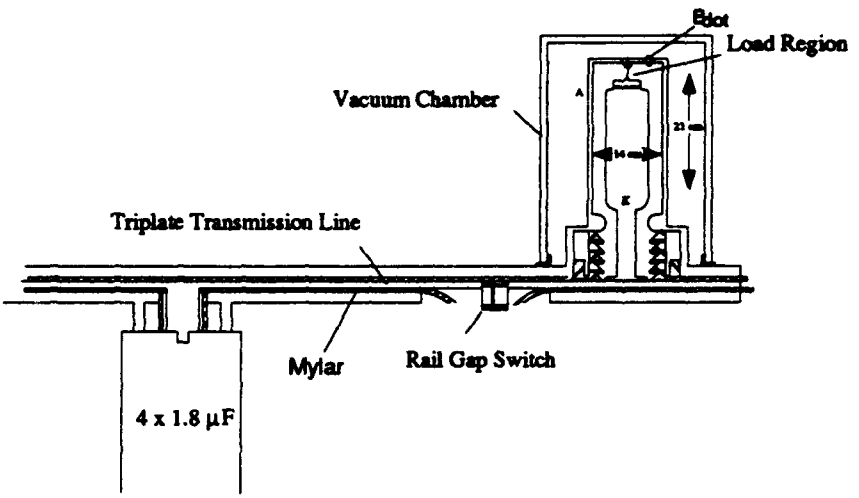


Figure 1. Key elements of the experimental apparatus.

Circuit Model

The z-pinch apparatus is shown in Figure 1. In this system four 1.85 μF capacitors are attached to a parallel plate transmission line and charged as a unit. Once the rail gap switch is fired the capacitors discharge and current flows into the coaxial electrode feed. The loop signals presented in this paper were obtained from the B_{dot} loop located near the load as indicated in Figure 1. The parallel plate transmission line and electrode system have a significant capacitance which cannot be neglected if dI/dt through the load is to be modeled accurately. Taking into account these capacitances, the circuit shown in Figure 2 is the result. For simplicity the nominal resis-

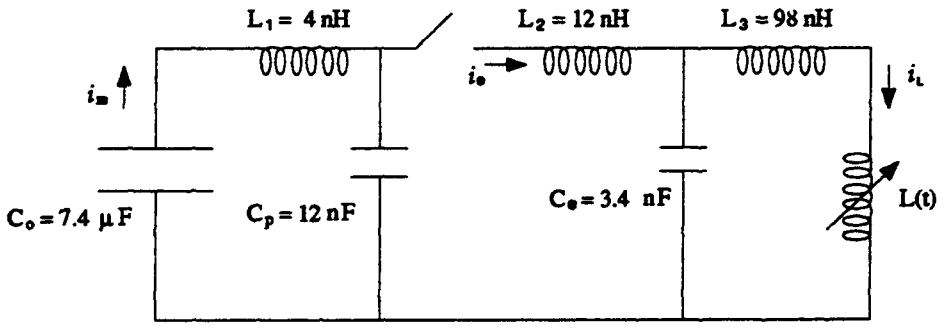


Figure 2. The circuit model for the apparatus in Figure 1. The load, L(t), is modeled as a time varying inductor.

tances have been omitted from the drawing. In the figure, C_o is the main capacitance, C_p the capacitance of the parallel plates, C_e the capacitance of the system after the switch, and L_1, L_2, and L_3 are the inductances of each respective section. For shots with aluminum wires the load is modeled as a time varying inductance, L(t). The currents and current derivatives were determined by integrating the appropriate differential equations using a 4^{th} order Runge-Kutta integration routine.

The values of the constant circuit elements were determined in the following manner. A shorting bar was placed in the system where the wire load would normally be and pickup loop signals were recorded. By looking at the long time scale behavior, the total inductance of the system was measured. On this time scale the stray capacitances were negligible and a simple LC circuit behavior was observed. On a much shorter time scale, about half of a quarter cycle, high frequency oscillations due to the capacitive coupling of the stray elements was observed. While maintaining the same total inductance in the model, the circuit elements were varied until the numerical solution produced a good match to the data. Of course reasonable estimates of some of these elements could be made given the geometry of the parallel plates, for instance. An example of the numerical solution compared to a shorted load signal is shown in Figure 3 where values

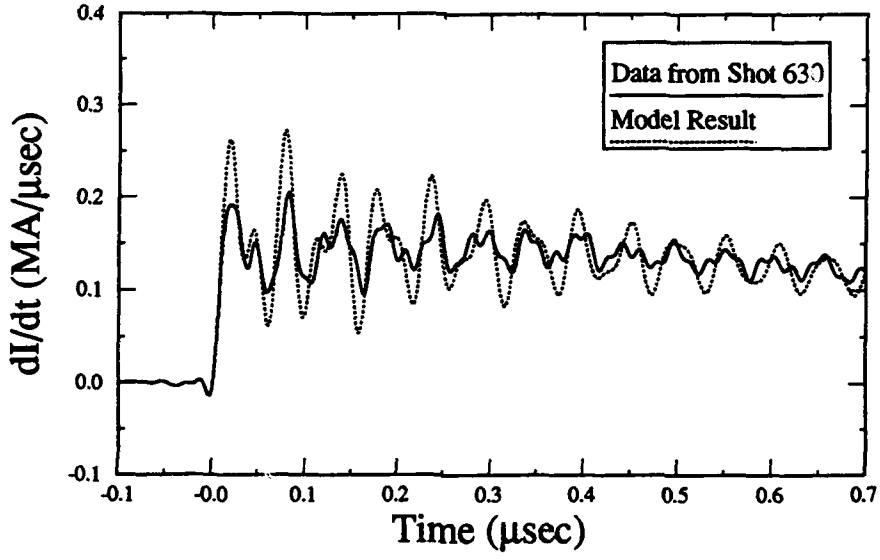


Figure 3. A comparison of the model result and the data obtained with a shorting bar at 25 kV.

for the circuit elements in Figure 2 were used. The data in this plot was obtained from the upper B_{dot} probe. A complication, which is not included in the model, is the coupling of the mini-Marx

bank which triggers the rail gap switch. This produces a very high frequency oscillation prevalent in the first few tenths of a microsecond. This is a very large effect with the shorting bar and the signal shown in Figure 3 has been filtered numerically. The mini-Marx coupling is much less prevalent with the higher inductive aluminum wire loads and the filtering was not necessary in those cases.

Some simplifications were made to determine L(t) for wire loads, namely that the wire was assumed to be a perfect conductor for all times and the radius was uniform along its 2 cm length. Given these assumptions the inductance of the load is a simple function of the wire radius. This function will be dependant on the electrode geometry for a given system. To determine this function, measurements were made with four 2 cm shorting bars with radii varying from 0.8 to 11 mm. The total inductance was measured in each case and it was found that the following function fit very well to the data,

$$L(r) = (7.3)\ln(142/r) + 119 \quad [nH], \qquad (1)$$

where r is the radius in millimeters. Figure 4 shows the data that was obtained along with the function in equation (1). If information as to the dependance of the wire radius with time can be measured, or guessed at, then L(t) can be determined using equation (1).

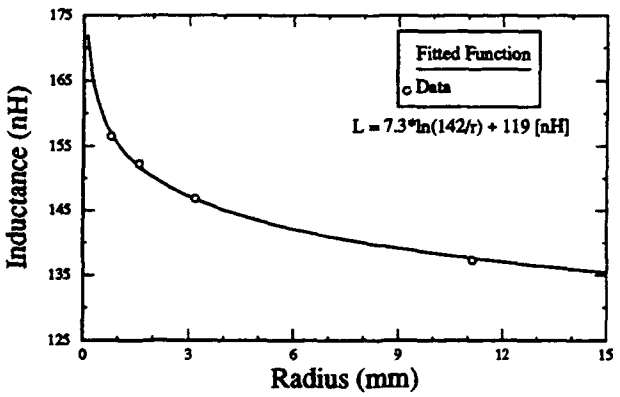


Figure 4. Data obtained from different size shorting bars with the fitted function.

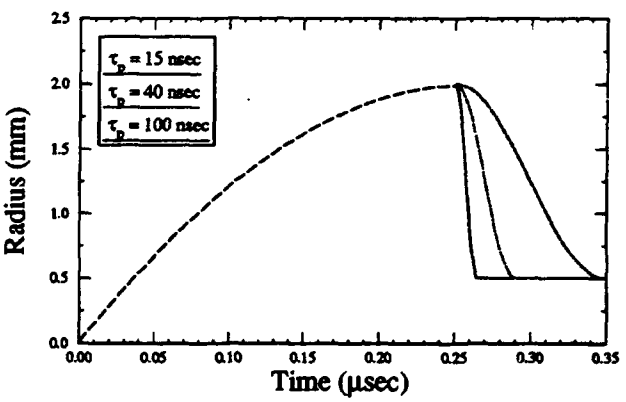


Figure 5. Radius as a function of time used in the model. Three different τ_i values are shown, 15, 40 and 100 nsec.

By observing streaked laser shadowgrams of exploding wires it was determined that the load expanded during the first 250 nsec of the discharge to a peak radius of about 2 mm.[5] After this time it became unclear what happened to the load using the streaked shadowgram. The expansion of the wire was very consistent and was monitored for many shots. Therefore, the circuit model

incorporated this expansion phase, followed by a quiescent phase where the radius was constant, and finally a pinching phase. Let us define the implosion time, τ_i, as the time to go from the maximum to minimum radius and the pinching time, τ_p, as the time when the implosion begins. The circuit model was set up so τ_p and τ_i could be varied, as well as the maximum and minimum radii. The duration of the expansion phase was kept constant at 250 nsec. The implosion profile used was the first quarter cycle of the cosine function adjusted so r(t) and dr/dt were both continuous. Figure 5 shows the function r(t) for the cases where the maximum radius is 2 mm, τ_p is 250 nsec, the minimum radius is 0.5 mm and τ_i is 15, 40 and 100 nsec respectively. These profiles, in conjunction with equation (1), determine L(t) and were used in the circuit model.

Comparison of Model and Aluminum Load Shots

The comparison of data with 25 μm aluminum loads to dI/dt obtained from the model revealed that pinching was occurring between 0.3 and 0.6 μsec into the discharge. Figure 6 shows this comparison for shot 658 where the dI/dt was calculated from the model using τ_i = 40 nsec, τ_p = 0.355 μsec, a maximum radius of 2 mm and a minimum radius of 0.2 mm. On this shot the charging voltage was 25 kV, which is half of the maximum. It can be observed that the pinch signature is a negative spike in the data which is also properly modeled in the calculation. Of the four parameters that can be varied in the model, the maximum radius is known accurately from the streaked shadowgram observations. The minimum radius at this point is purely a guess, and if a different minimum radius was used an accurate match to the data could also be obtained by adjusting the implosion time. For instance, if a larger minimum radius was assumed in the model, it would cause the negative spike to decrease in magnitude and sharpness. But if τ_i was decreased as well, than a match as close as the one in Figure 7 could be obtained. The bottom line is that without an independent measure of the minimum radius the matched solutions are not unique. The saving grace is that the calculation is more sensitive to both τ_i and τ_p than it is to the minium radius. Therefore, a reasonably accurate measurement of these parameters is possible despite the lack of information on the radius, simply by assuming a reasonable value. An example of this sensitivity is shown in Figure 7, displaying a calculation with τ_i = 15 and 40 nsec respectively. It can be seen that these signals are drastically different. We have been able to safely determine the time of the pinch to within 30 nsec and the implosion time to ± 15 nsec by using minimum radii between 0.1 and 0.2 mm. For our apparatus the pinch time, τ_p, varied between 0.3 and 0.6 μsec and the implosion time was about 40 nsec for most shots.

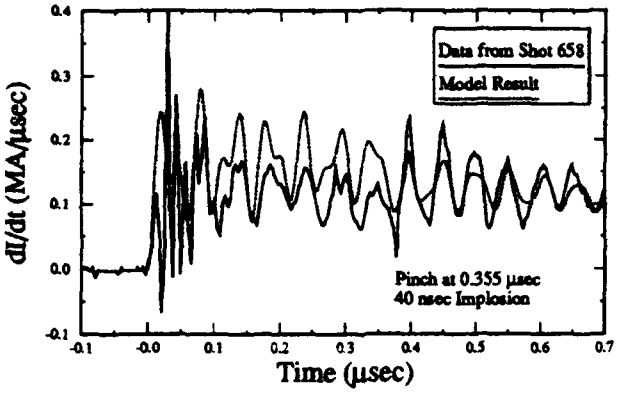


Figure 6. Data obtained from shot 658 along with the model results with τ_p=0.355 μs and τ_i = 40 ns. The dotted curve is the calculation.

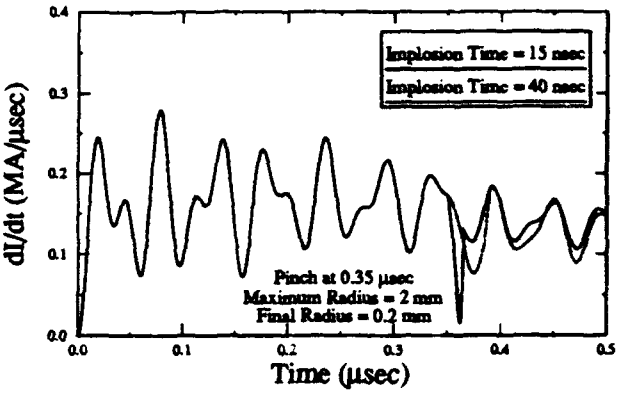


Figure 7. Results of the model for different values of τ_i equal to 15 and 40 nsec for τ_p=0.35 μs. The dotted curve has τ_i = 40 ns.

Discussion

The results indicate that a relatively long expansion phase, at least 300 nsec, is followed by a pinching phase which is 40 nsec in duration. One might expect that if the expanding wire was a highly ionized plasma, then pinching would occur earlier. Also, given the current rise time of our machine it seems unlikely for a plasma column to pinch in only 50 nsec. The model calculations also reveal, as can be clearly observed in Figure 6, that the magnitude of dI/dt before τ_p is lower than predicted. Since the constant circuit elements are determined, one conclusion is that the load is more inductive than the model assumes, and resistive effects should be included. It was assumed that the load was always a perfect conductor and therefore its inductance could be determined from its radius. If during the first 250 nsec the expanding wire was resistive, the current channel would penetrate into the column increasing the inductance and lower dI/dt. The short pinch times predicted by the calculations are more difficult to explain. It is quite possible that we are not imploding the wire as one would in a z-pinch but a vacuum spark is occurring. Very fast implosions have been observed in these devices for discharge periods similar to ours.

References

[1] N.R. Pereira, and J. Davis, J. Appl. Phys. **64**(3), R1 (1988).
[2] C. Deeney *et al.*, Phys. Rev. A **44**(10), 6762 (1991).
[3] E.S. Figura, G.H. McCall, and A.E. Dangor, Phys. Fluids B 3(10), 2835 (1991).
[4] W. Kies *et al.*, J. Appl. Phys. **70**(12), 7261 (1991).
[5] E.J. Yadlowsky, R.C. Hazelton, J.J. Moschella, and T.B. Settersten, these proceedings.
[6] V.A. Veretennikov, *et al.*, Sov. J. Plasma Phys. 7(2), 249 (1981).

PHENOMENOLOGICAL MODELING OF ARGON Z-PINCH IMPLOSIONS

K. G. Whitney and J. W. Thornhill
Naval Research Laboratory, Washington D.C. 20375
C. Deeney and P. D. LePell
Physics International Inc., San Leandro, CA. 94577
M. C. Coulter
Berkeley Research Associates, Springfield, VA. 22151

ABSTRACT

We investigate some of the effects of plasma turbulence on the K-shell emission dynamics of argon gas puff z-pinch implosions. The increases that turbulence produces in the plasma viscosity, heat conductivity, and electrical resistivity are modeled phenomenologically using multipliers for these quantities in the MHD calculations. The choice of multipliers was made by benchmarking a 1-D MHD simulation of a Physics International Inc. argon gas puff experiment against the inferred densities and temperatures achieved in the experiment. These multipliers were then used to study the parametric dependence of the K-shell emission on the energy input to the argon plasma for a fixed mass loading. Comparisons between turbulent and non-turbulent argon implosions are made.

INTRODUCTION

In two previous papers,[1,2] the analysis of a series of 1-D MHD aluminum calculations was carried out to quantify the roles that the imploding mass and final implosion velocity have in determining the yield of K-shell x-rays in z-pinch implosions. The yield behavior predicted in these papers was then investigated in a series of experiments conducted at Physics International Inc..[3] One of the basic ideas of the theoretical work was confirmed in the experiments; namely, that, to achieve bulk-plasma emission of K-shell x-rays from imploding z-pinch plasmas, it is necessary to achieve a minimum implosion velocity (dependent on the atomic number, Z, of the plasma). This velocity is essentially determined by the requirement that the maximum kinetic-energy-per-ion generated during run-in be larger than the minimum energy, E_{min}, needed to heat and ionize an ion into the K-shell once the plasma stagnates and thermalizes on axis. For elements up to krypton, $E_{min} \cong 1.012Z^{3.662}$ eV/ion. Therefore, for argon, $E_{min} \cong 40$ keV/ion.

An analysis of the x-ray data from the Physics International experiments also showed that the theoretical calculations produced ion densities on axis and K-shell power outputs that were 2 to 3 orders of magnitude larger than those seen in the experiments. Experimental K-shell yields were also generally larger than the calculated yields, which had been calculated on the basis of kinetic energy conversion alone. These observations can be taken as evidence for the presence of plasma turbulence in the experiments, whose effects had not been modeled in the calculations. There are two possible sources for this turbulence. The generation of ion-acoustic microturbulence would lead to an increase in plasma electrical resistivity;[4] whereas, the generation of hydromagnetic turbulence (as induced, for example, by Rayleigh-Taylor instabilities[5]) would lead to increases in the viscosities (Reynold's stresses) and heat conductivities needed in an average 1-D description of the flow.

In order to begin an assessment of the effect of enhanced transport coefficients on the z-pinch dynamics, we employ a phenomenological approach in the MHD calculations; namely, we multiply the coefficients of viscosity, heat conductivity, and electrical resistivity by constants (as is done, for example, in the treatment of inhibited heat transport in laser produced plasmas[6]). These multipliers were determined by varying them systematically until a reasonable agreement was obtained between a 1-D simulation of a Physics International Inc. experiment and the experimental data. The calculated quantities that were matched to the measured data were the K-shell yield and the average temperature and density of the K-shell x-ray emitting region. The latter quantities were inferred from the measured K-shell spectrum, pulsewidth, and pinhole picture.[7] The multipliers that we obtained by this process and that are used in the calculations described in this paper are: 24.5 for the artificial viscosity, 30 for the heat conductivity, and 20 for electrical resistivity. These multipliers correspond to physically realizable increases or decreases in the turbulent transport of momentum, heat, and charge, and they lead to reductions by 2 to 3 orders of magnitude in the densities that are calculated on axis.

We specifically discuss the effect that turbulence has, as modeled above, in softening the implosions generated in argon gas puffs and in altering the K-shell emission characteristics of these z-pinch implosions. The calculations that were carried out for this work are the same as those described in References 1 and 2, except that argon replaces aluminum. For the non-turbulent calculations, the current is ramped linearly and terminated when the plasma implodes to roughly 14% of its original radius. All the calculations are begun with the argon plasma at an average radius of 1 cm. 90% of its mass is concentrated in a 1 mm sized shell; the remaining mass is distributed in 6 inner cells inside the shell with a mass density that decreases exponentially toward the axis. This initialization procedure provides the calculations with numerical stability, but it also simulates the backpressure effects of plasma mass that is blown toward the axis by the gas jets or by the initial explosion of the (aluminum) wires. Each of the turbulence modeled calculations corresponds to a non-turbulent calculation. Thus, the current is linearly ramped in either case to prescribed values at prescribed times and then terminated whether or not the plasma has imploded to 14% of its initial radius.

In addition, in the following set of calculations, the argon mass is fixed at 200 μg/cm (or at 600 μg/cm for eight turbulence calculations) and the energy input to the plasma is varied by changing the strength of the final current as well as its risetime (see Ref. 1). Energy input to the plasma per ion, E_{inp}, is measured in terms of E_{min}, i.e., in terms of $\eta^* \equiv E_{inp}/E_{min}$, and E_{inp} is calculated as the sum of the $\mathbf{j} \times \mathbf{B}$ work and the Ohmic heating.

RESULTS

Figure 1 displays one of the major quality differences between the turbulent and non-turbulent implosions. In general, energy is delivered to the plasma during run-in in three ways: through Ohmic heating, through pdV work, and through the generation of kinetic energy. The kinetic energy generated per ion, K_{ion}, is also conveniently measured in units of E_{min}:[1] $\eta \equiv K_{ion}/E_{min}$. Figure 1 shows that most of the energy delivered to a 200 μg/cm argon load during run-in in a non-turbulent calculation is kinetic. The plasma is driven easily to radii of $\leq$1.4 mm with a negligible generation of back-pressure. Because the turbulently calculated implosions are much more viscous and distribute energy much more rapidly than their non-turbulent counterparts, they generate back-pressure much sooner than the non-turbulent implosions and produce roughly 35%

less kinetic energy. As Figure 2 shows, the Ohmic energy generated during run-in can also be a significant portion of the total energy input in a turbulent implosion when the coupled energy per ion is small, $\eta^* \leq 6$. Primarily, however, these calculations demonstrate that the generation of kinetic energy in a soft turbulent implosion is impeded by the early development of plasma back-pressure. Note finally that, in both Figures 1 and 2, the energy division within a turbulent implosion is only weakly mass dependent.

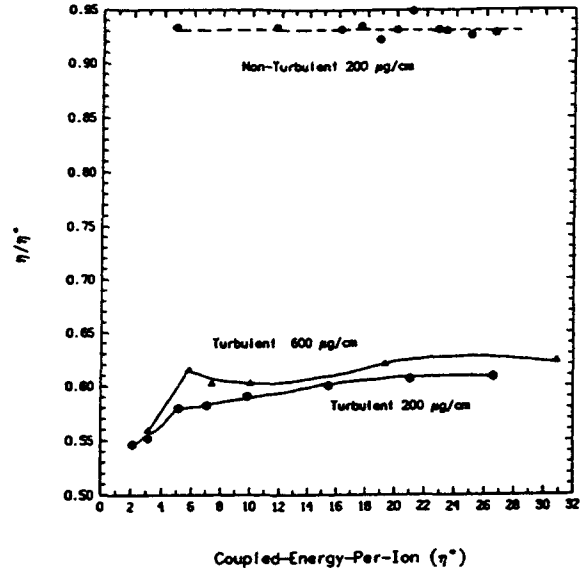


Figure 1. Ratios of the peak kinetic energy to the total coupled energy for turbulent and non-turbulent implosions.

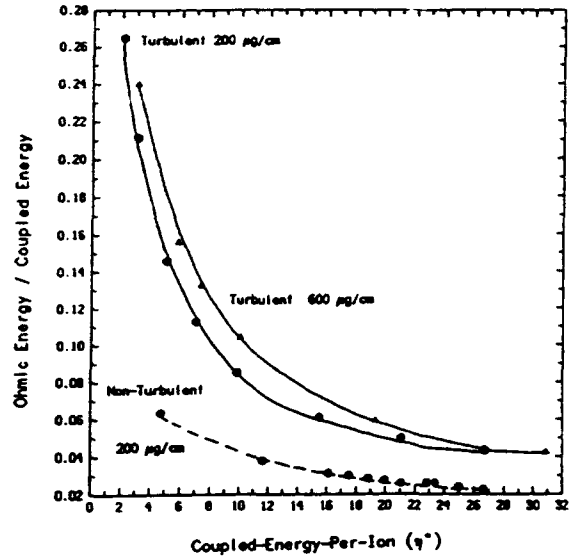


Figure 2. Ratios of the Ohmic energy input to the total coupled energy per ion for turbulent and non-turbulent implosions.

The way that the softening of the argon implosions affects the conversion of $\mathbf{j} \times \mathbf{B}$ work to K-shell x-rays is shown in Figure 3. In the non-turbulent, laminar calculations, the yield continues to rise until η^* values of ~22 are reached ($\eta \sim 20$), peaking at a yield of roughly 80 kJ/cm. By comparison, the same calculations for a 200 μg/cm aluminum plasma produced a peak K-shell yield of 54 kJ/cm at an η value of 27.5 (see Ref. 1). In the turbulence calculations with 200 μg/cm of argon, the K-shell yield quickly rose and essentially saturated at values slightly less than 20 kJ/cm for $\eta^* \geq 5$. When the imploded mass is raised to 600 μg/cm, the yield peaks near 130 kJ/cm for $\eta^* \geq 10$, and then it fell slowly, again not changing very much over a broad η^* range. Thus, much larger amounts of kinetic energy can be converted efficiently to K-shell emission in laminar than in turbulent implosions for a given load mass. One sees from Figure 4, in fact, that, in all cases, the conversion efficiency to K-shell emission eventually falls as the kinetic energy of the implosion increases. However, it falls much less rapidly in the laminar than in the turbulence calculations. Finally, Figure 4 suggests that as long as the conversion efficiency is larger than 20%, the yield will rise as the kinetic energy generated during the implosion is increased.

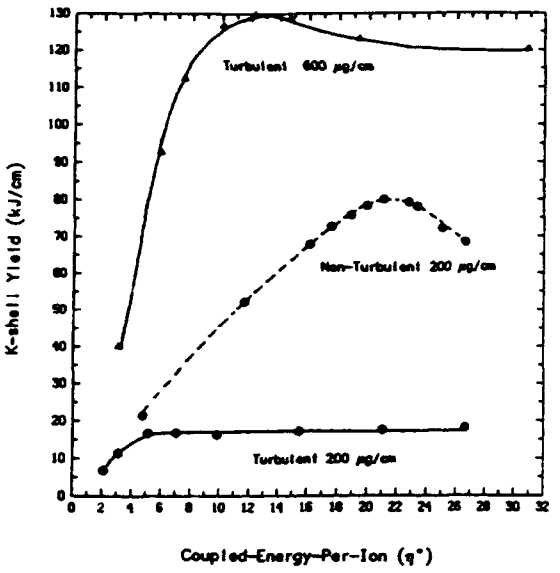


Figure 3. Calculated argon K-shell yields for turbulent and non-turbulent implosions.

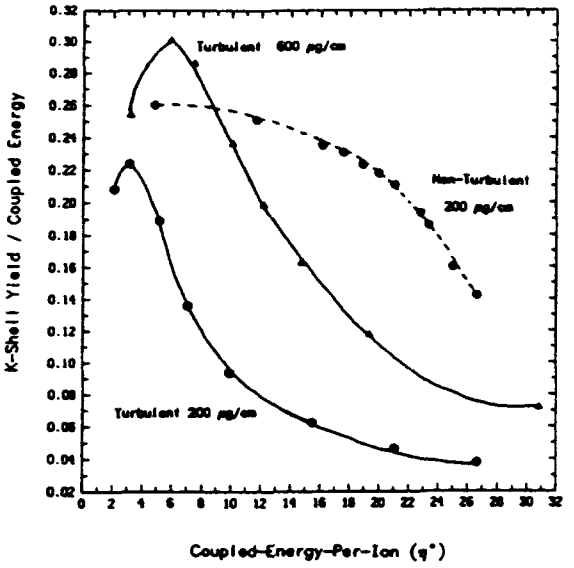


Figure 4. Ratios of the calculated argon K-shell yields to the total coupled energy for both turbulent and non-turbulent implosions.

The underlying reasons for the yield behavior in Figure 3 can be seen in Figures 5 and 6. In these figures, the maximum values of the average ion densities and charge states that were reached in the implosions are plotted. In the non-turbulent implosions, average ion densities in excess of 10^{22} ions/cm^3 were attained (Figure 5). These densities fell steadily as the kinetic energy of the implosion was increased. This fall is correlated with the continuous rise in the peak of the calculated average plasma temperature: from 1 to 8 keV between $\eta^* = 5$ and $\eta^* = 28$. As a result of the temperature increase and the density decrease, the plasma eventually can burn through the K-shell as seen in Figure 6 causing the x-ray yield to fall.

In the 200 μg/cm turbulence calculations, the average density, temperature, and charge state all increase as the kinetic energy of the implosion is increased. In these implosions, however, the densities are 2 orders of magnitude lower than in the laminar calculations, and, therefore, the plasma more quickly burns through the helium-like ionization stage ($16 \leq \langle Z \rangle \leq 17$), although its progression through the hydrogen-like system is slowed as the yield remains largely unchanging. By increasing the mass a factor of three in the turbulence calculations, the peak average densities are increased by more than a factor of 6. This, in turn, leads to a more rapid rise in the average charge state of the plasma as a function of energy input and to a more complete burn-through of the K-shell than occurred in the 200 μg/cm implosions.

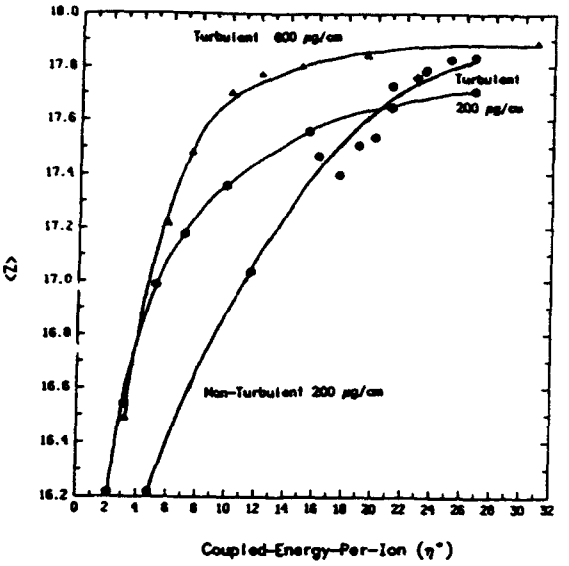


Figure 5. The peak of the average charge state calculated in each of the turbulent and non-turbulent implosions.

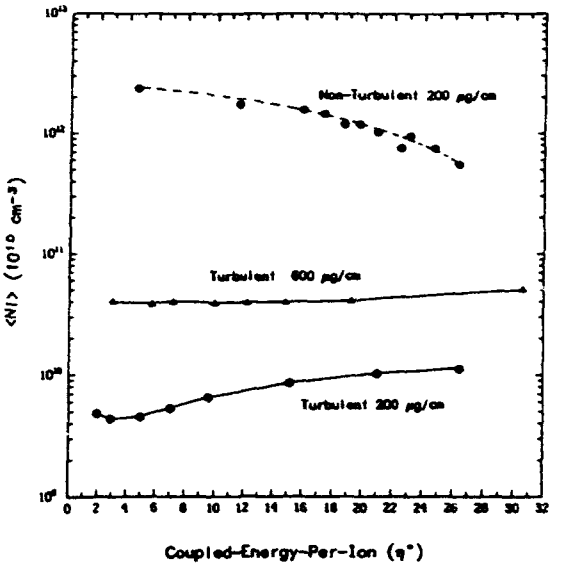


Figure 6. The peak of the average ion density calculated for each of the turbulent and non-turbulent implosions.

SUMMARY AND CONCLUSIONS

In two earlier papers,[1,2] a series of 1-D MHD calculations were described that showed how the imploded mass and the kinetic energy generated per ion influence the K-shell emission characteristics of a z-pinch. However, these calculations predicted an ideal implosion dynamics, which was not seen in experiments.[3] Based on the experimental evidence and on 2-D MHD z-pinch calculations,[5,6] it seems likely that some or all of the missing physics in the 1-D calculations is caused by plasma turbulence. To test this hypothesis, we employed a phenomenological approach in order to incorporate turbulence effects into our 1-D MHD calculations. Multipliers were introduced for the plasma (artificial) viscosity, the heat conductivity, and the electrical resistivity. It was then possible to make an appropriate choice for these multipliers so that the 1-D MHD calculations produced approximately the same plasma conditions and the same K-shell yield as a Physics International argon gas puff experiment. Again this provided supporting evidence for the presence of plasma turbulence in z-pinch experiments.

In order to continue to explore the consequences of this hypothesis, we utilized these same empirically determined multipliers in this paper to make a preliminary determination of how the altered energy, momentum, and charge conductivities would be expected to affect the K-shell emission characteristics of argon implosions. In general, phenomenological turbulence modeling does provide better agreement with experiment than non-turbulence modeling since the calculated ion densities and radiative powers are smaller and radiative pulsewidths are larger in the turbulence than in the non-turbulence calculations. In addition, some of the preliminary conclusions from the current-off calculations that were described in this paper are: (1) A larger mass loading is

required to achieve efficient K-shell yield scaling when turbulence is included in the modeling (for a given η), because turbulence lowers the stagnation mass density for a given mass loading, and consequently the ability of the plasma to radiate is diminished. The radiative capacity can be increased by imploding more mass. (2) When turbulence is included, the onset of K-shell burn-through and lower plasma densities severely limit the maximum K-shell yield that is attainable from a given mass (as opposed to the non-turbulent case). (3) The efficient scaling regime is much more restricted when turbulence is modeled, e.g., for the 200 μg/cm non-turbulent implosion, the efficient scaling region extends to $\eta \cong \eta^* = 22$; whereas, it extends to only $\eta \cong 2$ ($\eta^* \cong 4$) in the turbulence calculations.

While we have investigated in this work some of the effects that turbulence will have on the kinetic energy scaling of K-shell emission from z-pinch implosions, it is equally important to determine the scaling of turbulence effects with plasma mass, current, and kinetic energy and with the atomic number of the imploded plasma. To accomplish this, more theoretical justification for the phenomenological approach used in these calculations will be required, and more z-pinch experiments will need to be carried out and carefully analyzed for these effects.

ACKNOWLEDGEMENT

This work was sponsored by the Defense Nuclear Agency

REFERENCES

1. K. G. Whitney, J. W. Thornhill, J. P. Apruzese, and J. Davis, J. Appl. Phys. **67**, 1725 (1990).

2. J. W. Thornhill, K. G. Whitney, and J. Davis, J. Quant. Spectrosc. Radiat. Transfer **44**, 251 (1990).

3. C. Deeney, T. Nash, R. R. Prasad, L. Warren, K. G. Whitney, J. W. Thornhill, and M. C. Coulter, Phys. Rev. A **44**, 6762 (1991).

4. K. G. Whitney and P. E. Pulsifer, "Non-Maxwellian Electron Distributions in High Current Discharges", submitted to Phys. Rev. Lett. for publication.

5. T. W. Hussey, N. F. Roderick, and D. A. Kloc, J. Appl. Phys. **51**, 1452 (1980). 195:3-78 (1989).

6. see, for example, W. C. Mead, et. al., Phys. Fluids **26**, 2316 (1983).

7. M. C. Coulter, K. G. Whitney, and J. W. Thornhill, J. Quant. Spectrosc. Radiat. Transfer **44**, 443 (1990).

8. C. Deeney, P. D. LePell, F. L. Cochran, and M. C. Coulter, "Argon Gas Puff Implosion Experiments and Two Dimensional Modeling", submitted to Phys. of Fluids for publication.

RADIATION HYDRODYNAMICS OF AN IMPLODING ARGON PUFF GAS PLASMA

J. Davis
Plasma Physics Division
Radiation Hydrodynamics Branch
Naval Research Laboratory
Washington, D.C. 20375
and
F.L.Cochran
Berkeley Research Associates
Springfield, Va. 22151

ABSTRACT

The implosion dynamics of an argon puff gas plasma is investigated using a 2-D radiation hydrodynamics/circuit model. The focus of this research is to determine and evaluate the radiative properties and performance of the imploding plasma for conditions created by driving a rapidly rising current through the Z-pinch load with a terawatt generator characteristic of the Double Eagle and Saturn simulators.

INTRODUCTION

Z-pinch plasma loads driven by terawatt pulsed power generators produce a hot dense plasma accompanied by an intense burst of soft x-rays. In this paper we investigate the 2-D non-LTE radiation magnetohydrodynamics of a Z-pinch argon puff gas to evaluate and determine its radiative properties and performance on the Double Eagle and Saturn generators, respectively. In addition, numerical simulations have been performed both for a tilted and untilted nozzle design on the Double Eagle generator to asses its performance for improving radiative yields of the argon puff gas as a function of tilt angle.[1] Finally, it is well known that it is difficult to obtain agreement with the complete suite of experimental data: x-ray pulse widths and yield, temperature and density of the radiating region, and collapsed radius using 1-D numerical simulation models without enhancing some or all of the transport coefficients. A comparison of the x-ray pulse width as a function of linear mass density is made between a 2-D simulation and a number of 1-D simulations for Spitzer resistivity with multiplicative factors for a typical argon gas puff.

MODEL

The equations describing the model are presented below: they include the equations of hydrodynamics, Maxwell's equations, and rate equations representing the population of the atomic levels as well as the charge states.

$$d\rho/dt=-\rho\nabla\bullet u \qquad (1)$$

$$\rho du/dt = -\nabla(P_e + P_i + Q_a) + JXB/c\,, \tag{2}$$

$$d\varepsilon_e/dt + P_e dV/dt = -V\nabla\bullet q_e + V\eta J^2 + P_{rad} + V\dot{C}_{ei}(T_i - T_e)\,, \tag{3}$$

$$d\varepsilon_i/dt + (P_i + Q_a)dV/dt = -V\nabla\bullet q_i + V\dot{C}_{ei}(T_e - T_i). \tag{4}$$

To these equations are added Maxwell's equations, viz.,

$$\nabla \text{ X } B = 4\pi J/c, \tag{5}$$

$$\nabla \text{ X } E = -\partial B/c\partial t\,, \tag{6}$$

along with Ohm's law,

$$E = \eta J - u \text{ X } B/c. \tag{7}$$

In eqs. (1)-(6) $P_{e,i}$ are the material pressures for electrons and ions, $\varepsilon_{e,i}$ are the specific energies, ρ is the density, V is the inverse of the density, $q_{e,i}$ are the heat fluxes, $\dot{C}_{e,i}$ is the electron-ion energy exchange term. P_{rad} is the radiative power, and ηJ^2 is the ohmic heating. In eqs. (3) and (4), Q_a is an artificial viscosity used for numerical stability in regions of strong compression.

The atomic physics model contains all the ground states and 64 excited states distributed throughout the various ionization stages with particular emphasis in the K-shell and some in the L-shell. There are 74 spectral lines carried in the calculation. The local approximation is used to evaluate the line opacity within each computational zone. Equation Of State tables are constructed from this model and used in the dynamic calculations. Table lookups for P_{rad}, T_e, and <Z> based on internal energy and density are employed. The radiation spectra are produced in a static post-process calculation using a detailed atomic physics model and restart data from the dynamic simulations. The computational model is a 2D, cylindrically symmetric annular R-Z geometry and employs a Lagrangian push followed by an Eulerian remap phase. The simulation uses a voltage waveform to drive a circuit model characteristic of the load and generator to calculate a self-consistent current.

RESULTS

The first aspect of this investigation is to asses whether an inwardly tilted nozzle design on the Double Eagle generator improves the radiative yield of an imploding puff gas plasma. A comprehensive analysis based on a number of 2-D MHD simulations was performed to evaluate the influence of " zippering " on the implosions dynamics as a function of linear mass density and nozzle tilt angle. The results of the simulations can be succinctly summarized as follows: that for a linear mass density of about 55μgms/cm and a nozzle tilt of 10° the zippering effect is removed producing a more nearly uniform implosion

accompanied by an increased K-shell radiative yield. Fig. 1 shows the behavior of the normalized implosion parameter η, which is a measure of the ratio of the implosion kinetic energy/cm to the sum of the minimum amount of energy required to get into the K-shell plus the total thermal energy,[2] as a function of time. It is clear from the figure that for a 0° tilt (or straight) nozzle that motion along the z-axis corrupts the implosion. For the 10° tilt, motion along the z-axis is suppressed in favor of radial motion and improves the uniformity of the implosion and produces an increased K-shell radiative yield.

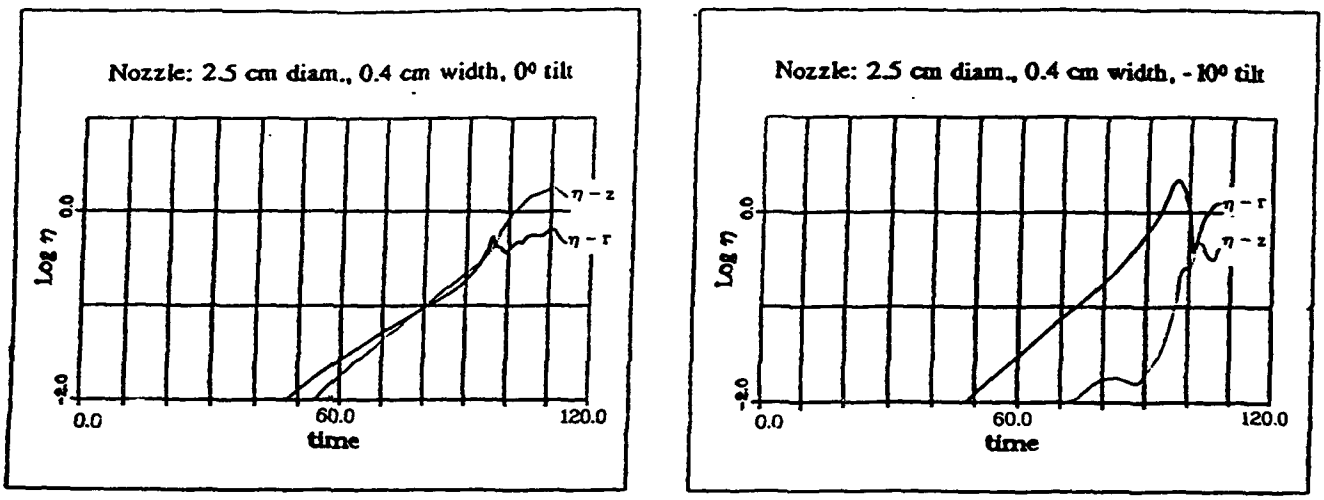


Figure 1. Radial and axial normalized kinetic energy for the untilted and tilted nozzle.

The influence of enhanced resistivity on the nozzle performance is also investigated. The resulting x-ray pulse width as a function of linear mass density is shown on Fig. 2 for different resistivities. It is clear that the 1-D simulations for 1, 10, and 100 x Spitzer resistivity underestimate the pulsewidth. The 2-D simulations are in fairly good agreement with the experimental observations.[1] In the case of zippering, motion and transport along the z-axis influences the collapsing plasma by creating a preheated plasma jet on axis onto which the main plasma implodes and results in a collapse with a moving localized emitting region which is limited in density. For a more nearly uniform implosion, i.e., the elimination of zippering, the 2-D modeling indicates that the collapsing plasma shell is able to achieve a higher density and smaller diameter and hence increased emission.

A typical numerical simulation for the Saturn generator using a straight nozzle is shown on Fig. 3. For the voltage pulse shown a self-consistently calculated current pulse is evaluated from a circuit model representing the generator characteristics. The argon puff gas load had a linear mass density of 350μgms/cm and length of 2 cm. A mass distribution with center radius of 1.25 cm, a width of 0.4 cm and a 10° was used. The maximum current achieved is slightly in excess of 8 MA and then decreases as a result of the increasing dL/dt of the load. The minimum pinch radius occurs at about 90 ns which coincides with the peak of the K-shell x-ray pulse. The peak K-shell radiated power is slightly less than 3 TW.

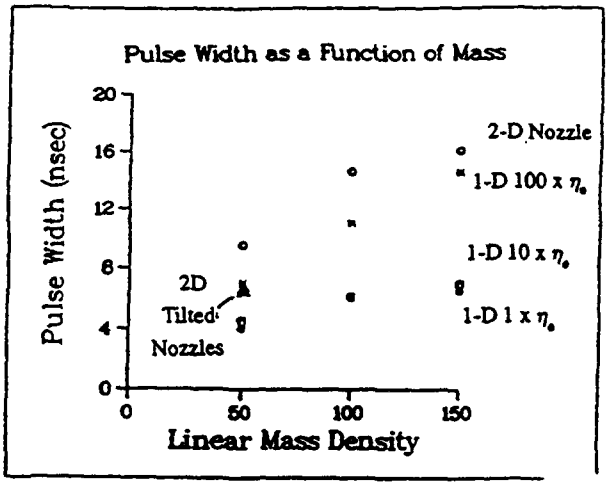


Figure 2. Pulse width as a function of mass for Double Eagle simulations.

The K-shell intensity spectrum for this simulation is shown on Figs. 4 and 5. At 85 ns, which is just prior to peak K-shell emission, the hydrogen- and helium-like lines are prominent with the resonance lines of each ionization stage dominating the spectrum. The free-bound or recombination continuum is well into the background in comparison with the lines. At peak implosion at 90 ns the lines from the K-shell are more pronounced but still dominate the spectrum. However, there is a noticeable increase in the continuum emission. The strongest line at both times is the helium-like resonance line indicating that the implosion was unable to burn through the hydrogenlike stage to the bare nucleus. No attempt was made to optimize the radiation characteristics.

The results for a series of 2 cm long puff simulations are presented in Table 1. For the 200μgms/cm case the plasma was heated to a peak temperature in excess of 4 keV and an average temperature of 650-700 eV. However, motion along the z-axis redistributed the hot plasma. Because of the low mass the plasma was overheated producing an inefficient K-shell radiator. For the case of a linear mass density of 300μ gms/cm three separate cases were considered using enhanced and classical resistivity in the 1-D calculation model and classical resistivity in the thin model. The comparison between 100 x Spitzer including opacity produces results in better agreement with experimental data than in the case of pure Spitzer resistivity with opacity. The comparison between the " thick " and " thin " results is, unfortunately, model dependent in the sense that it is essential to adequately include a sufficient number of L-shell levels and transitions in the atomic model in order to realistically predict the cooling rate. The limited model employed here can, at best, only suggest trends. By restricting the L-shell emission the cooling rate is also reduced. This allows the plasma to become hotter than it normally would and makes the K-shell more accessible. This is best seen in the comparison between the thick and thin results for classical resistivity. The L-shell radiates as a volume emitter in the thin case and produces copious quantities of subkilovolt x-rays that cool the plasma reducing the K-shell yield. The remainder of the entries in the Table should be self-explanatory .

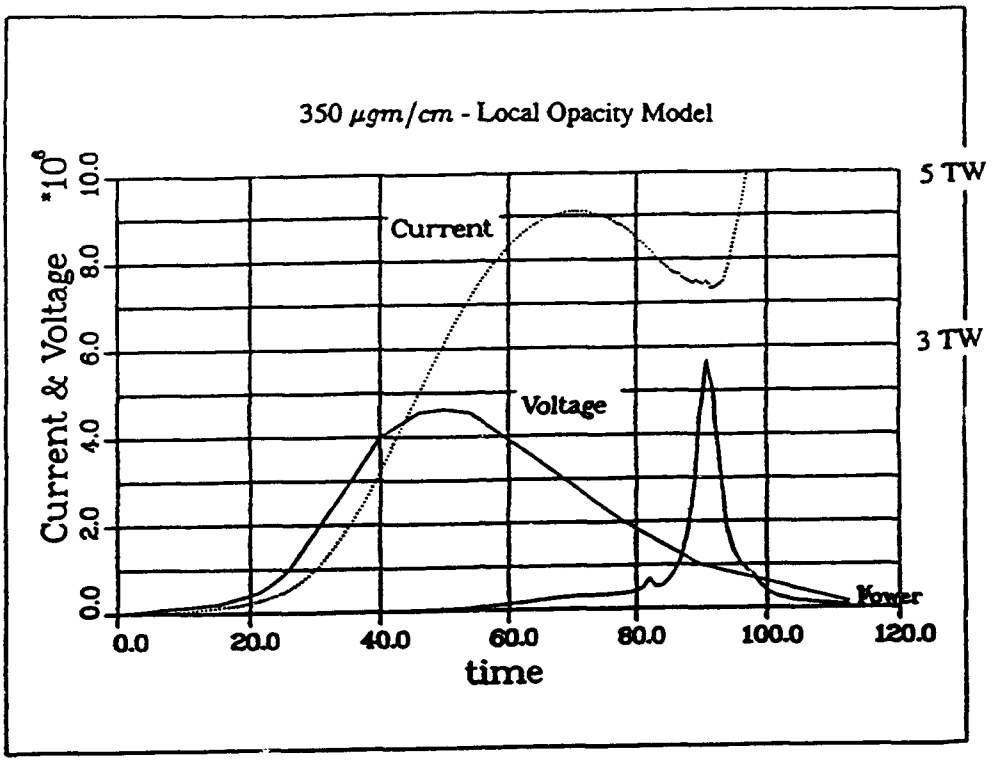


Figure 3. Saturn current, voltage, and K-shell power traces from the 350 μgms/cm

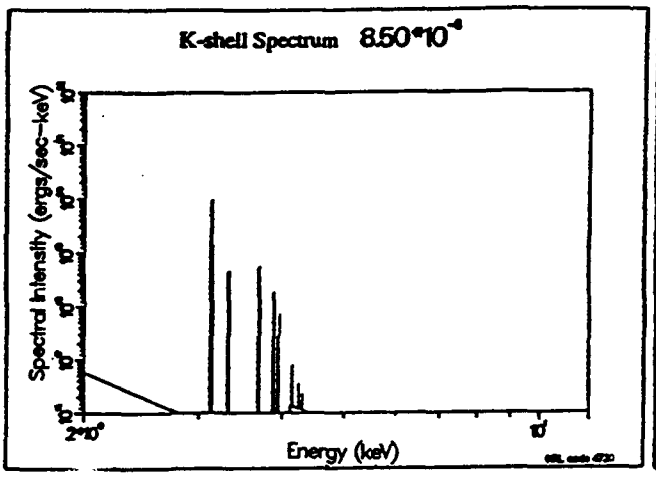


Figure 4. K-shell spectrum @ 85 ns.

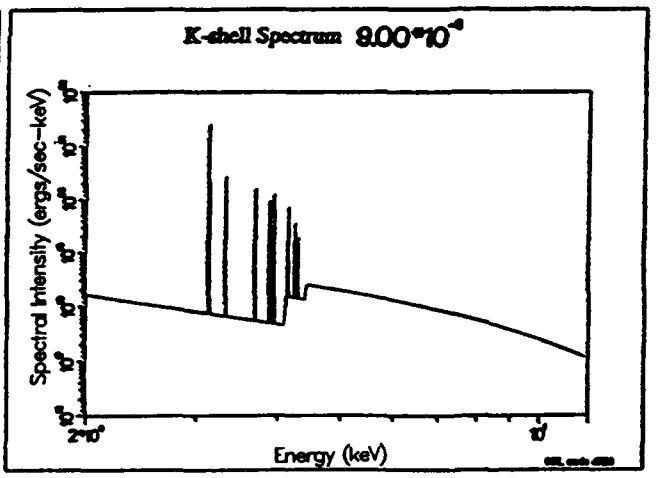


Figure 5. K-shell spectrum @ 90 ns.

MASS $\mu gm/cm$	RESISTIVE MODEL	OPACITY MODEL	PULSE FWHM (NSEC)	K SHELL YIELD (KJ)	TOTAL YIELD (KJ)	K SHELL YIELD (KJ)	TOTAL YIELD (KJ)
200		LOCAL	5	7	12		
300	ENHANCED	LOCAL	7	20	36		
300		LOCAL	5	13	17		
300		NONE	6	8	40		
350		LOCAL	6	21	27	17†	31†
400		LOCAL	6	24	29		
400		NONE	6	12	46		

†Approximate values obtained form detailed atomic physics post-process and assuming Gaussian pulse profile.

Table 1. Results from Saturn simulations.

SUMMARY AND CONCLUSIONS

The use of tilted nozzles reduces or removes the so-called "zippering" phenomena producing substantial improvements in the uniformity of the implosion and K-shell radiative yield. For the linear mass densities and gas puff lengths considered here the best implosions occurred for nozzle tilts of about 10°. For the straight nozzle Saturn simulations the K-shell spectrum moves up the z-axis during the implosion. The K-shell radiated power peaks when the implosion is centered along the axis. The pulsewidth is crudely defined by the maximum of the stagnation time and the time for the zipper to move up the axis. Enhanced resistivity improves the radiative yield. The limited L-shell atomic and opacity models profoundly affect the implosion dynamics by influencing the partitioning and distribution of available energy.

For the future, we will continue to simulate Saturn implosions with tilted nozzles for a variety of masses and gas puffs. We will also investigate self-consistently the effects that macroscopic turbulence has on the transport properties and how it affects the implosion dynamics.

REFERENCES

1. C. Deeney, et. al., " A REVIEW OF Z-PINCH RESEARCH AT PHYSICS INTERNATIONAL", INVITED PAPER OC-2, these PROCEEDINGS.
2. K. G. Whitney , J. W. Thornhill, J. P. Apruzese and J. Davis, J. Appl. Phys. 67, 1725 (1990)

ANOMALOUS RESISTIVITY IN A Z-PINCH SYSTEM

P.E. Pulsifer and K.G. Whitney
Radiation Hydrodynamics Branch
Plasma Physics Division
Naval Research Laboratory
Washington, DC 20375-5000

ABSTRACT

Microturbulence-mediated anomalous resistivity is a possible cause of observed anomalous heating in z-pinch implosions. Conditions seen in MHD z-pinch simulations suggest that the ion-acoustic instability could be a significant generator of turbulence. We employ a quasilinear kinetic theory to investigate electron heating in the presence of ion-acoustic turbulence in a moderately strong magnetic field. To lowest order, turbulence increases the effective electron-ion collision frequency. Simple scaling arguments for developed turbulence show that the collision frequency could be enhanced by one or two orders of magnitude in typical z-pinch plasmas. Turbulent, strong-magnetic field heating produces depressed-tail electron distributions, but with local enhancements. The effect on resistivity of distribution function shape depends on the magnetic field, but turbulence always increases resistivity because of the higher effective collision frequency. Electrical resistivity of z-pinch plasmas is calculated as a function of turbulence level.

INTRODUCTION

It has often been argued that z-pinch experiments exhibit the presence of significant resistive heating, with an effective resistivity 1 to 2 orders of magnitude higher than the Spitzer value [1,2,3]. This anomalous resistivity may result in a significant enhancement in radiative yield over Spitzer-based MHD estimates, which typically predict relatively little ohmic heating. A time-integrated energy balance has been carried out for a wire-array z-pinch [3], with reasonable assumptions made about time-integrated magnetic energy, inductive energy, and the work done in compressing the plasma; average pinch resistivities of about 100 times the Spitzer value were inferred. Anomalous heating is probably connected with other anomalous pinch behavior like long radiation pulse widths. Rapid field penetration into the pinch, as shown by runaways, also indicates a large plasma resistivity in the current-carrying region.

In low-density, non-collisional θ-pinch plasmas, anomalous resistivity typically results from saturated ion-acoustic or lower-hybrid-drift microturbulence [4]. Turbulence alters not only transport coefficients like resistivity but also significantly changes particle distribution functions and the radiative properties of the pinch plasma. A z-pinch has higher electron density and higher current density (but lower electron drift velocity) than a θ-pinch, and implosion timescales are much shorter (tens to hundreds of nanoseconds). The high z-pinch collisionality will influence the achievable saturation level of microturbulence, and the short timescales are still longer than the instability growth time. Therefore, the development and influence of these instabilities may need to be carefully examined.

Here, we study ion-acoustic turbulence, for which conditions in a typical high-power z-pinch are favorable. Using quasilinear theory, we obtain an expression for the change in the electron distribution function due to turbulence. This is included in a Fokker-Planck kinetic model that also contains effects of electron collisions with ions and other electrons, ohmic heating and strong magnetic fields. The quasilinear term directly increases the magnitude of ohmic heating, and also changes the shape of the heated distribution; both of these effects change the resistivity. The important parameters for turbulence are the electrostatic wave energy and the turbulent wave spectrum, which is determined initially by the scale length of the instability. Here, as a first step, we have assumed an isotropic spectrum of ion-acoustic turbulence. A single parameter then emerges, in terms of which we study the modification of plasma resistivity from the Spitzer value as well

as the deviation of the electron distribution function from a Maxwellian shape. Since the electron distribution shape ultimately drives the turbulence, this also gives some idea of the expected actual turbulence growth rates and saturation levels.

In the following, we consider a small, uniform cross-section of a z-pinch where there is current density j, ion density n_i and electron density $n_e = Zn_i$. There are two species: electrons, with charge $q_e = e$, mass $m_e = m$, and temperature T_e (thermal velocity v_{th}); and ions, with charge $q_i = Ze$, mass $m_i = Am_{amu}$, and temperature T_i. There is an electric field E and magnetic field B. The electron cyclotron frequency $\omega_c = eB/mc$ is large, but not larger than the electron-electron collision frequency ν_{ee}, the electron-ion collision frequency $\nu_{ei} = Z\nu_{ee}$, or the electron plasma frequency $\omega_e = \sqrt{4\pi ne^2/m}$. In the following, we denote the collision frequency at the thermal velocity by a bar, e.g., $\bar{\nu}_{ei} \equiv \nu_{ei}(v_{th})$.

Ion-acoustic microturbulence arises from the ion-acoustic instability, which is excited when two conditions are satisfied: 1) the electron drift velocity $v_d = j/en_e$ exceeds the ion sound speed $c_s = \sqrt{ZT_e/m_i}$; and 2) the electron and ion temperatures satisfy $ZT_e/T_i > 3$. This condition is less strict in more highly ionized plasmas. We can use non-turbulent MHD calculations to infer the presence of conditions favorable to growth of the ion-acoustic instability. In some regions of high-power argon z-pinch implosions, for example, $T_e > 5T_i$ before stagnation due to early electric-field acceleration, and $v_d \sim 3c_s$.

Once triggered, the ion-acoustic instability grows at a rate determined by plasma conditions and the electron and ion distribution functions. The maximum growth time τ for Maxwellian distributions is given by [5]

$$\omega_{pi}\tau \approx 200\sqrt{A/Z}\,\frac{c_s}{v_d}. \tag{1}$$

For typical (unstable-region) z-pinch parameters, τ is on the order of a nanosecond. As the instability grows it generates a large anomalous resistivity, thus increasing the potential difference across the pinch and reducing the pinch current until the plasma reaches a state where $v_d \sim c_s$ [4].

FOKKER-PLANCK KINETIC MODEL

We have developed a Fokker-Planck model to study electron kinetics in z-pinch implosions [6]. The model includes magnetic field effects on the distribution and on heating, and is ideal for studying systems like the z-pinch with moderate turbulence and collisionality. Turbulence has been included through a quasilinear term.

In the quasilinear approximation [4], the change in the electron distribution function due to turbulence is given by a diffusion tensor $\mathcal{D}_e$, in the same form as the Fokker-Planck diffusion term:

$$\left(\frac{\partial f}{\partial t}\right)_{QL} = \nabla_v \cdot [\mathcal{D}_e \cdot \nabla_v f(v)] \tag{2}$$

where

$$\mathcal{D}_e = \frac{8\pi^2 e^2}{m^2}\int d^3k\, W(\mathbf{k})\delta(\mathbf{k}\cdot\mathbf{v} - \omega(k))\,\hat{k}\hat{k} \tag{3}$$

and $W(\vec{k})$ is the Fourier transform of the electrostatic fluctuation wave energy $\delta E^2/8\pi$. For isotropic turbulence, only the "average" value, Ω, of the electrostatic wave energy is needed:

$$\Omega \equiv 4\pi \int kW(k)\,dk. \tag{4}$$

The integral in eq. (3) can be evaluated in a spherical coordinate system, with the result that

$$\mathcal{D}_e = \begin{cases} \dfrac{2\pi^2 e^2 \Omega}{m^2 v}\left\{(1 - \dfrac{c_s^2}{v^2})[\hat{u}_{\phi\phi} + \hat{u}_{\theta\theta}] + \dfrac{2c_s^2}{v^2}\hat{u}_{vv}\right\} & \text{if } v > c_s \\ 0 & \text{otherwise} \end{cases} \tag{5}$$

With this expression, the quasilinear term in eq. (2) can be evaluated. If terms proportional to $c_s^2/v_{th}^2 = 2.723 \times 10^{-4} Z/A \ll 1$ are then neglected, the lowest-order effect of ion-acoustic turbulence is an enhanced effective electron-ion collision frequency:

$$\nu_{eff} = \nu_{ei}(1+\beta) \tag{6}$$

where a turbulence strength parameter β has been introduced:

$$\beta \equiv \frac{4\pi^2 e^2 \Omega}{m^2 v_{th}^3 \bar{\nu}_{ei}} \tag{7}$$

The strength parameter is a function of ℓ, the turbulence length scale, divided by λ_D, the Debye length, and f_E, the fraction of thermal energy in fluctuations:

$$\beta \sim 2\pi \frac{\ell}{\lambda_D} \frac{\omega_p}{\bar{\nu}_{ei}} f_E \tag{8}$$

For fully developed but not strong turbulence [5], $f_E \sim N^{-\gamma}$, where N is the number of particles in the Debye sphere (the [inverse] plasma parameter) and $1/2 < \gamma < 1$. A common approximation in ion-acoustic turbulence is that $\ell \sim \lambda_D$. Also, the plasma approximation is that $\omega_p/\bar{\nu}_{ei} \sim N/Z$. Thus, the maximum value for β consistent with the quasilinear approximation is

$$\beta \approx 2\pi N^{1-\gamma}/Z. \tag{9}$$

N is is typically from 10–100 in an imploding pinch, and can reach 10^5 at stagnation. The resulting enhancement of the collision frequency could be significant. Since for fully developed turbulence β is a function only of the plasma conditions, this analysis can be used [7] to obtain a simple estimate of the increase in resistivity and the deviation from a Maxwellian distribution function as a function of pinch current, electron density and temperature. Note, however, that the β values obtained from these scaling arguments are not necessarily those actually found in the pinch; the actual values must be found by integrating the instability growth rate [5].

In the Fokker-Planck model [6], the time-evolving isotropic electron distribution function is found as a function of the normalized electron energy $\epsilon = \frac{1}{2}mv^2/kT$. The distribution is most influenced by two factors: electron-electron collisions, which tend to produce a Maxwellian, and ohmic heating, which is discussed below. The turbulence-enhanced collision frequency modifies the ohmic heating term, which has the form

$$\left(\frac{df}{dt}\right)_{ohmic} = a\mathcal{E}^2 \frac{\bar{\nu}_{eff}\bar{\nu}_{ee}}{\omega_c^2} \frac{1}{\sqrt{\epsilon}} \frac{\partial}{\partial \epsilon}\left[\frac{\epsilon^3}{(\bar{\nu}_{eff}/\omega_c)^2 + \epsilon^3} \frac{\partial f}{\partial \epsilon}\right] \tag{10}$$

where a is a constant of order unity and $\mathcal{E}$ is the electric field in units of the Dreicer field $E_D = mv_{th}^2 \bar{\nu}_{ee}/e$. In a strong magnetic field ($\omega_c \gg \bar{\nu}_{eff}$) the term in brackets in eq. (10) is just a constant times $\partial f/\partial \epsilon$, and ohmic heating produces distributions of the self-similar form [8]:

$$f_m(\epsilon) \sim e^{-(\epsilon/kT)^{m/2}}. \tag{11}$$

A phenomenological form for the exponent m in the presence of electron-electron collisions is [9]

$$m = 2 + \frac{3}{1 + 1.66/[(1+\beta)Z\mathcal{E}^2]^{0.724}} \tag{12}$$

In weaker fields or in strong turbulence, the self-similar form is only an approximation; the actual electron distribution has a strong enhancement, compared to a same-temperature Maxwellian,

near a focus energy. This focus energy ϵ_0 depends inversely on the magnetic field strength $\omega_c/\bar{\nu}_{eff}$: for high fields, ϵ_0 tends to zero and the self-similar, depleted-tail limit is recovered, whereas for low fields, ϵ_0 becomes very large and the zero-field runaway distribution is recovered. A simple approximation for ϵ_0 is that it is the inflection point of the ohmic heating shape function in eq. (10):

$$\epsilon_0 \approx \left[\frac{\bar{\nu}_{eff}\bar{\nu}_{ee}}{2\omega_c^2}\right]^{1/3} \tag{13}$$

Turbulence decreases the effective strength of the magnetic field ω_c and increases the relative importance of the ohmic heating term $\bar{\nu}_{eff}\mathcal{E}^2$, especially at ϵ_0. Results of the Fokker-Planck model for zero ($\beta = 0$) and moderate ($\beta = 10$) turbulence are shown in fig. (1), where focusing of plasma heating due to turbulence is evident.

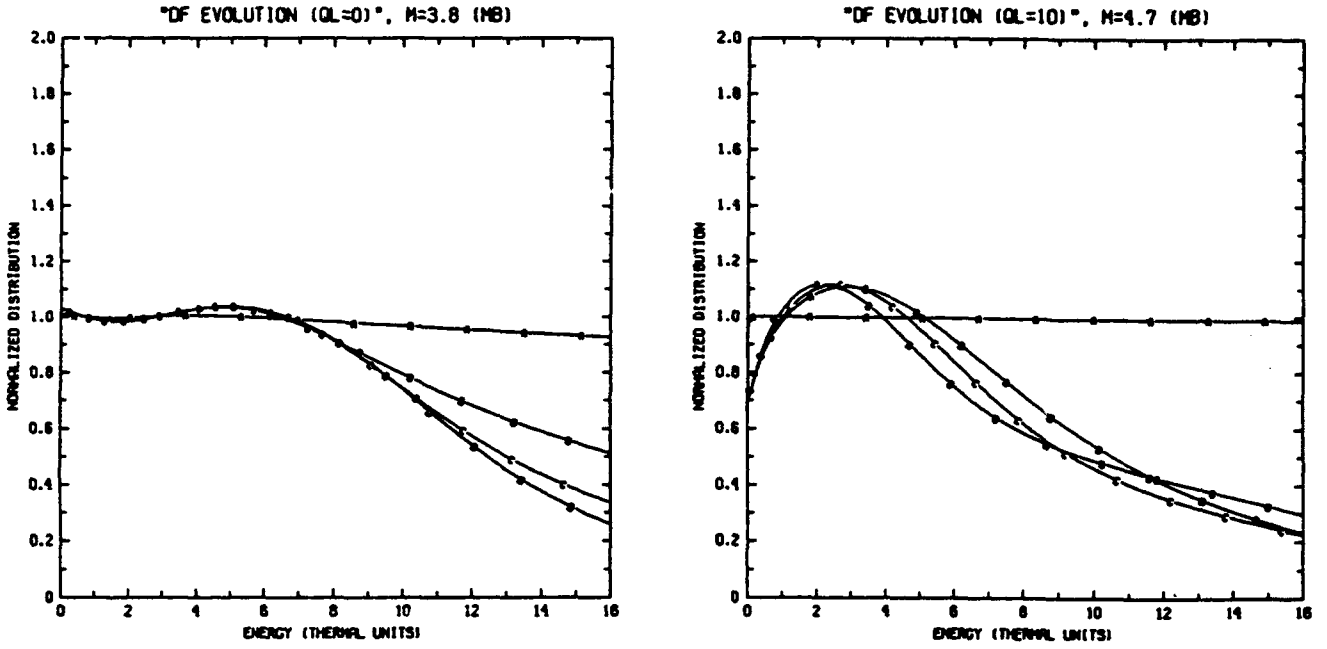


Figure 1. Model results: Electron distribution function evolution with a constant electric field of 200 kV/cm and a strong (200 kG) magnetic field. Plasma conditions: $n_e = 5 \times 10^{19}$, $Z = 10$, $T_e = 100\ eV$. Each curve gives the ratio of the distribution function with a same-temperature Maxwellian at intervals of $\bar{\nu}_{ee}^{-1} = 1.2$ ps: Curve A is earliest time, curve D is latest time. *Left:* zero turbulence. *Right:* medium turbulence ($\beta = 10$).

Turbulence affects electrical resistivity in two ways (see fig. (2)). The direct effect is a uniform increase in resistivity for all magnetic fields, due to the increased effective collision frequency. The indirect effect comes from turbulence-induced changes in the shape of the electron distribution function; turbulent-heated shapes have greater resistivity for weak magnetization, but lower resistivity for strong magnetization. This is because of the greater ability of the magnetic field to trap high-energy electrons, which carry relatively less current for depleted-tail distributions Overall, the direct effect dominates, and resistivity is always higher in the turbulent system. This can be seen in fig. (3), which gives the resistivity calculated with the Fokker-Planck model. Starting from an initial Maxwellian and a fixed level (β) of turbulence, plasma resistivity was calculated for a fixed, small electric field. In fig. (3), this resistivity is plotted as a function of turbulence level for several magnetic field strengths.

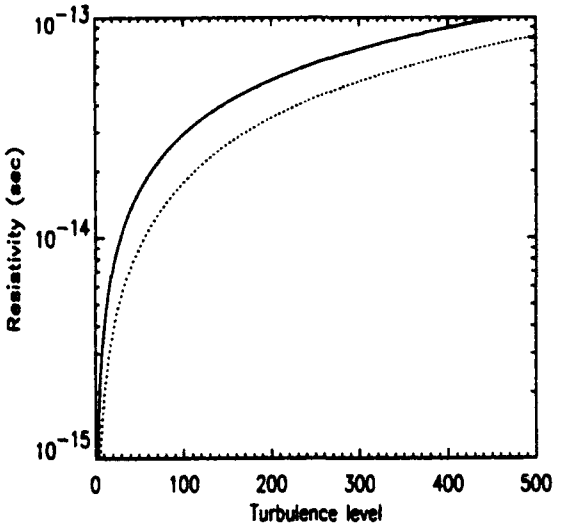


Figure 2a. Electrical resistivity (sec) as a function of ν_{eff}/ν_{ee}. Solid curve is for a Maxwellian, dashed curve is for the depleted-tail distribution of eq. (11), with m=5. A strong (1 MG) magnetic field emphasizes the difference between curves.

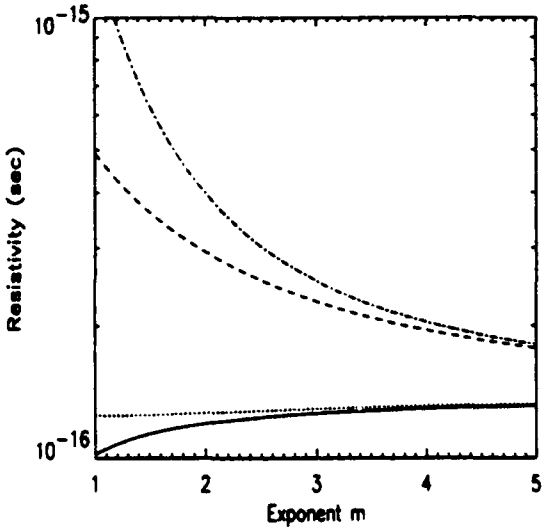


Figure 2b. Electrical resistivity (sec) for the depleted-tail distribution of eq. (11), as a function of exponent m. Larger m means greater tail depletion. Curves from bottom to top are for magnetic fields of 1, 100, 10^4 and 10^6 G, respectively.

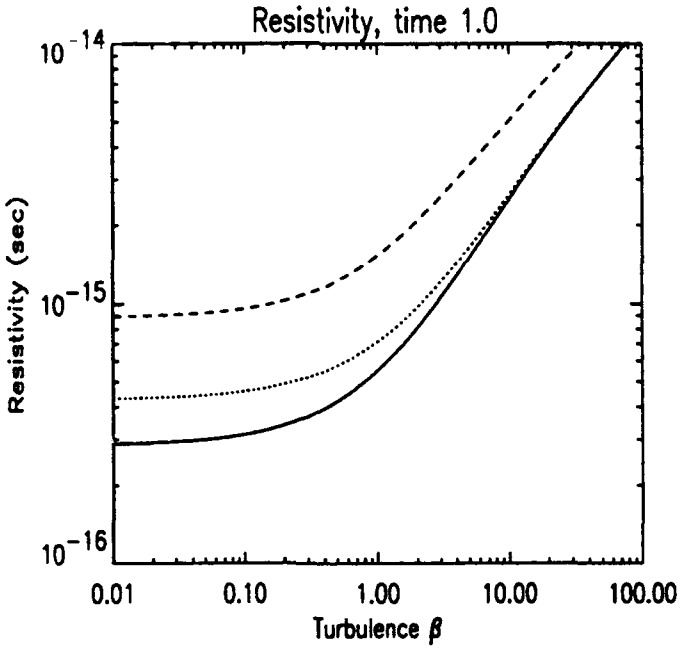


Figure 3. Model results: Resistivity (sec) as a function of turbulence strength β. Curves from bottom to top are for magnetic fields of 820 G, 82 kG and 8.2 MG, respectively. Other conditions: T_e = 100 eV, $n_e = 10^{19}$ cm^{-3}, and Z = 10.

CONCLUSIONS

1) We have investigated effects of a fixed level of isotropic ion-acoustic turbulence, measured by the parameter β. Despite high pinch collisionality, significant turbulence strength is possible, i.e., $\beta \gg 1$ is possible.

2) To lowest order, microturbulence effectively increases the electron-ion collision frequency. This effect dominates, and increases resistivity.

3) Microturbulence produces depleted-tail electron distribution functions, roughly approximated by $f_m(\epsilon)$ in eq. (11). Turbulently heated distributions are particularly enhanced relative to a Maxwellian at certain focus electron energies.

4) We have evaluated the anomalous resistivity from a given microturbulence level for simple but reasonable assumptions.

ACKNOWLEDGEMENT

This work was supported by the Defense Nuclear Agency.

REFERENCES

1. C. Deeney, P.D. LePell, T. Nash, B. Failor, S. Wong, R.R. Prasad, M. Krishnan, K.G. Whitney, J.W. Thornhill, F.L. Cochran, M.C. Coulter, J. Giuliani, J.P. Apruzese, F.C. Young, D. Hinshelwood and J.D. Sethian, paper OC-2, this conference.
2. D.H. McDaniel, M.K. Matzen, E.J. McGuire, T.J. Nash, R.B. Spielman, J. Seamen, S.F. Lopez, J.S. McGurn, L. Ruggles, T.L. Gilliland, D. Jobe and M. Vargas, paper OC-5, this conference.
3. M. Krishnan, "PRS – A critical assessment," Physics International Company Report PITR 3992-01 (1989).
4. R.C. Davidson and N.A. Krall, Nucl. Fusion 17,1313 (1977).
5. S. Ichimaru, *Basic Principles of Plasma Physics*, W.A. Benjamin, Inc., Reading, MA (1973), especially sections 7.3, 11.3 and 11.4.
6. P.E. Pulsifer and K.G. Whitney, "Non-Maxwellian electron distribution functions in z-pinch plasmas," NRL Memorandum Report 6662 (1990).
7. K.G. Whitney and P.E. Pulsifer, submitted to Phys. Rev. Lett. (1992).
8. A.B. Langdon, Phys. Rev. Lett. 44,575 (1980).
9. P. Alaterre, J.-P. Matte and M. Lamoureux, Phys. Rev. A34,1578 (1986).

A NUMERICAL STUDY OF THE STAGNATING COMPACT TOROID AND ITS APPLICABILITY AS A RADIATION SOURCE

Melissa R. Douglas, Robert E. Peterkin, Jr.,
Thomas W. Hussey, David E. Bell
Phillips Laboratory/WSP
Kirtland Air Force Base
Albuquerque, NM 87117-6008 USA

Norman F. Roderick
Dept. of Chemical and Nuclear Engineering
University of New Mexico
Albuquerque, NM 87131

Abstract

Using a compact toroid (CT) as a radiation source is one of the many applications being pursued by the MARAUDER CT program at the Phillips Laboratory. CT radiation production can be achieved via the stagnation of a high velocity plasma ring against a stationary object. A computational analysis of this process is underway using the 2 1/2-dimensional RMHD code MACH2. Preliminary simulations reveal that the stagnation process results in an inelastic collison between the CT and the wall. Estimates indicate a kinetic to radiation energy conversion of approximately 20% aiding in significant radiation output.

1.0 Introduction

A compact toroid is a magnetically confined plasma ring which is expected to have the ability to be compressed in a self-similar fashion (focused) and the capacity to remain intact when accelerated to large velocities. Such properties make the compact toroid well suited for a broad range of potential physical applications, one being that of a radiation source.

A possible method of radiation production involves the stagnation of a high velocity, high energy compact toroid against a stationary target. This process is currently being numerically simulated as part of the MARAUDER (Magnetically Accelerated Rings to Achieve Ultra-high Directed Energy and Radiation) compact toroid program at the Phillips Laboratory. To obtain the kinetic energy densities required for high radiation production, a compact toroid must be focused to smaller volume and accelerated to large velocity to insure MJ kinetic energies prior to stagnation. During the stagnation process itself, the plasma is further heated by a hypersonic shock wave travelling outward from the impact surface, resulting from the initial compression of the toroidal plasma against the target. If the electron-ion and electron-photon coupling time scales are small compared to the dynamical evolution of the system, the compact toroid will radiate via electron transitions and bremsstrahlung radiation. The spectrum of the radiation will naturally depend upon the material comprising the plasma and the kinetic and magnetic energies of the toroid upon impact.

To efficiently model this process and study the radiation output caused by the stagnation

numerically, the various material regimes through which the radiation travels must be considered. Order of magnitude estimates indicate that during the peak compression of the stagnation process, the density of the compact toroid is large enough that the plasma appears optically thick to any radiation. As the plasma begins to rebound and approach its original configuration, it is no longer fully opaque to the radiation, and outside of the boundaries of the toroid, the experimental conditions are near vacuum allowing the radiation to be free-streaming. These conditions imply the need for a radiation treatment which can address all regimes through which the plasma evolves. One way to accomplish this is to use a radiation diffusion approximation with a flux-limiter. Preliminary numerical simulations of the stagnation process have been performed using the 2 1/2-dimensional magnetohydrodynamic ALE code MACH2 [1] with a nonequilibrium flux-limited radiation diffusion treatment. These have been compared to simulations using emission and equilibrium diffusion radiation models [2] showing that the nonequilibrium radiation diffusion treatment is the most appropriate for the stagnation process. The code, stagnation calculations, and results will be discussed in the following sections.

2.0 The MACH2 code

MACH2 is a 2 1/2-dimensional, two temperature, nonideal magnetohydrodynamics code which has been utilized to model a variety of laboratory plasma experiments. The equations that are solved by the code include the dynamical equations for the material density, electron and ion specific internal energies, velocity, and magnetic field. These are solved in a simultaneous manner with an operator split method and an adaptive 2-dimensional grid comprised of quadrilateral cells. An equation of state is used to supplement the evolution equations and may be evaluated analytically or extracted from SESAME tables generated by the T-4 group at the Los Alamos National Laboratory [3].

To model the evolution of the radiation field during the stagnation process, a flux-limited nonequilibrium radiation diffusion treatment was added to the existing MACH2 code. This allows the radiation to evolve as a separate entity described by a Plankian distribution at the radiation temperature, T_R. The implementation of this radiation treatment introduced modifications to the momentum and the electron energy equations and added a dynamical equation for the radiation field. The following equations result:

Fluid Momentum Eqn.:

$$\rho\left[\frac{\partial \bar{V}}{\partial t} + \bar{V} \bullet \nabla \bar{V}\right] = -\left(p + \frac{1}{3} a_R T_R^4\right) + \bar{J} \times \bar{B} + \nabla \bullet \bar{\bar{\sigma}}.$$

Specific Internal Electron Energy Eqn:

$$\rho\left[\frac{\partial e_e}{\partial t} + \bar{V} \bullet \nabla e_e\right] = -p_e \nabla \bullet \bar{V} + \bar{J} \bullet \bar{E} - \nabla \bullet \left(\kappa_{T_e} \nabla T_e\right) + \phi_{ei} - a_R c \kappa_P \left(T_e^4 - T_R^4\right)$$

where ϕ_{ei} = electron-ion coupling term.

Radiation Energy Eqn.:

$$\frac{\partial (e_R)}{\partial t} + \bar{V} \bullet \nabla e_R = - (\frac{4}{3} e_R) \nabla \bullet \bar{V} + \kappa_{RAD} \nabla e_R + a_R c \kappa_P (T_e^4 - T_R^4)$$

where

$$\kappa_{RAD} = \frac{c}{3\rho\chi + \frac{|e_R|}{e_R}}, \qquad e_R = a_R T_R^4.$$

The diffusion of radiation is computed using a multigrid technique and Successive Over Relaxation algorithm to converge to a solution determined by boundary conditions. A flux-limited radiative conductivity is partially determined from a tabulated Rosseland mean opacity and used to find the radiative flux of the radiation energy density.

3.0 Computations and Results

Earlier calculations of compact toroid stagnation have been performed by M. Gee et al. [4,5], at the Lawrence Livermore National Laboratory. In their calculations, the hydrodynamic, magnetic, and radiation transport physics of the stagnation process were modelled using a one dimensional slab geometry. Radiation transport was accomplished using a flux-limited multigroup diffusion method and the atomic physics models used ranged from an LTE description to non-LTE models of average atom and detailed configuration accounting. In the numerical simulations reported in this paper, the stagnation process is treated two dimensionally with all three components of the magnetic field and the velocity. The radiation transport is modelled with a flux-limited mean opacity diffusion method and the material atomic physics is LTE and given by the Los Alamos generated SESAME tables.

Two different geometries have been considered in the present simulations. The first geometry is based on the MARAUDER experimental configuration while the second involves a more compressed toroid and is representative of the calculations made by M. Gee, et al. Both cases correspond to a less tightly focused compact toroid than reported in Refs. [4,5] and should result in a reduced system requirement on acceleration and focusing. In each geometry, the compact toroid has been conically focused before entering the target region. The main distinction between the two simulations lie in the existence of an inner conductor for the MARAUDER case which is not present in the more compressed problem.

The geometry of the stagnation process for the MARAUDER experiment is shown in Fig.1. The compact toroid is confined by inner and outer conductors, at radial positions 2 cm and 4 cm, respectively, The height of the toroid is taken to be 2 cm. The initial conditions are those predicted after

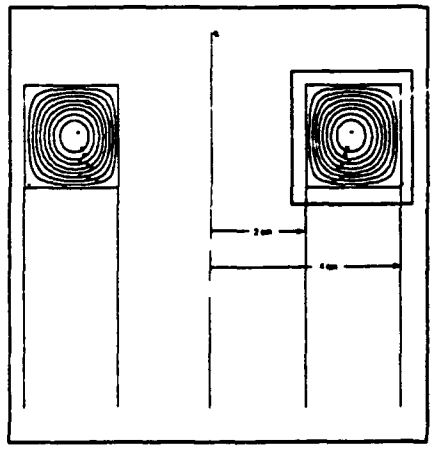


Fig.1 The geometry configuration for the coaxial geometry test problem.

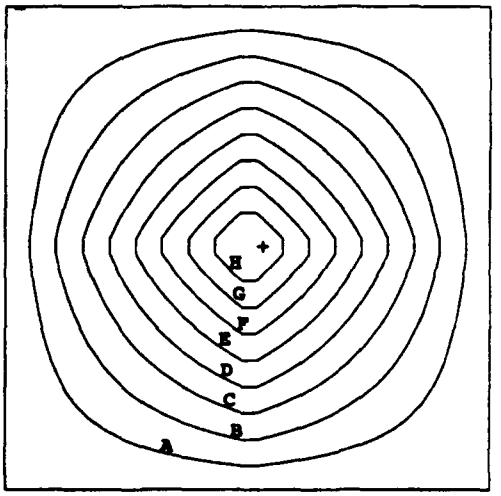


Fig.2 The initial density profile for the coaxial geometry test problem. Numerical values are in units of kg/m^3.

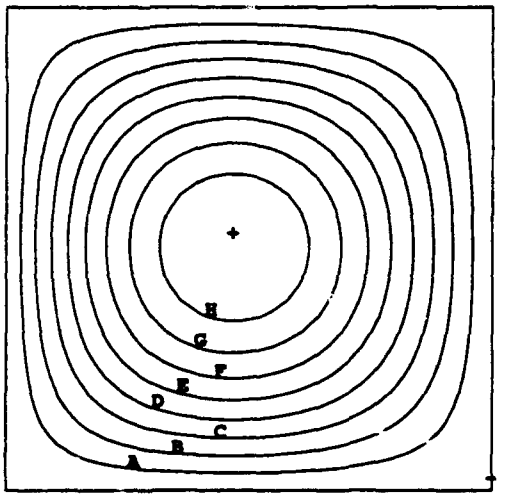


Fig.3 The initial magnetic field profile for the coaxial geometry test problem. Numerical values are in units of Tesla.

focusing and acceleration have been applied in the experiment. The compact toroid is taken to have a mass of 2.5 mg and travels towards the target region with a velocity of 2000 km/sec. This makes the kinetic energy of the toroid prior to stagnation 5 MJ. Within the toroid, the electron and radiation temperatures are both 100 eV and the ion te...perature is 1 keV. The magnetic field structure is "force free" ($\bar{J} \times \bar{B} = 0$) as shown in Fig.2, with a peak toroidal field of 3.8 MG. This results in a magnetic energy of 2.2 MJ. Figure 3 displays the initial density profile. Here the peak density is 0.12 kg/m^3 .

Maximum compression during stagnation occurs at approximately 5 ns. The magnetic field structure at this time is shown in Fig.4. The peak magnetic field is 11 MG, a factor of 2.89 larger than the initial peak magnetic field. The density has also increased from 0.12 kg/m^3 to 0.35 kg/m^3. In the vicinity of the shock layer in the region of the target, the electron temperature has reached 1.6 keV, the ion temperature 380 keV, while the temperature of the radiation field has increased to 470 eV (refer to Fig.5). Preliminary estimates indicate that the peak radiated power for this simulation is 1 x 10^{14} W.

In the second geometry considered (which will be denoted as cylindrical), the toroid is confined only by an outer conducting wall at 2 cm. Here the initial peak density is 0.39 kg/m^3 while the peak magnetic field is 6.8 MG. The initial velocity and temperatures are those presumed in the previous configuration, and the energies are essentially the same. At maximum compression, the peak toroidal magnetic field (Fig.6) is at 20 MG, a factor of 2.94 larger than the initial field. The ion, electron, and radiation temperatures within the shock layer are 1.9 keV, 410 keV and 510 eV, respectively. The radiation temperature profile is given in Fig.7. Preliminary estimates indicate that the peak radiated power for this simulation is 3.5 x 10^{14} W.

In conclusion, both geometries show temperatures that are uncoupled in the opaque region behind the shock layer reinforcing the idea that a three temperature diffusion approximation is

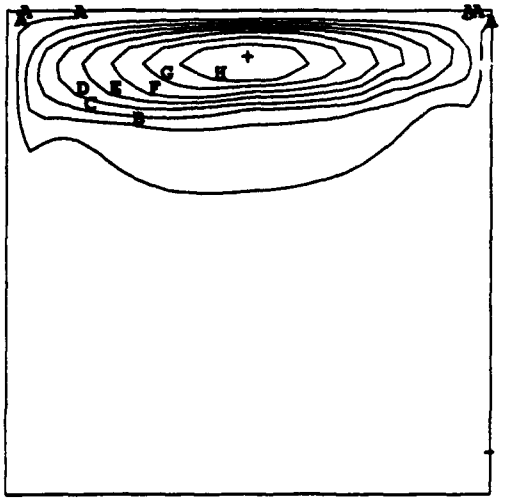


Fig.4 The magnetic field at peak compression for the coaxial geometry test problem. The peak magnetic field is 6.8 MG. Numerical values are given in units of Tesla.

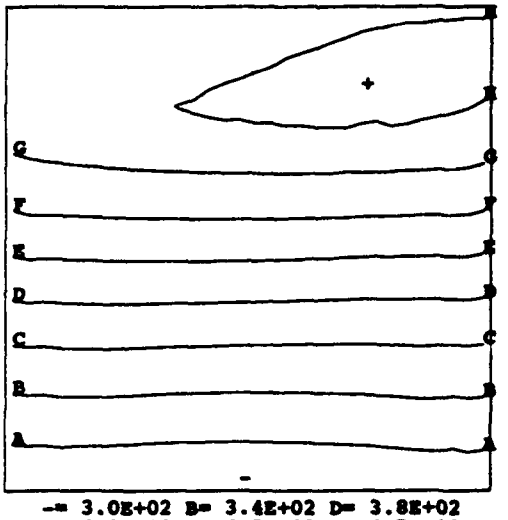


Fig.5 The radiation temperature at peak compression for the coaxial geometry test problem. The peak temperature is 470 eV. Numerical values are in units of eV.

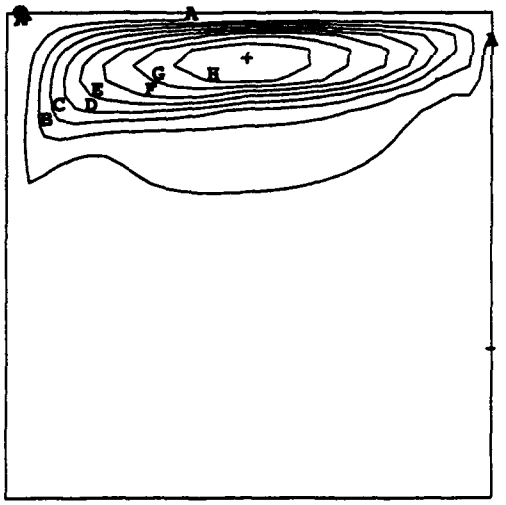


Fig.6 The magnetic field at peak compression for the cylindrical geometry test problem. The peak magnetic field is 20 MG. Numerical values are given in units of Tesla.

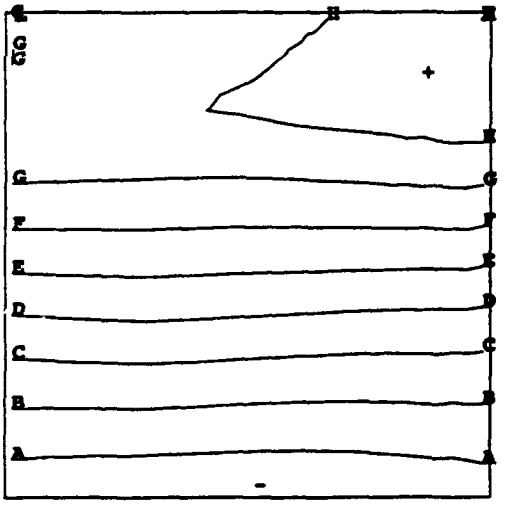


Fig.7 The radiation temperature at peak compression for the cylindrical geometry test problem. The peak temperature is 510 eV. Numerical values are given in units of eV.

appropriate for this process. An examination of the toroidal field structure throughout the stagnation process in both cases indicates that the impact involves an inelastic collision between the compact toroid and the wall. This is highly desirable since it produces a efficient conversion of kinetic energy (as evidenced by the numerical values) into radiation output. Moreover, these geometries are consistent with the results of M. Gee et al. [4,5], although they cannot be directly compared because of the physical differences noted earlier.

References

[1] Michael H. Frese, *MACH2: A Two-Dimensional Magnetohydrodynamic Simulation Code for Complex Experimental Configurations,* Technical Report AMRC-R-874, NTIS Document No. ADA 192285 (1987).

[2] Melissa R. Douglas, Norman F. Roderick, Carl R. Sovinec, and Robert E. Peterkin, Jr., *Computational Simulations of a Stagnating Compact Toroid,* Bul. Am. Phys. Society, Vol.36, No.9 (Oct 1991).

[3] M.Gee, P. Nowak, and G. Zimmerman, *Computational Analysis of a Compact Toroid X-Ray Source,* Technical Report UCRL-53951, Lawrence Livermore National Laboratory, Lawrence, California 94551, (August 1989).

[4] M. Gee, J.H. Hammer, P.F. Nowak, C.W. Hartman, and G.B. Zimmerman, *A Computatioal Analysis of a Compact Toroid X-Ray Source,* Technical Report UCID-21514, Lawrence Livermore National Laboratory, Lawrence, Californial, 94551 (Sept 1988).

[5] K.S. Holian, ed., *T-4 Handbook of Material Properties Data Base, vol. Ic: EOS,* LA-10160-MS, Los Alamos National Laboratory, Los Alamos, NM (Nov 1984).

HYDRODYNAMICS OF A STAGNATING RING-PUFF PLASMA

R. W. Clark and J. Davis
Radiation Hydrodynamics Branch
Plasma Physics Division
J. Les
Research Computation Division
Naval Research Laboratory
Washington, D.C. 20375

Abstract

The dynamics of an argon ring-puff plasma stagnating on a planar iron target is investigated theoretically and numerically. At stagnation, the high velocity argon ring-puff converts much of its kinetic energy to thermal and ionization energy which is then converted to radiation. The intensity, spectra, and pulselength of the emitted radiation produce an interesting x-ray radiation source with a potentially large number of applications. We present the results of our simulations and characterize the radiation source. During the plasma expansion phase population inversions were found in the hydrogen-like ionization stage of argon; their significance is discussed.

Introduction

Magnetically confined ring-puff plasmas have been experimentally[1,2] produced with velocities exceeding 10^8 cm/sec. They can create high density, high temperature plasmas on stagnation with a massive stationary target. These stagnation experiments were initially motivated by interest in alternative methods for producing efficient high temperature x-rays. We investigated the radiative properties and dynamics of an argon ring-puff plasma as it collided with and stagnated on a planar iron surface, as shown in Fig. 1. The ring-puff has major radius R_0 and minor radius r_0, and contains both poloidal and toroidal magnetic fields. The poloidal field becomes compressed between the target and the puff, which moves with an initial axial velocity of u_0. The interaction has been simulated with a one dimensional (1D) non-LTE multimaterial radiation hydrodynamics model which self-consistently includes the effects of opacity and line broadening[3]. The application of a 1D model, as shown in Fig. 1, is a reasonable approximation for timescales less than r_0/v_s, where v_s ($< u_0$) is the sound speed and r_0 corresponds to the transverse distance. Argon was used as the gas-puff, since for a high velocity stagnation on the order of 10^8 cm/sec, materials with substantially higher atomic number (Z) would not become fully stripped, and those with lower Z would not recombine quickly enough to the hydrogen-like ion. By modeling the problem in this manner, we have concentrated on the stagnation and radiation physics.

The stagnation has a simple analytic solution in the absence of ionization, radiation and thermal conduction: a layer of shocked argon is created (the iron remains cold), with a density ratio of 4:1 for large Mach numbers, and (assuming that the initial thermal energy of the puff is small compared with its kinetic energy) the temperature of the shocked gas-puff is given by $kT = {}^1/_3 m_i u_0^2$, where m_i is the mass of a gas-puff ion. Thus, for the idealized case (no wall or radiative losses, no ionization, etc.), the

stagnation temperature scales as the square of the puff velocity. A benchmark simulation was performed for this case, and reproduced the analytic model fairly well; it was a severe test of the code, since the gradients were very large and the computational mesh had to be severely stretched to provide adequate resolution in the interface region. In the non-adiabatic case, the stagnation temperature will generally be smaller, due to energy losses and ionization. Of course, when these energy sinks, including thermal conduction into the wall, are small relative to the kinetic energy of the puff, the solution will approximate the adiabatic solution during the stagnation phase.

Results

Radiation-hydrodynamic simulations with detailed atomic models for iron and argon were performed for an initial ring-puff velocity $u_o = 1.0 \times 10^8$ cm/sec. The iron target was assumed to be at solid density with a temperature of about 1 eV; the argon puff had a uniform ion density of about 10^{19} cm^{-3} and a temperature of 7.6 eV. A hot argon region was created initially at the interface with the iron that grew in thickness with time. When magnetic field effects on thermal conduction were ignored, a hot dense layer of iron formed adjacent to the interface, which ablated towards the puff plasma and efficiently radiated high temperature x-rays. However, the magnetic field of the ring puff becomes compressed by the stagnation and causes the inhibition of electron thermal conduction. We modeled this effect in a simplified manner by setting the heat flux equal to zero at the interface.

An energy history for this case is shown in Fig. 2. Initially, most of the energy in the system is in the kinetic energy of the argon puff. As the stagnation onto the wall proceeds, kinetic energy is converted into thermal energy, and the heated plasma ionizes (ionization energy) and

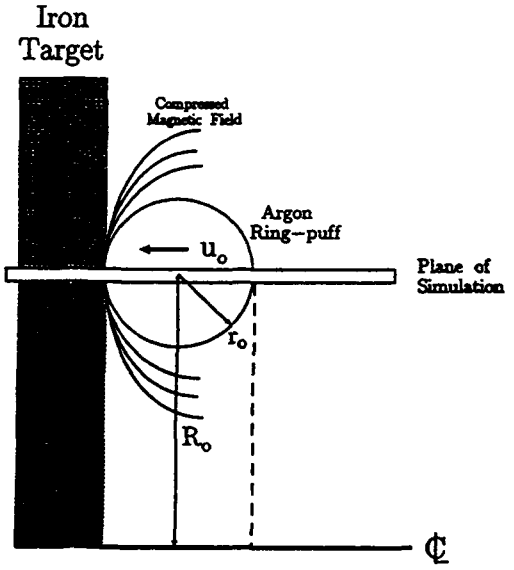


Fig 1. Compact toroidal argon plasma ring incident on a planar iron target.

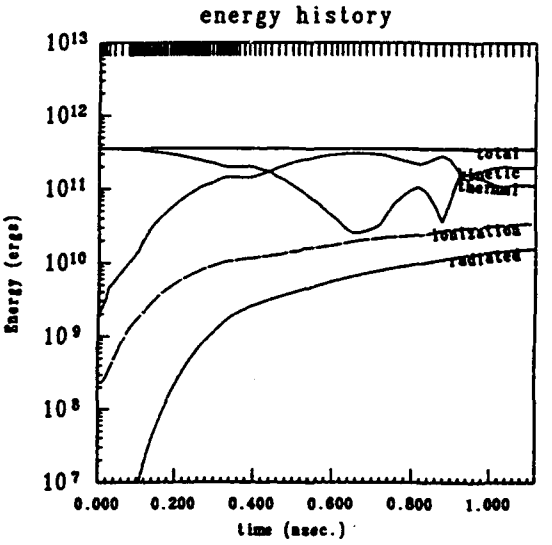


Fig 2. Energy history of the system. Total energy is the sum of kinetic, thermal, ionization and radiated energies.

radiates (radiated energy). Most of the kinetic energy has been thermalized by about 0.70 nsec, and the hot plasma begins to expand. In the expansion phase, thermal energy is converted into kinetic, and ionization energy is converted into thermal (and radiation) through recombination. The radiated energy is that which is lost from the system. The motion of the puff gas becomes complicated between about 0.70 and 0.90 nsec, as portions of the puff rebound and stagnate; two distinct minima in kinetic energy are evident near these times. Details of the stagnation at several times are shown in Figs. 3-6.

In Fig. 3, the hydrodynamic variables (density [g/cm^3], temperature [eV], pressure [$ergs/cm^3 x10^{-12}$], velocity [$cm/nsec\ x10^{-2}$] and radiative cooling [$ergs/nsec\text{-}cm^3 x10^{-14}$]) are plotted versus displacement in centimeters at 0.56 nsec., during the stagnation phase. The temperature in the puff reaches about 5.5 keV and is nearly isothermal due to thermal conduction. The shocked argon is, to a good approximation, stationary and fully stripped. A density jump of about 6:1 occurs at the shock front. The profiles at 0.72 nsec., near peak thermalization (where the kinetic energy is a minimum), are shown in Fig. 4. The peak temperature is about 6 keV and remains nearly isothermal in the puff; it decreases near the iron interface due to radiative cooling, and remains cold in the target. The strong shock wave in the puff is beginning to dissipate as the expansion proceeds, but the remnants can be observed near 0.022 cm, where a density jump of about 4:1 persists. The fluid velocity remains small behind the shock, but expansion of the shocked argon has commenced. The plasma between 0.026 and 0.054cm is still moving inwards, while the outer portion of the puff has begun to expand. Radiative cooling is sharply peaked near the iron interface.

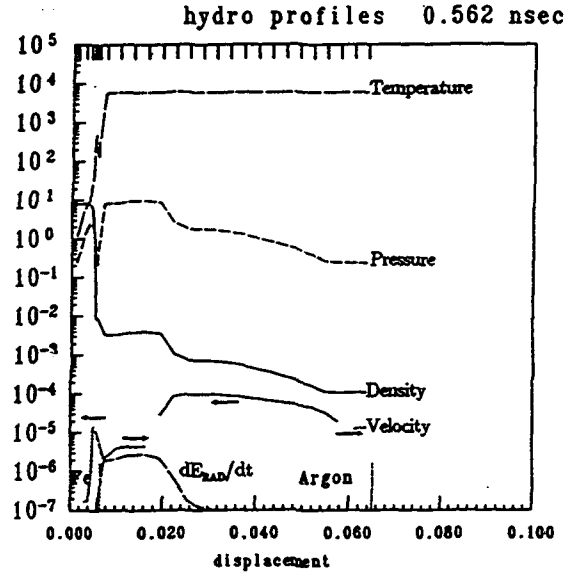


Fig 3. Hydrodynamical variables as a function of distance, at time 0.56 nsec.

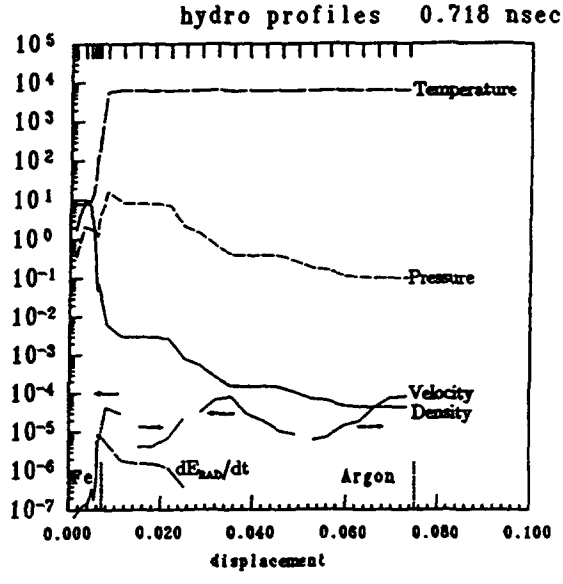


Fig 4. Hydrodynamical variables as a function of distance, at time 0.72 nsec.

In Fig. 5, the hydrodynamic variables are plotted at 0.92 nsec, when temperature is dropping rapidly due to expansion of the argon gas puff. The temperature decreases from about 3.6 keV in the bulk of the puff to 2.7 keV near the interface where radiative cooling, a strong function of density, is large. Radiation losses at the interface permit continuing local compression with a corresponding increase in the cooling rate. By 1.12 nsec., the argon temperature at the interface has dropped to about 600 eV, while the temperature in the remainder of the puff has fallen to 1.6 keV, see Figure 6. The rapid cooling near the interface is accompanied by recombination of fully stripped argon into the various excited states of the hydrogen-like ion. Collisional recombination preferentially populates high quantum n-states. The density in the vicinity of the interface is sufficiently high such that collisional recombination dominates over radiative for the levels of interest, but not so high that collisional excitations and deexcitations overwhelm the recombination processes[4,5]. Thus, conditions are favorable for the formation of population inversions in hydrogen-like argon.

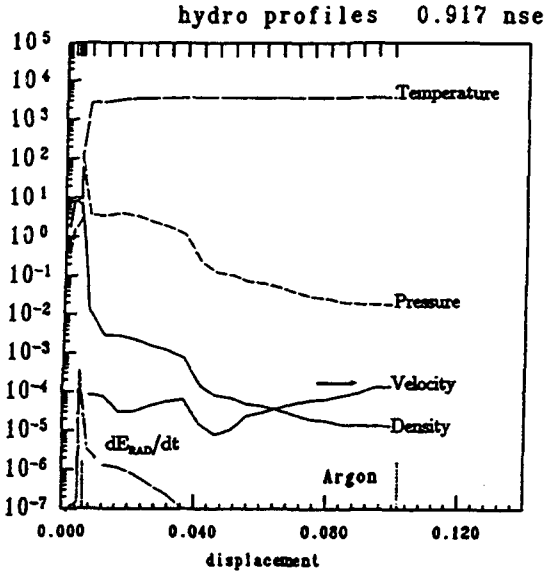


Fig 5. Hydrodynamical variables as a function of distance, at time 0.92 nsec.

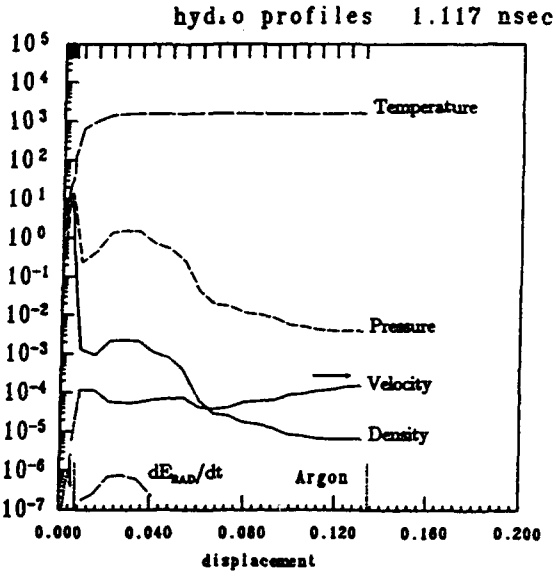


Fig 6. Hydrodynamical variables as a function of distance, at time 1.12 nsec.

Population inversions among the first ten quantum states of hydrogen-like argon during the cooling (expansion) phase were reported in reference 6. The recombination source, fully stripped argon, makes up more than half of the plasma near the target interface. Radiative processes (radiative recombination, spontaneous decay, etc.) dominate the lower n-states ($n < 4$), and collisional processes (collisional recombination, ionization, excitation and deexcitation) dominate the higher states. For this reason, population inversions are absent among the lower quantum states, but are possible among the higher states. In the highest states, collisional mixing becomes dominant. However, the existence of the states $n > 7$ is questionable; line broadening may cause these levels to overlap. The largest population inversions involve states $n>4$ relative to $n=4$, and range from 1.11 to 1.27. Because recombination from the fully stripped argon is relatively slow, these inversions will persist for at least a few tenths of a nanosecond.

Instantaneous emission spectra near peak thermalization (0.72 nsec) and in the expansion phase (1.12 nsec) are shown in Figures 7 and 8. The former spectrum is dominated by the emission from the hot 6 keV argon plasma. A few iron lines are in evidence, and a substantial portion of the continuum radiation (particularly free-free) comes from the warm iron plasma at the interface. The latter spectrum corresponds to a cooler (1.6 keV) argon plasma, with some contribution from the iron. We have found that the radiation efficiency increases substantially when thermal conduction into the wall is not inhibited. Clearly, the ring puff stagnation will be a more efficient x-ray source if the high density wall plasma can be made hotter. Similarly, the ring-puff plasma will be a more efficient radiator if its density can be increased. Radial compression has been accomplished with a focusing cone in recent experiments[1,2], but the density enhancements have been modest.

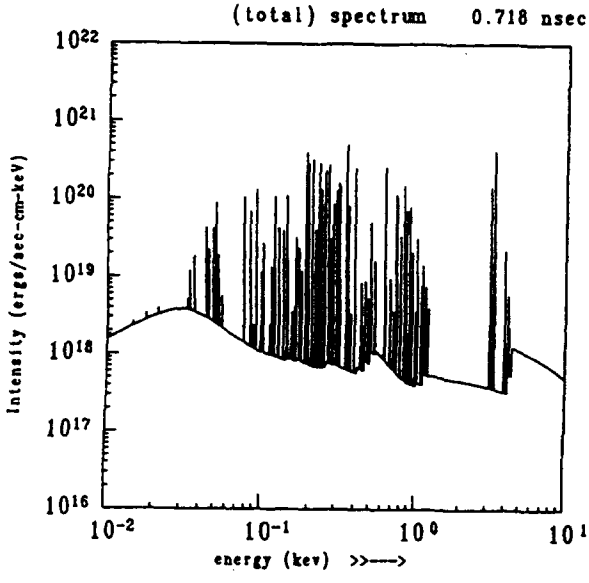


Fig 7. Instantaneous emission spectrum at time 0.72 nsec (near peak compression).

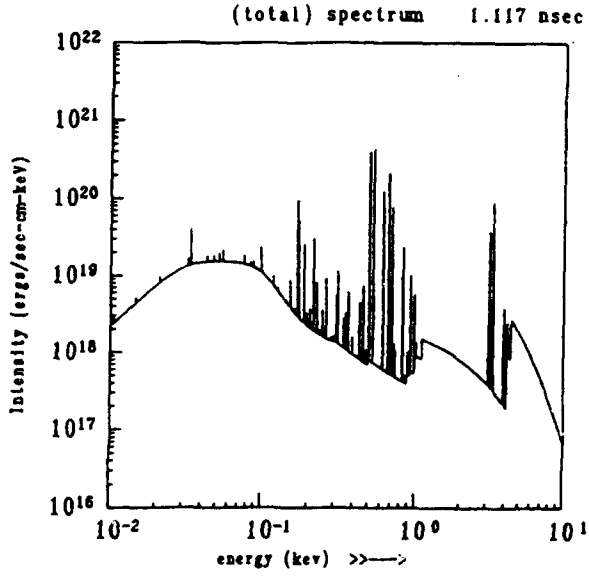


Fig 8. Instantaneous emission spectrum at time 1.12 nsec (expansion phase).

Summary

The stagnation of a high velocity ring-puff plasma on a planar solid density target can generate a high density, high-temperature plasma that can potentially be an interesting laboratory x-ray laser source. In addition, population inversions can be produced as the stagnated plasma expands and recombines. However, a number of questions need to be investigated. These include the importance of 2D effects which were ignored in this study, and the importance of non-fluid behavior at the puff-target interface. High-velocity ring plasma ions can penetrate the target, and in extreme cases, the interaction may resemble a beam deposition rather than a fluid stagnation. In addition, the adequacy of the model employed in this study for the inhibition of thermal conduction at the interface should be more

thoroughly investigated. Further, the magnetic (and electric) fields produced in the acceleration of the ring puff and in its interaction with the target could affect the dynamics. Finally, questions related to x-ray laser gain and the gain-length product need to be resolved.

Acknowledgements

We would like to thank Ward Thornhill for providing the method used in obtaining the nonequilibrium populations, and Paul Kepple for providing the detailed configuration argon and iron tables. This work was sponsored by the Defense Nuclear Agency.

References

1. C.W. Hartman and J.H. Hammer, Phys. Rev. Lett. **48**, 929 (1982).
2. J.H. Hammer, C.W. Hartman, J.L. Eddleman, and H.S. McLean, Phys. Rev. Lett. **61**, 2843 (1988).
3. D. Duston, R.W. Clark, J. Davis, and J.P. Apruzese, Phys. Rev. A **27**, 1441 (1983).
4. Y.B. Zel'dovich and Y.P. Raizer, Edited by W.D. Hayes and R.F. Probstein, *Physics of Shock Waves and High-Temperature Hydrodynamic Phenomena* , Vol. 1, (Academic Press, New York, 1966).
5. H.R. Griem, *Plasma Spectroscopy* , (McGraw-Hill, New York, 1964).
6. R.W. Clark, J. Davis and J. Les, Proc. International Conf on Lasers '91, (STS Press, Mc Lean, VA, 1992), in press.

Author Index

Abdullin E.N. - 419
Abe D.K. - 1607
Abe S. - 1758
Accelerator Physics Laboratory Staff - 1764
Adams R.G. - 800
Adcock J.L. - 333
Aiello N. - 203
Akiba T. - 1403
Akiyama H. - 627
Alberti S. - 1526, 1532
Alef M. - 756
Alexandrovich D.V. - 1574
Alexeev G.I. - 1312
Allen C.K. - 933
Allen S.L. - 247
Allison P. - 283
Alterkop B.A. - 1322
Althaus M. - 51
Ando R. - 1227, 1825
Anthouard P. - 1861
Antoniades J.A. - 99, 1245, 1251, 1257, 1263
Antonsen Jr. T.M. - 1497, 1607, 1613, 1728
Antoshkin M.Yu. - 1690
Aoki T. - 76
Apruzese J.P. - 159
Arad R. - 143, 633
Aragones J.M. - 1001
Armale R. - 890
Arzhannikov A.V. - 127, 431, 1117
Asahina T. - 976
Ashby S.R. - 385, 1855
Astrelin V.T. - 431, 756
Atanassov R. - 1700
Attelan S. - 2008
Averchenkov V.Ya. - 273
Babykin V.M. - 517
Bachmann H. - 51, 68, 735, 963
Bacon L.D. - 31
Bailey J.E. - 31, 788, 794, 903, 1397
Baksht R.B. - 2014
Balakirev V.A. - 1073, 1643
Baranov S.V. - 1574
Baranov V.Yu. - 1930
Bardy J. - 1752, 1861
Barnard J.J. - 297, 951
Bartsch R.R. - 88, 175, 615
Basmanov V.F. - 273, 505
Bastrikov A.N. - 1586
Batskikh G.I. - 449
Bauer W. - 51, 68, 735
Baumung K. - 51, 68, 963
Bayley J.M. - 474
Bekefi G. - 1715
Bell D.E. - 408, 2062
Benage J. - 175
Benford G. - 1631
Benford J. - 203, 341
Bennett L.F. - 1141
Bernard M. - 781
Beruchev N.G. - 436
Bessho I. - 1758
Beyec Y. Le - 939
Bidwell S.W. - 1728
Bieg K.W. - 794
Bishaev A.M. - 1312
Black W.M. - 1479
Bloomquist D.D. - 31
Bluhm H. - 51, 68, 735, 741
Bobylev V.B. - 431, 1117
Bobys M.P. - 1485
Bogachenkov V.A. - 1568
Bohacek V. - 1221
Boller J.R. - 375, 609, 871
Bolshakov E.P. - 1930
Bonnafond C. - 1752
Bossamykin V.S. - 273, 505, 511
Bottollier-Curtet H. - 1752
Boulais K.A. - 1087, 1300
Bourham M. - 1979
Bowers L.A. - 1649
Bowers R. - 175
Bratman V.L. - 1520
Bres M. - 237
Bromborsky A. - 1607, 1613, 1619
Brooks A.L. - 297
Brown D.J. - 1473
Brownell J. - 175
Bruggink D. - 1901
Brunelle A. - 939
Budakov A.V. - 505
Bugaev S.P. - 394, 419, 449, 1099, 1586
Bulan V.V. - 425
Bunkin B.V. - 195
Burdakov A.V. - 127, 1049, 1055
Burns M. - 283
Burtsev V.A. - 1930
Bushell M. - 1215
Buth L. - 51, 68, 735
Butler J.M. - 1637
Butler M.E. - 333
Buzzi J.M. - 237
Bystritskii V.M. - 529, 535, 812, 878
Calico S.E. - 1367
Caporaso G. - 283
Carlson A.L. - 794, 903
Carlson R.L. - 1881
Carlsten B.E. - 227, 1473, 1661
Carmel Y. - 1607
Chandler G.A. - 31
Chang C.L. - 927
Chavez J.R. - 781
Chen C. - 1526, 1807
Chen S.C. - 1135
Chen Y. - 1354
Chen Y.J. - 283
Chen Y.Q. - 1696
Chen Y.S. - 1696
Cherepenin V.A. - 1396
Chernin D.P. - 291, 1294, 1783
Chernobrovin V.I. - 1930
Chernyavsky I.A. - 1586
Chetvertkov V.I. - 1930
Chikin R.V. - 517
Chikunov V.V. - 127, 1043, 1049
Childers F.K. - 385
Ching C.H. - 1789
Chirko K.A. - 1625
Chishiro E. - 847
Chistov A.A. - 419
Chittenden J.P. - 474, 480
Choe J.Y. - 1087
Choi P. - 474, 480, 2008
Chu K.R. - 1491
Chumerin P.Yu. - 1685
Chun S.T. - 1087
Church B.W. - 1795
Chuvatin A.S. - 2008
Clark M.C. - 1649
Clark R.E.H. - 143
Clark R.W. - 2068
Clupek M. - 1221
Coats R.S. - 31, 781

Cochran F.L. - 159, 2050
Cochrane J. - 175
Coffield F. - 297
Coleman M. - 598
Colombant D.G. - 1783
Commisso R.J. - 167, 375, 603, 609
Conde M.E. - 1715
Cook D.L. - 31
Cooksey N. - 203
Cooper G.W. - 621
Cooperstein G. - 375, 871, 1159
Coulter M.C. - 159, 2044
Cravey W.R. - 646
Crawford M.T. - 1367
Cricket C.M. - 1776
Crist C.E. - 109
Cuneo M.E. - 31, 781
Czuchlewski S.J. - 1912
Dadusc G. - 143
Dangor A.E. - 474
Danko J.C. - 1954
Danly B.G. - 1135, 1526, 1532
Datsko I.M. - 2014
Davara G. - 143
Davis C.E. - 1649
Davis H.A. - 88, 615
Davis J. - 2050, 2068
Davis T.J. - 1601, 1667
Deadrick F. - 297
Deeney C. - 159, 167, 385, 2044
Degnan J.H. - 408
Deichuli M.P. - 1586
Denisov G.G. - 1520
Derzon M.S. - 31
Desjarlais M.P. - 31, 775
Destler W.W. - 1728
Deulin Yu.I. - 1015
Deutsch C. - 988
Devin A. - 1752
DeVore C.R. - 559
Didenko A.N. - 219, 1574, 1685, 1690
Ding B.N. - 665, 1176
Ding W. - 1734
Diyankov V.S. - 455, 1165
Dolezal F.A. - 1637
Dolgachev G.I. - 517, 523
Dolgopolov V.V. - 1073
Douglas M.R. - 408, 2062
Downing J. - 283
Drury D. - 1855
Dukart R.J. - 31
Duvall R.E. - 143
Eddy W. - 1979
Efremov A.M. - 419, 1948
Egorov O.G. - 425
Eisenhart R.L. - 1637
Ekdahl C. - 1887
Eliezer S. - 995
Eltchaninov A.S. - 195
Engelko V.I. - 436, 1935
Engelstad R.L. - 1901
Erickson A. - 227, 688
Ershov V.V. - 436
Esarey E. - 313, 1813
Etlicher B. - 2008
Eyharts P. - 1861
Eyl P. - 1861
Faehl R.J. - 88, 227, 688, 762, 1473, 1661
Faillon G. - 237
Failor B. - 159
Fan R.Y. - 1696
Fant K. - 1147
Fayne W.R. - 1649
Fazio M.V. - *227, 688, 1473,* 1661
Fedorov V. - 747
Fedotkin A.S. - 273
Fedotov A.V. - 1373
Fedushchak V.F. - 1194
Feher L. - 756
Feng B. - 1721
Fernsler R.F. - 99, 1245, 1251, 1276, 1282
Fidelskaya R.F. - 1930
Filipenko N.M. - 1574
Filippov V.O. - 505
Filippov V.V. - 1015, 1021
Filuk A.B. - 31, 788, 794
Finkelstein K.I. - 1930
Fischer R.P. - 1467
Fisher A. - 143, 357, 633, 812, 1631, 1746
Fisher R.C. - 609
Fisher V. - 143
Fleetwood R. - 1215
Fliflet A.W. - 1467
Fomenko G.P. - 1574, 1690
Foord M.E. - 143
Forman P. - 175
Fortov V.E. - 969
Foster J. - 1789
Fowler W.E. - 781
Freund H.P. - 263, 1709, 1728
Frost C.A. - 109, 492
Fruchtman A. - 143
Fu S. - 1354
Fukuzawa T. - 627
Furman E.G. - 1870
Furuuchi S. - 1971
Furuyama Y. - 841, 976
Gan Y.G. - 1918
Ganguly A.K. - 1514, 1709
Garate E. - 812, 1631
Gardelle J. - 1752
Gardes D. - 939
Gautier D.C. - 88
Gavrilov N.V. - 1105
George M. - 1141
Gerasimov A.I. - 273
Gerbelot N. - 237
Gerber R.A. - 800
Germain G. - 1752
Getman D.V. - 586
Getty W.D. - 1129
Giguet E. - 1526
Gilgenbach R.M. - *1789*
Gilligan J. - 1979
Ginzburg N.S. - 1740
Giuliani Jr. J.L. - 159, 167
Glazyring I.V. - 1165
Glidden S.C. - 349
Goebel D.M. - 1093, 1637
Goel B. - 68, 957, 969
Goez M.F. - 68
Goforth J. - 175
Gold S.H. - 1479
Golden J. - 1170
Golovanov Yu.P. - 517
Golub T.A. - 575
Golubev A.A. - 1312
Golubev A.V. - 2020
Goncharenko I.M. - 1948
Gondarenko N.A. - 575
Gonichon J. - 1135
Goodman D.L. - 1526
Goodrich P.J. - 375, 603, 609
Gordeev V.S. - 505, 511
Gorkunov V.S. - 273
Goyer J.R. - 385, 1385
Grabovsky E.V. - 425

Granatstein V.L. - 185, 1449, 1503, 1508, 1728
Green T.A. - 788
Greene A. - 175
Greenly J.B. - 43, 88, 615
Gregorian L. - 143
Grekhov A.V. Gaponov - 195
Gribov A.N. - 425
Gridasov A.P. - 505
Griffith L.V. - 297
Grigoryev V.P. - 1690
Grishin A.V. - 273
Grishin V.K. - 1770, 1776
Gritzina V.P. - 273
Grossmann J.M. - 375, 559, 603, 1159
Grothaus M.G. - 659
Gudovich V.A. - 1312
Guharay S.K. - 933
Gulotta G. - 1532
Gumennyj V.L. - 541
Gundersen M.A. - 1123
Gushenets V.I. - 1099
Guth H. - 68
Haber I. - 945
Hafizi B. - 1479, 1746
Haill T.A. - 31
Haines M.G. - 474
Hakansson P. - 939
Halbleib J.A. - 119
Hallal Jr. M.P. - 1153
Hammer D.A. - 349
Hankins O. - 1979
Hanson D.L. - 31, 781
Harden M.J. - 1141
Hardesty L.W. - 659
Harjes H.C. - 333
Harper-Slaboszewicz V.J. - 486
Harteneck B. - 203
Harvey R.J. - 1637
Hatfield L.L. - 1367
Haworth M.D. - 1649
Hayase H. - 835
Haynes W.B. - 227
Hazelton R.C. - 2032
Henderson J.L. - 1141
Hendricks K.J. - 1649
Henins I. - 88
Herniter M.E. - 1129
Hinshelwood D.D. - 159, 375, 603, 609
Hirshfield J.L. - 1514
Hoeberling R.F. - 227, 688, 1473
Hofmann I. - 969
Hogan B. - 185, 1449
Hogeland S. - 1328
Honrubia J.J. - 1001
Hoppe P. - 51, 68, 735, 741
Horioka K. - 806, 829, 835
Hoshino H. - 1971
Hou W.S. - 1984
Hsu T.Y. - 1123
Hu K. - 1354
Huang D. - 1343, 1349
Hubbard R.F. - 99, 945, 1245, 1251, 1257, 1276, 1282
Huber A.F. - 127, 1049
Hughes T.P. - 1881
Humphries Jr. S. - 1837, 1843, 1887
Hurley J. - 1979
Huseev A.P. - 394
Hushiki T. - 829
Hussey T.W. - 408, 2062
Hyman J. - 1637
Ignatov A.M. - 1373
Ihara S. - 627
Illy St. - 756
Imada G. - 323
Imasaki K. - 76, 884, 1403, 1758
Ingermanson R. - 553
Irwin K. - 1087
Isakov I.F. - 1966
Ishkhanov B.S. - 1770
Iskoldsky A.M. - 575
Itin V.I. - 1942, 1948
Ivanov I.B. - 1870
Ivanov V.V. - 1655
Ivanov Yu.F. - 1942, 1948
Ivers J.D. - 1081, 1601
Iyyengar S.K. - 1831
Jackson R.H. - 263
Jensen D. - 1147
Jeremkin V.V. - 1930
Jiang B. - 1123
Jiang W. - 323, 859
Jiang X. - 462, 468
Jiangjun S. - 1188
Johnson D.J. - 31, 788, 800, 903
Johnson D.L. - 333
Johnson W.A. - 499
Joyce G. - 313, 945, 1270, 1813, 1849
Judd D.L. - 297
Judy D.C. - 640, 1215
Jungwirth K. - 1337
Kablambajev B.A. - 581
Kadimov A.H. - 1312
Kalantar D.H. - 349
Kamada K. - 1227, 1825
Kanaev G.G. - 1870
Kanavets V.I. - 211, 1586
Kanazawa T. - 1825
Kandaurov I.V. - 1027, 1037
Kanel G.I. - 68, 963
Kang X.D. - 323, 1971
Kapitonov V.A. - 127
Karbushev N.I. - 1643
Karow H.U. - 51, 68, 735, 963
Karyukin A.V. - 127, 1015, 1049
Kasuya K. - 806, 829, 835
Katsuki S. - 627
Kawakita Y. - 829
Kawasaki S. - 255, 1825
Kawata S. - 76
Kazansky L.N. - 449
Keishi T. - 1758
Keller D.V. - 1391
Kellogg J.C. - 375, 603, 1159
Kerslick G.S. - 1081, 1601
Kharchenko I.F. - 1073
Kharlov A.V. - 878
Khomenko A.I. - 449
Khryapov P.A. - 1586
Kiekel P.D. - 333, 1328
Kim A.A. - 394, 586, 2014
Kimura T. - 1532
Kirbie H.C. - 297
Kirichenko Yu.V. - 1073
Kirkman G. - 1123
Kiselev V.N. - 394
Kishimoto Y. - 255
Kitamura A. - 841, 976
Klement'ev A.P. - 505
Klenov G.I. - 1312
Klimov V.I. - 1061, 1067
Knyazev B.A. - 1043
Kobayashi A. - 1758
Kobayashi T. - 255
Koc U.V. - 185, 1455
Koga A. - 1758

Koidan V.S. - 127, 431, 1021, 1049
Kojokhin E.P. - 425
Kokshenev V.A. - 394, 2014
Kolacek K. - 1337
Kolosov Yu.A. - 1643
Komarov O.L. - 436
Kondratiev N.A. - 1033
Kondratyev A.A. - 1165
Konovalov I.V. - 1655
Koontz R. - 1147
Kormilitsin A.I. - 455, 1165
Kornilov V.G. - 1655
Korovin S.D. - 195, 1580
Kortbawi D. - 385, 1385
Koshelev V.I. - 449, 1586
Kostas C. - 291, 1294
Kostin V.V. - 969
Kostov K.G. - 1700
Kotov Yu.A. - 670
Kou C.S. - 1491
Koval T.V. - 1690
Kovalchuk B.M. - 394, 419, 449, 1948
Kovalev N.F. - 1592
Kovalev V.G. - 436
Kovalev V.P. - 455
Kovalev Yu.I. - 517
Kovsharov N.F. - 394
Krall A. - 1087
Krall J. - 313, 1288, 1813, 1849
Krasik Ya.E. - 143, 529, 633
Kreindel M.Yu. - 1111
Kreindel Yu.E. - 1105
Krejci A. - 2020, 2026
Krishnan M. - 159
Kristiansen M. - 1367
Krousky E. - 2020
Kruglyakov Eh.P. - 1027, 1037
Kruse H. - 175
Kuang E. - 1601
Kueny C.S. - 305
Kukharenko I.N. - 425
Kulbeda V.E. - 1033
Kulcinski G.L. - 1901
Kuntz M. - 756
Kuo Y.Y. - 1984
Kurbatov K.V. - 425
Kusse B.R. - 43, 915
Kuznetsov V.E. - 1930
Kwan T.J.T. - 227, 688, 1562, 1661
Labrouche J. - 1752
Laderach G.E. - 333
Ladish J. - 175
Lai S.T. - 1907
Lampe M. - 99, 945, 1270, 1276, 1282
Laqua H. - 51, 741
Larionov V.P. - 1312
Latham P.E. - 185, 1449, 1455, 1461
Latinsky S.M. - 1073
Lats'ko E.M. - 1073
Lau Y.Y. - 1783
Launspach J. - 1752
Lawson W. - 185, 1449
Lazarenko A.V. - 1935
Lazarev S.A. - 273
Lebedev S.V. - 127, 1015, 1021, 1049
Leeper R.J. - 31
Lemke R.W. - 1649
Lenski I.F. - 1776
LePell P.D. - 159, 167, 2044
Les J. - 2068
***Levine* J.** - 203
Levush B. - 1461, 1497, 1607, 1613, 1619, 1728
Li T. - 676
Licht V. - 68, 963
Lin A.T. - 1491
Lin C.L. - 1135
Lindemuth I.R. - 1990
Linton T.W. - 88
Liou R.L. - 1123
Lisenko E.A. - 1073
Lisitsyn I.V. - 529, 535
Litvinov E.A. - 1111
Litwin C. - 143, 143
Litz M.S. - 1170
Liu J.R. - 1918
Lockner T.R. - 31, 788
Loginov S.V. - 419
Lomonosov I.V. - 969
Longcope D.W. - 769
Lopatin V.V. - 1586
Losev M.V. - 1037
Loskutov V.V. - 2014
Lotz H. - 68, 735
Lovberg R.H. - 1990
Lovell E.G. - 1901
Loza O.T. - 1550
Lu Z. - 1721
Luchinsky A.V. - 1194, 2014
Luhmann Jr. N.C. - 1485, 1491
Lujnov V.G. - 425
Lundin C.D. - 1954
Lykov S.V. - 1942, 1948
Ma W. - 1343
MacFarlane J.J. - 903, 1397, 1901
Maeda S. - 627
Maenchen J.E. - 781
Maglich B. - 357
Maidanovskii A.S. - 1574
Main W. - 185, 1449, 1455
Manheimer W.M. - 1467, 1479
Mankofsky A. - 927
Mann G.A. - 333
Markov A.B. - 1948
Maron Y. - 143, 633, 794
Martinez L.E. - 333
Martinez-Val J.M. - 995, 1001
Martynov V.F. - 1318
Maruyama X.K. - 1153
Mascureau J. d. - 1752
Mason R.J. - 547, 615
Masuda W. - 323
Masugata K. - 323, 682, 847, 853, 859, 1971
Masuzaki M. - 1227, 1825
Matsumura N. - 1825
Matsuura N. - 829
Matthews H.W. - 185
Mayhall D.J. - 652
Mazarakis M.G. - 109, 492, 1141
McClenahan C.R. - 333
McDermott D.B. - 1485, 1491
McGuire E.J. - 903
McKay P.F. - 781
McNally J.D. - 1485
Meachum J.S. - 136, 1385
Meek T.T. - 1954
Meger R.A. - 99, 1245, 1251, 1257, 1263
Mehlhorn T.A. - 31, 788
Mekler K.I. - 127, 1049
Melnikov G.V. - 1685, 1690
Melnikov P.I. - 127, 1021, 1043, 1049

Mendel Jr. C.W. - 31, 499
Mendenhall R.S. - 1385
Menge P.R. - 1789
Menninger W.L. - 1526, 1532
Merkel G. - 1215
Meshkov O.I. - 1027, 1037
Mesyats G.A. - 195, 394, 419, 449, 878, 1105, 1942
Mikhailov V.M. - 1322
Mikkelson K.A. - 119, 486
Miller A.R. - 402, 598
Miller J.D. - 1233
Miller R.B. - 1328
Miller S.M. - 1607, 1613
Minguez E. - 1001
Miram G. - 1147
Mitchell I.H. - 474, 480
Mitin L.A. - 1318, 1643
Mix L.P. - 31, 788
Miyai Y. - 829
Miyamoto S. - 76, 884, 1403
Miyauchi Y. - 1758
Miyoshi T. - 829
Mkheidze G.P. - 1061, 1067, 1924
Moats A.R. - 31
Mock R.C. - *119*
Mogahed E.A. - 1901
Moir D.C. - 283, 1881
Molina I. - 1328
Mondelli A.A. - 291, 927, 1294
Moran S.L. - 659
Morita H. - 1227
Morunov K.A. - 273
Moschella J.J. - 2032, 2038
Moses G.A. - 1397, 1901
Mosher D. - 60
Moya S.A. - 1141
Mozgovoy A.G. - 818, 824, 1867
Muenchausen R.E. - 88
Muirhead D. - 333
Mulbrandon M. - 167
Mullins B.W. - 408
Munz C.D. - 68
Murphy D.P. - 99, 1245, 1251, 1257, 1263
Musyoki S. - 255
Myers M.C. - 99, 1245, 1251, 1257, 1263
Myers T.J. - 1300
Myskov G.A. - 505
Mytnikov A.V. - 878
Nagai A. - 1758
Nagashima T. - 255
Nakai S. - 76, 884, 1403
Nakajima T. - 841, 976
Nakamura Y. - 255
Nakata K. - 829
Nardi E. - 982
Nash T. - 159, 903
Nation J.A. - 1081, 1601, 1667
Naugol'nyj I.N. - 541
Neau E.L. - 333, 1960
Neely S.M. - 486
Negra S. Della - 939
Neil V.K. - 297
Neri J.M. - 60
Newton M.A. - 297
Ngo M.T. - 1379
Nguyen K.T. - 1233
Ni A.L. - 68, 957, 969
Nianan C. - 1876
Nie L. - 1918
Nifanov A.S. - 211
Nikiforov A.A. - 127, 1049
Nikolaev V.S. - *127, 431,* 1117
Nikolov N.A. - 1700
Nishimura E. - 1758
Niu K. - 1895
Nolting E.E. - 1954
Noonan W.A. - 43
Novikov S.A. - 1685
Novikov S.S. - 1574
Novikov V.E. - 1073
Nusinovich G.S. - 185, 1461, 1497, 1503, 1619
Obenschain S.P. - 1912
Oda H. - 255
Ohashi M. - 1971
Ohshita E. - 829
Okano M. - 1758
Oliver B.V. - 921
Olson C.L. - 60, 897, 903
Olson J.C. - 915
Olson R.E. - 31
Olson W.R. - 1141
Oona H. - 175
Oppenheim M. - 1601
Oreshin A.A. - 449
Oreshkin V.I. - 2014
Osipov M.L. - 195
Ostrenskiy Ye.I. - 1643
Ostrovsky A.O. - 1073
Otlivantchik E.A. - 195
Ottinger P.F. - 60, 167, 375, 559, 1159
Ovsyannikov V.A. - 1930
Ozur G.E. - 1111, 1942
Panitz J. - 788
Papadichev V.A. - 818, 824, 1568
Parilis E. - 939
Parker J. - 175
Parks D. - 553, 598
Pashchenko A.V. - 541, 1073
Pasour J.A. - 1379
Paul A.C. - 297
Pavlovskii A.I. - 273, 505, 511, 1655
Pawley C.J. - 1912
Pearce K.D. - 1129
Pearson C. - 1147
Pechacek R.E. - 99, 1245, 1251, 1257, 1263
Pechersky O.P. - 436, 1930, 1935
Pena G.E. - *333*
Penn K.J. - 333
Pereira N.R. - 640
Perelmutter L. - 143
Perevodchikov V.I. - 1318
Perlado M. - 1001
Petelin M.I. - 195, 449
Peter W. - 1819
Peterkin Jr. R.E. - 408, 2062
Peterson D. - 175
Peterson R.R. - 909, 1901
Petillo J.J. - 291, 927, 1294
Petin V.K. - 1194
Petukhov A.A. - 436
Peyser T.A. - 99, 1245, 1251, 1257, 1263
Pichugin V.E. - 425
Piera M. - 995, 1001
Piffl V. - 1055, 1221, 2020, 2026
Pikunov V.M. - 1586, 1673
Pincosy P.A. - 646
Platonov Yu.Ya. - 2020
Platt R.C. - 1649
Pointon T.D. - 31, 775
Polevin S.D. - 1580

Polovkov A.I. - 1643
Poskonin V.A. - 581
Postupaev V.V. - 127, 1049, 1055
Poukey J.W. - 109, 119, 492, 781, 897, 1141, 1801
Poulsen P. - 646
Pozdeev V.V. - 1574
Prasad R.R. - 159
Prasol E.A. - 1073
Price D. - 203
Prikhod'ko I.G. - 1655
Prohaska R. - 812, 1631
Prokhorov A.M. - 195
Prokopenko V.F. - 1930
Proskurovsky D.I. - 1111, 1942
Pulsifer P.E. - 2056
Qi N. - 349
Qian M. - 1188
Qiu A.C. - 1918
Quintenz J.P. - 31
Radkevich O.I. - 1312
Rahman H.U. - 1996
Rashchikov V.I. - 219
Ratakhin N.A. - 581, 1194
Raus J. - *1221, 2020, 2026*
Razin S.V. - 1685
Reed K.W. - 333
Reginato L.L. - 297
Reinhardt N. - 1123
Reinovsky R. - 175
Reiser M. - 185, 933, 1182
Rej D.J. - 88, 615, 762
Remnev G.E. - 365, 1966
Ren S.Q. - 1918
Renk T.J. - 31, 794, 800
Renner O. - 2020
Renz G. - 1715
Rhee M.J. - 665, 1087, 1176, 1233, 1300
Richter S.H. - 1391
Rickel D.G. - 227, 688, 1661
Riley Jr. R.A. - 1990
Riordan J.C. - 136, 385, 1385
Ripa M. - 1337
Rix W. - 402, 598, 1887
Robertson K. - 598
Rochau G.E. - 31
Rodenz G. - 1473
Roderick N.F. - 175, 408, 2062
Rodgers J. - 1728
Rodiakin V.E. - 1673
Roitman A.M. - 1580
Romanov S.S. - 1073
Roques A. - 1861
Rose D.V. - 60
Rosenthal S.E. - 31, 499, 781
Rostoker N. - 357, 812, 890, 1996
Rostov V.V. - 195, 1580
Roth I.S. - 385, 1385
Rotshtein V.P. - 1942, 1948
Rouille C. - 2008
Roychowdhury P. - 1831
Rudakov L.I. - 565
Rudjak Yu.V. - 1306
Ruiz C.L. - 31
Rukhadze A.A. - 1322, 1556
Rukin S.N. - 670
Rullier J.L. - *1526, 1532*
Rusch D. - 51, 68, 735, 963
Russkich A.G. - 2014
Rust K. - 227, 688
Rutledge S. - 1901
Rybak P.V. - 1556
Ryne R.D. - 1661
Ryutov D.D. - *127, 1009*
Ryzhov V.V. - 1199
Saddow S.E. - 1087
Saeki K. - 1758
Saitou H. - 682
Sakagami T. - 859
Sakamoto K. - 255
Sakamoto M. - *1825*
Salberta E. - 553
Samarsky P.A. - 449
Samsonov S.V. - 1520
Sandalov A.N. - 1673, 1770
Sanford T.W.L. - 119
Sanin A.L. - 1037
Santoru J. - 1637
Santos J. - 99, 1245, 1251
Sapozhnikov A.A. - 1199
Saraev A.P. - 195
Saraph G.P. - 1497
Sarfaty M. - 143, 633
Sarid E. - 143
Sato M - 865
Sato S. - 1758
Savage M.E. - 621
Saveljev Yu.M. - 436
Savin A.A. - 1061, 1067, 1924
Sawan M.E. - 1901
Schachter L. - 1081, 1601, 1667
Schanin P.M. - 419, 1099
Scharlemann E.T. - 247
Schlitt L. - 385, 1855
Schmidt W. - 747, 756
Schneider A.J. - 1637
Schneider R.F. - 1233, 1954
Schuldt R. - 756
Schultheiss Ch. - 735
Schumacher R.W. - 1093, 1637
Schwirzke F. - 1153
Schwoebel P. - 788
Seidel D.B. - 31, 499
Sekimoto Y. - 323, 682
Seldner D. - 756
Selemir V.D. - 1655
Seleznev V.D. - 449
Selivanov I.A. - 1538
Semenov E.P. - 127
Serafim P. - 1746
Sethian J.D. - 159, 1912
Settersten T.B. - 2032
Shan Y. - 1343
Shapiro A.L. - *1318*
Sharp W.M. - 297, 951
Shatkus A.D. - 1643
Shay H.D. - 297
Shcheglov M.A. - 127, 431, 1015, 1021, 1049
Sheehey P. - 1990
Shibalko K.V. - 1655
Shibata K. - 682
Shigeta M. - 682
Shiho M. - 255
Shimotori Y. - 1971
Shinmura A. - 841
Shirai N. - 76, 1403
Shiyan V.D. - 1205
Shkolnikova S. - 143, 633
Shkvarunets A.G. - 1538, 1545
Shlapakovskii A.S. - 1625
Shokair I.R. - 1328
Shope S.L. - 109, 492
Shpitalnik R. - 143
Shterbina O.V. - 1312
Shubin O.A. - 1105
Shulov V.A. - 365
Shutov A. - 68

Shvedunov V.I. - 1770
Simpson W.W. - 621
Sincerny P.S. - 385, 1855
Sinebryukhov A.A. - 535, 878
Sinelshikov A.V. - 449
Singer J. - 68, 963
Singh A. - 1508
Sinilshikova I.V. - 1568
Sinitsky S.L. - 127, 431, 1117
Sisakyan I.P. - 195
Skogmo P.J. - 119, 1141
Skopec M. - 1954
Skripka G.M. - 273
Skvortsov V.A. - 969
Slepkov A.I. - 211, 1586
Slinker S.P. - 99, 945, 1270, 1276, 1282
Sloan M.L. - 305
Slutz S.A. - 31, 1801
Smetanin V.I. - 1033
Smirnov A.V. - 431
Smirnov L.V. - 436
Smirnov N.A. - 1194
Smith A.C. - 1960
Smith D.L. - 1141
Smith J.R. - 1328
Smith M. - 1215
Smith O.A. - 1568
Smith R. - 203
Smolenkova O.A. - 425
Smorgonsky A.V. - 195
Sochugov N.S. - 1586
Soln J. - 1211
Sonegawa T. - 323, 1971
Sotnikov G.V. - 1643
Spasovsky I.P. - 1700
Spielman R.B. - 2002
Spindler G. - 1715
Sprangle P. - 313, 1746, 1813
Sprehn D. - 203
Stallings C. - 385
Stark R.A. - 1233, 1954
Stearns W.F. - 781
Stein E. - 51, 735, 756
Stephanakis S.J. - 871, 1159
Stinnett R.W. - 31, 788
Stogov A.A. - 1673
Stoltz O. - 51, 68, 735, 741, 963
Strelkov P.S. - 1545, 1550
Streltsov A.P. - 1930
Stricklett K.L. - 640
Striffler C.D. - 185, 1449
Stringfield R.M. - 227, 688, 1473, 1661
Struckman C.K. - 43
Struve K.W. - 109, 1141, 1328, 1960
Stygar W.A. - 31
Sudan R.N. - 769, 921, 1795
Sugimura H. - 847
Sukhushin K.N. - 1586
Sulakshin A.S. - 1574
Sullivan C.A. - 1479
Sun R.F. - 1918
Sundquist B.U.R. - 939
Sunka P. - 1221, 1337
Suvorov V.A. - 195
Suvorov V.G. - 1655
Sviatoslavsky G. - 1901
Sviatoslavsky I.N. - 1901
Swanekamp S.B. - 1159
Swegle J. - 341
Syomin B.N. - 1360
Syutin O.N. - 273, 505
Tachibana T. - 847
Tahir N.A. - 988
Taillandier P. Le - 1752
Takahashi K. - 841
Tamagawa F. - 1825
Tananakin V.A. - 273
Tang C.M. - 1288
Tang H. - 676
Tantawi S.G. - 185, 1449, 1455
Tao Z. - 1876
Tarakanov V.P. - 1322, 1373, 1538, 1545, 1556
Tarasov A.D. - 273
Tazima T. - 853, 865
Temkin R.J. - 1123, 1135, 1526, 1532
Terry R. - 167
Thevenot M. - 1861
Thompson J. - 402, 598
Thompson J.R. - 305
Thompson L. - 1855
Thornhill J.W. - 159, 2044
Timofeyev V.V. - 1205
Ting A. - 313
Tisone G.C. - 31, 794, 800
Tkach Yu.V. - 541, 1073
Tkachenko K.I. - 436
Tokuda S. - 255
Tolkachev V.S. - 419
Tomimasu T. - 1758
Tomskikh O.N. - 1870
Trainor J. - 175
Trintchouk F.B. - 1924
Trotz S. - 1135
Troyansky L. - 143
Tsang K.T. - 291, 1294
Tskhai V.N. - 1318
Tsuchida S. - 682
Tsvetkov V.I. - 1690
Tukhfatullin A.A. - 1948
Turchi P.J. - 175, 408
Turman B.N. - 109, 492, 1141, 1328
Tzeng C.C. - 1984
Uhm H.S. - 1239, 1679
Ullschmied J. - 1221, 1337
Ushakov A.G. - 517, 523
Usher M.A. - 621
Usov Yu.P. - 1033, 1870
VanDeValde D. - 333
VanDevender J.P - 31
VanHaaften F.W. - 227, 688
Vasilevsky M.A. - 1930
Vasiljev V.V. - 1870
Vatrunin V.Y. - 1655
Vaysburd D.I. - 1360
Velarde G. - 1001
Velarde P. - 1001
Ventzek P.L.G. - 1789
Veresov V.P. - 273
Veron L. - 2008
Vijayan T. - 1831
Villate D. - 1861
Vladyko V.B. - 1306
Vlasov A. - 1619
Vlieks A. - 1147
Vodovosov V.M. - 1930
Volkov A.M. - 394
Volkov N.B. - 575
Volokitenkova I.L. - 1643
Vorobjev O.Yu. - 68, 957, 969
Voronkov S.N. - 1550
Voropaev S.G. - 127, 1015, 1021, 1049
Vyacheslavov L.N. - 1037
Waast B. - 939
Waganaar W.J. - 88
Wagner J.S. - 109
Waisman E. - 402, 553, 598
Walter M.T. - 1789

Wang D.X. - 1182
Wang J.G. - 1182
Wang L.G. - 1918
Wang L.H. - 1918
Wang M.C. - 1721
Wang P. - 903, 1397
Wang Q.S. - 1491
Wang X. - 462, 468, 1343
Wang X.H. - 1918
Wang Y. - 1343
Wang Z. - 676, 1721
Wang Z.X. - 1696
Warn C. - 1887
Wasierski R.F. - 227, 688
Watanabe A. - 255
Watkins R.M. - 1093, 1637
Wavrik R.W. - 333
Weber B.V. - 375, 603, 609, 871, 1159
Weber G.J. - 333
Wei Y.M. - 1918
Weidenheimer D.M. - 640, 1215
Weidman D.J. - 1233
Weingarten A. - 143, 633
Welch D.R. - 109, 119
Wen M. - 1984
Wenger D.F. - 31, 781
Werner P.W. - 1328
Wessel F.J. - 357, 1996, 2008
Westermann Th. - 735, 747, 756
Westfall R.L. - 486
Wheat R.M. - 1473
Whitney K.G. - 159, 2044, 2056
Whittum D.H. - 1270
Wilkinson M. - 402
Willey M. - 203
Wilson A. - 402, 598
Wilson J. - 297
Wittenberg L.J. - 1901
Wong S.L. - 136, 159
Worley J.F. - 474, 480
Wright E.L. - 1147
Wright J. Kinross - 1473
Wurtele J.S. - 1135, 1526
Xia N. - 676
Yadlowsky E.J. - 2032, 2038
Yalovets A.P. - 1165
Yamanaka C. - 76, 884, 1403
Yang D. - 462, 468
Yankovskiy B.D. - 443
Yao D.S. - 1918
Yasuike K. - 76, 884, 1403
Yasuoka J. - 1227
Yatsui K. - 323, 682, 847, 853, 859, 1971
Yee J.H. - 652
Yeh C.K. - 1984
Yeh T.R. - 1984
Yoshikawa M. - 1227
Young F.C. - 159, 871
Yu Q. - 806
Yu S.S. - 297, 951
Yu Y.J. - 1984
Yuan X. - 1918
Yushkov M.V. - 127, 1117
Yushkov Yu.G. - 1685
Zagulov F.Ya. - 195
Zajivikhin V.V. - 425, 592
Zakatov L.P. - 517, 523
Zakharov A.N. - 1586
Zakutayev A.N. - 1966
Zavialov M.A. - 1318
Zcherlitsin A.G. - 1685
Zeng N. - 462, 468, 1343
Zhai X. - 1631
Zhang D. - 1343
Zhang L. - 1721
Zhang M. - 1918
Zhang Q. - 676
Zhang S. - 1876
Zhang Y.M. - 1918
Zhang Z.X. - 1728
Zhao R. - 462, 468
Zhao X.Q. - 1918
Zhdanov V.S. - 1655
Zhdanov Yu.A. - 541
Zheng B. - 676
Zherlitsin A.G. - 1690
Zinamon Z. - 982
Zinchenko V.F. - 1205
Zorin V.B. - 419
Zotkin R.P. - 431, 1117

Registrant List

Beams 92 Statistics

	BULGARIA	CHILE	CZECHOSLOVAKIA	FRANCE	GERMANY	INDIA	ISRAEL	JAPAN	PEOPLES REPUBLIC OF CHINA	REPUBLIC OF CHINA	RUSSIA	SPAIN	SWEDEN	UKRAINE	UNITED KINGDOM	UNITED STATES OF AMERICA	TOTALS
Attendance	1		4	13	10		12	15	9	2	64	2		1	4	286	423
Abstracts Submitted	4	1	3	7	11	2	9	28	16		123	2	3	9	3	192	413
Papers Submitted	1		4	6	9	1	4	21	13		85	2		2	2	154	304

Abstract Distribution by Topic and Country

Ion Beams				3	9		1	14			8	2				31	68
Electron Beams	2		1			1		2	1		32					36	75
Pulsed Power							2	2	4		20			1	2	25	56
Microwaves	1			1					1		28			6		36	73
Free Electron Lasers	1			1	1			3	3		5				1	10	25
Advanced Accelerators				1		1	1	2	1		5			2		22	35
Plasma Discharges		1	2	1				1	1		8		3			14	31
Beam Diagnostics							5	1	4		3					7	20
Applications					1			3	1		14					11	30

NAME	AFFILIATION, ADDRESS	PHONE • FAX
Abe, D. K.	University of Maryland, Lab. for Plasma Res., Energy Res. Bld., College Park, MD, 20742, USA	301/474-4731 • 301/314-9437
Agee, Forrest	Harry Diamond Lab., Attn: SLCHD-NW-HP, 2800 Powder Mill Rd., Adelphi, MD, 20783, USA	301/394-4864 • 301/394-1416
Akiyama, Hidenori	Kumamoto University, Dept. of Elec. Eng., Kumorami 2-39-1, Kumamoto, 860, JAPAN	096/345-2111 • 096/345-1553
Alberti, Stefano	M.I.T., Plasma Fusion Center, NW16-17, 167 Albany St., Cambridge, MA, 02139, USA	617/258-9179 • 617/253-6078
Allen, Steven	Lawrence Livermore Nat. Lab., MFE Prog., P.O. Box 808, L-637, Livermore, CA, 94550-9900, USA	510/423-2676 • 510/423-2395
Allred, Daniel	Dept. of Defense, 9800 Savage Road, Ft. Meade, MD, 20755, USA	301/688-6485
Altgilbers, Larry	Strategic Defense Command, 3805 Jamestown Dr., Huntsville, AL, 35810, USA	205/955-1488 • 205/955-5722
Anthouard, Philippe	C.E.A. - CESTA, Service DT/PE, BP No 2, LeBarp, 33114, FRANCE	56 68 40 69 • 56 68 49 09
Antoniades, John	Naval Research Lab., Code 6751, 4555 Overlook Ave. S.W., Washington, DC, 20375, USA	202/767-2077 • 202/767-1607
Apruzese, John P.	Naval Research Lab., Code 6720, 4555 Overlook Ave. S.W., Washington, DC, 20375, USA	202/767-2939
Arzannikov, Andrei V.	Inst. of Nuclear Physics, Novosibirsk, 630090, RUSSIA	3832/35-60-31 • 3832/35-21-63
Atanassov, Rossen	Sofia University, General Physics Dept., 5 blvd. J. Bouchier, Sofia, 1126, BULGARIA	62-561-6386 • 359-2-46-3589
Ayral, Helene	C.E.A. Limeil - Valenton, DPAGAA/ECA, Villeneuve St. Georges, 94195, FRANCE	45956912 • 45959555
Back, Norman	Lawrence Livermore National Lab., M.S. L-281, P.O. Box 808, Livermore, CA, 94550, USA	510/422-0635 • 510/422-2383
Bailey, James	Sandia National Lab., Div. 1277, P.O. Box 5800, Albuquerque, NM, 87185-5800, USA	505/845-7203 • 505/845-7820
Baker, Mary C.	Texas Tech University, Elec. Eng. Dept., P.O. Box 4439, Lubbock, TX, 79409, USA	806/793-4716 • 806/742-1281
Baksht, Rina B.	High Current Electr. Inst., Academichesky Pr., 4, Tomsk, 634050, RUSSIA	• 128114 TAKT SU
Barker, Robert	Boiling Air Force Base, Office of Scientific Res., Bld. 410, Washington, DC, 20332-6448, USA	202/767-5011 • 202/767-4986
Barreto, Gilberto	Cornell University, Lab. of Plasma Studies, 369 Upson Hall, Ithaca, NY, 124853, USA	607/255-4127 • 607/255-3004
Bauer, Walter H.	Kernforschungszentrum, INR, Postfach 3640, Karlsruhe, D-W7500, GERMANY	07247-82-3869 • 07247-82-4874
Ben-Ari, Margalit	RAFAEL, Dept. 23, P.O. Box 2250, Haifa, 31021, ISRAEL	972-4-725905 • 972-4-795315
Benford, James	Physics International Co., HPM, 2700 Merced St., San Leandro, CA, 94577, USA	510/577-7157 • 510/577-7283
Bieg, Kevin W.	U.S. Dept. of Energy, DP-28, 19901 Germantown Road, Germantown, MD, 20585, USA	301/903-4323 • 301/903-5604
Blaugrund, Abraham	Weizmann Inst. of Sci., Dept. of Nuclear Physics, P.O. Box 26, Rehovot, 76100, ISRAEL	972/834-3458 • 972/834-4106
Bloomquist, Doug	Sandia National Lab., Dept. 1236, P. O. Box 5800, Albuquerque, NM, 87185, USA	505/845-7844 • 505/845-7864
Bluhm, Hans	Kernforschungszentrum, INR, Postfach 3640, Karlsruhe, D-W7500, GERMANY	0049-7247-822438 • 7247-824874
Bock, Gregory	P.O. Box 260, Herndon, VA, 22070, USA	
Bodner, Stephen	Naval Research Lab., Code 6730, 4555 Overlook Ave. S.W., Washington, DC, 20375, USA	202/767-2730 • 202/767-0046
Bonnafond, C.	C.E.A. - CESTA, Service de DT/PE, Le Barp 2, LeBarp, 33114, FRANCE	56-68-48-84 • 56-68-49-09
Bosamykin, Valeri S.	Inst. of Exp. Physics, Div. of Radiation Res., Shvernik St., Arzamas, 607200, RUSSIA	831/3013919 • 831/3054565
Boulais, Kevin A.	Naval Surface Warfare Ctr., MS R42, 10901 New Hampshire Ave., Silver Spring, MD, 20903, USA	301/394-2556 • 301/394-5062
Bourham, Mohamed	North Carolina State University, Dept. of Nuc. Eng., P.O. Box 7909, Raleigh, NC, 27695-7909, USA	919/515-7662 • 919/515-5115
Bowers, Richard L.	Los Alamos National Lab., B-259, Los Alamos, NM, 87545, USA	505/667-4726 • 505/665-7725

NAME	AFFILIATION, ADDRESS	PHONE • FAX
Brainard, John P.	Sandia National Lab., Div. 2564, P. O. Box 5800, Albuquerque, NM, 87185, USA	505/844-6462 • 505/844-2919
Brandt, Howard	Harry Diamond Lab., Code SLCHD-NW-TN, 2800 Powder Mill Rd., Adelphi, MD, 20783, USA	301/394-4143 • 301/394-4704
Bratman, Vladimir L.	Inst. of Applied Physics, Ulyanov St., 46, Nizhny Novgorod, 603600, RUSSIA	8312/36-58-10 • 8312/36-20-61
Brownell, John	Los Alamos National Lab., X-5, F669, P.O. Box 1663, Los Alamos, NM, 87545, USA	505/667-7780 • 505/665-7725
Bugaev, Sergey P.	High Current Electr. Inst., Academichesky Pr., 4, Tomsk, 634055, RUSSIA	3822/258 544 • 3822/259 410
Bulan, Vladimir V.	TRINITI, Troitsk, Moscow, 142092, RUSSIA	
Burdakov, Alexander	Inst. of Nuclear Physics, Novosibirsk, 630090, RUSSIA	3832/35-92-74 • 3832/35-21-63
Burns, Michael	Los Alamos National Lab., MS P-940, M-4, P.O. Box 1663, Los Alamos, NM, 87545, USA	505/665-2215 • 505/665-3359
Burtsev, Vitold A.	Efremov Inst., Metallostroje, St. Petersburg, 189631, RUSSIA	
Bystritskii, Vitaly M.	High Current Electr. Inst., Academichesky Pr., 4, Tomsk, 634055, RUSSIA	382-2-258534
Cable, Michael	Lawrence Livermore National Lab., Lasers/ICF, L-473, 7000 East Ave, Livermore, CA, 94550, USA	510/423-6536 • 510/422-8395
Carlsten, Bruce	Los Alamos National Lab., AT-7/MS H-825, P.O. Box 1663, Los Alamos, NM, 87545, USA	505/667-5657 • 505/667-8207
Carmel, Yual	University of Maryland, Lab. for Plasma Res., Energy Res. Bld., College Park, MD, 20742, USA	301/405-5046 • 301/314-9437
Chen, Chipping	M.I.T., Plasma Fusion Center, NW16-264, 167 Albany St., Cambridge, MA, 02139, USA	617/253-8506 • 617/253-0807
Cherepenin, Vladimir	Inst. of RadioEng. and Electr., Marx Avenue, 18, Moscow, 103907, RUSSIA	• 7-095-2038414
Choi, Jin Joo	Naval Research Lab., Code 6840, 4555 Overlook Ave. S.W., Washington, DC, 20375, USA	202/767-9202
Chuchem, David	NRC-Negev, Laser Unit, P.O. Box 9001, Beersheva, ISRAEL	972-57-568165 • 972-57554848
Church, Bruce W.	Cornell University, Lab. for Plasma Studies, 369 Upson Hall, Ithaca, NY, 14853, USA	607/255-4723 • 607/255-3004
Church, David	Student, address N/A, USA	
Clark, Robert	Naval Research Lab., Code 6720, 4555 Overlook Ave. S.W., Washington, DC, 20375, USA	202/767-6782 • 202/404-7596
Cochran, Frederick L.	Berkeley Res. Assoc., P.O. Box 852, Springfield, VA, 22150, USA	202/767-6783 • 703/750-3434
Coffey, Timothy	Naval Research Lab., Code 1001, 4555 Overlook Ave. S.W., Washington, DC, 20375, USA	202/767-3301
Coleman, Michael	Directed Technologies, Inc., 5945 Pacific Center Blvd. #510, San Diego, CA, 92121, USA	619/452-4231 • 619/452-0056
Colombant, Denis	Naval Research Lab., Code 6790, 4555 Overlook Ave. S.W., Washington, DC, 20375, USA	202/404-7721 • 202/767-0631
Commisso, Robert	Naval Research Lab., Code 6777, 4555 Overlook Ave. S.W., Washington, DC, 20375, USA	202/767-3066 • 202/767-0436
Cook, Donald L.	Sandia National Lab., Dept.1202, P. O. Box 5800, Albuquerque, NM, 87185, USA	505/845-7481 • 505/845-7864
Cooperstein, Gerald	Naval Research Lab., Code 6770, 4555 Overlook Ave. S.W., Washington, DC, 20375, USA	202/767-2290 • 202/767-0436
Corrigan, John	Harry Diamond Lab., SLCHD-NW-RS, 2800 Powder Mill Rd., Adelphi, MD, 20783, USA	301/394-2290 • 301/394-4706
Cravey, Ray	Lawrence Livermore National Lab., MS L-153, 7000 East Avenue, Livermore, CA, 94550, USA	415/422-9119 • 415/423-5080
Crawford, Mark	Texas Tech University, Dept. of Elec. Eng., P.O. Box 43102, Lubbock, TX, 79409, USA	806/742-3507 • 806/742-1281
Crouch, Dave	General Dynamics, P.O. Box 2507, Pomona, CA, 91769-2507, USA	714/945-7014 • 714/945-7945
Cuneo, Michael	Sandia National Lab., Div. 1231, P. O. Box 5800, Albuquerque, NM, 87185, USA	505/845-7547 • 505/845-7464
Danly, Bruce G.	M.I.T., NW16-172, 167 Albany St., Cambridge, MA, 02139, USA	617/253-8454 • 617/253-6078

NAME	AFFILIATION, ADDRESS	PHONE • FAX
Davis, Harold A.	Los Alamos National Lab., MS-E526, P.O. Box 1663, Los Alamos, NM, 87545, USA	505/667-8373 • 505/665-3552
Davis, John	Physical Sciences Inc., 635 Slaters Lane, MS G101, Alexandria, VA, 22314, USA	703/548-6410 • 703/684-0697
Davis, Joseph	UCLA, Dept. of Elec. Eng., 405 Hilgard Avenue, Los Angeles, CA, 90024-1594, USA	310/206-2039 • 310/206-8220
Davis, Tim	Cornell University, High Voltage Lab., 909 Mitchell St., Ithaca, NY, 14850, USA	607/255-3552 • 607/255-3004
Deeney, Christopher	Physics International Co., Plasma Physics Dept., 2700 Merced St., San Leandro, CA, 94577, USA	415/577-7139 • 415/577-7283
Degnan, James	Phillips Laboratory, Kirtland AFB, Albuquerque, NM, USA	
del Rosario, Jr., R.	Harry Diamond Lab., HIFX/HPM SLCHO-NW-RS, 2800 Powder Mill Rd., Adelphi, MD, 20783, USA	301/394-2238
Desjarlais, Michael	Sandia National Lab., Div. 1265, P.O. Box 5800, Albuquerque, NM, 87185, USA	505/845-7273 • 505/845-7890
Dewitt, Robert	U.S. Dept. of Energy, MS DP-241, Washington, DC, 20585, USA	301/903-3311 • 301/903-5604
Didenko, Andre N.	Moscow Eng. Phys. Inst., Charged Part. Accel., Kashirskoe Shosse, 31, Moscow, 115409, RUSSIA	324-80-00 • 7-095-4841729
Ding, Bainan	University of Maryland, Lab. for Plasma Res., Energy Res. Bld., College Park, MD, 20742, USA	301/434-8007 • 301/314-9437
Diyankov, Vladimir S.	Inst. of Technical Physics, Flat-1, Stoicovkogo-8, Chelyabinsk-70, Chelyabinsk, 454070, RUSSIA	8-351-72-2-41-68
Dolgachev, George I.	Kurchatov Inst., Moscow, 123182, RUSSIA	• 7-095-943-0073
Doucet, Henri	C.E.A. Limeil - Velenton, B.P. 12, Villeneuve St. Georges, F-94195, FRANCE	1-692-64711 • 1-692-66094
Douglas, Melissa	Phillips Laboratory, WSP, Kirtland AFB, Albuquerque, NM, 87117-6008, USA	505/846-8134 • 505/846-9900
Drobot, Adam T.	S.A.I.C., 1710 Goodridge Dr., P.O. Box 1303, McLean, VA, 22102, USA	• 703/821-1134
Dukart, Raymond	Sandia National Lab., Div. 1271, P.O. Box 5800, Albuquerque, NM, 87185, USA	505/845-7276 • 505/845-7664
Ekdahl, Carl	Los Alamos National Lab., P-14, Mail Stop D-410, P. O. Box 1663, Los Alamos, NM, 87545, USA	505/667-2470 • 505/667-7664
Esarey, Eric	Naval Research Lab., Code 6790, 4555 Overlook Ave. S.W., Washington, DC, 20375, USA	202/404-7720 • 202/767-0631
Eshhar, Shmuel	RAFAEL, Dept. 23, P.O. Box 2250, Haifa, 31021, ISRAEL	972-4-795100 • 972-4-795315
Etlicher, Bernard	Ecole Polytechnique, Laboratoire de Physique de Milieux Ionises, Palaiseau, F-91128, FRANCE	331-69-33-41-15 • -69-33-30-23
Evans, Kirk	Berkeley Scholars, P.O. Box 852, Springfield, VA, USA	703/750-3434
Eylon, Shmuel	Lawrence Berkeley Lab., AFRD/HIFAR, Bld. 47/112, 1 Cyclotron Road, Berkeley, CA, 94720, USA	510/486-5290 • 510/486-5392
Faehl, Rick J.	Los Alamos National Lab., MS B-259, P.O. Box 1663, Los Alamos, CA, 87545, USA	505/667-2806 • 505/665-4080
Faltens, Andris	Lawrence Berkeley Lab., AFRD/HIFAR Res. Gp, 47/112, 1 Cyclotron, Berkeley, CA, 94720, USA	510/486-7213 • 510/486-5392
Fazio, Michael V.	Los Alamos National Lab., Mail Stop H-851, P.O. Box 1663, Los Alamos, NM, 87545, USA	505/667-3281 • 505/667-8207
Fernsler, Richard F.	Naval Research Lab., Code 6790, 4555 Overlook Ave. S.W., Washington, DC, 20375, USA	202/767-6786 • 202/767-0631
Filuk, Alex	Sandia National Lab., Organization 1271, P.O. Box 5800, Albuquerque, NM, 87185, USA	505/845-7385 • 505/845-7890
Fischer, Richard	Naval Research Lab., Code 6793, 4555 Overlook Ave. S.W., Washington, DC, 20375, USA	202/767-3765 • 202/767-3950
Fisher, Amnon	Naval Research Lab., Code 6790, 4555 Overlook Ave. S.W., Washington, DC, 20375, USA	202/767-2674 • 202/767-0631
Fleurier, Claude	Universite d'Orleans, GREMI/CNRS, BP 6759, Orleans, F-45067, FRANCE	384-1-7123 • 384-1-7154
Forster, David	A.W.E. (MOD-PE), Dept. HWH, Bld. H36, Aldermaston, Reading, Berkshire, RG7 4PR, UK	0734-814111, X4396 •
Fortov, Vladimir E.	Inst. for High Temp., USSR Acad. of Sci., IVTAN, Izhorskaya, 13/19, Moscow, 127412, RUSSIA	485-79-88 • 485-79-90

NAME	AFFILIATION, ADDRESS	PHONE • FAX
Frazier, George	Physics International Co., Electr. Sys. Div., 2700 Merced St., San Leandro, CA, 94577-0599, USA	415/377-7122 • 415/577-7283
Freund, Henry P.	S.A.I.C., Applied Physics Operation, 1710 Goodridge Dr., McLean, VA, 22102, USA	703/734-5840 • 703/821-1134
Frost, Charles	Sandia National Lab., Div. 1248, P.O. Box 5800, Albuquerque, NM, 87185, USA	505/845-7135 • 505/845-7003
Fu, Shu-zhen	Inst. of Appl. Electr., China Acad. of Eng. Phys., POB 523, No. 65, Chendu, Sichuan, 610003, PRC	
Garate, Eusebio	UC Irvine, Physics Dept., PS II, Irvine, CA, 92717, USA	714/856-7095 • 714/725-2174
Gardes, Daniel	I.P.N. Orsay, Institut de Physics Nucleaire, BP No1, Orsay, Cedex, F-91606, FRANCE	69-41 72 17 • 69-284100
Gavrilov, Nikolay V.	Inst. of Electrophysics, Komsomolskaya St., 34, Ekaterinburg, 620219, RUSSIA	343/2-44-18-53
Geary, James	Berkeley Res. Assoc., 5532 Hempstead Way, Springfield, VA, 22151, USA	703/569-3924
Gee, Mark	AFRRI, NNMC, Bld. 42, Bethesda, MD, 20889-5145, USA	301/295-1288 • 301/295-3000
Gerbelot, Nathalie	Thomson Tubes Electr., 2 rue Latecoere - BP23, Velizy Villacoublay Cedex, 78141, FRANCE	30 70 24 37 • 39 46 30 95
Getty, Ward	U of Michigan, EE&CS, 1301 Beal Ave., 3403 EECS Bldg., Ann Arbor, MI, 48109-2122, USA	313/764-3347 • 313/747-1781
Giguet, Eric	M.I.T., Plasma Fusion Center, Nw16-17, Cambridge, MA, 02139, USA	617/258-9179 • 617/253-6078
Gilad, Pinchas	RAFAEL, Scientific Dept., P.O. Box 2250, Haifa, 31021, ISRAEL	972-4-795100 • 972-4-795315
Gilgenbach, Ronald	University of Michigan, Nuclear Eng. Dept., 2355 Bonisteel Blvd., Ann Arbor, MI, 48109-2104, USA	313/763-1261 • 313/763-4540
Ginzburg, Naum S.	Inst. of Applied Physics, 46 Uljanov St., Nizhny Novgorod, 630600, RUSSIA	• 9-0-8312362061
Giuliani, John L.	Naval Research Lab., Code 6723, 4555 Overlook Ave. S.W., Washington, DC, 20375, USA	202/767-9299 • 202/767-7596
Glazyring, Igor V.	Inst. of Technical Physics, P.O. Box 83, Chelyabinsk, 454070, RUSSIA	8-351-72-3-73-80
Godfrey, Brendan	Phillips Laboratory, PL/WS, Kirtland AFB, Albuquerque, NM, 87117-6008, USA	505/846-4040 • 505/846-0417
Goebel, Dan M.	Hughes Res. Labs., RL-58, 3011 Malibu Canyon Road, Malibu, CA, 90265, USA	213/317-5372 • 213/317-5483
Goel, Balbir	Kernforschungszentrum, GmbH - INR, Postfach 3640, Karlsruhe, D-W7500, GERMANY	07247-82-2445 • 07247-82-4874
Gold, Steven	Naval Research Lab., Code 6793, 4555 Overlook Ave. S.W., Washington, DC, 20375, USA	202/767-4004 • 202/767-3950
Golden, Jeffrey	Berkeley Res. Assoc., P.O. Box 852, Springfield, VA, 22150, USA	/03/750-3434 • 301/750-3106
Golub, T. A.	High Current Electr. Inst., Academichesky Pr., 4, Tomsk, 634055, RUSSIA	25-87-11 • 128114 TAKT SU
Gondarenko, N. A.	High Current Electr. Inst., Academichesky Pr., 4, Tomsk, 634055, RUSSIA	25-87-11 • 128114-TAKT SU
Goodrich, P.J.	Naval Research Lab., c/o Code 6770, 4555 Overlook Ave. S.W., Washington, DC, 20375, USA	202/767-2298 • 202/767-0436
Granatstein, Victor L.	University of Maryland, Lab. for Plasma Res., Energy Res. Bld., College Park, MD, 20742, USA	
Greenly, John B.	Cornell University, Lab. of Plasma Studies, 369 Upson Hall, Ithaca, NY, 14853, USA	607/256-5162 • 607/255-3004
Gregor, Joseph A.	University of Maryland, Lab. for Plasma Res., Energy Res. Bld., College Park, MD, 20742, USA	301/405-5027
Grigson, Mike	MOD Central Staffs, c/o M. Hubbard, British Emb., 3100 Mass.Ave., N.W., Wash., DC, 20008, USA	202/898-4398 • 202/898-4581
Grossmann, John M.	Naval Research Lab., Code 6771, 4555 Overlook Ave. S.W., Washington, DC, 20375, USA	202/404-7567 • 202/767-0436
Grothaus, Michael	Naval Surface Warfare Ctr., Code F45, Dahlgren, VA, 22448, USA	703/663-8057 • 703/663-8029
Guharay, Samar K.	University of Maryland, Lab. for Plasma Res., Energy Res. Bld., College Park, MD, 20742, USA	301/405-7369 • 301/314-9437
Gullickson, Richard	Defense Nuclear Agency, RAEV, 6801 Telegraph Road, Alexandria, VA, 22310, USA	703/325-7088 • 703/325-2959

NAME	AFFILIATION, ADDRESS	PHONE • FAX
Guo, H.	University of Maryland, Lab. for Plasma Res., Energy Res. Bld., College Park, MD, 20742, USA	
Gurr, Richard	Strategic Defense Command, Attn: CSSD-DE-N, P.O. Box 1500, Huntsville, AL, 35807-3801, USA	205/955-1568 • 205/955-5722
Haber, Irving	Naval Research Lab., Code 6790, 4555 Overlook Ave. S.W., Washington, DC, 20375, USA	202/767-3198
Hafizi, B.	Naval Research Lab., Code 6790, 4555 Overlook Ave. S.W., Washington, DC, 20375, USA	202/767-2874 • 202/767-0631
Hahn, Kyoung	Lawrence Berkeley Lab., AFRD/HIFAR GROUP, 47 -112, 1 Cyclotron, Berkeley, CA, 94720, USA	415/486-6372 • 415/486-5392
Hahn, Terry D.	Berkeley Res. Assoc., P.O. Box 852, Springfield, VA, 22150, USA	301/394-3657 • 301/394-3047
Hammer, David	Cornell University, Lab. of Plasma Sci., 369 Upson Hall, Ithaca, NY, 14853, USA	607/255-3916 • 607/255-3004
Hanson, David L.	Sandia National Lab., Div. 1231, P. O. Box 5800, Albuquerque, NM, 87185, USA	505/845-7547
Hendricks, Kyle J.	Phillips Laboratory, PL/WSR, Kirtland AFB, Albuquerque, NM, 87117-6008, USA	505/846-6770 • 505/846-9853
Hinshelwood, David	JAYCOR, 1608 Spring Hill Road, c/o Code 6771, Washington, DC, 22182-2270, USA	202/767-2298 • 202/767-0436
Hirshfield, J. L.	Omega-P, Inc., 2008 Yale Station, New Haven, CT, 06520, USA	203/288-6733 • 203/248-7071
Ho, Darwin	Lawrence Livermore National Lab., L-472, P.O. Box 808, 7000 East Ave, Livermore, CA, 94550, USA	510/423-9786 • 510/423-9969
Hoffman, Bruce	Thomson Components & Tubes, 40G Commerce Way, Totowa, NJ, 07511, USA	201/812-9000 • 201/812-9050
Hoppe, Peter	Kernforschungszentrum, INR, Postfach 3640, Karlsruhe, D-W7500, GERMANY	7247-822438 • 7247-825070
Horioka, K.	Tokyo Inst. of Tech., Dept. of Energy Sciences, Nagatsuta 4259, Midori-ku, Yokohama, 227, JAPAN	81 45 922-1111, X2661 • 921 1318
Hubbard, Richard F.	Naval Research Lab., Code 6790, 4555 Overlook Ave. S.W., Washington, DC, 20375, USA	202/767-2927 • 202/767-0631
Hughes, Thomas	Mission Res. Corporation, 1720 Randolph Road, S.E., Albuquerque, NM, 87106, USA	505/768-7719 • 505/768-7601
Hui, Bertram	DARPA/DSO, 1400 Wilson Blvd., Suite 111, Arlington, VA, 22209, USA	703/696-2239 • 703/696-2201
Humphries, Stan	University of New Mexico, Dept. of Elec. & Computer Eng., Albuquerque, NM, 87131, USA	505/277-5422 • 505/294-0222
Huttlin, George	Harry Diamond Lab., SLCHD-NW-RS, 2800 Powder Mill Rd., Adelphi, MD, 20783, USA	301/394-2290 • 301/394-4706
Hyder, Anthony	University of Notre Dame, 312 Main Bld., Notre Dame, IN, 46556, USA	219/239-8591 • 219/239-6630
Ignatov, Alexander	Inst. of General Physics, Vavilova, 38, Moscow, 117942, RUSSIA	
Johnson, Richard	FMC Naval Systems Div., Adv. Armaments/M170, 4800 East River Road, Minneapolis, MN, USA	612/572-6354 • 612/572-4903
Joyce, Glenn R.	Naval Research Lab., Code 6790, 4555 Overlook Ave. S.W., Washington, DC, 20375, USA	202/767-6785 • 202/767-0631
Jungwirth, Karel	Inst. of Plasma Physics, CSAV, Za Slovankou 3, P.O. Box 17, Prague, 18211, CZECHOSLOVAKIA	422 815-5268 • 42 2 858 6389
Kamada, Keiichi	Kanazawa University, Faculty of Sci., 1-1 Marunouchi, Kanazawa, Ishikawa, 920, JAPAN	0762-62-4281 X588 • 64-1059
Kanivets, Vasiliy I.	Moscow State University, Physics Faculty, Moscow, 119899, RUSSIA	095/939-30-04 • 095/939-11-66
Kapetanakos, C. A.	Naval Research Lab., Code 6795, 4555 Overlook Ave. S.W., Washington, DC, 20375, USA	202/767-2636 • 202/767-6900
Karow, Hans U.	Kernforschungszentrum, GmbH - INR, Postfach 3640, Karlsruhe, D-W7500, GERMANY	07247/82 24 63 • 07247/82 50 70
Kasuya, Koichi	Tokyo Inst. of Tech., Dept. of Energy Sciences, Nagatsuta 4259, Midori-ku, Yokohama, 227, JAPAN	45 922-1111 • 45 921-1318
Kato, Keith	General Dynamics, MS 800-10, P.O. Box 2507, Pomona, CA, 91769-2507, USA	714/945-7910 • 714/945-7945
Kawasaki, Sunao	Saitama University, Faculty of Sci., 255 Shimo-ohkubo, Urawa, Saitama, 338, JAPAN	048-852-2111 • 048-855-6295
Kehs, Alan	Harry Diamond Lab., SLCHD-NW-HP, 2800 Powder Mill Rd., Adelphi, MD, 20783, USA	301/394-4664 • 301/394-1416

NAME	AFFILIATION, ADDRESS	PHONE • FAX
Kenyon, Van	Naval Surface Warfare Ctr., M.S. H-23, 10901 New Hampshire Ave., Silver Spring, MD, 20903, USA	301/394-1889 • 301/394-3945
Kerslick, Graham S.	Cornell University, High Voltage Lab., 909 Mitchell St., Ithaca, NY, 14850, USA	607/255-3552 • 607/255-3004
Kessler, Gunther	Kernforschungszentrum, INR, Postfach 3640, Karlsruhe, D-W7500, GERMANY	07247/82-2440 • 07247/82-4874
Keys, Stephen	Advanced R&D, 3100 Clay Avenue, Orlando, FL, 32804, USA	
Kim, A. A.	High Current Electr. Inst., Academichesky Pr., 4, Tomsk, 634055, RUSSIA	3822/259 751 • 3822/259 410
Kirkman, George	Integrated Applied Physics, Inc., 50 Thayer Road, Waltham, MA, 02154, USA	617/489-1818 • 617/489-3521
Kirkpatrick, Douglas	S.A.I.C., Applied Physics Operation, 1710 Goodridge Dr., MS-2-3-1, McLean, VA, 22102, USA	703/821-4587
Kitamura, Akira	Kobe Univ.of Merc. Mar., Nuc. Eng., Fukaeminami-machi 5-1-1, Higashinada-ku, Kobe, 658, JAPAN	078-453-2332 • 078-412-9721
Klenov, Gennady I.	Moscow Radiotechnical Inst., Wazsavskoe Shosse, 132, Moscow, 113519, RUSSIA	3114312 • 7-095-3141053
Knyazev, Boris A.	Inst. of Nuclear Physics, Novosibirsk, 630090, RUSSIA	383/2-35-96-02 • 383/35-21-63
Koert, Peter	ARCO Power Tech, 1250 24th NW, Suite 850, Washington, DC, 20037, USA	202/223 8808 • 202/223-1377
Koidan, Vladimir S.	Inst. of Nuclear Physics, Novosibirsk, 630090, RUSSIA	35-95-89 • 3832/35-21-63
Kolb, Alan C.	Maxwell Laboratories, Inc., 8888 Balboa Ave., San Diego, CA, 92123, USA	619/576-7500 • 619/277-6754
Koshelev, Vladimir I.	High Current Electr. Inst., Academichesky Pr., 4, Tomsk, 634055, RUSSIA	• 128II4 TAKT SU
Kostas, Christopher	S.A.I.C., APO- M.S. T-II-3-1, 1710 Goodridge Dr., P.O. Box 1303, McLean, VA, 22102, USA	703/734-5805 • 703/821-1134
Kotov, Yury A.	Inst. of Electrophysics, Komsomolskaya St., 36, Ekaterinburg, 620219, RUSSIA	
Kova'Ichuk, B. M.	High Current Electr. Inst., Academichesky Pr., 4, Tomsk, 634055, RUSSIA	3822/259 654 • 3822/259 410
Kovalev, Nikolai F.	Inst. of Applied Physics, Uljanov St., 46, Nizhny Novgorod, RUSSIA	8312/36-58-10 • 8312/36-20-61
Krall, Jonathan	Naval Research Lab., Code 6791, 4555 Overlook Ave. S.W., Washington, DC, 20375, USA	202/404-7719 • 202/767-0631
Krejci, Ales	Inst. of Plasma Phys., CSAV, Pulse Plas. Sys., P.O. Box 17, Prague, 18211, CZECHOSLOVAKIA	422/815-3243 • 422/858-6389
Krishnan, Mahadevan	Science Res. Lab., Inc., 1150 Ballena Blvd., Suite 100, Alameda, CA, 94501, USA	415/521-8087 • 415/521-8292
Kristiansen, Magne	Texas Tech University, Dept. of Elec. Eng., P.O. 43102, Lubbock, TX, 79409-4439, USA	806/742-2224 • 806/742-1281
Kruglyakov, Eduard	Inst. of Nuclear Physics, Novosibirsk, 630090, RUSSIA	
Kusse, B. R.	Cornell University, Lab. of Plasma Studies, 369 Upson Hall, Ithaca, NY, 14853, USA	607/255-4127 • 607/255-3004
Kwan, Thomas	Los Alamos National Lab., MS-B259, P. O. Box 1663, Los Alamos, NM, 87545, USA	505/667-3447 • 505/665-4060
Lai, Shu T.	Phillips Laboratory, Mail Stop - WSVI, Hanscom AFB, MA, 01731, USA	617/377-2932
Lampe, Martin	Naval Research Lab., Code 6790, 4555 Overlook Ave. S.W., Washington, DC, 20375, USA	202/767-4041 • 202/767-0631
Latham, Peter	University of Maryland, Lab. for Plasma Res., Energy Res. Bld., College Park, MD, 20742, USA	301/405-5025 • 301/314-9437
Lau, Yue-Ying	Naval Research Lab., Code 6790, 4555 Overlook Ave. S.W., Washington, DC, 20375, USA	202/767-2675
Lawson, Wesley	University of Maryland, Lab. for Plasma Res., Energy Res. Bld., College Park, MD, 20742, USA	301/405-4972 • 301/314-9437
Lebedev, A. N.	Lebedev Inst., Leninsky Prospekt, 53, Moscow, 117924, RUSSIA	
Lebedev, Sergey	Inst. of Nuclear Physics, Novosibirsk, 630090, RUSSIA	3832-35-95-41 • 3832-35-21-63
Leeper, Ramon J.	Sandia National Lab., Organization 1277, P.O. Box 5800, Albuquerque, NM, 87185, USA	505/845-7185 • 505/845-7820

NAME	AFFILIATION, ADDRESS	PHONE • FAX
Len, L. K.	Naval Research Lab., c/o Code 6795, 4555 Overlook Ave. S.W., Washington, DC, 20375, USA	202/767-3135 • 202/767-6900
Leon, J. F.	Centre d'Etudes de Gramat, Gramat, F-46500, FRANCE	65105616 • 6510560g
Levush, B.	University of Maryland, Lab. for Plasma Res., Energy Res. Bld., College Park, MD, 20742, USA	301/405-5018 • 301/314-9437
Li, Hai	University of Maryland, Lab. for Plasma Res., Energy Res. Bld., College Park, MD, 20742, USA	301/405-4974 • 301/314-9437
Linford, James D.	Advanced R&D, 3100 Clay Avenue, Orlando, FL, 32804, USA	407/894-0111 • 407/894-0115
Lingerfelt, Chris	AFRRI, NNMC, Bld. 442, Bethesda, MD, 20889-5145, USA	301/295-1288 • 301/295-3000
Lisitsyn, Igor V.	High Current Electr. Inst., Academichesky Pr., 4, Tomsk, 634055, RUSSIA	382-2/25-85-34 • 382-2/25-94-10
Litz, Marc	Harry Diamond Lab., SLCHD-NW-RS, 2800 Powder Mill Rd., Adelphi, MD, 20783, USA	301/394-2238 • 301/394-3047
Liu, Jiangru	Northwest Inst. of Nuclear Tech., P.O. Box 69-13, Xian, Shanxi, 710024, PRC	029-363450 • 029-369313
Liu, Y. G.	Changsha Inst. of Tech., Dept. of Applied Physics, Changsha, Hunan, 410073, PRC	434601-83221 • 0731448307
Luhmann, Neville	UCLA, Elec. Eng. Dept./159410, 63-143 Eng. IV, Los Angeles, CA, 90024-1594, USA	310/825-4163 • 310/825-1528
MacFarlane, Joseph	University of Wisconsin, Fusion Tech. Inst., 1500 Johnson Dr., Madison, WI, 53706, USA	608/263-8485 • 608/263-4499
Maenchen, John	Sandia National Lab., Div. 1231, P. O. Box 5800, Albuquerque, NM, 87185, USA	505/845-8963 • 505/845-7841
Main, William T.	University of Maryland, Lab. for Plasma Res., Energy Res. Bld., College Park, MD, 20742, USA	301/405-5034 • 301/314-9437
Malouf, Perry	5308 Carlton St., Bethesda, MD, 20816, USA	301/229-2340 • 202/767-0082
Maron, Yitzhak	Weizmann Inst. of Sci., Dept. of Nuclear Physics, P.O. Box 26, Rehovot, 76100, ISRAEL	972-8-342560 • 972-8-466966
Marshall, Thomas	Columbia University, Appl. Physics Dept., Rm 213 S.W. Mudd Bld., NY, NY, 10027, USA	212/854-3116 • 212/854-8257
Martin, Theresa	Student, address N/A, USA	
Martinez-Val, Jose	Inst. of Nuclear Fusion, E.T.S.I.I., J. Gutierrez Abascal, 2, Madrid, 28006, SPAIN	34.1.5615891 • 34.1.5618618
Mason, Rodney J.	Los Alamos National Lab., P. O. Box 1663, X-1, MS F645, Los Alamos, NM, 87545, USA	505/667-4370 • 505/667-3389
Masuzaki, Masaru	Kanazawa University, Faculty of Sci., 1-1 Marunouchi, Kanazawa, Ishikawa, 920, JAPAN	0762-62-4281 • 0762-64-1059
Matzen, Keith	Sandia National Lab., Div. 1271, P. O. Box 5800, Albuquerque, NM, 87185, USA	505/845-7756 • 505/845-7864
Mayhall, David	Lawrence Livermore Nat. Lab., L156, 7000 East Ave., P. O. Box 808, Livermore, CA, 94550, USA	510/422-1510 • 510/422-3013
Mazarakis, Michael	Sandia National Lab., Div. 1242, P. O. Box 5800, Albuquerque, NM, 87185, USA	505/845-7138 • 505/845-7003
McDaniel, Dillon	Sandia National Lab., Dept. 1273, P.O. Box 5800, Albuquerque, NM, 87185-5800, USA	505/845-7494 • 505/845-7864
Meger, Robert	Naval Research Lab., Code 6750, 4555 Overlook Ave. S.W., Washington, DC, 20375, USA	202/767-2077 • 202/767-1607
Mehlhorn, T. A.	Sandia National Lab., Organization 1262, P.O. Box 5800, Albuquerque, NM, 87185, USA	505/845-7266 • 505/845-7890
Mendel, Clifford W.	Sandia National Lab., Div. 1273, P. O. Box 5800, Albuquerque, NM, 87185, USA	505/845-7492 • 505/845-7864
Menninger, William	M.I.T., Plasma Fusion Center, NW16-178, 167 Albany St., Cambridge, MA, 02139, USA	617/253-8646 • 617/253-6078
Merkel, George	Harry Diamond Lab., SLCHD-NW-TN, 2800 Powder Mill Rd., Adelphi, MD, 20783-1197, USA	301/394-2290 • 301/394-4706
Mesyats, Gennadi A.	Inst. of Electrophysics, Pervomaiskaya St., 91, Ekaterinburg, 620219, RUSSIA	• 7-095-938-2211
Mikkelson, Kenneth	Sandia National Lab., Div. 9343, P. O. Box 5800, Albuquerque, NM, 87185, USA	505/845-7238 • 505/845-7820
Miles, Louise	Naval Surface Warfare Ctr., H-23, 10901 New Hampshire Ave., Silver Spring, MD, 20903, USA	301/394-2119 • 301/394-3945

NAME	AFFILIATION, ADDRESS	PHONE • FAX
Miller, S. M.	University of Maryland, Lab. for Plasma Res., Energy Res. Bld., College Park, MD, 20742, USA	
Miller, Steve	AFRRI, Naval Medical Center, Bld. 42, Radiation Sources Dept., Bethesda, MD, 20889-5145, USA	301/295-1288 • 301/295-3000
Mitchell, Ian	Imperial College, PPG, Blackett Lab., Prince Consort Rd, London, SW7 2BZ, UNITED KINGDOM	071-589-5111 • 071-589-9463
Miyamoto, Shuji	Osaka University, Inst. of Laser Eng., 2-6 Yamada Oka, Suita, Osaka, 565, JAPAN	81-6-877-5111 • 81-6-877-4799
Moran, Stuart	Naval Surface Warfare Ctr., Code F-45, Dept. of the Navy, Dahlgren, VA, 22448, USA	703/663-8057 • 703/663-8029
Moschella, John J.	HY-Tech Res. Corp., Radford Industrial Center, 104 Centre Court, Radford, VA, 24141, USA	703/639-4019
Mosher, David	Naval Research Lab., Code 6770, 4555 Overlook Ave. S.W., Washington, DC, 20375, USA	202/767-6775 • 202/767-0436
Mourier, Georges	Thomson TTE, 2 Rue Latecoere, Velizy, 78140, FRANCE	
Mozgovoy, Alexander	Lebedev Inst., Leninsky Prospekt 53, Moscow, RUSSIA	
Murphy, Donald Paul	Naval Research Lab., Code 6751, 4555 Overlook Ave. S.W., Washington, DC, 20375, USA	202/767-2077 • 202/767-1607
Myers, Matthew	Naval Research Lab., Code 6751, 4555 Overlook Ave. S.W., Washington, DC, 20375, USA	202/767-2077 • 202/767-1607
Myers, T. J.	University of Maryland, Lab. for Plasma Res., Energy Res. Bld., College Park, MD, 20742, USA	
Nardi, Eran	Weizmann Inst. of Sci., Dept. of Nuclear Physics, P.O. Box 26, Rehovot, 76100, ISRAEL	972-8-34-3379 • 972-8-34-4106
Neau, Eugene L.	Sandia National Lab., Dept. 1243, P.O. Box 5800, Albuquerque, NM, 87185, USA	505/845-7120 • 505/845-7003
Nedoseev, Sergey L.	TRINITI, Troitsk, Moscow, 142092, RUSSIA	
Neri, Jesse	Naval Research Lab., Code 6773, 4555 Overlook Ave. S.W., Washington, DC, 20375, USA	202/404-7567 • 202/767-0436
Ngo, Mai T.	Mission Res. Corporation, 8560 Cinderbed Road, Suite 700, Newington, VA, 22122, USA	703/339-6500 • 703/339-6953
Nikolaev, Valentin S.	Inst. of Nuclear Physics, Novosibirsk, 630090, RUSSIA	3832-35-60-31 • 3832-35-21-63
Niu, Keishiro	Teikyo Univ. of Tech., Physics Lab., Ichihara, Chiba, 290-01, JAPAN	0436-74-5511 X3202 • -74-259 2
North, G. Gordon	Lawrence Livermore National Lab., Mail Stop L281, P. O. Box 808, Livermore, CA, 94550, USA	415/422-9869 • 415/422-2382
Nusinovich, Gregory	University of Maryland, Lab. for Plasma Res., Energy Res. Bld., College Park, MD, 20742, USA	301/405-5020 • 301/314-9437
O'Connell, James	Booz-Allen & Hamilton, Inc., Crystal Sq. 2, 1725 Jefferson Davis HW, Arlington, VA, 22202, USA	703/769-7416 • 703/685-6508
O'Shaughnessy, J.P	Colimer Semicond., 8000 Towers Crescent Dr., MS Tyson Towers 1350, Vienna, VA, 22182, USA	703/760-7877 • 703/760-7899
O'Shea, Patrick G.	Los Alamos National Lab., Apex Free-Electron Laser Lab., MS J-579, Los Alamos, NM, 87545, USA	505/667-1956 • 505/665-5823
Ogawa, Masao	Tokyo Inst. of Tech., Dept. of Energy Sciences, Nagatsuta 4259, Midori-ku, Yokohama, 227, JAPAN	45 922-1111 • 45-921-1318
Oliver, Bryan	Cornell University, Lab. for Plasma Studies, 369 Upson Hall, Ithaca, NY, 14853, USA	607/255-4723 • 607/255-3004
Olson, Craig L.	Sandia National Lab., Div. 1241, P.O. Box 5800, Albuquerque, NM, 87185, USA	505/845-7303 • 505/845-7890
Olson, Joseph C.	Cornell University, Lab. of Plasma Studies, 369 Upson Hall, Ithaca, NY, 14853, USA	607/255-4889 • 607/255-3004
Ossakow, Sidney L.	Naval Research Lab., Code 6700, 4555 Overlook Ave. S.W., Washington, DC, 20375, USA	202/767-2723 • 202/767-1607
Ottinger, Paul F.	Naval Research Lab., Code 6771, 4555 Overlook Ave. S.W., Washington, DC, 20375, USA	202/404-7567 • 202/767-0436
Papadichev, Vitaly A.	Lebedev Inst., Leninsky Prospekt 53, Moscow, 117924, RUSSIA	1326300 • 1357880
Park, Gun-Sik	Omega-P, Inc., c/o NRL, Code 6840, Washington, DC, 20375, USA	202/767-3936
Parker, R.K.	Naval Research Lab., Code 6840, 4555 Overlook Ave. S.W., Washington, DC, 20375, USA	202/767-6655

NAME	AFFILIATION, ADDRESS	PHONE • FAX
Parkes, David	DRA Malvern, c/o M. Hubbard, British Emb., 3100 Mass. Ave., N.W., Washington, DC, 20008, USA	202/898-4398 • 202/898-4581
Parks, Donald	S-Cubed Div. of MLI, 3398 Carmel Mountain Road, San Diego, CA, 92007, USA	619/587-8413 • 619/755-0474
Pasour, John A.	Mission Res. Corporation, 8560 Cinderbed Road, Suite 700, Newington, VA, 22122, USA	703/339-6500 • 703/339-6953
Pavlik, Dennis	Westinghouse Sci. & Tech. Ctr., MS 501-3E21, 1310 Beulah Road, Pittsburgh, PA, 15235, USA	412/256-1559 • 412/256-1948
Pavlovskii, Alexander	Inst. of Exp. Physics, Arsamas-16, Nizhny Novgorod, 607200, RUSSIA	
Pawley, Carl	Naval Research Lab., Code 6733, 4555 Overlook Ave. S.W., Washington, DC, 20375, USA	202/767-2705 • 202/767-0046
Pechacek, Robert E.	Naval Research Lab., Code 6751, 4555 Overlook Ave. S.W., Washington, DC, 20375, USA	202/767-2077 • 202/767-1607
Pechersky, Oleg P.	Efremov Inst., Metallostroje, St. Petersburg, 189631, RUSSIA	812/256-56-82 • 812/315-17-01
Peebles, David	UK Min. of Def., c/o M. Hubbard. British Emb.,3100 Mass. Ave., N.W., Wash., DC, 20008, USA	202/898-4398 • 202/898-4581
Pereira, Nino R.	Berkeley Res. Assoc., P. O. Box 852, Springfield, VA, 22150, USA	703/750-3434 • 703/750-3106
Perevodchikov, V. I.	Electrotechnical Inst., Krasnokazarmennaja Str. 2, Moscow, 111250, RUSSIA	361-53-84 •
Peter, William	Ben-Gurion University, Dept. of Physics, P.O. Box 653, Beersheva, 84105, ISRAEL	972-57-423-266 • 972-57-31340
Peterkin, Robert E.	Phillips Laboratory, WSP, Kirtland AFB, Albuquerque, NM, 87117-6008, USA	505/846-8134 • 505/846-9900
Peters, Gerald J.	U.S. Dept. of Energy, Div. of High /Energy Physics, ER-224, GTN, Washington, DC, 20585, USA	301/353-5228 • 301/353-2597
Peterson, Robert R.	University of Wisconsin, Fusion Tech. Inst., 1500 Johnson Dr., Madison, WI, 53706, USA	608/263-5646 • 608/263-4499
Petillo, John	S.A.I.C., Applied Physics Operation, MS-2-3-1, 1710 Goodridge Dr., McLean, VA, 22102, USA	
Piera, Mireia	Inst. of Nuclear Fusion, E.T.S.I.I., J. Gutierrez Abascal, 2, Madrid, 28006, SPAIN	34-1-4114148 • 34-1-5618618
Piffl, Vojtech	Inst. of Plasma Phys., CSAV, (REB), P.O. Box 17, Prague, 18211, CZECHOSLOVAKIA	422-815-3223 • 422-858-6389
Pina, Jose' F.	OSWR, P.O. Box 1925, Washington, DC, 20013, USA	
Prestwich, Kenneth	Sandia National Lab., Dept. 1240, P.O. Box 5800, Albuquerque, NM, 87185, USA	505/845-7000 • 505/845-7003
Prokopenko, A. A.	Inst. of Nuclear Physics, Novosibirsk, 630090, RUSSIA	
Pulsifer, Peter	Naval Research Lab., Code 6720, 4555 Overlook Ave. S.W., Washington, DC, 20375, USA	202/767-6704 • 202/404-7596
Quintenz, Jeffery P.	Sandia National Lab., Div. 1265, P.O. Box 5800, Albuquerque, NM, 87185, USA	505/845-7245 • 505/845-7890
Rains, Randolph G.	U.S. Army For. Sci. & Tech., IAAIF-RTB, 220 Seventh St., N.E., Charlottesville, VA, 22901USA	804/980-7887 • 804/980-7699
Ramirez, Juan J.	Sandia National Lab., Dept. 1204, P. O. Box 5800, Albuquerque, NM, 87185, USA	505/845-7051 • 505/845-7841
Ratajczak, Willi	Kernforschungszentrum, HVT/EA, Postfach 3640, Karlsruhe, D-W7500, GERMANY	07247-82-3013 • 07247/82-3186
Ratakhin, Nikolai A.	High Current Electr. Inst., Academichesky Pr., 4, Tomsk, 634055, RUSSIA	3822/259 335 • 3822/259 410
Reiser, Martin P.	University of Maryland, Lab. for Plasma Res., Energy Res. Bld., College Park, MD, 20742, USA	301/454-3188 • 301/314-9437
Rej, Donald J.	Los Alamos National Lab., P-1, Mail Stop E526, P.O. Box 1663, Los Alamos, NM, 87545, USA	505/665-1883 • 505/665-3552
Remnev, Gennadii E.	Nuclear Physics Inst., High Power Beam Lab. 52, P. O. Box 25, Tomsk, 634061, RUSSIA	440-097 • 128112 SU
Renk, Tim	Sandia National Lab., Div. 1231, P. O. Box 5800, Albuquerque, NM, 87185, USA	505/845-7491 • 505/845-7864
Rhee, Moon-Jhong	University of Maryland, Lab. for Plasma Res., Energy Res. Bld., College Park, MD, 20742, USA	301/405-4965 • 301/314-9437
Richter, Steven	Ktech Corporation, 901 Pennsylvania Avenue, N.E., Albuquerque, NM, 87110, USA	505/268-3379 • 505/266-4512

NAME	AFFILIATION, ADDRESS	PHONE • FAX
Riordan, John	Physics International Co., ASD Div./Dept. 7310, 2700 Merced St., San Leandro, CA, 94577, USA	510/577-7120
Rix, W.	Maxwell Laboratories, Inc., Balboa Div., 8888 Balboa Avenue, San Diego, CA, 92123-1506, USA	• 619/279-7794
Roberson, Charles	Office of Naval Res., Physics Div., Code 1112, 800 N. Quincy St., Arlington, VA, 22217, USA	703/696-4222 • 703/696-3945
Roderick, N.	University of New Mexico, Dept. of Chemical & Nuclear Eng., Albuquerque, NM, 87131, USA	505/277-5431 • 505/277-0813
Romary, Philippe	C.E.A. - CESTA, Service de Physique Experimentale, B.P. 2, Le Barp, F-33600, FRANCE	56684912 • 56684909
Rostoker, Norman	UC Irvine, Physics Dept., PS II, Irvine, CA, 92717, USA	714/856-6949 • 714/856-5903
Rowley, James	Defense Nuclear Agency, 6801 Telegraph Rd., Alexandria, VA, 22310, USA	
Rudakov, Leonid I.	Kurchatov Inst., Moscow, 123182, RUSSIA	
Rukhadze, Anri A.	Inst. of General Physics, Vavilova, 38, Moscow, 117942, RUSSIA	
Rullier, Jean-Luc	M.I.T., Plasma Fusion Center, Cambridge, MA, USA	
Russell, Robert	ANT Telecommunications, Inc., 205 Perry Parkway, Gaithersburg, MD, 20877, USA	301/670-9777 • 301/670-3992
Rutkowski, Henry	Lawrence Berkeley Lab., AFRD Res. Bld. 47/112, 1 Cyclotron Road, Berkeley, CA, 94720, USA	510/486-7209 • 510/486-5392
Ryutov, Dmitri	Inst. of Nuclear Physics, Novosibirsk, 630090, RUSSIA	• 3832-35-21-63
Salzborn, Erhard	Giessen University, Institut fur Kernphysik, Leihgesterner Weg 217, Giessen, D-W6300, GERMANY	0641-702-2658 • 0641-702-2672
Sandalov, A.N.	Moscow State University, Physics Dept., Moscow, 119899, RUSSIA	095/939-46-01 • 095/939-11-66
Sanford, Thomas W.	Sandia National Lab., Organization1231, P. O. Box 5800, Albuquerque, NM, 87185, USA	505/845-7816 • 505/845-7841
Santoru, Joseph	Hughes Res. Labs., 3185 Colchester Brook Lane, Fairfax, VA, 22031, USA	703/280-8194
Santos, Jonathan	SFA, Inc., c/o Naval Res. Lab., Code 4571, Washington, DC, 20375, USA	202/767-2077
Saraph, Girish	University of Maryland, Lab. for Plasma Res., Energy Res. Bld., College Park, MD, 20742, USA	301/405-4971
Sarfaty, M.	Weizmann Inst. of Sci., Physics Dept., Rehovot, 76100, ISRAEL	
Sato, Morihiko	Himeji Inst. of Tech., Dept. of Elec. Eng., 2167 Shosha, Himeji, Hyoga, 671-22, JAPAN	0792-66-1661 • 0792-66-8868
Savage, Mark	Sandia National Lab., Dept. 1273, P.O. Box 5800, Albuquerque, NM, 87185, USA	505/845-6920 • 505/845-7464
Savel'ev, Yury M.	Efremov Inst., Metallostroje, St. Petersburg, 189631, RUSSIA	
Schmidt, Winfried	Kernforschungszentrum, HDI-NP, Postfach 3640, Karlsruhe, D-W7500, GERMANY	07247-823728 • 07247-824972
Schneider, Ralph	Naval Surface Warfare Ctr., Code R-42, 10901 New Hampshire Ave., Silver Spring, MD, 20903, USA	
Schwirzke, Fred	Naval Postgraduate School, Dept. of Physics, Code PH/SW, Monterey, CA, 93943, USA	408/646-2635 • 408/646-2834
Seiler, Steven	Physical Sciences Inc., 635 Slaters Lane, MS G101, Alexandria, VA, 22314, USA	703/548-6410 • 703/684-0697
Selemir, Victor	Inst. of Exp. Phys., Dept. of Fund. and Appl. Res., Arsamas-16, Nizhny Novgorod, 607200, RUSSIA	8313012574 • 8313054565
Seleznev, Vladimir D.	Moscow Radiotechnical Inst., Wazsavskoe Schosse, 132, Moscow, 113519, RUSSIA	• 7 095/3141053
Sethian, John	Naval Research Lab., Code 6733, 4555 Overlook Ave. S.W., Washington, DC, 20375, USA	202/767-2705 • 202/767-1607
Sharp, William M.	Lawrence Livermore National Lab., Mail Stop L440, P.O. Box 808, Livermore, CA, 94550, USA	415/422-1688 • 415/423-2664
Shay, Henry	Lawrence Livermore National Lab., Comp. Org., L-66, 7000 East Ave, Livermore, CA, 94550, USA	510/422-4677 • 510/423-4820
Shcheglov, Mikhail A.	Inst. of Nuclear Physics, Novosibirsk, 630090, RUSSIA	

NAME	AFFILIATION, ADDRESS	PHONE • FAX
Sheehey, Pete	Los Alamos National Lab., MS-F645, Los Alamos, NM, 87545, USA	505/667-7879 • 505/665-3389
Shi, Jiangjun	Southwest Inst. of Fluid Physics, P.O. Box 523-55, Chengdu, Sichuan, 610003, PRC	0816-255839-4136 •
Shope, Steve	Sandia National Lab., Div. 1242, P. O. Box 5800, Albuquerque, NM, 87185, USA	505/845-7659 • 505/845-7003
Shpak, Valeri G.	Inst. of Electrophysics, Komsomolskaya St., 34, St. Petersburg, 620219, RUSSIA	3432/448085
Siambis, John G.	Litton Electron Device, 98 Mesa Court, Atherton, CA, 94207, USA	415/854-7881
Sincerny, Peter	Physics International Co., Adv. Simulator Dev. Div., 2700 Merced St., San Leandro, CA, 94577, USA	415/577-7138 • 415/577-7283
Sinebryukhov, A.	Inst. of Electrophysics, Ekaterinburg, 634055, RUSSIA	382-2/25-85-34 • 382-2/25-94-10
Singh, Amarjit	University of Maryland, Lab. for Plasma Res., Energy Res. Bld., College Park, MD, 20742, USA	301/405-5016 • 301/314-9437
Sinil'shikova, Irina V.	Lebedev Inst., Vavilova, 38, Moscow, 117924, RUSSIA	
Sirotinin, Yury V.	Kurchatov Inst., Moscow, 123182, RUSSIA	
Skopec, Marlene	Naval Surface Warfare Ctr.,R42, 10902 New Hampshire Ave., Silver Spring, MD, 20903, USA	301/394-2309
Slinker, Steven	Naval Research Lab., Code 6792, 4555 Overlook Ave. S.W., Washington, DC, 20375, USA	202/767- 3720
Sloan, M.L.	Austin Res. Associates, 1101 Capital of Texas Highway, South, Bld. B-210, Austin, TX, 78746, USA	512/328-9854 • 512/327-8906
Slutz, Stephen	Sandia National Lab., Div. 1265, P. O. Box 5800, Albuquerque, NM, 87185-5800, USA	505/845-7310 • 505/845-7890
Sluyter, Marshall	U.S. Dept. of Energy, Defense Program, DP-243/GTN, Washington, DC, 20585, USA	301/903-3345 • 301/903-6417
Smirnov, Valentin P.	TRINITI, Troitsk, Moscow, 142092, RUSSIA	• 7095-334-5776
Smith, David L.	Sandia National Lab., Div. 1242, P. O. Box 5800, Albuquerque, NM, 87185, USA	505/845-7141 • 505/845-7841
Smith, John R.	Titan/Spectron, P.O. Box 9254, Albuquerque, NM, 87119-9254, USA	505/764-5334 • 505/764-5399
Soln, Josip Z.	Harry Diamond Lab., Attn: SLCHD-NW-TN, 2800 Powder Mill Rd., Adelphi, MD, 20783, USA	301/394-4143
Spence, Philip W.	Pulse Sciences, Inc., 600 McCormick St., San Leandro, CA, 94577, USA	415/632-5100 • 415/632-5300
Spielman, Rick B.	Sandia National Lab., Div. 1273, P. O. Box 5800, Albuquerque, NM, 87185, USA	505/845-7470 • 505/845-7864
Spindler, Gerhard	German Aer. Res. Establ. (DLR), Pfaffenwaldring 38-40, Stuttgart 80, D-W7000, GERMANY	0711-6862-514 • 0711-6862-715
Sprangle, Phillip	Naval Research Lab., Code 6790, 4555 Overlook Ave. S.W., Washington, DC, 20375, USA	202/767-3493 • 202/767-0631
Stallings, Charles	Physics International Co., Div. 7000, 2700 Merced St., San Leandro, CA, 94577, USA	510/577-7111 • 510/577-7283
Stark, Robert	Naval Surface Warfare Ctr., Code R-42, 10903 New Hampshire Ave., Silver Spring, MD, 20903, USA	301/394-2278 • 301/394-5082
Stephanakis, Stavros	Naval Research Lab., Code 6773, 4555 Overlook Ave. S.W., Washington, DC, 20375, USA	202/767-2298 • 202/767-0436
Sternlieb, Abraham	Ministry of Defense, R&D Mafat, Hakirya, Tel-Aviv, 61909, ISRAEL	03/5630189 • 03/6376725
Stinnett, Regan W.	Sandia National Lab., Div. 1264, P. O. Box 5800, Albuquerque, NM, 87185, USA	505/845-7844 • 505/845-7864
Straw, David	W.J. Schaefer Assoc., 1901 North Fort Myer Dr., Suite 800, Arlington, VA, 22209, USA	703/558-7900 • 703/525-2691
Strelkov, Pavel S.	General Physics Inst., Plasma Physics Div., 38 Vavilova St., Moscow, 117942, RUSSIA	095/132-8216
Striffler, Charles D.	University of Maryland, Lab. for Plasma Res., Energy Res. Bld., College Park, MD, 20742, USA	301/405-5026 • 301/314-9437
Stringfield, Ray M.	Los Alamos National Lab., MS-H851, P.O. Box 1663, Los Alamos, NM, 87545, USA	505/665-3568 • 505/667-8207
Struve, Kenneth	Mission Res. Corporation, 1720 Randolph Road, S.E., Albuquerque, NM, 87106, USA	505/768-7720 • 505/768-7601

NAME	AFFILIATION, ADDRESS	PHONE • FAX
Sudan, Ravi	Cornell University, Lab. of Plasma Sci., 369 Upson Hall, Ithaca, NY, 14853, USA	607/255-4127 • 607/255-3004
Sullivan, Carol	Naval Research Lab., Code 6793, 4555 Overlook Ave. S.W., Washington, DC, 20375, USA	202/767-6999 • 202/767-3950
Sunka, Paval	Inst. of Plasma Phys., CSAV, Za Slovankou 3, P.O. Box 17, Prague, 18211, CZECHOSLOVAKIA	422-815-5268 • 422-858-6389
Swanekamp, Stephen B.	Naval Research Lab., Code 6770, 4555 Overlook Ave. S.W., Washington, DC, 20375, USA	202/404-7567 • 202/767-0436
Swegle, John	Lawrence Livermore National Lab., Mail Stop L377, P.O. Box 808, Livermore, CA, 94551, USA	510/423-0548 • 510/422-2485
Tang, Cha-Mei	Naval Research Lab., Code 6791, 4555 Overlook Ave. S.W., Washington, DC, 20375, USA	202/767-4148 • 202/767-0631
Tantawi, Sami G.	University of Maryland, Lab. for Plasma Res., Energy Res. Bld., College Park, MD, 20742, USA	301/405-5027
Tao, Zucong	Academy of Eng. Physics, P.O. Box 501, Chengdu, Sichuan, 610003, PRC	0816-25175 •
Tarakanov, Vladimir	Inst. of General Physics, Inst. of General Physics, Vavilov 38, Moscow, 117942, RUSSIA	
Tate, Jeffrey	U of MD, 1202C Energy Res. Bld., Lab. for Plasma Res., College Park, MD, 20742-3511, USA	301/405-5024 • 301/314-9437
Temkin, Richard	M.I.T., Plasma Fusion Center, NW16, 167 Albany St., Cambridge, MA, 02139, USA	617/253-5528 • 617/253-6078
Terry, Robert E.	Naval Research Lab., Code 6720, 4555 Overlook Ave. S.W., Washington, DC, 20375, USA	202/767-6782
Thompson, James R.	Austin Res. Associates, 1101 Capital of Texas Highway, South, Bld. B-210, Austin, TX, 78746, USA	512/328-9854 • 505/327-8906
Thornhill, Ward	Naval Research Lab., Code 6720, 4555 Overlook Ave. S.W., Washington, DC, 20375, USA	202/767-9299 • 202/404-7596
Tisone, Gary C.	Sandia National Lab., Div. 1275, P. O. Box 5800, Albuquerque, NM, 87185, USA	505/845-7270 • 505/845-7464
Tkach, Yuri V.	Kharkov Inst. of Physics & Technology, Ukraine	
Tokuda, Hachiroe	National Inst. for Def. Study, Japan Def. Agency, 2-2-1 Nakameguro, Meguro-ku, Tokyo, 153, JAPAN	03-3713-6111, X578 •-3713-6149
Tsang, Kang	S.A.I.C., 1710 Goodridge Dr., P.O. Box 1303, McLean, VA, 22102, USA	
Turman, Bobby	Sandia National Lab., P. O. Box 5800, Albuquerque, NM, 87185, USA	
Tzeng, C. C.	Inst. of Nuclear Energy Res., Physics Div., P. O. Box 3-4, Lung-Tan, Taiwan, ROC	03/471-2201 • 03/471-1408
Uhm, Han S.	Naval Surface Warfare Ctr., 10904 New Hampshire Ave., Silver Spring, MD, 20903, USA	301/394-1809 • 301/394-5135
Usov, Yuri P.	Nuclear Physics Inst., 2a, Lenina St., Box 25, Tomsk, 634050, RUSSIA	8-382-2-440100 •
VanDevender, J. Pace	Sandia National Lab., Dept. 1200, P. O. Box 5800, Albuquerque, NM, 87185, USA	505/845-7446 • 505/845-7464
Vaysburd, David I.	High Current Electr. Inst., Academicheski Avenue 4, Tomsk, 634055, RUSSIA	3822-25-86-11 • 3822-25-94-10
Vernier, Gilles	C.E.A., Pontfaverger, 51100, FRANCE	33-26037857 • 33-26037229
Vitkovitsky, Ihor	Logicon/RDA, 2100 Washington Blvd., Arlington, VA, 22204-5706, USA	703/486-3500 • 703/920-4710
Vyacheslavov, Leonid	Inst. of Nuclear Physics, Novosibirsk, 630090, RUSSIA	
Walchman, Karol	NRC-Negev, Laser Dept., P.O. Box 9001, Beer Sheva, 84190, ISRAEL	972/57-568107 • 972/57-554848
Walsman, Edwardo	S-Cubed Div. of MLI, 3398 Carmel Mountain Road, San Diego, CA, 92121, USA	619/587-8486 • 619/755-0474
Wang, Dun Xiong	University of Maryland, Lab. for Plasma Res., Energy Res. Bld., College Park, MD, 20742, USA	
Wang, Jian G.	University of Maryland, Lab. for Plasma Res., Energy Res. Bld., College Park, MD, 20742, USA	
Wang, Ming Chang	Shanghai Inst. of Optics & Fine Mech., P. O. Box 800211, Shanghai, 201800, PRC	21/953-4890 • 8621 9528885
Wang, Ping	University of Wisconsin, Nuclear Eng. & Eng. Physics, 1500 Johnson Dr., Madison, WI, 53706, USA	608/263-0807

NAME	AFFILIATION, ADDRESS	PHONE • FAX
Wang, Zhixiong	Northwest Inst. of Nuclear Tech., Mail Stop 15, P.O. Box 69, Xi An, Shan Xi, 710024, PRC	
Ware, Kenneth	Maxwell Laboratories, Inc., Adv. Simulation Tech., 9244 Balboa Ave, San Diego, CA, 92123, USA	619/576-7726 • 619/292-0546
Weber, Bruce	Naval Research Lab., Code 6773, 4555 Overlook Ave. S.W., Washington, DC, 20375, USA	202/767-2298 • 202/767-0436
Weidenheimer, D.	Berkeley Res. Assoc., Inc., P.O. Box 852, Springfield, VA, 22150, USA	301/394-2290
Weidman, Daniel	Advanced Tech. & Res. Corp., 14900 Sweitzer Lane, Laurel, MD, 20707, USA	301/498-8200 • 301/394-3026
Wells, Nikita	Rand Corporation - Consultant, 5332 Sherrier Place, N.W., Washington, DC, 20016, USA	202/244-5041
Wessel, Frank	Ecole Polytechnique, Laboratoire de PMI, Palaiseau, 91128, FRANCE	331-69-33-41-15 • -69-33-30-33
White, Roger	Maxwell Laboratories, Inc., 8888 Balboa Avenue, San Diego, CA, 92123, USA	619/576-7716 • 619/560-5092
Wilson, Andrew	Maxwell Laboratories, Inc., 8888 Balboa Avenue, Bldg. 2, San Diego, CA, 92123, USA	619/576-3755 • 619/277-6734
Wilson, Mark	U.S. Dept. of Energy, ER-543 GTN, Washington, DC, 20585, USA	301/903-5048 • 301/903-4716
Wong, Sik-Lam	Physics International Co., Nuclear Eff. Prog. Off., 2700 Merced St., San Leandro, CA, 94577, USA	510/577-7238 • 510/577-7108
Wright, Edward	Stanford Linear Acc., Klystr. & Microwave Dept., MS-33, P.O. Box 4349, Stanford, CA, 94309, USA	
Wu, Mien-Win	Inst. of Nuclear Energy Res., Physics Div., P.O. Box 3-4, Lungtan, Taiwan, 325, ROC	886-3-4711400 • 886-3-471-1408
Yadlowsky, Edward	HY-Tech Res. Corp., Radford Industrial Center, 104 Centre Court, Radford, VA, 24141, USA	703/639-4019 • 703/639-4027
Yalandin, Michael I.	Inst. of Electrophysics,, Komsomolskaya St., 34, Ekaterinburg, 620219, RUSSIA	3432/448065
Yampolsky, Iosif	JFS Vocational Div., 324A Essex St., Swampscott, MA, 01907, USA	617/595-8190
Yasar, Osman	University of Wisconsin, College of Eng., 1500 Johnson Dr., Madison, WI, 53706, USA	
Yasuike, K.	Osaka University, Inst. of Laser Eng., Beam Group, 2-6 Yamada-oka, Suita, Osaka, 565, JAPAN	81-6-877-5111 X6573 • -877-4799
Yatsui, Kiyoshi	Nagaoka Univ. of Tech., Lab. of Beam Tech., Nagaoka, Niigata, 940-21, JAPAN	0258 46-6105 • 0258-46-6506
Yonas, Gerald	Sandia National Lab., Organization 9000, P. O. Box 5800, Albuquerque, NM, 87185, USA	
Yoshikawa, Masayuki	Kanazawa University, Faculty of Sci., Marunouchi 1-1, Kanazawa, Ishikawa, 920, JAPAN	0762-62-4281 • 0762-64-1059
Young, Frank C.	Naval Research Lab., Code 6770, 4555 Overlook Ave. S.W., Washington, DC, 20375, USA	202/767-3066 • 202/767-0436
Zazhivikhin, Vladimir	TRINITI, Troitsk, Moscow, 142092, RUSSIA	334-58-14
Zeng, Naigong	China Inst. of Atomic Energy, Plasma Phys. and Laser Lab., P.O. Box 275-7, Beijing, 102413, PRC	861-935-7628 • 861-935-7008
Zhang, Qi	Academia Sinica, Inst. of Electronics, P.O. Box 2702, Beijing, 100080, PRC	86-1263943 • 0086-1-2567363
Zieher, Klaus W.	Texas Tech University, Elec. Eng. Dept., P.O. Box 4439, Lubbock, TX, 79409, USA	806/742-3506
Zinamon, Zeev	Weizmann Inst. of Sci., Dept. of Nuclear Physics, P.O. Box 26, Rehovot, 76100, ISRAEL	972-8-342063 • 972-8-344106





